

0  
A 030824

DISTRIBUTION STATEMENT A  
Approved for public release;  
Distribution Unlimited

AFGL-TR-76.0237

(1)

# THE GEOPHYSICAL USE OF SATELLITE BEACON OBSERVATIONS



## SYMPOSIUM PROCEEDINGS

Michael Mendillo, Editor

DDC  
REF ID: A6571  
OCT 15 1976

JUNE 1976  
BOSTON UNIVERSITY

DISTRIBUTION STATEMENT

Approved for public release by AFGL  
Distribution Unlimited

## Unclassified

SECURITY CLASSIFICATION OF THIS PAGE (When Data Entered)

<b>9 REPORT DOCUMENTATION PAGE</b>		READ INSTRUCTIONS BEFORE COMPLETING FORM	
<b>REPORT NUMBER</b> <b>AFGL-TR-76-0237</b>	<b>2. GOVT ACCESSION NO.</b>	<b>3. RECIPIENT'S CATALOG NUMBER</b>	
<b>4. TITLE (and Subtitle)</b> <b>PROCEEDINGS OF THE SYMPOSIUM OF THE COSPAR SATELLITE BEACON GROUP</b> on the Geophysical Use of Satellite Beacon Observations Held at Boston University on 1-4 June 1976.		<b>5. DATE OF REPORT &amp; PERIOD COVERED</b> <b>Final Report</b>	
<b>6. AUTHOR(S)</b> <b>Michael Mendillo</b>		<b>7. PERFORMING ORG. REPORT NUMBER</b>	
		<b>8. CONTRACT OR GRANT NUMBER(S)</b> <b>F19628-76-C-0128</b>	
<b>9. PERFORMING ORGANIZATION NAME AND ADDRESS</b> <b>Boston University 881 Commonwealth Avenue Boston, MA 02215</b>		<b>10. PROGRAM ELEMENT, PROJECT, TASK AREA &amp; WORK UNIT NUMBERS</b> <b>62101F 46430107</b>	
<b>11. CONTROLLING OFFICE NAME AND ADDRESS</b> <b>Air Force Geophysics Laboratory Hanscom AFB, Massachusetts 01731 Monitor/PHP/John Mullen</b>		<b>12. REPORT DATE</b> <b>4 Jun 76</b>	
<b>14. MONITORING AGENCY NAME &amp; ADDRESS (if different from Controlling Office)</b>		<b>13. NUMBER OF PAGES</b> <b>758</b>	
		<b>15. SECURITY CLASS. (of this report)</b> <b>Unclassified</b>	
		<b>16. DECLASSIFICATION/DOWNGRADING SCHEDULE</b>	
<b>16. DISTRIBUTION STATEMENT (of this Report)</b>  Approved for public release; distribution unlimited.			
<b>17. DISTRIBUTION STATEMENT (of the abstract entered in Block 20, if different from Report)</b>  <b>16 AF-4643</b> <b>17 464301</b>			
<b>18. SUPPLEMENTARY NOTES</b>			
<b>19. KEY WORDS (Continue on reverse side if necessary and identify by block number)</b> <b>Total electron content Group path delay Ionospheric propagation Ionospheric irregularities Ionospheric scintillation</b>			
<b>20. ABSTRACT (Continue on reverse side if necessary and identify by block number)</b> <b>This report contains the completed papers presented at the COSPAR Satellite Beacon Symposium of June 1976. The topics of the papers were ionospheric structure and dynamics, ATS-6 results, disturbed f region, scintillation and irregularities and specification of trans ionospheric functions for engineering purposes.</b>			

ACCESSION for		
RTIS	White Section <input checked="" type="checkbox"/>	
RRG	Buff Section <input type="checkbox"/>	
ANNOUNCED <input type="checkbox"/>		
JUSTIFICATION .....		
 BY DISTRIBUTION FACILITY CODES		
B1Z, C1C, D1D or SPECIAL		
<b>P</b>		

PROCEEDINGS

OF THE

SYMPOSIUM OF THE COSPAR  
SATELLITE BEACON GROUP

ON

THE GEOPHYSICAL USE OF SATELLITE BEACON OBSERVATIONS

1-4 JUNE, 1976  
Boston University  
Boston, Mass. USA

Coordinated by the Department of Astronomy,  
Boston University, with support from the  
Air Force Geophysics Laboratory

Sponsored by the Committee on Space Research,  
COSPAR, established by the International Council  
of Scientific Unions

Co-sponsored by the International Union of  
Radio Science, URSI

DISTRIBUTION SPECIAL

Approved for public release  
Distribution

## LOCAL PLANNING COMMITTEE

Prof. Michael D. Papagiannis (Chairman)

Prof. Michael Mendillo  
Mr. Jeffrey Baumgardner (Symposium Manager)  
Ms. Terry Pacheco (Administrative Assistant)

...Department of Astronomy  
Boston University

Dr. Jules Aarons  
Mr. John Mullen

...Air Force Geophysics Laboratory  
L. G. Hanscom A.F.B.

## SPOUSES' PROGRAM

Mrs. Maribeth Klobuchar  
Mrs. Joyce Mendillo

## SYMPOSIUM PROCEEDINGS

Prof. Michael Mendillo, Editor  
Mr. Michael Buonsanto, Assistant Editor  
Ms. Mary Ann Beacock, Editorial Assistant

Program Committee For The COSPAR  
Satellite Beacon Group Symposium  
The Geophysical Use of Satellite Beacon Observations

Prof. Michael Mendillo (Chairman)  
Department of Astronomy  
Boston University  
Boston, Massachusetts 02215 USA

Dr. Jules Aarons  
Air Force Geophysics Laboratory (LIR)  
L.G. Hanscom AFB  
Bedford, Massachusetts 01739 USA

Dr. Richard F. Donnelly  
Space Environment  
Laboratory  
NOAA  
Boulder, Colorado 80302

Prof. Ja. L. Al'pert  
IZMIRAN  
P/O Akademgorodok  
Moscow Region  
U.S.S.R.

Dr. Robert W. Kreplin  
Code 7125  
Naval Research Laboratory  
Washington, D.C. 20375

Prof. P.F. Checcacci  
IROE-CNR  
Via Panciatichi 56  
I-50127 Firenze  
ITALY

Dr. Rinehart Leitinger  
Institut für Meteorologie  
und Geophysik  
Universität Graz  
A-8010 Graz  
AUSTRIA

Dr. Kenneth Davies (on leave)  
Space Environment Laboratory  
NOAA  
Boulder, Colorado 80302

Dr. V.M. Sinel'nikov  
IZMIRAN  
P/O Academgorodok  
Moscow Region  
U.S.S.R.

Mr. Z. Niemirowicz  
Executive Secretary  
COSPAR  
81, Boulevard de Montmorency  
75016 Paris  
FRANCE



## Boston University

725 Commonwealth Avenue  
Boston, Massachusetts 02215  
617/353-2625

Department of Astronomy

1 June, 1976

Dear Colleagues:

It is a pleasure to welcome you to the City of Boston, often called the Athens of America, and in particular to Boston University. In the Boston area, there are eight major universities and over fifty colleges, with a total enrollment of nearly 200,000 students. Because of the city's rich heritage, Boston is one of the centers where America is celebrating this year's Bicentennial Anniversary. It was in Lexington, Massachusetts, only 15 minutes from Boston, where the first shots of the War of Independence were fired 200 years ago.

Boston has fine museums, outstanding hospitals, a famous symphony orchestra, and many excellent restaurants where you can taste some of the delicacies of New England.

We at Boston University are honored to have you with us and we want to express our congratulations to Dr. Aarons of the Air Force Geophysics Laboratory and to Professor Mendillo of our Department of Astronomy for their initiative and hard work to organize this fine symposium in our University.

Boston University was established in 1869 and it is now the third largest private University in the United States. Among its original faculty was Alexander Graham Bell, who one hundred years ago invented the telephone here in Boston. Boston University has 16 different schools including Schools of Medicine, Law, Education, Engineering, Nursing, Management, Dentistry, Fine Arts, etc. The Medical School receives more than ten million dollars per year in research grants and the Law School has on its faculty several past and present members of the Massachusetts Supreme Court. The School of Theology counts among its graduates Dr. Martin Luther King, the Nobel Laureate for Peace, and the President of Cyprus, Archbishop Makarios.

The Department of Astronomy is one of the twenty departments of the School of Arts and Sciences. Though there are nearly 2000 Physics Departments in the United States, there are less than one hundred independent Astronomy Departments. Boston University thus belongs to a small group of prestigious universities, including Harvard, Princeton, Columbia, Cal Tech, Berkeley, and Chicago, which have a Ph.D. granting Department of Astronomy.

During your stay with us, we hope we will have an opportunity to show you our faculty and student quarters, our library, our dark room, our observatory and our planetarium, which is now under construction. The department has five professors (Dr. Saul Adelman, Dr. Kenneth Janes, Dr. Lucas Kamp, Dr. Michael Mendillo and Dr. Michael Papagiannis), ten graduate students, including four teaching assistants, and about twenty undergraduate majors. We will all be more than happy to discuss our academic programs and our research work with you.

We are looking forward to a fine scientific meeting and the opportunity to exchange with all of you data and ideas on research work of common interest. We hope your visit to Boston and the COSPAR Symposium at Boston University will be culturally gratifying and scientifically rewarding. On behalf of the President of the University, the Dean of Arts and Sciences and the entire faculty of the Astronomy Department, I extend to all of you a most cordial welcome.

Sincerely yours,



Michael D. Papagiannis  
Professor and Chairman  
Department of Astronomy

TABLE OF CONTENTS

Preface.....	i
Local Arrangements.....	ii
Symposium Program Committee.....	iii
Welcoming Address - Prof. M.D. Papagiannis.....	iv
Contributed Papers	
I. Ionospheric Structure and Dynamics	
INVITED REVIEW: Satellite Beacon Contributions to Studies of the Structure of the Ionosphere - J.V. Evans (USA) .....	1
Early Results of the Ionospheric Experiment of the Apollo-Soyuz Test Project - M. Grossi and R.H. Gay (USA) .....	47
Structure and Morphology of the Main Plasma Trough in the Topside Ionosphere - P.J.L. Wildman, R.C. Sagalyn, and M. Ahmed (USA) .....	57
Early Results on INTASAT Beacon Data Recorded at El Arenosillo (Spain) - J.L. Sagredo (SPAIN) .....	67
Latitudinal Morphologies of TEC Deduced from Polar Orbiting Satellite INTASAT - K.H. Pai (TAIWAN) .....	82
Theoretical and Experimental Studies of TEC Measurements in the Transverse Zone - I.H. Keroub (ISRAEL) .....	96
Vertical Ion Drifts, Exospheric Temperatures and Neutral Winds Calculated from Simple Observations and Numerical Simulation of the Ionosphere - D.A. Antoniadis and A.V. da Rosa (USA) .....	116
Determination of Lunar-Dynamo Electric Fields From Total Electron Content Measurements - P.A. Bernhardt, D.A. Antoniadis, and A.V. da Rosa (USA) .....	138
Gravity Wave Induced Fluctuations in Total Electron Content - A. Sengupta, O.P. Nagpal, and C.S.G.K. Setty (INDIA) .....	153
Power Spectra of Acoustic Gravity Waves in the F-Region Ionosphere - R. DuBroff, K.C. Yeh, and C.H. Liu (USA) .....	163

The Meteorological Jet Stream As a Source of Medium Scale Gravity Waves in the Thermosphere: An Experimental Study - F. Bertin and J. Testud (FRANCE); L. Kersley and P.R. Rees (WALES, U.K.).....	182
Message from World Data Center A - J.V. Lincoln (USA).....	190
<b>II. ATS-6 Results</b>	
Simulation and Measurement of the Plasmaspheric Electron Content - D.A. Poletti-Liuzzi, K.C. Yeh, and C.H. Liu (USA).....	197
Comparative Study of ATS-6 Data from Lindau/Harz and From Graz/Austria - G.K. Hartmann and W. Degenhardt (W. GERMANY) and R. Leitinger (AUSTRIA).....	219
Diurnal, Day-to-Day, and Seasonal Variability of N <sub>F</sub> , N <sub>T</sub> , and N <sub>p</sub> at Fort Monmouth, New Jersey - H. Soicher (USA).....	231
Time and Latitude Dependence of Ionospheric Electron Content From the Combination of NNSS and ATS-6 Data - R. Leitinger (AUSTRIA) and G.K. Hartmann (W. GERMANY).....	244
Periodic Amplitude and Phase Fluctuations Ranging from 1 sec to 30 min Observed with the ATS-6 RBE at Lindau - W. Degenhardt and G.K. Hartmann (W. GERMANY).....	256
Multi-Station Investigations of Low Latitude Ionosphere Using Low Orbiting and Geostationary Satellites - The Ahmedabad Group (INDIA).....	268
<b><u>ATS-Discussion Notes</u></b>	
Measurements of Equatorial Ionosphere Irregularities With the IROE Multifrequency Receiving Station at the San Marco Range in Kenya - F. Bertini, P. Bruscaglioni, G. Fiori, M.T. De Giorgio, and P.F. Pellegrini (ITALY).....	289
VHF Scintillation Observations at Calcutta with Orbiting and Geostationary Satellites - S. Basu, B.K. Guhathakurta, G.N. Bhattacharyya, and A. Das Gupta (INDIA).....	295
Daytime VHF Scintillations at Huancayo Peru and their Possible Relationship to the Equatorial Electrojet - Santimay Basu and Jules Aarons (USA)....	301

### III. The Disturbed F-Region

- INVITED REVIEW: Satellite Beacon Studies of Global F-Region Disturbance Effects - M. Mendillo (USA)..... 307
- INVITED REVIEW: Storm-Time Coupling of Neutral Atmosphere and Ionosphere: ESRO 4 Results - G. Prölss (W. GERMANY)..... 323
- F-Region Enhancements Induced by Solar Flares - R.F. Donnelly, K. Davies, R.N. Grubb, and R.B. Fritz (USA)..... 345
- Multistation Observations of F-Region Response to Sudden Commencement Storms - L. Kersley and A. Das Gupta (WALES)..... 360
- Vertical Distortions of the Winter Nighttime Ionosphere Deduced From Simultaneous Satellite Beacon Observations and Ground-Based Ionosonde Data - M.J. Buonsanto and M. Mendillo (USA)..... 370
- Behavior of Auroral Zone Total Electron Content During Substorms - I.S. Mikkelsen and K. Damgaard (DENMARK)..... 384
- Geostationary Version of Non-Coherent Response Method as a Means for the Investigation of the Magnetospheric Plasma Discontinuities During Storms - J.V. Kovalevsky and T.V. Kuznetsova (USSR)..... 395
- Some New Phenomena Observed During Magnetic Storms and Solar Flares at Low and Equatorial Latitudes Using ATS-6 Radio Beacon Investigations - The Ahmedabad Group (INDIA)..... 412
- The Interdependence of Scintillation Index, Total Electron Content and Magnetic Activity at an Equatorial Station - J.R. Koster (GHANA)..... 423

### IV. Scintillations and Irregularities

- INVITED REVIEW: Scintillation Theory and its Relation to Satellite Beacon Transmissions - A.W. Wernik (POLAND), C.H. Liu (USA), and K.C. Yeh (USA).. 435
- Ionospheric Scintillations at Multiple Frequencies - R. Umeki, C.H. Liu, and K.C. Yeh (USA)..... 446
- A Two-Component Model for Scintillations - E.J. Fremouw, C.L. Rino, and R.C. Livingston (USA)..... 463
- Amplitude and Rate Characteristics of Intense Scintillations - H. Whitney (USA)..... 486

Correlated Measurements of Scintillations and In-Situ F-Region Irregularities from OGO-6 - S. Basu and S. Basu (USA).....	505
Anomalous Phase and Amplitude Scintillations of VHF Waves Within the Equatorial Electrojet Region - The Ahmedabad Group (INDIA).....	518
Scintillations in the VHF and UHF Range at the Magnetic Equator - B.V. Krishna Murthy, K. Krishna Murthy, C.R. Reddi, and S. Vaidyanathan (INDIA).....	532
A Nonlinear Model for Equatorial Spread F: Irregularity and Scintillation Calculations - B.E. McDonald, S.L. Ossakow, and A.J. Scannapieco (USA)...	544
The Stormtime Component of Scintillations - J. Aarons, S. Basu, and E. Martin (USA).....	552
Scintillation Observed Through the Magnetospheric Cleft - J.P. Mullen and J. Aarons (USA).....	569
Angle-of-Arrival Scintillations in the Region of the Polar Cleft - J.A. Fulford and P.A. Forsyth(CANADA) ..	576
Angle-of-Arrival and Doppler Fluctuations Caused by Ionospheric Scintillation - R.K. Crane (USA).....	583
The Structure of Signals Undergoing Scintillation as Inferred From ATS-6 and Transit Coherent Beacon Transmissions - C.L. Rino, E.J. Fremouw, and R. Livingston (USA).....	593
ATS-6 40 and 360 MHz Differential Phase Measurements - F. Slack (USA).....	605
V. Specification of Trans-Ionospheric Functions For Engineering Purposes, Equipment, and Systems Performance	
INVITED REVIEW: Review of Ionospheric Time Delay Limitations to Ranging Systems - J.A. Klobuchar (USA) .....	629
Space Variant Transfer Functions for the Characterization of Inhomogeneous Scattering Media - P.F. Checcacci and A.M. Scheggi (ITALY).....	634
Solar Cycle Variations in the Total Electron Content at Invariant Latitude 54 Degrees - Y.-N. Huang (TAIWAN) .....	643

Specification of Navigation and Radar Errors Caused by the Ionosphere - D.D. Du Long and R.S. Allen (USA).....	659
Ionospheric Refraction Errors in Satellite Tracking and Navigation in Low Latitudes - Y.V. Somayajulu and A.B. Ghosh (INDIA).....	669
Monitoring of the Troposphere Using Low Elevation Satellite Radio Beacons - Y.V. Somayajulu, T.R. Tyagi, and A.B. Ghosh (INDIA).....	681
Tropospheric Effects on Satellite-Earth Links - C. Fengler (CANADA).....	
Trans-Ionospheric Long Range Propagation Statistics Through the First Chinese Satellite Transmissions - P. Beni, F. Bertini, and P.F. Pellegrini (ITALY)....	699
Modelling of Line-of-Sight Ionospheric Electron Density Gradients - G. Nesterczuk, J.K. Kozelsky, and J. Behuncik (USA).....	706
The Performance of the ATS-6 Radio Beacon as a Measurement System - R.N. Grubb, R.B. Fritz, and J.E. Jones (USA).....	717
IROE Ground Equipment for ATS-6 - P.F. Checcacci, E. Capannini, and P. Spalla (ITALY).....	725
Research Program at IROE with the DNA-002 Experiment - F. Bertini, P.F. Pellegrini, P. Bruscaglione, and M. Pieralli (ITALY).....	736
VI. List of Participants.....	739
VII. List of Telex Numbers.....	744

SATELLITE BEACON CONTRIBUTIONS TO STUDIES OF THE  
STRUCTURE OF THE IONOSPHERE

J. V. Evans  
M.I.T. Lincoln Laboratory  
Lexington, Massachusetts 02173

ABSTRACT

The radio beacons on board artificial satellites have been widely used for studies of the earth's ionosphere. Following the launch of Sputnik 1, two lines of investigation quickly emerged — the study of the total columnar content of the ionosphere (up to the height of the satellite) and the study of the fine-scale irregularities within the layer responsible for causing scintillation of the received signal. Early studies of total content employed either the Faraday rotation or the differential doppler method and suffered because of an ambiguity in the results. In principle, the ambiguity could be resolved by assuming that the ionosphere is horizontally uniform, but in practice north-south gradients introduced, for example, by TIDs often rendered this difficult. This problem can be overcome using pairs of stations and/or local vertical-incidence measurements; the results then yield useful information concerning temporal changes of total content and large scale structure such as TIDs and the trough.

The advent of geostationary satellites has made possible long continuous records of total content for many fixed locations on the earth, and by using multiple frequencies it has also been possible to study the exchange of plasma between the ionosphere and the magnetosphere. An extension of these observations to higher latitudes could resolve the question of whether the shrinkage of the plasmasphere during magnetically disturbed periods is accomplished by "peeling away" the outer shells or an inward compression of the plasma into the ionosphere.

The morphology of ionospheric scintillation has been studied extensively using beacon signals. In addition, these studies have shown that the spectrum of irregularities is power law (rather than Gaussian), and at the equator can extend to very small spatial scales. While it is generally agreed that the irregularities responsible for scintillation are created by some form of plasma instability, there seems to be no generally accepted mechanism. It may be that different instability mechanisms operate at the equator, auroral zone and at midlatitudes and/or at different times.

## 1. INTRODUCTION

Prior to the advent of *in-situ* exploration of outer space employing artificial earth satellites, considerable study of the earth's ionosphere had been accomplished using ground-based HF soundings, and many excellent summaries of this era of exploration have been written (e.g., Rawer and Katz, 1957; Ratcliffe and Weekes, 1960; Alpert, 1963).

In addition, some rocket measurements had been carried out that provided measurements of E- and F-region electron density to altitudes of 200-300 km (e.g., Berning, 1951; Seddon, 1953; Seddon and Jackson, 1955). However, these were limited in number, and significant information concerning regions well above the peak of the F-layer did not become available until about the time that Sputnik I was launched (e.g., Gringauz, 1958; Nisbet, 1960). The early rocket results have been reviewed by Newell (1960). Finally, measurements of the total number of electrons in the ionosphere had been made by observing the Faraday rotation of moon-reflected radar signals (for review, see Evans, 1974). These showed that there were typically  $\sim 3$  times as many electrons above  $h_{\text{max}}^{\text{F2}}$  compared to the number below, implying that the F-layer was more complicated than a simple  $\alpha$ -Chapman layer at uniform temperature.

Somewhat surprisingly, the first really useful results of satellite investigations of the ionosphere came from observations of the satellite beacon signals, rather than *in-situ* sampling, and this has remained a valuable technique to this day. This paper attempts to summarize the types of measurements that are possible by observing the radio signals transmitted from satellite beacons. It is not intended to be an exhaustive review of the subject. (Such a review has been provided by Alpert, 1976.) The examples of the results presented have been chosen merely to illustrate the developments that were made, and are not meant to imply any priority of discovery.

In the section that follows we outline two methods of measuring the total electron content. Section 3 discusses observations of the gross structure of the F-layer from low altitude satellites and geostationary satellites, while Section 4 briefly comments on some of the physical processes that serve to control the total content as measured by either method. Section 5 describes observations of large scale features in the ionosphere such as the trough and the equatorial anomaly, and Section 6 deals with observations of Travelling Ionospheric Disturbances (TIDs). Finally, in Section 7, we discuss what can be learned concerning the ionospheric irregularities responsible for Spread F and radio star scintillation.

## 2. OBSERVING TECHNIQUES

### a. Faraday Rotation

At the time of the launch of Sputnik I (September 1957) the Faraday rotation of a linearly polarised electromagnetic wave was already being exploited as a means of measuring the integrated number of electrons through the

ionosphere by means of the moon echo technique (Browne et al, 1956; Evans, 1956, 1957). At frequencies  $f$  much higher than the plasma frequency  $f_p$  the one-way rotation  $\Omega$  of the plane of polarisation of the wave is given by

$$\Omega = \frac{K}{f^2} \int_0^{h_s} B_h \cos\theta_h \sec x_h N_h dh \text{ rotations.} \quad (1)$$

where

$$K = 3.75 \times 10^3 \text{ in mks units}$$

$B_h$  = the flux density of the earth's magnetic field at height  $h$

$\theta_h$  = the angle between the ray and the magnetic field direction

$x_h$  = the local zenith distance to the ray

$h_s$  = the height of the satellite

and  $N_h$  = the electron density ( $\text{el/m}^3$ ).

Equation (1) holds provided the ray path at no point becomes exactly normal to the magnetic field. As shown by many authors (e.g., Browne et al, 1956; Bauer and Daniels, 1958), the term  $B_h \cos\theta_h \sec x_h$  is usually slowly varying below about 2000 km. As a result some average value

$$M = \frac{1}{B_h \cos\theta_h \sec x_h} = \frac{\int_0^{h_s} B_h \cos\theta_h \sec x_h N_h dh}{\int_0^{h_s} N_h dh} \quad (2)$$

can be taken and placed outside the integral sign in Eq. (1), yielding

$$\Omega = KM \int_0^{h_s} N_h dh \quad h_s < 2000 \text{ km} \quad (3a)$$

$$= KMN_t \quad (3b)$$

where  $N_t$  is the ionospheric total content beneath the satellite.

In typical applications the number of rotations  $\Omega$  exceeds 1/2 introducing an ambiguity in the measurements. This may be removed if observations can be made simultaneously at two well-separated frequencies, or if a small frequency shift  $\Delta f$  can be introduced and the resulting change  $\Delta\Omega$  in  $\Omega$  observed, whence

$$\Omega = \frac{1}{2} \frac{\Delta f}{f} \Delta\Omega \quad \text{rotations.} \quad (4)$$

This was the approach originally employed in the moon reflection experiments (Evans, 1957) and later used in satellite experiments where multifrequency beacons were employed. For example, the satellite S-66 (1964-64a) carried beacons at 40 and 41 MHz expressly for this purpose.

For low altitude satellite measurements what is observed is a rate of change of  $\Omega$  introduced principally by the variation in  $M$  resulting from the changing geometry. That is the first term in

$$\frac{d\Omega}{dt} = K \int N_h dh \frac{dM}{dt} + MK \frac{d}{dt} \int N_h dh \quad (5)$$

is larger than the second. By making an assumption concerning the second, such as that the ionosphere is horizontally stratified and homogeneous, it is possible to solve for  $\Omega$ . In cases where the beacon frequency  $f$  exceeds the highest plasma frequency  $f_p$  along the path by only a few times the approximations leading to Eq. (4) may no longer be valid, and more general expressions which should then be used have been given by Garriott (1960a). At such frequencies, ionospheric refraction may also become important, and corrections for these effects have been developed by Yeh and Swenson (1961).

In early experiments, the assumption of no horizontal gradient in the ionosphere was widely employed in analysing the results (e.g., Garriott, 1960b), even though the error inherent in this approach was recognized. Garriott and Mendonca (1963) evaluated the probable errors encountered in the various methods of data reduction and concluded that a hybrid method using Faraday rotation and differential-doppler records (see below) simultaneously gave the least error.

For geostationary satellite experiments the second term of Eq. 5 dominates. It is then possible to solve the ambiguity if, at some time, bounds can be placed on  $\int N_h dh$  from some other measurement. Yuen et al (1969) and da Rosa (1973) have discussed how this might be accomplished using F-region critical frequency measurements. An excellent review of the satellite beacon Faraday rotation method of studying the ionosphere has been given by Garriott et al (1970), who also summarized the types of results obtainable.

b. Differential Doppler or Phase

An alternative method of studying the number of electrons along the line-of-sight to the satellite depends upon observing the phase of the received signal. This technique was employed originally by Seddon (1953) in early V-2 rocket experiments. The total phase path length to the satellite may be written

$$P = \frac{f}{c} \int_0^h \mu ds \quad \text{radian} \quad (5)$$

where  $\mu$  = the refractive index of the medium  
 $c$  = the free space velocity of light.

The phase path length  $P$  depends upon the actual distance to the satellite as well as on the properties of the troposphere and ionosphere.

The effect of the troposphere can be removed by making use of the fact that the ionospheric portion of the path introduces a phase change that is frequency dependent. Thus observations are made of a second frequency  $f'$  higher than the first that is harmonically related, i.e.,  $f' = mf$  ( $m > 1$ ). On reception both signals are observed to exhibit doppler shifts  $dP/dt$ ,  $dP'/dt$  caused chiefly by the satellite motion. A differential doppler signal  $F$  is developed in the receiver as

$$F = (dP'/dt) - m(dP/dt) \quad (6a)$$

Provided again that the lower frequency  $f$  is much larger than the ionospheric plasma frequency  $f_p$  anywhere along the path ( $f \gg f_p$ ), Eq. 6a reduces to

$$\begin{aligned} F &= (m - \frac{1}{m}) \frac{40.3}{cf} \frac{d}{dt} \int_0^h N_h ds \text{ Hz} \\ &= (m - \frac{1}{m}) \frac{40.3}{cf} \frac{d}{dt} \int_0^h N_h \sec x_h dh \text{ Hz} \end{aligned} \quad (6b)$$

where  $c$  is the velocity of light. By integrating  $F$  (i.e., counting radians of phase change over some finite time interval) it is possible to recover the total electron content along the line-of-sight to the satellite with an unknown constant of integration.

For a low-altitude satellite the plot of  $F$  vs. time will be an S-shaped curve whose slope at the point of closest approach will be proportional to the total electron content local to the station. Thus by assuming, either that there are no horizontal gradients in the ionosphere, or

some particular linear gradient it is possible to recover  $\int N_h dh$ . Alternatively, a solution may be sought that minimises the curvature of a plot of  $\int N_h dh$  vs. time during the pass. The accuracy of these approaches has been reviewed by Tyagi (1974).

If the absolute frequency of the satellite beacon is known with great precision, (or can be estimated by averaging many measurements over a period of time), then the time of closest approach can be inferred from observations of the doppler shift of the higher frequency  $f'$ . In this case, use can be made of any displacement observed in the times of closest approach and the time at which the differential doppler  $F = 0$  to infer the magnitude of any NS gradient (de Mendonça 1962).

Other methods of solving the ambiguity have been developed in which appeal is made to additional ionospheric measurements. For example, Evans and Holt (1973) described an approach in which local measurements of the electron density profile using incoherent scatter radar are employed to resolve the ambiguity, and the differential doppler record is then used to determine the latitudinal variation in the total electron content. Alternatively, a local measurement of the F-region critical frequency (made with an ionosonde) together with a model for the layer shape may be used to resolve the ambiguity and the differential doppler record then supplies information on the variation of  $N_{F2}^{\max}$  vs. latitude. Leitinger et al (1975) have described a method in which pairs of differential doppler records gathered at stations separated by a few hundred km are used to resolve the ambiguity.

For a geostationary satellite the differential doppler signal  $F$  will depend chiefly upon the time rate of change of total electron content and there will be a large ambiguity in the total number of cycles of phase difference along the path (da Rosa 1973). In this case it is preferable to measure the group delay or differential phase  $\Delta P$  between identical modulation signals applied to widely spaced carrier frequencies. These may be generated in the satellite by amplitude modulation. By employing two carriers it is possible to remove all ambiguity and the ATS-6 satellite was designed with this in mind (Hargreaves 1970; Davies et al 1975).

Measurements of the differential phase between a pair of widely spaced frequencies transmitted from geostationary satellites can be made to yield useful measurements of total electron content with an uncertainty of about  $10^{16} \text{ el/m}^2$  by using a hybrid technique in which the Faraday rotation is also measured (Almeida 1972).

### 3. GROSS STRUCTURE OF THE IONOSPHERE

#### a. Low-altitude satellite observations

Early efforts to measure the total content of the ionosphere  $N_t$  using the first Sputnik satellites were made by a number of groups employing the Faraday rotation and/or differential doppler methods. A detailed study of

8 months data gathered over the period September 1958 - April 1959 by observing Sputnik 3 at Stanford, California ( $37^{\circ}$ N), was published by Garriott (1960b). In this work two methods of analyzing the Faraday rotation records were tried yielding two estimates of  $N_t$  ( $= N_s$  in Garriott's paper). These are shown in Figure 1 as a function of local time over the 8 month period. Also shown is the total content up to the layer peak

$$N_b = \int_{100}^{h_{\max}} \frac{N_h F_2}{N_h dh} \quad (7)$$

obtained from ionosonde records.

Mixed together in Figure 1 are seasonal and diurnal variations, and in this respect these results are less useful than moon-echo observations in which the diurnal variation can be established over an interval of one month (e.g., Evans and Taylor 1961). Nevertheless, this work confirmed that the ratio  $N_s/N_b$  is of the order of 3-4 by day increasing to  $> 5$  by night, as observed in the early moon radar experiments (e.g., Evans 1957).

Total content measurements were made by a number of other groups over various shorter time intervals and by 1965, using moon radar and satellite data, it was possible to construct plots of total electron content in summer and winter at midlatitudes vs. 10.7 cm solar flux  $F_{10.7}$  (Taylor 1966). These suggested the existence of a linear dependence between  $N_t$  at noon on quiet days and  $F_{10.7}$ , with a winter value of  $15 \times 10^{16} \text{ el/m}^2$  at  $F_{10.7} = 100$  that is twice the summer value.

At about the same time, Bhonsle et al (1965) reported results gathered using the differential doppler technique while observing the Transit 4A satellite from Washington, D.C. ( $40^{\circ}$ N) and Ottawa ( $45^{\circ}$ ) over the 8 month interval February - September 1962. Figure 2 shows total content vs. local time determined for these two sites. From these data and earlier published results, Bhonsle et al were able to show that the largest noon values of total content actually occur in equinox for all parts of the sunspot cycle as may be seen from Figure 3. This is in contrast to  $N_t^{\max} F_2$  which maximizes in winter. Bhonsle et al were able to account for this behavior empirically in terms of variations in the slab thickness parameter

$$\tau = \frac{N_t}{N_{\max}} \quad \text{km} \quad (8)$$

as       $\tau = 270 (1 + 0.005 \bar{R}) \text{ km}$  summer  
            $\tau = 240 (1 + 0.005 \bar{R}) \text{ km}$  equinox  
            $\tau = 210 (1 + 0.005 \bar{R}) \text{ km}$  winter

where  $\bar{R}$  is the mean sunspot number.

That is the slab thickness maximizes in summer while  $N_t^{\max}$  maximizes in winter, and the combination of these two variations produces a maximum in  $N_t$  in equinox.

These conclusions were confirmed in a study by Yeh and Flaherty (1966) who made observations of Transit 4A from Urbana, Illinois ( $40^{\circ}$  N) over the period July 1961 to October 1964. Figure 4 shows the variation of  $N_t$  and  $\tau$  at noon reported by Yeh and Flaherty over the period July 1961 to December 1962. It is clear that  $N_t$  peaks in the equinoxes and has minima at the solstices with the summer minimum being deeper than the winter one (Fig. 4a). The slab thickness, on the other hand, shows a simple annual variation with a minimum in winter (Figure 4b).

While a nighttime dependence of slab thickness  $\tau$  on the magnetic activity index  $K_p$  had been recognized earlier (e.g., Evans and Taylor 1961), Yeh and Flaherty appear to be one of the earliest groups to identify a daytime dependence. This is shown in Figure 5. It can be explained as a consequence of the increased temperature of the neutral atmosphere associated with magnetically disturbed conditions (e.g., Jacchia and Slobey, 1964). Over the range  $0 < K_p < 5$ , this trend appears to be almost independent of time of day between about 06 and 15 hours.

#### b. Geostationary Satellite Observations.

Useful measurements of total electron content using radio transmissions from geostationary satellites became possible with the launch of Syncom 3 in August 1964. Garriott et al (1965) published results of a study made between September and November 1964 of the Faraday rotation at Stanford, California ( $40^{\circ}$  N) and Hawaii ( $20^{\circ}$  N). Figure 6ab shows the variations in  $N_t$  and  $\tau$  observed at the University of Hawaii in these measurements. It can be seen that the ability to obtain long continuous records permits much detail to be seen that otherwise might be missed. For example, the variation in slab thickness shown in Figure 6b is considerably more complicated than anticipated, exhibiting maxima immediately before sunrise and after sunset.

The ease with which geostationary satellites permit measurements of the gross structure of the ionosphere, and the absence of any appreciable motion of the subionosphere point with time, has rendered this method much more attractive than either low-altitude satellite or moon-radar observations. Thus, several groups, including those at Stanford University and the Air Force Research Laboratories, Cambridge, Massachusetts, have collected such data for long periods of time. Figure 7 shows the records obtained for the year 1968 by Klobuchar and Allen (1970) using Faraday rotation observations of the VHF beacon on ATS-3. Recognizing that the slab thickness  $\tau$  appears to exhibit smaller seasonal and diurnal variations than  $N_t^{\max}$ , these authors derived a simple analytical expression for  $\tau$  that would permit  $N_t$  to be predicted given an estimate of  $N_t^{\max}$ . This relation is

$$\tau = 261 + 26 \sin \frac{(H - 9) \pi}{12} + 73 \sin \frac{(D - 60) \pi}{183} \text{ km.} \quad (9)$$

where  $H$  is the local time (hours) and  $D$  the day number. Figure 8 shows the fit of the data points to the second term which describes the seasonal variation. Subsequently, the AFCRL group attempted to extend their model to storm time conditions by describing average percentage changes in  $\tau$  following storm sudden commencements (Mendillo et al, 1975).

The launch of ATS-6 in August 1975 permitted for the first time accurate simultaneous measurements of the electron content of the ionosphere (from Faraday rotation measurements) and total electron content beneath the satellite (via group delay measurements) (Davies et al, 1975). These permit observations of variations of total content (and hence density) in the magnetosphere and their relationship to variations in the underlying ionosphere. Interesting results are now beginning to emerge (e.g., Davies et al, 1976, Soicher, 1976) which suggest that within the plasmasphere there are only small day-to-night changes in total content, and during magnetically disturbed periods the protonosphere responds to (rather than drives) any changes in the ionosphere at the foot of the flux tube.

#### c. Magnetically Disturbed Behavior

Measurements of the variation of the total electron content during magnetic storms have been made by a number of workers (e.g., Titheridge and Andrews, 1967; Warren, 1969; Lanzerotti, 1975). In general  $N_t$  tends to vary in the same way as  $N_{t\max}^{F2}$ . A typical sequence of events following a storm sudden commencement is shown for Jodrell Bank ( $53^{\circ}\text{N}$ ) in Figure 9 (Taylor and Earnshaw, 1969). These observations were made with the Early Bird Satellite (1965 - 28a) with a sub-ionospheric point (i.e., the latitude of the ray path at 400 km altitude) of  $47^{\circ}\text{N}$ . On the day of the storm, the evening increases in  $N_t$  and  $N_{t\max}^{F2}$  were more pronounced than normal. This represents the positive phase of the storm. On the second day  $N_t$  was above normal while  $N_{t\max}^{F2}$  was depressed indicating a marked increase in the slab thickness parameter (here denoted by  $d$ ). On the third day, both  $N_t$  and  $N_{t\max}^{F2}$  were below normal but the slab thickness tended to remain above normal. These changes are thought to be brought about by the competing effects of 1) electric fields and winds which tend to raise the layer (and hence lower the loss rate) in the early phase of the storm, 2) increases in the scale height of the neutral atmosphere caused by heat deposited in the auroral zone, and 3) changes in the composition of the atmosphere brought about by the redistribution of the lighter constituents (e.g., He and O) as a result of the winds established by the auroral zone heating. Additional effects such as heating by thermal conduction from the magnetosphere (where energy is deposited through the decay of ring current protons), and from the precipitation of low energy electrons tend to be important only at night. All of these effects tend to vary from storm to storm and their importance depends considerably on the location of the station. As a result, much of our present understanding has come from other observations, such as those of particle temperature by the incoherent scatter technique and neutral composition by means of satellite-borne mass spectrometers.

One feature of the storm-time behavior, that has been pursued from satellite beacon studies, is the behavior during the positive phase. This increase is frequently much larger in  $N_t$  than in  $N_{max}$  (e.g., Goodman, 1968; Webb, 1969), and has been studied extensively by Mendillo et al (1970) and Papagiannis et al (1971, 1972). It has been established that the increase is observed only at stations lying on L-shells within the plasmasphere during the first 18 h. after the storm sudden commencement and is seen principally in the local time interval between noon and sunset. Figure 10 shows the behavior observed at 10 widely spaced stations for the storm of 8 March 1970 (Klobuchar et al, 1971). In this instance, increases were seen only at those stations that were lying in the sunlit hemisphere at the time of the storm commencement. Early theories advanced for this feature include the rapid diffusion of ionization from the magnetosphere into the ionosphere (Mendillo et al, 1970), 2) convergence of ionization in the dusk sector brought about by E-W drifts (Papagiannis et al, 1971; Evans, 1973a), and 3), the lifting of the layer into regions of low recombination rate either by electric fields (Evans, 1970; Somayajulu et al, 1971) or equatorward thermospheric winds (Jones and Rishbeth, 1971; Obayashi, 1972). The present view is that lifting of the layer by substorm electric fields causes the phenomenon (Tanaka and Hirao, 1973; Soicher, 1976), and hence by determining where it is seen it is possible to explore how the fields penetrate the plasmasphere.

#### 4. PHYSICAL INTERPRETATION OF TOTAL CONTENT MEASUREMENTS

##### a. Dependence Upon Temperature of the Neutral Atmosphere

Bauer (1960) stimulated interest in the possibility that studies of the gross structure of the ionosphere might lead to the determination of physically useful parameters such as the temperature of the upper atmosphere. He pointed out that for a Chapman layer formed in an isothermal atmosphere with scale height  $H$ , the slab thickness should be given by

$$\tau = 4.133 H \quad (10)$$

It transpires that this relation should hold for an isothermal F2 layer formed as a subsidiary layer (to the F1) by the competing processes of production, loss and diffusion (for review see Rishbeth, 1967). In a layer with a Chapman shape, the ratio of the number of electrons lying above  $h_{max}$  to the number below is

$$\frac{N_a}{N_b} = 2.15 \quad (11)$$

Hence, and the early observations which showed that in the daytime, this ratio is typically 3, cast doubt on the validity of Eq. (10). Bauer (1960) sought to account for this difference by supposing that the layer is formed in a region of increasing temperature. In this case the constant in Eq. (10) would be reduced in a manner depending upon the gradient assumed.

The discovery (in 1962) that the F-layer is not in thermal equilibrium and that, during the daytime the electron temperature  $T_e$  exceeds the ion temperature  $T_i$  (which above about 300 km exceeds the neutral temperature  $T_n$ ) further complicated any interpretation. In the years following, the effects of these temperature variations on layer shape have been examined in a number of papers (e.g., Thomas, 1966).

Additional difficulties with interpreting the slab thickness parameter in terms of exospheric temperature are introduced by changes in the composition of the F-layer with height (from predominantly  $O^+$  below 1000 km to predominantly  $H^+$  above). Upward fluxes of  $H^+$  exist in the daytime which markedly alter the transition altitude between the two species (Banks and Holzer, 1969). Titheridge (1973) showed, however, that in the daytime this latter complication should not be very important, and hence, if relationships between  $T_e$ ,  $T_i$  and  $T_n$  are adopted, it is possible to find a dependency between  $\tau$  and neutral temperature such as that shown in Figure 11.

Using the dependence of Figure 11, Titheridge (1973) obtained seasonal variations of the neutral temperature from data collected at Aukland ( $37^\circ S$ ) and Invercargill ( $46.5^\circ S$ ) when viewing Syncom 3 and ATS-1 (with subionospheric points at  $34^\circ S$  and  $42^\circ S$ , respectively). These indicated an average annual temperature of  $1200^\circ K$  with a summer to winter variation of  $\pm 250^\circ K$ . Incoherent scatter measurements (e.g., Salah and Evans, 1973) have shown that, in fact, the exospheric temperature at this level of solar activity is more typically about  $1000^\circ K$  and the seasonal variation only  $\pm 100^\circ K$ . While the model could be adjusted to yield lower mean values it seems that the seasonal variation will remain too large. This discrepancy is thought to reflect the neglect of the seasonal variation of the composition of the thermosphere which leads to marked changes in the shape of the F-layer (e.g., Strobel and McElroy, 1970; Tanaka and Hirao, 1972; Wu and Newell, 1972).

Given the enormous improvement in the models of the neutral atmosphere resulting from composition measurements made using satellite-borne mass spectrometers (Hedin et al, 1974) as well improvements modelling the F-region behavior gained from incoherent scatter measurements (e.g., Roble, 1975), it seems it should now be possible to recover useful information on the state of the upper atmosphere from measurements of  $N_t$ ,  $N_{max}$ , and  $\tau$ .

#### b. Dependence upon Solar Flux

The dependence of total content upon solar flux  $F_{10.7}$  measured at 10.7 cm wavelength has been discussed, among others by Taylor (1966), who showed the existence of a clear seasonal dependence. By constructing plots of 24-hour mean electron total content averaged over 31 days against the 183 day mean of  $F_{10.7}$ , da Rosa et al (1973) were able to obtain the average dependence of the total content on solar flux for all parts of the year. These regression formulae were then used to compute the expected variation in the 31 day average total content with  $F_{10.7}$  throughout the year. As may be seen in Figure 12, this empirical description permits much (though not all) of the variation seen at Stanford in 1965 and 1969 to be predicted. There remain however, marked discrepancies which may be associated with magnetically disturbed conditions (Kane, 1975).

### c. Dependence upon Topside Composition

Large nighttime increases in  $\tau$  (or  $N_e/N_{H_2}$ ) were observed in the early measurements. Titheridge (1973) succeeded in accounting for these in terms of the change in composition of the F-region that is known to occur with altitude. As noted above, there is a transition from predominantly O<sup>+</sup> to H<sup>+</sup> ions in the region above  $h_{F2}^{max}$ . The transition altitude i.e., the altitude at which  $N(O^+)^{max} = N(H^+)$  depends upon the abundances of each species, the presence of vertical fluxes and the ion and electron temperatures (for review, see Banks and Kockarts, 1973).

During the daytime, the vertical flux is usually upwards and together with a reduction in the abundance of neutral hydrogen (which is responsible for the production of H<sup>+</sup> via charge transfer) this leads to a height of the transition altitude at midlatitudes typically in the range 1500-2000 km. At night the transition altitude moves lower than 1000 km and reaches a minimum a little before ionospheric sunrise. This can lead to a marked increase in slab thickness  $\tau$  observed by the Faraday rotation technique, and Figure 13 illustrates this dependence for 3 values of the neutral exospheric temperature.

## 5. LARGE SCALE STRUCTURES IN THE IONOSPHERE

### a. Low-altitude Satellite observations

Faraday-rotation (or differential-doppler) measurements made with low-altitude satellites are naturally very sensitive to horizontal variations in the total electron content and have been undertaken to study the latitudinal variations. By observing polar orbiting satellites as a function of local time, it is possible to map the total content over a range of geocentric latitudes of  $\pm 15^\circ$  about the station. In this section we discuss those features of the ionosphere viz., the equatorial anomaly, the midlatitude trough, and the midlatitude winter night increase that have been studied in this fashion.

Early ionosonde measurements showed the existence during the daytime of crests of anomalously high F2-region critical frequencies at geographic latitudes separated by  $\pm 15^\circ$  from the geomagnetic equator (Appleton, 1946; Bailey, 1948). An explanation for this effect was given by Martyn (1947) in terms of the vertical lifting of ionization over the magnetic equator by the E-W electric field associated with the equatorial electrojet and subsequent diffusion of ionization north and south along magnetic field lines. This behavior has been reproduced in theoretical models of the ionosphere (e.g, Hanson and Moffett, 1966) and is now widely accepted.

The resulting ionisation irregularity is too large to be seen in total content measurements made observing low altitude satellites from a single station. However, Rastogi and Sharma (1971), Rastogi et al (1973) and others have studied the behavior of one of the crests as a function of local time and sunspot cycle. By combining data gathered at Singapore ( $1^\circ N$ ), Bangkok ( $14^\circ N$ ) and Hong Kong ( $22^\circ N$ ) using Faraday rotation observations of the Transit 4A satellite, Golton and Walker (1971) were able to reconstruct the total content variation across this feature as shown in Figure 14.

As was known from ionosonde records the anomaly develops between 09 and 10 hrs. and during the solstices is assymetric with the larger crest appearing in the winter hemisphere. This behavior is believed to be caused by the influence of interhemispheric F-region neutral winds, which blow from the summer to winter hemisphere (Sterling et al, 1969).

A region of low F-region ionisation located near  $60^{\circ}$  invariant latitude on the nightside of the earth was clearly identified in satellite-borne HF soundings by Muldrew (1965) and has been studied by a large number of workers (e.g., Rycroft and Thomas, 1970) since. This feature, now known as the trough, is generally thought to mark the boundary between the plasmasphere, i.e, that part of the earth's ionised envelope that corotates with the earth and the high latitude ionosphere where the field lines do not remain closed during the course of a whole day.

No completely accepted mechanism has been advanced to explain this feature, but the observation of enhanced  $\text{NO}^+$  abundance at F-region altitudes in the trough (Grebowsky et al, 1976) lends support to the view that it is formed as a consequence of an increase in the recombination rate. Such an increase could result from large  $O^+$  ion drift velocities caused by the large ionospheric electric fields that exist just outside the plasmasphere (Banks et al, 1974).

Anomalous variations of total content at auroral latitudes were seen in early moon-radar total content measurements conducted at Jodrell Bank ( $53^{\circ}\text{N}$ ) (Taylor, 1965) but not recognized as being caused by an E-W trough of low density until later (Earnshaw and Taylor, 1968). Liska (1966, 1967) appears to have been the first to clearly identify the trough in records of total electron content gathered from observations of a low altitude satellite (Figure 15). Using data gathered throughout the winter months in 1964-1965 Liska was able to construct a contour diagram of overhead electron content as a function of geographic latitude and local time that delineates this region of low electron density (Figure 16).

The position of the midlatitude trough has also been studied by Wand and Evans (1975) using the method described by Evans and Holt (1973) to determine the variation of peak electron density with latitude. In these observations the differential doppler signals of the Navy Navigation Series satellites were observed during some 2300 passes over the two year period (1971-1973). The records were divided into three levels of  $K_p$  activity ( $K_p = 0$  to  $1+$ ,  $2-$  to  $3+$  and  $> 4-$ ) and two seasons (summer and winter) and used to construct contour diagrams showing the average variation of  $\log_{10} N_{\text{max}}$  ( $\text{el/cm}^3$ ) as functions of latitude and local time. Two of the maps are given in Figure 17 a, b.

The observations of Liska (1967) from Kiruna were combined with measurements made at Val-Joyeux, France, by Bertin and Papet Lepine (1970) to obtain plots of total electron content vs. local time spanning the interval  $40^{\circ}$ - $70^{\circ}$  geographic latitude. An example of one of these for the 1965-1966 winter is shown in Figure 18. These maps reveal yet another feature of the midlatitude ionosphere, namely a post-midnight winter increase that is

seen near  $45^{\circ}$  latitude. This feature was studied by the incoherent scatter technique (Evans, 1965) and shown not to be caused by particle precipitation. Evans (1965) invoked downward transport from the protonosphere as the cause and assumed that this was initiated by conjugate sunset. It seems more probable, however, that it is related to the penetration of substorm electric fields into the plasmasphere (e.g., Park and Banks, 1974).

b. Geostationary Satellite Observations

Observations of geostationary satellites do not immediately lend themselves to studies of large scale horizontal structure in the ionosphere owing to the absence of appreciable motion of the subionospheric point. However, by using a network of stations, it is possible to reconstruct the variation over a limited geographic area. This has been attempted by Mendillo and Klobuchar (1975), who employed the network shown in Figure 19, and were able to derive contour maps of electron content vs. latitude and time such as that shown in Figure 20 for the two-day period 8-9 December 1971. This figure shows clearly the region of the trough (near  $\Lambda = 60^{\circ}$ ) as well as many other interesting features. It would seem that by combining measurements made at a number of geostationary satellites (which give essentially the time variation at different latitudes) with data from low altitude satellites, it should be possible to construct quite detailed maps showing the behavior within a given region as a function of time.

6. MEDIUM SCALE STRUCTURE IN THE IONOSPHERE

Little and Lawrence (1960) and Evans and Taylor (1961) drew attention to the presence of ionospheric irregularities with large spatial scale which were observed as quasi-sinusoidal fluctuations of  $N_t$  of the order of 1-2%. These irregularities were attributed to the presence of Travelling Ionospheric Disturbances (TIDs) seen originally in HF soundings (e.g., Munro, 1950). It is now established that TIDs represent the perturbation of the F-region produced by neutral air motions established by acoustic-gravity waves (Figure 21). The excitation and propagation of acoustic gravity waves has attracted considerable theoretical interest (for review, see Yeh and Liu, 1974), and the F-region perturbations they produce have been studied by a variety of methods (see Evans, 1975) that have included measurements of total electron content by means of satellite beacon experiments.

It would be beyond the scope of this article to attempt to review all this work and here we shall confine our discussion to a single study conducted at Millstone Hill (Evans, 1973). Medium scale TIDs move with velocities of  $\sim 100-250$  m/sec which are slow compared to the speed at which the subionospheric point moves during observations of a polar orbiting satellite. Thus the wave (Figure 21) can be regarded as frozen in place during a satellite transit. At midlatitudes most waves appear to have crests that are oriented E-W and propagate approximately in N-S directions. Faraday rotation records are particularly sensitive to the presence of the

irregularities, but the waves can also be seen in differential doppler records (Figure 22). The histograms shown in Figures 23 and 24 for the distribution of wavelengths and latitudes (of the mid points) for the TIDs observed at Millstone Hill in 1971-1973 were obtained from examining 2300 passes of the Navy Navigation Series satellites. The most frequently observed wavelength at the latitude of Millstone (42°N) is 250 km and while it seems that it is difficult to detect waves with lengths larger than 1000 km from such records, the peak (in Figure 23) is probably a real feature.

The waves are expected to be seen best when the ray path to the satellite is approximately parallel to the phase fronts of the perturbation (shown as broken lines in Figure 21). This will mean that the waves are more readily detected when travelling *away* from the station than when approaching it. Thus the detection of most of the waves to the south of Millstone (Figure 24) is consistent with a north-to-south direction of propagation and auroral zone origin.

While low-altitude satellite observations are useful for providing a near-instantaneous picture of the wave, they provide no information on its speed or direction, and it is usually not possible to recognize features of the wave pattern on satellite passes occurring about an hour apart. Observations made with geostationary satellites yield the wave period, but not the wavelength. However, by making measurements from 3 widely-separated stations, it is possible to recover the period, wavelength, phase speed and direction (e.g., Davis and da Rosa, 1969) provided that the form of the wave does not change with time, e.g., Francis (1974). By employing several such measurements, it should be possible to locate the wave source, but the interpretation of the records is complicated by the difference in the phase and group velocities, (Hines, 1974) and the effects of neutral winds, (Yeh, 1972). Here again it would seem that useful results could be obtained from simultaneous geostationary and low altitude orbitting satellite measurements, but to the knowledge of the author no such combined study has yet been undertaken.

#### 7. SMALL SCALE STRUCTURE IN THE IONOSPHERE

The existence of small scale irregularities in the ionosphere was first recognized from the observation that, at times, the intensity of cosmic radio sources appears to fluctuate e.g., Little and Maxwell (1951). Shortly thereafter, it was surmised that these irregularities were also the agent that gave rise to the appearance of Spread F on vertical incidence ionograms, e.g., Dagg, (1957a, b). Herman (1966) has reviewed the occurrence of Spread F and some of the early theories for its production.

Interest in ionospheric irregularities observed by means of radio-star scintillation and HF reflections reached a peak during the IGY when a large number of stations were established in an effort to measure the drift of

ionisation in the F-region by observing the motion of the diffraction pattern over the ground (Briggs, 1957; Huxley and Greenhow, 1957). Subsequently, interest in the radio astronomy community shifted to the study of irregularities in the solar wind responsible for "interplanetary" scintillation.

The observation of amplitude scintillation on records of satellite beacon signals provided new impetus to the subject especially when it was established that ionospheric irregularities are capable of introducing fading at frequencies well above 1000 MHz. Thus, over the past decade there has been lively interest in this field resulting in a large amount of effort which can be organized under the following headings, viz.:

- a. studies of the morphology of the irregularities (i.e., incidence vs. time of day, year, sunspot cycle and geomagnetic conditions).
- b. studies of the theory of propagation for plane electromagnetic waves traversing ionospheric irregularities (leading, for example, to the frequency dependence of the scintillation).
- c. theoretical and experimental studies of the production mechanism for the irregularities (presumed to be some form of plasma instability).

The irregularities responsible for Spread F and beacon signal scintillations are encountered chiefly at high latitudes — in the vicinity of the auroral ovals — and over the geomagnetic equator at night, as illustrated in Figure 25. Considerable effort has been expended in attempting to study the morphology of ionospheric scintillation which cannot be described here. Useful reviews have been given in a series of papers by Aarons (Aarons et al, 1970, 1971; Aarons and Allen, 1971; Aarons, 1973, 1975).

The problem of the propagation of radio waves through an irregular ionosphere was treated in a series of now classical papers by Booker et al (1950), Briggs and Phillips (1950), Hewish (1952) and reviewed by Ratcliffe (1956). In order to proceed, it was necessary to make certain assumptions concerning the shape and size of the irregularities. In early work it was assumed (for mathematical convenience) that the irregularities were local increases of electron density of equal amount and size and were either spherical or cylindrically symmetrical. The density across the irregularity was assumed to increase above the background and return to it in a gaussian fashion, and the peak departure from the mean was thought to be a few percent. This model proved incapable of accounting for the scintillation observed at very high frequencies, and was abandoned when radio star (Rufenach, 1972; Singleton, 1974) and *in-situ* sampling measurements (e.g., Dyson et al, 1974) showed that, in fact, there is a wide range of irregularity sizes describable by a power law. Extensions of the theory for this case have been made, among others, by Rufenach (1974), Crane (1974) and Rino (1976).

Many different approaches have been employed to describe the amplitude and phase fluctuations that develop as the wave traverses the irregular layer, and these all lead to the same result when the scintillation is weak (i.e., the rms phase fluctuations in the emerging wavefront are less than  $\pm 1$  radian). Theoretical difficulties are encountered when the fading becomes severe as this corresponds to the case where there is multiple scattering by the irregularities. Despite this, useful results can be obtained employing an approximation due to Rytov (1937) (see Crane, 1976a). A good review of our present understanding of the radiowave propagation effects has been given by Crane (1976a).

The relationship between the frequency spectra of the amplitude and phase of the received signals and spatial spectra of the ionospheric irregularities has been discussed by Rufenach (1974) and Crane (1976b). The frequency spectrum of the log of the amplitude fluctuations is found to depend only slightly on the shape of the irregularities and the manner in which the ray path cuts through them.

Figure 26 shows a match between the spectrum of the log amplitude of signals recorded at Millstone Hill at 400 MHz from a Navy Navigation Series satellite during scintillating conditions and theory (Crane, 1976b). In this figure,  $\alpha$  is the ratio of the length of the irregularities (assumed aligned along the magnetic field direction) to their width;  $\psi$  is the angle between the field direction and ray direction, and  $\xi$  is the angle between the normal to the plane containing the ray and field directions and the direction of motion of the ray path. For spatial scales less than the Fresnel zone size, the frequency fluctuations are expected to be related to the spectrum  $P(k)$  of the irregularities, where  $k$  is their wave number. A power-law type three-dimensional wave number spectrum  $P(k) \propto k^{-p}$  should cause the log amplitude spectrum to fall off with frequency at constant slope. The observed slope is  $f^{-3}$  and this is consistent with results of *in-situ* measurements ( $3.5 < p < 4.3$ ).

Observations of amplitude scintillation are insensitive to the presence of structures much larger than the Fresnel zone size appropriate to the radio wavelength and geometry of the observation (Rufenach, 1974). For beacon satellite observations conducted at VHF or UHF, this is typically  $\sim 1$  km. The smallest structure that may be detected usually depends upon instrumental limitations imposed by the signal-to-noise ratio or unwanted modulation of the signal frequency, and may be a few tens of meters.

As noted above, differential-doppler records are sensitive to the presence of irregularities of all scales. Thus by obtaining the power spectrum of the phase fluctuations it is possible to recover information of the presence of irregularities with scales much larger than the Fresnel zone size. This is one advantage provided by observations of satellite beacon signals over radio star measurements. Figure 27 shows the power spectral density of the VHF (differential doppler) signals observed at Millstone Hill at the same time as the data shown in Figure 26. Residual phase noise on the VHF signal

introduces the departure between the experimental and theoretical results at  $f > 10$  Hz. However, at all lower frequencies (larger spatial scales) the fit is very good, indicating that the ionospheric irregularities that are responsible for scintillation have a continuous distribution of sizes from meters to tens of kilometers.

No completely accepted theory for the production of these irregularities has yet been presented (Crane, 1976a), and it seems probable that more than one plasma instability may be responsible at different times and/or places. The continuous nature of the wave number spectrum suggests, however, that large scale irregularities are generated first and that these in turn stimulate the growth of smaller ones and so on down to some very small size set by the inability of the particles to behave collectively. Qualitatively, this is very similar to the manner in which atmospheric turbulence is generated in the troposphere.

#### 8. CONCLUDING REMARKS

We have described the use of observations of satellite beacon signals to study the over-all structure of the ionosphere, some irregular features, large scale gravity waves, and smaller scale irregularities. It is evident that the technique has and will continue to make valuable contributions to understanding the ionosphere. In the view of the author the most fruitful applications for further study appear to be in three areas, viz.:

- a. Measurements of total content and peak electron density in conjunction with realistic models for the ionosphere should permit some parameters (such as the solar EUV flux) to be monitored inexpensively.
- b. Measurements of the total content by a network of stations surrounding the auroral oval in conjunction with the incoherent scatter measurements should permit the study of the transient manner in which the energy input into the upper atmosphere by Joule heating is redistributed to other latitudes by planetary waves, acoustic gravity waves and winds.
- c. Studies of the morphology of scintillation in conjunction with satellite measurements of AC and DC electric fields should permit conclusions to be drawn concerning the production and redistribution of the small scale irregularities.

This work was supported by the National Science Foundation under Grant ATM-75-22193

- Figure 1** Measurements of the total electron content of the ionosphere (here  $N_t$ ) compared with the content below the layer peak  $N_b$  from observations of Sputnik 3 at Stanford, California (Garriott, 1960b).
- Figure 2** Measurements of the total electron content of the ionosphere (here  $N_t$ ) vs. local time observed (a) at Washington, D.C., and (b) at Ottawa using differential doppler measurements of Transit 4A (Bhonsle et al, 1965).
- Figure 3** Variation of the total electron content of the ionosphere at noon vs. mean sunspot number for 3 seasons (Bhonsle et al, 1965).
- Figure 4a, b** Variation with season of the mean total electron content and slab thickness observed at Urbana, Illinois, (Yeh and Flaherty, 1966). a.) total electron content. b.) slab thickness.
- Figure 5** Average variation of slab thickness  $\tau$  over the time intervals 06-09, 09-12 and 12-15 with the  $K_p$  index. (Yeh and Flaherty, 1966).
- Figure 6a, b** Variation of total content and slab thickness observed at the University of Hawaii in 1964, from Faraday rotation observations of the Syncom 3 geostationary satellite (Garriott et al, 1965). a.) total content. b.) slab thickness.
- Figure 7** Values of total electron content measured by the Air Force Cambridge Research Laboratories group at Hamilton, Massachusetts ( $43^{\circ}$ N) using Faraday rotation observations of the VHF beacon on ATS-3 in 1968 (Klobuchar and Allen, 1970).
- Figure 8** Seasonal variation of midday slab thickness (here denoted by  $S$ ) in 1968 obtained by Klobuchar and Allen (1970).
- Figure 9** Variation of  $K_p$ , total content (here  $n_t$ ), peak electron density ( $N_m$ ),  $P$  and slab thickness (here  $d$ ) following a storm sudden commencement (SSC) at  $47^{\circ}$ N (Taylor and Earnshaw, 1969).
- Figure 10** Variation of total electron content at 10 stations observed by means of Faraday rotation observations of ATS-1 and ATS-3 following the sudden commencement (denoted by the arrow) of a storm occurring on 8 March 1970 (Klobuchar et al, 1971).

- Figure 11** Variation of slab thickness at midlatitudes with neutral temperature according to a model by Titheridge (1973).
- Figure 12** Variation of the 24-hour mean total electron content averaged over 31 days for 1965 and 1969 as observed at Stanford (crosses). Also shown (solid line) is the variation predicted from regressions obtained between total content and solar flux (da Rosa et al, 1973).
- Figure 13** Dependence of the slab thickness parameter on the height of the transition between  $O^+$  and  $H^+$  in the upper F2-layer for three values of the exospheric temperature (Titheridge, 1973). The solid line corresponds to nighttime conditions where the plasma temperature  $(T_e + T_i)/2$  increases at  $0.5^\circ/\text{km}$  and the broken line the daytime situation where the gradient is  $4^\circ/\text{km}$ .
- Figure 14** Total content variations across the equatorial anomaly deduced from Faraday rotation observations of the Transit 4A satellite from three stations (Golton and Walker, 1971).
- Figure 15** Variation of total electron content with latitude deduced from Faraday rotation records made at Kiruna ( $68^\circ\text{N}$ ) by observing the S66 satellite in November 1964. Top: shortly before noon. Bottom: shortly after midnight (Liska, 1966).
- Figure 16** Variation of overhead total electron content as a function of latitude and local time derived by Liska (1966) from records such as those shown in Figure 15. Units are  $10^{-16}$  electrons/ $\text{m}^2$ .
- Figure 17** Maps of average  $\log_{10} N_{\text{max}}$  ( $\text{el}/\text{cm}^3$ ) constructed from 2300 records of the differential doppler records of the Navy Navigation Series satellites by Wand and Evans (1975). a.) Winter, low magnetic activity. b.) Summer, medium magnetic activity.
- Figure 18** Map of average overhead total electron content (units of  $10^{-16}$   $\text{el}/\text{m}^2$ ) vs. geographic latitude and local time obtained by Bertin and Papet Lepine (1970) by combined Faraday rotation measurements made in Sweden and France through observations of the Transit 4A satellite.
- Figure 19** The network of geostationary satellite observing stations employed by Mendillo and Klobuchar (1975) to construct the plot of total electron content shown in Figure 20.
- Figure 20** Contours of overhead total electron content (units of  $10^{-16}$   $\text{el}/\text{m}^2$ ) obtained from geostationary satellite observations by Mendillo and Klobuchar (1975).

- Figure 21** Contours of electron density in the F-layer when disturbed by a TID as computed by S. H. Francis (Evans, 1973b). Broken lines indicate the wave phase fronts for a wave that is propagating from left to right. Contours are labelled in units of the undisturbed peak electron density.
- Figure 22** Fluctuations in differential doppler, apparent elevation and azimuth observed for a very large TID at Millstone Hill (Evans, 1973b).
- Figure 23** Wavelength distribution of TIDs observed in differential doppler records (cf. Figure 22) gathered at Millstone Hill (Evans, 1973b).
- Figure 24** Latitude distribution of TID mid points observed in differential doppler records (cf. Figure 22) gathered at Millstone Hill (Evans, 1973b).
- Figure 25** Map showing the locations on the earth where ionospheric irregularities causing the scintillation of satellite beacon signals are most often found (Aarons et al, 1970). The hatched area represents the region in which deep fading may be encountered.
- Figure 26** Comparision with theory of the frequency spectra of the log of the amplitude of 400 MHz satellite beacon signals recorded at Millstone Hill during a period of scintillation (Crane, 1976b).
- Figure 27** Comparison with theory of the frequency spectra of the phase fluctuations of the 150 MHz satellite beacon signals recorded at Millstone Hill during a period of scintillation (Crane, 1976b).

## REFERENCES

- Aarons, J. (1973): A descriptive model of F-layer high latitude irregularities as shown by scintillation observations. J. Geophys. Res., 78:7441.
- Aarons, J. (1975): High latitude morphology of ionospheric scintillations. Effect of the Ionosphere on Space Systems and Communications, (ed. J. M. Goodman). U.S. Government Printing Office, Washington, D.C., pp. 1-7.
- Aarons, J. and Allen, R. S. (1971): Scintillation boundary during quiet and disturbed magnetic conditions. J. Geophys. Res., 76:170.
- Aarons, J., Whitney, H. E. and Allen, R. S. (1970): Global morphology of ionospheric scintillations. Air Force Cambridge Research Laboratories Report AFCRL-70-0672, Bedford, Massachusetts.
- Aarons, J., Whitney, H. E. and Allen, R. S. (1971): Global morphology of ionospheric scintillations. Proc. IEEE, 59:159.
- Almeida, O. G. (1972): VHF/UHF technique for the determination of the columnar electron content of the plasmasphere and of the protonosphere using geostationary satellite transmission: Observations during geomagnetic storms. Stanford University Technical Report SEL-72-019, Stanford, California.
- Al'pert, Ya. L (1963): Radiowave propagation and the ionosphere. (English translation.) Consultants Bureau Enterprises, Inc., New York, N. Y., 394 p.
- Al'pert, Ya. L. (1976): On ionospheric investigations by coherent radiowaves emitted from artificial earth satellites. Space Sci. Revs., 18:551.
- Appleton, E. V. (1946): Two anomalies in the ionosphere. Nature, 157:691.
- Bailey, D. K. (1948): The geomagnetic nature of the F2-layer longitude effect. Terrest. Magn. Atmospher. Elec. 53:35.
- Banks, P. M. and Holzer, T. E. (1969): Features of plasma transport in the upper atmosphere. J. Geophys. Res., 74:6304.
- Banks, P. M. and Kockarts, G. (1973): Physical processes in the topside ionosphere. Aeronomy, Part B, Academic Press, New York. Chapter 21.
- Banks, P. M., Schunk, R. W. and Raitt, W. J. (1974):  $\text{NO}^+$  and  $\text{O}^+$  in the high-latitude F-region. Geophys. Res. Lett., 1:239.

- Bauer, S. J. (1960): Inferred temperature variations at the F2 peak. J. Geophys. Res., 65:1685.
- Bauer, S. J. and Daniels, F. B. (1958): Ionospheric parameters deduced from the Faraday rotation of lunar radio reflections. J. Geophys. Res., 63:439.
- Berning, W. W. (1951): Charge densities in the ionosphere from radio doppler data. J. Meteor., 8:175.
- Bertin, F. and Papet Lepine, J. (1970): Latitudinal variation of total electron content in the winter at middle latitudes. Radio Science, 5:899.
- Bhonsle, R. V., da Rosa, A. V. and Garriott, O. K. (1965): Measurements of the total electron content and equivalent slab thickness of the midlatitude ionosphere. Radio Science J. of Res., NBS, 69D:929.
- Booker, H. G., Ratcliffe, J. A. and Shinn, H. D. (1950): Diffraction from an irregular screen with applications to ionospheric problems. Phil. Trans. Roy. Soc. (London), A242:579.
- Briggs, B. H. (1957): The determination of ionospheric-drift velocities from three-receiver fading records. Annals of the International Geophysical Year, Vol. III. (eds. W. J. G. Beynon and G. M. Brown) Pergamon Press, London, pp. 235-249.
- Briggs, B. H. and Phillips, G. H. (1950): A study of the horizontal irregularities of the ionosphere. Proc. Phys. Soc. (London), B63:907.
- Browne, I. C., Evans, J. V., Hargreaves, J. K. and Murray, W. A. S. (1956): Radio echoes from the moon. Proc. Phys. Soc. (London), B69;901.
- Crane, R. K. (1974): Morphology of ionospheric scintillation. Lincoln Laboratory Tech. Note 1974-29, Lexington, Mass. 84 p.
- Crane, R. K. (1976a): Ionospheric scintillation. Proc. IEEE, in press.
- Crane, R. K. (1976b): Spectra of ionospheric scintillation. J. Geophys. Res., 81:2041.
- Dagg, M. (1957a): The origin of the ionospheric irregularities responsible for radio-star scintillations and Spread F-1: Review of existing theories. J. Atmos. Terr. Phys., 11:133.
- Dagg, M. (1957b): Diurnal variations of radio star scintillations, Spread F and geomagnetic activity. J. Atmos. Terr. Phys., 10:204.

- da Rosa, A. V. (1973): Recent results from satellite beacon measurements. Technical Report No. 15, Stanford University, Radioscience Laboratories, Stanford, California. 36 p.
- da Rosa, A. V., Waldman, H., Bendito, J. and Garriott, O. K. (1973): Response of the ionospheric electron content to fluctuations in solar activity. J. Atmos. Terr. Phys., 35:1429.
- Davies, K., Fritz, R. B., Grubb, R. N. and Jones, J. E. (1975): Some early results from the ATS-6 radio beacon experiment. Radio Science, 10:785.
- Davies, K., Fritz, R. B. and Gray, T. B. (1976): Measurements of the columnar electron contents of the ionosphere and plasmasphere. J. Geophys. Res., 81:2825.
- Davis, M. J. and da Rosa, A. V. (1969): Traveling ionospheric disturbances originating in the auroral oval during polar substorms. J. Geophys. Res., 74:5721.
- de Mendonça, F. (1962): Ionospheric electron content and variations measured by doppler shifts in satellite transmissions. J. Geophys. Res., 67:2315.
- Dyson, D. L., McClure, J. P. and Hanson, W. B. (1974): In situ measurements of the spectral characteristics of F-region ionospheric irregularities. J. Geophys. Res., 79:1497.
- Earnshaw, R. D. and Taylor, G. N. (1968): Anomalous variations of the ionosphere total content at sub-auroral latitudes. J. Atmos. Terr. Phys., 30:1369.
- Evans, J. V. (1956): The measurement of the electron content of the ionosphere by the lunar radio echo method. Proc. Phys. Soc. (London), B69:953.
- Evans, J. V. (1957): The electron content of the ionosphere. J. Atmos. Terr. Phys., 11:259.
- Evans, J. V. (1965): Cause of the midlatitude winter night increase in  $F_o F2$ . J. Geophys. Res., 70:4331.
- Evans, J. V. (1970): The June 1965 magnetic storm: Millstone Hill observations. J. Atmos. Terr. Phys., 30:1629.
- Evans, J. V. (1973a): The causes of storm-time increases of the F-layer at mid-latitudes. J. Atmos. Terr. Phys., 35:593.

- Evans, J. V. (editor) (1973b): Millstone Hill radar propagation study: Scientific results - Part II. Lincoln Laboratory Tech. Rep. 509, Lexington, Mass. 80 p.
- Evans, J. V. (1974): Some post-war developments in ground-based radiowave sounding of the ionosphere. J. Atmos. Terr. Phys., 36:2183.
- Evans, J. V. (1975): A review of F-region dynamics. Revs. Geophys. and Space Phys., 13:887.
- Evans, J. V. and Holt, J. M. (1973): The combined use of satellite differential doppler and ground-based measurements for ionospheric studies. IEEE Trans. Antennas and Propagation AP-21:685.
- Evans, J. V. and Taylor, G. N. (1961): The electron content of the ionosphere in winter. Proc. Roy. Soc. (London), A 263:189.
- Francis, S. H. (1974): A theory of medium-scale traveling ionospheric disturbances. J. Geophys. Res., 79:5245.
- Garriott, O. K. (1960a): The determination of ionospheric electron content and distribution from satellite observations. Part I, Theory of the analysis. J. Geophys. Res., 65:1139.
- Garriott, O. K. (1960b): The determination of ionospheric electron content and distribution from satellite observations. Part 2. Results of the analysis. J. Geophys. Res., 65:1151.
- Garriott, O. K. and de Mendonça, F. (1963): A comparison of methods used for obtaining electron content from satellite observations. J. Geophys. Res., 68:4917.
- Garriott, O. K., da Rosa, A. V., Ross, W. J. (1970): Electron content obtained from Faraday rotation and phase path length variations. J. Atmos. Terr. Phys., 32:705.
- Garriott, O. K., Smith, F. L. and Yuen, P. C. (1965): Observations of ionospheric electron content using a geostationary satellite. Planet. Space Sci., 13:829.
- Golton, E. and Walker, G. O. (1971): Observations of ionospheric electron content across the equatorial anomaly at sunspot minimum. J. Atmos. Terr. Phys., 33:1.
- Goodman, J. M. (1968): Some measurements of electron content enhancements associated with magnetic storms. Planet. Space Sci., 16:951.
- Grebowsky, J. M., Chen, A. J. and Taylor, A. H., Jr. (1976): High-latitude troughs and the polar cap boundary. J. Geophys. Res., 81:690.

- Gringauz, K. I. (1958): Rocket measurements of the electron concentration in the ionosphere using an ultra-shortwave dispersion interferometer. Doklady AN (USSR), 120:1234.
- Hanson, W. B. and Moffett, R. J. (1966): Ionization transport effects in the equatorial F-region. J. Geophys. Res., 71:5559.
- Hargreaves, J. K. (1970): ATS-F: Observational opportunities. Proceeding of the Symposium on the Future Application of Satellite Beacon Experiments (June 1970), Max-Planck Institut für Aeronomie, Lindau/Harz, FRP. pp. 16-1 to 16-9.
- Hedin, A. E., Mayr, H. G., Reber, C. A., Spencer, N. W. and Carignan (1974): Empirical model of global thermosphere temperature and composition based on data from the OGO-6 quadrupole mass spectrometer. J. Geophys. Res., 79:215.
- Herman, J. R. (1966): Spread F and ionospheric F-region irregularities. Rev. Geophys., 4:255.
- Hewish, A. (1952): The diffraction of galactic radio waves as a method of investigating the irregular structure of the ionosphere. Proc. Roy. Soc. (London), 214:294.
- Hines, C. O. (1974): Propagation velocities and speeds in ionospheric waves: A review. J. Atmos. Terr. Phys., 36:1179.
- Huxley, L. G. H. and Greenhow (1957): The investigation of winds in the upper atmosphere by means of drifting meteor trails. Annals of the International Geophysical Year, Vol. III. (eds. W. J. G. Beynon and G. M. Brown). Pergamon Press, London. pp. 275-279.
- Jacchia, L. G. and Slowey, J. (1964): Atmospheric Heating in the Auroral Zones: A preliminary analysis of the atmospheric drag of the Injun 3 satellite. J. Geophys. Res., 69:905.
- Jones, K. L. and Rishbeth, H. (1971): The origin of storm increases of mid-latitude F-layer electron concentration. J. Atmos. Terr. Phys., 33:391.
- Kane, R. P. (1975): Day-to-day variability of ionospheric electron content at mid-latitudes. J. Geophys. Res., 80:3091.
- Klobuchar, J. A. and Allen, R. S. (1970): A first order prediction model of total electron-content group path delay for a midlatitude ionosphere. Air Force Cambridge Research Labs. Tech. Rep. AFCRL-70-0403, Cambridge, Mass. 19 p.

- Klobuchar, J. A., Mendillo, M., Smith, F. L., III, Fritz, R. B., da Rosa, A. V., Davis, M. J., Yuen, P. C., Roelofs, T. H., Yeh, K. C. and Flaherty, B. J. (1971): Ionospheric storm of March 8, 1970. J. Geophys. Res., 76:6202.
- Lanzerotti, L. J., Cogger, L. L. and Mendillo, M. (1975): Latitude dependence of ionospheric total electron content: Observations during sudden commencement storms. J. Geophys. Res., 80:1287.
- Leitinger, R., Schmidt, G. and Tauriainen, A. (1975): An evaluation method combining the differential doppler measurements from two stations that enable the calculation of the electron content of the ionosphere. Z. Geophys., 41:201.
- Liska, L. (1966): Latitudinal and diurnal variations of the ionospheric electron content near the auroral zone in winter. Electron Density Profiles in Ionosphere and Exosphere (ed. J. Frihagen). North Holland Publ. Co., Amsterdam, Netherlands. pp.549-554.
- Liska, L. (1967): The high-latitude trough in the ionospheric electron content. J. Atmos. Terr. Phys., 29:1243.
- Little, C. G. and Maxwell, A. (1951): Fluctuations in the intensity of radiowaves from galactic sources. Phil. Mag. (London), 42:267.
- Little, C. G. and Lawrence, R. S. (1960): The use of polarization fading of satellite signals to study the electron content and irregularities in the ionosphere. J. Res. NBS, 64D:335.
- Martyn, D. F. (1947): Atmospheric tides in the ionosphere - solar tides in the F2-region. Proc. Roy. Soc. (London), A129:241.
- Mendillo, M. and Klobuchar, J. A. (1975): Investigations of the ionospheric F region using multistation total electron content observations. J. Geophys. Res., 80:643.
- Mendillo, M., Buonsanto, M. J. and Klobuchar, J. A. (1975): The construction and use of storm-time corrections for ionospheric F-region parameters. Effect of the Ionosphere on Space Systems and Communications. (ed. J. M. Goodman), U.S. Gov. Printing Office, Washington, D.C. pp. 361-371.
- Mendillo, M., Papagiannis, M. D. and Klobuchar, J. A. (1970): Ionospheric storms at midlatitudes. Radio Science, 5:895.
- Muldrew, D. B. (1965): F-layer ionization troughs deduced from Alouette data. J. Geophys. Res., 70:2635.

- Munro, G. H. (1950): Travelling disturbances in the ionosphere. Proc. Roy. Soc. (London), A202:208.
- Newell, H. E., Jr. (1960): The upper atmosphere studied by rockets and satellites. Physics of the Upper Atmosphere (ed. J. A. Ratcliffe), Academic Press, New York, N.Y. pp. 102-108.
- Nisbet, J. S. (1960): Electron-density distribution in the upper ionosphere from rocket measurements. J. Geophys. Res., 65:2597.
- Obayashi, T. (1972): World-wide electron density changes and associated thermospheric winds during an ionospheric storm. Planet. Space Sci., 20:511.
- Papagiannis, M. D., Mendillo, M. and Klobuchar, J. A. (1971): Simultaneous storm-time increases of the ionospheric total electron content and the geomagnetic field in the dusk sector. Planet. Space Sci., 19:503.
- Papagiannis, M. D., Mendillo, M. and Klobuchar, J. A. (1972): Average behavior of the mid-latitude F-region parameters  $N_T$ ,  $M_{max}$  and  $\tau$  during geomagnetic storms. J. Geophys. Res., 77:4891.
- Park, C. G. and Banks, P. M. (1974): Influence of thermal plasma flow on the mid-latitude nighttime F2 layer: Effects of electric fields and neutral winds inside the plasmasphere. J. Geophys. Res., 79:4661.
- Rao, B. C. and Jain, V. C. (1974): Hydrogen and oxygen ion densities and fluxes in low and midlatitude topside ionosphere. Ind. J. Radio and Space Phys., 3:284.
- Rastogi, R. G. and Sharma, R. P. (1971): Ionospheric electron content at Ahmedabad (near the crest of equatorial anomaly) by using beacon satellite transmissions during half a solar cycle. Planet. Space Sci., 9:1505.
- Rastogi, R. G., Sharma, R. P. and Shodhan, V. (1973): Total electron content of the equatorial ionosphere. Planet. Space Sci., 21:713.
- Ratcliffe, J. A. (1956): Some aspects of diffraction theory and their application to the ionosphere. Proc. Phys. Soc. Progr. Phys., 19:188.
- Ratcliffe, J. A. and Weekes, K. (1960): The ionosphere. Physics of the Upper Atmosphere. (ed. J. A. Ratcliffe). Academic Press, New York, N.Y. pp. 377-470.
- Rawer, K. and Katz, L. (1957): The Ionosphere. Frederick Ungar Publishing Company, New York, N.Y.. 202 p.
- Rino, C. L. (1976): Some new results on the statistics of radiowave scintillation 2. Scattering from a random ensemble of locally homogeneous patches. J. Geophys. Res., 81:2059.

- Rishbeth, H. (1967): A review of ionospheric F region theory. Proc. IEEE, 55:16.
- Roble, R. G. (1975): The calculated and observed diurnal variation of the neutral thermospheric winds determined from incoherent scatter radar data. J. Geophys. Res., 79:2868.
- Rufenach, C. L. (1972): Power-law wavenumber spectrum deduced from ionospheric scintillation observations. J. Geophys. Res., 77:4761.
- Rufenach, C. L. (1974): Wavelength dependence of radio scintillation: Ionosphere and interplanetary irregularities. J. Geophys. Res., 79:1562.
- Rycroft, M. J. and Thomas, J. O. (1970); The magnetospheric plasmapause and the electron density trough at the Alouette I orbit. Planet. Space Science, 18:65.
- Rytov, S. M. (1937): Diffraction of light by ultrasound wave. Izv. AN SSSR Ser. Fiz., 2:223.
- Salah, J. E. and Evans, J. V. (1973): Measurements of thermosphere temperatures by incoherent scatter radar. Space Research XIII, Akademie-Verlag, Berlin. pp. 267-286.
- Seddon, J. C. (1953): Propagation measurements in the ionosphere with the aid of rockets. J. Geophys. Res., 58:323.
- Seddon, J. C. and Jackson, J. E. (1955): Absence of bifurcation in the E-layer. Phys. Rev., 97:1182.
- Singleton, D. G. (1974): Power spectra of ionospheric scintillations. J. Atmos. Terr. Phys., 36:113.
- Soicher, H. (1976): Response of electrons in ionosphere and plasmasphere to magnetic storms. Nature, 259:33.
- Somayajulu, Y. V. Sehgal, A. K., Tyagi, T. R. and Nagi, N. K. (1971): Changes in electron content during the 25-26 May 1967 magnetic storm event. Indian J. Pure and Applied Phys., 9:548.
- Sterling, D. L., Hanson, W. B., Moffett, R. J. and Baxter, R. G. (1969): Influence of electromagnetic drifts and neutral air winds on some features of the F2-region. Radio Science, 4:1005.
- Strobel, D. F. and McElroy, M. B. (1970); The F-layer at middle latitudes. Planet. Space Sci., 18:1181.
- Tanaka, T. and Hirao, K. (1972): Numerical study of the seasonal variations of the ionosphere. Rep. Ionos. and Space Res. in Japan, 26:216.

- Tanaka, T. and Hirao, K. (1973): Effects of an electric field on the dynamical behavior of the ionosphere and its application to the storm time disturbance of the F-layer. J. Atmos. Terr. Phys., 35:1443.
- Taylor, G. N. (1965): Some curious anomalies in the Faraday rotation of lunar echoes. J. Atmos. Terr. Phys., 27:118.
- Taylor, G. N. (1966): The seasonal anomaly in electron content. Electron Density Profiles in the Ionosphere and Exosphere (ed. J. Frihagen). North Holland Publ. Co., Amsterdam, Netherlands. pp. 543-548.
- Taylor, G. N. and Earnshaw, R. D. S. (1969): Changes in the total electron content and slab thickness of the ionosphere during a magnetic storm in June 1965. J. Atmos. Terr. Phys., 31:211.
- Thomas, L. (1966): Electron density distributions in the daytime F2-layer and their dependence on neutral gas, ion and electron temperatures. J. Geophys. Res., 71:1357.
- Titheridge, J. E. (1973): The slab thickness of the midlatitude ionosphere. Planet Space Sci., 21:1775.
- Titheridge, J. E. and Andrews, M. K. (1967): Changes in the topside ionosphere during a large magnetic storm. Planet. Space Sci., 15:1157.
- Tyagi, T. R. (1974): Determination of total electron content from differential Doppler records. J. Atmos. Terr. Phys., 36:1157.
- Wand, R. H. and Evans, J. V. (1975): Morphology of ionospheric scintillations in the auroral zone. Effect of the Ionosphere on Space Systems and Communications (ed. J. M. Goodman). U.S. Govt. Printing Office, Washington, D.C. pp. 76-83.
- Warren, E. S. (1969): The topside ionosphere during geomagnetic storms. Proc. IEEE, 57:1029.
- .bb, H. D. (1969): Solar flares and magnetic storm of May 21 to 28, 1967. J. Geophys. Res., 74:1880.
- Wu, M-F, and Newell, R. E. (1972): Computer simulation of the F-region seasonal anomaly. J. Atmos. Terr. Phys., 34:1635.
- Yeh, K. C. (1972): Traveling ionospheric disturbances as a diagnostic tool for thermospheric dynamics. J. Geophys. Res., 77:709.
- Yeh, K. C. and Flaherty, B. J. (1966): Ionospheric electron content at temperate latitudes during the declining phase of the sunspot cycle. J. Geophys. Res., 71:4557.

- Yeh, K. C. and Liu, C. H. (1974): Acoustic-Gravity waves in the upper atmosphere. Revs. Geophys. and Space Phys., 12:193.
- Yeh, K. C. and Swenson, G. W. (1961): Ionospheric electron content and its variations deduced from satellite observations. J. Geophys Res., 66:1061.
- Yuen, P. C., Roelofs, T. H. and Young, D. M. L. (1969): The use of foF2 data to remove the ambiguity in total electron content data. J. Atmos. Terr. Phys., 31:877.

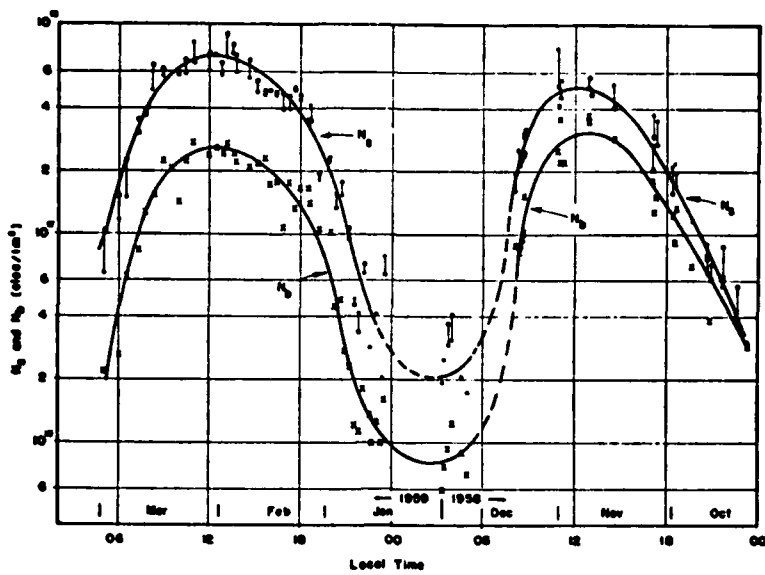


Figure 1

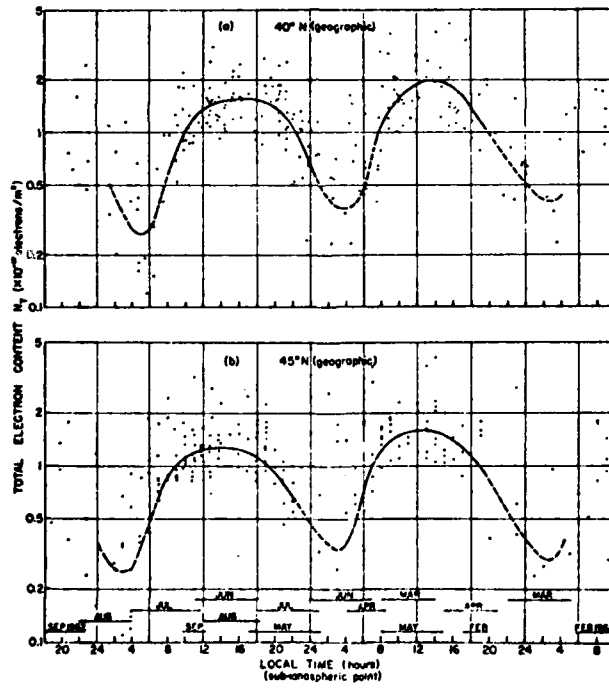
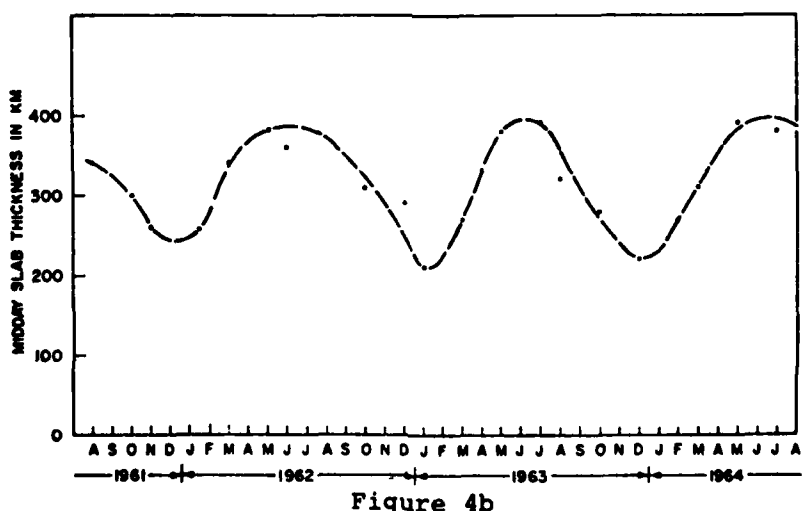
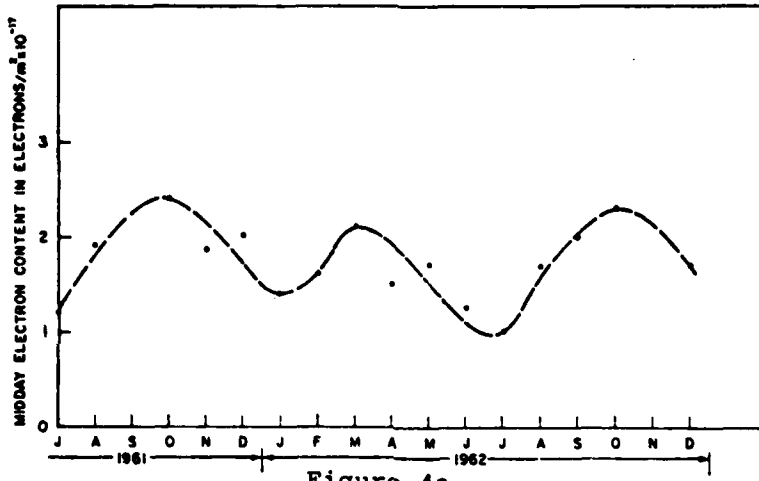
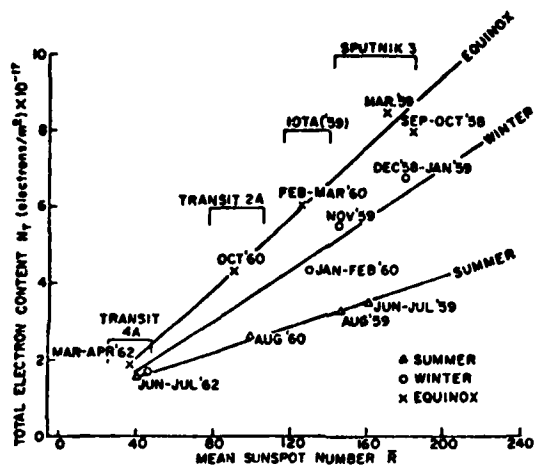


Figure 2



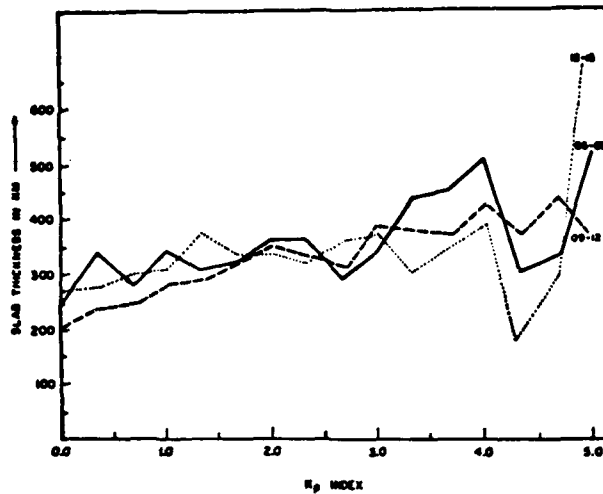


Figure 5

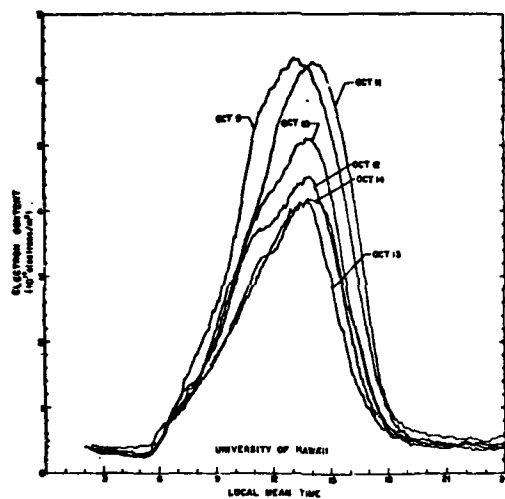


Figure 6a

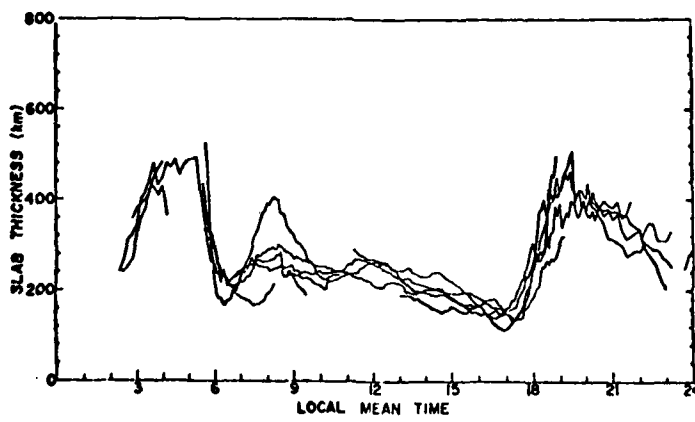


Figure 6b

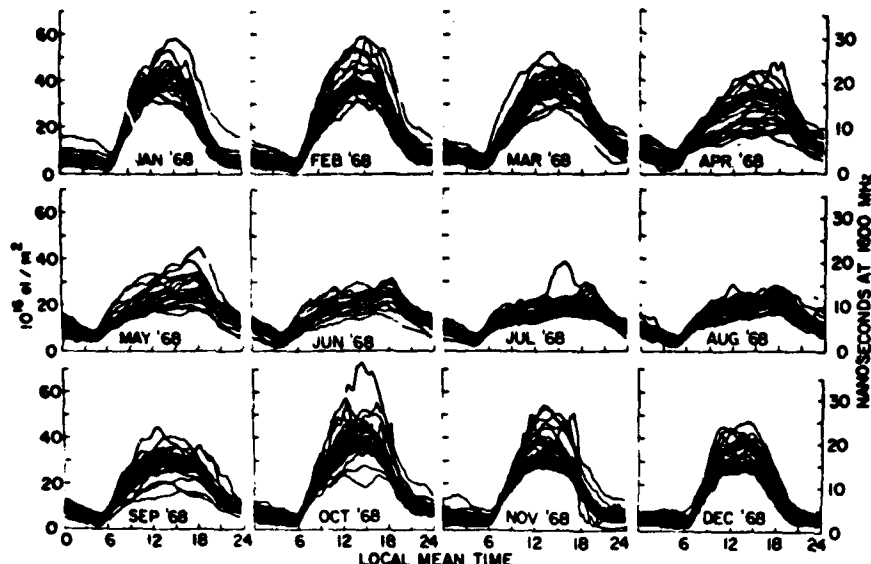


Figure 7

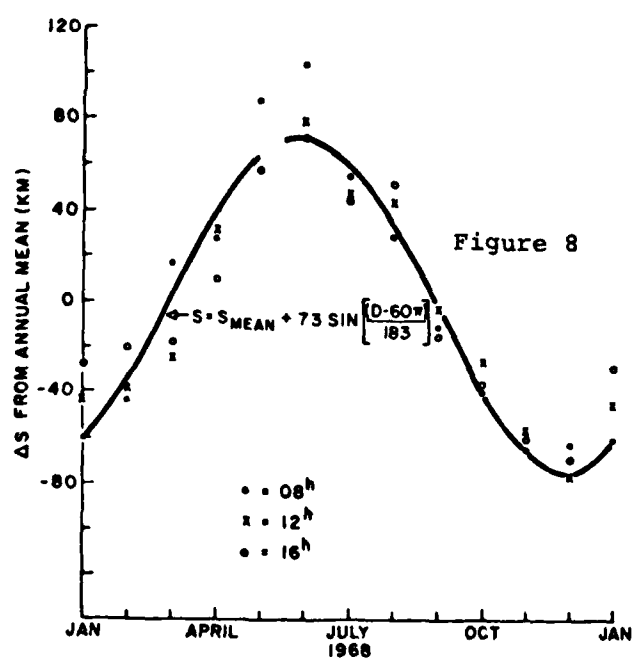


Figure 8

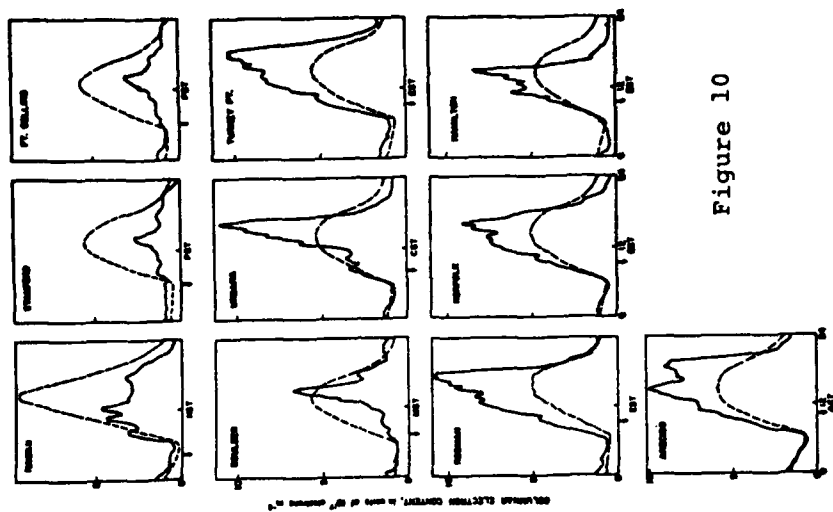


Figure 10

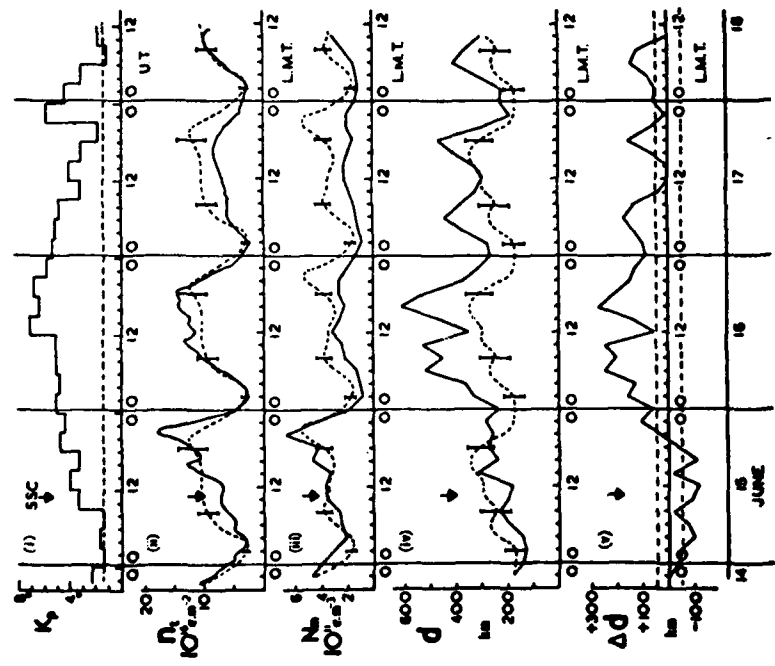


Figure 9

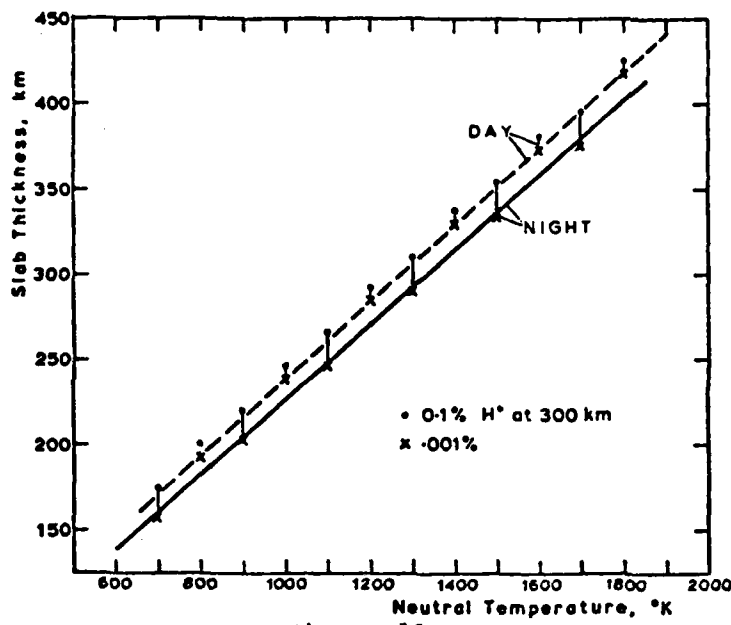


Figure 11

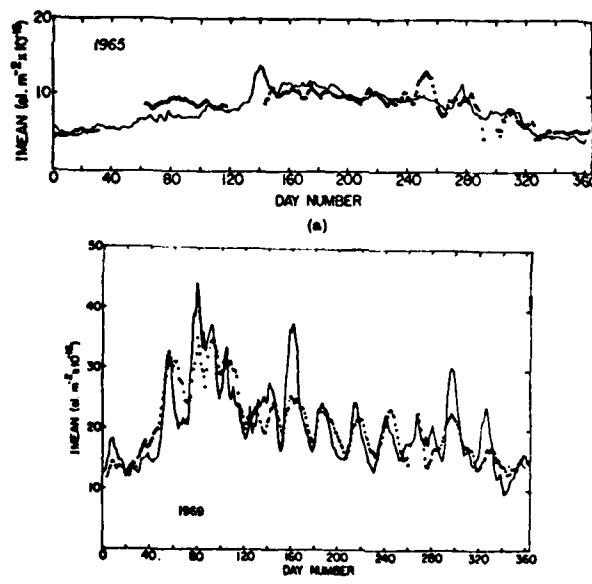


Figure 12

Figure 13

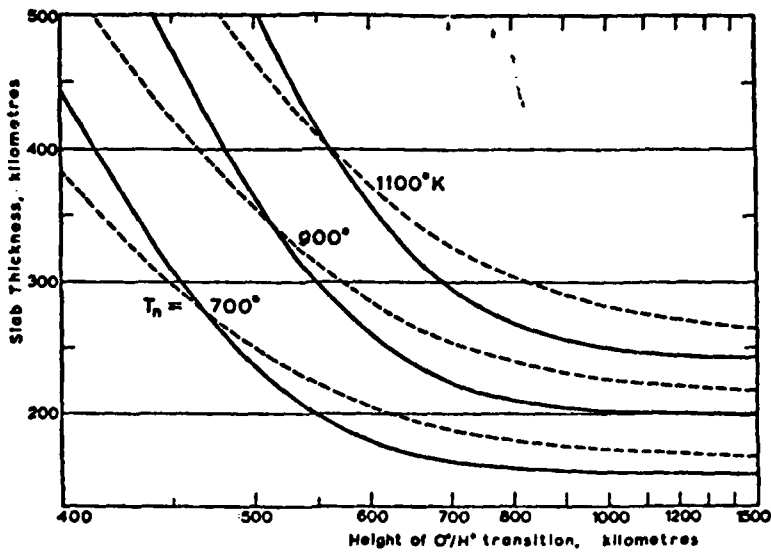
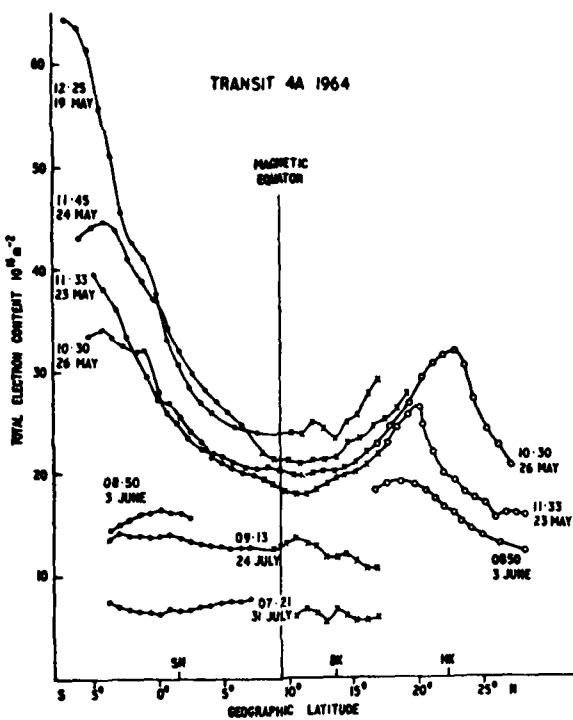


Figure 14



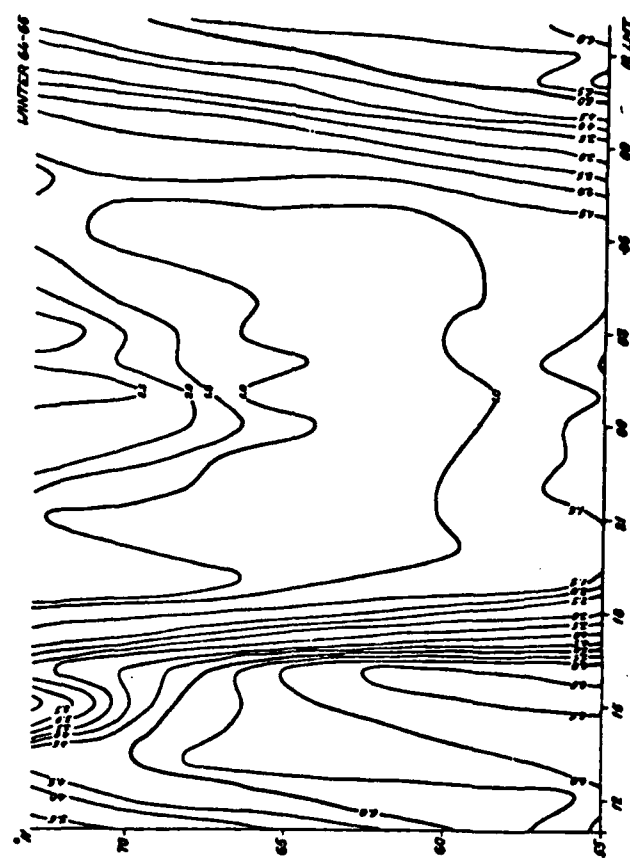


Figure 16

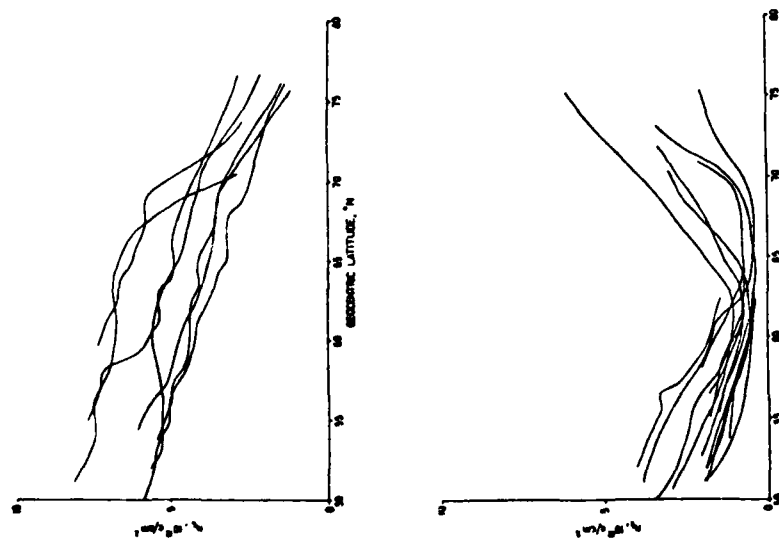


Figure 15

CONTOURS OF  $\log_{10} \bar{N}_{\text{MAX}}$ , WINTER,  $K_p 0_0$  to  $1_+$   
(Millstone Hill 1971 to 1973)

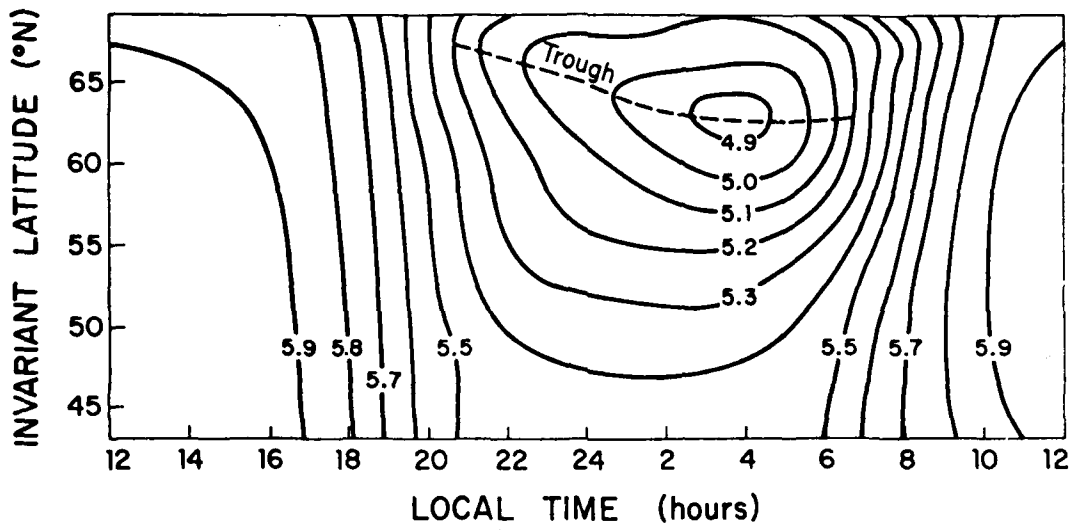


Figure 17a

CONTOURS OF  $\log_{10} \bar{N}_{\text{MAX}}$ , SUMMER,  $K_p 2_-$  to  $3_+$   
(Millstone Hill 1971 to 1973)

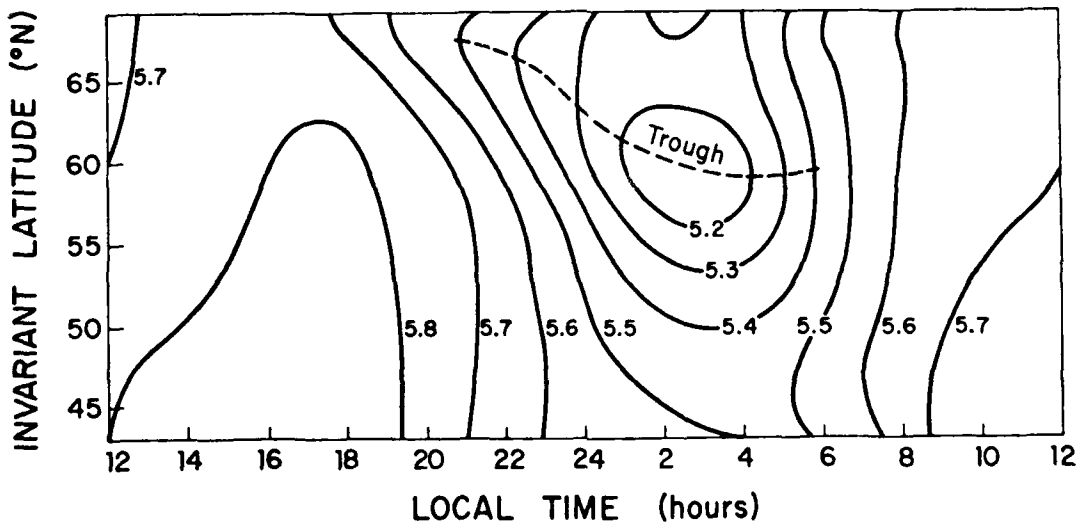


Figure 17b

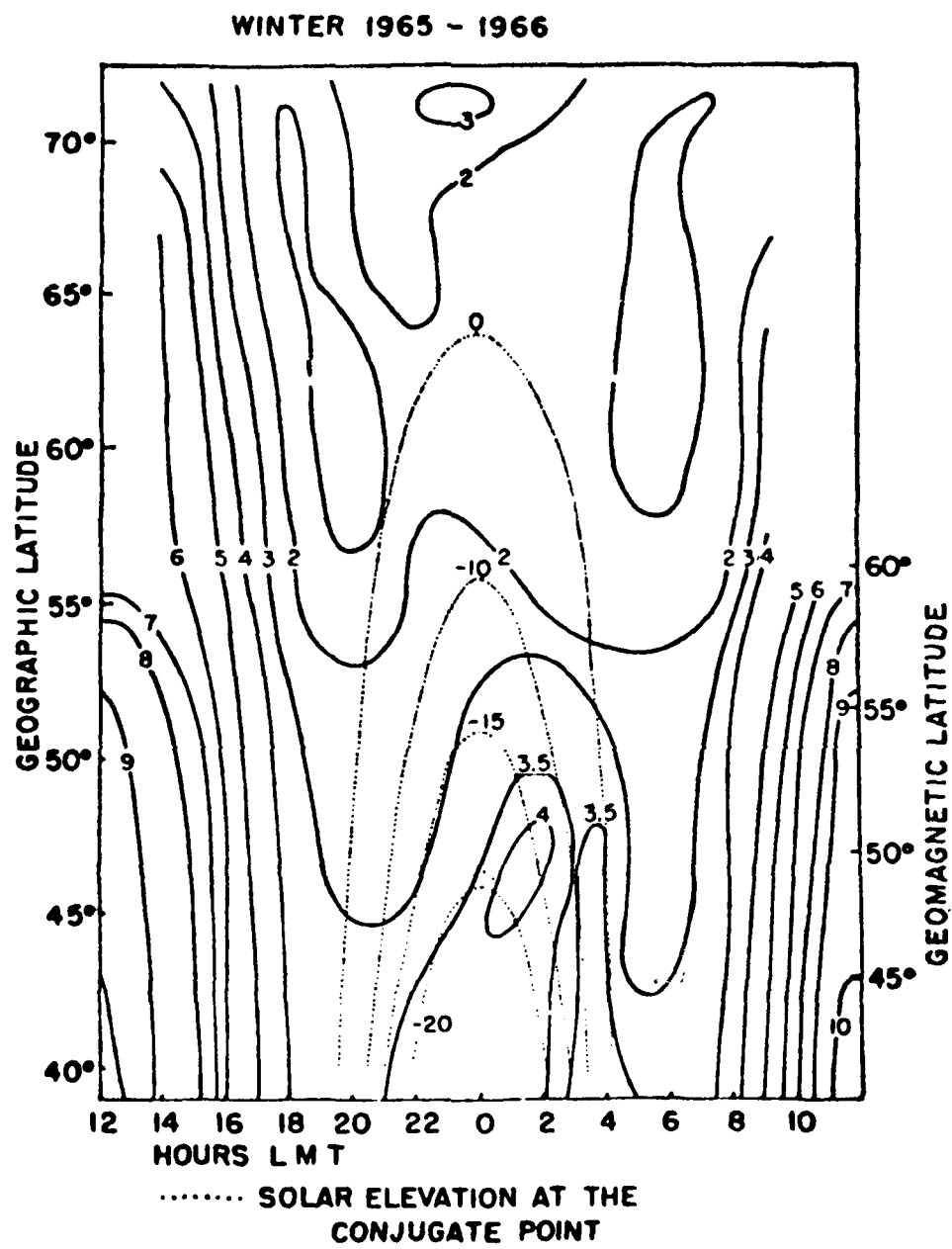


Figure 18

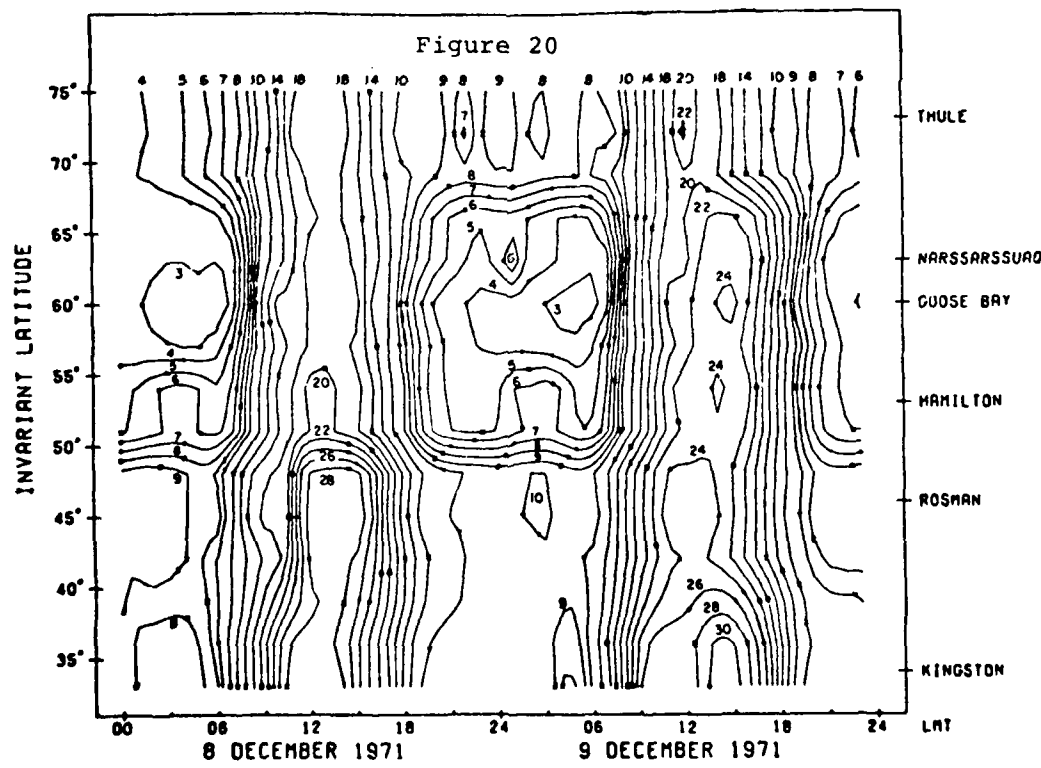
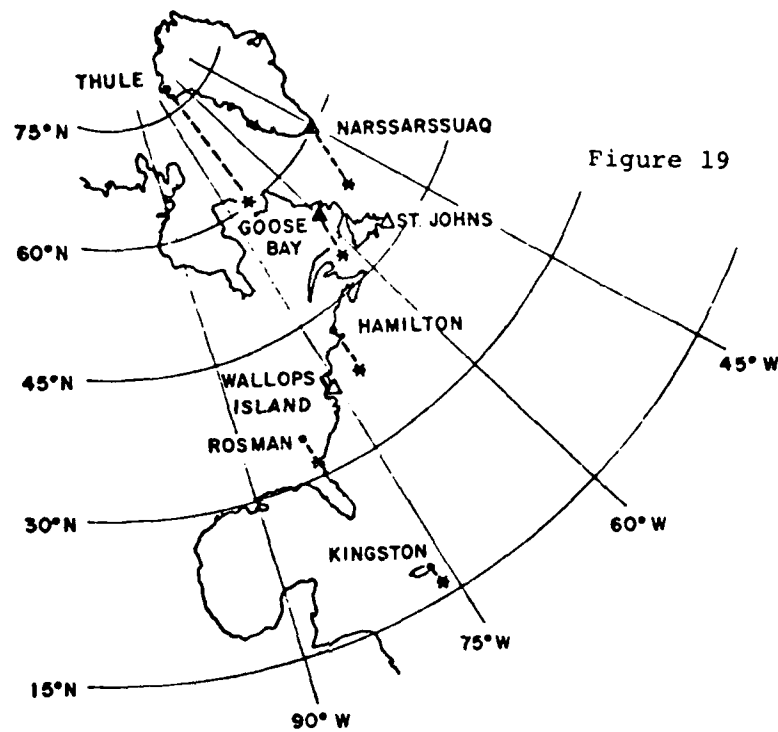
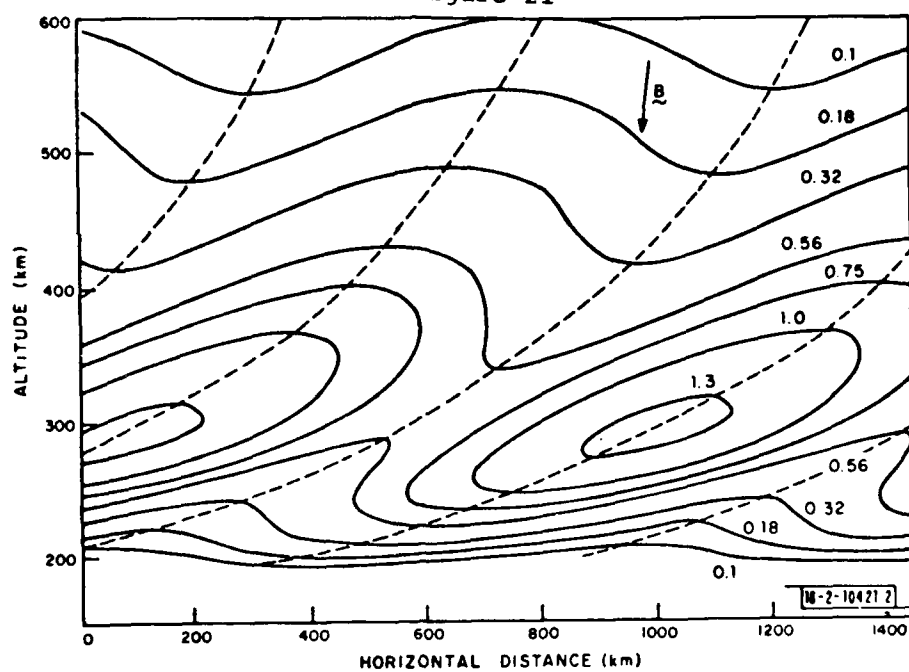


Figure 21



OBJECT 3133  
1000 EST

M-2-13400-1

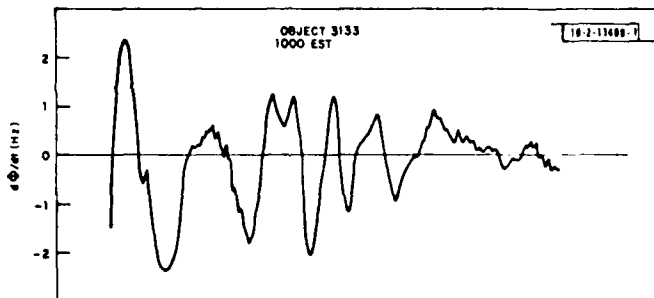
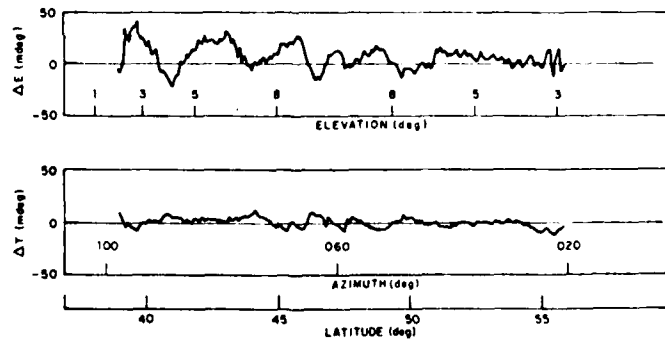
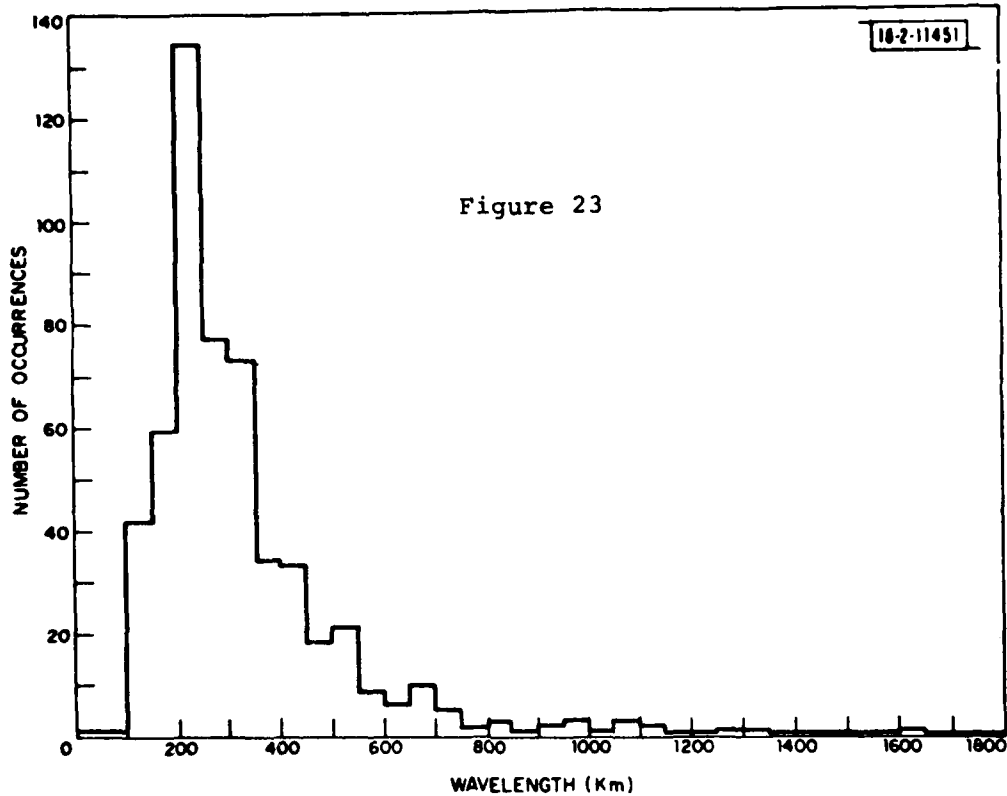


Figure 22



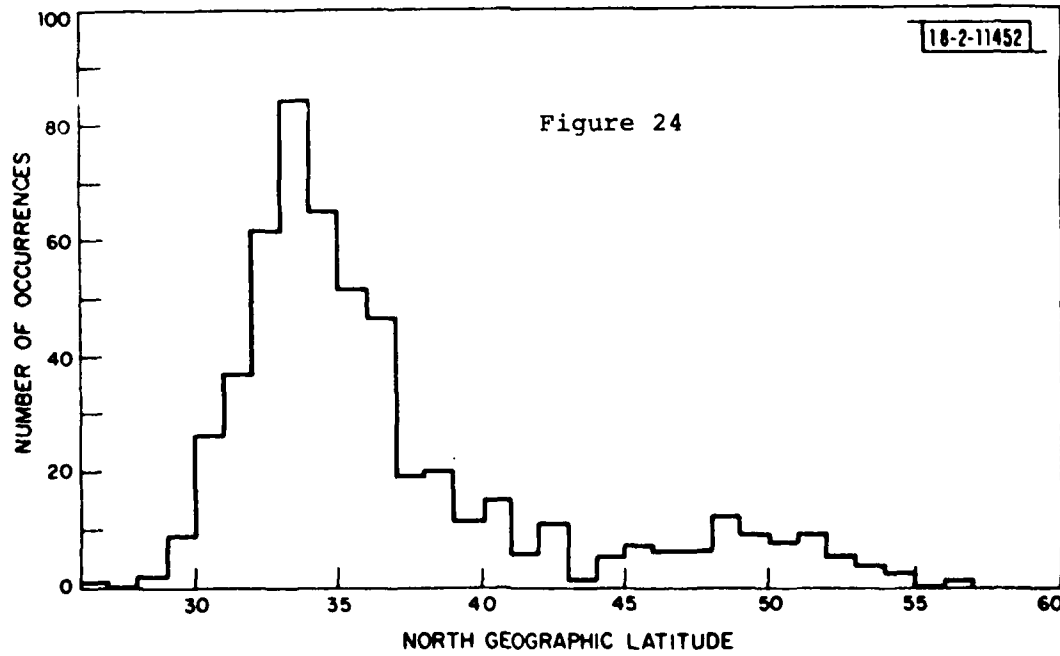
18-2-11451

Figure 23



18-2-11452

Figure 24



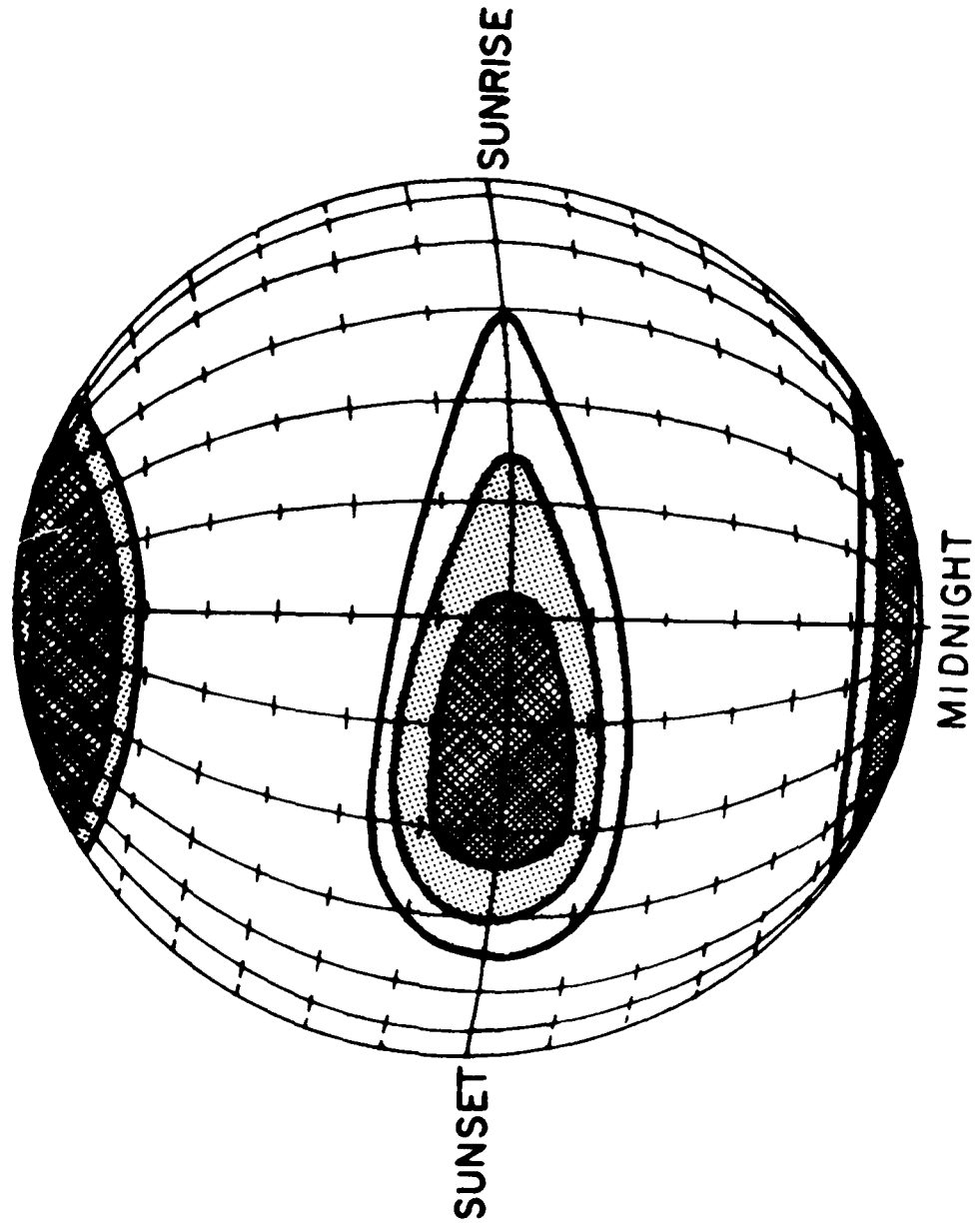


Figure 25

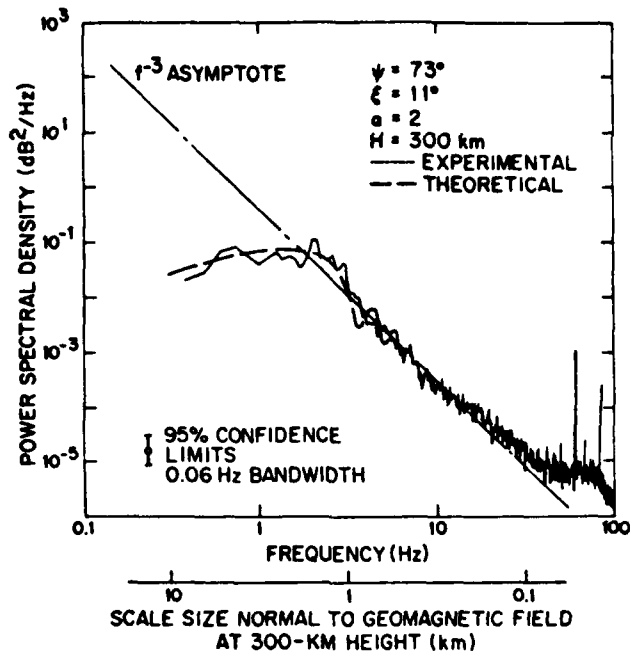


Figure 26

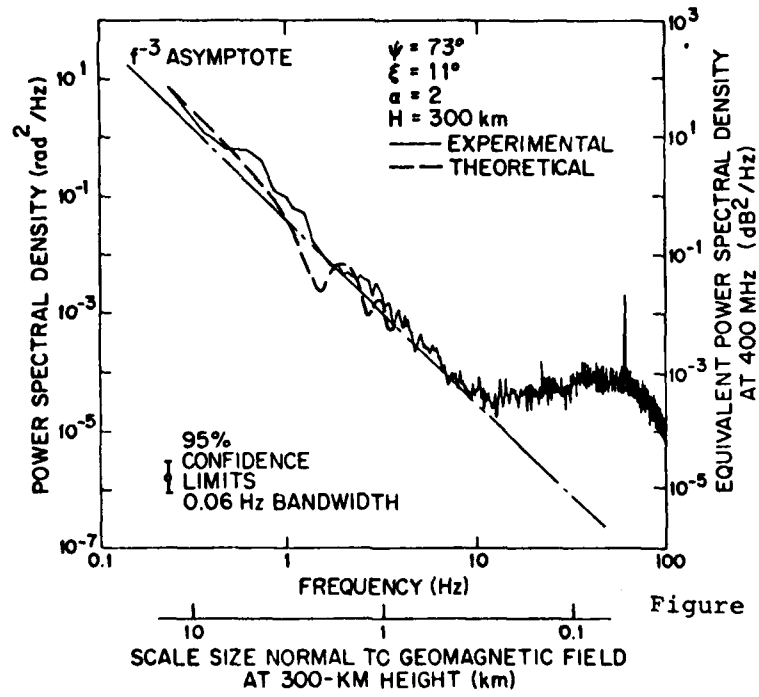


Figure 27

## EARLY RESULTS OF THE IONOSPHERIC EXPERIMENT OF THE APOLLO-SOYUZ TEST PROJECT

M. D. Grossi and R. H. Gay

Smithsonian Astrophysical Observatory, Cambridge, Massachusetts 02138

### 1. INTRODUCTION

A spacecraft-to-spacecraft doppler-tracking experiment was performed by the Smithsonian Astrophysical Observatory on the occasion of the Apollo-Soyuz Test Project (ASTP). Launched in orbit on July 15, 1975, the ASTP was the first joint USA/USSR space effort.

The experiment consisted of measuring, by means of doppler tracking, the relative velocity between the ASTP docking module (DM) and the Apollo command service module (CSM). The DM and the CSM both orbited at a height of approximately 200 km and kept a relative distance of about 400 km during the 24-hour period of data taking. The main scope in collecting relative-velocity data was to invert them into anomalies of the earth's gravity field with a threshold sensitivity of the order of 10 mgal in 10-sec integration time. In addition, by using the transmitter installed on board the DM as a dual-frequency beacon (operating at two-frequency-coherent carriers of 162 and 324 MHz), an ionospheric experiment was also performed, with differential doppler data collected in both DM-to-CSM and DM-to-earth paths. Figure 1 schematically represents the links used by the experiment.

The goals of the ionospheric experiment were as follows (Refs. 1-4):

- A. To measure the time changes of the columnar electron content between the two spacecraft, from which horizontal gradients of electron density at the height of 220 km (along the orbital path of the DM/CSM pair) could be derived.
- B. To measure the time changes of the spacecraft-to-ground columnar electron content, from which an averaged columnar content and the electron density at the DM could be derived under some simplifying assumptions. Because horizontal gradients at orbital heights are measured simultaneously, a secondary goal was to investigate the increase in accuracy obtained by performing these inversions.
- C. To observe traveling ionospheric disturbances (TID) with both the DM-to-CSM and the DM-to-earth links.
- D. To detect boundaries of turbulent regions of the ionosphere, such as the aurora oval and the equatorial region.

The data-collection phase of the experiment was highly successful. The DM-to-CSM link collected samples of differential doppler data over a period of nearly 14 hours from nine orbital revolutions on July 24. Through the courtesy of the Defense Mapping Agency, DM dual-frequency emissions were recorded on

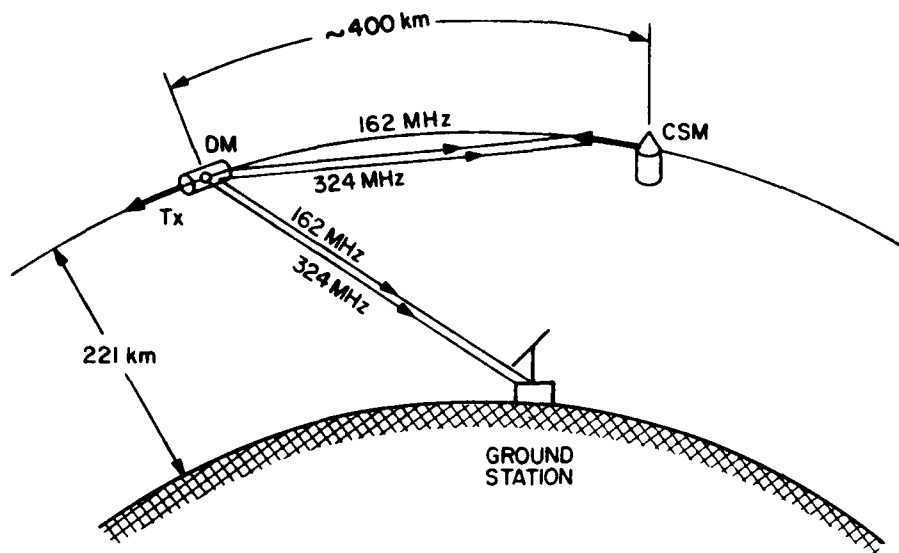


Figure 1. Measurement links of the ASTP doppler-tracking experiment.

earth by eight Tranet and Geoceiver tracking stations on 235 passes. Table 1 provides orbital data for both the DM and the CSM.

The resolution in the doppler measurements was  $1\sigma \approx 3$  mHz in 10-sec integration time, consistent with preflight expectations. The oscillators of the doppler links performed as specified, with stability of a few parts in  $10^{12}$  over a 10- to 100-sec integration interval.

Block diagrams of the instrumentation can be found in Reference 1. Figures 2 and 3 provide a schematic representation of the raw data utilized by the experiment and of the data reduction and processing flow adopted.

Table 1. Orbital data for DM and CSM (epoch 42617.008305567 MJD).

Orbital element	DM	CSM
Semimajor axis	6590.8184769 km	6590.8434884 km
Eccentricity	0.0011944815576	0.0012376262770
Inclination	51°770492247	51°765736753
True anomaly	98°984865652	97°558757298
Longitude of the ascending node	81°308688226	81°311408223
Argument of perigee	220°53048262	219°30088626

## 2. BASIC ALGORITHMS USED IN DATA REDUCTION

Let us define  $\delta\dot{\phi} = \dot{\phi}_1 - (f_1/f_2)\dot{\phi}_2$ , where  $\dot{\phi}_1$  and  $\dot{\phi}_2$  are the doppler shifts at the higher ( $f_1$ ) and lower ( $f_2$ ) frequencies of the link. In our case,  $f_1 = 324$  MHz and  $f_2 = 162$  MHz; therefore,

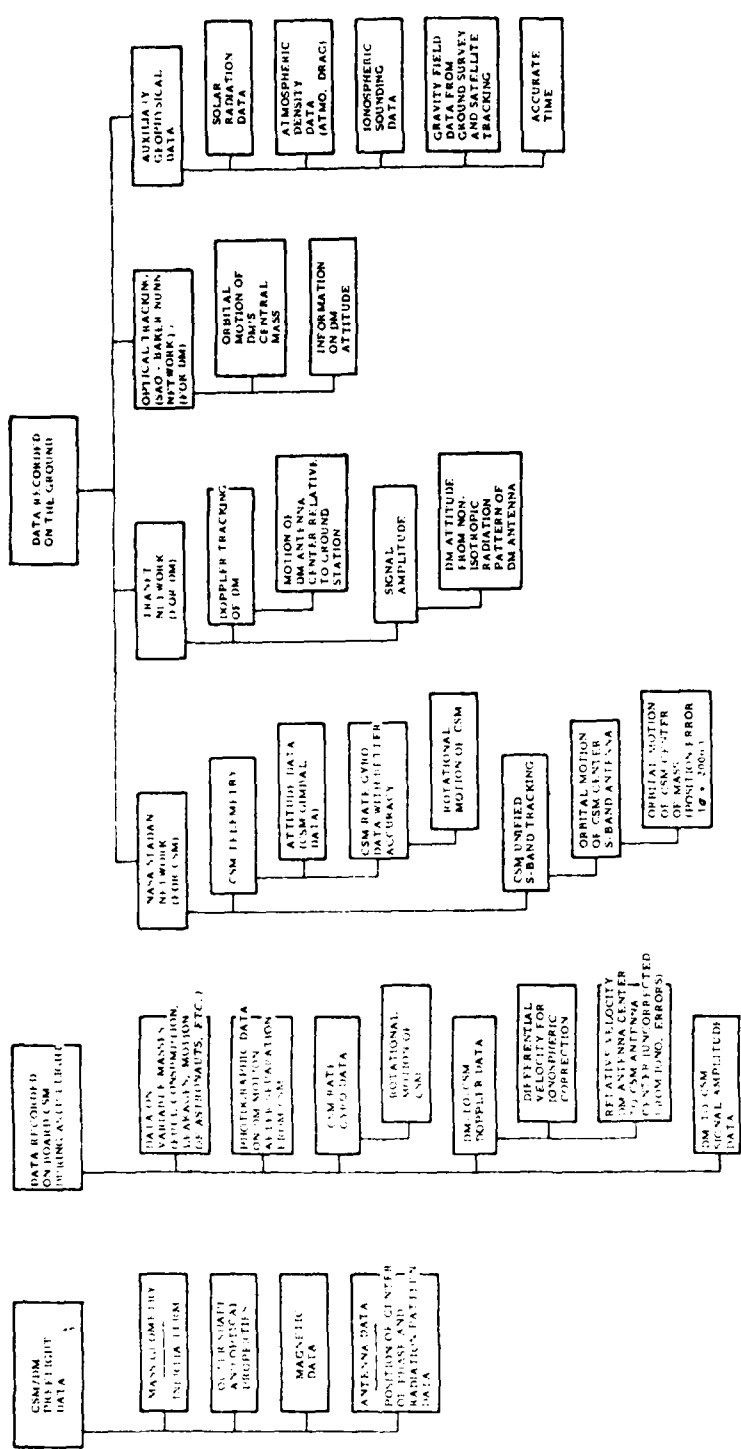


Figure 2: Block diagram of the raw data.

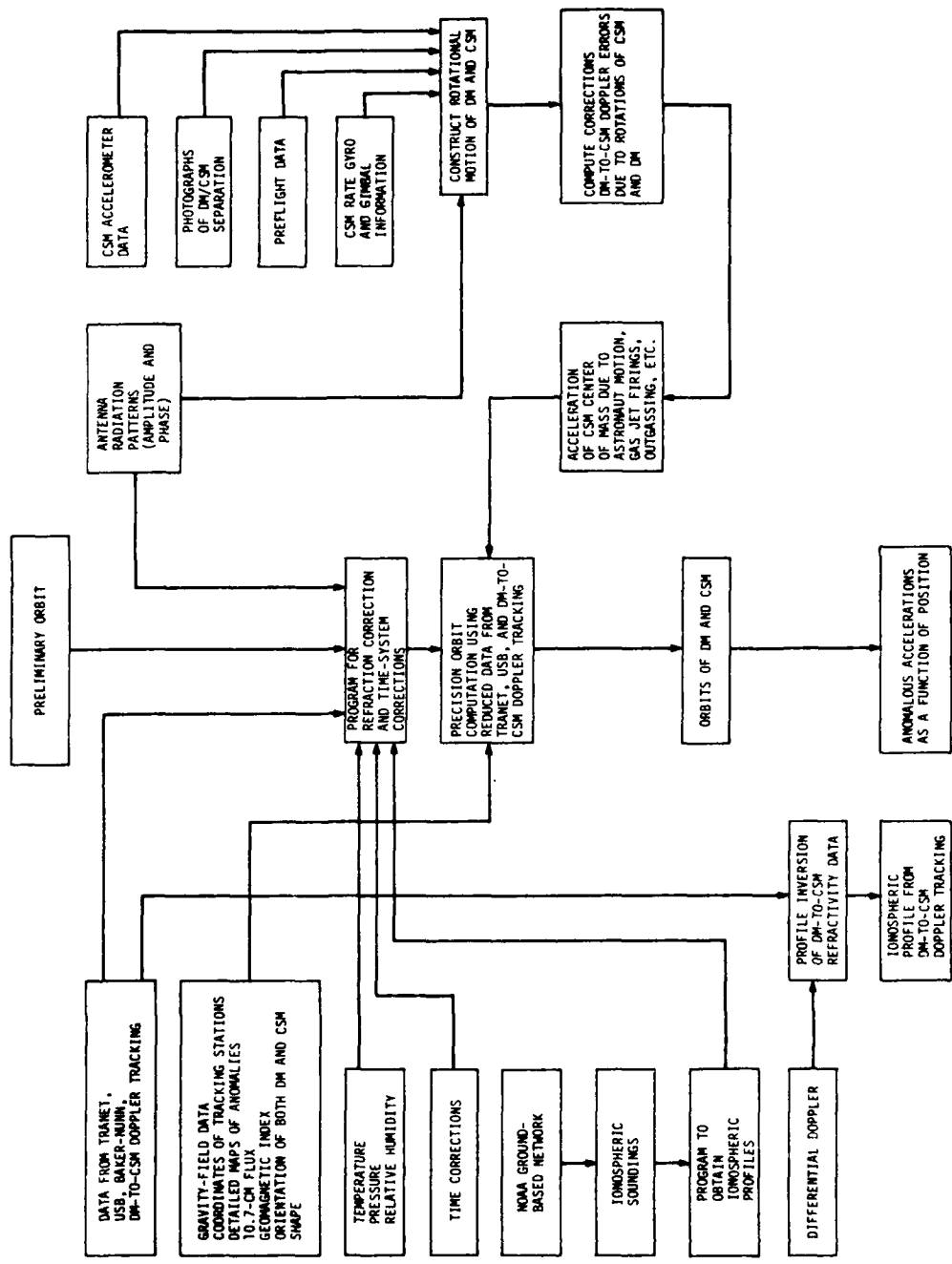


Figure 3. Simplified scheme of data reduction and processing.

$$\delta\dot{\phi} = \dot{\phi}_1 - 2\dot{\phi}_2 .$$

In the path from the DM to the CSM, the following relationship applies:

$$\delta\dot{\phi} = (40.3/2\lambda_1) [(1/f_2^2) - (1/f_1^2)] d/dt \int_{DM}^{CSM} N ds ,$$

where  $\lambda_1 = c/f_1$ ,  $c$  being the velocity of light in free space.

Under the assumptions that the two terminals of the link are in nearly coincident circular orbits and that the temporal variations of the ionosphere can be disregarded while the doppler samples are being taken, the differential doppler shift  $\delta\dot{\phi}$  is a measure of the electron-density gradients at the ASTP orbital altitude averaged over the DM-to-CSM separation  $\Delta x$ :

$$\overline{\frac{\partial N}{\partial x}} = \frac{\lambda_1 f_1^2 f_2^2}{40.3(f_2^2 - f_1^2)} \frac{\delta\dot{\phi}}{v_0 \Delta x} ,$$

where  $v_0$  is the common orbital velocity of the two terminals.

In DM-to-earth paths, the following relationships apply (see Figure 4 and Ref. 5):

$$\delta\dot{\phi}(t) = a_0 \left[ -\frac{\dot{z}_s}{\cos \phi_s} N_s + \left( \dot{r}_s + \frac{\dot{z}_s}{\cos \phi_s} \right) \bar{N} \right]$$

if horizontal gradients are neglected. When horizontal gradients are taken into account, we have (Ref. 5)

$$\delta\dot{\phi} = a_0 \left[ -N_s \frac{\dot{z}_s}{\cos \phi_s} + \bar{N}_x \left( \dot{r}_s + \frac{\dot{z}_s}{\cos \phi_s} \right) - \bar{N}_y \dot{y}_s - N_t \right] .$$

In these expressions,

$$a_0 = \frac{2\pi e^2}{m} \frac{\omega_1}{c} \left( \frac{1}{\omega_1^2} - \frac{1}{\omega_2^2} \right) , \quad \bar{N} = \frac{1}{z_s} \int_0^{z_s} N dz ,$$

and, for a planar approximation,

$$\bar{N}_x = \frac{1}{z_s} \int_0^{z_s} N dz + \frac{1}{z_s \sin \phi_0 \cos \phi_0} \int_0^{z_s} \frac{\partial N}{\partial x} z dz ,$$

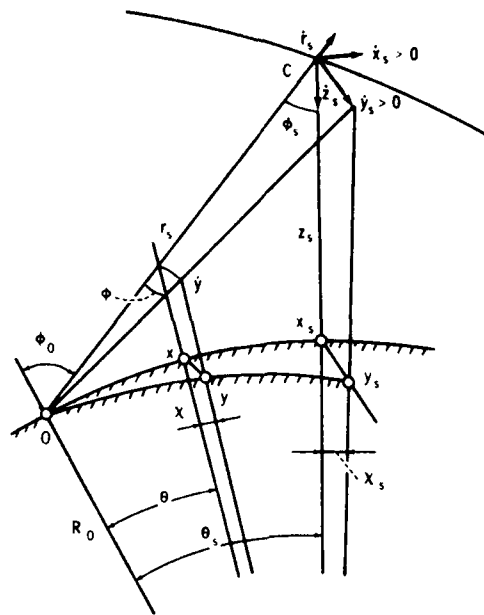


Figure 4. Geometry of space-to-ground observations.

$$\bar{N}_y = \frac{1}{z_s \cos \phi_0} \int_0^{z_s} \frac{\partial N}{\partial y} z \, dz , \quad N_t = \frac{1}{\cos \phi_0} \int_0^{z_s} \frac{\partial N}{\partial t} \, dz .$$

### 3. PRELIMINARY RESULTS OF DATA PROCESSING AND ANALYSIS

Figures 5 and 6 reproduce the DM-to-CSM differential doppler records obtained from revolutions 127 and 131. Table 2 gives the starting time of each orbit and the serial number of the frame-word recorded when the DM crossed the meridian containing the subsolar point (SSP). Each frame has 73 words, each 10 sec long, so that, for example, the start of revolution 126 corresponds to  $(47 \times 73 + 31) \times 10 = 34,620$  sec from reference time zero, which was set at the beginning of the link operation.

It can be seen that sharp horizontal gradients of electron density have been detected. As introduced in Section 2,  $\partial N / \partial x = 2.62 \times 10^5 \times \delta \phi$  (el m<sup>-3</sup>/m). The figures show that gradients up to  $\sim 10^6$  el m<sup>-3</sup>/m are not uncommon for a day such as July 24, which was magnetically quiet and was characterized by an electron density at 220-km height that varied from  $\sim 3 \times 10^9$  el/m<sup>3</sup> (night side) to  $\sim 5 \times 10^{11}$  el/m<sup>3</sup> (day side). Most of the gradients are encountered at the equatorial crossings and are most likely related to the equatorial F-layer irregularities.

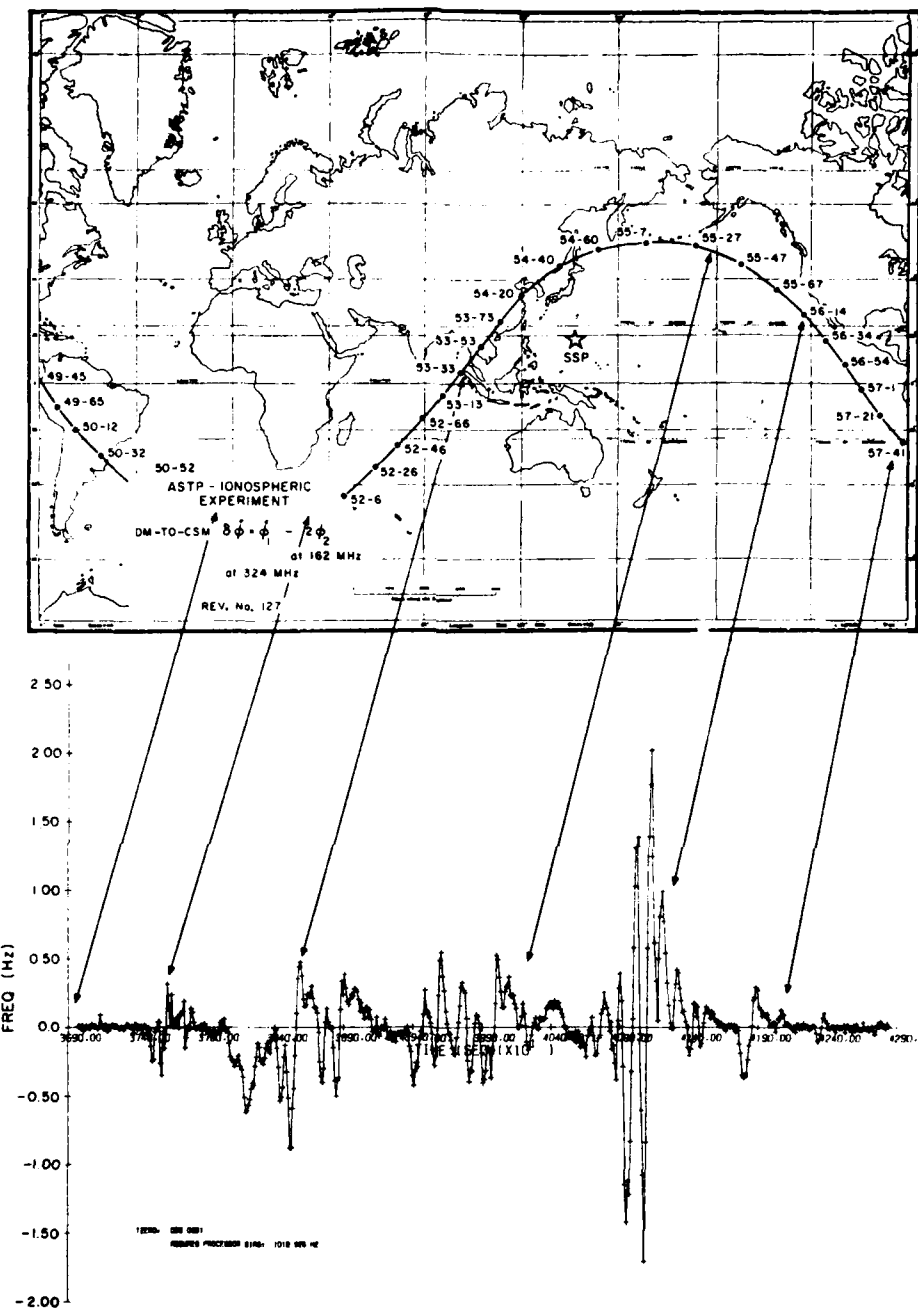


Figure 5. Map of revolution 127 with differential-doppler plot.

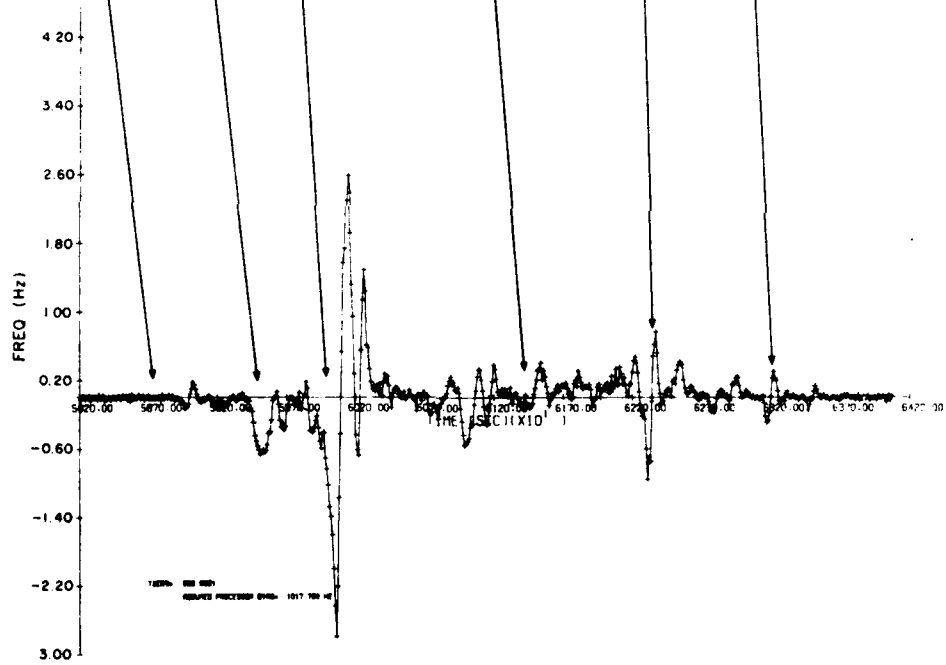
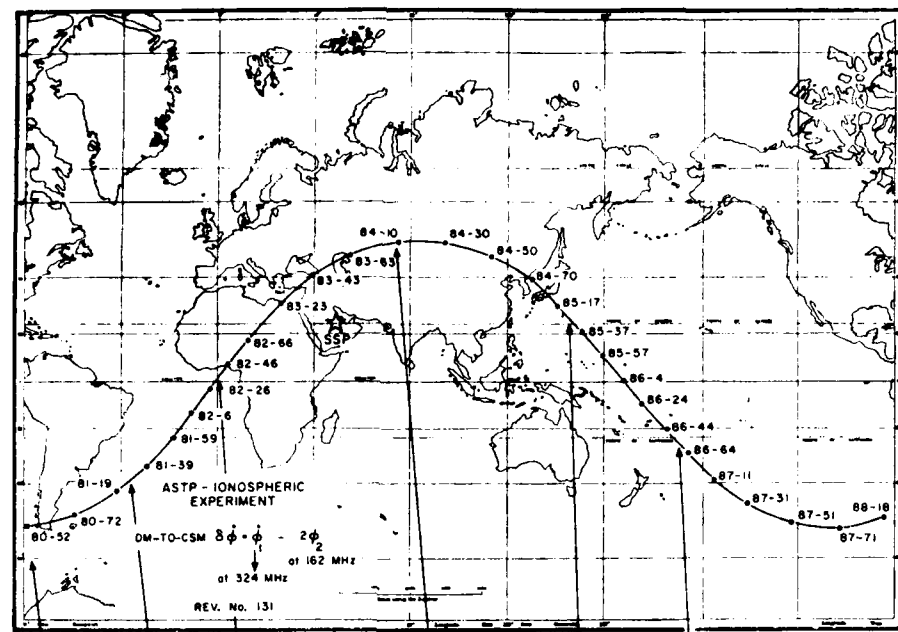


Figure 6. Map of revolution 131 with differential-doppler plot.

Table 2. Times of data take, July 24.

Revolution number	Revolution start time (GMT)	Frame-word at meridian crossing
126	0h56m	47-31
127	2 34	54-50
128	4 12	61-69
129	5 47	69-15
130	7 20	76-34
131	8 52	83-56
132	10 24	91-03
133	11 58	98-22
134	13 34	105-41

The nine-cycle waveform shown in Figure 5 is suggestive of a day-side TID characterized by the following parameters (preliminary model):

Apparent spatial wavelength along the orbital track at 220-km height:	~800 km
Estimate of the spatial wavelength as it would be observed from the ground:	690 km
Spatial extent along orbital track at 220-km height:	~7200 km
Estimate of peak-to-peak electron-density perturbation:	35%
Estimate of velocity:	~700 m/sec
Estimate of the period as it would be observed from the ground:	16 min

Data analysis still continues at this time, both for the data collected with the DM-to-CSM link and for the space-to-ground data collected by the ground-based network of stations that participated in the experiment.

#### 4. CONCLUSIONS

The ionospheric experiment on board the ASTP performed the first space-craft-to-spacecraft horizontal sounding of the ionosphere at a height of 220 km and acquired data that are expected to add new and useful information to the literature on ionospheric electron-density structures at a height that is important and that had never been probed before.

In addition, it is expected that the experiment will contribute to a better understanding of how horizontal gradients of electron density influence the accuracy of ionospheric columnar measurements performed by transmitting radio emissions from satellites to the earth.

#### 5. ACKNOWLEDGMENT

This work was supported in part by Contract NAS 9-13837 from the National Aeronautics and Space Administration.

## 6. REFERENCES

1. Grossi, M. D., Spacecraft-to-spacecraft ionospheric measurements on occasion of the Apollo-Sovuz Test Project. In Proceedings of the Beacon Satellite Investigations of the Ionosphere Structure and ATS-6 Data, Acad. Sci. USSR, Moscow, vol. 1, pp. 84-91, 1975.
2. Grossi, M. D., and Gay, R. H., Doppler measurements of the ionosphere on the occasion of the Apollo-Soyuz Test Project. Part I: Computer simulation of ionospheric-induced doppler shifts. Smithsonian Astrophys. Obs. Spec. Rep. No. 366, 54 pp plus appendix, 1975.
3. Gay, R. H., and Grossi, M. D., Doppler measurements of the ionosphere on the occasion of the Apollo-Soyuz Test Project. Part II: Inversion of differential and rotating doppler shifts. Smithsonian Astrophys. Obs. Spec. Rep. No. 367, 37 pp., 1975.
4. Gay, R. H., and Grossi, M. D., The ionospheric experiment of the Apollo-Soyuz Test Project. Presented at the American Geophysical Union Meeting, Madison, Wisconsin, September 1975.
5. Al'pert, Ja. L., On ionospheric investigations by coherent radiowaves emitted from artificial earth satellites. Space Sci. Rev., vol. 18, pp. 551-602, 1976.

STRUCTURE AND MORPHOLOGY OF THE MAIN PLASMA

TROUGH IN THE TOPSIDE IONOSPHERE

P.J.L. Wildman and R.C. Sagalyn

Air Force Geophysics Laboratory  
Hanscom AFB, MA

and

M. Ahmed

Regis College  
Weston, MA

The main trough is a region where thermal plasma density depletions are consistently observed at mid latitudes in the night side ionosphere. It is considered to indicate the boundary between regions of the ionosphere having different primary source processes. Firstly the low latitude ionosphere or plasmasphere, resulting principally from solar radiation, and secondly a high latitude region due primarily to magnetospheric particle precipitation. Characteristics of the main trough in the F region and topside ionosphere have been studied by several workers including Muldrew (1965), Sharp (1966), Rycroft and Thomas (1970), Tulunay and Sayers (1971), Wrenn and Raitt (1975). These studies have established the location of the trough, its variation with magnetic activity, its relation with the plasmapause position, concentrating on the night side.

In this paper a study of the morphology of several features of the main trough is presented, based on 3 year's data obtained from thermal plasma sensors flown on the ISIS-I and INJUN V satellites. Boom mounted spherical electrostatic analyzers were biased to measure positive ions on ISIS-I and electrons on INJUN V. The dayside trough is also examined and the trough structure, that is, its width, depth, equatorial and poleward gradients are determined as a function of local time and season, for  $K_p \leq 3$ . Additional plasma depletions observed on the dayside between  $L = 2$  and 4 at altitudes greater than 1500 km are also described.

## METHOD

In Figure 1 the orbital parameters for the satellites utilized are given.

It is seen that both are polar orbiting satellites and data is obtained throughout the topside ionosphere.

Approximately 1000 individual troughs were examined from 12,000 whole or partial orbits. A representative trough obtained on orbit 6864 is shown in Figure 2. It is shown to define the properties we have measured.

The equatorial edge of the trough, point a, is the location of the intercept of two lines drawn through the density just equatorward of the trough, and the equatorial trough wall, i.e. the midpoint of the knee.

The poleward edge, point d, is the intercept of lines drawn through the first ionization maximum in the precipitation region, and the poleward trough wall.

The width is taken to be the latitude range between points a and d.

The depth of the trough is defined for both its equatorial and poleward edge since the densities at points a and d and at the base b and c are frequently very different. The equatorial depth is the ratio of the density at a over the density at b. The poleward depth is the density at d over the density at c.

In order to minimize the effects of varying density with height normalized gradients were evaluated at the equatorial and poleward walls. Then the gradient at the equatorial edge is the density a minus density b divided by the latitude a minus latitude b all over the average density between points a and b.

Figure 3 illustrates the variability of individual troughs at different local times and altitudes. On the left side of the figure troughs measured within 2 hours of local noon at varying altitudes between 600 and 2300 km are illustrated. On the right side results obtained within 2 hours of midnight are given for 600 km and 3500 km. The nightside troughs tend to be broader and deeper than the dayside troughs.

The trough occurrence frequency as a function of local time is shown in Figure 4. The results for each hour of local time are based on data from at least 2 seasons. It is seen that in the night hours between 1900 hrs and 0400 hrs the occurrence frequency is high, >95%. After 0400 hrs the occurrence frequency decreases reaching a minimum of 48% around noon. This is followed by a steady increase to 1900 hrs. These nighttime results are in good agreement with results reported earlier by Tulunay and Sayers (1974). They concluded, however, that the trough was primarily a nighttime phenomenon. The difference in the daytime results is probably due to the selection process for each study. Tulunay and Sayers used the criterion that the ratio of the maximum density to minimum density in the trough must be greater than 2:1 for a trough to be noted. It will be seen from our results on trough amplitude in Figure 9 that this criterion would eliminate most of the midday troughs which we have identified, where values as low as 1.25:1 are identified.

#### TROUGH LOCATION

The mean location of the equatorial edge of the trough as a function of time is shown for the winter and summer seasons on Figure 5. It is seen in the polar plot that the seasonal variation of the trough position at a given local time is small, within the limits of the standard deviation indicated on the figure except for the hours between 6 and 9 am. In the summer the invariant latitude of the trough increases steadily between 0400 and 1000 hrs. In the winter the trough position remains close to the nighttime value of about  $60^{\circ}$  up to 0900 hours. This is followed by a rapid increase between 0900 and 1000 hrs. These differences are considered to be due to the varying tilt angle of the sun with season.

The relatively high invariant latitude of the trough on the dayside around  $72^{\circ}$  near local noon should be noted. Throughout the day and night the trough is found at the equatorward edge of the auroral precipitation zone.

The next few figures show some results on the trough structure. First the width - In Figure 6, the trough width exhibits a simple diurnal variation with a maximum between 0300 and 0500 hours and a minimum of about  $4^{\circ}$  around local noon. It then increases gradually to the early morning maximum. There is a pronounced seasonal variation in the night hours. For example at 0500 hours the width is nearly  $12^{\circ}$  in winter and  $5^{\circ}$  in summer. Spring and

fall values lie between these limits. The strong influence of solar radiation on the width is evident from the onset times of the rapid decrease in width in the morning hours in each season.

The standard deviations for all trough parameters are large. This is illustrated in Figure 7 where the mean width data for summer and winter shown in the previous slide, is given with calculated standard deviation. The standard deviation in width is approximately  $\pm 2^{\circ}$ . We have searched for factors contributing to the standard deviation including altitude, Kp, previous magnetic history and have been unable to account for the variability. It probably reflects the complicated plasma processes contributing to the formation of the trough including plasma convection, E-fields and charge exchange.

#### TROUGH GRADIENTS

Plasma density gradients at the equatorial edge of the trough as a function of local time for each season are shown in Figure 8. The amplitude of the diurnal variation is greatest in winter when there is observed an 80% change in density per degree latitude at 20:00 hrs and a minimum value of 25% per degree latitude around local noon. In summer the gradients are reduced with a maximum of 45% per degree at 2000 hrs and a minimum of 17% per degree at 1300 hrs.

The diurnal and seasonal variation of the poleward gradients are similar to the results obtained at the equatorwards edge (Figure 9). The most noticeable difference is that the poleward gradients are consistently found to be about 30% higher in the night hours.

#### TROUGH DEPTH

The depth or amplitude of the trough, that is, the ratio of the plasma density at the trough edge to the value at the base of the trough wall has been evaluated for both poleward and equatorial edges. It is seen in Figure 10 that the amplitude is a minimum around local noon and a maximum near midnight. The depth changes by a factor of 10 throughout the day in winter and by a factor of 2.3 in summer. The results for spring and fall lie between these limits.

Similar results were obtained for the amplitude at the poleward edge with the exception of winter nights when the ratios are 2 to 3 times smaller than for the equatorial depth. This

reflects primarily the smaller contribution of solar radiation to the ionization in the polar regions on winter nights.

In this paper we have presented only results for low  $K_p$ , ( $K_p \leq 3_0$ ). We have carried out a similar analysis of a smaller sample of high  $K_p$  data. The results on the trough structure are found to be surprisingly similar to the results at low  $K_p$  with the location moved to lower latitudes.

It is instructive to relate these results on the trough location to independent measurements of the plasmapause location from the same satellite by Brace and Theis (1974), and by Miller (1974) as well as with other higher altitude measurements of the plasmapause.

Brace and Theis reported gradients in electron density above 2000 km on the dayside from ISIS-I. They associate these gradients with the plasmapause location. We observe similar gradients with our own ion probe on ISIS-I on over 60% of the data near this location at altitudes above 2000 km. Figure 11, for example, gives results for the midday pass 6325. A low latitude density gradient is seen at about  $L = 3$  together with a high latitude trough observed at  $78^\circ$  latitude. We consider that the low latitude gradients indicate the partial filling of flux tubes at low latitudes. The high latitude dayside trough would not normally be seen in the analysis carried out by Brace and Theis since they used a spatial resolution of about  $9^\circ$  in their analysis.

In Figure 12, we compare the equatorward edge of the trough with the plasmapause location observed by others. In addition, the cross-hatched region on the dayside (between  $L = 2$  and 4) indicates the location of low latitude high altitude depressions mentioned above. It is seen that on the nightside the trough location agrees with the plasmapause location reported by other workers. On the dayside two regions of plasma depletion are observed. First the high latitude trough observed at all altitudes located at the equatorward edge of the cusp. Second, plasma depletions between  $L = 2$  and 4 at altitude  $> 1500$  k. Since they occur on lower  $L$  shells than the normal plasmapause we consider that they represent partial filling of plasmasphere flux tubes as described by Banks and Doupinik (1974).

Finally we must consider how these data add to our understanding of the formation of the trough. Since they are real data, gathered on a global scale over several years we cannot dismiss them if they do not fit current theories of the formation and maintenance of the trough. In particular the existence of daytime troughs means that solar UV cannot always be the major determining

cause of trough formation. Since the daytime trough has a lower probability of occurrence and is also less pronounced than at night we must conclude that competing processes control the plasma density and motion at different times, and that these can sometimes overcome the constant replenishment of ionization by solar UV on the dayside. The most important of these is convective drift across the polar cap to supply plasma at night.

Other processes which influence the trough and its location include, on the nightside: 1. Auroral particle precipitation, causing ionization to give the poleward boundary; 2. The escape of light ( $H^+$  and  $He^+$ ) along open field lines to give depletion of plasma within the trough; 3. The presence of electric fields within the trough regions. This causes bulk motion of the plasma (direct depletion) in addition to Joule heating as this flow takes place. This heating increases the reaction rate of  $O^+ + N_2 \rightarrow NO^+ + N$ , further reducing the total ionization present above the F region peak.

The processes induced by E fields become very important in the formation of the trough at latitudes and altitudes where  $H^+$  is not the dominant ion, and where the more classical picture of ion escape along magnetic field lines is usually invoked as the major cause of ion depletion.

On the dayside the poleward edge is again set by the particle precipitation. At the equatorward edge, however, the location shown in Figure 12, around  $L = 8 - 12$  for several hours each side of local noon, fits more closely with the cusp location than with the plasmapause.

#### CONCLUSION

1. The trough is found to exist at all local times. It is not only a nighttime phenomenon. It is consistently found at the equatorial edge of the precipitation zone.

2. Significant variation of the widths, amplitude, and gradients at both the equatorward and trough wall are found with local time and season. Maximum values are observed on winter nights.

#### REFERENCES

Banks, P.M. and J.R. Doupinik, 1974, "Thermal proton flow in the plasmasphere: The morning sector", *Planet. and Space Sci.*, 22, p. 79-94.

Brace, L. and R.F. Theis, 1974, "The behavior of the plasmapause at mid-latitudes: ISIS I Langmuir probe measurements", J. Geophys. Res., 79, p. 1871-1884.

Muldrew, D.B., 1965, "The main electron trough during the rising solar cycle", J. Geophys. Res., 70, p. 2635-2650.

Rycroft, M.J. and J.O. Thomas, 1970, "The magnetospheric plasma-pause and the electron density trough at the Alouette I orbit", Planet. and Space Sci., 18, p. 65-80.

Sharp, G.W., 1966, "Mid-latitude trough in the night ionosphere", J. Geophys. Res., 71, p. 1345-1356.

Tulunay, Y. and J. Sayers 1971, "Characteristics of the mid-latitude trough as determined by the electron density experiment on Ariel III", J. Atmos. and Terr. Phys., 33, p. 1737-1761.

Wrenn, G.L. and W.J. Raitt, 1975, "in-situ observations of mid-latitude plasma associated with the plasmapause", Ann. Geophys., 31, p. 17-28.



Figure 1

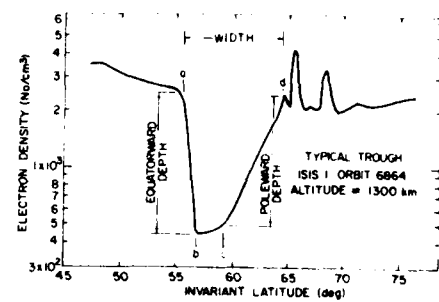


**Figure 2**

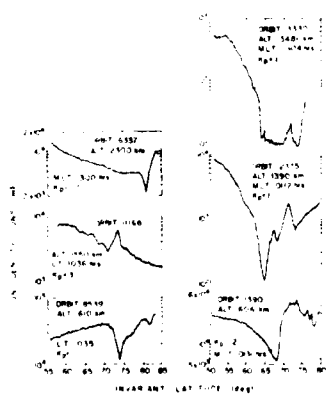
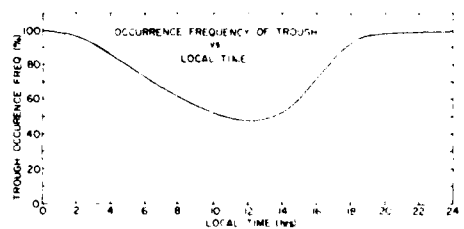
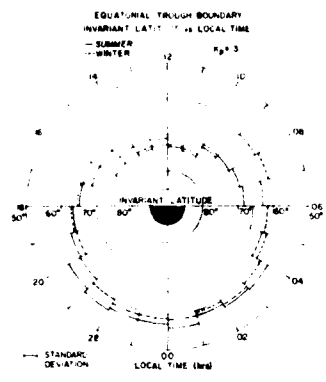


Figure 3  
Trough Variability



**Figure 4**



**Figure 5**

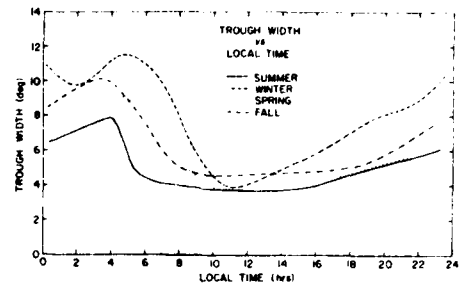


**Figure 6**

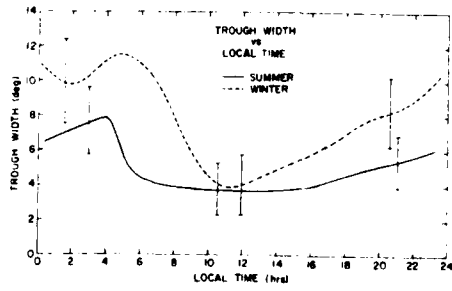


**Figure 7**

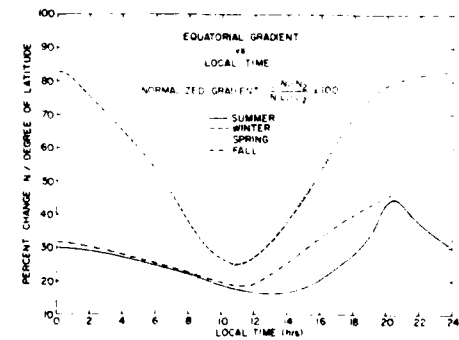


**Figure 8**

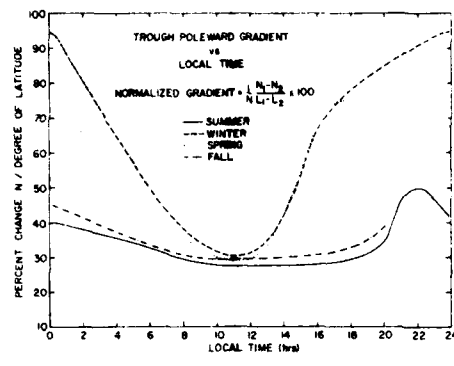


Figure 9

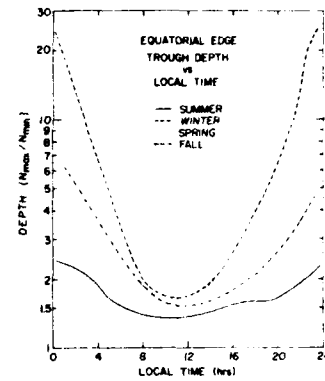


Figure 10

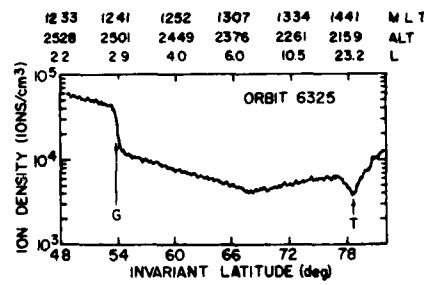


Figure 11  
Trough and Low Latitude Gradient

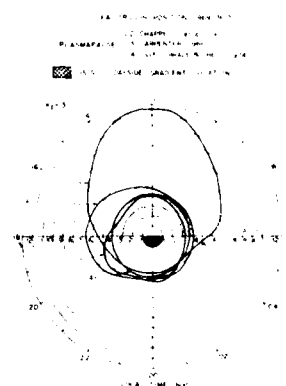


Figure 12

EARLY RESULTS ON INTASAT BEACON DATA RECORDED AT EL  
ARENOSILLO (SPAIN)

José L. Sagredo  
INTA  
Spain

ABSTRACT

The INTASAT satellite, equipped with a radio beacon transmitter at frequencies of 40.0100 MHz and 41.01025 MHz, was launched on November 15, 1974 into a sun-synchronous, nearly circular orbit, with an inclination of 101.7° and an altitude of 1460 Km.

A receiver installed in El Arenosillo (37.1°N, 353.57°E) records INTASAT beacon data for two orbits per day, one in the local morning (~ 0900 LT) and the other later in the evening (~ 2100 LT). The recording time of the latter which is roughly the same during the whole year sweeps along the year the region of solar zenith angles between 80° and 110° where important gradients of electron density are to be expected.

Faraday rotation data recorded during the equinox periods March 2 to April 4, 1975 and September 11 to November 17, 1975 have been analyzed and the vertical ionospheric electron content obtained are shown as a function of the solar zenith angle. Apart from a sharp decrease of electron content of about 40% which occurs during the days 19/20 May, the ionospheric electron content at solar zenith angles of about 60° appears to decrease by about 1% per degree of SZA.

In the records of El Arenosillo it is not unusual to observe inversions of the apparent Faraday rotation angle, specially in the northern end of the records which roughly correspond to a subionospheric latitude of about 40°. Using linearized propagation theory, it is shown in the paper that a Northern gradient of electron density must exist to account for the existence of such inversions.

1. INTRODUCTION

The INTASAT satellite is a sun-synchronous orbiting satellite equipped with a radio-beacon transmitter.

The beacon transmits continuous unmodulated plane polarized radiowaves at frequencies 40.0100 MHz and 41.01025 MHz. The satellite was launched on November 15, 1974 into a nearly circular orbit at an altitude of 1460 Km, inclination 101.7°. The equator

crossing in the North to South direction occurs at 0835 LT.

The signals from the beacon are recorded in El Arenosillo ( $37.1^\circ\text{N}$ ,  $353.57^\circ\text{E}$ ) during two passes per day. Due to the characteristics of the INTASAT orbit, the two passes recorded occur nearly at the same local time during the whole year. The pass recorded in the morning ( $\sim 0900$  LT) is in the North to South direction while the orbit recorded in the late local evening ( $\sim 2100$  LT) corresponds to a South to North pass.

The data recorded at a single station from a low orbiting satellite such as the INTASAT do not allow a good coverage of local time. At El Arenosillo the evening recordings occur at a time not far from the local dusk, and data recorded along the year for these orbits sweep the zone of solar zenith angles between  $80^\circ$  and  $110^\circ$  at ionospheric F-region heights where important gradients of electron content are to be expected.

The range of latitude covered by the data lies between  $32^\circ\text{N}$ - $42^\circ\text{N}$ .

## 2. DATA REDUCTION

The polarization of a plane polarized radiowave which propagates through a non-isotropic medium such as the Ionosphere rotates continuously (Faraday effect). The total angle rotated by the wave polarization plane on its way through the ionosphere from the satellite to the receiver is given, in linearized theory, by

$$\Omega = \frac{K}{f^2} \int_0^h NH \cos\theta \sec\chi dh \quad (1)$$

where  $f$  is the frequency of the radiowave,  $N$  the electron density of the ionospheric plasma,  $H$  the earth's magnetic field intensity,  $\theta$  the angle between the earth's magnetic field and the wave normal,  $\chi$  the angle between the ray path and the local vertical and  $K$  a constant of value  $2.97 \times 10^{-2}$  in MKS units, and the integral is extended from the ground to the altitude of the satellite.

The above expression can be simplified by taking the mean value along the propagation path of the slowly varying quantity  $H \cos\theta \sec\chi$ .

Thus

$$\Omega = \frac{K}{f^2} \bar{M} N_T \quad (2)$$

where  $\bar{M} = \overline{H \cos\theta \sec\chi}$  and  $N_T = \int_0^h N dh$  is the vertical electron

content in a column of unit cross section up to the satellite height.

Due to the Faraday rotation the signals recorded appear modulated in amplitude and a fading null is observed every time that the total angle rotated by the polarization plane has increased or decreased by  $\pi$  radians. On a record several fading nulls are observed and therefore relative variations of the rotation angle can be measured directly. To compute the total electron content from equation (2) the absolute values of  $\Omega$  are needed and these cannot be read on the records. To overcome this difficulty two close frequencies,  $f_1$  and  $f_2$ , are emitted by the beacon and at the point at which a fading null of the two frequencies coincides in time (coincidence), the differential Faraday rotation between the two frequencies is an integer of  $\pi$  radians.

At any point, the rotation undergone by the polarization plane of the upper frequency ( $\Omega_{f_2}$ ) can be expressed as a function of the differential Faraday rotation between the two frequencies by

$$\Omega_{f_2} = \frac{f_1^2}{f_2^2 - f_1^2} (\Omega_{f_1} - \Omega_{f_2}) \quad (3)$$

At the point of coincidence the differential Faraday rotation has the value  $n\pi$  and  $n$  takes usually an integer value between 1 and 4. Thus at this point the absolute rotation angle  $\Omega_{f_2}$  is

$$\Omega_{f_2} = \frac{f_1^2}{f_2^2 - f_1^2} n\pi$$

For the INTASAT beacon ( $f_1 = 40$  MHz,  $f_2 = 41$  MHz)

$$\Omega_{41} = 19.75 n\pi \quad (4)$$

If no coincidence is seen on the record, its position can be determined by fitting a straight line of slope  $\frac{1}{f_2^2 - f_1^2}$  to the differential Faraday rotation for each null, in the way described by Klobuchar and Aarons (1968) or of undetermined slope as described by Kersley and Taylor, (1974).

Once the appropriate value of  $n$  has been determined, the rotation  $\Omega_{41}$  at the coincidence is known (eq.4) and the corresponding angle of rotation for the successive nulls of the record are obtained simply by adding or subtracting  $\pi$  radians starting from that of

the coincidence.

The integer  $n$  is unambiguously obtained in most cases by comparing the intervals of time between consecutive fading nulls with those obtained if no horizontal gradients of total electron content occur ( $dN_T/dt \equiv 0$ ) (Crooker, 1970).

The method of determining  $n$  is described with the aid of figure 1. Let  $\Omega(t)$  be the total rotation of the polarization plane. The semi-period of the modulated signal obtained in the register, i.e. the time interval between consecutive nulls is given by

$$P = \frac{\pi}{|d\Omega/dt|}$$

which using equation (2) gives

$$P = \frac{\pi f^2}{k} \frac{1}{|N_T(d\bar{M}/dt) + \bar{M}(dN_T/dt)|}$$

If no horizontal gradients of total electron content occur, the above expression becomes

$$P^*(n) = \frac{\pi f^2}{k} \frac{\Delta t}{N_T^*(n) |\Delta \bar{M}|}$$

where  $N_T^*(n)$  is the columnar electron content obtained from equation (2) corresponding to a point of occurrence of a fading null at  $t = t^*$  where  $\Omega$  takes successively the values given by equation (4) for  $n = 1$  to 4.

In figure 1(b) the measured values of  $P$  for each null corresponding to one of the frequencies are plotted as a function of subionospheric latitude together with the curves  $P^*(n)$  for different values of  $n$ . Comparing these curves it is possible in most cases to select the curve  $P^*(n)$  which best fits to the experimental curve  $P$ , thus allowing the identification of the appropriate value of  $n$  to be used in equation (4).

When the slope of the  $P$  curve differs sensibly from that of the  $P^*(n)$  curves, a horizontal gradient of electron density exists. For example if, as in figure 1(b),  $dP/d\theta > dP^*/d\theta$ , the electron density increases toward the south. As the time  $t^*$  is taken at the northern end of the record, the appropriate value for  $n$  is  $n = 1$  which corresponds to the upper curve.

### 3. EXPERIMENTAL RESULTS

Over sixty orbits of Data recorded at Arenosillo during the periods March 2 to April 4, 1975 and September 11 to November 17, 1975 have been analyzed. Figure 2 shows examples of the analysis performed on two orbits. In the lower orbit the period of the fading nulls as measured in the records (curve +---+) fits well to one of the curves obtained assuming constant electron content (curve ▶-▶-▶), indicating that the value of  $n$  corresponding to this curve is the appropriate to use in equation 4. In the orbit corresponding to the upper curves the slope of the curve for the measured periods is greater than that for the curves with constant electron content, indicating the existence of a southern gradient of electron density. As the constant electron density was taken at a northern point of the record the upper curve (▶-▶-▶) is selected for the determination of the integer  $n$ .

It has to be pointed out that in some orbits it is not easy to identify the curve that fits best to the data. In such cases the selection of  $n$  is done by comparing with similar orbits of previous days.

Figure 3 shows the vertical electron content for the morning orbits of the first period analyzed, as a function of the peak F region solar zenith angle ( $\chi$ ). In this figure straight lines have been fitted to the data, which indicate a decrease of about 1% of total electron content per degree of solar zenith angle. Interesting in these data is the observation of a sharp decrease of about 40% of total electron content during two days (19/20 May).

Data for the same period corresponding to the evening passes are shown in figure 4. Here the solar zenith angle at the F region peak is greater than  $100^\circ$ , and therefore the zone sounded is in the shadow. The scattering of the data is somehow greater than the corresponding for the morning data, but the decrease in electron density during the days 19/20 May is also apparent in coincidence with the morning data. Important diurnal changes in total electron content have been reported in several works. In the present case, the decrease occurs very neatly between two periods for which the total electron content as a function of solar zenith angle repeats itself during several days. It is to be noted that the planetary

conditions do not show any important change during the days under study:  $\Sigma K_p = 18+$  for May 19 and  $\Sigma K_p = 23$  for May 20; in previous days the index range from  $\Sigma K_p = 36-$  to  $22-$ , and the following day corresponds to a rather quiet day with  $\Sigma K_p = 6-$ .

Figures 5 and 6 show examples of the total electron content deduced from several orbits as a function of latitude. They corresponded to orbits registered in the morning and evening respectively.

During the second period analyzed (September 11 to November 17) only the morning orbits provide sufficient data for analysis. The variation of total electron content as a function of solar zenith angle is shown in figure 7. The scattering of the data is somehow greater than that for the corresponding data of March/April (figure 3). The straight line fitted to the data indicates again a decrease of about 1% of total electron content per degree of solar zenith angle.

In the records of Arenosillo it is not unusual to observe inversions of the sense of rotation of the signal. These inversions which normally appear in pairs occur in the northern end of the record where the  $\bar{M}$  factor takes small values ( $< 10$  ampere-turns/m), indicating that these inversions are due to critical propagation conditions rather than to large local gradients of electron density. However gradients of electron content must exist since the condition for inversion is

$$\frac{\Delta N_T}{N_T} + \frac{\Delta \bar{M}}{\bar{M}}$$

Thus on a Northbound orbit ( $\bar{M}$  decreases) the gradient of electron content must be positive ( $\Delta N_T > 0$ ) whereas on a Southbound orbit this gradient has to be negative ( $\Delta N_T < 0$ ).

Figure 9 shows examples of inversions in two orbits. The upper record corresponds to a north to south pass and the lower is a south to north pass. In both cases the inversion occurs in the northern end of the record and typical size of the region where the inversion occurs is of the order of 200 Km at F-peak heights.

#### References

- CROOKER, U.S. (1970) J. Atmosph. Terr. Phys. 32, 179.  
KEPSLEY, L. and TAYLOR, G.N. (1974). J. Atmosph. Terr. Phys., 36, 93  
KLOBUCHAR, J.A. and AARONS, J. (1968). Annls. Géophys. 24, 885.

- - - - -

### FIGURE CAPTIONS

Fig.1 - Illustrative description of the method for determining the absolute rotation of the polarization of a radiowave. See text.

Fig.2 - Examples of analysis of two INTASAT passes recorded at Arenosillo.

+---+--- Periods of fading nulls

->->->- Periods of fading nulls assuming constant electron content.

-□-□-□-

-◆-◆-◆- Solar zenith angle at the satellite height.

-▼-▼-▼- Solar zenith angle at the F region peak.

Fig.3 - Total electron content versus solar zenith angle for the morning passes during the period 2 March/4 April 1975.

Fig.4 - Total electron content versus solar zenith angle for the evening passes during the same period.

Fig.5 - Examples of total electron content versus latitude for several morning passes during the same period.

Fig.6 - As for Fig.6 for evening passes.

Fig.7 - Total electron content versus solar zenith angle for the morning passes during the period 11 Sept./17 Nov 1975.

Fig.8 - Examples of records of two orbits. The upper record is a south to north pass on April 1976 and the lower pass a north to south pass on 17 April 1976. The upper part of each orbit corresponds to  $f = 40$  MHz and the lower to  $f = 41$  MHz.

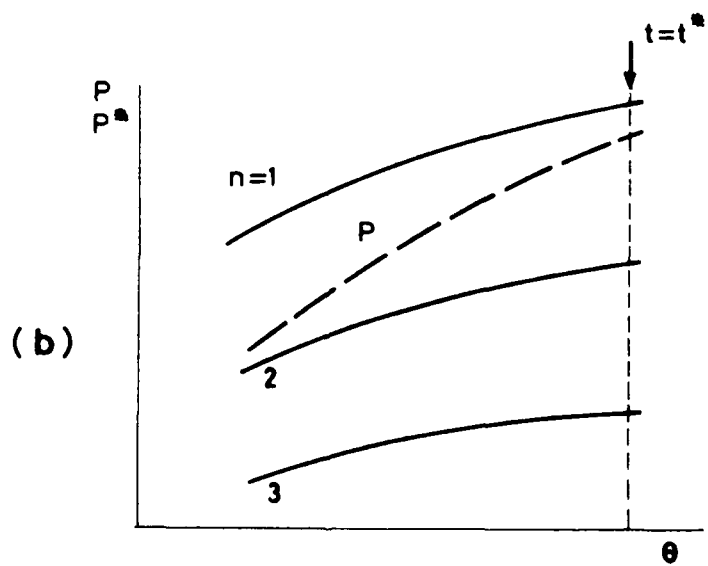
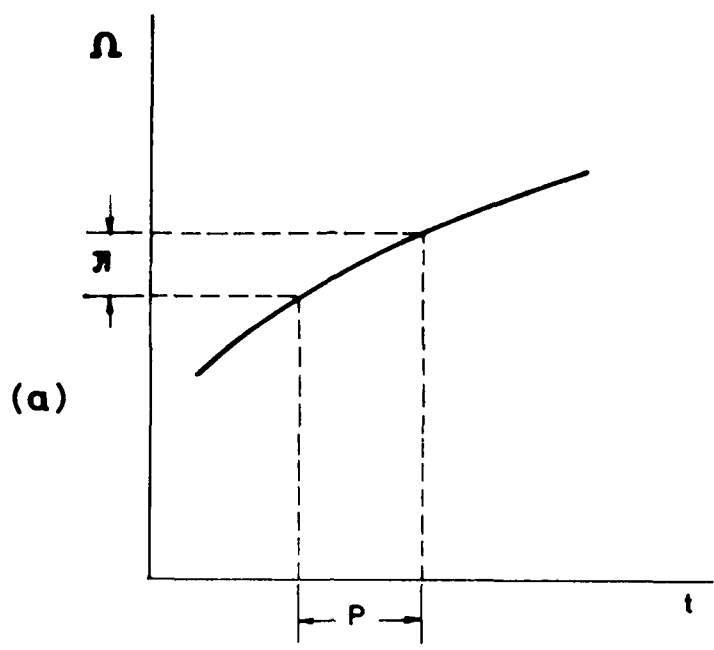


FIGURE 1

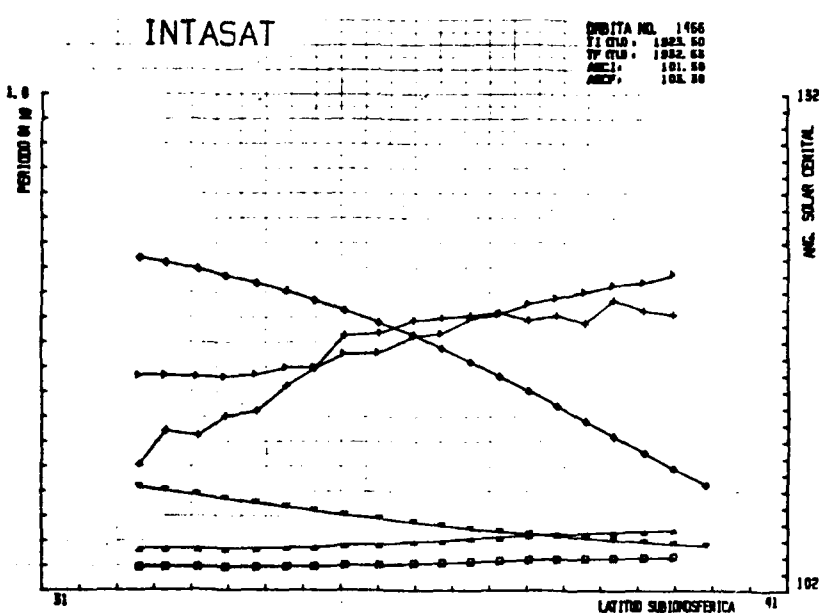
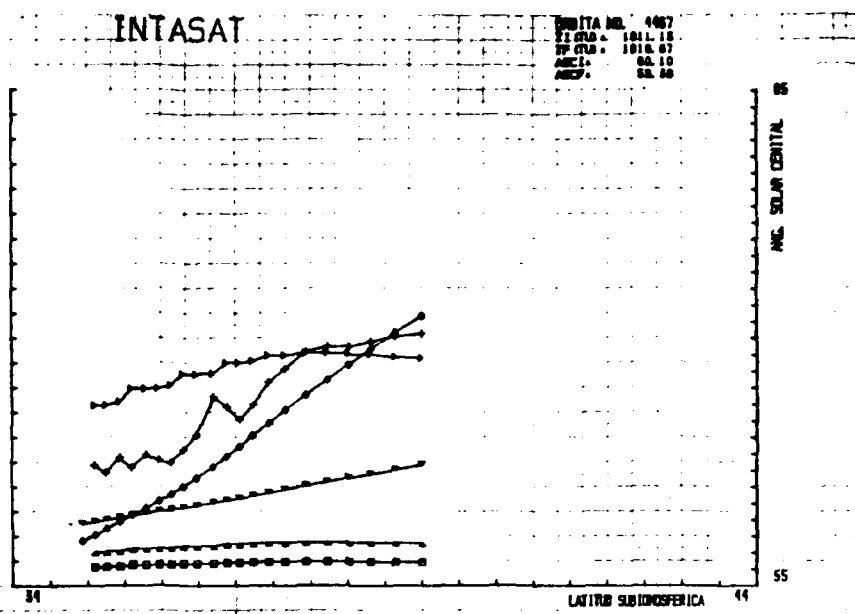


FIGURE 2

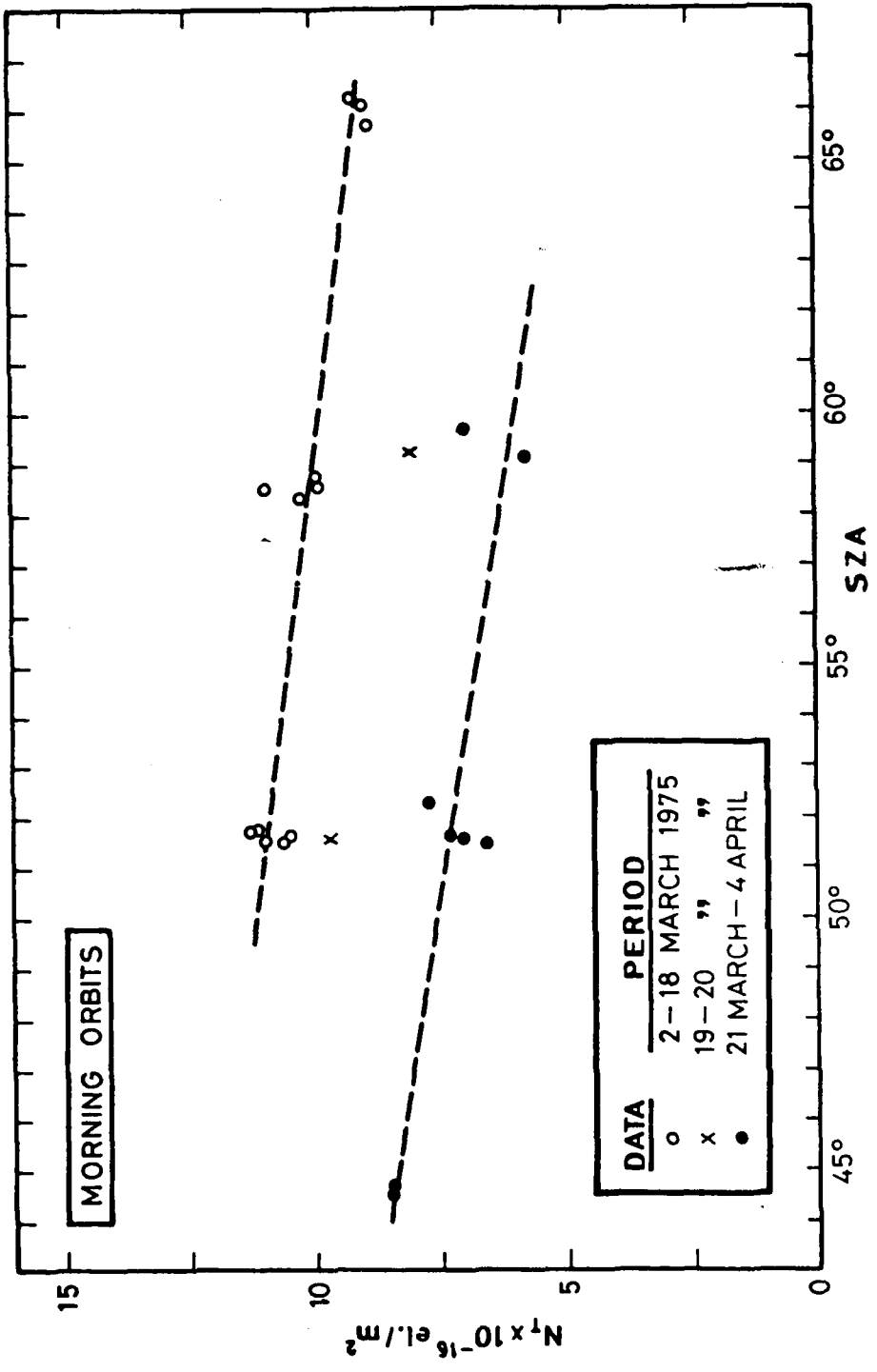
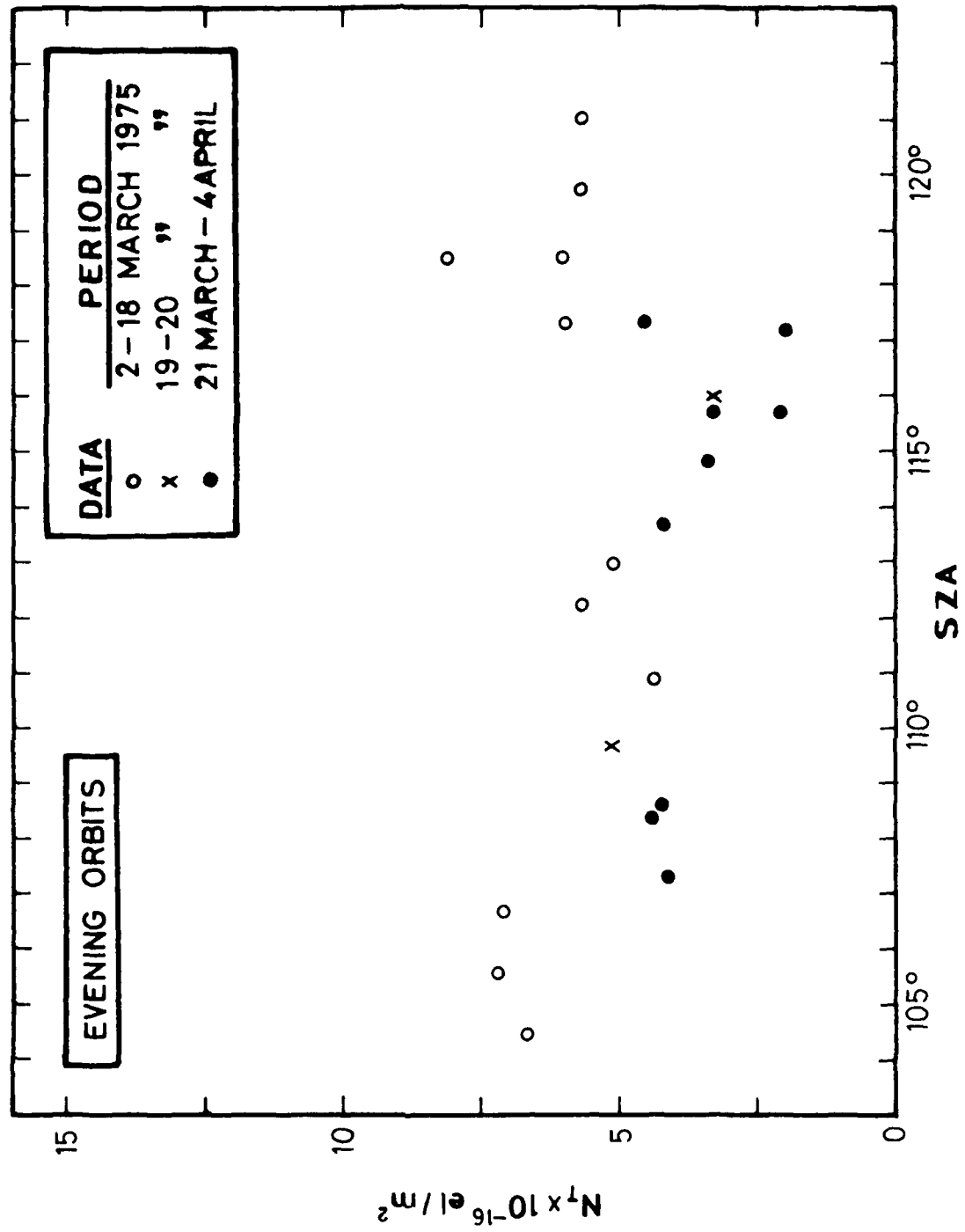


FIGURE 3



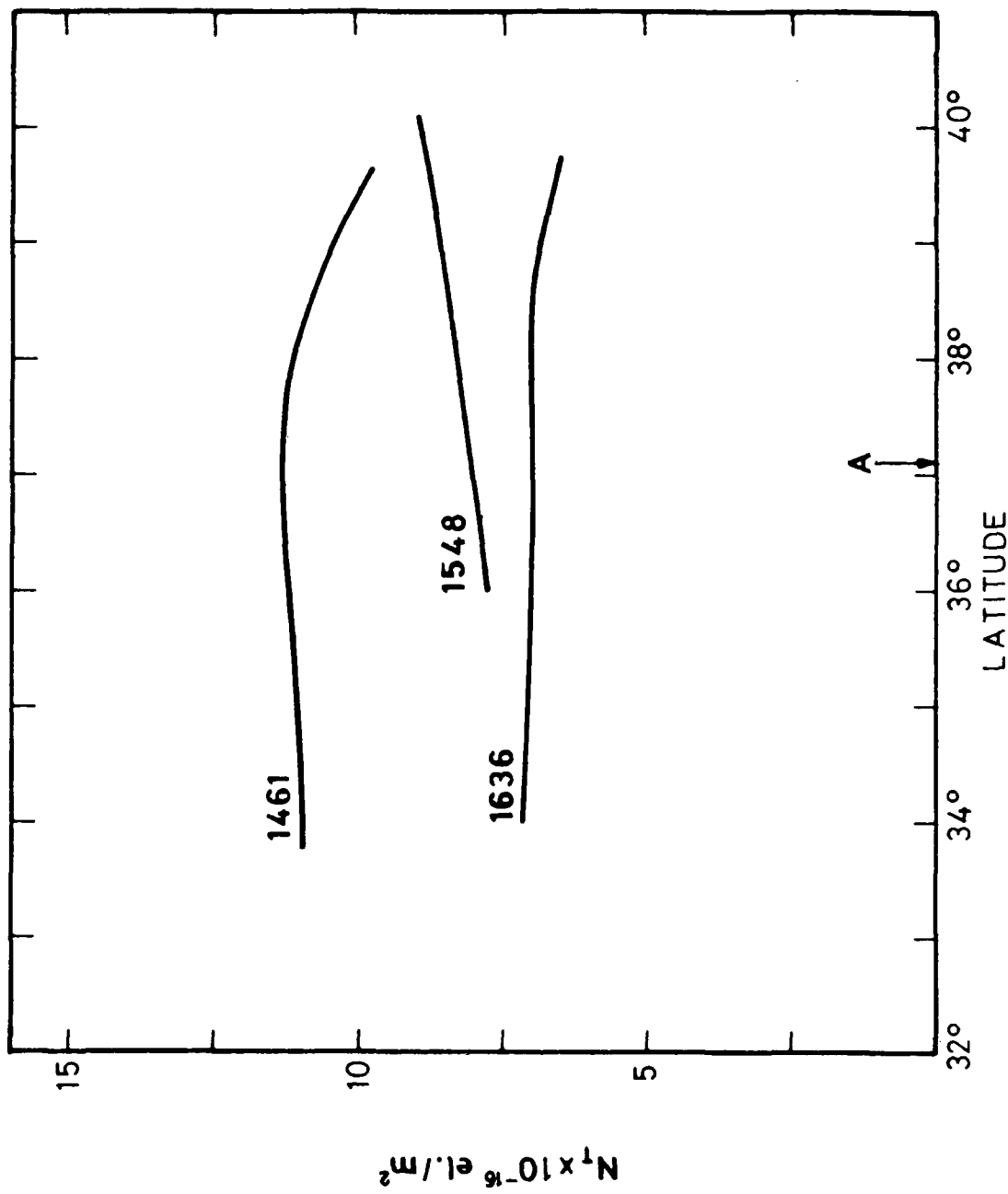


FIGURE 5

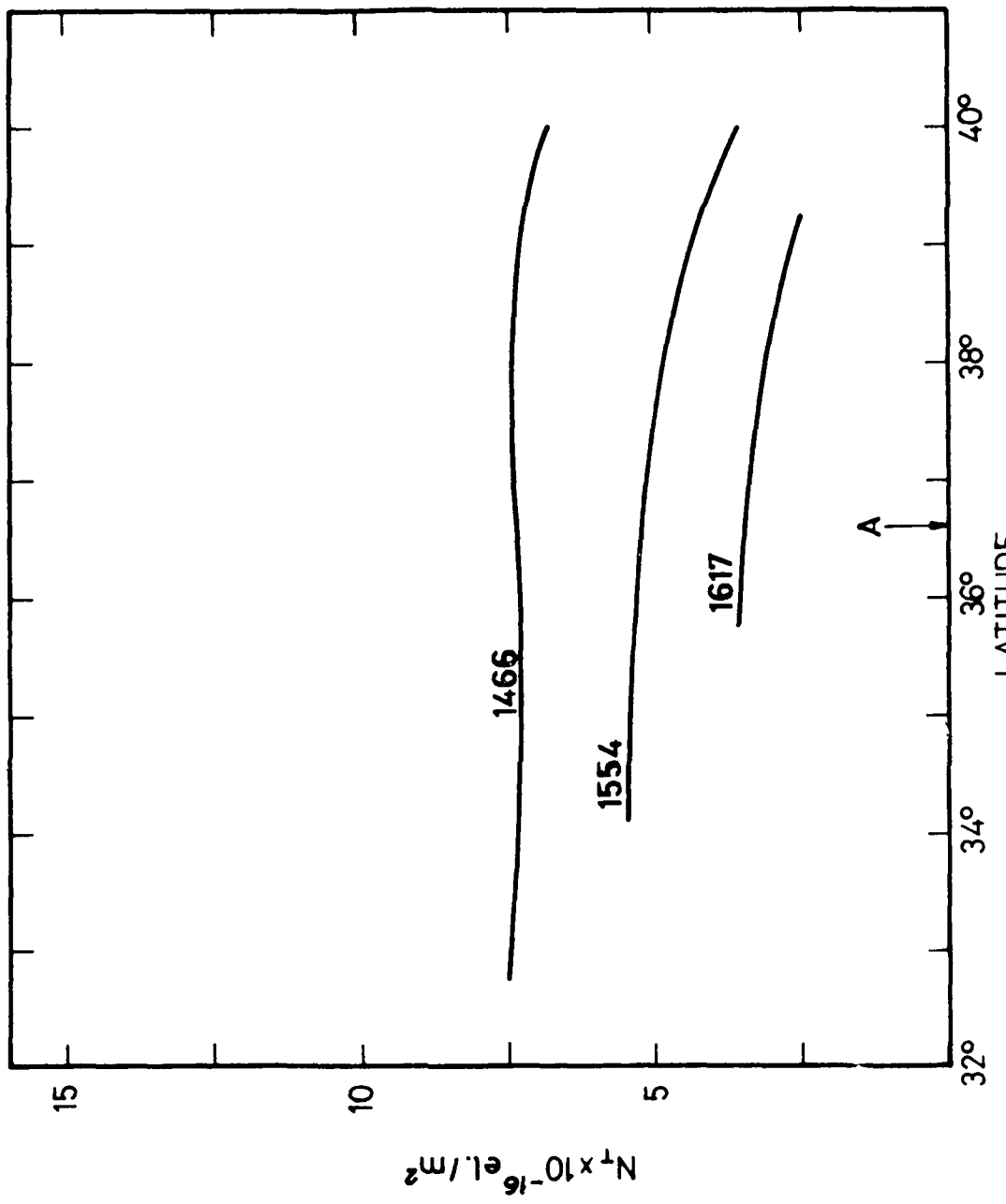


FIGURE 6

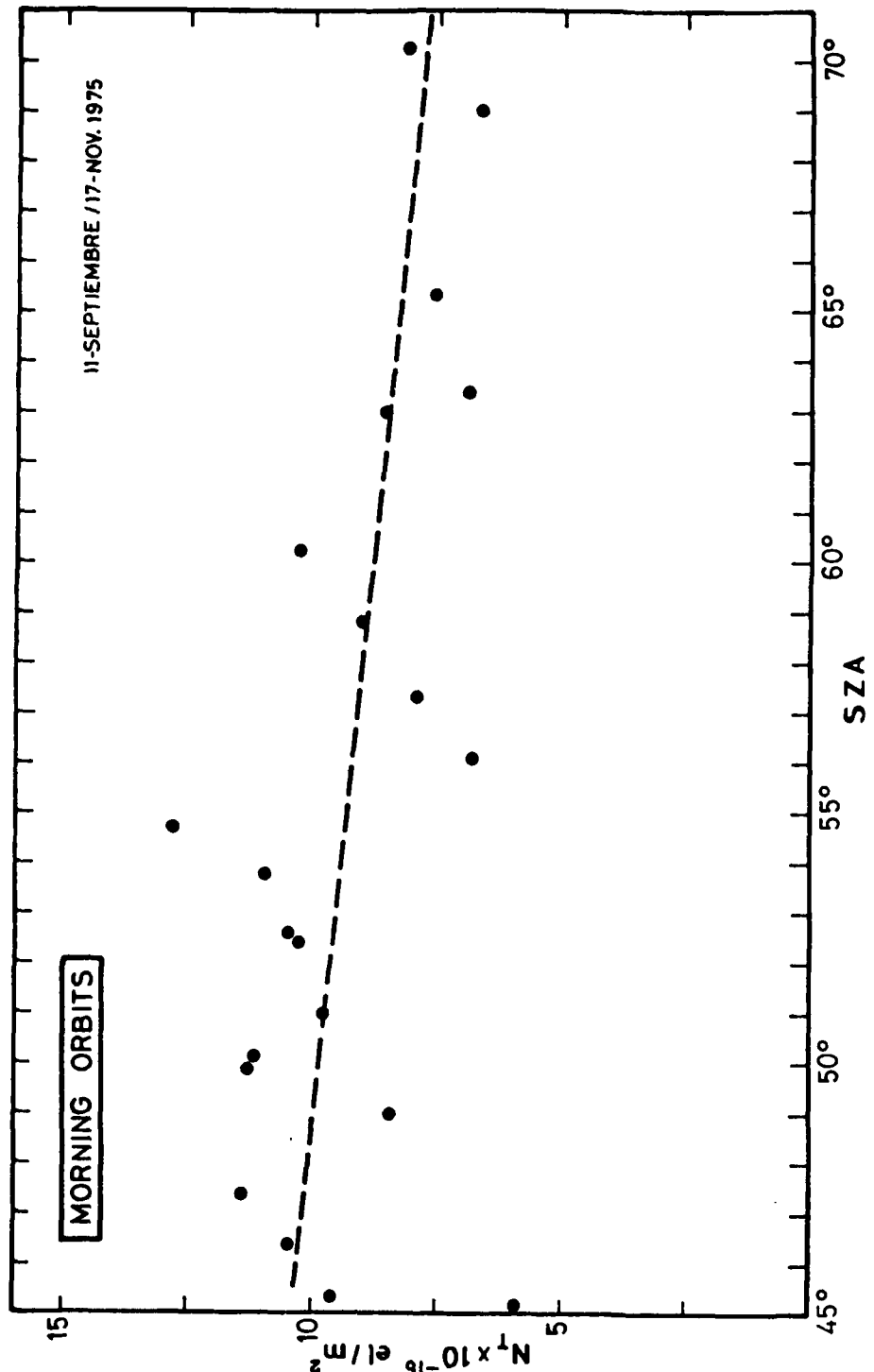
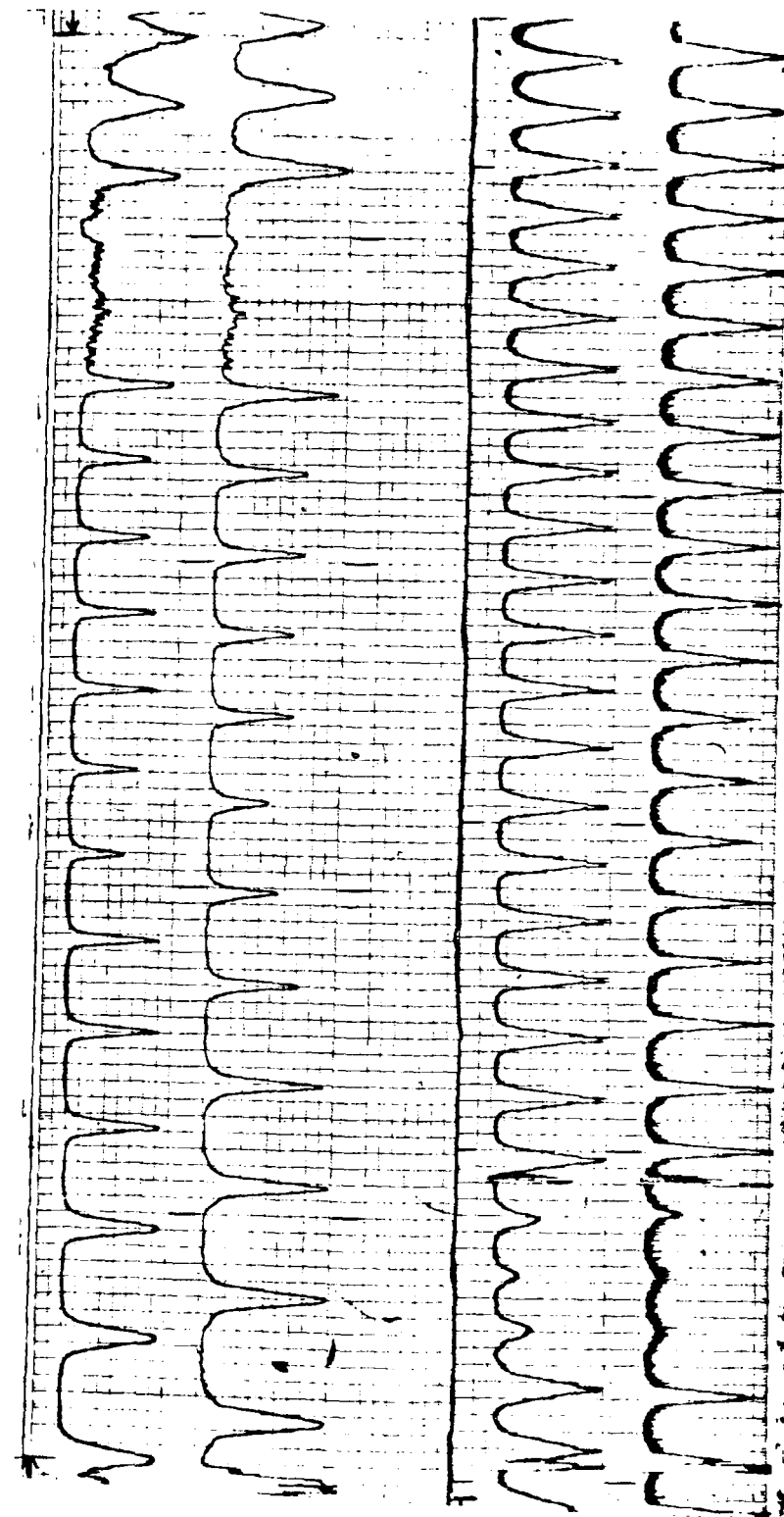


FIGURE 7

FIGURE 8



Latitudinal Morphologies of TEC Deduced  
from Polar Orbiting Satellite INTASAT

K. H. PAI

Dept. of Electrical Engineering  
National Taiwan University  
Taipei, Taiwan, Republic of China

ABSTRACT

The radio beacon signals transmitted by the polar orbiting satellite INTASAT have been observed since Feb. 1975 at Radio Wave Research Laboratory (Geographic latitude 25° N, longitude 121.5° E, magnetic dip 34° N) of National Taiwan University. This satellite transmits beacon signals of 40 and 41 MHz which enables a determination of electron content by using the differential Faraday rotation method. Because of low latitude of Taiwan the quasi-transverse propagation condition is met at some point of nearly every satellite pass. At the point of transverse propagation, there generally occur coincident shallow nulls at 40 and 41 MHz. This gives an alternate but easier method of determining the electron content value and has been applied to more than two hundred INTASAT records in an effort of studying the latitudinal morphologies.

The present paper shows that the variation of the monthly mean total electron content versus sub-ionospheric latitude exhibit a strong equatorial anomaly. A comparative analysis also has been carried out in the latitudinal variation of TEC for magnetically disturbed days ( $\sum k_p > 16$ ) and quiet days ( $\sum k_p < 16$ ). Almost all of the data deduced from south-bound passes under the low sun-spot number near 0800 to 0900 local time.

## 1. INTRODUCTION

The Spanish orbiting satellite INTASAT was successfully launched from Vandenberg Air Force Base on November 15, 1974. This satellite was designed for measurement of total electron content of the ionosphere. [1]

At present about forty observation stations scattered throughout the world are making observations. [2] Because the INTASAT transmits continuous stable unmodulated linearly polarized signals at 40.01 MHZ and 41.01 MHz, the differential Faraday technique may be applied for the determination of total electron content in the ionosphere.

Owing to the high orbital inclination ( $i = 101.735$  degrees) and almost circular orbit (apogee = 1457.97 km, perigee = 1440.39 km, and orbiting period = 114.86 min) [3], INTASAT travels nearly in south-north or north-south direction at Taipei, Taiwan. During the 1975-1976, the satellite tracking station of Radio Wave Research Laboratory, National Taiwan University at Taipei have been observing the geostationary satellite IIF-2 and IIF-3 by using a rotating linearly polarized antenna as well as cross-polarized antenna with polarimeter. Therefore, we have an excellent opportunity to compare the TEC values deduced by differential Faraday technique with that of single-frequency Faraday rotation method.

## 2. METHOD OF ANALYSIS

It is well known fact that when a linearly polarized wave transmitted by the satellite under the quasi-longitudinal approximation undergoes a continuous rotation in the direction of propagation. This effect is called the Faraday rotation. The Faraday rotation angle  $\Omega$  in a magneto-ionic medium is given by

$$\Omega = \frac{k}{f^2} \bar{M} \int_0^{h_s} N dh \\ = \frac{k}{f^2} \cdot \bar{M} \cdot N_t \quad \text{degrees} \quad (1)$$

where  $K$  is a constant (-1.699 in International System of Units),  $\bar{M}$  ( $-B \cos \theta \sec x$ ) is the geomagnetic factor in amp-turn/meter,  $f$  is the satellite signal frequency in Hz and  $N_t$  is the total electron content in electrons per square meter. Because the Spanish satellite INTASAT transmits at two closely spaced frequencies 40 and 41 MHz, one can apply differential Faraday technique for the determination of total electron content  $N_t$ . Applying eq(1) to two frequencies  $f_1$  and  $f_2$ , the absolute Faraday rotation  $\Omega_1$  of the signal at frequency  $f_1$  is given by [4]

$$\Omega_1 = -\frac{f_2^2}{f_1^2 - f_2^2} (\Omega_2 - \Omega_1) \quad (2)$$

Let  $f_1 = 40$  MHz and  $f_2 = 41$  MHz, we obtain

$$\Omega_{40} = 20.75 (\Omega_{40} - \Omega_{41}) \quad (3)$$

and

$$\Delta \Omega = \Omega_{40} - \Omega_{41} = k \bar{M} N_t \left[ \frac{1}{40^2} - \frac{1}{41^2} \right] \quad (4)$$

In evaluating the total electron content  $N_t$  from Faraday fading chart, one can employ the following two methods. (a): Time coincidence of 40 and 41 MHz nulls. (b): Measurement of differential Faraday rotation by using eq(4).

If a coincidence of Faraday nulls at the two frequencies occurs at any particular time during the satellite passage, the differential rotation at that time is equal to an integral multiple of  $\pi$  radians. If no null time coincidence is found, the value of  $\Delta\Omega$  are found from linear interpolation. [5]

The geographical variation of the electron content is determined by the total number of rotation measured from the transverse position  $T_0$  by using the geomagnetic factor  $M$ . [6]

In particular, if the transverse propagation condition is met at some point during the pass, the total rotation can be obtained by merely counting the Faraday fading chart at a single frequency. Taiwan is fortunately situated at a location where the transverse propagation condition is met for nearly every pass.

Near the transverse propagation condition the Faraday fading is usually slower and at the transverse point the nulls are shallow and coincident. The point of transverse propagation can therefore be identified easily. Both analysis methods have been applied to our data. But we have found the counting of Faraday rotation from transverse point much simpler. A typical chart record is shown in Fig 1. This is a record of voltage induced in a 3-element vertically directed Yagi receiving antenna by 40 and 41 MHz unmodulated signal transmitted by the satellite INTASAT. Fig 2 shows the south-going of the INTASAT passage (revolution number 5602) on February 6, 1976.

The fading pattern shown in Fig 1 is caused by the resultant polarization vector of the received downcoming signal alternately in parallel to or orthogonal to the linearly polarized antenna. Because of the south-going satellite passage, the number of Faraday rotation in every minute is increasing toward the magnetic equator. The transverse point  $T_0$  is easily visible near the local time 0902:13 and this time correspond to the sub-ionospheric point at  $33.70^\circ$  N and  $123.30^\circ$  E. Some investigators discuss the measurement of total electron content from Faraday effect and concludes that the correct conversion of polarization data to equivalent vertical TEC values is mainly dependent upon the choice of the

$\bar{M}$  factor which appear in the Faraday equation. [7] The geomagnetic factor  $\bar{M}$  value for the present analysis is based on the computer data which was supplied by Air Force Geophysics Laboratory (AFSC) and under the assumption of a mean ionospheric height of 350 km. All total electron content was computed at every minute during the south-going of the satellite passage.

### 3. RESULTS

Fig 3. illustrates the monthly mean value of TEC versus sub-ionospheric latitude for Spring, Summer, Autumn in 1975 and January in 1976. The maximum total electron content of the four seasons was found around a sub-ionospheric latitude of  $20^{\circ}$  N (magnetic dip =  $16.5^{\circ}$  N) and decreases both poleward and equatorward from this latitude.

The maximum value of TEC at the equatorial anomaly for the four representative months are  $20.1 \times 10^{16}$  el/m<sup>2</sup> (October),  $16.5 \times 10^{16}$  el/m<sup>2</sup> (April),  $11.4 \times 10^{16}$  el/m<sup>2</sup> (July) in 1975 and  $13.3 \times 10^{16}$  el/m<sup>2</sup> (January) in 1976. A comparative analysis also has been carried out in the latitudinal variation of TEC for magnetically disturbed days ( $\sum k_p > 16$ ) and quiet days ( $\sum k_p < 16$ ).

In Fig.4 latitudinal variations of TEC are plotted for four seasons on a meridian of  $110^{\circ}$  -  $135^{\circ}$  East. It is noted that the average latitudinal gradient varies from  $1.0 \times 10^{16}$  el/m<sup>2</sup>/deg in Autumn and Summer to  $0.2 \times 10^{16}$  el/m<sup>2</sup>/deg in Winter under the low sun-spot number near 0800 to 0900 local time for south-going passages. The difference of TEC between disturbed days and quiet days is biggest in Autumn (about  $4.0 \times 10^{16}$  el/m<sup>2</sup>) and smallest in Winter (approx.  $0.4 \times 10^{16}$  el/m<sup>2</sup>).

An interesting point is that in Summer the TEC for those quiet days is greater than that for disturbed days and the difference of TEC is about  $1.5 \times 10^{16}$  el/m<sup>2</sup>.

#### 4. DISCUSSION

Twelve months of observations of INTASAT signals enable us to deduce the monthly mean total electron content versus sub-ionospheric latitude as shown in Fig.5. The highest TEC was found in October 1975 while lowest TEC happened in January 1976. A steep slope occurred in November 1975 and a shallow slope occurred in July 1975. It may be observed that the electron content is maximum around a sub-ionospheric latitude  $20^{\circ}$ - $22^{\circ}$  N and decreases towards the magnetic equator and higher latitude. From Fig. 5 we obtain the TEC contour map as shown in Fig. 6. The contour map in Fig. 6 illustrates the relation between sub-ionospheric latitude and 12 months (from April 1975 to March 1976), and the parameter is total electron content (unit is  $10^{16}$  el/m<sup>2</sup>). From this map it is easily seen that maximum TEC are located near vernal equinox in March 1975 and 1976 also in autumnal equinox in 1975.

The peak value of the former is about  $16.5 \times 10^{16}$  el/m<sup>2</sup> while for the latter is approximately  $20-21 \times 10^{16}$  el/m<sup>2</sup>. Their minimum values are  $10-11 \times 10^{16}$  el/m<sup>2</sup> (in Summer) and  $8.5 \times 10^{16}$  el/m<sup>2</sup> (in Winter). It will be noted that the peak of TEC in vernal equinox was situated near  $20.5-22^{\circ}$  N of the sub-ionospheric latitude and this situation well meet the equatorial anomaly in the low latitudinal region.

An outstanding feature is that another valley is located in May 1975 and its minimum TEC is approximately equal  $10 \times 10^{16}$  el/m<sup>2</sup>. As indicated by the dashed lines, the location of the valleys is shift from  $28^{\circ}$  N (in May 1975) to  $31^{\circ}$  N (in Dec-Jan 1975-1976) via  $27.8^{\circ}$  N (in July-August) of the sub-ionospheric latitude. In contrast of the valley, peak TEC is located in lower sub-ionospheric regions. In March 1975 it is situated at  $20.6^{\circ}$  N while in March 1976 is located near  $22^{\circ}$  N. In Autumn, TEC is highest and is situated at about  $18.5^{\circ}$  North. The relation between TEC, months, and sub-ionospheric latitude is shown in the following table.

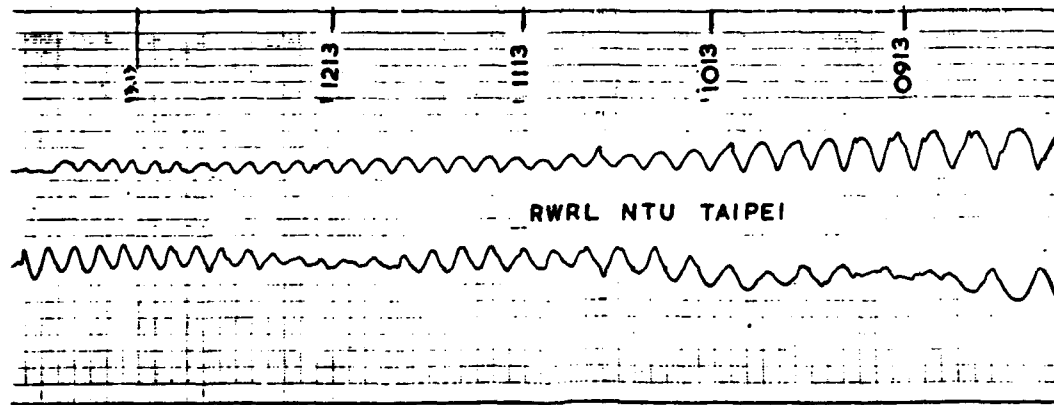
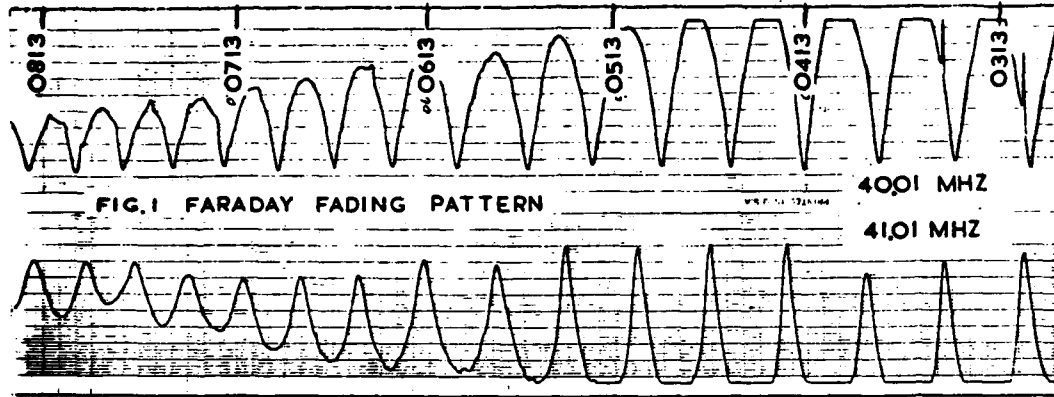
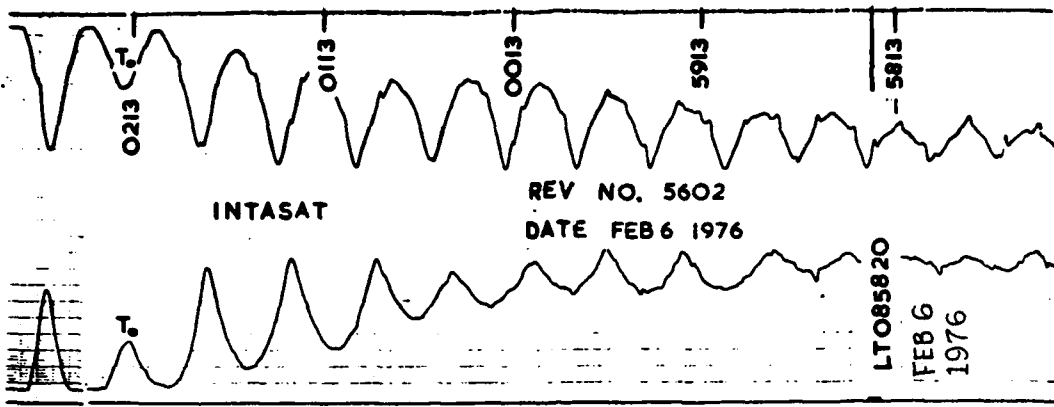
Total Electron Content (unit: el/m <sup>2</sup> )		Sub-Ionospheric Latitude	Months	
Max. value	$20 \times 10^{16}$	$18.5^\circ$ N	Oct	1975
Min. value	$8.5 \times 10^{16}$	$31^\circ$ N	Jan	1976
	$10 \times 10^{16}$	$27.8^\circ$ N	July	1975
	$10 \times 10^{16}$	$28.0^\circ$ N	May	1975
Medium value	$16-16.5 \times 10^{16}$	$20.5-21^\circ$ N	Mar	1975
			Mar	1976

Acknowledgments. We gratefully acknowledge the assistance of the U. S. Air Force Geophysics Laboratory (AFSC), NASA Goddard Space Flight Center and Atlantic Science Corporation for supplying the necessary satellite ephemeris and data concerning geomagnetic M factor. I wish to express my gratitude to Prof. K. C. Yeh University of Illinois at Urbana for helpful discussions during the preparation of this paper. Data collection was carried out under the supervision of Mr. H. J. Li. We are also grateful to the International Programs Division of National Science Council Republic of China for the financial support in carrying this research work.

#### REFERENCES

1. GODDARD NEWS. December 1974. Vol 22, NO. 9
2. CONVERSION FACTORS FOR FARADAY ROTATION DATA. Atlantic Science Corporation. 5711 Sarvis Ave. Riverdale, MD 20840 USA
3. Letter from Mr. William R. Witt Jr. INTASAT Project Manager NASA GSFC. Greenbelt, MD 20771 U.S.A.

4. N. Narayana Rao and K. C. Yeh. Comparizon of Faraday and Doppler Methods of Obtaining Ionosperic Electron Content. J. Geophys. Res., vol 73 NO.7 p.2447 1968
5. J.A. Klobuchar. Total electron computation from two frequency Faraday rotation. PP 18-24. Report of Joint Satellite Studies Group. JSSG Report NO.2 October 1966 France
6. Clifford. L. Rufenach et al. Faraday Rotation Measurement of Electron Content near the Magnetic Equator. J. Geophys. Res. vol 73. NO.7 PP2459-2468 1968.
7. J. A. Klobuchar and Michael Mendillo. Total Electron Content from the Faraday Effect. PP 7-11 AGARD NO.166  
Editted by J. Aarons.



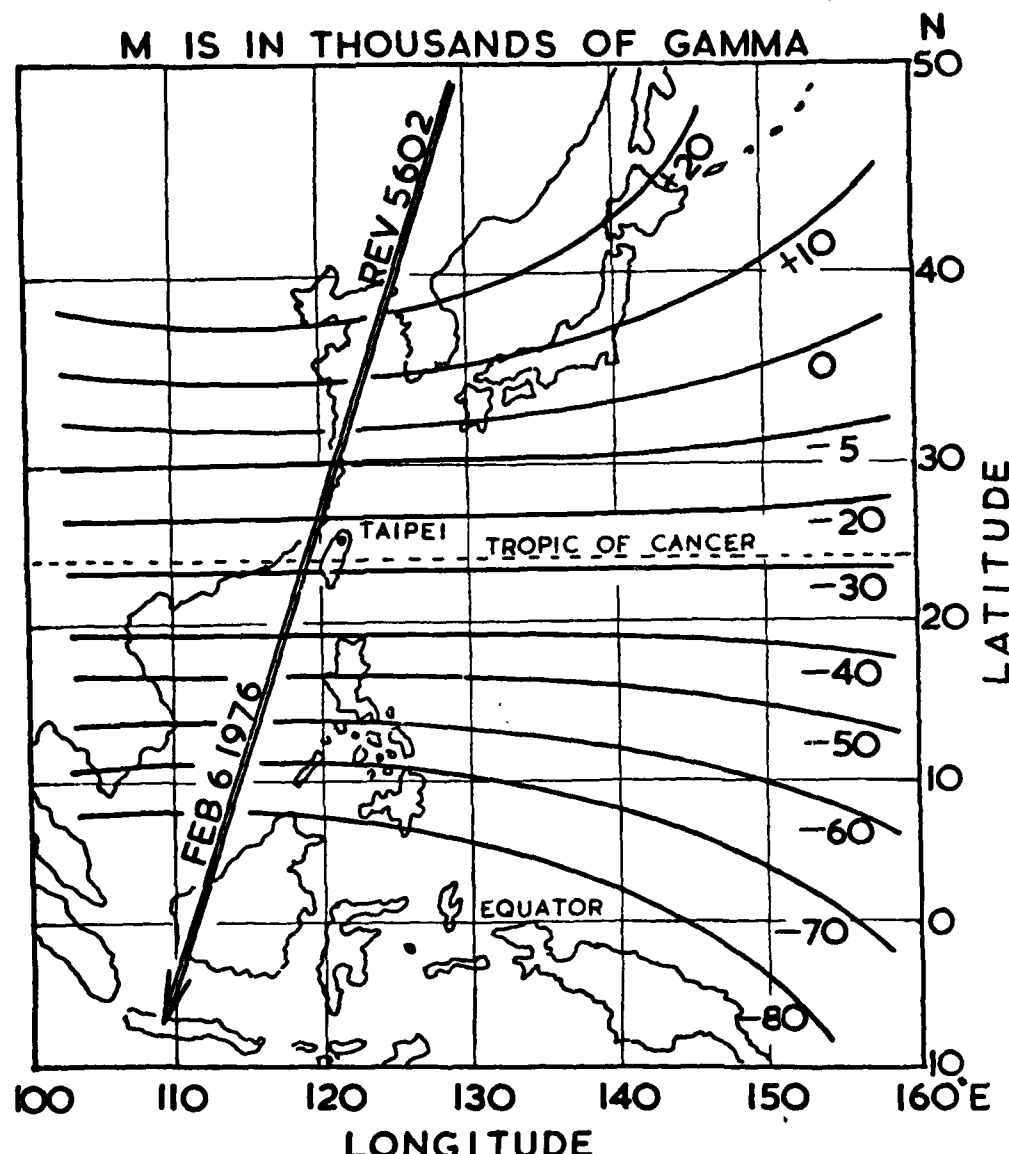


FIG 2 SOUTH GOING OF INTASAT  
PASSAGE REV 5602 ON FEB 6 1976

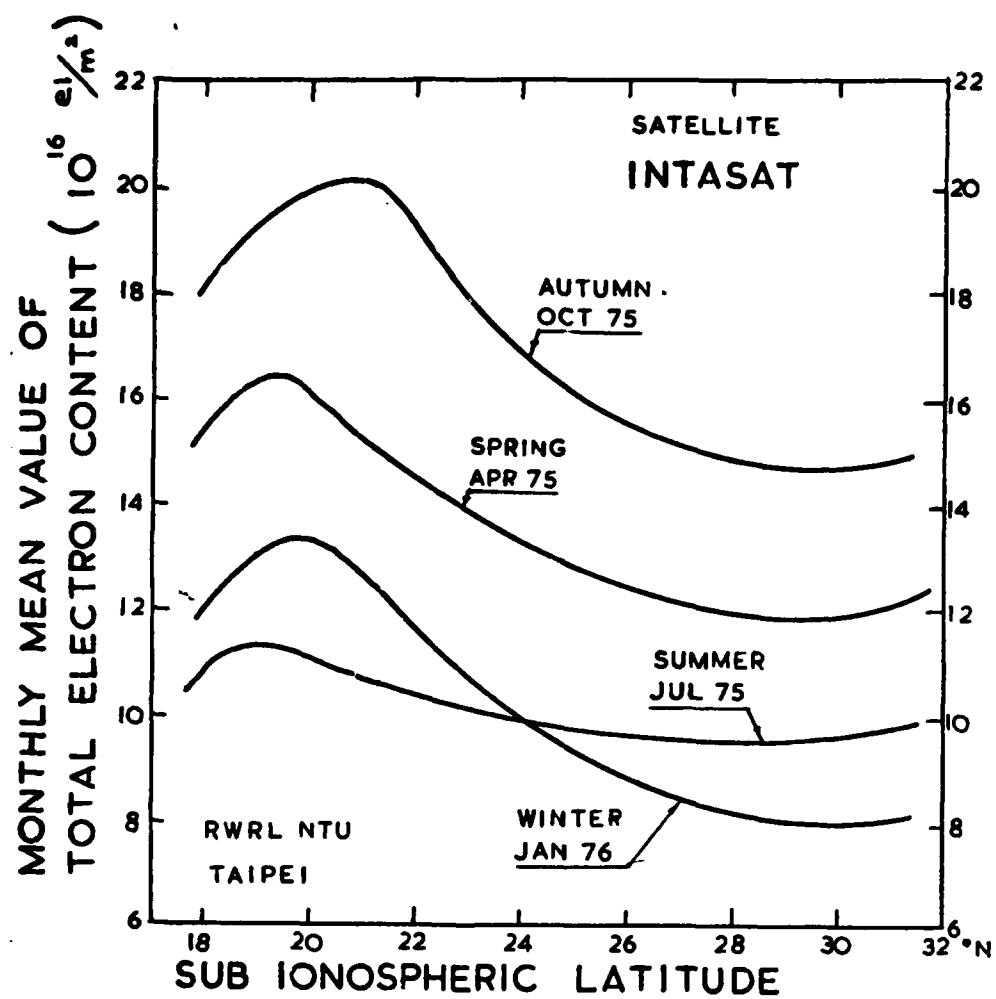


FIG 3 MONTHLY MEAN VALUE OF TEC  
VERSUS SUB-IONOSPHERIC LATITUDE  
IN FOUR SEASONS DURING 1975-1976

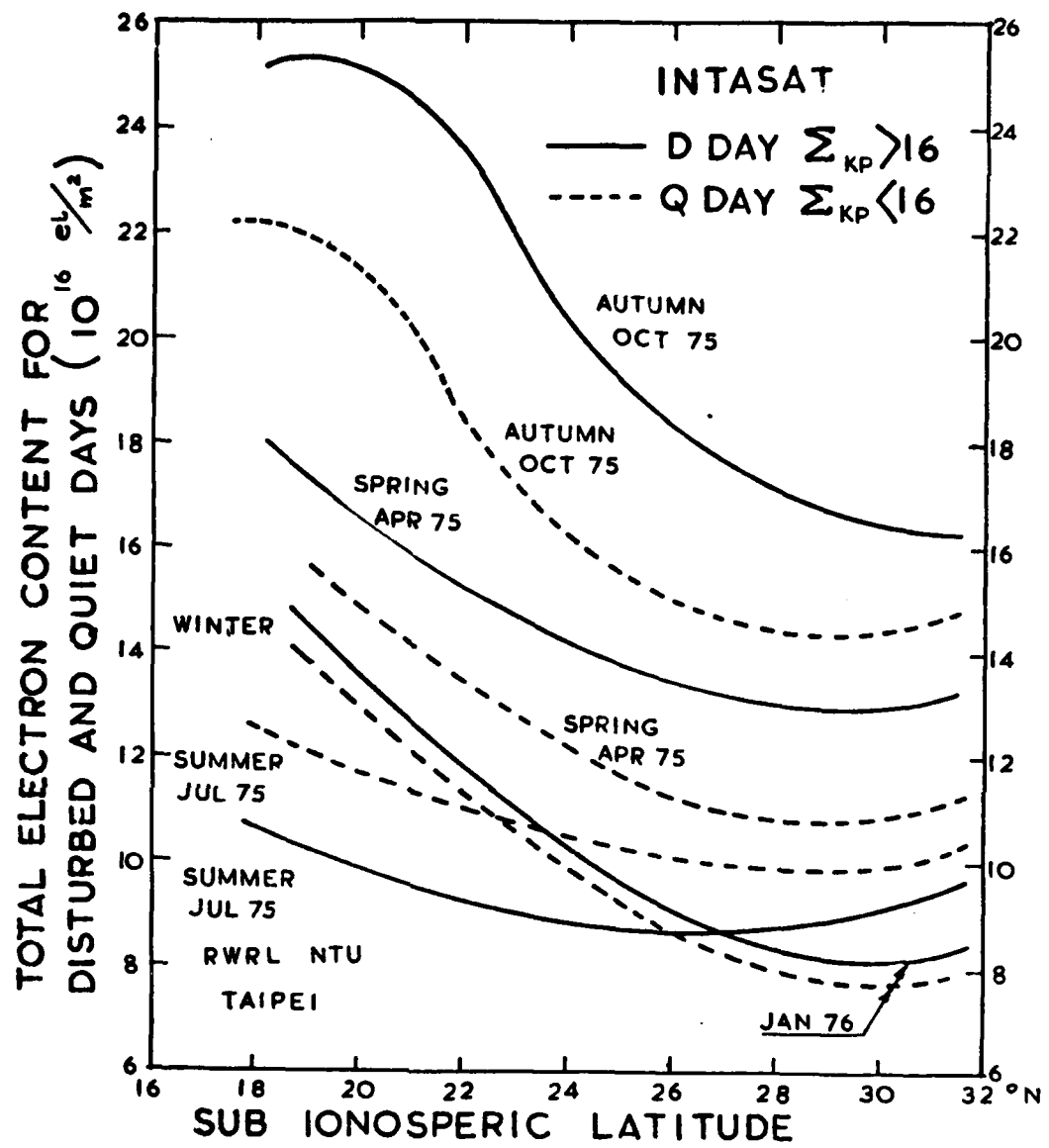


FIG 4 LATITUDINAL VARIATION OF TEC FOR DISTURBED AND QUIET DAYS IN FOUR SEASONS DURING 1975-1976

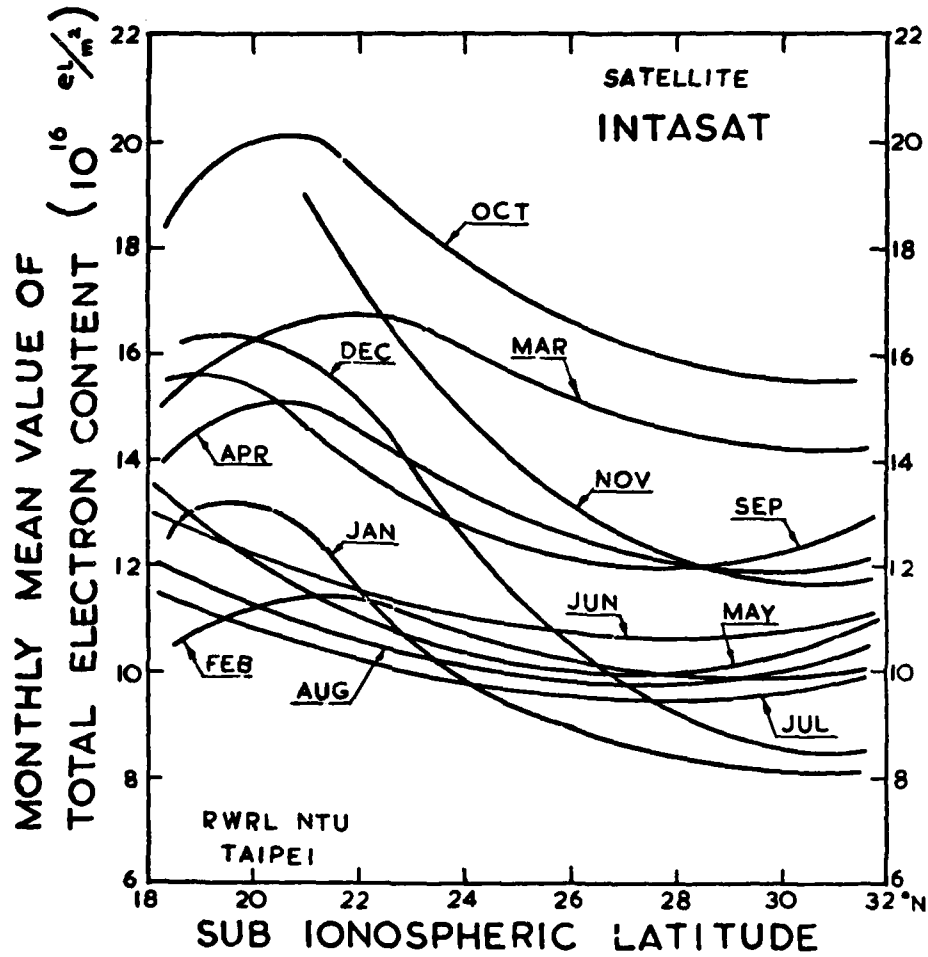


FIG 5 LATITUDINAL VARIATION OF  
TEC FOR 12 MONTHS DURING  
1975—1976

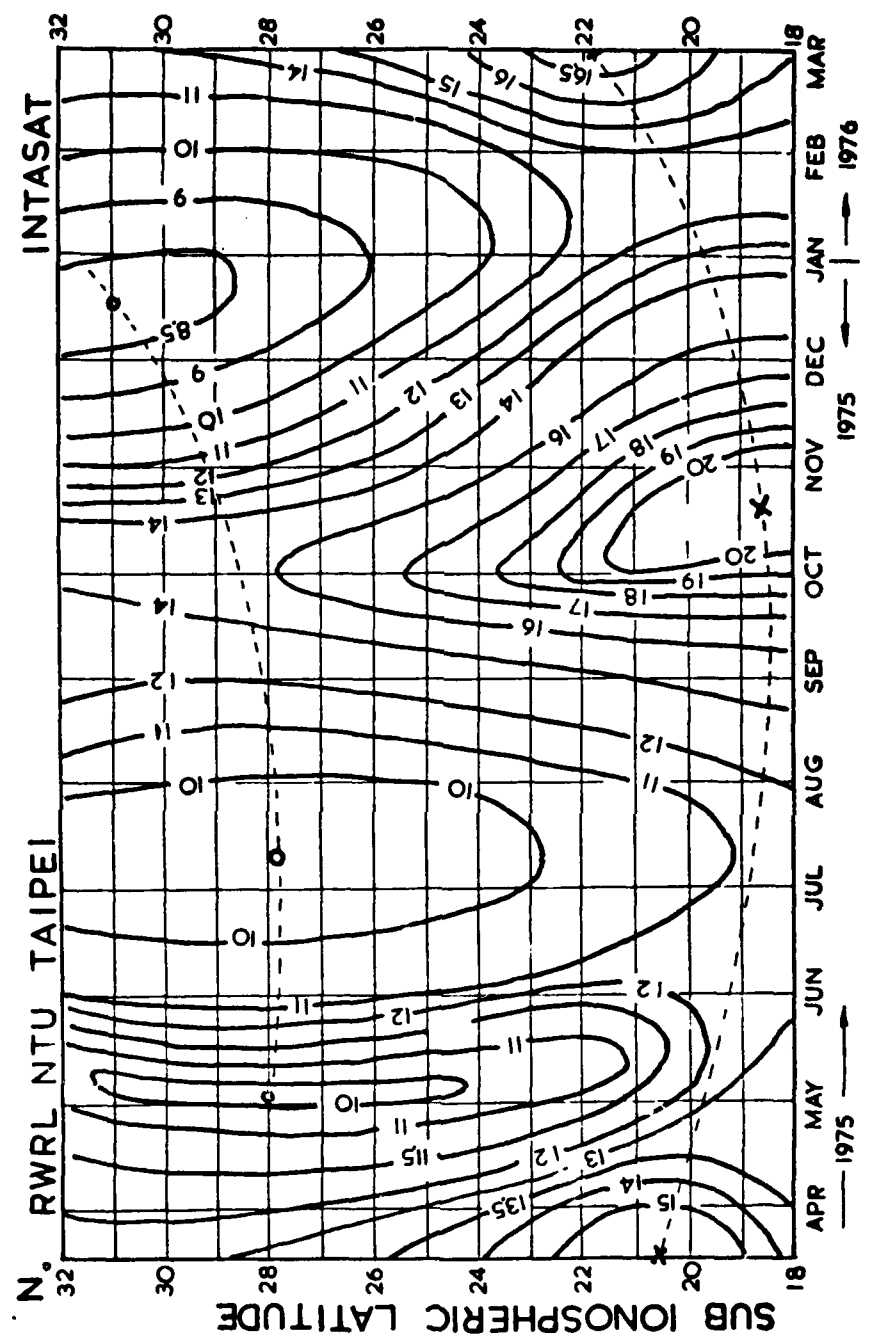


FIG 6 CONTOUR MAP OF TOTAL ELECTRON  
CONTENT FOR 12 MONTHS DURING 1975—1976

# THEORETICAL AND EXPERIMENTAL STUDIES OF TEC MEASUREMENTS IN THE TRANSVERSE ZONE

I.H. KEROUB

NATIONAL COMMITTEE FOR SPACE RESEARCH  
RADIO OBSERVATORY

P.O.B. 4651, Haifa ISRAEL

## ABSTRACT

The theoretical principles of the transionospheric Faraday effect are reviewed, using the properties of conformal transformations. The total Faraday rotation is effectively calculated through a ray tracing algorithm, without postulating the well known quasi-longitudinal approximations of "divers" orders. This treatment makes it possible to overcome the difficulties which are in fact encountered in the neighborhood of the transverse zone. It is shown that this treatment enables substantial advances to be made in the concepts involved in the geophysical interpretation of the Faraday effect recordings in the transverse zone, for stations situated at moderate geomagnetic mid-latitudes. An interesting example of such an application is furnished by the classical methods as compared with our own analysis of a recording from the region of New Delhi. However, our most important contribution is a quantitative method for the correction of systematic TEC error gradients which become particularly large in the vicinity of the transverse zone. The trend of the latitudinal TEC gradients thus obtained agrees with the results given by several other independent determinations. In this way, optimum geophysical use can be made of satellite beacons observations performed at moderate geomagnetic latitudes such as Haifa.

## **1. INTRODUCTION**

The optimum geophysical utilization of satellite beacon observations performed from a single station such as Haifa involves the determination of the TEC by using synchronous and low-altitude satellites; the synchronous satellites ensure the time coverage, unlike a low-altitude satellite, which can be usefully observed only during a few minutes each day. Nevertheless, the typical advantage of a low-altitude over a synchronous satellite is the fact that the low-altitude satellite can give an extended coverage of TEC gradients from a single station\*.

However,-especially so when approaching the transverse zone for a moderately mid-latitude situated station - the classical (i.e. counting from the transverse point) method for TEC determination may introduce systematically erroneous TEC gradients, and thus eliminate the principal advantage of the low altitude satellite.

The large relative size of the recorder tracings representing this zone in these stations, resulted in the development of rigorous specific methods for accurate determination of TEC in the transverse zone (Keroub, 1976).

Following a brief survey of the fundamental principles of the Faraday rotation, and a brief review of the ray tracing program employed, this study illustrates the application of new concepts to the geophysical interpretation concerning the transverse recording zone; it also shows that it is possible to make a quantitative correction of systematic error gradients produced by the classical methods. We shall also show that the new methods are a powerful tool in the geophysical interpretation and analysis of the available recordings.

---

\* Gradient studies with the aid of synchronous satellites necessitate the establishment of a network of stations (Mendillo - Klobuchar, 1975).

## 2. THEORETICAL PRINCIPLES OF TOTAL FARADAY ROTATION THROUGH THE TRANSVERSE ZONE

### 2.1. General

This section deals with Faraday Rotation as observed from "low altitude" satellites. These are satellites for which the changes in phase path length are dominated by effects resulting from the change in the direction of the source as seen from the receiving station. Their orbits often lie above much of the ionization layer, but the general results of this study are also valid if the satellite's orbit penetrates deeply into the denser parts of the ionosphere.

The polarization rotation becomes small when extended into the Transverse Propagation Region (Garriott et al, 1970), so that if such an observation of the transverse point is possible, the rotation at other points can be accurately determined within the framework of first order analysis by simple counting.

However, this simple first order analysis assumes a thin ionospheric layer in which the whole total electron content is concentrated. An advanced study in this field must include a study of the behaviour of the Faraday Rotation along the whole path of the ray between the satellite and the receiving station. For this purpose we consider the behaviour of the Faraday Rotation in the general case, and describe a ray tracing program which computes the total Faraday Rotation for any position of a satellite relative to an observing station.

### 2.2. Behavior of Faraday Rotation in the General Case

If the eikonal solution and the properties of conformal transformation are used (Keroub; 1975), the Faraday Rotation ( $n_2 - n_1$ ) along the propagation path (from satellite to station)  $\vec{r}_1$  to  $\vec{r}_2$  is obtained as the result of an integration which depends on the physical behavior of the ionosphere between the transmitter and the receiver, and on the relative geometrical location at any given instant.

In general, in the "transverse region" of a recording chart of Faraday fading, it is quite impossible to make any simple assumption which gives a simple fit to the real behavior of the propagation (quasi-longitudinal, first order, second order, third order; quasi-transversal, etc.). The only rigorous assumption that can be made is that the period of Faraday fading is related to changes in the phase path length by the relationship

$$2(\alpha_2 - \alpha_1) = \frac{\int_1^2 dr \cdot k_+}{\hat{r}_1} - \frac{\int_1^2 dr \cdot k_-}{\hat{r}_1}$$

whatever the conditions of the propagation between the transmitter and the receiver.

It follows that the way to find the phase path length is to determine the directions of the ray. This will be discussed in the next sub-section.

### 2.3. Determination of the Ray

In the case of free propagation without absorption, the Poynting vector of an individual mode, averaged over the cycle of the wave, has the direction of the ray; deviation from the normal is thus a consequence of the presence of a longitudinal E component (the  $E_n$  component in the direction of the wave normal). The polarization of propagation modes is usually elliptical, with one longitudinal and two transverse E components and two transverse H components of the wave field. The derivation of the average Poynting vector requires the study of all these field components. Now let us consider an infinite number of plane waves whose wave normals vary slightly. They may be superimposed, and the location of the wave packet is where all of them are in phase. They turn out to be in phase on an entire line. This line is the ray. In other words, this is the line along which the wave packet travels. It is thus seen that the variation of the refractive index with a slight variation of the direction of the wave normal is of decisive significance for the direction of the ray.

It is seen that it is not very easy to determine the path along which the energy will travel. In general, the path of the ray cannot be determined analytically. It has to be determined by a step-by-step process.

There are varying degrees of sophistication in ray tracing; thus, for instance, in its simplest form we assume that the ionosphere is plane. In the more sophisticated ray-tracing programs, the effects of curvature of the ionosphere, electron density variations (provided they are compatible with the eikonal hypothesis), magnetic-field changes and collision frequency are all taken into account.

Several methods exists for ray-tracing computation (Booker, Bremer, Hazelgrove, Poeverlein). The Bremmer method is useful in visualizing what is happening to the ray, and was chosen for this reason (see Fig. 1).

#### 2.4. Conclusion

The theoretical principles underlying the most general case of trans-ionospheric Faraday effect are outlined.

The properties of conformal transformations are utilized in order to obtain the exact results valid in all cases of trans-ionospheric propagation of electromagnetic waves.

In order to overcome the difficulties encountered in calculating the Faraday Rotations, for which the conventional classical quasi-longitudinal approximation fails, especially so in the case of recorder tracings of the transverse zone of mid-latitude geomagnetic stations, the suitable method seems to be the use of an exact formulation of the phase path lengths involved. The several possible options in the choice of a ray-tracing program are stated, and the Bremmer method is chosen.

Such an approach could bring about substantial progress in the geophysical exploitation of the Faraday Effect. We shall attempt to demonstrate this point in the following sections.

### 3. A NEW CONCEPT IN THE GEOPHYSICAL INTERPRETATION OF THE FARADAY EFFECT RECORDINGS IN THE TRANSVERSE ZONE

#### 3.1. General

Having recalled the interpretation which follows from the application of the classical methods of TEC determination, we shall describe an algorithm which leads to a new concept for the geophysical interpretation in the transverse zone.

#### 3.2. Classical Study of the Revolution of BEB-S 66 Satellite

In order to ensure an objective attitude towards the classical interpretation, we chose the results already published for New Delhi, which is a station located at a moderate geomagnetic latitude.

Figs. 2 and 3 clearly illustrate the classical interpretation of a day pass of the BEB-S 66 satellite in terms of rotation reversals. More details will be found elsewhere (Mitra et al, 1970).

#### 3.3. The Algorithm Employed

We simulated, with the aid of our ray tracing program, several passes of polar satellites of BEB-S 66 type for moderate geomagnetic latitudes.

Whatever the ionosphere model adopted, and whatever the actual magnitude of the latitudinal TEC gradient, the "rotation reversals" referred to above (para. 3.2) were never observed.

In order to give some idea of the results obtained by simulation, the reader is referred to the curves published by the author elsewhere (Keroub, 1976). Here we shall give another typical curve obtained by simulation. The curve represents the total Faraday rotation  $\Omega$  as a function of  $\Delta\Omega$ , which is the difference between the Faraday rotations at

40 and 41 MHz shown in the selected recording. Fig. 4 shows the result obtained for a day pass.

It is noteworthy that a change in the geophysical parameters employed in the simulation produces no significant changes in the topology of the curve in Fig. 4. In the following sub-section we shall give an interpretation based on this topology.

#### 3.4. Proposed Interpretation

It is seen in Fig. 4 that in the case of day passes the minimum Faraday Rotation does not become zero for a station located at a moderate geomagnetic latitude, but assumes a minimum value (e.g.,  $\alpha_{0E}$  on the curve in Fig. 4).

On the other hand, on both sides of this minimum, the synchronisms between 40 and 41 MHz are compatible with the theory of the differential Faraday effect - especially so starting from the first synchronism adjacent to the transverse zone (point A, in the present case). In the case of synchronisms taking place to the north of the transverse recording zone (above point B), i.e., towards low elevations of ray paths, the validity of the classical analysis is limited owing to the refraction effect.

As far as we are concerned, two general results may be stated.

1. The minimum of the total Faraday rotation does not pass through zero at the transverse point.
2. Counts starting from synchronisms must allow for  $\alpha_{0E}$ , in order to avoid the difficulties presented by the classical interpretation (systematic error giving rise to "multiple reversal polarizations" concept as stated above).

#### 3.5. Conclusion

It is seen that the treatment proposed in the present study may introduce new concepts in the geophysical interpretation connected with the transverse zone.

In the following section, we shall give a quantitative example of the use of our algorithm to correct systematic TEC error gradients.

#### **4. QUANTITATIVE CORRECTION OF SYSTEMATIC TEC ERROR GRADIENTS**

##### **4.1. General**

This chapter will give a quantitative description of the use of the methods we have developed, and the results obtained in this manner will be compared with those obtained by the conventional counting methods.

##### **4.2. Study of TEC Gradient as a Function of the Latitude**

As an example, we shall study the variation of TEC with time during pass No. 22,591 of the quasi-polar BEB S-66 over the Haifa station.

In order to be able immediately to compare our results with those obtained by the classical method, the magnitude  $\Omega_E/\Omega_L$  is plotted on the ordinate of Fig. 5 as a function of time;  $\Omega_E$  is the experimental angle of Faraday rotation determined by our method, while  $\Omega_L$  is the total Faraday Rotation angle read on the recording in the counting method.

Let  $\Omega_{OE}$  be the residual Faraday Rotation of the above pass for the frequency of 20 MHz. To determine  $\Omega_{OE}$ , we shall use our algorithm (for more details, see Keroub, 1976); as a result, the simple relationship  $\Omega_E = \Omega_L + \Omega_{OE}$  is obtained.

Table I lists the experimental data and the magnitudes used in determining the curve in Fig. 5.

We have plotted similar pass curves with different TEC's. The curves describe BEB S-66 passes No. 22,509 of 5th April 1969 at 7:23 U.T., and No. 22,468 of 2nd April 1969 at 7:23 U.T. These passes are described, respectively, in Tables II and III and in Figs. 6 and 7.

TABLE I

Satellite: BEB S-66  
 Pass No.: 22,591  
 Date: 11 April 1969, 06<sup>h</sup>35 U.T.  
 Frequency: 20 MHz

T	0"	19"	29"	59"	89"	119"	149"	179"	209"
$n_E$	21	29	37	63	91	123	155	192	230
$n_L$	0	28	16	42	70	102	134	171	209
$n_E/n_L$	-	3.62	2.31	1.50	1.30	1.22	1.16	1.12	1.10

TABLE II

Satellite: BEB S-66  
 Pass No.: 22,509  
 Date: 5 April 1969, 7<sup>h</sup>23 U.T.  
 Frequency: 20 MHz

T	0"	14"	24"	54"	84"	114"	144"	174"	209"
$n_E$	32	37	51	87	121	156	191	228	276
$n_L$	0	5	19	55	89	124	159	196	244
$n_E/n_L$	-	7.4	2.68	1.58	1.36	1.26	1.20	1.16	1.13

TABLE III

Satellite: BEB S-66  
 Pass No.: 22,468  
 Date: 2 April 1969, 7<sup>h</sup>45 U.T.  
 Frequency: 20 MHz

$t_0$	0	10"	30"	1'	90"	2'	150"	3'	3'3"
$n_E$	55	65	82	135	182	227	275	324	331
$n_L$	0	10	27	80	127	172	220	269	276
$n_E/n_L$		6,5	3	1,68	1,43	1,32	1,25	1,204	1,2

The three selected passes of the polar satellite BEB S-66 are north-south passes.

The origins of the curves in Figs. 5, 6 and 7 are the times of the minimum Faraday Rotation for each pass.

The dimensionless magnitude  $n_E/n_L$ , plotted on the ordinate, is the number by which we must multiply the TEC value obtained by the classical method in order to obtain the true result, not distorted by the systematic error. The relative systematic error, which distorts the determination of TEC at a given moment, will thus be:

$$\epsilon = (n_E/n_L - 1)$$

In the vicinity of the transverse zone, this error is greater than 200%. At the transverse point, it becomes infinitely large.

One minute after the satellite has passed through the minimum point of Faraday Rotation, the error is still 50% or larger when the satellite is already about  $3^{\circ}$  of geographical latitude away from the position it occupied at minimum Faraday Rotation.

Since the TEC's corresponding to Figs. 5, 6 and 7 are in increasing sequence, it is seen in the figure that the magnitude of the correction to be introduced also increases with the TEC.

Thus, the assumption that the residual angle  $\alpha_{OE}$  is negligibly small or zero strongly affects the estimated value of the TEC; an artificial latitudinal gradient is introduced, which rapidly becomes intolerable for latitudes to the north of the listening station (in the northern hemisphere).

#### 4.3. Conclusion

Two points must be made.

1. The residual angle of Faraday Rotation given by our algorithm makes it possible to extend the improvements of our technique into the range of quasi-longitudinal propagation. In fact, a quantitative correction is thus made of the systematic error introduced by most classical methods of determination of the TEC latitudinal gradient, which is an important magnitude.
2. The results of any study of TEC which is exclusively based on counting from the minimum point of Faraday Rotation must be treated with caution.

## **5. CONCLUSION**

In the case of stations located at moderate geomagnetic latitudes such as Haifa, there are two main difficulties involved in the study of TEC latitudinal morphologies, starting from a single station:

1. The correct geophysical interpretation of the transverse zone, which occupies a major part of the recording;
2. The introduction of systematic errors into the determination of latitudinal TEC gradients. These errors are due to the fundamental assumptions (quasi-longitudinal propagation, etc.) which are usually made in such determinations.

We have drawn attention to the fact that by the use of a theoretically rigorous algorithm these difficulties can be overcome. Having outlined the fundamental principles employed, we have introduced new concepts in the interpretation of the experimental recordings concerning the transverse zone. We have also shown that this approach makes it possible to effect a quantitative correction of the systematic TEC error gradients, which become particularly large in the vicinity of the transverse zone.

Thus, the present study makes for the best possible utilization of the available satellite beacons observations.

**6. REFERENCES**

- GARRIOTT, O.K., A.V. DA ROSA, and W.J. ROSS (1970),  
"Electron Content Obtained from Faraday Rotation and Phase  
Path Length Variations",  
Jour. Atmos. Terrestr. Phys., 32, p. 710.
- KEROUB, I.H. (1975),  
"Fundamental Theoretical Principles of the Total Faraday Rotation  
through the Transverse Region",  
Haifa Radio Observatory, Fascicule No.: 1975 - 1.
- KEROUB, I.H. (1976),  
"New Methods of Determination of the Total Electron Content in the  
Transverse Zone",  
In Press.
- MENDILLO, M. and J.A. KLOBUCHAR (1975),  
"Investigations of the Ionospheric F Region Using Multistation Total  
Electron Content Observations",  
Jour. Geophys. Res., 80, p. 643-650.
- MITRA, A.P., and T.R. TYAGI (1970),  
"Some Geographic and Geophysical Aspects of Electron Content Measurements  
from Satellite Radio Beacon Transmissions",  
Jour. Atmos. Terrestr. Phys., 32, p. 1807-1818.

Fig. 1: shows an example of a part of the output of this program.  
For the drawing of 10 curves simultaneously the abscissae should be  
linear and the ordinates should correspond to the height above a spherical  
earth.

1. Electron density in the proximity of ordinary ray.
2. Electron density in the proximity of extraordinary ray.
3. Electron density above observatory.
4.  $K_1 \cos\theta$ ,  $\theta$  as in the Appleton-Hartree formula.
5.  $K_2 H$ ,  $H$  intensity of terrestrial magnetic field.
6.  $K_3 X$ ,  $X$  distance from ray to plane vertical to the observatory and  
passing through the satellite.
7.  $K_4 Y$ ,  $Y$  horizontal projection of the distance from station to satellite.
8.  $K_5 Z$ ,  $Z$  distance between ordinary and extraordinary rays.
- 9,10. Relative gradient factor of electronic densities for ordinary and  
extraordinary rays.

$K_1$  to  $K_5$  are constants.

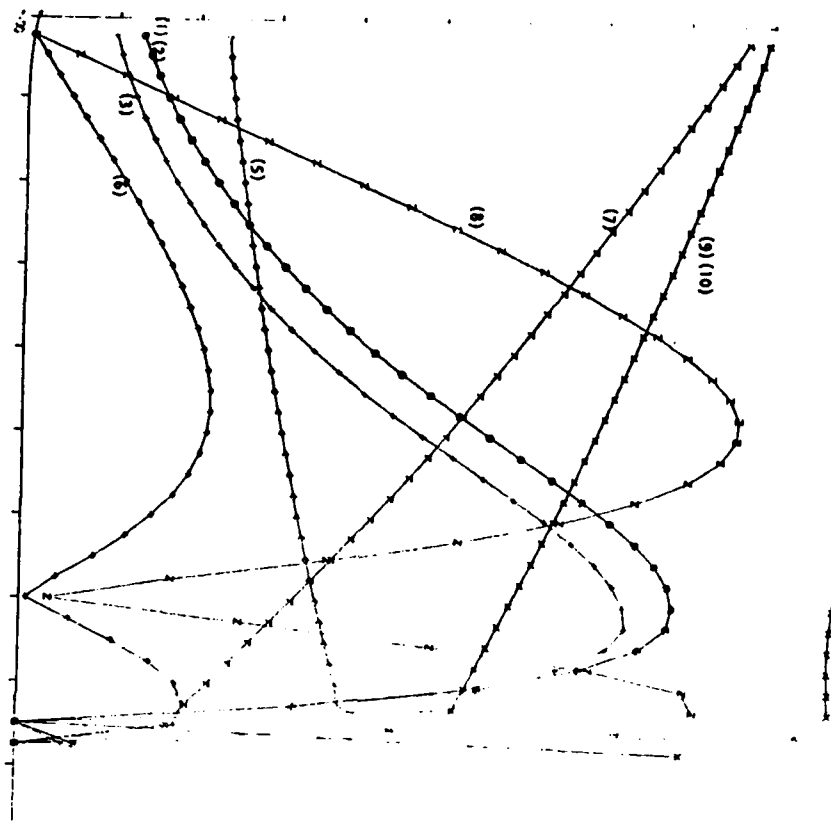


FIGURE 1: Plotter Output.

The quantities were multiplied by scaling constants to make the simultaneous drawing possible. The 10 curves are described on the following page. For more details, see Keroub, I. (1972), "An Ionospheric HF Ray Tracing Program", Haifa Radio Observatory, Report No.: 724.

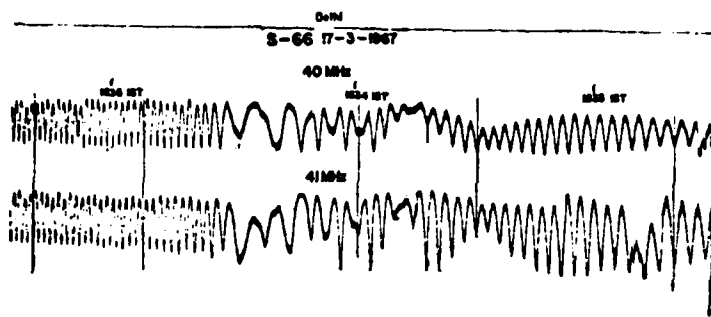


FIGURE 2: A Faraday Rotation record showing four rotation reversals.

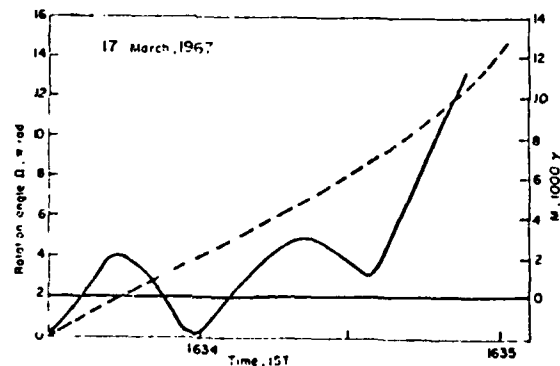


FIGURE 3: Variation of rotation angle with time for the record shown in Fig. 2.

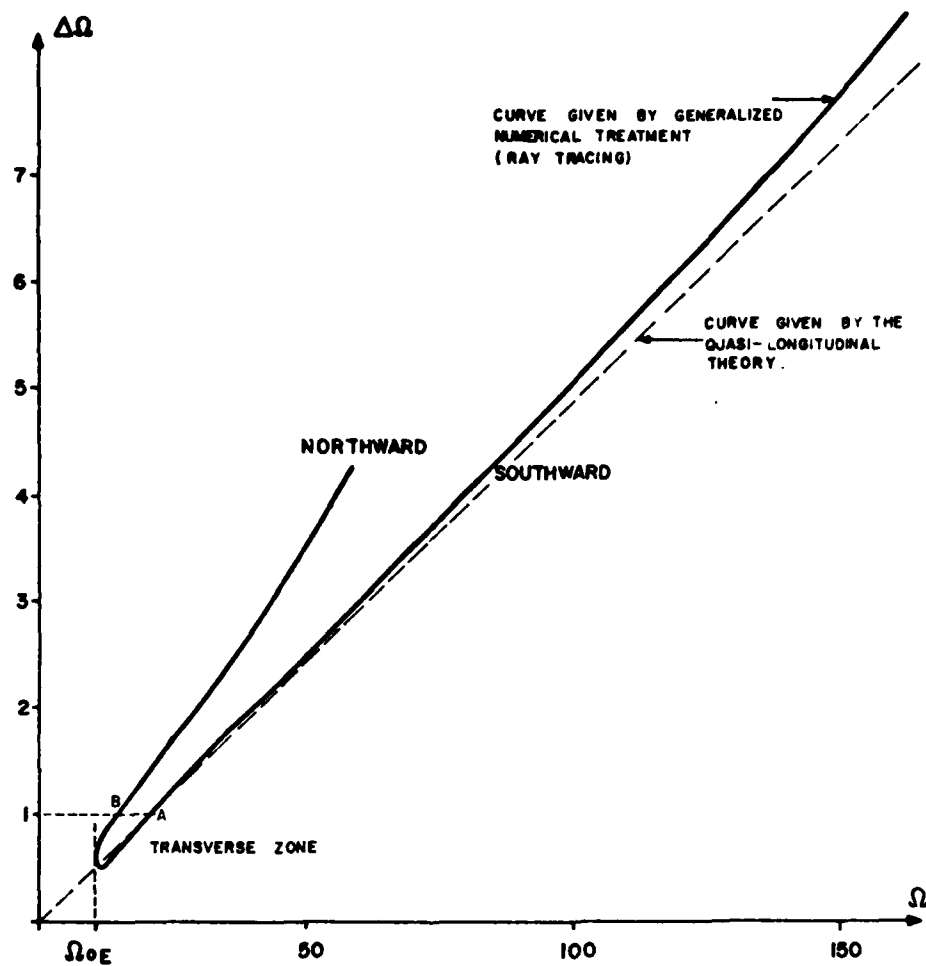


FIG. 4: VARIATION OF  $\Delta\Omega$ , DIFFERENCE BETWEEN THE TOTAL FARADAY ROTATIONS AT 40 AND 41 MHz AS A FUNCTION OF THE TOTAL FARADAY ROTATION  $\Omega$  AT 41 MHz.

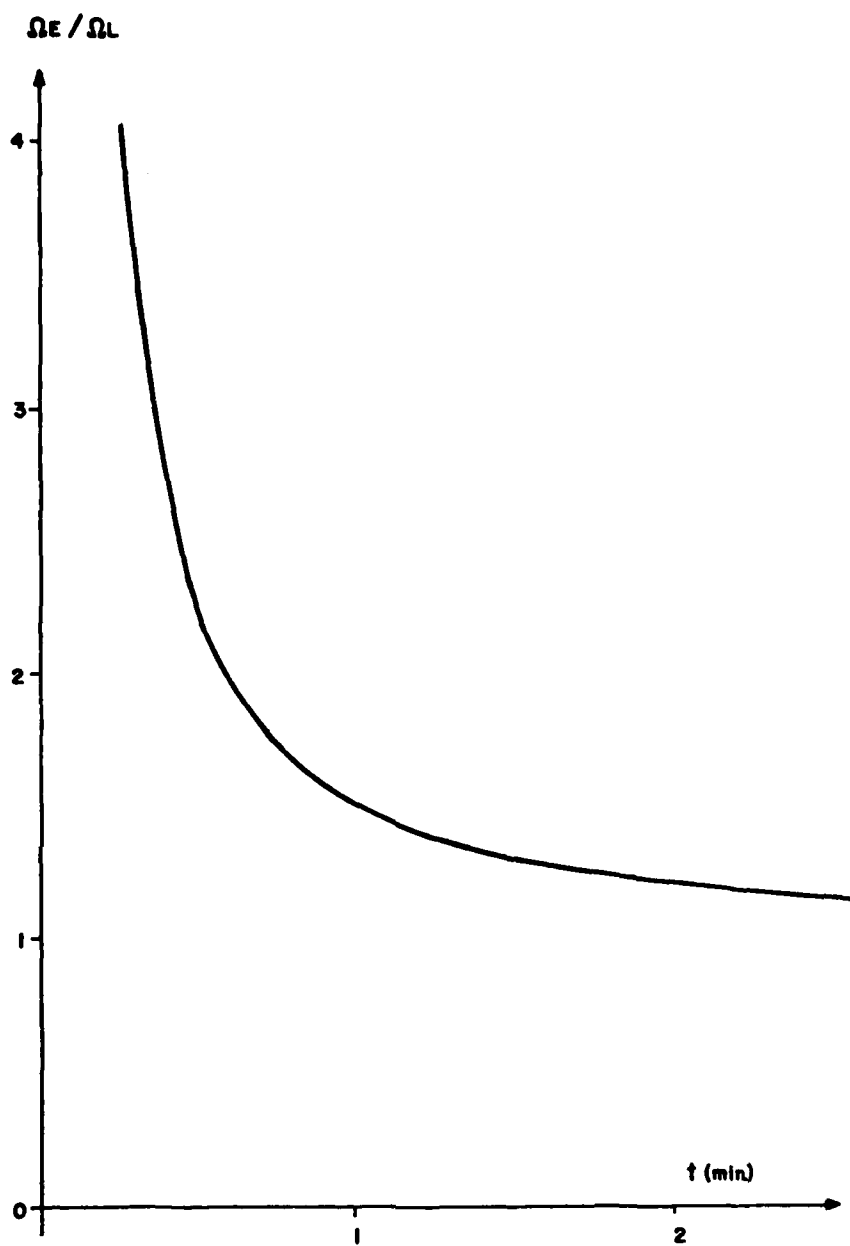


FIG. 5 :CALCULATED FOR PASS No. 22,591  
OF BEB S-66 SATELLITE(II APRIL 1969)

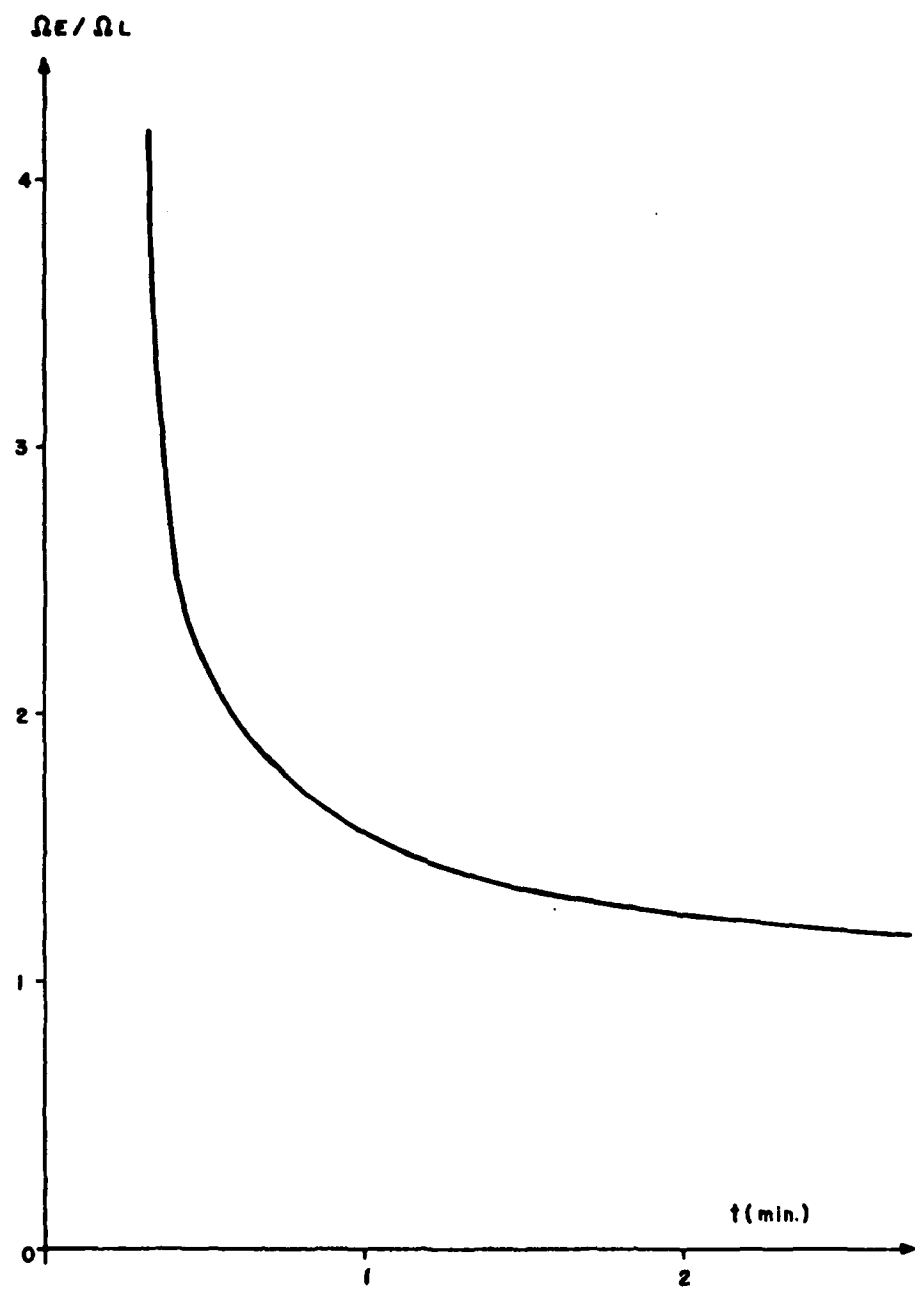
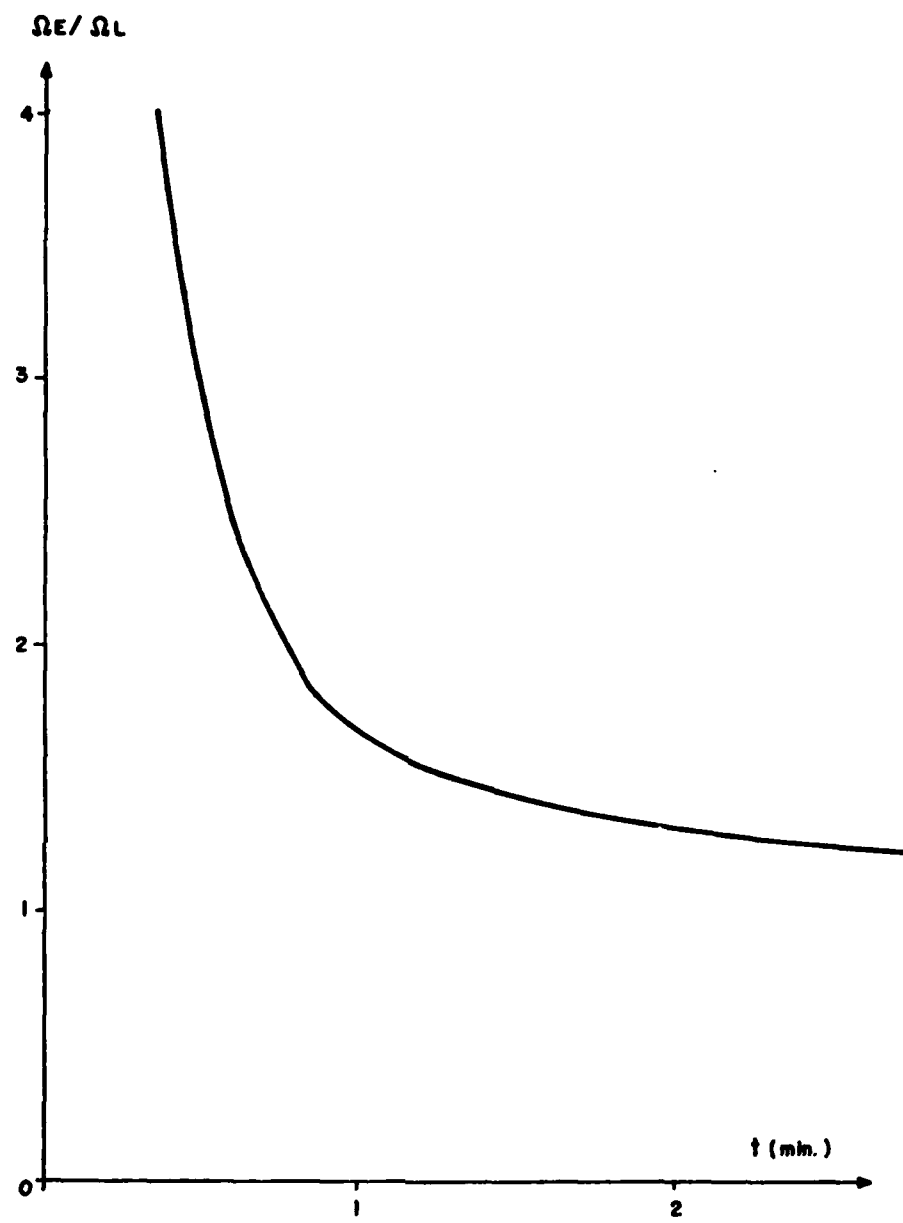


FIG. 6 : CALCULATED FOR PASS No. 22,509  
OF BEB S-66 SATELLITE (5 APRIL 1969)



**FIG. 7 : CALCULATED FOR PASS No. 22,468  
OF BEB S-66 SATELLITE (2 APRIL 1969)**

VERTICAL ION DRIFTS, EXOSPHERIC TEMPERATURES AND NEUTRAL WINDS  
CALCULATED FROM SIMPLE OBSERVATIONS AND NUMERICAL SIMULATION  
OF THE IONOSPHERE

by

D. A. Antoniadis and A. V. da Rosa  
Radioscience Laboratory  
Stanford University  
Stanford, California 94305

ABSTRACT

A method was developed for the determination of induced ionospheric plasma drifts by means of a dynamic simulation technique using columnar electron content as the only measured input. The method can be extended to yield also exospheric neutral temperatures if, in addition to the electron content data, values of peak electron concentrations are available. The method was tested with data collected both in the East and the West coasts of the USA during the 23-24 March 1970 period. The values of drifts and temperatures as well as those of some other ionospheric parameters obtained were compared with corresponding results from radar measurements made at Millstone Hill. A good agreement was found between the two sets of measurements. Meridional exospheric temperature gradients and the corresponding neutral winds, compatible with the calculated plasma drifts were derived through the use of a dynamic model of the thermosphere.

1. INTRODUCTION

It has long been recognized that both neutral winds and electric fields induce ionospheric plasma motions that strongly influence the behavior of the ionosphere. Of greatest interest concerning the F-layer ionosphere are the induced, magnetic field-aligned, plasma motions, often termed vertical plasma drifts. Following the terminology in Rishbeth [1972], the word "drift" in the present article refers to a bulk motion of plasma, due to either winds or electric fields. Such motions are indirectly observed with incoherent radars [c.f. Vasseur, 1969; Evans et al., 1970; Taylor, 1974]. When electric fields can be estimated, it is possible to calculate the neutral winds that are compatible with those plasma drifts [Salah and Holt, 1974; Roble et al., 1974; Antoniadis, 1976a].

Numerous theoretical studies of neutral winds have been presented [for a review see Rishbeth, 1972], and the most important aspects of this phenomenon have been analyzed in detail. Similarly electric fields affecting the ionospheric F-layer have been studied in several papers and some models have been proposed [Maeda et al., 1966; Matsushita, 1969, 1971; Stening, 1973; Kirchhoff and Carpenter, 1975].

Ionospheric dynamic models, coupled with theoretical neutral wind and electric field models, have been used by a number of workers [for example:

Kohl et al., 1968; Bailey et al., 1969; Stubbe, 1970; Rüster, 1971] to explain various aspects of ionospheric behavior, especially during quiet periods. More recently, Roble [1975] has used a dynamic ionospheric model with reasonable success in simulating the diurnal ionospheric behavior in realistic terms, by using neutral winds derived from incoherent scatter radar observations of plasma motions.

It is possible to invert the problem and attempt to determine vertical plasma drifts from the ionospheric behavior by using simulation techniques. In this paper, we present and evaluate a simulation technique through which one or more observable ionospheric parameters are directly introduced to a dynamic ionospheric model to yield information about one or more processes (or physical quantities) affecting the behavior of the ionosphere. Limitations of our technique arising from the necessity of additional inputs to the ionospheric simulation are identified and discussed. The basic mode (mode 1) of our simulation technique is used to derive vertical plasma drifts, at the East coast of USA from vertical electron content data,  $I_z$ , during an equinoxial day of 1970. These drifts are compared with those obtained during the same day by incoherent scatter radar at roughly the same geographical location. A second variation (mode 2), which employs peak electron concentration,  $N_e^{\max}$ , data in addition to  $I_z$ , is used to derive both vertical drifts and exospheric temperatures at the West coast of USA during the same day as above, bringing out some interesting similarities and differences between quantities in the East and West coasts. A third variation (mode 3), which is a combination of mode 2 with a thermospheric model, presented by Antoniadis [1976a], is used to derive horizontal wind profiles and meridional exospheric temperature gradients at the East coast.

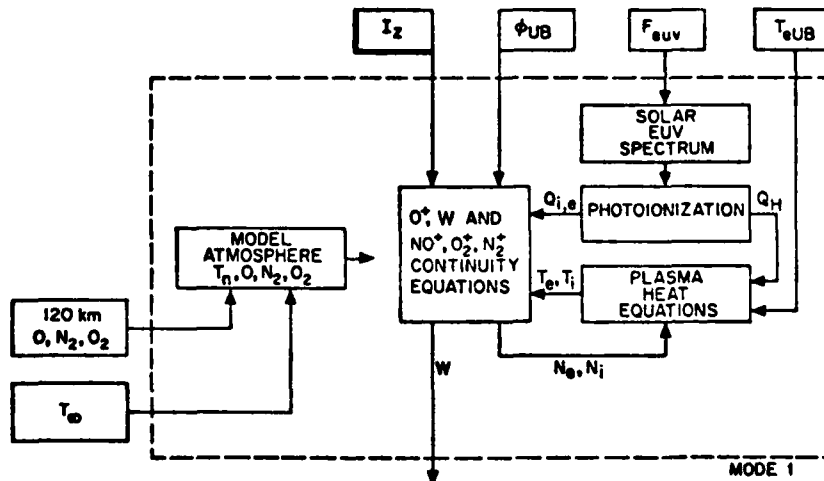


Figure 1. Block diagram of the ionospheric model. Also shown are the input parameters required for the basic mode (mode 1) of simulation. This mode is used to calculate the induced vertical plasma drift,  $W$ , from electron content data.

## 2. THE IONOSPHERIC MODEL

A block diagram of our basic ionospheric model is shown in Figure 1. Many of the details of this model are given by Antoniadis [1976b] and thus, only a brief description will be given here.

The neutral atmosphere is assumed to be in diffusive equilibrium and the vertical distributions of O, O<sub>2</sub>, N<sub>2</sub> and T<sub>n</sub> are given by the analytic expression of Bates [1959]. The necessary inputs to this atmospheric model are the concentrations at the bottom of the thermosphere, at 120 km, and the exospheric neutral temperature, T<sub>∞</sub>.

The considered ionospheric constituents are, O<sup>+</sup>(<sup>4</sup>S), O<sup>+</sup>(<sup>2</sup>D), N<sub>2</sub><sup>+</sup>, O<sub>2</sub><sup>+</sup> and NO<sup>+</sup>. The concentration of O<sup>+</sup>(<sup>4</sup>S), N<sub>1</sub>, and the vertical ion drift velocity, W, are derived from the continuity equation of O<sup>+</sup>(<sup>4</sup>S), in the form:

$$\frac{\partial N_1}{\partial t} = Q_1 - \beta N_1 - \frac{\partial(N_1 W)}{\partial z} + D_z \left[ \frac{\partial^2 N_1}{\partial z^2} + A \frac{\partial N_1}{\partial z} + BN_1 \right] \quad (1)$$

where Q<sub>1</sub> is the net production rate of O<sup>+</sup>(<sup>4</sup>S) resulting from photoionization processes and calculated using the solar EUV spectrum of Hinteregger [1970] multiplied by an adjustable factor F<sub>EUV</sub>; β is the O<sup>+</sup>(<sup>4</sup>S) loss rate coefficient; D<sub>z</sub> the effective diffusion coefficient for vertical transport related to the ambipolar diffusion coefficient by D<sub>z</sub> = D<sub>z</sub> sin<sup>2</sup>I, where I is the geomagnetic inclination or dip angle. The coefficients A and B are functions of altitude and of neutral and plasma temperatures. The exact expression for W is:

$$W = \left( \frac{E_x}{B} - U_y \sin I \right) \cos I \cos D \\ + \left( \frac{E_y}{B} - U_x \sin I \right) \cos I \sin D + U_z \sin^2 I \quad (2)$$

where x, y, z are our cartesian coordinates correspondingly eastward, northward and upward, E the electric field, U the velocity of neutral wind and D the magnetic declination. It can be seen from (2) that because of U, W would, under most circumstances, be altitude dependent. However, in order to keep the solution of (1) in terms of W and N<sub>1</sub>, as simple as possible, we have made the assumption of an altitude independent "effective" W. It turns out, as will be seen later on, that the value of this effective W is very close to the value of an altitude dependent drift at the peak of the F2 layer.

The boundary conditions, b.c., for (1) are: chemical equilibrium at the lower boundary (z<sub>l</sub> = 120 km) and plasma flux, φ<sub>UB</sub>, and the upper (z<sub>U</sub> = 800 km). In addition, the vertical O<sup>+</sup>(<sup>4</sup>S) content, I<sub>0</sub>, is used as a b.c. so that a simultaneous solution for the altitude profile of N<sub>1</sub> and the vertical plasma drift, W, is obtained. Details of the numerical technique are given in Antoniadis [1976b]. In order to derive I<sub>0</sub> from the vertical electron content, I<sub>z</sub> (which is obtained from measurements as discussed in the next section), it is necessary to determine the contribution of the other ions (primarily O<sub>2</sub><sup>+</sup> and NO<sup>+</sup> and also N<sub>2</sub><sup>+</sup> and O<sup>+(2D)</sup>) to I<sub>z</sub>. This is accomplished by solving the

continuity equations of those ions to yield their concentration profiles. These equations however can be and are simplified substantially by assuming negligible transport, and, for  $N_2^+$  and  $O^+(2D)$  further assuming chemical equilibrium.

The electron and ion temperatures are obtained from the heat balance equations [Herman and Chandra, 1969]:

$$\begin{aligned}\frac{\partial T_e}{\partial t} &= \frac{Q_H - L_{ei} - L_{en}}{\frac{3}{2} k N_e} + \frac{\sin^2 I}{\frac{3}{2} k N_e} \frac{\partial}{\partial z} (K_e \frac{\partial T_e}{\partial z}) \\ \frac{\partial T_i}{\partial t} &= \frac{L_{ei} - L_{in}}{\frac{3}{2} k N_i} + \frac{\sin^2 I}{\frac{3}{2} k N_i} \frac{\partial}{\partial z} (K_i \frac{\partial T_i}{\partial z})\end{aligned}\quad (3)$$

where  $T_e$ ,  $T_i$  are the electron and ion temperatures;  $Q_H$  the electron heat input given by Swartz et al. [1972];  $L_{ei}$ ,  $L_{en}$ ,  $L_{in}$  the electron-ion, electron-neutral, ion-neutral heat loss rates;  $K_e$ ,  $K_i$  the electron and ion thermal conductivities;  $k$  Boltzmann's constant and  $N_e$ ,  $N_i$  the electron and ion concentrations. Equations (3) are by no means complete since mechanisms such as convection and non-local heating are neglected. However, they are adequate for our purposes. Boundary conditions for (3) are:  $T_e = T_i = T_n$  at the lower boundary and the electron temperature at the upper boundary,  $T_{eUB}$ .

The differential equations of the model are solved numerically as discussed in Antoniadis [1976b]. The resulting computer program is very efficient; for example, a complete solution for a single time step with 70 altitude cells, requires approximately 2 seconds on a SDS Σ-5 computer.

### 3. THE DATA

Referring to Figure 1, the input data to the ionospheric simulation can be classified into three categories:

- (a) Directly (and simply) observable ionospheric parameters such as  $I_z$  and  $N_{max}$  (in mode 2, Figure 5).
- (b) Indirectly observable geophysical parameters such as EUV flux ( $F_{euv}$  in our case) and  $T_\infty$  which may be related through models to the observable solar radio flux parameters  $F_{10.7}$ .
- (c) Modeled parameters such as neutral composition at the lower boundary (120 km), protonospheric plasma flux  $\Phi_{UB}$  and heat flux or alternatively,  $T_{eUB}$ , that generally cannot be related on a day-to-day basis to observable quantities.

It should be noted that though  $T_\infty$ ,  $\Phi_{UB}$  and  $T_{eUB}$  are all quantities that can be measured by incoherent scatter radar techniques and thus might all fit category (a), we have reserved this category for those data that can be measured in a simple manner. This reflects the basic philosophy behind our simulation technique which is to use as primary input only easily obtainable

quantities. Thus, radar data, whenever available, can be used to support our simulation but are not a required input.

Ideally, the results of our simulation technique should exhibit large sensitivity to parameters in (a) and small to parameters in (b) and (c). Due to the complexity of the ionospheric model and to the great variety of possible conditions to which this simulation might be applied, a general sensitivity analysis is almost impossible and, the best approach to this task is to evaluate the reliability of the results for each particular application or perhaps class of applications. As we proceed in the following section with the presentation of our results, we will be discussing the sensitivity aspect in terms as general as possible. In the rest of this section we will consider the determination of  $I_z$  from beacon satellite measurements.

The data from which  $I_z$  has been determined, for the applications in the following section, have all been produced by the Faraday rotation method. With this method a slant electron content,  $I_s$ , is determined from the measured rotation angle (in radians),  $\Omega_F$ , by:

$$I_s = \frac{\Omega_F}{G} \quad (4)$$

where G is known as the layer shape factor and is defined by

$$G = \frac{Q_F}{f^2} \frac{\int_0^{s_{sat}} N_e B_L ds}{\int_0^{s_{sat}} N_e ds} \quad (5)$$

where  $Q_F$  is a constant with a numerical value of  $2.36 \times 10^4$  in m.k.s. units, f the frequency in Hz,  $N_e$  the concentration of electrons in  $m^{-3}$ ,  $B_L$  the longitudinal component of the geomagnetic flux in  $wbm^{-2}$  and  $I_s$  an element of length along the ray path, s, in meters. Since  $B_L$  is not constant with respect to s, G depends on the shape of the  $N_e$  distribution along s (but not on the magnitude of  $N_e$ ). Because of this dependence on the layer shape factor, G cannot be uniquely defined.

Figure 2 is a plot of  $B_L$  with respect to altitude along s, for two different observer-satellite geometries. Since  $B_L$  decays rather quickly with altitude and the bulk of the plasma exists at lower altitudes, most workers often define a constant shape factor G and use (4) to determine the plasma content below a certain (rather loosely determined) altitude. For example, Titheridge [1972], using a collection of ionization profiles and the centered dipole approximation for the geomagnetic field has pointed out that, by adopting a constant or "effective shape factor"  $\bar{G}$  determined by:

$$\bar{G} = \frac{Q_F}{f^2} B_L \quad (6)$$

with  $B_L$  evaluated at a point on s and at an altitude of 420 km, the plasma content below about 2000 km can be determined with an estimated accuracy of  $\pm 5\%$ .

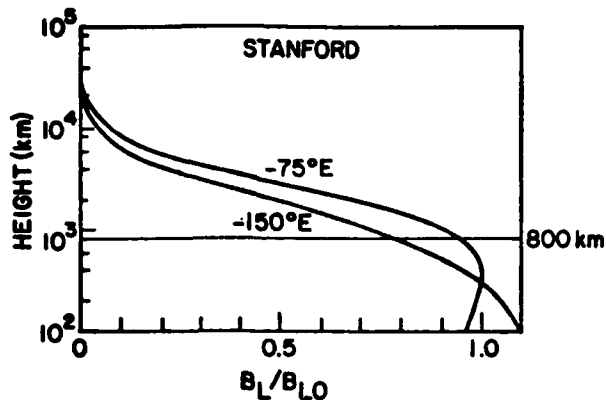


Figure 2. Vertical profile of the normalized longitudinal component of  $\bar{B}$  for Stanford and two different geostationary satellite locations. [Adapted from Almeida, 1973].

It is common practice (and a necessity in our work) to convert the slant content obtained, as described above, to a vertical content. This involves the assumption of horizontal stratification and is described by the following equation:

$$I_{zt} = \frac{\Omega_F}{\bar{G}} \sec x_s \quad (7)$$

where  $I_{zt}$  is the estimated vertical content up to 2000 km and  $x_s$  is the zenithal angle of the line of sight at the point, often referred to as ionospheric point, where  $\bar{G}$  is evaluated. Thus,  $I_{zt}$  is considered as the representative vertical content at the geographic coordinates of the ionospheric point and not of the observer.

Perhaps it can be appreciated that, the Faraday method is indeed more appropriate than the group delay or phase path difference methods in our case, because it is relatively insensitive to electron concentrations outside the region of interest to us. Ideally, we would like  $B_L$  to be non-zero and constant up to 800 km and zero beyond. This is, of course, a physically unrealizable requirement and, as it is obvious from Figure 2, we might expect some contamination from ionization above 800 km.

In deriving  $I_z$  from  $I_{zt}$ , in the present work we have used the simplest possible scheme, namely, scaling of  $I_{zt}$  by a constant factor  $r < 1$ :

$$I_z = r I_{zt} . \quad (8)$$

The value of  $r$  depends of course on the value of  $\bar{G}$  that was used in determining  $I_{zt}$ . This scheme was found quite satisfactory for the applications of our

simulation technique, presented in the following section. As mentioned there, we have used data of  $I_{zt}$  from two stations and, the value of  $r$  was .9 for the East coast data and .8 $^{zt}$  for the West coast (Stanford) data. These values were arrived at by comparing the measured  $I_{zt}$  with the electron content up to 800 km derived from a plausible electron concentration profile at a given time near local midday. The shape of this profile was assumed similar to that measured with the Millstone Hill radar at the same local time, and its absolute magnitude was determined from the measured  $N_{max}$  at each location of interest. We estimate a probable error in  $r$  of about  $\pm .05$ .

#### 4. APPLICATIONS

##### 4.1. Mode 1

Mode 1 of our ionospheric simulation technique (Figure 1) was used to derive the behavior of vertical plasma drifts,  $W$ , for a 24 hour period during days 23-24 March 1970. The single, directly observable ionospheric parameter required by this mode is  $I_{zt}$  and it was derived as discussed in the previous section, from Faraday rotation data obtained at Sagamore Hill, Massachusetts, using the geostationary satellite ATS-3, then at  $80^{\circ}\text{W}$  longitude. A 420 km ionospheric point with geographic coordinates of  $39^{\circ}\text{N}$ ,  $72^{\circ}\text{W}$ , was assumed for the derivation of  $I_{zt}$  and the scaling factor  $r$  was estimated to be about .9.

Vertical plasma drifts for the same period had been derived by Salah and Holt [1974], from radar data obtained at Millstone Hill ( $42.6^{\circ}\text{N}$ ,  $71.5^{\circ}\text{W}$ ). This proximity provides an excellent opportunity for evaluation of our technique.

The upper boundary electron temperature,  $T_{eUB}$ , the plasma flux,  $\phi_{HB}$  and the exospheric neutral temperature,  $T_{\infty}$ , were established consistent with the incoherent radar measurements [Evans, 1971a, b; Salah and Evans, 1973]. These data are shown in Figure 3.

A comparison of our results with the observations is presented in Figure 4. Shown from top to bottom are: the electron content,  $I_{z}$ ; the vertical ion drift deduced from our calculations together with the drift at 300 km from radar data [Salah and Holt, 1974]; the calculated peak electron concentration,  $N_{max}$ , together with the  $N_{max}$  measured by the Wallops Island ionosonde ( $38^{\circ}\text{N}$ ,  $75^{\circ}\text{W}$ ); the calculated peak height of the F-layer,  $h_{max}$ , together with the  $h_{max}$  observed by the incoherent scatter radar at Millstone Hill. The good agreement between calculations and observations is self-evident.

In the above simulation we have used  $F_{UV} = 2$ . This is consistent with the fact that the analyzed period of time occurred during relatively high solar activity (see section 4.5). The neutral composition at 120 km was kept constant throughout the 24 hours at the following concentrations:

$$[O] = 1.35 \times 10^{11}, [N] = 3.0 \times 10^{11}, [O_2] = 0.5 \times 10^{11} (\text{cm}^{-3}).$$

These concentrations are in general agreement with those used by Roble [1975]. However, it was not found necessary to vary the concentration of monatomic oxygen at 120 km between day and night, as he did.

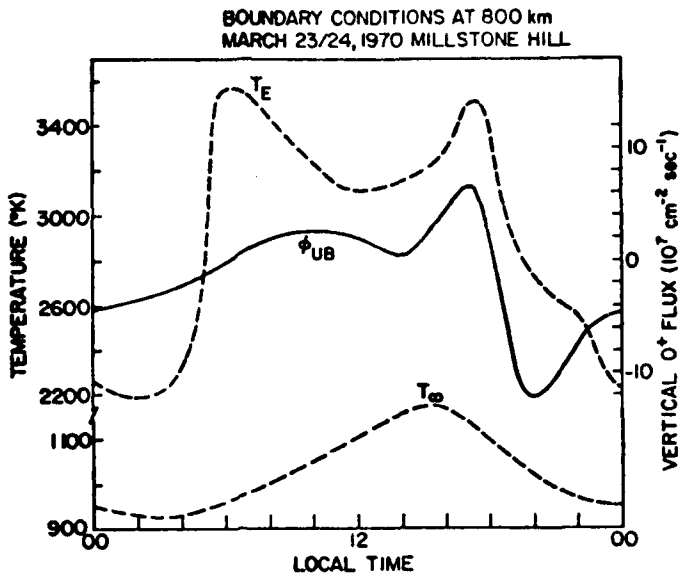


Figure 3. The 800 km boundary conditions for day 23-24 March, 1970 at Millstone Hill. Adapted from Roble [1975].

In a complex numerical simulation, such as the one presented here, the only meaningful way of estimating the sensitivity of calculated quantities to input parameters, is through controlled numerical experiments. We have performed such a series of experiments and the results are presented in the remainder of this section. However, some insight into the expected sensitivities may be gained by discussing briefly, in physical terms, the way in which  $W$  is calculated through our ionospheric model. This can be easily done by considering the continuity equation for  $O^+(^4S)$  (which is the fundamental equation of the model), in its integrated form:

$$\dot{I}_z = \int_{z_L}^{z_U} Q_1 dz - \int_{z_L}^{z_U} \beta N_1 dz - \phi_{UB} \quad (9)$$

where:

$$I_z = \int_{z_L}^{z_U} N_1 dz , \quad (10)$$

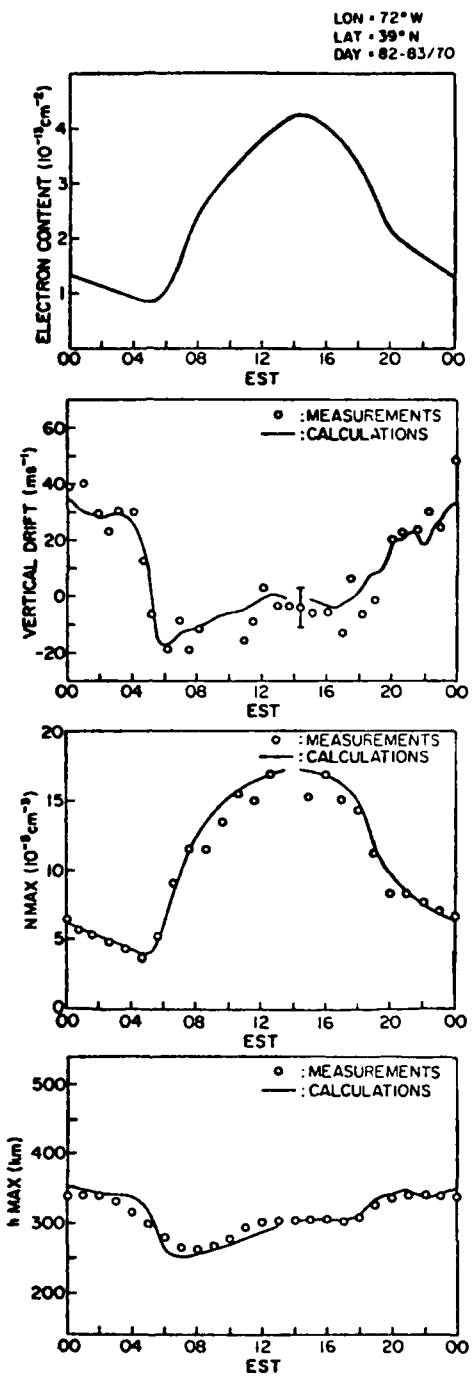


Figure 4. Day 23-24 March, 1970, East Coast. From top to bottom: observed (corrected) vertical electron content,  $I_z$ ; calculated and observed  $N_{\text{max}}$ ; calculated and observed  $h_{\text{max}}$ .

and where for discussion purposes we have assumed that the  $O^+(^4S)$  content is equal to  $I_1$ . At any given time,  $I_1$  and  $I_2$  are known from observations. The effect of vertical drifts,  $W$ , is to control the shape of the ionization distribution and in particular, the altitude of the peak of the F-layer,  $h_{max}$ . The ion loss rate coefficient,  $\beta$ , is a function of atmospheric concentration and consequently it decreases exponentially with height. Therefore, the net result of  $W$  in (9) is to control the magnitude of the second term at the right hand side (the integrated ionization loss rate).  $W$  is not explicitly contained in (9) but is implicitly calculated from this equation by finding the shape of  $N_1(z)$  that satisfies both (9) and (10).

It follows from the preceding discussion that, the sensitivity of the calculated  $W$  (and therefore of  $h_{max}$ ), to the values of  $F_{euv}$  and to the assumed atmospheric composition at 120 km, should be quite large since, the first controls  $Q_1$  while the second controls both  $Q_1$  and  $\beta$ . For instance, at midday, for the conditions of the application presented here (which may be considered typical of equinox conditions during medium and high solar activity) a change of 7 m/s to the calculated  $W$ , with a corresponding change of about 18 km in  $h_{max}$ , would result from: a) -25% change in  $F_{euv}$  or, b) -25% change in the concentration of oxygen at 120 km,  $[O]_{120}$ , or c) -60% change in  $[N_2]_{120}$  or, d) -110% change in  $[O_2]_{120}$ . The experimental error in deducing field aligned plasma drifts from incoherent radar measurements is about +10 m/s [Evans et al., 1970; Salah and Holt, 1974]. Thus, the uncertainty of the calculated  $W$ , from our method, due to any of the above uncertainties is well within the limits of radar measurement errors. We may add here, that since  $h_{max}$  can be obtained from ionosonde measurements, comparisons between calculated and observed  $h_{max}$  can be used to adjust either  $F_{euv}$  or, say,  $[O]_{120}$  (whichever is less reliably known).

It also follows from equation (9) that  $\phi_{UB}$  can play a significant role in our calculations only if it is of magnitude comparable to the integrated production or loss of ionization or, to  $I_1$ . Of course, since  $\phi_{UB}$  is not known a priori, we might resort to a plausible value for such comparisons. Thus, assuming that  $\phi_{UB}$  will not be larger than about  $2 \times 10^8 \text{ cm}^2 \text{ sec}^{-1}$  (generally values reported by incoherent radar investigators are quite smaller than this [Evans, 1975]), under most circumstances,  $\phi_{UB}$  can be assumed negligible, provided the solar zenithal angle is smaller than about  $95^\circ$ . However, during nighttime a much closer examination of individual cases is necessary. In the particular period under investigation the rate of decay of nighttime ionization,  $I_1$ , is larger than  $2 \times 10^8 \text{ cm}^{-2} \text{ sec}^{-1}$ . Since the average downward flux observed at Millstone Hill was less than  $5 \times 10^7 \text{ cm}^{-2} \text{ sec}^{-1}$  the sensitivity of our results to  $\phi_{UB}$  of that order is small. Indeed setting  $\phi_{UB} = 0$  for the complete diurnal run barely affects our results.

The sensitivity of the calculated  $W$ , as well as of most ionospheric parameters, is very small with respect to  $T_{eub}$ . This quantity reflects the protonospheric heat flux which controls the electron temperature,  $T_e$ , down to an altitude of about 400 km (for the conditions considered here) and, thus, affects the behavior of only a small amount of the ionospheric ionization. For instance, setting  $T_{eub}$  constant and equal to 2000 K, 2500 K or, 3500 K in the present simulation, affects our results by a negligible amount. It is therefore estimated that for most applications a simple model of  $T_{eub}$  (or of the protonospheric heat flux) would suffice. Nevertheless, this point must be examined more closely in applications during summer conditions. Summers are

characterized by low electron concentrations resulting to deeper penetration of the heat flux into the ionosphere and generally high  $T_e$  at relatively low altitudes [Evans, 1971c, 1973, 1974].

Finally, the sensitivity of  $W$  to  $T_\infty$  was found to be rather small. We tested this by adding a constant bias ( $+100^\circ\text{K}$ ), to the observed values of  $T_\infty$  and also by forcing  $T_\infty$  to remain constant through the day at  $1050\text{ K}$ , with only small effects in the calculated  $W$ . This observation combined with the fact that  $N_{\max}$  is very sensitive to  $T_\infty$ , has led to the development of mode 2 of our simulation which is presented in the following section.

#### 4.2. Mode 2

The functional block diagram of mode 2 of our ionospheric simulation is shown in Figure 5. As can be seen, the input parameter  $T_\infty$  has been replaced by the observable  $N_{\max}$ , so that  $T_\infty$  now becomes an output of the simulation. The  $T_\infty$  controller corrects successively  $T_\infty$  by means of the empirical equation:

$$\Delta T_\infty = \frac{T_\infty}{\tau} \Delta \tau \quad (11)$$

where  $\tau \equiv I_z / N_{\max}$ , is often referred to as "slab thickness". Equation (11) is solved at every time step using the expected  $\tau$  and the value of  $T_\infty$  and  $\tau$  at the previous step.

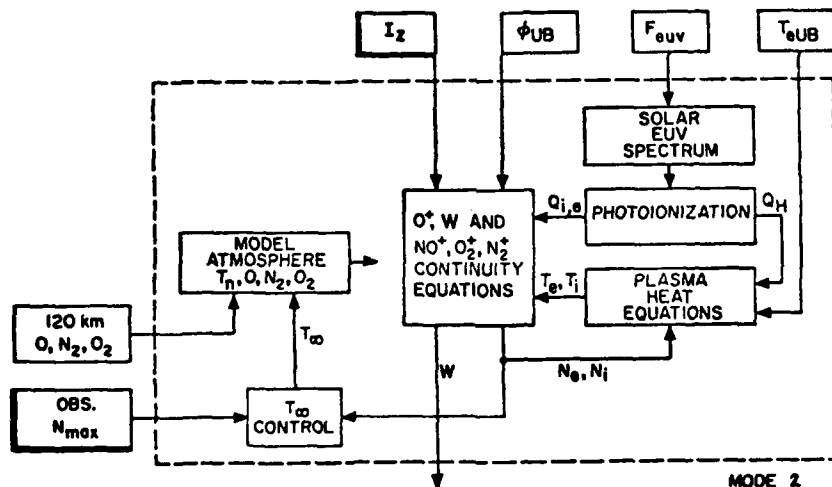


Figure 5. Block diagram of the ionospheric model (mode 2) used to calculate time dependent, induced vertical plasma drift,  $W$ , and exospheric neutral temperature,  $T_\infty$ , from electron content and  $N_{\max}$  data.

We have applied mode 2 with electron content data obtained at Stanford during the same period (23-24 March 1970), as the data in the preceding section. The Faraday rotation method was used with signals from the ATS-1 satellite, parked at 150°W. The 400 km ionospheric point with coordinates 34.2°N, 125.5°W was located just 5° west of the Point Arguello ionosonde station (34.6°N, 120.6°W), where the  $N_{\max}$  data used here were obtained. In this case the scaling factor 2 for the determination of  $I_z$  (equation 8) was estimated, as discussed in Section 3, to be about .8.

Figure 6 presents the vertical electron content,  $I_z$ , that was used in the simulation, the calculated vertical ion drift,  $W$ , the calculated and observed (P. Arguello ionosonde)  $h_{\max}$  and, the calculated exospheric temperature which is compared with the same temperature at Millstone Hill. The latter was shifted in time by about 3 hours in order to coincide with the local time in this simulation. Owing to the fact that this period of time was geomagnetically quiet and that the difference in geographic latitude between Millstone Hill and the location of this simulation is only 8°, this comparison of exospheric temperatures may be considered valid.

The observed  $h_{\max}$  has been plotted directly from the routine table of hourly ionogram data, produced at Point Arguello. We believe that the relatively large discrepancy between calculated and observed  $h_{\max}$  from 0500 to about 1700 is very probably due to errors introduced by the approximate methods of routinely scaling ionograms, manifested mainly by an increase of the estimated  $h_{\max}$  due to incorrect accounting of the bottom side ionization which is quite significant during daytime [Rishbeth and Garriott, 1969].

Several differences between the electron content behavior at the two locations (East and West Coast) can be seen by comparing Figures 4 and 6. For instance, the maximum value of  $I_z$  at Stanford is significantly larger than that at Sagamore Hill. Also the ionization in the East coast decays continuously throughout the night but never reaches values as low as those at Stanford which remain unaltered from a little after midnight to sunrise.

The different behavior of  $I_z$  is reflected in the difference between the calculated vertical drifts at the two locations. Thus, though the change from upward to downward drifts in the early morning occurs at roughly the same local time at the two locations, at the West coast, the drift becomes again positive at 1000 LT and remains so until about 1500 LT while, at the East coast the drift is negative throughout the day. Since negative drifts tend to increase the integrated loss rate (equation 9), the build-up of ionization at the East is slower than at the West coast where it reaches a larger maximum as stated before. On the other hand the opposite may be observed in the afternoon. Then, the drift in the West coast becomes more negative than that in the East coast and remains so until much later in the early evening. This results in a steeper decline of the ionization in the first location.

Referring to the definition of  $W$  (equation 2), repeated here for convenience, the difference of the behavior of  $W$  can be, at least partially explained by the different magnetic field declination at the two locations:

$$W = -(U_y \cos D + U_x \sin D) \cos I \sin I \quad (12)$$

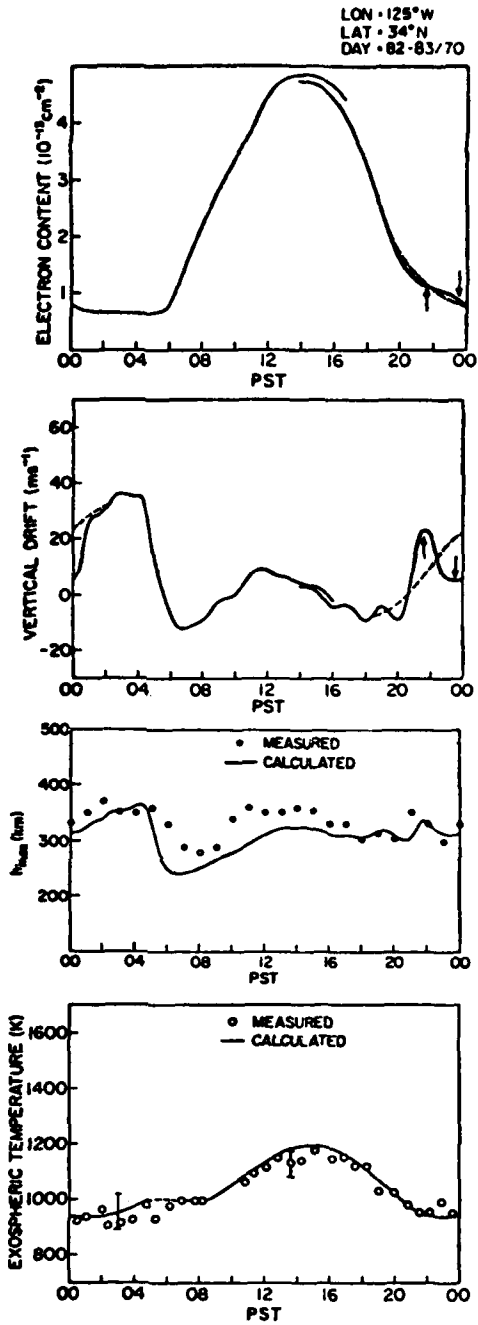


Figure 6. Day 23-24 March, 1970, West Coast. From top to bottom: observed (corrected) vertical electron content,  $I$ ; calculated vertical plasma drift,  $W$ ; calculated and observed  $z_{\text{h}}^{\text{max}}$ ; calculated and observed  $T_{\infty}$ . The dashed lines and the arrows are explained in the text.

where we have assumed that  $W$  is due purely to neutral winds. The magnetic declination is positive (eastward) at the West coast location ( $D=15^\circ$ ) and negative at the East coast location ( $D=-15^\circ$ ). Thus, the contribution of the zonal winds,  $U_x$ , is negative at the West and positive at the East coast. Since neutral winds tend to be westward, i.e.  $U_x$  is negative, from midnight to about 1500 LT and positive in the remaining time, we may indeed expect  $W$  to be algebraically larger at the West in the former period of time and at the East in the latter.

We must add here that, such differences in the behavior of the ionosphere at the same latitude but at different longitudes were spotted rather early from  $N_{max}$  observations at various locations on the Earth and Eyfrig [1963] suggested that they might result from the neutral wind action at different magnetic declinations. Later Kohl et al. [1969] carried out theoretical calculations which confirmed the plausibility of Eyfrig's suggestion.

An interesting result of the steep decay of ionization at the West coast is that the nighttime plasma concentrations are quite small. This leads to a different nighttime situation from that at the East coast. It may be seen from Figure 6 that  $I_z$  is constant from about 0100 LT to 0530 LT. Referring to equation (9)<sup>z</sup> and assuming that nighttime production of ionization is negligible [Fujitaka et al., 1971], the only way for  $I_z$  to be zero is if the protonospheric flux,  $\Phi_{UB}$ , is significant and negative (downward). Thus for this simulation,  $\Phi_{UB}$  cannot be neglected during nighttime and, therefore  $W$  will depend on the assumed value of  $\Phi_{UB}$ .

In order to determine  $\Phi_{UB}$ , we decided to use a very simple model of its behavior namely, we assumed that  $\Phi_{UB}$  is zero between 0700 LT and 2000 LT and has a constant non zero value, during the rest of the time. Then, we adjusted this value by making several trial runs and comparing the calculated  $h_{max}$  with that observed at Point Arguello. Since it is the balance between the action of  $W$  (which controls  $h_{max}$ ) and  $\Phi_{UB}$  that makes  $I_z = 0$ , this approach is justifiable. The estimated plasma flux was  $1.3 \times 10^8 \text{ cm}^2 \text{ sec}^{-1}$  and it must have been present at least between 0100 LT and 0530 LT. This is a substantially larger nighttime flux than that observed at Millstone Hill.

Finally, we would like to discuss briefly the behavior of the calculated  $W$  in the early night hours. The maximum and minimum of  $W$ , both indicated by the arrows in Figure 6, arise (in our simulation) from the rapid change of ionization rate of decay,  $I_z$ , and coincide with the lowest and the highest  $I_z$  respectively (of course, in nature, the causality is reversed). This feature of  $I_z$  was persistent during this period at the West coast, roughly at constant local<sup>z</sup>time and, thus, it seems to represent a regular phenomenon in the behavior of vertical drifts, as further testified by the agreement between calculated and observed  $h_{max}$  at this time. Since, a rapid change in neutral winds that would give rise to such behavior of  $W$  is rather unlikely, a possible cause for this behavior could be a large travelling ionospheric disturbance, TID, or rapidly changing electric fields. In the latter case, because of the small conductivities of the E-layer at this time, a probable origin for the electric fields could be the F-region dynamo [Rishbeth, 1971], or magnetospheric convection. The dashed lines in Figure 6 represent a hypothetical smooth change of electron content,  $I_z$ , for this period of time and the resulting effective vertical drift,  $W$ ; they have been included to

emphasize the large fluctuation of  $W$  necessary to produce the relatively small changes in  $I_z$  and to provide a baseline for the estimation of the amplitude of this fluctuation. As can be seen, this amplitude is about 20 m/s. If this fluctuation is of electromagnetic nature, the necessary electric field amplitude would be about 2 mV/m, an order of magnitude which is well within plausibility limits [c.f. Kirchhoff and Carpenter, 1975].

#### 4.3. Mode 3

Up to this point we have derived vertical plasma drifts by means of modes 1 and 2 of our ionospheric simulation without specifically considering their origin. These drifts have been assumed altitude independent as described in Section 2 where we defined such drifts as "effective", meaning that they have the same effect on the plasma content as altitude dependent drifts under the same circumstances. If the calculated drifts were entirely the result of electric fields then, they could be immediately related to the eastward component of the electric field (assuming  $D \approx 0^\circ$ ), as can be seen from equation (2). However, since at midlatitudes (under geomagnetically quiet conditions), vertical plasma drifts are primarily driven by neutral winds, it is reasonable to relate the calculated drifts to these neutral winds.

Neutral winds and the meridional gradient of exospheric temperature can indeed be calculated from the results of our ionospheric simulation under mode 2 through a dynamic thermospheric model in a way very similar to that presented by Antoniadis [1976a]. In the present case, instead of using incoherent radar data, the data produced by the ionospheric simulation are coupled directly to the thermospheric model. We refer to this mode of coupled ionospheric-thermospheric simulation as "mode 3". A functional block diagram of this mode is given in Figure 7.

As discussed in Antoniadis [1976a], the altitude dependent horizontal components of the wind are specified through the thermospheric model from the value of the vertical plasma drift at a given height. At present the assumption is made that the value of this drift is equal to the value of the effective drift and that the appropriate height is the peak of electron concentration,  $h_{\max}$ , calculated through the ionospheric model.

We have tested the above assumption by comparing the plasma content  $I_z$ , calculated through our model in two ways (note that  $I_z$  in this case was not an input): a) the model was used with an altitude independent plasma drift  $W$ , and b) the model was used with a wind compatible (i.e. altitude dependent)  $W$ , which at  $h_{\max}$  had the same value as the drift in (a). All other model parameters were kept the same. The results of the two runs are shown in Figure 8. It can be seen that during most of the day the calculated contents agree well. The larger differences at night are due to the sharp increase of vertical drift with decreasing altitude below  $h_{\max}$ , associated with the low ion drag in these regions resulting from the small nighttime concentrations of ions (see Figure 10).

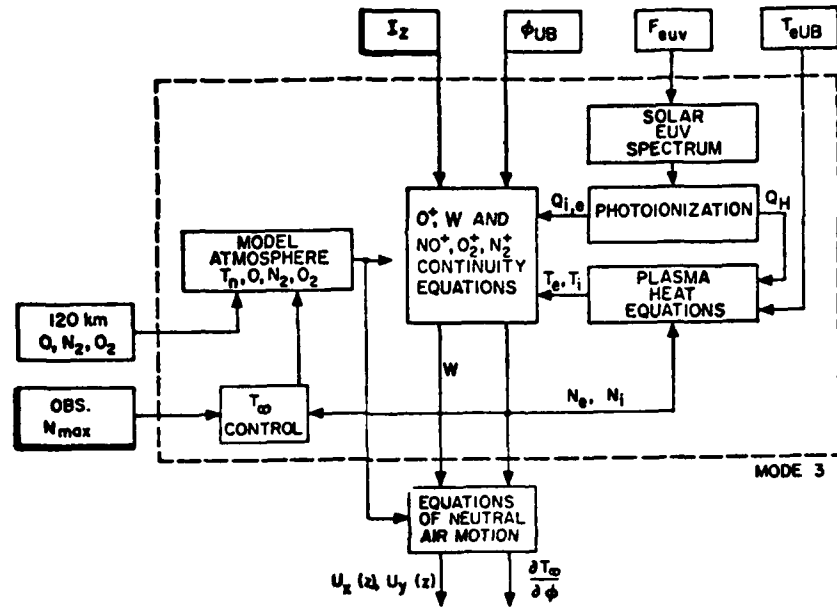


Figure 7. Block diagram of the combined ionospheric-thermospheric model (mode 3). This mode allows the calculation of vertical profiles of neutral winds as well as exospheric temperature and its gradients, from electron content and  $N_{max}$  data.

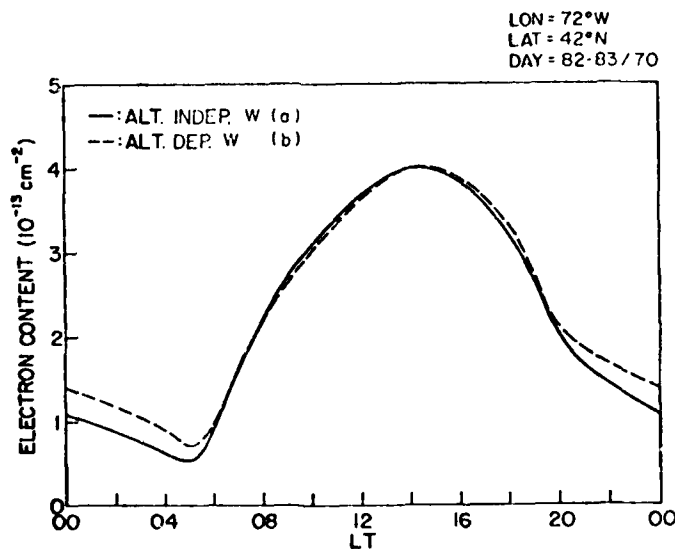


Figure 8. Electron content calculated with: (a) altitude independent vertical plasma drift and (b) neutral wind induced (altitude dependent) drift.

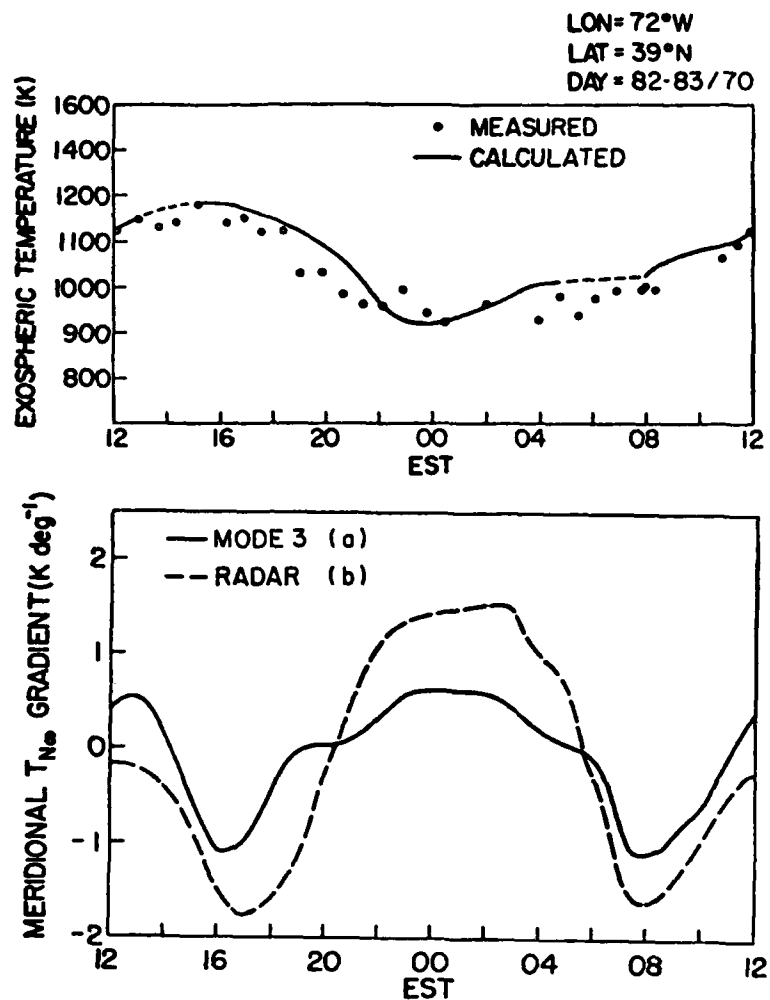


Figure 9. Day 23-24 March, 1970, East coast. Top: the calculated and observed exospheric temperature,  $T_{\infty}$ . Bottom: the calculated meridional exospheric temperature gradient (a), by means of ionospheric-thermospheric simulation (mode 3) and (b), by means of thermospheric simulation and incoherent data [Antoniadis, 1976a].

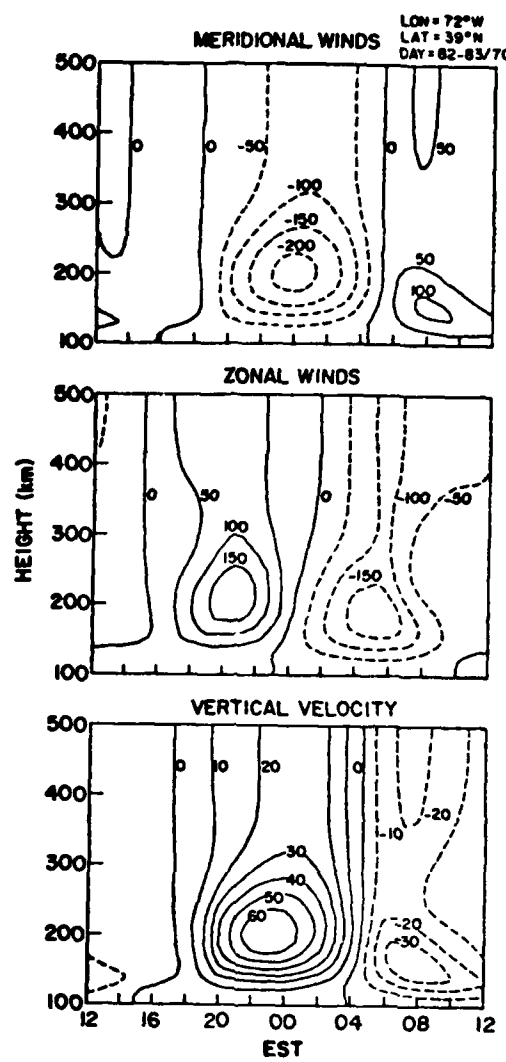


Figure 10. Day 23-24 March, 1970, East coast. From top to bottom: time dependent vertical profiles of the meridional winds, of the zonal winds and of the vertical plazma drift velocity induced by these winds. All quantities were calculated through mode 3 of simulation. Contours annotated in  $\text{ms}^{-1}$ .

We have used mode 3 with the East coast data already discussed in Section 4.1. The  $N_{max}$  data which are also an input in this mode, were obtained from the Wallops Island ionosonde. All other parameters were the same as in Section 4.1. Figure 9 (top) presents the calculated exospheric temperature,  $T_\infty$ , in comparison with the temperature obtained by the Millstone Hill incoherent scatter radar. In the bottom part of this figure, the meridional gradient of  $T_\infty$  calculated here is shown in comparison with the gradient calculated from radar data during the same period in Antoniadis [1976a]. Though several differences between the two calculations can be observed, the agreement is quite remarkable considering the greatly different types of information from which they were derived. Besides we have reason to believe that a more careful treatment of the effective drift used here would result in smaller discrepancies, particularly during nighttime.

Finally, Figure 10 presents the calculated wind components, which may be compared with those obtained in Antoniadis [1976a]. Also shown in the same figure is the altitude dependent vertical drift velocity resulting from those wind components.

#### 4. CONCLUSIONS

A new technique, for determining vertical plasma drifts in the F-region, has been presented and its application during a geomagnetically quiet equinox day was evaluated by comparing values calculated using electron content data with those measured independently by incoherent scatter techniques. Although electron content provides the most important b.c. in the analysis, it is necessary to establish the neutral exospheric temperature,  $T_\infty$ , and upper boundary electron temperature and flux by models or radar data. Under many circumstances, the sensitivity to the last two parameters is small and it was demonstrated that  $T_\infty$  can be obtained by using  $N_{max}$  as additional information, thus, effectively freeing the application of our technique from the need of radar support. Finally, neutral winds and meridional exospheric temperature gradients were derived by coupling the ionospheric model to a thermospheric dynamic model that was presented in a previous paper. In view of the simplicity in acquisition of the required ionospheric input parameters, it is believed that the simulation technique presented here, will be a useful new source of neutral wind and exospheric temperature data.

#### ACKNOWLEDGMENTS

Many valuable discussions with Dr. O. K. Garriott are greatly appreciated. The present work was supported by NASA grant NGR-05-020-001.

## REFERENCES

- Almeida, O.G., Protonospheric columnar electron content determination - I. Analysis, J. Atmos. Terr. Phys., 35, 1657 (1973).
- Antoniadis, D.A., Thermospheric winds and exospheric temperatures from incoherent scatter radar measurements in four seasons, J. Atmos. Terr. Phys. 38, 187 (1976a).
- Antoniadis, D.A., Determination of thermospheric quantities from ionospheric radio observations using numerical simulation, Tech. Rept. No. 18, SU-SEL-76-013 (1976b).
- Bailey, G.J., R.J. Moffett and H. Rishbeth, Solution of the coupled ion and neutral air equations of the mid-latitude ionospheric F2-layer, J. Atmos. Terr. Phys., 31, 253 (1969).
- Bates, D.R., Some problems concerning the terrestrial atmosphere above the 100-km level, Proc. R. Soc. A253, 451 (1969).
- Evans, J.V., Observations of F-region vertical velocities at Millstone Hill: 1. Evidence for drifts due to expansion, contraction and winds, Radio Sci. 6, 609 (1971a).
- Evans, J.V., Observations of F-region vertical velocities at Millstone Hill: 2. Evidence for fluxes into and out of the protonosphere, Radio Sci. 6, 843 (1971b).
- Evans, J.V., Millstone Hill Thomson Scatter Results for 1967, Tech. Rept. 482, Lincoln Laboratory, M.I.T. (1971c).
- Evans, J.V., Millstone Hill Thomson Scatter Results for 1968, Tech. Rept. 499, Lincoln Laboratory, M.I.T. (1973).
- Evans, J.V., Some post-war developments in ground-based radiowave sounding of the ionosphere, J. Atmos. Terr. Phys., 36, 2183 (1974).
- Evans, J.V., A review of F-region dynamics, Rev. of Geophys. and Space Phys. 13, 887 (1975).
- Evans, J.V., R.A. Brockleman, R.F. Julian, W.A. Reid and L.A. Carpenter, Determination of F-region vertical drifts at Millstone Hill, Radio Sci. 5, 27 (1970).
- Eyfrig, R.W., The effect of magnetic declination on the F2-layer, Ann. Geophys. 19, 102 (1963).
- Fujitaka, K., T. Ogawa and T. Tohmatsu, A numerical computation of the ionization redistribution effect of the wind in the nighttime ionosphere, J. Atmos. Terr. Phys., 33, 687 (1971).
- Herman, J.R. and S. Chandra, The influence of varying solar flux on ionospheric temperatures and densities: a theoretical study, Planet. Space Sci., 17, 815 (1969).

- Hinteregger, H.E., The extreme ultraviolet solar spectrum and its variation during the solar cycle, Ann. Geophys.. 26, 547 (1970).
- Kohl, H., J.W. King and D. Eccles, Some effects of neutral air winds on the ionospheric F-layer, J. Atmos. Terr. Phys., 30, 1733 (1968).
- Kohl, H., J.W. King and D. Eccles, An explanation of the magnetic declination effect in the ionospheric F2-layer, J. Atmos. Terr. Phys., 31, 1011 (1969).
- Maeda, K. and S. Kato, Electrodynamics of the ionosphere, Space Sci. Rev., 1, 57 (1966).
- Matsushita, S., Dynamo currents, winds and electric fields, Radio Sci., 4, 771 (1969).
- Matsushita, S., Interactions between the ionosphere and the magnetosphere for Sq and L variations, Radio Sci., 6, 279 (1971).
- Rishbeth, H., The F-layer dynamo, Planet. Space Sci., 19, 263 (1971).
- Rishbeth, H., Thermospheric winds and the F-region: A review, J. Atmos. Terr. Phys., 34, 1 (1972).
- Rishbeth, H. and O.K. Garriott, Introduction to ionospheric physics, Academic Press, New York (1969).
- Roble, R.G., The calculated and observed diurnal variation of the ionosphere over Millstone Hill on March 23-24, 1970, Planet. Space Sci. 23, 1017 (1975).
- Roble, R.G., B.A. Emery, J.E. Salah and P.B. Hays, Diurnal variation of the neutral thermospheric winds determined from incoherent scatter radar data, J. Geophys. Res., 79, 2868 (1974).
- Rüster, R., Solution of the coupled ionospheric continuity equations and the equations of motion for the ions, electrons and neutral particles, J. Atmos. Terr. Phys., 33, 137 (1971).
- Salah, J.E. and J.V. Evans, Measurements of thermospheric temperatures by incoherent scatter radar, Space Research XIII, 267 Akademie-Verlag, Berlin (1973).
- Salah, J.E. and J.M. Holt, Midlatitude thermospheric winds from incoherent scatter radar and theory, Radio Sci., 9, 301 (1974).
- Stening, R.J., The electrostatic field in the ionosphere. Planet. Space Sci., 21, 1897 (1973).
- Stubbe, P., Simultaneous solution of the time dependent coupled continuity equations, and equations of motion for a system consisting of a neutral gas, an electron gas, and a four component ion gas, J. Atmos. Terr. Phys., 32, 865 (1970).

- Swartz, W.E. and J.S. Nisbet, Revised calculations of F-region ambient electron heating by photoelectrons, *J. Geophys. Res.* 77, 6259 (1972).
- Taylor, G.N., Meridional F2-region plasma drifts at Malvern, *J. Atmos. Terr. Phys.* 36, 267 (1974).
- Titheridge, J.E., Determination of ionospheric electron content from the Faraday rotation of geostationary satellite signals, *Planet. Space Sci.*, 20, 353 (1972).
- Vasseur, G., Dynamics of the F-region observed with Thomson Scatter-I. Atmospheric circulation and neutral winds, *J. Atmos. Terr. Phys.*, 31, 397 (1969).

DETERMINATION OF LUNAR-DYNA MO ELECTRIC FIELDS  
FROM TOTAL ELECTRON CONTENT MEASUREMENTS

by

P. A. Bernhardt, D. A. Antoniadis, and A. V. da Rosa  
Radioscience Laboratory  
Stanford University  
Stanford, California 94305

Temporal variations in the ionospheric electron content result from movement of the sun and the moon with respect to a fixed point in the F-layer. The solar electron content component contains diurnal effects due to photoionization, neutral winds driven by pressure gradients, and electric fields. The solar thermal contribution masks the solar gravitational contribution to tidal variations in electron content. Relatively small lunar variations in electron content are produced by atmospheric tides resulting from fluctuations in the lunar gravitational potential. Since the lunar gravitational potential contains frequency components that are significantly different from the solar frequency components, filtering may be used to separate the lunar and solar effects in the electron content measurements. A finite-duration impulse-response digital filter is used in the separation process. Theoretical analysis of the filtered electron content variation is used to determine electric fields produced by the lunar dynamo.

INTRODUCTION

Tidal variations in ionospheric electron content have been previously observed by Rao and Stubenrauch [1967]. Their analysis produced an estimate of the content variation at the lunar semi-diurnal ( $M_2$ ) frequency. The ionosphere is a nonlinear medium in which the solar photoionization and the lunar gravitational field interact resulting in the mixing of the solar and lunar frequencies. Thus, the  $M_2$  tidal component produces variations at several frequencies. In our analysis, all the frequency components, generated by the  $M_2$  tidal frequency are considered.

It has been shown that the established methods of tidal analysis (such as given by Bartels and Johnston [1940], Chapman and Bartels [1940], and Chapman and Miller [1940]) which involve grouping of data by fixed periods of time are equivalent to processing by a finite-duration impulse-response digital filter (or, equivalently, delay filter) [Bernhardt, 1974]. The transfer function of the delay filter has narrow stopbands and passbands for the rejection or acceptance of harmonic components in data. By cascading several delay filters, a wide range of filter characteristics may be achieved [Bernhardt and Schlapp, 1976].

In this paper we present an optimized delay-filter which is used to estimate the variations of the total electron content produced by the main lunar tidal component  $M_2$ . The lunar variations in electron content are used to derive the F-layer plasma drifts necessary to produce these variations by means of the ionospheric simulation technique developed by Antoniadis [1976]. These plasma drifts are attributed to electric fields resulting from the E-region lunar-dynamo.

## THE FILTER

The electron content data are analyzed by the use of the generalized delay filter illustrated in Figure 1. The filter consists of  $2N$  elements each with a delay of  $T$  (days). The data input,  $U(t)$ , is fed into the first element in the delay line. The taps of the delay line are multiplied by weights  $a_m$ ,  $-N \leq m \leq N$ . The outputs of the multiplicative weights are averaged to produce the output of the filter  $X(t)$ . Thus,  $X(t)$  is the weighted average of the data  $N$  delays before and after the data value at a time  $t - NT$ .  $U(t-NT)$ , the unfiltered representative of  $X(t)$ , is tapped from the center of the delay line.

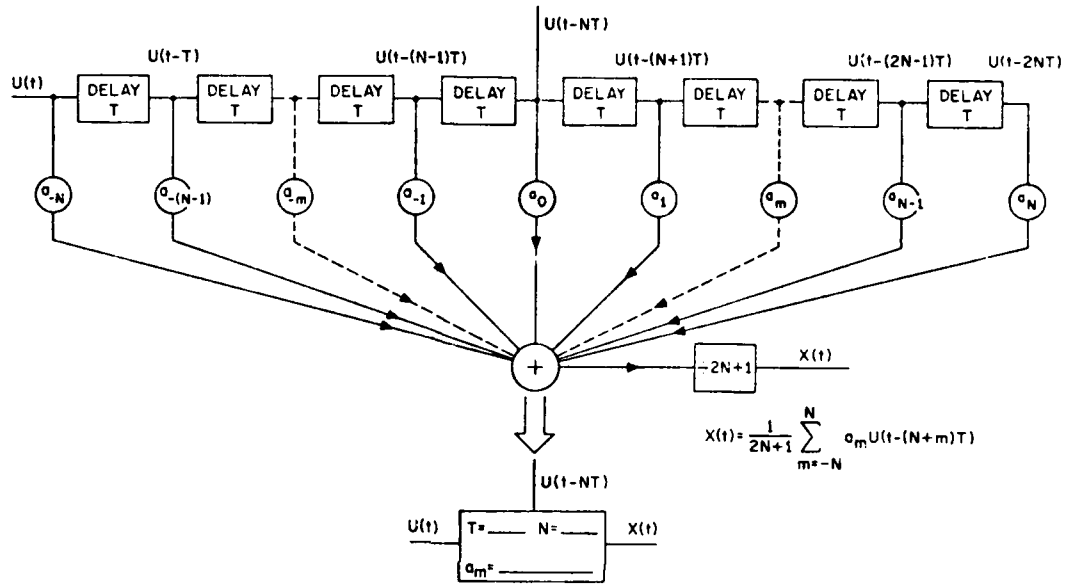


FIGURE 1. Generalized delay-filter model.

$$T(f) = \frac{1}{2N+1} \sum_{m=-N}^{N} a_m \exp[-j2\pi f(N+m)T] \quad (1)$$

where  $T(f)$  is the Fourier transform of the impulse response of the filter and  $f$  is frequency in cycles per day. The procedure of calculation of the filter transfer function is given by Bernhardt [1974].

We have developed an easily implementable filter which is used to isolate the solar harmonic components (with frequencies that are multiples of one cycle per day) from the lunar semi-diurnal component  $M_2$  (at frequency  $f_{M2} = 1.93227$  cycles per day) and the frequency components resulting from mixing between the solar harmonics and  $M_2$ . The notation for the components of the measured electron content variations is as follows:

$I = I_S + I_L + I_R$  is the unfiltered data.

$I_S$  is the variation due to the sun.

$I_L$  is the luni-solar variation resulting from nonlinear interaction between the semi-diurnal lunar ( $M_2$ ) input and the solar harmonics.

$I_R$  is the residue after  $I_S$  and  $I_L$  have been subtracted from the data.

The filter was designed to efficiently sort out each of these data components.

The solar variation can be written as a Fourier series

$$I_S(t) = \sum_{n=0}^{\infty} b_n \cos(2\pi nt + \beta_n) \quad (2)$$

where  $t$  is time in days,  $b_n$  is the amplitude of the component with frequency  $n$  cycles per day and  $\beta_n$  is the phase of each component. The solar filter with narrow passbands around 0, 1, 2, 3 etc. cycles/day may be constructed from the generalized delay filter by setting all the weights to unity (i.e.,  $a_m = 1$ ,  $-N \leq m \leq N$ ) and setting the length of each delay element to  $T = 1$  day. The transfer function of the solar delay-filter is calculated from (1) to give

$$T_S(f) = \exp[-j2\pi fT] \frac{\sin[(2N+1)\pi fT]}{(2N+1)\sin(\pi fT)} \quad (3)$$

The width of the bandpass lobes in the filter is inversely proportional to the length  $(2N+1)$  of the delay line. All the filtering in this paper is done with  $N = 29$  delay filters requiring 59 days (two months) of data. The magnitude response of the  $N = 29$  solar filter is illustrated in Figure 2a.

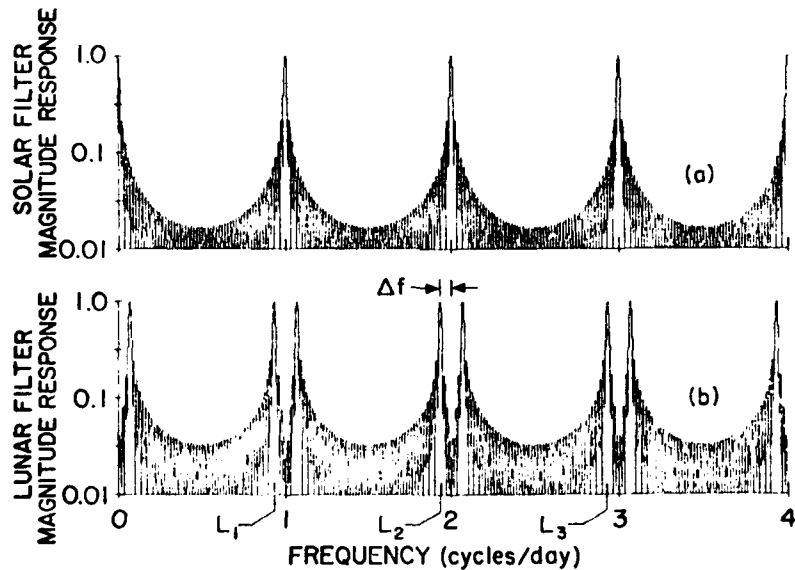


FIGURE 2. Comparison of response of the (a) solar and (b) lunar filters.

The lunar semi-diurnal frequency component is written as

$$I_{M2} = a_{M2} \cos (2\pi t f_{M2} + \alpha_{M2}) \quad (4)$$

where  $I_{M2}$  is the electron content variation at the lunar frequency  $f_{M2}$ , and  $a_{M2}$  and  $\alpha_{M2}$  are the amplitude and phase of this variation, respectively. The luni-solar lines resulting from nonlinear mixing in the ionosphere have the form

$$\begin{aligned} I_L(t) &= \sum_{n=0}^{\infty} c_{n+} \cos [2\pi(f_{M2}+n) t + \delta_{n+}] \\ &+ \sum_{n=1}^{\infty} c_{n-} \cos [2\pi(f_{M2}-n) t + \delta_{n-}] \end{aligned} \quad (5)$$

where  $c_{n+}$  and  $\delta_{n+}$  are the amplitude and phase, respectively. The  $\pm$  sign denotes the solar sidebands around the  $M_2$  frequency. Redefining the amplitudes and phases, and noting that  $f_2 = 1.93227$  is close to the solar semi-diurnal frequency (2 cycles per day), the equation for  $I_L(t)$  can be written in terms of sidebands around the solar harmonic frequencies:

$$I_L(t) = \sum_{m=0}^{\infty} \{d_{m+} \cos[2\pi(m+\Delta f)t + \gamma_{m+}] + d_{m-} \cos[2\pi(m-\Delta f)t + \gamma_{m-}]\} \quad (6)$$

where  $\Delta f = 2 - f_{M2} = .0677262$  cycles/day, and  $d_{m+}$  and  $\gamma_{m+}$  are the amplitudes and phases of the luni-solar sidebands about the solar line at  $m$  cycles/day.

The main luni-solar lines are denoted according to the convection adopted by Gupta and Chapman [1969].  $L_1$  is the lower sideband of  $M_2$  produced by mixing with the solar diurnal component  $S_1$  at one cycle per day.  $L_2$  and  $M_2$  are equivalent.  $L_3$  is the upper solar sideband of  $M_2$ . The frequencies of the main lines are

$$\begin{aligned} f_{L1} &= f_{M2} - 1 = .93227 \text{ cycles/day} \\ f_{L2} &= f_{M2} = 1.93227 \text{ cycles/day} \\ f_{L3} &= f_{M2} + 1 = 2.93227 \text{ cycles/day} \end{aligned}$$

In Eq. (6), the amplitudes of the  $L_1$ ,  $L_2$  and  $L_3$  lines are  $d_{1-}$ ,  $d_{2-}$ , and  $d_{3-}$ , respectively.

Several methods of estimating  $I_L(t)$  come to mind. For instance, the amplitude of each line could be estimated by using a separate filter with a narrow passband at the appropriate frequency. Or, equivalently, the discrete Fourier transform may be used to estimate the spectral components in the data. After the strength of each luni-solar frequency component has been obtained, they may be summed to give  $I_L(t)$ . We have devised a scheme which directly evaluates  $I_L(t)$  without separate filtering of each component in the summation.

By appropriate choices of the weights in the generalized filter, a lunar filter with passbands at the frequency components of  $I_L(t)$  is obtained.

The weights are given by

$$a_m = 2 \cos (2\pi\Delta f m T) \quad (7)$$

where  $T = 1$  day. Substituting the cosine weights into (1) and simplifying yields the transfer function of the lunar filter

$$T_L(f) = T_S(f + \Delta f) + T_S(f - \Delta f) \quad (8)$$

where  $T_S(f)$  is the solar filter transfer function given by (3). Using the cosine weights instead of constant weights shifts the passbands of the solar filter by plus or minus  $\Delta f$  (Figure 2b). The passbands of the lunar filter coincide exactly with the luni-solar frequencies produced by mixing of the  $M_2$  frequency with the solar harmonics. The location of the main luni-solar frequencies  $L_1$ ,  $L_2$ , and  $L_3$  are indicated in Figure 2b.

The weighted delay filter is flexible and easy to implement. By changing  $\Delta f$  in the cosine weights, the passbands around the solar lines may be located at any desired frequency. Thus, using this filter, the frequency mixing between the solar harmonics and any lunar line may be investigated.

Notice that in both the solar and lunar filters, the length of each delay is one day. Thus, data recorded at intervals which divide an integer number of times into 24 hours may be used directly by the filters without any interpolation.

The solar and lunar delay-filters are cascaded as shown in Figure 3. The output of the solar filter,  $I_S$ , is subtracted from the central delay-line point of this filter. This effectively suppresses the solar harmonics [Bernhardt and Schlapp, 1976]. The data are further processed by the lunar filter.  $I_L$  is subtracted from the center of the lunar delay-filter leaving the residue,  $I_R$ .

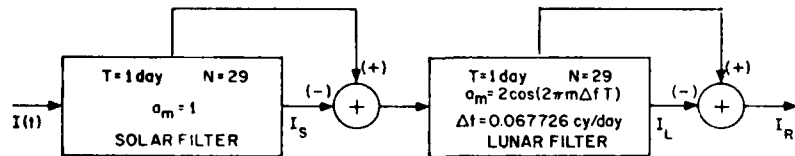


FIGURE 3. Implementation of solar and lunar delay filters in the analysis of electron content data.

In summary, the delay filter is an efficient method of processing long data streams containing harmonically related frequency components. A filter composed of cascaded delay filters seems to be the optimum solution for separating solar variations from luni-solar variations in electron-content data.

### THE FILTERED DATA

Half-hour samples of electron content data obtained at Stanford during the winter and spring of 1971 were processed by the delay filter. Missing data points were rare, and when they occurred linear interpolation was used. The results in this section are typical of the first 6 months of 1971.

Figure 4 shows a sequence of five days for which the electron content was split in the manner described in the preceding section. Figure 4a shows the diurnal variation of the observed electron content days 80 through 85 of 1971. Figure 4b shows the diurnal variation of the solar component which can be seen to exhibit negligible day-to-day changes owing to the 59 day averaging process and to the fact that the solar activity changed little over the period considered. Figure 4c shows the lunar component displaying a systematic maximum near the time of upper transit (marked "U" in the plots). Finally, Figure 4d displays the residue component,  $I_R$ .

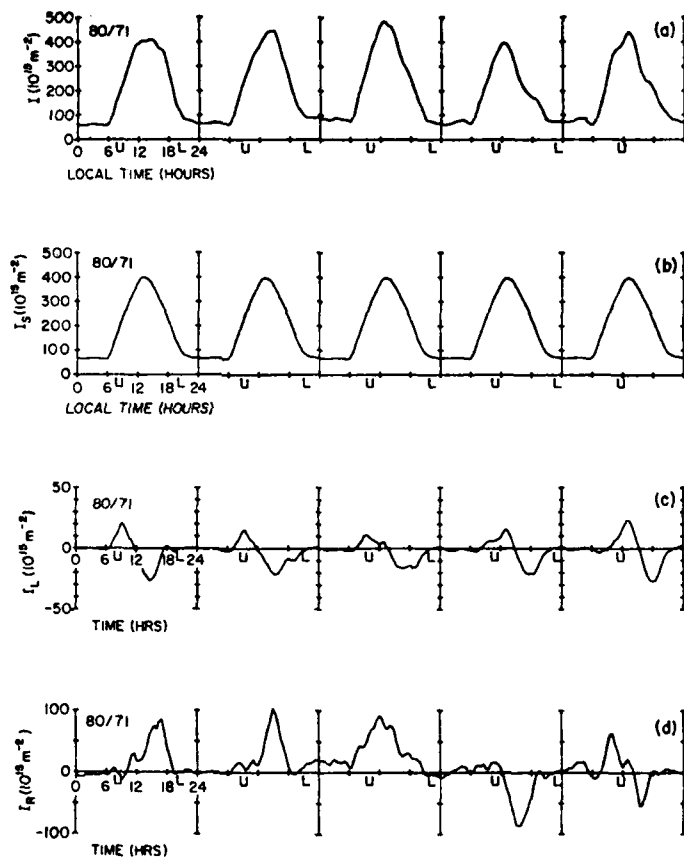


FIGURE 4. A sequence of five days for which the electron content was split, as discussed in the text. (a) The diurnal variation of the observed electron content during 80 through 85, 1971. (b) The diurnal variation of the solar component. (c) The diurnal variation of the lunar component. The time of lunar upper transit is marked "U". (d) The diurnal variation of the residue component.

The magnitude spectrum of the unfiltered data is shown in Figure 5a. A logarithmic scale is used in all such spectra. The solar harmonics ( $S_0$ ,  $S_1$ ,  $S_2$ ,  $S_3$ , etc.) dominate the spectrum. The lunar semi-diurnal component  $L_2$  ( $\delta r M_2$ ) is much weaker than the neighboring solar semi-diurnal component  $S_2$ . The major solar sidebands around  $M_2$  are denoted by  $L_1$  and  $L_3$ .

The solar filter removes most of the fluctuations in the unfiltered data so that only the solar harmonics are present in the spectrum of  $I_S$  (Figure 5b).

The frequency spectrum at the output of the lunar filter is illustrated in Figure 5c. The  $L_2$  frequency component and the symmetric sidebands at  $L_1$  and  $L_3$  clearly stand out. The significance of the  $L_1$ ,  $L_2$ , and  $L_3$  lines may be estimated by comparing their magnitudes with those of the complementary lines just above the solar harmonic frequencies. The three main luni-solar lines are greater than their complements. In all the data examined, the magnitude of  $L_1$  is about 15% higher than the magnitude of  $L_3$ . We attribute this to contamination of the  $L_1$  line by the lunar tidal line  $O_1$  at frequency .92954 cycles per day. The passband of the delay filter is not narrow enough to completely reject the  $O_1$  line.

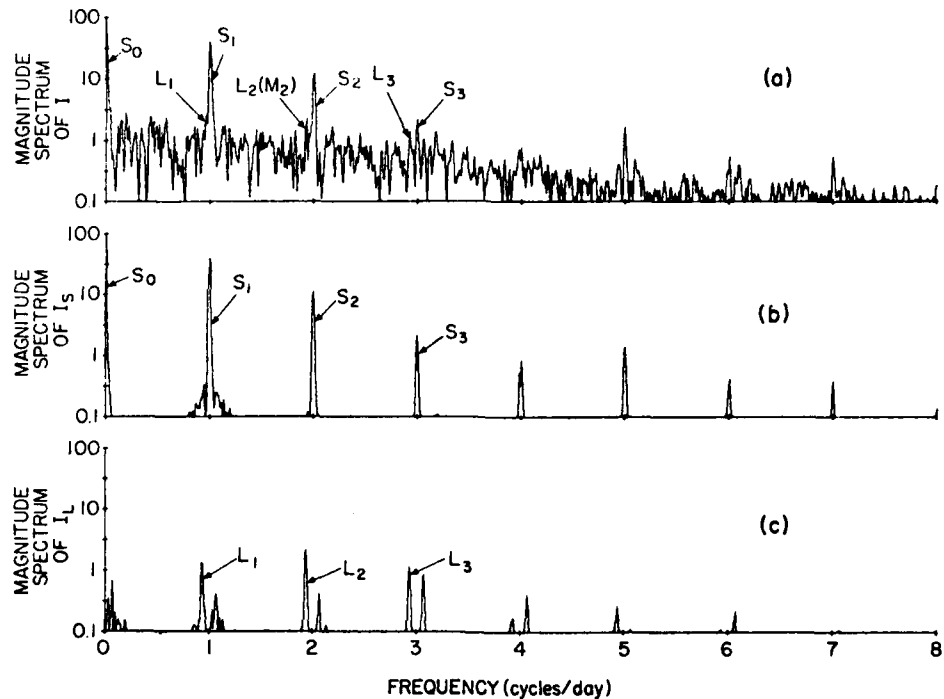


FIGURE 5. (a) Spectrum of unfiltered electron content data. (b) Spectrum of output of solar filter. (c) Spectrum of output of lunar filter.

If lines  $L_1$  and  $L_3$  are produced by mixing of the solar  $S_1$  component with the lunar  $L_2$  component, the phase of  $L_1$  and  $L_3$  should be the difference and sum, respectively, of the phases of  $S_1$  and  $L_2$ . For all the data analysed, the phase of  $L_3$  stays within  $2^\circ$  of the sums of the phases of  $S_1$  and  $L_2$ .

However, the phase of  $L_1$  differs by as much as  $20^\circ$  from the difference between the phases of the  $S_1$  and  $L_2$  lines. This is again attributed to the presence of the  $O_1$  lunar line.

Although the  $O_1$  line can be removed by using a longer delay-filter which has narrower passbands, no attempt has been made to do this because the interference of  $O_1$  with  $L_1$  was considered unimportant.

The luni-solar fluctuations,  $I_L$ , correlate well with the position of the moon. Figure 6 illustrates the behavior of  $I_L$  over a period of half a month. It is immediately evident that the lunar influence is small at night. During daytime, the lunar upper (U) and lower (L) transits are associated with positive values of  $I_L$ . When the moon is either rising or setting,  $I_L$  reaches its most negative values.

A comparison of the fluctuations in  $I_L$  (which can amount to  $5 \times 10^{16}$  electrons  $m^{-2}$ , peak to peak) with those in  $I_S$  (some  $35 \times 10^{16}$  electrons  $m^{-2}$ , peak to peak) shows that the lunar effects on the electron content have amplitudes some 14% of those of the solar effects.

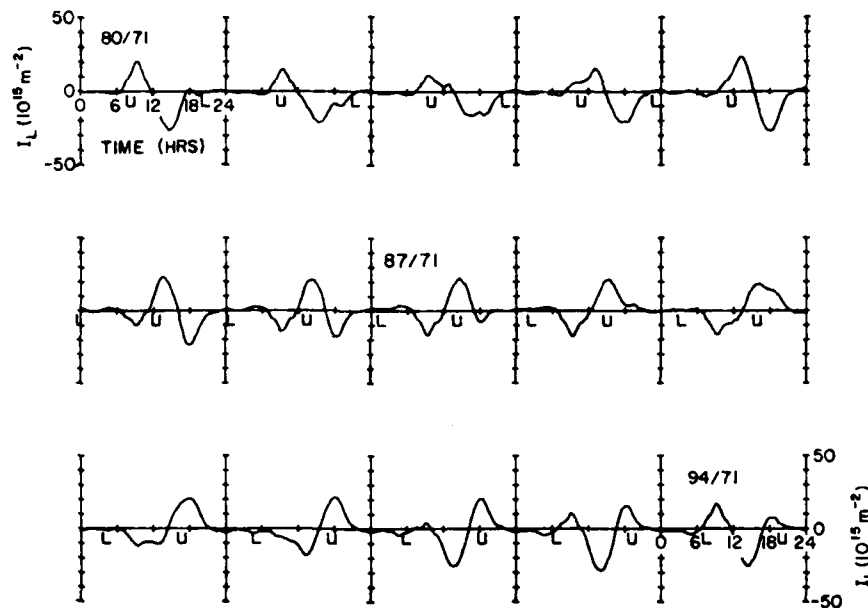


FIGURE 6. Temporal variation of lunar component in electron content data.

#### THE LUNAR DYNAMO ELECTRIC FIELDS

Before we present the analysis of the electron content data, a short review of the atmospheric dynamo theory is in order. Lunar tidal variations in the gravitational potential set up pressure gradients in the atmosphere. These gradients produce winds,  $\bar{U}$ , that cause ions and electrons to move in different directions owing to the presence of the geomagnetic field. Thus,

a current of density  $\bar{J}$  flows piling up charges that produce polarization electric fields  $\bar{E}$ . The currents and fields are coupled by the conductivity tensor  $\tilde{\sigma}$  in the generalized Ohm's law equation:

$$\bar{J} = \tilde{\sigma}[\bar{E} + \bar{U} \times \bar{B}]$$

where  $B$  is the flux density of the geomagnetic field. The conductivity has daily fluctuations due to the variations in the E-region plasma concentration caused by the variation of the solar zenith angle. Multiplication of the solar harmonics in the conductivity tensor by the lunar frequencies in the tidal winds produces the luni-solar fluctuations in the electrostatic fields and currents. Both currents and electric fields in the E-region manifest themselves indirectly by affecting the behavior of observable quantities. Currents affect the behavior of the geomagnetic field as initially suggested by Stewart [1882], while electric fields are mapped along the highly conductive magnetic field lines into the F-region, thus affecting the behavior of the ionospheric plasma distribution. This coupling between the dynamo region and the F-region was suggested by Martyn [1955] and Dagg [1957] and was subsequently pursued by Farley [1959, 1960, 1961] and Spreiter and Briggs [1961a,b]. Equivalent electric current distributions resulting from the lunar dynamo can be deduced by analyzing the measurements of geomagnetic variations at the surface of the Earth (c.f. Chapman and Bartels [1940]; Matsushita [1968]). Such measurements have attracted a lot of attention over the years. On the other hand, electric fields resulting from the lunar dynamo cannot be determined from localized geomagnetic measurements and thus have been primarily deduced theoretically from models of lunar tides and of E-region conductivities (c.f. Matsushita [1969]; Tarpley [1970]; Abur-Robb and Dunford [1975]). Maeda and Fujiwara [1967] have determined experimentally the lunar dynamo electric fields by using the procedure developed by Maeda [1955] for the calculation of electric fields resulting from the solar dynamo. This procedure consists of converting global measurements of geomagnetic variations into currents and, through theoretical models of conductivity, producing a tidal wind and electric field pattern consistent with the currents.

Our technique for determining electric fields makes use of measurements of electron content at only one location on the globe. The electron content is influenced by plasma drifts induced by electric fields in the F-region. These drifts are related to the electric fields by:

$$\bar{V}_d = \frac{\bar{E} \times \bar{B}}{B^2}$$

The vertical component of the drift raises or lowers the F-layer into regions of higher or lower ion loss rate and, thus, modulates the ionospheric plasma content. This modulation is recovered by the filtering technique, as already discussed.

The procedure for determining vertical plasma drifts from electron content measurements has been presented by Antoniadis [1976] and Antoniadis and da Rosa [1976]. It consists of a dynamic ionospheric simulation technique which allows the calculation of the time dependent vertical plasma drifts from the behavior of the observed electron content. The coupled equations of ion continuity and of plasma heat balance are solved in the 120 km and 800 km altitude range

subject to some externally imposed boundary conditions. The sensitivity of the absolute values of the calculated vertical drifts to these boundary conditions has been discussed in the above papers. It was concluded that the sensitivity is small with respect to changes in  $T_{\infty}$  (neutral exospheric temperature), negligible with respect to changes in  $T_{eUB}^{\infty}$  (upper boundary electron temperature), and negligible with respect to changes in  $\phi_{UB}$  (upper boundary plasma flux, provided that the integrated O<sup>+</sup> production (and loss) and the rate of change of the electron content are larger than about  $2 \times 10^8 \text{ cm}^{-2} \text{ sec}^{-1}$ ). During the particular day under investigation here, these requirements were met between 0530 LT and 2130 LT. On the other hand, the sensitivity to the solar EUV flux is quite significant. The value of this flux is adjusted by comparing the calculated and observed behavior of  $h_{max}$ . In our simulation, the external model parameters were established as follows:

- a)  $T_{\infty}$  and  $T_{eUB}^{\infty}$  are the same as those reported for days 28-29 September 1970 at Millstone Hill (Roble et al [1974] and Salah [1975, private communication]). The solar activity during these days matches closely the activity during the simulated period.
- b) The solar EUV flux was taken as the flux given by Hinteregger [1970] multiplied by a factor  $F_{EUV} = 1.5$ .
- c) The atmospheric model lower boundary conditions were:  $T$  (neutral temperature) = 355 K,  $[O]$  (monoatomic oxygen concentration) =  $1.35 \times 10^{11} \text{ cm}^{-3}$ ,  $[N_2]$  (nitrogen concentration) =  $3 \times 10^{10} \text{ cm}^{-3}$  and  $[O_2]$  (diatomic oxygen concentration) =  $8 \times 10^{10} \text{ cm}^{-3}$ .
- d) The protonospheric flux  $\phi_{UB}$  was assumed to be zero between 0600 LT and 1900 LT and  $1.3 \times 10^8 \text{ cm}^{-2} \text{ sec}^{-1}$  from the remaining time.

A comparison (not shown here) has indicated good agreement between calculated and observed values of  $N_{max}$  and  $h_{max}$  at Point Arguello, which is close to the subionospheric point of the electron content measurement. This fact indicates that the external parameters used here and the calculated absolute values of vertical drifts are realistic.

The lunar variation in the vertical plasma drift is calculated by using the ionospheric model twice as shown diagrammatically in Figure 7. First, the solar driven component of the plasma drift is calculated from the solar component of the electron content data. Second, the sum of the lunar and solar components of the electron content data are used to calculate the sum of the lunar and solar components of the vertical plasma drift. The solar drift velocity is then subtracted from the lunar plus solar drift velocity, leaving the lunar component of the drift velocity. This procedure is probably valid since the lunar component is only a small perturbation of the large solar component of the vertical plasma drift.

One component of the electric field can be calculated from the vertical drift  $w_L$  using the equation

$$w_L = (E_x \cos D + E_y \sin D) \frac{\cos \theta}{B}$$

where  $\theta$  is the dip angle and  $x$  and  $y$  are the geographic eastward and poleward directions, respectively. It is clear that the sum inside the parenthesis is simply the component of the electric field in the magnetic eastward

direction. Denoting this direction by  $x'$ , we have

$$E_{x'} = W_L B / \cos \theta$$

The magnetic dip at Stanford is  $\theta = 61^\circ$  and  $B$  may be taken as  $4.8 \times 10^{-5}$  Webers/m<sup>2</sup>. Then, the relation between the eastward electric field and the vertical drift becomes:

$$E_{x'} = 10^{-4} W_L$$

where  $E_{x'}$  is in V/m and  $W_L$  in m/sec.

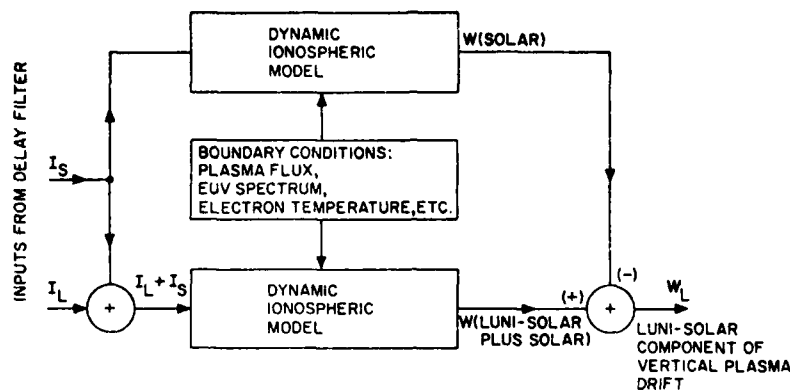


FIGURE 7. The ionospheric model is used twice to produce an estimate of the lunar fluctuations in the vertical plasma drift.

The vertical plasma drift,  $W_L$  and the lunar dynamo electric field,  $E_x$  (the magnetically eastward component) are illustrated in Figure 8 for days 80/71, 83/71, and 87/71. The calculated  $W_L$  shows a strong semidiurnal variation as might have been anticipated from the behavior of  $I_L$ . A closer observation, however, reveals that there is a phase difference between  $I_L$  and  $W_L$ ;  $I_L$  seems to lag  $W_L$  about 2 hrs. This can be seen more clearly in Figure 9 where  $I_L$  and the calculated perturbations to  $N_{max}$  and  $h_{max}$  are shown together with the  $W_L$  obtained for day 80/71. Starting from the bottom of this figure, the ionospheric quantities are shown in the sequence in which one affects the other. Thus, the lunar perturbation of the vertical drift,  $W_L$ , causes the perturbation,  $h_{maxL}$  in  $h_{max}$ , which in turn causes the perturbation,  $N_{maxL}$ , in  $N_{max}$ .  $N_{maxL}$  is, of course, tied very closely to  $I_L$ . The progressive lag in phase from bottom to top is clearly evident.

A delay of up to several hours between observed  $h_{maxL}$  and  $N_{maxL}$  has been reported in previous studies [Matsushita, 1967]. The reported delay was a function of latitude. The corresponding delay of about 1 hr. calculated here is smaller than what would be expected at the latitude of Stanford, from Matsushita's work, but it is in the same direction.

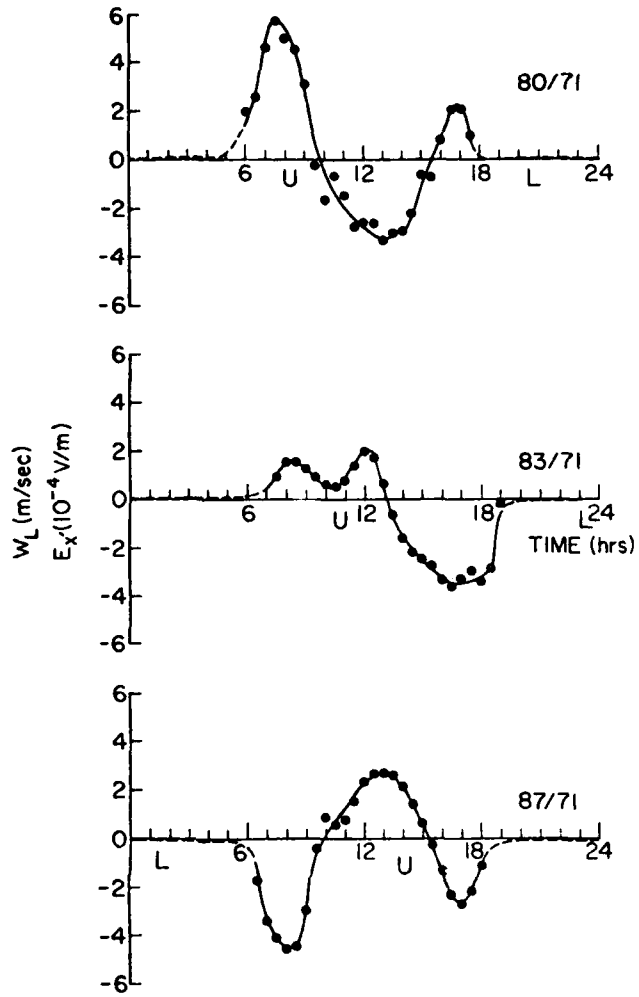


FIGURE 8. Calculated electric field and vertical drift fluctuations for three days. The fluctuations are closely coupled to the times of upper or lower transit of the Moon.

The lunar electrostatic fields have peak excursions of  $\pm .4$  millivolts per meter. These values are consistent with fields obtained by Maeda and Fujiwara [1967], Matsushita [1969], and Matsushita and Tarpley [1970].

#### CONCLUSIONS

A generalized delay filter has been used to decompose the ionospheric electron content into solar, luni-solar and residual components. This type of filter is a flexible and easily implementable tool and is particularly suitable for the analysis of long streams of data, such as geophysical data,

containing periodic fluctuations at various frequencies.

The luni-solar component of electron content was found to be on the order of 10% of the solar component for the period analyzed. This luni-solar component was attributed to the perturbation of the F2 region by electro-magnetic drifts resulting from the lunear dynamo electrostatic field in the E region. By means of a dynamic ionospheric simulation technique, the magnitude of this lunar electrostatic field was calculated to be approximately .4 mV/m.

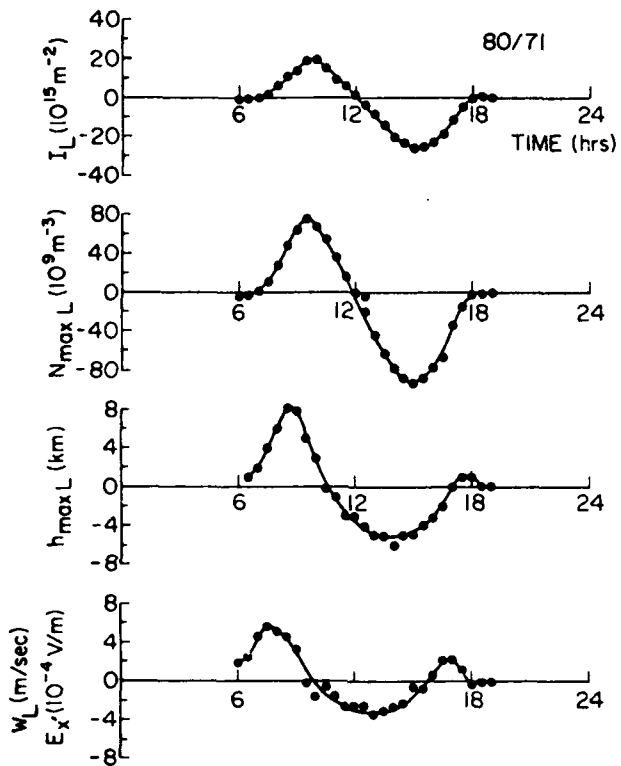


FIGURE 9. Temporal variation in  $I_L$ ,  $N_{\max L}$ ,  $h_{\max L}$ , and  $E_x$ -(or  $w_L$ ) over day 80/71.

#### ACKNOWLEDGMENTS

The authors would like to thank Dr. O. K. Garriott for many useful discussions during the course of this work. This research was supported by the National Aeronautics and Space Administration under Grant NGR-05-020-001.

## REFERENCES

- Abur-Robb, M. F. K., and E. Dunford, A theoretical evaluation of the lunar tidal variations in the ionospheric F2-layer, Planet. Space Sci., 23, 1071, 1975.
- Antoniadis, D. A., Determination of thermospheric quantities from simple ionospheric observations using computer simulation (submitted to J. Atmos. Terr. Phys., 1976).
- Antoniadis, D. A., and A. V. da Rosa, Vertical ion drifts, exospheric temperatures, and neutral winds calculated from simple observations and numerical simulation of the ionosphere (to be published in the Proceedings of the COSPAR Satellite Beacon Group Symposium, June 1-4, 1976).
- Bartels, J., and H. F. Johnston, Geomagnetic tides horizontal intensity at Huancayo, Terr. Magn. Atmos. Elect., 45, Pt. I, 369, Pt. II, 485, 1940.
- Bernhardt, P. A., Separation of lunar and solar periodic effects in data, J. Geophys. Res., 78, 4343, 1974.
- Bernhardt, P. A., and D. M. Schlapp, Suppression of the unwanted variations in data, J. Geophys. Res., 81, 1976.
- Chapman, S., and J. Bartels, Geomagnetism, Vol. I and II, Oxford Univ. Press, 1940.
- Chapman, S., and J. C. P. Miller, Statistical determination of lunar daily variations in geophysical data, Mon. Not. R. Astr. Soc., Geophys. Suppl. 4, 649, 1940.
- Dagg, M., The origin of the ionospheric irregularities responsible for radio star scintillations and spread F (II), J. Atmos. Terr. Phys., 11, 139, 1957.
- Farley, D. T., Jr., A theory of electrostatic fields in a horizontally stratified ionosphere subject to a vertical magnetic field, J. Geophys. Res., 64, 1225, 1959.
- Farley, D. T., Jr., A theory of electrostatic fields in the ionosphere at nonpolar geomagnetic latitudes, J. Geophys. Res., 65, 869, 1960.
- Farley, D. T., Jr., Discussion of paper by John R. Spreiter and Benjamin R. Briggs on "Theory of Electrostatic Fields in the Ionosphere at Polar and Middle Geomagnetic Latitudes," J. Geophys. Res., 66, 3965, 1961.
- Gupta, J. C., and S. Chapman, Lunar daily harmonic geomagnetic variation as indicated by spectral analysis, J. Atmos. Terr. Phys., 31, 233, 1969.
- Hinteregger, H. E., The extreme ultraviolet solar spectrum and its variation during the solar cycle, Ann. Geophys., 26, 547, 1970.

Maeda, H., Horizontal wind systems in the ionospheric E-region deduced from the dynamo theory of the geomagnetic Sq variation, Part I, J. Geomag. Geoelect., 7, 1214, 1955.

Maeda, H., and M. Fujiwara, Lunar ionospheric winds deduced from the dynamo theory of geomagnetic variations, J. Atmos. Terr. Phys., 29, 917, 1967.

Martyn, D. F., Interpretation of observed F2 wind as ionization drifts associated with the magnetic variations, Physics of the Ionosphere, The Physical Society, London, 163, 1955.

Matsushita, S., Lunar tides in the ionosphere, Handbuch der Physik, 49, 547, 1967.

Matsushita, S., Sq and L current systems in the ionosphere, J. Geophys. Res., 73, 109, 1968

Matsushita, S., Dynamo currents, winds and electric fields, Radio Sci., 4, 771, 1969.

Matsushita, S., and J. D. Tropley, Effects of dynamo-region electric fields on the magnetosphere, J. Geophys. Res., 75, 5433, 1970.

Kao, N. N., and C. F. Stubenrauch, Lunar tidal variations in the equivalent slab thickness of the ionosphere over Hawaii, J. Geophys. Res., 72, 5547, 1967.

Roble, R. G., B. A. Emery, J. E. Salah, and P. B. Hays, Diurnal variation of the neutral thermospheric winds determined from incoherent scatter radar data, J. Geophys. Res., 79, 2868, 1974.

Spreiter, J. R., and B. R. Briggs, Theory of electrostatic fields in the ionosphere at polar and middle latitudes, J. Geophys. Res., 66, 1931, 1961a.

Spreiter, J. R., and B. R. Briggs, Theory of electrostatic fields in the ionosphere at equatorial latitudes, J. Geophys. Res., 66, 2345, 1961b.

Stewart, B., Hypothetical views regarding the connection between the state of the sun and terrestrial magnetism, Ency. Britannica (9th ed.) 16, 181, 1882.

Tropley, J. D., The ionospheric wind dynamo - I lunar tide, Planet. Space Sci., 18, 1075, 1970.

## GRAVITY WAVE INDUCED FLUCTUATIONS IN TOTAL ELECTRON CONTENT

By

A. Sengupta, O.P. Nagpal and C.S.G.K. Setty

Ionosphere Research Centre

Department of Physics and Astrophysics,  
University of Delhi, Delhi-110007, India.

### Abstract

Continuous records of the electron content at Delhi (Geog. Lat.  $28^{\circ}$ N,  $77^{\circ}$ E; Sub Ionospheric Point  $26.5^{\circ}$ N,  $72.9^{\circ}$ E) obtained by monitoring the Faraday angle variations of signals at 140 MHz transmitted from geostationary satellite ATS-6 have revealed the presence of atmospheric gravity waves in the F-region of the ionosphere with periods ranging from 10 to 100 minutes. The records obtained from August 1, 1975 have been examined for the purpose of the present study. Some tens of continuous daytime records have been chosen which show clear periodicities. Variations produced by these waves were very common in the range of 10-60 min with a marked dip near 15 min period. The amplitudes of electron content fluctuations have been estimated to be in the range of 0.5 to 6.0%. Theoretical computations based on a simple model of the ionosphere gravity wave interaction have been carried out. The integrated response to gravity waves is found to be dependent on the satellite observed ray path geometry, magnetic dip and the wave azimuth. The observed average spectrum agrees qualitatively with the computed spectrum if a meridional propagation is assumed.

### Introduction

Ionospheric irregularities have been studied for many years. One class of these irregularities known as travelling ionospheric disturbances (TID's) have been detected by a number of techniques. Recent work (Hines, 1960; Thome, 1964, 1968; Testud and Vasseur, 1969; Georges, 1968; Titheridge, 1960, 1971; Davis and Da Rosa, 1969; Klostermeyer, 1969; Yeh, 1972; Gupta and Nagpal, 1973) has revealed that these disturbances are caused by propagation of atmospheric gravity waves. The TID's are generated by an interaction between the neutral atmospheric wave and the ambient ionization (Hooke, 1968, 1970). VHF Radio signals received from the geostationary satellites provide a convenient means for studying the temporal variations of columnar electron content, between the satellite and the observer, in the ionosphere over continuous periods. In this paper we present the results of analysis of continuous records of the polarisations angles of the 140 MHz signals received at

the University of Delhi from the satellite ATS-6, of wavelike perturbations in the total electron content. The Faraday polarimeter used to obtain these records has been described elsewhere (Sengupta and Setty, 1976). The records often show fluctuations in the total electron content. The records obtained from August 1975 - December 1975 have been used to determine the number of occurrences of these fluctuations each day provided the record exhibits atleast two or more complete cycles of the same period. The periods ranged from 70 min down to a sharply defined lower limit of 10 min agreeing with the permitted spectrum of gravity waves in the F-region.

#### Experimental Results

The polarization rotation due to Faraday effect is proportional to the electron density integrated along the way path. Therefore, the experimental records represent variations of the integrated electron density (or electron content). These records show small fluctuations superimposed on the larger variations caused by the production and loss processes. These small fluctuations, believed to be caused by propagating atmospheric gravity waves, are extracted from the records (Cowling et al., 1970) and spectrum analysed. About thirty non overlapping records (each of which lasted for about 9 hrs) of data taken during day time were selected for the present analysis.

Sample records of the polarisation angle variations are reproduced in Figures 1 and 2. It is seen that the fluctuations in these records are not random but are of a sustained type. Some periodicity is usually evident on every record. Periods greater than 100 min and any overall trend has been removed by visual inspection from the data before it is subjected to spectral analysis. The spectral estimate is followed by a process of smoothing using Hanning weight (Blackman and Tukey, 1958). The spectra of the sample records are shown in Figures 1 and 2 respectively as insets. Three dominant oscillations of about 10, 25 and 50 min periods are seen on the spectrum of Fig. 1. The spectral estimates were made for each record separately and dominant periods were read. The periodicities thus obtained were divided into the following ranges: 7.5 - 12.5, 12.5 - 17.5 --- and so on. The lowest period was chosen to be greater than the Nyquist period of about 5 min. The distribution of significant periodicities are noted at 10, 25, and 45 min with a well defined minimum at about 15 min. Of these three at least the two at 10 and 25 min are clearly distinct. These features are visible even on the spectrum of individual records (see insets of Figs. 1 and 2). The average distribution of periods shown in Fig. 3 is characterised by a short period cut off near 8 minutes, a long period cut off near 60 min., and a sharp dip near 15 min. It appears that the short cut off period may be associated with the increased damping near the Brunt period (Yeh and Liu, 1974), neutral winds and temperature gradients (Gupta et al., 1973). The shape of the spectral distribution is related to the gravity wave -

ionosphere interaction. Hence the following sections have been devoted for discussions of a theoretical model of the ionospheric response to atmospheric gravity waves and the conclusions that can be drawn by comparing the theoretical model with the experimental results.

#### Theoretical Background

Our theoretical analysis in the following will be made with the understanding that the theory will be applied to the electron content data. Since the electron content is heavily weighted by electrons with a few scale heights away from the F2 peak, many simplifications can be made in the analysis. In a lossy isothermal atmosphere, the wave induced neutral air parcel velocity,  $\vec{V}'$ , can be expressed as

$$\vec{V}' = \vec{V}_0 \exp[-i(\omega t - \vec{k} \cdot \vec{r}) + z/2H - \int \beta dz] \quad (1)$$

where  $\vec{V}_0$

$\vec{V}_0$  = velocity amplitude which may depend on  $\omega$  and  $\vec{k}$ .

$\omega$  = angular wave frequency

$\vec{k}$  = wave vector

H = scale height

z = height

$\beta$  = damping coefficient which usually depends on z.

In the F region of the ionosphere the perturbation in the ion velocity is constrained to be along the geomagnetic field lines. Hence, the ionization velocity is

$$\vec{V}_i = (\vec{V}' \cdot \hat{\vec{B}}_0) \hat{\vec{B}}_0 \quad (2)$$

where  $\hat{\vec{B}}_0$  is the unit vector in the direction of the geomagnetic field lines. Substituting equation (2) into the continuity equation (1), and assuming that the background ionization density  $N_0$  depends only on z, we find that the perturbed ionization density  $N'$  is of the form

$$N' = \bar{\omega} \vec{V}' \cdot \hat{\vec{B}}_0 \hat{\vec{B}}_0 \left[ \vec{k} + iz\left(\beta - 1/2H - \frac{\partial}{\partial z}\right) \right] N_0(z) \quad (3)$$

where  $\hat{\vec{z}}$  is the unit vector in the vertical direction. If we neglect the dissipation (putting  $\beta = 0$ ) and the exponential growth of the wave with z (putting  $1/2H$  to zero) we can see that (3) reduces to the result obtained by Hooke (1968). However, the integration of equation (3) from the ground based observer to the satellite, results in an equation for the perturbation in electron content,  $I_{ob}'$ , along an oblique path. With the time factor  $\exp(-\omega t)$  omitted it becomes

$$I_{ob}' = \frac{\vec{k}_h (\vec{V}_0 \cdot \hat{\vec{B}}_0) g}{\omega \cos^2 \chi} \int N_0(z) \exp \left[ i(k_z \cos \eta / \cos \chi) + z/2H - \int \beta dz \right] dz \quad (4)$$

where

$\vec{k}_h$  = the horizontal component of  $\vec{k}$

$g$  = the geomagnetic factor  $(\hat{r} \times \hat{B}_0) \cdot \hat{xz} \cdot \vec{k}_h$

$\chi$  = the satellite zenith angle (the angle between  $\hat{r}$  and  $\hat{z}$ )

$\eta$  = the angle between  $\hat{r}$  and  $\vec{k}$

For an  $\alpha$ -Chapman layer, the integration of equation (4) gives

$$\left| \frac{I'}{I_0} \right| = \sqrt{\frac{2}{\pi}} \left| \frac{(\vec{V}_m \cdot \hat{B}_0) g}{V_h \cos \chi} K_{1p}(\xi) \right| \quad (5)$$

where

$V_m$  = the amplitude of the air parcel velocity at the ionization peak.

$V_h = \omega/k_h$  = the horizontal phase velocity

$K_{1p}(\xi)$  = the modified Bessel function of the third kind with an imaginary order and a real argument.

$p = k H \cos \eta / \cos \chi$

$\xi = (2H\beta(z_m))^{1/2}$

$I' = I_{ob}' \cos \chi$  = perturbed electron content converted to the vertical direction

$I_0$  = the background vertical electron content.

When the dissipation and growth are both neglected (or when these two effects cancel), the equation corresponding to equation (5) is (Yeh, 1972):

$$\left| \frac{I'}{I_0} \right| = \frac{\vec{k}_h \cdot (\vec{V}_m \cdot \hat{B}_0)}{\omega \cos \chi} \frac{g}{\sqrt{\cosh(\pi k H \cos \eta / \cos \chi)}} \quad (6)$$

As seen in equation (5) the ratio between  $I'$  and  $I_0$  depends upon two factors : (i) the interaction geometry involving the air parcel velocity, wave vector, magnetic field, and the satellite direction and (ii) the dissipative processes. Both of these will be discussed in the next section.

#### Comparison of Experimental and Theoretical Results:

The geomagnetic factor,  $g$ , appearing in both the equations (5) and (6) causes the electron content to be sensitive to certain waves, and insensitive to others (Georges and Hooke, 1970; Davis, 1973). The angle  $\theta$ , between the neutral air parcel velocity and the geomagnetic field vector is given by

$$\cos \theta = \cos I \cos \phi \cos \alpha - \sin I \sin \phi \quad (7)$$

where

$\phi$  = the tilt of the wave front ( $\sin \phi = \frac{g}{\tau_g}$ )

$\tau_g$  = the Brunt period

$T$  = the wave period

$I$  = the dip angle

$\alpha$  = the azimuth of  $\vec{k}_h$ .

Equation (6) has been studied for various azimuthal angles of  $\vec{k}_h$ . The Brunt period has been assumed to be 13 minutes at 300 km altitude and the constant scale height to be 60 km. The wave wave number,  $k$ , was chosen to be  $0.02 \text{ km}^{-2}$  on the basis of several disturbances observed by Cowling et al., (1970). The use of these quantities in equation (6) allows the amplitude of  $|I'/I_0|$  to be computed as a function of the wave period for several different azimuths, as shown in Fig. 4. These curves are symmetric with respect to the magnetic meridian and hence are plotted only for  $\alpha$  varying from  $0^\circ$  to  $180^\circ$ . It may be noted that a clear bite out is present for small angles. However, this bite out is not so pronounced as those reported for mid latitudes (Setty et al., 1973) for fluctuation in the electron density observed at the F2 peak.

Let us first assume that the gravity waves occur with equal probability in all azimuths. Then a composite spectrum can be constructed theoretically by averaging over all the azimuths with equal weighting. This theoretical spectrum appears in Figure 5. The theoretical spectrum for northsouth propagating waves is shown in Figure 4 (top left). Comparing the experimental results of Figure 3 with the theoretical spectra of Figures 4 and 5 appears to agree with our earlier conclusions (Gupta and Nagpal, 1973) that the gravity waves have a tendency to travel close to the magnetic meridian.

### Conclusions

The fluctuations induced in the electron content by the atmospheric gravity waves have been studied both experimentally and theoretically. Following conclusions are shown by comparing the experimental results (Fig. 3) with the theoretical results (Fig. 4):

- (a) The fluctuations in total content are generally weaker than the fluctuation in the electron density at a fixed height.
- (b) The amplitude of fluctuation in total content for higher periods are greater than those for shorter periods and
- (c) The response of the electron content to the 15 min wave is generally relatively weak and anisotropic.

Generally, studies of the wave induced fluctuations in the ionosphere are aimed at getting information about the character of the wave propagating in the neutral atmosphere. However this task is quite involved as has been stressed by Hooke. This is particularly so when one is dealing with the integrated effects as in the present case of total electron

content measurements. Hence the conclusion drawn in this paper can at best be compared with those arrived at using a single parameter such as fluctuations in FOF2.

#### Acknowledgement

The work reported in this paper was carried out under the project 'Studies of the Ionosphere' sponsored by the University Grants Commission, India. One of the authors (A.S.) is indebted to the NCERT for the award of a Junior Research Fellowship.

#### REFERENCES

- Blackman, R.B. and J.W. Tukey (1958), Bell Syst. Tech.Jour., 37, 185 and 485.
- Cowling, D.H., H.D. Webb and K.C. Yeh (1970), Tech. Rept. No.38, Ionosph. Res. Lab., Univ. of Illinois, Urbana.
- Davis, M.J. (1973), J. Atmosph. Terr. Phys., 35, 929-959.
- Davis, M.J. and A.V. da Rosa (1969), J. Geophys. Res., 74, 5721.
- Georges, T.M. (1968), J. Atmosph. Terr. Phys., 30, 735.
- Georges, T.M. and W.H. Hooke (1970), J. Geophys. Res., 75, 6295.
- Gupta, A.B., O.P. Nagpal and C.S.G.K. Setty (1973), Ann. Geophys., 29, 301.
- Gupta, A.B. and O.P. Nagpal (1973), Ann. Geophys., 29, 307.
- Hines, C.O. (1960), Can. J. Phys., 38, 1441.
- Hooke, W.H. (1968), J. Atmosph. Terr. Phys., 30, 795.
- Hooke, W.H. (1970), J. Geophys. Res., 75, 5535.
- Klostermeyer, J. (1969).J. Atmosph. Terr. Phys., 31, 25.
- Sengupta, A. and C.S.G.K. Setty (1976), Paper presented at the Symposium on 'Ionosphere and Magnetosphere', Andhra Univ., Waltair, Jan. 7-9, 1976.
- Testud, J. and G. Vasseur (1969), Ann. Geophys., 25, 525.
- Thome, G.D. (1964), J. Geophys. Res., 69, 4047.
- Thome, G.D. (1968), J. Geophys. Res., 73, 6319.
- Titheridge, J.E. (1968), J. Geophys. Res., 73, 243.
- Titheridge, J.E. (1971), Planet. Space Sci., 19, 1593.
- Yeh, K.C. (1972), J. Geophys. Res., 77, 709.
- Yeh, K.C. and C.H. Liu (1974), Rev. Geophys. Space Phys., 12, 193.

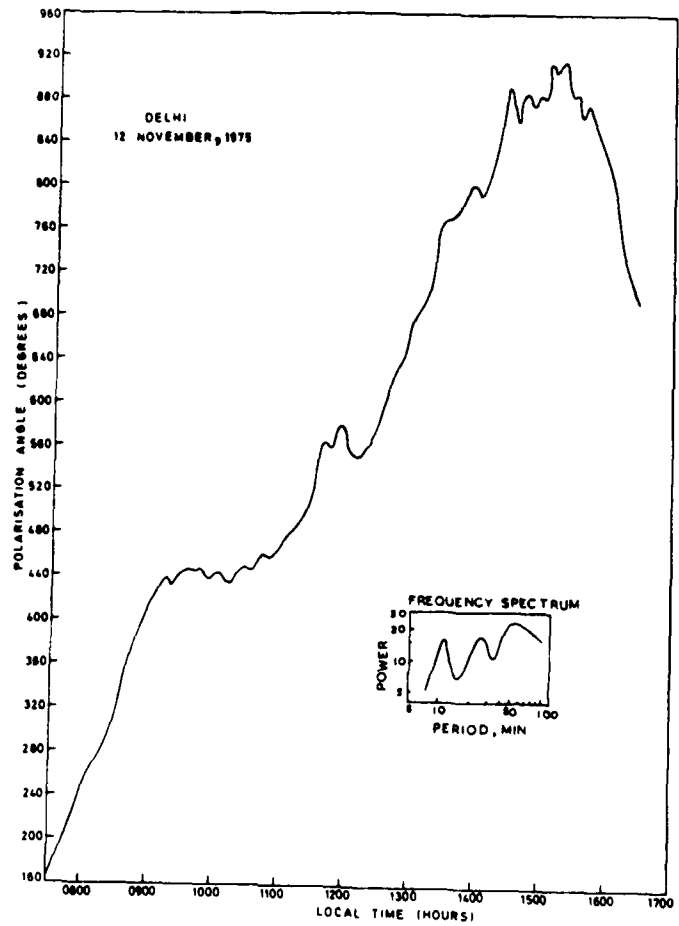


Fig.1. A typical continuous record made on 12 November 1975 of the Faraday angle variations showing sustained fluctuations superimposed on the diurnal trend. The inset shows the frequency spectrum of the fluctuations.

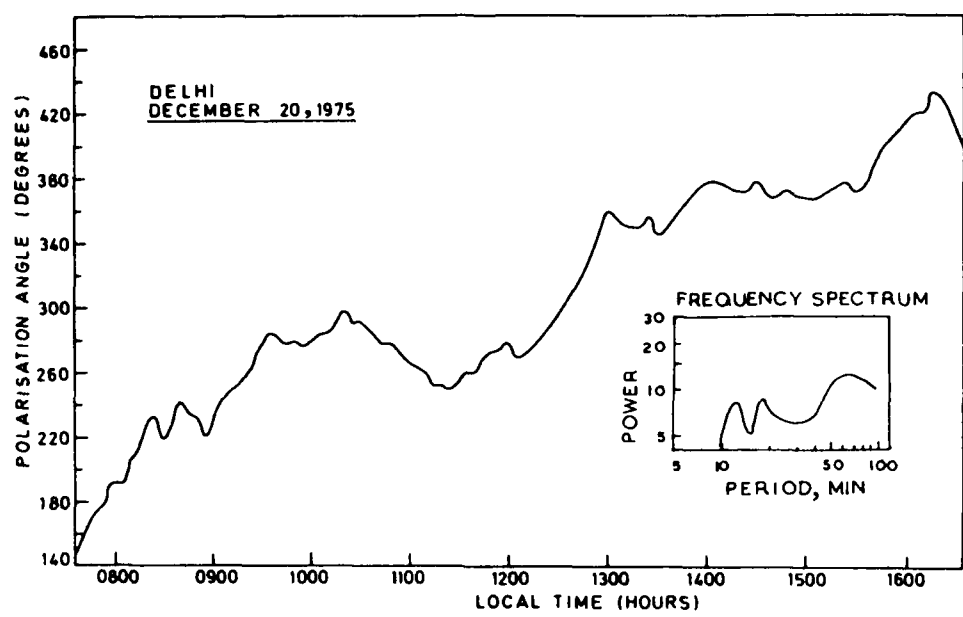


Fig.2. Another typical record made on 20 December 1975 alongwith the frequency spectrum.

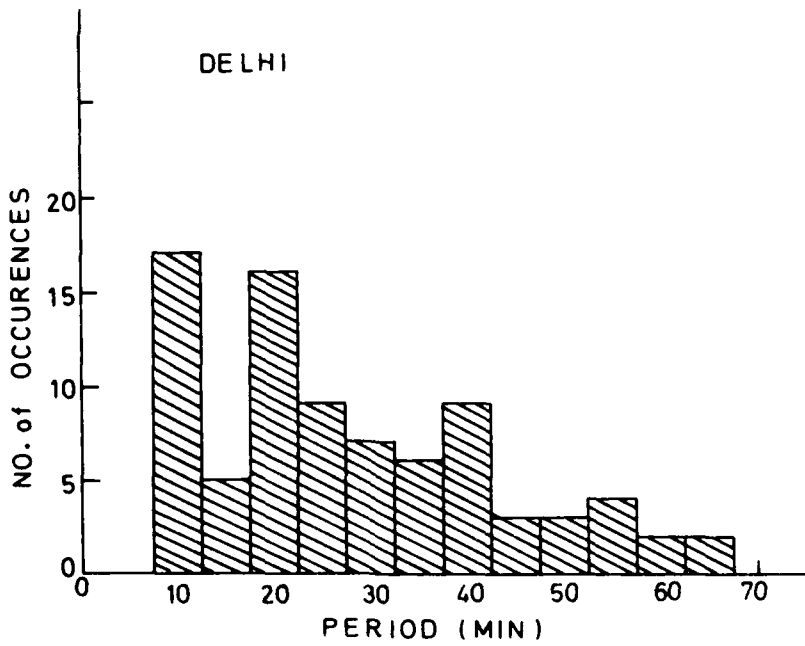


Fig.3. Histogram showing the relative occurrence of various periods.

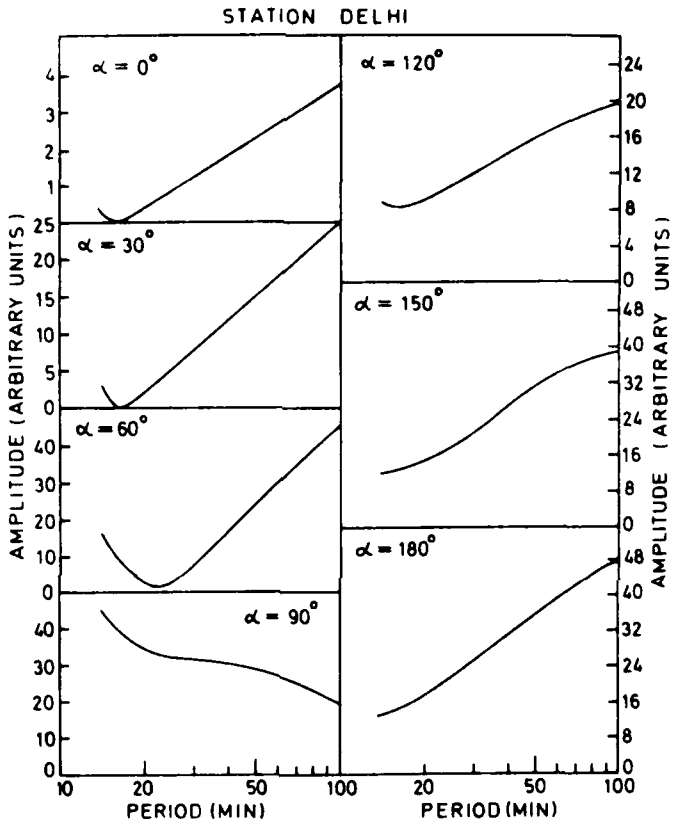


Fig.4. Theoretically computed spectrum for Delhi representing the ionospheric response to gravity waves propagating at different azimuths. The amplitude along the ordinate has arbitrary units.

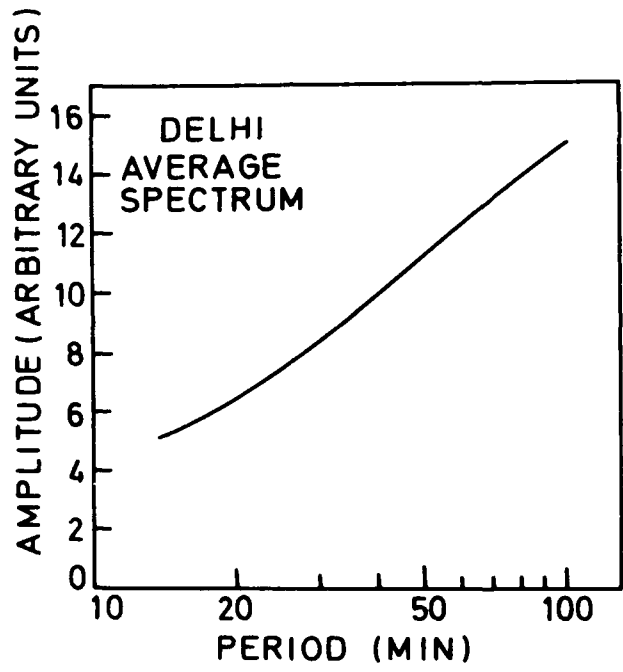


Fig.5. Average theoretical spectrum for Delhi. The average is taken over the azimuth angles from  $0^\circ$ - $180^\circ$ .

POWER SPECTRA OF ACOUSTIC GRAVITY WAVES IN  
THE F-REGION IONOSPHERE

R. DuBroff, K. C. Yeh and C. H. Liu

Department of Electrical Engineering  
University of Illinois  
Urbana, Illinois 61801

Abstract

Maximum entropy power spectrum analysis was applied to the travelling ionospheric disturbances (TID's) observed in the electron content data obtained from the ATS-III satellite. Assuming that the TID's are caused by atmospheric internal gravity waves, the power spectra should provide some indication of the frequency dependent dissipative effects of atmospheric loss mechanisms. In this regard, a theoretical model of the attenuation of acoustic gravity waves was utilized to compute the frequency dependence of thermal conduction and viscous damping of internal gravity waves in the thermosphere. The experimentally obtained power spectra are then compared with the theoretical predictions.

In particular it has been found that the experimentally observed spectral peak, occurring at a frequency of about .04 cycles/min, generally corresponds to the theoretical prediction of minimum attenuation.

## I. Introduction

The primary purpose of the present work is directed towards a comparison between a theoretical consideration of the effects of dissipative processes upon the propagation of acoustic gravity waves and the experimentally obtained power spectra of fluctuations in ionospheric electron content. Within the context of theoretical models of dissipative processes, a number of different methods have been proposed. For example, full wave and coupled mode (also known as WKB) methods have been applied to the linearized lossy hydrodynamic equations by Klostermeyer [1972], Liu and Klostermeyer [1975], Volland [1969] and others. On the other hand, Yeh et al. [1975] and Yeh and Liu [1974] have considered the problem from the viewpoint that the dissipative effects may be evaluated by determining the imaginary part of the wave vector which, in a weakly dissipative medium, should be equal to the rate of energy dissipation divided by twice the energy flux [Lindau and Lifshitz, 1959]. The present approach to the theoretical model falls somewhere between these two methods, and is, perhaps, most similar to the method of Pitteway and Hines [1963], as will become more apparent in the next section.

Experimental power spectra of ionospheric electron density perturbations have been investigated by many authors [Titheridge, 1968; Schödel, 1972; Toman, 1976]. In this paper, power spectra of wave-like perturbations in ionospheric electron content data are computed and compared with the theoretical results in an attempt to interpret the general features of the spectra in terms of the atmospheric filtering effects due to dissipative processes.

## II. A theoretical model of the effects of dissipation upon the propagation of acoustic gravity waves.

Since acoustic gravity waves are governed by the linearized hydrodynamic equations [e.g. Hines, 1960], the effects of dissipation are also contained in the linearized hydrodynamic equations. Although these equations may be written in many forms, the form which was discussed by Yeh and Liu [1974] provides a basis for the present discussion -- i.e.

$$\frac{\partial \rho'}{\partial t} + \vec{v}' \cdot \nabla \rho_0 + \rho_0 \nabla \cdot \vec{v}' = 0 \quad (1)$$

$$\rho_0 \frac{\partial \vec{v}'}{\partial t} + \nabla p' - \rho' \vec{g} = \eta \nabla \cdot [(\nabla \vec{v}')^T + (\nabla \vec{v}')^T] - \frac{2}{3} \vec{I} (\nabla \cdot \vec{v}') \\ - \nu \rho_0 (\vec{v}' - \vec{v}_i')$$
(2)

$$\frac{\partial p'}{\partial t} + \vec{v}' \cdot \nabla p_0 - c^2 \frac{\partial p'}{\partial t} - c^2 \vec{v}' \cdot \nabla p_0 = (\gamma - 1) \nabla \cdot \kappa V T' \quad (3)$$

with pressure  $\equiv p_0 + p'$ ; density  $\equiv \rho_0 + \rho'$ ; velocity  $\equiv 0 + \vec{v}'$ ; temperature  $\equiv T_0 + T'$ ; speed of sound  $\equiv c$ ; ratio of specific heats  $\equiv \gamma$ ; gravitational acceleration  $\equiv \vec{g}$ ; coefficient of thermal conduction  $\equiv \kappa$ ; collision frequency  $\equiv \nu$ ; and ion velocity  $\equiv v_i'$ . The viscous stress tensor,  $\tau'$ , has been written explicitly as a function of  $\vec{v}'$ , and  $\eta$  is the coefficient of viscosity. The perturbed quantities are primed and subscript 0 indicates background quantities. Assuming that the horizontal and temporal variation of the first order perturbations may be represented by  $e^{-i(t - k_x x - k_y y)}$ , then it should be possible to write equations (1) through (3) in the form of a set of coupled first order differential equations, i.e.

$$\frac{\partial \vec{F}(z)}{\partial z} = \tilde{\vec{A}}(z) \cdot \vec{F}(z) \quad (4)$$

where the components of  $\vec{F}(z)$  generally involve some combination of the first order perturbed quantities and/or their derivatives.

In any case, the eigenvalues ( $\lambda$ ) of  $\tilde{\vec{A}}(z)$  are defined implicitly by some dispersion equation of the form

$$G(\omega, k_x, k_y, \lambda, \eta, \nu, \kappa, z) = 0. \quad (5)$$

If it is now assumed that  $\eta$ ,  $\nu$ ,  $\kappa$  each represent a small departure from lossless ( $\eta = \nu = \kappa = 0$ ) conditions, then the deviation of  $\lambda$  from its lossless ( $\lambda_0$ ) value may be obtained by expansion of equation (5) as:

$$0 = G(\omega, k_x, k_y, \lambda_0, 0, 0, 0, z) + G_\eta(\omega, k_x, k_y, \lambda_0, 0, 0, 0, z) \eta \\ + G_\nu(\omega, k_x, k_y, \lambda_0, 0, 0, 0, z) \nu + G_\kappa(\omega, k_x, k_y, \lambda_0, 0, 0, 0, z) \kappa \quad (6) \\ + G_\lambda(\omega, k_x, k_y, \lambda_0, 0, 0, 0, z) \lambda' + \dots$$

with  $\lambda' \approx \lambda - \lambda_0$ . The first term, of course, vanishes since  $\lambda_0$  is defined as the solution of the lossless dispersion equation. Thus, when the losses are small, the modification of the real part of the eigenvalue (the attenuation coefficient) in the case of thermal conduction, for example is

$$\lambda'_r = R : [\lambda - \lambda_0] = -R : \frac{G_k(\omega, k_x, k_y, \lambda_0, 0, 0, 0, z) \kappa}{G_\lambda(\omega, k_x, k_y, \lambda_0, 0, 0, 0, z)} . \quad (7)$$

Similar expressions can be obtained for the contributions to the attenuation coefficient by viscosity and ion drag. These expressions can then be used for the computations of the attenuation coefficient.

On the other hand, in the method used by Yeh et al. [1975], it is assumed that the effects of a dissipative process upon the pseudo energy flux,  $\Gamma_z = \frac{1}{2} R : [p'v_z^*]$ , may be adequately represented by multiplying the lossless pseudo energy flux by  $\exp \int_{z_0}^z 2\lambda'_r d\zeta$ . Therefore, the attenuation coefficient can be computed by dividing the rate of energy dissipation by twice the energy flux. It is found that the two methods yield the same value of  $\lambda'_r$  when thermal conduction, viscosity and ion drag are considered.

To study the effects of the dissipative processes, let us define a transmittivity function,  $\Xi(\omega, k_h)$  as:

$$\Xi(\omega, k_h) \equiv \exp \int_{z_0}^z [\lambda'_r(\zeta)] d\zeta \quad (8)$$

when, in our computations,  $z_0 = 150$  km,  $z = 350$  km. The transmittivity function represents the change of amplitude of a wave due to dissipation when propagating from height  $z_0$  to height  $z$ . In the case of thermal conduction the functional dependence of  $\Xi(\omega, k_h)$  is shown in Figure (1). The effects of viscosity are shown in Figure (2). The atmosphere between 150 km and 350 km was assumed to be described by the CIRA [1965] atmospheric model no. 5 at 12:00. In both cases, the general features of  $\Xi(\omega, k_h)$  are similar to the results obtained by Yeh et al. [1975].

Figures (1) and (2) represent the cumulative effects of dissipation as it acts over a range of altitudes for several given horizontal wave numbers  $k_h$ . The experimental data, however, does not contain any spatial information, and as a result cannot be compared directly to these two figures. In order to allow the data to be compared to the theoretical model, therefore,  $\Sigma(\omega, k_h)$  was averaged over a range of values of  $k_h$ . If the sources exciting the gravity waves are relatively broad band (in the sense of wave numbers), then this approach may be reasonable. The result of averaging over  $k_h$  is shown in Figures (3) and (4) (for viscosity and thermal conduction, respectively). In both cases, it would appear that the two dissipative processes exert a similar filtering effect upon the frequency components of the acoustic gravity waves.

### III. Experimental measurements

The electron content was obtained from Urbana, Illinois ( $40.069^\circ\text{N}$ ,  $88.225^\circ\text{W}$ ) by monitoring the Faraday rotation of signals from ATS-III. After sampling the data at 2 minute intervals, thirteen records, each lasting 8 hours, were selected for spectrum analysis. Although no systematic attempt was made to select the records on either a seasonal or time of day basis, most of the records lasted from mid-morning to mid-afternoon in the Fall of 1971. The data was selected on the basis of visible indications of the presence of wavelike fluctuations superimposed upon the slowly varying diurnal trend. Four additional records were selected on the basis of visible indications of the absence of wavelike fluctuations, in order to assess the possible effects of the diurnal variations upon the spectrum. In order to remove at least part of the contribution of very low frequency components to the power spectrum, each of the thirteen records were passed through a weighted running mean filter [Webster and Lyon, 1973]. Figure 5 represents the frequency response of this particular filter, corresponding to a cut off frequency of  $(1/120)\text{min}^{-1}$ . The effect of the filter on one of the records is shown, as an example, in Figure (6).

Having filtered the raw data, the power spectrum of each of the thirteen records was evaluated by using maximum entropy spectrum analysis. This technique, as described by Burg [1967, 1968], was implemented by two different methods, both of which are described by DuBroff [1976]. The thirteen power spectra were then averaged, and the resulting average spectra were compared with the theoretical predictions of the weak dissipation theory.

#### IV. Interpretation of Results

The average spectrum of the thirteen records is shown in Figure (7). Although there is a substantial amount of power at low frequencies, there would also appear to be a broad local maximum and a sharp peak within the shaded region of Figure (7). The frequency band, in which the maximum occurs, extends from about .03 to .06 cycles/min. This would seem to correspond to the predictions of the theoretical model, as represented by Figures (1) and (2). This maximum becomes even more prominent if the power spectrum shown in Figure (7) is multiplied by  $\omega^2$  in order to partially compensate for the frequency dependent nature of the response of the ionosphere due to acoustic gravity waves in a neutral atmosphere [Hooke, 1968]. This result is shown in Figure (8).

A second method of maximum entropy spectrum analysis was used, and the results shown in Figures (9) and (10) compare favorably with Figures (7) and (8), respectively. Conventional spectrum analysis also reveals the same general features -- a maximum extending from .03 to .06 cycles/min.

In order to interpret the sharp peak which occurs within the shaded region in the four figures, the thirteen individual spectra were renormalized before averaging. In particular, each of the thirteen spectra were, in effect, multiplied by a number which was inversely proportional to the variance of each record. After averaging the thirteen renormalized spectra together, it was found that the sharp peak which is exhibited in Figures (7) through (10) does not appear. However, a local maximum was still found to extend from about .03 to .06 cycles/min.

Finally, in order to determine the possible effects of the diurnal variation of the electron content upon the spectra, the four specially selected records were considered. After passing each of the four records through the weighted running mean filter shown in Figure (5), evaluating the maximum entropy spectra, and averaging the four spectra together, Figure (11) was obtained. Figure (11) indicates the presence of a low frequency spectral peak, (~.005 cycles/min) as well as a general downward trend from about .01 to .08 cycles/min. The low frequency peak occurs outside of the passband of the weighted running mean filter, and therefore is difficult to interpret. Nevertheless, a similar low frequency peak occurs in Figure (7) and (9). The general downward trend, however, would appear to be a common feature of all of the spectra which have been presented in Figures (7) through (10). Thus, the large downward trend occurring in the spectra might not be associated with the observed wavelike fluctuations in electron content.

## V. Conclusion

In summary, it should be noted that the observation of wavelike fluctuations in the ionosphere with periods corresponding to the minimum attenuation (from about 15 to 30 minutes), as shown in Figures (1) and (2), has been fairly well substantiated by other experiments (e.g. Titheridge [1968], and Toman [1976]). While the limitations in the theoretical models and uncertainties in the experimental data prevent us from carrying out more quantitative comparisons in this paper, the general agreement between the experimental and theoretical results would seem to indicate that the dissipative processes indeed play a role in the propagation of acoustic-gravity waves in the upper atmosphere and this filtering effect can be investigated using the theoretical model discussed in the paper.

## REFERENCES

- Burg, J. P., A new analysis technique for time series data, presented at the NATO Advanced Study Institute on Signal Processing with Emphasis on Underwater Acoustics, Enschede, Netherlands, 1968.
- Burg, J. P., Maximum entropy spectral analysis, presented at 37th Annual International SEG Meeting, Oklahoma City, Oklahoma, 1967.
- CIRA, COSPAR International Reference Atmosphere, North Holland Publishing Company, Amsterdam, 1965.
- DuBroff, R. E., Unpublished Ph.D. thesis, 1976.
- Hines, C.O., Internal atmospheric gravity waves at ionospheric heights, Can. J. Phys., 38, 1441-1481, 1960.
- Hooke, W. H., Ionospheric irregularities produced by internal atmospheric gravity waves, J. Atmos. Terr. Phys., 30, 795-829, 1968.
- Klostermeyer, J., Numerical calculation of gravity wave propagation in a realistic thermosphere, J. Atmos. Terr. Phys., 34, 765-774, 1972.
- Landau, L. D., and E. M. Lifshitz, Fluid Mechanics, Pergamon Press, 1959.
- Liu, C. H. and J. Klostermeyer, Excitation of acoustic gravity waves in a realistic thermosphere, J. Atmos. Terr. Phys., 37, 1099-1108, 1975.

- Pitteway, M. L. V. and C. O. Hines, The viscous damping of atmospheric gravity waves, Can. J. Phys., 41, 1935-1948, 1963.
- Schödel, J. P., A phenomenological investigation of amplitude and spectra of gravity waves, in Effects of Atmospheric Acoustic-Gravity Waves on Electromagnetic Wave Propagation, Conf. Proc. 115, 18-1-18-11, AGARD, Harford House, London, 1972.
- Titheridge, J. E., Periodic disturbances in the ionosphere, J. Geophys. Res., 73, 243-252, 1968.
- Toman, Kurt, On wavelike perturbations in the F region, Radio Sci., 11, 107-119, 1976.
- Webster, A. R. and G. F. Lyon, On the use of running means in the power spectrum analysis of ionospheric data, Planet. Space Sci., 21, 153-157, 1973.
- Volland, H., The upper atmosphere as a multiple refractive medium for neutral air motions, J. Atmos. Terr. Phys., 31, 491-514, 1969.
- Yeh, K. C. and C. H. Liu, Acoustic-gravity waves in the upper atmosphere, Rev. Geophys. Space Phys., 12, 193-216, 1974.
- Yeh, K. C., C. H. Liu and M. Y. Youakim, Attenuation of internal gravity waves in model atmospheres, Ann. Geophys., 31, 321-328, 1975.

#### ACKNOWLEDGMENT

This work was supported in part by a contract from the Air Force Cambridge Research Laboratory, No. F19628-74-C-0044; and in part, by a Grant GA-42857 from the Atmospheric Sciences Section of the National Science Foundation.

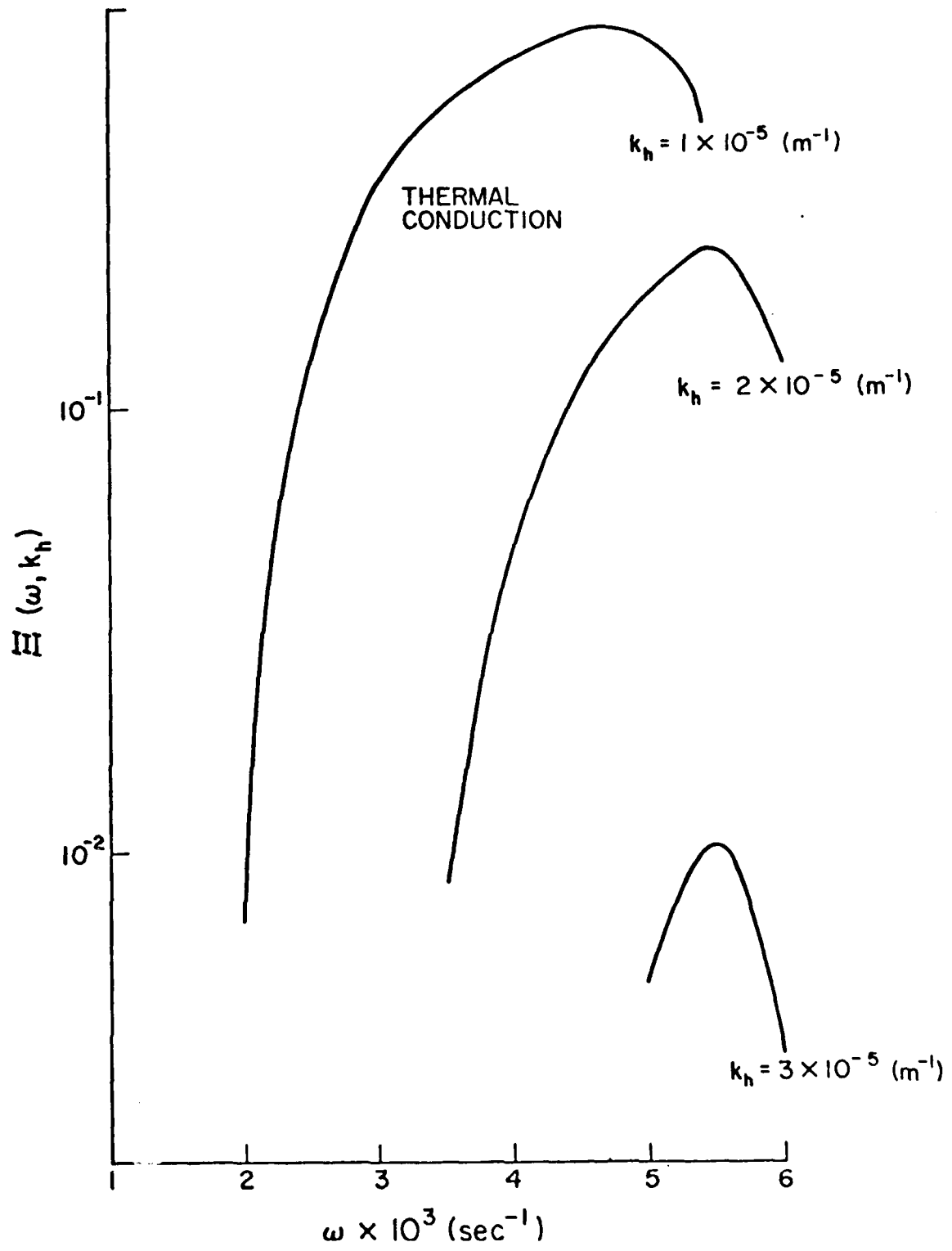


Figure (1) Transmittivity function (thermal conduction)

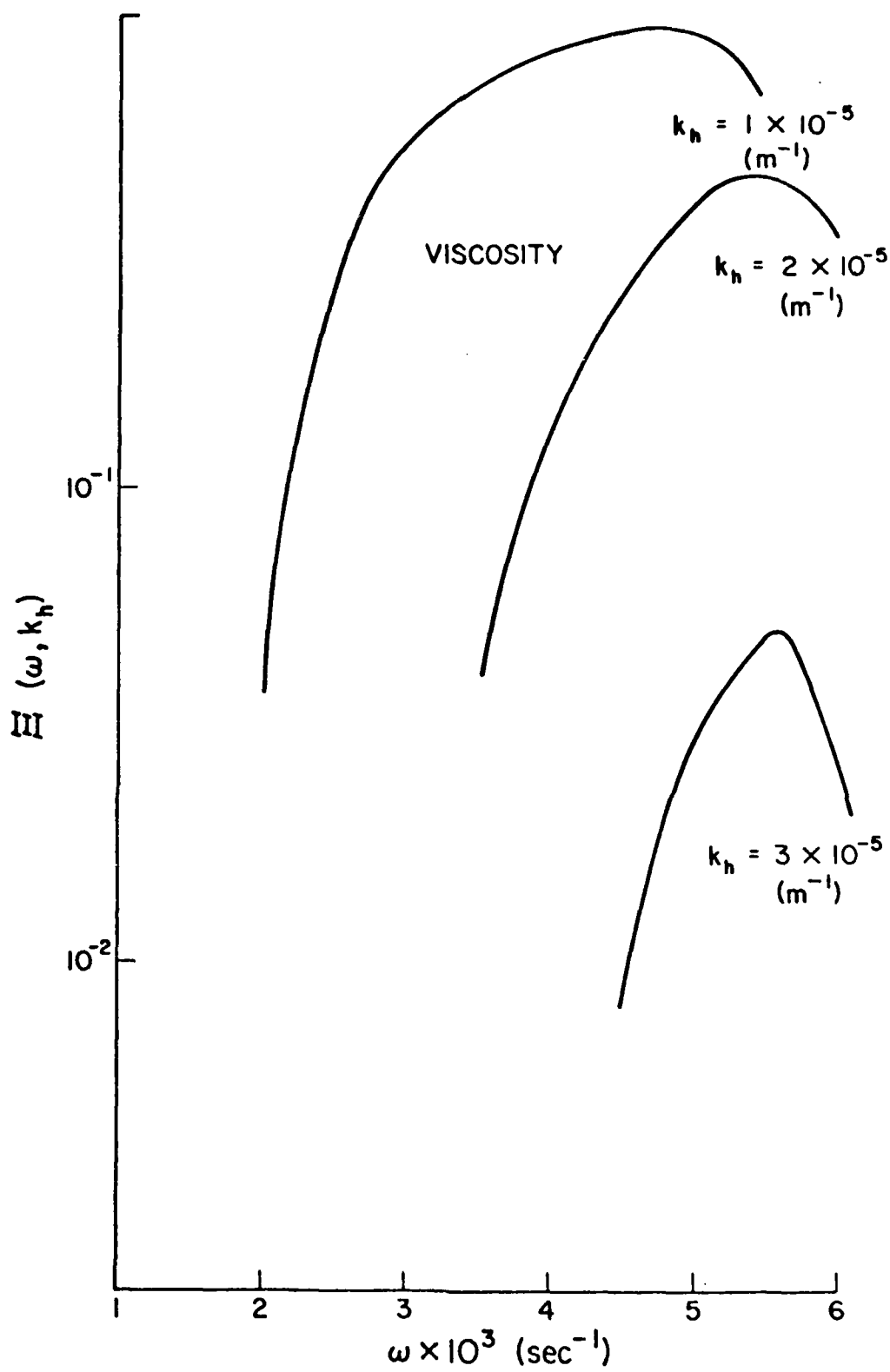


Figure (2) Transmittivity function (viscosity)

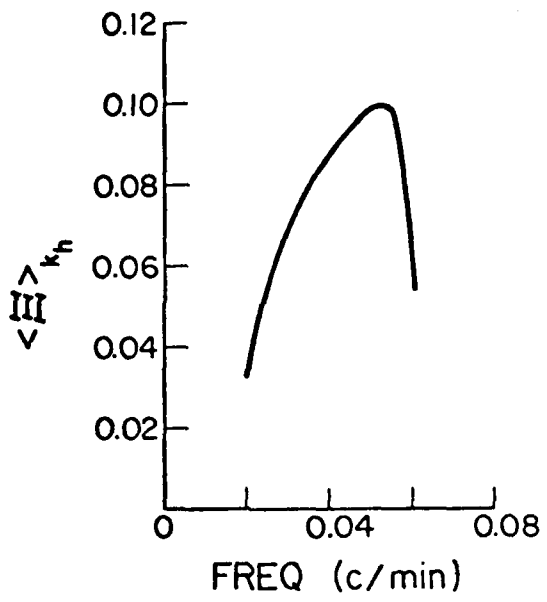


Figure (3) Transmittivity function (thermal conduction)  
averaged over  $k_h$

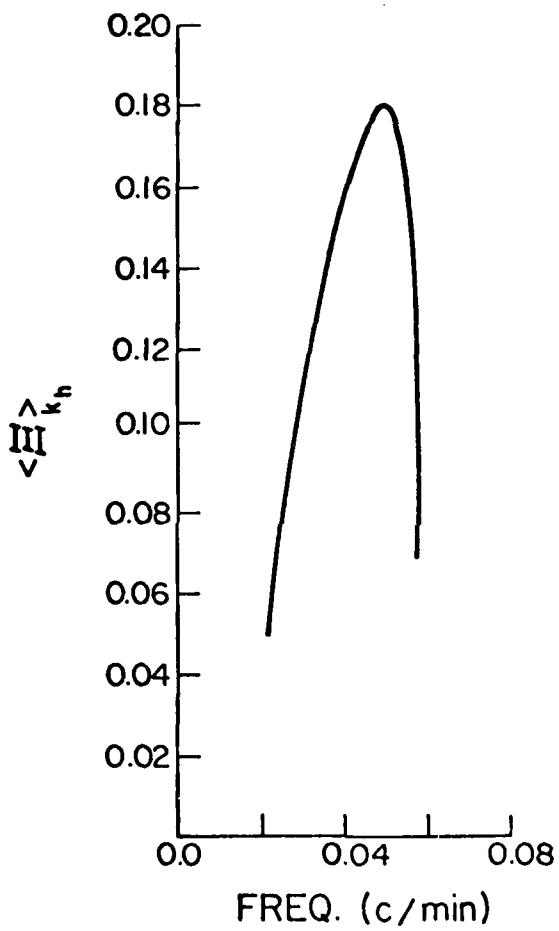


Figure (4) Transmittivity function (viscosity) averaged over  $k_h$

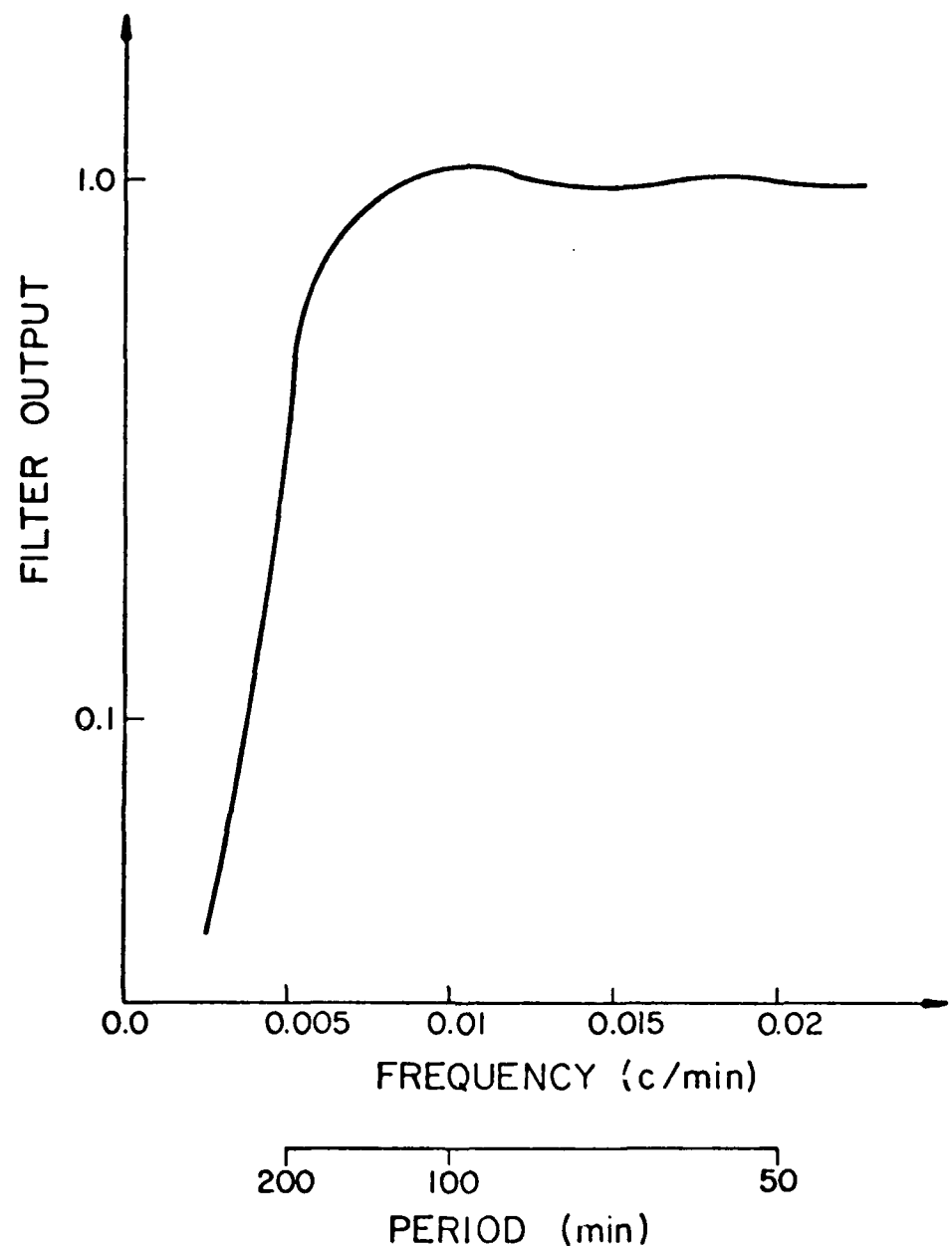


Figure (5) Frequency response of weighted running mean filter

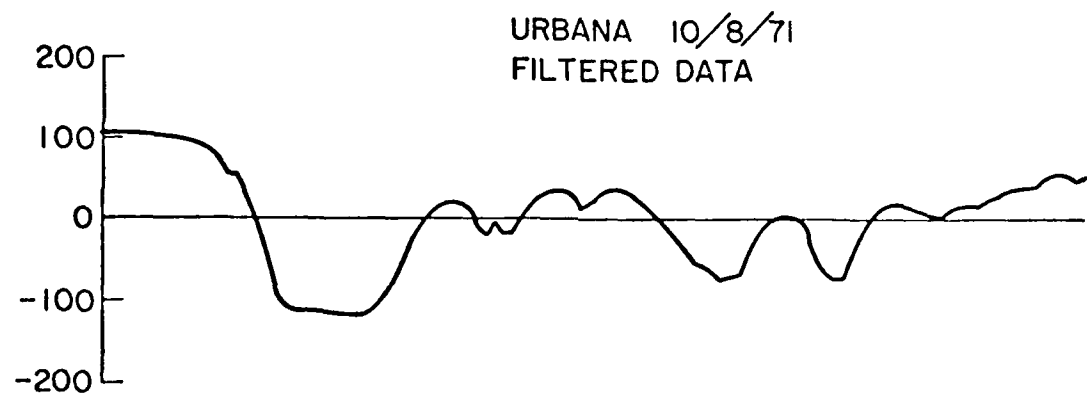
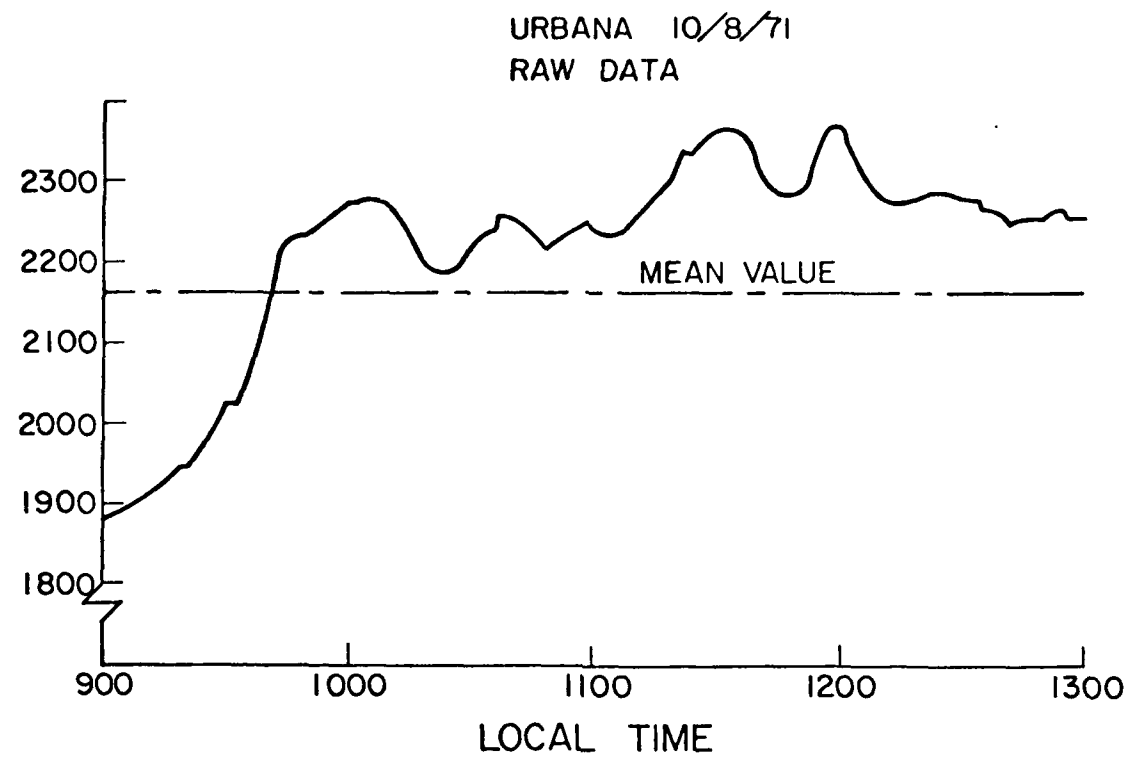


Figure (6) Raw and filtered data -- an example

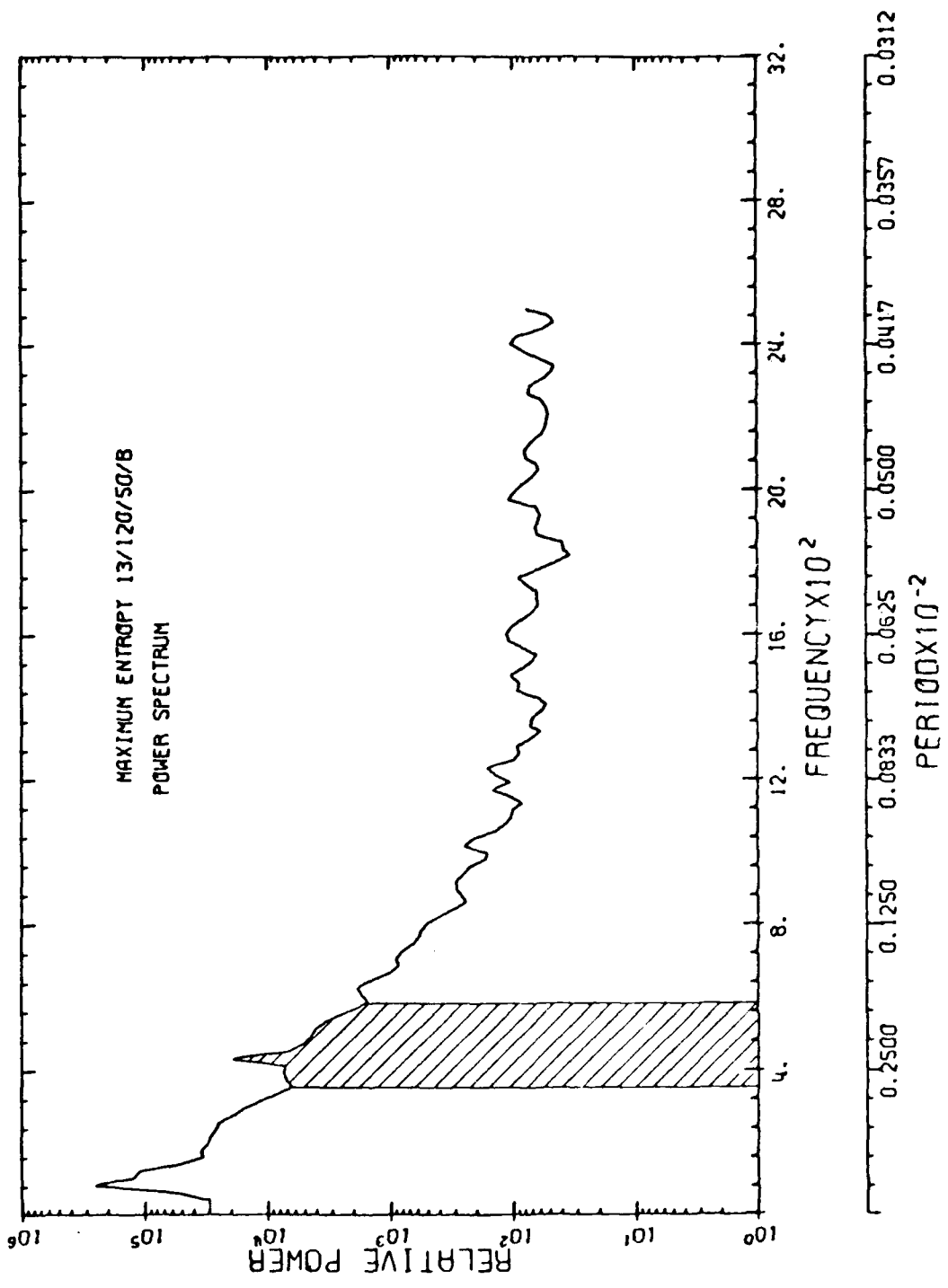
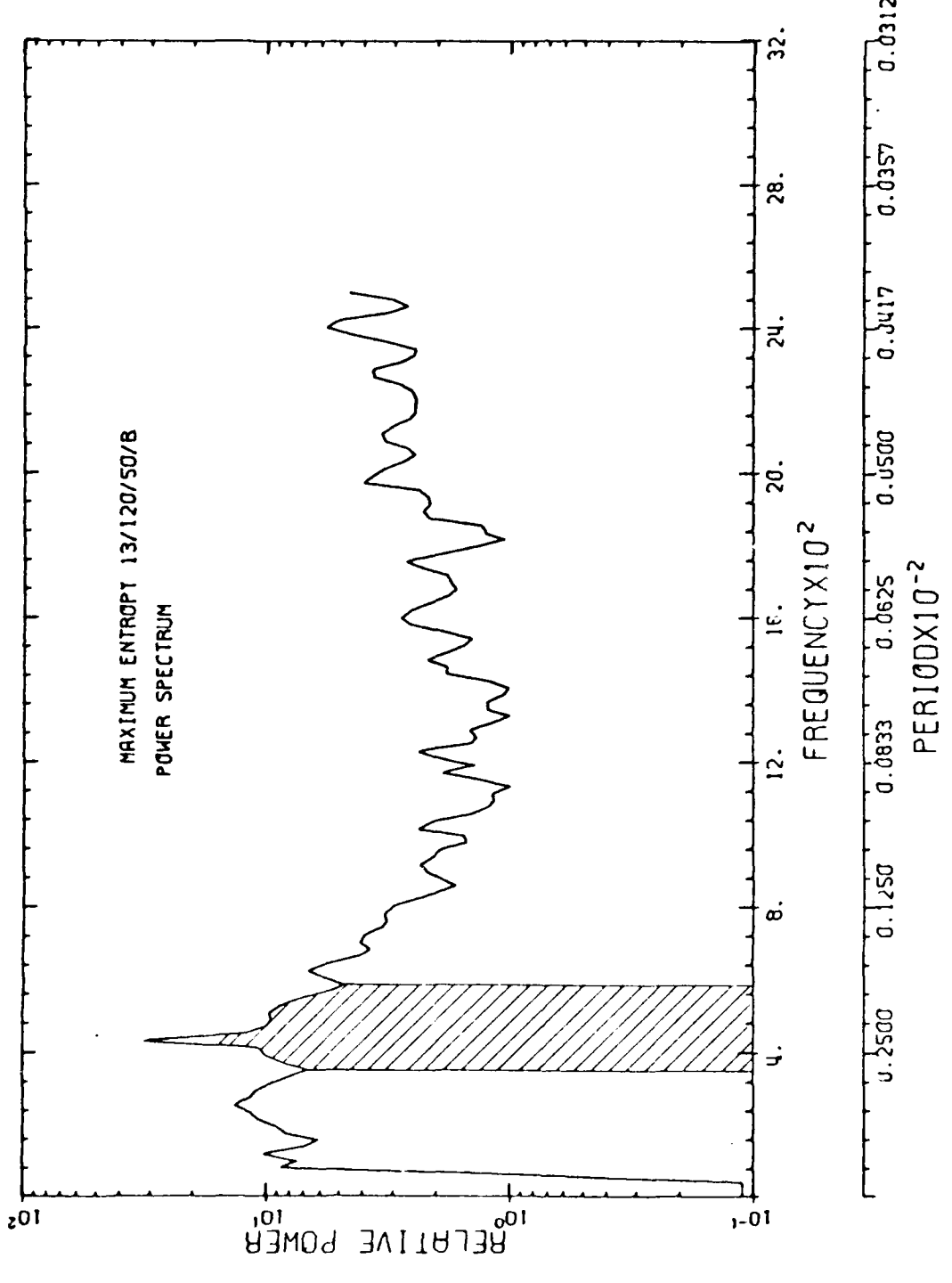
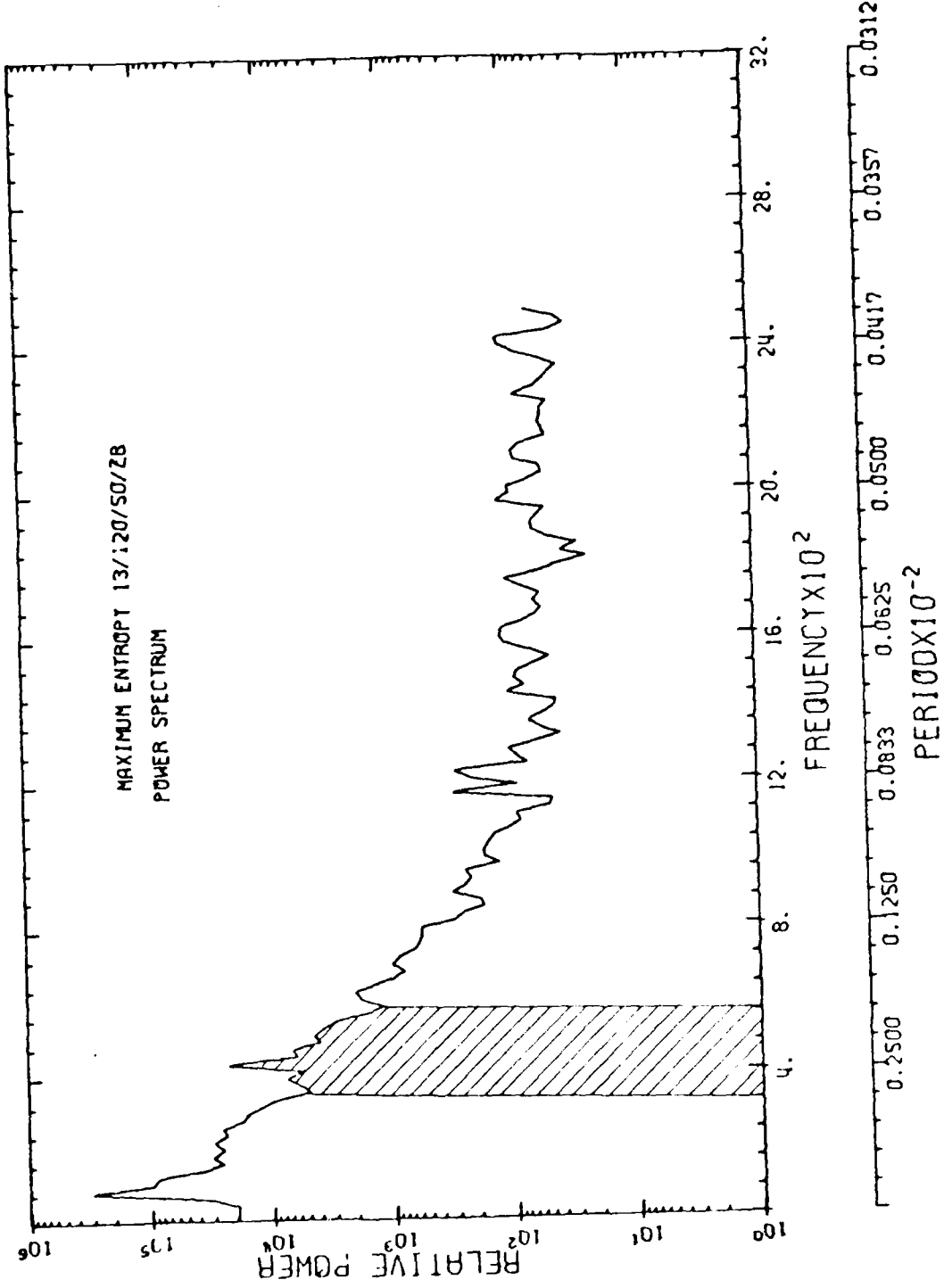


Figure (7) Power spectrum of electron content fluctuations  
(Method I)



178

Figure (8) Power spectrum of electron content fluctuations with compensation (Method I)



179

Figure (9) power spectrum of electron content fluctuations  
 (Method II)

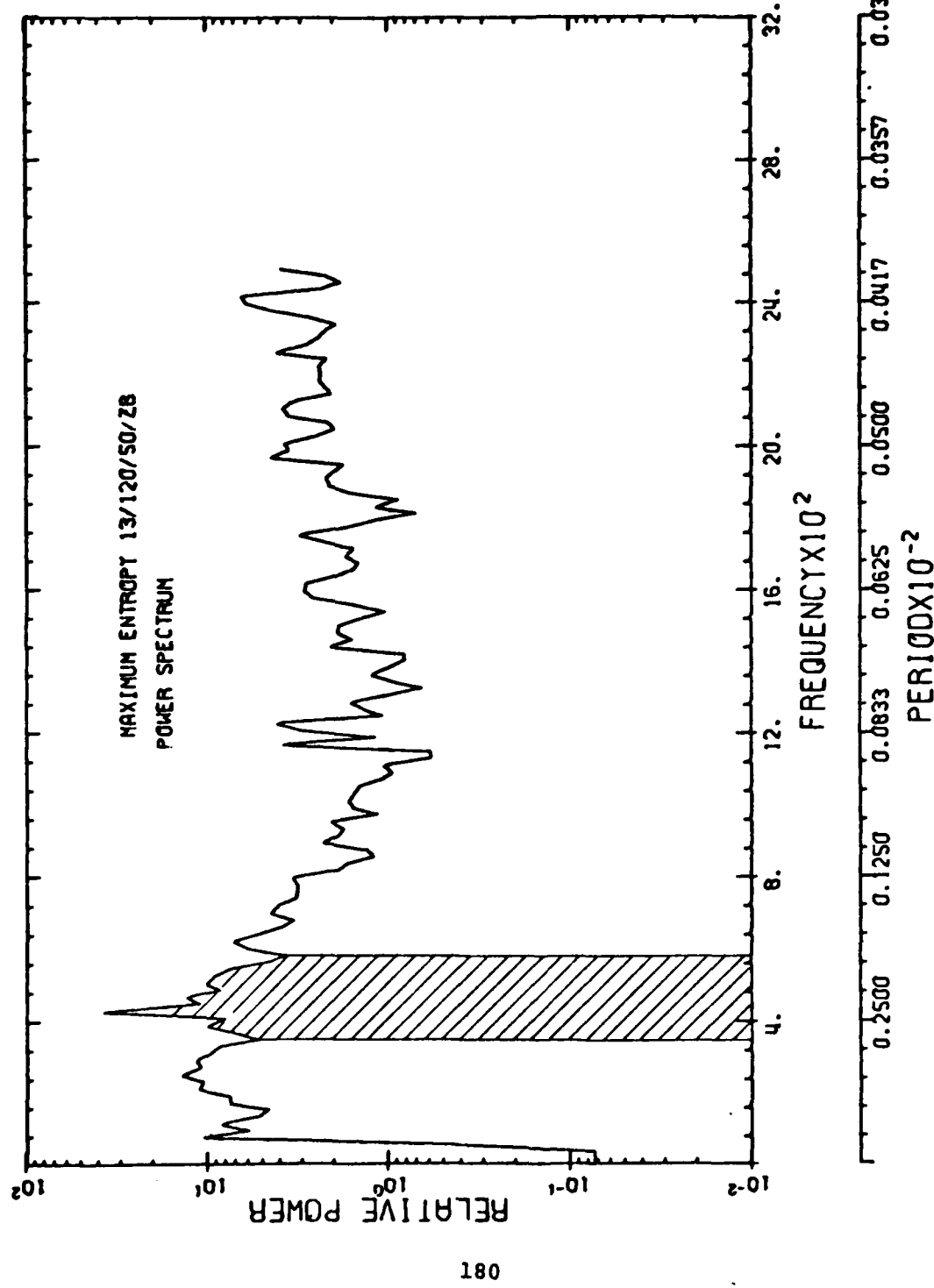


Figure (10) Power spectrum of electron content fluctuations with compensation (Method II)

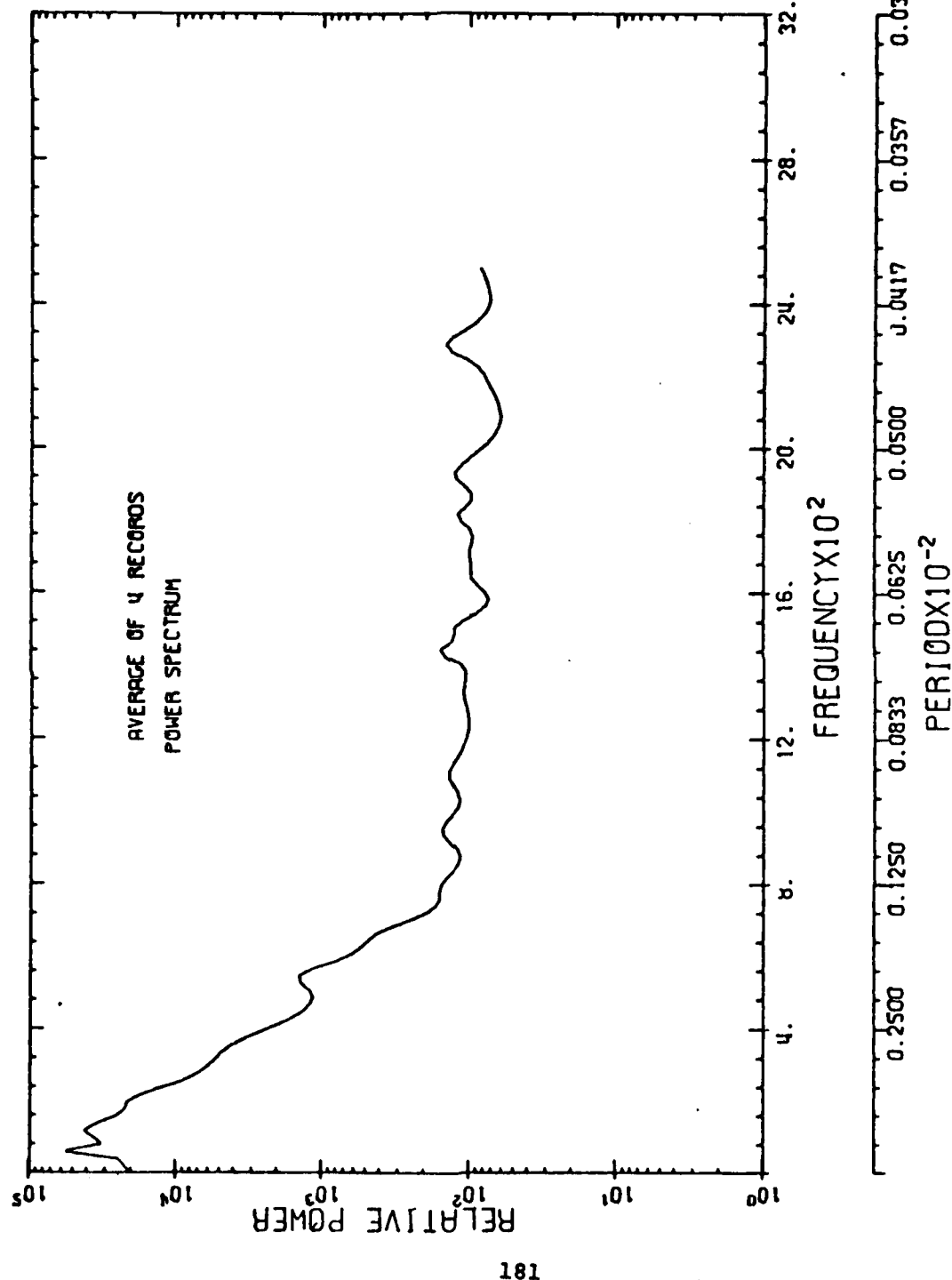


Figure (11) Power spectrum of electron content in the absence of noticeable wavelike fluctuations

THE METEOROLOGICAL JET STREAM AS A SOURCE OF MEDIUM SCALE GRAVITY  
WAVES IN THE THERMOSPHERE : AN EXPERIMENTAL STUDY

by F. Bertin and J. Testud

CNET, Issy les Moulineaux, France

and

L. Kersley and P.R. Rees

UCW, Aberystwyth, U.K.

INTRODUCTION

In an earlier paper BERTIN et al (1975) presented results which linked atmospheric gravity waves observed at ionospheric heights to possible sources of a meteorological nature in the troposphere. The present work represents a continuation in which attempts have been made in the first place to allay possible objections to the earlier study and secondly to define more precisely the source regions.

EXPERIMENTAL NETWORK AND DATA ANALYSIS

The experimental basis of this preliminary paper was a coordinated campaign carried out in July 1974. The investigations involved use of the quadristatic incoherent scatter sounder at St. Santin-Nancay-Mende-Montpazier together with a system of six spaced polarimeters, two networks of three each in France and U.K., receiving transmissions from a geostationary satellite and providing measurements of ionospheric electron content fluctuations. Figure 1 shows the geographic location of the observations.

In the thermosphere, the incoherent scatter technique provides a quasi-direct means of observing gravity waves as it gives access over a wide altitude range (100 to 500km) to parameters, ionic temperature and velocity, which are strongly coupled to the temperature and velocity of the neutral atmosphere; in addition the effect of the wave on electron density is observed simultaneously. The horizontal structure of the wave, which is not accessible by incoherent scatter, can be derived from spaced polarimeter measurements. Thus, taken together, the two techniques constitute a powerful method of observing gravity waves.

Correlation analysis is used to determine the characteristics of the wave : amplitude, period, speed and azimuth of propagation. Five consecutive days have been analysed by this method, and for each wave detected a reverse ray tracing has been computed to look for the source of the phenomenon. Performing such a ray tracing requires an atmospheric model. From the point of view of gravity wave propagation, the neutral atmosphere can be characterised at different heights by the scale height, the ratio of the specific heats and the background wind. For medium scale gravity waves, with periods in the 20 or 30 minute range and propagation speeds 70 to 200 m s<sup>-1</sup>, the interaction between the wave and the neutral wind can be very important, so that special care must be exercised in the choice of the background wind model. The wind model used in the present study is based on tidal observations (steady, 24-hour and 12-hour components), provided by

the incoherent scatter sounder in the altitude range 100 to 300km and by the meteor radar measurements at Garchy (France) between 70 and 100km. These are complemented by meteorological data in the range 0 to 30km, while between 30 and 70km the theoretical model of MURCATROYD (1965), zonal circulation with a westwards maximum around 50km, is assumed representative. The uncertainty in the wind model can be estimated, for example from the day to day variation in the incoherent scatter or meteor radar data, so that the error in the reverse ray tracing is calculated systematically for each observed wave.

## RESULTS

This preliminary paper presents the results of a study of approximately 100 waves. For 20 per cent of the waves the vertical wave number becomes zero at around the 110km level. The speed of many of these waves approximates to the speed of sound at this altitude. It is suggested that the observed waves at ionospheric F2-layer heights represent an energy escape of Lamb waves propagating in the middle atmosphere.

For 80 per cent of the waves detected the reverse ray tracing could be continued down to the 15km level, indicating that no critical or reflection level is encountered by the wave between the F2-peak and the tropopause. For each wave satisfying this condition, the point where the wave reaches the 15km level is plotted on a tropopausic meteorological chart. Figures 2 and 3 show examples of such plots. In these figures the sizes of the circles represent the errors resulting from uncertainties in the wind profile used in the ray tracing procedure. The positions of the circles correspond in most cases to geographical areas where strong winds blow at the tropopause level, indicating the presence of the jet stream. The significance of the relationship is enhanced by the fact that ray tracings are performed for waves observed at two locations, in U.K. and France, separated by about one thousand kilometers.

The distance of each source location from the jet stream axis has been determined, distinguishing between sources lying on the polar and tropical sides of this axis as shown in the distribution of Figure 4. The histogram shows an asymmetry with respect to the jet stream axis and strongly suggests that in fact it comprises two component distributions, one centred on the axis with a second displaced towards the polar side by some 400km. The sources lying in this latter region have been re-examined individually and appear to fall into two categories only one of which can be linked genuinely to the jet stream. The other group can be illustrated by the example of the sources marked by the hatching in Figure 5. These show no obvious association with either of the jet streams present at this time, but lie in the strongly convective region on the polar side of the jet stream axis. It is suggested that these sources are associated with convective instability, thunderstorm activity having been reported from these regions on the days in question.

## CONCLUSIONS

It is important to try to understand the significance of and to appreciate the objectives of a study of this kind. It is believed that work of the type described above is of use in three areas.

1. The method developed to study the gravity waves is in itself a good tool to understand the meteorological instability process. (GOSSARD and BOOKE, 1975).

2. From the results already obtained work is in progress on energy balance considerations and there are indications that a study of this kind can lead to a greater understanding of the waves and their sources. The velocity amplitude in the neutral atmosphere of the waves observed by the St. Santin incoherent scatter at 250km was about  $15 \text{ m s}^{-1}$ . Assuming an exponential growth the corresponding amplitude at 15km would be about  $1/2000$  of this value. However, consideration of damping effects, like resonant interaction with the wind (YEH and LIU, 1970), suggests that the actual amplification is much less. A full wave calculation for one of the waves in the present study has given an amplification factor in the range 15 to 40 (VIDAL MADJAR, private communication). This would imply that the velocity amplitude at the tropopause would have a magnitude in the range  $0.3$  to  $1.0 \text{ m s}^{-1}$ . Thus for a source of finite size, say 20km horizontal extent, the total energy launched would be very large.

3. If the indications outlined above are correct, namely that the wave spectrum is characteristic of the source type, then studies of this kind may assist in the evaluation of theoretical work on the wave generation process (MASTRANTONIO et al., 1976).

#### Acknowledgements

Thanks are due to Dr. J. Papet-Lepine for management of experimental aspects of this study in France and to Mr. K.J. Edwards for design, construction and operation of the polarimeters in U.K.

#### REFERENCES

- GOSSARD E.E. and HOOKE W.H. 1970, Waves in the Atmosphere, Elsevier Scientific Publ.Co., Amsterdam-Oxford-New York.  
MASTRANTONIO G. EINAUDI F., FAU D. and LALAS D.P. 1976, To be published.  
YEH K.C. and LIU C.H. 1970, Radio Sci., 5, 39.

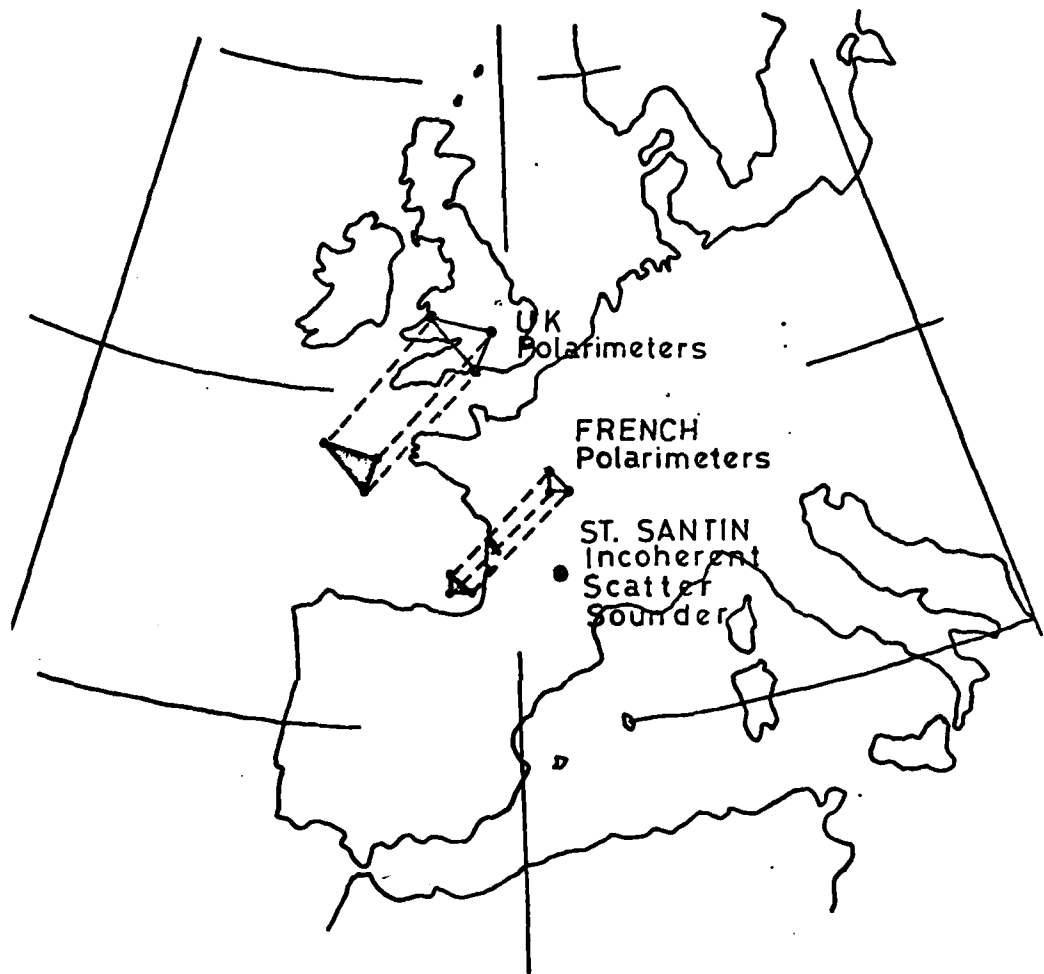
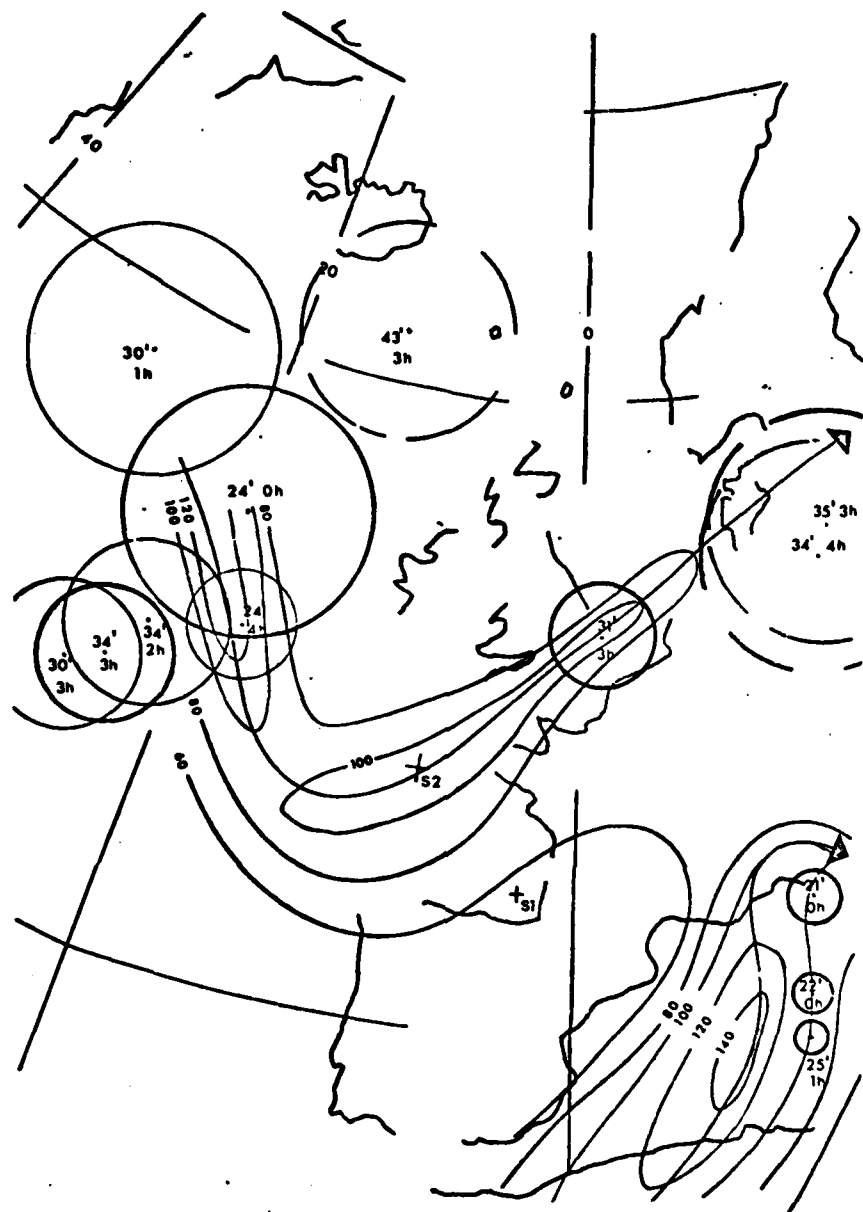


Fig.1. Geographic locations of the experimental observations.



**Fig.2.** The geographic location of the source regions of the observed waves. The contours are of constant wind speed at tropopause level, labelled in knots, for 00000.U.T. on 16 July 1974. The lines terminating in arrows show the jet-stream axis. The general locations of the ionospheric observations are depicted by S<sub>1</sub> and S<sub>2</sub> for French and U.K. station networks respectively. The source regions at tropopause level of the observed waves are depicted by the circles, the numbers within each circle giving the period of the observed wave and the approximate time (U.T.) of launching. The continuous and broken circles refer to the French and U.K. observation respectively, while the size of the circle gives a measure of the uncertainty of the source position due to the accuracy of the wind profile used in the ray tracing procedure.

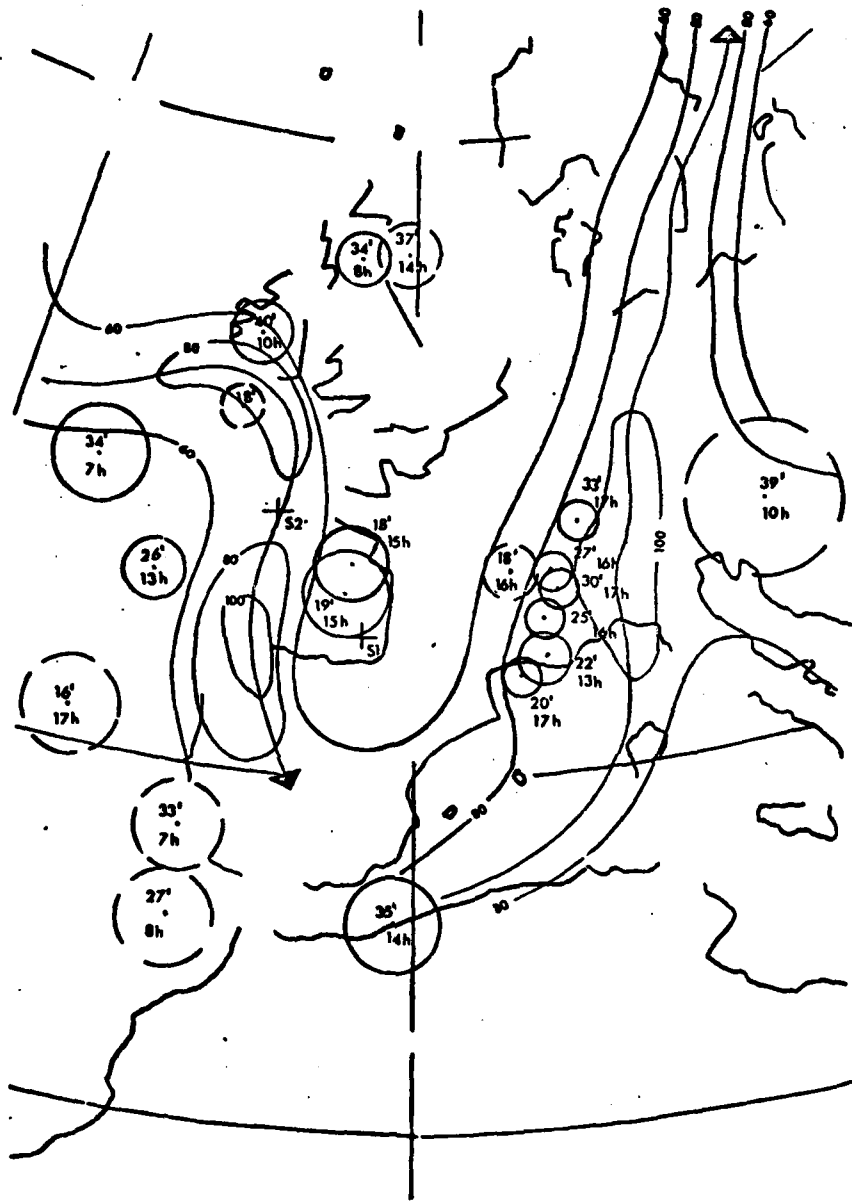


Fig.3. As for Fig.2 except that observations are for 1200U.T. on 17 July 1974.

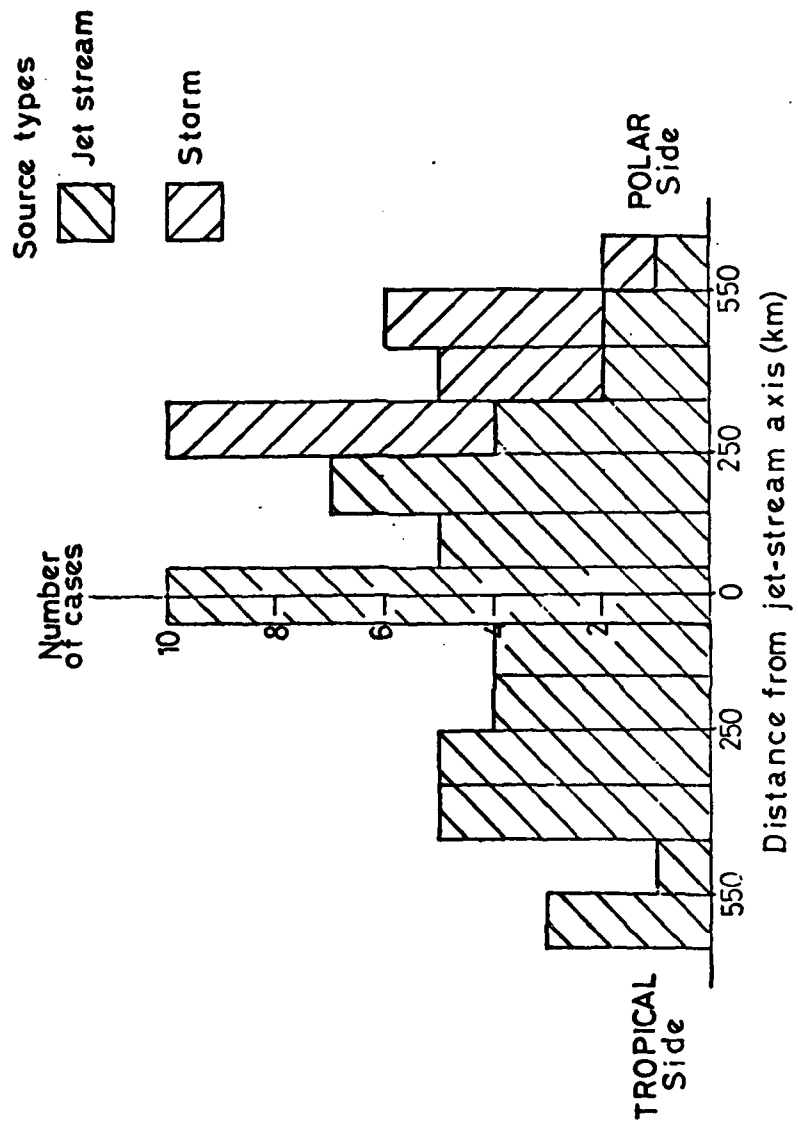
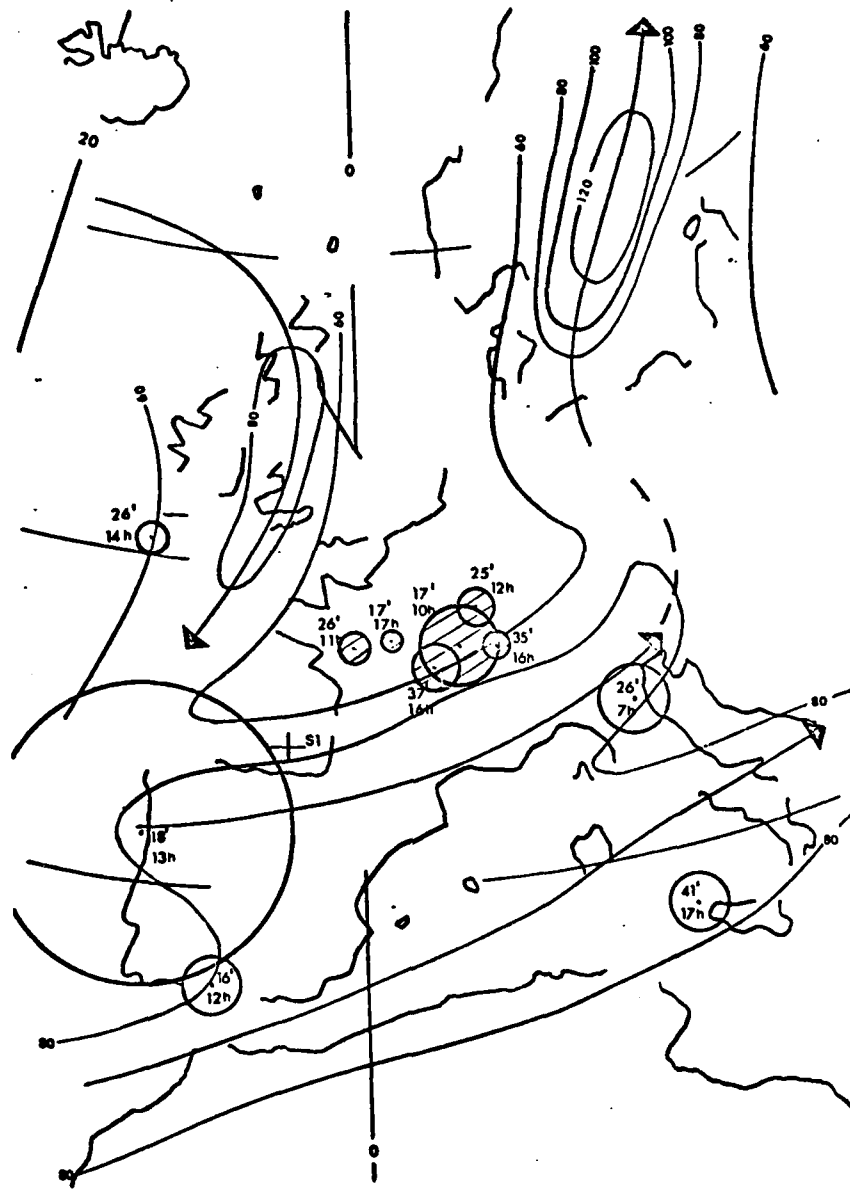


Fig.4. Distribution of source distance from jet-stream axis. Two source types are distinguished, the jet stream and thunderstorms.



**Fig.5.** As for Fig.2 except that the observations are for 1200U.T. on 18 July 1974. The sources marked with the hatching are associated with a region of thunderstorm activity.



## WORLD DATA CENTER A for SOLAR-TERRESTRIAL PHYSICS



National Oceanic and Atmospheric Administration  
Boulder, Colorado 80302 U. S. A.

### MESSAGE FROM WORLD DATA CENTER-A FOR SOLAR-TERRESTRIAL PHYSICS

by J. Virginia Lincoln

I have brought 25 copies of 3 handouts. The first is an updated version of the Catalog of B.6 Total Electron Content data from Satellite Beacons presently in the World Data Center. You will note it consists of very little actual data in our hands at present. What we do hold are copies of reports made by various institutions, universities, or government laboratories for limited periods. We feel the WDC could be more helpful to the total electron content and scintillation data community if your data were supplied to a WDC, particularly if in computerized format as recommended by the COSPAR Working Group some years ago; however, hard copy data are still welcome.

The second handout is the format for hourly electron content data on punched cards as prepared by J. Klobuchar. I am happy to announce that he has just mailed some of these data to us. The only change is the asterisk indicating that WDC-A needs columns 74-80 for control use, and, therefore, would prefer that the information optionally suggested for columns 74-80 be placed on information header sheets.

The third handout is pages from the *Second Edition of the URSI Handbook of Ionogram Interpretation and Reduction*, Report UAG-23 of World Data Center-A for Solar-Terrestrial Physics. This handout indicates that if the proposed Klobuchar format is used, it readily fits into the internationally adopted scheme for preparing hourly values of ionospheric characteristics in computer format. In fact, the two formats are identical for the electron content data.

I must, however, confess that my own agency NOAA is submitting computer tapes in a different format. It is as described by K. Davies, R. B. Fritz, R. N. Grubb and J. E. Jones at an earlier COSPAR meeting. These NOAA data are additionally expected to be published in a UAG Report of World Data Center-A for Solar-Terrestrial Physics. Though we prefer standardized data formats, we will happily accept data on punched cards or magnetic tape as long as they are in fully documented form. I believe you are all aware of the problems of converting data tapes from one computer system to another, hence the need for documentation. If you have any questions on format, please write our data center, and our programmers will respond.

We have just recently issued our Catalog of B.1 Ionospheric Vertical Soundings Data, and if any of you (or your organization) did not receive a copy, please let me know. It includes all of our holdings, not just the data from the IGY onward. We hope to publish the other ionospheric holdings catalog by the end of the year. Therefore, I beg you to submit your electron content and scintillation data and indices in the near future (or at least tell us what data are to be available on query). Replies to the MONSEE-STP questionnaire have provided a little such information, but complete details are still needed from many of you.

By supplying equivalent amounts of data to you on request in exchange for your data (or supplying larger amounts of data at the cost of reproduction) we feel we can relieve you of such copying burdens from bilateral type requests.

May I close with other advertisements of our data center services. Mini-catalogs are presented in the flyers 1976 (A), Monthly Composite Data - h'f and N(h), and 1976 (B) for Whistler Data - 1956-1966, available from our archives.

June 1, 1976

6/22/76 SB

B.6 TOTAL ELECTRON CONTENT - SATELLITE BEACONS

AT BOULDER

STATION	GEOGRAPHIC	YEAR																				
			LAT	LONG	57	58	59	60	61	62	63	64	65	66	67	68	69	70	71	72	73	74
WNULE	77N 24E																	Q	Q	Q	Q	Q
KIRUNA	68N 21																					
OLU	69N 25																					
WZELLER	60N 43																					
COLD BAY	55N 197																					
MUHLENBERG	54N 12																					
LINDAU	52N 10																					
BREISACH	48N 8																					
EDMONTON	47N 239																					
INVERGARGILL	46S 168																					
FLORENCE	44N 11																					
VAL-JOYEUX	44N 4																					
FT COLLINS	41N 255																					
GRAZ	47 46N 15																					
TORTOSA	41N 0																					
UNIV PARK	41N 282																					
BOULDER	40N 254																					
URBANA	40N 272																					
AHMEDABAD	37N 50																					
PALO ALTO	37N 242																					
CHINA LAKE	35N 243																					
TOKYO	35N 139																					
CORONA	36N 243																					
UCLA	36N 242																					
CLARK LAKE	33N 243																					
HAMILTON	33N 25																					
SAGAMORE HILL	42 32N 289																					
ROSHAN	32N 279																					
COLLEGE STA	30N 264																					
DELHI	28N 77																					
TAIPEI	25N 121																					
AHMEDABAD	23N 72																					
MONG KONG	22N 114																					
KONOLULU	21N 201																					
PIAHUATLAN	18N 264																					
BANGKOK	13N 100																					
ADDIS ABABA	09N 39																					
ACRA	05N 359																					
SINGAPORE	01N 103																					
NAIROBI	01S 36																					
DAR ES SALAAM	06S 39																					
TSUMEB	19S 17																					
SAN JOSE	39S 345																					
TUGUAN	27S 205																					
BRISBANE	28S 153																					
AUCKLAND	37S 175																					
PORT STANLEY	51S 303																					
FT MONMOUTH	40N 286																					

KEY TO SYMBOLS

- A = 12 Months
- B = 6-11 Months
- C = 1-5 Months
- W = World Days Only
- Q = Data exist but not held at WDC-A;  
QUERY WDC-A to assist in obtaining data
- P = Data PRESUMED to exist but not held at WDC-A;  
WDC-A will attempt to ascertain availability
- S = Program STOPPED operations (see PASTP  
STATION LIST for actual date)

B.6 TOTAL ELECTRON CONTENT - SATELLITE BEACONS

AT GREENBELT

SPACECRAFT, EXPERIMENT INVESTIGATOR, NSSDC ID	DATE SET AT NSSDC MONTH - DAY - YEAR FROM TO	LAUNCH DATE
PIONEER 6: TWO-FREQUENCY RADIO RECEIVER ESMLEMAN (65-105A-C4)	121665 271166 - 121665	
PIONEER 7: TWO-FREQUENCY BEACON RECEIVER ESMLEMAN (66-C75A-C4)	091966 252369 - 101766	
PIONEER 8: TWO-FREQUENCY BEACON RECEIVER ESMLEMAN (67-06CA-C2)	081966 112167 - 161457	
ATS 1: FARADAY ROTATION DARLSSA (66-11FA-15)	012157 123171 - 124755	
PIONEER 9: TWO-FREQUENCY BEACON RECEIVER ESMLEMAN (67-123A-C3)	121457 232771 - 121367	
PIONEER 9: TWO-FREQUENCY BEACON RECEIVER ESMLEMAN (68-10CA-C3)	121967 132771 - 132868	

**Proposed Format for Hourly Electron Content Data on Punched Cards (from J. Klobuchar)**  
 (for submission of data to WDC)

<u>Card Column</u>	<u>Description</u>	<u>Remarks</u>
1	Type Card	Ionospheric Data: "1"
2	Hours	Hours 00 - 11: "1" (assumed to be local standard time unless Hours 12 - 23: "2" noted otherwise in column 80.)
3-5	Station Code	See master list or write WDC-A (Boulder) for new code.
6-11	Date Code	Year-Month-Day (YYMMDD)
12-13	Characteristic Code	"70": Ionospheric Electron Content to 2000 km, Faraday Rotation, geostationary satellite. "71": Total Electron Content up to the geostationary satellite
14-18, 19-23, . . . 69-73	Hourly Data	Divided into five columns per hour: first three columns: hourly value in units of $10^{15}$ electrons-meter <sup>-2</sup> vertical column, right justified, no decimal pt. If more than 999 use M or N descriptive letter. fourth column: qualifying letter fifth column: descriptive letter
74-76	Sub-ionospheric latitude	In whole degrees (positive North), right justified. Use 420km height.
77-79	Sub-ionospheric longitude	In whole degrees East, right justified. Use 420km height.
80	Time standard	"U": Universal Time "L": Local Standard Time "S": Sub-ionospheric longitude time

Optional\*

Header Card Information (for use with hourly electron content data)

<u>Column</u>	<u>Description</u>
1	Identifier for electron content: "7"
2	Blank
3-20	Station name
21-30	Satellite name
31-34	Satellite East Longitude
35-40	Beacon Frequency ('Hz)
41-45	Sub-ionospheric point Latitude (use 420 km height)
46-50	Sub-ionospheric point East Longitude (use 420 km height)
51-60	East Longitude Time Zone used for data.
61-70	Conversion factor (unit of ambiguity) in units of electrons per meter squared per unit of ambiguity (e.g. pi radians) times $10^{-15}$ .
71-80	Method of data reduction (e.g. Faraday Rotation = FR, Group Delay = GD, Differential Carrier Phase = DCP, etc.)

This information is not processed in any mathematical way. It is used in the heading to explain the hourly values which follow. A decimal point may be used on the Header Card, but all hourly data values must be integers.

Qualifying and Descriptive Letters for Total Content Data

Qualifying Letters developed for ionosonde data which may be applicable to Electron Content data:

D Greater than ...

E Less than ...

I Missing value has been replaced by an interpolated value.

Descriptive Letters developed for ionosonde data which may be applicable to Electron Content data:

C Measurement influenced by, or impossible because of any non-ionospheric reason, e.g. equipment failure.

S Measurement influenced by, or impossible because of, interference or atmospheric, including scintillations.

The following Descriptive Letters are to be used in this way only for Electron Content data:

M To add 1000 to value reported

N To add 2000 to value reported

\* WDC-A for Solar-Terrestrial Physics requests that these columns 74-80 be left blank for WDC control use.

## TABULATION OF HOURLY VALUES

JKL MNOPQR

Fig. 7.2 "Eleven punch" for station codes

(c) Date

Columns 6 and 7 identify the year (e.g. 57 implies 1957).  
Columns 8 and 9 identify the month (e.g. 09 = September).

Columns 8 and 9 identify the month (e.g. 09 = September).  
Columns 10 and 11 identify

columns 10 and 11 identify

(1) for hourly measurements: the day  
(e.g. 08 signifies 8th of month).

(ii) for monthly summaries:

40 the median,  
50 the median

50 the median count,  
60 the upper quartile

60 the upper quartile,  
70 the lower quartile.

80 the quartile range

77 the upper decile

87 the lower decile

### 3. The Voter Section

(d) Characteristic

Columns 12 and 13 identify the ionospheric characteristic by using the unified two-digit code given in Table 7.2 in section 7.34. Characteristics normally interchanged are marked with an asterisk.

Hourly measurements: The ionospheric data for one characteristic for 12 (or 13) hourly observations are punched on a single card. Five columns are devoted to each observation as follows:

(a) Characteristics normally expressed as numerical values

Columns 14, 15, 16 (for example): The numerical value. This is always punched with three digits in the following way:

a 7.9	value of	foF2	is punched as 079,
a 3.5	value of	foF1	is punched as 350,
a 2.45	value of	foE	is punched as 245,
a 9.4	value of	foEs	is punched as 094,
a 3.7	value of	fbEs	is punched as 037,
a 2.6	value of	fmin	is punched as 026,
a 2.95	value of	M(3000)F2	is punched as 295,
a 245	value of	h'F	is punched as 245,
a 97	value of	h'E's	is punched as 097,
27.6	value of	MUF(3000)F2	is punched as 276.

PUNCHED CARDS

Column 17 (for example): Qualifying letter.  
 Column 18 (for example): Descriptive letter.

Further groups of five columns are used in the same way.

(b) Type of Es

To accommodate the standard 5-column allotment to each hourly observation, Es types are punched in the following way:

Column 14 (for example): First tabulated type.  
 Column 15 Number of Es traces of type punched in preceding column (maximum of 9 traces permitted).  
 Columns 16, 17 (for example): Type and number of traces for second tabulated type.  
 Column 18 (for example): Type (only) for third tabulated type.

Nothing is punched for vacant spaces on the tabulation sheets.

Code of characteristics: It is essential that all groups use the same characteristic code for key punching ionospheric data. The standard characteristic code assignments of Table 7.2 was adopted internationally in January 1970, for punch card columns 12 and 13.

Table 7.2  
 Codes of Characteristics, Card Columns 12 and 13  
 Characteristics normally interchanged are marked with an asterisk (\*).

CHARACTERISTIC CODES											
USED FOR IONOSPHERIC MEASUREMENTS Jan. 1970											
		FREQUENCIES			PARAMETERS			HEIGHTS			
CARD COL 13	CARD COL 12	0	1	2	3	4	5	6	7	8	9
LAYER	0	00	01	02	03	04	05	06	07	08	09
F2		foF2*	fxF2	fzF2	M(3000)F2*	h'F2*	hpF2	h'0x	MUF(3000)F2	hc	qc
F1	1	10	11		13	14		16	17		
		foF1*	fxF1		M(3000)F1*	h'F1		h'F*	MUF(3000)F1		
E	2	20		22		24		26			
		foE*		foE2		h'E*		h'E2			
Es	3	30	31	32	33	34		36			
		foEs*	fxEs	fbEs*	fEs	h'Es*		Type Es*			
Other	4	40		42	43	44			47	48	49
		foF1.5		fmin*	M(3000)F1.5	h'F1.5			fm2	hm	fm3
Spread F and Oblique	5	50	51	52	53	54			57		
		fol	fxI*	fml	M(3000)I	h'I			dfs		
N(h)	6	60	61		63	64	65	66	67	68	69
		fh'F2	fh'F		h'mF1	h1	h2	h3	h4	h5	H
T.E.C.	7	70	71	72							79
		I(2000)	I	I(xxxx)							T

## TABULATION OF HOURLY VALUES

The table lists characteristics that should be exchanged internationally by all stations, with the addition of some characteristics regularly measured at some stations for voluntary interchange by special arrangement. In a few cases, an arbitrary code assignment was adopted, but, in general, the WWSC system has been followed.

This table differs slightly from that given in the first edition. The following changes and additions have been adopted: Card column 12 (Layer identification), index 5 was originally reserved for solar indices, but has not been used for this purpose since an independent solar code has been developed. Therefore, index 5 in column 12 was adopted for parameters associated with spread F and oblique reflections. Index 6 is adopted for electron density profile parameters and index 7 for total electron content parameters.

- 02 fzF2 (new)
- 07 MUF(3000)F2 (change of code number)
- 17 MUF(3000)F1 (change of code number)
- 26 h'E2 (new)
- 44 h'F1.5 (new)
- 47 fm2 (minimum frequency of second order trace) (new)
- 49 fm3 (minimum frequency of third order trace if required) (new)
- 50 Reserved for foI if required
- 51 fxI (new standard parameter)
- 52 fmi, lowest frequency of spread (in use at some stations only) (new)
- 53 M(3000)I, factor deduced from upper frequency edge of spread traces and fxI (in use at some stations on experimental basis only) (new)
- 54 h'I, minimum slant range of spread (in use at some stations only) (new)
- 70 I<sub>2000</sub> or I(2000) Definition: Ionospheric electron content up to 2000 km (for a geo-stationary satellite measured by Faraday technique).
- 71 I Definition: Total electron content up to a geostationary satellite.
- 72 I<sub>xxxx</sub> or I(xxxx) Definition: Ionospheric electron content up to satellite height xxxx for nongeostationary satellites.

The following allocations have been requested to facilitate interchange of electron density profile data. They will be reviewed in the future to see whether they have been used in practice, and may be changed.

Additional parameters needed to enable profiles to be calculated using conventional parameters (e.g., foF2, M(3000)F2, h'F2, foF1, M(3000)F1, h'F, foE, h'E, fmin).

- 60 fh'F2 Definition: The frequency at which h'F2 is measured.
- 61 fh'F Definition: The frequency at which h'F is measured.
- 63 hmF1 Definition: The maximum virtual height in the o-mode F1 cusp.  
(i.e., the value of h' at foF1).

Profile characteristics calculated using Titheridge's method (Chapter 10).

- 48 hm Definition: The height of maximum density of the F2 layer calculated by Titheridge's method.
- 79 T Definition: The total sub-peak content calculated by Titheridge's method.
- 69 H Definition: The effective scale height at hmF2 calculated by Titheridge's method (H is similar to qc physically but liable to greater experimental errors).

PUNCHED CARDS

64 h1      |  
65 h2      |      Definition: True heights calculated by Titheridge's method at the sampling  
66 h3      |      frequencies f1, f2, f3, f4, f5.  
67 h4      |  
68 h5      |      Note: At night h1 represents f1.

Among the recent additions only fxI (51) is now recommended for general use, but data available for other additions should conform to the recommended code when punched.

The following definitions are generally accepted but have not been standardized internationally. It should be noted that such local conventions may change with development and research.

x- and z-mode characteristics: For extraordinary-wave mode or z-wave mode (columns 1 and 3 Table 7.2), follow the corresponding definitions for o-wave mode characteristics.

44 h'F1.5 This is defined to be analogous to h'F2.

05 hpF2 This code may also be used for parameters analogous to hpF2 where this parameter is not measured at the station, e.g., hmF2 deduced by curve fitting without correction for underlying ionization, but a note showing the exact parameter used must be included with the cards.

06 h'0x Height of extraordinary-wave trace at frequency equal to foF2.

57 dfS Frequency range of spread. This is normally equivalent to fxI-foF2, but can denote total frequency range of spread when foF2 or fxF2 cannot be identified, e.g., for equatorial scatter, when dfS = fxI - fmi may be used.

Note: The URSI/STP Vertical Incidence consultant or members of the INAG should be consulted when preparing local conventions for regional use to insure that scaling and reduction personnel receive instructions consistent in form with those of standard characteristics included in the current international exchange program.

Some typical ionospheric data punched cards are shown in Fig. 7.3, 7.4, 7.5 and 7.6. The interpretation of the punched codes and data is printed at the top of each card and in the figure caption.

SIMULATION AND MEASUREMENT OF THE  
PLASMASPERIC ELECTRON CONTENT

D. A. Poletti-Liuzzi, K. C. Yeh and C. H. Liu

Department of Electrical Engineering  
University of Illinois  
Urbana, Illinois 61801

Abstract

By combining the Faraday rotation, differential group delay and the differential Doppler techniques, attempts have been made in the ATS-6 beacon experiments to measure the plasmaspheric electron content. However, the sensitivity of the techniques depend on the ionospheric parameters. Therefore, in order to obtain consistent results from the data, computer simulations investigating the sensitivity of the techniques to different ionospheric models are carried out. It is shown that in order to obtain consistent results from the experiments, a pair of optimal values for Faraday height and averaged magnetic field strength used in the analysis of Faraday data should be found which are applicable to a wide range of variations of model parameters. Such a pair is obtained and used to analyze the ATS-6 data from our Danville, Illinois station. Our results show that during magnetic quiet periods in the summer, the plasmaspheric content  $I_p$  is quite large, of the order of 20% of the total content during the day and can be as high as 50% during night time. No appreciable diurnal variations are found in  $I_p$ . Also, increase of  $I_p$  during the few hours following sudden commencement of magnetic storms is observed. These results as well as those from computer simulations will be presented.

## 1. Introduction

The ATS-6 satellite (ATS-F before launch) carries a multi-frequency radio beacon which permits a continuous monitoring of the integrated electron content in the ionosphere [Davies et al., 1972]. This is done by measuring from ground stations the effect of the ionosphere upon radio signals transmitted by the satellite.

Two experiments are of particular interest to us. One is the Faraday rotation experiment, which consists of measuring the rotation of the plane of polarization of a radio wave that has travelled across the ionosphere. Since this effect is strongly dependent on the earth's magnetic field, whose strength decreases approximately with the cube of the distance from the center of the earth, it is rather insensitive to the electrons encountered in the upper parts of the ray path. Consequently, it gives a measure of the electron content of the lower ionosphere, where most of the ionization is known to occur. We call this quantity Faraday content.

The differential group delay experiment, which measures the difference in transit times of two radio waves across the ionosphere, is equally sensitive to all electrons regardless of their position along the ray path. The total content integrated along the entire ray path can be computed from this observation.

The plasmaspheric content is then found by subtracting from the total content the Faraday content. In this work we are concerned with studying the techniques for measuring the plasmaspheric electron content from both a theoretical and an experimental standpoint. In section 2 we analyze the behavior of the electron contents for model ionospheres. The experimental results are presented in section 3. Some conclusions are discussed in section 4.

## 2. Simulation

Let us consider the radio ray path from the satellite to the ground as shown in Figure 1. We will represent the distance from the ground station to a point on the ray path by  $h$ , the height, and the elemental path length by  $ds$ . The slant electron content from ground level to a height  $h$  is defined as

$$I(h) = \int_0^h N(s) ds \quad (1)$$

and the corresponding slab thickness obtained by dividing (1) by the peak density,  $N_m$ , is

$$\tau(h) = I(h)/N_m \quad (2)$$

$h = 0$  at the ground station,  $h_s = 37623$  Km at the ATS-6 satellite. The total content and slab thickness are then

$$\begin{aligned} I_T &= I(h_s) \\ \tau_T &= \tau(h_s) \end{aligned} \quad (3)$$

The Faraday height,  $h_F$ , is defined so that the equation

$$I_F = I(h_F) = \int_0^{h_F} N(s) ds \quad (4)$$

is satisfied. Then  $\tau_F = \tau(h_F)$ . Let us recall that the Faraday rotation angle undergone by the wave in its entire path is

$$\Omega = K \int_0^{h_s} N(s) H_L(s) ds \quad (5)$$

where  $K = 2.97162 \times 10^{-2}/f^2$  (S.I. units) and  $H_L$  is the magnetic field intensity in the direction of wave propagation. Our ultimate aim is to relate linearly  $I_F$  to  $\Omega$ . Since  $H_L$  is variable, we must account for its effect on  $\Omega$  by finding a weighted average value,  $\bar{H}_L$ . Furthermore, we must answer this very crucial question: Does a unique  $h_F$  exist such that equation (5) can be written as

$$I_F = \Omega/K\bar{H}_L \quad (6)$$

for the different model ionospheres? If such a quantity is plausible then, for the particular ray path geometry, we will have a unique  $\bar{H}_L$  value that will allow us to determine  $I_F$  from the measured value of  $\Omega$  for a range of varying conditions of the ionosphere. In the next section, computer simulations are carried out to study this problem.

The geomagnetic field is modelled by the dipole approximation (Sec Yeh and Liu, 1972, pp. 148-149). The lines of force of the dipole, together with the ray path geometry, are shown in Figure 1. The equatorial distance to the satellite is given both in kilometers and by the L-value.

Notice that the radio path encounters different field lines at different angles, and that it encounters some lines twice. Our station in Danville is at  $L \sim 2.45$ . Progressing upwards  $L$  decreases to  $\sim 2.1$  at a height of  $\sim 2100$  Km, then it increases monotonically up to the satellite ( $L \sim 6.8$ ). The lines corresponding to  $L = 2.45$  to  $2.1$  are encountered twice.

The model for the electron density consists of four different parts. Above 500 Km the profile is that given by Angerami and Thomas [1964], modified to make the temperature variable with height. Below 500 Km, three layers are used.

Since we would like the model to be valid for any actual magnitude of the peak density, we will normalize its value to unity. In this way, an evaluation of equations such as equation (1) will actually yield the slant slab thickness.

The model uses three parameters: the transition height,  $h_T$ , which is the level of the  $O^+$  to  $H^+$  transition; the peak height,  $h_M$ , and the exospheric plasma temperature,  $T_\infty$ . The ranges of variation for the parameters are  $500 \text{ Km} \leq h_T \leq 1500 \text{ Km}$ ,  $200 \text{ Km} \leq h_M \leq 400 \text{ Km}$ , and  $1000^\circ\text{K} \leq T_\infty \leq 5000^\circ\text{K}$ . The illustrations that follow, unless otherwise stated, will correspond to  $h_T = 1000 \text{ Km}$ ,  $h_M = 300 \text{ Km}$ , and  $T_\infty$  ranging from  $1000^\circ\text{K}$  to  $5000^\circ\text{K}$ , in  $1000^\circ$  steps.

The density profiles change appreciably as the parameter values are changed. In Figure 2 we can observe how strongly the electron density at heights above  $h_M$  is affected by changes in  $T_\infty$ .

From equations (4), (5), and (6) we obtain

$$\int_0^{h_s} \frac{N(s)}{N_m} H_L(s) ds = \bar{H}_L \int_0^{h_F} \frac{N(s)}{N_m} ds . \quad (7)$$

The left hand side can be readily evaluated since the integrand, as well as the limit of integration  $h_s$ , are known. The right hand side, on the other hand, has two unknowns to be determined, the constant  $\bar{H}_L$  and the limit of integration,  $h_F$ . Since there is only one equation, we need to impose another condition in order to solve both  $\bar{H}_L$  and  $h_F$  from equation (7). The idea is to make  $h_F$  as independent of the model parameters as possible. Evidently, we have to use a trial-and-error procedure for the solution. The results are shown in Figure 3.

The curves show that there exists an optimum  $\bar{H}_L = 35.1 \text{ A/m}$  that minimizes the changes in the Faraday height due to variations of the model parameters. Although we cannot achieve a perfectly constant  $h_F$ , its total variation is of the order of 270 Km, which is about 10% of its median value of 2715 Km. The significance of these numbers can be understood better if we take a look at the other curves. Any small deviation from the optimum  $\bar{H}_L$ , either above or below, produce drastic changes in  $h_F$ . This fact can give us an idea of how critical the value of  $\bar{H}_L$  is. Let us emphasize that these results,  $\bar{H}_L = 35.1 \text{ A/m}$ , and  $h_F \sim 2700 \text{ Km}$ , apply only to the geometry corresponding to the station at Danville, Illinois.

The ratio  $I_F/I_T$  at the satellite gives a good indication of the behavior of the plasmaspheric content, for the ratio of the content in the exosphere to the total content is simply

$$\frac{I_P}{I_T} = 1 - \frac{I_F}{I_T} . \quad (8)$$

We can now use the obtained value of  $\bar{H}_L$  to compute this ratio. The effects of each parameter upon  $I_F/I_T$  are shown in Figure 4 which shows the contours of constant value of this ratio for all the parameter values used in this study. By fixing two of the parameters and letting the other vary we can draw the following conclusions:

- (i) An increase in  $T_\infty$  makes  $I_F/I_T$  to decrease
- (ii) An increase in  $h_M$  makes  $I_F/I_T$  to decrease
- (iii) An increase in  $h_T$  makes  $I_F/I_T$  to increase

Also, using our model, we can simulate the behavior of the plasmaspheric content during magnetic storms. During magnetic storms, the plasmapause shrinks. As remarked earlier, the ray path to the Danville Station intercepts an L-shell twice for  $2.1 < L < 2.45$ . If the plasmapause should shrink to such low levels, then the radio wave will travel through regions essentially depleted of electrons, both below and above the L-shell. The model is adapted to the magnetic storm conditions by neglecting all electrons outside the plasmapause without other changes in the density profile. We can now compute the Faraday and total slant slab thickness as a function of the plasmapause position for different parameter values. The results are shown in Figure 5 for the total (full lines) and Faraday (broken lines) cases.

The Faraday slab thickness is unchanged as the plasmapause moves inward, provided  $L > 2.45$ , because the Faraday height is below the plasmapause. On the other hand, for the same range

of L-values the total slab thickness does decrease with L. The decrease is almost negligible for  $T_e = 1000^\circ\text{K}$ , but becomes more noticeable for higher temperatures, because the plasmasphere is reduced more and more. Now, if the plasmapause is further shrunk below  $L = 2.45$ , both quantities will decrease very sharply because of the special configuration of the ionosphere.

Figure 6 shows how the ratio  $I_F/I_T$  changes during a magnetic storm. The abscissa represents the L-value. Starting from the satellite and progressing down the ray path, as L becomes smaller the ratio increases until a maximum is reached, and then decreases again. The position of the maxima for different temperatures varies between  $L = 2.45$  and  $2.7$ .

An important conclusion is that the ratio  $I_p/I_T$  is likely to drop considerably as the plasmapause progresses inward, unless it passes  $L = 2.45$ , a rather unlikely event. The magnitude of the change of this ratio depends heavily on the temperature and on the magnitude of the change in L. For example, a change of L from 6.8 to 3.0 will provoke, if the temperature remains constant throughout the process, a reduction in the ratio  $I_p/I_T$  of 31% at  $5000^\circ\text{K}$ , 37% at  $4000^\circ\text{K}$ , 43% at  $3000^\circ\text{K}$ , and of 53% at  $2000^\circ\text{K}$ . These values are quite considerable.

### 3. Data analysis and results

Records of the ATS-6 beacon experiment have been gathered at the Danville station for a time span of almost one year (5 July 1974 to 9 June 1975). We have attempted to analyze some of these records. Two periods of data were chosen for analysis. The first was during a long string of quiet and normal days in August 1974. The second was in October 1974, for a period of sharp changes in geomagnetic activity with two major storms.

In Figures 7 through 16, the results are shown in the following manner. The bottom frame shows, in dashed lines, the  $K_p$  value, together with the plots in full lines of the integrated slant electron content, total,  $I_T$ , and Faraday,  $I_F$ . The middle frame depicts the integrated slant plasmaspheric content,  $I_p$ , in a scale twice as large as that for  $I_T$  and  $I_F$ . In the upper frame the value of the ratio  $I_F/I_T$ , or  $I_p/I_F$ , is plotted. The time is given in Central Standard Time (CST = UT - 6).

The August period analyzed is fairly distant from the previous moderately strong magnetic storm on 2 - 4 August. The magnetic activity tends to decrease, with the last four days (12 - 15 August) being very quiet ( $K_p < 2+$ ).

The behavior of  $I_p$  and  $I_F$  is very much in line with what was previously observed for  $I_F$  for this month [Flaherty and

Narayana Rao, 1972]. The daytime increases in  $I_T$  and  $I_F$  above their nighttime values are small. Figures 7 and 8 show the typical behavior for this period. The plasmaspheric content,  $I_p$ , is rather large, of the order of  $3 - 5 \times 10^{16} \text{ el/m}^2$ . It is essentially constant throughout the day. There appears to be some substantially large oscillations in  $I_p$  (of the order of  $2 \times 10^{16} \text{ el/m}^2$ , peak-to-peak), which we think are mostly due to errors in equipment and data scaling. The most representative values are probably given by the mean of the oscillations.

The ratio  $I_p/I_F$  for all these days follows the same general daily variations. The maximum seems to occur between 0300 and 0400 with very large values, 0.5 to 0.6. After sunrise this ratio experiences a very marked decrease in a period of one to two hours, then remaining fairly constant with values between 0.15 to 0.25, depending on the day. It starts to increase again before sunset, at a slower pace than the sunrise decrease, and continues doing so until reaching the peak on the following day.

The progressive behavior of  $I_p$  during this period is less evident, yet noticeable. At the beginning of our observation period  $I_p$  was from  $3$  to  $4 \times 10^{16} \text{ el/m}^2$ , and towards the end, with much quieter conditions, it rose to about  $5 \times 10^{16} \text{ el/m}^2$ .

The period of 10 - 20 October 1974 consists of two quiet days, 10 and 11 October and two important magnetic storm periods with SC on the 12 and 14 October. The storm of 12 October had two SC reported, one at 0645 and the other at 1415. Following the first SC the  $K_p$  index remained high for the remainder of the day and part of 13 October. On 14 October, another storm had an SC at 1034 and lasted for a few days. The  $K_p$  index has risen sharply by five units at SC, and remained in general fairly high until the end of our data.

The behavior of  $I_T$  and  $I_F$  during the two quiet days at the beginning of the period can be considered as normal for that time of the year (See Figure 9 for 11 October). The plasmaspheric content has a very much flat behavior (save for the oscillations) of an average level of  $3 - 3.5 \times 10^{16} \text{ el/m}^2$ . The ratio  $I_p/I_T$  is larger at nighttime than during the daytime, with a typical nighttime value of 0.35, decreasing gradually after sunrise and remaining at an average of 0.11 before gradually increasing at the time  $I_T$  and  $I_F$  begin their afternoon decrease.

On 12 October, the  $K_p$  index increased after the first SC from 4 to a high of 7- at midnight. In Figure 10, the curves for  $I_T$  and  $I_F$  are in general higher than for the preceding day, especially in the time period that follows the second SC until 0200 to 13 October. The plasmaspheric content showed a slow increase in its mean behavior, from the nighttime value of  $2.5 \times 10^{16}$  to about  $3.7 \times 10^{16}$  after 1200; it remained at that level until midnight. On 13 October the  $I_T$  and  $I_F$  curves were very depressed and showed little daily variation (Figure 11).

The  $I_p$  curve showed a marked decrease from  $3.7 \times 10^{16}$  at 0000 to about  $1.5 \times 10^{16}$  at 0600, staying at that low level until midnight. On 14 October  $I_p$  slowly increased from midnight until SC of the storm, to a value of  $2 \times 10^{16}$  (Figure 12).

The ratio  $I_p/I_T$  on 12 October followed the same morning behavior for 11 October but in the afternoon its increase was very slow, reaching a maximum at 0300 of 13 October. During the rest of 13 October it was at a low 0.1 to 0.15 value, rising only after midnight to a maximum at 0300, 14 October.

The storm on 14 October had some interesting effects upon the ionosphere. It caused a very large peak of  $I_T$  and  $I_F$  about four hours after SC; followed by a rapid decrease in the next three hours, and a slower one until 0500 of 15 October. The plasmaspheric content was  $\sim 2 \times 10^{16}$  el/m<sup>2</sup> before SC, increased in a perceptible manner to  $\sim 4 \times 10^{16}$  el/m<sup>2</sup> at the peaks of  $I_T$  and  $I_F$ , and afterwards decreased to  $2 \times 10^{16}$  by 1800. Its value remained roughly constant until sunrise of 15 October. We are inclined to believe that the actual value of  $I_p$  did not increase afterwards during the remainder of 15 October. The ratio  $I_p/I_T$  for 14 and 15 October were not much different from the corresponding ones for the 12 - 13 October period. Similar to what happened on 13 October, the  $I_T$  and  $I_F$  curves were very depressed on 15 October (Figure 13).

During the last five days of the storm period, 16 - 20 October (Figures 14 through 16), the general pattern of  $I_T$  and  $I_F$  appears to be that of depressed contents, except for 17 October. The exact behavior of the plasmasphere during 16 and 17 October is difficult to recognize because of the large sizes of the oscillations. But averaging over them it is apparent that the plasmasphere is essentially depleted of electrons. The mean value is only around  $10^{16}$  el/m<sup>2</sup> on 17 October. It is even lower for 16 October. On 18 October it appears to start to increase to  $2 \times 10^{16}$  and to  $2.5 \sim 3 \times 10^{16}$  on 19 October. The average  $I_p$  for 20 October has dropped to  $2.5 \times 10^{16}$  el/m<sup>2</sup>.

It is of great interest to observe the daytime ratio  $I_p/I_T$  during those days. On 16 and 17 October it reached a very low level of 0.05. As compared with the daytime ratio observed before the storm. This is in agreement with our simulation results. The nighttime value on 17 October was of the order of 0.25, and that of 16 October was about 0.1. The discrepancy in the nighttime ratios may be due to different phase errors; also, at 0400 on 16 October,  $I_T$  was extremely small, and even a small error in  $I_T$  can influence a large error in  $I_p/I_T$ . On 18, 19, and 20 October the ratio seems to go back to the behavior of the pre-storm days.

#### 4. Discussion of the results

From the results, we note that under normal geomagnetic conditions the plasmaspheric content exhibits a very flat daily behavior, with an essentially constant value throughout the day. The oscillations observed in  $I_p$  are a consequence of errors in equipment calibrations and scaling. Taking the median values of these oscillations, we find that the ratio  $I_p/I_T$  is quite large at nighttime, but low during daytime. This is due to the relatively stable level of  $I_p$  and to the large diurnal changes undergone by  $I_T$  and  $I_F$ . This implies that the free exchange of plasma between the plasmasphere and the underlying ionosphere, where the ionization is produced during daytime, is hindered to the extent that the plasmasphere is unable to respond to the large diurnal changes in total electron content. Therefore, most of the ionization produced during the day is confined to remain in the regions below the plasmasphere, which in our measuring technique is below 2700 Km, and contributes only to the Faraday content. With respect to this fact, Park [1970] mentioned the existence of a diffusive barrier hindering the free exchange of ionization between the two regions. Since the major ion constituent of the plasmasphere is  $H^+$  while the corresponding constituent of the underlying layers is  $O^+$ , the large Coulomb cross sections may be responsible for impeding the free movement of the  $H^+$  ions in a region largely dominated by  $O^+$  ions.

Nonetheless, it was suggested that the plasmasphere acts as a reservoir of ionization, by receiving excess plasma from the lower layers during daytime, and providing the plasma necessary to maintain the nighttime ionosphere. Park [1970] estimated that the flux along tubes of magnetic force between both regions is sufficient to sustain the processes mentioned above. To investigate this coupling we should compute the magnitude of the flux. This, unfortunately, is hampered by the uncertainties in the true variation of the contents created by the oscillations. For this reason we did not seek to determine the flux.

During the quiet period of August we notice that the level of  $I_p$  tends to increase from day to day. This may be due to the replenishing of the plasmasphere occurring during quiet days after storm periods. The preceding storm was already distant at the beginning of our observation (7 August), so the plasmaspheric content was already at a high level but it continued to rise to even higher levels as quiet conditions persisted. Park [1970] found from whistler data that the content of a whistler duct continued to rise beyond the monthly median value (which was reached five days after the storm) as the geomagnetic conditions remained quiet.

During the two storms in October, the content behavior was characterized by a general increase in the plasmaspheric content after SC. This can be explained by the lifting of the F-layer during the positive phase of the storm [Mendillo et al., 1972]. The ensuing decrease in  $I_p$  and the depletion occurred at least during the following day, or, when the disturbed magnetic conditions persisted, for three days. This was caused by large inward motions of the plasmapause, which also diminished the plasmaspheric contribution to the total content to one half of the pre-storm levels. This behavior is predicted by the simulation study in section 2.

In conclusion, we note that from both our simulation studies and experimental data it is possible to study the plasmaspheric electron content using the Faraday and group delay techniques.

#### ACKNOWLEDGMENT

This work was supported in part by a grant from the National Oceanic and Atmospheric Administration, Grant No. NOAA 4-5-022-10, and in part, by a Contract F-19628-74-C0044, from Air Force Cambridge Research Laboratory.

#### REFERENCES

- Angerami, J. J. and J. O. Thomas, "Studies of planetary atmospheres - 1, The distribution of ions and electrons in the earth's exosphere," J. Geophys. Res., 69, 4537-4560, 1964.
- Davies, K., R. B. Fritz and R. N. Grubb, "The ATS-F/G radio beacon experiments," J. Environ. Sci., 31-35, March/April, 1972.
- Flaherty, B. J. and N. Narayana Rao, "Atlas of electron content values observed at Urbana, Illinois, for the period December 1, 1967 through December 30, 1970," Tech. Rep. No. 47, Ionosphere Radio Laboratory, University of Illinois, 1972.
- Mendillo, M., M. D. Papagiannis and J. A. Klobuchar, "Average behavior of the midlatitude F-region parameters  $N_T$ ,  $N_{max}$ , and  $\tau$  during geomagnetic storms," J. Geophys. Res., 77, 4891-4895, 1972.
- Park, C. G., "Whistler observations of the interchange of ionization between the ionosphere and protonosphere," J. Geophys. Res., 75, 4249-4260, 1970.
- Yeh, K. C. and C. H. Liu, "Theory of Ionospheric Waves," Academic Press, New York and London, 1972.

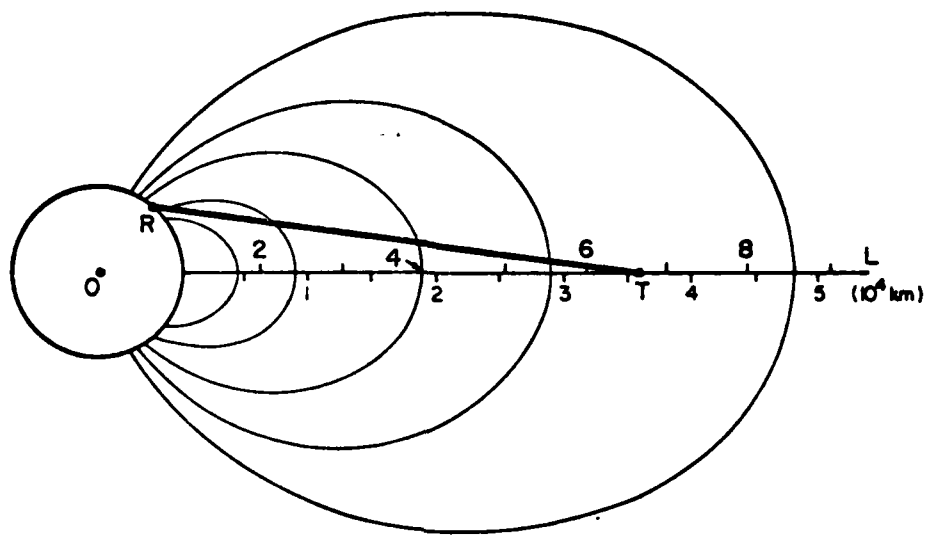
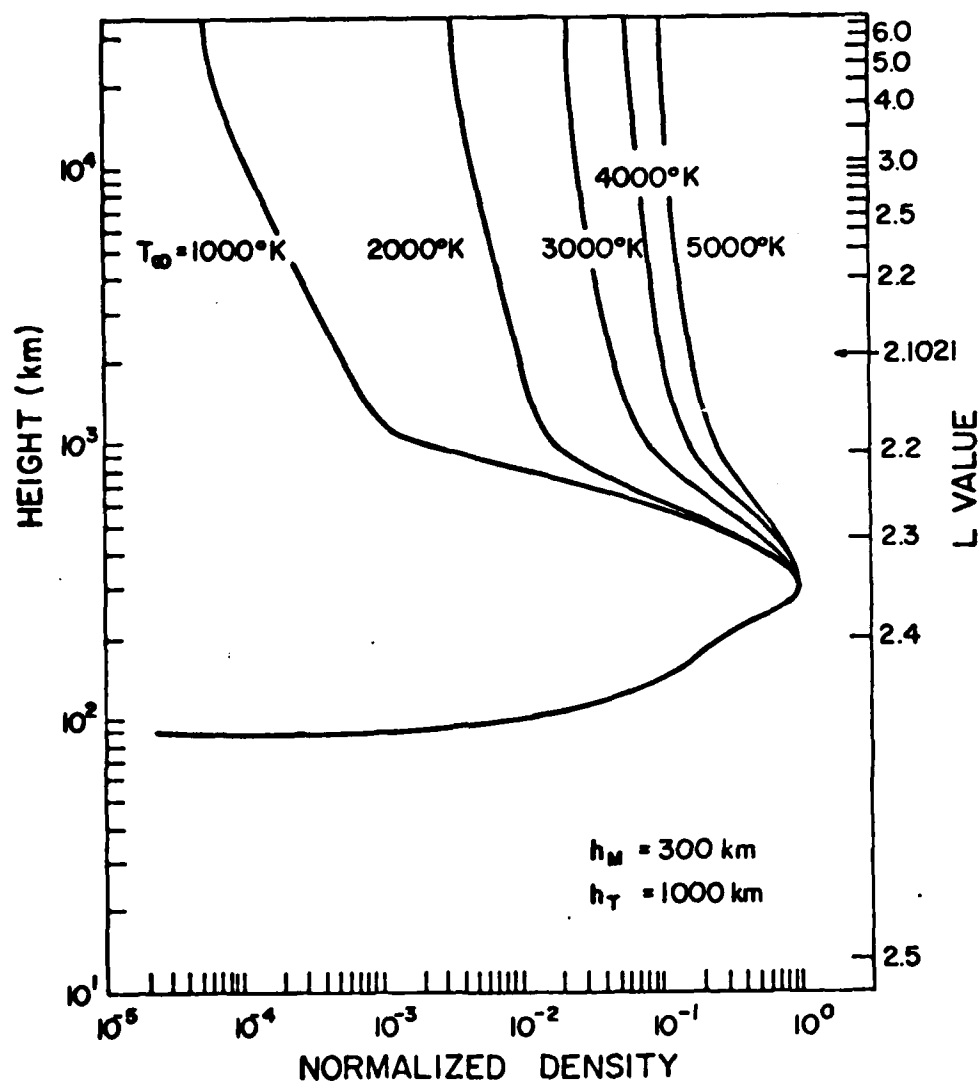


Figure 1. Geometry of the ray path and earth's magnetic dipole model.



**Figure 2.** Ionosphere model, electron density profiles as a function of height.

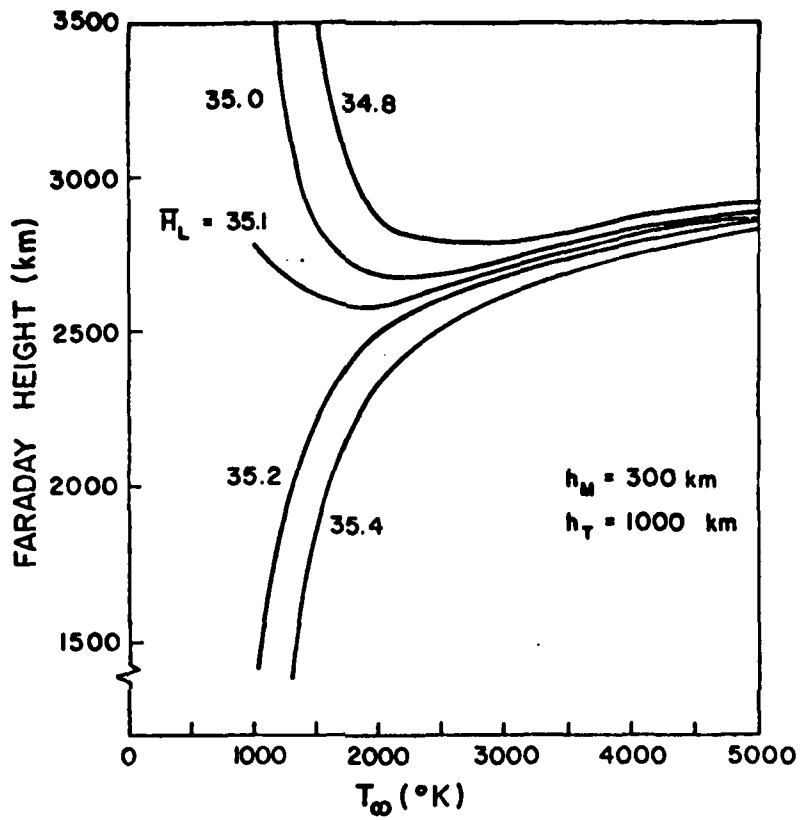


Figure 3. Contours of  $h_F$  for different  $\bar{H}_L$  values.

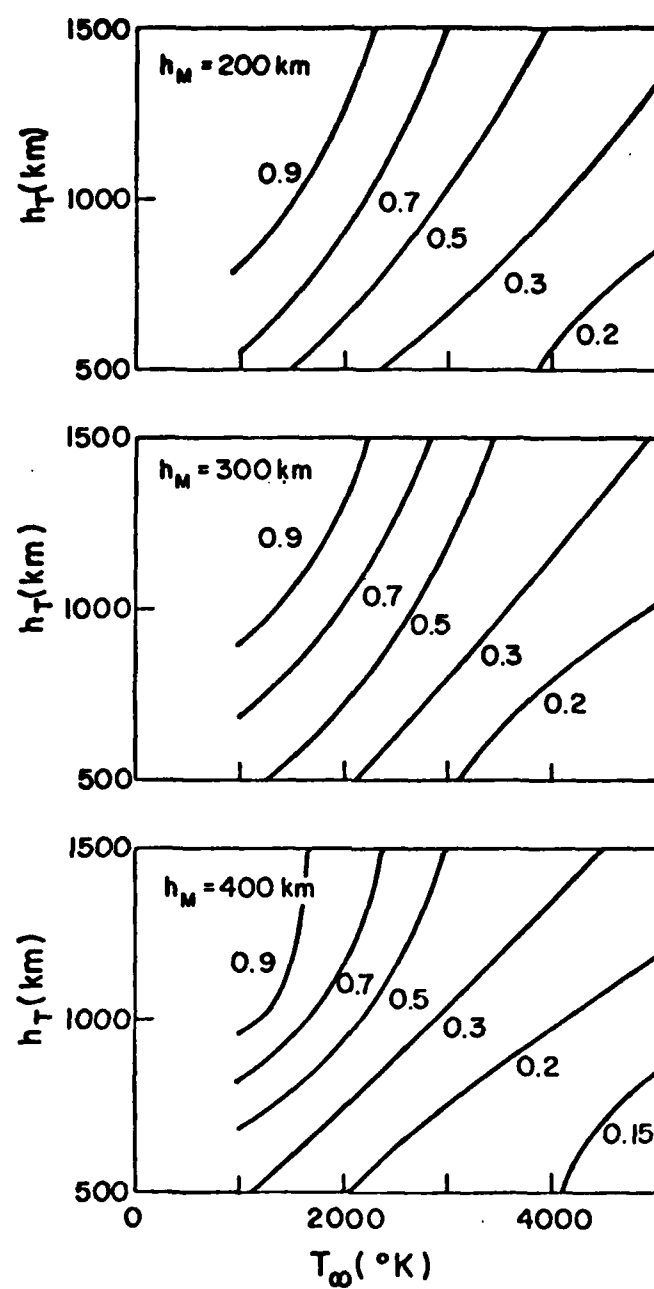


Figure 4. Contours of constant  $I_F/I_T$  values for all parameter values used in the simulation.

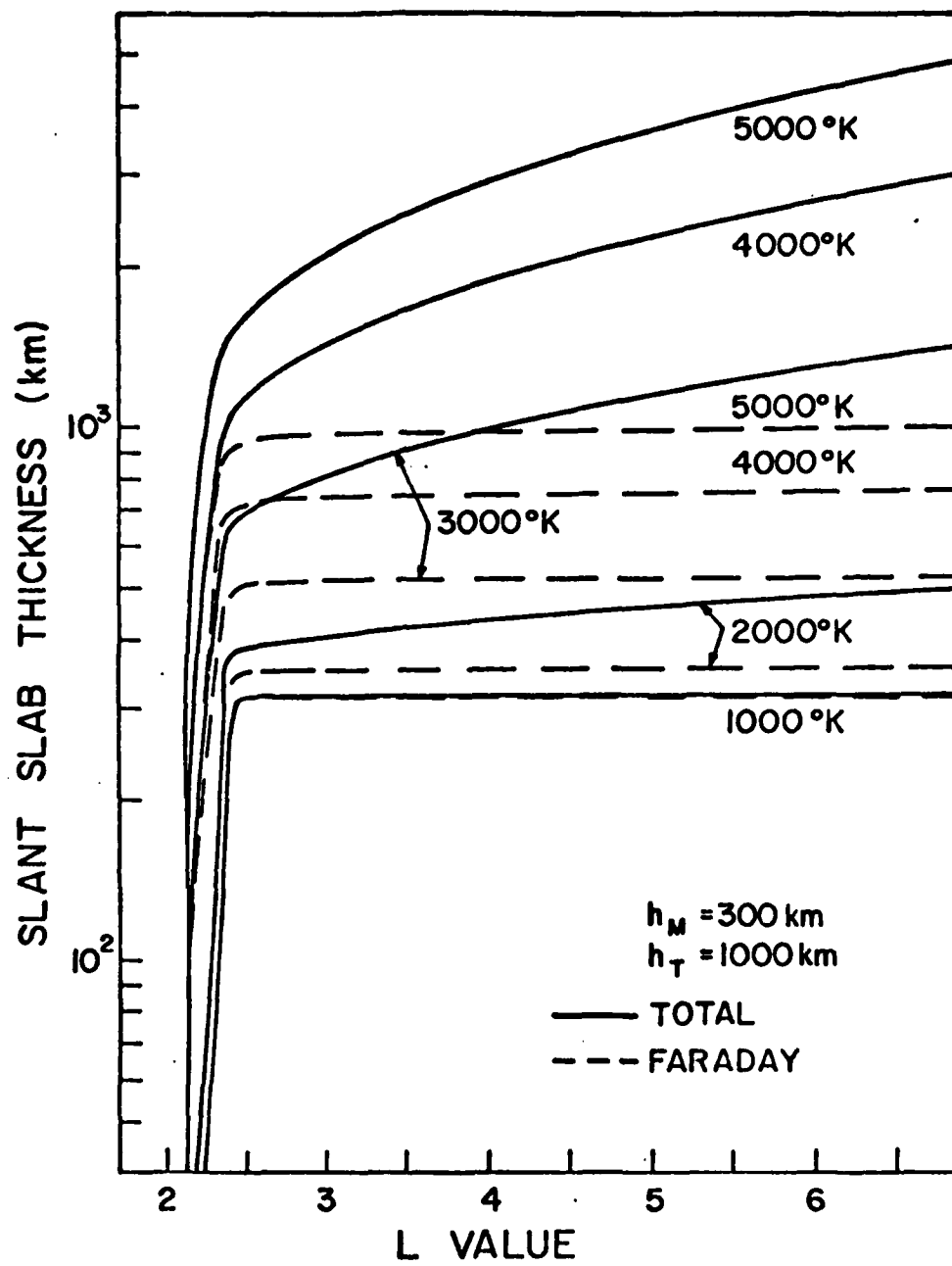


Figure 5. Faraday and total slant slab thickness for different positions of the plasmapause.  
(L-value)

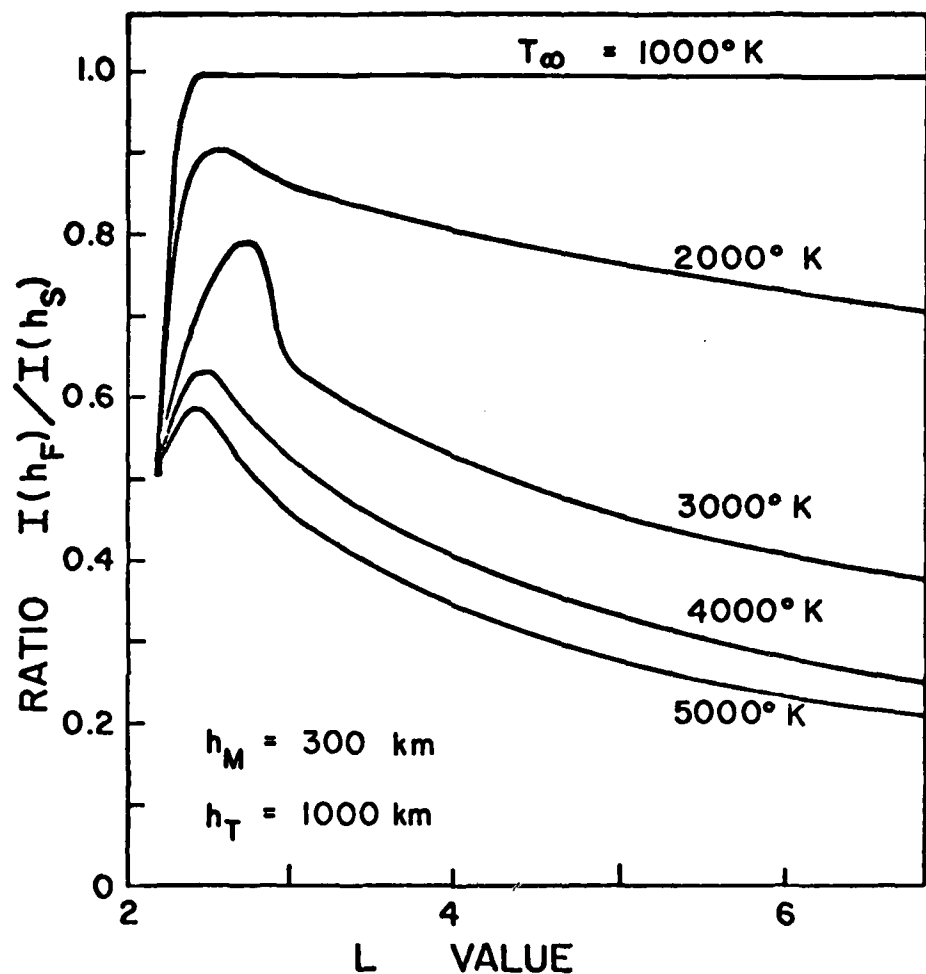


Figure 6. Behavior of the ratio  $I_F/I_T$  for different positions of the plasmapause. (L-value)

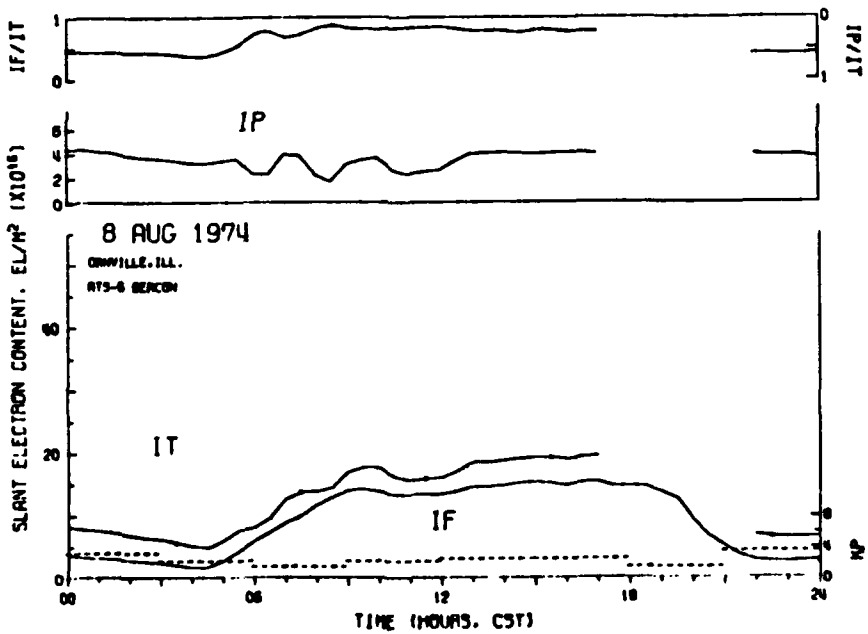
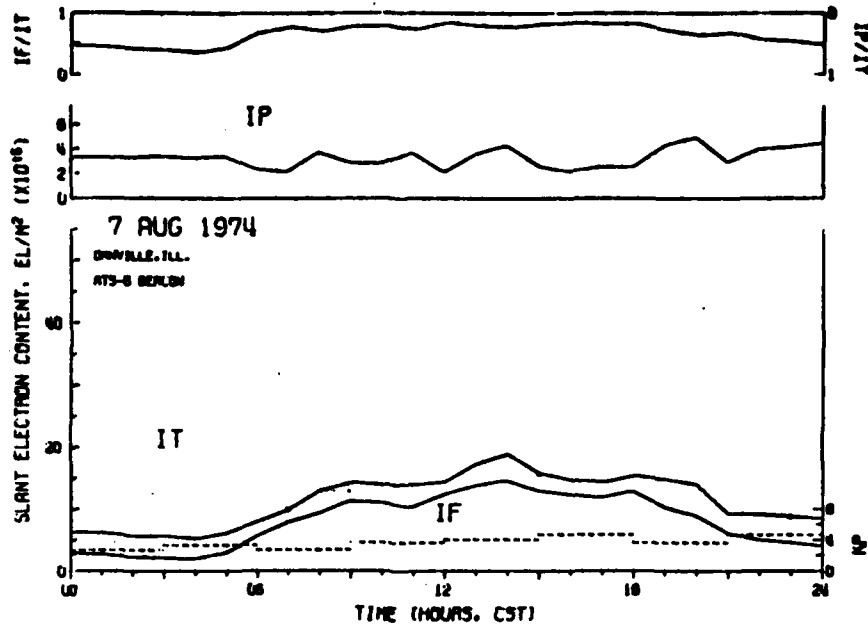
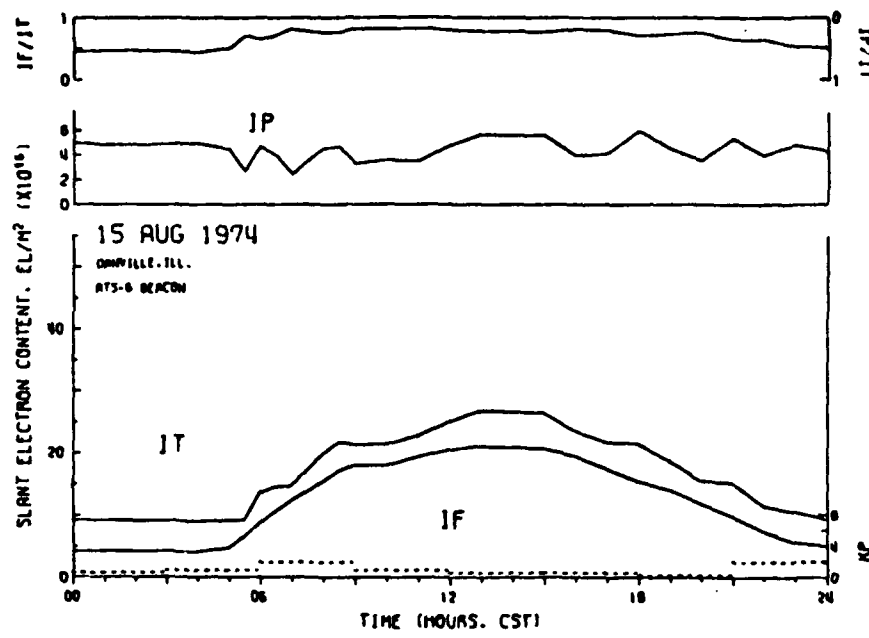


Figure 7. Faraday, Total and Plasmaspheric Contents for 7 and 8 August 1974.



**Figure 8.** Faraday, Total and Plasmaspheric Contents for 15 August 1974.

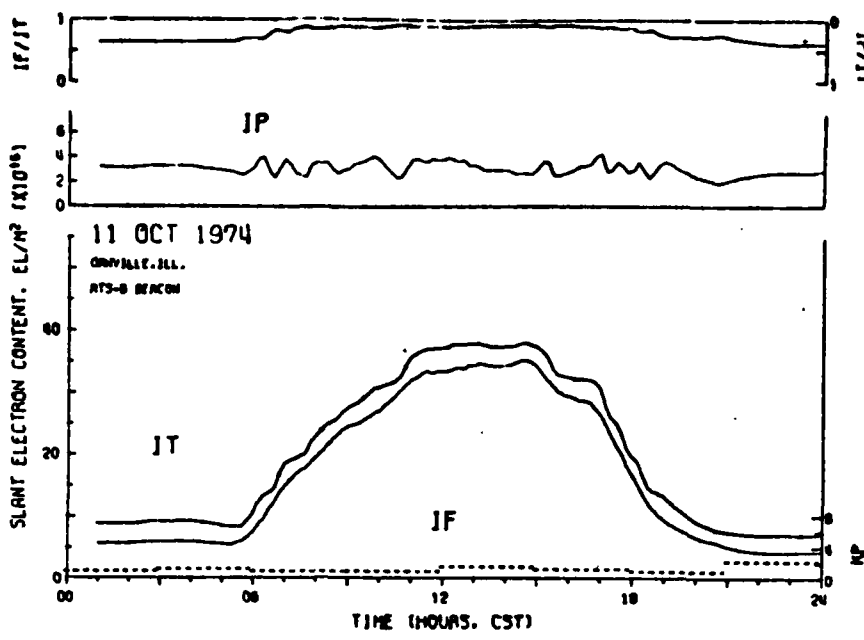


Figure 9. Faraday, Total and Plasmaspheric Contents for 11 October 1974.

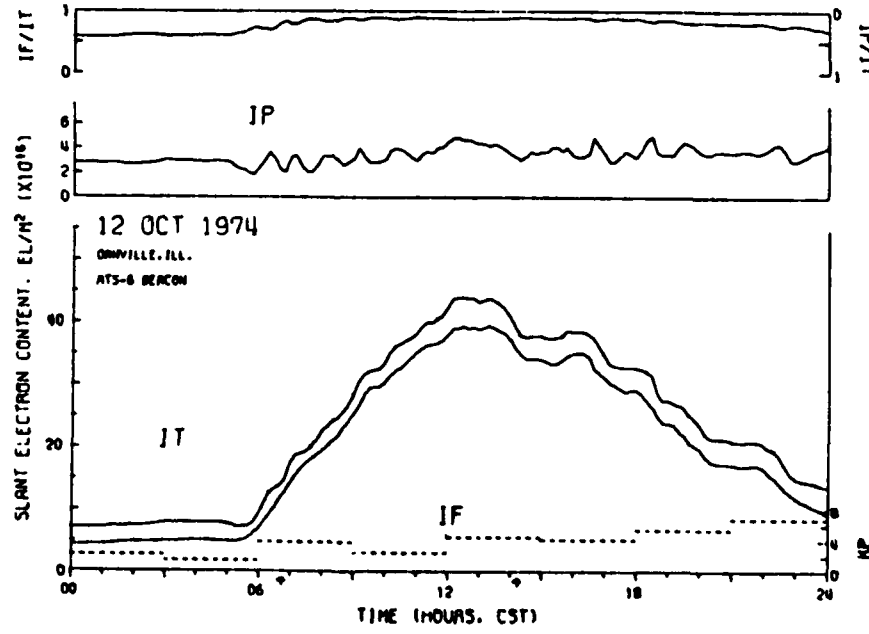


Figure 10. Faraday, Total and Plasmaspheric Contents for 12 October 1974.

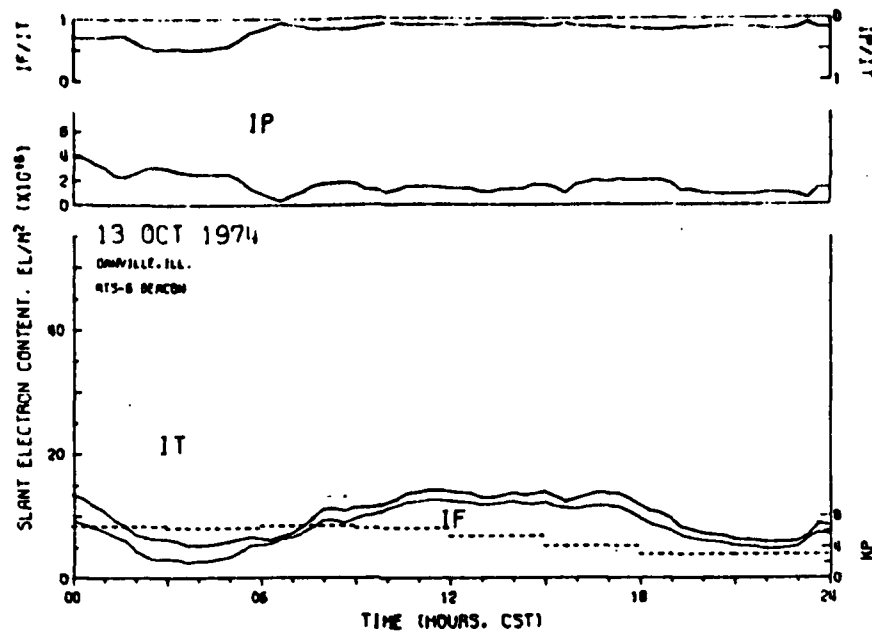


Figure 11. Faraday, Total and Plasmaspheric Contents for 13 October 1974.

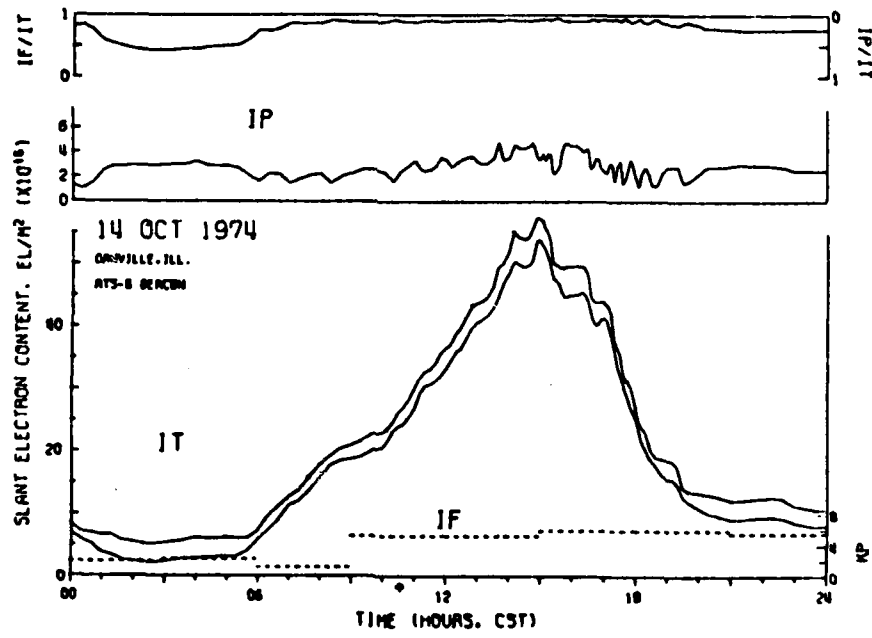


Figure 12. Faraday, Total and Plasmaspheric Contents for 14 October 1974.

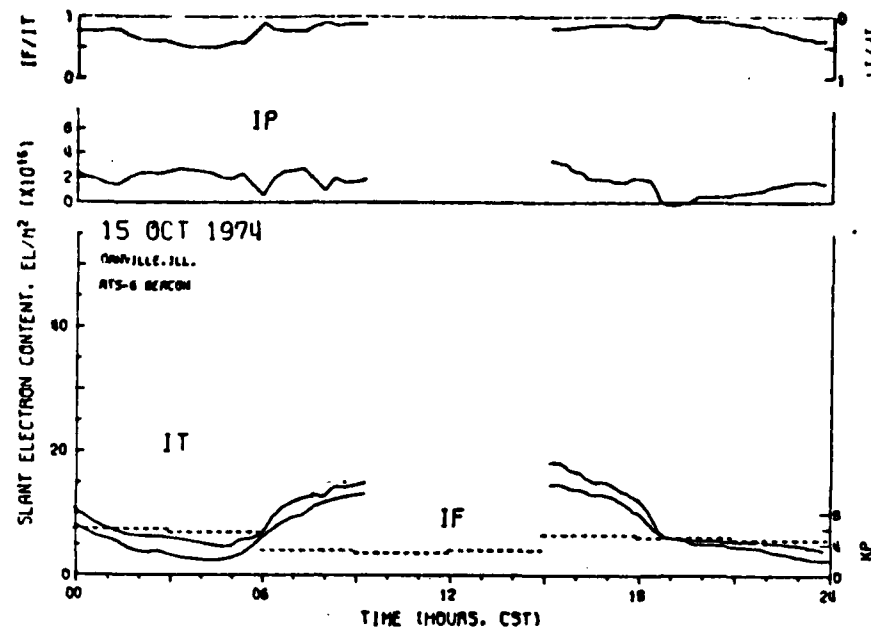


Figure 13. Faraday, Total and Plasmaspheric Contents for 15 October 1974.

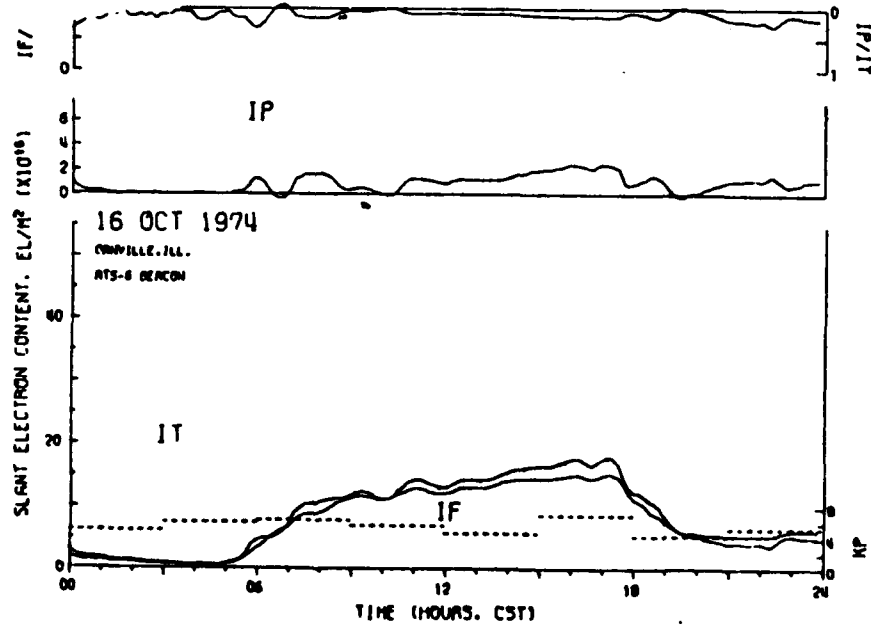


Figure 14. Faraday, Total and Plasmaspheric Contents for 16 October 1974.

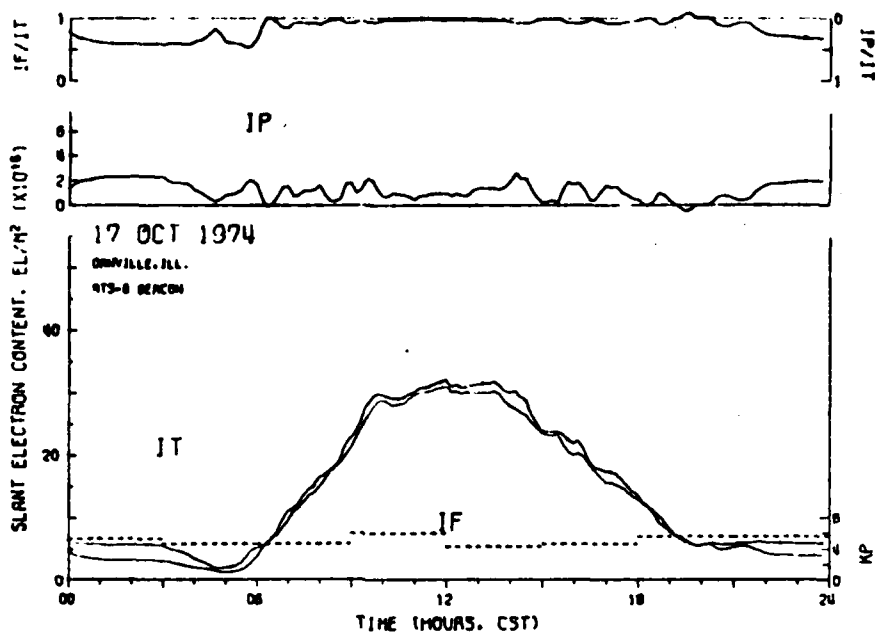


Figure 15. Faraday, Total and Plasmaspheric Contents for 17 October, 1974.

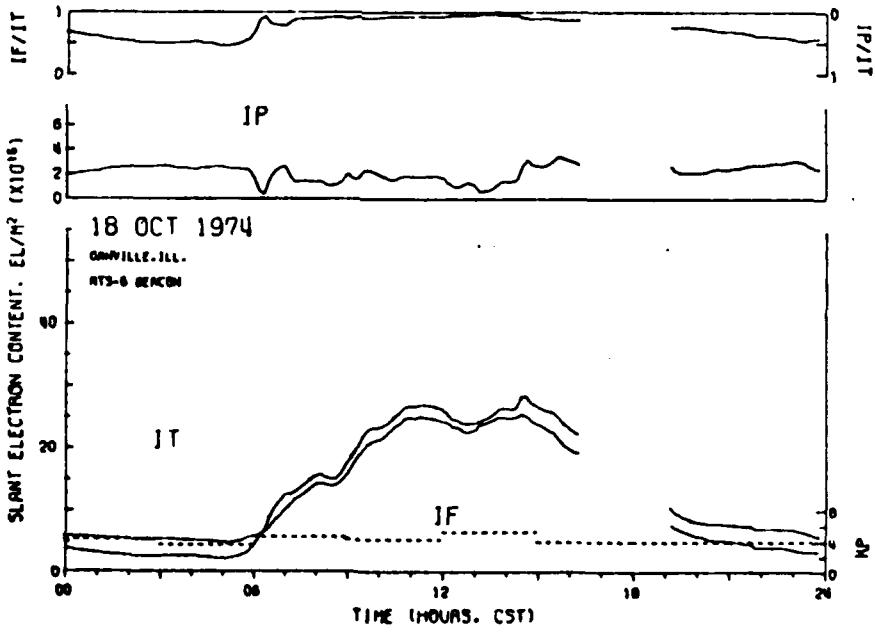


Figure 16. Faraday, Total and Plasmaspheric Contents for 18 October 1974.

COMPARATIVE STUDY OF ATS-6 DATA FROM LINDAU/HARZ  
AND FROM GRAZ/AUSTRIA

G.K. Hartmann and W. Degenhardt, Max-Planck-  
Institut für Aeronomie, Lindau/Harz, FRG,  
R. Leitinger, University of Graz, Austria

1. Introduction.

Fig. 1 shows a map with the stations Lindau/Harz (FRG) and Graz (Austria) and the projections of the rays from the stations to ATS-6. One can see that the rays are very close which means that the signals from ATS-6 propagate to the stations essentially through the same longitude region.

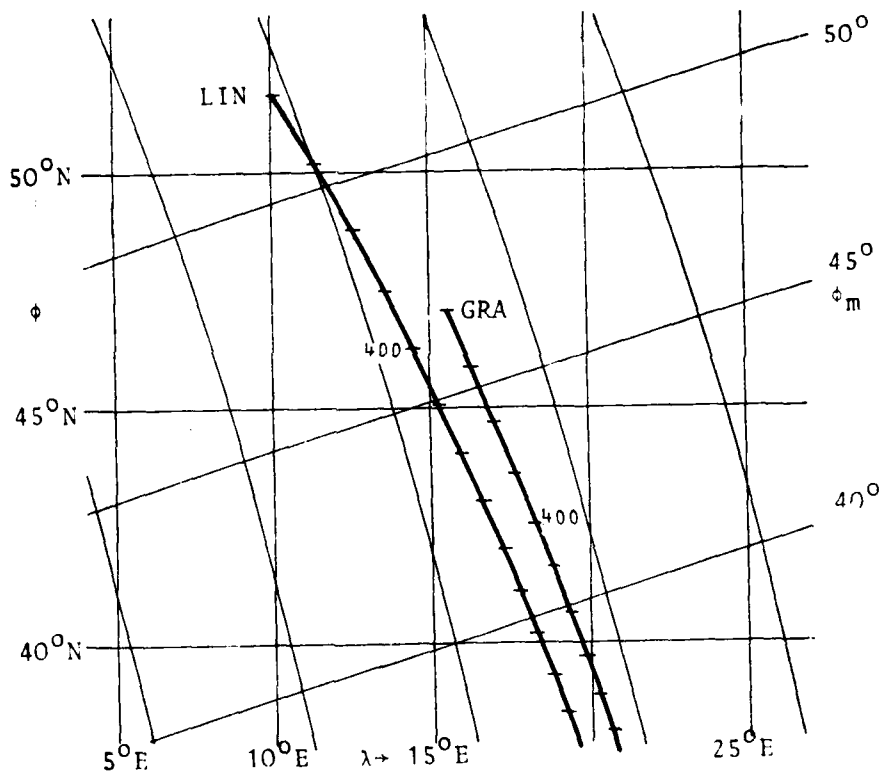


Fig. 1: Map with ray projections for ATS-6 observations from the stations Lindau and Graz. Geographic and geomagnetic coordinates. The rays are marked to indicate height (every 100 km).

h	$\phi$	x	B	L	I	$\phi_m$	$ \vec{a} $
			$\lambda$	sec x	$B_L$	D	Az( $\vec{a}$ )
0	51.6	63.2	0.480	2.66	67.5	52.2	0.675
	10.1	2.214	0.346		- 2.2		-36.24
300	47.5	58.4	0.413	2.30	63.6	47.6	0.562
	13.5	1.910	0.335		- 1.3		-37.20
400	46.3	57.1	0.392	2.22	62.3	46.2	0.525
	14.4	1.840	0.327		- 1.2		-37.96
500	45.1	55.8	0.373	2.16	61.1	45.0	0.490
	15.2	1.780	0.319		- 1.2		-38.96
2000	33.1	42.8	0.181	1.83	46.3	32.1	0.165
	21.9	1.362	0.177		- 2.4		72.66
35869	0.0	7.7	0.001	6.65	- 7.2	- 2.7	
	34.0	1.009	0.000		-10.4		
0	47.1	57.1	0.473	2.14	63.9	46.8	0.545
	15.5	1.838	0.390		0.1		-35.13
300	43.6	53.3	0.405	1.96	60.0	43.0	0.434
	17.7	1.672	0.353		- 0.0		-38.62
400	42.6	52.1	0.384	1.92	58.8	41.9	0.400
	18.3	1.629	0.347		- 0.1		-40.34
500	41.6	51.1	0.365	1.89	57.6	40.9	0.367
	18.8	1.592	0.335		- 0.2		-42.39
2000	30.9	39.7	0.177	1.74	43.3	29.5	0.192
	23.8	1.299	0.172		- 2.2		40.08
35869	0.0	7.3	0.001	6.65	- 7.2	- 2.7	
	34.0	1.008	0.000		-10.4		

Table 1: Geographic and geomagnetic constants for ATS-6 observations from Lindau and Graz. Points in the rays from the stations to ATS-6. h: altitude (km);  $\phi$ : geogr. latitude ( $^{\circ}$ N);  $\lambda$ : geogr. longitude ( $^{\circ}$ E); x: zenith angle ( $^{\circ}$ ); B: geomagnetic induction ( $\Gamma$ );  $B_L$ : component of B in the direction of the ray ( $\Gamma$ ); L: L-value; I: geomagn. inclination ( $^{\circ}$ ); D: geomagn. declination ( $^{\circ}$ );  $\phi_m$ : geomagn. dipole-latitude ( $^{\circ}$ );  $\vec{a}$ : vector to calculate the aspect sensibility of slant electron content for waves in the neutral gas (after Georges and Hooke, 1970).  $\vec{a} = (\vec{r} \times \vec{b}) \times \vec{z}$  ( $\vec{r}, \vec{b}, \vec{z}$ : unit vectors in the directions of the ray, of the geomagn. induction, of the vertical, resp.).  $\vec{a}$  is a horizontal vector,  $Az(\vec{a})$  gives the azimuth of its direction (N over E to S). The aspect sensitivity is given by  $\vec{a} \cdot \vec{k}$  ( $\vec{k}$ : unit vector in the direction of the wave vector). Geomagnetic data B,  $B_L$ , I, D,  $\vec{a}$  calculated from IGRF 1965, updated to 1974,0 (IAGA 1969), L,  $\phi_m$  from geoc. dipole (pole:  $78.51^{\circ}$ N,  $290.32^{\circ}$ E).

Identical receiving equipment is operating at the two stations. In this study data from two channels have been used: a) Group delay (modulation phase) data using the 1 MHz modulation on the ATS-6 carriers 140 MHz and 360 MHz (carriers and upper sidebands, channel symbol: GD 141); b) Faraday rotation data for the 140 MHz carrier (derived from the phase difference of circular components, channel symbol: F 140).

Data reduction has been done with the following formulae:

$$N_T = \int_0^{ATS} N ds = C_{GD} \Phi_{GD}; \quad N_F = \int_0^{2000} N ds = C_F \Omega / \bar{B}_L.$$

$N$ : electron density ( $m^{-2}$ );  $N$  with subscript: electron content (subscript T for slant content from ground to ATS-6, F for slant content from ground to appr. 2000 km);  $ds$ : ray path element ( $m$ );  $C_{GD}$  and  $C_F$ : constants;  $\Phi_{GD}$  measured modulation phase (radian);

$\Omega$ : Faraday rotation angle (radian);  $\bar{B}_L$ : longitudinal component of geomagnetic induction ( $r$ ) in a suitable mean field height.

A fieldheight of 400 km has been used in this study which is close enough to the value recommended by Titheridge (1972).

The following values have been used for the constants:

$C_{GD} = 27.99 \times 10^{15} m^-$ ,  $C_F = 8.295 \times 10^{15} m^{-2} r$ ,  $\bar{B}_L = 0.3274 r$  (Lindau),  $\bar{B}_L = 0.3471 r$  (Graz). Some additional geometrical and geomagnetic data for the rays from the stations to ATS-6 are given in Table 1.

It is the purpose of this study to show in which way the results of ATS-F observations from the stations Lindau and Graz differ and which quantities are essentially identical. This is done by means of a detailed comparison for four selected days, by comparing diurnal curves for a period of 14 days and by studying mean values over a longer period of time.

## 2. Comparison of daytime structure of electron content.

The diurnal curves of four days are studied in detail. The choice of these days has been made with the purpose to show one particularly interesting case and three typical examples. For the latter we could have found many other equally suitable days in the period for which we have had fully reduced data (November 15, 1975 to February 10, 1976).

For the detailed comparison of those four days we have taken total electron content from group delay measurements. The comparison would have been possible with essentially the same results using Faraday observations.

From the original diurnal curves in Fig. 2 it can be seen that there is some similarity in the behaviour of electron content for Lindau (field station Gillersheim) and for Graz but one can easily distinguish large differences during daytime when one compares values for a given time (e.g. around 9:20 UT on day 14, or around 12:40 UT on day 5, 1976). A more detailed inspection shows that peaks and other prominent features can be identified in the diurnal

curves for both stations but that there is a time delay and a change in amplitude and a change in shape. Examples for day 9: the peaks at 10:02, 11:36, 12:35, 13:32 (UT) in the curve for Lindau can be identified in the curve for Graz and are found at the times 10:59, 12:17, 13:19, 14:26 (UT), resp. If these peaks are taken to be the signature of Travelling Ionospheric Disturbances (TID's) one can interpret the time delay as the travel time from Lindau to Graz. With the distance of the ionospheric points (542 km for a mean ionospheric height of 400 km) one can calculate travel velocities. For the four peaks of day 9 the results are 158, 220, 205, 167 m sec<sup>-1</sup>, resp. (mean: 188 m sec<sup>-1</sup>). A shift in the height of ionospheric points of +100 km / -100 km changes the distance to 525 km / 561 km and would change the velocities by -3.1 % / +3.5 % (the mean ionospheric height is not a critical parameter in the calculation of travel velocities). The results agree with the general ideas on TID's or on the ionospheric signature of gravity waves but it is our feeling that no far reaching conclusions should be drawn: Apart from a strong hint that the features identified in the two diurnal curves are "travelling" we have no chance to derive parameters which would allow to test theories. In the case that the gravity wave concept is adopted the travel velocity of above could be used for an approximate value of the meridional component of the horizontal group velocity but this would be the only parameter to be derived from our comparison.

Not all identifiable features are travelling: The long period structure immediately after the morning rise on days 5 and 9 (but not on day 14!) is stationary: it appears synchronously in the diurnal curves. Such a morning structure can be identified on many days during December, 1975 and January, 1976. The duration of this structure is about equal for the two stations, the amplitudes differ.

A more detailed analysis for the days 5, 9, 11 and 14 (1976) has been done by means of digital filtering. We have applied bandpass filters which have no phaseshift. The results of the filtering process are shown above the diurnal curves in Fig. 2: a short-period and a long-period component have been separated. The residual electron content (diurnal curve minus short-period component and diurnal curve minus both components) is shown in Fig. 2 in the system of the diurnal curves.

It is easily seen from Fig. 2 that the short-period components do not correlate. (This is in agreement with the general view that the correlation length for such fluctuations is quite short, c. Davis and da Rosa, 1969). In the short-period component for Lindau (but not for Graz) one can distinguish longer "wave trains" with periods around 30 min. (morning of day 9) and 20 min. (afternoon of day 14).

In the long-period range one has very good correlation of the two stations if one looks at "stationary" and "travelling" components separately. A comparison shows that it is better to discuss the travelling component in terms of characteristic features in the original diurnal curves rather than in terms of the filtered components: the wavelike structure is not sinusoidal but shows sharp peaks and shallow troughs.

Day 11 is a special case: it has the weakest structure of all days in December, 1975 and January, 1976 (c. Fig. 3 and 4). It is very interesting to find such a smooth diurnal curve in the middle of a magnetic storm! <sup>1</sup> The aspect sensibility for Graz and for Lindau is such that gravity waves with meridional components should have signatures in the electron content observed at the two stations (Table 1). The phase cancellation effect (Georges and Hooke, 1970) could obliterate a short period component, but components with longer periods ( $T > 1$  hour) would probably have signatures in the electron content for Graz and Lindau. Therefore one can conclude that probably no gravity waves (or large scale TID's) with periods longer than one hour have propagated southwards from the auroral regions to Central Europe. The weak long period structure of day 11 is in marked contrast to the behaviour of the day before the onset of the storm (day 9, s. Fig. 2) and of the days after the storm (e.g. day 14, s. Fig. 2). The days 10, 12, 13 show structures which are a bit weaker than the structures seen on days 9 and 14 (c. Fig. 3). No features can be seen which would allow to distinguish the days 10, 12, 13 from magnetically quiet days in January, 1976.

One important conclusion should be drawn from the comparison of diurnal curves for Lindau and Graz: One should be very careful with selected daytime values from one station. The use of selected noon values, of daytime maxima, of the times when the maximum occurred etc. could be misleading because long period structures of considerable amplitude could be present (highest relative amplitude of the structure superimposed on the filtered diurnal curves of the sample days 5, 9, 14: 30%). One should be very careful to separate the smoothed diurnal curve and the superimposed structure (e.g. for the calculation of integrated production or loss rates).

It can be seen from Fig. 2 (day 14) that even the filtered diurnal curves could show a quite different behaviour for the two stations. This is probably a filter effect: the large peak in the morning leaves a residual in the smoothed curve. This peak could lead to the conclusion that the electron content had reached a maximum in the morning at Graz (around 9:01 UT or 10:14 LT of ionospheric point) and a secondary maximum in the afternoon (around 12:00 UT or 13:13 LT). For Lindau one could claim an absolute maximum in the early afternoon and a secondary maximum in the morning ...

A look at the means for the whole day (means of 720 values read every second minute from 00:01 UT to 23:59 UT) shows no peculiar situation for day 14: the mean slant electron content for Lindau is  $95.7 \times 10^{15}$ , the corresponding value for Graz is  $86.7 \times 10^{15}$  ( $m^{-2}$ ). Using a ionospheric height of 400 km one would get for the mean vertical content  $52.0 \times 10^{15} m^{-2}$  (Lindau) and  $53.2 \times 10^{15} m^{-2}$  (Graz).

In this respect day 14 is no exception at all: we have found that the means for the whole day in vertical electron content agree very well for the two stations, the values for Graz being slightly higher in the average than the values for Lindau.

---

<sup>1</sup> SSC on day 10, 6:24 UT, end day 13, 10 UT (Irkutsk). Ap = 47 on day 10, Ap = 40 on day 11, Ap = 13 on day 12.

3. Parameters for which the two stations show similar behaviour.

a) Mean over a whole day.

The mean of electron content over a hole day is one parameter which behaves in a similar way for Lindau and Graz. Geomagnetic disturbances show in this parameter quite well: among others a depression can be observed during the magnetic storm of January 10, 1976. This is summarized in Table 2.

day (1976)	$N_T$		$N_T \cos x$		$\times 10^{-15}$ (station)
	LIN	GRA	LIN	GRA	
08	121.4	105.7	66.0	64.9	
09	116.2	100.8	63.2	61.9	
10	116.2	104.8	63.2	64.3	
11	95.4	89.9	51.8	55.2	
12	80.5	75.5	43.7	46.3	
13	78.2	71.6	42.5	43.9	
14	95.7	86.7	52.0	53.2	
15	106.9	96.2	58.1	59.0	
16	110.3	98.3	59.9	60.3	
17	111.0	101.3	60.3	62.2	

Table 2: Mean of electron content over a hole day, slant ( $N_T$ ) and projected on the vertical ( $N_T \cos x$ ) for Lindau and Graz.

b) Plasmaspheric content.

Plasmaspheric electron content is defined as the difference  $N_p = N_T - N_F$  (Davies et al. 1975). From the vicinity of the rays to ATS-6 it follows that plasmaspheric content should behave similarly at the two stations. This is the case as can be seen from Fig. 3.  $N_p$  is strongly depressed during the magnetic storm. The depression begins at both stations suddenly a few hours after Sudden Storm Commencement (which occurred at 6:24 UT on day 10 at the observatory Irkutsk). The recovery phase is quite long, it can be considered to end on day 16 (c. Fig. 3).

c) Nighttime values of electron content.

During nighttime the electron content behaves in a very similar way at Lindau and at Graz. This can be seen from Fig. 3 and from Fig. 4. When small scale fluctuations are smoothed by averaging over a period of half an hour (over 15 values read every second minute) the nighttime values show nearly perfect correlation (Fig. 4, values centered at 21:15 and at 03:15 UT). In the period covered by this study the correlation is very good from about 17:00 UT until shortly after sunrise. As can be seen from Fig. 4 some similarities in the behaviour of  $N_T$  exist during daytime as well but the correlation is much better during the night. (As has to be expected for the wavelike structures which are responsible for the daytime differences the correlation is improved when some smoothing is applied which removes the day to day scatter.)

The nighttime values show a distinct depression during the storm of January 10. The depression is comparable with the depression seen in the mean over a whole day (case a). A preliminary evaluation revealed that increases in Ap which surpass a lower limit ( $Ap \approx 25$ ) are followed by a depression in nighttime  $N_T$  with a timelag of 1 to 3 days. The depth of the depression seems to be correlated with the magnitude of the increase of Ap. In Fig. 4 such depressions are centered on the days December 1 and 28 and January 13. Probably depressions occurred on November 24 and on February 2, too (no proof: lack of data).

#### 4. Concluding remarks.

From our study it can be concluded that daytime electron content derived from observations of geostationary satellites may differ considerably from one station to another, even when longitudinal effects are excluded and when the distance of the stations is only a few hundred kilometers.

One reason for the differences observed are long period TID's (or signatures of gravity waves) of sometimes considerable amplitude. An other reason is the "morning overshoot", a stationary feature, which could show large differences in amplitude for Graz and Lindau.

All daytime differences seem to be traces of dynamical processes: we have found that the mean values for a whole day are in excellent agreement for the two stations. This means probably that in the average daytime production and loss rates are nearly equal for the two stations.

Nighttime values (smoothed to remove noise and small period fluctuations) are nearly equal whereas the means over a whole day are slightly higher at Graz. This could be an image of the solar zenith angle dependence of electron production.

We have found that selected daytime values could have very large differences for the two stations (up to 50 % if one station happens to see a "trough" at the time the other station sees a "peak"). Therefore we feel that selected values are not a suitable indicator of solar activity or of geomagnetic influence, at least not for the European sector and for the period of time covered by our study. For studies of geomagnetic influence we would recommend the use of means over a whole day or of smoothed nighttime values.

Similar behaviour of electron content at two stations aligned as Lindau and Graz is to be expected during nighttime, for means taken over periods longer than 4 hours during daytime, for smoothed values of plasmaspheric content. Short period fluctuations do not correlate but rms values are nearly equal. When long period TID's (signatures of gravity waves) are present they are seen from both stations.

Acknowledgements.

The MPI research program was supported by Reserach Grant Di 32/33 from Deutsche Forschungsgemeinschaft. The research program in Graz was supported by the Fonds zur Förderung der wissenschaftlichen Forschung and by Österreichische Akademie der Wissenschaften. In Graz ATS-6 receiving equipment of MPI Lindau is used. For a part of the computations the facilities of the Rechenzentrum Graz have been used.

References.

- Davies, K. 1975 Determination of the total electron content of the ionosphere and the plasma-sphere, Proc. Symp. on the beacon satellite investigations of the ionosphere structure, II, IZMIRAN, Moscow, 146-158
- Fritz, R.B.  
Hartmann, G.K.  
Leitinger, R,  
Paul, A.K.  
Schmidt, G.
- Davis, M.J. 1969 Travelling ionospheric disturbances originating in the Auroral Oval during polar substorms, J. Geoph. Res. 74, 5721-5735
- da Rosa, A.V.
- Georges, T.M. 1970 Wave-induced fluctuations in ionospheric electron content: a model indicating some observational biases, J. Geoph. Res. 75, 6295-6308
- Hooke, W.H.
- IAGA, Comm. 2 1969 International Geomagnetic Reference Field 1965.0, J. Geoph. Res. 74, 4407-4408
- Titheridge, J.E. 1972 Determination of ionospheric electron content from the Faraday rotation of geo-stationary satellite signals, Planet. Space Sci. 20, 353-369

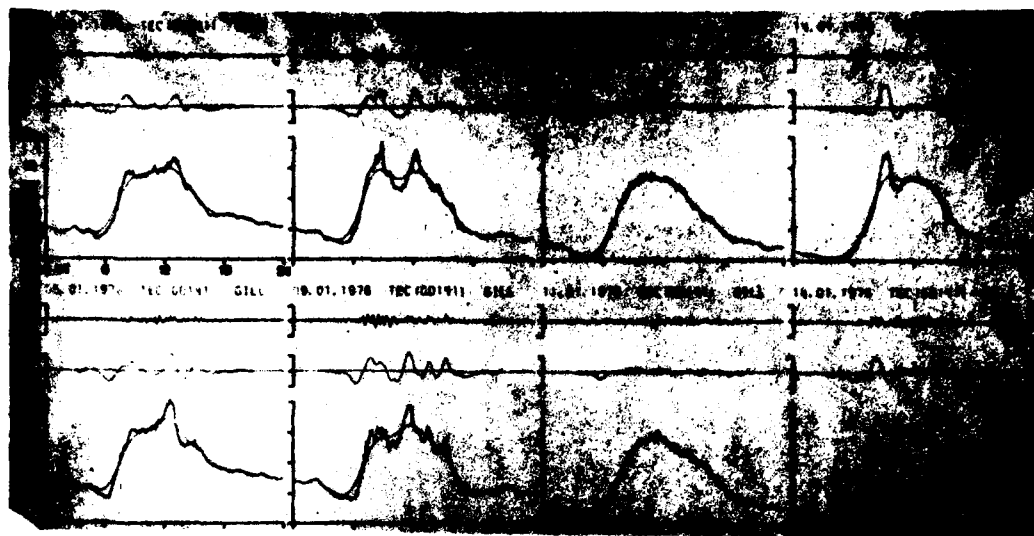


**Figure 2:** Diurnal curves of slant electron content  $N_T$  from group delay observations on signals of the ATS-6 Radio Beacon Experiment. Receiving stations Lindau (field station GILLERSHEIM) and GRAZ. Original diurnal curves and smoothed curves gained by digital filtering. Above the diurnal curves: filtered components (short period and long period). Electron content ( $m^{-2}$ ) vs. Universal Time (UT). Local time for Lindau (ionospheric point 400 km): UT+0.96 hours, local time for Graz (ionospheric point 400 km): UT+1.22 hours. Vertical scale:  $40 \times 10^{15}$  to  $200 \times 10^{15} m^{-2}$  (the origin is not zero!). Dates (January 1976): a) day 5; b) day 9; c) day 11; d) day 14.



Figure 3: Diurnal curves of slant electron content for a series of days in January 1976. Total electron content from group delay ( $N_T$ ), ionospheric electron content from Faraday effect ( $N_F$ ) and plasmaspheric electron content ( $N_p = N_T - N_F$ ). Note that  $N_p$  has a larger scale. Stations and data source as for Fig. 2.

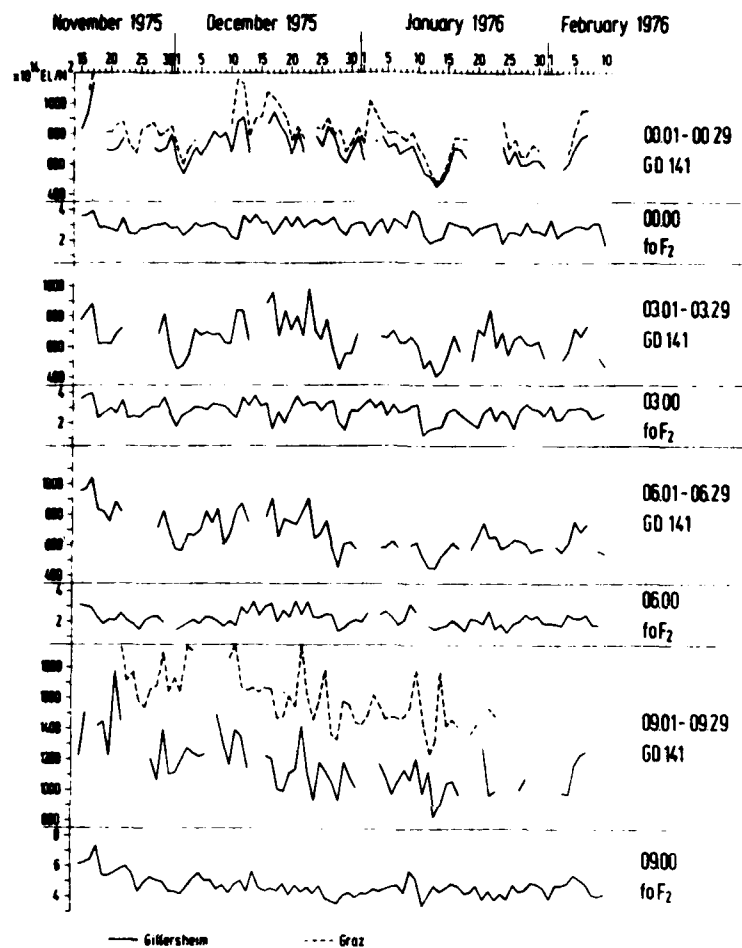


**Figure 4:** Comparison of half hour mean values of electron content  $N_T$ . The values used for the means have been read at every odd minute UT. The means have been gained by summing all available values within the time interval indicated and dividing by the number of the values (when no loss of data occurred: 15 values; e.g. readouts from 00:01 to 00:29; this interval is centered at 00:15). Stations and data source as for Fig. 2.  
 Values for Graz: dashed, values for Lindau (field stations Gillersheim): solid. foF<sub>2</sub> values from the ionosonde Lindau are shown in addition to  $N_T$ . Abscissa: days 1975/1976.

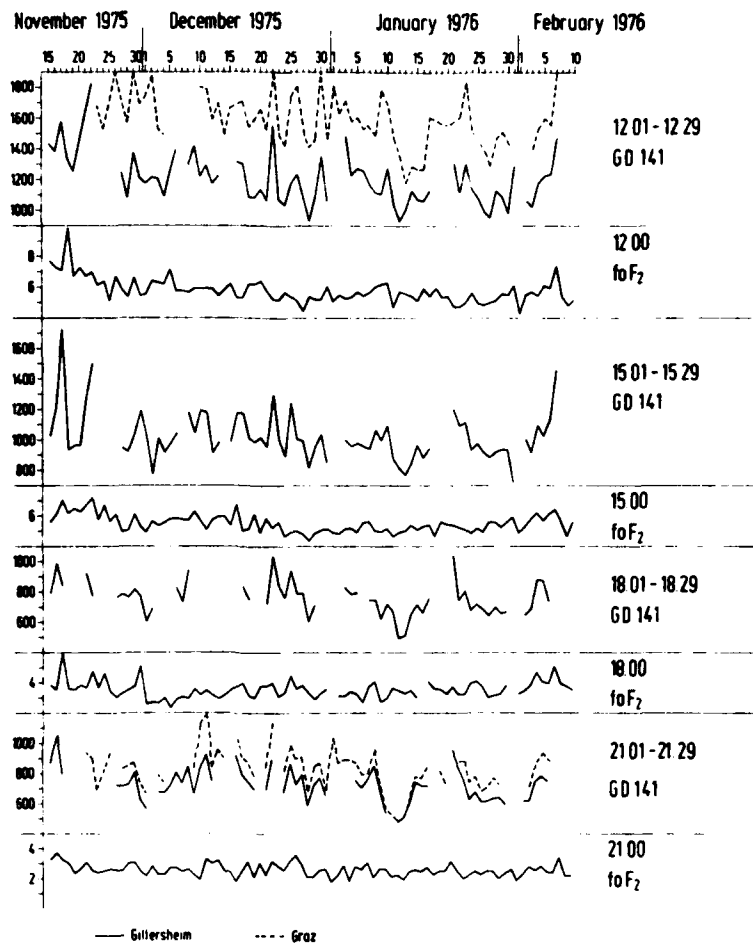


Figure 4b

DIURNAL, DAY-TO-DAY, AND SEASONAL VARIABILITY  
OF  $N_F$ ,  $N_T$ , AND  $N_p$  AT FORT MONMOUTH, NEW JERSEY

H. SOICHER

Communications/Automatic Data Processing Laboratory  
U. S. Army Electronics Command, Fort Monmouth, New Jersey 07703

INTRODUCTION

The ATS-6 Satellite was launched into a geostationary orbit at  $94^{\circ}$ W in late May 1974 and, according to plan, drifted eastward in June 1975. During this period, measurements of the total electron content (TEC) utilizing the Faraday polarization rotation technique and the dispersive-group-delay technique were conducted at Fort Monmouth, New Jersey ( $40.18^{\circ}$ N;  $74.06^{\circ}$ W)<sup>1,2,3</sup>. The total Faraday rotation from signal-source to observer is directly proportional to (TEC) and to the mean magnetic field component along the propagation path. Since the magnetic field decreases inversely with the cube of the geocentric distance and the electron density decreases exponentially with altitude above layer maximum, the rotation is heavily weighted near the earth, and hence is considered to provide TEC below ~1500 km ( $N_F$ ). The dispersive-group-delay technique, which involves comparison of the phase of the modulation envelope between the carrier and its sideband at two frequencies, is insensitive to the earth's magnetic field. For this reason it is considered to yield the total number of electrons along the path from signal-source to observer ( $N_T$ ). The difference between the two, i.e.,  $N_T - N_F$ , yields the plasmaspheric content,  $N_p$ , which is the total electron content above ~1500 km.

THE DATA

The daily variations in vertical TEC measured by the Faraday technique and by the dispersive-group-delay technique for January through April 1975 are shown in Figs. 1 through 8, respectively. Also indicated in these figures are the equivalent signal-delay-times normalized to a frequency of 1.6 GHz. The data gaps which appear in these figures were the result of beacon transmitter turnoff at the satellite. The normal diurnal variations in  $N_F$  and  $N_T$  are also depicted in the figures. The absolute value of  $N_F$  during these months varied from a predawn minimum of <1 TEC unit (1 TEC unit  $\equiv 10^{16}$  e/m<sup>2</sup>) to an afternoon maximum of ~22 TEC units. For the same times,  $N_T$  varied from ~2 TEC units to ~24.2 TEC units. The mean monthly averages of  $N_F$  varied from a predawn minimum of ~1.8 TEC units in April to an afternoon maximum of ~12 TEC units in February. The mean monthly averages of  $N_T$  varied from a predawn minimum of ~3.9 TEC units in February and March, to an afternoon maximum of ~13.5 TEC units in January.

The daily variations in the vertical plasmaspheric content,  $N_p$ , for January through April 1975 are shown in Figs. 9 through 12, respectively. During these months the absolute value of  $N_p$  varied from a minimum of ~0.1 TEC units to a maximum of ~4.4 TEC units. Monthly averages, throughout this period however, varied from ~1.3 TEC units and 2.6 TEC units. Diurnal changes, although noticeable, were relatively small in comparison to the diurnal changes in  $N_F$  and  $N_T$ . During February, when the diurnal variation of  $N_p$  was most pronounced, double maxima of  $N_p$  occurred during the pre-dawn period and during the decay phase of the ionospheric content variation; the double minima occurred during the period of maximum daytime ionospheric content and at the end of its decay phase at night. During April, the diurnal variation of  $N_p$  was also pronounced.  $N_p$  had reached a minimum during the build-up phase of the ionospheric content variation, and a maximum during the maximum phase of the ionospheric content variation. During January and March, there was very little variation in the diurnal trend of  $N_p$ . The day-to-day variations of  $N_p$  were quite pronounced, often exceeding the diurnal variation ranges. The day-to-day variation, as determined by the standard deviation about the mean, varied from ~0.35 TEC units to ~0.9 TEC units.

The daily variations in the plasmaspheric-to-ionospheric ratio ( $N_p/N_F$ ) for January through April 1975, are shown in Figs. 13 through 16, respectively. During this period, the ratio varied from a minimum of a few percent to a maximum of more than 200%. The mean monthly averages, however, generally varied between ~12% during the day, and ~130% prior to dawn. For all the months, the ratio minimum was reached during ionospheric maximum content. During January and February, the maximum ratio was attained shortly after midnight; it was maintained until sunrise, when it decreased rapidly. During March and April, the ratio gradually increased until sunrise, when it decreased rapidly.

The daily variations in the ratio of plasmaspheric-to-total contents,  $N_p/N_T$ , for January through April 1975 are shown in Figs. 17 through 20, respectively. The behavior of this ratio was similar to that of the plasmaspheric to ionospheric ratio. The mean monthly averages throughout this period generally varied between ~10% during the day and ~56% at nighttime.

#### DISCUSSION

The mean monthly values of  $N_F$  and  $N_T$  for the four months considered were roughly equal throughout the diurnal period. The only discernible differences were the gradual content increases which occurred during the eight-hour period centered at midnight from January through April. Content

maxima were also somewhat larger in January and February than in March and April. On the average,  $N_F$  and  $N_T$  varied diurnally by a factor of ~4. The day-to-day variations in  $N_F$  and  $N_T$  as determined by the standard deviations were comparable throughout the period, although the most pronounced deviations occurred prior to and after midnight in April. The standard deviation throughout the period varied from ~0.5 to ~3.2 TEC units.

The mean monthly values of  $N_p$  were comparable for January and April as well as for February and March, with the former pair being larger in absolute value than the latter pair, especially at night. The mean monthly values never varied diurnally by more than 1 TEC unit; they generally varied by much less. The day-to-day variations in  $N_p$  were comparable throughout the period.

The minimum ratios of  $N_p/N_F$  and  $N_p/N_T$  during daytime and nighttime occurred in February. The seasonal behavior of these ratios is exhibited in the trend of the nighttime ratio during January and February when compared to that for March and April. The nearly constant value of the nighttime ratio in January and February was replaced by a gradually increasing ratio in March and April. The maximum ratio usually attained just prior to sunrise, increased from February to March and again to April.

#### REFERENCES

<sup>1</sup>Soicher, H., *Nature*, vol. 253, Jan. 24, 1975, pp. 252-254.

<sup>2</sup>Soicher, H., *Nature*, vol. 259, Jan. 1 & 8, 1976, pp. 33-35.

<sup>3</sup>Soicher, H., AGARD Conference Proceeding No. 173 (AGARD-CP-173), *Radio Systems and the Ionosphere*, January 1976, pp. 6-1 to 6-11.

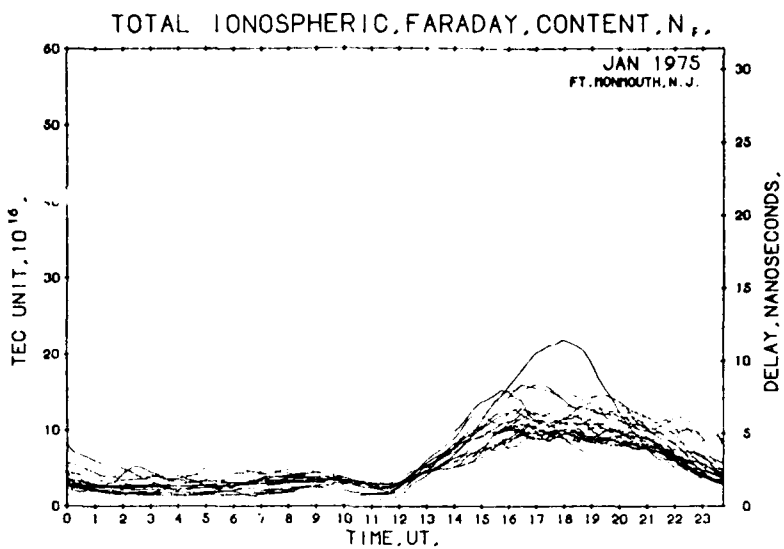


Fig. 1. Total ionospheric (Faraday) electron content ( $N_F$ ) at 15-minute intervals at Ft. Monmouth, NJ., during January 1975 (left ordinate: 1 TEC unit  $\equiv 10^{16} \text{ e/m}^2$ ; right ordinate: delay normalized to 1.6 GHz).

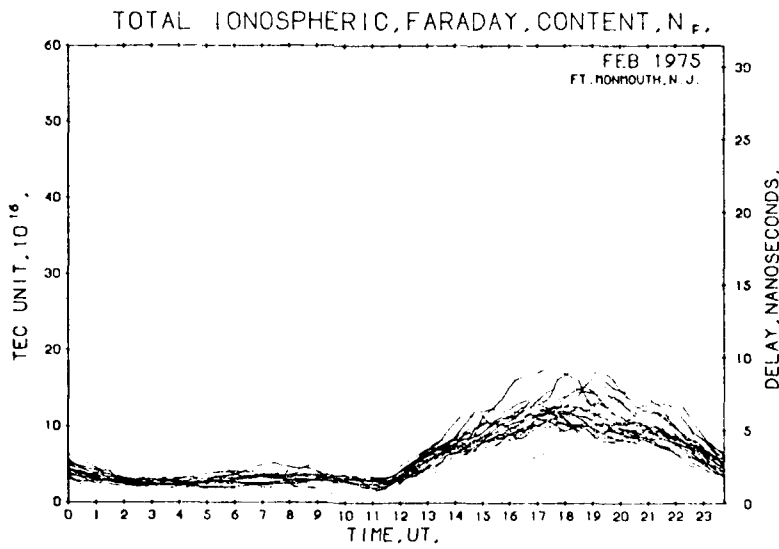


Fig. 2. Same as Fig. 1, but for February 1975.

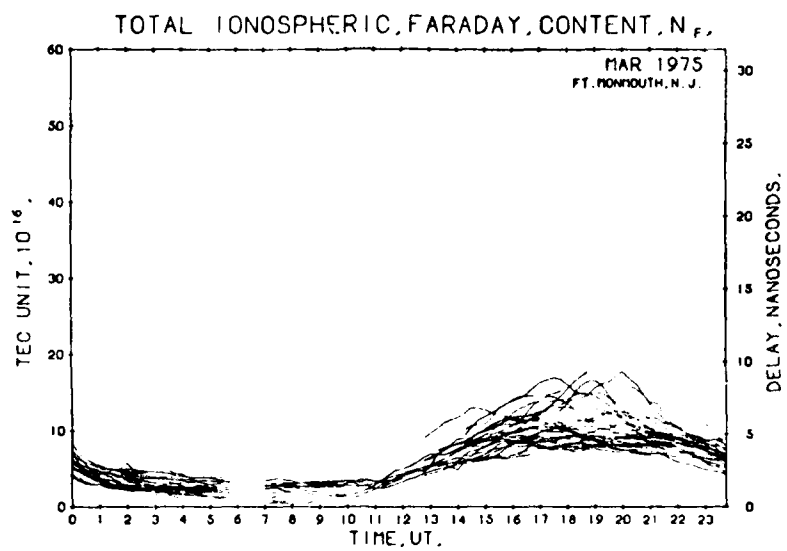


Fig. 3. Same as Fig. 1, but for March 1975.

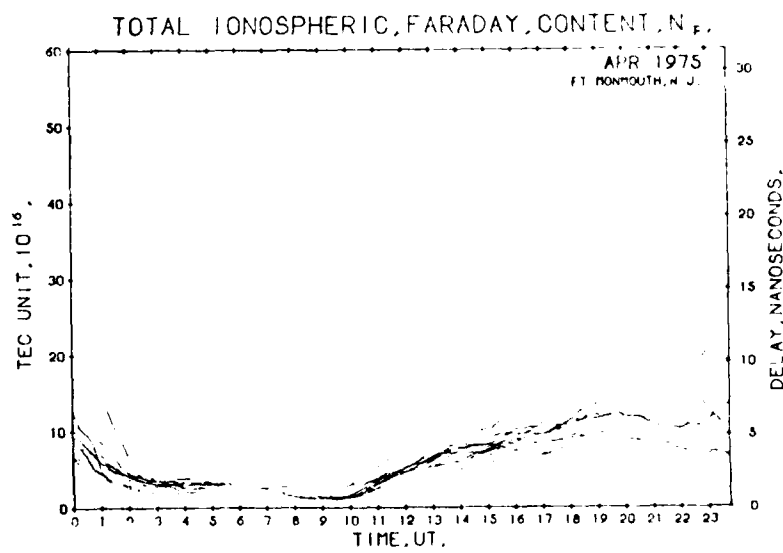


Fig. 4. Same as Fig. 1, but for April 1975.

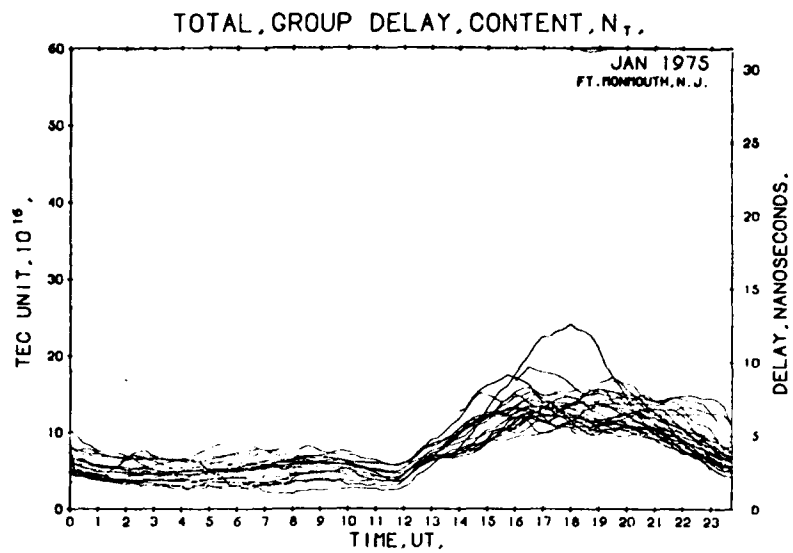


Fig. 5. Total (dispersive-group-delay) electron content ( $N_T$ ) at 15-minute intervals at Fort Monmouth, N.J., during Jan 1975.

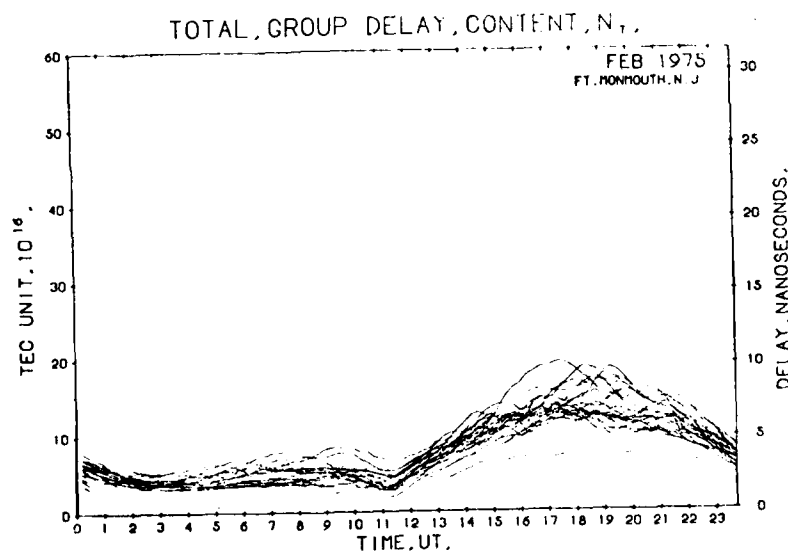


Fig. 6. Same as Fig. 5, but for February 1975.

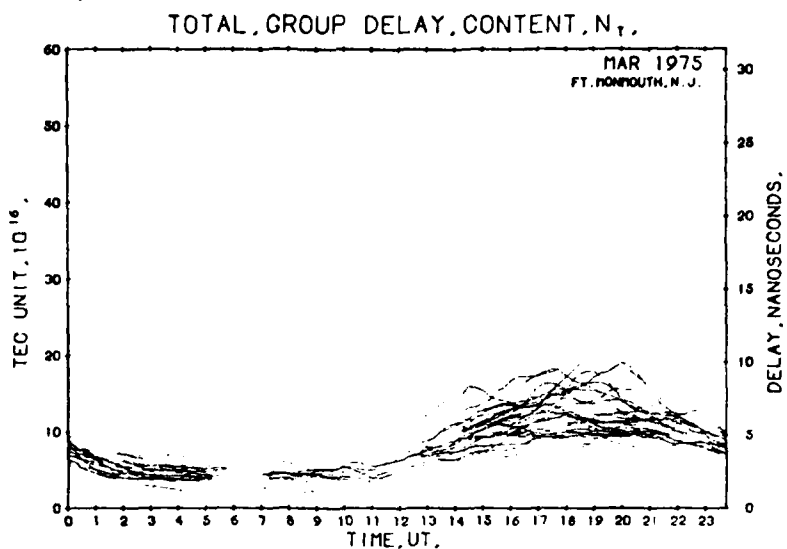


Fig. 7. Same as Fig. 5, but for March 1975.

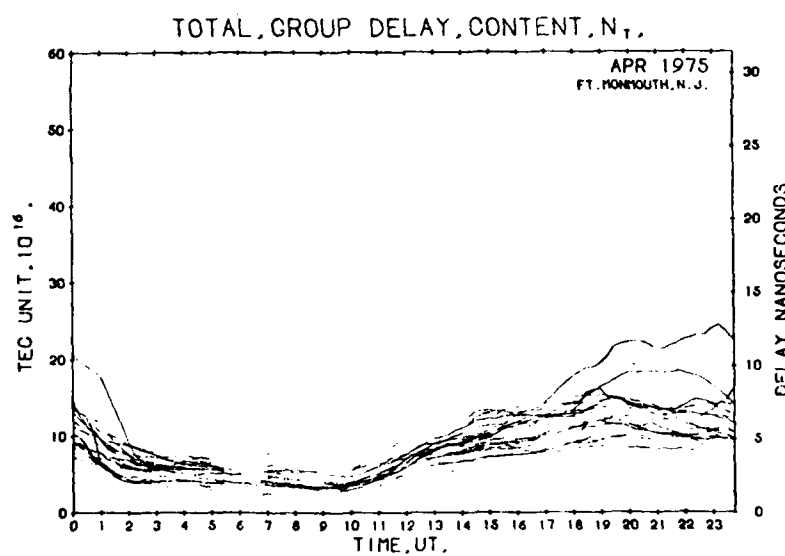


Fig. 8. Same as Fig. 5, but for April 1975.

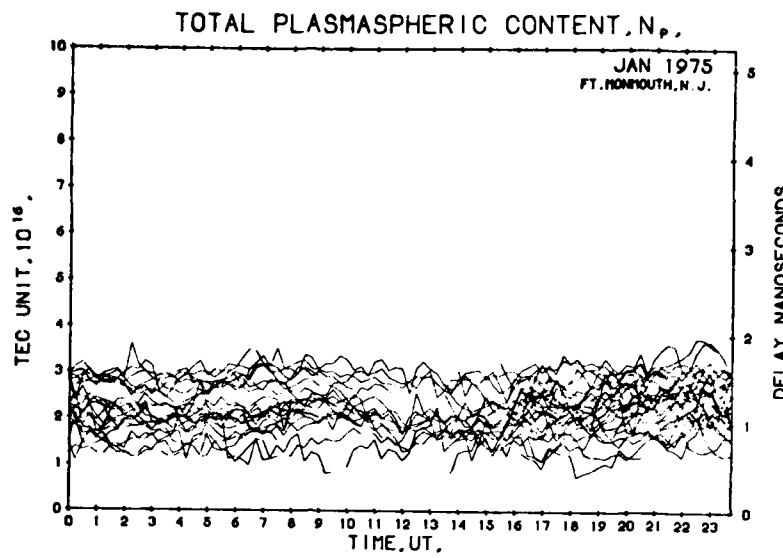


Fig. 9. Total plasmaspheric electron content ( $N_p$ ) at 15-minute intervals, Fort Monmouth, N.J., January 1975.

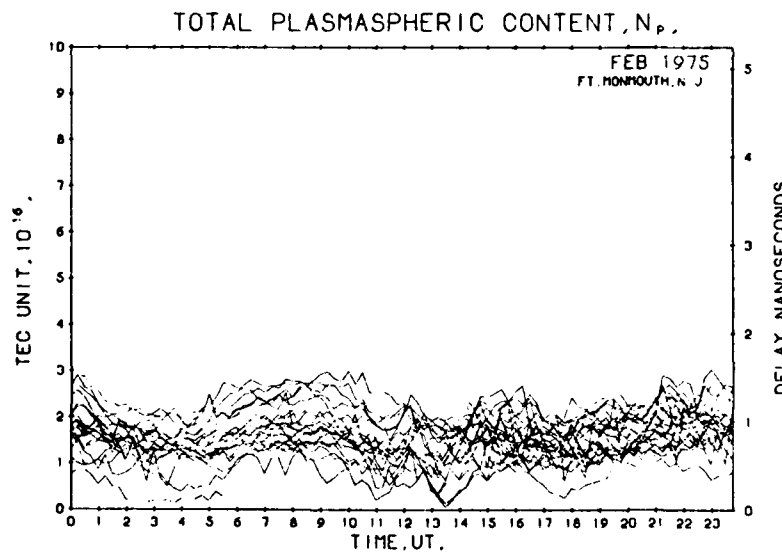


Fig. 10. Same as Fig. 9, but for February 1975.

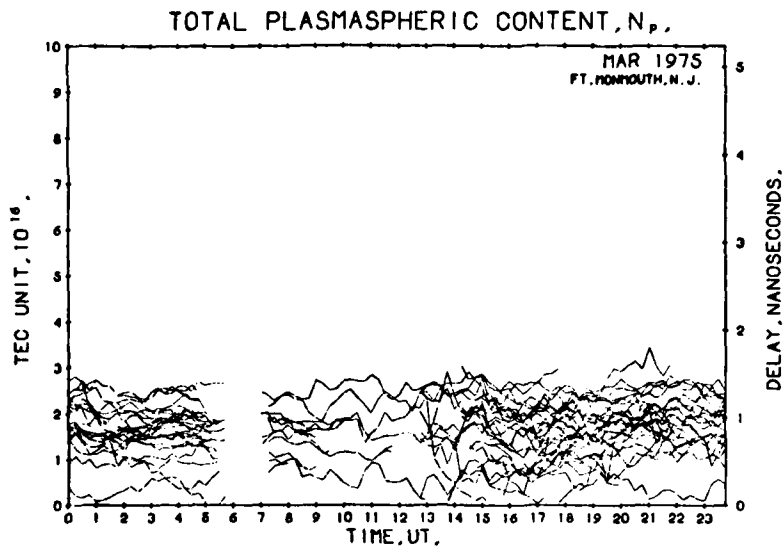


Fig. 11. Same as Fig. 9, but for March 1975.

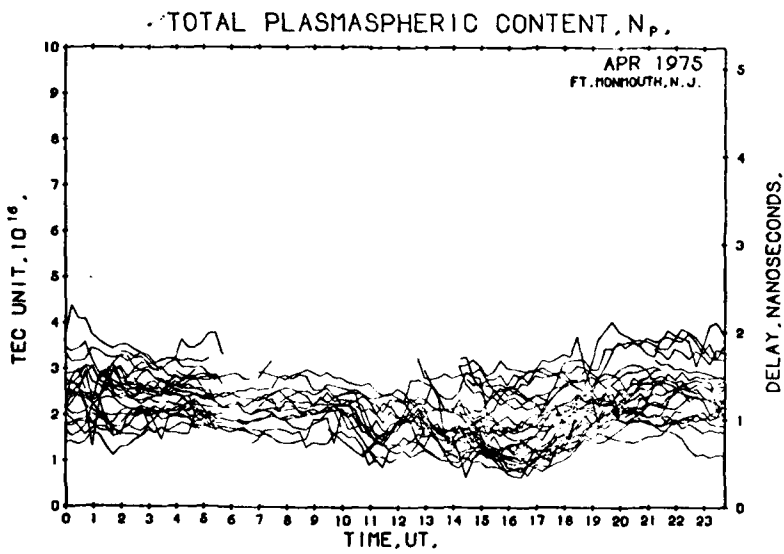


Fig. 12. Same as Fig. 9, but for April 1975.

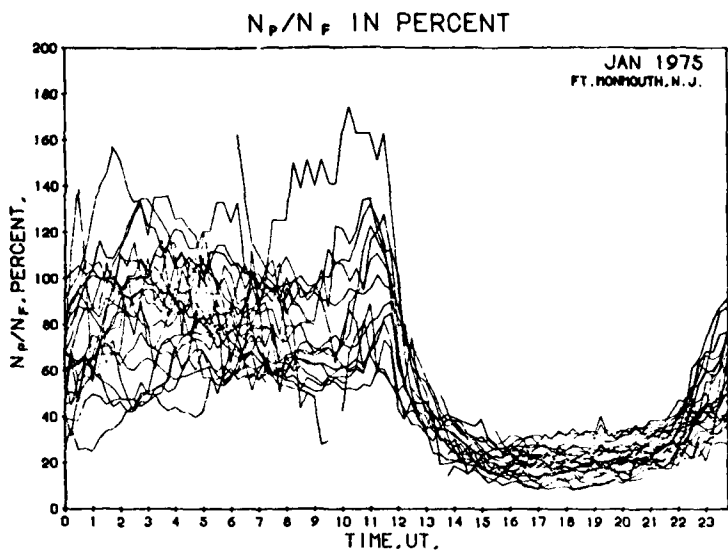


Fig. 13. Ratio of plasmaspheric to ionospheric contents ( $N_p/N_F$ ) at 15-minute intervals, Fort Monmouth, N.J., during January 1975.

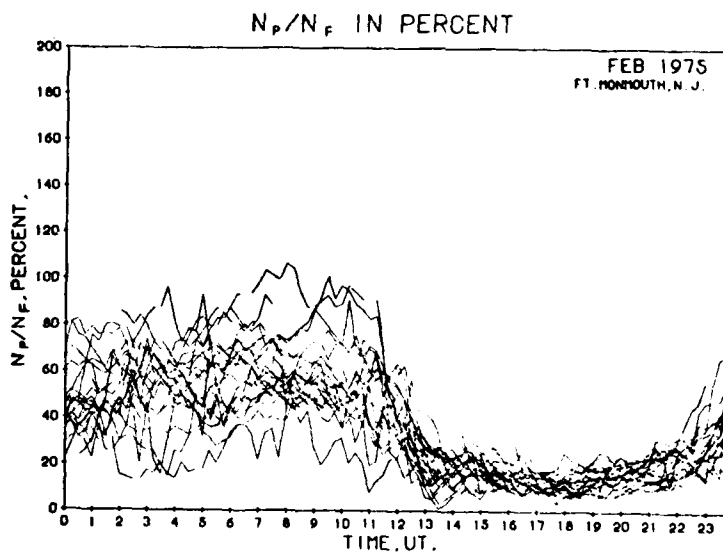


Fig. 14. Same as Fig. 13, but for February 1975.

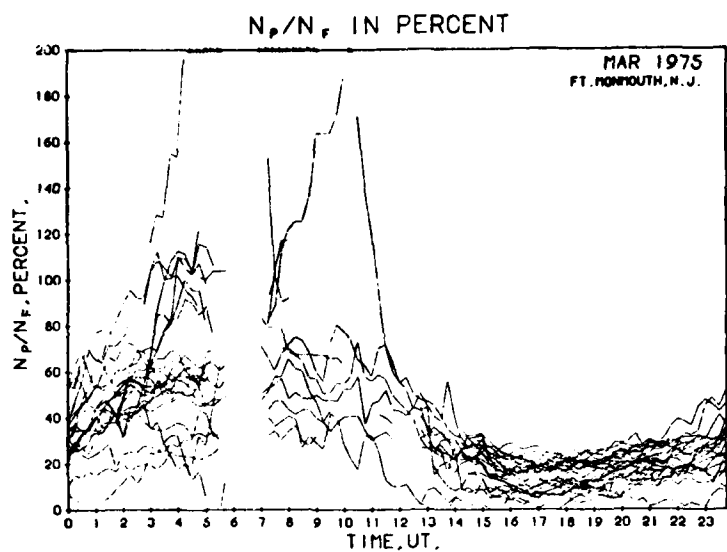


Fig. 15. Same as Fig. 13, but for March 1975.

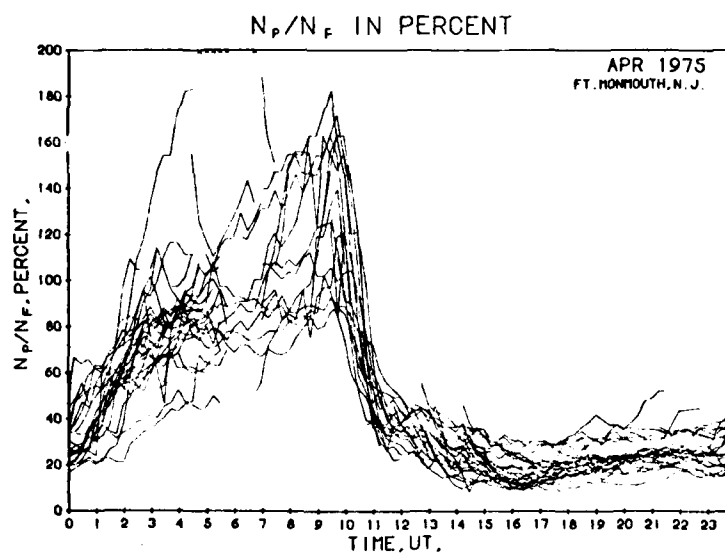


Fig. 16. Same as Fig. 13, but for April 1975.

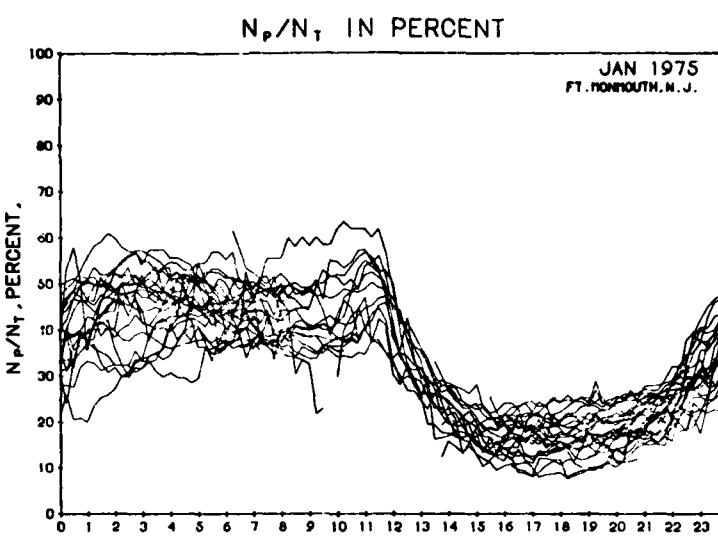


Fig. 17. Ratio of plasmaspheric-to-total content ( $N_p/N_T$ ) at 15-minute intervals, Fort Monmouth, N. J., during January 1975.

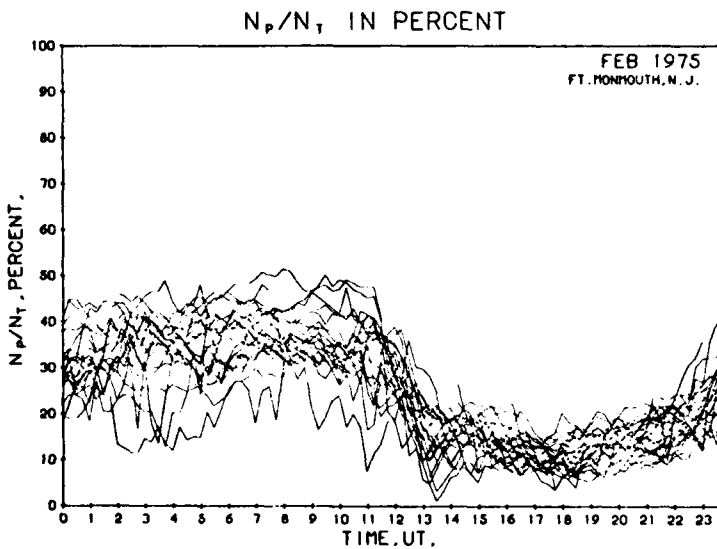


Fig. 18. Same as Figure 17, but for February 1975.

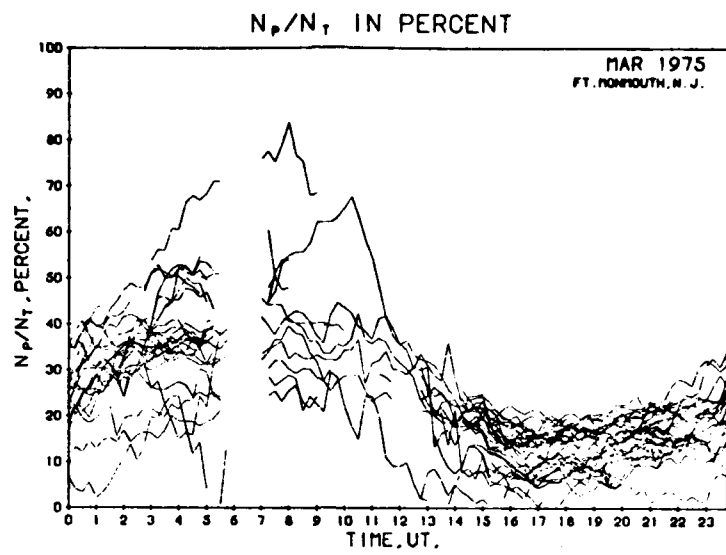


Fig. 19. Same as Figure 17, but for March 1975.

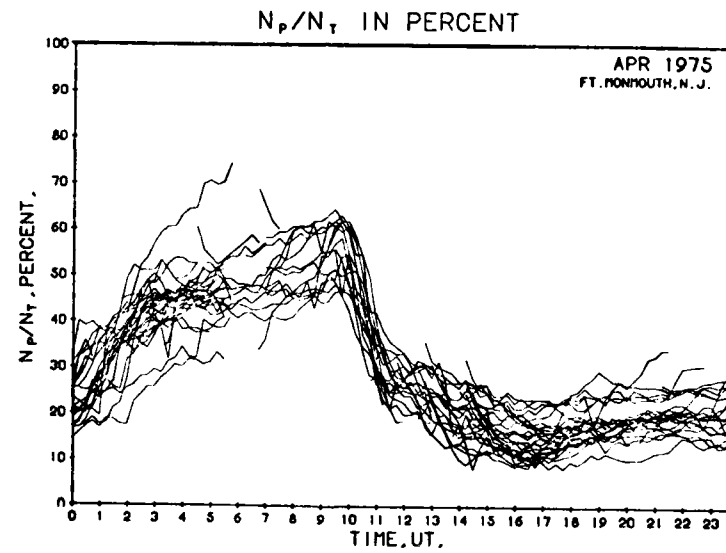


Fig. 20. Same as Figure 17, but for April 1975.

TIME AND LATITUDE DEPENDENCE OF IONOSPHERIC ELECTRON  
CONTENT FROM THE COMBINATION OF NNSS AND ATS - 6 DATA

R. Leitinger, University of Graz, Austria,  
G.K. Hartmann, Max-Planck-Institut für Aeronomie,  
Lindau/Harz, FRG

Abstract.

Geostationary satellites allow the observation of time changes in the ionospheric electron content under nearly constant geometrical conditions. From low orbiting satellites one can derive primarily spatial changes of electron content, the time for a scan provided by a pass of the satellite is short compared with timescales typical for ionospheric processes (except scintillations). Polar orbiting satellites have the additional advantage that they provide a scan in latitude for nearly constant local time if the observed electron content is referred to a ionospheric point in a given height. The disadvantage of low orbiting satellites is the bad time resolution even when several satellites can be observed: the time interval from one useful pass to the next is of irregular length. On the other hand geostationary satellites provide no spatial resolution at all when only one observing station is used.

The combination of data from low orbiting and from geostationary satellites could be used to override these disadvantages.

It was found that a suitable way to combine data from both sources into a presentation which yields the highest amount of geophysical information is to draw contour lines of constant electron content in a local time versus latitude coordinate system covering longitudes of  $\pm 5\%$  around the central satellite receiving station. It should be emphasized that no averaging process was applied, i.e. the displayed data give the real time changes in ionospheric electron content and are very useful in studying the day to day changes. Not only the effects of magnetic disturbances can be studied under new aspects but also during quiet days the effects of the dynamics of the neutral atmosphere which lead to very different day to day latitudinal and time dependent electron content distributions, despite the fact that the overall amount of ionization remains almost constant. To improve the interpretation the data should be supplemented by relevant ionogram data.

Some first results are presented here.

### 1. Introduction.

Geostationary satellites allow the observation of time changes in the ionospheric electron content under nearly constant geometrical conditions. From low orbiting satellites one can derive primarily spatial changes of electron content, the time for a scan provided by a pass of the satellite is short compared with timescales typical for ionospheric processes (except scintillations). Polar orbiting satellites have the additional advantage that they provide a scan in latitude for nearly constant local time if the observed electron content is referred to a ionospheric point in a given height. The disadvantage of low orbiting satellites is the bad time resolution even when several satellites can be observed: the time interval from one useful pass to the next is of irregular length. On the other hand geostationary satellites provide no spatial resolution at all when only one observing station is used.

The combination of data from low orbiting and from geostationary satellites could be used to override these disadvantages. We have found that a suitable way to combine data from both sources into a display which is easy to interpret is to draw lines of constant electron content in a local time vs. latitude system. It should be emphasized that we use no averaging of data: our display gives real time changes and is especially useful in studying the day to day changes in ionospheric electron content.

### 2. Construction procedure for isolines of ionospheric electron content.

The following data are used: Faraday effect data from the 140 MHz channel of the ATS-6 Radio Beacon Experiment (ATS-6 RBE) and Differential Doppler data from the six fully operational satellites of the Navy Navigational Satellite System (NNSS) (carrier frequencies: 150 MHz and 400 MHz). For our purpose ATS-6 is a very good approximation to a geostationary satellite and the NNSS satellites have nearly polar orbits in a height range of 900 to 1200 km. As is the case with all Radio Beacon observations the primary data give information on integrals along the slant radio path from the satellite to the receiver. To derive any useful information in a local time vs. latitude system it is necessary to project the data onto the vertical and to refer them to a well defined point on the surface of the earth.

A considerable amount of work has been devoted to this problem in the past. We did not want to ignore or to neglect some of the results but the only practicable way to project and to refer the data was to use a simple and constant procedure. Possibly the errors in our results could be reduced with some kind of iterative process but it is doubtful whether this would improve the results in view of possible uses to such an extent that the efforts are justified.

In the reduction of ATS-6 Faraday observations we used the following formulae for electron content:

$$N_{A\text{/}} = C_F \Omega / \bar{B}_L; \quad N_{A\perp} = N_{A\text{/}} \cos x$$

$N$  with subscript: electron content (subscript A: refers to ATS-6 as the data source; symbols  $\text{/}$  and  $\perp$ : to indicate slant and vertical content, resp.);  $C_F$ : Faraday constant;  $\Omega$ : observed Faraday rotation angle;  $\bar{B}_L$ : longitudinal component of geomagnetic induction in a mean field height;  $x$ : zenith angle of the ray in a mean ionospheric height. For the 140 MHz carrier of ATS-6  $C_F$  has the value  $8.295 \times 10^{15} \text{ m}^{-2} \text{ radian}$ , when  $N_{A\text{/}}$  is expressed in  $\text{m}^{-2}$ ,  $\Omega$  in radian and  $\bar{B}_L$  in  $\text{G}$ .

The geometry for the projection from slant into vertical content is shown in Fig. 1:

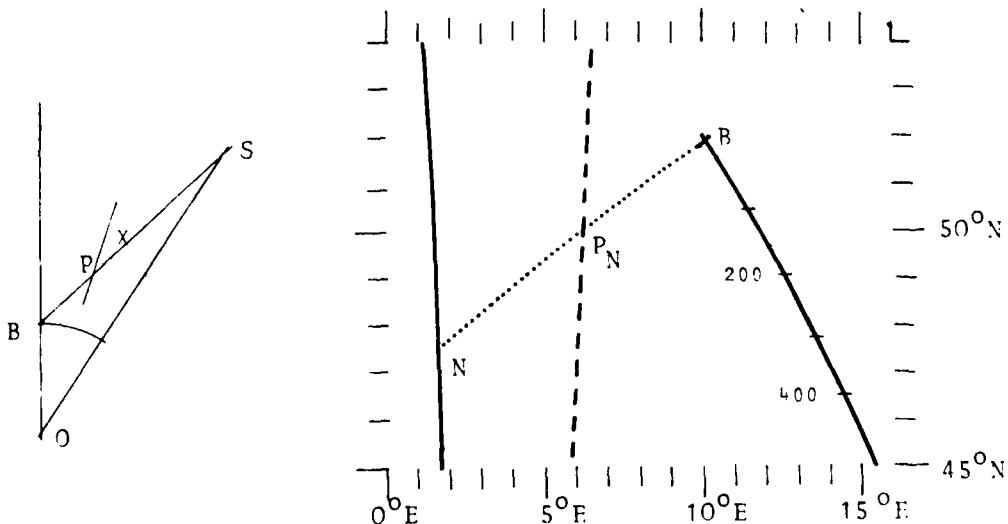


Fig. 1: Map with ray from Lindau to ATS-6 and with an NNSS orbit (solid lines) and the corresponding trace of ionospheric points (400 km). On the left: Geometry for the projection of slant content onto the vertical. O: center of the earth; S: satellite; B: observer; P: ionospheric point; x: zenith angle in P.

The projection is done in the ionospheric point which is found in the ray (straight line) from the satellite (S) to the observing station (B). The vertical electron content gained from the projection is referred to a point on the surface of the earth with the coordinates of the ionospheric point ( $P_A$ , the subscript indicating ATS-6, with latitude  $\phi_A$  and longitude  $\lambda_A$ ).  $x$  is the zenith angle of the ray in  $P_A$ .

Titheridge (1972) has shown that  $N_{A\perp}$  can be interpreted as the vertical electron content from ground to 2000 km with an accuracy of  $\pm 5\%$  if a height of 420 km is taken for  $P_L$  and for  $x$ . We have taken 400 km for  $P_L$  and for  $x$ . The difference in the results is very small.

For the reduction of Differential Doppler observations an integration constant has to be determined which cannot be derived from Differential Doppler data without additional information (Leitinger et al. 1975). Electron content can than be evaluated by means of the formulae

$$N_{N\perp} = C_D (\phi_0 + \psi) ; \quad N_{N\perp} = N_{N\perp} \cos x .$$

The subscript N refers to the NNSS satellites;  $C_D$ : Differential Doppler constant;  $\phi_0$ : integration constant;  $\psi$ : observed Differential Doppler phase angle;  $x$  is again the zenith angle of the ray from NNSS (N) to the receiver (B) in the ionospheric point  $P_X$  (Fig. 1). The information which is necessary to get a value for  $\phi_0$  is provided by the ATS-6 - data:  $\phi_0$  is adjusted in such a way that vertical electron content values from observations of the two satellites match in the latitude  $\phi_A$  at the local time  $t_N$ . For this purpose the (vertical) electron content values from ATS-6 are considered to define a function of local time  $N_A = N_A(t_L)$ ,  $t_L$  being the local time of the ionospheric point  $P_A$  (from now on the symbol  $\perp$  is omitted; all electron content values are vertical). From NNSS Differential Doppler one has a set of measured values  $\psi$  which can be considered to define a function of Universal Time  $t$ :  $\psi = \psi(t)$ . From the orbital parameters of the NNSS pass one can calculate the corresponding coordinates of the ionospheric points (400 km) and the zenith angle on the ray to the satellite (lat.  $\phi_i = \phi_i(t)$ , long.  $\lambda_i = \lambda_i(t)$ , zenith angle  $x_i = x_i(t)$ ). Vertical electron content would follow from the formula

$$N_N(t) = C_D (\phi_0 + \psi(t)) \cos x_i(t) ; \quad t \text{ is to be considered as parameter which connects coordinates and } \psi\text{-values.}$$

Now one looks for the ionospheric point which has the latitude  $\phi_i = \phi_A$ . This point is crossed by the ray to the satellite at the time  $t^*$ . Its coordinates are  $\lambda_i(t^*)$ ,  $\phi_A$ , resp., the corresponding  $\psi$ -value is  $\psi(t^*)$ , the local time is  $t_N = t^* + \lambda_i(t^*) / 15.0$  ( $t_N$  and  $t^*$  in hours,  $\lambda_i$  in  $^{\circ}$ E).

With  $t_N$  one gets  $N_A(t_N)$  and using this value the integration constant  $\phi_0$  follows:

$$\phi_0 = N_A(t_N) \sec x_i(t^*) / C_D - \psi(t^*)$$

With  $\phi$  one can calculate the vertical electron content for the ionospheric points of the NNSS pass and using the formula given above one gets the corresponding local times. These are nearly constant for a pass of the satellite.

The  $N_A$  values from ATS-6 together with the  $N_N$  values would give enough information to draw isolines of electron content provided that the time interval from one NNSS pass to the next is not too long. The situation is improved if ATS values from stations in other latitudes can be used for interpolation. But the inclusion of another station requires that the difference in the longitudes of their ionospheric points is not larger than a few degrees. (It was not possible to combine values from the Boulder region with values from the West coast of the US kindly provided by J.A. Klobuchar from AFCRL. Values from Bozeman and Boulder and from Lindau and Graz, resp., could be combined very well; values from Dallas had to be adjusted slightly in some cases before they could be used for interpolation of NNSS values gained at Boulder.) One has to be careful with NNSS passes which ionospheric points are too far West or East of  $P_A$ : the adjustment of local times described above requires the assumption that there is only a local time and a latitude dependence but no longitude dependence of ionization. No NNSS passes should be used which have zenith angles larger than  $60^\circ$  in the point of closest approach.

### 3. Sample isoline plots.

In the Fig. 2 to 4 three examples are shown for the isoline method. Each plot was drawn for a series of three to four days. For Fig. 2 and Fig. 3 we used values from the American sector gained in late summer and in fall 1974, for Fig. 4 we used values from the European sector gained in winter 1975/76. The station coordinates are summarized in Table 1.

station	lat. $^{\circ}$ N	long. $^{\circ}$ E	observations
<b>American sector</b>			
Bozeman (BOZ)	45.66	-111.05	ATS-6
Boulder (BOU)	40.13	-105.24	ATS-6, NNSS
Las Vegas, NM	35.60	-105.17	NNSS
Dallas (DAL)	32.98	-96.75	ATS-6
<b>European sector</b>			
Uppsala	59.80	17.60	NNSS
Lindau (LIN)	51.62	10.09	ATS-6, NNSS
Graz (GRA)	47.08	15.49	ATS-6, NNSS

Table 1: Coordinates of the stations used for the construction of isolines in Fig. 2 to 4. Coordinates of ATS-6 for American sector: lat.:  $0^\circ$ , long.:  $-94^\circ$ E, height: 35869 km; for European sector: lat.:  $0^\circ$ , long.:  $34^\circ$ E, height: 35869 km.

The solar and geomagnetic conditions have been quite different for the three series of days shown in Fig. 2 to 4. The first series (August 29 to September 1, 1974) could stand for a typical period of time at low solar activity with average values of magnetic indices and no storm of which ionospheric effects could be expected (a weak storm without SSC has been reported from only 4 observatories for August 29). This contrasts strongly with the series of Fig. 3 (October 12 to 14, 1974): the solar activity has been higher and the days have been heavily disturbed magnetically: two principal magnetic storms with Sudden Commencement have been reported (onset in Boulder: October 12, 12:45 UT and October 14, 16:34 UT). Weaker storms without SSC have been reported for October 8 and 9 (no reports from Boulder). The third period has been magnetically very quiet indeed (December 10 to 13, 1975).

The solar flux values and some geomagnetic parameters are summarized in Table 2.

date	S <sub>F</sub>	Ap	k <sub>p</sub>	date	S <sub>F</sub>	Ap	k <sub>p</sub>
Aug. 26, 1974	72.3	7	2	Oct. 12, 1974	144.7	17	4+
27	71.2	18	4	13	127.2	86	7
28	70.4	20	4+	14	113.8	30	6
29	71.0	31	4+	Dec. 7, 1975	76.0	4	1+
30	72.8	17	4+	8	78.3	18	4
31	74.2	21	4+	9	75.6	16	3
Sep. 1, 1974	76.4	24	5	10	75.6	8	0+
Oct. 9, 1974	129.5	39	5+	11	76.7	5	2+
10	129.7	10	5+	12	75.7	3	1+
11	138.1	6	3	13	75.1	3	0+

Table 2: Solar flux values and geomagnetic parameters for the series of days shown in Fig. 2 to 4. (Begin of the table: three days before the begin of the figures). S<sub>F</sub>: solar flux (2800 MHz) for Ottawa; Ap: daily index of geomagnetic activity (linear scale); k<sub>p</sub>: maximum k<sub>p</sub>-value for this day. All values from Solar-Geophysical Data (World Data Center A, issues of 1974, 1975 and 1976).

Before discussing the Figures 2 to 4 some remarks have to be made. As the time intervals from one NNSS pass to the next are of irregular length there are differences in the resolution of the isolines: in regions with a high density of observed values features of smaller scale could be resolved than in regions for which the bearing of the isolines had to be guessed. In the larger gaps (e.g. in Fig. 2, Aug. 29, 8:15 to 19:45 LT) even larger features are necessarily doubtful outside the region covered by ATS-6 observations. An other warning: it is in the very nature of observation by means of orbiting satellites that the spatial structures are seen through a "low pass filter" which suppresses small scale irregularities (higher spatial frequencies). The (spatial) cutoff

frequency decreases with increasing zenith angle (Leitinger et al. 1975). It can clearly be seen from the Figures that much more details are shown in the center near the ATS-traces than in the northern and southern regions. The (absolute and relative) accuracy of the isolines is highest in the center of the displays: (~10%) distortions increase with increasing zenith angles of NNSS passes. One should bear in mind that the "slant electron content projected onto the vertical" differs from "true electron content" when a ionospheric point is used which differs from the center of the electron distribution along the ray and that the resulting error increases with increasing zenith angle. For the center our estimate of the absolute accuracy is  $\pm 10\%$  for daytime and magnetically quiet periods.

Having given these warnings the displays of isolines can be discussed:

a) Display shown in Fig. 2 (August 29 to September 1, 1974). The following characteristics are seen immediately: a nighttime trough which changes its position from night to night (probably identical with the main F-layer polar trough), the value of the nighttime minimum changes too. The morning increase and the evening decrease of electron content can vary considerably in steepness from day to day in the whole latitude region. The overall electron content could be nearly equal for the series of days shown in the display: On August 29 the electrons appear to be swept southwards, forming a broad daytime maximum, on August 30 the peak is smaller (shorter) but much more electrons are found in the region of 50°N. Large scale irregularities are seen on all four days.

The characterization of days by the number of daytime maxima of the diurnal curve cannot give much insight in ionospheric processes: the number depends on the day and on the latitudes of the station. On each day there is a latitude region for which two maxima exist. On August 30, to give an example, this region is limited to the North and to the South.

Some secondary peaks and troughs are seen in the display. In this case the warning given above should be applied: the existence of other secondary peaks and troughs cannot be excluded in regions not covered by observations (e.g. north of 42°N on August 29 during daytime).

It can be concluded from Fig. 2 that strong dynamic processes must have acted to account for the day to day variability and for the large scale irregularities seen in the display.

b) Display shown in Fig. 3 (October 12 to 14, 1974). A comparison with Fig. 2 reveals that the electron content behaves completely different during this heavily disturbed period: The daytime values on October 12 and on October 14 are much higher than the daytime values seen in Fig. 2, whereas the electron content is strongly depleted on October 13. In this case the overall electron content has certainly changed considerably from day to day: the depletion is seen in the whole latitude region of the display.

Nighttime values are higher, too; on October 14 one can see a clear nighttime increase of ionization but the region affected by the increase seems to be comparatively small.

It seems that the strong disturbance has not produced an unusual amount of large scale irregularities.

A very important property is the steep decrease of ionization in the afternoon of October 14.

c) Display shown in Fig. 4 (December 10 to 13, 1975).

This is one example from the European region. It has been possible to extend the latitude region to the North because NNSS observations from Uppsala (Sweden) could be used in addition to values gained at Lindau and at Graz. Fortunately a large number of NNSS passes could be disposed of, therefore the accuracy of the isolines is better than in the samples for the American sector.

It is interesting to see that no criteria can be derived to qualify the ionosphere to be "very quiet" as has been the case for the geomagnetic indices (Table 2). Large scale irregularities are seen during daytime together with secondary peaks and troughs. A nighttime increase of ionization is seen on December 11 which extends far in the North but is centered around 45°N. A complicated pattern of isolines is revealed for the night Dec. 11/12. As is the case for the previous night, a midlatitude ridge has formed.

The total amount of ionization during daytime shows nearly no differences as should be expected for a very quiet period with nearly constant solar flux. The daytime pattern of isolines is very complicated from the action of large scale TID's, but it can be seen quite clearly that in the average the daytime electron content increases from North to South and that by a suitable smoothing process one would get a diurnal maximum near local noon in all latitudes.

Some statements on the dynamics of the polar trough could be made from Fig. 4: in the nights Dec. 11/12 and Dec. 12/13 it wandered southwards in the evening, reached its lowest latitude around 1 LT and wandered northwards in the morning.

#### 4. Discussion.

From the samples shown it can be seen that the isoline display for ionospheric electron content allows an easy inspection in the behaviour of the ionosphere over a wide range of latitudes. The method described can be successfully used to combine data from geostationary and from low orbiting satellites if gained from the same station. It is an effective way to reduce a large amount of data to have an optical display which allows a quick evaluation. With present possibilities it is probably not feasible to construct isolines for a longer series of days: ATS-6 RBE operates with interruptions and the distribution of NNSS passes changes with time: there could be very long gaps from one useful pass to the next (when two or more satellites are above the station horizon in the same time interval the signals interfere etc.). The ever present equipment failures produce additional gaps in the data. Nevertheless we think that even isoline displays with interruptions could be a very useful tool in studies based on ionospheric electron content. Not only the effects of magnetic disturbances can be studied under new aspects but also during quiet days the effects of the dynamics of the neutral atmosphere which lead to very different day to day electron content distributions in latitude and time, despite the fact that the overall amount of ionization remains almost constant. To improve the interpretation the data should be supplemented by relevant ionogram data.

### Acknowledgements.

The authors thank Dr. K. Davies, NOAA-ERL, for having made available ATS-6 data from Boulder. In the collection and analysis of the data from the American sector a number of people has been involved to whom we express our thanks (see acknowledgements in Davies et.al. 1975 for details). We thank Dr. R. Hedberg, Ionospheric Observatory Uppsala, who has made possible the operation of NNSS equipment in Uppsala. We thank Dr. W. Degenhardt, MPI Lindau, and Mag.rer.nat. E. Putz, University of Graz, for assistance in the reduction of ATS-6 and NNSS data. The MPI research program was supported by Research Grant Di 32/33 from Deutsche Forschungsgemeinschaft. The research program in Graz was supported by the Fonds zur Förderung der wissenschaftlichen Forschung. In Graz ATS-6 receiving equipment of MPI Lindau is used. For a part of the computations the facilities of the Rechenzentrum Graz have been used.

### References.

- |   |      |   |
|---|------|---|
| Davies, K.<br>Fritz, R.B.<br>Hartmann, G.K.<br>Leitinger, R.<br>Paul, A.K.<br>Schmidt, G. | 1975 | Determination of the total electron content of the ionosphere and the plasmasphere, Proc. Symp. on the beacon satellite investigations of the ionosphere, v. II, IZMIRAN, Moscow, 146-158                 |
| Leitinger, R.<br>Schmidt, G.<br>Tauriainen, A.  | 1975 | An evaluation method combining the Differential Doppler measurements from two stations that enables the calculation of the electron content of the ionosphere, J. Geophysics (Zs. Geophysik), 41, 201-213 |
| Titheridge, J.E.  | 1972 | Determination of ionospheric electron content from the Faraday rotation of geostationary satellite signals, Planet. Space Sci. 20, 353-369  |

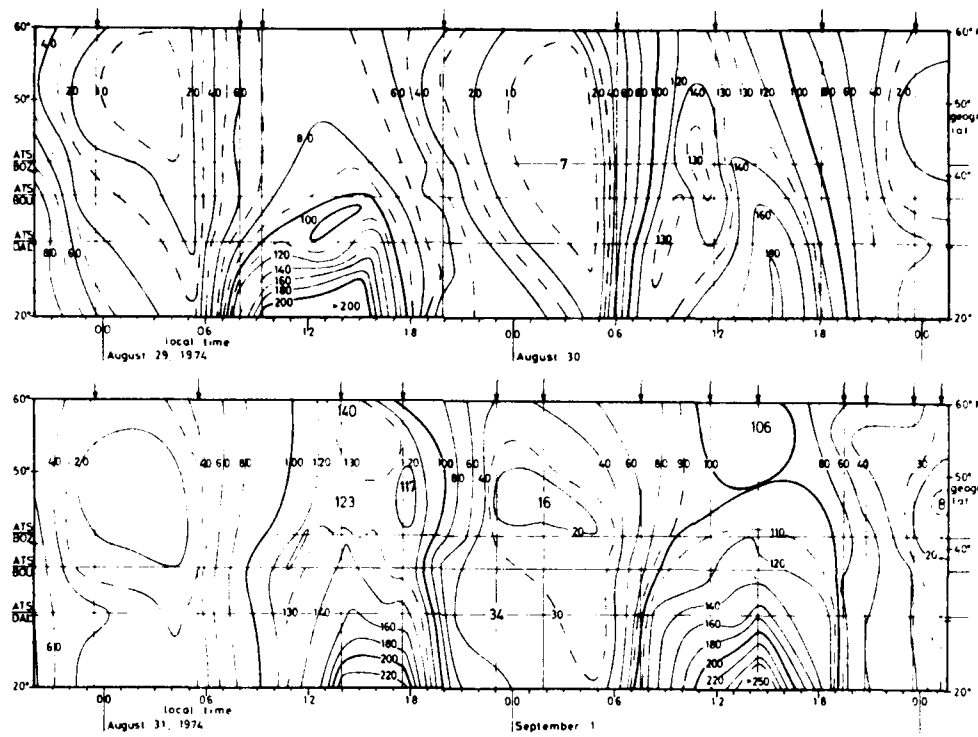


**Figure 2:** Lines of constant electron content (isolines) in a local time vs. latitude system. Vertical ionospheric electron content in  $10^{15} \text{ m}^{-2}$ . Distance of solid lines:  $20 \times 10^{15} \text{ m}^{-2}$ . In some regions isolines for odd multiples of  $10 \times 10^{15} \text{ m}^{-2}$  have been drawn (dashed). Isolated numbers: values in minima, maxima or saddle points.

Location of ionospheric points (400 km) of ATS-6 stations indicated by horizontal lines (when interrupted: no data available). Local times of NNSS observations indicated by horizontal lines with arrows on the top of the plot. In some cases the NNSS data are restricted to the central parts of the plot. ATS-stations for this figure: BOZ eman, BOU lder, DAL las. NNSS values have been used from the stations Boulder and Las Vegas, N.M. (for coordinates see Table 1). ATS-6 at  $-94^\circ\text{E}$ . Local time of the ionospheric point in the Boulder-ATS-6 ray. LT = UT - 6.93 hours. Longitude range about  $\pm 5^\circ$  around the central observing station.

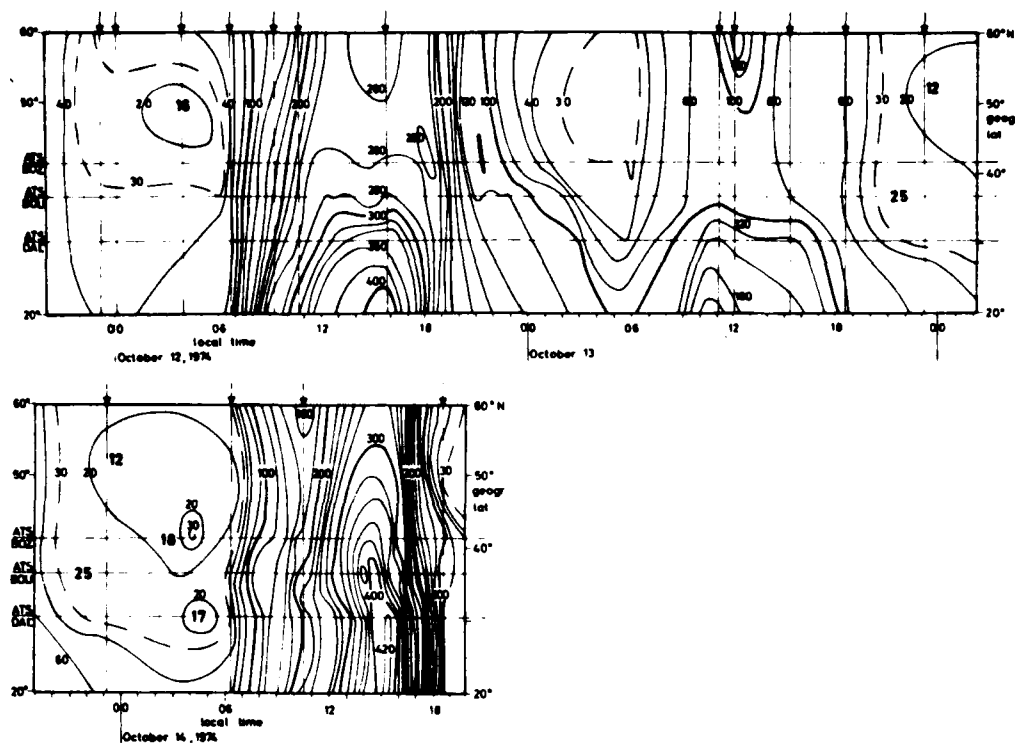
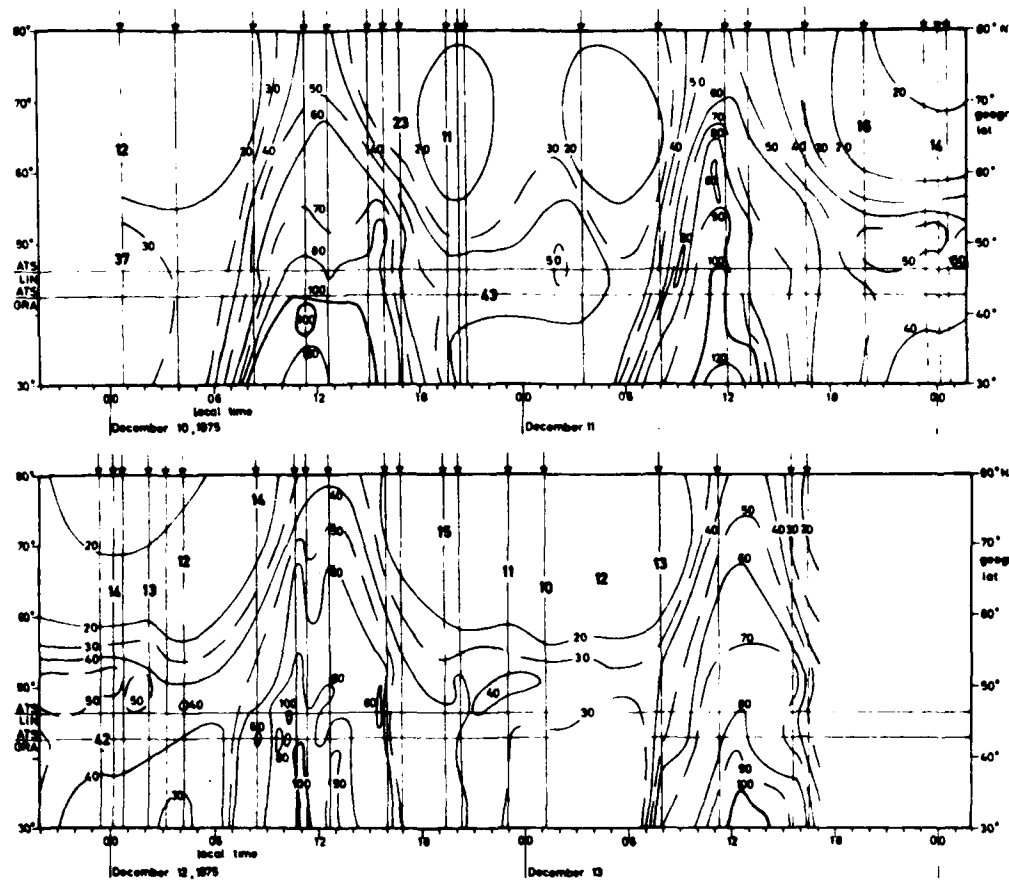


Figure 3: Isolines of ionospheric electron content as in Fig. 2.



**Figure 4:** Isolines as in Fig. 2, but stations from the European sector: observations from LINdau and GRAz (location of ionospheric points indicated by horizontal lines). Additional NNSS observations from Uppsala (Sweden) (for coordinates see Table 1). Local time of the ionospheric point in the Lindau - ATS-6 ray. LT = UT + 0.96 hours.

Periodic amplitude and phase fluctuations ranging from 1 sec  
to 30 min observed with the ATS-6 RBE at Lindau

by

W. Degenhardt and G.K. Hartmann

Max-Planck-Institut für Aeronomie - IfL  
D-3411 Lindau/Harz, FRG, P.O. Box 80

April 1976

### Abstract

#### I. Fluctuations caused by the troposphere

Periodic fluctuations in the range of duration between 1 and 10 minutes were observed on the 140 MHz and 141 MHz Faraday channels of two Single Frequency Polarimeters (SIPOL) using two Yagi antennas with  $\pm 30^\circ$  beamwidth. Data from November and December 1975 were evaluated. Examples for Nov 23, Nov 25, Nov 26 and Dec 18/19 1975 are presented. During night periods between 5 and 6 minutes are typical with a maximum of occurrence around midnight. During day 1 to 3 minute periods are dominant. These effects were not observable with a simultaneous Multi Frequency Polarimeter (MEPOL) and Short Backfire antennas with  $\pm 150^\circ$  beamwidth. The elevation angle of ATS-6 at Lindau is  $28^\circ$  thus it is concluded that the SIPOL effects are not caused in the ionosphere but in the troposphere and might possibly be caused by microclimatic effects close to the surface of the earth. 360 MHz amplitude fluctuations, which were observed during times when neither the 140 MHz amplitude nor the 40 MHz amplitude showed relevant fluctuations are very likely caused in the troposphere. One out of ten very clear examples is presented here.

#### II. Fluctuations caused by the ionosphere

For detailed investigations three subsequent days in December 1975 were selected, Dec 11, 12, and 13.

On December 11 around 1955 UT 7 sec periods were observed on the 140 MHz and 141 MHz amplitudes lasting for about 1 minute. Simultaneously on the 40 MHz amplitude and Dispersive Doppler 40 MHz 15 sec periods. Furthermore periods less than 5 sec were observed. In addition to that longer periodic fluctuations up to about 30 min were observed during day and night. Due to the high resolution of the DD 40 measurement ( $\sim 200$  times more sensitive than Faraday rotation 140 MHz) for the first time real significant effects on TEC at midlatitudes due to gravity waves could be shown in the middle of the night. DD 140-, Faraday rotation- and Group delay measurements are too insensitive and marginal for displaying any effect of gravity waves on the TEC during the night. Furthermore the daily variations of the scintillation indices  $S_4$  at 40 MHz and 140 MHz are presented as well as a graph for the frequency of occurrence of scintillations for the three months period Oct 1975 -

Dec 1975.  $S_4$  includes any type of periodic and unperiodic fluctuations and depends from the data sampling rate and from the receiving antenna beamwidth.

### Introduction

#### The ATS-6 geostationary satellite and the Radio Beacon Experiment (RBE).

There are three carrier frequencies, 40 MHz, 140 MHz, and 360 MHz. Amplitude modulation frequencies are 100 kHz on the 40 MHz and 360 MHz signals and 1 MHz on the 360 MHz, 140 MHz, and 40 MHz signals. The RBE is designed for several types of measurements, principally: Faraday Rotation, differential carrier phase (Dispersive Doppler), modulation phase (Differential Group Delay), and signal amplitude (Absorption). [1], [5], [6], [19].

From September 1974 through April 1975 observations were carried out at several locations in the US in the frame of cooperative programs with NOAA ERL, Boulder, Colo; Montana State University, Bozeman, Mt; and University of Texas at Dallas, Dallas, Texas. [7], [9], [10], [11], [18]. In summer 1975 the satellite moved from  $94^{\circ}$  W to  $35^{\circ}$  E and is now observable from Europe. Some preliminary results obtained from October 1975 through February 1976 will be presented here.

### Location

The receiving station Gillersheim is a field site of the MPI f. Aeronomie and is located at  $51.65^{\circ}$  N and  $10.13^{\circ}$  E about 7 km spaced from the main institute at Lindau. ATS-6 is positioned at  $35^{\circ}$  E, 36000 km above the surface of the Earth. Its tropocentric coordinates with respect to the receiving site Lindau are azimuth:  $30^{\circ}$  from south towards east, elevation:  $28^{\circ}$ . The line of sight between ATS-6 and Gillersheim intersects between  $50^{\circ}$  and  $40^{\circ}$  geogr. latitude the ionosphere in altitudes between 100 km and 1000 km and has a relevant length of 1600 km. Thus the results are due to medium latitudes, in our case geographic and geomagnetic coordinates are nearly identical.

### Equipment

Several receiving equipments, designed at Lindau are in use.

1. Multifrequency-polarimeter receiving units (MEPOL) [3], [20]
  2. Single frequency polarimeter receiving units (SIPOL) [14]
- The Multifrequencypolarimeter (MEPOL) is operated with One-Element-Short-Backfire-Antennas, having a beamwidth (3 dB points) of about  $30^{\circ}$ . [13]. The single frequency-polarimeter (SIPOL units are operated with commercially fabricated Yagi antennas having beamwidth of about  $60^{\circ}$ .

### I. Fluctuations caused by the troposphere

#### A) $F_{140}$ and $F_{141}$ measurements

With two single frequency polarimeter (SIPOL) units - inclusive two Yagi antennas - the Faraday effect was recorded at 140 MHz and 141 MHz. Analog chart recorders were used with a chart speed of 120 mm/h and a chart width (resolution) of 200 mm per  $180^{\circ}$  Faraday rotation. During the nights we observed several times significant periodic variations with a duration of about 5 min and rotation angle variations of more than  $\pm 1^{\circ}$ . Figure 1 displays a section of such a recording.

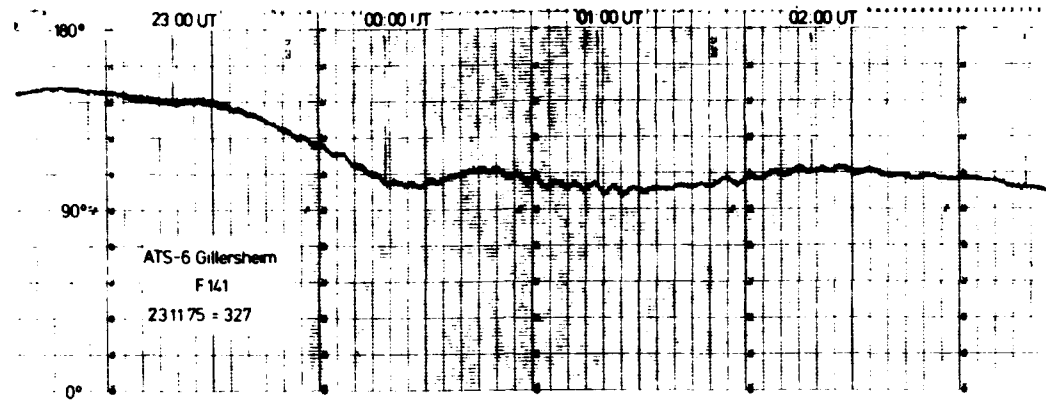


**Figure 1:** Recording of the Faraday effect at 141 MHz in the early night at Nov 23, 1975 at Gillersheim

The periodic variations are observable on the 140 MHz recording and on the 141 MHz recording. There seems to be a small time delay between the two events.

For a better identification (amplification) of these effects we measured additionally the differential Faraday effect  $F_{140/141}$ , where the daily TEC variation is nearly eliminated.

Figure 2 shows quasiperiodic variations on  $F_{140/141}$  in the night from Dec 18 to Dec 19, 1975 of about 5 to 6 min duration and shorter periods during the following day hours.

Until now the period November and December 1975 was investigated.

During the night the sinusoidal fluctuations seem to be a rather regular phenomenon with a maximum of occurrence before midnight. During the day periods between 1 to 3 minutes are typical. The short period fluctuations are superimposed on longer period fluctuations (gravity waves).

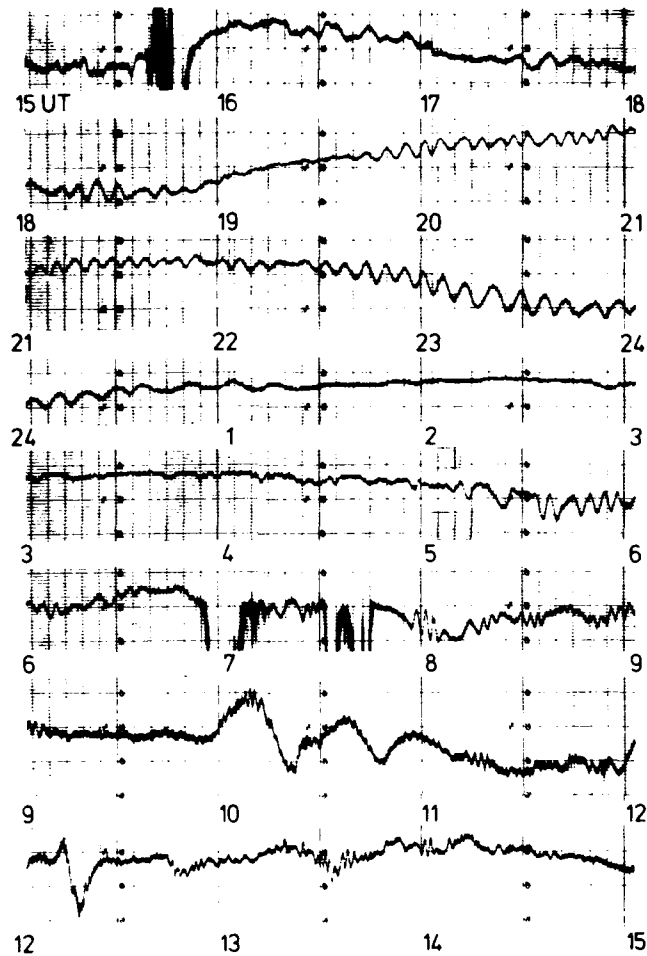


Figure 2: Faraday effect 140/141 MHz recording at Gillers eim  
Comparison with simultaneous multifrequencypolarimeter (MEPOL) measurements

The "Single frequency polarimeter (SIPOL)-effects" were not visible on the multifrequencypolarimeter (MEPOL) recordings.  
 We have to conclude that the fluctuations measured with single frequency polarimeter (SIPOL) can only be due to the different beamwidth of the Short Backfire (SBF) antenna and Yagi antenna (SBF antenna  $\pm 15^\circ$ ; Yagi antennae  $\pm 30^\circ$ ).  
 Due to the fact that ATS-6 is visible from Gillersheim with an elevation angle of  $28^\circ$  and that the beamwidth of the Yagi antennas is  $\pm 30^\circ$

the Yagi antennas "see" tropospheric regions very close to the ground where the microclimate plays the dominant role [16]. The Short Backfire (SBF) antenna with a beamwidth of  $\pm 15^\circ$  does not cover these lower regions.

### 8) 360 MHz amplitude variations

Tropospheric effects can play an important role. This was demonstrated by the ATS-6 RBE 360 MHz amplitude recordings obtained at Bozeman, Montana, with a multifrequency polarimeter (MEPOL) receiving unit when ATS-6 was located  $94^\circ$  W. [2].

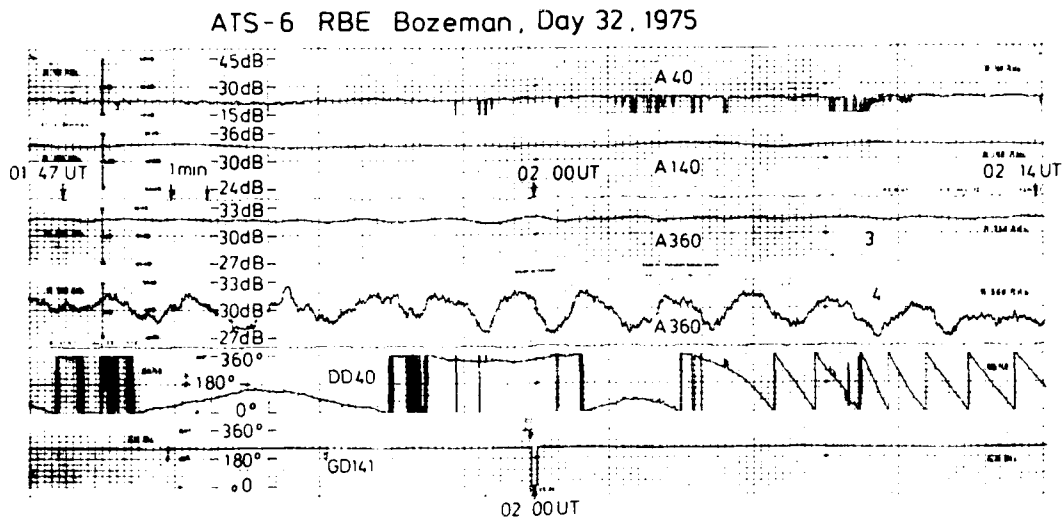


**Figure 3:** ATS-6 RBE recording taken at Bozeman, Montana, USA

Figure 3 shows part of a recording taken on Feb 1, 1975 (day 32) at Bozeman. Channel 3 displays the ATS-6 360 MHz carrier amplitude (intensity) recorded with the multifrequency (MEPOL) receiver and a 1-element Short Backfire antenna.

Channel 4 at this time was connected to a separate phaselock receiver with a  $\lambda/2$  dipole  $\lambda/4$  above ground. We see amplitude (intensity) variations with periods between 1 and 3 minutes. The amplitude of these fluctuations strongly depends on antenna type.

Model calculations show that the amplitude variations are proportional to the wave frequency. Refraction effects in the ionosphere show an opposite frequency behaviour. [17]

Figure 4 shows a portion of a 360 MHz amplitude recording obtained around 0600 UT on Nov 20, 1975 at Gälleråsheim.

The effect is clearly to be seen on the 360 MHz channel but neither the 140 MHz amplitude nor the 40 MHz amplitude showed simultaneously fluctuations. If the effect would be due to the ionosphere we would expect the opposite behaviour. Thus we conclude - like in Bozeman - that these 360 MHz amplitude variations are very likely caused in the troposphere. [16]

20.11.1975 Day 324 ATS-6 RBE Gillersheim

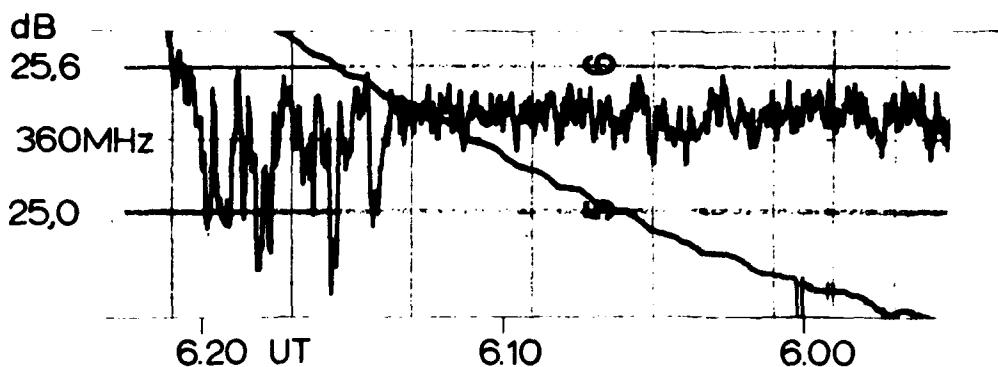


Figure 4: 360 MHz amplitude variations of tropospheric origin

The occurrence of tropospheric effects observed on the 360 MHz amplitude from Nov 1975 through Jan 1976 is shown in Fig. 5 together with various ionospheric effects. The amplitude fluctuations at 360 MHz are given by open rectangles. There is to be seen no dependence on daytime. [17], [18].

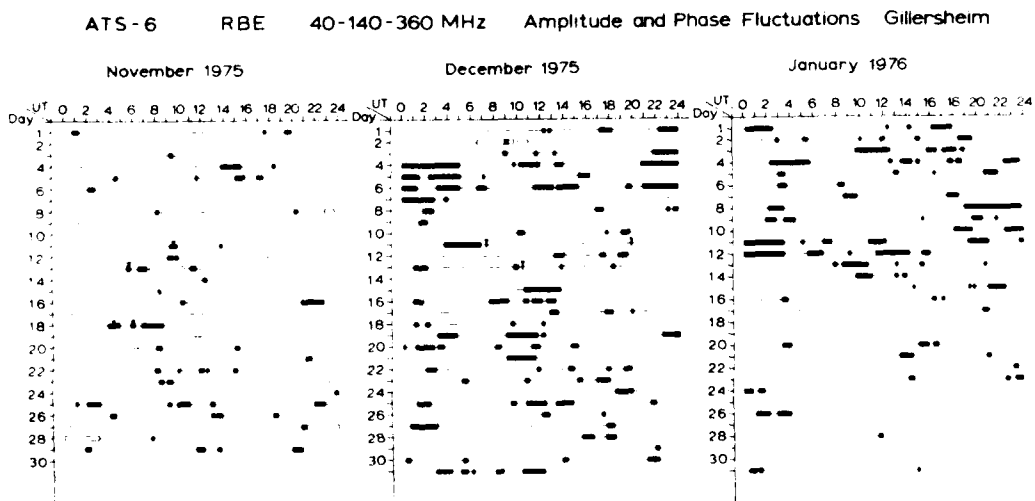


Figure 5: Occurrence of various fluctuation effects

□ tropospheric effects on the 360 MHz amplitude  
 █ scintillation events at 40 MHz and/or 140 MHz and/or 360 MHz  
 ▽ quasi-periodic fluctuations with periods between 1 and 60 sec.  
 The line indicates periods where ATS-6 data were available

## II. Fluctuations caused by the ionosphere

In this section various types of fluctuations will be presented which - as we believe - are caused in the ionosphere.

### A) Quasiperiodic fluctuations with periods less than 1 minute.

The occurrence of quasiperiodic fluctuations is shown in figure 5 by small arrows. The quasiperiodic fluctuations with periods between 1 and 60 sec always occur during scintillation periods. [4], [8], [11], [15].

The occurrence of clearly detectable scintillation events at 40 MHz and/or 140 MHz and/or 360 MHz from Nov 1975 through Jan 1976 is shown in fig. 5 by black rectangles. There seems to be no dependence from day-time and the maximum of occurrence seems to be in December. There are many more events than were expected.

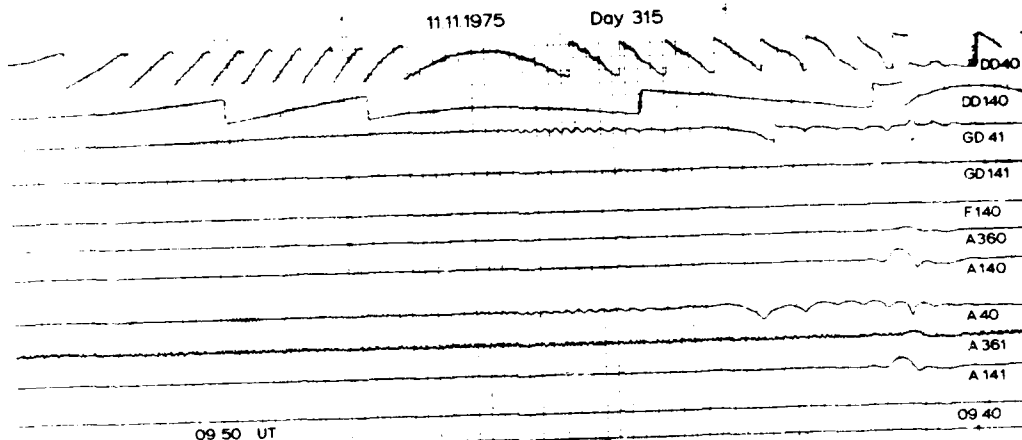


Figure 6: Quasiperiodic fluctuations at 40 MHz

Fig. 6 shows a portion of an analog recording with periodic fluctuations. The analog recording - taken at Gillersheim on Nov 11, 1975 between 0940 UT - displays the following channels:

- 1) DD 40 (Dispersive Doppler 40 MHz or carrier phase 40 MHz)
- 2) DD 140 (Dispersive Doppler 140 MHz or carrier phase 140 MHz)
- 3) GD 41 (Differential Group delay 41 MHz or modulation phase 41 MHz)
- 4) GD 141 (Differential Group delay 141MHz or modulation phase 141MHz)
- 5) F 140 (Faraday rotation angle at 140 MHz)
- 6) A 360 (Amplitude 360 MHz)
- 7) A 140 (Amplitude 140 MHz)
- 8) A 40 (Amplitude 40 MHz)

9) A 361 (Amplitude 361 MHz)      10) A 141 (Amplitude 141 MHz)  
11) 1 hour markers                    12) 10 minute markers

Chart speed was 1 mm/sec. All channels have a chart width of 20 mm except channel 1 that has 40 mm chart width. Time is increasing from right to left.

Resolution of the channels:

1) DD 40	0°	... 360°	90°/mm	2) DD 140	0°	... 360°	18°/mm
3) GD 41	0°	... 360°	18°/mm	4) GD 141	0°	... 360°	18°/mm
5) F 140	0°	... 180°	9°/mm	6) A 360	22	... 28 dB	0.3 dB/mm
7) A 140	24	... 36 dB	0.6 dB/mm	8) A 40	15	... 45 dB	1.5 dB/mm
9) A 361	22	... 28 dB	0.3 dB/mm	10) A 141	24	... 36 dB	0.6 dB/mm

The quasiperiodic fluctuations follow a time period when most channels show fairly strong variations (scintillations). Between 0944 UT and 0947 UT about 20 periods at DD40, GD41, and A40 are visible with a decreasing period duration from 14 sec. to 5 sec. They are followed by several further wave trains with periods between 3 and 4 sec.

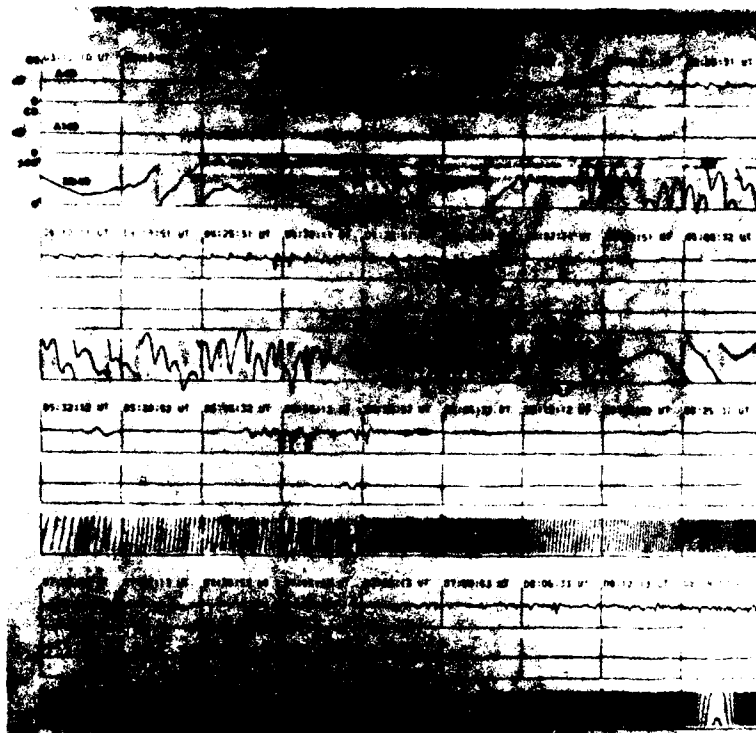


Figure 7: Quasiperiodic oscillations of the carrier phase  
(dispersive doppler) measurements at 40 MHz (DD40)

Fig. 7 shows a portion of a plot obtained from a digital recording taken

at Nov 18, 1975 at Gillersheim between 0312 UT and 0512 UT. The sampling rate was 0.1 sec for A40, A140, and DD40. Between 0340 UT and 0450 UT quasiperiodic (sinusoidal) oscillations are to be seen at DD40 with periods of about 1 min. duration. The corresponding A40 channel shows quasiperiodic fluctuations which are different from these at DD40. We see that phase and amplitude measurements do not necessarily give always the same information. The lower portion of fig.7 shows also other types of fluctuations between 0530 UT and 0630 UT and between 0725 UT and 0825 UT. These fluctuations are nonperiodic and are normally called scintillations.[17],[18].

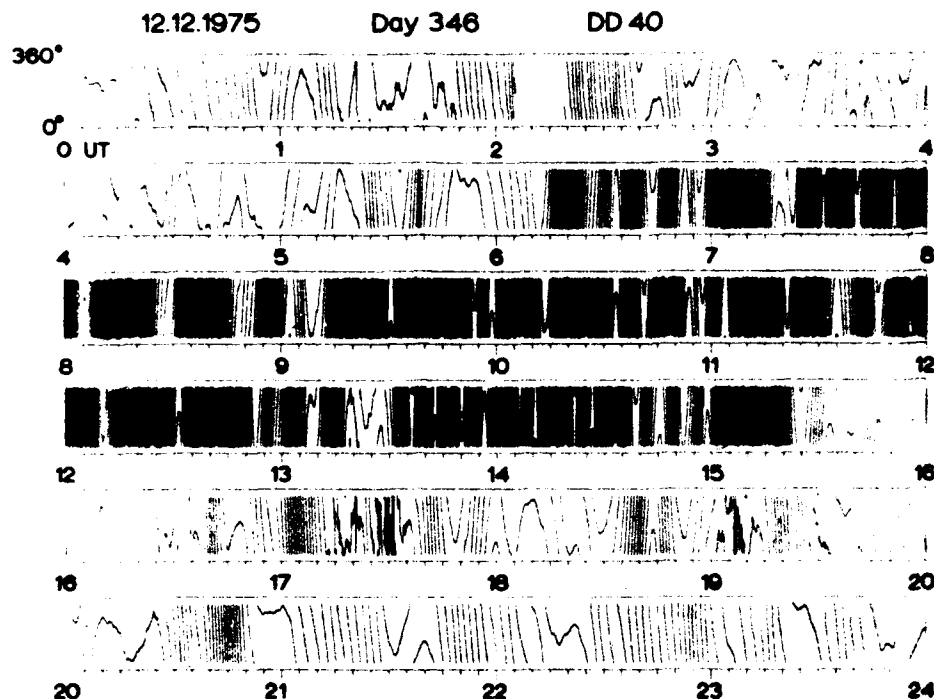


Figure 8: DD40 variations at Gillersheim

B) Long-periodic fluctuations with periods more than five minutes

Figure 8 shows the DD40 variations between 0 and  $2\pi$  on Dec. 12, 1975 between 0000 UT and 2400 UT. The variations of DD40 produce a density modulation as a function of time. Its meaning is shown in the next figure.

Figure 9 shows the DD40 variations between 0 and  $2\pi$  on Dec. 12, 1975 between 0800 UT and 1600 UT. Simultaneously the number of integer  $2\pi$  changes of DD40 is displayed together with 1/2 hour mean values and 2 hour mean values to work out the shorter and longer periodic fluctuations superimposed on the daily TEC variations. It can be seen how the density fluctuations of the DD40 variations correspond with the short period fluctuations displayed by the  $2\pi$  changes.

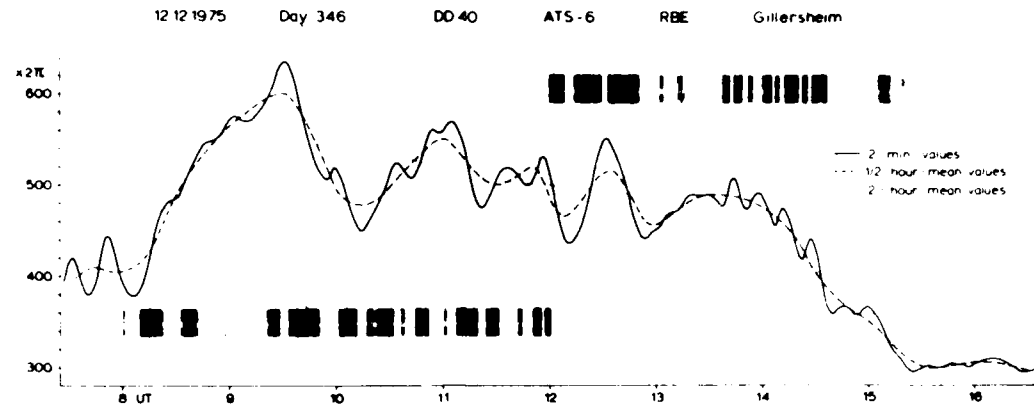


Figure 9: DD40 variations in two different presentations

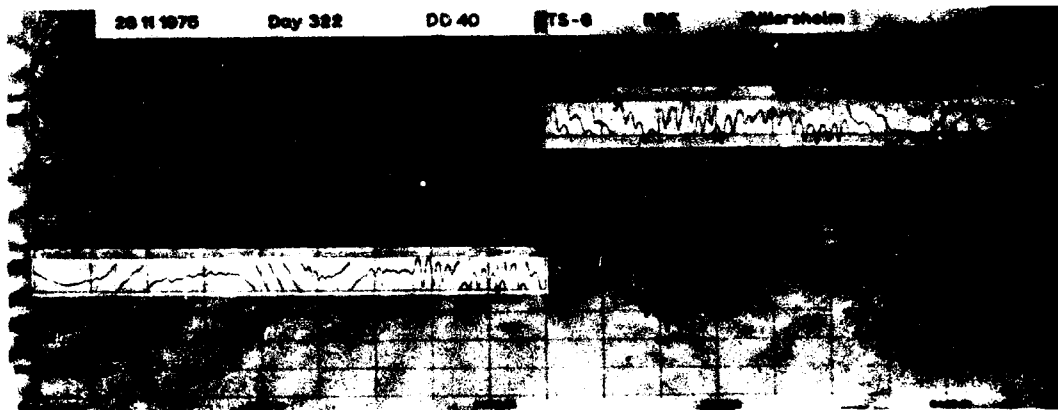


Figure 10: DD40 nighttime variations in two different presentations

Figure 10 shows the DD40 data from fig. 7 (Nov. 28, 1975) in a different presentation. It can be seen that the 1 minute oscillations are superimposed on longer periodic TEC variations with a period of about 30 minutes, which are very likely caused by gravity waves [12] and which are only clearly visible at DD40, due to the very high resolution of the dispersive doppler effect DD40 (carrier phase) as compared to F140 and GD141 etc. This is just one example out of many.

#### Acknowledgement

The authors thank the staff at the field site of the MPI f. Aeronomie at Gillersheim for the operation of the equipment and for the valuable

help in the analysis of data. We extend our thanks to the computing center staff at the MPI f. Aeronomie at Lindau for the help with the digital data processing and display. The MPI research program was supported by research grant Di 32/33 from the Deutsche Forschungsgemeinschaft.

#### References

- [1] ATS-6 "Applications Technology Satellite -6", IEEE Transaction on Aerospace and Electronic Systems, vol AES 11, no 6, pp 981-1206, 1975
- [2] Barrett, L.  
Hartmann, G.K.  
Leo, R.L.  
Weiß, W.  
Zwick, R.  
"Tropospheric irregularity effects on the 360 MHz ATS-6 Radio Beacon". Submitted for publication to Radio Science, 1975
- [3] Becker, H.  
Engelhardt, W.  
Eulig, K.O.  
Fuhrmann, W.D.  
v.d.Grinten, H.J.  
Güttler, W.  
Hartmann, G.K.  
Loidl, A.  
Schmidt, G.  
Weiß, W.  
Zwick, R.  
"MEPOL Empfangsanlage"  
MPI f. Aeronomie, Interne Bericht,  
Mai 1975
- [4] Campbell, W.H.  
"Geomagnetic pulsations, chapter N-3" in:  
Physics of Geomagnetic Phenomena, eds.  
S. Matsushita and W.H. Campbell, pp 821-909,  
New York, Academic Press, 1967
- [5] Davies, K.  
Fritz, R.B.  
Grubb, R.N.  
Jones, J.E.  
"The ATS-F/G radio beacon experiments"  
J. Environ. Sci. XV, (2), pp 31-35, 1972
- [6] Davies, K.  
Fritz, R.B.  
Grubb, R.N.  
Jones, J.E.  
"ATS-6 Radio Beacon Experiment. The first year".  
IEEE Transactions AES-11, no 6, p.1103-1109,  
1975
- [7] Davies, K.  
Hartmann, G.K.  
"The NOAA/MPI observation program for the ATS-6  
radio beacon experiment". Proc. of Symp. of  
COSPAR Beacon Satellite Group, Moscow, USSR,  
Nov. 1974. 1975a
- [8] Davies, K.  
Hartmann, G.K.  
"Kurzperiodische Schwanungen im totalen Elek-  
troneninhalt". Kleinheubacher Tagung im Okt.75.  
Kleinheubacher Berichte, Nr.19, im Druck  
1975b

- [9] Davies, K.  
Fritz, R.B.  
Grubb, R.N.  
Jones, J.E. "Some early results from the ATS-6 Radio Beacon Experiment". Radio Science, vol 10, no 8, 9, pp 785-799, 1975c
- [10] Davies, K.  
Fritz, R.B.  
Gray, T.B. "Measurements of the columnar electron contents of the ionosphere and plasmasphere". Manuscript no IPA-75-16, NOAA ERL, Boulder, Colo.80302, USA, 1975d
- [11] Davies, K.  
Hartmann, G.K. "Short Period Fluctuations in total Columnar Electron Content. To be published in J.Geophys.Res.1976
- [12] Dieminger, W.  
Hartmann, G.K.  
Schmidt, G.  
Schödel, J.P. "Recording gravity waves by means of geostationary beacon satellites". J.Atmos. Terr. Phys., vol 32, pp 1615-1617, 1970
- [13] Engelhardt,W.  
Hartmann, G.K. "Dispersion measurements of one element Short Back-fire (SBF) antennas". IEEE APS, vol Ap - 23, no 2, pp 289-293, 1975
- [14] Fuhrmann, W.D.  
Tyagi, T.R. "The 140 MHz ATS-6 Radio Receiving System". To be published in Indian Journal of Radio & Space Physics, in 1976. 1975
- [15] Garriott, O.K.  
Risbeth, H. "Relationship between simultaneous Geomagnetic and Ionospheric Oscillations". Radio Science, vol.68D, no 3, pp 339-343. 1964
- [16] Hartmann, G.K. "Tropospheric diffraction phenomena of radio signals from the beacon satellite Explorer 22".J.Atmos. Terr.Phys., vol31, p 663-669. 1969
- [17] Hartmann, G.K. "HF and UHF propagation studies of the midlatitude ionosphere"(Review). Ann.Geophys.,vol 31, 1, pp 39-52. 1975a
- [18] Hartmann,G.K. "Amplitude and phase scintillations with the ATS-6 RBE". Presented at USNC/URSI Meeting, Oct.20-24, 1975, Colorado Univ.at Boulder, USA. 1975b
- [19] NASA GSFC "The ATS-F Data Book". Goddard Space Flight Center, Greenbelt, Maryland 20771. 1974
- [20] Schmidt, G.  
Weiß, W.  
Zwick, R. "Mehrfrequenzempfangsanlage zur Messung der Phasenbeziehung von Satellitensignalen". Erscheint in NTZ 1976. 1975

MULTI-STATION INVESTIGATIONS OF LOW LATITUDE IONOSPHERE USING  
LOW ORBITING AND GEOSTATIONARY SATELLITES

by

M.R. Deshpande<sup>1</sup>, R.G. Rastogi<sup>1</sup>, R.V. Bhonsle<sup>1</sup>, H.S. Sawant<sup>1</sup>,  
K.N. Iyer<sup>1</sup>, Banshi Dhar<sup>1</sup>, A.V. Janve<sup>2</sup>, R.K. Rai<sup>2</sup>, Malkiat  
Singh<sup>3</sup>, H.S. Gurm<sup>3</sup>, A.R. Jain<sup>4</sup>, B.N. Bhargava<sup>4</sup>, V.M. Patwari<sup>5</sup>,  
and B.S. Subbarao<sup>5</sup>.

ABSTRACT

Some investigations of low latitude Ionospheric Total Electron Content (TEC) in Indian zone using BE-B, BE-C, and ATS-6 satellites are reported in this paper. The results may be summarized as follows:

(1) Integrated production rates at Ahmedabad (dip 34°N) calculated from the mean daily curves of TEC obtained from BE-B and BE-C satellites show a semiannual variation with equinoctial peaks and increase linearly with 10.7 cm solar flux.

(2) The effective loss coefficient in the F region also shows a seasonal variation with larger values around equinoxes and lesser values around solstices.

(3) A conclusive evidence for the effectiveness of blanketing type of sporadic E in producing satellite signal scintillations is presented.

(4) TEC over the Indian sub-continent using ATS-6 measurements is studied. Equatorial anomaly in TEC is described.

(5) Occurrence of Traveling Ionospheric Disturbances (TID's) and their movements are investigated using the network of stations in India. TID's move north-eastward in morning hours and reverse in the afternoon, with a speed of about 50 m/sec. The time of occurrence, amplitude and period of TID's are also studied.

(6) A time sharing radio polarimeter and Dicke switched radiometer were used to record ATS-6 signals at 40 and 860 MHz at Ahmedabad. Observation of scintillations at both frequencies, on a few occasions, is reported.

INTRODUCTION

For more than a decade, using low orbiting satellites at an altitude of about 1000, Total Electron Content (TEC) of the Ionosphere has been studied at high, middle and low latitudes. Although such satellites are superior in respect of study of spatial variations, they lack the continuity of observations and time resolution. Geostationary satellites have been used at a number of middle and high latitude stations to study the TEC (Garriott et al. 1965, Titheridge 1966 and Mendillo et al.

- 
1. Physical Research Laboratory, Ahmedabad 380 009, India.
  2. University of Udaipur, Udaipur 313 001, India.
  3. Punjabi University, Patiala 147 022, India.
  4. Indian Institute of Geomagnetism, Bombay 400 005, India.
  5. A.V. Parekh Technical Institute, Rajkot 360 001, India.

1970). At low and equatorial latitudes relatively sparse measurements using such satellites have been made and these are mainly again in African and American sectors (Garriott et al. 1965, Yuen and Roclofs 1967 and Yeboah-Amankwah and Koster 1972). With the positioning of ATS-6 at 35°E longitude in mid 1975, a unique opportunity has arisen to study the equatorial and low latitude in Indian zone ionosphere in order to augment the information obtained from the **S-66** satellite (Basu and Basu 1971, Rastogi and Sharma 1971, Somayajulu et al. 1972 and Rastogi et al. 1973, 1975) and from previous near geostationary satellites that drifted across our longitudes (Basu et al. 1975 and Deshpande and Rastogi 1975). In this paper some new phenomena observed at low and equatorial latitudes are presented using results of ATS-6 satellite at a chain of stations in India and the **S-66** satellite at Ahmedabad, Kodaikanal and Thumba.

#### EXPERIMENTAL SET UP

(a) For S-66 Satellite: The equipment consists of simple half wave dipole antenna at 20 and 40 MHz, followed by preamplifier, receiver and paper chart recorder. All passes of both the satellites BE-B and BE-C were analysed to obtain the Faraday rotation at every minute during the pass at the stations Ahmedabad (dip 34°N), Kodaikanal (dip 3.4°N) and Thumba (dip 0.4°S), all lying around 75°E longitude.

(b) For ATS-S Satellite: Rotating antenna type polarimeters at 140 MHz were set up at Waltair (dip 19°N), Bombay (dip 25°N), Rajkot (dip 33°N), Ahmedabad (dip 34°N), Udaipur (dip 35°N), and Patiala (dip 45°N). At Jaipur (dip 39°N), polarimeter of X, Y component type was set up. In addition a complete ATS-6 receiving system was also set up at Ootacamund (dip 4°N) in collaboration with NOAA, Boulder. The Faraday rotation data is analysed at every 15 minutes for total electron content studies and for special studies like solar flares scaling at every minute or less was used.

#### RESULTS

(a) S-66 Satellite: Detailed study of TEC and equivalent slab-thickness at Ahmedabad for a period covering half a solar cycle from 1964-1969 was done by Rastogi and Sharma (1971). Studies of TEC at Thumba and Kodaikanal did not show the noon bite-out in TEC similar to the one in  $f_0F_2$ ; but the latitudinal variation of TEC obtained by combining the observations at Kodaikanal and Ahmedabad did show the equatorial anomaly in TEC with peak values of EC around 20°N dip latitude (Rastogi et al. 1973, 1975). In this note some of the associated parameters such as integrated production rate for an overhead Sun ( $Q_o$ ), the effective loss rate ( $\beta$ ) are investigated following the method of Garriott and Smith (1965), Titheridge (1966) and Smith (1968). Using the early morning build up rate of TEC, integrated production rate  $Q_o$  is given by  $Q_o = (\partial N_T / \partial t)_{\text{SUNRISE}} \text{Ch}(\chi, H)$  where  $(\partial N_T / \partial t)_{\text{SUNRISE}}$  is the slope of  $N_T$  vs time curve at sunrise and  $\text{CH}(\chi, H)$  is the Chapman function which takes up a value of 15 for a scale height  $H = 50$  km and  $\chi$  between 87° and 93°. From the decay rate of TEC after sunset, the effective loss rate is calculated using the equation

$$(N_T)_t = (N_T)_{\text{SUNSET}} e^{-\beta't} \quad (1)$$

Defining  $t_{\gamma_2}$  as the time required by  $N_T$  to reduce to half its value at sunset (approximately half life) we can write

$$\beta' = \frac{0.693}{t_{\gamma_2}} \quad (2)$$

The seasonal variation of  $Q_0$  obtained separately using the northbound and southbound passes of BE-B and BE-C satellites is shown in Fig.1. A semiannual variation in  $Q_0$  with equinoctial peaks and solstitial minima is clearly seen for all the years 1965 through 1967. This semiannual variation may be explained in terms of semiannual variation of O/N<sub>2</sub> ratio seen by Mayr and Mahajan (1971) of amplitude about 1.5:1.0. Having observations over the period 1964 through 1969, the dependence of  $Q_0$  on solar activity was investigated. The published data of FEC from Delhi is also used in this study.  $Q_0$  shows a linear increase with 10.7 cm solar flux with varying slopes in different seasons which is seen from Fig.2.

The effective loss rate  $\beta'$  was calculated for different months, and average values for the different months are shown in Table 1. It is seen from Table 1 that  $\beta'$  also shows a seasonal variation with summer values around  $0.6 \times 10^{-4} \text{ sec}^{-1}$  and equinoctial values of about  $1.1 \times 10^{-4} \text{ sec}^{-1}$ .

Scintillations are seen at polar latitudes during day and night and are known to be caused by irregular ionization due to charged particle precipitation. At equatorial latitudes Chandra and Rastogi (1974) have shown that scintillations are well correlated with spread F and the night time scintillation belt spreads over 1000 km centered at  $\pm 5^\circ$  from dip equator. In this paper evidence is presented for blanketing type sporadic E patches causing day time scintillations. One such example is shown in Fig.3 where the burst of deep scintillations seen between  $23.4^\circ$  and  $23.7^\circ$  N geographic latitude is caused by the strongly blanketing type Es, of critical frequency more than 7 MHz, recorded in the ionograms shown. This illustrates the effectiveness of sporadic E patches in causing scintillations by day and also shows that the Es patches are much less in horizontal extent (about  $.5^\circ$  of latitude) than spread F clouds.

(b) ATS-6 Satellite: The chain of ATS-6 receiving stations is shown in Fig.4. It can be seen that a latitudinal coverage right from the dip equator (about  $4^\circ$  N) to and beyond the equatorial anomaly region is obtained by this chain of stations.

Contours of constant elevation angles over a grid of latitude versus longitude covering the Indian zone when ATS-6 is at  $35^\circ$  E longitude over the equator are presented in Fig.5. It can be seen that ATS-6 signals can be received at elevation angles between  $42^\circ$  and  $22^\circ$  from the different stations in India. Elevation angle is more dependent on the longitude of the station.

For correlating the TEC data obtained from ATS-6 satellite with other ionospheric data like  $f_0F_2$ , it is necessary to know the sub-ionospheric point where the ray path crosses the ionosphere. This again varies with the height of the ionosphere considered. Therefore we have computed the ionospheric points corresponding to different ionospheric heights from 100 to 500

km in steps of 100 km and these are shown in Fig.6. The projection of the ray from ATS-6 to the different stations is also indicated in the figure.

Another important parameter in deducing TEC from Faraday rotation records is the magnetic field factor  $M = B \cos \theta \sec \chi$ . This is generally computed at a height known as the mean field height. This is generally taken as 400 km for our latitudes. We have the information of ionospheric TEC obtained from previous measurements using BE-B and BE-C satellites. From such known TEC and the computed  $M$  at 400 km height we have calculated the expected Faraday Rotation at Ahmedabad at 40 and 140 MHz for typical solstitial and equinoctial months of low sunspot years. This is shown in Fig.7. For comparison with the actually observed Faraday Rotation, the experimental measurements at Ahmedabad from ATS-6 are also plotted (circles) in the diagram. There is a good agreement between the two. This will also help to remove the  $n \pi$  ambiguity in determining the absolute Faraday rotation at any station.

Typical daily variation of  $\Delta\Omega/\bar{M}$  (proportional to  $\Delta\text{TEC}$ ) are now studied. The normalization with respect to  $\bar{M}$  is done in order to obtain the genuine latitudinal effect due to ionosphere rather than being contaminated by geometrical effects. In Fig.8 a typical plot of  $\Delta\Omega/\bar{M}$  is given for the day 24 October 1975 for 140 MHz, at the different stations Ootacamund, Bombay, Rajkot, Ahmedabad, Udaipur and Patiala. For comparison, we also plot  $f_0F2$  obtained at Ahmedabad. The diurnal maximum is quite flat at Ootacamund. As one goes to high latitudes, the amplitude of the daily curves (and hence the diurnal range of TEC) increases reaching maximum around Ahmedabad and, with further increases of latitude, the diurnal range again decreases. This suggests the equatorial anomaly in the latitudinal variation of TEC.

To further understand the latitudinal variation of TEC, the daily maximum of  $\Delta\Omega/M$  is plotted against the sub-ionospheric dip latitude. It is seen that TEC reaches peak values around  $14^\circ$  dip latitude indicating the presence of Appleton anomaly.

Next we investigate the passage of TID's through Indian sub-continent. Percentage occurrence of TID's at different times of the day at the stations Bombay, Ahmedabad, Udaipur, and Patiala is shown in Fig.10. TID's predominantly occur in daytime with peak occurrence at about 1400 hr LT at all the stations. The period of investigation is from 15 September 1975 to 15 March 1976.

The statistics of the occurrence of TID's with different periods and amplitudes is investigated next. Daytime and night-time cases were separately treated. Histograms of TID periods for the stations Bombay, Ahmedabad, Udaipur, and Patiala are given in Fig. 11, separately for day and night. It can be seen that by day most of the TID's have a period of about 20 minutes in all the stations. At night also a period of about 20-30 minutes is predominant at Bombay, about 10-15 minutes at Ahmedabad and Udaipur and no preferential period at Patiala. The TID amplitude histogram is shown in Fig.12. By day, lower amplitudes of  $\Delta\Omega \sim 10-20^\circ$  is preferred while by night the spread is large except at Ahmedabad where a predominant amplitude of about  $10^\circ$  is seen.

Daily variation of TID period, averaged for the period 15 September 1975 to 15 March 1976, is shown in Figure 13. At all the stations TID's have a period of about 20 minutes, roughly constant throughout the day. The periods seem to increase towards nighttime hours reaching values as large as 60 minutes. These nighttime peaks are more visible at higher latitudes, Patiala and Udaipur, as compared to Ahmedabad and Bombay.

Daily variation of TID amplitude is shown in Fig.14. Nighttime peaks in amplitude are seen at stations Bombay, Ahmedabad, and Udaipur, but not at Patiala. The mean amplitude of TID's is about  $20^\circ$  ( $\Delta\Omega$ ).

From the above studies of TID's the vector velocity of daytime TID's is plotted in Fig.15. It may be noted that TID propagation is dominantly in the northwest or outheast direction during daytime. The median speed is about 70 m/sec.

Vector velocities of nighttime scintillations are shown in Fig. 16. The median speed is found to be about 140 m/sec and the predominant propagation direction of TID's seems to be eastwest.

In addition to these investigations, a time-sharing radio polarimeter was used to measure the Stokes polarization parameters of ATS-6 40 MHz signals. These data contain information regarding the Faraday rotation; typically 30 to 40 rotations from the time of layer-sunrise to that of maximum electron content were observed. This amounts to a total ionospheric electron content of the order of  $4 \times 10^{17}$  electrons/m<sup>2</sup>. There were indications of large-scale ionospheric irregularities manifested by variations in the Faraday rotation rate.

From Fig.17 it can be seen that scintillation is normally weak as seen on the I-channel on 9-1-1976 in the post midnight period. Of particular interest is the evidence that scintillations were seen to start simultaneously with the commencement of a magnetic storm in the presunrise period on 10-1-76. On the following night, strong scintillations with fast fading rates were observed throughout the night. After sunrise on 11-1-76, it is found that the fading rate was considerably reduced.

Table 1  
Effective loss rate at Ahmedabad ( $\beta'$ )  
for different months

Month	$\beta'$
January	0.85
February	1.10
March	1.10
April	0.50
May	0.55
June	0.65

Table 1, Continued

Month	$\beta'$
July	0.90
August	0.95
September	1.10
October	0.65
November	0.63
December	0.60

REFERENCES

- Basu Sunanda and Basu S., J. Geophys. Res., 76, 5337 (1971).  
Basu S., Guhathakurta B.K., Bhattacharyya G.N. and Das Gupta A., Proc. Symposium on Beacon Satellite Investigations of Ionosphere Structure and ATS-6 Data, Moscow, I, 210 (1975).  
Chandra H. and Rastogi R.G., Curr. Sci., 43, 567, (1974).  
Deshpande M.R. and Rastogi R.G., Proc. Symposium on Beacon Satellite Investigations of Ionosphere Structure and ATS-6 Data, Moscow, I, 221 (1975).  
Garriott O.K. and Smith F.L., Planet. Space Sci., 13, 839(1965).  
Garriott O.K., Smith F.L. and Yuen P.C., Planet. Space Sci., 13, 829 (1965).  
Mayr H.G. and Mahajan K.K., J. Geophys. Res., 76, 1017 (1971).  
Mendillo M., Papagiannis M.D. and Klobuchar J.A., Rad. Sci., 5, 895, (1970).  
Rastogi R.G. and Sharma R.P., Planet. Space Sci., 19, 1505 (1971).  
Rastogi R.G., Sharma R.P. and Shodhan V., Planet Space Sci., 21, 713 (1973).  
Rastogi R.G., Iyer K.N. and Bhattacharyya J.C., Curr. Sci., 44, 531 (1975).  
Smith III, J. Geophys. Res., 73, 7385 (1968).  
Somayajulu Y.V., Tyagi T.R. and Nagi N.K., Ind. J. Rad. Space Phys., 1, 62 (1972).  
Titheridge J.E., J. Atmos. Terr. Phys., 28, 1135 (1966).  
Yuen P.C. and Roclofs, J.H., J. Atmos. Terr. Phys., 29, 321 (1967).  
Yeboah-Amankwah and Koster, J.R., Planet. Space Sci., 20, 395 (1972).

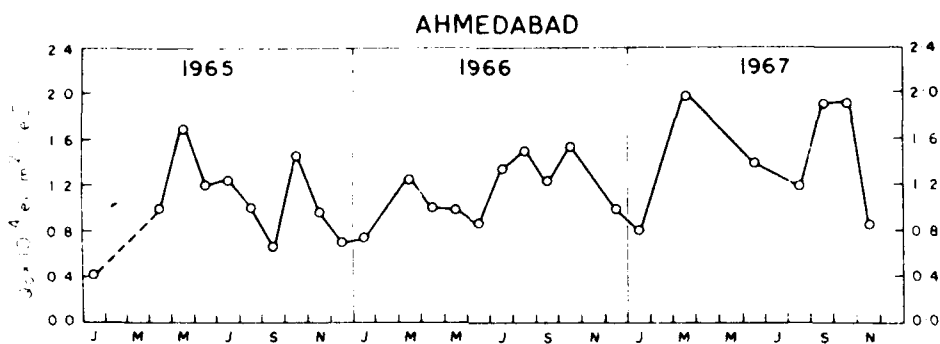


Figure 1 : Seasonal variation of integrated production rate ( $Q_o$ ) at Ahmedabad.

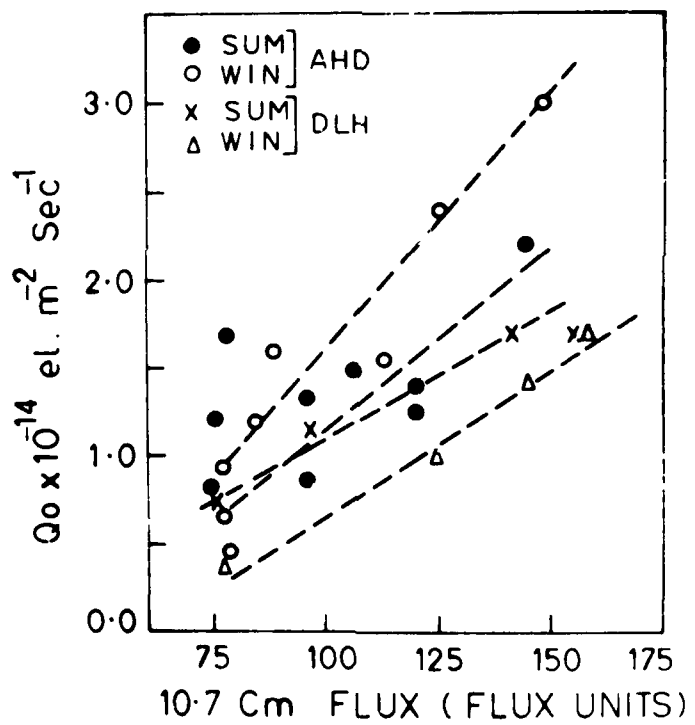
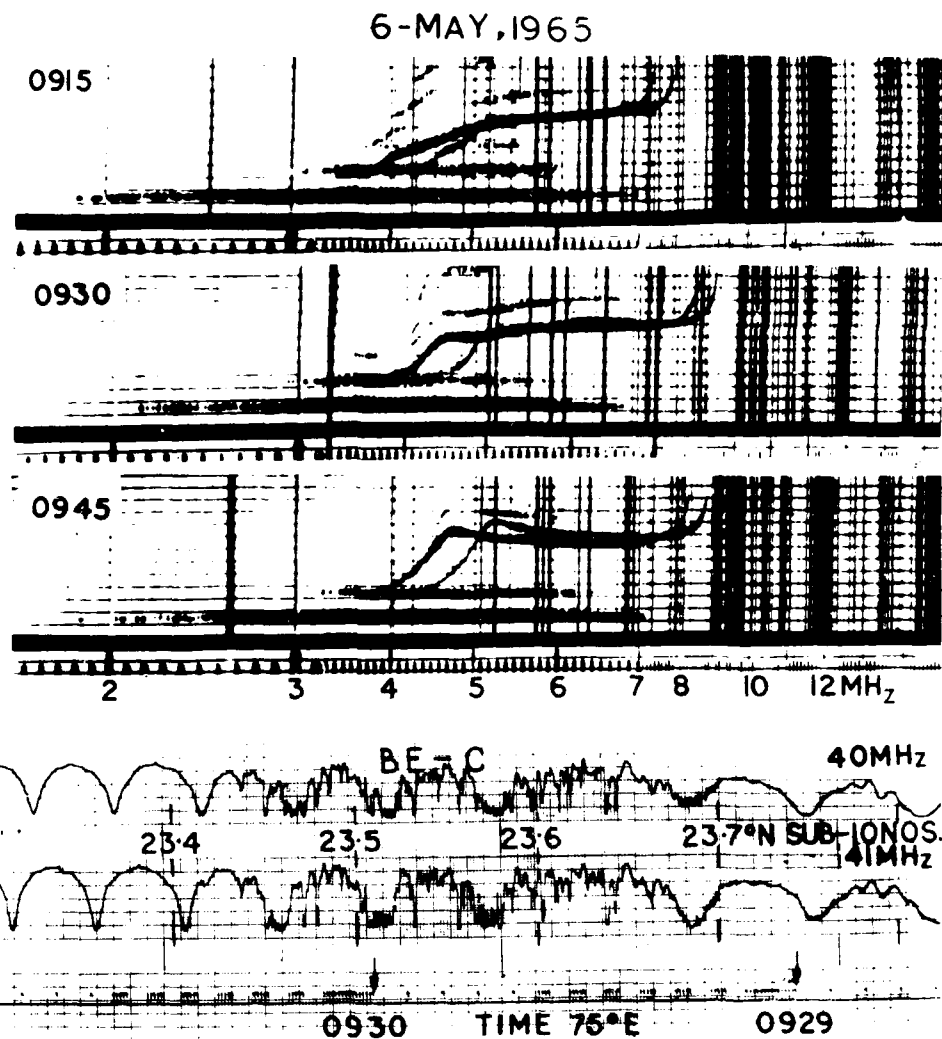
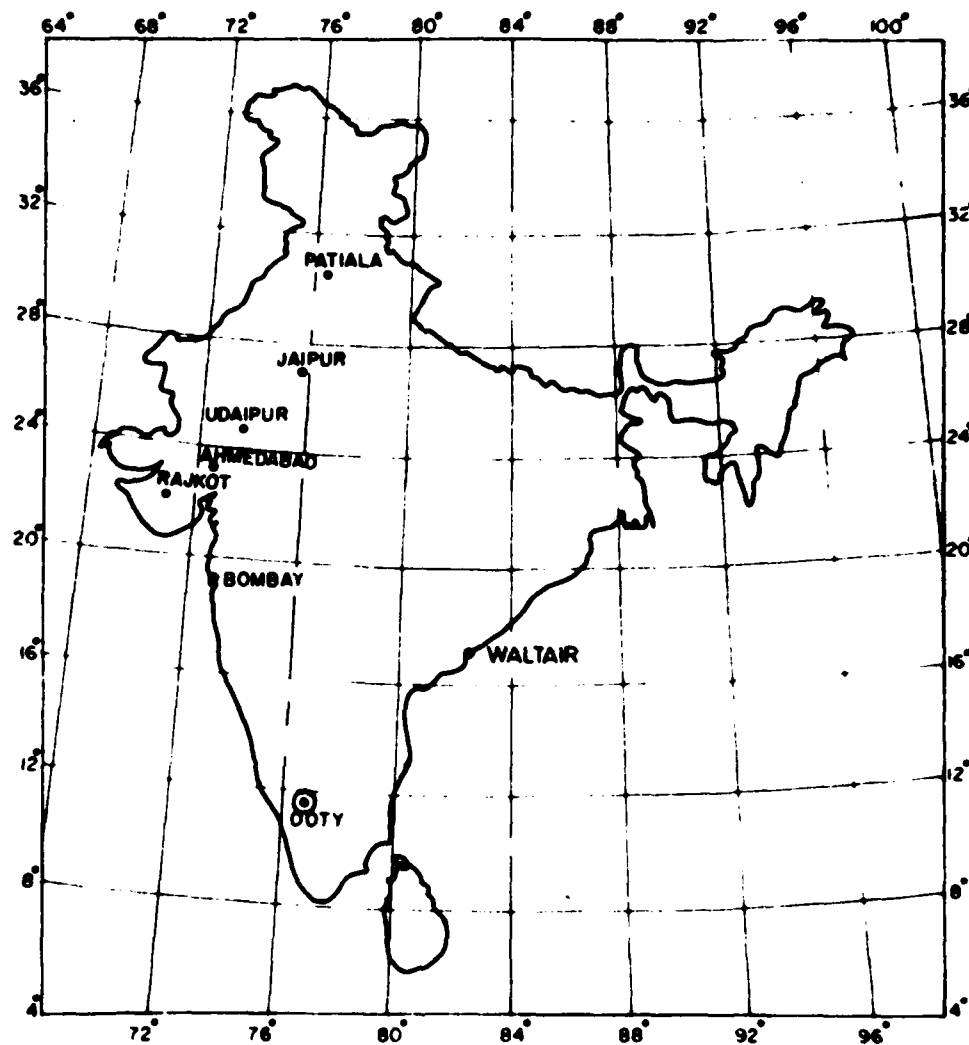


Figure 2 : Variation of integrated production rate ( $Q_o$ ) with 10.7 cm solar flux.



**Figure 3 :** Faraday rotation records at 40 and 41 MHz at Ahmedabad on 6 May 1965 showing burst of scintillations between 0929 and 0930 hr 75° EMT. Ionograms taken at Ahmedabad at 0915, 0930 and 0945 hr 75° EMT are also shown. Intense sporadic E seen on the ionograms is the cause of these scintillations.



**Figure 4 : Map of India showing locations of ATS-6 radio beacon experiment.**

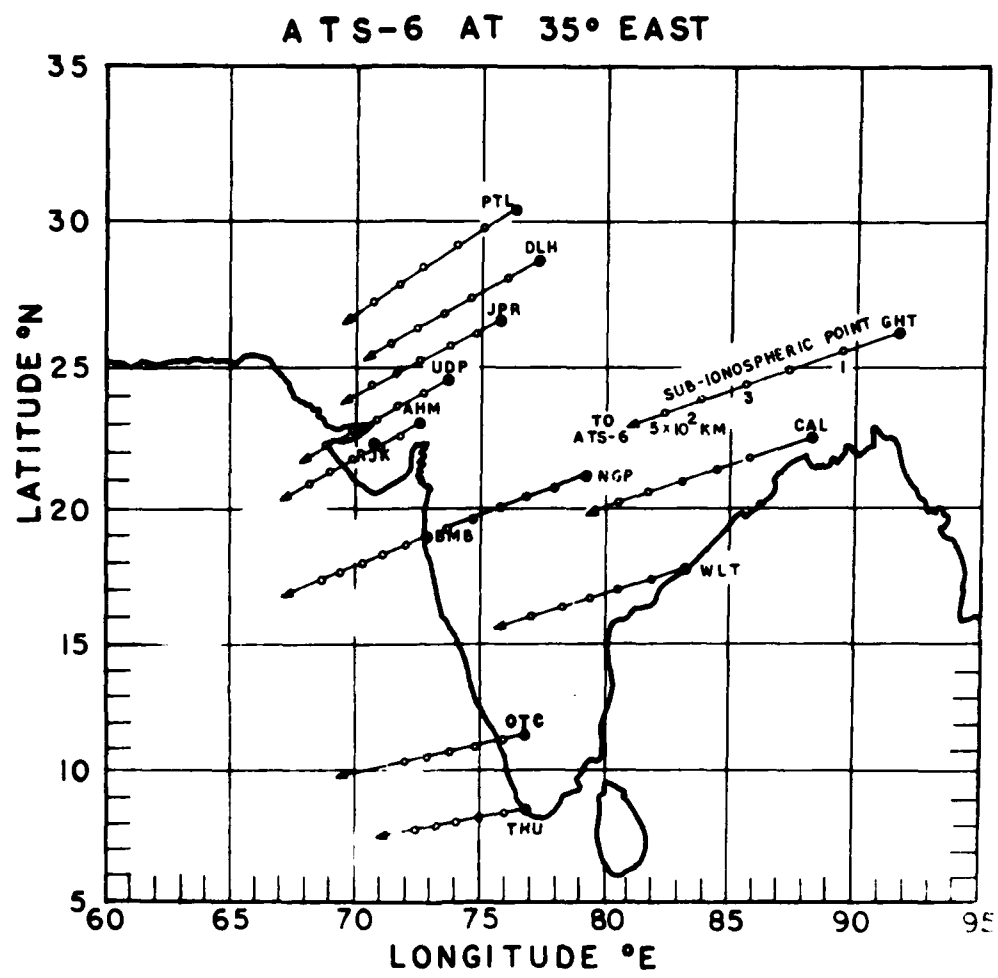


Figure 6 : ATS-6 ray directions to different receiving stations, the sub-ionospheric points for ionospheric height of 100 to 500 kms at intervals of 100 kms are also shown.

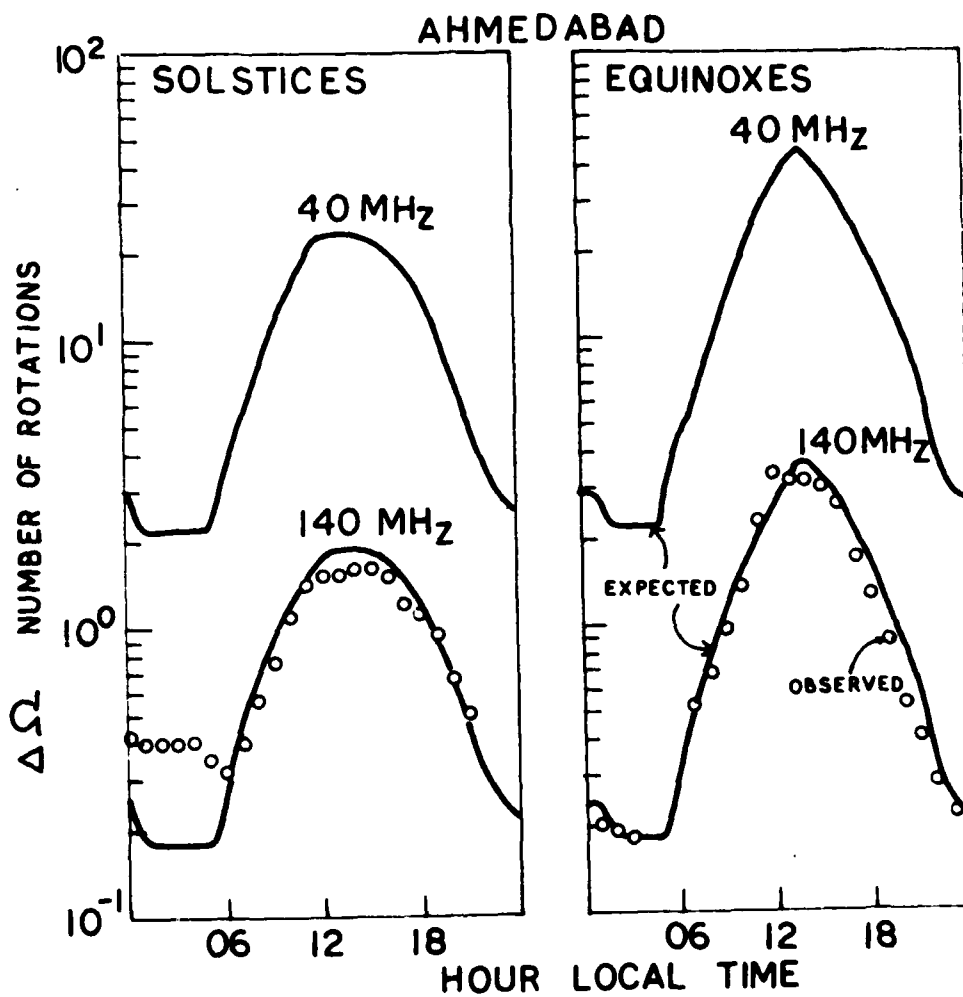


Figure 7 : Faraday rotation of 40 and 140 MHz signals from ATS-6 at Ahmedabad for solstices and equinoxes of low sunspot period. Full lines are the computed Faraday rotation using B-E-B results of TEC and M computed at 400 km altitude. 'O' indicates measured Faraday rotation from ATS-6 at Ahmedabad.

ATS-6 140 MHz  
24-OCTOBER, 1975

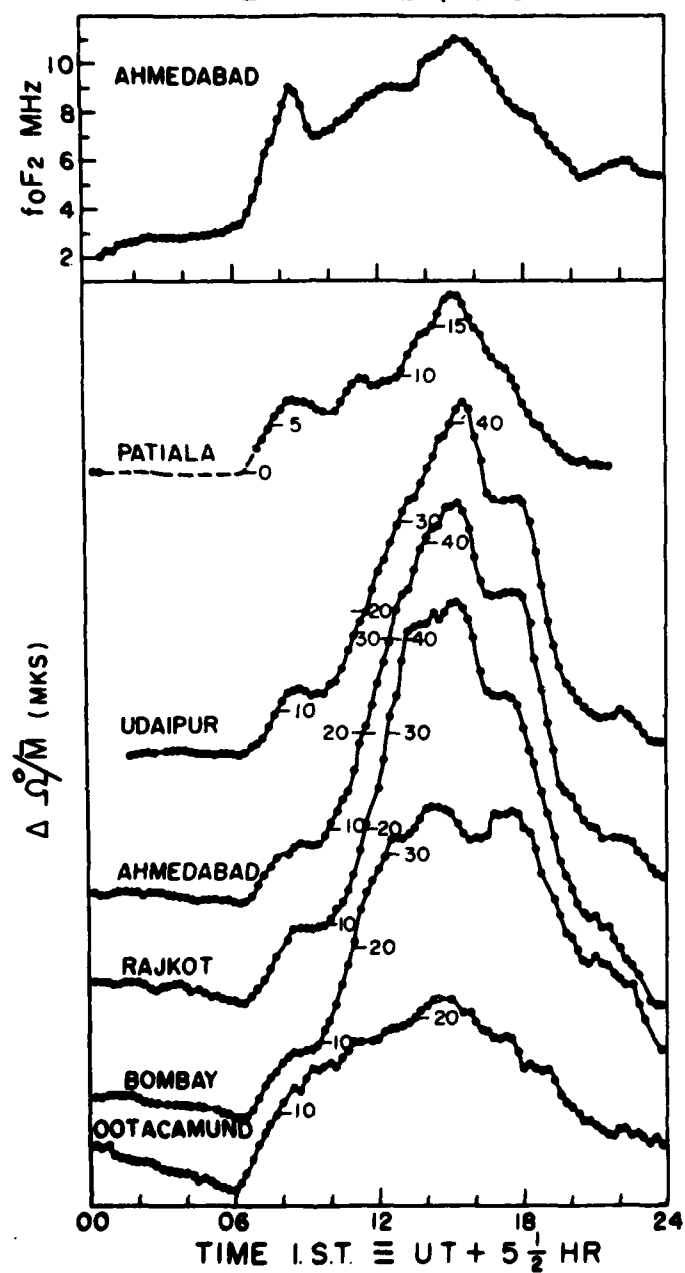


Figure 8 : Daily variations of  $\Delta \Omega^{\circ}/M$  at Ootacamund, Bombay, Rajkot, Ahmedabad, Udaipur and Patiala, and foF<sub>2</sub> at Ahmedabad on 24 October 1975.

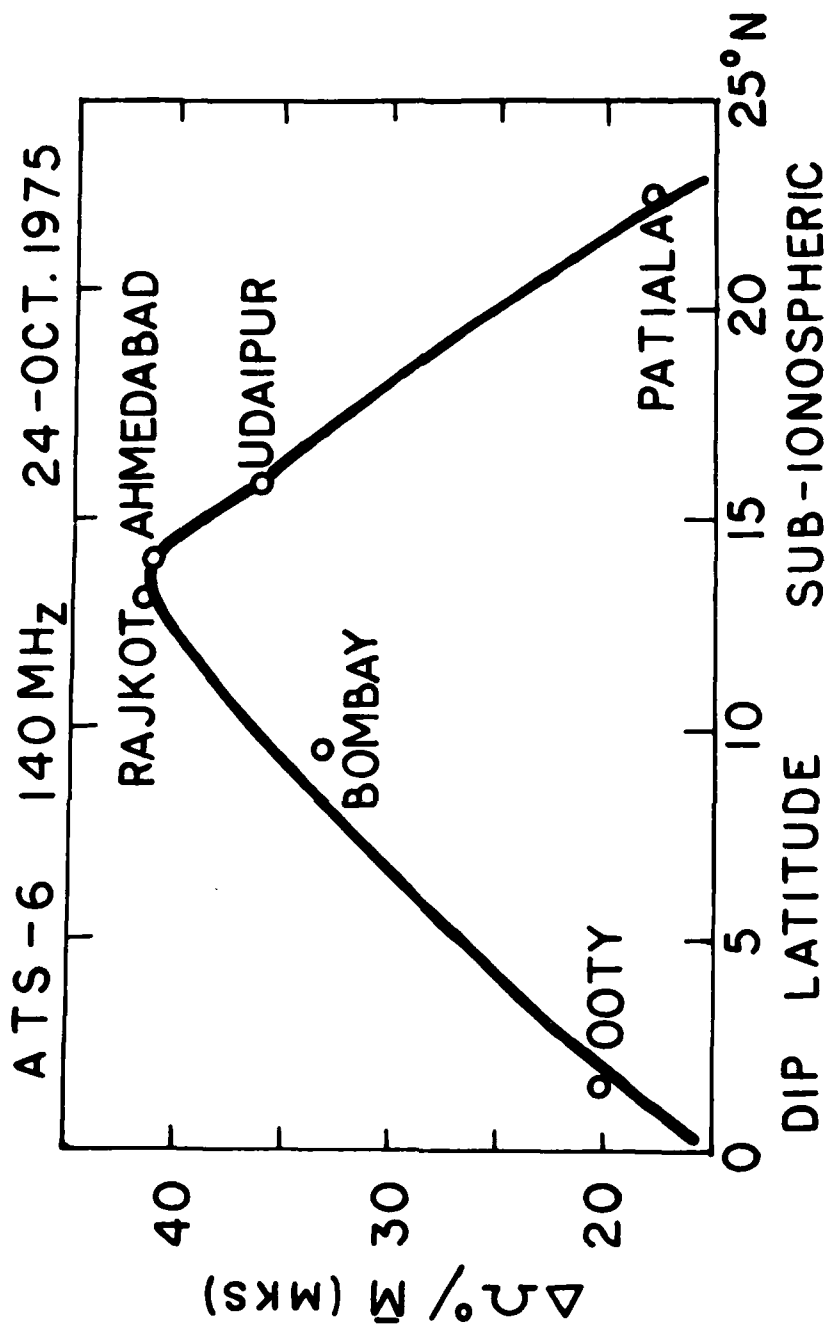


Figure 9 : Latitudinal variation of  $\Delta\Omega_0/\Delta M$  showing the equatorial ionospheric anomaly in  $\text{TEC}$  on 24 October 1975.

DAILY VARIATION OF THE OCCURRENCE OF TID

ATS-6, 140 MHz

15-SEP, 1975 TO 15-MARCH, 1976

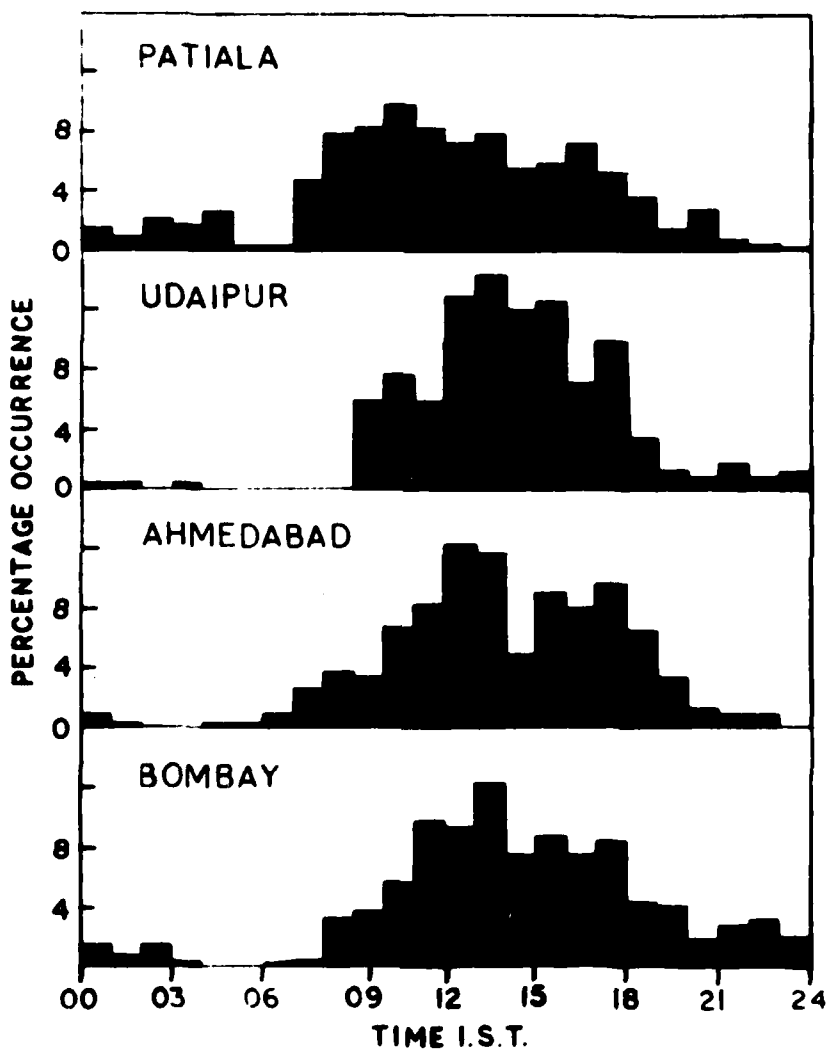


Figure 10 : Daily variation of occurrence of TID at Bombay, Ahmedabad, Udaipur and Patiala.

**ATS-6, 140MHz TID**  
**15-SEP,1975 TO 15-MARCH,1976**

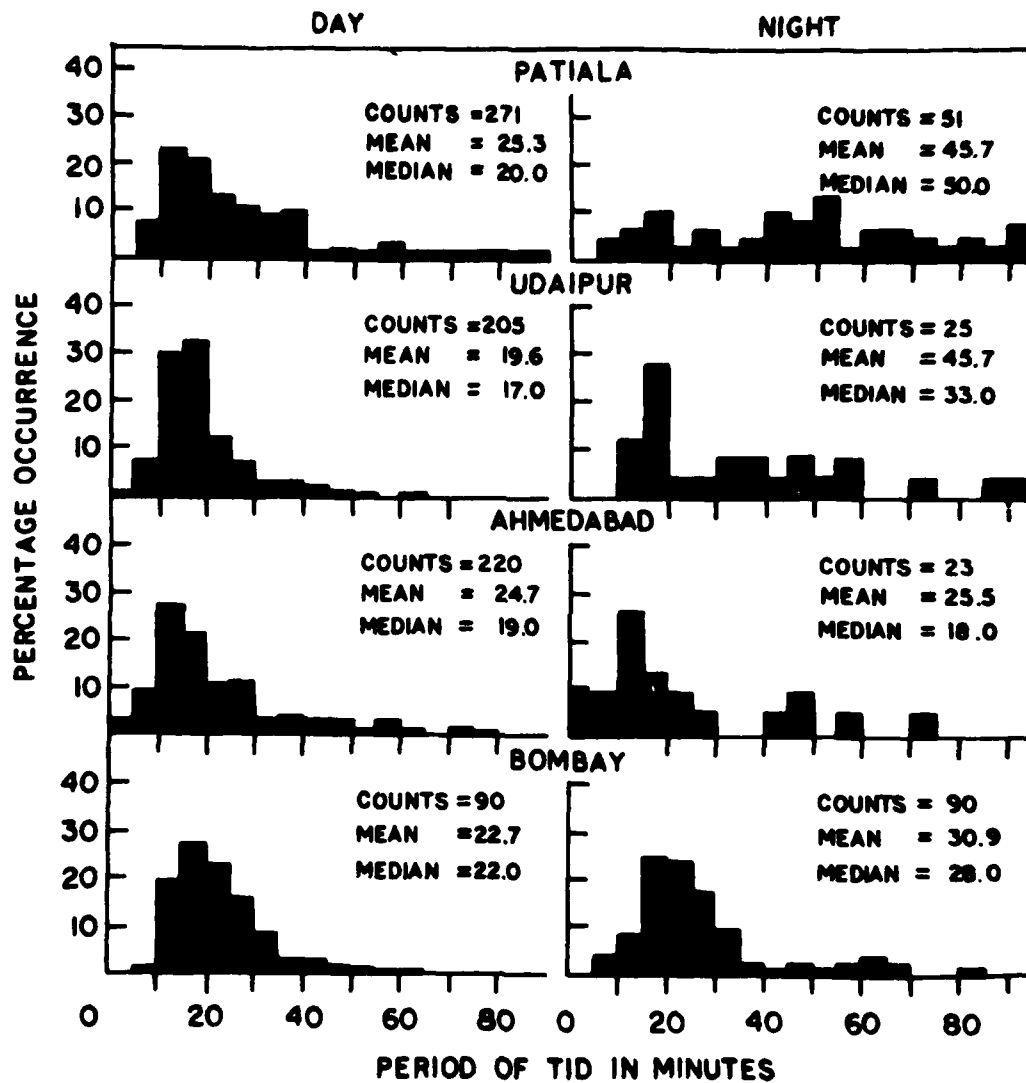


Figure 11 : Histogram of TID period at Bombay, Ahmedabad, Udaipur and Patiala.

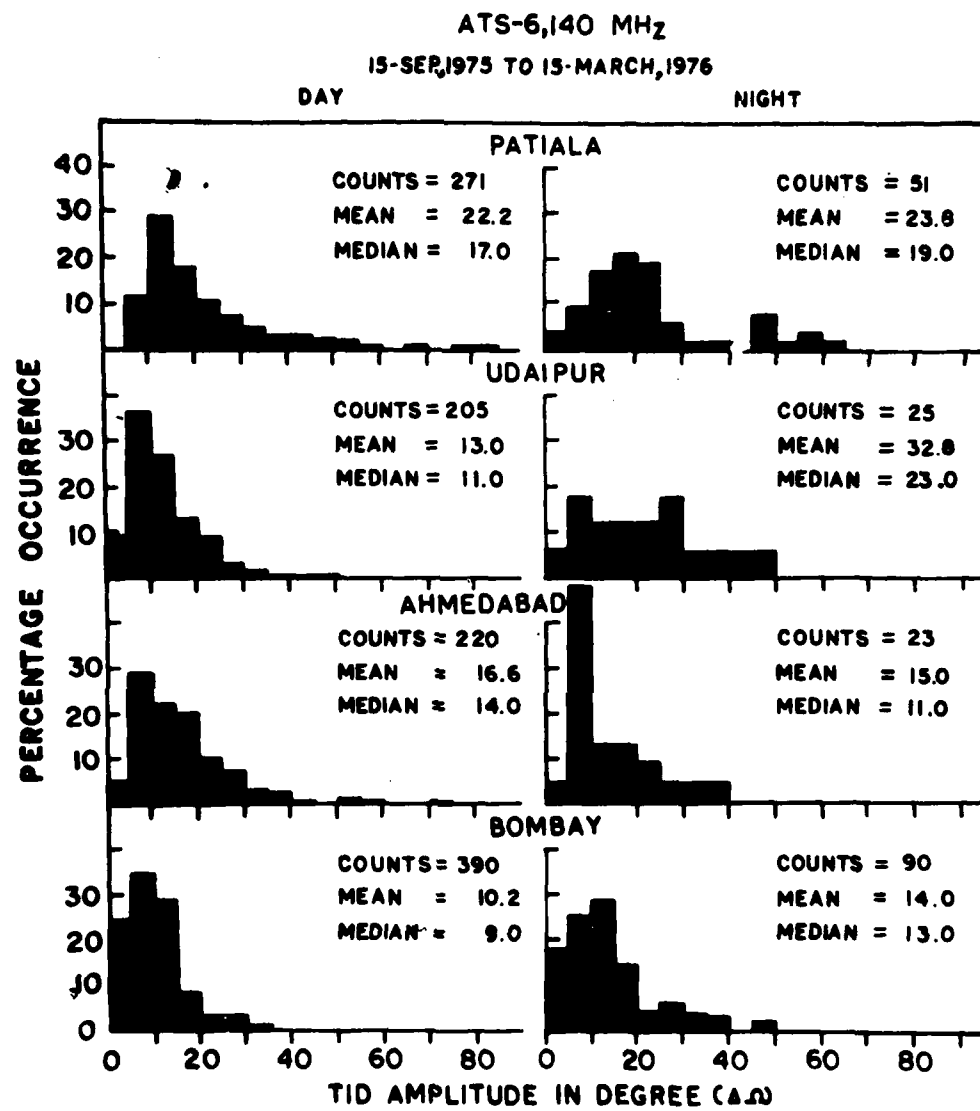


Figure 12 : Histogram of TID amplitude at Bombay, Ahmedabad, Udaipur and Patiala.

**ATS-6 140 MHz**  
**MEAN DAILY VARIATION OF TID PERIOD**  
**15-SEP.,1975-15-MAR.,1976**

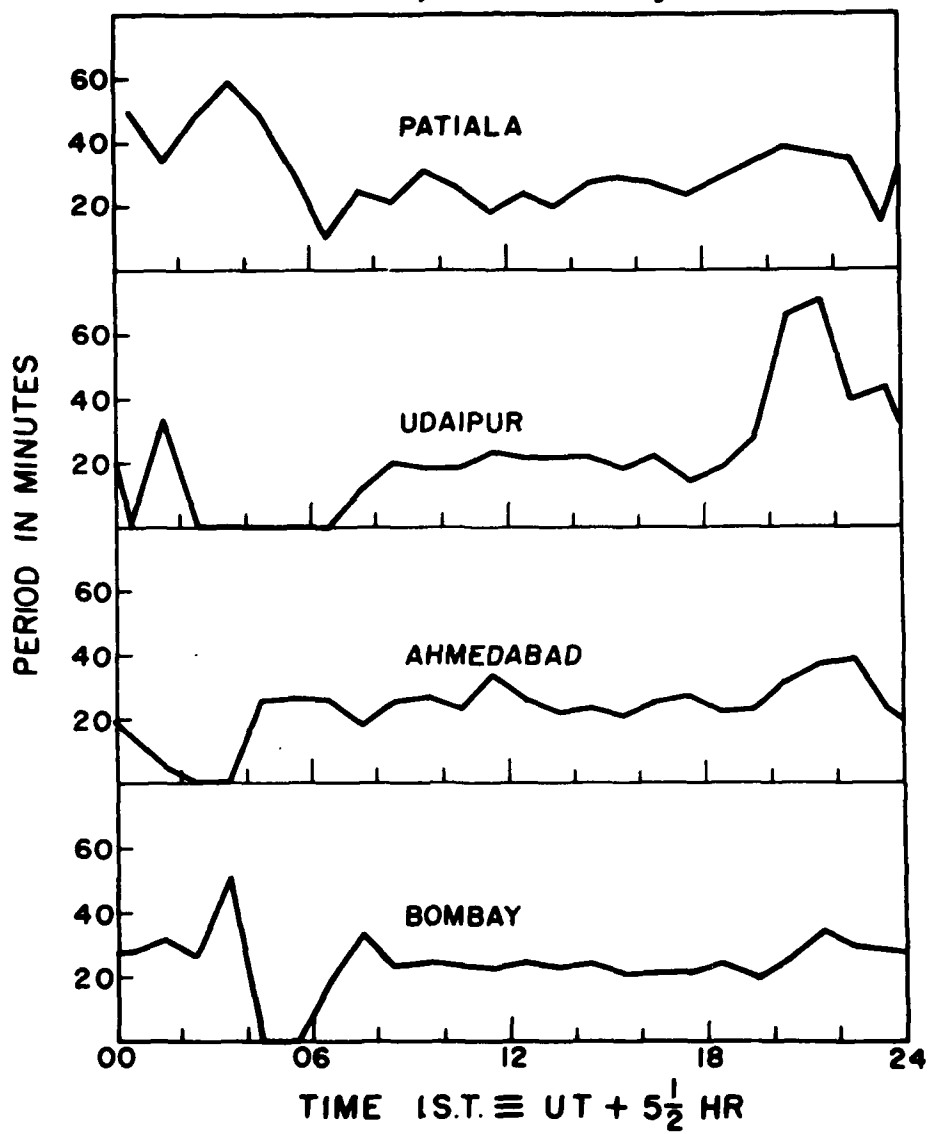


Figure 13 : Daily variation of TID period at Bombay,  
Ahmedabad, Udaipur and Patiala.

DAILY VARIATION OF ( $\Delta\Omega$ ) OF TID

ATS-6, 140 MHz

15-SEP., 1975 TO 15-MARCH, 1976

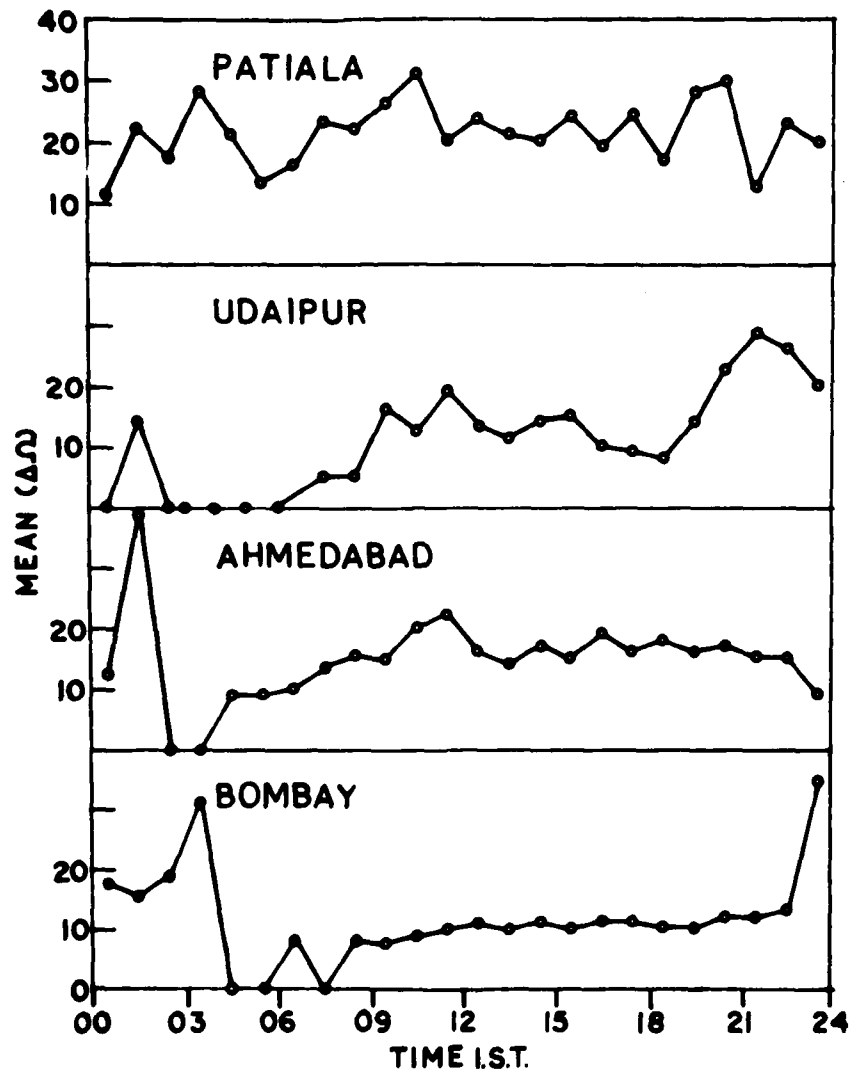


Figure 14 : Daily variation of TID amplitude at Bombay, Ahmedabad, Udaipur and Patiala.

ATS - 6 140 MHz  
TID VELOCITY VECTOR  
15-SEP.,1975—15-MAR.,1976

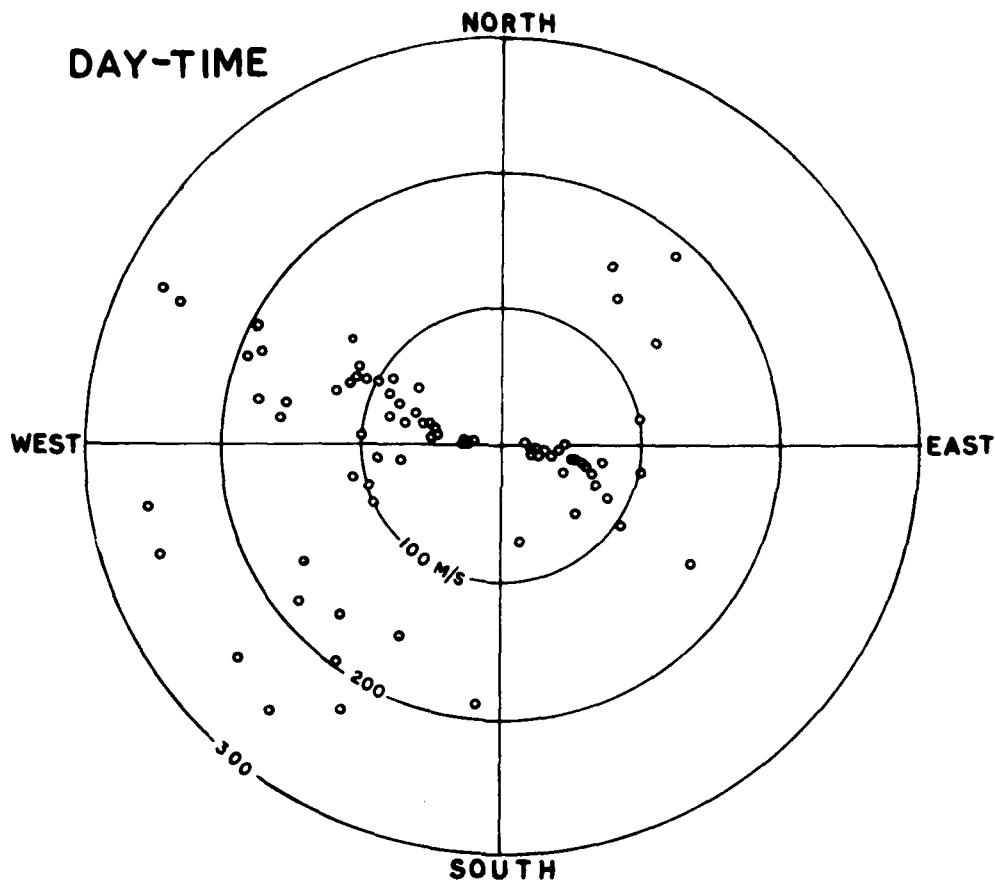


Figure 15 : Polar diagram of TID velocity vector during daytime hours.

ATS-6, 140 MHz  
TID VELOCITY VECTOR  
15 SEP., 1975 - 15 MAR., 1976

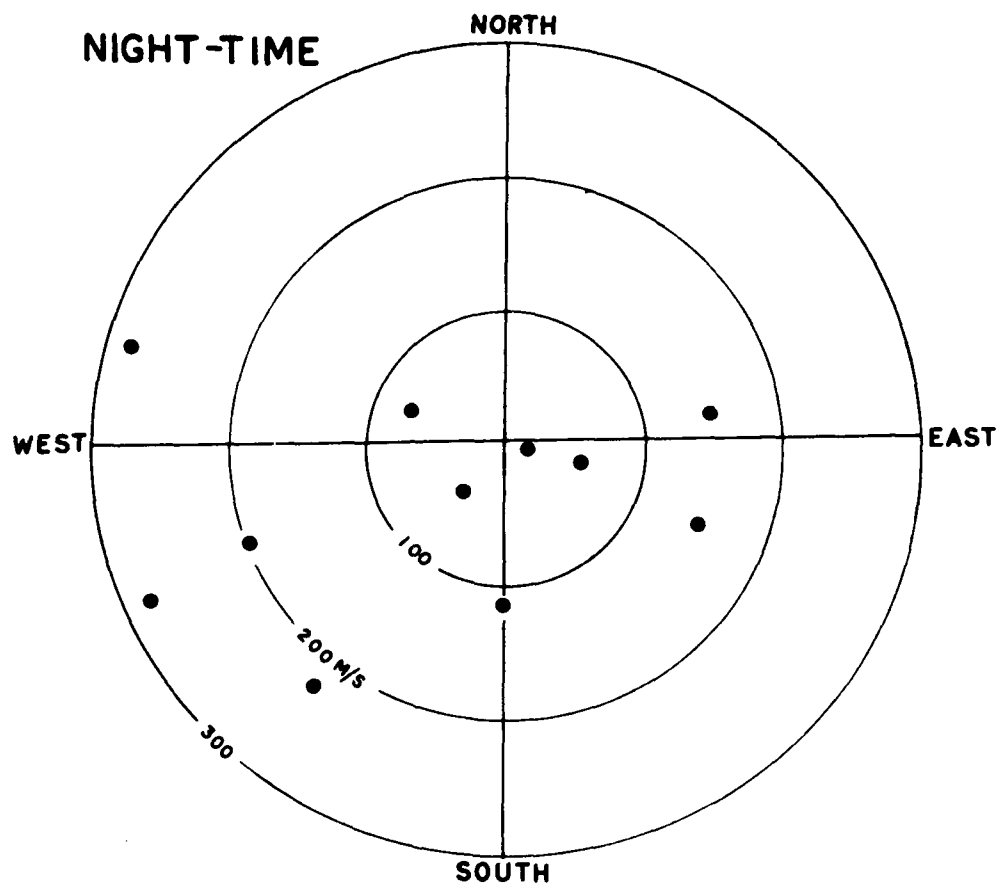
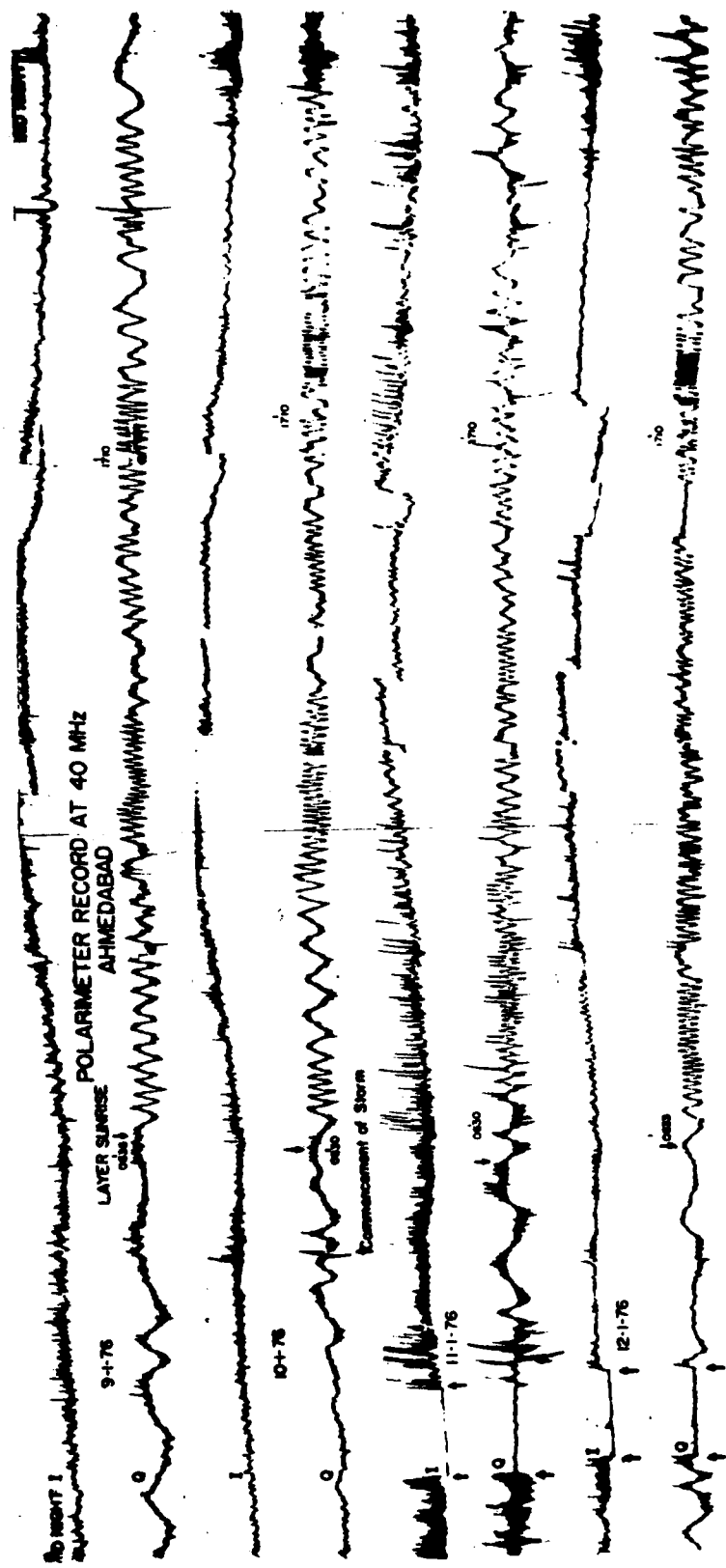


Figure 16 : Polar diagram of TID velocities vector during nighttime hours.



288

Figure 17 : 40 MHz polarimeter record at Ahmedabad from 9-1-76 to 12-1-76 indicating the onset of scintillation simultaneous with the commencement of geomagnetic storm on 10.1.76.

MEASUREMENTS OF EQUATORIAL IONOSPHERE IRREGULARITIES WITH THE  
IROE MULTIFREQUENCY RECEIVING STATION AT SAN MARCO RANGE IN  
KENYA

F.Bertini, M.T.de Giorgio, P.F.Pellegrini  
Istituto di Ricerca sulle Onde Elettromagnetiche, C.N.R.  
Firenze, Italy

P.Bruscaglioni, G.Fiori  
Università degli Studi, Firenze, Italy

During the periods December 74 January 75 and July 75 September 75, a receiving station, assembled at IROE was used at the Italian Equatorial Range San Marco in Kenya ( $40^{\circ}11,4'E$ ,  $2^{\circ}59,6'S$ ) to receive the signals of the orbiting satellites Intasat and Intercosmos 12 and of the ATS-6 geostationary satellite.

The station is assembled in a standard container and can receive simultaneously the signals from the satellites, through a group of different antennas. A cross dipole was used for the 40 MHz band. A 4 cross Yagi (6 elements) antenna was used for the 140 MHz band. A 6 cross Yagi (8 elements) antenna was used for the 360 MHz band.

Figure 1 shows the block diagram of the station. A single reference oscillator at 1 MHz is the basis of the whole RF section, which is completely synthesized. A computer (HP 2100A) controls the operation of two RF receivers with respect to frequency, bandwidth, gain and choice of the receiving mode.

The computer takes into account the frequency shift due to Doppler effect by changing periodically the frequency of the receivers. The computer also controls the A/D converter connected to the output of the receivers. The received signals are recorded on digital tape together with time information. The computer also controls the multiplexer, which selects the antennas to be electrically connected to the station. During the campaign the beacon signals of Intercosmos and Intasat satellites were recorded for about 70 passages. As for the ATS 6,30 records each about 1 h long have been obtained.

Fig.2 shows an example of the ATS records in a quick-look form representation (one point in the drawing represents an average over 1 second). One of the two channels was on a fixed frequency, the lowest beacon frequency, while the other channel is switched for the other 12 beacon frequencies, once every 30 seconds.

Fig.3 is an analogous quick-look representation for an or-

biting satellite (Intercosmos: 40 MHz upper channel, 41 MHz lower channel, night passage).

As the analysis of the data has just only begun, we only say that our purposes are to study the scintillation of phase and amplitude and to connect scintillation, when it is possible, to the characteristics of the ionization irregularities.

Then, as allowed by the recorded signals at the different beacon frequencies of ATS-6, we will study the communication channel, through the determination of the time-frequency correlation function of the complex envelope, and of the scattering function of the channel.

As a first example of the work we refer to Fig.3 and to the analysis of scintillation of amplitude and phase. During the reception, after conversion of the beacon frequency to few hundreds Hz, the signal was sampled at a frequency of 6500 samples per second. For our analysis first the real part and the imaginary part of the complex envelope of the signal have been evaluated by multiplying the samples by  $\cos\omega t$  and by  $\sin\omega t$  respectively, where  $\omega$  is an estimation of the low frequency carrier frequency. A low pass digital filter was then used. The amplitude and phase of the obtained complex envelope was then evaluated. As for the phase yet one has to take into account the fact that a residual low frequency (few tenths, ore-say-1 Hz) is still present after filtering, together with a doppler shift, giving a continuous variation of phase to which random oscillations (scintillation) in superimposed. We tried two type of corrections: a linear correction for very short periods of time ( $1/3$  second) and a second order polynomial correction for longer periods of time (5 seconds).

Fig.4 shows the variance of phase (dots) and the normalized variance of amplitude (crosses) after this second type of correction.

Each circle and each cross represent the average over an interval of 5 seconds.

The power spectra of phase, obtained after linear detrending are shown in figure 5. The spectra shown are evaluated for successive intervals of time of 20 seconds (time is growing from spectrum 1 to spectrum 7). Small oscillations in spectra are smoothed out. One has to note that linear or second order polynomial correction of phase led to practically the same spectra only for frequencies higher than 1-2Hz. Lower frequency spectra resulted substantially different.

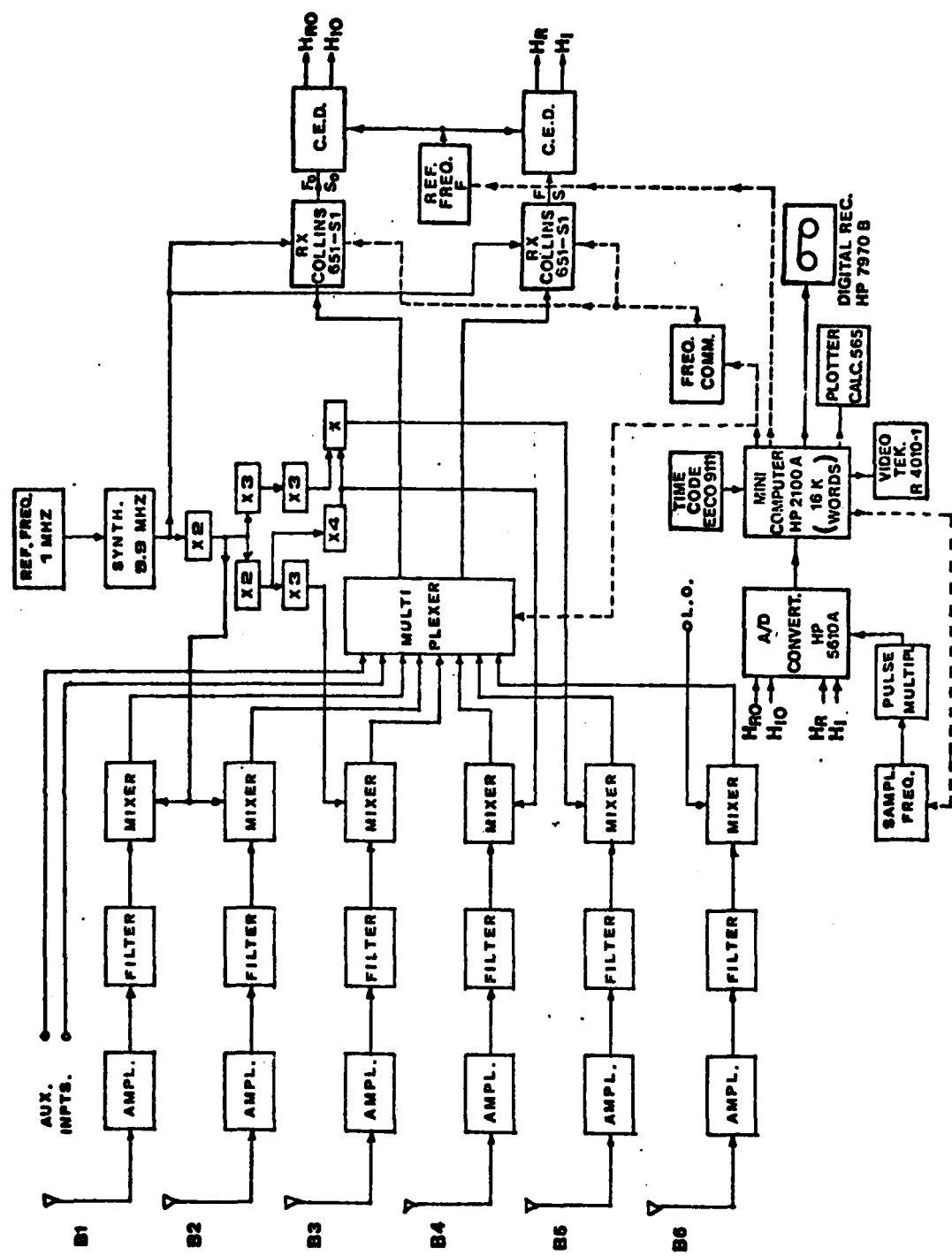


Fig. 1. Block diagram of the receiving station

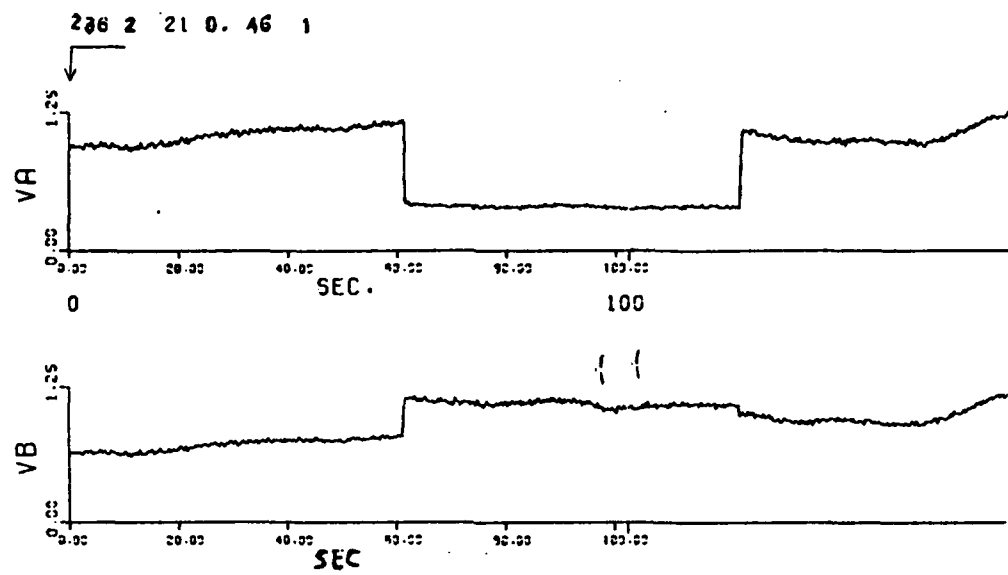


FIG. 2

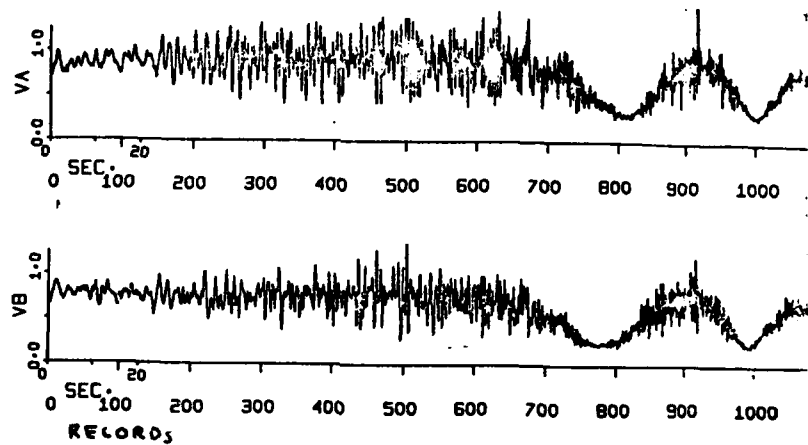


FIG. 3

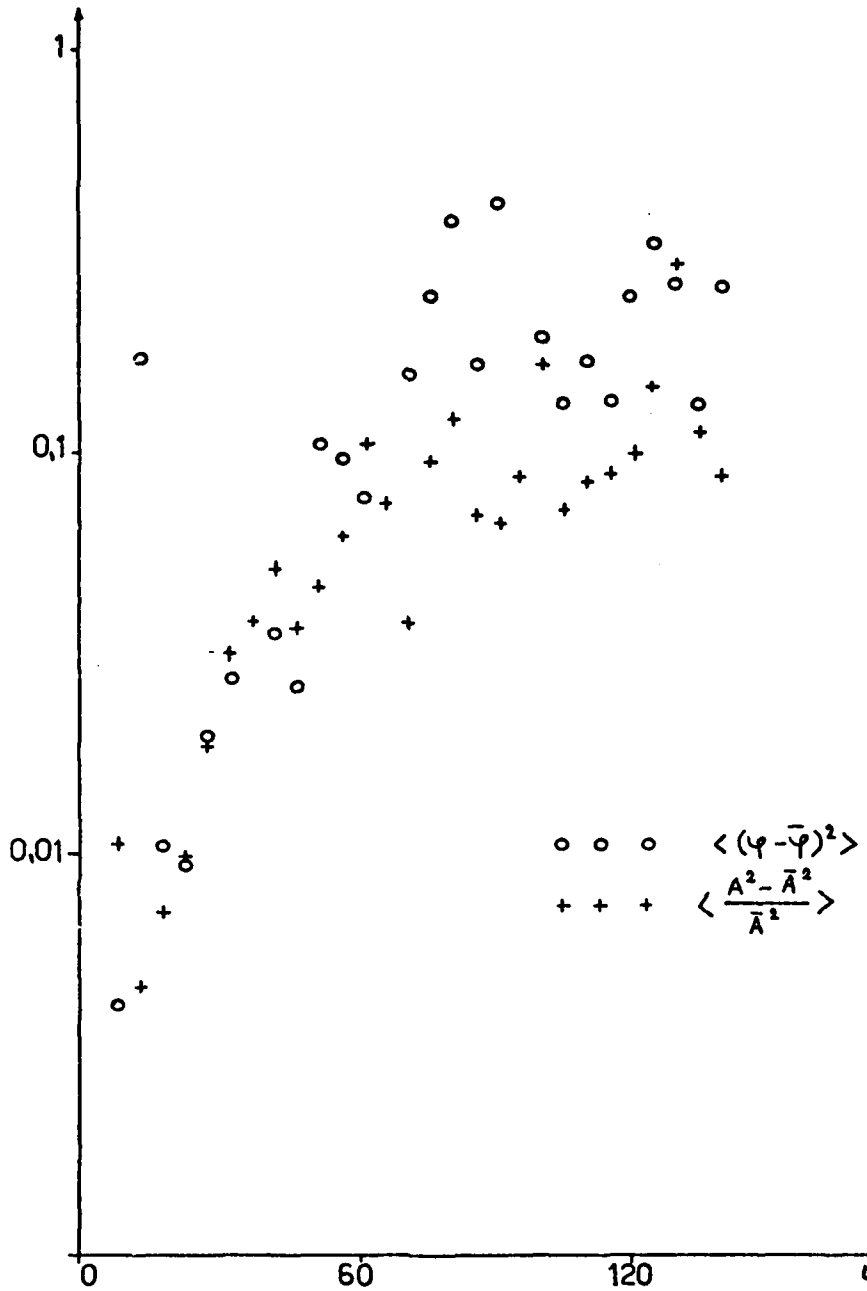


Fig.4 VARIANCE OF PHASE ( $\varphi$ ) AND NORMALIZED VARIANCE OF AMPLITUDE (A). (SEE TEXT AND FIG 3 )

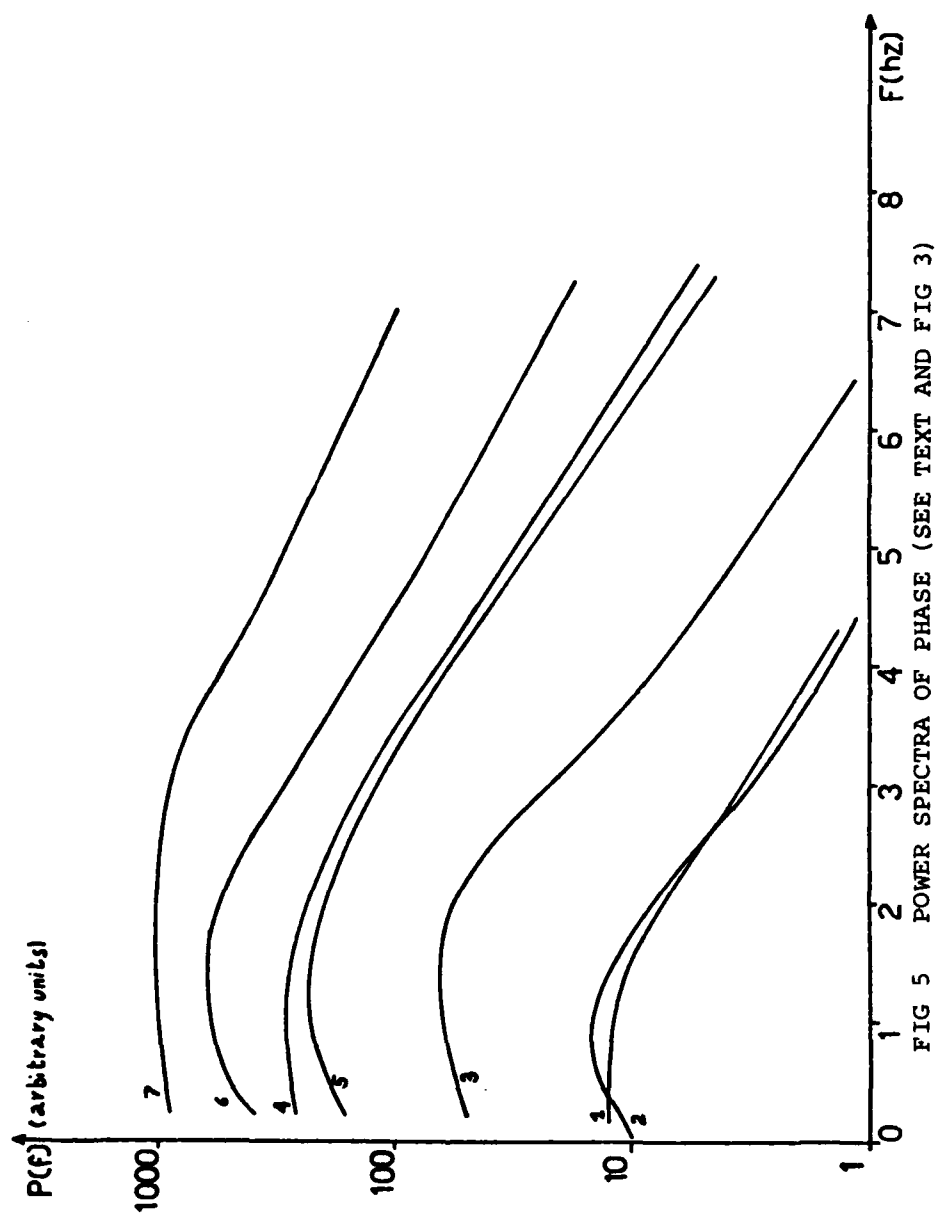


FIG 5 POWER SPECTRA OF PHASE (SEE TEXT AND FIG 3)

## VHF Scintillation Observations at Calcutta with Orbiting and Geostationary Satellites

S. Basu, B.K. Guhathakurte,  
G.N. Bhattacharyya and A. DasGupta  
Institute of Radio Physics and Electronics  
92 Acharya P. C. Road  
Calcutta 9, India

### Abstract

The results of VHF scintillation observations carried out at the Ionosphere Field Station of Calcutta University (Geographic lat: 22°58' N, long: 88°30' E; Dip lat: 17°21' N) during the period November - April, 1972-73 and August to October, 1975 are reported. 136 MHz transmissions from Intelsat 2F2 located to the south of the station, 137 MHz from ATS-6 in near westerly direction as well as 40 MHz transmissions from orbiting satellite Intasat were received at the station. The results indicate that the occurrence of scintillations > 3 dB at 40 MHz did not exceed 20% in the pre-midnight hours (when Intasat transits occurred) whereas in the telemetry channels at 136 and 137 MHz the occurrence was lower than 5%. Even though the occurrence was low, scintillations were found to be intense, attaining levels as large as 9 dB at 136 MHz. From a combined study of scintillations with orbiting and geostationary satellites the spatial extent of the irregularities and their characteristics have been derived.

### Introduction

The Field Station (Geographic latitude: 22°58' N, longitude: 88°30' E; Magnetic latitude: 17°21' N) of the University of Calcutta is located below the northern crest of equatorial F2 anomaly. As such, the equatorial geomagnetic control plays a prominent role in governing the plasma transport from the magnetic equator to ionospheric locations in the vicinity of the station. Prior to 1971, orbiting beacon satellite transmissions at the low frequencies of 20 and 40 MHz were only available to the Indian observers. Explorer 22 and 27 observations in 1966-1969 indicated that 20 and 40 MHz scintillations are observed at the station primarily during the summer months (Bhar et al., 1970). although other equatorial stations have recorded an equinoctial maximum. During 1971-1972,

observations at a higher frequency namely, 136 MHz, could be carried out at the station on a continuous basis when Intelsat 2F2 made its transit over the Indian longitudes. A very low occurrence of 136 MHz scintillation during November, 1971 to April, 1972 was reported (Basu et al., 1975). Since August, 1975 136 MHz transmissions from Intelsat 2F2, drifting across the longitude of the station, and 137 MHz transmissions from ATS-6 at 35° E longitude could be received at the station. The above observations have been supported by 40 MHz scintillation studies carried out with the help of orbiting satellite Intasat. The continuous observations of the geostationary satellites were used to obtain the percentage occurrence of 136-137 MHz scintillation. The observations of the orbiting satellite Intasat, transiting between 1800-2100 local time, were used to obtain the distribution of irregularities of electron density causing 40 MHz scintillation.

### Results

Figure 1 shows sections of data exhibiting scintillations at 136 and 137 MHz. The top channel shows scintillations on 136 MHz Intelsat 2F2 transmissions received with a rotating yagi antenna. The two bottom channels of the figure exhibit Intelsat 2F2 signals received with a rotating yagi antenna and 137 MHz transmissions received from ATS-6 with a circularly polarized antenna. ATS-6 was viewed nearly to the west of the station and Intelsat 2F2 to the south. Scintillations due to a sharp edge irregularity may be viewed on ATS-6 channel in addition to the random type of scintillation. The characteristic sudden onset of scintillation may be noted in all cases. The decrease of ATS-6 signal level has been caused by the movement of the satellite antenna at this time. It may be mentioned that the fading period of scintillation is about 4-5 seconds for strong scintillation but is as large as 40 seconds when scintillations are weak.

Figure 2 shows the percentage occurrence of 136 and 137 MHz scintillations  $> 3$  dB obtained during November-April, 1972, 1973 and August to October, 1975. It is found that the occurrence of 3 dB scintillation at 137 MHz does not exceed 5% at the station during the above period.

It is interesting to note that the global model of equatorial scintillations recently developed by Basu et al. (1976) on the basis of in-situ measurements of ionospheric irregularities indicated a remarkable longitude variation of equatorial scintillation. The low occurrence of scintillations at this longitude is in agreement with the model which also shows that over the African sector a station with a similar magnetic latitude would have observed 3 dB scintillations at 140 MHz for 60% of the time.

During the above period of August-November, 1975, when continuous observations of geostationary satellites were carried out, the transits of orbiting satellite Intasat occurred between 1800-2100 ( $82^{\circ}$  E time). Figure 3 shows the portions of subionospheric track (400 km altitude) over which 40 MHz scintillation was obtained. The figure shows that the irregularities are mostly localized towards the north. An east-west asymmetry in the irregularity distribution may also be noted. Let us consider that the irregularity patches in the north are confined within magnetic field tubes and that the irregularity amplitude,  $\Delta N/N$ , ( $\Delta N$ , the electron density deviation and  $N$ , the ambient electron density) is preserved, as is usually assumed, when the irregularities are mapped along field lines. As these field lines are traced southward (i.e., equatorward) the field lines map higher in altitudes where the ambient  $N$  is reduced. The assumption of constant  $\Delta N/N$  requires a proportionate reduction of  $\Delta N$ . The reduced value of  $\Delta N$  is probably insufficient to cause scintillations towards the south of the station. It is to be noted that the northern patch of irregularities would correspond to those in the topside portion of the ionosphere above the magnetic equator. The southernmost location viewed from Calcutta corresponds to a magnetic latitude as low as  $5^{\circ}$  N. The low occurrence of irregularities at this position indicates that the width of the equatorial belt of strong scintillation is indeed very narrow in this longitude zone for the above period of observation.

Considering that the irregularities which give rise to strong scintillations at the magnetic equator are located around the F peak, the narrow width of the scintillation belt signifies a limited irregularity layer thickness above the magnetic equator in this longitude zone. The northern irregularity patches observed from the present station probably indicate the presence of isolated irregularities at altitudes greater than 700 km above the magnetic equator.

#### References

- Bhar, J. N., A. Das Gupta and S. Basu, Radio Science, 5, 939-942, 1970.
- Basu, S., G.K. Guhathakurta, G.N. Bhattacharyya and A. Das Gupta, Proceedings of symposium on beacon satellite investigations of the ionosphere and ATS-6 data, Ya. L'Alpert ed., Moscow, U. S. S. R., 1975.
- Basu, Sunanda, S. Basu and B. K. Khan, Model of equatorial scintillations from in-situ measurements, submitted for publication to Radio Science, 1976.

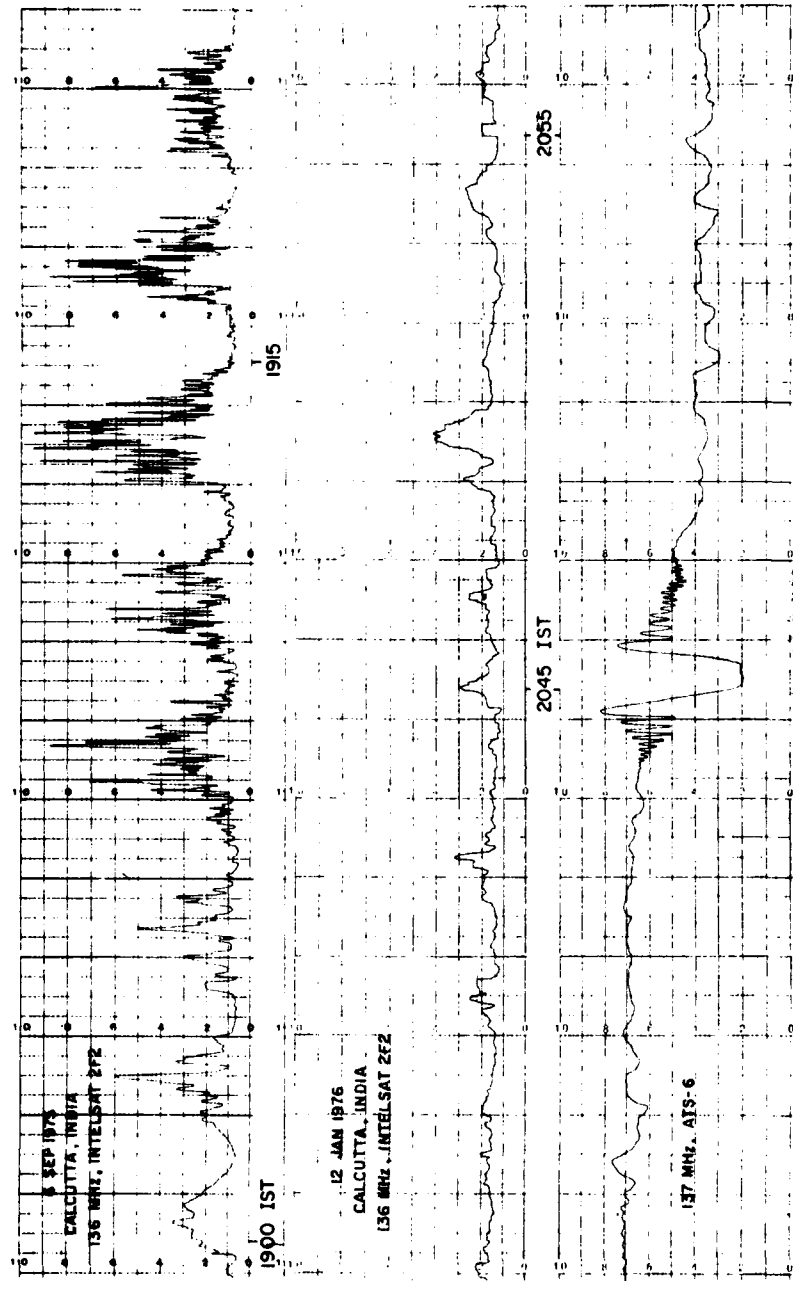


FIGURE I. VHF SCINTILLATION AT CALCUTTA, INDIA

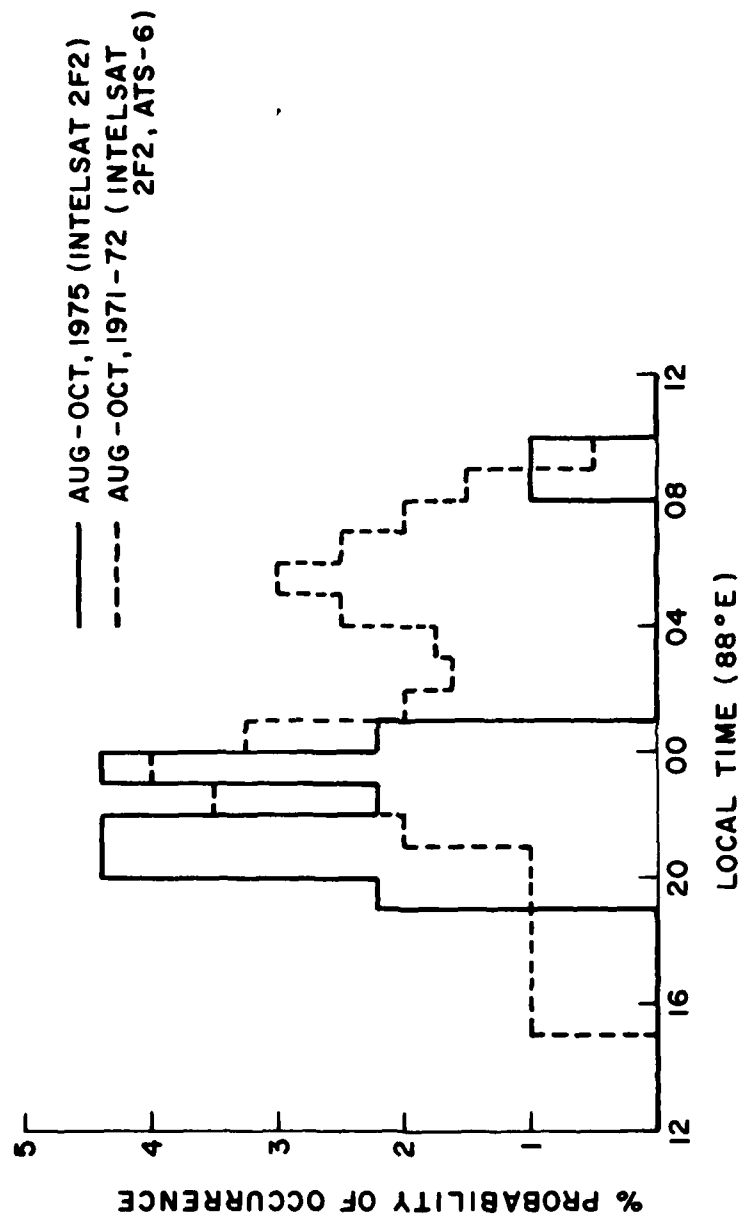


FIG. 2 OCCURRENCE OF 137 MHz SCINTILLATIONS AT CALCUTTA  
(DIP: 32°N; GEOGRAPHIC LONGITUDE: 88°30' E)

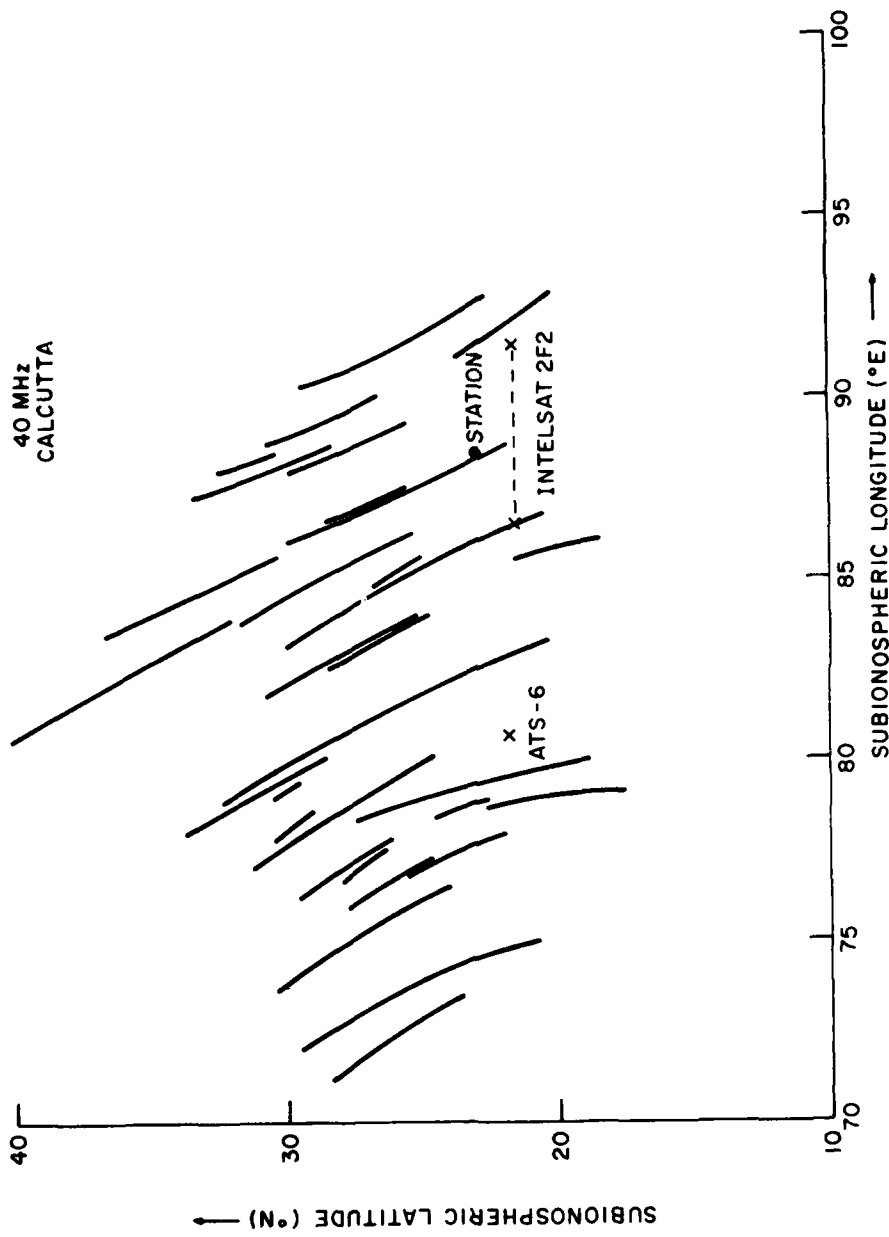


FIG. 3 NORTH-SOUTH AND EAST-WEST ASYMMETRY OF IRREGULARITY DISTRIBUTION  
OBTAINED FROM INTASAT OBSERVATIONS AT 40 MHz, AUGUST-OCTOBER  
1975, 1930-2230 LMT.

Daytime VHF Scintillations at Huancayo, Peru and  
their Possible Relationship to the Equatorial Electrojet

S. Basu\*  
Emmanuel College  
Boston, MA 02115

Jules Aarons  
Air Force Geophysics Laboratory  
Air Force Systems Command  
Hanscom AFB, MA 01731

Abstract

Daytime VHF scintillation observations at Huancayo, Peru, during February to May, 1975 indicate that it is a regularly occurring phenomenon and is possibly related to the equatorial electrojet. The level of daytime scintillation at 41 MHz is typically of the order of 10 dB peak-to-peak and 1 dB at 140 MHz. On certain days, the scintillation is, however, found to be inhibited. The spectral index of daytime scintillation has been shown to depend on the level of scintillation.

Introduction

The characteristics of nighttime VHF scintillation near the magnetic equator caused by the irregularities of electron density at F region heights have been well documented (Aarons, 1976 and references therein). On the other hand, the daytime VHF scintillation at this location, though less intense, has not been fully explored. It is found, however, that daytime VHF scintillation near the magnetic equator is a regularly occurring phenomenon except on a few days. The most viable portion of the equatorial ionosphere where plasma irregularities are generated during the daytime corresponds to the altitude range of 100-110 km where an intense equatorial electrojet current is located. The presence of irregularities in this region is revealed in equatorial sporadic E ( $E_{s\acute{e}}$ ) signature on ionograms. In recent years, the powerful Jicamarca radar facility, capable of covering the frequency range of 15-150 MHz, has been used to make an extensive study of the irregularity characteristics in this region (Balsley et al., 1976)

\*On leave from the University of Calcutta

Since backscatter radars are only sensitive to the irregularities having scale lengths one half the transmitted wavelength, the E<sub>1</sub> echoes obtained by conventional ionosonde provide information on irregularity wavelength of 30-300 m. whereas Jicamarca radar operated between 15-150 MHz probes the irregularities with wavelengths ranging between 1-10 m. On the other hand, the scintillation experiment being sensitive to irregularity wavelengths of the order of a Fresnel dimension, 41 and 140 MHz scintillation observations effectively sample E region irregularities having scale lengths of the order of 0.5-1 km.

### Results

Figure 1 shows daytime scintillation data at 41 MHz obtained from ATS-6 at Huancayo, Peru on April 28, 1975. The three sections of the figure correspond to three intervals of time on the same day. The left hand section corresponding to local noon exhibits intense scintillation at 41 MHz with a peak-to-peak fluctuation of 13 dB.

Figure 2 shows the typical features of daytime VHF scintillation at Huancayo. The top panel shows the diurnal variation of scintillation index (SI) at 41 MHz and 140 MHz on successive days covering April 25-29, 1975. On April 27, the transmission was interrupted for the major part of the day and the limited data is not shown. From the figure it may be observed that daytime scintillation was consistently present on successive days at both frequencies between 0600-1800 (75°W time). This time period coincides with the daytime equatorial electrojet activity. The SI index at 41 MHz ranges between 70-90% corresponding to a peak-to-peak fluctuation of 7-13 dB. At 140 MHz, the SI index is found to range between 1-1.5 dB. The departure from the normal daytime scintillation behavior is shown in the bottom panel of Figure 2. It may be observed that although normal daytime scintillation was observed on March 19 and March 21, no conspicuous scintillation was present on March 20 and March 22. The inhibition of daytime scintillation is probably related to a weakening of electrojet activity (Matsushita, 1957; Knecht, 1959; Egan, 1960; Rastogi, 1976).

From simultaneous measurements of scintillation at 41 and 140 MHz, the frequency dependence of daytime scintillation was studied. The spectral index,  $\eta$ , of the theory based scintillation index  $S_4$  was derived from the relation  $S_4 \propto f^{-\eta}$ , where  $f$  is the frequency. Figure 3 shows the variation of spectral index  $\eta$  with  $S_4$  index at

41 MHz as obtained from an analysis of five days observations. It is interesting to note that the spectral index,  $\eta$ , varies from a value of about 0.6 to 1.2 with an increase of  $S_4^4$  index at 41 MHz from 0.2 to 0.4. It has been shown (Lovelace et al., 1970; Jokippi and Hollweg, 1970) that for weak-scattering, the spectral index of scintillation,  $\eta = (p+2)/4$  where  $p$  is the spectral index of the 3-dimensional power-law irregularity power spectrum. Based on this relation, the plot in Figure 3 indicates that the irregularity power spectrum is very flat at low levels of scintillation but tends to a value of 3 at increased levels of scintillation satisfying the weak scatter criterion.

Simultaneous studies of VHF scintillation, equatorial sporadic E and radar backscatter are being conducted to obtain information on the characteristics of daytime ionospheric irregularities over the magnetic equator with scale lengths ranging from a meter to a kilometer.

#### References

- Aarons, J., Equatorial Scintillations: A Review, submitted for publication in IEEE Trans. Antennas Propagation, 1976.
- Balsley, B.B., A. Rey and R.F. Woodman, J. Geophys. Res., 81, 1391, 1976.
- Egan, R.D., J. Geophys. Res., 65, 2343, 1960.
- Jokippi, J.R. and J.V. Hollweg, Astrophys. J., 160, 745, 1970.
- Knecht, R.W., J. Atmos. Terr. Phys., 14, 348, 1959.
- Lovelace, R.V.E., E.E. Salpeter and L.E. Sharp, Astrophys. J., 159, 1045, 1970.
- Matsushita, S., J. Atmos. Terr. Phys., 10, 163, 1957.
- Rastogi, R.G., J. Geophys. Res., 81, 687, 1976.

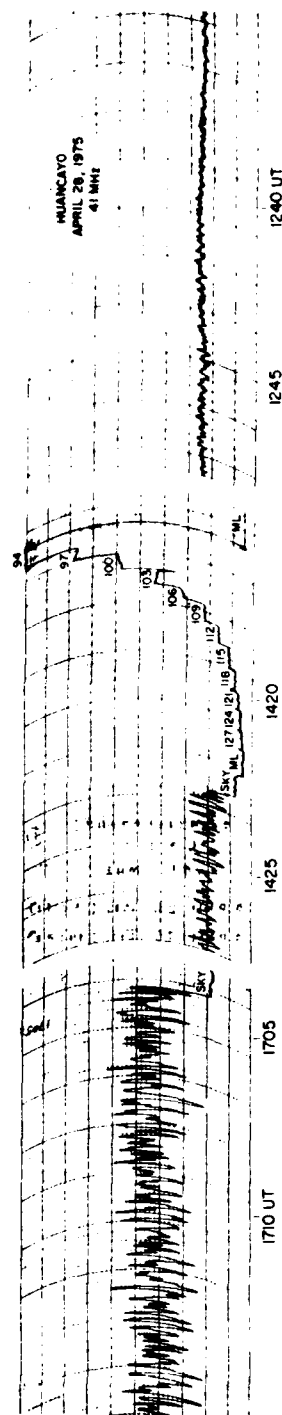


FIGURE 1. DAYTIME 41 MHz SCINTILLATIONS  
OBSERVED AT HUANCAYO, PERU.

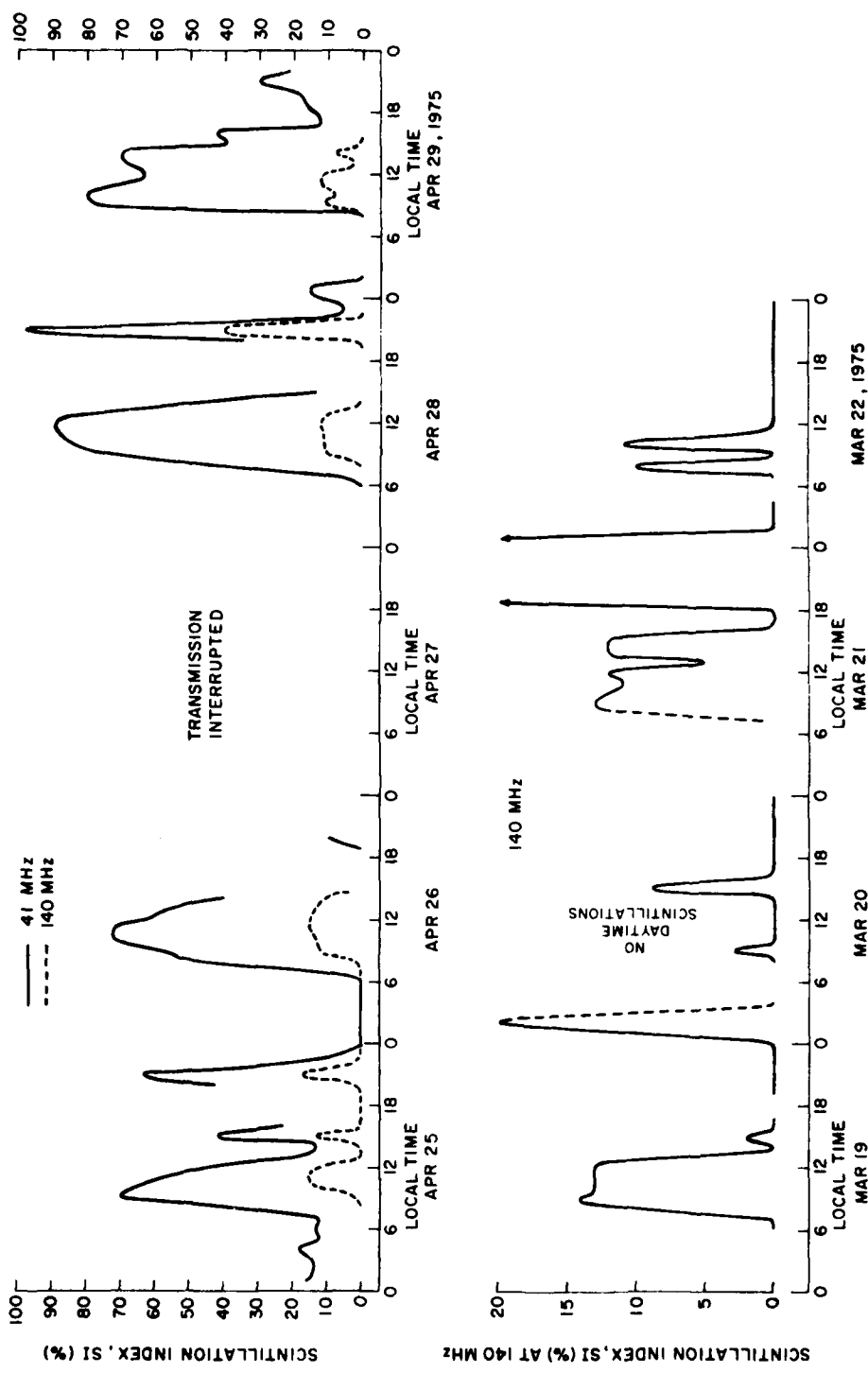


FIG. 2 VHF SCINTILLATIONS DURING DAYTIME AT HUANCAYO, PERU

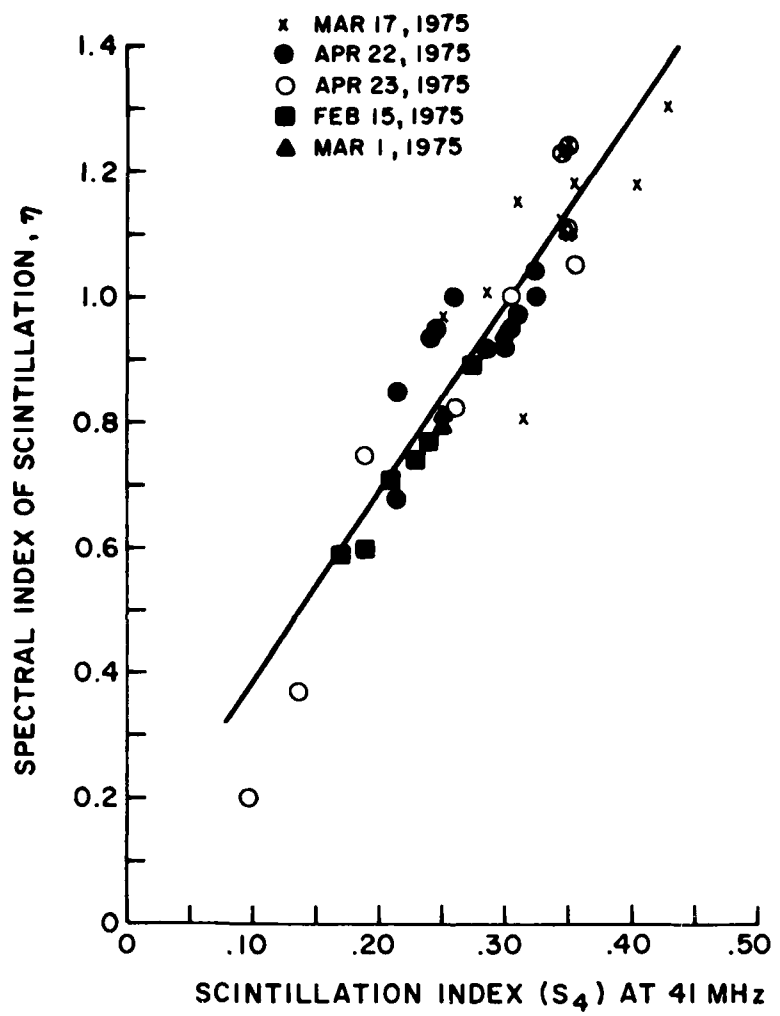


FIGURE 3. VARIATION OF THE SPECTRAL INDEX OF SCINTILLATION ( $\eta$ ) WITH SCINTILLATION INDEX ( $S_4$ ) AT 41 MHz.

SATELLITE BEACON STUDIES OF GLOBAL F-REGION  
DISTURBANCE EFFECTS

Michael Mendillo  
Astronomy Department  
Boston University  
Boston, Massachusetts 02215

ABSTRACT

Satellite radio beacon observations have made a major contribution to the geophysical sciences in the area of solar terrestrial disturbances. The monitoring of VHF signals from geostationary satellites has provided a most effective way to study solar flare and geomagnetic storm induced perturbations upon the ionospheric F-region. A high time resolution, relative accuracy, and potential for data continuity make the satellite beacon measurements a valuable technique for the specification of ionospheric disturbances.

The present review concentrates on the use of the satellite beacon derived parameter total electron content (TEC) as a means of studying F-region plasma disturbance effects. A semi-global network of TEC monitoring stations has presented the most detailed morphology of an F-region solar flare effect recorded to date (7 August, 1972), and a summary of these observations is presented. The satellite beacon community has also made significant contributions to the study of magnetic storm effects upon the F-region. Two approaches have been used: (1) the construction of "average storm patterns" at a single site, and (2) the "case study" approach of describing a few particularly large events as observed by a network of stations. Both of these schemes are reviewed, as applied to large geomagnetic storm-induced perturbations. Finally, attention is drawn to the great potential of using the ATG-6 satellite to study storm effects in the plasmaspheric content. This area is in its infancy, and thus future work should add appreciably to our understanding of the coupled ionosphere-plasmasphere response to geomagnetic disturbances.

## I. INTRODUCTION

Since the first days of the Space Era, satellite radio beacon transmissions have been used to study the behavior of the propagation medium they traverse. In addition to specifying quiet-time or "normal" ionospheric morphology, satellite beacon observations have made significant contributions to the study of F-region disturbance effects. At least five areas are particularly well documented: (1) radio scintillation studies of F-region irregularities in electron density, (2) atmospheric gravity wave investigations using total electron content TID data, (3) solar flare effects upon the ionosphere, (4) geomagnetic storm associated disturbances upon the ionosphere and plasmasphere, and (5) artificial modification effects upon the F-region.

In this brief review, only topics (3) and (4) will be touched upon. Time does not permit a complete documentation of all those who have made contributions to these areas; the figures and references chosen are thus intended to be illustrative of the type of investigations carried out by the satellite beacon community, but in no way constitute a definitive summary.

Satellite beacon studies of the ionosphere are now chiefly made using signals from geostationary satellites. Faraday rotation, differential Doppler and group-path delay techniques furnish integrated electron content data for the study of F2-region disturbances over semi-global regions. These measurements distinguish themselves from other ionospheric diagnostic techniques in three main ways: (1) a very high time-resolution capability, over long periods of time, at a fixed location, (2) a high relative accuracy ( $<1\%$ ) of measurement upon an absolute capability of about 10%, and (3) no loss of data due to the severity of the event under study, obviously a necessity for the investigation of solar-terrestrial disturbances.

## II. SOLAR FLARE EFFECTS

The most complete description of a solar flare effect upon the F-region was presented through the collaborative efforts of the satellite beacon community (Mendillo et. al., 1974). The event of 7 August 1972 was monitored along 13 separate ray paths spanning the latitude range  $5^{\circ}4'N$  to  $62^{\circ}3'N$  and the local time period 0600-1700. The sudden increases in total electron content (STECs, a term first suggested by Matsoukas et. al. (1972) for an effect first documented by Garriott et. al. (1967)) were in the range  $1.8$  to  $8.6 \times 10^{16} el/m^3$ . The individual events (shown in Figure 1),

when examined in detail, showed several new facets of SITEC morphology.

(1) The magnitude of the flare induced total content enhancement,  $\Delta$ TEC, showed a correlation with the geographic latitude of the subionospheric point, and not with the zenith angle ( $\chi$ ) at the sub-ionospheric point, as would be predicted by simple production function models (see Figure 2).

(2) Simultaneous measurements made at the incoherent scatter facility at Millstone Hill showed that the height distribution of the electron concentration enhancements responsible for the overall  $\Delta$ TEC extends throughout the ionosphere, and is not limited to heights below hmF2.

(3) High time resolution of the rate of change of TEC during the flare showed a remarkable correlation with simultaneous solar radio burst data in the cm-range. Since  $d$ TEC/ $dt$  relates directly to the solar production function ( $q$ ), the correlation presented in Figure 3 points out how well the 35,000 MHz behavior describes the solar EUV and X-ray burst characteristics responsible for the SITEC.

More recent advances in the description and simulation of SITEC events are dealt with in the paper by Donnelly et. al. (1976). The incoherent scatter study of the 7 August 1972 event showed that significant thermal and plasma dynamic effects contribute to the overall SITEC (Mendillo and Evans, 1974). The computer simulation of these effects are actively being pursued (Donnelly (1976), Oran et. al. (1976), Antoniadis, private communication).

### III. GEOMAGNETIC STORM EFFECTS UPON THE IONOSPHERE

The response of the F-region to magnetic storms has been one of the main areas studied by geostationary satellite techniques. Most of these studies were made using Faraday rotation measurements of TEC. The clear demonstration that the F-region experiences both positive and negative phases depending upon storm-time, local time, season and latitude has been a well documented achievement of recent years. While it is naive to search for the "single mechanism" responsible for ionospheric storms (in the sense of choosing electrodynamic, neutral wind or composition changes as the exclusive agent for disturbance effects), there is a growing case for suggesting electrodynamic drift effects as the primary cause for the positive phase at mid-latitudes and neutral composition variations as the chief source of the Ne depletions found during the negative phase.

The construction of average storm patterns at a single site has added to our knowledge of dominant characteristics and mechanisms operating at different locations. Figure 4

gives average TEC patterns for mid and low latitude stations (Sagamore Hill, Massachusetts, and Honolulu, Hawaii). These two sites have received the most extensive analysis to date for ionospheric storms (Mendillo and Klobuchar (1974), Huang et. al. (1974), Basu et. al. (1975)). The type of local time (SD) analysis shown in Figure 4 should be pursued since average patterns according to storm-time ( $Dst$ ) or simple correlations with magnetic indices (such as  $K_p$ ) rarely add physical insight to the discussion.

To understand more fully the global aspects of the electrodynamic, neutral wind and thermal mechanisms operating during storms, multi-station and semi-global networks of stations studying the same events are needed. The satellite beacon community has, in fact, already carried out several excellent studies in this area. Figure 5 gives the local time patterns for two mid-latitude stations (Sagamore Hill (Hamilton, MA),  $L=2.8$  and Stanford (Calif.),  $L=1.7$ ) using the same 28 storm period in 1967-69 described by Mendillo (1971). Note that the two stations exhibit both positive and negative phases. The nighttime effects are particularly interesting in that the recurrent post-midnight minima at  $L=2.8$  correspond to recovery periods at  $L=1.7$ . The severe latitudinal gradient thus evident suggests that strong trough/plasmapause dynamics are confined to a narrow band of upper mid-latitudes. Figure 6, taken from Lanzerotti et. al. (1975), compares the  $L=2.8$  response with simultaneous Arecibo data ( $L=1.4$ ) for 12 storm periods from 1968-1970. While the Hamilton SD curves in Figures 4, 5, and 6 are all in basic agreement (showing a definite long-term consistency at that site), the  $L=1.7$  (Stanford), the  $L=1.4$  (Arecibo), and the  $L=1.1$  (Honolulu) results from Figures 5, 6, and 4 do not fit into an obvious latitudinal pattern. The storm-time response of the equatorial to lower mid-latitude ionosphere is complicated by motions of and longitudinal asymmetries in the so-called "Appleton Anomaly." The equatorwards extent of storm-induced composition changes and neutral winds further complicates the attempt to obtain "characteristic morphologies" as consistent as those found at upper mid-latitudes. Huang et. al. (1974), in fact, reported that their analysis of 72 weak storms ( $Ap < 30$ ) yielded more well-defined SD patterns than their analysis of 29 strong storms ( $Ap > 30$ ).

The most extensive analysis of the SD (TEC) characteristics for the same set of storms as observed at different stations has been carried out by Hearn (1974). A total of 23 storms (both weak and strong) were used to obtain LT patterns at 11 western hemisphere station spanning longitudes from  $67^{\circ}1W$  (Arecibo) to  $160^{\circ}6W$  (Cold Bay, Alaska), and magnetic latitudes  $55^{\circ}$  (Edmonton) to  $20^{\circ}$  (Honolulu). Several features coming from their study are:

(1) Nearly all of the SD (TEC) average patterns, with the exception of Honolulu's, exhibit the dusk sector enhancement discussed by Mendillo et. al. (1970) and Papagiannis et. al. (1971).

(2) The enhanced periods for stations showing the dusk effect in  $\Delta$ TEC on the first day of the storm all begin near the same LT, but the lower latitude stations maintain the enhancement longer.

(3) The SD (TEC) patterns for two stations, at the same magnetic latitude (Urbana and Cold Bay, 48° geomagnetic) suggest that there exists some longitudinally dependent enhancement mechanism that accounts for the earlier starting and longer lasting enhancement in TEC at Cold Bay with respect to Urbana.

The comparison of average storm patterns derived from the same set of storms as recorded at several stations is not the only way to study global F-region storm effects. An equally valid approach is to examine individual events from a large network of stations. There have been at least five "Great Storms," studied in this way by the satellite beacon community:

(1) The 15 June, 1965, event has been reviewed by Somayajulu (1972).

(2) The 25 May, 1967, event first drew attention to the large TEC enhancements which occur near dusk (Goodman, 1968; see Somayajulu (1971) for a review of this storm).

(3) The 7 March, 1970, event instigated the first "joint study" of TEC storm effects (Klobuchar et. al., 1970) by the satellite beacon community. The TEC data collected for this event was confined to northern latitudes in the American sector. It pointed out a remarkable longitudinal gradient in the daytime response to the storm suggesting that strong heating effects, beginning near local sunrise, can cause F-region loss enhancements to be so large as to overpower the positive phase mechanism which clearly dominated the TEC response at easterly longitudes (see Figure 7).

(4) The 17 December, 1971, period was the most widely documented TEC storm event studied to date (Schödel et. al., 1974). It exhibited the largest positive phase enhancement ever recorded at many of the individual stations.

(5) The 17 June, 1972, storm period was monitored by a similar network of 20 sites, but its full description has not yet been reported.

The study of individual storms can be used to check aspects of the statistical studies described earlier. For example, the Illinois study (Hearn, 1974) suggested that the beginning and end of the positive phase afternoon TEC enhancement had a longitudinal dependence. The global data set for 17 December 1971 and 17 June 1972 were used to examine this possibility. At American longitudes, both

storms produced large TEC enhancements which had extremely well defined temporal peaks. For both events, the peaks of the enhancements were plotted on a longitude vs. local time grid (see Figure 8). If the time of the  $\Delta$ TEC maximum depends only on LT, then all points should fall on a vertical line, above say 1700 LT. If the  $\Delta$ TEC maxima occurs at the same instant of storm-time (say, perhaps, during the most magnetically active UT-period), then all points would fall along the diagonal from upper left to lower right. In Figure 8, the analysis for December 1971 shows a strong clustering along the single storm-time (i.e., same UT) diagonal. For the June 1972 case, however, an opposite type of diagonal is observed, indicating a definite longitudinal dependence in the peak of the  $\Delta$ TEC enhancements.

#### IV. SUBSTORM EFFECTS IN TEC

The study of magnetospheric substorm effects upon TEC is an area of growing interest. The initial studies made by Essex and Watkins (1973), Mikkelsen (1975) and Mendillo and Klobuchar (1975) indicate that the F-region's sensitivity to substorms is a strong function of latitude. The effects are much smaller in magnitude and shorter in duration than large storm effects---usually taking the form of nighttime increases in TEC.

In satellite beacon studies of substorm effects, particular attention must be paid to the geometry of the satellite-station ray path. A geostationary satellite signal arriving at high latitudes often crosses regions of the ionosphere dominated by a trough and/or auroral precipitation regions. These effects occur at different heights along the ray path, and the TEC data integrates through them. Yet, the different signatures of E and F region contributions to TEC enhancements can, in principle, be used to infer the spatial as well as temporal development of substorm effects. Several "case studies" of substorm effects in TEC are currently being organized by the satellite beacon community.

#### V. PLASMASPERIC STORMS

The Radio Beacon Experiment (RBE) package placed on board the ATS-6 satellite ushered in a new era for satellite beacon studies. The great promise of the ATS-6 experiments is the determination of so-called "plasmaspheric contents." In principle, the ATS-6 group-delay experiment gives the integral of the electron densities along the entire length of the station-satellite ray path (called the total content,  $N_T$ ). The ATS-6 Faraday rotation experiment also gives an integral measure of electron densities along the ray path, but an integral weighted by the geomagnetic field. The rapid

fall-off of the magnetic field strength with distance results in the Faraday rotation experiment being basically insensitive to electrons above the height of a few thousand kilometers. The measurement thus determines the ionospheric electron content, denoted  $N_I$ . The subtraction of  $N_I$  from  $N_T$  (both simultaneously determined along the same ray path) offers an attractive scheme to determine the "plasmaspheric content ( $N_p$ )"--- the integral of the number of electrons in the interesting region which begins above the ionosphere and extends to  $L=6.6$  (geostationary orbit).

The initial results of this experiment (Davies et. al., 1975, Solcher, 1976), as well as those presented in detail during this Symposium, show some very interesting (and sometimes confusing) results. The main problem encountered in deriving  $N_p$  lies in the evaluation of  $N_I$ . The traditional scheme of converting the measured amount of Faraday rotation to the ionospheric content via a constant conversion factor seems to break down for the high degree of accuracy needed to get  $N_p$  by subtracting  $N_I$  from  $N_T$ . The main uncertainty contributing to variations in the conversion factor is the shape of the ionospheric  $N_e(h)$  profile. The problem is not too severe for the derivation of average or monthly median  $N_p$  results, but can introduce significant uncertainties during geomagnetically active periods when the  $N_e(h)$  profile shape is known to vary substantially.

Almeida (1974) was the first to present plasmaspheric storm effects derived from satellite beacon techniques. Using the Faraday/differential Doppler experiment on ATS-3, definite evidence for the shrinkage of the plasmasphere following a SSC was presented. An initial study of  $N_p$  storm effects using ATS-6 (Solcher, 1976) shows a remarkable similarity between the  $N_I$  and  $N_p$  phases of the storm-induced variations. Davies et. al. (1975) examined the same storm period (14-15 September, 1974) and reported no appreciable change in plasmaspheric contents. Several more studies are obviously needed in order to establish  $N_p$  storm morphology and the role the underlying ionosphere plays in determining the observed behavior.

#### REFERENCES

- Almeida, O. G., J. Atmosph. Terr. Phys., 36, 305, 1974.  
Basu, S., Guhathakurta, B. K., and S. Basu, Ann. Geophys.,  
31, 497, 1975.  
Davies, K., Fritz, R. B., Grubb, R. N., and J. E. Jones,  
Radio Sci., 10, 785, 1975.  
Donnelly, R. F., Davies, K., Grubb, R. N., and R. B. Fritz,

Proc. COSPAR Sat. Beacon Group Symposium on "The Geophysical Use of Satellite Beacon Observations," Boston University, 1-4 June, 1976.

Essex, E. A., and B. J. Watkins, *J. Atmosph. Terr. Phys.*, 35, 1015, 1973.

Garriott, O. K., da Rosa, A. V., Davis, M. J., and O. G. Villard, *J. Geophys. Res.*, 72, 6099, 1967.

Goodman, J. H., *Planet. Space Sci.*, 16, 951, 1968.

Hearn, A. L., *Nature*, 249, 133, 1974.

Huang, Y.-N., Najita, K., Roelofs, T. H., and P. C. Yuen, *J. Atmosph. Terr. Phys.*, 30, 9, 1974.

Klobuchar, J. A., Mendillo, M., Smith III, F. L., Fritz, R. B., da Rosa, A. V., Davis, M. J., Yuen, P. C., Roelofs, T. H., Yeh, K. C., and B. J. Flaherty, *J. Geophys. Res.*, 76, 6202, 1971.

Lanzerotti, L. J., Cogger, L. L., and M. Mendillo, *J. Geophys. Res.*, 80, 1287, 1975.

Matsoukas, D. A., Papagiannis, M. D., Aarons, J., and J. Klobuchar, *J. Atmosph. Terr. Phys.*, 34, 1275, 1972.

Mendillo, M., *Nature*, 234, 23, 1971.

Mendillo, M., and J. A. Klobuchar, An atlas of the mid-latitude F-region response to geomagnetic storms, Tech. Rep. 74-0165, AFCRL, Bedford, Mass., 1974.

Mendillo, M., and J. A. Klobuchar, *J. Geophys. Res.*, 80, 643, 1975.

Mendillo, M., Klobuchar, J. A., Fritz, R. B., da Rosa, A. V., Kersley, L., Yeh, K. C., Flaherty, B. J., Pangaswany, S., Schmid, P. E., Evans, J. V., Schodel, J. P., Matsoukas, D. A., Koster, J. R., Webster, A. R., and P. Chin, *J. Geophys. Res.*, 79, 665, 1974.

Mendillo, M., Papagiannis, M. D., and J. A. Klobuchar, *Radio Sci.*, 5, 395, 1970.

Mikkelsen, I. S., *Planet. Space. Sci.*, 23, 619, 1975.

Oran, E., Baker, L., and T. R. Young, The Effects of Solar Flares on the Ionosphere, NRL Memorandum Report, 1976.

Papagiannis, M. D., Mendillo, M., and J. A. Klobuchar,  
Planet. Space Sci., 19, 503, 1971.

Schödel, J. P., Mendillo, M., da Rosa, A. V., Klobuchar,  
J. A., Roelofs, T. H., Fritz, R. D., Essex, E. A.,  
Flaherty, B. J., Hibberd, F. H., Kersley, L.,  
Koster, J. R., Liszka, L., and Y. Nakata, J. Atmosph.  
Terr. Phys., 36, 1121, 1974.

Soicher, H., Nature, 259, 53, 1976.

Somayajulu, Y. V., Sci. Report 404, Penn. St. Univ., Univ.  
Park, PA., 1972.

Somayajulu, Y. V., Sehgal, A. K., Tyagi, T. R., and N. K.  
Negi, Ind. J. Pure Applied Phys., 9, 548, 1971.

## FIGURES

FIGURE 1. Changes in Faraday rotation associated with the solar flare of 7 August, 1972 (from Mendillo et. al., 1974).

FIGURE 2.(a) A comparison of the observed SITEC and the corresponding solar zenith angles at the subionospheric points on August 7, 1972; triangles, stations in the western United States; dots, stations in the eastern United States, Canada, and Greenland; crosses, stations in Europe and Africa. Local time, 0600-1700; geographic latitude, 5°-65°N.

FIGURE 2.(b) A comparison of the observed SITEC and the corresponding latitudes of the subionospheric points: dots, stations in eastern United States, Canada, and Greenland (0900-1200 LT); crosses, stations in Europe and Africa (1400-1700 LT); triangles, stations in the western United States (0630-0820 LT). (from Mendillo et al., 1974).

FIGURE 3. A comparison of the rate of change of TEC along the Boulder-ATSI ray path with simultaneous measurements of the August 7 radio burst at 35,000 MHz. (from Mendillo et al., 1974).

FIGURE 4. Average local time patterns for the storm response (SD) of TEC at (a) Sagamore Hill, Massachusetts derived from 75 strong storms ( $Ap > 30$ ), (b) Honolulu, Hawaii, for 72 weak storms ( $Ap < 30$ ). (from Huang et al., 1974)

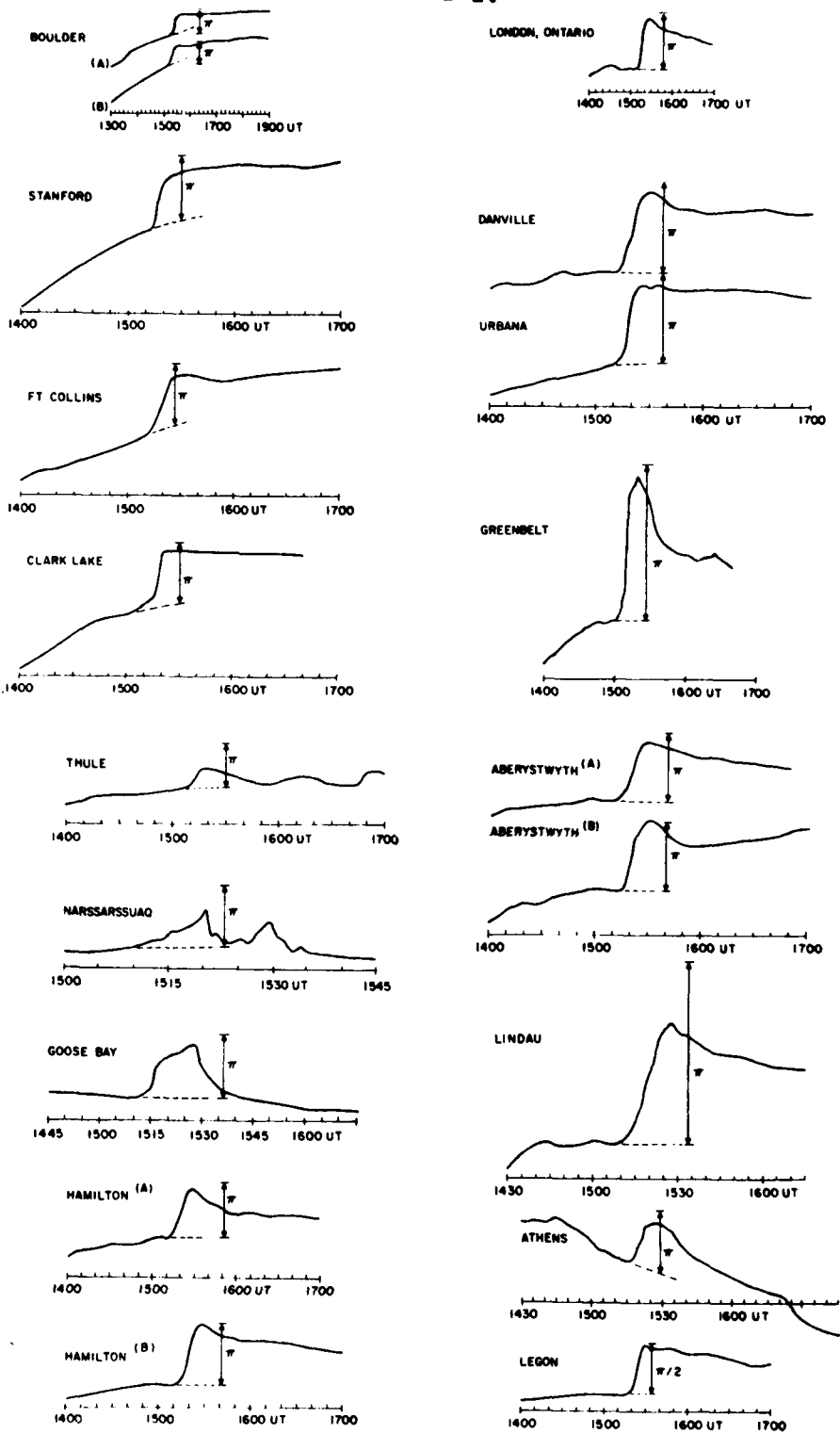
FIGURE 5. SD (TEC) patterns for 28 storms derived from stations at Sagamore Hill, Hamilton, Mass., and Stanford, California.

FIGURE 6. SD (TEC) patterns for 12 storms derived from stations at Sagamore Hill, Hamilton, Mass., and Arecibo, Puerto Rico (from Lanzerotti et. al., 1975).

FIGURE 7. TEC observations made from a network of stations in the western hemisphere during the large magnetic storm of 8 March 1970 (from Klobuchar et. al., 1971).

FIGURE 8. The time of the diurnal TEC peak on the storm days of 17 December, 1971, and 17 June, 1972, plotted on a longitude/local time grid (see text). Station code: SH = Sagamore Hill, UR = Urbana, BO = Boulder, ST = Stanford, FC = Fort Collins, CL = Clark Lake, ROS = Rosman.

FIGURE 1.



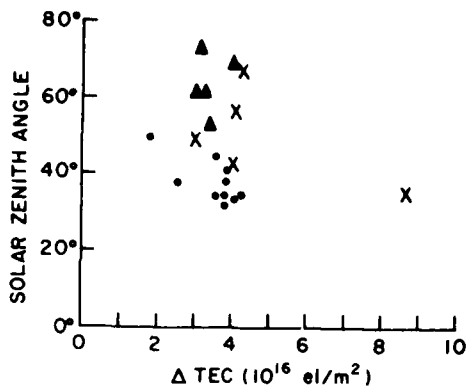


FIGURE 2(a).

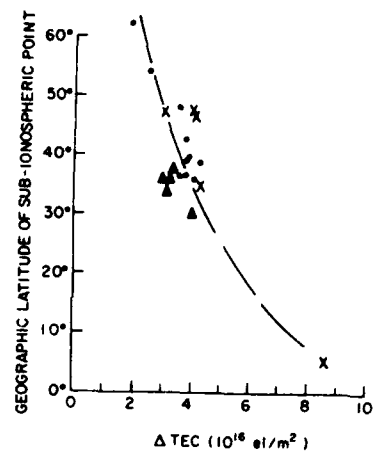
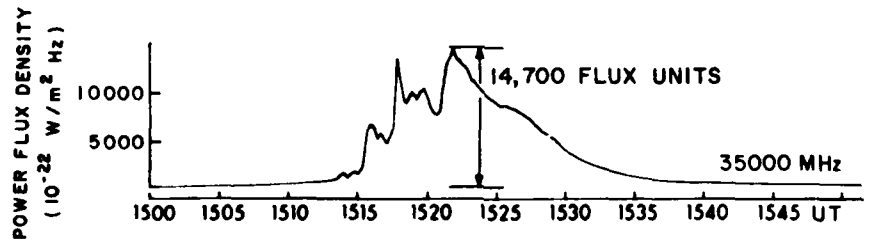
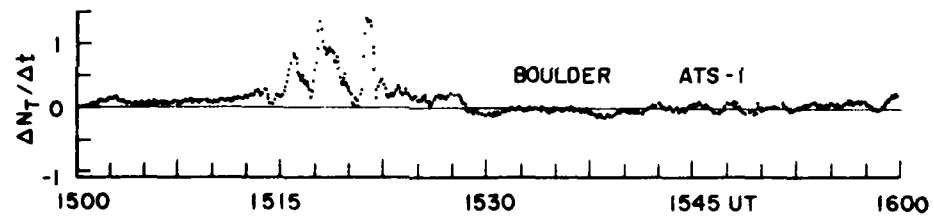


FIGURE 2(b).

RATE OF IONOSPHERIC ELECTRON CONTENT CHANGE

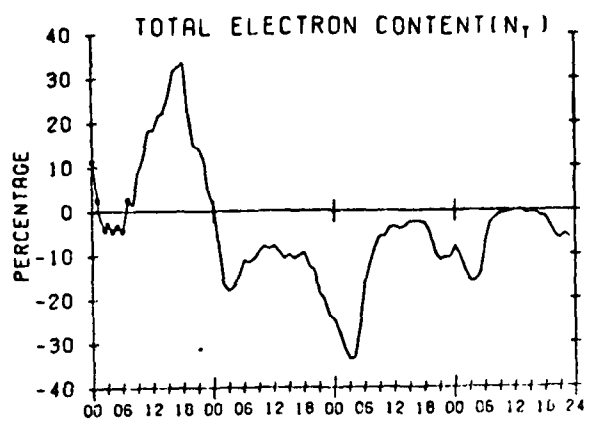
7 AUGUST 1972

( UNITS OF ELECTRONS - METER<sup>-2</sup> - SEC<sup>-1</sup>  $\times 10^{-14}$  )



GREAT BURST OBSERVED 7 AUGUST 1972 AT SAGAMORE HILL RADIO OBSERVATORY, HAMILTON, MASS.

FIGURE 3.



LOCAL TIME  
SD1 SD2 SD3 SD4  
AVERAGE DISTURBED DAILY VARIATIONS  
SD FOR 75 STORMS

SAGAMORE HILL, MA.

## HONOLULU, HAWAII

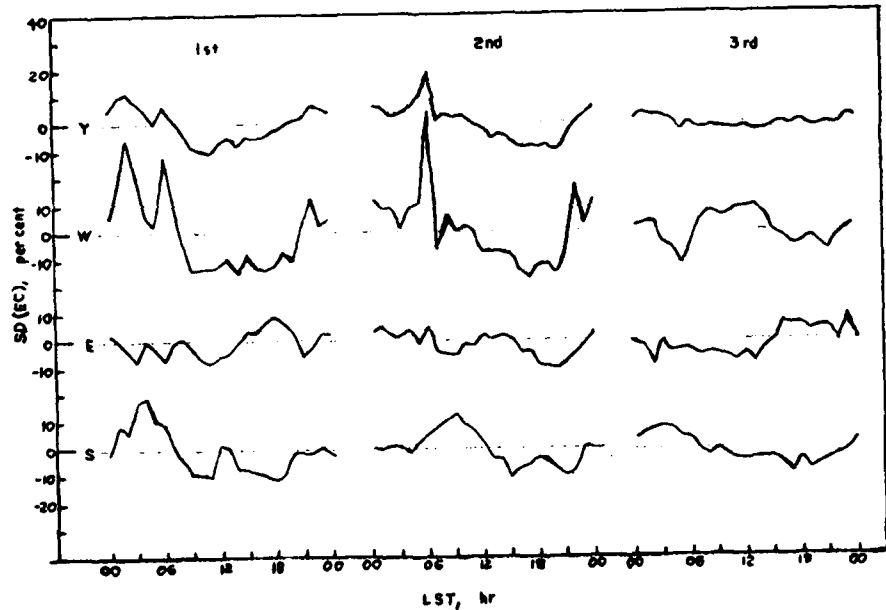


#### FIGURE 4.

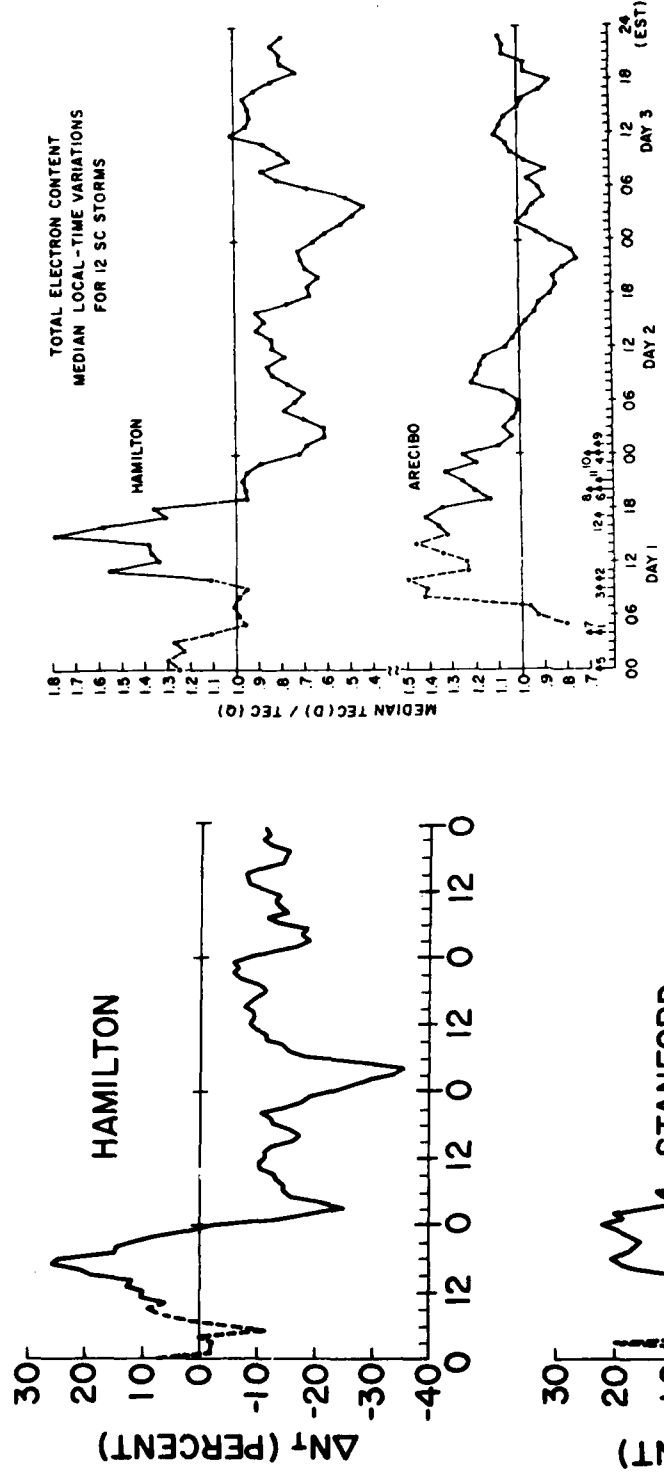


FIGURE 6.

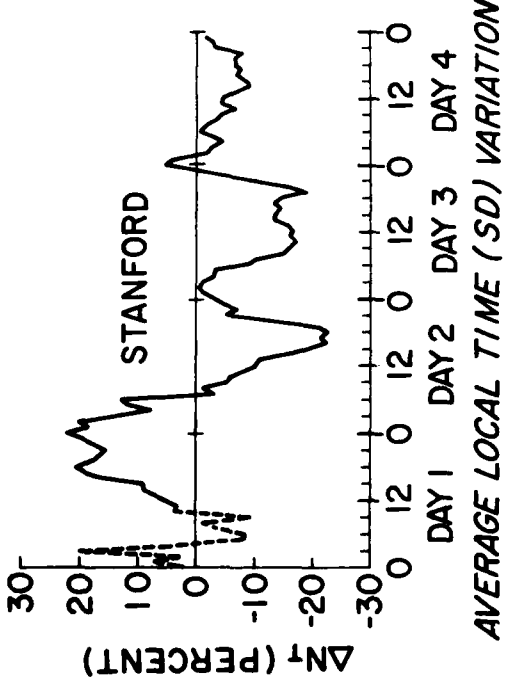


FIGURE 5.

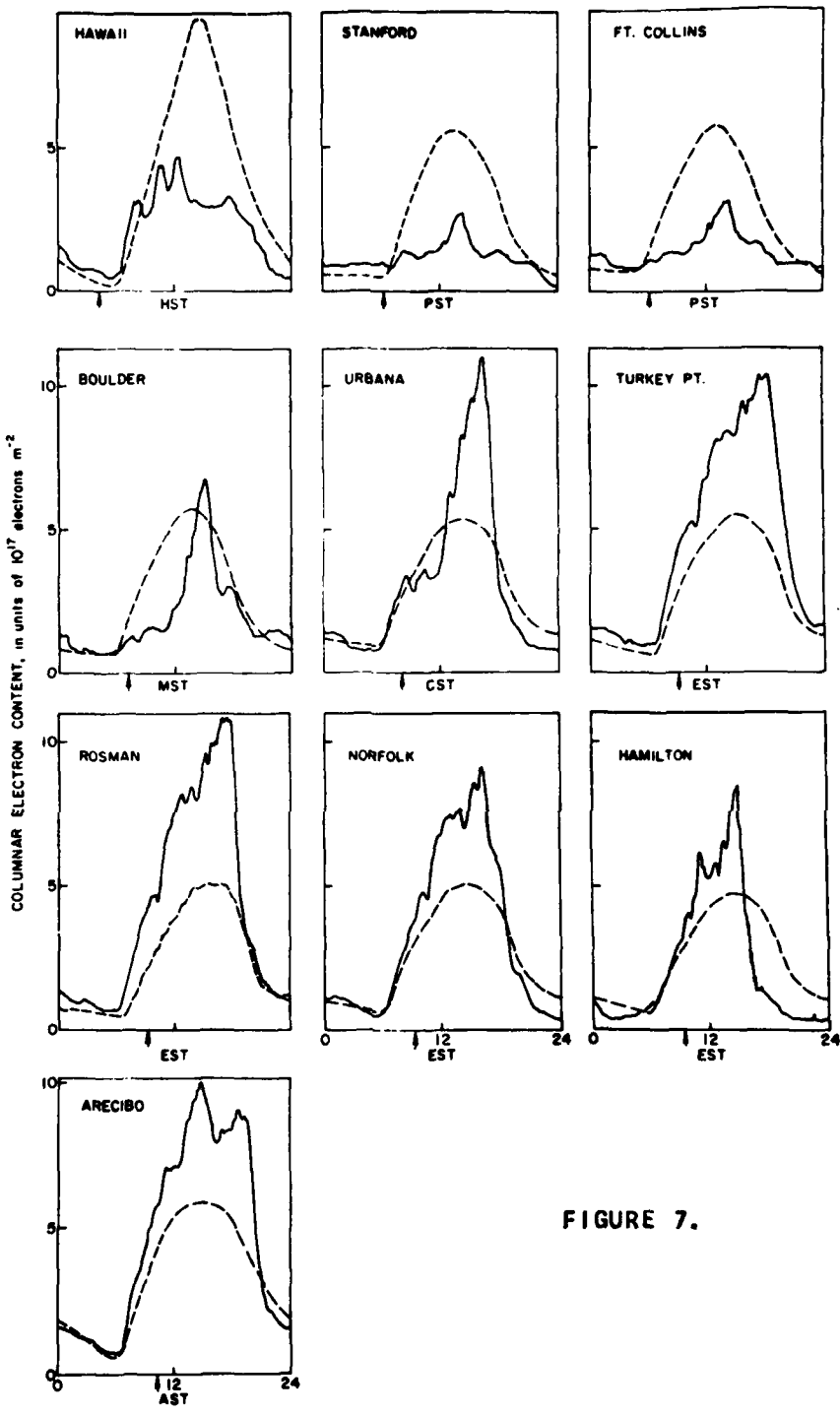
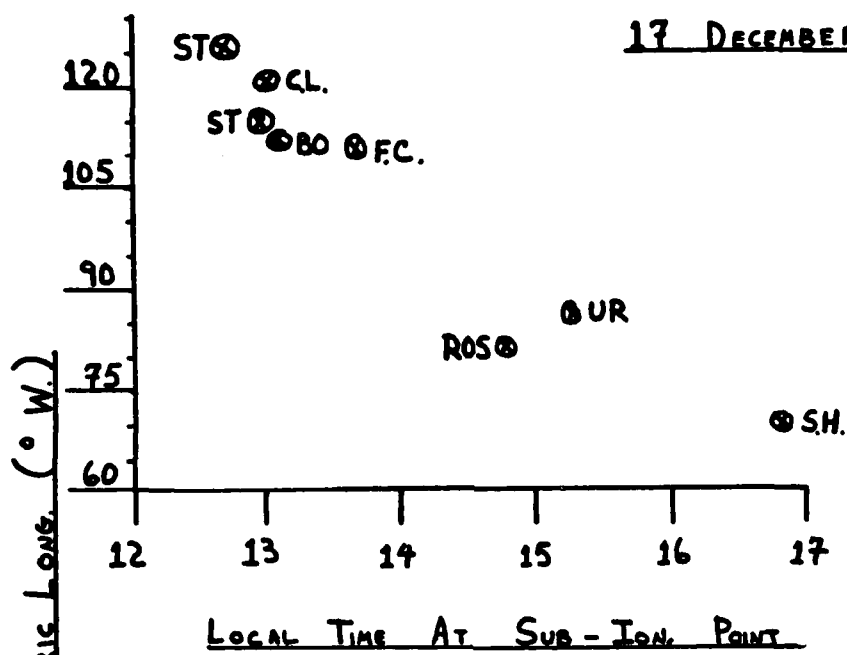


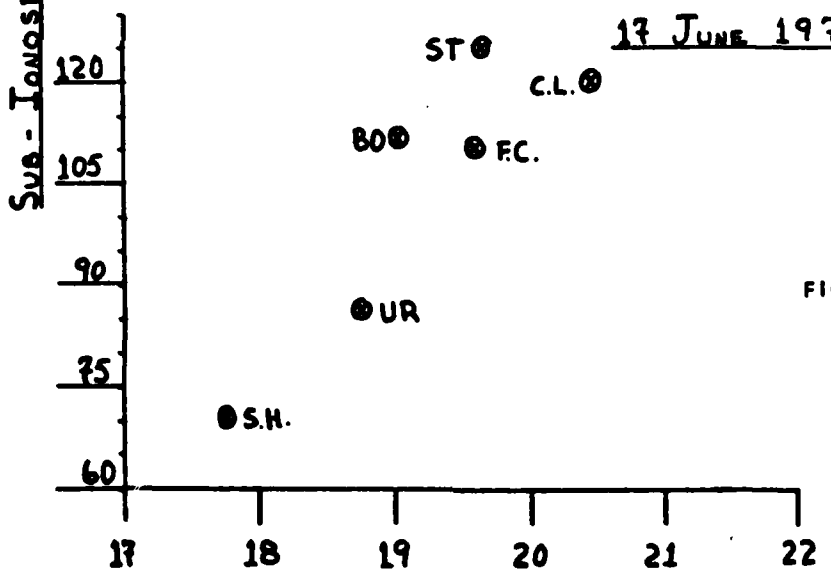
FIGURE 7.

17 DECEMBER 1971



LOCAL TIME AT SUB-ION POINT

17 JUNE 1972



LOCAL TIME AT SUB-ION POINT

FIGURE 8.

STORM-TIME COUPLING OF IONOSPHERE AND NEUTRAL  
ATMOSPHERE: ESRO 4 RESULTS

G. W. Prößl

Institut für Astrophysik und  
extraterrestrische Forschung  
Auf dem Hügel 71  
53 Bonn, Fed. Rep. of Germany

Abstract:

The storm-time interaction of the neutral and ionized atmosphere is investigated using neutral composition data obtained by the ESRO 4 satellite and plasma data obtained from ground-based stations. A close coupling is found between the O/N<sub>2</sub> ratio and the maximum F2-layer electron density, thus supporting previous suggestions that negative storm effects are caused by changes in the neutral composition. Given this connection a number of common features of atmospheric-ionospheric disturbances are discussed. These include the basic latitudinal structure of the disturbance, its systematic variation with invariant latitude, and its dependence on local time. Seasonal variations of ionospheric storm effects are attributed to directly observed seasonal changes in the O/N<sub>2</sub> ratio. Finally, we note that positive storm effects are not due to changes in the neutral composition.

One of the basic input parameters in modeling the ionospheric behavior is the neutral composition of the upper atmosphere. Recently satellite-borne gas analyzers have provided for the first time detailed information on this important state variable. In this study we discuss neutral composition data obtained by the ESRO 4 satellite which are essential for understanding the ionospheric behavior during magnetically disturbed periods. They are discussed within the framework of a model which tries to explain certain features of negative ionospheric storms (Prölss, 1976). Although open to discussion this model allows us to organize the observations in a suitable way.

### 1. Storm-time coupling between F2-layer plasma density and neutral composition

In 1956 Seaton suggested that the negative phase of ionospheric storms is caused by changes in the neutral composition. Subsequent theoretical studies (e.g. King, 1971; Chandra and Stubbe, 1971) and direct evidence obtained by satellite-borne gas analyzers (Prölss and von Zahn, 1974; Prölss et al., 1975) confirmed the validity of the proposed concept. In this section we present data which illustrate the close coupling between the neutral and ionized atmosphere during disturbed conditions.

Figure 1 shows a comparison between the day-to-day variation of the atomic oxygen to molecular nitrogen ratio and that of the maximum electron density in the F2 layer. Plotted are data from six mid-latitude stations during a nine-day interval in February 1973. Hermanus (HE) is located in South Africa, Salisbury (SR), Townsville (TV), and Brisbane (BR) in Australia, and Port Stanley (PS) and South Georgia (SG) in the South American sector. Both data sets have been normalized to values observed on a reference day ( $R(N_{max}) = R(O/N_2) = 1$ ). In addition the  $O/N_2$  ratios have been corrected for changes in observation height. Local solar time is approximately 11 hours. As is evident the variations of both parameters show a high degree of conformity. This is especially obvious during the magnetic-atmospheric-ionospheric disturbance starting on February 21 when a significant decrease in the  $O/N_2$  ratio causes a similar drop in the plasma density.

Using the same form of data presentation, Fig. 2 shows the relative day-to-day variations in the  $O/N_2$  ratio and in the maximum electron density for a six-day interval in October 1973. Point Arguello (PA), Boulder (BC), and Wallops Island (WP) are located in North America, Leningrad (LD) and Tomsk (TK) in Russia, and Brisbane (BR) in Australia. Local solar time of observation is approximately 9 hours. Again we note the close coupling between the two data sets, especially during the major magnetic storm of October 29/30, 1973.

Not all data investigated show this close coupling, and deviations are observed, especially for (geographic) mid-latitude stations located in the South American and Asian sectors (see section 6). However, in general, composition and plasma data are well correlated. This is demonstrated in Fig. 3 which combines the data from a larger number of stations and for

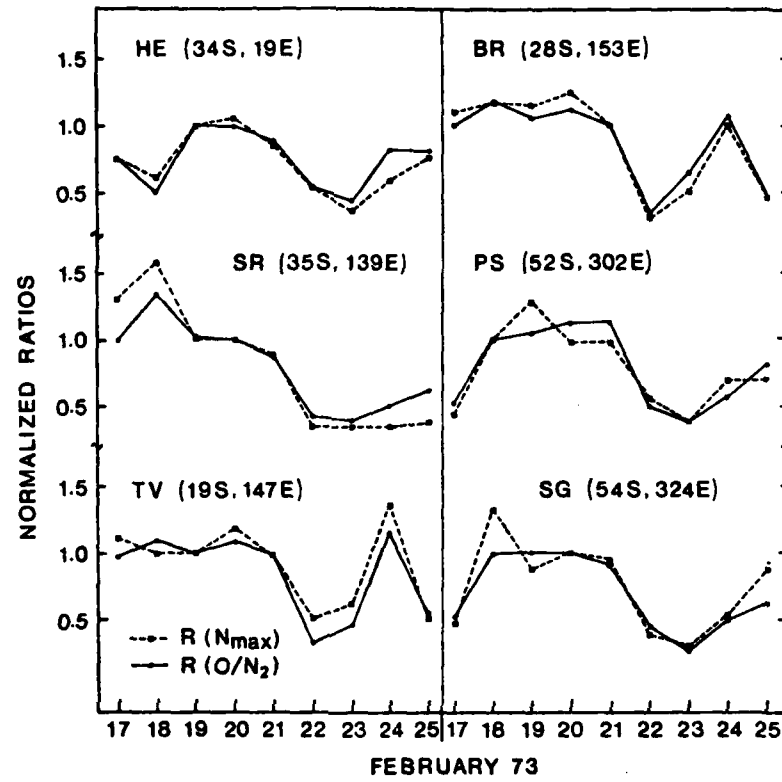


**Fig. 1:** Relative day-to-day variations in F2-layer maximum electron density and O/N<sub>2</sub> ratio above 6 mid-latitude stations (position in geographical coordinates) during a nine-day interval in February 1973.

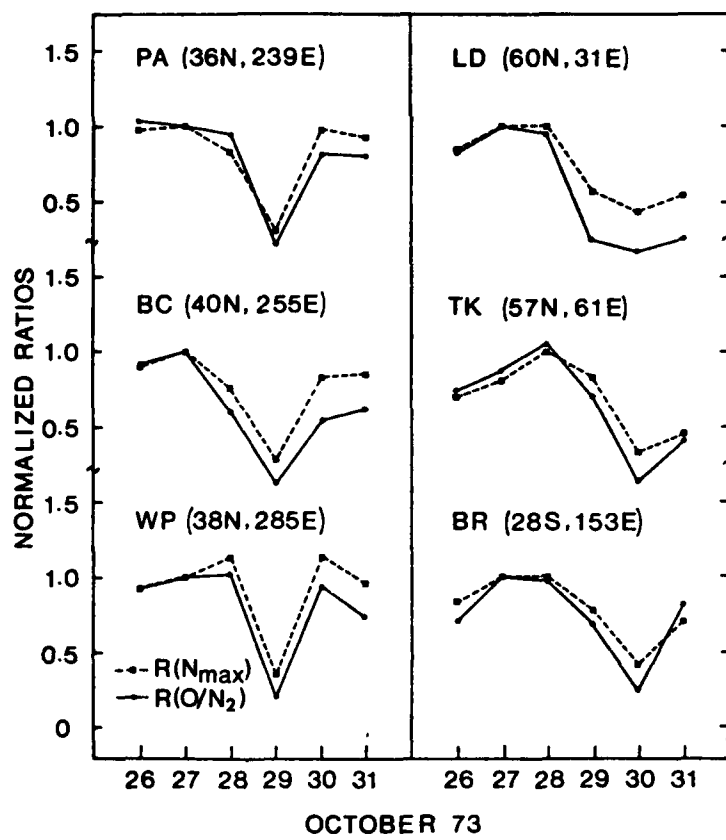
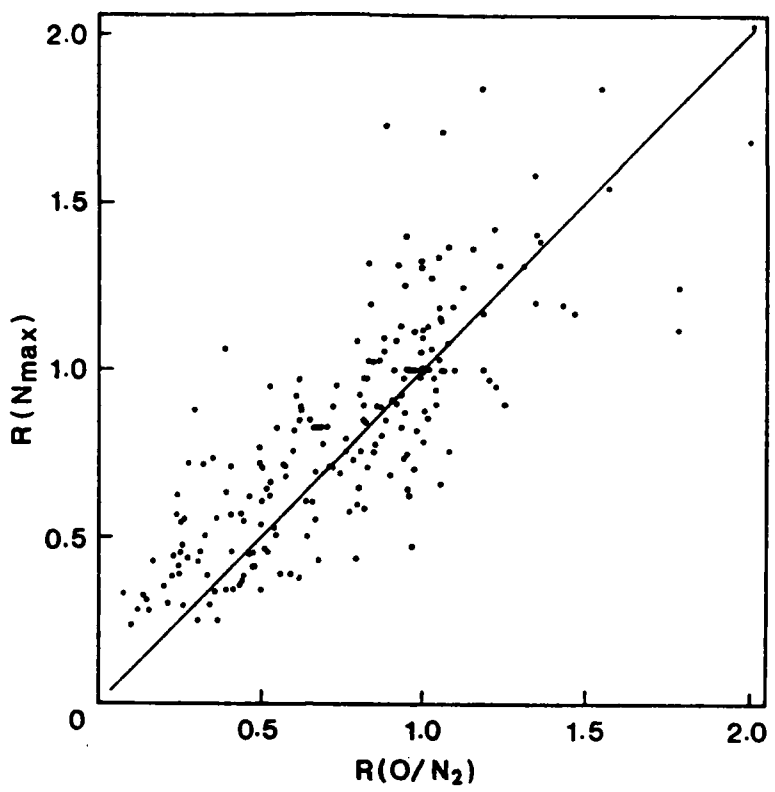


Fig. 2: Same as Fig. 1 for six-day interval in October 1973.



**Fig. 3:** Relative day-to-day variations in neutral composition  $R(O/N_2)$  versus relative day-to-day variation in maximum electron density  $R(N_{max})$  as observed above some 30 stations during February and October storm events.

both time intervals in the form of a scatter diagram. The close connection between the two data sets is evident.

From a theoretical point of view the positive correlation between neutral composition and plasma density is not surprising. Assume, for simplicity, a photochemical equilibrium situation for which the ionospheric production is proportional to the atomic oxygen density and the ionospheric loss is proportional to both the molecular nitrogen density and the electron density. In this situation relative changes in the  $O/N_2$  ratio should be equal to relative changes in the electron density ( $R(O/N_2) = R(N_{max})$ ), as is indicated by the straight line in Fig. 3. Even if plasma transport and dynamical processes are taken into account, this relationship should be approximately valid.

## 2. Basic latitudinal structure of atmospheric-ionospheric disturbances

In the previous section we have presented observational evidence for the close coupling between the neutral and ionized atmosphere. If we assume then that negative storm effects are caused by changes in the neutral composition, certain features of ionospheric storms will be determined by the morphology of the disturbed neutral atmosphere. In this section we discuss the basic latitudinal structure of an atmospheric disturbance and examine to what extent it is reflected in the ionospheric behavior.

It is well known that magnetospheric storms deposit a large amount of energy in the higher latitude region (e.g. Cole, 1966). Recent satellite measurements have shown that this energy injection leads to the development of disturbance zones in the neutral composition which are - among other things - characterized by a marked increase in the  $N_2/O$  ratio (e.g. Taeusch et al., 1971; Prölss and Fricke, 1976). This is schematically illustrated in Fig. 4. Actual data showing the basic latitudinal structure of these disturbance zones are presented in Fig. 5. The upper panel shows the time variation of the auroral electrojet index AE during a five-day interval in October 1973 which includes a period of enhanced magnetic activity. The lower panel illustrates the atmospheric response to this disturbance. Plotted are relative changes in the  $N_2/O$  ratio along the satellite orbit. In this kind of presentation  $R(N_2/O) = 1$  serves as a reference, meaning no change with respect to quiet times. Figure 5 clearly documents the following points: (1) Magnetic activity leads to the development of disturbance zones in the  $N_2/O$  ratio in the high and mid-latitude regions of both hemispheres; (2) The magnitude of the disturbance increases with increasing magnetic activity; (3) The latitudinal extent of the disturbance zone also increases with increasing activity; in addition it varies with the invariant latitude.

The latitudinal structure of the atmospheric disturbance shown in Fig. 5 is closely matched by similar variations in the ionospheric storm effects. This is demonstrated in Fig. 6. The upper panel shows again the relative changes in the  $N_2/O$  ratio as observed during orbit 5086. The lower part shows the time variation of the critical frequency as observed at Brisbane (BR) in Australia, at Yamagawa (YG) in Japan, and at Yakutsk (YA) in

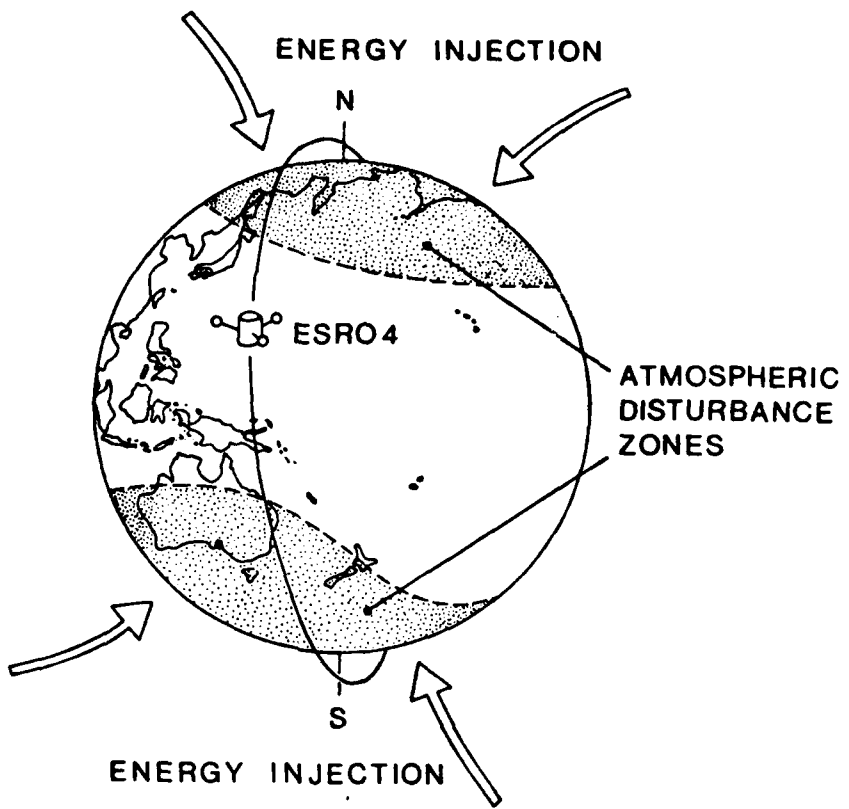


Fig. 4: Energy injection and formation of atmospheric disturbance zones during magnetospheric storm event. Also shown is a sample ESRO 4 orbit.

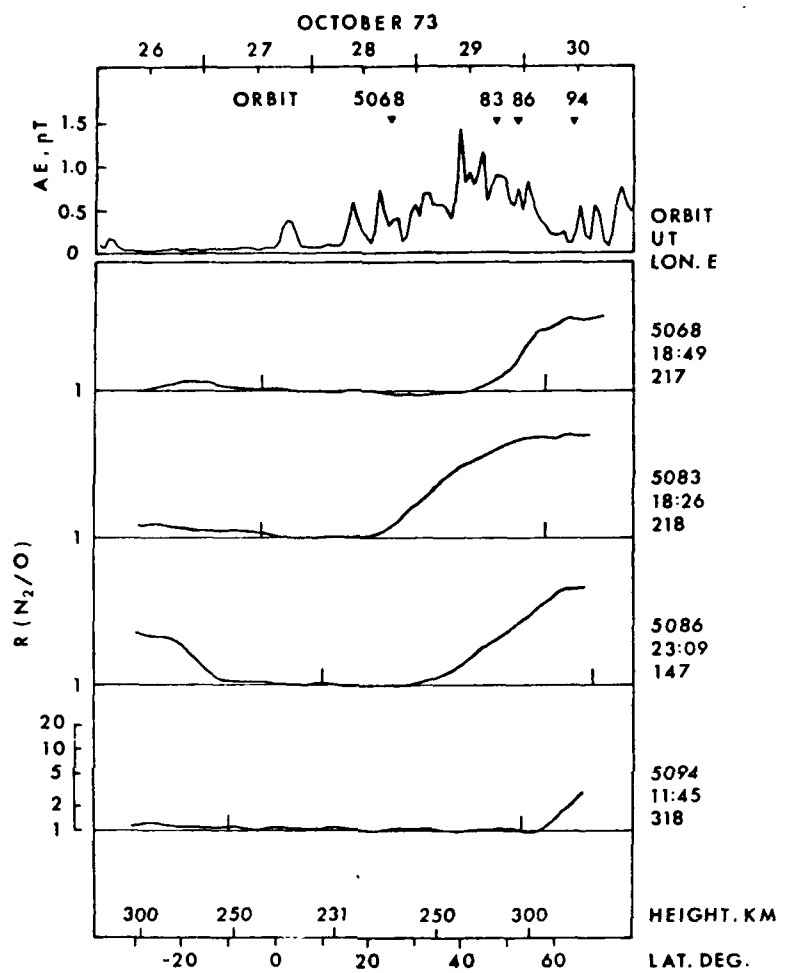
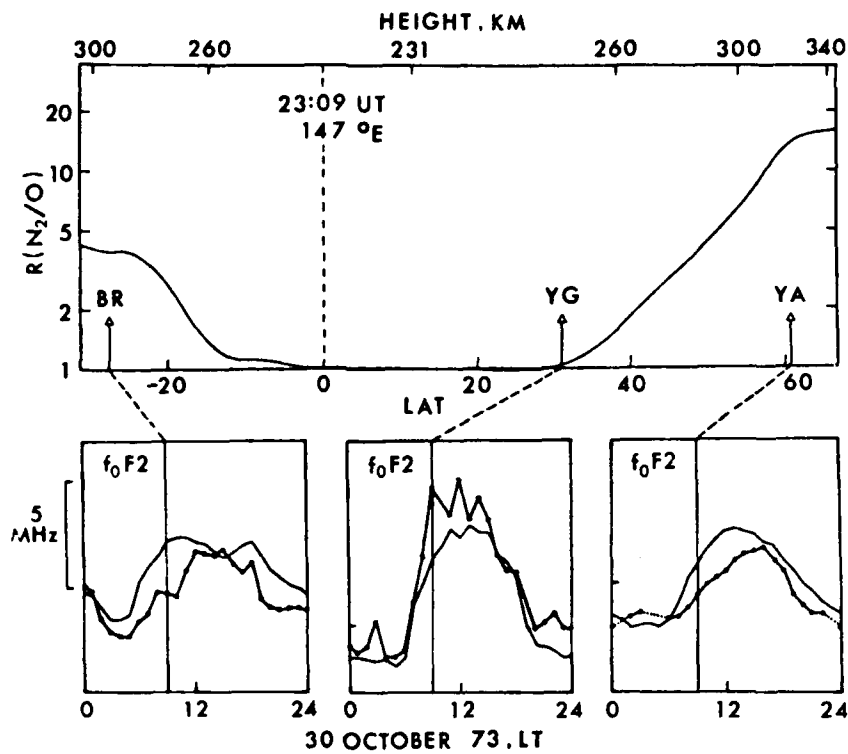


Fig. 5: Magnetic activity associated changes in neutral composition. The upper panel shows the magnetic AE index during five days in October 1973. The lower panel shows the associated changes in the  $N_2/O$  ratio as observed during 4 representative orbits. Geographic latitude and approximate height of observation are given at the bottom of the figure. At the right orbit numbers and UT and geographic longitude (east) of equator crossings are given. The vertical bars indicate  $0^\circ$  and  $60^\circ$  N invariant latitude.



**Fig. 6.** Comparison between latitudinal variation of neutral composition and plasma density. The upper panel shows the relative changes in the  $N_2/O$  ratio as observed during orbit 5086 on October 30, 1973. The lower part shows the local time variation of the F2-layer critical frequency (fat dotted line) as observed at three ionosonde stations whose relative positions with respect to the atmospheric disturbance zones are indicated by arrows. Also shown for comparison is the monthly median of  $f_0F2$  for October 73 (thin line).

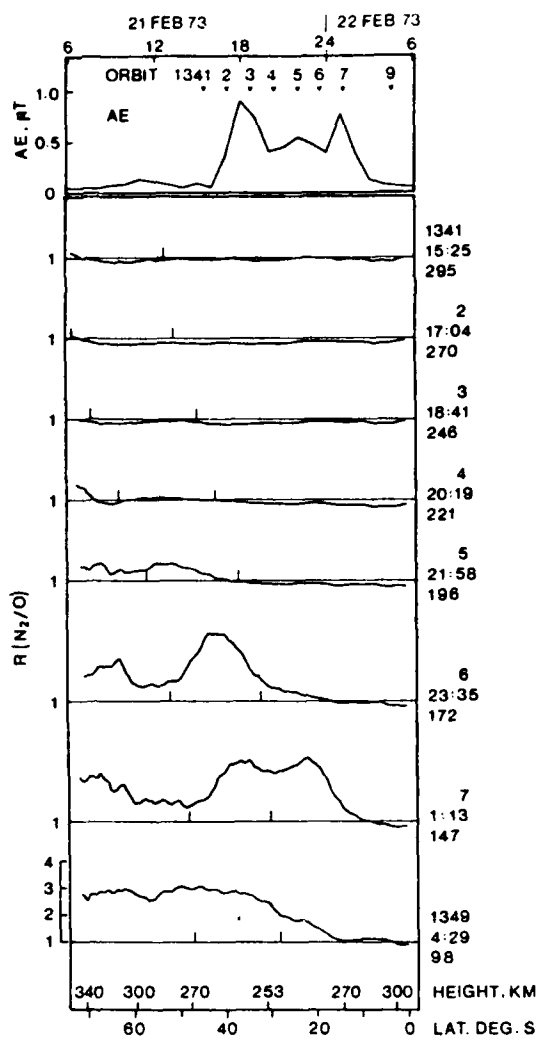
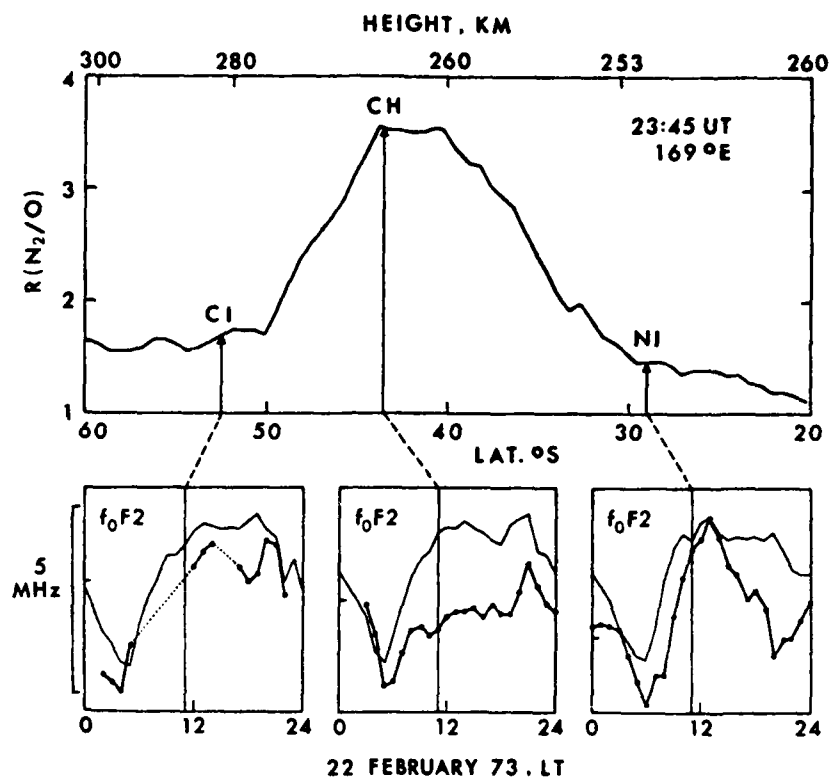


Fig. 7: Same as Fig. 5 for February storm event.



**Fig. 8:** Same as Fig. 6 for orbit 1346 and data from 3 ionosonde stations located at different positions relative to the atmospheric disturbance zone.

Russia, all stations being located at longitudes close to that of orbit 5086. Both Yakutsk and Brisbane, located inside the northern and southern disturbance zones, respectively, show considerable negative storm effects. On the other hand Yamagawa, situated just outside the northern disturbance zone, shows positive storm effects. We conclude that only ionosonde stations located within the disturbance zones of the enhanced  $N_2/O$  ratio are liable to observe negative storm effects.

Atmospheric disturbances do not always exhibit smooth latitudinal (and longitudinal) variations (Prölss and von Zahn, 1974; Trinks et al., 1975). This is illustrated in Fig. 7, which shows data obtained during the magnetically disturbed period of February 21/22, 1973. The format of data presentation is the same as in Fig. 5. We note that interesting latitudinal structures are observed during orbits 1345 to 1349. A comparison with ionosonde data shows that these structures are accurately reproduced by similar variations in the plasma density. This is shown in Fig. 8. The upper panel again shows the mid-latitude disturbance observed during orbit 1346. The lower part shows the time variation of the critical frequency as observed at Campbell Island (CI), Christchurch (CH), and Norfolk Island (NI), all located in the New Zealand sector and at longitudes close to that of orbit 1346. Both Campbell Island and Norfolk Island, located south and north of the disturbance zone, respectively, exhibit much weaker negative storm effects than Christchurch, which is near the center of the disturbance. This is to show that even localized structures in negative storm effects may be attributed to similar variations in the atmospheric disturbances.

### 3. Longitudinal variations of atmospheric-ionospheric disturbances

The magnetospheric storm associated energy injection in the higher latitude region is controlled by the geomagnetic field. The basic longitudinal variation of the resulting atmospheric disturbance in a geographic coordinate system should therefore be that associated with the varying displacement between magnetic and geographic latitudes. This is indeed observed (e.g. Prölss et al., 1975; Jacchia et al., 1976). The lower panels of Figs. 9 and 10 show a comparison between the variation of the  $N_2/O$  ratio and the variation of the magnetic invariant latitude as a function of the geographic longitude along constant geographic latitude and at constant height. There is good agreement between the systematic variation of both parameters, clearly demonstrating the invariant latitude control of atmospheric disturbances.

Satellite data do not allow us to separate spatial from temporal effects. To demonstrate that the observed variations in the  $N_2/O$  ratio are not due to similar temporal changes in the magnetic activity, the upper panels of Figs. 9 and 10 show the AE index for the time intervals of interest: As is evident, no comparable variations in AE and  $N_2/O$  or  $\Lambda$  are observed.

Figures 9 and 10 also show that in the southern hemisphere the atmospheric disturbance maximizes in the Australian sector (AU) and is weakest in the South American sector (SA), whereas in the northern hemisphere it peaks in the North American sector (NA) and is weakest in the Asian sector

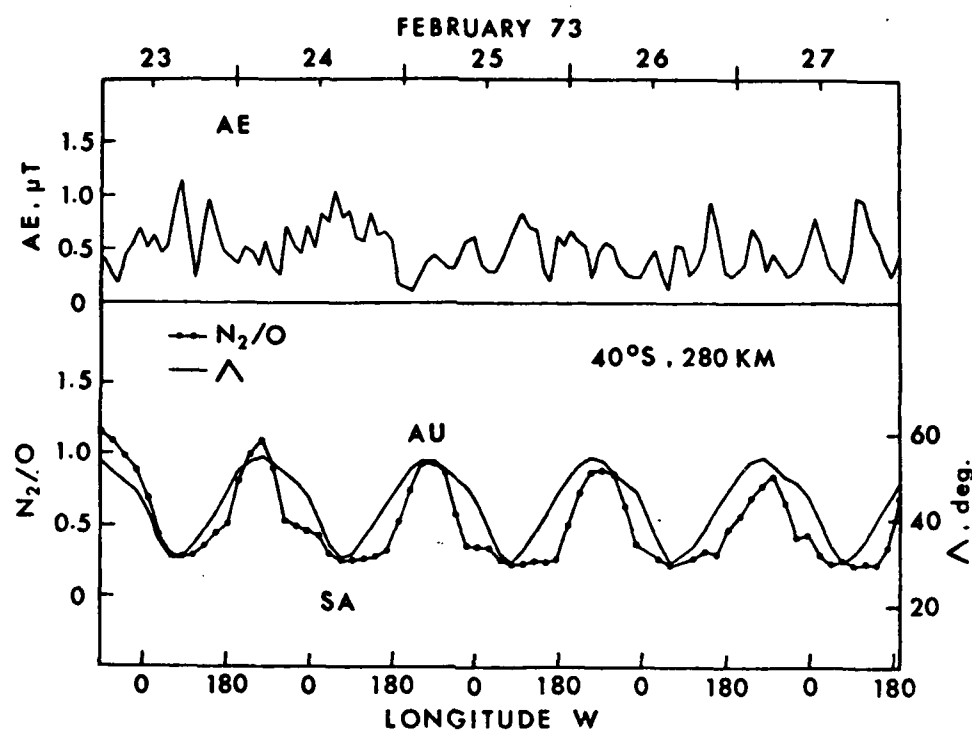


**Fig. 9:** Comparison between the variation of the  $N_2/O$  ratio and the variation of the magnetic invariant latitude  $\Lambda$  as a function of the geographic longitude along constant geographic latitude and at constant geographic height during five days in February '73 (lower panel). The level of magnetic activity during this time interval is shown in the upper panel using the AE index as an indicator.

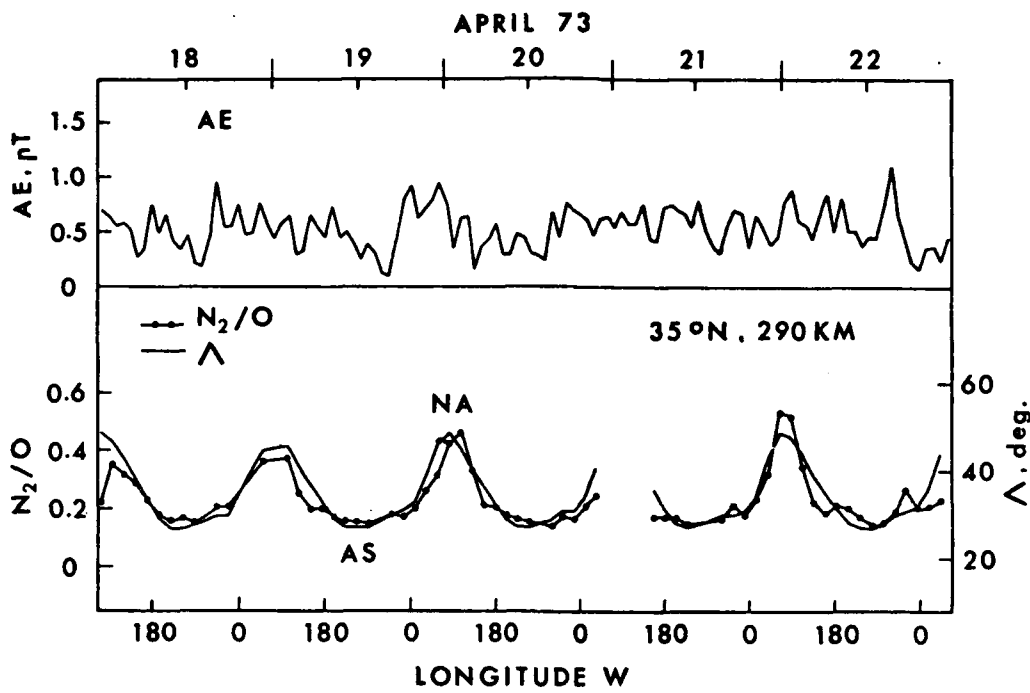


Fig. 10: Same as Fig. 9 for five-day interval in April '73.

(AS). Whether this distribution is solely due to the varying displacement of an energy source located at a fixed invariant latitude is not clear at this time. A preliminary analysis of other atmospheric-ionospheric storms appears to indicate that in addition to this displacement effect there may also be an amplitude modulation effect with maximum energy injection (at a constant magnetic activity level as indicated by the AE and Dst indices) in the Australian and North American sectors.

The longitudinal variations in the  $N_2/O$  ratio are closely matched by similar variations in the negative storm effects. During most of the ionospheric disturbances investigated so far, including those considered in Figs. 9 and 10, significant negative effects are observed in the Australian and North American sectors while stations located in the South American and Asian sectors tend to be scarcely disturbed or show positive storm effects.

#### 4. Local-time control of atmospheric-ionospheric disturbances

As was the case for the longitudinal variation, the local-time control of an atmospheric-ionospheric disturbance should be coupled to that of the primary energy source. Using auroral emissions and magnetic substorm activity as diagnostic tools the following picture emerges. First of all there is strong evidence that the energy injection maximizes along the auroral oval, which is not symmetric in local time but displaced toward the dark hemisphere (e.g. Akasofu, 1968). Thus the atmospheric disturbance should extend to lower latitudes in the night sector rather than in the day sector. Secondly, we note that substorm activity appears to be most intense in the early morning sector (Allen and Kroehl, 1975). The atmospheric disturbance should therefore be largest at these local times. Figure 11 schematically illustrates these points.

An experimental verification of these ideas by means of ESRO 4 data is difficult. A search for suitable orbits unambiguously demonstrating the day-night asymmetry in the atmospheric disturbances was largely unsuccessful so far because of the many conditions imposed by us (the most stringent of which being that no corrections for changes in observation height should be necessary). One of the few examples meeting most requirements is shown in Fig. 12. As is evident, the disturbance in  $N_2$  is significantly larger in the early morning than in the afternoon sector.

A determination of the most disturbed local-time sector proves to be even more difficult because on one hand the satellite samples at the most two different local time sectors at a time, and on the other hand a separation of temporal and spatial effects is nearly impossible in the high latitude region. Also a statistical study will be impeded by the limited data base. Further work on this problem is in progress.

Turning to ionospheric data we note that negative storm effects are most conspicuous during sunlit hours. To be consistent with the local time variation of the disturbing energy source we have to assume that the night time F2 layer is less sensitive to changes in the neutral composition. Theoretical studies support this assumption with different arguments (Jones,

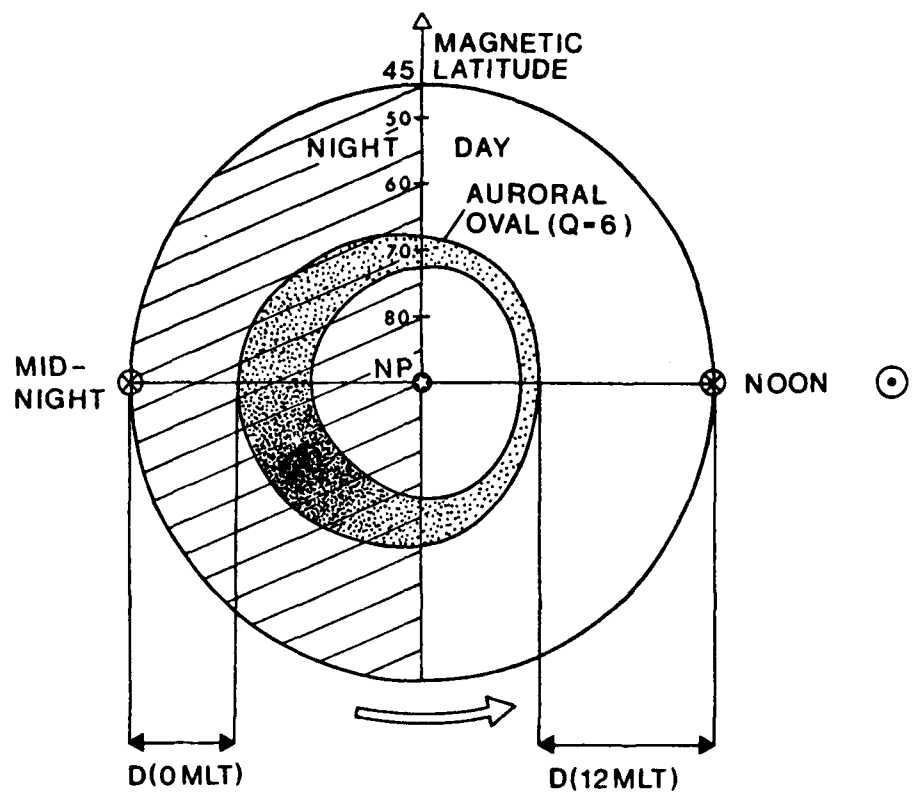


**Fig. 11:** Auroral oval during disturbed conditions illustrating the local-time dependence of location and strength of primary energy source.

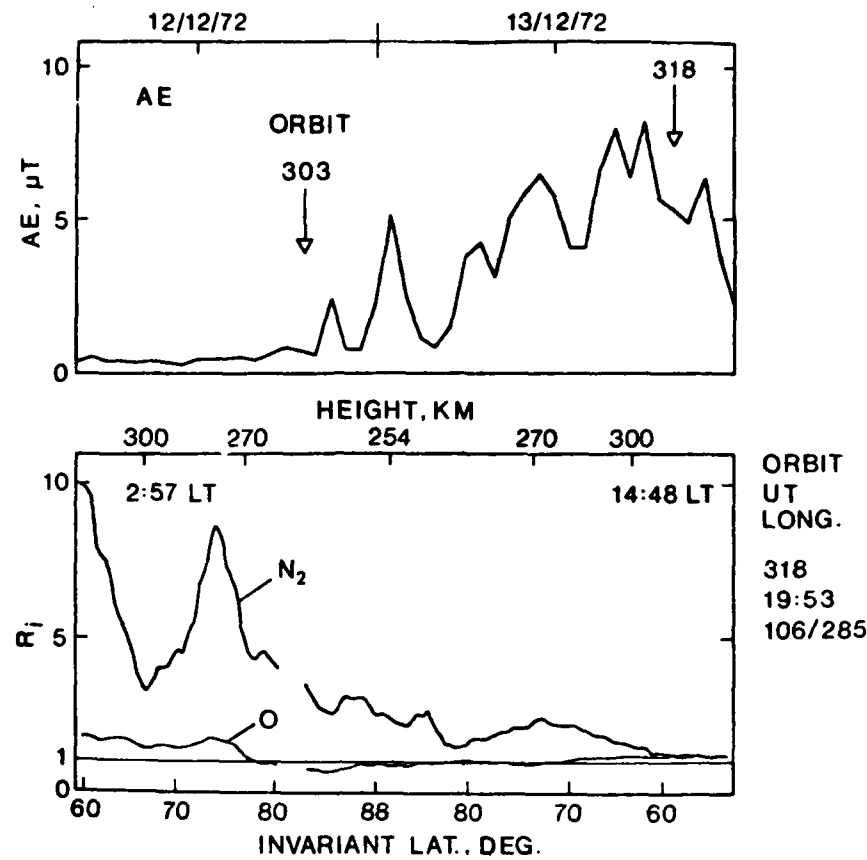


**Fig. 12:** Relative changes in the  $\text{N}_2$  and O densities as observed during orbit 318 illustrating the day-night asymmetry in the atmospheric disturbance (lower panel). The upper panel shows the level of magnetic substorm activity during reference orbit 303 and disturbed orbit 318.

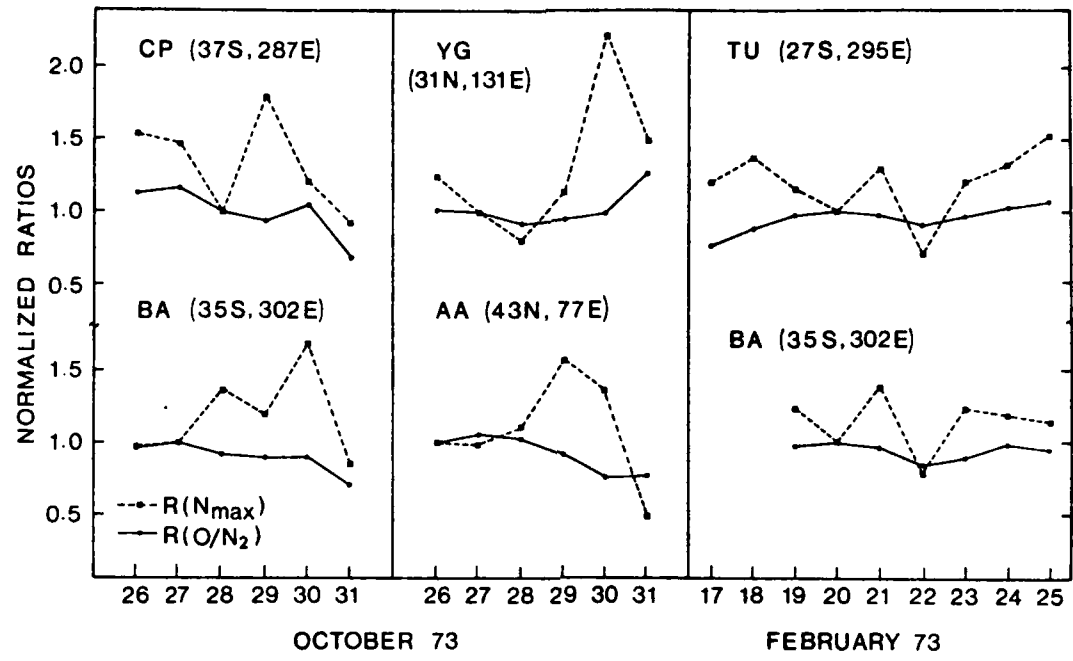


Fig. 13: Same as Figs. 1 and 2 for 6 stations located in the South American and Asian sectors during October and February at storm events.

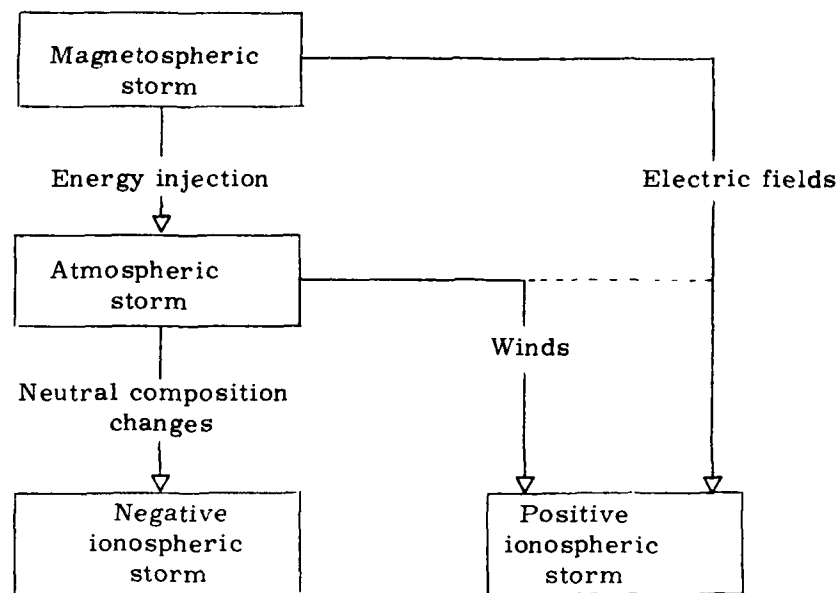
1973; Park and Banks, 1974). Work to verify this important point by means of ESRO 4 data is in progress. Finally, we note that the local-time control of the energy source together with the low night-time sensitivity of the F2-layer to composition changes may explain why negative storm effects are so often delayed until the day following the beginning of the magnetic storm.

##### 5. Seasonal variations of atmospheric-ionospheric disturbances

Duncan (1969) suggested that magnetic storm effects and seasonal variations are supporting each other in the summer hemisphere and are out-of-phase in the winter hemisphere, thus explaining the seasonal behavior of ionospheric storm effects. His explanation was based on the assumption that both variations are caused by changes in the neutral composition. ESRO 4 data provide direct evidence that this assumption is correct. In section 1 we discussed the storm-time coupling of the neutral and ionized atmosphere. Here we note that Köhnlein et al. (1975) using quiet-time ESRO 4 data derived considerable seasonal variations in the O/N<sub>2</sub> ratio. Thus for 45° N and 250 km altitude ( $ap = 5$ ,  $F_{10.7} = 100$  r.u.) they obtained an increase by a factor 3.4 in the O/N<sub>2</sub> ratio from the summer to the winter season. The mechanism causing this seasonal change will be in phase with the magnetic storm associated changes during the summertime. During the winter this same mechanism will oppose the build up of the disturbance zone as well as speed up the recovery to prestorm conditions.

##### 6. Positive storm effects

Neutral composition changes are by no means the only factors determining the ionospheric storm behavior. Thus no correlation was found between positive storm effects and corresponding changes in the neutral composition. This is demonstrated in Fig. 13, which shows the relative day-to-day variations in the O/N<sub>2</sub> ratio and in the F2 layer maximum electron density for 6 (geographic) mid-latitude stations during the October and February storm events. Concepcion (CP), Buenos Aires (BA), and Tucuman (TU) are located in South America, and Yamagawa (YG) and Alma Ata (AA) in Asia. No correlation is found between the enhancements and fluctuations in  $N_{max}$  and changes in the O/N<sub>2</sub> ratio. This supports previous suggestions that positive and negative storm effects are caused by different and sometimes competing mechanisms (e.g. King, 1971; Jones, 1971). If we assume that winds and electric fields are responsible for positive storm effects, the following block diagram illustrates the principle interactions during magnetospheric-atmospheric-ionospheric disturbance (MAID) events:



## 7. Conclusions

In this study data are presented which show the close coupling between the neutral and ionized atmosphere. This connection is used to identify a number of systematic variations in the disturbance behavior. A combination of these effects can explain the typical morphology of atmospheric-ionospheric storms, although departures from the expected behavior may occur for a number of reasons. For example, the spatial and temporal morphology of magnetospheric substorms is not well known at the present. Although neither the atmosphere nor the ionosphere will act as a passive tracer, the properties of this primary energy source will strongly influence their behavior. A better understanding of this mechanism will certainly help to improve the proposed model.

**Acknowledgments:** I am greatly indebted to U. von Zahn, who is the principle investigator of the ESRO 4 gas analyzer experiment. The help of his co-workers K.H. Fricke, H. Trinks, and U. Laux is appreciated. Thanks are also due to K. Schrüfer for carefully reading the manuscript. The ionospheric data used in this study were obtained from World Data Center A. This research was supported by the Deutsche Forschungsgemeinschaft through grant Pr 19/9.

### References

- Akasofu, S.-I. (1968). Polar and magnetic substorms, D. Reidel, Dordrecht, Netherlands.
- Allen, J.H., and Kroehl, H.W. (1975). Spatial and temporal distributions of magnetic effects of auroral electrojets as derived from AE indices. *J. Geophys.* 80, 3667.
- Chandra, S. and Stubbe, P. (1971). Ion and neutral composition changes in the thermospheric region during magnetic storms. *Planet. Space Sci.* 19, 491.
- Cole, K.D. (1966). Magnetic storms and associated phenomena. *Space Sci. Rev.* 5, 699.
- Duncan, R.A. (1969). F-region seasonal and magnetic-storm behavior. *J. Atmos. Terr. Phys.* 31, 59.
- Jacchia, L.G., Slowey, J.W. and von Zahn, U. (1976). Latitudinal changes of composition in the disturbed thermosphere from ESRO 4 measurements. *J. Geophys. Res.* 81, 36.
- Jones, K.L. (1971). Storm time variation of F2-layer electron concentration. *J. Atmos. Terr. Phys.* 33, 379.
- Jones, K.L. (1973). Wind, electric field and composition perturbations of the mid-latitude F-region during magnetic storms. *J. Atmos. Terr. Phys.* 35, 1515.
- King, G.A.M. (1971). The ionospheric F-region storm. *J. Atmos. Terr. Phys.* 33, 1223.
- Köhnlein, W., Trinks, H. and Volland, H. (1975). The density ratio O to N<sub>2</sub> in the thermosphere derived from ESRO-4 data. *Space Res.* 15, 287.
- Park, C.G. and Banks, P.M. (1974). Influence of thermal plasma flow on the mid-latitude nighttime F2 layer: Effects of electric fields and neutral winds inside the plasmasphere. *J. Geophys. Res.* 79, 4661.
- Prölss, G.W. and von Zahn, U. (1974). Magnetic storm associated changes in neutral composition of the atmosphere at mid-latitudes observed by the ESRO 4 gas analyzer. *Space Res.* 14, 158.
- Prölss, G.W. and von Zahn, U. (1974). ESRO 4 gas analyzer results, 2., Direct measurements of changes in the neutral composition during an ionospheric storm. *J. Geophys. Res.* 79, 2535.
- Prölss, G.W., von Zahn, U. and Raitt, W.J. (1975). Neutral atmospheric composition, plasma density, and electron temperature at F region heights. *J. Geophys. Res.* 80, 3715.

- Prölss, G.W., Fricke, K.H. and von Zahn, U. (1975). Observations during an atmospheric storm in late October 1973. *Space Res.* 15, 215.
- Prölss, G.W. and Fricke, K.H. (1975). Neutral composition changes during a period of increasing magnetic activity. *Planet. Space Sci.* 24, 61.
- Prölss, G.W. (1976). On explaining the negative phase of ionospheric storms. *Planet. Space Sci.* 24 (in press).
- Seaton, M.J. (1956). A possible explanation of the drop in F-region critical densities accompanying major ionospheric storms. *J. Atmos. Terr. Phys.* 8, 122.
- Taeusch, D.R., Carignan, G.R. and Reber, C.A. (1971). Neutral composition variation above 400 kilometers during a magnetic storm. *J. Geophys. Res.* 76, 8318.
- Trinks, H., Fricke, K.H., Laux, U., Prölss, G.W. and von Zahn, U. (1975). ESRO 4 gas analyzer results, 3, Spatial and temporal structure of the midlatitude atmosphere during a geomagnetic storm. *J. Geophys. Res.* 80, 4571.

## F-REGION ENHANCEMENTS INDUCED BY SOLAR FLARES

R. F. Donnelly, K. Davies, R. N. Crubb and R. B. Fritz  
NOAA Environmental Research Laboratories  
Boulder, Colorado 80302

ATS-6 total electron content  $N_T$  observations during solar flares exhibit four types of response: (1) a sudden increase in  $N_T$  (SITEC) for about 2 min. with several maxima in  $dN_T/dt$ , then a maxima ( $N_{T1MAX}$ ) or a distinct slowing in growth, followed by a slow smooth increase to a flat peak ( $N_{T2MAX}$ ) and finally a slow decay in  $N_T$ ; (2) a SITEC that occurs during ionospheric storms, where  $N_T$  decays abruptly after  $N_{T1MAX}$ ; (3) slow enhancements devoid of distinct impulsive structure in  $dN_T/dt$ ; and (4) no distinct response in  $N_T$ , even for relatively large soft X-ray flares. Flare induced increases in  $N_T$  are dominated by low-loss F2 ionization produced by 90-911A emission. The impulsive flare component  $\phi_1$  is relatively intense in the 90-911A range, but is short lived and is weak for flares near the edge of the visible solar disk and for certain slow flares.  $\phi_1$  produces the rapid rise, the sharp  $dN_T/dt$  maxima, and  $N_{T1MAX}$  in SITECs. The slow flare components are strong in the 1-20A range but relatively weak in the 90-911A range and accumulatively contribute to  $N_{T2MAX}$  in type 1 and 3 events, except during storms when F2 loss rates are abnormally high in type 2 events.

### 1. OBSERVATIONS

The ATS-6 total electron content measurements  $N_T$  at Boulder from June 1974 through May 1975 (Davies et al., 1975) were analyzed during solar flares. Figure 1 shows the largest SITEC (sudden increase in total electron content) observed where  $\Delta N_{T1MAX} \approx 2 \times 10^{16}$  electrons  $m^{-2}$  and  $dN_T/dt_{MAX} \approx 3.7 \times 10^{14}$  electrons  $m^{-2} s^{-1}$ , for a radial path. Note that the rise to maximum lasts only two minutes. The solar flare involved was an intense white-light flare, like that of the well-known event of August 7, 1972 (Mendillo et al., 1974).  $\Delta N_{T1MAX}$  was comparable but smaller than that of the event of August 7, 1972, while  $dN_T/dt_{MAX}$  was larger.

Twenty-five events of flare-induced enhancements were identified (Donnelly and Fritz, 1975) including a large variety of time structures. The most common

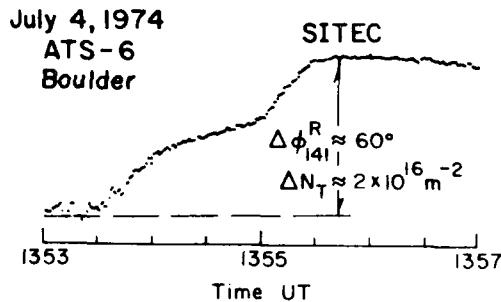


Figure 1. A large fast SITEC. The modulation phase  $\phi_{1411}^R$  is proportional to  $\pi_m$ .

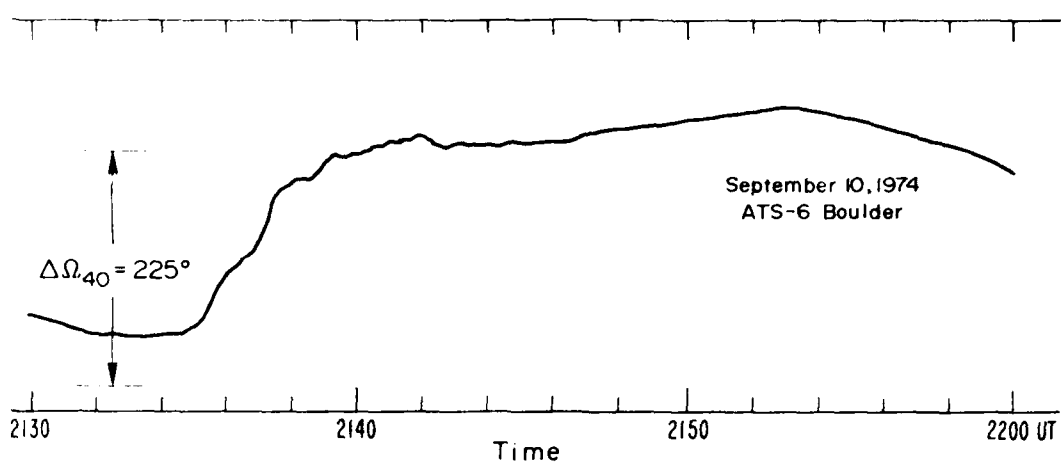


Figure 2. A sustained SITEC with early maxima  $\Delta N_{T1MAX}$  near 2139 and 2142 UT and a slow maximum  $\Delta N_{T2MAX}$  near 2153 UT. The Faraday rotation  $\Omega$  is proportional to the columnar electron content.

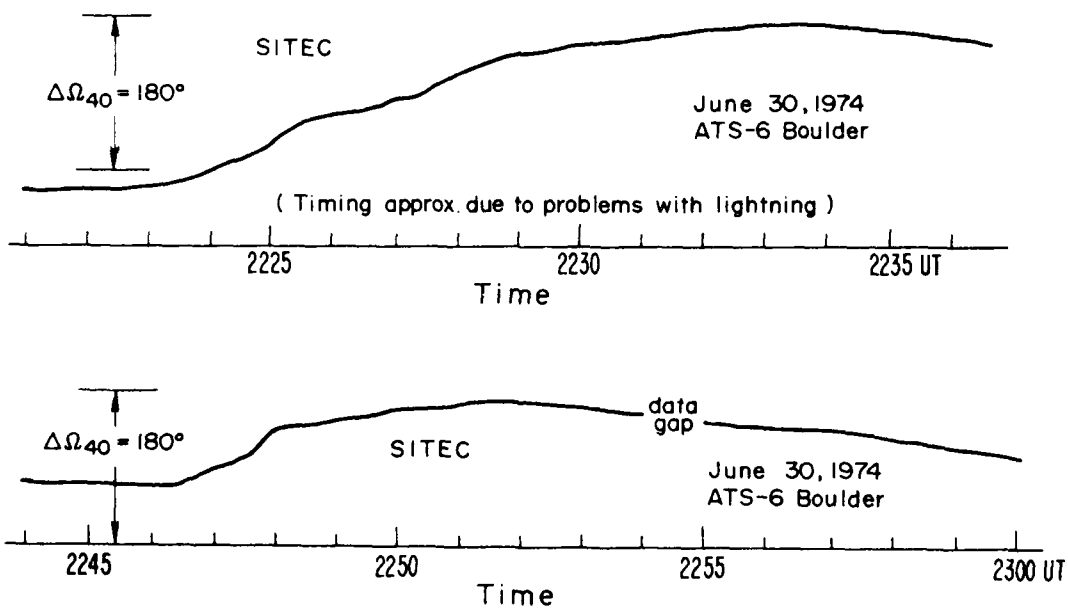


Figure 3. Sustained SITECs with points of marked decline in the rate of increase of  $\Delta N_T$  with the only maximum being  $\Delta N_{T2MAX}$ .

type of event, a sustained SITEC, involved a rapid rise in  $N_T$  to an early maximum  $N_{T1\text{MAX}}$ , followed mainly by a slow increase to a flat or gradual maximum  $\Delta N_{T2\text{MAX}}$ , and then a gradual decay. Figure 2 illustrates a sustained SITEC where  $\Delta N_{T1} \approx 4.7 \times 10^{15}$  electrons  $\text{m}^{-2}$  at 2141.8 UT and  $\Delta N_{T2\text{MAX}} \approx 6.7 \times 10^{15} \text{ m}^{-2}$  for a radial path. In other sustained SITECs, for example those in Figure 3, the first type of maximum is replaced by a marked decrease in the growth rate of  $\Delta N_{T1}$ .

A second type of SITEC involves a rapid decay right after the rapid rise. Figure 4 shows the most extreme example of this type observed at Boulder. These events occur only during ionospheric storms when  $f_0F2$  is depressed. Only the first type of maximum  $\Delta N_{T1\text{MAX}}$  occurs in this case, the second maximum does not. The event in Figure 1 is another example of this type of event.

A third type of flare-induced event is shown in Figure 5, where the enhancement is not sudden but rather very slow. These events are not nearly as distinct as are SITECs and appear much like other ionospheric variations unrelated to solar flares. Unlike these nonflare variations, the slow flare enhancements are simultaneous over the sunlit hemisphere as shown by observations from different longitudes and latitudes. The event in Figure 5 is devoid of the impulsive fine structure in  $dN_T/dt$  that is strong in SITECs. SMS-1 (Synchronous Meteorological Satellite) soft X-ray measurements in the 1/2 - 4A and 1 - 8A bands were used to identify solar flares and the concurrent ATS-6 data were searched for corresponding enhancements. Besides the three types of events discussed above, a fourth case was observed wherein some soft X-ray bursts lacked any distinct total content enhancement even though the 1 - 8A peak flux exceeded that of other bursts that were accompanied by SITECs (cf Garriott et al., 1967, p. 6012). For example, the 1 - 8A soft X-ray flare of 1910 UT October 12, 1974 was more than twice as large as that at 1722 UT, yet the later event was not accompanied by any distinct evidence of a flare-related enhancement whereas the earlier event definitely produced a SITEC. The lack of a distinct ionospheric event can, of course, result because the solar flare is too small or because the ionosphere is so disturbed by other processes that a small flare-induced enhancement cannot be observed clearly. But in addition, there are flares with soft X-ray emission comparable to other flares that produce total content enhancements where the 90 - 911A emission is too weak to produce a SITEC or distinct slow enhancement, as will be discussed later. For a detailed report of the ATS observations of flare-induced enhancements in total content, see Donnelly and Fritz (1975).

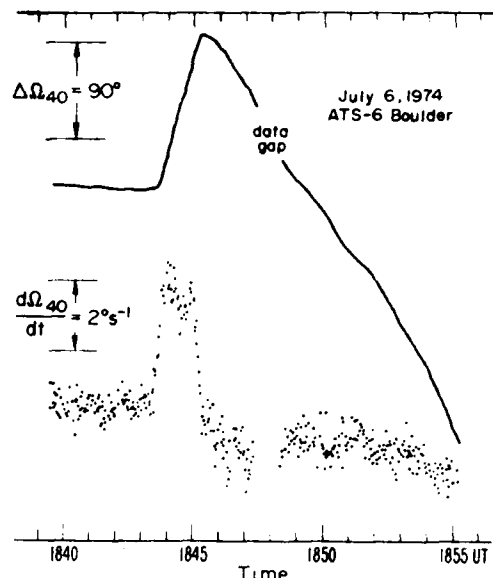


Figure 4. Rapid-decay SITEC. The bottom graph is proportional to the time rate of change of electron content.

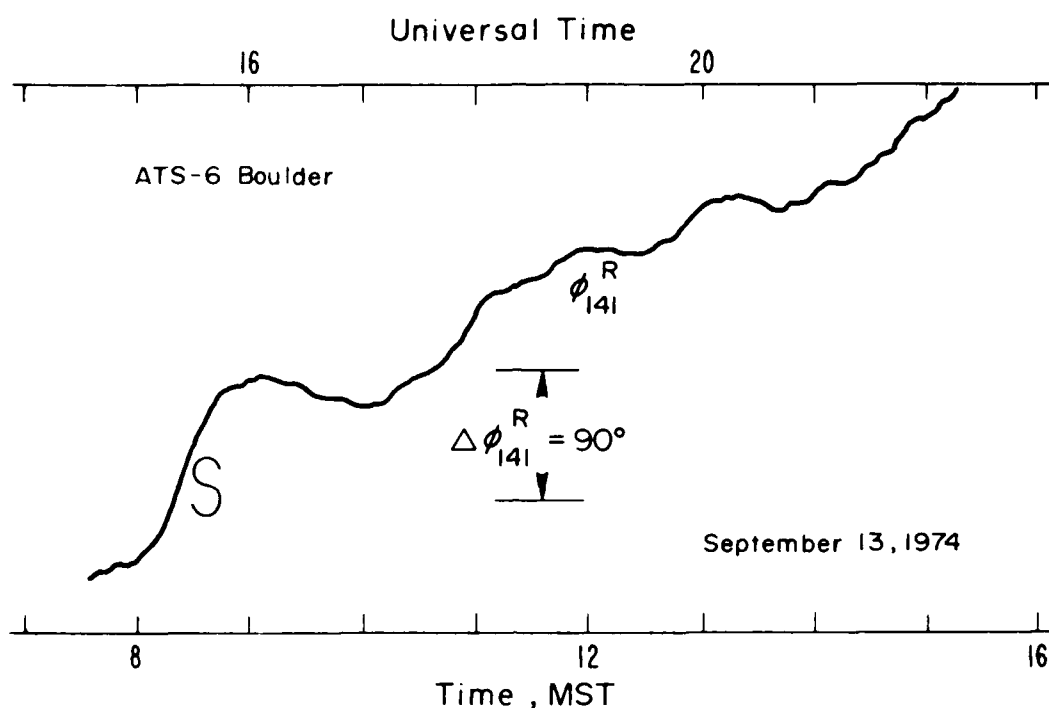


Figure 5. Slow enhancement of total electron content marked "S."  
The modulation phase  $\phi_{141}^R$  is proportional to  $N_T$ .

## 2. SOLAR FLARE X-RAY AND EUV EMISSION

The interpretation of SID's (Sudden Ionospheric Disturbances) has been complicated mainly by a lack of absolute-flux measurements over all the X-ray and extreme ultraviolet (EUV) wavelengths capable of affecting the upper atmosphere. Donnelly (1976) has developed empirical models of the flare energy flux  $\Phi$  based on various OSO, SMS and SOLRAD satellite experiments. These models will be described briefly and used to interpret the ATS-6 observations of enhancements in total electron content induced by solar flares. Figure 6 illustrates the three types of time components used in the model, namely:  $\Phi_1(t)$  the impulsive component,  $\Phi_2(t)$  the related slow component, and  $\Phi_3$  the very slow component. The two components  $\Phi_1$  and  $\Phi_2$  are approximately related by

$$\Phi_2(t) \propto \int_0^t \Phi_1(u) e^{-(t-u)/\tau_s} du, \text{ Wm}^{-2}, \quad (1)$$

where  $\tau_s$  is a decay time constant that is a function of the emission temperature appropriate for the particular wavelength  $\lambda$  for which  $\Phi_2$  is considered.  $\Phi_2$  starts when  $\Phi_1$  starts, rises most rapidly when  $\Phi_1$  peaks, and peaks just before  $\Phi_1$  ends.  $\Phi_3$  can occur by itself, but when it occurs with  $\Phi_1$  and  $\Phi_2$ , the latter usually occur during the rise of  $\Phi_3$ .

The rise and decay times of the fine structure in the impulsive bursts is typically several seconds to several tens of seconds. The rise and decay times

for the ensemble of impulsive bursts is typically several minutes in the large solar flares involved in SITECs. The combined slow components have rise and decay times ranging from several minutes to several hours. The emission at any particular wavelength in general involves a combination of all three components. The impulsive component is very strong in the 90 - 1027A range while the slow components are very strong in the soft X-ray range 1 - 90A.

The intensity of the impulsive EUV burst depends on the location of the flare on the sun, probably because of absorption of these emissions in the surrounding nonflaring solar atmosphere. The slow soft X-ray emission of flares is relatively independent of the flare location as long as it is not behind the sun. For flares located near the edge or limb of the visible sun, the EUV intensity is quite weak, more than an order of magnitude weaker than flares at the solar central meridian. The absorption effect is more complicated than that from a spherical concentric absorbing layer because flares near the center of the sun are more intense relative to those at intermediate central meridian distances than can be explained by a spherical absorbing layer. For flares within a given region on the sun, there are probably variations in EUV intensity according to the location of the flare within the solar active region and the amount of relatively cool solar material between the flare and Earth (Donnelly, 1976).

### 3. E- AND F-REGION EFFECTS OF SOLAR FLARES AND SITECS

Donnelly (1976) showed that the height-profile of the ionospheric electron production rate  $q(h)$  produced by the impulsive component is very similar in shape to that produced by the nonflare solar spectrum while that produced by the slow components is drastically different, as shown in Figure 7. The impulsive component has a relatively strong effect in the F region because it is strong in 90 - 911A emission. The slow component is very strong in absolute enhancement of  $q$  near 105 km because of the strong X-ray emission and because the K-shell absorption (below 31A for  $N_2$ , 23A for  $O_2$ ) causes the photoionization from 8 - 31A emission to occur over the same heights as that from the 31 - 90 emission. The percentage increase in  $q$  below 100 km produced by the slow components is extremely large because the percentage increase in  $\Phi(1 - 8A)$  is so large.

Figure 8 illustrates the ionization enhancement as a function of altitude and time computed for a sustained SITEC like that in Figure 2. The photoionization calculations were discussed by Donnelly (1976). Boulder ionograms were

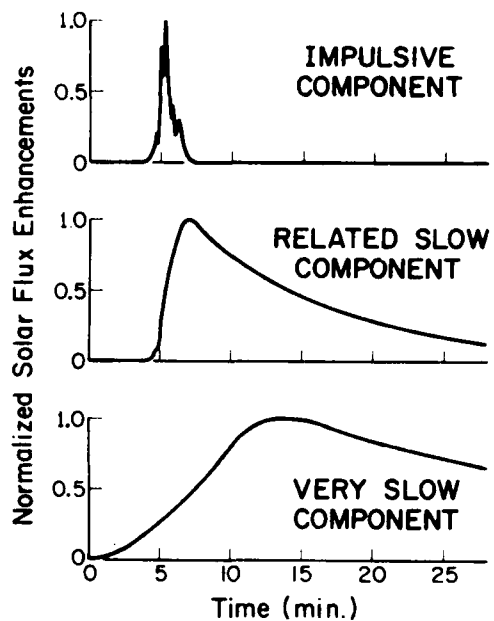


Figure 6. Characteristic time components of solar X-ray and EUV flares.

that from a spherical concentric absorbing layer because flares near the center of the sun are more intense relative to those at intermediate central meridian distances than can be explained by a spherical absorbing layer. For flares within a given region on the sun, there are probably variations in EUV intensity according to the location of the flare within the solar active region and the amount of relatively cool solar material between the flare and Earth (Donnelly, 1976).

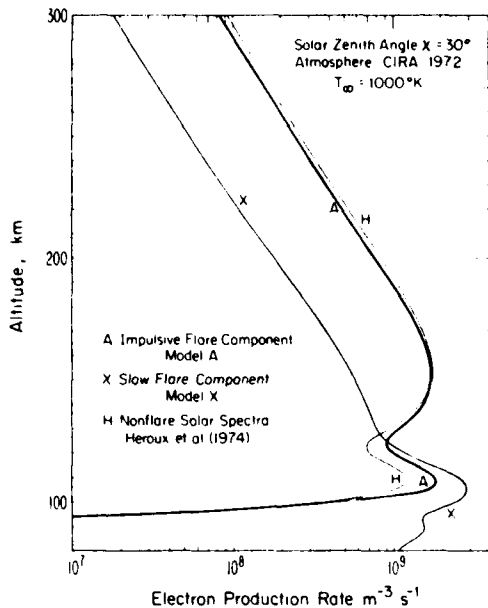


Figure 7. Electron production rate profiles for normalized  $\Phi(1/2-1027\text{A}) = 10^{-3}\text{Wm}^{-2}$  for a nonflare spectrum and for the impulsive and slow flare components.

The main features in Figure 8 can be approximately described by the electron continuity equation for the flare enhanced ionization  $\Delta N_e(z,t)$ ,

$$\frac{d}{dt} \Delta N_e(z,t) = \Delta q(z,t) - \frac{\Delta N_e}{\tau_i(z)} - \alpha_{eff}(z) \Delta N_e^2 - \nabla \cdot (\vec{v} \Delta N_e) \quad (2)$$

where  $\Delta q(t) \propto \Delta \Phi(t)$ ,  $\tau(z) \approx \beta^{-1}(z)$  and  $\alpha_{eff} \rightarrow 0$  above about 200 km and  $\tau(z) \approx 1/[2\alpha_{eff} N_0(z)]$  in the E region. The electron loss time constant is several tens of sec. in the 100 to 200 km range but increases with increasing altitude to very large values in the F region.

The fine structure of the impulsive component is the only flare structure with time constants shorter or comparable to the ionospheric electron-loss time constant at the altitudes of major photoionization. Consequently, the largest values of  $d\Delta N_e/dt$  are caused by this fast fine structure in  $\Delta \Phi$  and  $\Delta q$  and are dependent on the solar zenith angle  $\chi$ , particularly below 200 km. The ensemble of impulsive bursts for large flares rises and decays in times somewhat greater than  $\tau$  in the 100 - 200 km altitude range, consequently  $\Delta N_e(z,t)$  begins to decline there shortly after  $\Phi_{MAX}$ . The portion of the SIEC produced by the impulsive emissions and at altitudes, where the electron loss rates are high ( $z \leq 200$  km,  $t < 2245$  UT) and the transport term in (2) is small, can be approximately described by:

$$\Delta N_e(z, t) \approx \int_0^t \Delta q(z, u) e^{-(t-u)/\bar{\tau}_i} du. \quad (3)$$

Integrating over altitude, the impulsive E- and F-region contribution is

$$\Delta N_e(z, t) dz \approx \bar{\mu}_1 \cos X \int_0^t \Phi_1(1/2 - 1027A, u) e^{-(t-u)/\bar{\tau}_i} du \quad (4)$$

where  $X$  is the solar zenith angle,  $\bar{\mu}_1$  is the average of  $\mu = \eta(hc/\lambda)^{-1}$  over the  $1/2 - 1027\text{A}$  wavelength range when weighted by the impulsive energy flux  $\Phi_1(\lambda)$ ,  $\eta$  is the ionization efficiency, and  $\bar{\tau}_i$  is the average  $\tau_i$  over the  $100 - 200$  km altitude range.

The slow radiations are slow enough that below about  $200$  km their resultant ionization enhancement is approximately in quasi-equilibrium, i.e.  $d\Delta N_e/dt \approx 0$ . Because of the combination of the ionization production from the

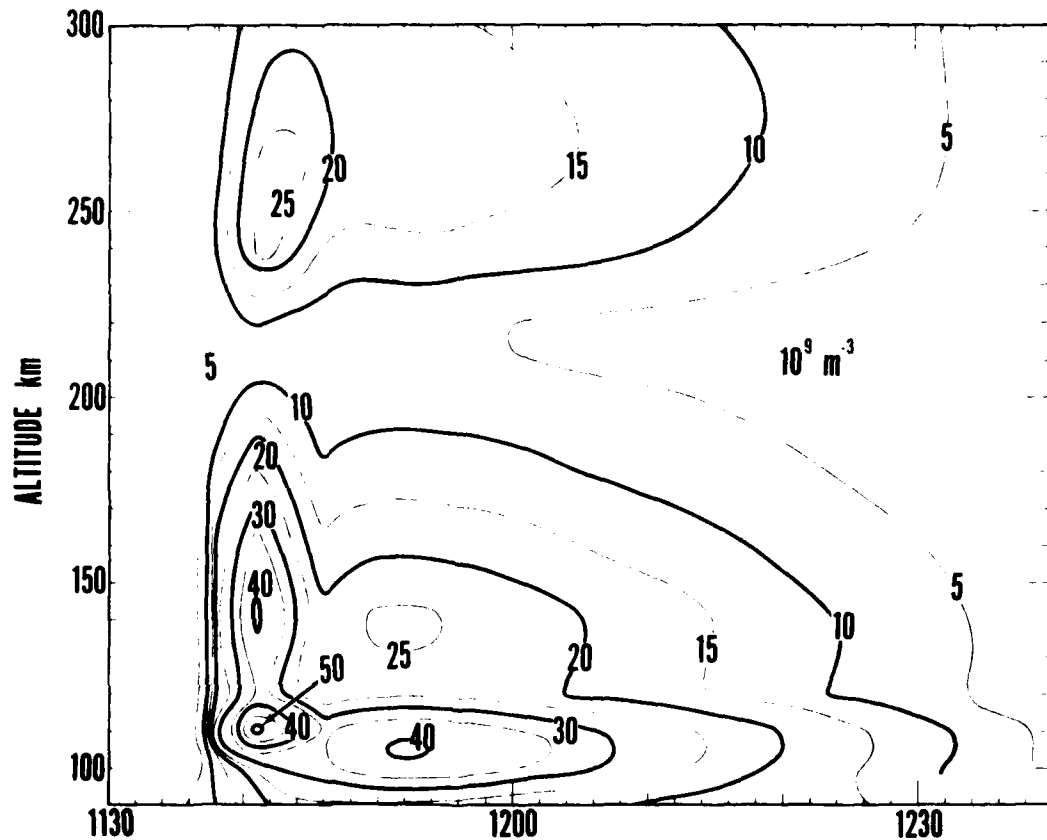


Figure 8. Computed electron enhancement as a function of altitude and local time.

strong and slow emissions in the 8 - 31A and 31 - 90A ranges, the ionization enhancement near 105 km is large and long lasting. Because the photoionization from the slow component decreases rapidly with altitude and because the electron loss rates are fast at altitudes below about 200 km,  $\Delta N(z,t)$  drops to very small values near 200 km near the end of the impulsive emissions. The portion of the SITEC produced by the slow emissions at altitudes where the electron loss rates are high is approximately given by

$$\Delta N_{\text{slow}}(z,t) \approx \left[ \frac{q_0 + \Delta q(z,t)}{\alpha_{\text{eff}}(z)} \right]^{1/2} - N_0(z), \quad (5)$$

where the "0" subscripted terms refer to the preflare values. Below the bottom of the preflare E layer,  $q_0$  and  $N_0$  in (5) are small. Above the bottom of the E layer,  $\Delta N \approx \tau_i \Delta q$ , except for extremely large events where a nonlinear loss term should be included. Integrating with altitude, the slow E-region contribution is

$$\int_0^{200} \Delta N_e(z,t) dz \approx \tau_{E_{2+3}}^{\bar{\mu}} \cos \chi \Phi(8 - 1027A) + \left[ \frac{\cos \chi h_s \Phi(1 - 8A)}{E_0 \bar{\alpha}_{\text{eff}}_D} \right]^{1/2} \quad (6)$$

where  $\tau_{E_{2+3}}$  is the average  $\tau_i$  over the 100 - 130 km altitude range,  $\bar{\mu}$  is the average of  $\eta \lambda / hc$  over the 8 - 1027 A range weighted by the combined slow emissions,  $E_0$  is the average energy expended per electron-ion pair formed by 1 - 8 A X-rays,  $h_s$  is the slab thickness of the enhancement below 100 km, and  $\bar{\alpha}_{\text{eff}}_D$  is the average effective reaction loss rate in the 70 to 100 km altitude range. (The last term in (6) is a very crude representation of the complicated nonlinear enhancement of ionization below 100 km, which is permissible here only for describing  $N_T(t)$  where that term contributes little).

Above 200 km, transport processes are usually important; and the atmosphere is optically thin for most wavelengths. Also,  $\Delta q(z)$  is relatively weak, decreases exponentially with altitude, and is relatively independent of the solar zenith angle for  $\chi < 80^\circ$ . Furthermore, for a quiet preflare ionosphere, the loss rates for O<sup>+</sup> are slow and decrease very rapidly with altitude. The result is that the O<sup>+</sup> ionization enhancement accumulates with time.  $\Delta N_2$  and related molecular enhancements still have a high loss rate. Because the impulsive emissions are strong in the 90 - 911A range and the loss rates are low,  $\Delta N_e(h,t)$  rapidly rises to large values. The fact that the photoionization rate is smaller than at lower altitudes is offset by the low loss rates. Above 200 km, neglecting the transport processes

$$\Delta N_e(z) \approx \int_z^t \Delta q(u) e^{-(t-u)\bar{\beta}} du. \quad (7)$$

For the F2-region contribution from the impulsive burst,

$$\int_{200}^{\infty} \Delta N_e(z) dz \approx \bar{\sigma}_1 [0]_{200} H_0 \int_0^t I_1(90 - 911A, u) e^{-(t-u)\bar{\beta}} du, \quad (8)$$

where  $I$  is the photon flux,  $\bar{\sigma}_1$  is the atomic oxygen absorption cross section averaged over the 90 - 911A range, and  $H_0$  is the scale height for the oxygen density [O] at 200 km. The 90 - 911A band is used here because the 1 - 90A and 911 - 1027A impulsive emissions contribute little to the ionization above 200 km. Including photoionization of He and H would increase (8) by only about 1/2, since  $(\bar{\sigma}_{He} [He]_{200} H_{He} + \bar{\sigma}_H [H]_{200} H_H)/\bar{\sigma}_1 [O]_{200}$ ,  $H_0$  is about that.

Although the slow flare components have a lower  $O^+$  production rate at high altitudes relative to the impulsive components, their longer duration accumulates ionization above 200 km to  $\Delta N_e$  values comparable to those during the impulsive enhancement. From (7), the F2-region contribution from the slow flare emission is

$$\int_{200}^{\infty} \Delta N_e dz \approx \bar{\sigma}_{2+3} [O]_{200} H_0 \int_{2+3}^{\infty} I_{2+3}(90 - 911A, u) e^{-(t-u)\bar{B}} du \quad (9)$$

The complete  $\Delta N_T(t)$  is given approximately by the sum of (4), (6), (8) and (9).

Figure 9 shows ATS-6  $N_T(t)$  observations together with results based on the above approximate expressions. SMS-1 soft X-ray measurements in the 1/2 - 4A and 1 - 8A wavelength ranges were used to estimate the time dependences and intensity of the slow flare emission, where the 1/2 - 4A flux peaks earlier and decays faster than the 1 - 8A flux, while the net 8 - 1027A flux is slower. The 8.8 GHz radio burst observed at Manila Observatory was used to estimate the time dependence of the impulsive component  $\Phi_1(t)$ . Equation (1) with  $\Phi_1(t)$  estimated by  $\Phi(8.8 \text{ GHz})$ , provided a good fit for  $\Phi_2(t) \approx \Phi(1/2 - 4A, t)$  with  $\tau_s = 20 \text{ min}$ . The 8 - 1027A flux was estimated using  $\tau_s = 45 \text{ min}$ . The impulsive component for this flare consists of a long lasting series of impulsive bursts where the peak flux of the ensemble of impulsive bursts is mildly weak relative to the slow emission, which was very long lasting. Note that in this flare the F2-region contribution exceeds that from the E and F1 regions after 2232 UT and the F2-region contribution from the slow emissions is apparently larger than that from the impulsive component. The various parameters used are as follows:

$\Phi_1 (1/2 - 1027A)_{MAX}$	$= 0.001 \text{ Wm}^{-2}$ at 2239 UT,	$\bar{\tau}_1 = 25 \text{ sec}$ ,
$\Phi_{2+3} (8 - 1027A)_{MAX}$	$= 0.002 \text{ Wm}^{-2}$ at 2250 UT,	$\bar{\tau}_E = 15 \text{ sec}$ ,
$\Phi (1 - 8A)_{MAX}$	$= 0.00017 \text{ Wm}^{-2}$ at 2248 UT,	$\bar{B} = 1/300 \text{ sec}^{-1}$ ,
$\bar{\mu}_1 = 1.9 \times 10^{17} (\text{Ws})^{-1}$	$\bar{\tau}_1 = 6 \times 10^{-22} \text{ Wm}^{-2}$ ,	$H_0 = 50 \text{ km}$ ,
$\bar{\mu}_{2+3} = 1.6 \times 10^{17} (\text{Ws})^{-1}$	$\bar{\tau}_{2+3} = 4.6 \times 10^{-22} \text{ Wm}^{-2}$ ,	$h_s^0 = 20 \text{ km}$ ,
$\alpha_{effD} = 10^{-12} \text{ m}^3 \text{s}^{-1}$ ,	$[O]_{200} = 5.5 \times 10^{15} \text{ m}^{-3}$ , and $E_0 = 5.6 \times 10^{-18} \text{ Ws}$ .	

The closeness of the fits should not be construed to mean that each of the above parameters or approximations are that correct, or that neglected ionospheric processes like transport processes are really negligible. Too many parameters are not known precisely enough for a unique accurate solution to be determined. The results do show that the general features of this sustained SITEC are consistent with the above interpretation.

The rapid rise in  $N_T$  until about 2239 UT in Figure 9 occurs during the rise of the ensemble of impulsive bursts for this flare. After the peak in  $\Phi_1$ ,  $N_T$  continues to grow but at a slower rate.  $\Delta N_e$  actually decreases in the high

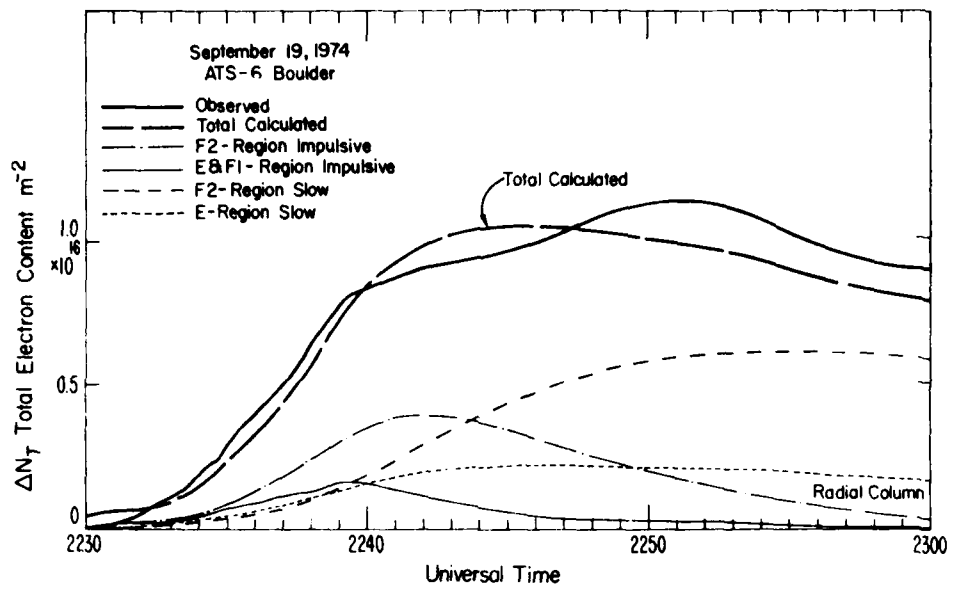


Figure 9. Observed and computed electron content enhancements.

loss region below 200 km but the continued accumulation above 200 km produces a net slow increase in  $N_T$ . In this flare,  $\Phi_1$  decreased from 2239 UT to about 2250 UT. If the decrease had been much more rapid as it is in some flares, the decrease in  $\Delta N_T$  below 200 km could dominate  $N_T$  and cause a maximum  $N_{T1MAX}$  at 2239 UT followed by a decrease in  $N_T$ . The slow emissions then offset the decay of the ionization produced by the impulsive flare emission producing the continued slow rise, smooth flat peak and then slow decay.

The above analysis implied that the portion of  $N_T$  occurring above 200 km varies significantly with time during the solar flare, with the smallest portion occurring during the rise of the impulsive component of flare emission. Then during the slow maxima  $\Delta N_{T2MAX}$  and the final decay of the sustained SITEC, the portion contributed from above 200 km dominates  $N_T$ . Mendillo et al. (1974) and Mendillo and Evans (1974) used Millstone Hill incoherent scatter measurements with low time resolution (~8 min) to determine that about 70% of the columnar electron content enhancement occurred above 200 km during the large flare of August 7, 1972. Thome and Wagner (1971) and Garriott et al. (1967) presented similar measurements with moderate time resolution (~1 min) for several large flares on May 21 and 23, 1967 where the structure in Figure 8 is evident and the portion of  $N_T$  contributed from above 200 km dominated  $N_T$  after the impulsive phase of the flare. The computed enhancement in Figure 9 includes about 77% of the total from above 200 km at 2250 UT. Because the high altitude contribution dominates  $\Delta N_{T2MAX}$ , and because the photoionization that produces this part involves the optically-thin high altitude portion of  $q(h)$ , which is independent of solar zenith angle for  $\chi < 80^\circ$ , then  $\Delta N_{T2MAX}$  should be fairly independent of the solar zenith angle. Mendillo et al. (1974) used SITEC measurements from 20 different ground stations for the flare of August 7, 1972, with  $\chi$  in the range 32 to 73°, and found  $\Delta N_{TMAX}$  to have no simple relation to  $\chi$  or  $\sec \chi$ .

Prölss et al. (1974a,b) and Tranks et al. (1975) have shown that the ratio  $[N_2]/[O]$  increases appreciably at mid- and high-latitudes and at altitudes

above 200 km during ionospheric storms. This greatly increases the F-region electron loss rates and would then greatly decrease the contribution to  $N_T$  from above 200 km. This would cause a SITEC to be smaller and to have a marked decrease after the impulsive flare emissions, i.e. after  $\Delta N_{T1\text{MAX}}$ . This is consistent with the fact that rapid-decay SITECs occur only during ionospheric storms, for example the events in Figures 1 and 4. The rapid decay of  $\Delta N_T$  would be even more rapid when the flare radiations decay more rapidly than usual. Since solar flares tend to occur in groups as flare-prolific solar active regions rise and rotate across the solar disk, large flares frequently occur during ionospheric storms produced by earlier flares from the same group. Consequently, ionospheric storms probably cause the SITECs of many large flares to be smaller and shorter-lived than if they had not been preceded by other major flares. The effects of ionospheric storms vary greatly with time and latitude, where storm-like effects are frequent at high latitudes and rare at low latitudes. Therefore, rapid decay SITECs are probably more common at high latitudes. Sustained SITECs were observed to be the most common at mid-latitudes. Mendillo et al. (1974) found a marked latitude dependence in the SITECs observed during the flare of August 7, 1972, which occurred during the recovery from the ionospheric storm of August 4-6, 1972, where  $\Delta N_T$  decreased with increasing latitude. This may have resulted from the electron loss rates in the 200 - 400 km altitude range being higher at higher latitudes.

Since flares located near the solar limb have weak impulsive EUV emission, the rapid rise portion of the  $\Delta N_T$  event would be smaller, however the slow  $\Delta N_T$  enhancement may still be quite sizeable. The result would be a slow  $\Delta N_T$  enhancement, e.g. like the events observed at Boulder at 0040 UT, September 22, 1974 and 1540 UT November 5, 1974. Slow flares on the solar disk that are dominated by the  $\Phi_3$  component or have very weak impulsive EUV emission will also have  $\Delta N_T$  enhancements like the slow portions in Figure 8 or in equations (6) and (9), e.g. the event in Figure 5. The lack of a distinct  $\Delta N_T$  enhancement can occur because the flare radiation as a whole is too small or because other ionospheric variations mask the flare-induced event. But the lack of a  $\Delta N_T$  event probably also occurs for events having soft X-ray emissions comparable to that of events with distinct  $N_T$  enhancements because the EUV emission is too weak, e.g. for flares near the solar limb or flares involving the  $\Phi_3$  component alone, and/or because the F-region loss rates are abnormally high.

#### 4. COMPARISON OF SITECS AND SOFT X-RAY DATA

For the SITECs observed at Boulder (Donnelly and Fritz, 1975), the soft X-ray data was dominated by the  $\Phi_2$  component, i.e. its time dependence was consistent with  $\Phi_2$  in (1). Because of the similarity of (1), (4) and (8), because  $\tau \sim 1/\beta$  for most flares, and because (4) and (8) dominate  $\Delta N_{T1}$ , then  $\Delta N_{T1\text{MAX}}$  and  $S\Phi(1 - 8A)$  should be correlated, even though  $\Phi(1 - 8A)$  physically contributes little to  $\Delta N_{T1}$ . Donnelly and Fritz (1976) studied this relation and found correlation coefficients of 0.9 when corrections were made for the location of the soft X-ray flare on the sun.  $\Phi(1 - 8A)$  itself is relatively independent of the location of the flare, but here  $\Phi(1 - 8A)$  is being used to estimate the time integral of  $\Phi_1(1/2 - 1027A)$  in (1) and this latter term varies with the central meridian distance (CMD) of the flare location. For a vertical path,

$$\Delta N_{T1\text{MAX}} \approx 7 \times 10^{19} D(\text{CMD}) \Phi(1 - 8A), \text{ m}^{-2}, \quad (10)$$

where the units of  $\Phi$  are  $\text{Wm}^{-2}$  and  $D$  is unitless.  $D = 1$  for  $\text{CMD} \approx 0$ , 0.6 at

12°, 0.5 at 18°, 0.4 at 33°, 0.3 at 63°, 0.2 at 73°, 0.1 at 82°, 0.05 at 87° and 0.015 at 90° (Donnelly, 1976). This relation is useful because  $\Phi(1 - 8A)$  has been measured for most of the last ten years and is currently being monitored by the SMS and GOES satellites in real time more than 99% of the time. Because of the physical indirectness of this relation, the precision of predicting  $\Delta N_{T1\text{MAX}}$  from  $\Phi(1 - 8A)$  is not high, particularly for events during ionospheric storms, but is usually within  $\pm 60\%$  for the Boulder data. The correlation of  $\Phi(1 - 8A)_{\text{MAX}}$  with  $\Delta N_{T2\text{MAX}}$  was significant, but much lower, probably because of the variability of the net electron loss rates at altitudes above 200 km. With the advent of SOLRAD-HI monitoring of solar EUV emission, a much closer relation with  $\Delta N_T(t)$  using equations (4), (6), (8) and (9) should be attainable.

Figure 10 illustrates the relation between the time dependences of the flare radiation and  $\Delta N_T(t)$  features. Radio data were used to estimate the peak time of the impulsive EUV emission  $t_1$ . Note that  $dN_T/dt|_{\text{MAX}}$  occurs at about the same time but slightly ahead of  $t_1$  on the average. The time of maximum of the 1 - 8A SMS soft X-ray data was used to estimate the time of maximum emission for the slow components  $t_s$ . Actually,  $\Phi(8 - 1027A)_{\text{MAX}}$  will occur later than  $\Phi(1 - 8A)_{\text{MAX}}$ , so part of  $\Delta t_s$  corresponds to our error in estimating  $t_s$ . The large variation in  $\Delta N_{T2\text{MAX}}$  probably results from the large variation in time characteristics of flare radiation, and probably more importantly, from large variations in ionospheric conditions above 200 km, e.g. transport and loss rates. The average time from the SITEC start to  $\Delta N_{T1\text{MAX}}$  is about 5 min. (median  $\approx 4$  min). The events used above are reported in detail by Donnelly and Fritz (1975).

### 5. COMPARISON OF $dN_T/dt$ AND SFDs

SFDs (Sudden Frequency Deviations) are another type of SID wherein the frequency of a received CW radio wave transmitted from ground stations and reflected in the ionosphere has rapid deviations induced by impulsive EUV bursts of solar flares. The observed frequency deviation  $\Delta f(t)$  is proportional to an integral of  $dN/dt$  over heights below reflection. SFDs are dominated by the effects of  $\Phi_1$  and the time rate of change of equation (3). In Figure 8, the region from about 100 to 200 km and before 1141 dominates the large values of  $\Delta f$ .

Donnelly and Fritz (1976) have studied the relation between  $dN_T/dt$  and SFD data and found the following results. The impulsive fine structure is concurrent to within our noise, timing and scaling accuracies. Figure 11 compares the two types of observations for the same flare for which  $\Delta N_T$  is shown in Figure 2. The large peaks in  $\Delta f$  or  $dN_T/dt$  correspond to fast peaks and rapid rises in  $\Phi_1$ . For these peaks,  $dN/dt$  and  $d\Phi/dt$  are the two dominant terms in (2)

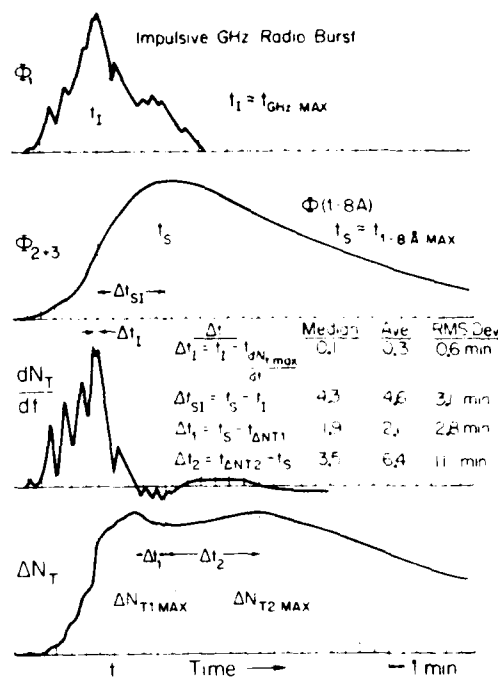


Figure 10. Approximate relation of  $\Delta t$  and flare radiation time features.

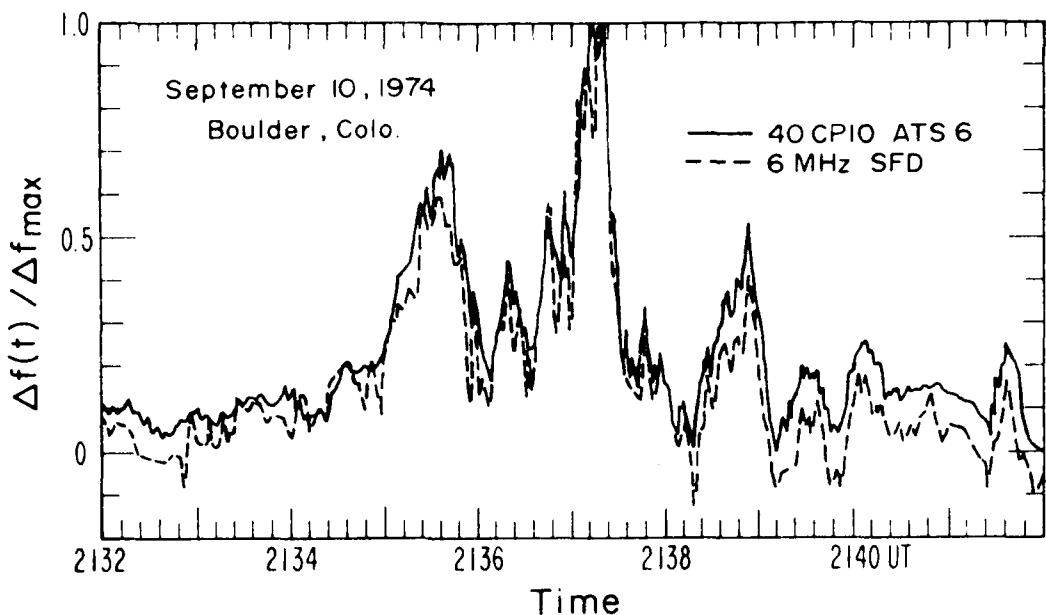


Figure 11. Comparison of ATS-6 and ground-based SFD observations. 40CP10 is the 40MHz carrier phase observed at an IF frequency of 10MHz.

where the large values of  $\Delta q$  in the altitude region of high electron loss rates contribute most to  $\Delta f$ . There are differences between the ATS-6 and ground-based SFDs that increase as the height of reflection of the ground-based measurement decreases. The ATS-6  $\Delta f(t)$  measurements often indicate that  $dN_t/dt$  remains small but positive after  $\Delta f(t)$  for the ground-based SFD measurements become negative, up until  $\Delta N_{T2}^{\text{MAX}}$  occurs. For example, for the event in Figure 11,  $\Delta f(t)$  for 6 MHz remains negative after 2149 UT while  $\Delta f(t)$  from ATS-6 remains small but positive until after 2153 UT. Also the valleys in  $\Delta f$  tend toward lower values relative to  $\Delta f$  for the ground-based measurements. These differences result from the ionospheric electron-loss time constant decreasing with altitude (Donnelly and Fritz, 1976).

## 6. CONCLUSIONS

A large variety of events occur in total electron content during solar X-ray and EUV bursts. Four types of events were identified in the Boulder ATS-6 measurements. Although a much larger set of events may exhibit a smooth distribution of events rather than four distinctly different groups, the four classifications are useful for understanding the variation in physical parameters involved. The variety of events probably results from the variety in time dependence and spectra in flare radiation and from the variety of ionospheric conditions just above 200 km, e.g. electron loss rates and transport processes. The types of total content responses to solar flare X-ray and EUV emissions are as follows:

1. Sustained SITEC (Sudden Increase in Total Electron Content).  $N_t$  increases rapidly for several minutes while  $dN_t/dt$  has several sharp maxima. Then an early type of maxima  $\Delta N_{T1}^{\text{MAX}}$  may occur, sometimes several of them, or else the rate of growth of  $N_t$  abruptly decreases. This portion of the

event is produced mainly by impulsive EUV emission, particularly that producing  $\Phi_1$  at high altitudes,  $\Phi_1(90 - 911A)$ .  $\Delta N_{T1MAX}$  occurs after the maximum of  $\Phi_1$  while the impulsive enhancement below 200 km proceeds to decay rapidly. The decrease after  $\Delta N_{T1MAX}$  is short-lived because of the short E and F1 region decay time and because the slow flare emissions increase the ionization in the 80 - 150 km altitude range, where the X-ray photoionization rates are large, but more importantly, above 200 km where the electron loss rates are extremely low,  $\Delta N_T$  can accumulate to fairly large values. This slow increase results in a smooth slow rise in  $\Delta N_T$  to a peak  $\Delta N_{T2MAX}$  after  $\Phi(1 - 8A)_{MAX}$  when transport and electron loss processes finally overcome the accumulation of high altitude ionization leading to a slow decay. The time delay after  $\Phi(1 - 8A)_{MAX}$  until  $\Delta N_{TMAX}$  occurs varies greatly from one event to another, probably because of variations in the decay time of the slow flare components  $\Phi_{2+3}$  and because of variations in transport and electron loss processes above 200 km.

2. Rapid-Decay SITEC. Some events are like the above type, but after  $\Delta N_{T1MAX}$ , they decay to much smaller values. This type of event occurs only during ionospheric storms and probably results from an abnormally high net electron loss rate above 200 km, which eliminates the slow portion of the SITEC above 200 km. Such events where the X-ray burst is still long-lasting probably drop to a small long-lasting tail in  $\Delta N_T(t)$ . Both of the above types of SITECs are preferentially produced by flares located away from the edge of the visible solar disk because their fast rise is produced by impulsive EUV emission which is relatively weak for flares near the solar limb.

4. Slow  $N_T$  Enhancements. These events can occur devoid of any impulsive  $\Phi_1/\Phi_2$  structure, although most events like this may have a small impulsive component. These events result mainly from the slow accumulation of ionization above 200 km. Flares near the limb will tend to produce this type but slow solar flares can occur near the center of the sun that are dominated by the  $\Phi_3$  component and lack significant impulsive emission.

4. No Distinct Enhancement. Some flares with soft X-ray emission comparable to that of other flares that produce SITECs, do occur but do not produce a distinct enhancement in  $N_T$ . These flares are too weak in the 90 - 911A range, since it is this radiation that mainly produces  $\Delta N_T$ . Slow flares probably produce smaller values of  $\Delta N_T$  during ionospheric storms. Other ionospheric disturbances may cause some small flare-induced enhancements to be too indistinct to identify.

The analysis in Section 3 should be improved to include transport processes, electron temperature enhancements, and multiple-charged ions. The above analysis does describe the main features of SITECs.

#### ACKNOWLEDGMENTS

We are thankful for NASA Order No. W-13,938, which made possible our analysis of ATS-6 total content data. We thank our colleagues Mr. J. E. Jones for construction of the Boulder ATS-6 antennas and receiving systems, Mr. J.H. Taylor for designing the digitizing system, and Mr. L. Matheson, Mrs. J. Falcon, and Mr. H. Ishonyo for data processing.

#### REFERENCES

- Davies, K., R. B. Fritz, R. N. Grubb and J. E. Jones (1975), Some early results from the ATS-6 radio beacon experiment, Radio Science, 10, 785-99.
- Donnelly, R. F., and R. B. Fritz (1975), ATS Observations of Sudden Increases of Total Electron Content Induced by EUV and X-Ray Bursts of Solar Flares, NOAA Tech. Rept. ERL 347-SEL 35 (U.S. Government Printing Office, Washington, DC 20402).
- Donnelly, R. F. (1976), Empirical models of solar flare X-ray and EUV emission for use in studying their E- and F-region effects, submitted to J. Geophys. Res..
- Donnelly, R. F. and R. B. Fritz (1976) SITECs, SFDs and the X-Ray and EUV Bursts of Solar Flares, to be submitted to Radio Sci..
- Ferguson, E. E. (1974), Laboratory measurements of ionospheric ion-molecule reaction rates, Rev. of Geophys. Space Phys., 12, 703-13.
- Garriott, O. K., A. V. da Rosa, M. J. Davis and O. G. Villard, Jr., (1967), Solar flare effects in the ionosphere, J. Geophys. Res., 72, 6099-6103.
- Mendillo, M. and J. V. Evans (1974) Incoherer scatter observations of the ionospheric response to a large solar flare, Radio Sci., 9, 197-203.
- Mendillo, M., J. A. Klobuchar, R. B. Fritz, A. V. da Rosa, L. Kersley, K. C. Yeh, B. J. Flaherty, S. Rangaswamy, P. E. Schmid, J. V. Evans, J. P. Schödel, D. A. Matsoukas, J. R. Koster, A. P. Webster, and P. Chin (1974), Behavior of the ionospheric F region during the great solar flare of 7 August 1972, J. Geophys. Res., 79, 665-72.
- Prölss, G. W. and U. von Zahn (1974a), Magnetic storm associated changes in neutral composition of the atmosphere at mid-latitude observed by ESRO 4 gas analyser, Space Res., XIV, Academie-Verlag, Berlin, 157-61.
- Prölss, G. W., and U. von Zahn (1974b), ESRO 4 gas analyzer results: 2 direct measurements of changes in the neutral composition during an ionospheric storm, J. Geophys. Res., 2535-9.
- Trinks, H., K. H. Fricke, U. Laux and G. W. Prölss (1975), ESRO 4 gas analyzer results, 3, spatial and temporal structure of the mid-latitude atmosphere during a geomagnetic storm, J. Geophys. Res., 4571-5.
- Thome, G. D. and L. S. Wagner (1971), Electron density enhancements in the E and F regions of the ionosphere during solar flares, J. Geophys. Res., 76, 6833-95.

MULTISTATION OBSERVATIONS OF F-REGION  
RESPONSE TO SUDDEN COMMENCEMENT STORMS

by

L. KERSLEY AND A. DAS GUPTA\*

University College of Wales, Aberystwyth, U.K.

1. INTRODUCTION

The response of the ionospheric F-region to geomagnetic activity has been investigated for many years. Both the maximum ionisation density of the F2-layer ( $N_{mF2}$ ) and the total electron content ( $N_T$ ) have been widely used. Early studies were for a single station only, but recently attempts have been made to combine observations from several widely separated stations for a few selected storms (SCHODEL et al., 1974, MENDILLO and KLOBUCHAR, 1975). While studies of the latter kind provide a description of the global and latitudinal evolution of the large scale manifestations of storm development observations from stations separated by only a few degrees enable the progress of individual features to be followed. The present paper reports observations of the response of electron content to a number of sudden commencement type storms obtained at a multistation network where the locations are separated by only a few hundred kilometers.

2. EXPERIMENTAL OBSERVATIONS

Observations of polarisation rotation of the 137MHz transmissions from the quasi-geostationary satellite Intelsat IIF3 were made at a number of locations in UK for about eight months during 1974. The locations of the stations and the corresponding sub-ionospheric points for 420km altitude are shown in Figure 1. The present study is confined to seven sudden commencement type geomagnetic storms in the summer and autumn for which total electron content data were available at more than one station.

3. RESULTS

The observations of the local time development (approximately UT for the station network) of the total electron content of the individual storms are presented in Figures 2 to 7. Only relative values are considered for each station and,

\* Permanent Address: University of Calcutta, India.

for clarity of presentation, the individual total electron content plots are displaced with respect to each other. The mean diurnal variation of electron content for Aberystwyth for five days prior to the storm is also plotted to allow direct comparison with the storm days. For the two storms in September following in close succession the same mean curve for the five days before the earlier storm is used. Some of the more important features of the individual storms are described below.

a. 10 - 11 June 1974

The sudden commencement occurred at 1850 UT when the planetary magnetic index  $K_p$  was 4+. Within 100 minutes of storm commencement the electron content shows an increase maximising at 2120 UT at Hawick and slightly later at Aberystwyth with the more northerly station showing the larger effect (Figure 2). This increase may be interpreted as a positive effect generated by the initial heat input from a source in the auroral region. From the time delay of the maxima observed at the two stations the apparent meridional propagation speed is estimated to be about  $500 \text{ m s}^{-1}$ . A rapid drop in ionisation follows the peak. It is interesting to note that the curve for 10 June shows considerable departure from the mean curve even prior to the sudden commencement. This may be due to the higher than average level of geomagnetic activity throughout the day where the  $K_p$  sum for the six three-hour intervals before 1800 UT was 17.

On 11 June a positive effect maximising around 1300 UT is observed with a fall to a minimum value around 1730 UT, an increase to 2100 UT and a subsequent sharp drop. There is a remarkable similarity between the recording around 2100 UT on 10 and 11 June. Since it is difficult to envisage a positive effect due to initial heat input on 11 June it may be that on both days this feature has its origins in an electrodynamic mechanism induced by storm enhanced electric fields of magnetospheric origin. (MENDILLO, 1975).

The nighttime content shows some depletion below the mean level during the early morning of 11 June with a more marked fall the following night. It is interesting to note the onset of the post sunrise increase in ionisation is delayed by approximately one hour on 11 June compared to the mean curve.

b. 25 - 26 June 1974

The storm with sudden commencement at 2335 UT on 25 June and  $K_p = 5$  was observed at all four stations. Figure 3 gives no indication of any initial positive effect and the nighttime content does not depart significantly from the mean except that the onset of the morning rise is delayed by some 30 mins. The daytime values on 26 June are higher than average and have marked fluctuations. The time delays between corresponding structures show that the disturbances are propagating from directions within the north-west to north-east quadrant with speeds in the range from  $350 \text{ m s}^{-1}$  to  $600 \text{ m s}^{-1}$ . The high speeds and large amplitudes of these wave-like features indicate that they may be associated with ducted mode gravity waves having their origins in auroral electrojet activity (FRANCIS, 1973).

c. 4 - 6 July 1974

During early July there was a complex sequence of geomagnetic activity with sudden commencements at 1535 UT on 4 July and 0321 UT on 6 July and K<sub>p</sub> values of 5 and 8+ respectively. Figure 4 shows that a small increase in ionisation is observed after the first sudden commencement which corresponds to a disturbance propagating from the north-west at some 400 m s<sup>-1</sup>. Once again the post-sunrise build up is delayed, this time by about one hour on 5 July and the content remains below normal for the rest of this day.

The storm of 6 July is the only pre-noon sector storm occurring in the present study but unfortunately residual effects from the storm two days earlier were still present making interpretation of the observations difficult.

It is interesting to note that there were four sudden increases in electron content occurring simultaneously (within the one minute time resolution) at all stations : 0648 UT and 1352 UT on 4 July, 1507 UT on 5 July and 1111 UT on 6 July. These can be identified with the solar flares reported at these times.

d. 2 August 1974

The sudden commencement was at 1227 UT with K<sub>p</sub> = 4-. It can be seen from Figure 5 that an ionisation build up started at about 1400 UT with a positive effect continuing till almost 2000 UT. The disturbance producing the maximum just after 1700 UT can be identified as propagating southwards in the magnetic meridian at about 480 m s<sup>-1</sup> while that at 1940 UT, representing the negative effect onset, appears to come from the north-north-east at some 600 m s<sup>-1</sup>. The post-dawn increase is again delayed on 3 August.

e. 15 September 1974

Figure 6 shows the total electron content variations at Hawick, Aberystwyth and Buckingham on 15 September. The order of the stations has been reversed in the diagram to minimise confusion due to cross-over of the curves. Equipment malfunction limited the useful portion of the Buckingham record and a non-linearity in the polarimeter response has resulted in distortions in the electron content curve for this station; however, the times of the turning values are unambiguous even though the magnitudes of the features themselves may be distorted.

The storm commencement was at 1344 UT when K<sub>p</sub> = 7. An enhancement of the electron content is apparent even before the commencement but from 1500 UT the slope of the curves shows a rapid increase in ionisation which appears first at the highest latitude station. The electron content maximises about 1800 UT, followed by a very rapid depletion. The sharp drop is preceded by wave-like features of large amplitude with quasi-periodicities of 15 to 25 minutes, which, before 1800 UT, appear to have a meridional speed of some 500 m s<sup>-1</sup>. The shape of the records is not well preserved between stations during

the fall, but it is estimated that the disturbance is propagating from the north-north-east at  $170 \text{ m s}^{-1}$  and there are indications of very large north-south gradients in ionisation.

f. 18 September 1974

On 18 September the sudden commencement was at 1434 UT when  $K_p = 5$ . A rapid build up in ionisation started within one hour of the storm (Figure 7) with its onset apparently propagating in the magnetic meridian at only  $170 \text{ m s}^{-1}$ . The maximum positive effect occurs about 1700 UT with its termination propagating from the north-north-east at about  $500 \text{ m s}^{-1}$ . A rapid depletion follows with the nighttime values being depressed considerably. For both September storms the dawn build-up starts slightly earlier than the mean curve.

It should be noted that for all the storm periods described above the records show a fine structure of a quasi-periodic nature usually associated with gravity waves. As only simple analysis techniques, involving identification of similar features, have been used the velocities quoted for the storm associated effects may have been contaminated by the wave velocities. However, it is believed that the values given are representative of the storm effects as attempts have been made to eliminate the waves in cases where a systematic train of, fine structure fluctuations allowed identification.

The results of the apparent propagation of storm associated features are summarised in the table, which lists observed speeds and directions of positive effect onset and negative effect onset for each storm where these parameters could be determined.

4. DISCUSSION

The local time development of an F-region storm at mid-latitudes involves the complex interplay of several effects whose importance may vary, not only with local time during a single storm, but also from storm to storm as is evidenced by the differing characteristics of the storms described above.

The multistation observations provide examples of storms where an increase in ionisation is found within two hours of commencement. The speed of this positive disturbance was generally about  $400 \text{ m s}^{-1}$  which is considerably lower than the near-thermal speed proposed by JONES and RISHBETH (1971) for this initial disturbance. The direction of the initial positive disturbances was from higher to lower latitudes but there was no evidence of a source located consistently at a particular magnetic time in the auroral zone. The observed speeds are in the range to be expected for large scale gravity waves and it appears that in general the first appearance of a storm associated feature in mid-latitude total electron content takes the form of a signature of a large scale gravity wave propagating from an auroral zone source. For 18 September the observed speed was only  $170 \text{ m s}^{-1}$ , too slow for the disturbance to have reached mid-latitudes within 90 minutes of storm commencement. Consequently, it seems likely that some localised effect like an electric field change rather than an impulse or wind propagating from the auroral zone was responsible for the ionisation increase.

The velocities of subsequent positive effect features in the afternoon sector are in general in the range  $400 \text{ m s}^{-1}$  to  $600 \text{ m s}^{-1}$  which may be compared to the value of  $400 \text{ m s}^{-1}$  quoted by JONES and RISHBETH (1971). These workers propose a mechanism for enhancement

involving lifting of the plasma under the influence of a neutral wind whose poleward motion has been weakened or even reversed by the storm modified temperature gradient (DAVIES and RUSTER, 1974). An additional lifting effect in the daytime sector is the electrodynamic ( $\vec{E} \times \vec{B}$ ) drift associated with the penetration to ionospheric heights of the storm enhanced magnetospheric convection field. (MENDILLO, 1975).

Using the criterion that the maximum of the positive effect represents the negative onset (DAVIES, 1974) it has been found that the disturbances propagate essentially in the magnetic meridian at high speed ( $\sim 500 \text{ m s}^{-1}$ ). The intersection of the propagation vector with the auroral oval does not show any consistent pattern of source location like the magnetic noon meridian envisaged by DAVIES and the speeds are, in general, too high to be related to his 'bow wave' model. The apparent propagation speeds are comparable to that of SPURLING and JONES (1975) and appear to be consistent with a composition change mechanism, namely an advection from high latitudes of neutral gas with increased  $[N_2]/[O]$  ratio, for the ionisation depletion. KING (1967) has suggested atmospheric gravity waves as a means of propagating composition changes. The present study shows that wave-like features propagating from the north at high speed are an important feature of almost every storm and can play a dominant role as on 26 June. It is probable that these disturbances are associated with large scale gravity waves, generated by substorm related auroral electrojet activity (FRANCIS, 1973).

The storm of 15 September had a spectacular negative onset which propagated at only  $170 \text{ m s}^{-1}$ . MENDILLO et al. (1974) showed that motion of the mid-latitude trough could result in large drops in ionisation and it is suggested that it is motion of the trough which is being observed in this case. It should be noted that the speed of  $40 \text{ m s}^{-1}$  for trough motion reported by TAYLOR (1973) applied to the night sector and the present observation is probably consistent with the expected motion around 1800 LT.

The large amplitude waves which appear as precursors of the trough on 15 September deserve further comment. The quasi-period ranges from 25 to 15 minutes with the largest amplitudes and shortest periods just before the negative onset, while the propagation is from high latitudes at some  $500 \text{ m s}^{-1}$ . These waves differ from the short period fluctuations generally seen in total electron content, which are associated with medium scale gravity waves, in that the speed is comparable to that of large scale auroral electrojet generated waves. For such short period, large amplitude waves to be an ionospheric manifestation of neutral atmospheric gravity waves, either internal or ducted mode, the source would have to be close to the observing region. It is thus possible that these waves, precursors to the trough, represent an instability in the ionospheric plasma which may be associated with contraction of the plasmapause or the peeling-off of the plasmasphere in the afternoon sector, although the mechanism is not clear at the moment.

Finally, the storm induced changes in nighttime ionisation deserve comment. In particular, the delayed onset of the morning increase in summer, when sunrise was before 0600 UT, suggests that a downwards electrodynamic drift plays an important role in producing the nighttime depletions often found during storms.

### Acknowledgements

The authors are indebted to Mr. K.J. Edwards for assistance with the experimental observations. In addition, thanks are due to Messrs. J. Barker, I.C. Beckett and V.W.L. Kersley for accommodating and monitoring the receiving equipment at the outstations. ADG acknowledges the financial support of the British Council.

### REFERENCES

- Davies K. 1974 Planet. Space Sci. 22, 237.
- Davies K. and Ruster R. 1975 Proc.Symp.Beacon Satellite Investigations of the Ionosphere structure and ATS-6 Data, II, IZMIRAN, Moscow,p7.
- Duncan R.A. 1969 J.Atmos.Terr.Phys. 31, 59.
- Francis, S.H. 1973 J.Geophys.Res. 78, 2278.
- Jones K.L. and Rishbeth H. 1971 J.Atmos.Terr.Phys. 33, 391.
- King G.A.M. 1967 J.Atmos.Terr.Phys. 29, 161.
- Mendillo M. 1975 Proc.Symp.Beacon Satellite Investigations of the Ionosphere structure and ATS-6 Data, II, IZMIRAN, Moscow,p60.
- Mendillo M. and Klobuchar J.A. 1975 J.Geophys.Res. 80, 643.
- Mendillo, M. Klobuchar J.A. and Hajeb-Hosseinieh H. 1974 Planet. Space Sci. 22, 223.
- Schodel, J.P., da Rosa A.V., Mendillo M., Klobuchar J.A., Roelofs T.H., Fritz R.B., Essex E.A., Flaherty B.J., Yeh K.C., Hibberd F.H., Kersley L., Koster J.R., Liszka L. and Nagata Y. 1974 J.Atmos.Terr.Phys. 36, 1121
- Spurling P.H. and Jones K.L. 1975 J.Atmos.Terr.Phys. 37, 1385.
- Taylor G.N. 1973 J.Atmos.Terr.Phys. 35, 647.

STORM	SSC UT	Kp	INITIAL POSITIVE EFFECT	POSITIVE ONSET			NEGATIVE ONSET		
				TIME	SPEED $\text{ms}^{-1}$	AZIM deg	TIME	SPEED $\text{ms}^{-1}$	AZIM deg
10 - 11 June	1850	4+	X ---	1900	500				
25 - 26 June	2335	5					1800	350	348
4 July	1535	5	X	1740	460	300	2030	460	348
6 July	0321	6+	X ---	0800	210	52			
2 August	1227	4-					1940	600	13
15 September	1344	7	X				1830	170	22
18 September	1434	5	X	1530	170	5	1700	480	13

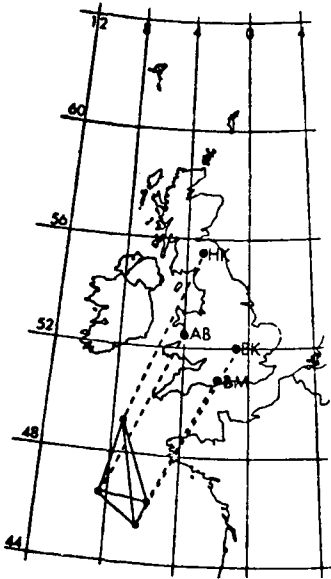


Figure 1. Locations of the observing stations at Aberystwyth (AB), Bournemouth (BM), Buckingham (BK) and Newark (NW) together with the corresponding sub-ionospheric points for 420 km altitude.

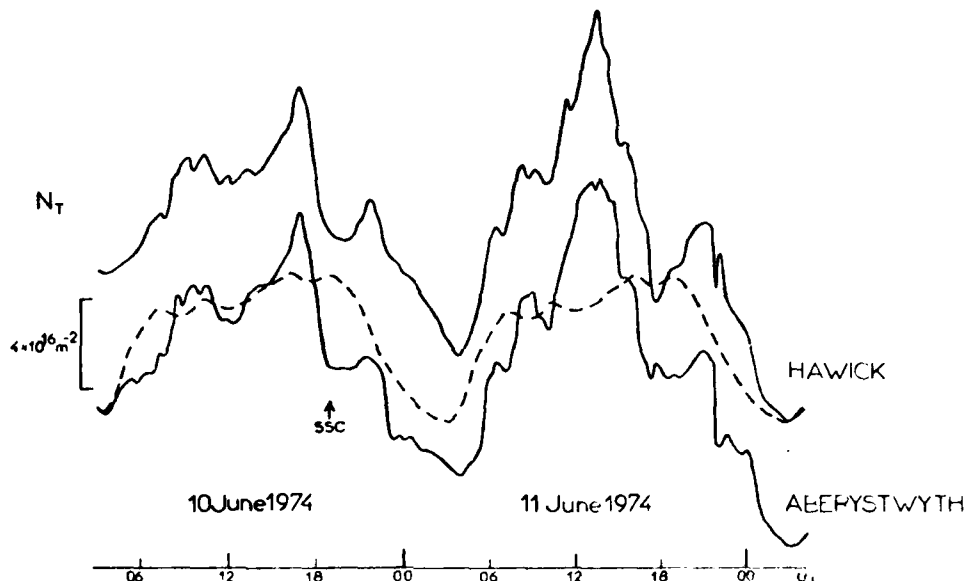


Figure 2. The relative total electron content variations measured at the stations listed for the storm period 10 - 11 June 1974. For clarity of presentation the curves are displaced vertically with respect to each other. The dashed curve represents the mean diurnal variation for Aberystwyth for the five days prior to the storm which can be compared directly to the storm period curve for this station.

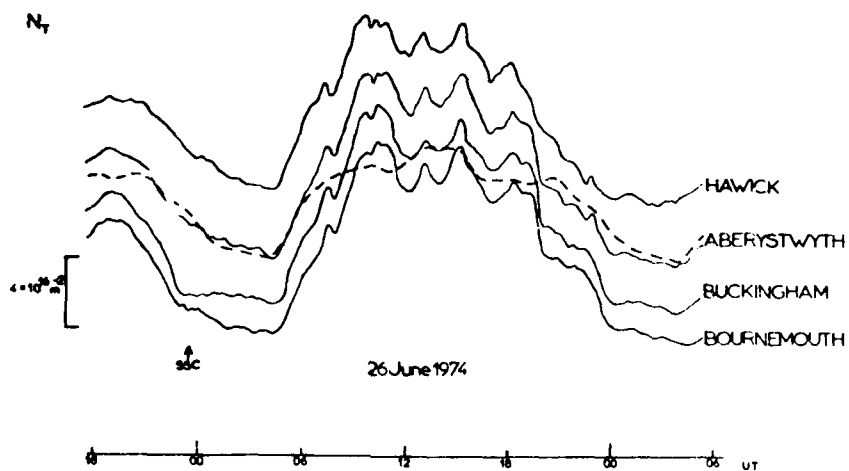


Figure 3. The relative total electron content variations measured at the stations listed for the storm period 26 June 1974.

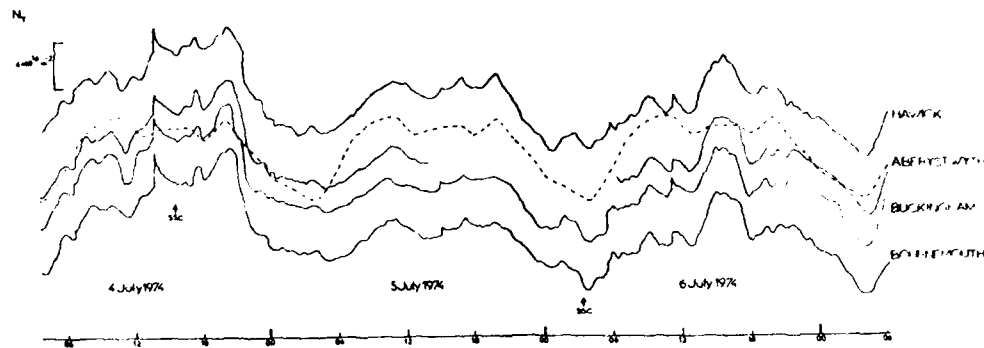


Figure 4. The relative total electron content variations measured at the stations listed for the storm period 4 - 6 July 1974.

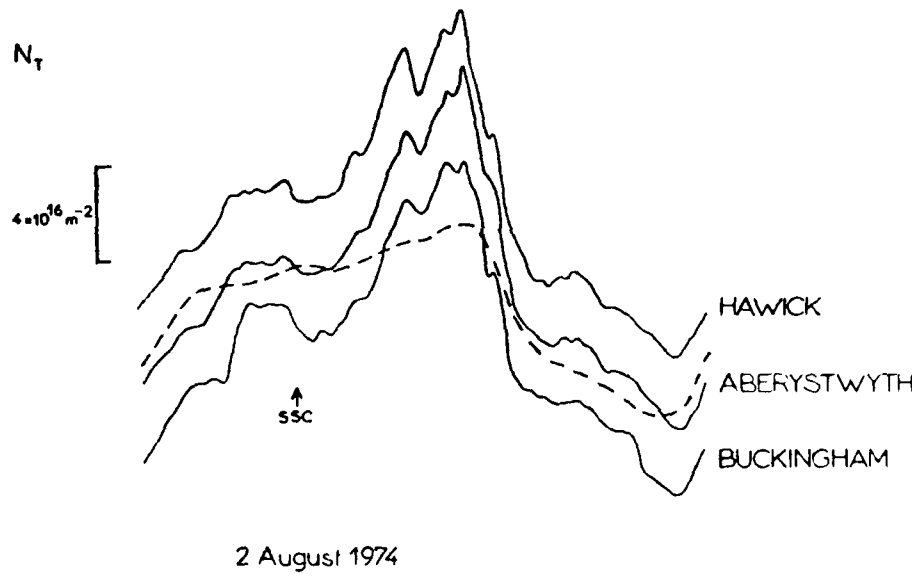
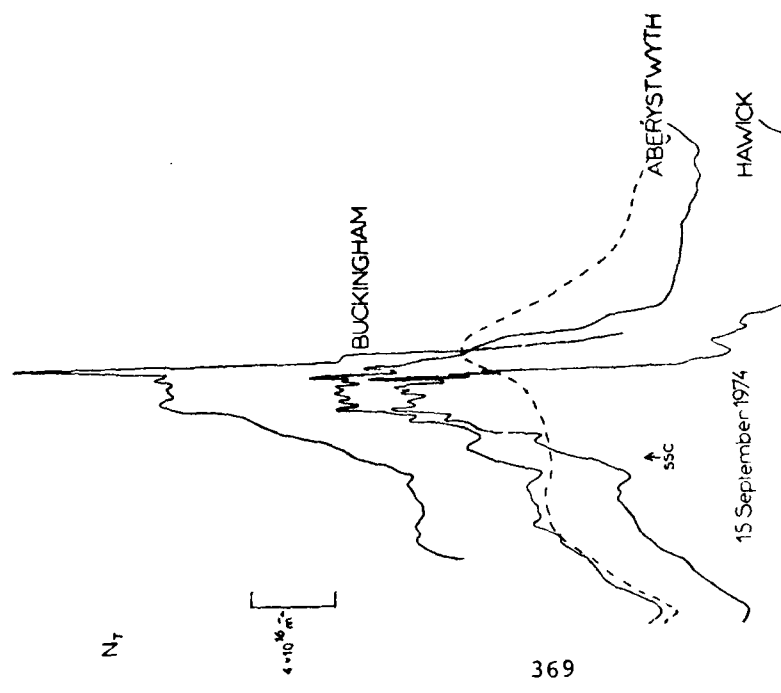


Figure 5. The relative total electron content variation measured at the stations listed for the storm period 2 August 1974.



369

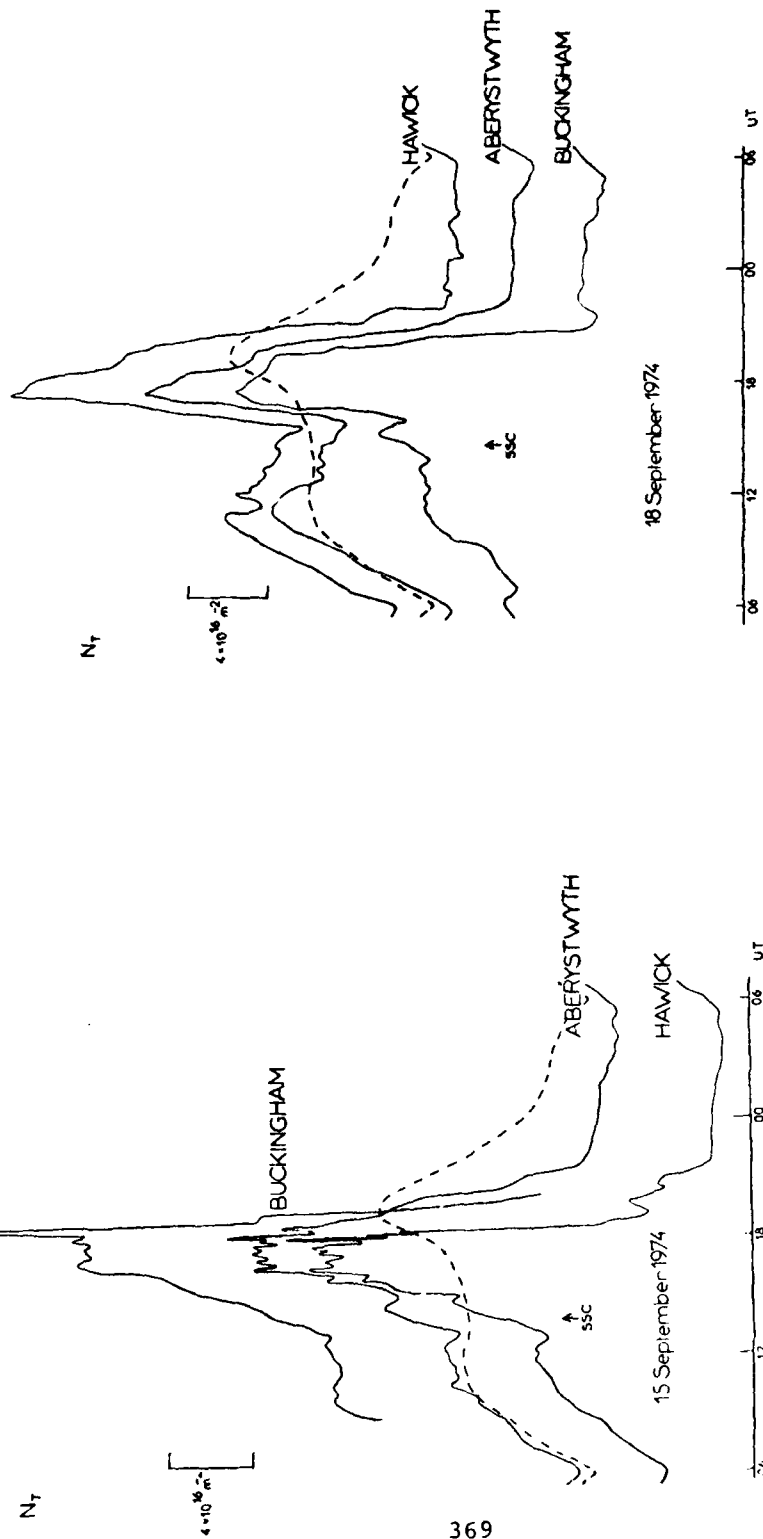


Figure 6. The relative total electron content variations measured at the stations listed for the storm period 15 September 1974.

Figure 7. The relative total electron content variation measured at the stations listed for the storm period 15 September 1974 and the dashed curve represents the mean diurnal variation for Abeyazith for the five days prior to 15 September 1974.

VERTICAL DISTORTIONS OF THE WINTER NIGHTTIME IONOSPHERE  
DEDUCED FROM SIMULTANEOUS SATELLITE BEACON OBSERVATIONS  
AND GROUND-BASED IONOSONDE DATA

Michael J. Buonsanto and Michael Mendillo  
Department of Astronomy  
Boston University  
Boston, Mass. 02215

ABSTRACT

Continuous observations of the Faraday rotation of geostationary satellite signals have been made at Goose Bay, Labrador ( $53^{\circ}31'N, 60^{\circ}31'W$ ) since mid-November, 1971. These measurements provide the total electron content (TEC) of an equivalent vertical column intersecting the 420-km point at  $47^{\circ}5'N, 62^{\circ}2'W, L=4$ . The Goose Bay measurements provide TEC values for a point close to St. John's, Newfoundland ( $47^{\circ}6'N, 52^{\circ}7'W$ ), where over 30 years of ionosonde data have been collected. Examination of 24 years of December foF2 data reveals that at least a 0.3MHz increase in foF2 occurred during 71% of the nights. During the first winter of simultaneous foF2 and TEC observations (1971), increases in foF2 were relatively frequent, while such increases in the TEC data were rare. During December, 1971, foF2 increases were observed on 21 of 25 nights for which data were available; comparable increases in TEC occurred during only 8 of 27 nights. Two nights during which foF2 increased while TEC did not, Dec. 8-9 and 14-15, were studied in detail. A semi-empirical model, developed for Ne(h) vs. latitude from h=0 to geostationary satellite height, showed that substorm induced vertical distortions of the ionosphere are in quantitative agreement with the observed increases in NmF2 accompanied by constant TEC.

## I. INTRODUCTION

Observations of the Faraday rotation of 137 MHz signals from the geostationary satellite ATS-3 have been made at Goose Bay, Labrador ( $53^{\circ}5'N, 60^{\circ}3'W$ ) since mid-November, 1971. These measurements have been used to deduce the total electron content (TEC) of the vertical column which intersects the slanted ray path to ATS-3 at a height of 420km (Titheriuge, 1972; Mendillo and Klobuchar, 1974). Buonsanto (1976) has shown that the choice of 420km height for the location of the derived vertical column results in 10% accuracy for the typical winter nighttime conditions we are concerned with here. This result holds for the Goose Bay ray path on nights when a severe latitude gradient in the electron density profiles is absent.

For the Goose Bay ray path, the 420km point is located at ( $47^{\circ}5'N, 62^{\circ}2'W, L=4$ ). This is almost precisely the same latitude (both geographic and geomagnetic) as that of St. John's, Newfoundland ( $47^{\circ}6'N, 62^{\circ}7'W$ ) where over 30 years of ionosonde data have been collected. Figure 1 shows several TEC stations, ionosonde stations, and sub-ionospheric (420km) points, including those for the Goose Bay/ATS-3 ray path. St. John's foF<sub>2</sub> observations, which directly give the peak density of the F-region, may be combined with simultaneous Goose Bay TEC results to give information about the variability of the F-region at L=4.

## II. IONOSONDE DATA AT L=4

In order to study the occurrence frequency of winter nighttime increases in foF<sub>2</sub> at St. John's, we chose two types of periods for analysis: (1) the October to March periods for 1971-1973, and (2) 24 years of December data spanning the years 1945-1974. A quantitative scheme was devised for classifying the variations in foF<sub>2</sub> during winter nights. Based on the two October to March periods, we found that foF<sub>2</sub> increases are basically a winter phenomenon, with most increases in December. The 24 years of December foF<sub>2</sub> data showed increases of at least 0.3 MHz during 71% of the night, for which data were available. During December, 1971, a 0.3 MHz increase in foF<sub>2</sub> occurred on 21 of the 25 nights available for analysis. Our statistical survey of winter nighttime foF<sub>2</sub> variations did not yield a clear correlation between the occurrence of foF<sub>2</sub> increases and the sunspot number. The larger increases, however, were a little more likely to occur during mid-winter and during high sunspot years. The variability from year to year was observed to be substantial, and thus, there is no apparent way to predict whether there will be a large number of increases in a given year.

## III. DECEMBER, 1971 F-REGION DATA AT L=4

As mentioned above, simultaneous measurements of Goose Bay TEC and St. John's foF<sub>2</sub> yield information about F-region

variability at  $L=4$ . As seen from Goose Bay, a winter nighttime increase in total electron content of about 20% is comparable to a 0.3 MHz increase in foF2. In December, 1971, increases of 20% in TEC occurred on only 8 of the 27 nights for which data were available. This is in sharp contrast to the foF2 increases, which occurred, as previously mentioned, on 21 of 25 nights.

Overplots of Nmax and TEC for December, 1971, are shown in figure 2. On the left half of the figure, the two parameters are plotted for all of the nights for which data were available. To the right, ten of the nights during which substantial increases in Nmax were observed are plotted. If one ignores December 17 (when a large magnetic storm occurred), an envelope drawn around the plots would extend from about 5 to 15 ( $10^{12}$  el/cm $^3$ ) for Nmax and from about 2.5 to 5.0 ( $10^{12}$  el/cm $^3$ ) for TEC. This demonstrates the significantly greater variability of peak density compared with TEC at  $L=4$  during nighttime periods of December, 1971.

#### IV. CASE STUDIES

In figure 3, TEC and Nmax are plotted for 5 of the nights during which Nmax increased, while TEC did not. Note that there was some magnetic activity each night, but except for the Dec. 9 case, the peak of the Nmax increases occurred a few hours after the highest level of geomagnetic activity.

Two nights during which this increasing Nmax-constant TEC effect occurred, Dec. 8-9 and Dec. 14-15, were studied in detail. In figures 4 and 5, this effect is clearly shown in the upper left, where plots of TEC and Nmax at  $L=4$  are drawn. To the upper right, comparable midlatitude results are given. Notice that both TEC and Nmax showed increases at mid-latitudes during both nights. Glancing at the lower left of the figures, we note that the greatest magnetic activity coincided with the increase on Dec. 9, but preceded the greatest part of the increase on Dec. 15. At the lower right in the two figures are plotted bottomside profiles obtained from World Data Center A For Solar-Terrestrial Physics. The times of these profiles are indicated and correspond to the times marked on the St. John's Nmax plots. One can see a considerable amount of filling in of the bottomside profile in both cases. For the 15th, a period of enhancements at all heights up to the peak is followed by depletions at lower levels, apparently due to an increased rate of recombination.

We wished to find out if this increasing Nmax-constant TEC effect is due exclusively to vertical distortions, or if a latitudinal motion of an electron density trough could account for it. To investigate this question, a semi-empirical model was developed for the array of  $Ne(h)$  vs. latitude from  $h=0$  to geostationary satellite height. A diffusive equilibrium model was used above 1000km if the field line intersecting the ray path was inside the plasmasphere, a collisionless model if outside the plasmasphere. Isis II topside sounder  $Ne(h)$  interpolated data was

used from 1000km down to the F2-peak, and matched with profiles from ground-based ionosondes, where available.

$Ne(h)$  vs. latitude arrays were constructed, using this model, for both Dec. 9 and Dec. 15, the two nights referred to above.

Much evidence exists that electron density troughs move equatorward at night. To investigate whether this alone could have caused the increasing  $N_{max}$ -constant TEC effect, the arrays for Dec. 9 and Dec. 15 were shifted equatorward in one degree steps. Moving the trough poleward edge over St. John's will clearly increase  $N_{max}$ . We wanted to see what would happen to TEC, obtained from the Faraday rotation along a slanted ray path, under the conditions of the trough and poleward edge moving equatorward.

In figure 6, the Dec. 15 array in its original position is shown in the top half of the figure; the same array, shifted six degrees equatorward, appears in the bottom half. Note that the trough's poleward edge, at the right-hand side in the top half of the figure, has been moved to cross the ray path near 400km height. In examining the ionosphere now sampled by the ray path, we see that the great increase in electron densities near the peak of the F-region is partially off-set by the fact that the upper regions along the ray path are now in the electron density trough. This effect alone, however, does not keep the TEC along the ray path constant, although the percentage increase in TEC is substantially lower than the  $N_{max}$  enhancement. We found that adjusting the height ( $h_0$ ) where the bottomside  $Ne(h)$  goes to zero could reduce the  $Ne$  contributions along the lower portions of the ray path to such an extent that a nearly constant TEC was obtained. For example, using this technique, an  $N_{max}$  increase of 72% was produced, coincident with only a 7% TEC increase for  $h_0=230$ km north of the poleward edge and  $h_0=120$ km in the trough. Considering that the  $Ne$  enhancement of the poleward edge is produced by energetic particles, one would suspect that  $h_0$  should be lower north of the poleward edge as compared to that in the trough minimum, rather than higher. Our scheme of low  $h_0$  in the trough and high  $h_0$  north of the poleward edge was chosen to reproduce the temporal sequence shown in figure 5 by simple latitudinal motions. In applying similar latitude shifts to the December 9 case, the  $N_{max}$  and TEC computed with this method showed large increases, although the  $N_{max}$  increase was about twice the TEC increase. Therefore, while we can make TEC increase much less than  $N_{max}$  does, we cannot reproduce the observations under study merely by shifting the  $Ne(h)$  vs. latitude arrays.

The second method tried was a vertical distortion of the  $Ne(h)$  array over a wide latitude range, without a latitude shift. We applied distortion factors to the arrays based on vertical drifts caused by an enhanced magnetospheric dawn-dusk electric field ( $E_{d,d}$ ) mapped along field lines to the ionosphere (Mendillo,

1973).

In figures 7 and 8, we show the type of distortions which have been invoked. These are not vertical profiles, but rather plots of  $Ne(h)$  along the ray path for both the Dec. 9th (figure 7) and Dec. 15th (figure 8) events. Note how the increases in  $N_{max}$  are compensated for by decreases at higher heights, and yet at bottomside heights,  $h_0$  is lower and the  $Ne$  values show large increases (comparable to those shown in figures 4 and 5).

For Dec. 15, our calculations, using this vertical distortion method, gave constant TEC; and we reproduced in detail the Dec. 9 observations using this method. Not only was the equivalent vertical TEC constant, but the actual vertical columnar TEC in the model arrays were constant to within 10%, which indicates that any net influx of plasma into the columns were small. This seems to be a clear case of having a vertical distortion of the existing profile.

A final method was tried, a combination of the previous two, i.e., shifting a distorted  $Ne(h)$  vs. latitude array. We were not able doing this to reproduce the Dec. 9 observations. The calculations did give, however, a 12% decrease in TEC for Dec. 15, which compares well with the observed 17% decrease.

## V. Discussion

Our calculations described above have shown that vertical distortions are primarily responsible for the increasing  $N_{max}$ -constant TEC effect so often observed in December, 1971 from the Goose Bay-St. John's pair of stations which monitor the ionosphere at  $L=4$ . It seems clear that this effect is substorm related. Substorms were recorded at Narssarssuaq, 8.6 degrees east of St. John's on all 5 nights which were shown in figure 3. On four of the five nights, however, the substorm occurred a few hours before the greatest part of the  $N_{max}$  increase. We suspect that the later increases were due to highly localized geomagnetic disturbances not recorded at Narssarssuaq, or other stations of the AE network (see Allen and Kroehl, 1975, for a description of how the AE index is formed). Also, the electric fields needed to account for the effects are small (e.g.,  $E_{B\parallel}=0.2$  to  $0.7$  mV/m), and thus, the types of F-region disturbances reported here may in fact be sensitive indicators of small and localized westward electric fields in the post-midnight sector.

## ACKNOWLEDGEMENTS

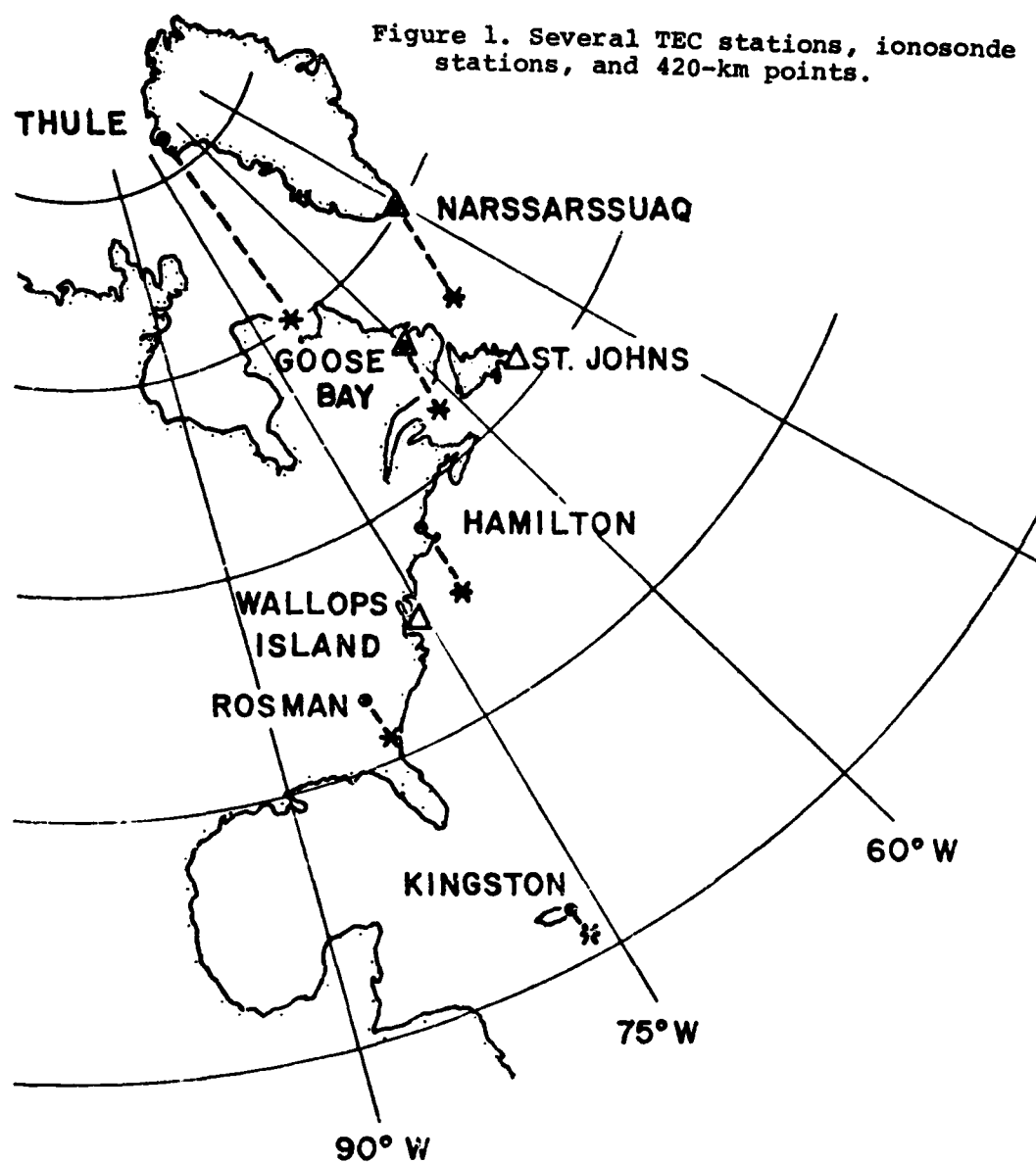
The authors wish to thank J. A. Klobuchar of the Air Force Geophysics Laboratory for supplying the TEC data used in this analysis, and also for his valuable comments and suggestions. foF2 data and topside Isis II profiles were obtained from the Canadian Department of Communications. Bottomside profiles and

some foF2 data were obtained from World Data Center A for Solar-Terrestrial Physics. This work was supported by the United States Air Force (Contract No. F19628-75-C00044).

#### REFERENCES

- Allen, J. H., and Kroehl, H. W., Spatial and temporal distributions of magnetic effects of auroral electrojets as derived from AE indices, *Jour. Geophys. Res.*, **80**, 3667, 1975.
- Buonsanto, M. J., Behavior of the ionosphere near sixty degrees magnetic latitude, A. M. thesis, Boston University, 1976.
- Mendillo, M., Magnetospheric convection at ionospheric heights, AFCRL Tech. Report-73-0358, 1973.
- Mendillo, M., and Klobuchar, J. A., An atlas of the midlatitude F-region response to geomagnetic storms, AFCRL Tech. Report-74-0065, 1974.
- Titheridge, J. E., Determination of ionospheric electron content from the Faraday rotation of geostationary satellite signals, *Planet. Space Sci.*, **20**, 353, 1972.

Figure 1. Several TEC stations, ionosonde stations, and 420-km points.



TEC OBSERVING STATIONS •

TEC 420 KM SUB-ION. PTS. \*  
(ATS - 3 AT 70° W)

IONOSONDE STATIONS △

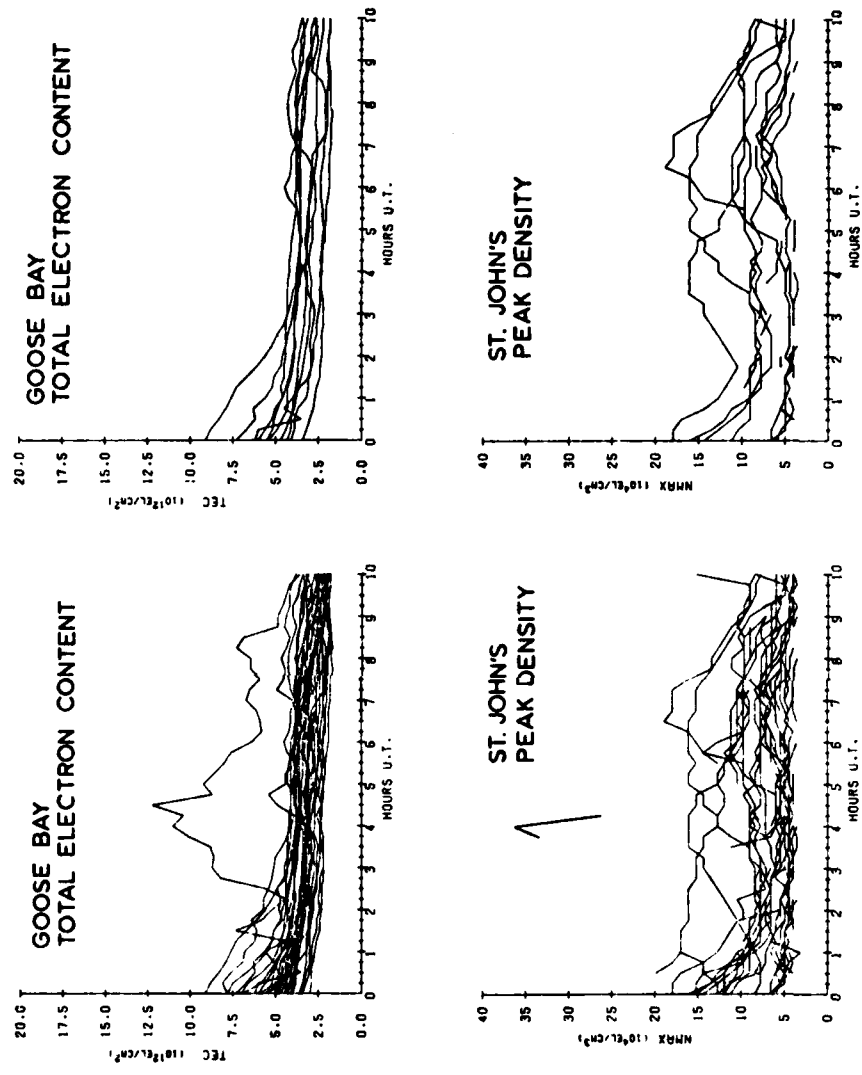


Figure 2. Goose Bay TEC and St. John's Nmax nighttime overplots for December, 1971. At left, entire month; at right, ten nights with substantial foF2 increases.

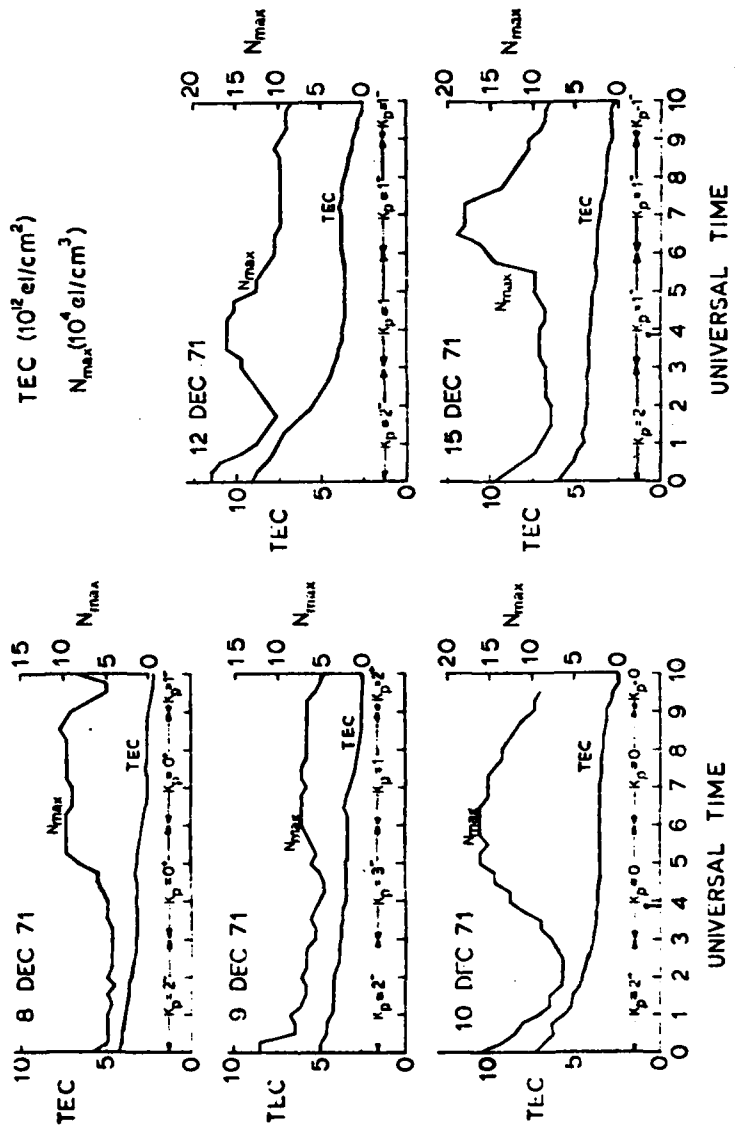
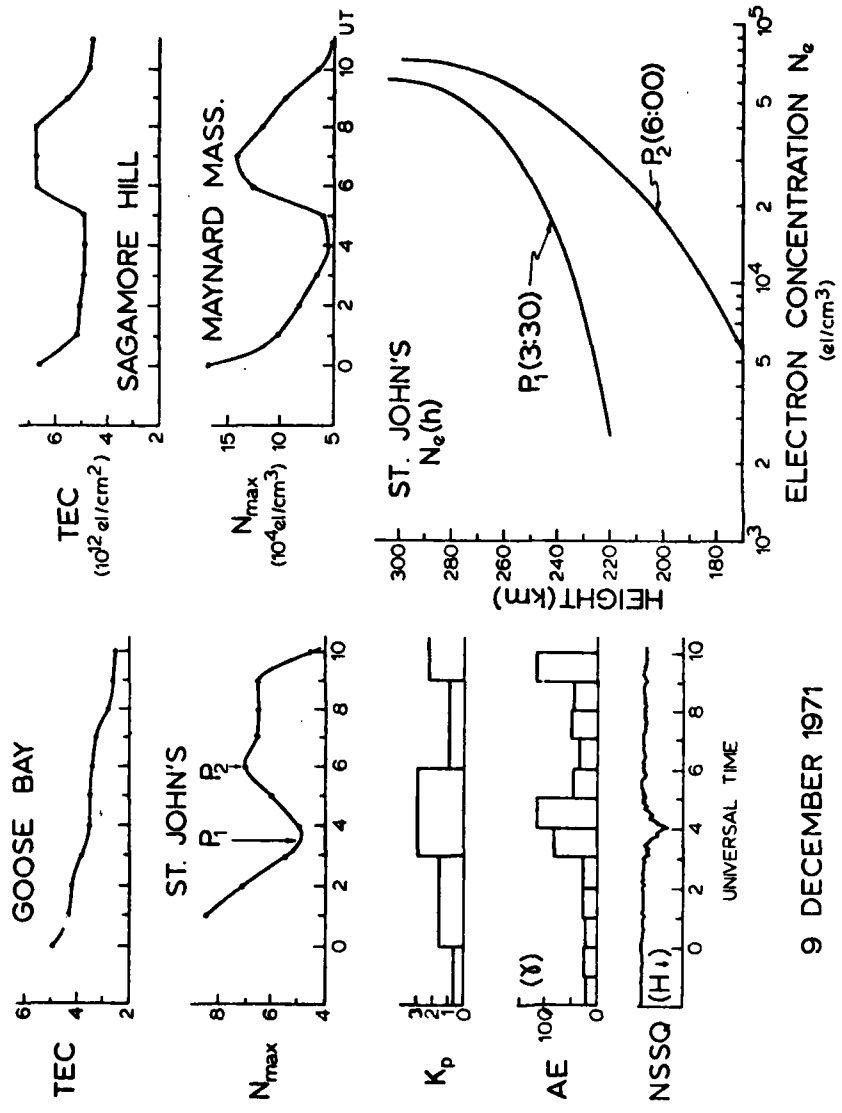


Figure 3. Five nights during which increasing  $N_{max}$ -constant TEC effect occurred at  $L=4$ .



9 DECEMBER 1971

Figure 4. Some of the available data used in the Dec. 8-9 case study.

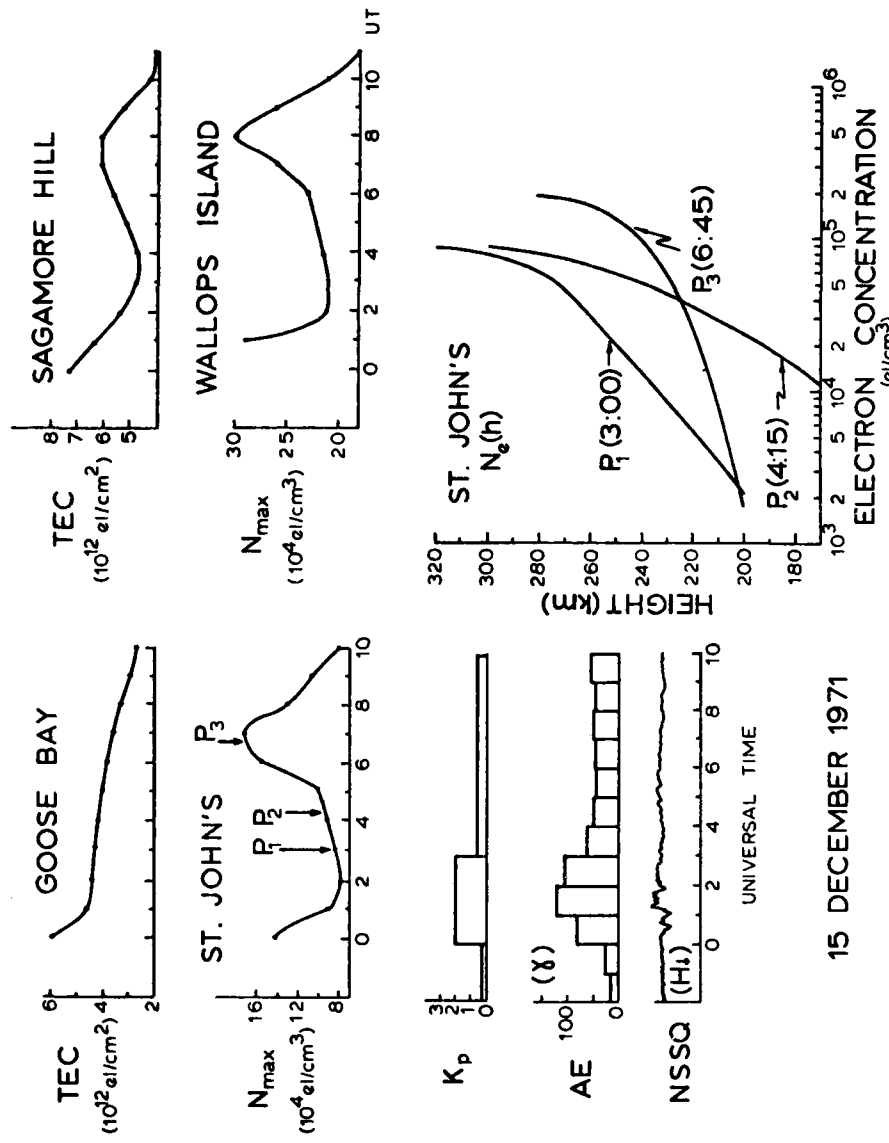


Figure 5. Some of the available data used in the Dec. 14-15 case study.

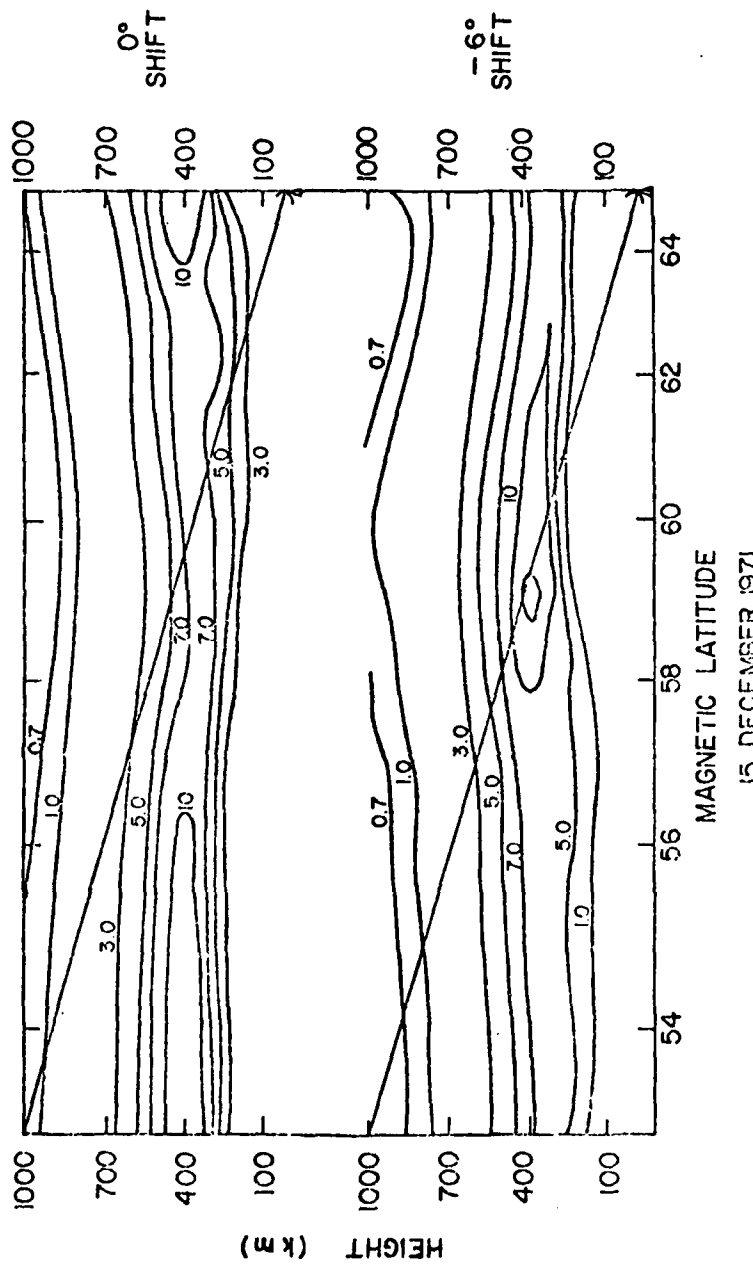


Figure 6. Electron Density Contours ( $10^4 \text{ el}/\text{cm}^3$ ) with Ray Path from Goose Bay to ATS-3  
 15 DECEMBER 1971

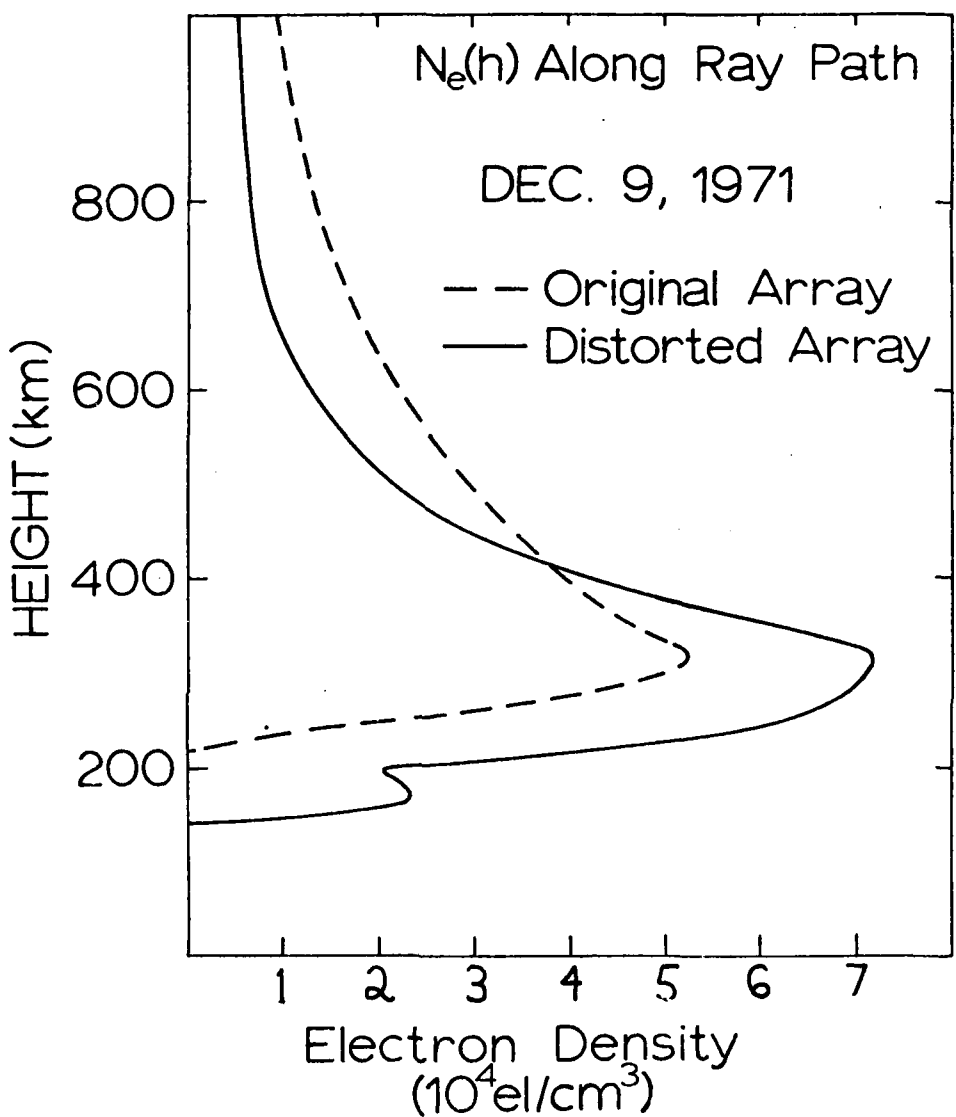


Figure 7.  $N_e(h)$  along oblique ray path, original and distorted arrays, December 9, 1971.

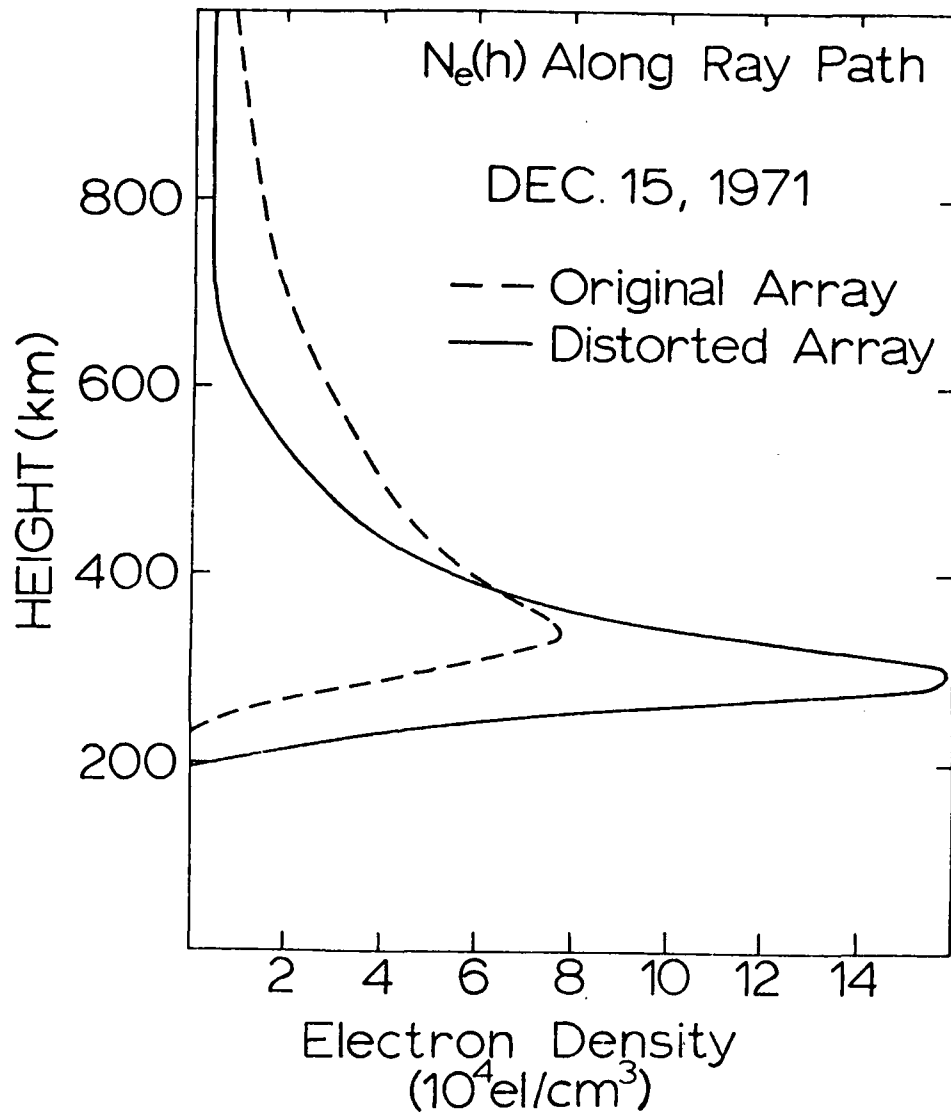


Figure 8.  $N_e(h)$  along oblique ray path, original and distorted arrays, December 15, 1971.

Name: I.S. Mikkelsen and K. Damgaard  
Address: Geophysical Section, Danish Meteorological Institute,  
Lyngbyvej 100, DK-2100 Copenhagen Ø, Denmark  
Paper: Behavior of auroral zone total electron content during substorms

**Abstract:**

The auroral zone total electron content TEC as computed from the ATS-3 Faraday-rotation shows systematic changes during magnetic activity. These changes depend upon local time, season, sunspot-cycle and the prehistory of the magnetic activity.

During summer and equinox the daytime TEC both shows a positive and negative phase, which probably are related to the prehistory of the magnetic activity. During winter the daytime TEC is dominated by enhancements as responses to the substorms. The magnitude of these enhancements is determined by the activity prior to sunrise. Thus if the activity is low prior to sunrise, the substorms during the subsequent day cause the TEC to blow up. In contrast if the pre-sunrise activity is high the daytime TEC is similar to the quiet time level.

In the late afternoon the TEC is depleted at all seasons as a response to the substorms.

In the night enhancements are observed due to the precipitation of substorm-injected electrons. These enhancements are very large during winter. During summer other factors cause a depletion of TEC. At sunspot maximum the net result is a depletion and at sunspot minimum an enhancement.

**Introduction.**

The behavior of the auroral oval F region ionization during magnetic activity is of special interest. This is so, because the electric fields, joule heating and particle precipitation which influence the neutral atmosphere and ionosphere have their maxima in the auroral oval.

By recording the Faraday-rotation of a geostationary satellite signal the total ionospheric electron content, abbreviated TEC, can be monitored almost continuously. TEC is simply proportional to the total Faraday-rotation.

Since 1969 the geostationary satellite ATS3 has been recorded at the auroral zone station Narssarssuaq, Greenland. Data from 1970 and 1971 have not been reduced, but the data from 1969 and recent data allow us to compare sunspot maximum and sunspot minimum behavior. The ATS3 signal crosses the F-region at  $63^{\circ}$  invariant latitude. During the night this latitude is within the main ionospheric trough. During the day the F-region at  $63^{\circ}$  shows mid-latitude behavior. With increasing magnetic activity the oval expands to lower latitudes such that oval conditions prevail at night. At noon TEC still shows mid-latitude behavior during very disturbed periods. First we discuss the statistical behavior of TEC with increasing magnetic activity. Next we go back to the original data and look for this statistical behavior of TEC in individual days. This is important because the statistical analysis only takes into account the instantaneous level of activity. Thus the prehistory of magnetic activity as well as the onset time (local time) of the activity is disregarded in the statistical analysis. Finally we discuss the proposed influences of electric fields, neutral winds and electron precipitation.

#### Statistical results.

To see the influence of magnetic activity all 3 hour pieces of the TEC curve are sorted according to the simultaneous  $K_p$ -indices. To see the seasonal variation, the data are collected in groups of 27 days. This is a short period compared to the seasonal variations. The 27-day period is chosen, because it is equal to the periodicity of the magnetic activity. Thus each group is expected to contain a typical distribution of quiet and disturbed days. Furthermore since the solar UV-flux also has a 27-day period the effect of the varying UV-flux is expected to be averaged out within each group of 27 days.

Figure 1 shows the daily and seasonal variation of TEC at  $63^{\circ}$  invariant latitude. It is a contour-map of quiet time ( $K_p = 0,1$ ) TEC. At the top are indicated the TEC levels (in units of  $10^{16} \text{ el m}^{-2}$ ) of the different shadings. The + and - show the changes of TEC, when the magnetic activity goes up. These changes are discussed later. The horizontal axis is cor-

rected geomagnetic local time. Corrected geomagnetic midnight takes place at 02 UT. Local solar midnight is at 03.30 UT. The vertical axis is season starting with May 1972 and terminating with March 1975. The contour map has been constructed by combining the median daily curves of quiet-time TEC from each group of 27 days.

Behavior of quiet time TEC.

The large white areas of figure 1 show the extent in local time and season of the very low TEC-values. Since the quiet winter night TEC is constant for several hours and also is the lowest of all observed TEC values it is probably also the bottom of the latitudinal profile during winter night. This minimum in both longitude and latitude is identified as the main ionospheric trough. Whether the daily minimum during summer night is also the minimum of a latitudinal profile is not known. It is probably so, when considering the  $K_p$ -value ( $=0,1$ ) and the invariant latitude ( $=63^\circ$ ,  $L=5$ ). The highest TEC values are observed during the summer daytime. In contrast to the TEC data from 1969, (Mikkelsen, 1972) which showed a pronounced winter anomaly, the ratio between winter and summer content is reversed at sunspot minimum. This is similar to  $f_o F_2$  behavior. (King and Smith, 1968).

Changes of TEC in connection with magnetic activity.

Like the contour map shown in figure 1 contours of TEC have also been constructed for higher levels of magnetic activity. In figure 1 we have indicated the sign of the difference TEC-median ( $K_p > =4$ ) - TEC-median ( $K_p =0,1$ ). Because of incomplete data the transition from positive to negative areas is not well defined in a few places. This is indicated by stipled lines.

The significant changes of TEC can be listed as follows:  
1) In the late afternoon after 18 CGLT TEC is lower during disturbed than during quiet conditions. Looking at the upper quartile of disturbed TEC it is also lower than the lower quartile of quiet TEC values at this local time. This

means that most disturbed days show a depletion of TEC after 18 CGLT. This is the case for all seasons and independent of the TEC level prior to the depletion.

2) During winter the late afternoon depletion is followed by an enhancement due to precipitating electrons. (Mikkelsen 1975). This winter night enhancement lasts until sunrise for very disturbed conditions as demonstrated by figure 2. The onset of the afternoon depletion is probably due to the onset of the mechanisms, which form the main ionospheric trough. Subsequently the auroral oval expands equatorward into the trough and fills it up with ionization. This is not very clear from figure 1 and 2, but when considering only moderately disturbed days ( $K_p=2,3$ ) a clear separation can be seen between the depletion and subsequent enhancement of TEC.

3) During summer the depletion which started in the late afternoon extends into the night. Thus an enhancement due to electron precipitation, which is centered at corrected geomagnetic midnight, is not evident. During 1969 (Mikkelsen, 1972) at sunspot maximum, the TEC showed a more pronounced depletion during night. Figure 1 shows, that there is a gradual change from a negative to a positive response of TEC when approaching the sunspot minimum.

4) The winter day-time TEC shows a very pronounced enhancement at disturbed days. This is also a very significant effect, since the lower quartile of the disturbed TEC values is also bigger than the upper quartile of the quiet TEC values. This enhancement is seen during all years both at the maximum (Mikkelsen, 1972) and the minimum of the sunspotcycle.

5) During the summer and equinox day changes which are repeatable from year to year can be seen in figure 1. In the equinox day the TEC goes down. The summer day both shows a positive and negative phase. The statistics shows, that the quartiles of quiet and disturbed TEC are not separated. Going back to the individual days it means, that a very variable behavior is seen.

Dependence of TEC upon prehistory of magnetic activity and local time onset of activity.

Mendillo (1973) has found a systematic behavior of the mid-

latitude TEC during sudden commencement storms. In many cases TEC shows a positive phase at the first day of the storm and a negative phase at the subsequent days. According to Mendillo (1973) the positive phase or enhancement of TEC which occurs near dusk is only observed, when a nearby magnetic observatory shows a positive bay, the signature of an eastward ionospheric current. Furthermore if the storm starts at such a local time, that the magnetic observatory encounters a strong negative bay (westward electrojet) as the first event of the storm, the positive bays on the subsequent days do not have connected with them TEC enhancements. We have looked for the same pattern in the auroral zone. Until now only the winter data have been analyzed. The summer and equinox (apart from a few cases) await a future analysis.

The winter day time TEC is enhanced during magnetic activity. Figure 2 shows, that the enhancement starts at sunrise. TEC continues to grow at a bigger rate than during quiet conditions until the maximum is reached. The time of maximum is coincident with the quiet time maximum. Shortly after the maximum is passed, TEC decays more rapidly than during quiet conditions, which leads to the afternoon depletion. This median behavior of TEC is the same in the three winters studied, that is 72/73, 73/74 and 74/75.

Going back to the original data especially the winter 72/73 shows many days, where TEC goes to very high values. It is common to these days, that the Kp-index increases during the hours 6-15 UT. The median behavior of Kp is such, that Kp equals 1, 2, and 4 in the three-hour intervals 6-9, 9-12, and 12-15 respectively. To test the relationship, we have searched for all days having this development of Kp-index. Indeed there are not more days, than those, which show the very big TEC-values. Thus, if Kp is low during the hours 6-12 UT, the auroral oval following the normal diurnal pattern migrates northward. This means, that the separation between the oval and the F-region observed is big, such that the F-region is left untouched of the physical processes active along the oval. In that case a subsequent in-

crease of magnetic activity during the day-time causes the TEC to blow up. There is no dependence of TEC upon the very long prehistory of magnetic activity. The pronounced TEC enhancements discussed here are not related to sudden-commencement storms.

If on the contrary the magnetic activity is high during the hours 6-12 UT, TEC the following day shows a smaller enhancement as a response to magnetic activity. If the period 6-12 UT is very disturbed TEC remains at the quiet time level the following day. (During the late afternoon the depletion is still present). The above description applies to the winters 72/73 and 73/74. The behavior of TEC during the winter 74/75 does not fit into the systematics described above. The winter is more disturbed. K<sub>p</sub> is equal to or greater than 4 or 20% of the time. During the winters 72/73 and 73/74 this is only the case 10% of the time. Examining the individual days, the long periods of high activity both show positive and negative days. In contrast to the two winters 72/73 and 73/74 the "negative days," during 74/75 are definitely below the quiet level. There is no simple clue in the K<sub>p</sub>-index to these positive and negative days.

Discussion of proposed mechanisms influencing the auroral zone TEC.

The seasonal variation of the ionospheric substorm is believed to be caused by a seasonal enhancement of the ratio n(0)/n(N<sub>2</sub>) from summer to winter. (Mayr et al., 1976). This is supported by Prölss and Zahn (1974), who find a good correlation between the relative changes of f<sub>0</sub>F2 and the relative changes of the ratio n(0)/n(N<sub>2</sub>) during ionospheric storms. Theoretically Park and Banks (1975) have computed that Nmax goes down by a factor 2, when the concentration of N<sub>2</sub> is enhanced by a factor 5. Thus the low abundance of N<sub>2</sub> during winter means, that the processes which enhance TEC may dominate the loss due to charge exchange with N<sub>2</sub> both at quiet and disturbed conditions. According to Mayr et al. 1976 the reversal of the winter anomaly at sunspot minimum may be caused by a relative enhancement of

$n(O_2)/n(N_2)$  from summer to winter - at sunspot minimum. Although this enhancement of  $O_2$  can remove the winter anomaly it is not able to create a negative phase during the winters 72/73 and 73/74. Whether the negative days of the winter 74/75 are caused by an extra high abundance of  $O_2$  or by the particularly high magnetic activity during that winter can not be decided here.

Considering the foregoing discussion of the seasonal variation of the thermospheric composition it is tempting to suggest, that the positive phase of the ionospheric substorm during the winter day (which includes the dusk-effect) is created by the same mechanism, which causes the positive dusk effect at midlatitudes as described by Mendillo (1973).

Many authors have suggested that the positive phase of the ionospheric substorm is caused by a lift of the plasma to greater altitudes, where the recombination is slower. Horizontal transport may also cause changes of TEC, if horizontal gradients of the plasma are moved past the observation point. But such effects can not explain the positive phase. For example, the quiet time latitudinal TEC gradients shown by Mendillo and Klobuchar (1975) are too small to explain the enhancements even if we imagine a very big (and unrealistic) poleward plasma convection at midlatitudes. The same can be seen from latitudinal profiles of TEC obtained from the polar orbiting satellite S66 (Mikkelsen, 1971).

A downward flow of plasma would also increase the TEC. This mechanism is active south of the plasmapause, but according to Park and Banks (1975) it is only a minor modification to the day time F-region.

Thus the only possible mechanism to explain the positive phase is to lift the plasma to greater altitudes. This can be done by southward neutral winds or by a northward plasma convection. The latitudinal profiles published by Mikkelsen (1971) show that the dusk enhancement terminates at a high latitude, where TEC drops by a sharp gradient to a low value. We can not explain this behavior, but we can incorporate the different mechanisms proposed into a model. The relative importance of the equatorward neutral winds and the poleward plasma convection may vary with local time. The neutral winds originate from a high pressure region along the oval created by Joule heating and/or particle precipitation. Schunk and Banks (1975b) suggest that  $N_2$  molecules are excited  $N_2 \rightarrow N_2^*$  in the oval. The neutral winds blow these excited molecules equatorward. Because the charge exchange reaction

$O^+ + N_2 \rightarrow NO^+ + N$  is more rapid, when  $N_2$  is excited, the  $O^+$  ions are depleted. This process would prevent the creation of the enhancement. Therefore, if it exists, the  $N_2^{++}$  molecules must be removed before the neutral wind reaches the region of the observed enhanced TEC.

There is another process proposed, which could explain the steep slope, which is the poleward termination of the enhancement. According to Schunk et al. (1975a), the process  $O^+ + N_2 \rightarrow NO^+ + N$  is speeded up, if the relative speed of the two reactants  $O^+$  and  $N_2$  is enhanced. This can be done by neutral winds (moving  $N_2$ ) or by electric fields moving the plasma (of which  $O^+$  is part). The neutral winds are too small to be of importance, but rapid plasmaconvection has a very drastic effect. We have integrated the electron density profiles shown by Schunk et al. (1975) to find that TEC is decreased by a factor 2, when the electric field is shifted from 0 to 100 mv/m. It is well known, that the regions of plasma return flow expands equatorward and the plasma speed is also enhanced in connection with magnetic activity. This means, that the F-region at  $63^\circ$  invariant latitude comes in touch with the plasma-return flow at an earlier local time of the afternoon during disturbed conditions. This could explain the late afternoon depletion of TEC. Recently Brinton (1975) has measured, that the concentration of  $NO^+$  goes up within regions of enhanced plasma flow. This further supports the proposed mechanism.

Acknowledgments. The research in this paper has been sponsored by the Air Force Cambridge Research Laboratories under Grant AFOSR-72-2161. Thanks are given to H. Hartmann for valuable computer programming and to Greenfort, who did the scaling of the Faraday-rotation.

References.

- Brinton, H.C., In situ measurements of plasma drift velocity and enhanced NO<sup>+</sup> in the auroral electrojet by the Bennett mass spectrometer on AE-C, *Geophys. Res. Letters*, 2, 243, 1975.
- King, J.W. and P.A. Smith, The seasonal anomaly in the behavior of the F<sub>2</sub> layer critical frequency, *J. Atmos. Terr. Phys.*, 30, 1707, 1968.
- Mayr, H.G., P. Bauer, H.C. Brinton, and L.H. Brace, Diurnal and seasonal variations in atomic and molecular Oxygen inferred from atmosphere Explorer-C, *Geophys. Res. Letters*, 3, 77, 1976.
- Mendillo, M., A study of the relationship between geomagnetic storms and ionospheric disturbances at midlatitudes, *Planet. Space Sci.*, 21, 349, 1973.
- Mendillo, M., and J.A. Klobuchar, Investigations of the ionospheric F-region using multistation total electron content observations, *J. Geophys. Res.*, 80, 643, 1975.
- Mikkelsen, I.S., Knee of total electron content and scintillation boundary, Danish Meteorological Institute, Geophysical Papers, R-21, 1971.
- Mikkelsen, I.S., Seasonal, diurnal and magnetic dependence of ionospheric total electron content at 63° invariant latitude. 1972, available through the author.
- Mikkelsen, I.S., Enhancements of the auroral zone ionization during substorms, *Planet. Space Sci.*, 23, 619, 1975.
- Park, C.G., and P.M. Banks, Influence of thermal plasma flow on the daytime F<sub>2</sub> layer, *J. Geophys. Res.*, 80, 2419, 1975.
- Prölss, G.W., and U. von Zahn, Esro 4 gas analyzer results 2, Direct measurements of changes in the neutral composition during an ionospheric storm, *J. Geophys. Res.*, 79, 2535, 1974.
- Schunk, R.W., W.J. Raitt, and P.M. Banks, Effect of electric fields on the day-time high-latitude E- and F-region, *J. Geophys. Res.*, 80, 3121, 1975a.
- Schunk, R.W., and P.M. Banks, Auroral N<sub>2</sub> vibrational excitation and the electron density trough, *Geophys. Res. Letters*, 2, 239, 1975b.

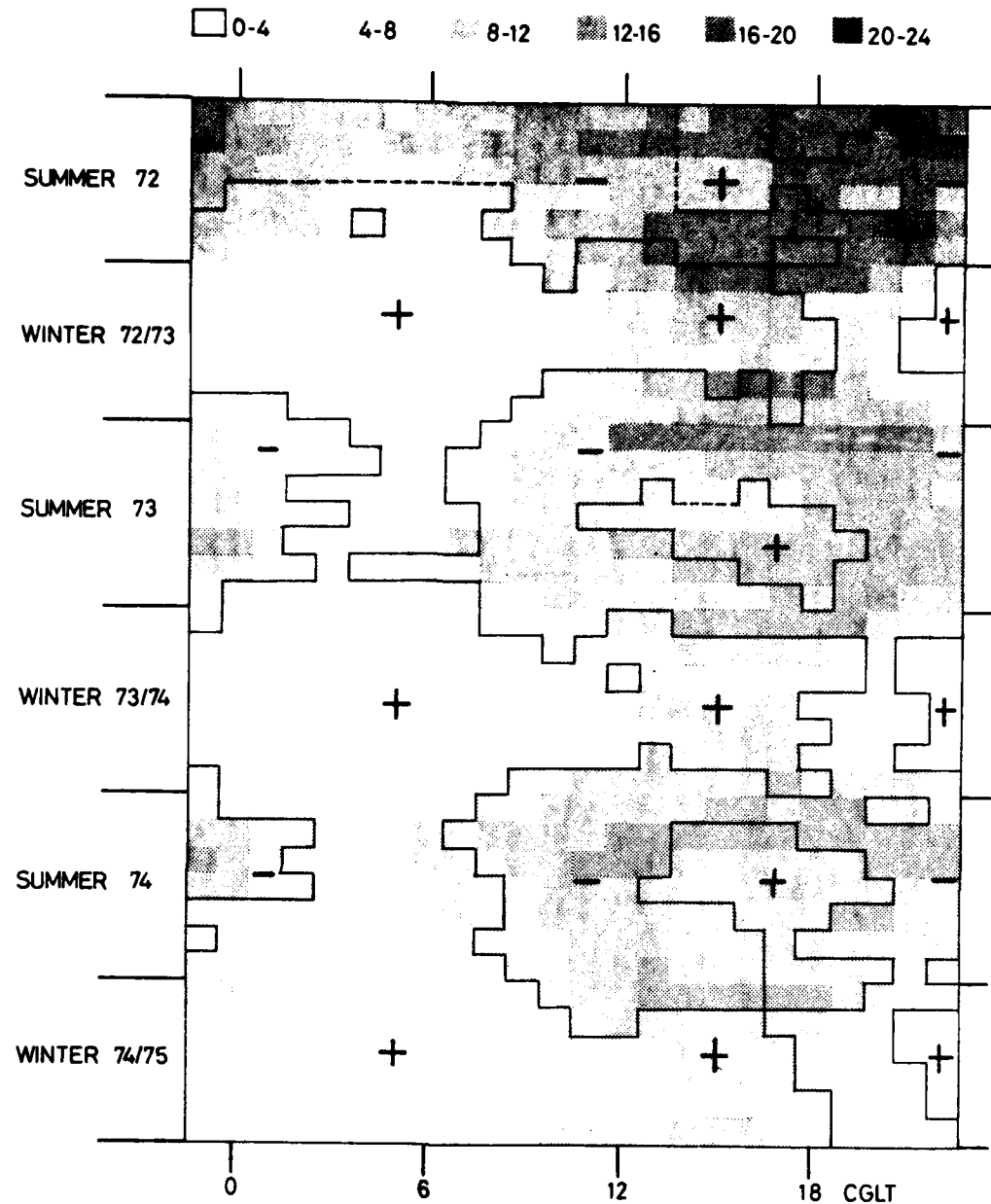


Figure 1. Contours of quiet time auroral zone TEC in units of  $10^{16} \text{ el m}^{-2}$ . Horizontal axis is corrected geomagnetic local time and vertical axis shows seasons. + and - indicate changes during ionospheric substorms.

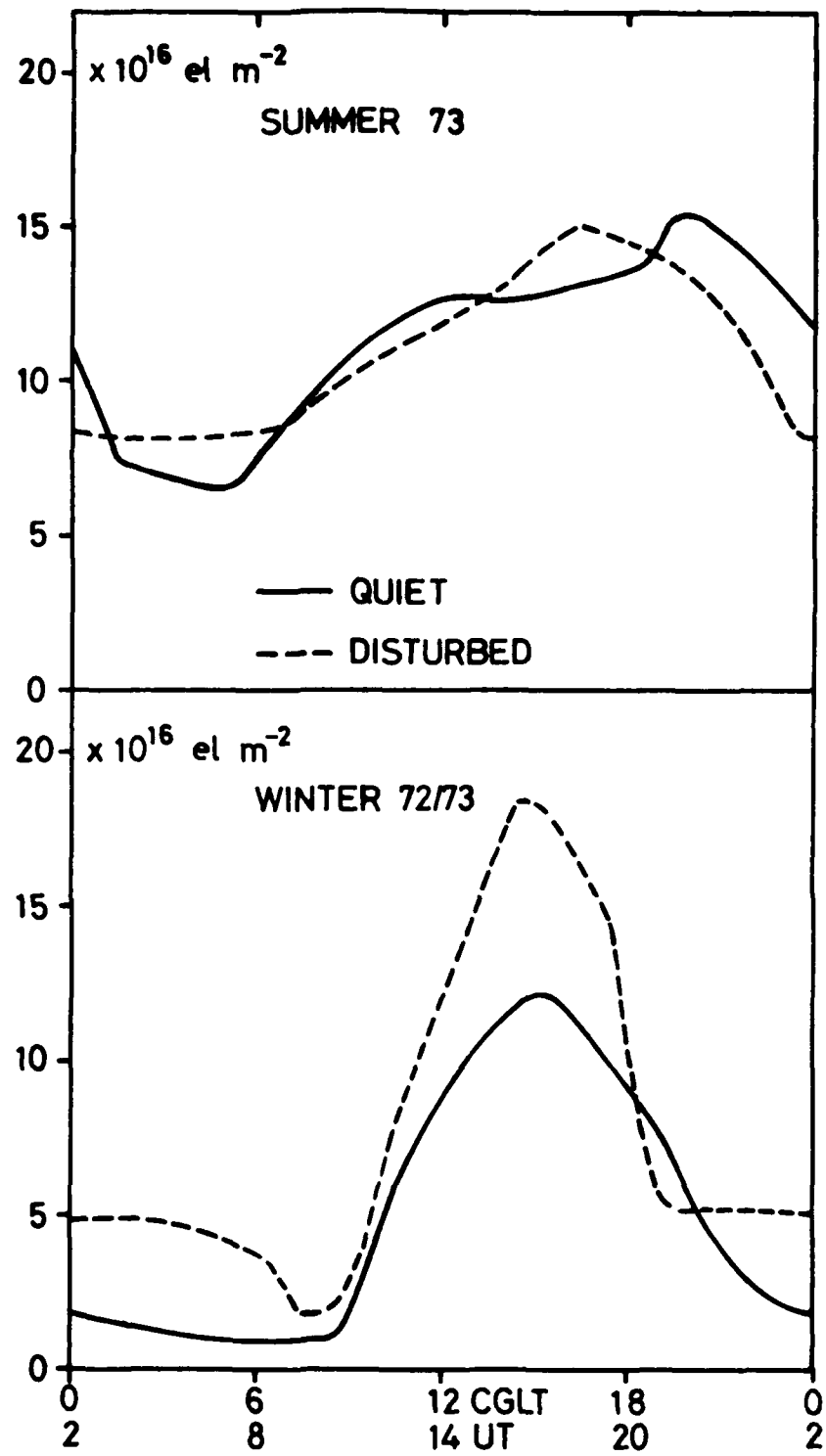


Figure 2. Quiet and disturbed TEC.

GEOSTATIONARY VERSION OF NON-COHERENT RESPONSE METHOD AS  
A MEANS FOR THE INVESTIGATION OF THE MAGNETOSPHERIC PLASMA  
DISCONTINUITIES DURING STORMS

J.V. Kovalevsky, T.V. Kuznetsova

Institute of Terrestrial Magnetism, Ionosphere and Radio Wave  
Propagation of the USSR Academy of Sciences  
142092, Moscow Region, p/o Academgorodok, USSR

Abstract

It is shown that by means of the geostationary version of the non-coherent response method at the root of which is the idea of transformation of a signal transmitted from a sounding station (a geostationary satellite) and received by a response one (the Earth), that permits to change the sign of frequency shift and of phase lag, it is possible to investigate the dynamics of the plasmapause, the plasmasphere plasma tails, the plasma sheet and magnetosheath boundaries of the geomagnetosphere. By measuring on board of the geostationary satellite the phase difference of the sounding and response signals  $\Delta\Phi$ , the time of its increase (fast beating frequency  $\Delta f$ ) it is possible to get the information about the location, the motion velocity of the magnetosphere plasma discontinuities and the concentration drop on their fronts. The establishment of communication between appropriately spaced ground stations and a satellite with a quasi-polar orbit will permit to study the midlatitude plasmapause dynamics, and those of the ionosphere trough, polar cusps boundaries and of polar cap inhomogeneities. For registering (for  $\Delta\Phi = 10^{-4}$  - tens of rad. and for  $\Delta f = 10^{-5}$  - tens of Hz) the most dynamical events occurring in radiopath during storms it is needed the equipment with the stability being  $10^{-11} - 10^{-12}$ .

Introduction. During magnetospheric storms and substorms a shift of the plasmasphere boundary (the plasmapause) towards the Earth down to the magnetic shell  $\lambda \leq 2$  [1-4] may be observed, as well as plasma detachment from the plasmasphere mainly in the evening sector (that <sup>may</sup> be self-drifting towards the magnetopause detached plasma regions [1, 5] or a formation of plasma tails connected with the plasmasphere [6, 7]) and the approach to the Earth (down to the plasmapause) of the geomagnetosphere plasma sheet inner boundary (Alfven layer) [4, 8-11].

The plasmapause, plasma tails or detached plasma regions sides on which plasma concentration  $\eta$  changes, as a rule, by drop by 1-2 orders or more [1, 4, 5] are moving with the velocity  $U$  of about 1-10 km/sec [4, 12-16]. The plasma sheet inner boundary at which the concentration may change from 0,1 to  $1-10 \text{ cm}^{-3}$  [16-18] moves at  $U = 40-200 \text{ km/sec}$  [19].

It should be noticed that a co-existence of several plasmapauses is possible (which will appear on the profile  $\eta$  in the form of several steps), due to the past erosions and to several successive substorms losses pile-up [1, 4]. Besides this, large-scale dips may occur in the plasmapause [1]. The plasmasphere and the plasma sheet inner boundary dynamics is, apparently, determined by the magnetosphere convection time-changing electric field directed from the day side to the evening one [10, 20, 21]. It should be born in mind that according to theoretical computations [22] the Alfven layer occurring as a result of charges separation near the moving inner boundary of plasma sheet will considerably alter and

complicate the electric fields pattern, will weaken considerably the field from inside the Alfvén layer region and will intensify it from the outside. However experimental data are poor concerning a real behaviour of the inner boundary and its effects. That is why when investigating the plasmopause, plasma tails and plasma sheet boundaries an information may be obtained on plasma convection and large-scale electric fields non-stationary character during storms and substorms and, consequently, on the Earth magnetosphere dynamics as a whole.

Still a recording of the above mentioned events by space-crafts is rather difficult since the above spacecraft has to be near a corresponding boundary when the event occurs. Then, to estimate a distance for which the boundary shifts under the effect of a disturbance, the spacecraft has to follow it as it shifts otherwise it is necessary to use several appropriately sited space-crafts. The both seem rather improbable at the present time. The difficulty consists in that the probe methods of plasma investigations permit to get information only on such events that occur directly in the neighbourhoods of the space-craft.

On the other hand, familiar radiointerference methods (e.g. coherent frequencies or Faraday rotation ones) give information only about plasma integral characteristics giving no possibility to localize the events in time and space. In this case the overwhelming contribution to the recorded phase difference belongs to the Earth ionosphere which restricts considerably these methods in the study of magnetospheric and interplanetary plasma dynamics.

From that point of view it seems of some interest to investigate a possibility of events recording by means of measurement of the phase shift  $\Delta\Phi$  of a sounding and a response signals transmitted at a same frequency  $f$  [23]. The sounding station being placed on board the spacecraft and the response one on the Earth, the ionosphere effect (influence) may be almost completely eliminated; may be also singled out the phase shifts occurring due to cosmic plasma discontinuities [24] (e.g. run over the radio path of interplanetary shock and tangential discontinuities; the magnetopause and the Earth bow shock motion [25]); they may be localized in space and time (non-coherent response method).

Let us notice that the non-coherent response method had for base the idea of transformation of a signal transmitted from a sounding station and received by a response one which permits to change the signs of the frequency shift and of the phase lag [26, 27]. Thus transformed, the signal has been transmitted from the response station and received by the sounding one. Such a procedure permitted to obtain effects on  $\Delta\Phi$  and  $\Delta\omega$  caused by a run-over of plasma disturbances in the radiopath (independently of the near-the-response-station-medium conditions).

#### Possibilities of plasmapause dynamics investigation.

Formulae obtained in [24, 25] for phase shifts may be also applied to intramagnetosphere plasma discontinuities shifts. It may be shown [28] that by measuring the phase shift between a sounding and a response signals  $\Delta\Phi$  and its increase rate  $\Delta\omega = \Delta\Phi/\Delta t$ , the following data on plasmasphere and plasma tails boundaries and on the plasma layer inner boun-

dary may be obtained: concentration change at the boundaries  $\Delta n$ , shift velocities  $u$  for moments of the beginning and the end of the motion, space and time coordinates of these events. Consequently parameters will be obtained forming the basis of our ideas on magnetosphere non-stationary character during storms and substorms.

Let us assume that a sounding signal is transmitted from a station situated within the magnetosphere boundaries (i.e. inside the magnetopause and the inner boundary of the plasma sheet but outside the plasmasphere) from a geostationary satellite, for example. Recording of phase shifts of a sounding and a response signals is performed on board the spacecraft. Some time after the response signal comes which has passed through the plasmapause in that moment when the latter started moving a phase difference occurs; in a time  $\Delta t_1 = \frac{2R_1}{c}$  ( $R_1$  - a distance from Earth to the magnetopause in the beginning of the motion) it reaches its maximal value equal to (see fig. 1)

$$\Delta_1 \Phi = \frac{\omega_{re}^2}{\omega \cdot \cos \alpha} \frac{R_1}{c} \frac{u}{c}, \quad (1)$$

where  $\omega_{re}^2 = \frac{4\pi e \Delta_1 n}{m}$ ,  $\Delta_1 n = n' - n'' \approx n' - n$  - a concentration drop at the plasmapause boundary,  $n'$  - plasma concentration in the plasmasphere near its boundary,  $\alpha$  - the angle between the line connecting a sounding and a response stations and a normal to the plasmapause surface.  $R_1$  may be determined from a time of phase growth  $\Delta t_1$  and the value  $\Delta_1 n u / \cos \alpha$  - from  $\Delta_1 \Phi$ . Plasmapause motion at a constant velocity leads but to very slow changes of phase difference

which could not be registered nowadays. Still in the instant the plasmapause stops in a time  $\Delta t_2 = \frac{2R_2}{c}$  a considerable change of a sounding and response signals phase shift will occur once more; it will be equal to a value

$$\Delta_2 \Phi = \frac{\omega_{2e}^2}{\omega \cdot \cos \alpha} \frac{R_2}{c} \frac{U}{c},$$

where  $\omega_{2e}^2 = \frac{4\pi e^2 \Delta_2 n}{m}$ ,  $\Delta_2 n$  - concentration drop at the plasmapause at the instant it stops. Measuring  $\Delta t_2$  and  $\Delta_2 \Phi$  one may determine a new position of the plasmapause  $R_2$  and  $\Delta_2 n U / \cos \alpha$ . From the difference of  $R_1$  and  $R_2$  and the time that has passed from the beginning of the motion to its stop one may determine the mean velocity of the motion

$$U / \cos \alpha \text{ and, thus, } \Delta n, \text{ and } \Delta_2 n, \text{ too.}$$

It has been assumed above that the time of the plasmapause slowing-down is short enough ( $< 2R_2/c$ ). If the relaxation of electric fields causing the plasmapause shift passes in a time  $\Delta t$  more than  $2R_2/c$ , the right-hand side of the plot in fig.1 will somewhat change its character (see a dash-and dots line).

In order to estimate the frequency stability level necessary for the recording of the above considered phase shifts calculations of  $\Delta f = \frac{\Delta \Phi}{\Delta t \cdot 2\pi}$  have been carried out the signal frequency being  $f = \omega / 2\pi = 40 \text{ MHz}$ ,  $\cos \alpha = 1$ ,

$U = 0,2; 1; 10 \text{ km/sec}$ . Real concentration drops at the plasmapause have been taken as  $\Delta n$ ; they have been experimentally measured for the day (0600 - 1500 LT), night (2200 - 0600 LT) and evening-side (1500 - 2200 LT) regions, all-in-all 21 cases (N) [1, 5, 29-33]. In fig.2 are given the computed phase change rates, i.e. the values of relations

$\frac{\Delta \Phi}{2\pi \cdot \Delta t} = \Delta f$  (•, ▲, ■ correspond to  $U = 0, 2; 1; 10$  km/sec respectively) when the plasmapause comes into motion or stops. The same figure gives frequency drifts  $\delta_{\gamma} f$  because of the instability of a sounding and a response generators, stabilization levels  $\xi$  being different (the horizontal solid lines designate respectively  $\delta_{\gamma} f = 4 \cdot 10^{-6}, 4 \cdot 10^{-5}$  and  $4 \cdot 10^{-4}$  Hz for corresponding  $\xi = 10^{-13}, 10^{-12}, 10^{-11}$ ). The fig.2 evidences that for registering the majority of phenomena under consideration a stabilization to an accuracy of  $\xi = 10^{-11}$  is sufficient. It would be recalled that modern quantum standards of frequency permit to obtain a stability of  $10^{-12} + 10^{-14}$  [33]. Let us also notice that the stationary plasmapause (as well as stationary plasma tails and plasma sheet boundaries) will not give rise to any phase shift of signals in the method in consideration. Ionospheric disturbance level lies below  $10^{-6}$  Hz.

#### On double plasmapause and its large-scale dips recording.

There is no fundamental difficulty for a non-coherent response method in registering a multi-step concentration profile, i.e. practically any number of "plasmapauses". A characteristical example of a double plasmapause has been registered on 12. III. 1968 from the day side as well as from the night one [32, 33]. If we assume both plasmapauses shift under the effect of some process with a velocity  $U \approx 1$  km/sec the equipment with  $\xi = 10^{-12}$  will be able to register signals both from the outer  $\Delta f \approx 7 \cdot 10^{-5}$  Hz,  $\Delta \Phi = 2 \cdot 10^{-4}$  rad with  $\Delta n \approx 44 \text{ cm}^{-3}$  and from the inner plasmapauses  $\Delta f \approx 3 \cdot 10^{-3}$  Hz,  $\Delta \Phi = 8 \cdot 10^{-3}$  rad with  $\Delta n \approx 980 \text{ cm}^{-3}$  (see also fig.2, cases 22-29).

Given the presence of some short-time local source of an intensive electric field a small part of the plasmasphere may shift towards the inside [1]; in this case a large-scale dips in plasmasphere density may occur (as it has been found by "OGO-5" 30.III. 1968 at  $L \approx 2,8$  [33]). If the base of the dip, being in radiopath, started shifting at  $U = 10$  km/sec (with  $\Delta L \approx 4600$  cm<sup>-3</sup>), this event could be easily registered from  $\Delta f$  ( $\approx 10^{-1}$  Hz) and  $\Delta \Phi$  (0,4 rad) (see fig.2 cases 30-32).

In the case of a stationary dip with pronounced sides and base it could be detected from  $\Delta f$  and  $\Delta \Phi$  in the moments on the radiopath entering into it and its issuing from it, for the azimuthal velocity of the radiopath making several km/sec. This condition is met at a level  $L = 3-6$  if the equipment is set up on a geostationary satellite.

#### Plasmasphere corotational plasma tails.

The near-equator plasmasphere is customary subdivided into three sectors regions as to its character [1]: the day, the night and the evening (or the bulge region) ones. In the evening, day and very seldom in the night sectors of the plasma trough a cold and a very dense plasma regions are observed (as a rule, during magnetic storms and substorms when the electric field changes sharply) [1, 5, 7]; they are considered as detached plasma regions not connected with the plasmasphere or as plasma tails connected with the plasmasphere [2, 6, 7] (the latter assumption is physically better-reasoned and qualitatively better worked out [20, 21]).

Though in such periods a situation in radiopath in the day and the evening sectors becomes more complicated, never-

heless the process of co-rotational plasma tails formation, the non-uniformity of the shift towards the day side magneto-pause and subsequent dynamics may be investigated by a non-coherent response method.

Co-rotational plasmasphere plasma tails may be, apparently, approximated in the form of dense plasma layers with rather pronounced boundaries submerged in a strongly rarefied plasma trough medium. A radiobeam transmitted from a sounding station will find on its way a quasirectangular concentration pulse and then it will pass through the plasmapause.

From theoretical models [1, 2, 6] it follows that an sharp enhancement of the convection electric field shifts the plasma tails towards the Sun and broadens it, i.e. its boundaries will shift in opposite directions. The electric field's attenuation after a substorm will make the layer shift eastwards narrowing it at the same time, i.e. the boundaries will meet one another in the viewing field of the radio beam.

As this takes place it may be shown that in the beginning of a sharp shift of plasma tails boundaries and during their instantaneous stops (independently of their quantity) as well as in the instants the boundaries issue from the limits of a sounding station a phase difference occurs which may be determined from (1) by substituting corresponding  $R$ ,  $u$ ,  $\alpha$ ,  $\omega$ . The phase difference change rate is

$$\Delta f = \frac{1}{4\pi} \frac{\omega_e^2}{\omega \cdot \cos \alpha} \frac{u}{c} . \quad (2)$$

The carried out estimates have shown that plasma tails

boundaries (with  $\Delta/l = 64(3-310) \text{ cm}^{-3}$  [1, 6] and assuming  $U = 10 \text{ km/sec}$  [4, 16]) will cause in the radiopath  $\Delta f \approx 2 \cdot 10^{-3}(2 \cdot 10^{-4} - 10^{-2}) \text{ Hz}$  and  $\Delta \Phi \approx 6 \cdot 10^{-3}(5 \cdot 10^{-4} - 3 \cdot 10^{-2}) \text{ rad}$  (fig.3; cases 1-32) which may be registered with  $E = 10^{-11} - 10^{-12}$ . It should be added that it seems possible to note a lateral intrusion into radiopath and the emergence from it of detached plasma regions from a short-time enhancement of  $\Delta \Phi$  [35].

Signals from plasma sheet boundaries and magnetosheath.

Let us notice that in plasmasphere study from a geostationary satellite some new signals (commensurable as to the amplitude) may occur in day-side radiopaths besides the registered signals caused by the plasmapause and plasma tails boundaries; the former are caused by an intrusion on the sounding station first of the magnetopause and then of a bow shock of the Earth [25]. For example, such situation could have occurred on 8. III. 1970 when a magnetopause and a bow shock shifter inside the satellite ATS-5 orbit [36]. Assuming the transition region (magnetosheath) boundaries shifting with  $U = 200 \text{ km/sec}$ ,  $\Delta \Phi \approx 7 \text{ rad}$ ,  $\Delta f \approx 0,1 \text{ Hz}$  in this case.

According to the phenomenological model of a substorm [11, 37, 38] the interplanetary magnetic field vector's changing its direction to a southward one is accompanied by plasma sheet narrowing and by its inner boundary shift towards the Earth. As the substorm origin phase develops, the inner boundary becomes more steep and the shift velocity goes increasing. Therefore, in the plasmasphere study in night-side radiopaths signals may be recorded on the plasma sheet inner boundaries intrusion in the radiopath from the soun-

ding station and then on their leaving it ( $\Delta f \approx 10^{-3} - 10^{-4}$  Hz,  $\Delta \Phi \approx 10^{-4} - 10^{-2}$  rad); the analysis of these signals may supply an important information on plasma layer.

Conclusion.

Thus we see that in the study of plasmasphere dynamics by a non-coherent response method (in its geostationary version) the recording conditions depend significantly on the sector (i.e. on local time) and on the position of the bow shock, magnetopause and the plasma layer inner boundary (i.e. on the magnetospheric activity and in the final analysis on the conditions of interaction of the interplanetary medium and the Earth magnetosphere). In the night sector radiopaths signals depending on the plasmapause dynamics and sometimes on the plasma layer inner boundary will be mainly recorded. In the day and evening sectors radiopaths there will be also signals caused by plasma tails boundaries and sometimes by the bow shock and the magnetopause, too.

A mounting of equipment complying with the sounding station on a satellite with a quasipolar orbit and an appropriate choice of ground-based stations for a set-up of the response equipment would permit a considerable enlargement of a non-coherent response method scope: e.g. to study the midlatitude plasmapause dynamics and those of the ionosphere trough, of polar cusp boundaries and even of inhomogeneities above the polar cap.

It should be particularly emphasized that all events in the radiopath may be recorded and localized in time and space. This is one of the most important advantages of the

non-coherent response method. Among other advantages there should be also mentioned a great time resolution (0,1-0,2sec).

Besides all this the method permits to obtain data on  $\Delta U$  and  $\Delta Z$  for discontinuities inside the magnetosphere. If, moreover, there are data on the magnetic field then one may obtain information on the non-stationary electric field.

It follows from the foregoing that the non-coherent response method is a promising one for investigation of intra-magnetospheric plasma discontinuities dynamics.

#### References

1. C.R. Chappell. Rev. Geophys. Space Phys., 1972, 10, 951.
2. J.M. Grebowsky, Y. Tulinay, A.J. Chen. Planet. Space Sci., 1974, 22, 1089.
3. L.H. Brace, E.J. Maier, J.H. Hoffman, J.Whittaker, G.G. Shepherd. J. Geophys. Res., 1974, 79, 5211.
4. K.I. Gringauz. In "Physics of the Magnetosphere". Izdatelstvo "MIR", M. 1972, 413 and 566.
5. C.R. Chappell. J. Geophys. Res., 1974, 79, 1861.
6. A.J. Chen, J.M. Grebowsky. J. Geophys. Res., 1974, 79, 3851.
7. N.C. Maynard, A.J. Chen. J. Geophys. Res., 1975, 80, 1009.
8. L.A. Frank. J. Geophys. Res., 1971, 76, 2265.
9. U.M. Vasiliunas in Solar Terrestrial Physics / 1970 (ed E.R. Dyer), D. Reidel Publ. Co., Dordrecht-Holland, Part III, 1972, 192.
10. L.D. Kavanagh, J.W. Freeman, A.J. Chen. J. Geophys.

- Res., 1968, 73, 5511.
11. S.I. Akasofu. In Solar Terrestrial Physics / 1970 (ed. E.R. Dyer), D. Reidel Publ. Co., Dordrecht-Holland, Part III, 1972, 137.
  12. C.J. Park, D.L. Carpenter. J. Geophys. Res., 1970, 75, 3825.
  13. A.D. Richmond. Radio Sci., 1973, 8, 1019.
  14. M.G. Kivelson, C.T. Russell. Radio Sci., 1973, 8, 1035.
  15. O.M. Raspov. In "Solar-Terrestrial Physics", Izdatelstvo VINITI, M. 1969, 1, 243.
  16. I.V. Kovalevsky. In "Probl. Kosmich. Phys.", 1972, 1, 23.
  17. A. Nishida, E.F. Lyon. J. Geophys. Res., 1972, 77, 4086.
  18. V. Villante. Riv. ital. geofis., 1974, 23, 1-2, 27.
  19. S.I. Akasofu, E.W. Hones, C.I. Meng. J. Geophys. Res., 1970, 75, 7296.
  20. J.M. Grebowsky. J. Geophys. Res., 1970, 75, 4329.
  21. A.J. Chen, R.A. Wolf. Planet. Space Sci., 1972, 20, 483.
  22. R.K. Jagg, R.A. Wolf. J. Geophys. Res., 1973, 78, 2852.
  23. C.S. Ivanov-Kholodny, A.A. Korchak, L.A. Lobachevsky, I.P. Stakhanov and B.M. Chikhachev. Geomagn. and Aeronomiya, 1972, 12, 398.
  24. I.P. Stakhanov. Dokl. AN USSR, 1975, 220, 1310.
  25. I.P. Stakhanov, I.V. Kovalevsky. Geomagn. and Aeronomiya, 1976, 16, 511.
  26. R.S. Badessa, R.L. Kent, J.W. Nowell. Phys. Rev. Letters, 1959, 3, 79.
  27. R.S. Badessa, R.L. Kent, J.W. Nowell, G.L. Searle. Proc. I R E, 1960, 48, 758.

28. I.V. Kovalevsky, T.V. Kuznetsova, V.D. Novikov, I.P. Stakhanov. Geomagn. and Aeronomiya, 1976, 16, 204.
29. K.K. Harris, G.W. Sharp, C.R. Chappell. J. Geophys. Res., 1970, 75, 219.
30. H. Kikuchi, H.A. Taylor. J. Geophys. Res., 1972, 77, 131.
31. D.L. Carpenter, C.R. Chappell. J. Geophys. Res., 1973, 78, 3062.
32. C.R. Chappell, K.K. Harris, G.W. Sharp. J. Geophys. Res., 1970, 75, 3848.
33. C.R. Chappell, K.K. Harris, G.W. Sharp. J. Geophys. Res., 1971, 76, 7632.
34. P. Kartashov, D.A. Burns. In "Time and Frequency", Izdatelstvo "MIR", M. 1973, 29.
35. I.V. Kovalevsky, V.D. Novikov, I.P. Stakhanov. Izvestiya Vys. Uch. zav. - Radiophysica, 1976, (in press).
36. S.E. De Forest. J. Geophys. Res., 1973, 78, 1197.
37. E.W. Hones, A.T.Y. Lui, S.I. Bame, S. Singer. J. Geophys. Res., 1974, 79, 1385.
38. M.P. Aubry. In Earth's Magnetospheric Processes (ed. B.M. McCormac), D. Reidel Publ. Co., Dordrecht-Holland, 1972, 361.

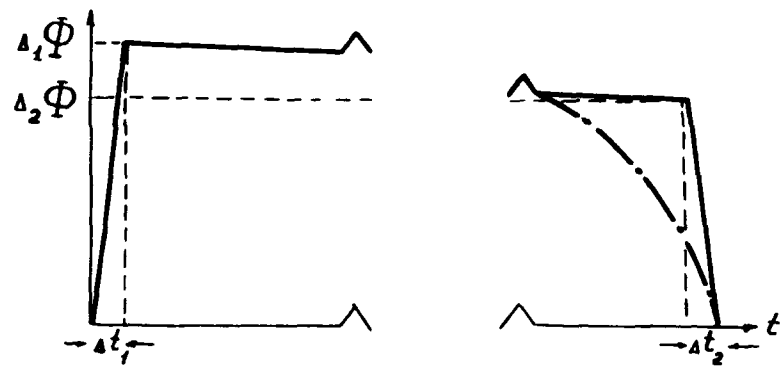


**Fig.1.** Time dependence of the phase shift  $\Delta\Phi$  of a sounding and a response signals crossing an instantaneously shifting plasmapause.

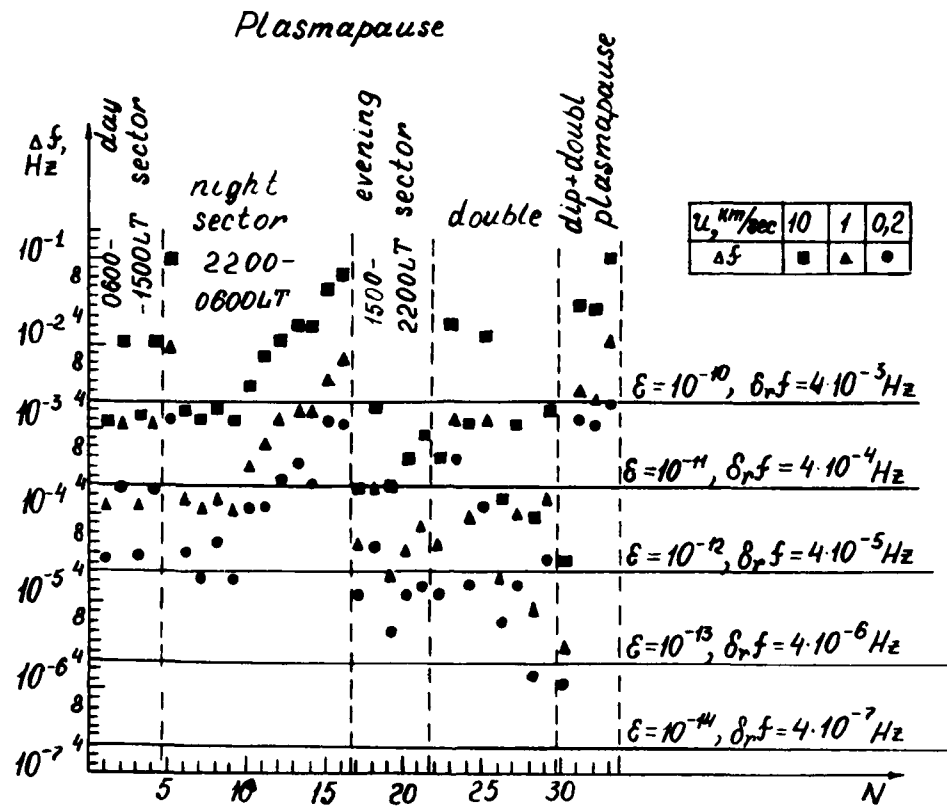


Fig.2. Fast  $\Delta f$  beating frequencies occurring as the plasmapause and the dip sides are moving in radiopath with the velocity  $u$  (with  $f = 40 \text{ MHz}$ ) for the cases ( $N = 33$ ).  $\delta_r f$  - possible frequency drifts the stability of generators being  $\epsilon = 10^{-11} - 10^{-14}$ .

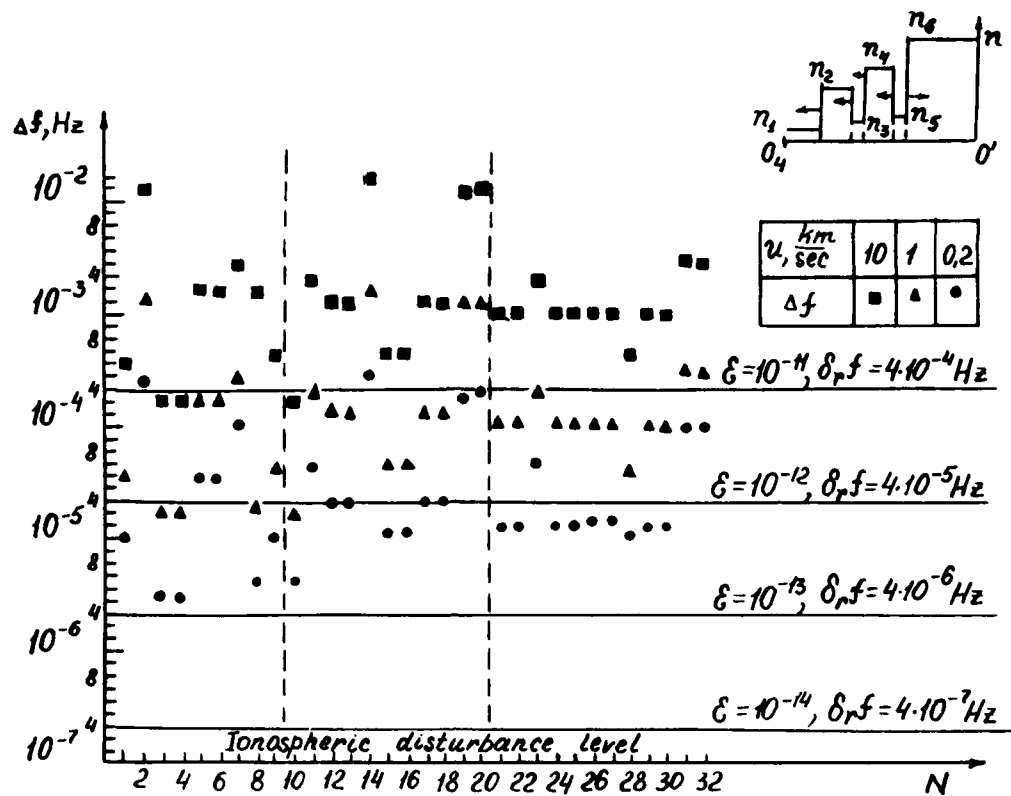


Fig.3. Fast  $\Delta f$  beating frequencies occurring as the detached from the plasmasphere plasma tails (regions) are moving with the velocity  $u$  in radiorack (with  $f = 40$  MHz) for the 32 cases ( $N$ ). Above (to the right) is shown a possible concentration profile at radiopath.

SOME NEW PHENOMENA OBSERVED DURING MAGNETIC STORMS AND SOLAR FLARES AT LOW AND EQUATORIAL LATITUDES USING ATS-6 RADIO BEACON INVESTIGATIONS

by

M.R. Deshpande<sup>1</sup>, R.G. Rastogi<sup>1</sup>, Malkiat Singh<sup>2</sup>, H.S. Gurm<sup>2</sup>,  
A.V. Janve<sup>3</sup>, R.K. Rai<sup>3</sup>, A.R. Jain<sup>4</sup>, B.N. Bhargava<sup>4</sup>, V.M.  
Patwari<sup>5</sup>, and B.S. Subbarao<sup>5</sup>

ABSTRACT

The emphasis in this article is to bring out some new features associated with the magnetic storms and solar flares at low and equatorial latitudes. Three important discoveries need special attention:

(i) Scintillations are triggered during storm time at low latitudes with phase lags at different stations.

(ii) Travelling Ionospheric Disturbances are induced during magnetic storms and their movement direction suggests that the heat input at high latitudes induces equatorial motions.

(iii) Solar flare enhancements exceeding 5% of total electron content are seen. Such large changes cannot be accounted for the enhancement of ionization in D-region during solar flare.

Additional production mechanisms in E, F<sub>1</sub> and F<sub>2</sub> regions are also believed to be contributing to the observed large TEC changes during the flare. The zenith angle effect of solar flares is discussed. The above results are derived from ATS-6 beacon experiments conducted at seven sights in India.

INTRODUCTION

In the past decade, extensive investigations of ionospheric storms (Goodman 1968, Klobuchar et al. 1968, Taylor and Earnshaw 1969, Aarons 1970, Mendillo et al. 1970, Klobuchar et al. 1971, Papagiannis et al. 1971, Mendillo 1973 and Schödel et al. 1974) and solar flares (Matoukas et al. and Mendillo et al. 1974) have been carried out. In most of these investigations, effects of storms on total electron content, stormtime behaviours, and effects of solar flares are discussed.

In this paper some new phenomena associated with storms and flares are given.

EXPERIMENTAL SET UP

Six polarimeters of rotating antenna type at 140 MHz were installed in collaboration with various institutions and universities at Patiala (Geog. Long. 76.3°E, Geog. Lat. 30.3°N, Dip. 45°N), Udaipur (Geog. Long. 73.6°E, Geog. Lat. 24.6°N, Dip. 35°N), Ahmedabad (Geog. Long. 72.6°E, Geog. Lat. 23.0°N, Dip. 34°N), Rajkot (Geog. Long. 70.7°E, Geog. Lat. 22.3°N, Dip. 33.8°N), Bombay (Geog. Long. 72.9°E, Geog. Lat. 19.1°N, Dip. 24.8°N) and Waltair (Geog. Long. 83.3°E, Geog. Lat. 17.7°N, Dip. 19°N).

- 
1. Physical Research Laboratory, Ahmedabad 380 009, India.
  2. Punjabi University, Patiala 147 002, India.
  3. University of Udaipur, Udaipur 313 001, India.
  4. Indian Institute of Geomagnetism, Bombay, 400 005, India.
  5. A.V. Parekh Technical Institute, Rajkot 360 001, India.

In addition, a X,Y type polarimeter and scintillation recorder have been set up at Jaipur (Geog.Long. $75.8^{\circ}$ E, Geog.Lat. $26.9^{\circ}$ N, Dip. $39^{\circ}$ N). At Ootacamund (Geog.Long. $76.7^{\circ}$ E, Geog.Lat. $11.4^{\circ}$ N, Dip.  $4^{\circ}$ N), in collaboration with NOAA Laboratories, a complete ATS-6 receiving set up has been established to study the equatorial scintillations, total electron content, differential faraday rotation, etc. All these experiments are planned so as to have complete coverage of Indian sub-continent along more or less same longitude. The locations of these stations are shown in a companion paper.

#### EFFECT OF SOLAR FLARE

For investigating solar flare effects, 5 December 1975 has been selected. In Fig. 1 are shown Faraday rotation records for Patiala, Udaipur, Ahmedabad, Rajkot, Bombay and Ootacamund. The flare started at 1317 hr IST and ended at 1411 hr IST. At all these places the effect of flare can be seen. To investigate the zenith angle dependence of flare enhancements of total electron content,  $\Delta N/M$  are plotted against  $\cos \chi$  in Fig.2. A linear fit on log scale is found with n value as 1.25. Mendillo et al. (1974) carried out 7 August 1972 flare analysis for 17 stations in North America, Europe and Africa and found no correlation of zenith angle dependence of flare time enhancement. It should be noted that most of the stations were above  $30^{\circ}$  latitude. In our investigations all stations are below  $30^{\circ}$  latitude and conclude that solar flare effects do show zenith angle dependence. The latitudinal variation of  $\Delta N/M$  during flare is shown in Fig.3. It is seen that the flare time enhancement decreases with increase of latitude. The flare time enhancements are of the order of 5% of total electron content. Such large enhancements cannot be accounted from the increase in electron density in D region during flare. Additional production mechanisms are to be invoked at higher altitudes to explain the observed results.

#### EFFECT OF STORMS AND TRAVELLING IONOSPHERIC DISTURBANCES

During magnetic storms, the ionosphere also gets perturbed and some new effects seen over Indian sub-continent are presented. As an example, the magnetic storm of 10-11 January 1976 is discussed. The sudden commencement was seen at 1534 hr IST. Following night severe scintillations were seen (Fig.4) at all stations except Patiala, the northern most station. The scintillations were quite severe and lasted about 2 hrs at all stations. The onset times of scintillations were however different (see Table 1).

Table 1

Station	Geog.Lat.	Onset Time of Scintillation
Bombay	$19.1^{\circ}$ N	2130 hr - 0100 hr IST. (next day)
Rajkot	$22.3^{\circ}$ N	2210 hr - 1000 hr IST. (next day)
Ahmedabad	$23.0^{\circ}$ N	2140 hr - 2343 hr IST

Station	Geog.Lat.	Onset Time of Scintillation
Udaipur	24.6°N	2243 hr - 0100 hr IST. (next day)
Patiala	30.3°N	Not seen
Ooty (Ootacamund)	11.4°N	2116 hr - 0130 hr IST. (next day)

It is therefore suggested that irregularities causing scintillations drift during storm. In addition, a group of Traveling Ionospheric Disturbances (TID's) are seen at Udaipur, Ahmedabad, Rajkot and Bombay. Again at Patiala this effect is not seen. The mean TID velocity is 230 m/sec and its direction and propagation are almost eastward. TID's with such high velocities are not seen during quiet nights. Hence it is concluded that during the initial phase of the storm severe scintillations and high velocity TID's are seen from the equator up to 30°N. Such a phenomenon has not been observed earlier. The scintillation zone is shown in Fig. 5 for the first night (2200-0100 hr IST) following sudden commencement of storm. In addition, TID velocity vector is also shown. On the following pre sunrise time, scintillations were again seen (Fig.6) as localized patches. The scintillation zone this time appears to be shifted northward up to Patiala. On the next day (Fig.7), 11 January 1976, at 1300-1400 IST the scintillations were again seen. It is to be noted that on quiet days during daytime, scintillation is a very rare phenomenon. Again the scintillation zone seems to have moved northward and no scintillation is seen near the equator. From Figures 5 and 7 it is clear that during the storm an elliptical belt of scintillation zone is seen near the equator. As the storm progresses the belt shows a tendency to move northward.

#### CONCLUSIONS

(1) Flare enhancements of total electron content shows zenith angle dependence at low and equatorial latitudes. Such a dependence was not found at mid and high latitudes (Mendillo et al. 1974).

(2) The  $\cos^n \chi$  fit of flare time enhancement in total electron content has yielded  $n = 1.25$ .

(3) During magnetic storm scintillations are seen in the low and equatorial latitudes. These scintillations with time appear and disappear and are not seen continuously for more than 3 hours at a time. The onset of scintillation at different places is different and suggests that the irregularities causing scintillation move over, and the direction of their motion is eastward.

(4) The scintillation patches during the early part of the storm extend right up to equator; on the subsequent day they tend to move northward.

(5) The scintillation zones are of elliptical in shape.

(6) TID's are seen during storm with very high velocities.

These characteristics we believe are due to perturbations introduced in the ionosphere during magnetic storms.

REFERENCES

- Aarons J., 1970, Rad. Sci., 5, 959-966.
- Goodman J.M., 1968, Planet. Space Sci., 16, 951-952.
- Klobuchar, J.A., Aarons J. and Hosseineigh H.H., 1968, J. Geophys. Res., 73, 7530-7534.
- Klobuchar J.A., Mendillo M., Smith III F.L. Fritz R.B., da Rosa A.V., Davis M.J., Yuen P.C., Roclofs T.H. Yeh K.C. and Flaherty B.J., 1971, J. Geophys. Res., 76, 6202-6207.
- Matsoukas D.A., Papagiannis M.D., Aarons J. and Klobuchar J.A., 1972, J. Atmos. Terr. Phys., 34, 1275-1283.
- Mendillo M., Papagiannis M.D. and Klobuchar J.A., 1970, Rad. Sci., 5, 895-898.
- Mendillo M., 1973, Planet. Space Sci., 21, 349-358.
- Mendillo M., Klobuchar J.A., Fritz, R.B., da Rosa A.V., Kersley L., Yeh K.C., Flaherty B.J., Rangaswamy S., Schmid P.E., Evans J.V., Schodel J.P., Matsoukas D.A., Koster J.R., Webster A.R. and Chin P., 1974, J. Geophys Res., 79, 665-671.
- Papagiannis M.D., Mendillo M. and Klobuchar J.A., 1971, Planet. Space Sci., 19, 503-511.
- Schödel J.P., da Rosa A.V., Mendillo M., Klobuchar J.A., Roclofs T.H., Fritz R.H., Essex E.A., Flaherty B.J., Yeh K.C., Hibberd F.H., Kersley L., Koster J.R., Liszka L. and Nakata Y., 1974, J. Atmos. Terr. Phys., 36, 1121-1134.
- Taylor G.N. and Earnshaw R.D.S., 1969, J. Atmos. Terr. Phys., 31, 211-216.

ATS-6-140 MHz FARADAY RECORDS  
5 DEC. 1975 FLARE

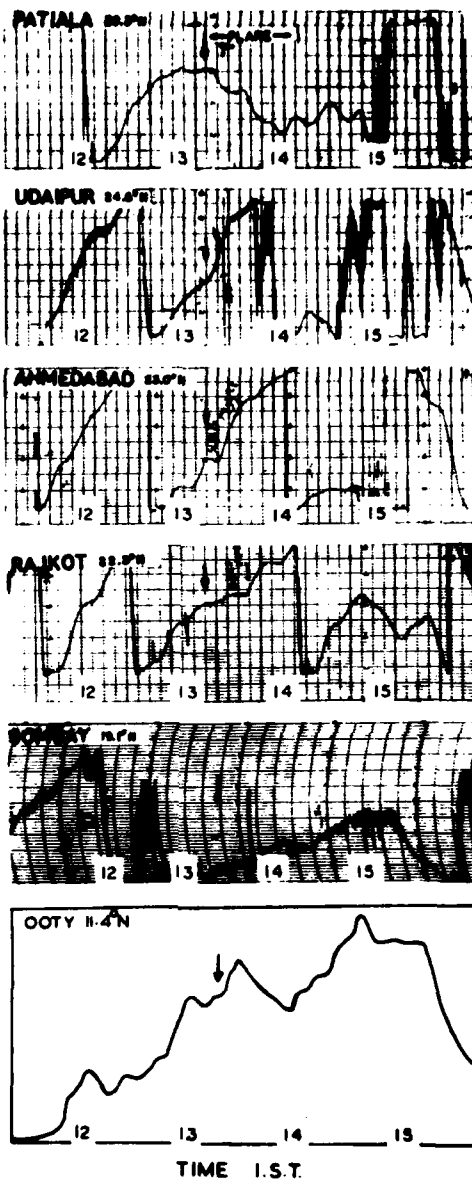


Figure 1 : Faraday records showing the effect of solar flare on 5 December 1975 at Ooty, Bombay, Rajkot, Ahmedabad, Udaipur and Patiala.

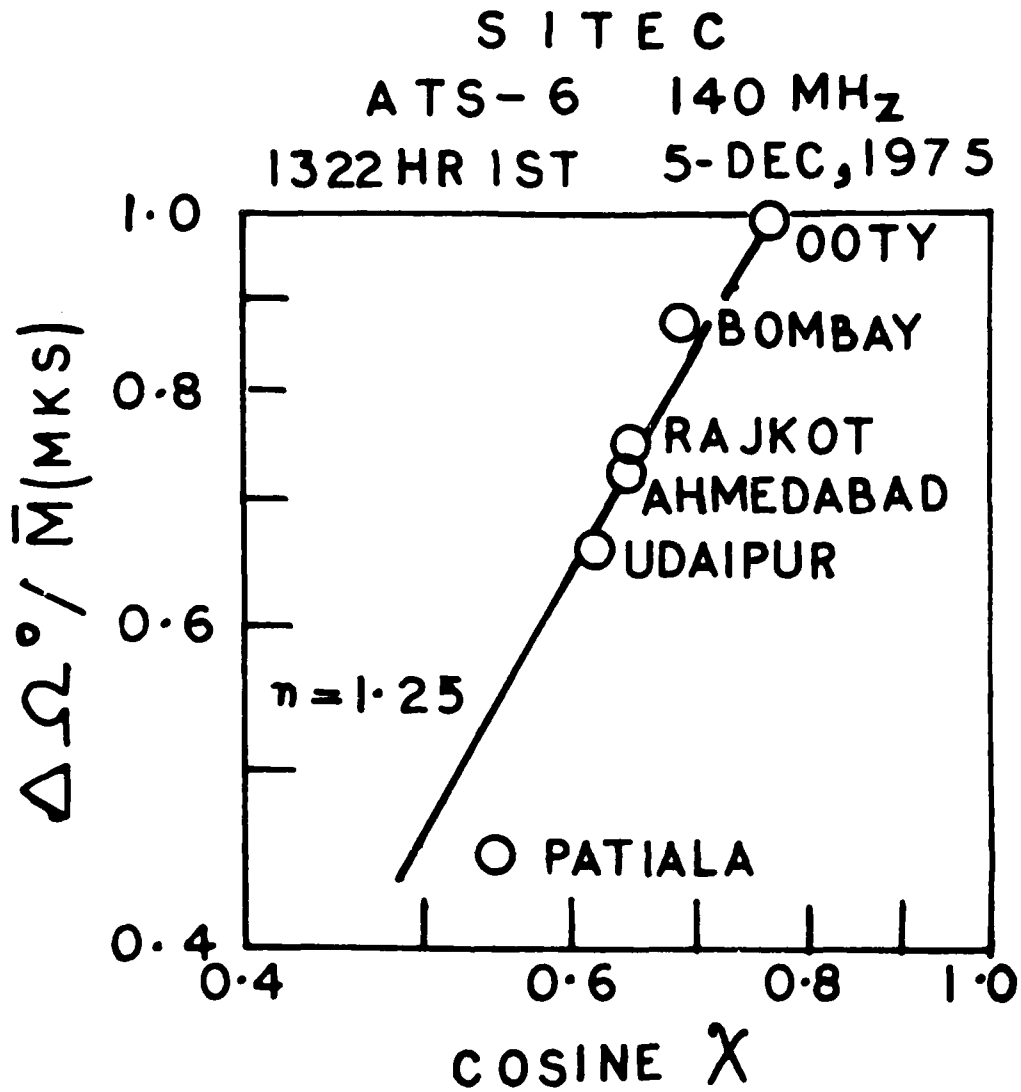


Figure 2 :  $\cos \chi$  variation of flare enhancements in  $\Delta\Omega^\circ / \bar{M}$  at Patiala, Udaipur, Ahmedabad, Rajkot, Bombay and Ooty for 5 December 1975 solar flare.

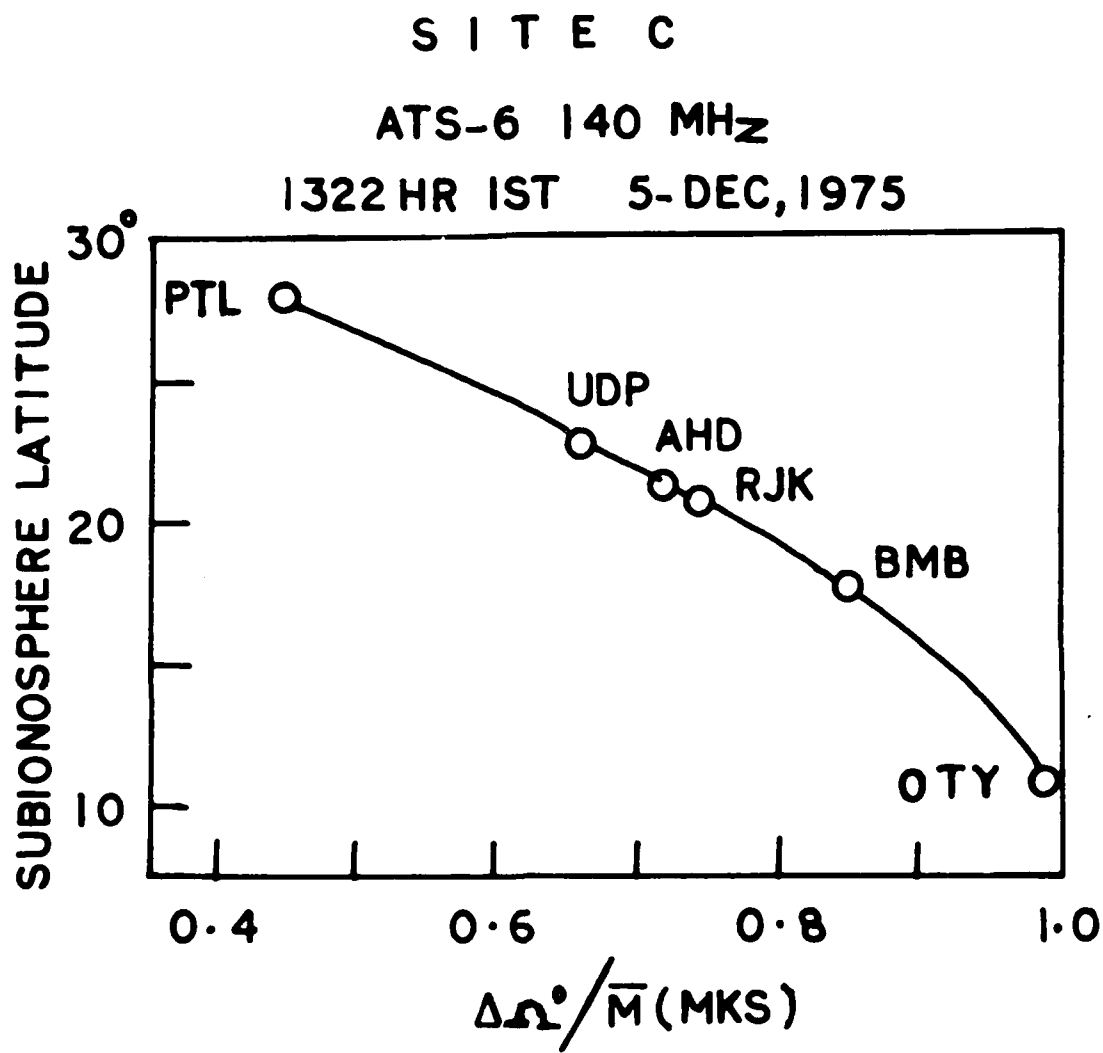


Figure 3 : Variation of flare enhancements in  $\Delta\bar{\Omega}/\bar{M}$  with sub-ionospheric geographic latitudes of Ooty, Bombay, Hajkot, Ahmedabad, Udaipur and Patiala for 5 December 1975 solar flare.

ATS-6 140 MHz FARADAY ROTATION  
SCINTILLATION TRIGGERED BY STORM  
10-11 JAN. 1976

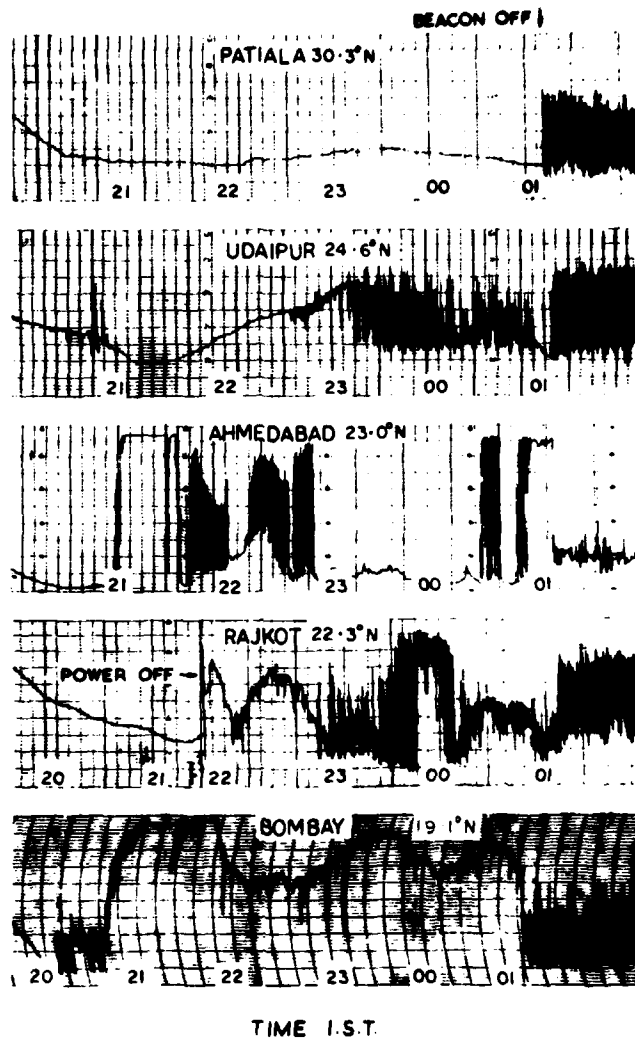


Figure 4 : Faraday records showing scintillations and TIDs triggered by magnetic storm at Udaipur, Ahmedabad, Rajkot and Bombay on the night of 10-11 January 1976. Note the absence of scintillation and TIDs at Patiala.

ATS 6 140 MHz  
STORM TRIGGERED SCINTILLATION ZONE  
10-11 JAN 1976 2200-0100 IST

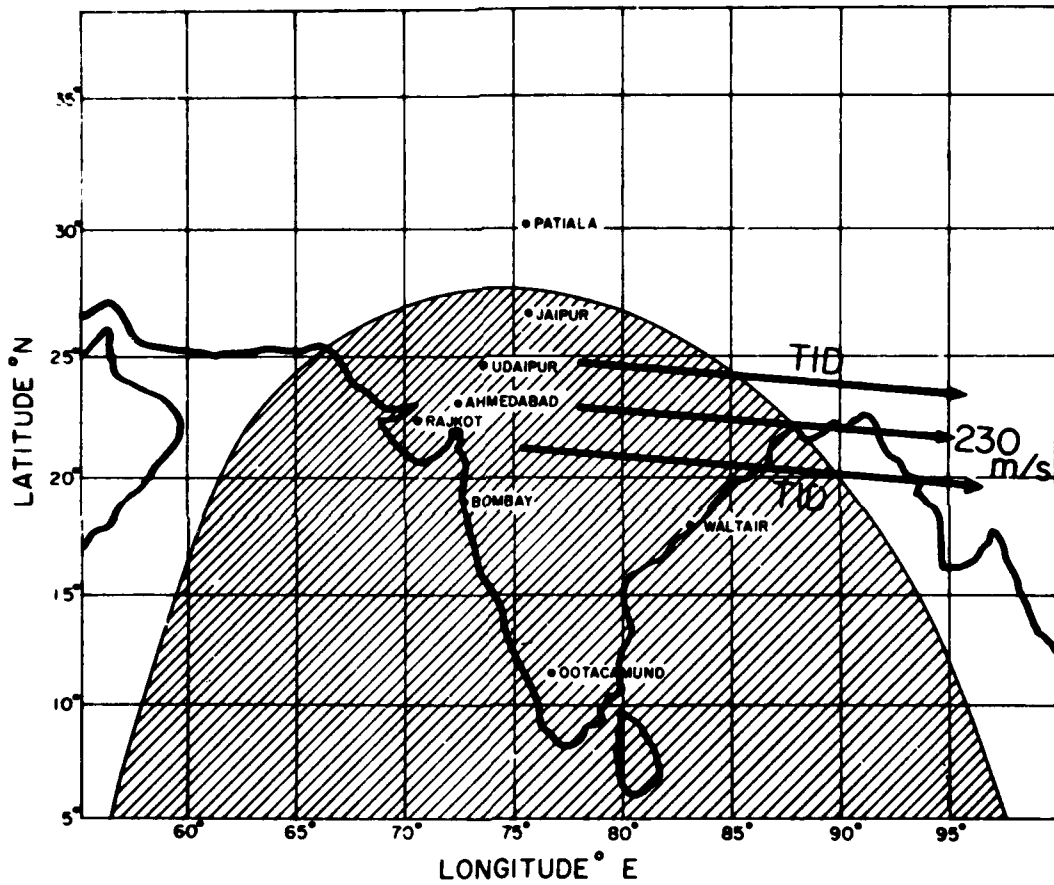


Figure 5 : Map showing storm triggered scintillation zone and TID velocity vector on the night following sudden commencement (10-11 January, 1976).

ATS-6 140 MHz  
STORM TIME SCINTILLATION ZONE  
11 JAN 1976 0630-0830 IST

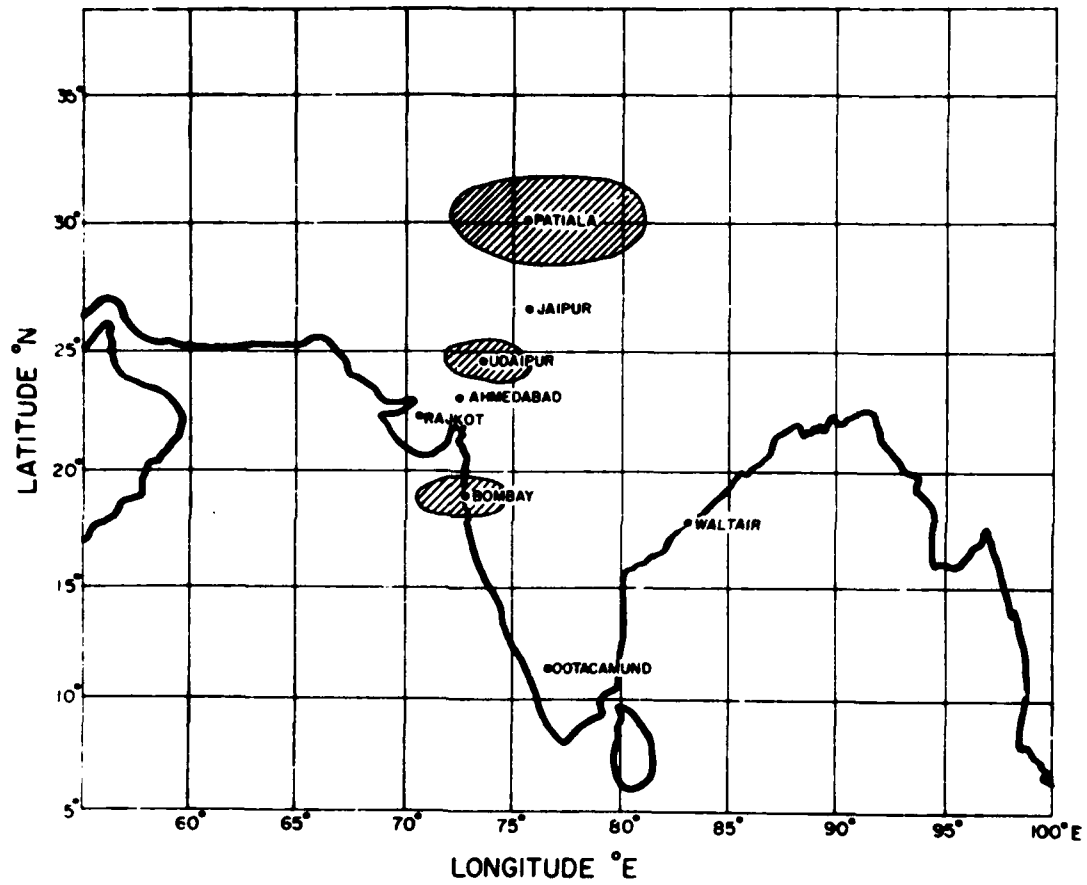


Figure 6 : Map showing storm time scintillation zones at Patiala, Udaipur and Bombay in the following morning of sudden commencement (11 January 1976). Note that at equator no scintillation effect is seen.

ATS-6 140 MHZ  
STROM TIME SCINTILLATION ZONE  
11 JAN 1976 1300-1400 IST

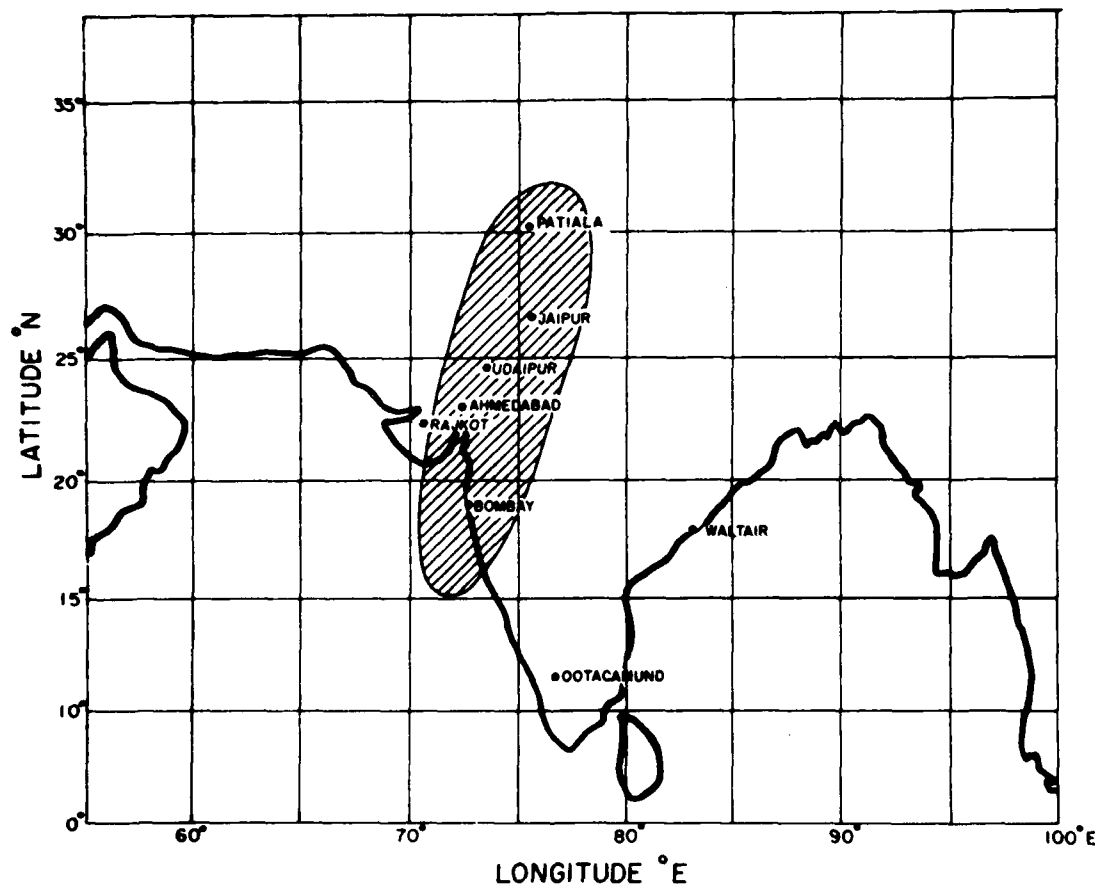


Figure 7 : Map showing storm time scintillation zone at Patiala, Udaipur, Ahmedabad and Bombay on the afternoon hours of 11 January 1976.

THE INTERDEPENDENCE OF SCINTILLATION INDEX,  
TOTAL ELECTRON CONTENT AND MAGNETIC ACTIVITY  
AT AN EQUATORIAL STATION

J.R. Koster  
Physics Dept.  
University of Ghana  
P.O.Box 63  
Legon, Accra  
Ghana

ABSTRACT

The total columnar electron content (TEC) and the scintillation index (SI) determined at Legon, Ghana, exhibit a negative correlation between sunset and midnight; a positive correlation around sunrise. This relationship can be explained in terms of the dependence of these two parameters on magnetic activity. It is shown that the total electron content is increased at all hours during magnetic disturbances, while scintillation is suppressed before midnight, somewhat enhanced around dawn. Both phenomena exhibit a 9 to 10 hour time lag behind magnetic activity. All the phenomena have a pronounced seasonal minimum around the June solstice. It is suggested that the reduction of ionospheric electric fields can account most easily for all the observed dependencies. These fields are probably due to neutral winds.

## THE INTERDEPENDENCE OF SCINTILLATION INDEX, TOTAL ELECTRON CONTENT AND MAGNETIC ACTIVITY AT AN EQUATORIAL STATION

### 1. INTRODUCTION

Since September 1971 recordings have been made at Legon, Ghana (Longitude 0.19°W, latitude 5.63°N, dip angle 8°S) of both the scintillation and the Faraday rotation experienced by the 136.47 MHz signal radiated by the synchronous satellite ATS-3. During this period of time the satellite has been kept on station at approximately 70°W longitude. Hence these records can be compared without the usual uncertainty due to the variation of the Scintillation index and other parameters with elevation. All the comparisons made below are based on continuous data, extending from September 1971 to October 1975 inclusive, a period of 50 months.

### 2. SCINTILLATION INDEX AND TOTAL ELECTRON CONTENT

Scintillation at Legon is quantified using the definition of scintillation index (SI) adopted by the Joint Satellite Studies Group (Aarons et. al. 1971). The relationship between this index and the total electron content (TEC) of the ionosphere was first studied. Hourly values of the two parameters SI and TEC were divided into 50 one month segments, and each segment analyzed separately. Twenty four hourly correlation coefficients were produced for each segment.

A plot of correlation coefficient versus hour of day appears in Figure 1A. This figure represents the mean of 34 of the monthly segments, the four months around the June solstice (May, June, July and August) being omitted for reasons given below. Figure 2A shows the seasonal variation of the dependence of scintillation on total electron content. The correlation coefficients between SI and TEC for the periods 04-07 hours, and 20-23 hours local time are averaged separately for each month of the year. Both curves show a predominantly annual variation, with the effect virtually disappearing around the June solstice. Because the correlation coefficients fall near or below the 1% significance level during this period, these months were omitted in the determination of Figure 1A. It may be mentioned here that this same pattern of minimum correlation around the June solstice is found in the interrelationship of all three parameters considered in this paper.

#### 2.1. SUMMARY OF THE RESULTS OF THE COMPARISON

The following conclusions can be drawn from Figures 1A and 2A:

- (a) There is a significant positive correlation between SI and TEC from 04 to 08 hours local time.
- (b) There is a significant negative correlation between them from 20 to 01 hours local time.

- (c) There is no significant correlation between the two parameters from 09 to 19 hours (scintillation is rare during these hours) and during the hours of crossover from negative to positive correlation (02 to 03 hours).
- (d) There is a marked seasonal effect, correlation amplitudes showing a deep minimum around the June solstice. It is to be noted that the 1% significance levels appear as dotted lines in the figures.

## 2.2. SOME SPECULATIONS ABOUT THE INTERPRETATION OF THESE RESULTS

A significant correlation between two variables indicates some connection between them, but not necessarily a causal relationship. They may well be related to one another through some third variable. This consideration gives rise to the following speculation:

- (a) Consider the sunset to midnight period. It is fairly well established, at least at Legon, that during this time:

- i. magnetic activity is accompanied by an increase in TEC.
- ii. magnetic activity is accompanied by a decrease in SI.

Hence, it could well be that magnetic activity accounts for all, or at least some, of the negative correlation found between SI and TEC during this part of the day.

- (b) Consider the period centred on sunrise. If it can be shown that:

- i. magnetic activity is accompanied by an increase in TEC during this daily period as well, and
- ii. that scintillation increases with magnetic activity during these hours, then,

we could explain the early morning positive correlation by a dependence on magnetic activity as well.

In support of (ii) we can mention that we have previously reported from Legon that scintillation around the time of sunrise seems to be more probable during magnetic storms. Mullen and Whitney (1974) have found that there is a definite increase in scintillation with magnetic storms at these hours during some seasons at Huancayo. If we consider the night as a whole, as we have previously done at Legon, the negative correlation of SI with KP dominates the results, since it is much the larger of the two effects.

## 2.3. INVESTIGATIONS SUGGESTED BY THESE RESULTS

The above speculation strongly suggests that it would be profitable to investigate the dependence of SI and TEC separately on magnetic activity. This will give some basis for accepting or rejecting the possibilities given in (2.2) above.

### 3. TOTAL ELECTRON CONTENT AND MAGNETIC ACTIVITY

We next give the results of a study of the variation of total electron content with magnetic activity. We here use the planetary K figure  $K_p$  as an index of magnetic activity, and for the sake of convenience we shall refer to it as KP. The TEC data were again divided into 50 one-month segments, and hourly values were correlated with the corresponding values of KP. Thirty four of the segments (again omitting the four June solstice months) were averaged for the final plot of correlation coefficient versus hour as shown in Figure 1B. The dotted curve in 1B shows the enhanced correlation values that are found when the KP values lead the TEC values in time by nine hours. This time shift is discussed more fully below in section 5. The seasonal variation appears in Figure 2B.

#### 3.1. SUMMARY OF THE RESULTS OF THE COMPARISON

The following conclusions can be drawn from Figures 1B and 2B:

- (a) There is a positive correlation between KP and TEC for all hours.
- (b) The value of the correlation coefficient is above the 1% significance level at all times.
- (c) The correlation is much larger still when one uses KP values which lead the TEC values by 9 hours.
- (d) There is a seasonal minimum in the correlation around the June solstice. The value for May is especially low. This is the only month in which the value of the correlation coefficient falls below the 1% significance level.

#### 3.2. SOME POSSIBLE INTERPRETATIONS

This result is consistent with the negative correlation found in the comparison of SI and TEC from sunset to midnight. If the TEC value increases during storms, as we show here, and if SI decreases, as has been shown by Koster (1972), we should expect the result that we actually find in the SITEC curve.

Whether we can explain the 04 to 08 H results of SITEC is not as yet clear. We have a definite rise in TEC with KP at these hours. We shall have to investigate the early morning behaviour of SI and KP before we can draw any conclusions.

### 4. SCINTILLATION AND MAGNETIC ACTIVITY

The relationship between SI and KP has been studied before (Koster, 1972) but never with so much data available, and with the satellite at constant elevation, so that one cause of uncertainty is removed. Also, all the scintillation records used here have been reduced by the same person, using the same method throughout. As was done above, the data were divided into 50

one-month segments, and correlation coefficients were found for each hour in each segment. Figure 1C shows the hourly correlation coefficients resulting from thirty four segments (the months of May, June, July and August were again omitted). The relationship is precisely what earlier results have led us to expect. The correlation coefficients are negative from sunset to midnight; positive around sunrise. But the amplitude of the correlation coefficients is rather small. After other results (to be described later) indicated that a time lag probably occurs between magnetic disturbances and perturbations in SI or TEC, correlation coefficients were computed afresh introducing a nine-hour time delay. The results are plotted as the dotted curve in Figure 1C. Correlation coefficients are now very much larger.

The seasonal effect is given in Figure 2C. Since the SIKP curve shows a positive correlation in the morning at 6 and 7 hours local time, and a negative correlation in the evening from 21 hours to 02 hours, the seasonal variation of the correlation is shown separately for these two time intervals. The evening hours show the usual June minimum; the morning hours have, in addition, a second minimum in January.

#### 4.1. SUMMARY OF THE COMPARISON OF SI AND KP

- (a) There is a significant positive correlation from 05 hours to 08 hours local time.
- (b) There is a significant negative correlation from 20 H to 02 H.
- (c) Correlation is not significant during most of the day (from 09 H to 19 H). Since daytime scintillation is comparatively rare, this is not surprising. Correlation is also not significant during the hours of change from negative to positive correlation (03 H and 04 H).
- (d) The correlation coefficients are somewhat smaller than those found in SITEC and KPTEC, but they increase substantially when a 9 hour time lead is introduced in the KP values, as is shown in the dotted curve in Figure 1C.
- (e) The evening hours (20 H to 02 H) show the usual June solstice minimum; the morning hours (07 H and 08 H) show a January minimum as well.

#### 4.2. DISCUSSION OF THE SIKP RESULTS

These results are quite consistent with the SITEC and KPTEC investigations, and suggest that the increase in TEC during magnetic storms may account for the SITEC results. The picture that emerges seems quite consistent:

- (a) Magnetic disturbances result in increased TEC at Legon at all hours (See the KPTEC curve).

- (b) This increased TEC is accompanied by the suppression of scintillation from sunset to midnight (see the SIKP curve). Hence a negative correlation between SI and TEC is to be expected, and is in fact found, at this time.
- (c) The increased TEC is accompanied by a somewhat enhanced scintillation around sunrise (see the SIKP curve). Hence we expect, and indeed find, a positive correlation between SI and TEC around dawn.
- (d) All the above dependences are reduced significantly around the time of the June solstice.

If, as seems to be the case, magnetic activity appears to be the common factor relating scintillation and total electron content, it would be worth while investigating the dependence of both TEC and SI on magnetic activity more closely. And the first question worth asking would seem to be the following: 'Do increases in TEC and the variations in SI follow the variations in the KP index immediately, or is there a discernible time lag between them?' The dotted curves in Figures 1B and 1C give our answer, but this answer will now be investigated more fully.

##### 5. THE TIME LAG FOR MAXIMUM CORRELATION BETWEEN KP AND TEC

The procedure followed in this part of the investigation was the following:

- (a) First get the correlation coefficient between TEC and KP using simultaneous values of the two parameters.
- (b) Shift KP in time relative to TEC, and repeat. Current values of TEC were correlated with values of KP taken L hours ago, where L is referred to as the LAG of TEC in time behind KP. In the computer program used, LAG assumed values from -9 to 33 hours. For each value of LAG, the usual 24 correlation coefficients were evaluated.
- (c) For all values of the correlation coefficient above the 1% significance level, the time shift (LAG) giving maximum correlation was noted. Since the correlation between KP and TEC is always positive, the mean of the 24 hourly values of the correlation coefficient was used.
- (d) The above process was gone through for each two-month segment of the 50 months of data on hand.

Results found for each of the 25 two-month segments are summarized in Table 1 below.

TABLE 1

MONTH YEARS	J-F	M-A	M-J	J-A	S-O	N-D
1971					.35(07)	.43(04)
1972	.31(06)	.18(07)	.10( )	.05( )	.16(14)	.47(16)
1973	.32(10)	.24(10)	.00( )	.29(14)	.37(11)	.20(04)
1974	.32(11)	.14(11)	-.07( )	.22(09)	.29(04)	.29(10)
1975	.35(11)	.46(15)	.31(12)	.01( )	.29(05)	

TABLE 1: The first figure in each entry is the maximum correlation coefficient between KP and TEC for the two-month period in question. The figure in parentheses is the time lag in hours giving maximum correlation. No time lag is given in cases where the correlation coefficient is below the 1% significance level (0.12).

The following points should be noticed in these results:

- (a) The 1% significance level for these data is 0.12.
- (b) One of the four entries for the months of May-June reaches this value.
- (c) Two of the four entries for July-August are significant on this level.
- (d) All other entries are significant.
- (e) Maximum values of the correlation coefficient occur in November-December.
- (f) The mean time lag for maximum correlation in the case of the 20 significant entries is 9.6 hours, with a standard deviation of 3.7 hours.

The above table shows that the correlation coefficient between KP and TEC is enhanced if a time lag is introduced. To give a better indication of the magnitude of the enhancement, curves KPTEC (Figure 1B) and SIKP (Figure 1C) were re-calculated introducing a nine-hour time lag. The results appear as the dotted curves in the two figures. It is obvious that the enhancement is far from trivial.

It was explained above that correlation coefficients were calculated on a monthly basis; these were then combined to give the result over the total period of 50 months. This was initially done for practical reasons, so that the seasonal variations could be studied using the same results. Later, when all the data were stored on a computer disk it became possible to determine the correlation coefficients over a period of any length. When calculations are made on a yearly basis, the 24 hourly correlation coefficients give a similar picture each year. And the curves for the total period of 50 months do not differ significantly from those given above.

The above experimental results suggest the following simplified picture:

- (a) Energy of solar origin is injected into the magnetosphere during magnetic storms.
- (b) Most of this energy would seem to be deposited initially in the auroral zones.
- (c) Effects are produced at the equator after an average time lag of the order of 9 to 10 hours. Principal among these are an increase in the value of TEC, and a delay in the production of the irregularities in the F region which give rise to scintillation effects.

Magnetic storms are apparently very complex phenomena, and quite a number of physical processes are operative during them. It is our aim here to try to identify that process or those processes which can most simply account for the TEC increase, the scintillation evening decrease and dawn enhancement, and the time lag.

#### POSSIBLE PHYSICAL MECHANISMS

##### (a) A Temperature Increase

It is well known that magnetic disturbances are accompanied by an increase in exospheric temperature. Such temperature changes may well contribute to an enhancement of the electron content of the ionosphere. This would be consistent with the seasonal variation in TEC, where low exospheric temperatures at the June solstice coincide with the annual minimum in ionospheric electron content. But it is not immediately evident why this is so. The effective loss coefficient  $\beta$  is indeed dependent on temperature. Some published results (Rishbeth and Garriot, 1969) suggest that  $\beta$  increases with temperature. If this alone were operative, a temperature increase would be accompanied by a decrease in TEC. Beer (1974) suggests that a temperature increase would indeed give an increase in TEC. Even if we accept his result, it is difficult to see how an increase in temperature could bring about a delay in the onset of scintillation. Scintillation indices tend to be maximum during seasons of maximum exospheric temperature. We summarize as follows:

- i. There is a temperature increase during magnetic storms;
- ii. This increase might account for an increase in TEC, but it is not clear how this might be effected, and
- iii. A temperature increase alone can hardly explain the evening suppression of scintillation, or the morning enhancement.

##### (b) Composition changes in the neutral atmosphere.

A change in the composition of the upper atmosphere, especially a change in the O/N<sub>2</sub> ratio, could result in a dramatic change in TEC.

Duncan (1969) discussed this in some detail, and more recently Titheridge (1974) has considered it. Rishbeth (1975) has summarized current thinking about the atmospheric circulation following the injection of energy into the polar regions during magnetic storms and its effect on atmospheric composition. Such composition changes are currently believed to account for the dramatic decrease in electron content observed at middle latitude stations during the later phases of magnetic storms. We note that these decreases are not observed at Legon. An attempt to detect composition changes in the atmosphere over Legon through the determination of the initial zenith angle (Koster, 1976) yielded negative results.

(c) Quasi Trapped Particles

It is not inconceivable that particles trapped in the inner Van Allen belt at low heights over the equator may make a contribution to an enhanced TEC during magnetic storms. Goldberg (1974) gives some experimental evidence for the presence of a quasi trapped distribution of soft energetic particles at low equatorial heights, with flux densities approaching auroral levels. It is difficult to account for the presence of such particles in terms of present day models of magnetic storms, but the experimental evidence is such that we would not ignore the possibility. Even if this could, however, account for an increase in TEC, there is no obvious connection between the injection of such particles and the suppression of scintillation in the evening; its enhancement in the morning.

(d)  $E \times B$  Forces

Another mechanism which is operative at the equator under normal conditions, and which is perturbed during magnetic storms, is the following.

Daytime eastward equatorial electric fields give rise to an  $E \times B$  force on charged particles, causing them to rise. This upward motion, combined with diffusion along magnetic field lines, gives rise to the so called "fountain effect" through which a considerable amount of ionization can be removed from the equator to low latitudes on either side. At night an oppositely directed (i.e. westward) electric field gives rise to a downward  $E \times B$  force which probably contributes significantly to the observed downward movement of equatorial F region ionization after sunset. This ionization moves to heights where recombination is rapid, and is quickly removed. If these electric fields should disappear, or be reduced during magnetic storms, it could lead to a large daytime increase in TEC over the equator due to the cessation of the fountain effect. Similarly, a reduction in the night-time downward velocity of ionization could contribute to the maintenance of a relatively high electron content throughout the night.

It is well known (Farley et al, 1970) that equatorial irregularity production is closely associated with the rather dramatic increase in upward ionization velocity around the time of ground sunset. Unless the base of the layer rises above a certain minimum level, irregularity production is inhibited. The disappearance or diminution of the usual daytime eastward electric field during magnetic disturbances would produce the observed

suppression of evening scintillation. As for the morning enhancement of scintillation, one might note that the morning TEC is frequently so small that no scintillation is possible. The suppression of the usual westward field at night would reduce the downward drift of ionization. Hence the electron content would remain relatively high throughout the night, and the possibility of morning scintillation would be enhanced.

It seems likely that the production of the above mentioned electric field is associated with winds in the neutral atmosphere. Energy injected into the auroral regions would eventually, after a suitable delay, give rise to winds at low latitudes. This, in turn, could reduce the electric fields present near the equator under normal conditions.

We may summarize our proposed "simple" mechanisms as follows:

- (a) Energy is injected into the auroral regions. This sets up a circulation (wind) that affects equatorial latitudes some hours later, resulting in a reduction of the E-W electric fields normally present.
- (b) Suppression of the fountain effect enhances equatorial electron content during the day; and the diminution of the downward velocity at night keeps the content abnormally high during the night.
- (c) Inhibition of the evening rise inhibits evening scintillation; the morning high electron content favours scintillation around sunrise.
- (d) The injection of additional energy into the summer hemisphere causes relatively small changes there; hence the effects are less pronounced during local summer.

ACKNOWLEDGEMENT: This work was carried out under Research Grant AFOSR 74-2828, Air Force Cambridge Research Laboratories, United States Air Force.

#### REFERENCES

AARONS, J. et al	1971	Proc. IEEE <u>59</u> , 159
BEER, T.	1974	Atmospheric Waves Adams Hilger, London p. 254.
DUNCAN, R.A.	1969	J. Atmos. terr. Phys. <u>31</u> , 59
FARLEY, D.T. et al	1970	J. geophys. res. <u>75</u> , 7199
KOSTER, J.R.	1972	Planet. Space Sci. <u>20</u> , 1999
KOSTER, J.R.	1976	J. geophys. res. (in the press)
RISHBETH, H & CARRIOT, O.K.	1969	Introduction to Ionospheric Physics Academic Press, New York & London p. 172ff.
GOLDBERG, R.A.	1974	J. Geophys Res. <u>79</u> , 5299
RISHBETH, H.	1975	J. Atmos. terr. Phys. <u>37</u> , 1055
TITTERIDGE, J.E.	1974	J. Atmos. terr. Phys. <u>36</u> , 1249

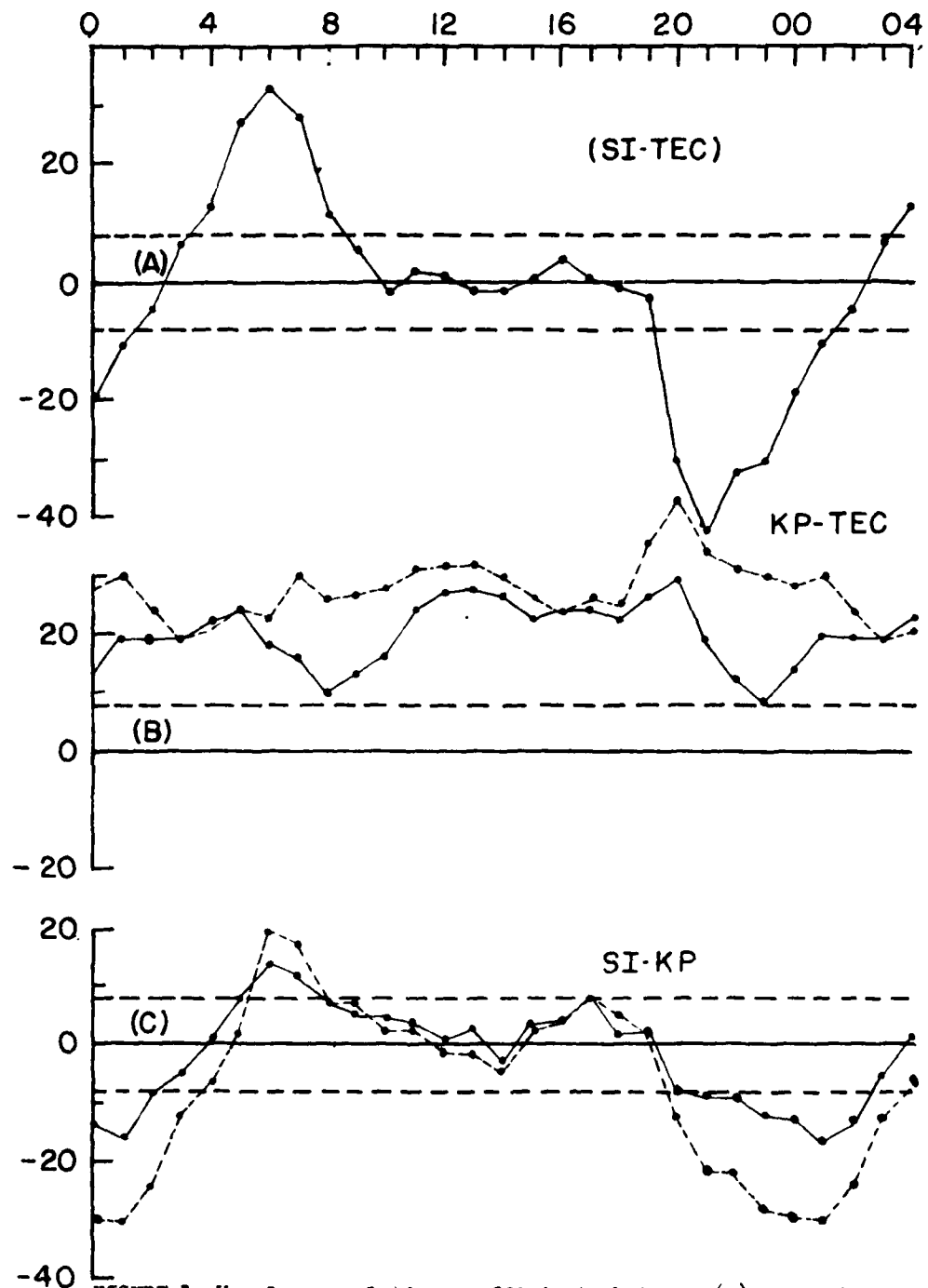


FIGURE 1 Hourly correlation coefficients between (A) scintillation index and total electron content, (B) total electron content and magnetic activity, and (C) magnetic activity and scintillation index. The horizontal dashed line shows the 1% significance level. The dashed curve in (B) and (C) has KP leading by nine hours.

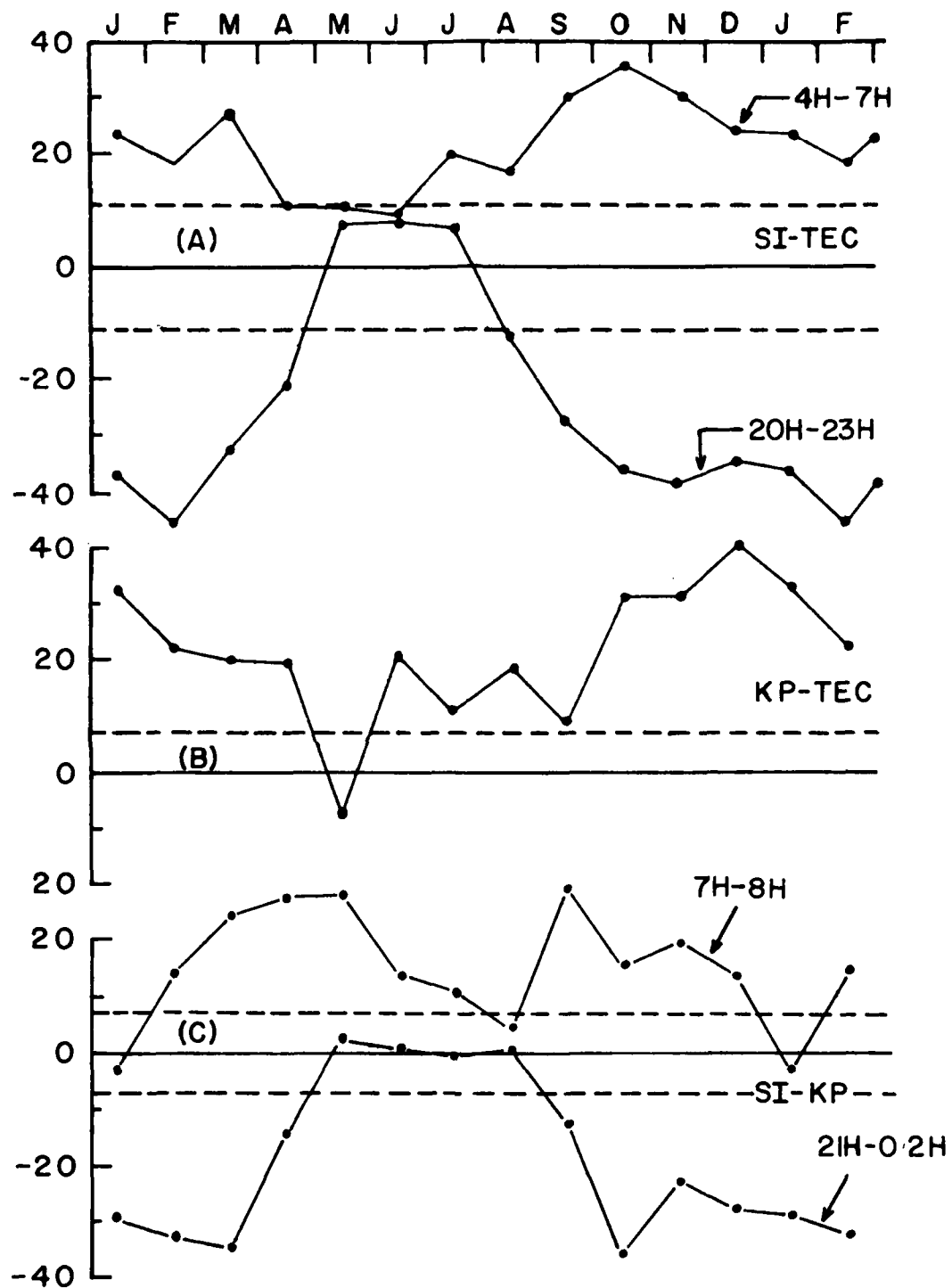


FIGURE 2 The seasonal variation of the correlation coefficients between scintillation index (SI), total electron content (TEC) and magnetic activity (KP).

SCINTILLATION THEORY AND ITS RELATION TO  
SATELLITE BEACON TRANSMISSIONS

A. W. Wernik\*, C. H. Liu\*\*, and K. C. Yeh\*\*

\*Institute of Geophysics, Polish Academy of Sciences,  
ul. Pasteura 3, 00-973 Warsaw. P.O. Box 155, Poland

\*\*Department of Electrical Engineering, University of  
Illinois at Urbana-Champaign, Urbana, Illinois 61801

Abstract

The recent advances in the scintillation theory are reviewed. Different approaches are compared and discussed. Parabolic equation method and resulting equations for the field moments give a unified theory of weak and strong scintillation. Results of the theory are reviewed. It is also shown that the single scattering theory can be easily improved by taking into account the extinction. Shortcomings of the scintillation theory as related to the interpretation of beacon signal observations are pointed out.

## 1. Introduction

The scintillation study on random fluctuations of wave parameters passing through the ionosphere has 30 years of history. During that time the problem has been investigated both experimentally and theoretically (for reviews refer to: Aarons et al., [1971], Aarons [1975], Wernik and Liu [1975]). It is now understood that the scintillation is a consequence of existence of random electron density fluctuations in the ionosphere. The main goal of the scintillation theory is to relate the observed wave statistics to the properties of the irregular ionosphere.

Three main physical processes cause scintillation: scattering, diffraction or phase mixing, and extinction. All three processes have to be considered jointly, although their relative importance may vary depending on the wave length, irregularity scale-size, irregular slab thickness, observers distance from the slab etc.

Ionospheric irregularities responsible for scintillation are large compared to the wave-length and the dielectric permittivity does not differ much from unity. Waves scattered by such irregularities maintain the state of polarization and the scattering process leads practically only to the change of wave phase. The direction of propagation of scattered wave is very close to the direction of incident wave. For the observer very close to the thin irregular slab the diffraction is of no importance and the scintillation can be considered in the frame of geometrical optics.

In reality the diffraction can not be ignored both inside the irregularity slab and outside it. For the thick slab the diffraction leads to the wave leaving the slab which is not only phase but also amplitude fluctuating. The diffraction causes increase of the intensity scintillation when the distance between observer and the slab increases. Far from the slab, in the far zone, the intensity scintillation saturates.

The extinction is closely related to scattering and causes attenuation of the wave. The extinction is usually ignored when weak scintillation is considered. This leads to the non-conservation of energy in the weak scattering theories.

## 2. Scintillation theories

The geometry of the problem is shown in Fig. 1. A plane wave is assumed to be incident on the irregularity slab at  $z = 0$ . The thickness of the slab is  $l$ . The receiver is on the ground at  $(0, 0, z)$ . The presence of the irregularities causes irregular variations of the refractive index in the slab. As the wave passes through the slab, these irregular variations act to distort the original plane wavefront, giving rise to a randomly phase-

and amplitude-modulated wave. After the wave emerges from the bottom of the slab at  $z = l$ , it propagates in a regular medium (often taken as the free space) toward the receiver. During this passage, further phase-mixing occurs changing the modulation of the wave and eventually producing a complicated diffraction pattern on the ground. In general, the irregularities are assumed to be "frozen" during the passage of the wave and drift across the propagation path with constant speed. This causes the diffraction pattern on the ground to drift and at the receiver it appears as a temporal pattern. Under the assumptions of "frozen in" and ergodicity, the temporal variations can be used to obtain the various statistics of the signal.

To study the scintillation problem we begin by formulating the problem of wave propagation in random media. Let us assume that the irregularity slab can be characterized by a relative dielectric permittivity  $\epsilon(r, t)$  which is a random function of position and time. The spatial and temporal variations of  $\epsilon(r, t)$  are assumed to be slowly varying as compared to the wavelength and period of the wave respectively. For the case where the drift velocity of the irregularities is small compared with the velocity of light and the characteristic size of the irregularity is much larger than the wavelength the above formulated problem reduces to the solution of the Helmholtz wave equation

$$\nabla^2 u + k^2 \epsilon u = 0 \quad (1)$$

where  $u$  is a component of the electric field. It must be noted that in considering the scalar wave equation the depolarization effect is neglected.

Equation (1) is a partial differential equation with stochastic coefficient. At present no exact method of solving this equation exists. We are forced to make various simplifying assumptions. It is believed that in the real ionosphere these assumptions are valid under certain conditions.

The wave equation (1) is linear in terms of the wave function but nonlinear in terms of the fluctuating coefficient  $\epsilon$ . If the fluctuating part  $\epsilon_1$  of the dielectric permittivity is much less than its mean value  $\langle \epsilon \rangle$  equation (1) can be linearized by expanding the wave function  $u$  in terms of a series in ascending powers of the small parameter  $\epsilon_1/\langle \epsilon \rangle$ . Such linearization leads to the well known Born approximation, which takes into account only waves which are scattered once. The application of the Born approximation is limited to weak scintillation.

If instead of the complex amplitude, the complex phase of wave is expanded the smooth perturbation or Rytov approximation can be obtained.

In the Born approximation the statistics of wave amplitude and phase is obtained, while the Rytov approximation leads to the logarithmic amplitude and phase statistics. Approximate solution of the stochastic wave equation at the bottom of irregularity slab can be used as the initial condition for the free space wave equation. Its solution gives the complex amplitude or phase at any point below the irregularity slab. Correlation functions, scintillation spectra and scintillation index can be obtained by averaging procedure. Statistics of scintillation is then expressed in terms of the irregularity spectrum and some filter function depending on the geometry and wave-length.

Figure 2 shows the amplitude filter functions computed from the Rytov approximation for two values of wave number  $k = 2\pi/\lambda$  together with the two types of irregularity spectra corresponding to exponential and Gaussian correlation functions. Due to the decaying character of the irregularity spectrum and oscillatory behavior of the filter function the main contribution to the amplitude scintillation comes from that part of irregularity spectrum which corresponds to the first maximum of the filter function.

The phase filter function has a first maximum at  $\kappa = 0$  which means that the phase scintillation is sensitive to the large scale irregularities. In the weak scattering regime the spatial scintillation spectrum is just the product of the filter function and irregularity spectrum. The motion of the irregularities causes the diffraction pattern to drift and if irregularities are "frozen in" the spatial spectrum can be easily converted to the frequency scintillation spectrum.

The Fourier transform of the spatial scintillation spectrum gives the correlation function of the diffraction pattern which can be measured on the ground by an array of receivers.

A very useful and simple model of scintillation is obtained when the scattering slab is replaced by a thin screen which changes only the wave phase in the same manner as the scattering slab. Usually it is assumed that inside the slab the geometrical optics approximation is valid which allows the computation of the phase variance and phase correlation function at the screen. Below the screen the wave propagates in the free space with the phase mixing being the only process leading to the development of amplitude scintillation. If the screen is placed at the middle of irregularity slab the phase screen model leads to the result in agreement with the weak scattering scintillation theory.

The weak scintillation theory is well developed although some questions remain concerning the validity range of different approximations.

Theoretical studies of strong scintillation are much more difficult and incomplete. Different approaches have been used

(Mercier [1962], Uscinski [1968a, 1968b], Tatarski [1971]) but it seems that the most promising is the so called parabolic equation method (PEM) Tatarski [1974]). In this method we seek the solution of the parabolic equations for the wave function moments. Various conditions must be satisfied in order to apply the PEM. (Tatarski [1971]) Discussion of these conditions show that the PEM can be used for the ionospheric scintillation. Depending on the parameters chosen the PEM allows us to study scintillation for a wide range of conditions, in the weak and strong scattering regimes.

For a plane incident wave the equations for the first and second moment of the field can be solved exactly. However, most interesting is the fourth moment which gives the intensity correlation function and scintillation index directly related to the measured quantities. The fourth moment equation can be solved only numerically. Because of various simplifications the solution gives only semiquantitative results. For instance, only normal incidence on a plane-parallel, homogeneous irregularity slab with isotropic irregularities have been considered. In spite of this, this solution explains the observed scintillation frequency dependence over broad range of frequencies and allows us to discuss multiple scattering effects, such as focusing, saturation and reduction of the scintillation correlation distance for low frequencies.

As an example, Fig. 3 shows the scintillation correlation distance dependence on frequency (Yeh et al., [1975]). For high frequencies, for which we may expect that the weak scattering takes place, the correlation distance increases with decreasing frequency because of the Fresnel filtering. For frequencies less than about 500 MHz, multiple scattering plays an important role and the correlation distance decreases with decreasing frequency. For thicker slab, when the multiple scattering is more important, the correlation distance at low frequencies is smaller.

The weak scattering results can be improved by taking the extinction into account (Wernik [1976]). The so called single scattering approximation of the radiative transfer theory (Tatarski [1971]) includes the extinction effects exactly, while the scattering is included only approximately. The improvement of the results for the scintillation index  $S_4$  can be seen from Fig. 4. In this figure  $S_4$  dependence on the wave parameter  $kr_o^2/z$  is compared for the scintillation index computed using the Rytov approximation, fourth moment equation and single scattering approximation of the radiative transfer theory.

Despite the extensive computations made for the effects of multiple scattering, the results are not a general theory. More study is needed to develop a comprehensive scintillation theory that can be applied to all situations in the ionosphere.

### 3. Application of scintillation theory for data interpretation

The scintillation theory relates the measured quantities, such as the scintillation index, frequency or spatial scintillation spectra, correlation distance for the diffraction pattern over the ground etc. to the properties of the irregular ionosphere. The inverse problem of the theory is to find the irregularity parameters: scale-size, elongation, spectrum, irregular slab thickness and height from the measured scintillation statistics. Results of the inverse problem solution may be in error if the validity of the theoretical simplifications is not carefully checked before applied to a particular situation. For example, when weak scattering scintillation theory is applied, only such data can be interpreted which were taken under the validity of weak scattering assumption. There is no unique criterion which can be used to check whether the weak scattering assumption is valid. The often used criterion requiring that for weak scattering the amplitude (or intensity) scintillation is weak may be misleading because the weak scattering may lead to stronger amplitude scintillation than strong scattering depending on the irregularity slab thickness and observer's distance from the slab. The phase measurements are not going to help to solve the problem, because the phase variance measured on the ground is not the same as variance at the bottom of the irregularity slab, which is a measure of scattering strength.

From the point of view of the theory of irregularity generation and evolution it is of interest to know the shape of the irregularity spectrum and its sizes. Formally, some information about these parameters can be gained from the scintillation data analysis. For instance, the correlation distance for the diffraction pattern measured on the ground can be related to the correlation distance of the electron density fluctuations. However, this is not a direct relationship and some parameters, like slab thickness and observer's distance from the slab, must be assumed or known from other independent measurements.

In the past few years extensive studies have been made on irregularity spectrum. The method is based on a close correspondence between the power spectrum of scintillation and irregularity spectrum. In applying the theory to interpret the data, however, again certain assumptions were made. First of all, the "frozen in" assumption assumes that the diffraction pattern drifts over the ground with constant velocity. For data taken with synchronous beacon satellites the analyzed sample must be long enough to gain required accuracy of spectral analysis. However, it can not be too long to avoid possible velocity changes. The problem of choice of appropriate sample length is not so serious for transit satellites.

The weak amplitude scintillation power spectra agree quite well with those theoretically predicted (Fig. 5) and indicate the irregularity spectrum of the power-law type is in agreement with the in-situ measurements of electron density fluctuations.

Strong scintillation spectra have not been investigated theoretically due to the lack of adequate theory. The single scattering approximation of radiative transfer theory give, however, some indication of spectrum broadening and smearing under conditions of moderately strong scintillation (Wernik [1976]). Similar results have been obtained using the phase screen approximation (Rumsey [1975], Marians [1975]). It is worthwhile to mention that strong scintillation intensity and log-amplitude spectra differ in shape. More studies on strong scintillation spectra are desirable.

The important parameters are the height and thickness of the irregular slab. The common observational method is the spaced receiver technique. In the paper by Paul et al. [1970] a critical discussion of the method is given. It was pointed out that the method is applicable only when the irregular slab is thin. For observations based on the low-orbiting beacon satellites the main contribution to the scintillation comes from those irregularities which are at a half-way distance between the satellite and the ground (Yeh [1962]). This will lead to a greater irregularity height for higher satellites. On the other hand, it was also shown (Liu [1967]) that if the background electron density has a peak the main contribution to observed scintillation comes from irregularities at the peak height. All this makes it very difficult to determine the true height and thickness of the irregular slab.

Singleton [1970] using the scintillation data and phase screen approximation was able to estimate the electron density fluctuations. Essentially Singleton has used a plot of contours of the constant scintillation index on the plane  $2z\lambda/\pi r^2 - \phi_0$  (a phase variance on the screen) and with some assumed values of  $z$  and  $r$  determined  $\phi_0$  from which, with the reasonable guess about the slab thickness, electron density variance was obtained. With simultaneous multi-frequency scintillation observations it is possible to avoid some of the assumptions and get better values of the electron density fluctuations.

#### 4. Discussion

In spite of the great advances both in the theory and data interpretation further studies of the scintillation phenomenon are needed. Below we wish to point out some of the outstanding problems and suggestions for the future work.

Strong scintillation theory needs further development. The phase scintillation, scintillation spectra, geometry effects have not been considered in detail.

Verification of the "frozen in" assumption is needed, especially for the case of geostationary satellite beacon signals scintillation. The problem of the probability distributions of amplitude and phase scintillation is still uncertain. Opinions differ in whether the

joint Gaussian distribution of the phase and amplitude, or of phase and log-amplitude, or of in-phase and quadrature components of the signal fits best the observed probability distributions (Rino et al. [1976], Fremouw et al. [1976], Crane [1976]).

The in-situ measurements and scintillation spectra show the upper scale size of ionospheric irregularities is probably around few tens of kilometers rather than less than 1 km as was believed in the past. With such big upper scale size the phase scintillation should be expected to be very strong indicating multiple scattering conditions. At the same time the observed amplitude scintillation is often rather weak and in agreement with the weak scintillation theory. The question then arises: is the condition of small phase fluctuations the necessary condition for applying the weak scintillation theory to interpret amplitude scintillation data? A closer look at the problem is needed to answer this question.

Global models of ionospheric scintillation based on the in-situ electron density data and scintillation theory should be further developed.

Scintillation phenomenon depends in a complicated manner on many parameters which usually are not known in advance. More complete and complex scintillation measurements, simultaneously performed with other irregularity measurements, may help to verify the scintillation theory and at the same time to get more information on the irregular ionospheric structure.

#### References

- Aarons, J., H. E. Whitney and R. S. Allen, Proc. IEEE, 59, 159, (1971)  
Aarons, J., Proc. COSPAR Symp. on the Beacon Satellite Investigation of the Ionospheric Structure and ATS-6 Data, IZMIRAN, Moscow, 184 (1975)  
Crane, R. K., J. Geophys. Res., 81, 2041 (1976)  
Fremouw, E. J., C. L. Rino and R. C. Livingston, Proc. COSPAR and URSI Symp. on the Geophysical Use of Satellite Beacon Observations, 1 - 4 June 1976, Boston, (this volume)  
Liu, C. H., Radio Sci., 2, 961 (1967)  
Marians, M., Radio Sci., 10, 115 (1975)  
Mercier, R. R., Proc. Camb. Phil. Soc., 58, 382 (1962)  
Paul, L. M., K. C. Yeh and B. J. Flaherty, Radio Sci., 5, 967 (1970)  
Rino, C. L., R. C. Livingston and H. E. Whitney, J. Geophys. Res., 81, 2051 (1976)  
Rumsey, V. H., Radio Sci., 10, 107 (1975)  
Singleton, D. G., J. Atmos. Terr. Phys., 32, 187 (1970)  
Tatarski, V. I., "The Effects of the Turbulent Atmosphere on Wave Propagation", U. S. Dept. Commerce, National Technical Information Service, Springfield, VA (1971)

- Uscinski, B. J., Phil. Trans. Roy. Soc. London A., 262, 609 (1968a)  
 Uscinski, B. J., Proc. Roy. Soc. London A., 307, 471 (1968b)  
 Wernik, A. W. and C. H. Liu, Artificial Satellites ed. Committee  
     on Research and Peaceful Uses of Outer Space, Polish Ac.  
     Sci., 10, 37 (1975)  
 Wernik, A. W., Publ. Inst. Geophys. Polish Ac. Sci., E-1(100),  
     43 (1976)  
 Yeh, K. C., J. Res. NBS, 66D, 621 (1962)  
 Yeh, K. C., C. H. Liu and M. Y. Youakim, Radio Sci., 10, 97  
     (1975)

#### Figure Captions

- Fig. 1. Geometry of the scintillation problem.  
 Fig. 2. Amplitude filter function multiplied by the factor  
 $\pi L/(4k)^{-2}$  for waves of frequency 40 MHz ( $k = .84 \text{ m}^{-1}$ )  
     and 4 GHz ( $k = 84 \text{ m}^{-1}$ ) and irregularity spectra for  
     the Gaussian and exponential correlation functions  
     with different scale sizes  $r_o$ .  
 Fig. 3. Correlation distance for the amplitude scintillation  
     as a function of frequency.  
 Fig. 4. Scintillation index  $S_4$  vs. wave parameter  $D_z = (z-L)/kr_o^2$ .  
     Broken curve-Rytov approximation, solid curve-single  
     scattering approximation of the radiative transfer  
     theory, dashed curve-multiple scattering theory. Numbers  
     by the curves =  $L/kr_o^2$ .  $C = \langle \epsilon^2 \rangle k^3 r_o^3 / 4$ .  
 Fig. 5. Comparison of the experimental and theoretical, weak  
     scattering spectra.

#### Acknowledgment

The work of CHL and KYC was partially supported by a grant ATM-75-21755 from the Atmospheric Sciences Section, National Science Foundation.

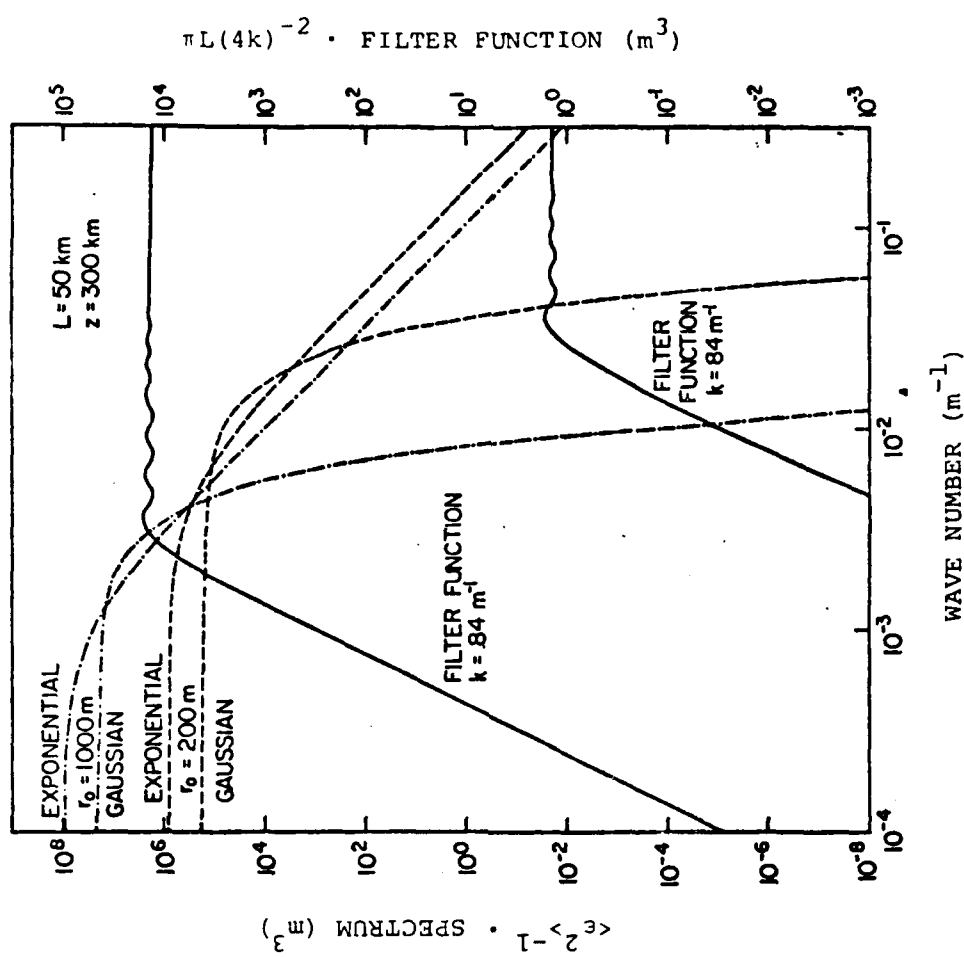


Figure 2

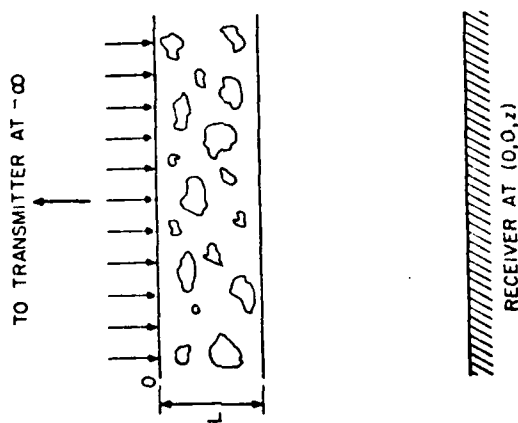


Figure 1

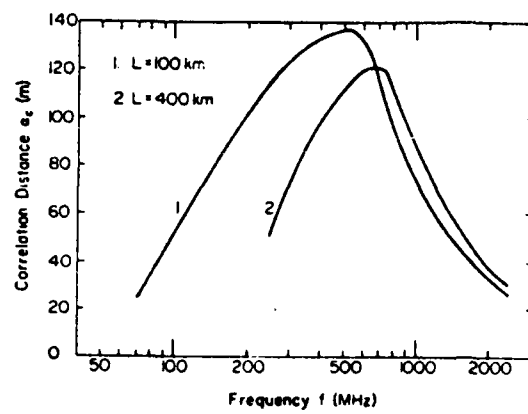


Figure 3

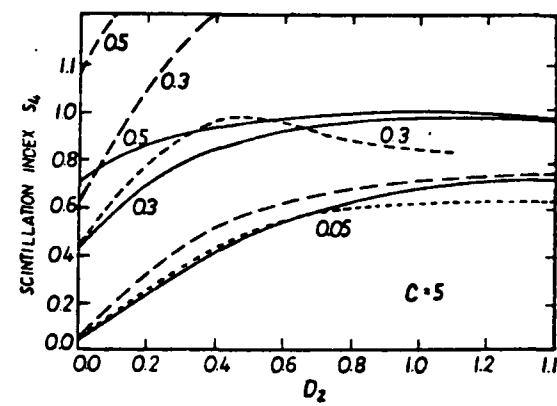


Figure 4

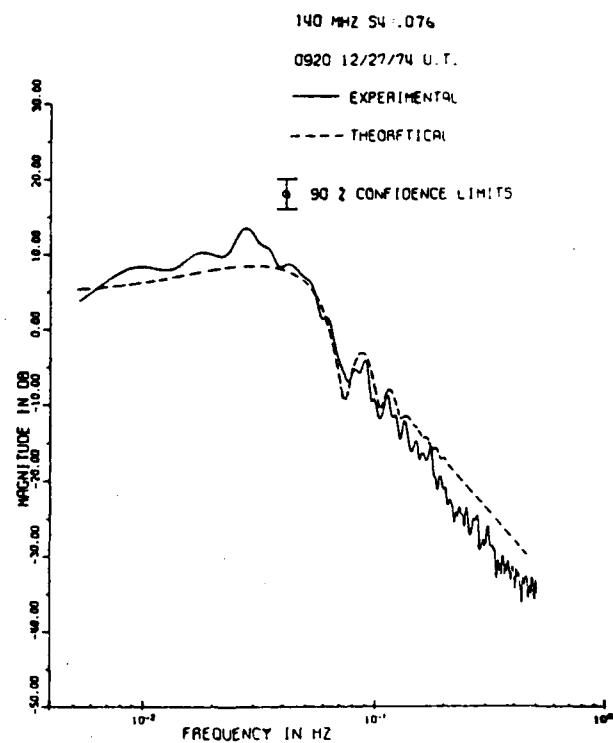


Figure 5

IONOSPHERIC SCINTILLATIONS AT  
MULTIPLE FREQUENCIES

R. Umeki, C. H. Liu and K. C. Yeh

Department of Electrical Engineering  
University of Illinois  
Urbana, Illinois 61801

Abstract

In the study of scintillation of transitionospheric radio signals, the frequency dependence of the intensity scintillation index  $S_4$  is a subject of both experimental and theoretical interest. It is well known that the dielectric permittivity fluctuation in the ionosphere varies as  $f^{-2}$ , where  $f$  is the signal frequency. Under the conditions of weak scattering, for power law irregularity spectrum of the form  $\kappa^{-p}$ , the scintillation frequency dependence will be  $f^{-n}$  with  $n = (p+2)/4$ . However, when the strength of scintillation increases, multiple scattering becomes important and there is no simple relation for the frequency dependence of  $S_4$ . Simultaneous scintillation data from ATS-6 Beacon Experiments for signals at 40, 140 and 360 MHz offer the opportunity to study the frequency dependence of the scintillation phenomenon. Analysis of some of this data for weak scintillations has shown that the power index  $p$  is about 4, while results for strong scintillations indicate the saturation effects on the scintillation index  $S_4$  and the modifications of the power spectrum caused by multiple scattering. These results plus those obtained from the use of the Bessel spectrum analysis will be presented.

## 1. Introduction

When a radio wave propagates through the ionosphere, the random irregularities present will cause the parameters of the wave to fluctuate. This is what is known as the scintillation phenomenon. Amplitude, phase as well as angle-of-arrival scintillations have been observed at frequencies ranging from 10 MHz to several gigahertz. By studying these fluctuations, we can learn much about the characteristics of the ionosphere (Aarons et al., 1971; Elkins et al., 1969; Rufenach, 1972; Singleton, 1974). Early observations were made mostly of single frequencies. It is well known that the departure of the relative dielectric permittivity from its background value in the ionosphere is inversely proportional to the square of the signal frequency. Therefore, under the condition for which fluctuations occur at higher frequencies, signals at lower frequencies will suffer much more severe scintillations. In fact, at times the scintillation will be so intense that the multiple scattering effects will become important (Yeh et al., 1975). The Radio Beacon Experiments on ATS-6, with the three frequencies at 40, 140 and 360 MHz, provide us with a good opportunity for simultaneous multi-frequency observation of the scintillation phenomenon. In this paper, some results of our analysis of the ATS-6 scintillation data will be presented.

In section 2 the scintillation index  $S_4$  is studied. The emphasis will be on the frequency dependence of  $S_4$  under both weak and strong scintillation conditions. Some theoretical models will be discussed in an effort to interpret the data. The power spectra of the amplitude and intensity of the fluctuating signals will be investigated in section 3. Some conclusions will be discussed in section 4.

## 2. Frequency dependence of scintillation index $S_4$

Linearly polarized signals were transmitted from the ATS-6 satellite ( $0^\circ\text{N}$ ,  $94^\circ\text{W}$ ) at carrier frequencies of about 40, 140 and 360 MHz respectively. The amplitudes, among other parameters of the signals, were received in Boulder, Colorado ( $40.13^\circ\text{N}$ ,  $105.24^\circ\text{W}$ ) by the Space Environmental Laboratory of NOAA using short backfire type antennas (Davies et al., 1975). Elevation angle was  $42.2^\circ$  at an azimuth of  $162.9^\circ$ . The receiver's post detection bandwidth was .16 Hz and the sampling rate was 10 Hz. Each second, ten .1 second samples were taken, averaged together, and the resultant amplitude recorded digitally on magnetic tape via mini computer. The final sampling rate was thus 1 Hz.

After obtaining the tape from NOAA the data was plotted to locate periods of scintillation. We found that this phenomena was most likely to occur between the hours of 2100 and 0300 local time. A number of segments of data which appeared stationary to the eye and were of sufficient time duration (usually 45 min.) were chosen for analysis. Before proceeding further, the data was detrended using a high pass digital filter with a pass band beginning at .005 Hz.

To obtain a measure of the intensity of the fading and its statistics, we computed the scintillation index  $S_4$  which is defined as

$$S_4^2 = \frac{\langle A^4 \rangle - \langle A^2 \rangle^2}{\langle A^2 \rangle^2} \quad (1)$$

where  $A$  is the amplitude of the received signal. We also used this as an added check for stationarity by verifying that  $S_4$  was relatively constant throughout the periods being analyzed. In Table 1 we have tabulated the dates and times for the data sets we used.

TABLE 1

	<u>Date</u>	<u>Time (U.T.)</u>
Set 1	12/27/74	0920
Set 2	05/09/74	0500
Set 3	01/09/75	0700

At this point, we can investigate the frequency dependence of the scintillation index which for small  $S_4$  and power-law irregularity spectrum proportional to  $\kappa^{-p}$  has been found to satisfy the relation

$$\frac{S_{4a}}{S_{4b}} = \left( \frac{f_b}{f_a} \right)^n \quad (2)$$

where  $n = \frac{p+2}{4}$ ,  $\kappa$  is the spatial frequency, and  $f_b$  and  $f_a$  are the transmitting frequencies (Jokipii and Hollweg, 1970). For our data Set 1 in which  $S_4 \leq 0.5$  we have found  $n$  to be about 1.6 corresponding to  $p \approx 4.4$  (see Table 2) which is consistent with

TABLE 2 (Set 1)

<u>S<sub>4a</sub></u>	<u>S<sub>4b</sub></u>	<u>f<sub>a</sub></u>	<u>f<sub>b</sub></u>	<u>n</u>
.54	.076	40	140	1.57
.076	.016	140	360	1.65
.54	.016	40	360	1.6

results observed by others (Rufenach, 1972). In fact, using single-scatter theory, it is possible to model the irregularity layer in the ionosphere that will produce this multi-frequency scintillation data. We assumed a power-law irregularity spectrum of the form

$$\Phi_N(K_x, K_y, 0) = \frac{<(\Delta N/N_o)^2> \eta r_o^3 \Gamma(p/2)}{2\pi \Gamma(3/2) \Gamma(\frac{p-3}{2}) [1 + r_o^2 (K_x^2 + \eta^2 K_y^2)]^{p/2}} \quad (3)$$

where  $<(\Delta N/N_o)^2>$  is the variance of the electron density fluctuation,  $\eta$ , the anisotropy factor;  $r_o$ , the outer scale of the irregularities and  $\Gamma(x)$  is the gamma function.

The geometry of the model is shown in Figure 1. The scintillation index can be computed by the formula (Wernik and Liu, 1974)

$$S_4^2 = \frac{k^2 L}{2} \left( \frac{f_p}{f} \right)^4 \int_0^\infty \left\{ 1 - \frac{2k}{K^2 L} \sin \left( \frac{K^2 L}{2k} \right) \cos \left[ \frac{K^2}{k} (z - \frac{L}{2}) \right] \right\} \Phi_N(K) K dK \quad (4)$$

where  $k = 2\pi f/c$  is the wave number of the signal at frequency  $f$ ,  $f_p$  is the electron plasma frequency for the background ionosphere.

Theoretical computations of  $S_4$  were made for various parameters of the ionosphere. The results of one such model computation with the chosen parameters were shown in Table 3. We note that the results match the experimental data quite well except at 40 MHz. Here we must realize that we are using the single scatter model, and at 40 MHz when  $S_4 \approx 0.5$  some multiple scattering effects are already beginning to show.

For the cases of strong scintillation, multiple scattering effects are important. Theoretical computations (Liu et al., 1974; Yeh et al., 1975) have shown that under multiple-scatter theory it is no longer possible to obtain a constant exponent

TABLE 3

Frequency	Experimental $S_4$	Theoretical $S_4$
40	.54	.59
140	.076	.077
360	.016	.017

$$\text{Parameters : } f_p = 9 \text{ MHz} \quad z = 400 \text{ Km}$$

$$L = 90 \text{ Km} \quad r_o = 9 \text{ Km}$$

$$\frac{\Delta N}{N} = 3.18 \quad \eta = 3$$

n that describes the frequency dependence of the scintillation index  $S_4$  as indicated in equation (2). Rather, the frequency dependence varies as a function of the signal frequency and other parameters of the irregularity slab. In particular, under certain conditions, the scintillation index can be greater than unity. This is referred to as the focussing (Yeh et al., 1975). The focussing occurs at a distance  $z_{foc}$  from the center of a thin irregularity slab where  $z_{foc}$  is given by (Shishov, 1971)

$$z_{foc} \propto k/\phi_o \quad (5)$$

$$\text{where } \phi_o^2 = k^2 (f_p/f)^4 r_o L \langle (\Delta N/N_o)^2 \rangle / 4.$$

We note that  $z_{foc}$  is proportional to  $f^2$ . Therefore, at higher frequencies, for certain ionospheric parameters, the distance  $z$  from the irregularity slab to the ground may be much smaller than the focusing distances for such frequencies. However, for signals with lower frequency the focusing distance is smaller and the same distance  $z$  may be comparable to  $z_{foc}$ . Therefore, at this lower frequency the receiver may be in or near the focusing region.

Our data sets II and III indicate strong scintillation conditions (see Tables 4, 5, and 6). In both sets, we note the presence of the focussing phenomenon at 40 MHz.

TABLE 4 (Set 2)

<u>S<sub>4a</sub></u>	<u>S<sub>4b</sub></u>	<u>f<sub>a</sub></u>	<u>f<sub>b</sub></u>	<u>n</u>
1.31	.23	40	140	1.39
.23	.058	140	360	1.46
1.31	.058	40	360	1.42

TABLE 5

<u>Frequency</u>	<u>Experimental S<sub>4</sub></u>	<u>Theoretical S<sub>4</sub></u>
40	1.31	1.50
140	.23	.23
360	.058	.056

Parameters:  $f_p = 8 \text{ MHz}$        $z = 400 \text{ Km}$   
 $L = 100 \text{ Km}$        $r_o = 8 \text{ Km}$   
 $\frac{\Delta N}{N} = 10\%$        $n = 1$

TABLE 6 (Set 3)

<u>S<sub>4a</sub></u>	<u>S<sub>4b</sub></u>	<u>f<sub>a</sub></u>	<u>f<sub>b</sub></u>	<u>n</u>
1.5	.55	40	140	.8
.55	.12	140	360	1.61
1.5	.12	40	360	1.15

Since at the higher two frequencies, the scintillation level is still low enough, single-scatter modeling based on data at these frequencies can be carried out. Using the parameters obtained for the models, in principle we can then apply equation (5) to check if indeed the computed  $z_{foc}$  for 40 MHz signal is

approximately equal to the assumed distance between the irregularity slab and the receiver. However, due to the difficulties involved in the omission of the inner scale in the assumed irregularity power spectrum, no quantitative computations can be made. Qualitatively, the data and the model do indicate that for the 40 MHz signal, the receiver is in or near the focusing zone.

Another quantity of interest is  $\sigma_x^2$ , the variance of the log-amplitude, which is defined as

$$\sigma_x^2 = \langle x^2 \rangle - \langle x \rangle^2 \quad (6)$$

where  $x = \ln A$ . For weak scattering,  $\sigma_x$  is directly proportional to  $S_4$  and using the Rytov approximation, the same frequency dependence is predicted (Crane, 1976). This behavior is best illustrated by plotting  $\sigma_x$  values obtained at two different frequencies (140 and 360 MHz) as is done in Figure 2. Since all of the scintillation observed at these frequencies was weak, the single scatter model should be valid and a linear relationship should exist between the  $\sigma_x$  at the two frequencies.

Comparing the experimental results and the Rytov solution, we can see that this is indeed the case. However with increased scintillation levels, multiple scatter becomes important and saturation of the fluctuation takes place. We can see this effects in Figure 3, where we plot  $\sigma_x$  at 40 and 140 MHz. Since

most of our data is for either strong or weak scintillation we cannot see too much about what is happening between the two extremes. However, Rytov solution seems to agree well with the data up to  $\sigma_x \approx 5$  db or so. Then, the saturation occurs.

### 3. Power spectra of scintillation:

In recent years, the use of the power spectrum of temporal amplitude fluctuations to study the ionospheric irregularities has gained recognition. To compute our spectra we first calculated autocorrelations for 200 lags. In the case of the Fourier spectra, the Hanning window was then applied to the auto-correlation function and the product Fast Fourier Transformed (Blackman and Tukey, 1958).

Bessel spectra were computed using a prewhitened Bessel transform of the autocorrelation function ( $A(\tau)$ ) given as (Lovelace et al., 1970)

$$f_B(f) = - \left( \frac{1}{2\pi} \right)^2 \int_0^\infty \tau J_1(2\pi f\tau) \frac{dA(\tau)}{d\tau} d\tau . \quad (7)$$

The differentiated autocorrelation function was multiplied by a Gaussian lag window ( $\exp(-\gamma(\tau/\tau_m))$ ) with  $\gamma=4$  to suppress sidelobs of the frequency response. The expression was then integrated using Simpson's rule. Before plotting, the pre-whitening was removed by dividing each frequency component by its frequency.

The stability of the spectra is found by establishing the number of degrees of freedom as follows:

$$\text{Fourier: } k = 2.5 (T/\tau_m)$$

$$\text{Bessel: } k = 2 (T/\tau_m) (\gamma/f\tau_m)$$

where  $T$  is the duration of the data and  $\tau_m$  is the number of logs. Frequency resolution (full width  $e^{-1}$ ) for the Fourier and Bessel spectra are respectively  $1/\tau_m$  and  $\gamma^{(1/2)}/\tau_m$  (Lovelace et al., 1970).

The computed Fourier spectra for case I (weak scintillation) are shown in Figures 4, 5, 6. The drop-off rate at high frequency is proportional to  $f^{-3.5}$ . This is consistent with spectra observed by others (Elkins et al., 1969; Rufenach, 1972). The theory predicts a drop off of  $f^{-(P-1)}$  for power law irregularity spectrum and it is gratifying to note that the  $P$  obtained here corresponds quite well with that obtained from the frequency dependence of  $S_4$ . The 360 MHz curve starts to fall at the proper rate, but then the slope gradually decreases. Since  $S_4$  for this case is only .016, this may be due to receiver noise or round off noise from digitizing. The Fresnel frequency which corresponds to the frequency at which the spectrum rolls off is theoretically proportional to the square root of the transmitted frequency. Again our results correspond quite well with the theory as the 140 and 360 MHz spectra break at frequencies at about 2 and 3 times higher than the 40 MHz spectrum. From the spectra, it is possible to estimate that the horizontal drift speed of the irregularities is approximately 45m/sec.

We used the parameters obtained from the theoretical modeling of  $S_4$  to compute theoretical power spectra for this set of data.

For weak scintillation, the power spectra for the amplitude, the log-amplitude as well as the intensity are all equivalent to each other and proportional to

$$F_X(\Omega) = \frac{\pi k^2 (f_p/f)^4 \langle (\Delta N/N_0)^2 \rangle}{4v} \left\{ 1 - \left( \frac{2k}{Q^2 L} \right) \sin \left( \frac{Q^2 L}{2k} \right) \cos \left[ \frac{Q^2}{k} (z-L/2) \right] \right\} \phi_N(\Omega/v, K_y) dK_y \quad (8)$$

$$Q^2 = \Omega^2/v^2 + K_y^2$$

where  $\Omega$  is temporal frequency (rad/sec),  $v$  is the drift velocity of the irregularity, and  $\phi_N$  is given by (3). The theoretical spectra are plotted over the corresponding experimental curves in Figures 4, 5, and 6. The slope of the roll off matches the experimental data fairly well in all cases and in the case of the 140 MHz, some of the minima also coincide. The drop in power in the low frequency end of the spectra is evidently due to anisotropy. In the theoretical spectra, this is modeled by setting  $n$  greater than 1. For this set of data, a value of about 3 seems to provide a good fit to the experimental results. This is significant since the theory predicts that the spectra should be modulated by the Fresnel filtering function which produces minima at  $f_1 \sqrt{n}$  where  $n$  is an integer and  $f_1$  is the frequency of the first minimum. For these minima to be seen in the Fourier spectra we must have  $n \gg 1$  (Singleton, 1974). Thus our Fourier spectra do not show any significant minima. Although Bessel spectrum is defined only for the isotropic case, however, for the purpose of comparison, the Bessel spectrum for the 140 MHz signal was also computed and shown in Figure 7. We note that the Bessel spectrum does show some modulation but not quite at the right pattern. Apparently, the anisotropy ( $r=3$ ) is large enough to disrupt but not completely invalidate the Bessel spectrum. It is interesting to note that the minima show good correspondence between the Bessel and Fourier spectra.

Now with some confidence that our analysis techniques are correct, we turn to the spectra for strong scintillations. Figure 8 shows amplitude, log amplitude and intensity spectra for the 40 MHz signal in data set 1' where  $S_4 = 1.31$ . The log

amplitude spectrum shows considerable broadening and is quite different from the amplitude and intensity spectra. The intensity spectrum on the other hand is almost the same as the amplitude spectrum except a slight narrowing at the high frequency end. The relations among the three spectra depend on the probability distribution of the scattered signal. Our data indicate that for weak scintillation (although we show no examples), the amplitude, log amplitude, and intensity spectra are all identical, which is to be expected. For strong scintillations, however, the spectral behavior of the log-amplitude and the amplitude are quite different. Thus, in the study of power spectra for strong scintillation case, a distinction must be made among the spectra discussed.

In Figure 9, we superimpose the amplitude spectra from the 3 frequencies in data set II. The 140 and 360 MHz which are still in the weak scattering regime show distinct frequencies where roll off begins. There is broadening of the 40 MHz spectrum as it rolls off almost on top of the 140 MHz curve. This did not happen in data set #1 where we had only weak scintillation. A more extreme case of this broadening is seen in our third data set (Figure 10). Here  $S_4 = 1.5$  at 40 MHz, and the spectrum rolls off at a frequency higher than the 360 MHz case. Although the 40 MHz spectra for these two cases do show broadening, the slope of the roll off is the same as for the cases of weak scintillation. Using a thin phase screen model, Rumsey (1975) and Marians (1975) have studied the power spectra for strong scintillations. Our results seem to agree, at least qualitatively, with their findings.

#### 4. Conclusions

Simultaneous multi-frequency scintillation data from ATS-6 have been analyzed and studied in this paper. We have shown that for weak scintillation the existing models fit the experimental data quite well giving us an  $f^{-n}$  frequency dependence for  $S_4$ . However, for increasing scintillation multiple scatter becomes important and this simple relationship no longer is valid. We have demonstrated that it is possible to model the ionospheric irregularities based on the scintillation data at higher frequencies and the single-scatter theory and then use this model to investigate the strong scintillation phenomena, such as focussing for the 40 MHz signal. In our power spectrum analysis we have seen evidence that the irregularities are slightly anisotropic and have power-law spectrum with the power index  $p$  ranging between 4 and 4.5. The behavior of the power spectra changes considerably when the scintillation level increases. The most noticeable feature is the broadening of the spectra while at the same time maintain the same high frequency asymptote as that for the weak scintillation spectra. This behavior seems to agree qualitatively with preliminary theoretical predictions. Also, for strong scintillations,

log-amplitude spectrum has been found to be quite different from the amplitude or intensity spectra. Since their relations depend closely on the probability distribution of the fluctuating signal, investigation of the spectra may also be useful in the effort to determine the distributions.

#### ACKNOWLEDGMENT

We thank the Environmental Research Laboratories of National Oceanic and Atmospheric Administration for making the ATS-6 data available to us. The work was supported by grants ATM 74-08765 and ATM 75-21755 from the Atmospheric Sciences Section of National Science Foundation.

#### REFERENCES

- Aarons, J., Whitney, H. E. and Allen, R. S., (1971), Global morphology of ionospheric scintillations, Proc. IEEE, 59, 159-172.
- Blackman, R. B. and Tukey, J. D., (1958), The Measurement of Power Spectra, Dover Publications, New York.
- Crane, R. K., (1976), Spectra of ionospheric scintillation, To appear in J. Geophys. Res.
- Davies, K., Fritz, R. B., Grubb, R. N., Jones, J. E., (1975), ATS-6 radio beacon experiment: The first year., IEEE Trans. Aerospace and Elect. Sys., AES-11, 1103-1107.
- Elkins, T. J. and Papagiannis, M. D., (1969), Measurement and interpretation of power spectrums of ionospheric scintillation at a sub-auroral location, J. Geophys., Res., 74, 4105-4115.
- Jokipii, J. R. and Hollweg, J. V., (1970), Interplanetary scintillation and the structure of solar-wind fluctuations, Astrophys. J., 160, 745-753.
- Liu, C. H., Wernik, A. W., Yeh, K. C., and Youakim, M. Y., (1974), Effects of multiple scattering on scintillation of trans-ionospheric radio signals, Radio Sci., 9, 599-607.
- Lovelace, R. V. E., Salpeter, E. E., and Sharp, L. E., (1970), Analysis of observations of interplanetary scintillations, Astrophys. J., 159, 1047-1055.
- Marians, M., (1975), Computed scintillation spectra for strong turbulence, Radio Sci., 10, 115-119.

Rufenach, C. L., (1972), Power-law wavenumber spectrum deduced from ionospheric scintillation observations, J. Geophys. Res., 77, 4761-4772.

Rumsey, V. H., (1975), Scintillations due to a concentrated layer with a power law turbulence spectrum, Radio Sci., 10, 107-114.

Shishov, V. I., (1971), Diffraction of waves by a strongly refracting random phase screen, Radiofizika, 14, 85-92.

Singleton, D. G., (1974), Power spectra of ionospheric scintillations, J. Atmos. Terr. Phys., 36, 113-133.

Wernik, A. W. and Liu, C. H., (1974), Ionospheric irregularities causing scintillation of GHz frequency radio signals, J. Atmos. Terr. Phys., 36, 871-879.

Yeh, K. C., Liu, C. H. and Youakim, M. Y., (1975), A theoretical study of the ionospheric scintillation behavior caused by multiple scattering, Radio Sci., 10, 97-106.

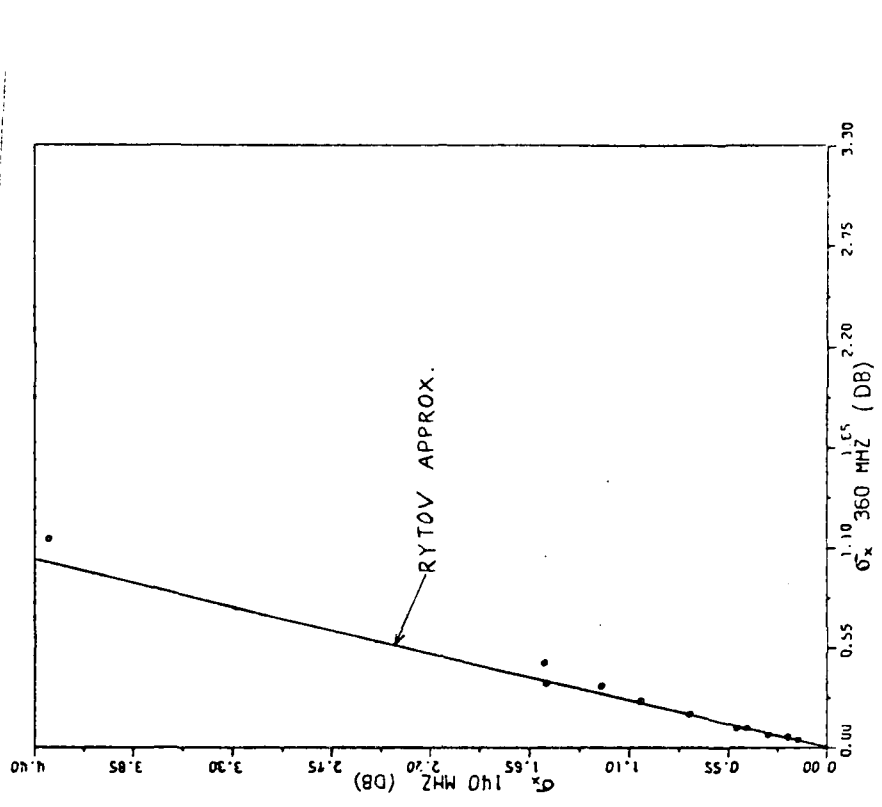


Fig. 2  $\sigma_X$  at 140 MHz vs.  $\sigma_X$  at 360 MHz

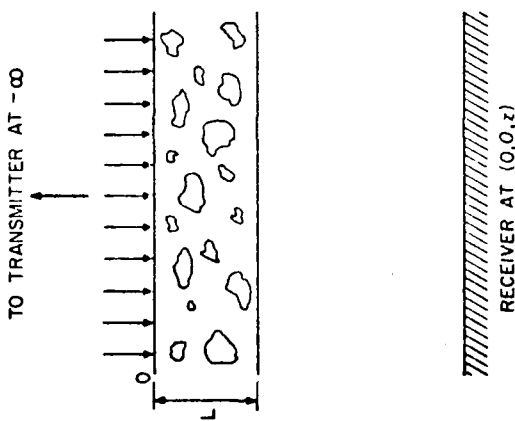
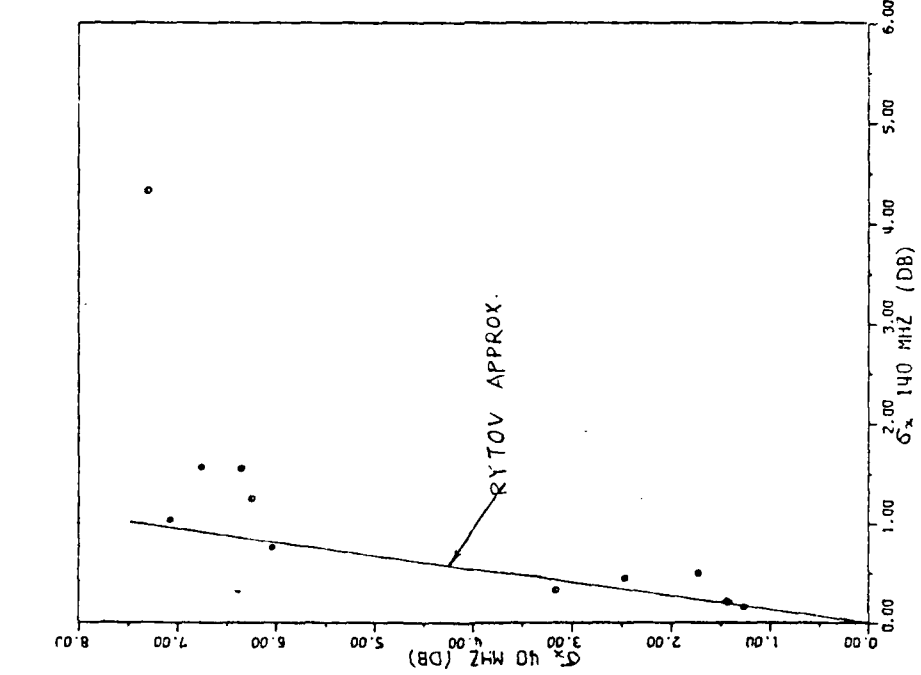


Fig. 1 Geometry of the problem



459

Fig. 3  $\sigma_{\chi}$  at 40 MHz vs.  $\sigma_{\chi}$  at 140 MHz

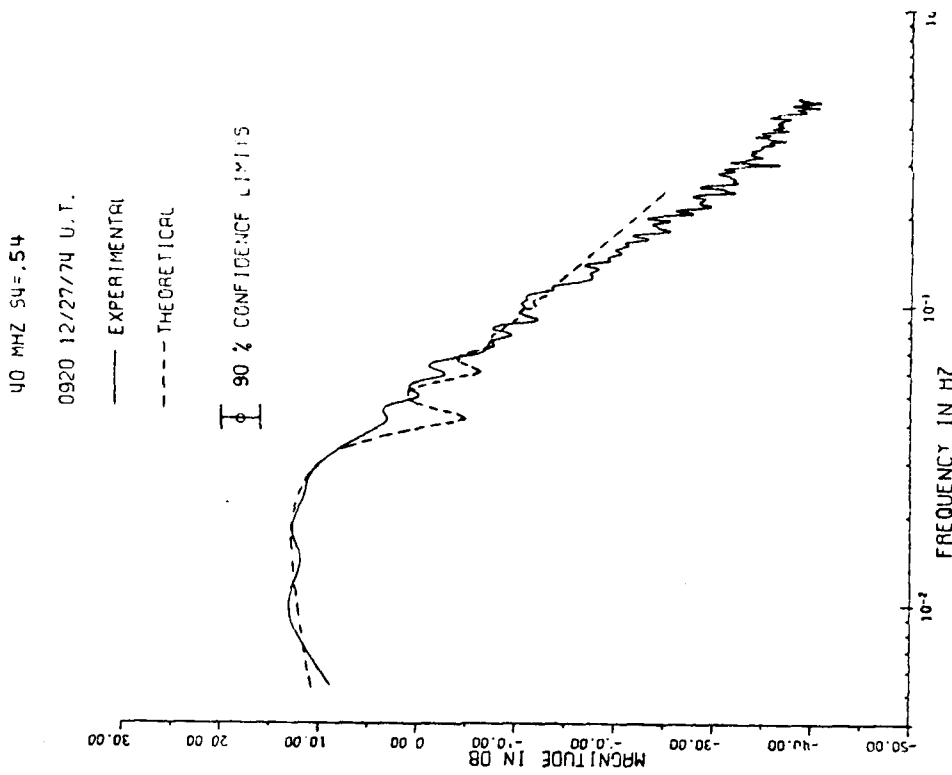


Fig. 4 Amplitude spectra for 40 MHz signal

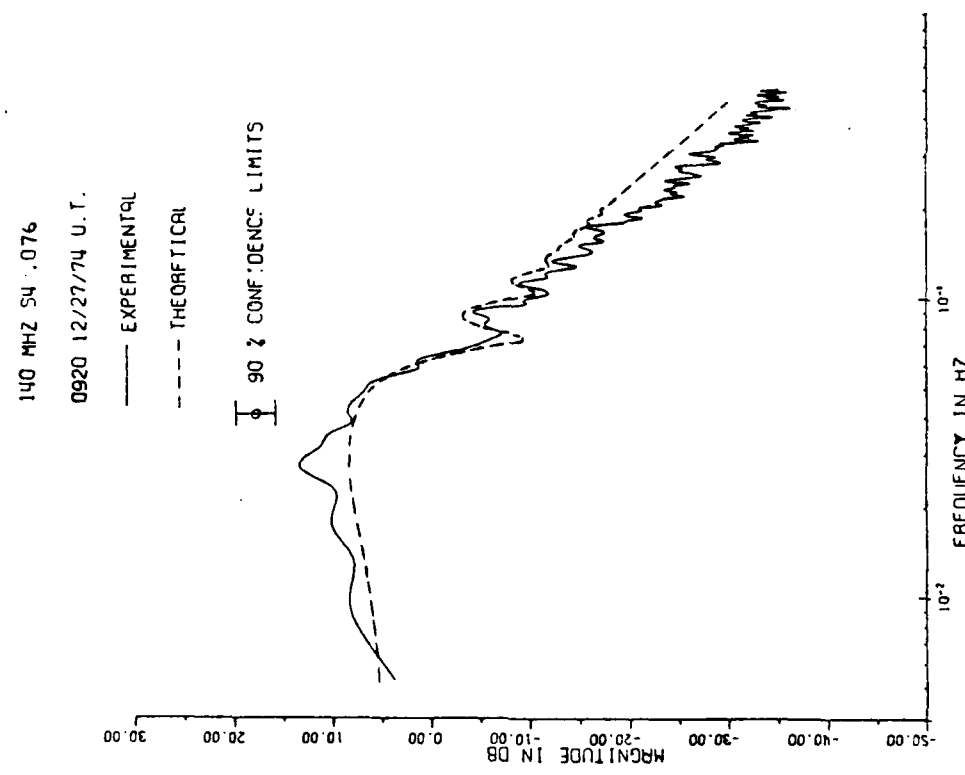


Fig. 5 Amplitude spectra for 140 MHz signal

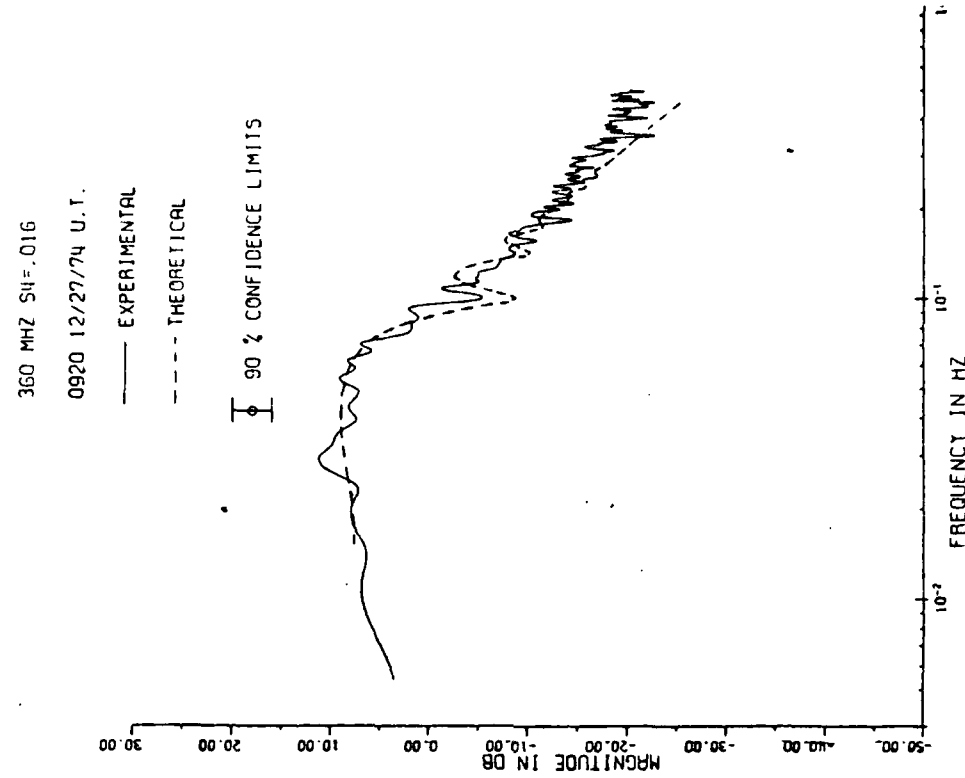
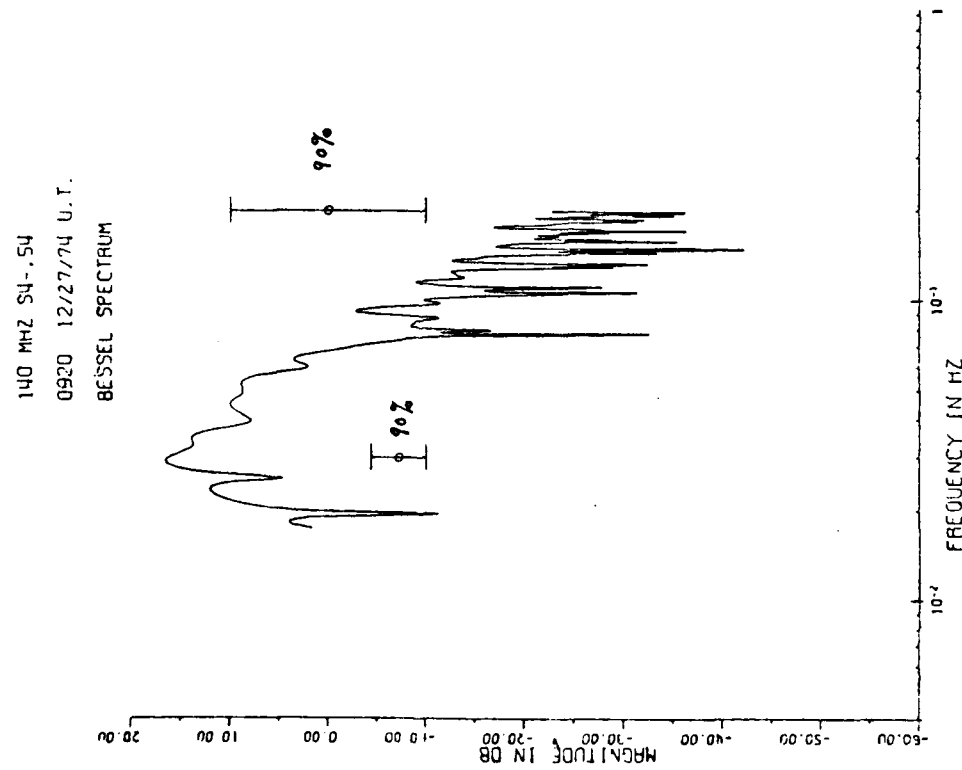


Fig. 6 Amplitude spectra for 360 MHz signal



461

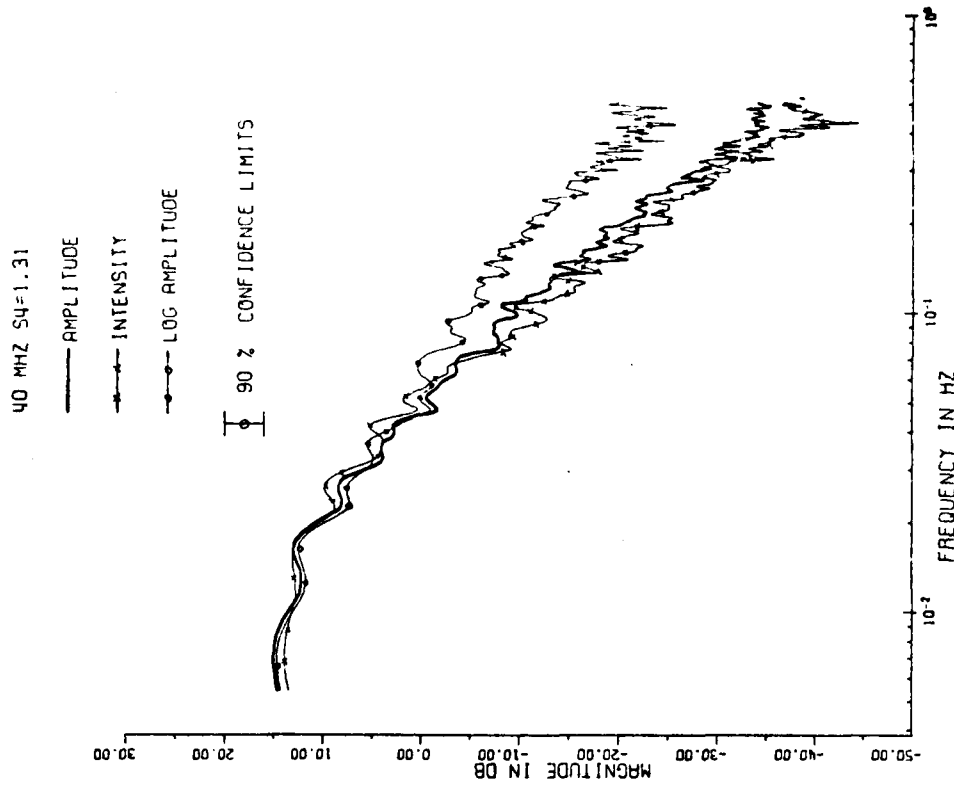


Fig. 7 Bessel spectrum for 140 MHz signal

Fig. 8 Amplitude, intensity and log-amplitude spectra for 40 MHz signal

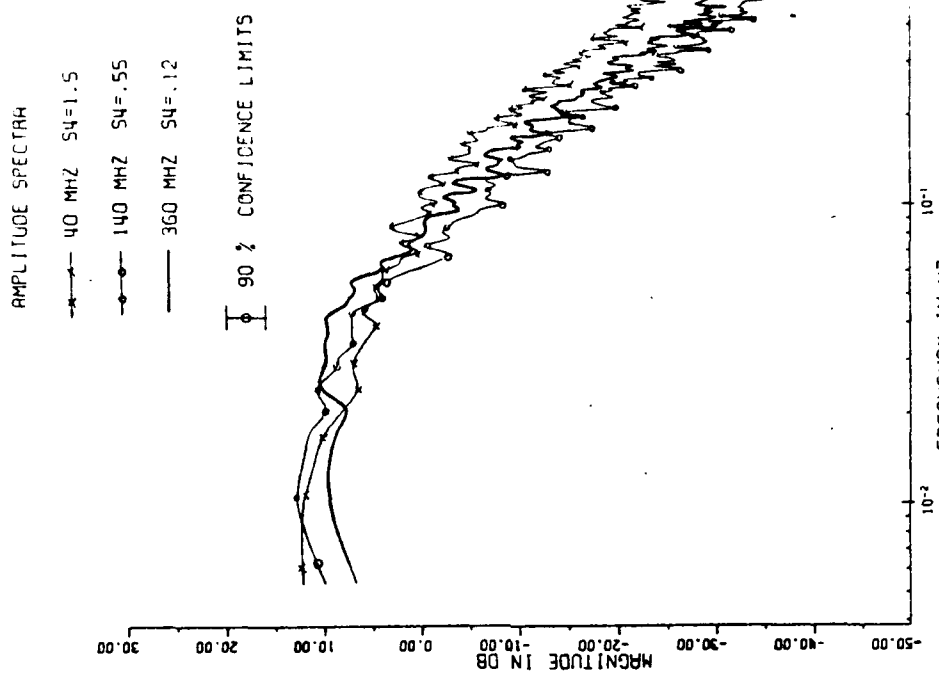
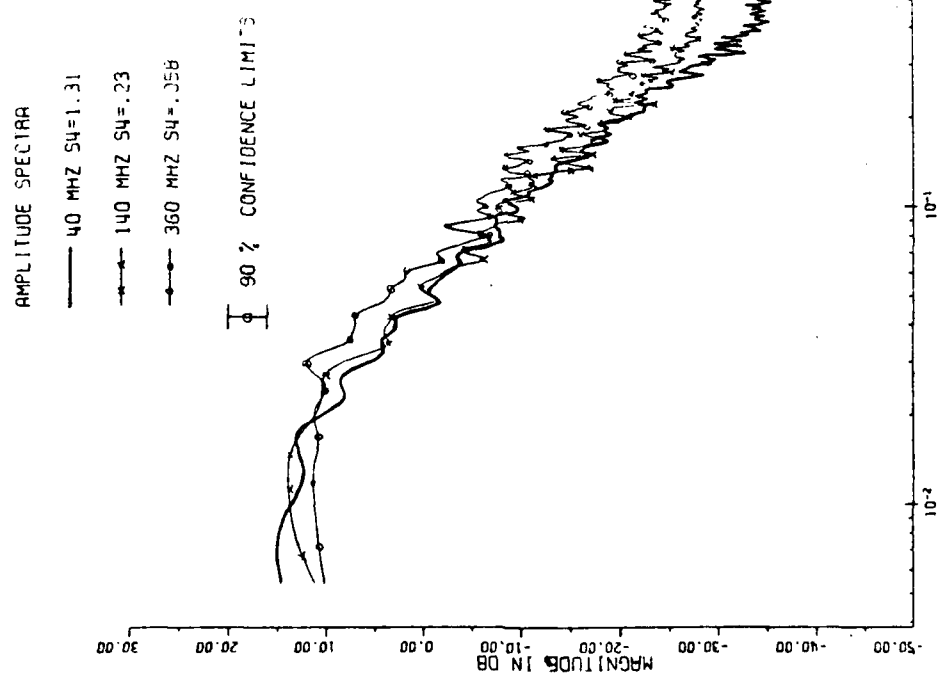


Fig. 9 Amplitude spectra for 3 frequencies

Fig. 10 Amplitude spectra for 3 frequencies

## A TWO-COMPONENT MODEL FOR SCINTILLATION

By

E. J. Fremouw, C. L. Rino, and R. C. Livingston  
Stanford Research Institute  
Menlo Park, Ca. 94025

### ABSTRACT

When the complex envelope of the signal received from a coherent beacon such as those transmitting from the Navy Navigation (Transit) satellites (150 MHz with a 400-MHz reference) and ATS-6 (40 and 140 MHz with a 360-MHz reference) is recorded, a mixture of information is obtained. The record contains data pertaining to the traditional studies of both total electron content (TEC) and (intensity) scintillation. Since TEC information is gleaned from relatively slow dispersive-phase variations and scintillation involves faster phase and amplitude fluctuations, (complex) scintillation can be isolated by high-pass filtering the recorded phase. A reasonable choice for the filter cutoff is the highest frequency that leaves the intensity scintillation index ( $S_4$ ) unchanged when the same filter is applied to amplitude. We have performed such phase "detrending" in order to analyze the complex-signal statistics associated with scintillation. We find that the first-order statistics can be described in terms of two multiplicative signal components. One component, which is isolated by continuing the amplitude and phase detrending past the invariant- $S_4$  criterion, obeys bivariate Gaussian signal statistics, which we believe to prevail under conditions of single, first-Born scatter. The remaining signal component displays strong phase variations and weak, correlated amplitude variations that may be the signature of a Gaussian phase screen observed in the near zone. This paper will describe the first-order probability density functions, and pertinent moments thereof, of the two (complex) signal components and of their product, the total scintillating signal.

## 1. INTRODUCTION

Satellite beacons have been used traditionally for two quite distinct kinds of ionospheric study: measurement of total electron content (TEC) and observation of scintillation. Both kinds of investigation depend on the (dispersive) phase perturbation imposed on the radio wave by the ionospheric plasma, but the two techniques have been used almost exclusively to study plasma variations and structures having such very different scale sizes that the propagation models employed have been quite different. For TEC studies, the transitionospheric propagation path usually is viewed deterministically, and geometric optics is employed in a very straightforward way for record analysis. On the other hand, scintillation is nearly always viewed in statistical terms, and the importance of radiowave diffraction has been appreciated for a very long time (Little, 1951).

Recent in-situ (Dyson et al., 1974; Phelps and Sagalyn, 1976) and radio (Rufenach, 1972; Crane, 1975) measurements suggest the need for a more unified approach to analyzing beacon records. That is, it is quite clear now that F-layer structure exists on all scales from those small compared with typical radio Fresnel zones to those approaching deterministic features (e.g., plasmapause boundary) of the ionosphere. Furthermore, most of the measurements show a continuous spatial spectrum of structure with no naturally imposed spectral separation between random irregularities that produce scintillation and deterministic gradients in TEC.

In this paper we describe a two-component scintillation model that has been suggested to us by observation of the complex signals received from ATS-6 and the Transit satellites, and that we hope will lead to more unified analyses of beacon records. The model is presented in Section 3, following a brief description of our data-processing procedure in Section 2. Section 4 contains a discussion of the model's internal consistency, followed, in Section 5, by our conclusions.

## 2. DATA PROCESSING

Following launch failure of the P72-2 satellite carrying the DNA-002 beacon payload, we modified two of the three observing stations we had deployed for observations of the beacon's coherent signals. The receiver located at Ancon, Peru, was retuned for observations of the ATS-6 ionospheric beacon for a few weeks before ATS-6 moved from its initial position, and then this receiver and the receiver at Poker Flat, Alaska, were retuned for two frequency coherent observations of the Transit signals. The ATS-6 observations were straightforward, and we devised a means for purging the Transit records of the imposed phase modulation.

It happens that the tri-state, phase-switching waveform used to modulate the Transit carriers returns to the zero state periodically 100 times per second, regardless of the message (i.e., for an arbitrary stream of logical ones and zeros). If one can sample the signal at these times, the resulting record is usable for scintillation measurements with a Nyquist rate of 50 Hz. Our procedure is to lock our coherent receiver to the (modulated) 400-MHz Transit signal and to record the quadrature components of the (modulated) 150-MHz signal. By employing a bandwidth sufficient to pass the modulation, we digitally record both the modulation and the ionospherically imposed complex-signal scintillation and (TEC-related) dispersive-phase signature.

Our initial off-line data-processing step is to cross-correlate the complex signal against a reference signal generated by a sequence of Transit-like logical ones and zeros. By searching in time for a high correlation (preferably during a record segment containing little scintillation), the computer "locks" to the modulation waveform and synchronously decimates the original record, keeping samples from only the zero-phase state. The decimated record is virtually free of modulation effects but contains all dispersive-phase variations and scintillations up to the sample rate of 100 Hz. The strong and spectrally pure signals from the ATS-6 beacon require no decimation, and its geostationary orbit permits a lower sampling rate; we employed a rate of 10 Hz.

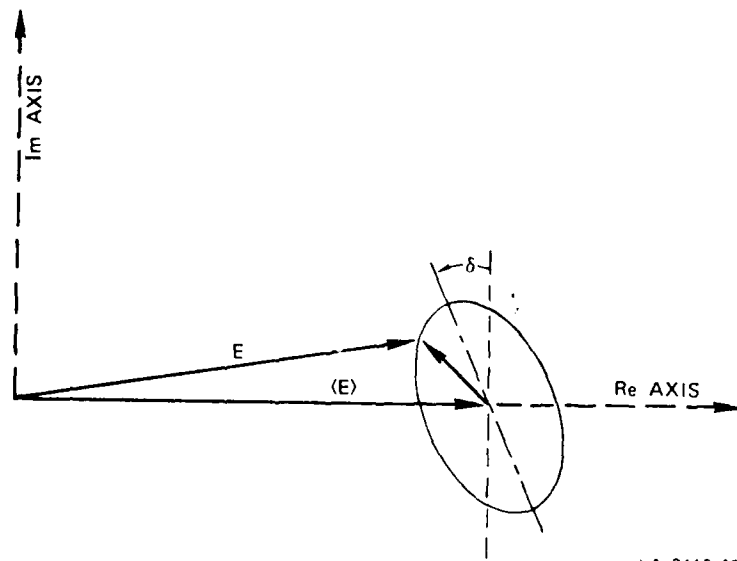
The sample rate, of course, sets the high-frequency cutoff of our records for scintillation studies. As is often the case, the nature of the low-frequency cutoff is not so obvious. Transmitter and receiver stability, antenna-pattern structure and geometry, and statistical non-stationarity in ionospheric structure all may play a role in determining the signal-fluctuation spectrum at the low-frequency end, as does the actual spatial-spectrum shape of large-scale ionospheric structure. In general, some form of data detrending is needed.

Since our emphasis is on scintillation, we need a criterion for distinguishing scintillation from other fluctuations of the complex signal. Our preconception was of spectrally separable signal fluctuations--i.e., relatively rapid fluctuations of the quadrature components representing complex scintillations, and very much slower phase trends due to changing TEC (which are possibly contaminated with experimental artifacts arising from the various factors mentioned above). Thus, we envisioned a single detrending operation with a cutoff period in the range of 10 seconds to a minute for Transit, and 10 to 30 times as long for ATS-6. As we shall see in the next section, there is no gap in the spatial spectrum of ionospheric structure that permits a geophysical separation between scintillation and phase variations related to TEC.

### 3. DEVELOPMENT OF THE MODEL

A good deal of attention has been given to the statistical nature of a scintillation signal (Ishimaru, 1975), with most observations being of signal amplitude or intensity only, but with some theories addressing the question of the distribution of the complex signal. Whether based on observation (Cohen et al., 1967), direct calculation of multiple moments (Mercier, 1962), or loose application of the central limit theorem, most signal-statistical discussions have centered on the question of whether the amplitude distribution of a scintillating signal is log-normal or arises from a complex signal having a Nakagami-Rice distribution. In recent years, the joint Gaussian generalization to Nakagami-Rice statistics has been offered as appropriate for characterizing the complex signal (Rino and Fremouw, 1973; Rino et al., 1976a), and the log-normal distribution has been found lacking as a description of intensity fluctuations (Wang and Strohbehn, 1974; Crane, 1975).

On the basis of past theoretical work and amplitude-only observations, we anticipated that we would find the quadrature components of our detrended scintillating signals to be jointly Gaussian variates. A necessary (but not sufficient) condition for Gaussian statistics is that a contour of equal probability, on the complex plane, for the received voltage will be an ellipse (Beckman and Spizzichino, 1963), such as that shown in Figure 1.



LA-3416-12

FIGURE 1 CONTOUR OF EQUAL PROBABILITY FOR A SCINTILLATING SIGNAL,  $E$ , IF THE QUADRATURE COMPONENTS OBEY GAUSSIAN STATISTICS. Correlation between the quadrature components orients the contour at an angle  $\delta$ .

In this idealization, the scintillating signal  $E$  is characterized by its long-term average value  $\langle E \rangle$  and an additive complex random variable, the quadrature components of which have zero means but in general have unequal variances and a nonzero covariance. If such a signal were received in the far (Fraunhofer-diffraction) zone of all scattering irregularities, the correlation ellipse would be expected to reduce to the circle characteristic of Nakagami-Rice statistics.

When one accounts for the dispersive-phase change due to a deterministic trend in TEC during the course of a scintillation observation, he would expect the entire phasor diagram appearing in Figure 1 to rotate at the differential Doppler frequency, producing a circular scatter diagram enclosing the complex-plane origin. Indeed, such a scatter diagram is produced from our raw (i.e., non-detrended) data, as shown in Figure 2 (top) together with the signal recorded during a portion of a Transit pass over Alaska.

If the scatter diagram shown at the top of Figure 2 were produced simply by rotation of a diagram such as that in Figure 1 through one or more quasi-deterministic dispersive-phase cycles, then removal of the dispersive-phase "ramp" by detrending should recover an elliptical scatter diagram. As illustrated in Figure 3 for the data set shown in Figure 2, an elliptical scatter diagram indeed is recovered when detrending is performed, using a cutoff of 2.5 s.

The detrending procedure employed is as follows. From the quadrature-component recordings, instantaneous values of log-amplitude and phase are computed and then smoothed by means of a low-pass numerical filter. The smoothed log-amplitude and phase are subtracted from the raw data, the residuals representing the (detrended) complex envelope of the recorded signal after passage through a coherent AGC circuit.

As noted above, when a 0.4-Hz cutoff is used for the detrending filters, the resulting complex-plane scatter diagram is that expected if the signal obeys generalized Gaussian statistics (i.e., if its quadrature components are jointly Gaussian variates). If such a statistical model characterized the entire scintillating signal, a similar diagram should be found for any cutoff that effectively removes the quasi-deterministic dispersive-phase ramp. That is, one would expect to find a family of elliptical scatter diagrams as the filter cutoff is lowered in frequency, with a sudden transition to a diagram such as that in Figure 2 when no detrending is employed. What is actually found, however, is a family of arc-like diagrams making a smooth transition from Figure 3 to Figure 2, a typical one of which is shown in Figure 4.

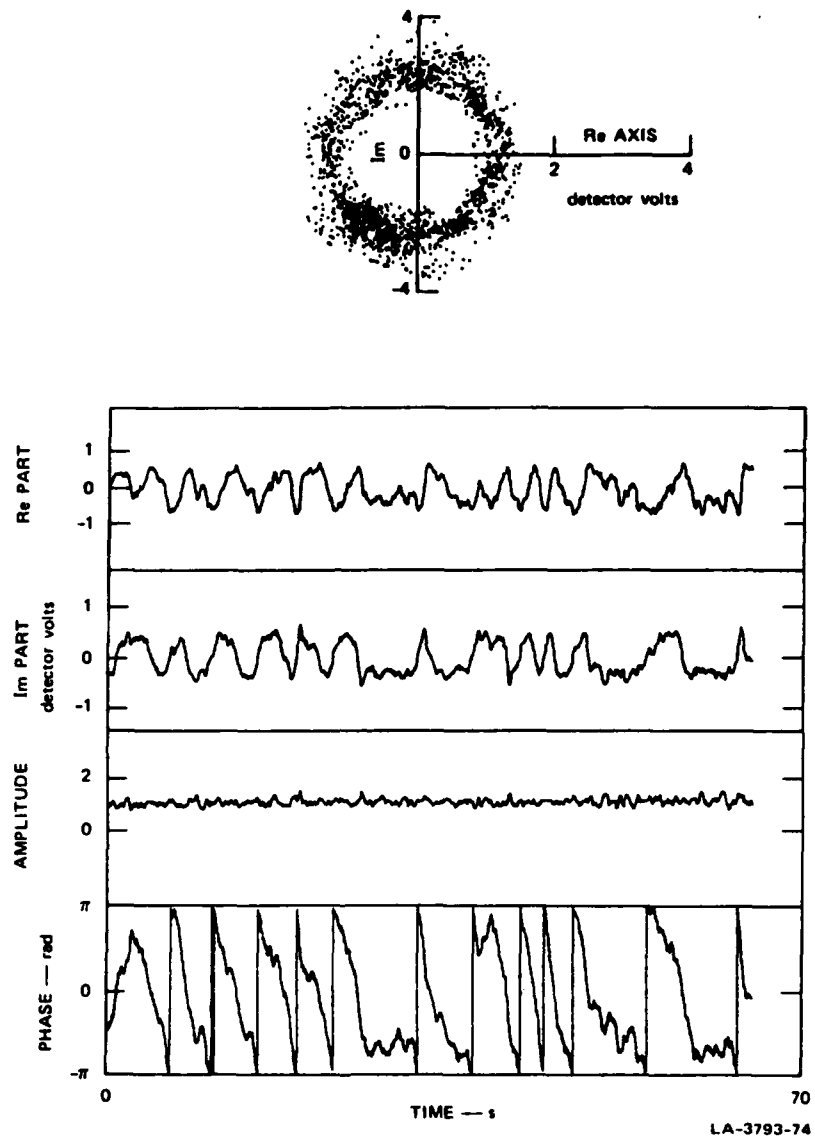
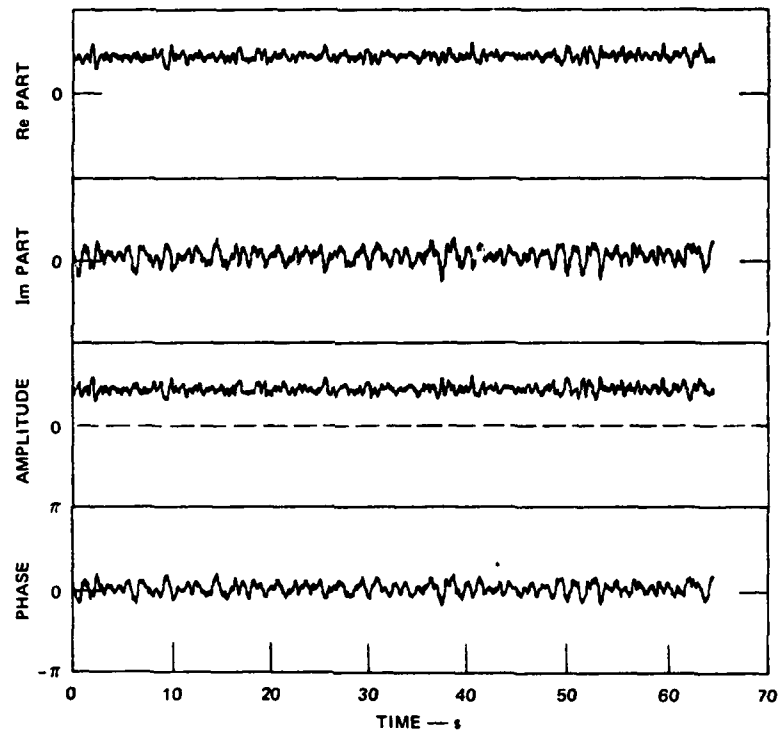
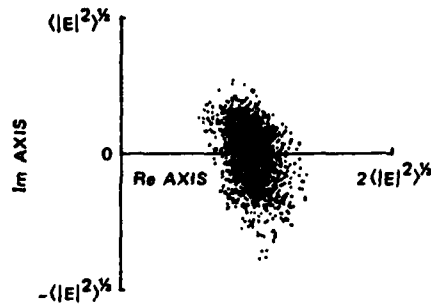


**FIGURE 2** RAW DATA RECORDED FROM THE 150-MHz SIGNAL (with 400 MHz as a coherent reference) RECEIVED FROM ONE OF THE TRANSIT SATELLITES DURING 65 s OF A PASS OVER POKER FLAT (near Fairbanks), ALASKA, STARTING AT 2025:05 GMT ON 3 OCTOBER 1975.



LA-3793-64

**FIGURE 3** FIRST-ORDER SIGNAL-STATISTICAL RESULTS FROM (logarithmic) DETRENDING OF THE RAW DATA DISPLAYED IN FIGURE 2.  
The detrending filters were ten-pole Butterworths with a cutoff of 0.4 Hz.

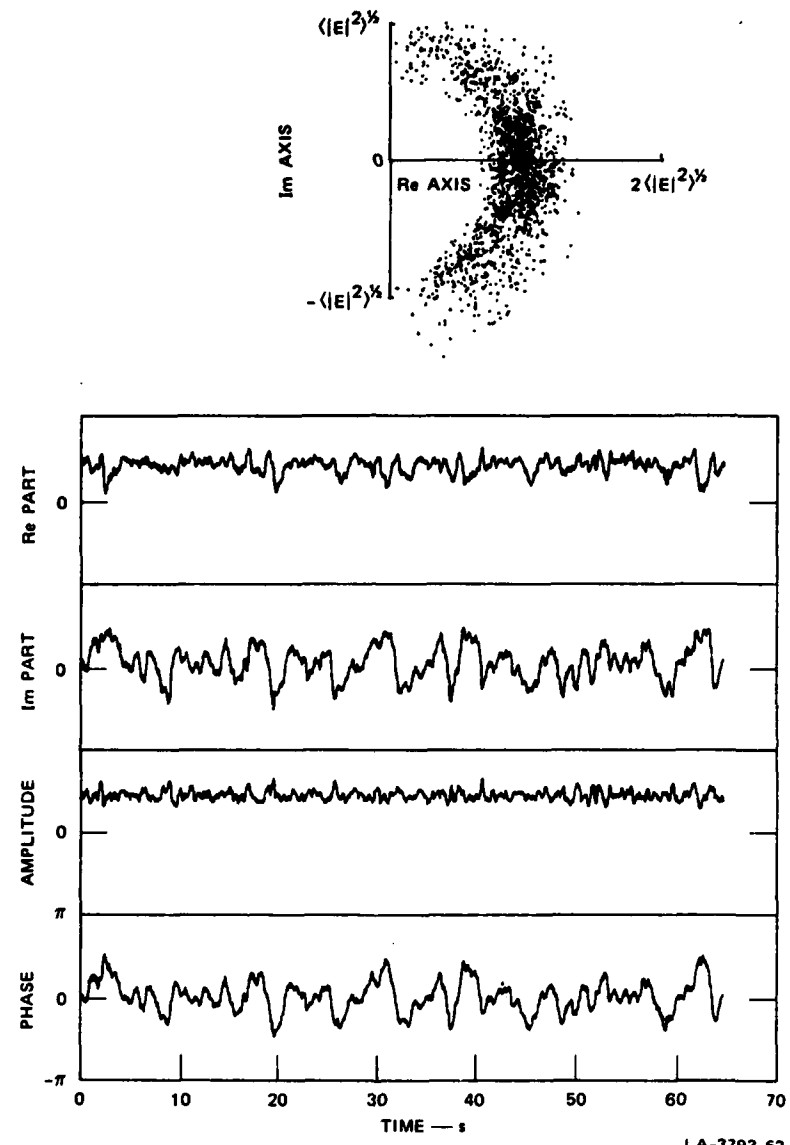


**FIGURE 4** FIRST-ORDER SIGNAL-STATISTICAL RESULTS WHEN THE RAW DATA IN FIGURE 2 ARE DETRENDED USING FILTERS WITH A LOWER FREQUENCY CUTOFF THAN THAT USED FOR FIGURE 3. The detrending filters were six-pole Butterworths with a cutoff of 0.1 Hz. Measured  $S_4 = 0.29$ .

Obviously, the data in Figure 4 are dominated by phase variations. There is clear evidence, however, that the large and relatively slow phase variations producing the crescent shape of the scatter plot are accompanied by (and correlated with) amplitude variations on the same time scale. The evidence is that the overall shape of the plot is not that of a true crescent, but rather resembles a portion of a shallow spiral. That is, as the phase advances, the signal tends preferentially to fade; and as the phase retards, the signal preferentially is enhanced. This behavior is exactly what would be expected from weak focusing and defocusing by lens-like ionospheric structure and it is very persistent from data set to data set.

The characteristic behavior described above suggests that the signal variations illustrated in Figure 4 are to be viewed as (complex) scintillations and that the distinction between scintillations and (phase) variations due to (slow but essentially random) changes in TEC is nebulous. We have developed a procedure, as follows, for separating our data into spectral regimes for TEC and scintillation studies, recognizing that there will be some overlap and ambiguity.

From Transit data sets obtained in Alaska we selected several that appeared subjectively, and on the basis of calculated  $S_4$ , to maintain reasonable statistical stationarity over periods of a few tens of seconds. These data sets were used to arrive empirically at a detrend cutoff for separation of TEC trends and scintillation, employing the same detrend filter for log-amplitude as for phase. While there are trends in signal intensity, due mainly to such artifacts as changing range, changing structure in antenna patterns, and so forth, the spectral density of log-amplitude is very much less than that of phase at very low frequencies. If one calculates  $S_4$  from the raw (non-detrended) records and then again from detrended records having successively shorter-time cutoffs, one finds a cutoff beyond which detrending begins to decrease the measured  $S_4$ .

We chose as a criterion for establishing our routine detrend cutoff that the measured value of  $S_4$  should not be decreased "significantly" (typically, a couple of percent) by the procedure. We found from our selected Transit data sets that a detrend cutoff of 0.1 Hz met this criterion, and we have adopted this value. That is, we regard all phase and log-amplitude variations with periods shorter than about 10 s as complex-envelope scintillations to be analyzed, for the most part, statistically. Slower phase variations are regarded as arising from TEC changes, to be treated deterministically for a given data set.

The corresponding (i.e., slow) log-amplitude variations are due mainly to the experimental artifacts mentioned above, although some focusing effects could be included on occasion. The latter effects, in addition

to special features such as the so-called "ringing-irregularity" signature and other results of deterministic diffraction, are amenable to special analysis after visual identification on either the raw records, the smoothed (TEC) records, or the detrended (scintillation) records.

Our emphasis is on signal-statistical analysis of scintillation. What the data-processing experience described in the foregoing has revealed to us is two-fold. First, as illustrated in Figure 3, we have found that scintillations faster than about 2.5 s for low-orbiting (altitude  $\approx$  1000 km) satellites such as the Transits (the line of sight to which scans the F layer at about 3 km/s) may be characterized by generalized Gaussian signal statistics. Second, as illustrated in Figure 4, we have found that such a model falls short of fully describing the first-order statistics of a scintillating signal. In particular, we can isolate a Gaussian-statistics component only by detrending past the inviolate- $S_4$  criterion, which is the only workable criterion we have found for defining scintillation, as distinguished from dispersive-phase variation.

The above dilemma leads us to postulate a two-component, multiplicative signal-statistical model for characterizing scintillation. The model is defined by the following simple equation:

$$E = E_s E_f = (\bar{x} + x_s + iy_s) \exp(\epsilon + X_f + i\phi_f) \quad (1)$$

where  $\bar{x}$  and  $\epsilon$  are real constants;  $x_s$  and  $y_s$  are jointly Gaussian, zero-mean random variables; and  $X_f$  and  $\phi_f$  are a second (statistically independent) pair of jointly Gaussian, zero-mean random variables. The first component,  $E_s$ , which we think arises from diffractive scatter by relatively small irregularities, is illustrated in Figure 3, whereas Figure 4 illustrates the composite scintillating signal,  $E$ . The second component,  $E_f$ , which we think arises from refractive focusing and defocusing by relatively large irregularities behaving as a phase screen observed in the near zone, is illustrated in Figure 5.

The composite scintillating signal is obtained by removing the TEC signature in a first detrend operation, using a six-pole Butterworth filter having a cutoff (3 dB rejection) of 0.1 Hz. The two scintillation components are separated by means of a second detrending procedure, using a 10-pole Butterworth filter having a cutoff of 0.4 Hz. The focus component is simply the reference signal applied in the second coherent AGC operation (obtained by smoothing the log-amplitude and phase of the composite scintillating signal), and the scatter component is the (residual) output of the second coherent AGC. The two components are multiplicative by virtue of the nature of the coherent AGC operation--namely, subtraction of complex logarithms.

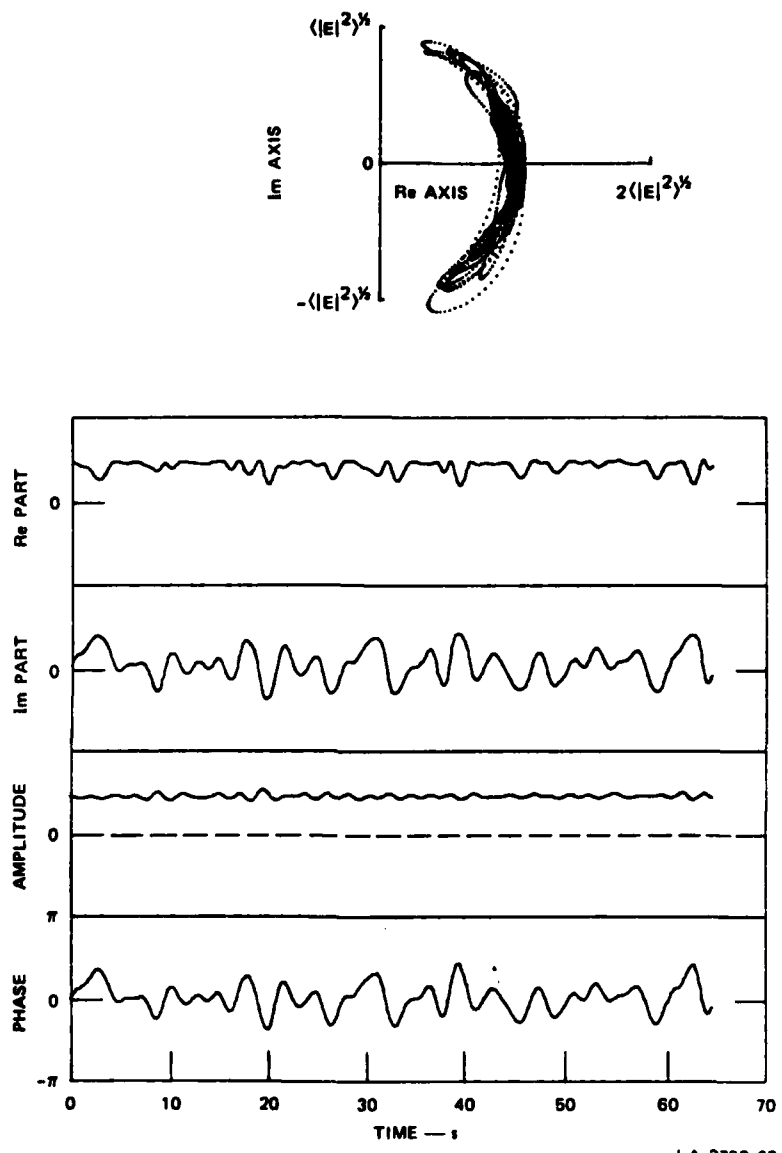


**FIGURE 5** THE "FOCUS" COMPONENT OF THE SCINTILLATING SIGNAL IN FIGURE 4,  
CONSISTING OF PHASE AND LOG-AMPLITUDE VARIATIONS IN THE  
SPECTRAL RANGE FROM 0.1 TO 0.4 Hz.

A key simplifying assumption in the model is that the two components are statistically independent. Isolation of two statistically independent components is achieved by using a very sharp cutoff filter (ten poles) in the second detrend operation. By means of the model, we are simply postulating that the composite scintillating signal can be characterized as the product of two statistically independent components having, respectively, Gaussian and log-normal statistics.

#### 4. INTERNAL CONSISTENCY OF THE MODEL

There are two reasons for developing a signal-statistical model of scintillation. First, such a model should permit characterization of the transitionospheric communication channel for engineering purposes by means of a few parameters. Second, those parameters (moments of the signal-statistical distribution) should be relatable to ionospheric structural parameters by means of propagation theory. Useful moments for these purposes are  $\langle E \rangle$  and the following:

$$R_o \triangleq \langle EE^* \rangle - |\langle E \rangle|^2 \quad (2)$$

$$B_o \triangleq \langle EE \rangle - \langle E \rangle^2 \quad (3)$$

$$S_4 \triangleq \frac{\langle (EE^* - \langle EE^* \rangle)^2 \rangle^{1/2}}{\langle EE^* \rangle} \quad (4)$$

For the postulated two-component model, we have calculated the above moments in terms of the moments describing each of the two components. The results are as follows:

$$\langle E \rangle = \eta_e e^{\epsilon_e} + \epsilon_f / 2 \quad (5)$$

$$R_o = 1 - (1 - \sigma_s^2) e^{-\sigma_f^2} \quad (6)$$

$$B_o = B_{os} e^{-2\sigma_{of}^2 + 4iC_f} + B_{of} (1 - \sigma_s^2) \quad (7)$$

$$S_4^2 = [(S_{4s}^2 + 1)][(S_{4f}^2 + 1)] - 1 \quad (8)$$

where, by the normalization condition ( $\langle E_s E_s^* \rangle \approx 1 \equiv \langle E_f E_f^* \rangle$ ),

$$\eta^2 = 1 - \sigma_s^2 \text{ and } \epsilon = -\sigma_{x_f}^2 \quad (9)$$

and where

$$\sigma_s^2 \triangleq \sigma_{x_s}^2 + \sigma_{y_s}^2 \quad (10)$$

$$\sigma_f^2 \triangleq \sigma_{x_f}^2 + \sigma_{\phi_f}^2 \quad (11)$$

$$\beta_f \triangleq (\sigma_{x_f}^2 - \sigma_{\phi_f}^2) + 2i C_f \quad (12)$$

$$B_{os} \triangleq (\sigma_{x_s}^2 - \sigma_{y_s}^2) + 2i C_s \quad (13)$$

$$B_{of} \triangleq (e^{2\beta_f} - e^{\beta_f}) e^{-2\sigma_{x_f}^2}. \quad (14)$$

In the above,  $\sigma$  represents the standard deviation of the subscripted quantity, and  $C$  represents the covariance of the real and imaginary parts of the subscripted signal component (e.g.,  $C_f$  = covariance of  $x_f$  and  $\phi_f$ ).

Equation (8) gives the intensity scintillation index for the composite signal in terms of the index for each component. As written, the only condition on which the equation depends is that of statistical independence for the two components. We have investigated the importance of component independence by varying the roll-off sharpness of the filter used in the second detrend process. A gradual roll-off permits the two components to share Fourier components, which can introduce correlation between them. A sharp cutoff virtually assures statistical independence. To investigate this behavior, we inserted measured values of  $S_4$  for each of the components into Eq. (8) and compared the result with a measured value of  $S_4$  for the composite signal. When we used a filter having only a few poles, the calculation consistently underestimated the measured value. Increasing the number of poles consistently improved the agreement. It is for this reason that we employ ten poles in our second detrend filter, which we find produces agreement within a couple of percent.

Now, besides statistical independence of the components, our model contains postulates of Gaussian and log-normal statistics for the two components. Based on these postulates, one can calculate the component  $S_4$  values as follows:

$$(S_4^2)_s = 4\sigma_x^2 (1 - \sigma_s^2) + \sigma_s^4 + |B_{os}|^2 \quad (15)$$

$$(S_4^2)_f = \exp(4\sigma_x^2_f) - 1 \quad . \quad (16)$$

Performing these calculations and using the results in Eq. (8) for comparison with the measured value of  $S_4$ , obtained from the composite scintillating signal, is one means for checking internal consistency of the model. The results of such a comparison for six data sets are listed in Table 1. (Data Set 1 is that illustrated in Figures 2 through 5.)

Table 1  
A CHECK ON INTERNAL CONSISTENCY

Data Set	Observed $S_4$	Calculated $S_4$
1	0.29	0.27
2	0.37	0.37
3	0.37	0.36
4	0.38	0.39
5	0.43	0.45
6	0.89	1.02

Various other consistency checks are possible, employing the relations described by Eqs. (5) through (14), but their significance is not so readily grasped as is that of the  $S_4$  comparison. In any case, the main utility of the various relations listed is that all the quantities are determined by the four variances and two covariances ( $\sigma_x^2$ ,  $\sigma_y^2$ ,  $C_s$ ,  $\sigma_x^2$ ,  $\sigma_y^2$ ,  $C_f$ ) that specify the two components, and that these six (co)variances should be calculable in terms of ionospheric structural parameters by means of propagation theory. The theoretical relation of our two-component scintillation model to ionospheric structure will be explored in a separate paper presented at this symposium (Rino et al., 1976b).

An intuitive demonstration of the model's consistency with observation is provided by Figure 6, which shows contours of equal probability density, on the complex plane, for the composite scintillating signal, calculated from the six measured component (co)variances. Comparison of Figure 6 with the scatter diagram at the top of Figure 4 shows that the dominant statistical features of the composite signal are reproduced, including the spiral nature of the scatter plot caused by correlation between amplitude and phase scintillations. The calculation leading to Figure 6 is essentially a two-dimensional convolution of the two-component probability density functions (pdf), yielding the joint pdf for amplitude and phase of the composite signal, as follows:

$$p_{A\phi}(A, \phi) = \frac{1}{A} \int_{-\infty}^{\infty} \int_{-\infty}^{\infty} e^{2x_s} p_{x_s y_s} [ (e^{x_s} \cos \phi_s - 1), e^{x_s} \sin \phi_s ] p_{x_f \phi_f} [ (\ln A - \epsilon - x_s), (\phi - \phi_s) ] dx_s d\phi_s \quad (17)$$

where  $p_{x_s y_s}$  and  $p_{x_f \phi_f}$  are the (joint Gaussian) pdf's that specify the scatter and focus components, respectively.

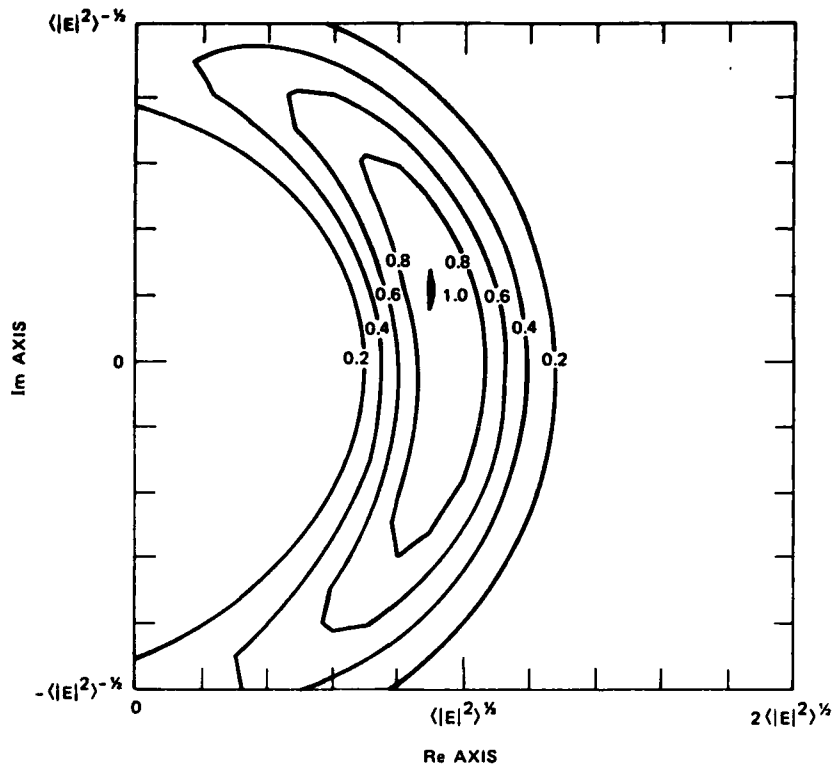
Integration of Eq. (17) over one variable leads to the following convolutions for the pdf for amplitude and the pdf for phase, respectively:

$$p_A(A) = A^{-1} \int_{-\infty}^{\infty} e^{x_s} p_{x_s} (e^{x_s}) p_{x_f} (\ln A - \epsilon - x_s) dx_s \quad (18)$$

where  $p_{x_s}$  is the amplitude pdf arising from Gaussian complex-signal statistics (Fremouw and Rino, 1975), and  $p_{x_f}$  is the normal pdf for  $x_f$ ,

$$p_\phi(\phi) = \int_{-\infty}^{\infty} p_{\phi_f} (\phi - \phi_s) d\phi_s \quad (19)$$

where  $p_{\phi_s}$  is the Hatfield distribution (Hatfield and Rino, 1975) for phase arising from Gaussian complex-signal statistics, and  $p_{\phi_f}$  is the normal pdf for  $\phi_f$ .



LA-4259-17

**FIGURE 6** CONTOURS OF PROBABILITY DENSITY, ON THE COMPLEX PLANE, CALCULATED FROM THE MODEL BASED ON EQ. (1), USING COMPONENT-SIGNAL MOMENTS DETERMINED FROM DATA SET 1. Compare with observed scatter plot in Figure 4.

Figure 6 and Table 1 show a favorable degree of consistency between the signal-statistical model and the data, for moderate scintillation index. The final entry (Data Set 6) in Table 1 suggests that the model may be less accurate for very strong scintillation, although this conjecture must be checked with more data sets. It must be noted that the disturbed conditions involved in this data set surely resulted in signal perturbations on our reference frequency of 400 MHz. More reliable scintillation modeling under such conditions will be possible after launch\* of a backup DNA-002 beacon, which will transmit a reference signal at 2891 MHz.

---

\* Launch of Satellite P76-5, carrying DNA-002, is scheduled for 0040 GMT on 20 May 1976.

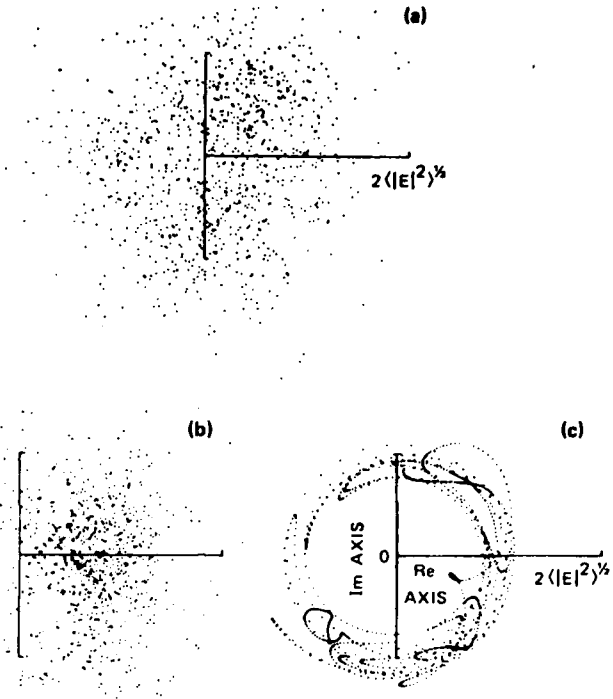
It may be worth noting that the difference between the calculated and observed  $S_4$  in Data Set 6 stemmed not from the postulate of two statistically independent, multiplicative components, but rather from the statistics postulated for the two components. In particular, the component  $S_4$  values calculated from Eqs. (15) and (16) were both larger than the values measured for the corresponding components; the discrepancy was greater for the scatter (i.e., supposed Gaussian-statistics) component than for the focus (i.e., supposed log-normal) component.

The complex-plane scatter diagrams for the two components and for the composite scintillating signal recorded in Data Set 6 are shown in Figure 7. The composite-signal diagram attests to the highly disturbed nature of the received signal (recorded a few minutes earlier in the same Transit pass over Poker Flat on which the data in Figures 2 through 5 were recorded). An interesting feature in Figure 7(b) is the presence of a nonscattered component (i.e., the offset in the cloud of points along the real axis), which nonetheless has its phase and amplitude perturbed by refractive focusing and defocusing. Of considerable interest in Figure 7(c) is the persistence of the tendency for correlation between amplitude and phase even when the phase variations are considerably in excess of a radian (including extrema greater than  $\pm\pi$ ).

In addition to the Transit data from our own stations at Poker Flat and Ancon (the latter recorded for us by colleagues at the Instituto Geofisico del Peru), we have received some ATS-6 data from Ancon, from Boulder (recorded by our NOAA colleagues), and from Ootacamund (through the cooperation of colleagues at the Indian Physical Research Laboratory, Ahmedabad). We have just begun to adapt the analysis procedure described in the foregoing to these geostationary-satellite data. In general, the procedure and the two-component model look quite applicable, using a pair of detrend cut-off periods more than 10 but no more than 60 times those chosen for Transit (10 and 2.5 s). Once detrend cut-offs have been firmly established, we shall perform internal-consistency checks on the ATS-6 data similar to those discussed herein for the Transit data.

##### 5. DISCUSSION AND CONCLUSIONS

We have proposed the two-component scintillation model described in Section 3 in order to resolve the following dilemma: Amplitude-scintillation data analyzed in the past (Crane, 1975; Rino et al., 1976a) have been more consistent with the Gaussian family of complex-signal statistics (of which Nakagami-Rice is a member) than with log-normal statistics, yet even a cursory glance at the first-order statistics of the initial complex scintillation data available to us showed them to be inconsistent with Gaussian statistics but possibly consistent with log-normal statistics.



LA-3793-75

FIGURE 7 SCATTER PLOTS OF (a) COMPOSITE SCINTILLATING SIGNAL, (b) SCATTER COMPONENT, AND (c) FOCUS COMPONENT RECORDED UNDER STRONG SCINTILLATION ( $S_4 = 0.89$ ) CONDITIONS. Transit over Poker Flat, Alaska, 2022:41 to 2023:21 GMT, 3 October 1975.

By means of our double-detrend procedure, we found that we could isolate a component consistent with Gaussian statistics and another consistent with log-normal statistics. Since the former consists of relatively rapid signal fluctuations, it is the signature of relatively small-scale structure in a diffraction pattern arising from scatter in small-scale irregularities and therefore dominates the statistics of amplitude. The slower-fluctuation component dominates the phase statistics, and because of the low-pass nature of the ionospheric spatial spectrum, also dictates the gross appearance of signal scatter plots on the complex plane. A model that incorporates both these components can resolve the dilemma.

We have not yet proven that the two components we have isolated are distributed according to the statistics we postulate; we have noted only that the appearance of scatter plots on the complex plane is consistent

with these postulates. In effect, we have tacitly assumed that physics related to the central-limit theorem will contrive to produce a normal distribution for some signal parameter.

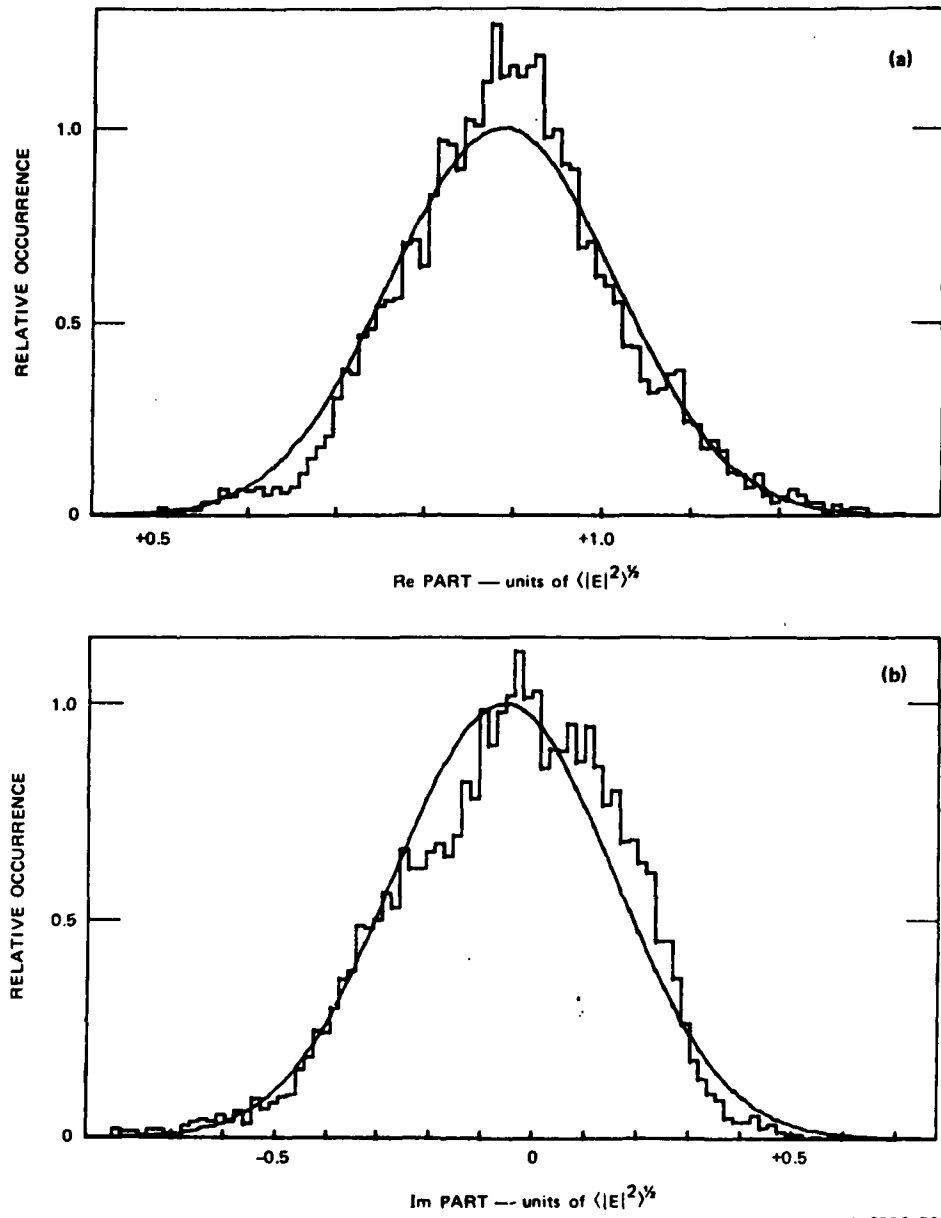
One might suppose a signal random-walking through a thick phase screen to have its phase (and subsequently its amplitude or log-amplitude) normally distributed, and our "focus" signal component appears consistent with this supposition. Similarly, for wider-angle scatter by smaller-scale structure observed in the intermediate-to-far zone, one might suppose the signal itself (i.e., its quadrature components), rather than its amplitude and phase, to be normally distributed because it is the sum of a number of more or less independent contributions; our "scatter" component appears consistent with this view. Thus, our two-component signal-statistical model simply marries two long-standing intuitive views.

We now must perform more quantitative statistical tests of our hypotheses. A first step in this direction is illustrated in Figures 8 and 9. Figure 8 compares histograms of the quadrature components of  $E_s$  from the data in Figure 3 with the normal distributions calculated from the measured moments. Figure 9 is a similar comparison for the log-amplitude and phase of  $E_f$ , using the data from Figure 5. We have not yet calculated meaningful goodness-of-fit estimators, but subjectively the fits in Figure 8 are reasonably satisfactory. Interestingly, in Figure 9 the log-amplitude fit appears better than that of phase.

Probably the most significant point evident in Figures 8 and 9 is the poor phase fit in 9(b). This is very likely due at least in part to the finite duration (65 s) of the record used, for analysis of fluctuations in the period range between 2.5 and 10 s, which corresponds to spatial periods in the F layer between about 7.5 and 30 km. Statistical homogeneity over regions much larger than this seems to be rather uncommon, at least in the auroral-latitude ionosphere. Thus, the signal fluctuations included in our "focus" component may be near the spectral limit where statistical analysis is meaningful, at least under the usual assumption of strict statistical homogeneity.

A more satisfactory approach might be developed, however, on the basis of locally homogeneous statistics (Rino, 1976). In the meantime, we intend to perform hypothesis testing to establish the degree to which our two-component model may improve the mathematical description of amplitude statistics as compared with a one-component Gaussian model, which is already known to be better than a one-component log-amplitude model.

Acknowledgment. The work reported herein was sponsored by the Defense Nuclear Agency under Contract DNA001-75-C-0111 and by ARPA under RADC Contract F30602-75-C-0236.



LA-3793-76

**FIGURE 8** OCCURRENCE HISTOGRAMS OF QUADRATURE COMPONENTS OF  $E_s$  COMPARED WITH GAUSSIAN DISTRIBUTIONS CALCULATED FROM MEASURED MOMENTS. Data Set 1 (Figure 3).

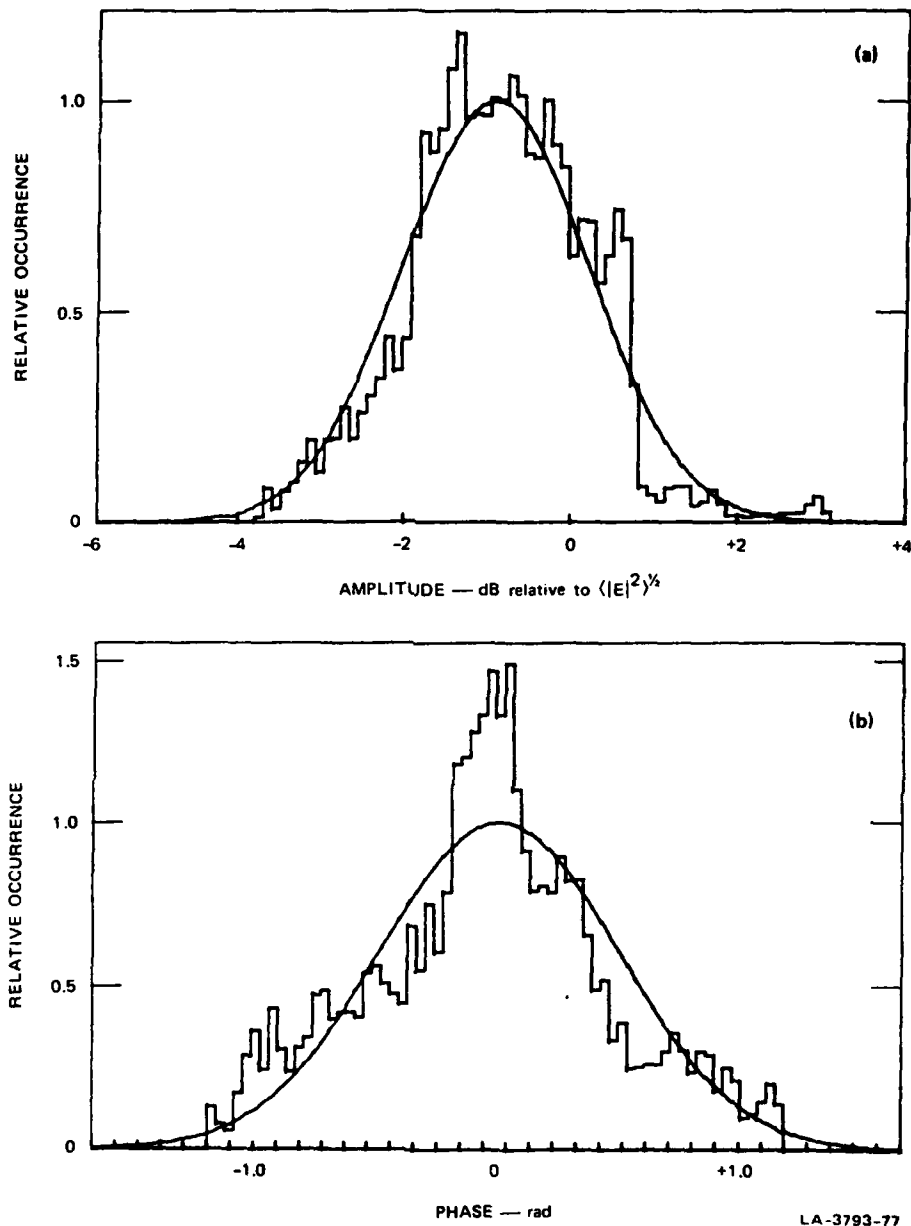


**FIGURE 9** OCCURRENCE HISTOGRAMS OF (a) LOG AMPLITUDE, AND (b) PHASE OF  $E_f$  COMPARED WITH NORMAL DISTRIBUTIONS CALCULATED FROM MEASURED MOMENTS. Data Set 1 (Figure 5).

REFERENCES

Beckman, P., and A. Spizzichino, The Scattering of Electromagnetic Waves from Rough Surfaces, pp. 119-136 (Pergamon Press, New York, N.Y. 1963).

Cohen, M. H., E. J. Gundermann, H. E. Hardebeck, and L. E. Sharp, "Interplanetary Scintillations. II. Observations," Astrophys. J., Vol. 147, No. 2, pp. 449-466 (1967).

Crane, R. K., "Spectra of Amplitude and Phase Scintillation," in Proceedings of the 1975 Symposium on the Effect of the Ionosphere on Space Systems and Communications, Arlington, Va., 20-22 January 1975.

Dyson, P. L., J. P. McClure, and W. B. Hanson, "In Situ Measurements of the Spectral Characteristics of F Region Ionospheric Irregularities," J. Geophys. Res., Vol. 79, No. 10, pp. 1497-1502 (1 April 1974).

Fremouw, E. J., and C. L. Rino, "First-Order Signal-Statistical Modeling of Scintillation," paper presented at the NRL Symposium on The Effect of the Ionosphere on Space Systems and Communication, Washington D.C., 20-22 January 1975.

Hatfield, V. E., and C. L. Rino, "Non-Rician Statistics and Their Implications for Modeling Effects of Scintillation on Communication Channels," paper presented at NRL Symposium on The Effect of the Ionosphere on Space Systems and Communications, Washington, D.C., 20-22 January 1975.

Ishimaru, A. (editor), Radio Science, Special Issue: "Waves in Random Media," Vol. 10, No. 1, (1975).

Little, C. G., "A Diffraction Theory of the Scintillation of Stars on Optical and Radio Wave-Lengths," Mon. Nat. Roy. Ast. Soc., Vol. III, pp. 289-302 (1951).

Mercier, R. P., "Diffraction by a Screen Causing Large Random Phase Fluctuations," Proc. Camb. Phil. Soc., Vol. 58, pp. 382-400 (1962).

Phelps, A. D. R., and R. C. Sagalyn, "Plasma Density Irregularities in the High-Latitude Top Side Ionosphere," J. Geophys. Res., Vol. 81, No. 4, pp. 515-523 (1976).

Rino, C. L., "Some New Results on the Statistics of Radio-Wave Scintillation: B. Scattering from Locally Homogeneous Irregularity Layers," in press, J. Geophys. Res. (1976).

Rino, C. L., and E. J. Fremouw, "Statistics for Ionospherically Diffracted VHF/UHF Signals," Radio Science, Vol. 8, No. 3, pp. 223-233 (1973).

Rino, C. L., R. C. Livingston, and H. E. Whitney, "Some New Results on the Statistics of Radio-Wave Scintillation: A. Empirical Evidence for Gaussian Statistics," in press, J. Geophys. Res. (1976a).

Rino, C. L., E. J. Fremouw, and R. C. Livingston, "The Structure of Signals Undergoing Scintillation as Inferred from ATS-6 and Transit Coherent Beacon Transmissions," paper to be presented at COSPAR Beacon Satellite Group Symposium, Boston, Mass., 1-4 June 1976b.

Rufenach, C. L., "Power-Law Wavenumber Spectrum Deduced from Ionospheric Scintillation Observations," J. Geophys. Res., Vol. 77, No. 25, pp. 4761-4772 (1972).

Wang, T.-I., and J. W. Strohbehn, "Log-Normal Paradox in Atmospheric Scintillations," J. Opt. Soc. Am., Vol. 64, No. 5, pp. 583-591 (1974).

## **Amplitude and Rate Characteristics of Intense Scintillations**

Herbert E. Whitney  
Air Force Geophysics Laboratory (AFSC)  
Hanscom AFB, MA 01731

### **Abstract**

Intense periods of scintillation were analyzed in order to provide design information for evaluation of the performance of satellite communication links. Data is available for the auroral and equatorial regions. The amplitude fluctuations are described by cumulative amplitude distributions and indicate that a Rayleigh distribution is a worst case condition. Rate of fading is described by power spectra and correlation functions.

### **Introduction**

Satellite communication links at UHF can be subject to the effects of ionospheric scintillations which are principally related to the occurrence of F-layer irregularities. Scintillations cause both enhancements and fading about the median level as the radio signal transits the disturbed ionospheric region. When scintillations occur which exceed the fade margin, performance of the communications link will be degraded. This degradation is most serious for propagation paths which transit the auroral and equatorial ionospheres. The degree of degradation will depend on how far the signal fades below the margin, the duration of the fade, the type of modulation and the criteria for acceptability.

The occurrence of scintillations has been studied for several years and its morphology has been documented for the auroral, mid-latitude and equatorial regions<sup>(1,2,3)</sup>. This report concentrates on the analysis of specific periods of intense scintillations and applies the results to the evaluation of communication system performance.

### **Data - Format and Analysis**

Data from Huancayo, Peru and Narssarssuaq, Greenland were used for this study. The data were analyzed in fifteen minute intervals as earlier studies<sup>(4)</sup> had shown that this length was a good choice for scintillation studies using synchronous satellites. The periods covered by each set of data are listed in the following table.

Site	Freq (MHz)	Date	Time (UT)	No. 15 Min. Intervals
Peru	137/360	2Nov74	0315-0500	7
Peru	137/360	5Nov74	0118-0433	10
Narssarssuaq	137	20Jul74	0500-0830	14

This selection of data provided a total of 31 periods of quite intense scintillations. These data were not selected to represent 'worst' case conditions but only a sampling of strong scintillations that can occur in the polar, auroral and equatorial regions. The 360 MHz data from Peru was at a frequency of direct interest to AFSATCOM, while only 137 MHz data was available on magnetic tape from Narssarssuaq. The Peru data was emphasized because it exhibited the strongest scintillation and had two frequencies which provided a measure of the spectral index or frequency dependence of scintillation for this frequency range.

The signal strength level from satellite beacons was recorded on FM analog tape and then digitized at 6 samples per second for computer processing. A relative calibration of the complete receiving and recording equipment was accomplished near the time of each scintillation record.

A computer program was written that provided the following outputs:

- a. IBM plot of the signal level
- b. Cumulative probability amplitude distribution. cdf
- c. Fade rate distributions
- d. Message reliability
- e. Power spectrum
- f. Autocorrelation
- g. Cross-correlation

A 15 minute section of the chart recording at each frequency and the resulting cdf is shown in fig. 1. The cdf is a first order statistic and is useful for defining the minimum margin requirements for the communications link of nondiversity systems. The various scintillation indices defined by Briggs and Parkins<sup>(5)</sup>, i.e.,  $S_1$ ,  $S_2$ ,  $S_3$  and  $S_4$  are calculated for each 15 minute sample.  $S_4$ , which depends on the rms value of the power, is the most commonly used index. The Nakagami m-distribution<sup>(6)</sup> has been shown<sup>(4)</sup> to be practically useful for describing the effects of scin-

tillations on satellite communication links. Christopher<sup>(7)</sup> has described a useful application of the moments of a log-Nakagami distribution. Also calculated for each 15 minute interval are the Nakagami m-value, ( $m = 1/S_4^2$ ); a Chi-square fitness test of the experimental data to both Nakagami and log-normal distributions over the 2-98 percentile range; and the first four moments, MU, of the log-Nakagami pdf. The circles in fig 1 are points for a Rayleigh distribution ( $m = 1$ ) and show the agreement with the experimental data.

In addition to the information on the amplitude of the fades which is given by the cdf, statistical descriptions of the fading rate is needed in order to fully characterize the effects of scintillations on the communications channel. Information on the fading rate can either be produced by level-crossing techniques or by Fourier techniques which produce the power spectra and time correlation functions. The level-crossing data give measurements of the distribution of the fades and enhancements at various levels relative to the median level. The duration and separation of the fades are counted and tabulated against time intervals for 1dB changes in signal level down to -10dB. Intervals shorter than 0.25 second and longer than 60 seconds were not resolved. Fig. 2 shows the distribution of fades below several levels for both 137 MHz and 360 MHz. For this particular sample the occurrence of fades of a given duration at 137 MHz was approximately twice that occurring at 360 MHz. The presentation of enhancements of signals for various levels can be done in a similar manner.

Fig. 3 shows a plot of the message reliability for both frequencies. This gives an estimate of the increase in margin which is required over the value specified by the cdf to obtain a given probability of receiving perfect messages. Message reliability was measured by determining the number of time intervals or messages that completely fit within the signal enhancements or increases above specified calibration levels compared with the total possible number in a 15 minute period. Since the calibration levels are relative to the median level they can represent various values of fade margin. The data sample is long (15 minutes) compared with typical message lengths. Therefore changing the time of synchronization results in only a minor variation to the calculated value of message reliability. As the time interval (message length) approaches zero the message reliability approaches the percentile given by the cdf at that fade level. Therefore the cdf gives the maximum possible value of message reliability. The curves show message reliability approaches zero as the message length increases. For example, for a 4 second message length, approximately 40% of the messages would be perfectly received at the -8dB fade margin level at 137 MHz and 70% at 360 MHz. As the fading rate increases the curves will fall off more rapidly. If the fading rate becomes so rapid that the inter-fade separations are less than the message length, no messages will be received without error.

Fig. 4 shows the 137 MHz and 360 MHz power spectra for this data sample. The rate of the scintillation fading is characterized by the power spectrum. In general the spectral shape consists of a relatively flat low frequency spectrum and a high frequency roll-off with a slope of approximately  $f^{-5}$  for intense scintillations. A 'cut-off' frequency denotes the break point between the low and high frequency slopes. Some spectra had a fairly abrupt transition in the 0.1 to 1Hz range between the low and high frequency bands and the intersection of straight line fits to the slopes give the 'cut-off' frequency. Other spectra did not exhibit a 'cut-off' frequency and only a single slope was measured. The strong discrete lines are associated with the satellite spin modulation.

Fig. 5 shows the 137 MHz and 360 MHz autocorrelation functions for the data sample. The autocorrelation function is another way of characterizing the rate of scintillation fading. It is the Fourier transform of the power spectrum and therefore has a width which is inversely proportional to the bandwidth of the power spectrum where the bandwidth is defined by the 'cut-off' frequency. The autocorrelation interval gives an estimate of the effectiveness of time diversity. Coding techniques can be an effective means of achieving time diversity improvement. The correlation for the full period is plotted and in addition the first 16 seconds is expanded. The correlation interval,  $\tau$ , is printed out for coefficients of approximately 0.5, 0 and at the first inflection point.

Fig. 6 shows the cross-correlation function of the 137 MHz and 360 MHz channels. It indicates the effectiveness of applying frequency diversity techniques to overcome the degradation due to scintillations. The cross-correlation coefficient was less than 0.2 for this sample and also was low ( $< .4$ ) for two other data samples that were analyzed. It is expected that the cross-correlation values would be low for this wide a frequency difference (137/360 MHz) under conditions of intense scintillations. Since Schwartz et al<sup>(8)</sup> indicates only a very small improvement in diversity gain for correlation coefficients between 0.5 and 0 the computation of the cross-correlation function was not done for all the two frequency data. From the standpoint of the needs of the AFSATCOM program it would have been more desirable to have been able to measure the cross-correlation interval for a smaller frequency separation. However, the 137/360 MHz data were the only available two frequency data.

### Results

The Nakagami m-parameter is related to the rms value of the intensity of the scintillations. It completely describes the distribution. Reference 4 has shown that the distribution function of ionospheric scintillations closely approximates the theoretical Nakagami distribution. While m can have any value  $> 0.5$ , all the data that has been analyzed indicates that m=1 is the limiting case

which corresponds to the Rayleigh distribution. The circles in Fig. 1 are points for a Rayleigh distribution, ( $m=1$ ), and show the agreement of the 137 and 360 MHz data with the Nakagami distribution. The Chi-square test indicates that there is a better fit of the data to the Nakagami distribution than to the log-normal distribution. Fig. 7 is a plot of the Nakagami distribution in cumulative form for several values of  $m$ . The experimental data indicates that the Rayleigh distribution or the  $m=1$  curve in Fig. 7 is a limiting case for scintillations in the 200-400 MHz band. Fig. 7 can therefore be used to estimate the expected fading under 'worst' case conditions for various percentiles.

Reference 4 has shown that the spectral index or frequency dependence of scintillations can be related to the  $m$ -parameter in the following way:

$$n_m = \frac{\log^{m_1/m_2}}{\log f_1/f_2} \quad \text{where } n_m \text{ is the spectral index}$$

and  $m_1$  and  $m_2$  are the Nakagami values measured at the two frequencies,  $f$ . This assumes that the scintillation index or  $m$  remains a constant power of frequency over the measurement range. The values of the spectral index were calculated from the measured values of  $m$  for the 17 sets of two frequency data and the distribution is plotted in Fig. 8. While the scintillations at 360 MHz did not have the intensity to actually measure a value of

$n_m = 0$ , it is expected that this could be achieved as the 'worst' case condition. There were several measured values of  $n_m$  in the lowest range of 0.2 which indicates very little decrease of scintillation intensity with frequency. This is another indication that the 'worst' case fading in the 200-400 MHz band can be approximated by a Rayleigh distribution.

In addition to the information on the depth fading, information on the rate of fading is also required to fully understand the effects of scintillation on the communications channel. The statistics on the fading rates has been measured and presented in three ways: (1) the autocorrelation function, (2) the power spectrum, and (3) the tabulation of the results of the level crossing technique in the form of the duration of fades below and increases above given levels and message reliability. Since time diversity is effectively achieved in the application of coding techniques to the AFSATCOM system, it is felt that the autocorrelation information is the easiest to apply in evaluating the fade rate data.

When correlation data is available it can be used to determine the improvement in performance that can be obtained through the application of diversity techniques. Autocorrelation data can be used to evaluate time diversity techniques; cross-correlation data from multifrequency measurements can be used to evaluate the effectiveness of frequency diversity; and, if spaced receiver measurements are available, then the cross-correlation information can

evaluate space diversity. Fig. 9 is adapted from Ref. 8 and shows the improvement in performance that is possible with dual-diversity techniques. The probability of achieving diversity gain is given for several values of  $\rho$ , the correlation coefficient. It is based on slow, multiplicative Rayleigh fading and equal signal-to-noise ratios in both branches of a dual diversity system. Ref. 8 used  $|\rho|$ , the magnitude of the complex cross-correlation, while Fig. 9 uses the envelope cross-correlation. Most of the diversity improvement is achieved by the time  $\rho = 0.6$ . For example the improvement at the 1% point is approximately 8 dB for  $\rho = 0.6$  and 10dB for  $\rho = 0$  or complete decorrelation.

The correlation intervals for  $\rho = 0.5$  of the 17 sets of 137/360 MHz data are plotted in Fig. 10 to show the relationship that holds for this very limited set of data. For small delays the 360 MHz value is approximately twice the 137 MHz value. At longer delays the values tend to be the same.

The variation of the correlation interval with intensity of scintillation is shown in Fig. 11. The measured values at each frequency for the 17 sets of data are plotted against the Nakagami m-parameter which was measured from the corresponding cdf. An ellipse has been drawn to encompass the data at each frequency and an axis drawn to give the apparent variation with m.

The values of the correlation interval for the Narssarssuaq data were generally greater than for the Peru data, even though they were both measured at the same frequency, 137 MHz. It is felt that this is not a difference between the equatorial and auroral regions but rather it is caused by the Narssarssuaq data having less intensity of scintillations than the Peru data.

#### Conclusions and Recommendations

From a large collection of observations a limited amount of VHF/UHF data has been analyzed to determine the amplitude and rate characteristics of intense scintillations. The results are in the form of amplitude distributions, level crossing tabulations, power spectra and correlation data. While a Rayleigh distribution was not exactly measured, it was judged that this would be the limiting case up to at least 400 MHz. This is in agreement with the spectral index data which indicated that fading of the most intense samples was almost independent of frequency. The auto-correlation and power spectra data defined the fading rates and provided a base for the evaluation of time diversity techniques. Only three samples of cross-correlation (137/360 MHz) were processed and coefficients less than 0.4 were obtained. However, this frequency separation was really too great to determine the applicability of frequency diversity techniques within the bandwidth normally available to satellite communication systems.

Much remains to be done to characterize the intense scintillations that are observed in the equatorial region. Multi-frequency observations are necessary to determine the frequency dependence and the evaluation of diversity techniques in the UHF range.

1. Aarons, J., Whitney, H.E., and Allen, R.S. (1971) Global Morphology of Ionospheric Scintillations, Proc. IEEE 59:159
2. Crane, R.K. (1974) Morphology of Ionospheric Scintillation, Technical Note. Lincoln Laboratory, 1974-29, Air Force Contract F19628-73-C-0002.
3. Aarons, J. (1975) Global Morphology of Ionospheric Scintillations II, AFCRL-TR-75-0135.
4. Whitney, H.E., Aarons, J., Allen, R.S. and Seeman, D.R. (1972) Estimation of the Cumulative Amplitude Probability Distribution Function of Ionospheric Scintillations, Radio Science 7:1095-1104 Vol. 7 No. 12.
5. Briggs, B.H. and Parkin, I.A., (1963) On the Variation of Radio Star and Satellite Scintillations with Zenith Angle, J. Atmos. Terr. Phys., 25, 330-366.
6. Nakagami, M. (1960), Statistical Methods, in Radio Wave Propagation, edited by W.C. Hoffman, pp. 3-36, Pergamon, N.Y.
7. Christopher, P., Moments of a Log-Nakagami Distribution and Application, Mitre Corporation Memo D91-M-4025, 20 March 1975.
8. Schwartz, M., Bennet, W.R., and Stein, S., (1966) Communication Systems and Techniques McGraw-Hill

### Figure Captions

- Fig. 1. Example of intense scintillations recorded on 137 and 360 MHz and resulting cumulative amplitude distributions. A Rayleigh distribution as indicated by the circles.
- Fig. 2. Distribution of the fade durations for the period of intense scintillations shown in fig. 1.
- Fig. 3. Effect of the scintillations in fig. 1 on the reception of perfect messages for various message lengths.
- Fig. 4. Typical power spectra for intense scintillations.
- Fig. 5. Typical autocorrelation data for intense scintillations.
- Fig. 6. Typical cross-correlation plot for 137 and 360 MHz scintillations.
- Fig. 7. Cumulative form of the Nakagami m-distribution valid for  $m > 0.5$ .
- Fig. 8. Occurrence of spectral index values which were calculated from the measured m-values of 17 sets of simultaneous 137 and 360 MHz scintillations.
- Fig. 9. Effectiveness of dual-diversity techniques for various degrees of correlation under conditions of Rayleigh fading.
- Fig. 10. Relationship of the 137 and 360 MHz correlation intervals for  $\rho = 0.5$ .
- Fig. 11. Variation of the correlation interval with intensity of scintillations.

0400 UT ATS - 6 137 / 360 MHz HUANCAYO, PERU NOV. 2, 1974 0345 - 0400 UT  
0355 0350 0345

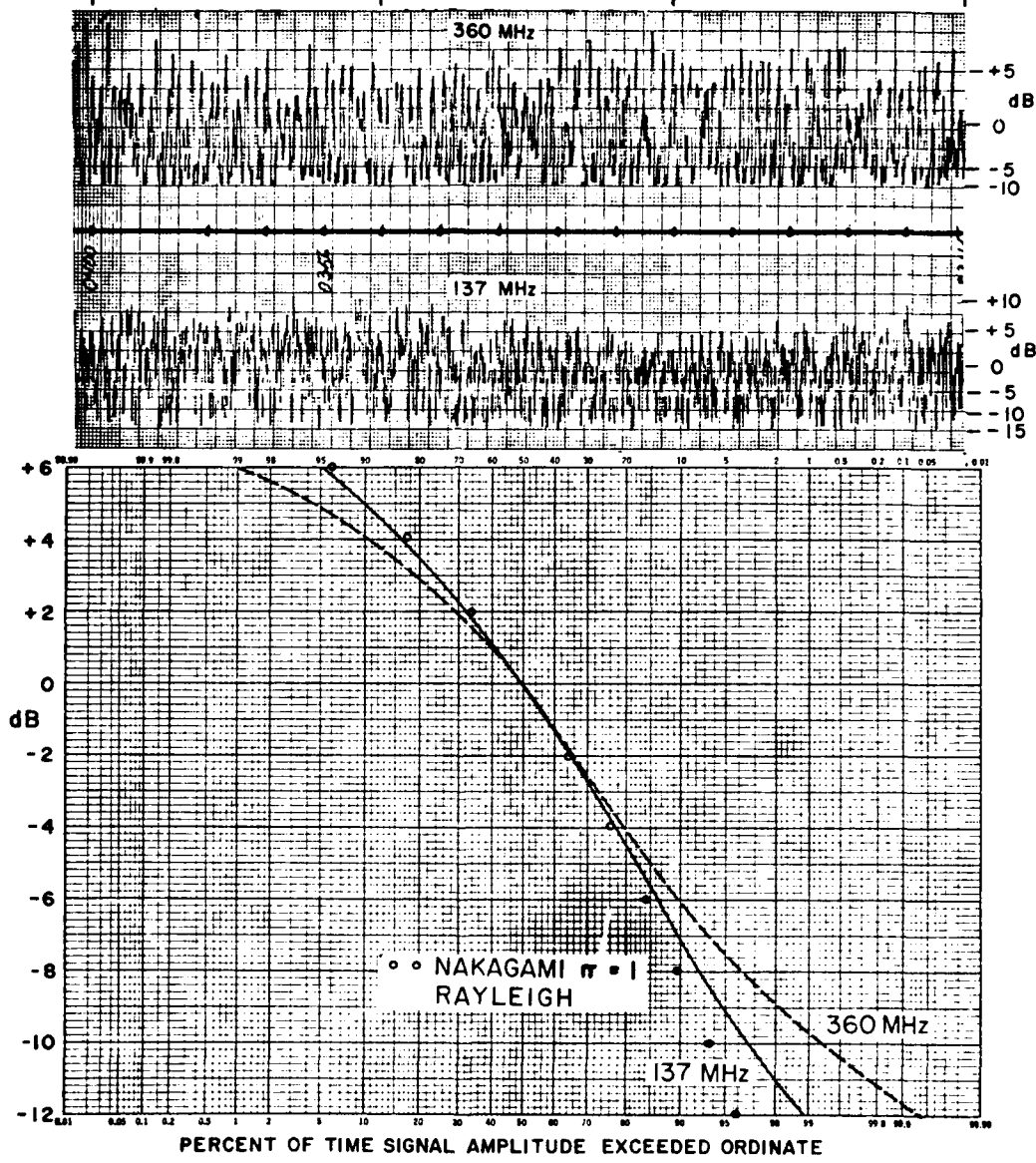


FIG. I

CUMULATIVE DISTRIBUTION OF FADE DURATIONS

ATS-6 2 NOV. 1974 0345 - 0400 UT

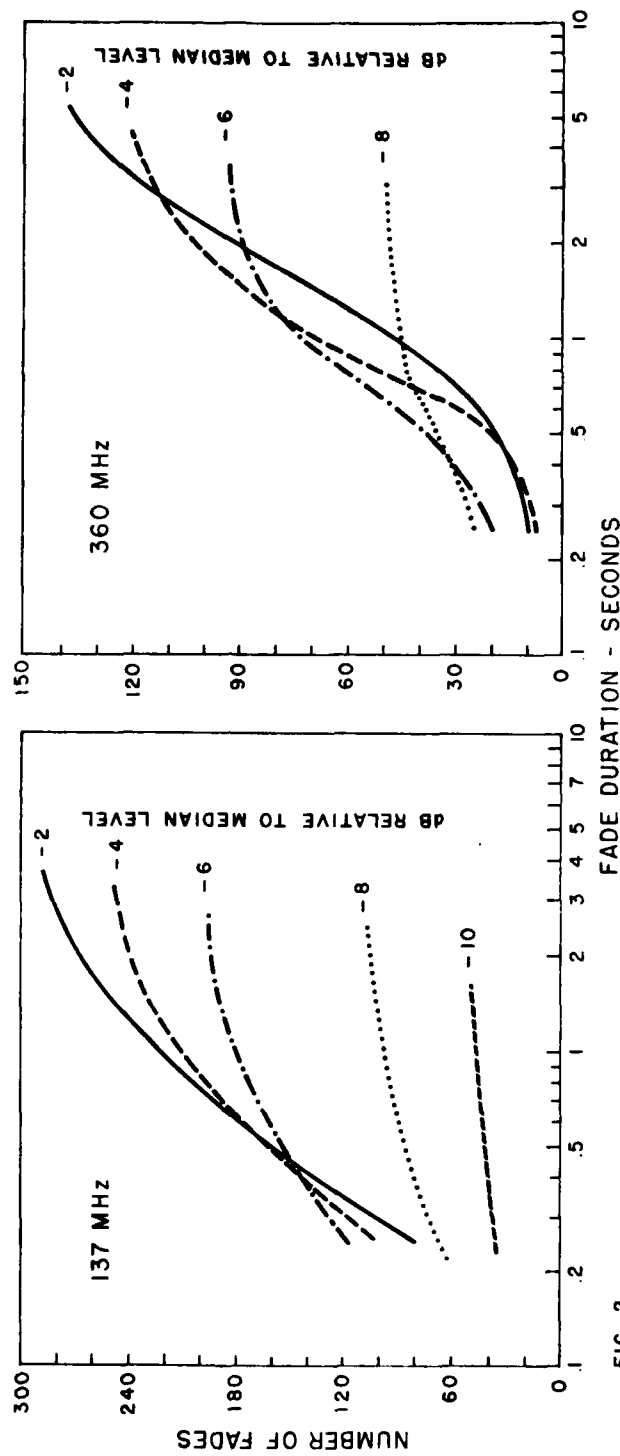


FIG. 2

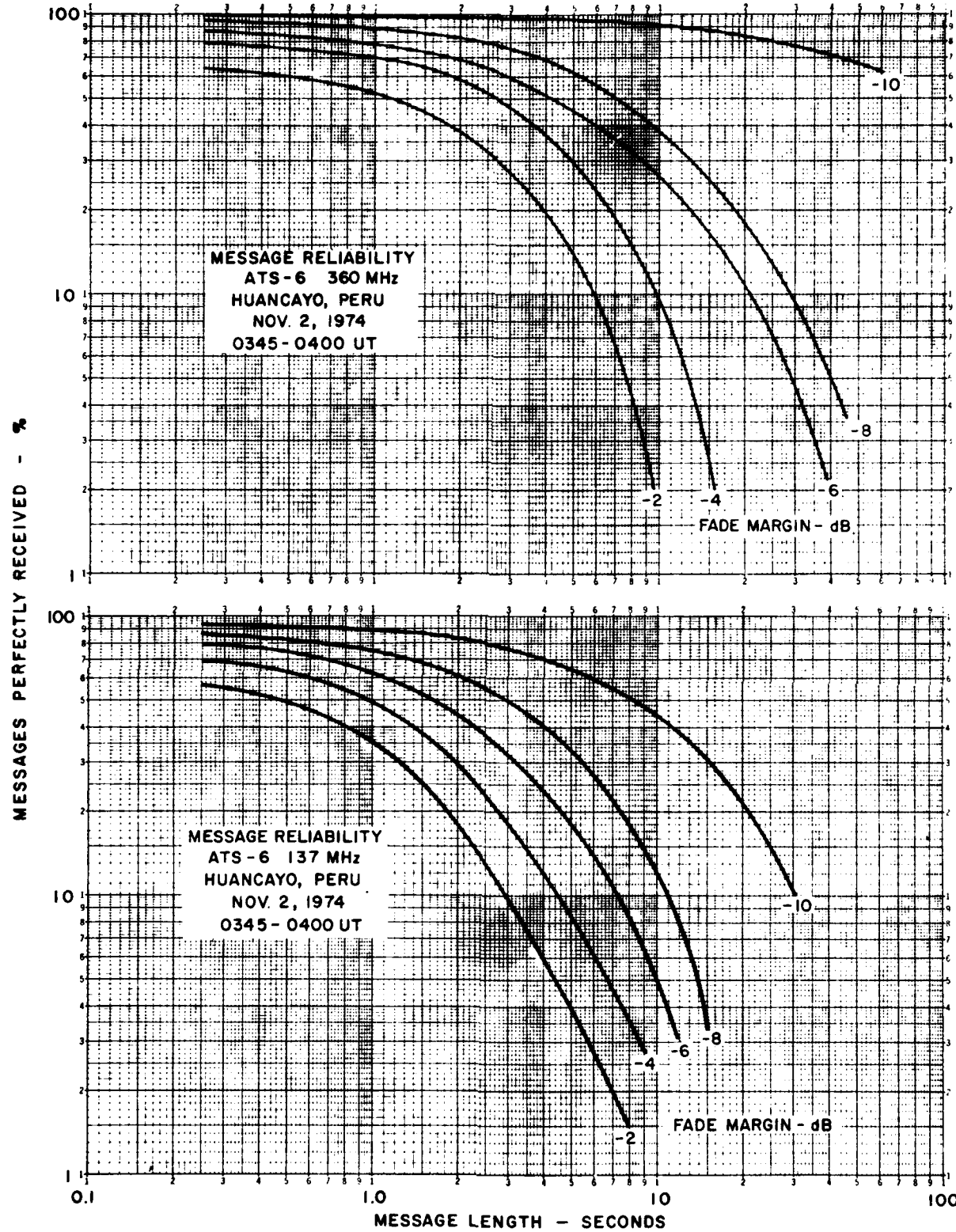


FIG. 3

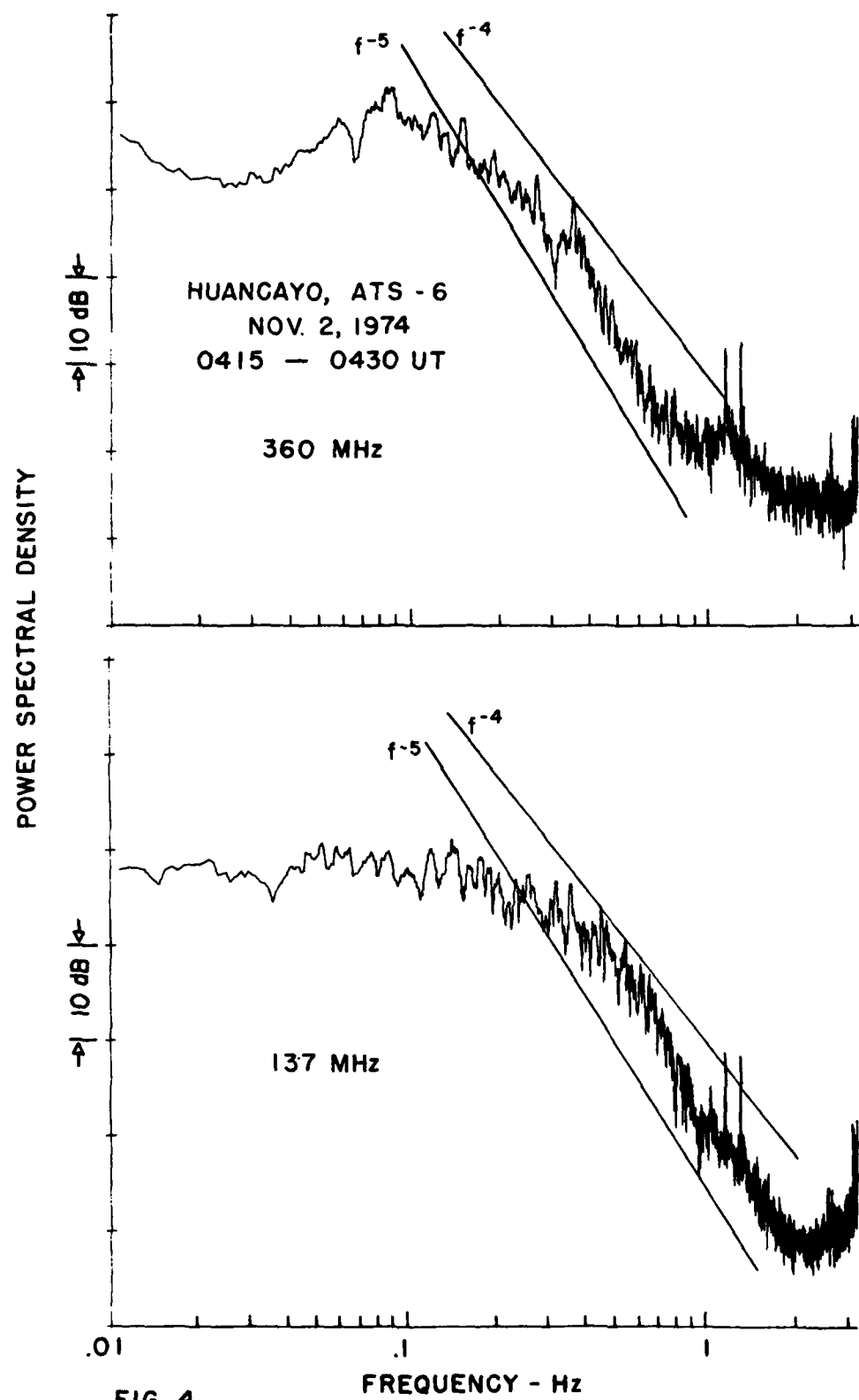


FIG. 4

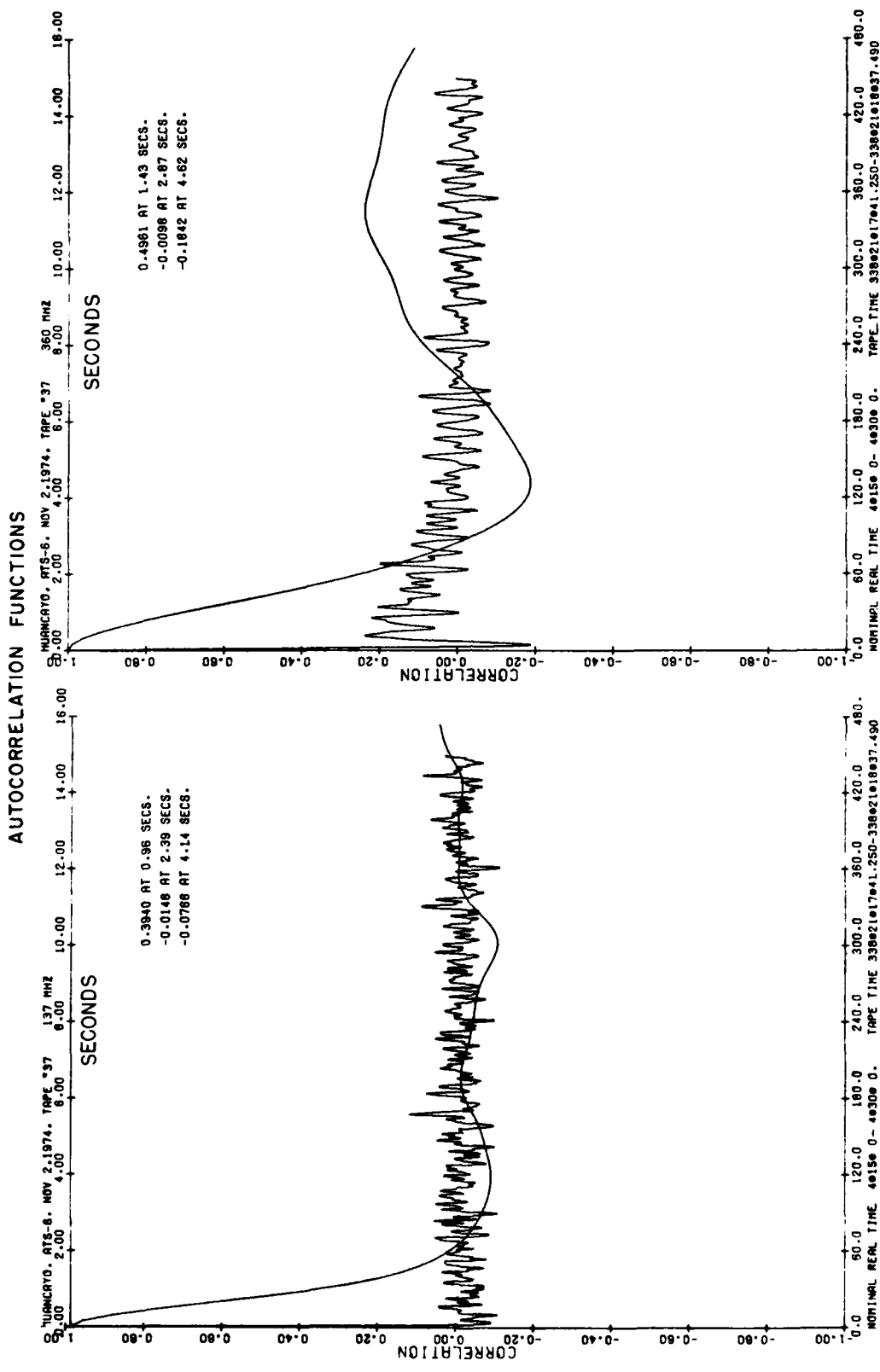


FIG. 5

CORRELATION INTERVAL -  $\tau$  (SECONDS)

CROSS-CORRELATION FUNCTION

MURCAYO, ATS-6, NOV 2-1974, TAPE #37      137 MHz vs. 360 MHz

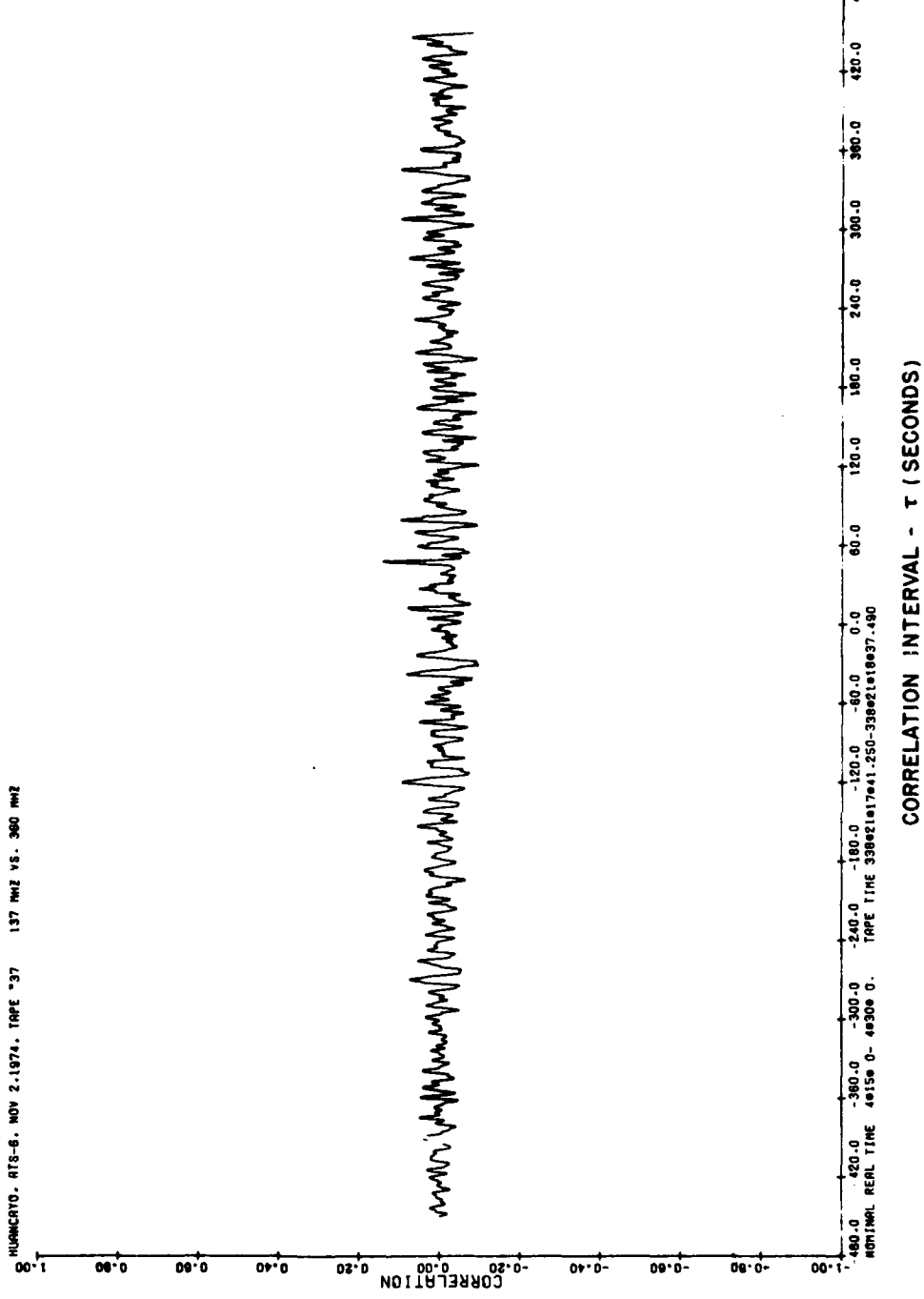


FIG. 6

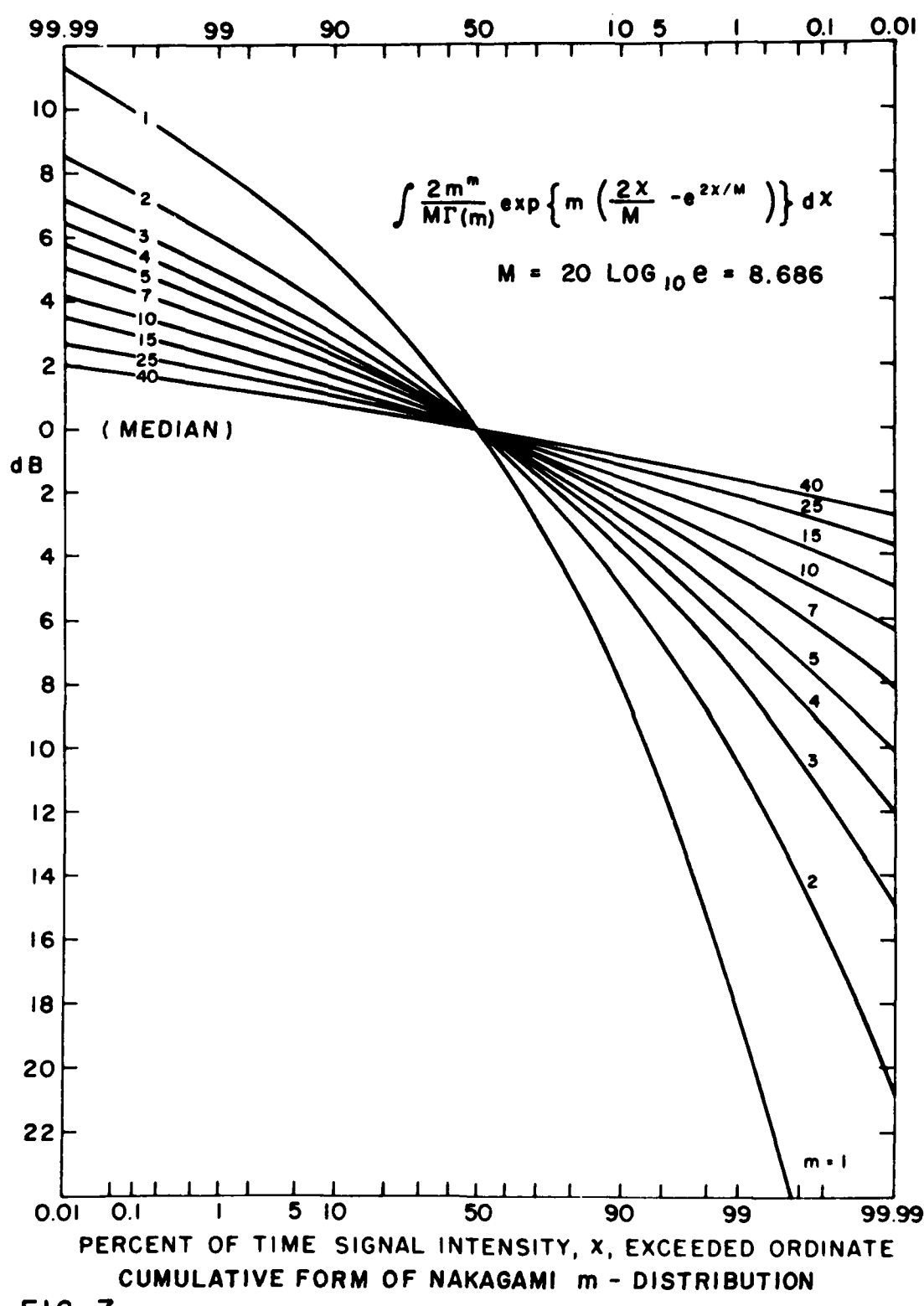


FIG. 7

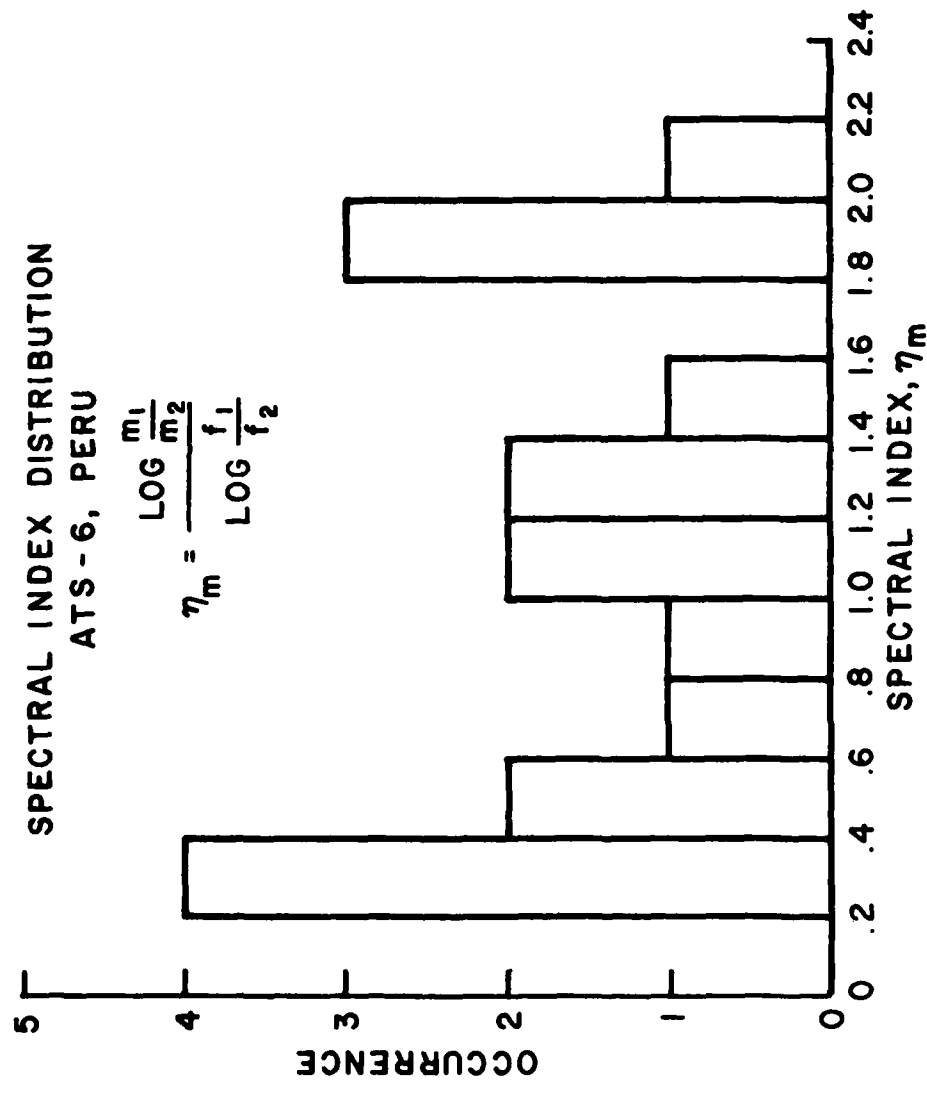


FIG. 8

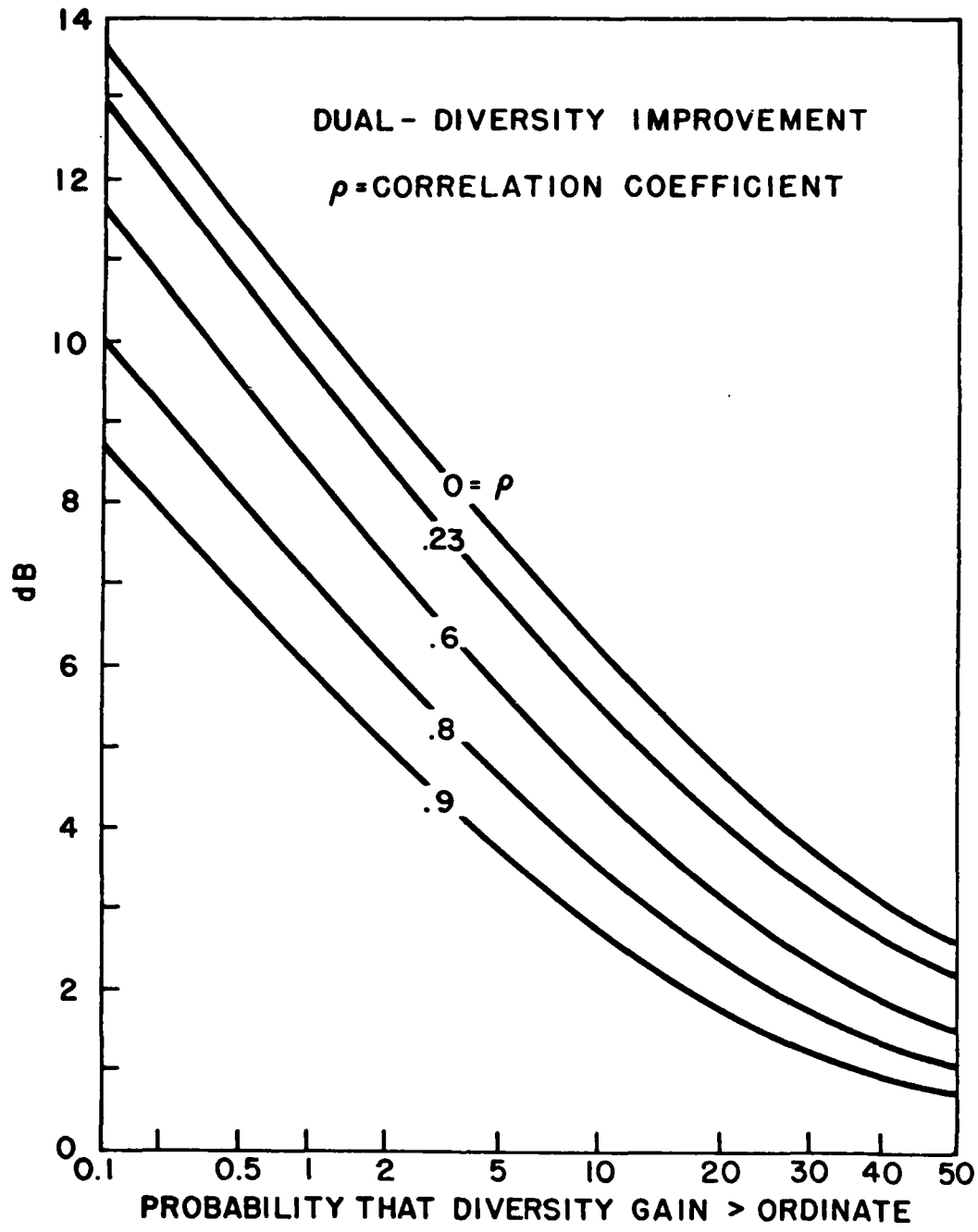


FIG. 9

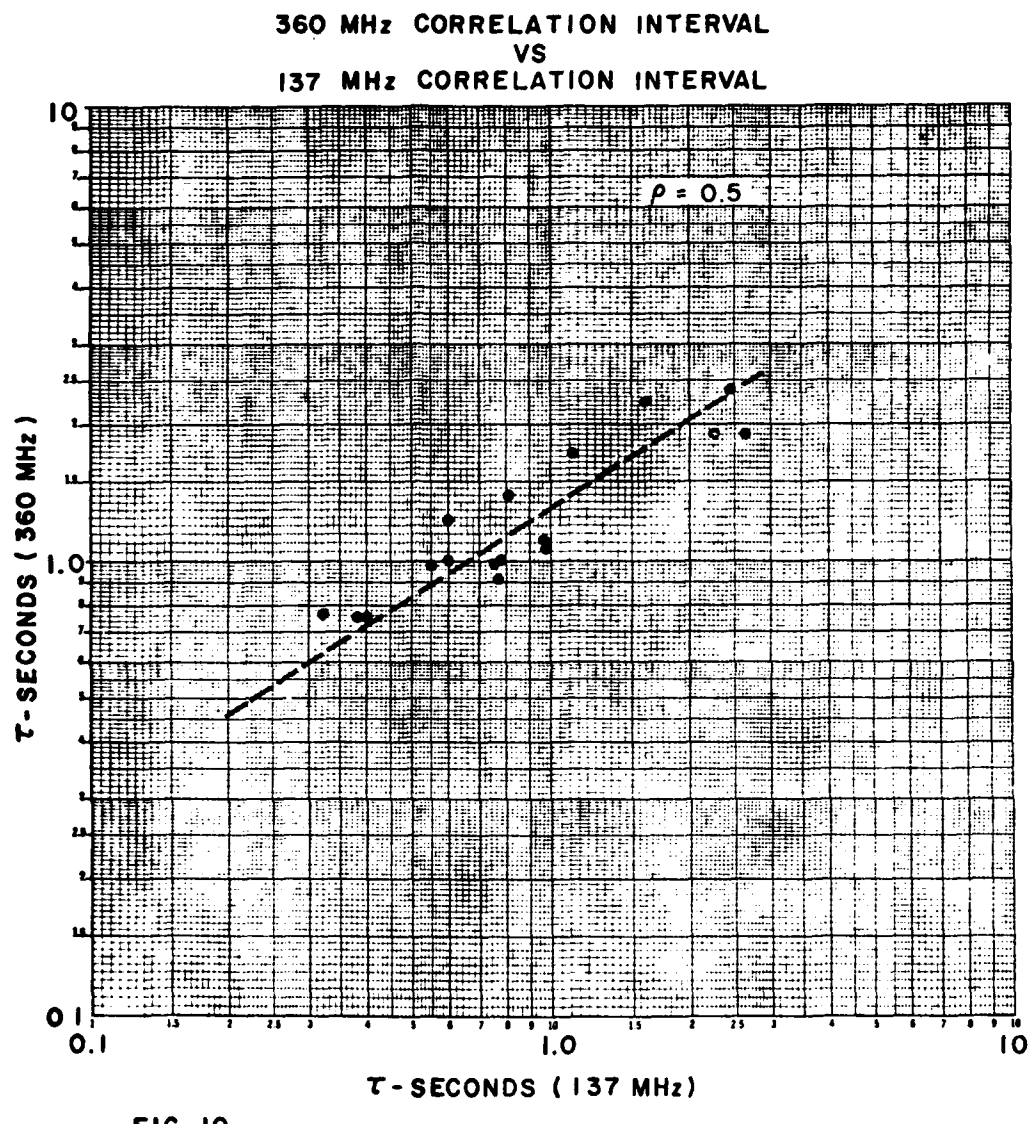


FIG. 10

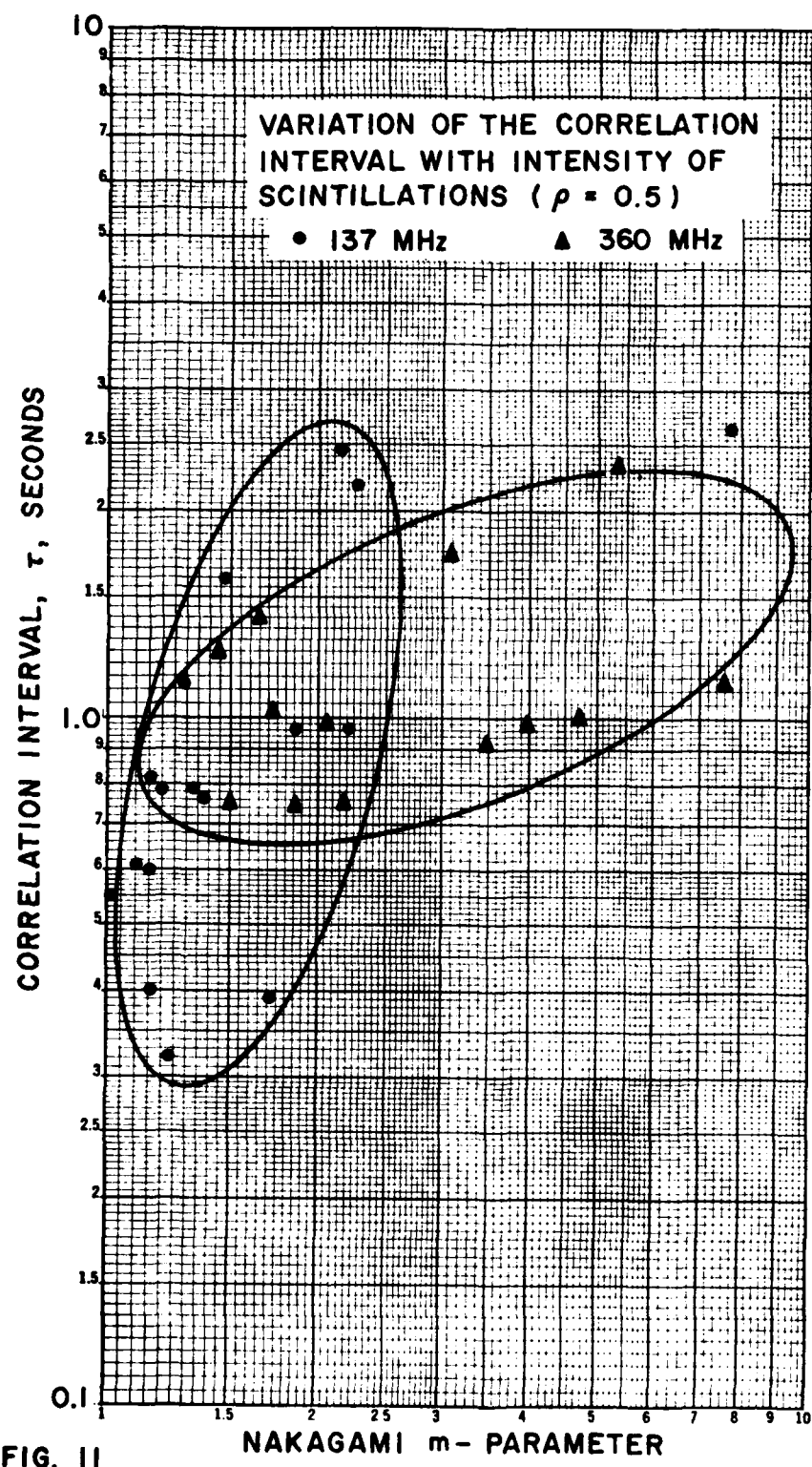


FIG. II

Correlated Measurements of Scintillations and  
In-Situ F-Region Irregularities from OGO-6

Sunanda Basu\*  
Air Force Geophysics Laboratory  
Air Force Systems Command  
Hanscom AFB, MA 01731

S. Basu<sup>+</sup>  
Emmanuel College  
Boston, MA 02115

Abstract

Near simultaneous in-situ measurements of F-region irregularities obtained from Ogo-6 satellite and ground based scintillation observations at 137 MHz and 6 GHz are available over the American and African sectors for selected days in the period November-December, 1969 and November, 1970. Scintillation estimates obtained from in-situ irregularity measurements are compared with scintillations actually recorded on ground to obtain information regarding the spectral characteristics of equatorial irregularities. In general, the equatorial irregularity amplitudes, particularly at Legon in the African sector, are large so that a monotonic power law spectrum for the irregularities with a spectral index of 4 and an outer scale dimension of 20 km yields scintillation estimates large enough to be in the multiple scatter regime. Simultaneous VHF scintillation measurements at Legon indicate the effects of saturation in agreement with the estimates.

The observed irregularity amplitude and ambient electron density are also found to be large enough near Ascension Island and Tangua, Brazil so that 6 GHz scintillations at these stations can be explained on the basis of a weak-scatter theory and the previously assumed monotonic power law irregularity spectrum. However, at Huancayo, the irregularity amplitudes are sometimes not large enough to explain even the VHF scintillation measurements on the basis of the above irregularity characteristics. This disagreement is discussed on the basis of magnetic declination in the Huancayo sector in relation to the orbital inclination of Ogo-6.

\*NRC Resident Research Associate

<sup>+</sup>On leave from the University of Calcutta

## Introduction

The observation of unexpected ionospheric scintillations at frequencies up to 6 GHz in the vicinity of the magnetic equator (Taur, 1973) has lead to an in-depth study of spectral characteristics of both in-situ and scintillation measurements. Both types of measurements have been interpreted in terms of a power law variation in wavenumber spectrum (Rufenach, 1974; Dyson et al., 1974). Though a continuous power-law type of wavenumber spectrum between an outer and inner scale is the most generally observed spectral characteristic, Dyson et al. (1974) found occasionally the existence of wavelike irregularities near the magnetic equator which yielded a non-monotonic form of irregularity spectrum. Wernik and Liu (1974) also postulated a non-monotonic spectrum to explain the magnitude as well as frequency dependence of 4 and 6 GHz scintillation. Rufenach (1975) has pointed out that such inferred spectral shapes must be considered tentative until simultaneous in-situ and scintillation measurements are available.

In this study, we wish to present such correlated scintillation and in-situ irregularity measurements made in the equatorial region. The in-situ observations were obtained from the retarding potential analyzer (RPA) on board the Ogo-6 satellite while the scintillation observations were obtained from Legon and Huancayo at a frequency of 137 MHz during November-December, 1969. We were also fortunate enough to obtain a limited amount of data at 6 GHz from Ascension Island and Tangua on a few days in November, 1970. These near-simultaneous measurements are examined to obtain information regarding the scattering regime as well as constraints on the form of irregularity spectrum.

## Results

In order to obtain equivalent scintillation indices from in-situ F-region irregularity measurements, it is necessary to use either diffraction or scattering theory. Basu et al., (1976) have provided a detailed discussion for such conversion on the basis of a thin phase screen approximation using Rufenach's (1975) equations. They also obtained a statistical model of equatorial scintillations from these in-situ measurements which is shown in Figure 1. Here we shall present a comparison between actual scintillation measurements and that estimated from individual closely matched Ogo-6 passes to determine the scattering regime. Also the high resolution RPA irregularity waveform data will be used to indicate the irregularity spectrum in such cases.

a) VHF Scintillation Observations at Legon

From Figure 1 we note that Legon is situated in a high occurrence zone of scintillations. In fact, a statistical comparison presented by Basu et al (1976) showed that Legon observes scintillations  $> 7.5$  dB for 80% of the time during November-December 1969 in the time slot 1900-2300 LT. These statistics were based on ATS-3 observations at 137 MHz at an elevation angle of  $38^\circ$  corresponding to ionospheric zenith angle  $x = 48^\circ$ . Figure 2 shows an Ogo-6 pass on November 14, 1969 close to the ionospheric intersection point of Legon ( $5^\circ$  S dip latitude,  $4^\circ$  W longitude). The arrow marks the latitude position of Legon. The irregularity amplitude  $\Delta N/N$  at that position is 100% and the corresponding ambient density  $N$  is  $6 \times 10^{11} \text{ m}^{-3}$ . There is a considerable amount of  $\text{Fe}^+$  ion present though not exactly at the location of Legon. Since there is a small difference in longitude between the equatorial crossing and the intersection point (about  $5^\circ$ ) we utilized the 5%  $\Delta N/N$  observed over  $-20^\circ$  to  $+10^\circ$  dip rather than the sharp peak amplitude of 100% and obtained  $S_4 > 1$  in conjunction with the other model parameters ( $L_o$ , outer scale;  $\alpha$ , axial ratio;  $\psi$ , propagation angle;  $L_e$ , layer thickness;  $z$ , slant range) shown in Figure 2. We wish to emphasize that Rufenach's (1975) equation is invalid for such large levels of scintillation and the  $S_4$  figure is quoted merely to give an idea of the saturation condition represented by the computations. At the same time the scintillation index (Whitney et al, 1969) reported by Legon is 90% (J. R. Koster, private communication, 1975), a value also close to saturation. Thus an irregularity amplitude of 5% is capable of producing saturation even with a large outer scale  $L_o$  of 20 km. Since the amplitudes observed in this sector are usually much greater than 5%, it is evident that saturation is the rule rather than the exception during this time period for any reasonable value of irregularity layer thickness  $L_e$ .

b) GHz Scintillation Observations at Ascension Island & Tangua

Systematic observations of microwave scintillations at frequencies of 4 and 6 GHz started from September, 1970 using the INTELSAT network (Craft and Westerlund, 1972). The occurrence of scintillations at these frequencies is considered to be a problem for space communications and it is important to understand their mechanism. Taur (1973) found that GHz scintillations occur sporadically in the early evening hours after local sunset at equatorial stations.

In Figure 3 we show an Ogo-6 pass on November 18, 1970 which is very close to the intersection point ( $15^\circ$  S dip latitude,  $15^\circ$  W longitude) of the ray path from Ascension Island (AS). The large irregularity structure is not symmetrical over the equator and extends from the equator to  $20^\circ$  S dip latitude. At the position of Ascension Island a very large irregularity of 70% amplitude is observed. On the same day, the scintillation at 6 GHz ranged between 1 to 2 dB during 2040 to 2330 LT (R. Taur, private communication, 1976). The Ogo pass occurred

at 2220 LT and using the same model parameters as used for the VHF case it was found possible to obtain  $S_4 = .08$  equivalent to 1.1 dB. Thus no special tailoring of the spectra such as a decrease of the outer scale size or introduction of a bump was found necessary to explain the observed magnitude of 6 GHz scintillation. If at anytime during that evening the irregularity amplitude had become as large as 100% it would be possible to model a 2 dB scintillation magnitude leaving all other model parameters unaltered. Considering the fact that the Ascension Island observations were essentially for overhead conditions (ionospheric zenith angle  $x = 14^\circ$ ) it seems quite possible to model 6 GHz scintillations up to 3 dB simply by considering a low elevation angle geometry with similar irregularity characteristics. The magnitude of scintillations rarely exceeds 3 dB at 6 GHz (Taur, 1973). Thus, based on such a limited comparison we may infer that GHz scintillations may be explained by a monotonic power law spectra with large outer scale of 20 km if the irregularities are assumed to be undiminished in intensity over a region of 200 km. It should be noted that the height of the satellite varied between 450 and 550 km over the magnetic equator in the large irregularity region where a high ambient density was simultaneously measured. Now, current radar and rocket observations indicate that equatorial irregularities are created in the bottomside and are buoyed up to the topside against gravity thus creating small scale irregularities (Woodman and La Hoz, 1976; Kelley et al, 1976). If this is coupled with the information obtained from this Ogo-6 orbit, we may be justified in using a relatively thick irregularity layer lying between 350 and 550 km.

In Figure 4, we show two consecutive Ogo-6 orbits obtained on November 25, 1970, straddling the Ascension Island longitude. From the position of the arrow we note that the large irregularity structure observed over the equator in both orbits do not reach the  $15^\circ$  S dip latitude intersection point of Ascension Island. No GHz scintillation was observed that evening (R. Taur, private communication, 1976).

An Ogo-6 orbit on November 4, 1970 close to the Tangua, Brazil intersection point ( $10^\circ$  S dip latitude,  $40^\circ$  W) is shown in Figure 5. There were several periods of 6 GHz scintillation reported earlier that evening with the last one of 1 dB magnitude observed between 2331-2350 LT (R. Taur, private communication, 1976). The Ogo-6 transit occurred 20 minutes later and it is interesting to note from Figure 5 that the computed scintillation is  $\ll 1$  dB in agreement with the GHz observation. The irregularity amplitude at Tangua is 10% while the ambient density observed is  $1.4 \times 10^{12} \text{ m}^{-3}$ . An irregularity amplitude of 50% would have produced a 1 dB level of scintillation at this density. Thus it seems that an actual decay of the irregularity amplitude rather than the ambient density is responsible for the absence of scintillation

at the time of the Ogo-6 orbit. Recent observations (Woodman and La Hoz, 1976) have shown that irregularity plumes rising into the topside are generally observed between the post-sunset and pre-midnight hours.

c) VHF Scintillations at Huancayo

The stations that have so far been used for comparison with matched Ogo-6 orbits have all been in longitude sectors where the declination of the earth's magnetic field has been westwards as may be observed from Figure 1. As a matter of fact all three stations, Legon, Tangua and Ascension Island are situated near the position of maximum westward declination of  $18^{\circ}$  found in the vicinity of the magnetic equator. The orbital inclination of Ogo-6 is  $82^{\circ}$  so that in sectors with large westward declinations the Ogo-6 orbits cut magnetic field lines at a considerable angle. In the Huancayo sector and further west, the declination is eastwards which makes the magnetic field lines almost exactly parallel to the Ogo-6 orbits. This has important implications for the interpretation of the in-situ data as we shall show in the following section.

An Ogo-6 orbit on November 13, 1969 in the Huancayo sector ( $0^{\circ}$  dip latitude,  $75^{\circ}$  W) is shown in Figure 6 during the time when the Huancayo station reported a scintillation index of 100% for several hours. Using the model parameters indicated earlier we find that the computed  $S_4$  index is in disagreement with the observed saturated scintillations at 137 MHz.

The detailed irregularity wave forms obtained near the Huancayo intersection point for the orbit shown in Figure 6, as well as those obtained near Legon in the orbit of Figure 2, are depicted in Figure 7. The dots (each separated by 1.1 km) are obtained from the electrometer output while the line output obtained from the differential amplifier has a spatial resolution of one-third of the dots (McClure and Hanson, 1973). The dots are displayed on a relative amplitude scale of 0, 1, 2 while the solid line differential amplifier often saturates at less than  $\pm 5\%$ . It may be observed from Figure 7 that while the irregularity waveforms have only large wavelength components, the orbit in the Legon sector shows that spectral power exists over a much larger range of wavelengths particularly at the small wavelength range  $< 1$  km. It is to be noted, however, that simultaneous ground-based measurements for both these orbits show the occurrence of 100% scintillations at 137 MHz.

An examination of many other such orbits in the Huancayo sector and in other regions of eastward declination (particularly around  $180^{\circ}$  longitude) shows that the irregularity waveforms tend to be sinusoidal in character with the irregularity wavelengths being of the order of a few km. For such orbits

also the irregularity amplitudes show much less randomness as evidenced by the close agreement of the five point average thick line with the fine line showing individual irregularity measurements. It is our tentative conclusion that the sinusoidal spectra obtained by Dyson et al (1974) were most probably seen in orbits which were aligned along the magnetic field. The origin of this sinusoidal structure along magnetic lines should provide further clues for the determination of processes creating these irregularities.

#### Acknowledgement

We wish to thank Professor W. B. Hanson and Dr. J. P. McClure for generously making their Ogo-6 RPA data available to us and for many helpful discussions. Dr. J. Aarons kindly put the Huancayo scintillation data at our disposal and contributed many discussions on the scintillation problem. Professor J. R. Koster and Dr. R. Taur kindly provided their respective VHF and GHz observations.

#### References

- Basu, Sunanda, S. Basu and B. K. Khan, Model of equatorial scintillations from in-situ measurements, submitted for publication to Radio Science, 1976.
- Craft, H. D. and L. H. Westerlund, AIAA Paper No. 72-179, American Institute of Aeronautics and Astronautics Library, 750 Third Avenue, New York, 1972.
- Dyson, P. L., J. P. McClure and W. B. Hanson, J. Geophys. Res., 79, 1495, 1974.
- Kelley, M. C., G. Haerendel, H. Kappler, A. Valenzuela, B. B. Balsley, D. A. Carter, W. L. Ecklund, C. W. Carlson, B. Hausler and R. Torbert, Evidence for a Rayleigh-Taylor type instability and upwelling of depleted density regions during equatorial spread-F, submitted for publication to Journal of Geophysical Research Letters, 1976.
- McClure, J. P. and W. B. Hanson, J. Geophys. Res., 78, 7431, 1973.
- Rufenach, C. L., J. Geophys. Res., 79, 1562, 1974.
- Rufenach, C. L., Radio Science, 10, 155, 1975.
- Taur, R. R., Comsat Tech. Rev., 3, 145, 1973.
- Wernik, A. W. and C. H. Liu, J. Atmos. Terr. Phys., 36, 871, 1974.
- Woodman, R. F. and C. La Hoz, Radar observations of F-region equatorial irregularities, submitted for publication to Journal of Geophysical Research, 1976.

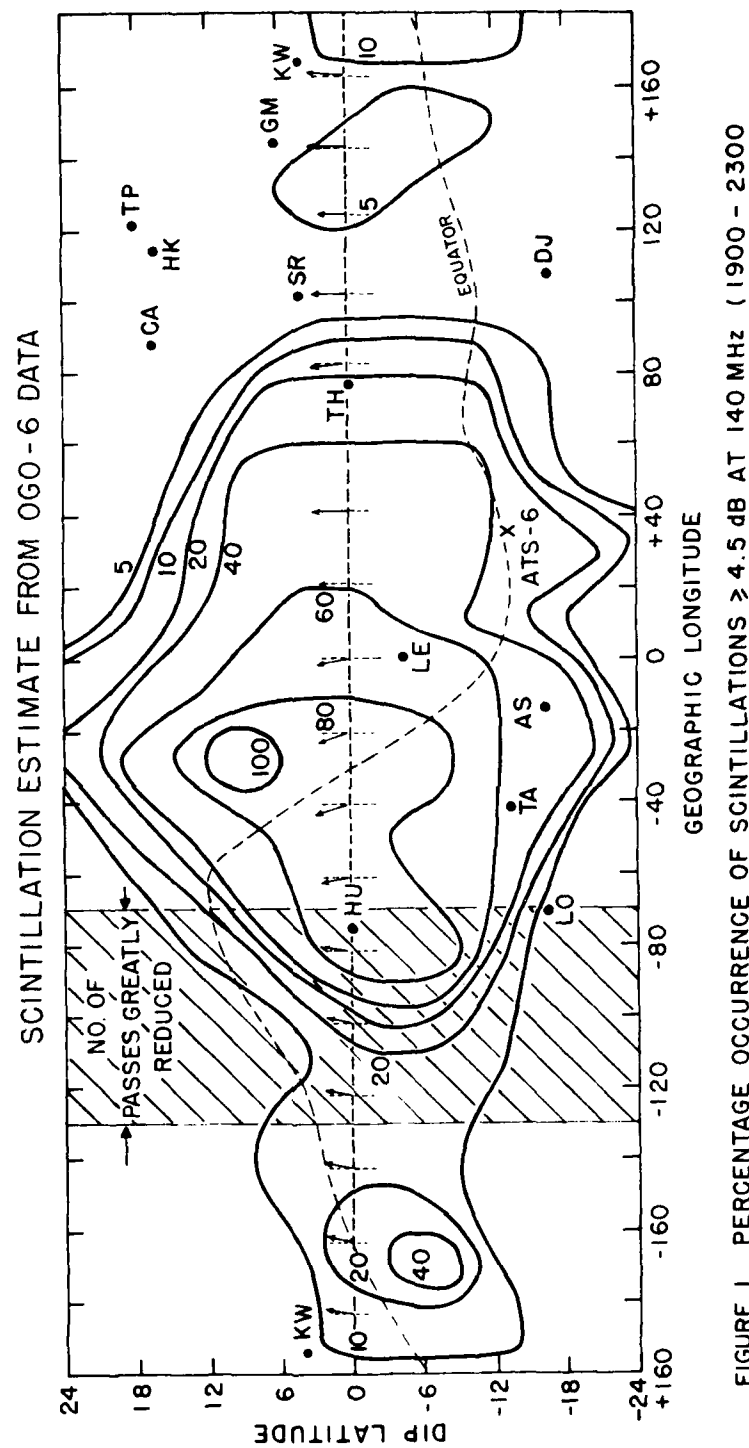


FIGURE 1. PERCENTAGE OCCURRENCE OF SCINTILLATIONS  $\geq 4.5$  dB AT 140 MHz ( 1900 - 2300 LMT, NOV - DEC 1969, 1970 )  $A_p \leq 12$

$$\Delta N = 3 \times 10^{10} \text{ m}^{-3}$$

$$L_o = 20 \text{ km}$$

$$\alpha = 5; \psi = 81^\circ$$

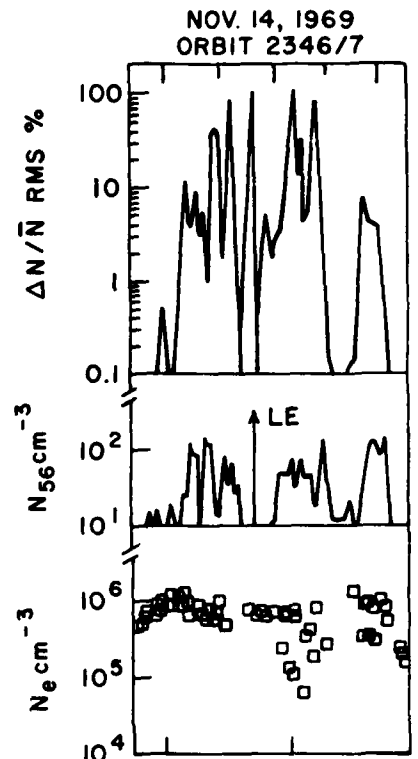
$$L_e = 200 \text{ km}$$

$$x = 47^\circ$$

$$z = 700 \text{ km}$$

COMPUTED  $S_4 > 1$  AT 137 MHz

OBSERVED SI = 90% AT 137 MHz  
BETWEEN 1950 - 0220 LT



LT	22.16	22.29
----	-------	-------

LNG	-10.97	-9.14
-----	--------	-------

LAT	-15.00	8.27
-----	--------	------

ALT	452.92	402.43
-----	--------	--------

UT	22.76	22.86
----	-------	-------

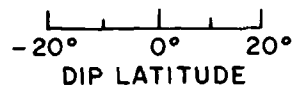


FIGURE 2. OGO-6 ORBIT IN LEGON SECTOR DURING VHF SCINTILLATION EVENT.

$\Delta N = 7 \times 10^{11} \text{ m}^{-3}$   
 $L_0 = 20 \text{ km}$   
 $\alpha = 5, \downarrow = 53^\circ$   
 $L_e = 200 \text{ km}$   
 $x = 14^\circ$   
 $Z = 450 \text{ km}$

COMPUTED  $S_4 = .08$  (1.1 dB) AT 6 GHz  
 OBSERVED SI = 1-2 dB AT 6 GHz  
 BETWEEN 2040 - 2330 LT

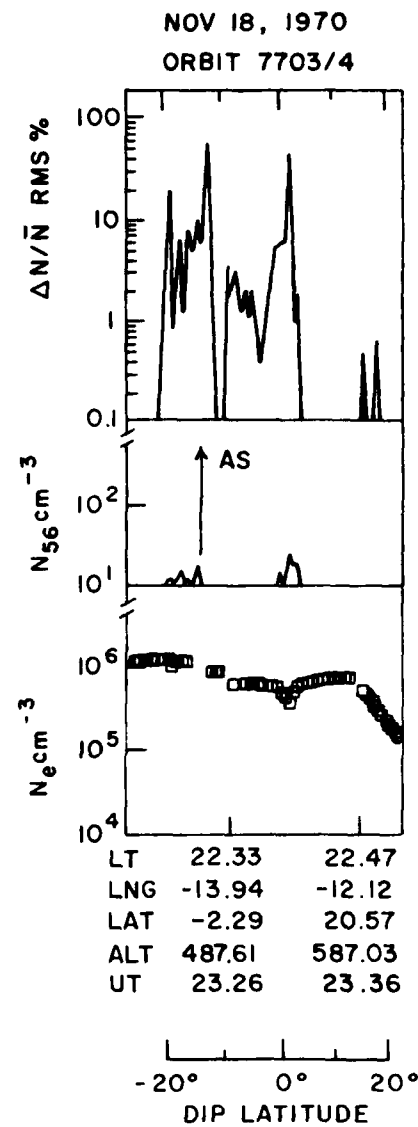


FIGURE 3. OGO-6 ORBIT IN ASCENSION ISLAND SECTOR DURING GHZ SCINTILLATION EVENT.

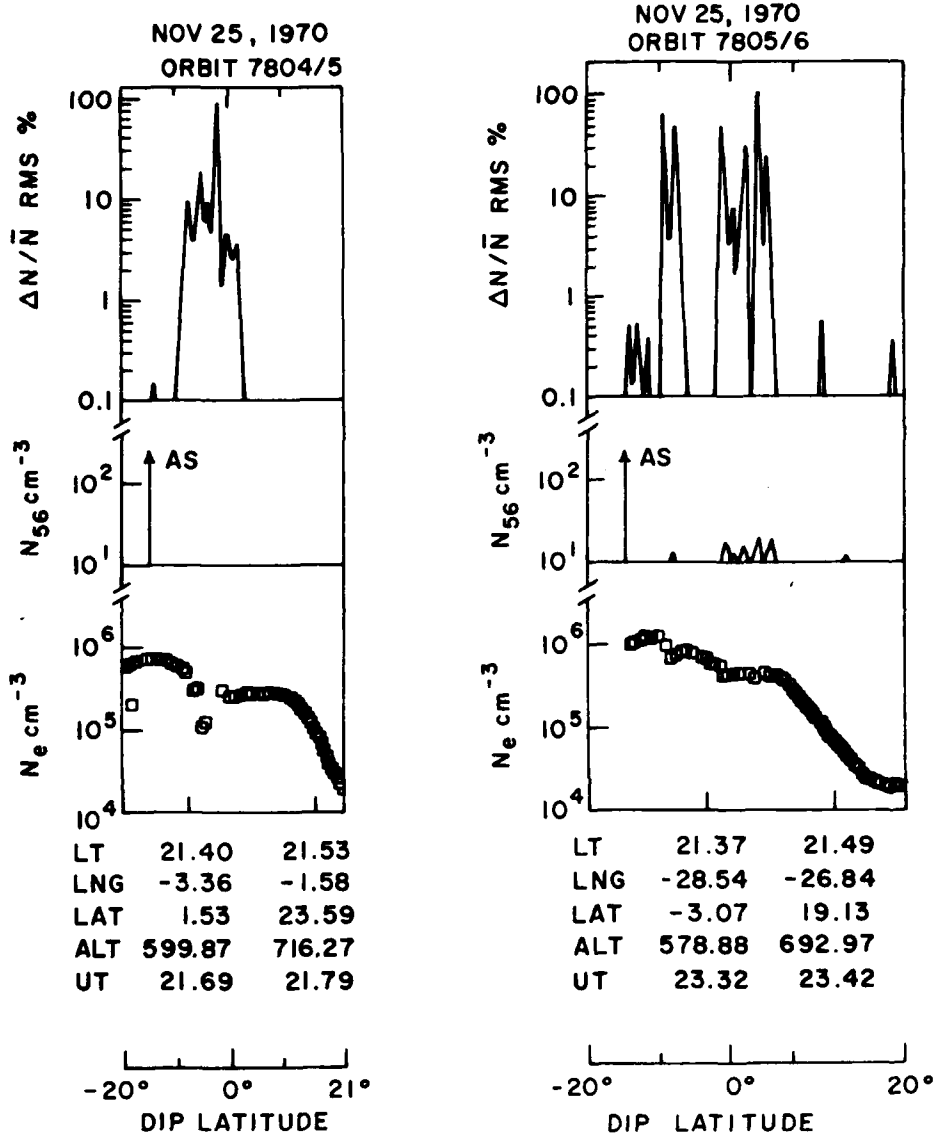


FIGURE 4. OGO-6 ORBITS NEAR ASCENSION ISLAND WHEN NO GHz SCINTILLATION WAS REPORTED.

$\Delta N = 1.4 \times 10^{11} \text{ m}^{-3}$   
 $N = 1.4 \times 10^{11} \text{ m}^{-3}$   
 $L_o = 20 \text{ km}$   
 $a = 5^\circ; \psi = 54^\circ$   
 $L_e = 200 \text{ km}$   
 $x = 30^\circ$   
 $Z = 525 \text{ km}$

COMPUTED  $S_4 = .014$  ( $\ll 1 \text{ dB}$ ) AT 6 GHz  
 OBSERVED SI = 1 dB AT 6 GHz  
 BETWEEN 2331 - 2350 LT

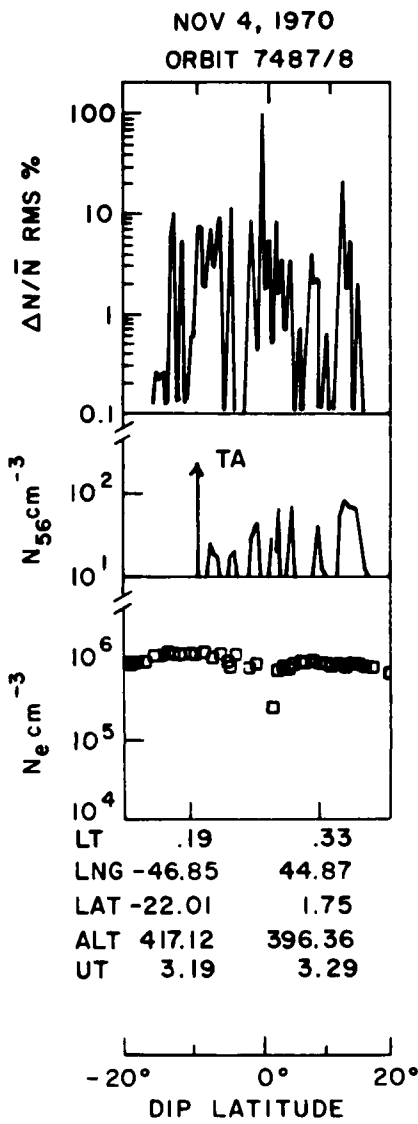
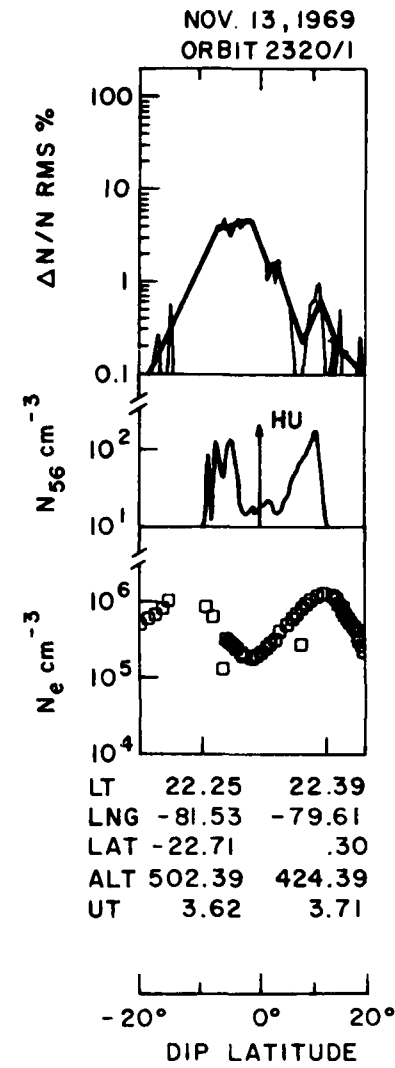


FIGURE 5. OGO-6 ORBIT IN TANGUA SECTOR NEAR THE TIME OF GHz SCINTILLATION.

$\Delta N = 6 \times 10^9 \text{ m}^{-3}$   
 $N = 2 \times 10^{11} \text{ m}^{-3}$   
 $L_o = 20 \text{ km}$   
 $a = 5; \psi = 80^\circ$   
 $L_e = 200 \text{ km}$   
 $x = 14^\circ$   
 $Z = 450 \text{ km}$   
**COMPUTED  $S_4 = .15$  (2.5 dB) AT 137 MHz**  
**OBSERVED SI = 100 % (> 20 dB) AT 137 MHz**



**FIGURE 6. OGO-6 ORBIT IN HUANCAYO SECTOR DURING VHF SCINTILLATION EVENT.**

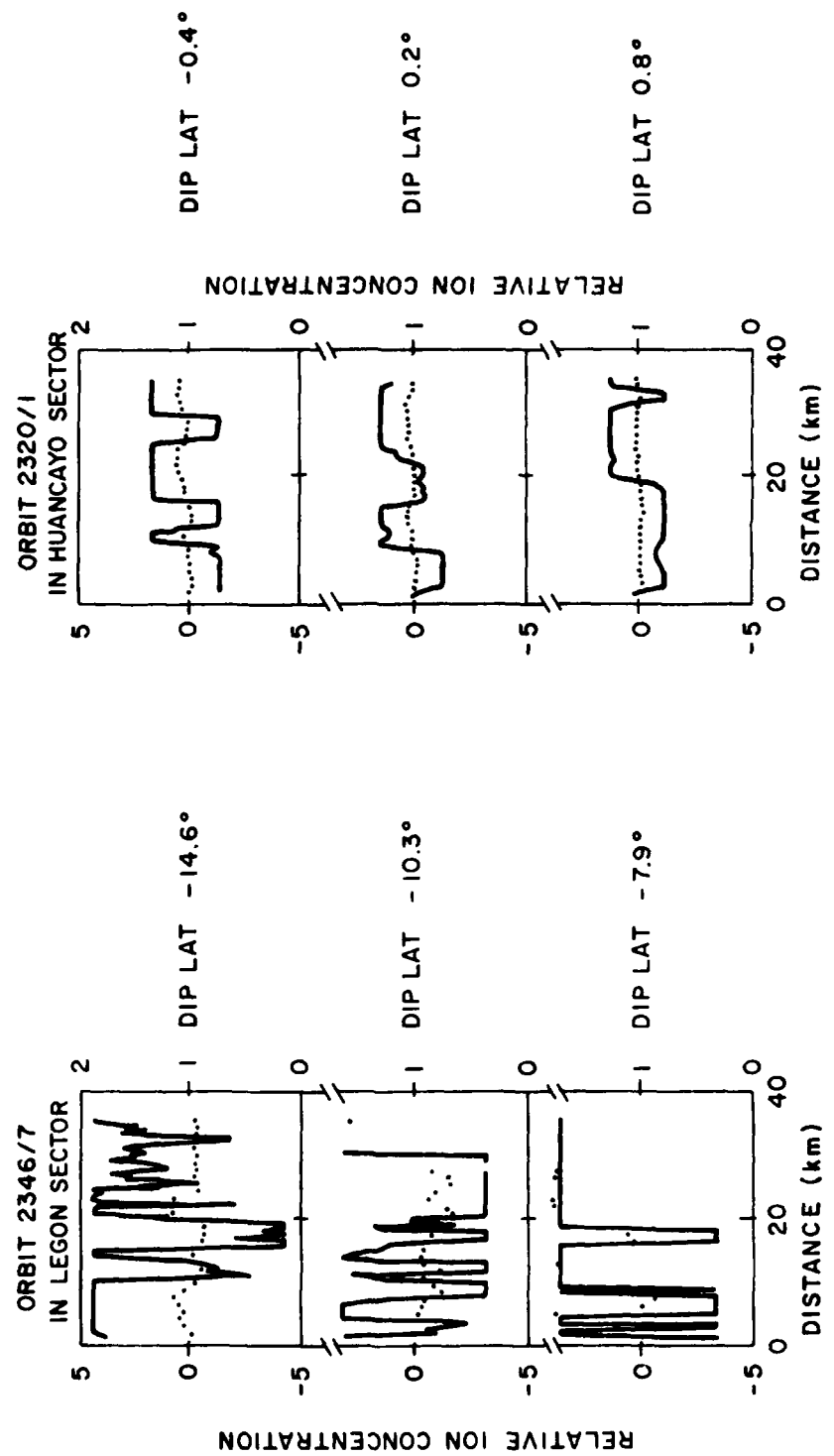


FIGURE 7. OGO-6 IRREGULARITY WAVEFORMS.

ANOMALOUS PHASE AND AMPLITUDE SCINTILLATIONS OF VHF WAVES  
WITHIN THE EQUATORIAL ELECTROJET REGION AND OTHER NEW PHENOMENA

by

R.G. Rastogi<sup>1</sup>, M.R. Deshpande<sup>1</sup>, A. Sen<sup>1</sup>, K. Davies<sup>2</sup>, R.N. Grubb<sup>2</sup>,  
and J.E. Jones<sup>2</sup>.

ABSTRACT

For the first time, phase scintillations within the equatorial electrojet region are measured using ATS-6 beacons at 40 and 140 MHz at Ootacamund (11.43°N, 76.70°E) in India. The r.m.s. phase fluctuations, at times, exceed well above one radian and also the spectrum of fluctuation shows high frequency components. Further, these results are not consistent with the thin screen approximation, which requires r.m.s. phase variations to be less than a radian. It is suggested that at equatorial latitudes thick screen theory needs to be worked out.

Severe daytime amplitude scintillations, even at 360 MHz, are observed with periodicities as low as one second. During daytime, scintillations occur more frequently around 1500 hr local time. The depth of scintillation is maximum at 40 MHz and least at 360 MHz. These scintillations are believed to be due to equatorial blanketing sporadic E irregularities which are seen commonly during afternoon hours. During nighttime, mostly the scintillation depths reverse with most deep fluctuations seen at 360 MHz. This implies a reversal of frequency law of scintillation. The period of scintillations seen at 40 MHz, 140 MHz and 360 MHz is as low as one second.

During sunrise and sunset periods scintillations are never seen. It is suggested that the irregularities causing scintillations die out during these periods due to the reversal of equatorial electric field at E region heights.

The above results, all new, are being reported in this paper with possible explanations.

INTRODUCTION

In the past decade, extensive radio beacon experiments have been carried out particularly at high latitudes using orbiting satellites. The advantage of orbiting satellites is that large spatial coverage can be achieved; however time resolution is limited. Better time resolved data can be obtained from geostationary satellites and hence these have also been employed for radio beacon experiments. Most of the geostationary satellites have largely concentrated their coverage to the western hemisphere. A few drifting geostationary satellites like Intelsat 2F2, Syncrom III have been available over the Indian sub-continent.

- 
1. Physical Research Laboratory, Ahmedabad 380 009, India.
  2. NOAA Environmental Research Laboratories, Space Environment Laboratory, Boulder, Colorado 80302, USA.

The positioning of ATS-6 over 35°E has therefore provided an excellent opportunity for the first time to carry out radio beacon experiments over the Indian sub-continent. For scintillation studies, this is particularly opportune, as it affords us an opportunity to investigate the equatorial region, which has hitherto not been studied extensively. In this paper we will report some of the findings on amplitude and phase scintillations measured at the equatorial station of Ootacamund (4° dip N).

#### EXPERIMENT AND DATA ANALYSIS

The experiment at Ooty has been carried out in collaboration with NOAA Laboratories, Boulder, Colorado, USA, and the equipment was designed by Davies et. al.(1975). The equipment consists of short back fire antenna system at 40 MHz, 140 MHz and 360 MHz. The cables to the receiver room are run underground to avoid phase fluctuations caused by temperature variations. The receiver has been designed on phase lock loop principles and can be operated with low bandwidths (as low as 3 Hz).

Analyses of amplitude as well as phase scintillations have been carried out for every 15 min with a width of  $\pm 7.5$  min. In addition, frequency law indices of amplitude and phase scintillations are also being calculated.

#### RESULTS AND DISCUSSIONS

Some typical amplitude scintillation records are shown in Figures 1 and 2 for 40 MHz, 140 MHz and 360 MHz. The records of Fig. 1 (Nov. 7, 1975, Nov. 5, 1975 and Nov. 3., 1975) are representative of day time scintillations where one typically observes that the scintillation depth decreases rapidly with increasing carrier frequency. This can be interpreted normally in the weak scattering approximation where for low levels of electron density fluctuation the r.m.s. fluctuation in the refractive index is inversely proportional to the square of the signal frequency. We also notice from the present observations that the fading rate is almost independent of the carrier frequency. The night time scintillation records (Figs. 2a, 2b) however show a different behaviour. As seen in the records for October 19 and 20, 1975, the scintillation depths are quite large even for the higher frequencies and the fading rate appears to be inversely proportional to the signal frequency. Such anomalous behaviour, which is found to be a common occurrence in our night time observations, cannot be explained on the basis of single scattering theory. As some recent calculations indicate, when the level of turbulence rises beyond a certain value, multiple scattering effects become important and are likely to predominate at the higher frequency end. A fairly good index of the turbulence level is the scintillation index itself, of which several standard definitions have now been given ( $S_0, S_1, S_2, S_3$ , and  $S_4$ ) (Briggs and Parkin 1963 and Whitney 1970). We have used

$$S_0 = \frac{P_{\max} - P_{\min}}{P_{\max} + P_{\min}}$$

as a crude index for a quick analysis and also calculated  $S_4$  for detailed and accurate comparisons. Typically for single scattering theory to hold,  $S_4$  has to be less than 0.25. For the night time records showing anomalous behavior  $S_4$  is found to be about 0.86 (Fig. 2c, which shows normal scintillations at night has  $S_4 = 0.18$  at 360 MHz). An independent and perhaps more direct assessment of the validity of the weak scatter approximation can be obtained from the r.m.s. value of phase fluctuations. Normally  $\phi_{\text{rms}} < 1$  radian and this is found to hold for the day time scintillations. However for many of the night time records  $\phi_{\text{rms}}$  turns out to be between 1 and 3 radians. We find therefore a distinct difference in the nature of signal fading for our day time and night time observations.

In Fig. 3 we have plotted the diurnal pattern of scintillation occurrence. We find that on all frequencies the maximum occurrences are observed just before midnight. In addition there are two day time occurrence peaks - one around 1000 hr and the other around 1400 hr. This is further suggestive of the differences in the nature of the ionospheric irregularities. The night time scintillations seem to have their origin in the spread F irregularities whereas the day time scintillations are probably caused by the blanketing type of equatorial sporadic E which is frequently seen on equatorial ionograms during low solar activity around forenoon and afternoon hours (Chandra and Rastogi 1974). Such a conjecture is further supported by the fact that scintillations are found to vanish during sunrise and sunset periods, when E region irregularities are known to disappear due to a possible field reversal.

It is further important to note (Fig. 4) that the night time scintillations show a very large percentage occurrence (98%) of high levels of scintillation (90%). Day time scintillations are by contrast weaker and rarer. Another interesting aspect of the night time scintillations is the structure in the histograms for the 140 and 360 MHz histograms which seem to indicate the presence of a weaker component. This fact has to be investigated more carefully to delineate the possibilities of a mixing effect on scintillations due to the presence of different layers of irregularities.

In Fig. 5 we present the diurnal variation of the mean scintillation index for the period 26 September 1975 to 10 November 1975. In general there appears to be a strong level of scintillations for the 40 MHz during both day and night hours whereas for the 140 MHz and 360 MHz signals, the nighttime scintillation level is significantly higher than that during daytime. The dramatic fall in scintillation level during dawn and dusk is also very clearly seen.

Next, we have attempted to look at the frequency dependence of the scintillations a little more closely. From single scattering theory, the scintillation index is expected to follow the

inverse frequency law,  $S_o \propto f^{-n}$  where  $n$  the power law index is normally expected to be between 1 and 2. In Fig. 6 we have plotted histograms of  $S_o$  ratios between sets of two frequencies. If the inverse frequency law is valid then the expected  $S_o$  ratios for 40 MHz to 140 MHz, 40 MHz to 360 MHz and 140 to 360 MHz (assuming  $n = 1$ ) are 3.5, 9.0, and 2.6 respectively. During day time, the observed ratios are seen to be fairly close to these expected values. However, during pre-midnight and post-midnight periods the results depart considerably from the theoretical ratios indicating that  $n$  gets considerably less than unity. This is seen even more clearly in Fig. 7, where the diurnal variation of  $n$  values are plotted for the various frequencies. During day time, the average value of  $n$  is around 2 whereas during night hours there is a considerable variability in  $n$  ranging from -0.2 to 1.5. The negative values indicate a reversal in the frequency law when higher frequency carriers could experience severe fade outs.

So far, our analysis is based on the simple visual index  $S_o$  which affords a quick qualitative feel for the results. A more reliable index is  $S_4$  which is actually the normalized variance of the amplitude. This index is also related to the  $m$  value of the so called Nakagami  $m$ -distribution (Chytil 1967) for the probability distribution function of the instantaneous values of the amplitude and phase of scintillations. Plotting the amplitude distribution is also another convenient way of classifying the scintillation levels and has been used by several workers in the past. Normally  $m > 1$ , in which case the Nakagami  $m$ -distribution goes over to the commonly observed Rice distribution. However, for strong levels of scintillation  $m$  could become less than unity leading to Rayleigh distribution ( $m = 1$ ) or normal distribution ( $m < 1$ ). Fig. 8 shows probability distribution for amplitude and phase for weak scintillation example on 3 November 1975. The corresponding amplitude scintillation record is shown in Fig. 1. It is to be noted that even in this case 40 MHz does show moderate scintillations. The  $\phi$  rms for 40 MHz is 1.47 radians. The scintillation at 140 MHz is relatively weak and shows  $\phi$  rms = 0.1 radian.

Referring to a strong scintillation case (Fig. 9 and Fig. 2a) the amplitude distributions show  $m \leq 1.0$  indicating Rayleigh and normal distributions. The  $\phi$  rms for 40 MHz exceeds 1.5 radians.

#### CONCLUSIONS

- (1) During day time, severe scintillations have been observed within the equatorial electrojet region even up to 360 MHz. The scintillation decreases with increasing frequency but the fading rate is independent of the frequency.
- (2) During night time, intense scintillations are observed even up to 360 MHz. Scintillation does not decrease as frequency increases as expected by inverse frequency law. At times scintillation at 360 MHz exceeds those at 140 MHz and 40 MHz. The fading rate, unlike during day time, decreases with increasing frequency.

(3) The scintillation occurrences are most common during pre-midnight hours. In addition, two day-time peaks are seen and are suggested to be due to Es-b irregularities which also show similar behaviour. Night-time scintillations are suggested to be due to spread F irregularities.

(4) During sunrise and sunset periods no scintillation is observed. This we suggest is owing to the destruction of irregularities due to the reversal of electric field in the E region.

(5) During most of the night hours  $\phi$  rms exceeds 1 radian indicating that thin screen approximation is not valid at the equator.

(6) The amplitude distributions during weak scintillations show Rice distribution. During strong scintillations normal and Rayleigh distributions are seen.

#### REFERENCES

- Briggs, B.H. and Parkin, I.A., 1963, J. Atmos. Terr. Phys., 25, 339.  
Chandra, H and Rastogi, R.G., 1974, Curr. Sci., 43, 533.  
Chytil, B., 1967, Studia Geoph. et Geod., 11, 221.  
Davies, K., Fritz, R.B., Grubb, R.N., and Jones J.E., 1975, Rad. Sci., 10, 785.  
Whitney, H.E., 1970, A survey of scintillation data and its relationship to satellite communications, edited by J. Aarons, AFCRL Special Report No. 106, pp. 5-14.

## ATS-6 OOTACAMUND

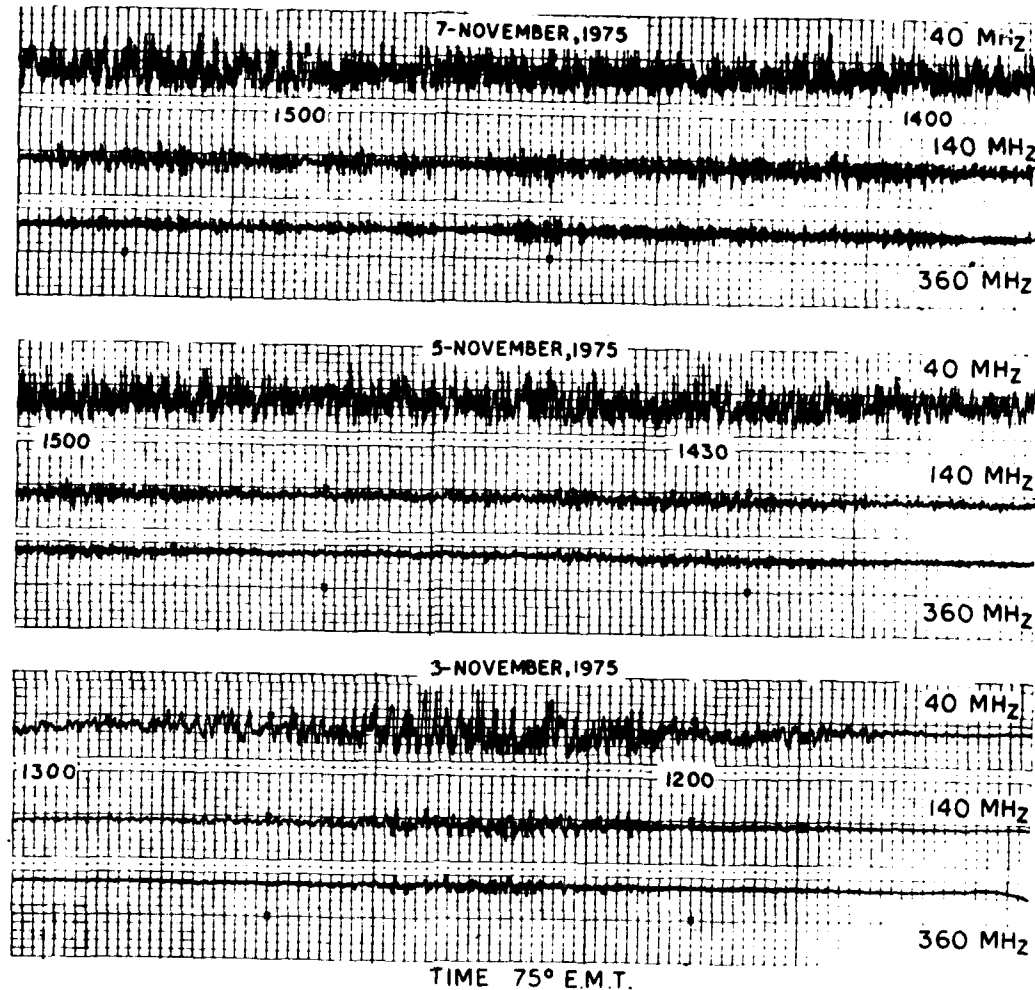
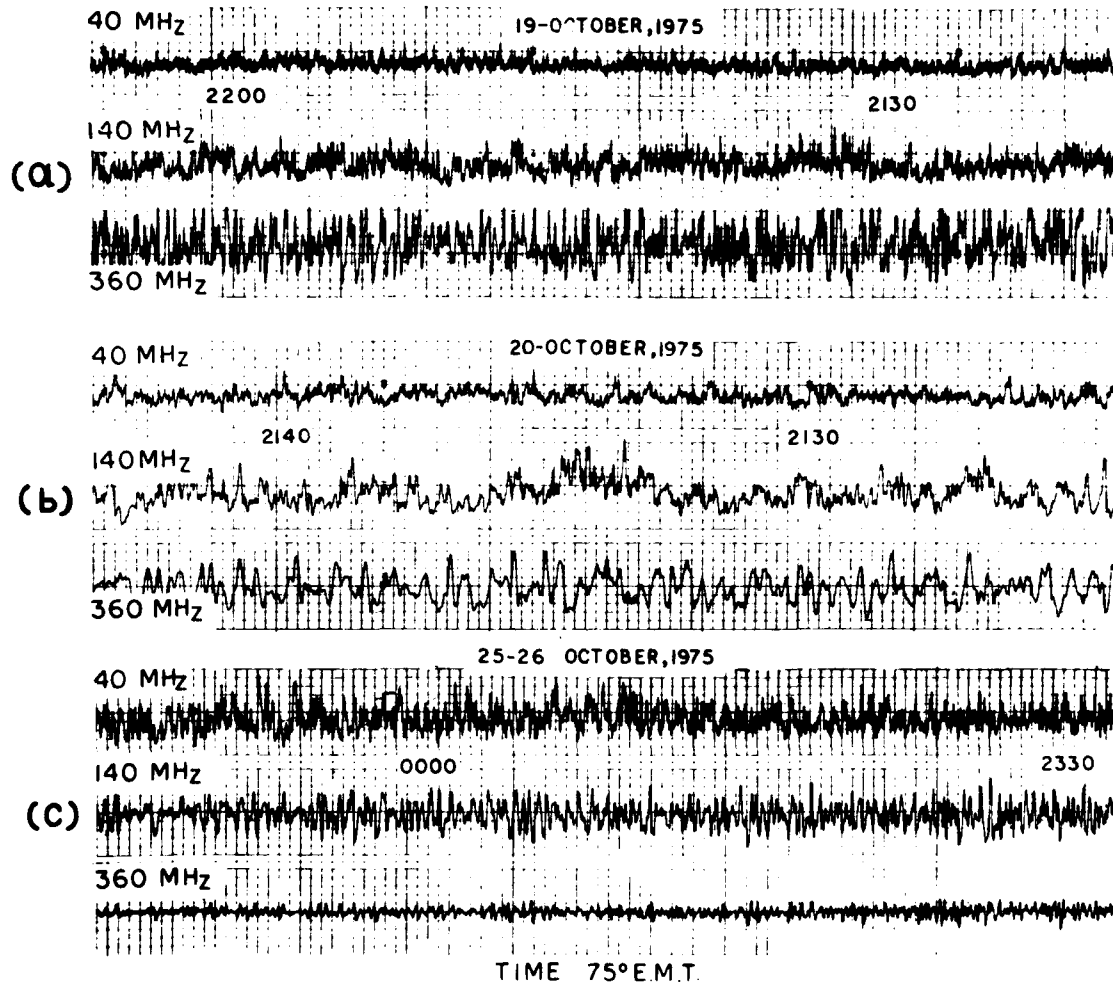


Figure 1 : Records of amplitude scintillation of 40 MHz, 140 MHz and 360 MHz beacon radio waves emitted from ATS-6 received at Ootacamund, India during daytime hours.

**ATS-6 OOTACAMUND**



**Figure 2 : Records of the amplitude scintillation of 40 MHz, 140 MHz and 360 MHz beacon radio waves emitted from ATS-6 received at Ootacamund, India during nighttime hours.**

ATS-6 OOTACAMUND  
26 SEP. 1975 TO 10 NOV. 1975

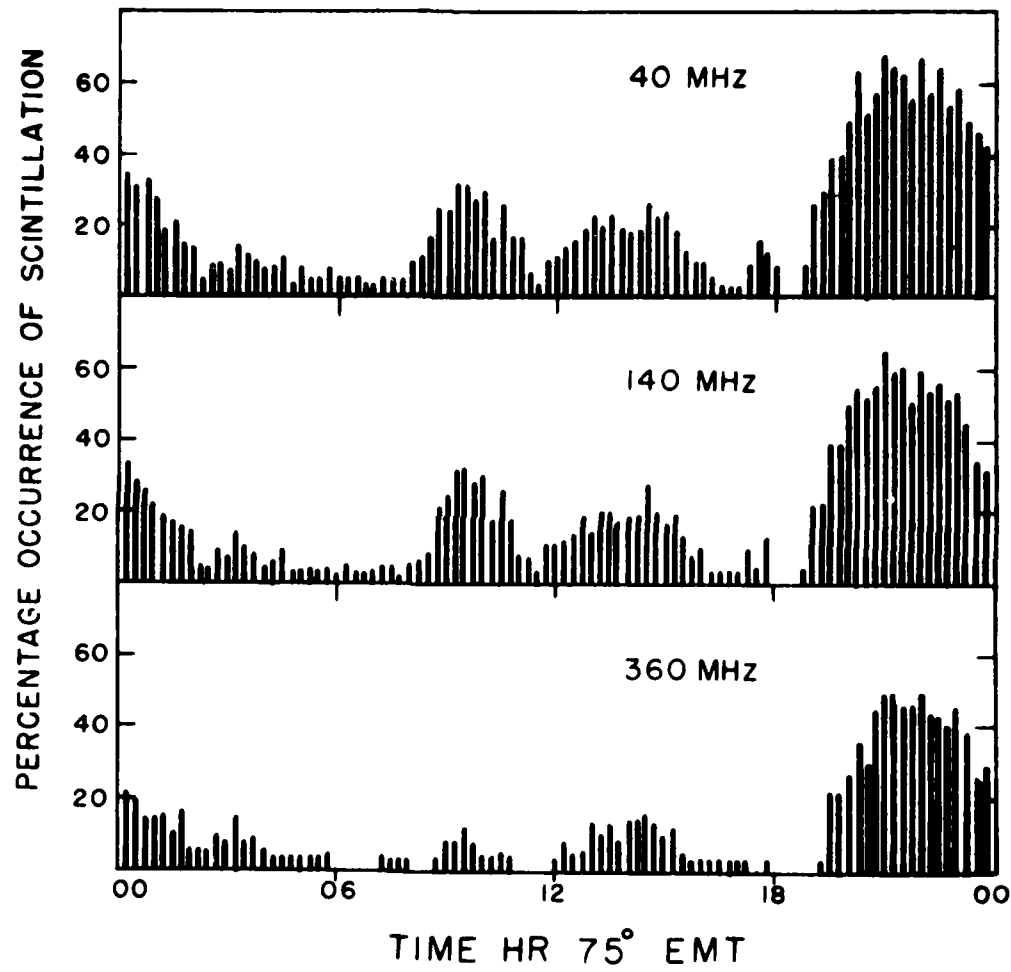


Figure 3 : Daily variations of the occurrence of scintillation of 40 MHz, 140 MHz and 360 MHz radio waves from ATS-6 received at Ootacamund, India.

ATS-6 OOTACAMUND  
26 SEP. 1975 TO 10 NOV. 1975

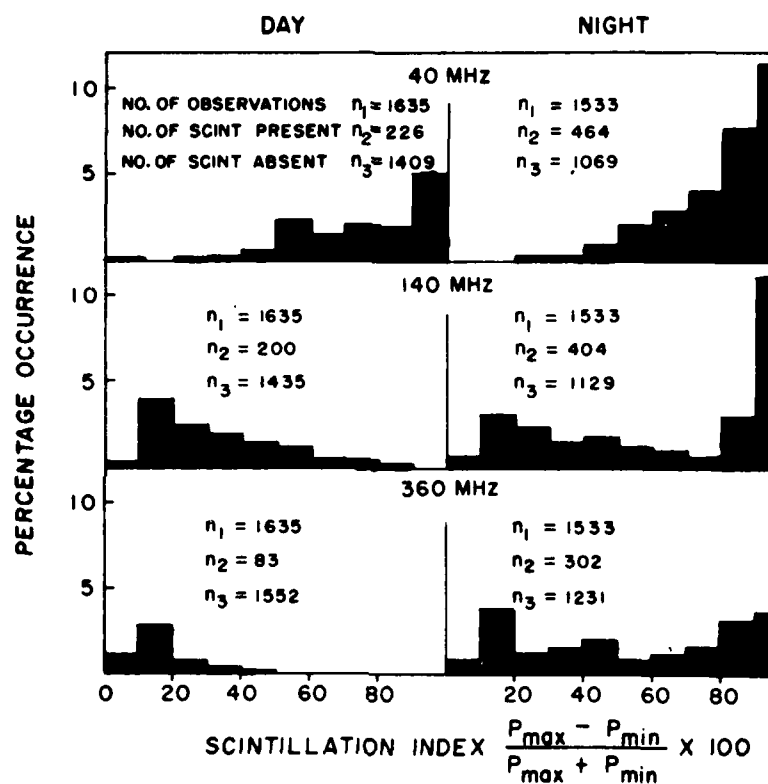
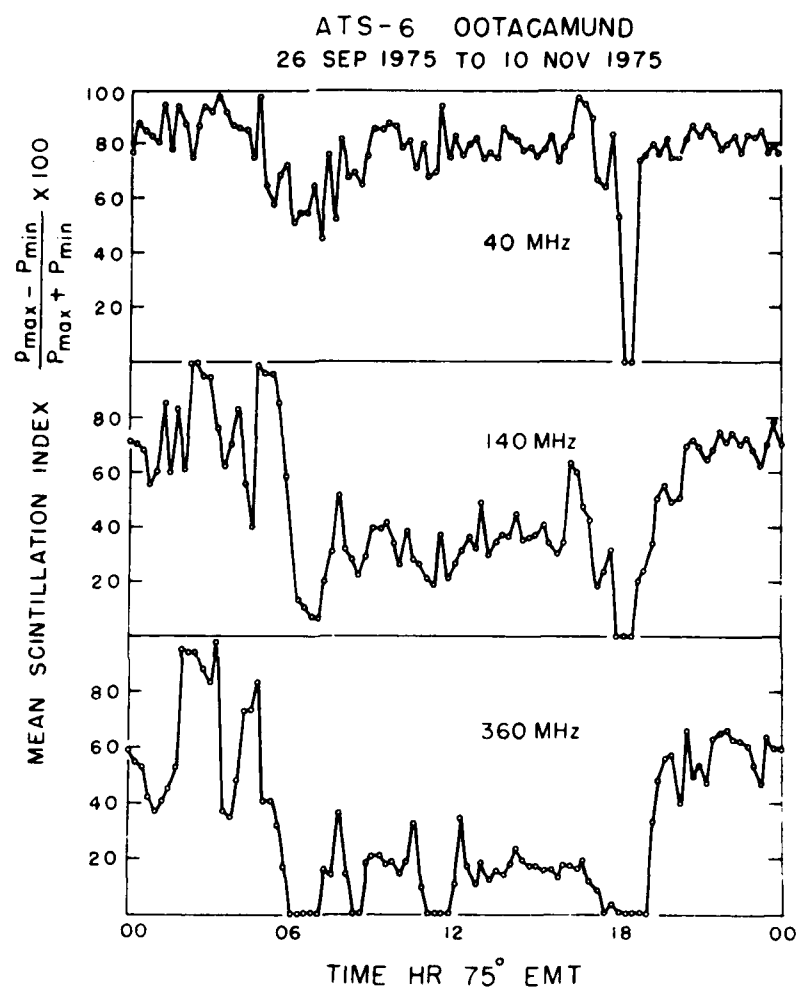


Figure 4 : Percentage occurrence of scintillation index of 40 MHz, 140 MHz and 360 MHz radio waves from ATS-6 received at Ootacamund, India.



**Figure 5 : Daily variation of scintillation index of 40 MHz, 140 MHz and 360 MHz radio waves from ATS-6 received at Ootacamund, India.**

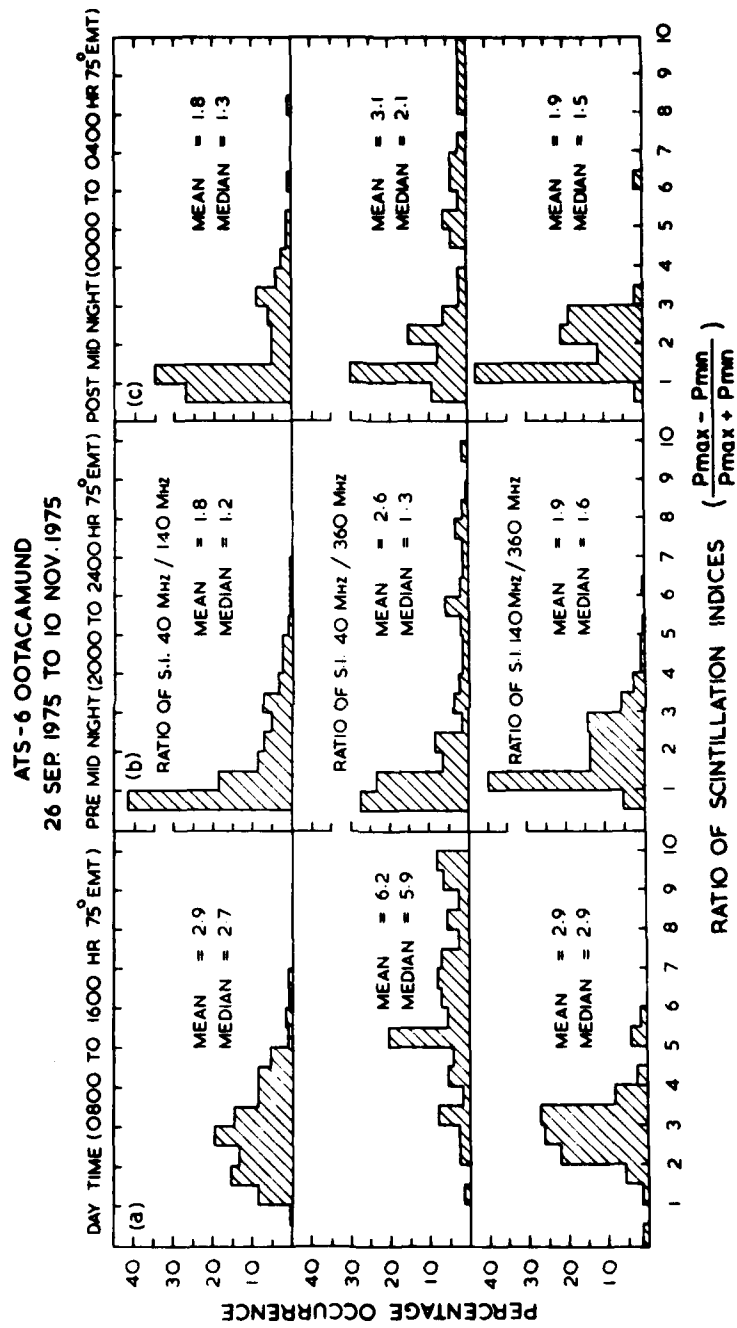


Figure 6 : Histograms of the ratio of scintillation index on two different frequencies (40 MHz/140 MHz, 40 MHz/360 MHz, 140 MHz/360 MHz) radiated from ATS-6 received at Ootacamund, India.

ATS-6 OOTACAMUND  
26 SEP. 1975 TO 10 NOV. 1975

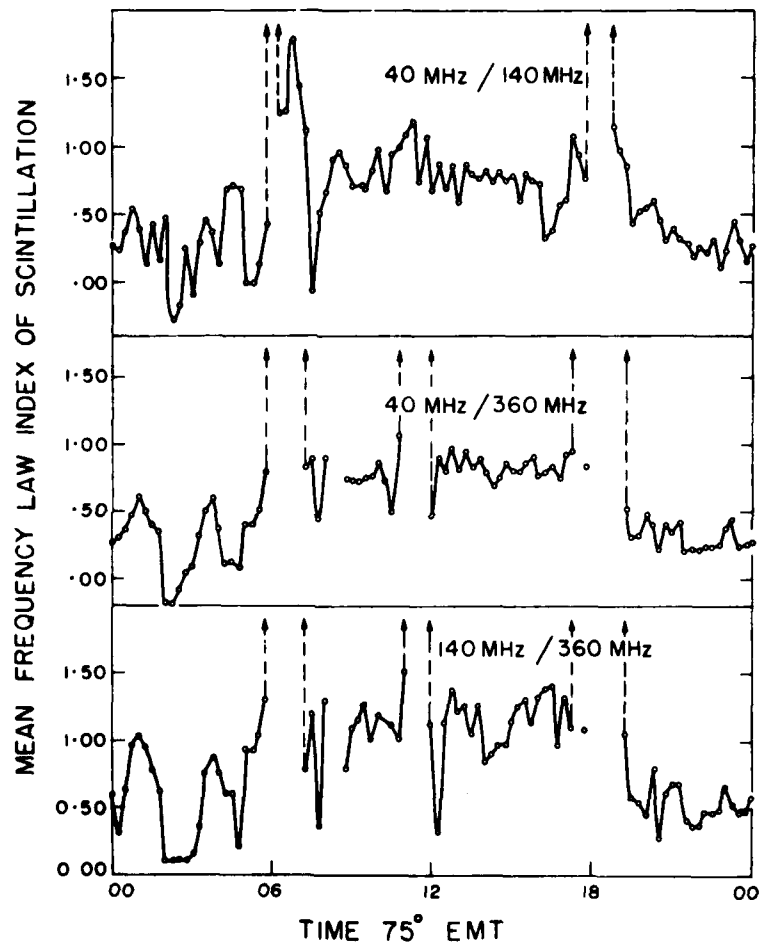


Figure 7 : Daily variations of frequency law index of scintillation ( $n$ ), calculated from a set of two frequencies radiated from ATS-6 received at Ootacamund, India.

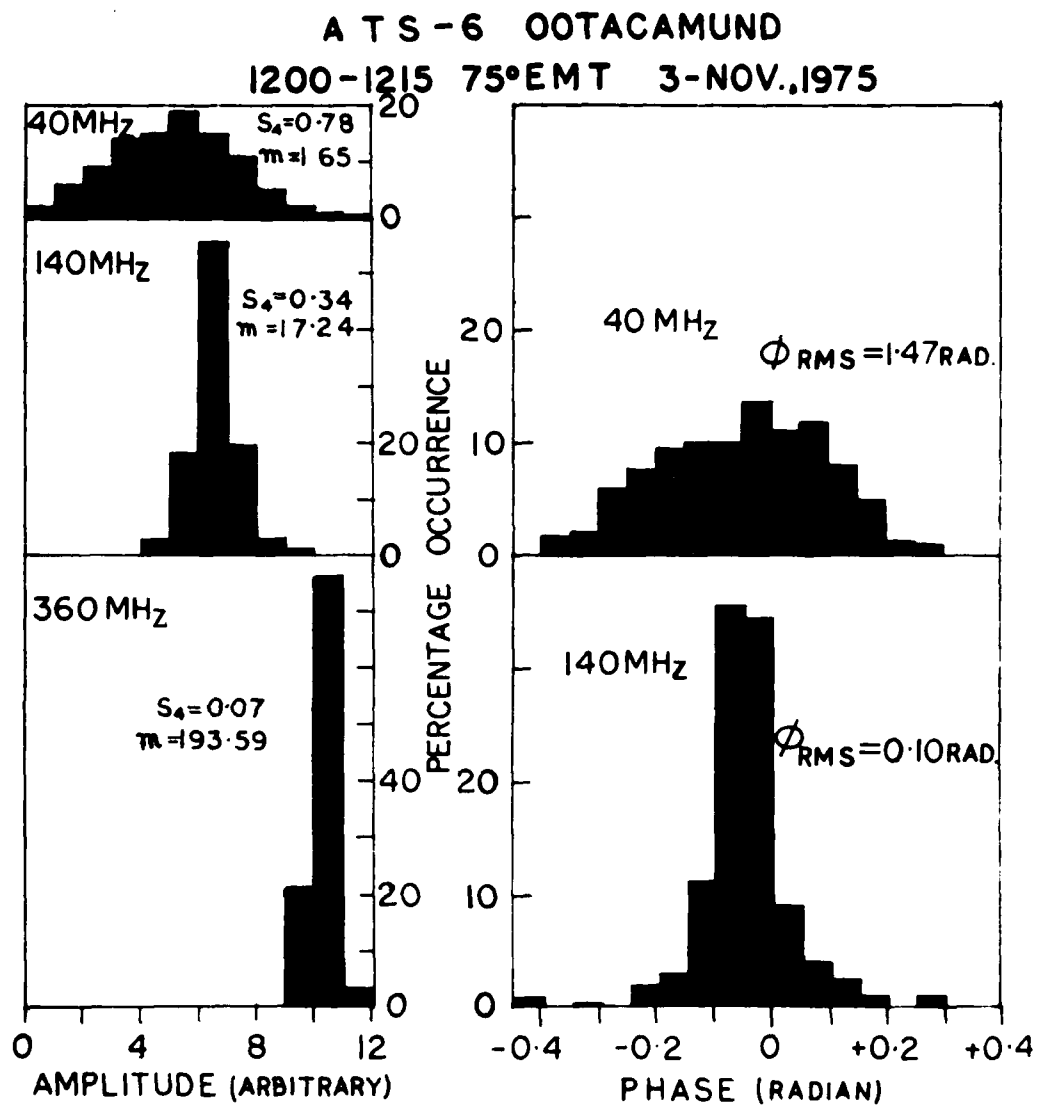


Figure 8 : Amplitude distribution of 40 MHz, 140 MHz and 360 MHz and phase distribution of 40 MHz and 140 MHz radio waves radiated from ATS-6 received at Ootacamund, India on 3 November 1975 between 1200 and 1215 hr 75° EMT.

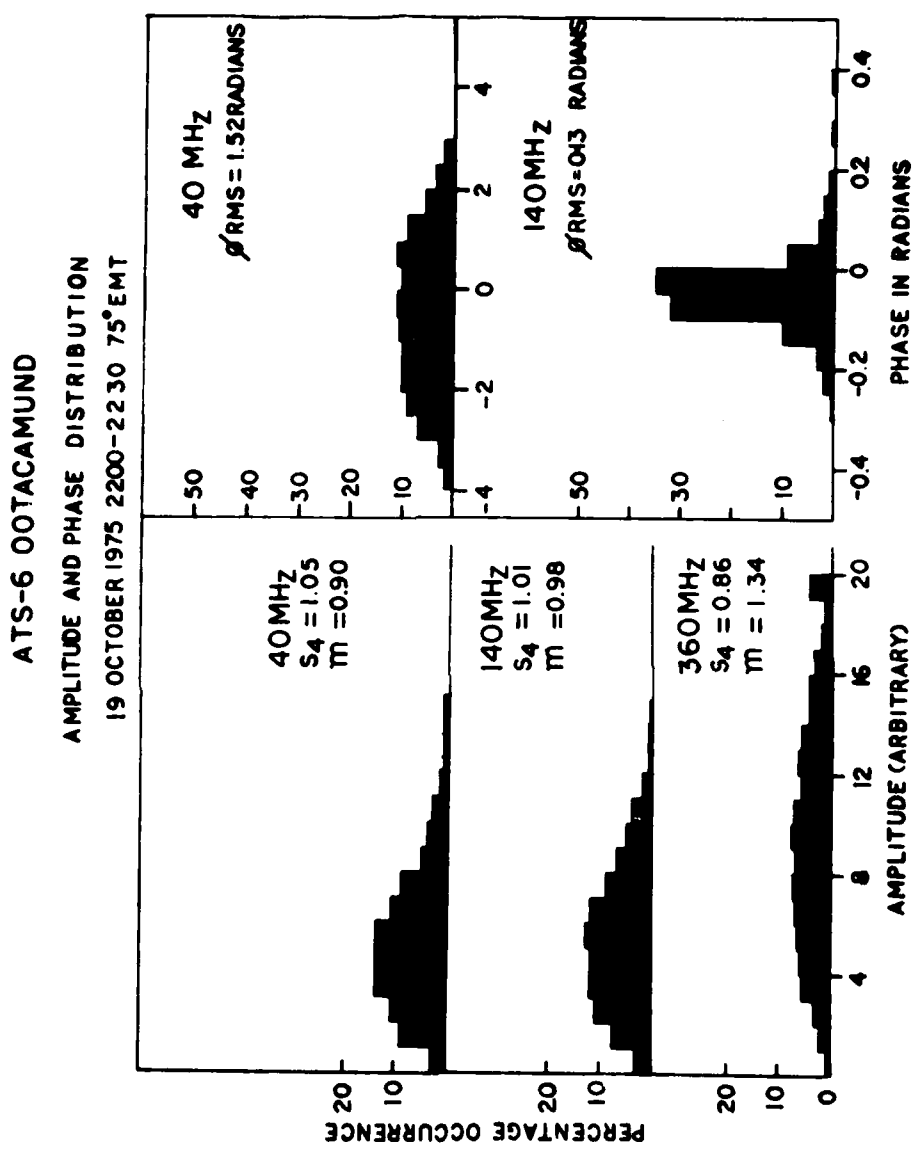


Figure 9 : Amplitude distribution of 40 MHz, 140 MHz and 360 MHz and Phase distribution of 40 MHz 40 MHz and 140 MHz radio waves radiated from ATS-6 received at Ootacamund, India on 19 October 1975 between 2200 and 2230 hr 75° EMT.

## SCINTILLATIONS IN THE VHF AND UHF RANGE AT THE MAGNETIC EQUATOR

B.V. Krishna Murthy, K. Krishna Murthy,  
C. Paghava Reddi and S. Vaidyanathan  
Space Physics Division  
Vikram Sarabhai Space Centre  
Trivandrum 695022, India.

Abstract: Amplitude scintillations recorded at Trivandrum (Mag. dip. 0.6°S) at four frequencies namely 40, 140, 360 and 860 MHz, have been studied using transmissions from ATS-6 satellite situated at 35°E. Frequency index of scintillation has been evaluated and it is found that the index is about 1.1 for weak scintillations. Cumulative amplitude probability distributions (CDF) have been obtained for all the frequencies under different scintillation conditions. It is found that these experimental distributions agree well with the theoretical Nakagami distributions for weak scintillations, whereas for strong scintillations, they differ considerably. The association between the scintillation index ( $S_4$ ) and bottomside spread F has also been investigated.

Introduction: Since July 1975, when the ATS-6 satellite was positioned at 35°E longitude, the phase and amplitude informations on the RBE transmissions from that satellite are being recorded at Trivandrum (Mag. dip 0.6°S), geograph. long 76°57'E). In addition, the amplitude of 860 MHz SITE TV transmissions are being recorded. Using the amplitude records on all the four frequencies, namely, 40, 140, 360 and 860 MHz, characteristics of the nighttime scintillations observed at Trivandrum have been studied. The results of these studies are presented in the following sections. The data analysed, corresponds to that recorded in the period July-December 1975.

Frequency Variation of Scintillations: The data for some of the scintillation nights has been scaled at intervals of 1.2 sec or its multiples, depending upon the fading periods encountered. Using the scaled data,  $S_4$  scintillation indices (Briggs and Parkin, 1963) have been obtained for data ensembles of about 10-20 min duration. This is sufficiently long enough not to cause errors in the  $S_4$  indices considering the observed quasiperiods of scintillations which are generally in the range of few seconds to few tens of seconds.

The frequency variation of  $S_4$  is expressed by the relation

$$S_4 = \frac{k}{f^n}$$

where  $f$  is the exploring frequency,  $n$  is the frequency index and  $k$

is a constant depending only upon the scintillation conditions. The above equation can be rewritten as

$$\log \frac{(S_4)_1}{(S_4)_2} = n \log \frac{f_2}{f_1} \quad (1)$$

where  $(S_4)_1$  and  $(S_4)_2$  are the scintillation indices at the frequencies  $f_1$  and  $f_2$ . Using the observed  $S_4$  values,  $\log (S_4)_1$  is plotted against  $\frac{(S_4)_1}{(S_4)_2}$

$\log \frac{f_2}{f_1}$  and shown in Fig.1. A careful examination of the  $S_4$  indices

showed that they can be divided into two groups depending upon whether  $S_4$  index at 360 MHz is greater or less than about 0.5. The conditions corresponding to  $S_4$  at 360 MHz greater than 0.5 can be termed as strong scintillation conditions and those corresponding to  $S_4$  at 360 MHz less than 0.5 as relatively weak scintillation conditions. When  $S_4$  at 360 MHz exceeds 0.5,  $S_4$  at 140 MHz usually would be around 0.8 or greater. Depending upon this classification, data representing weak scintillation conditions are shown as aided points and those representing strong scintillation conditions, as crosses in Fig 1. Mean straight lines are drawn through these points. The frequency index  $n$  for weak scintillation condition is 1.1 and for strong scintillation conditions is 0.47 as can be seen from the figure. It has been found that under very strong scintillation conditions, the  $S_4$  index at 140 MHz and 40 MHz are about same indicating no frequency variation of  $S_4$ . This is shown by the triangulated point close to the abscissa in Fig 1.

Rufenach (1974) had shown from theoretical considerations that for weak scattering case the frequency index  $n$  is between 1.4 and 1.6 depending upon the exponent of the irregularity spectrum, in the range 3.5 to 4.5. Yeh et al (1975) had shown from a theoretical analysis of multiple scattering case, that  $n$  is less than unity for the VHF range of frequencies and strong scintillation conditions and it approaches a value of 1.5 for higher frequencies and weak scintillation conditions. The results presented here appear to be in general agreement with these theoretical considerations.

Cumulative Amplitude Probability Distribution Functions (CDF): The scaled scintillation data as described above, has been first converted to dB scale. Using these, the cumulative amplitude probability distributions have been obtained.

Chyttil (1967) has shown that the probability distribution function can be represented by the theoretical Nakagami distribution (Nakagami 1960) given by  $P(S) = \frac{2m^m}{M^m} \exp^{-m} \left( \frac{2S}{M} - \exp \frac{2S}{M} \right) \dots (a)$

where  $S$  is the signal strength in dB,

$M = 20 \log e$ ,  
and the Nakagami parameter  $m = \frac{1}{S_4}$ .

The theoretical cumulative Nakagami distributions for values of  $m$  corresponding to the observed  $S_4$  indices have been estimated for comparison with the observed distributions. Typical distributions for all the four frequencies are shown in Figs 2, 3, 4 and 5.

As SITE TV transmissions in the evening are restricted to only 2½ hours, scintillations at this frequency have been observed only on few occasions with  $S_4$  values in the range 0.15 to 0.22. The distributions for the highest and lowest  $S_4$  values observed, are shown in Fig 2. The agreement between the theoretical and experimental distributions is good. For higher  $m$  value (lower  $S_4$  index) the agreement seems to be slightly better.

For 360, 140 and 40 MHz distributions are shown for high and low values of  $m$  in Figs 3, 4 and 5. It can be seen from these figures that the agreement between theoretical and experimental distributions is better for high  $m$  values than for low  $m$  values. This is particularly evident in Fig 5 (40 MHz) for  $m = 0.8$  corresponding to a severe scintillation condition. The deviation of the experimental distributions from the theoretical ones for low  $m$  values is prominent when the signal is below 0 dB.

From the above, it is clear that Nakagami distribution represents well the experimental distributions for low  $S_4$  indices but fails for high  $S_4$  indices.

Comparison with Spread F: The nocturnal variation of scintillation indices is compared with that of spread F as seen on the bottomside ionograms. Two such comparisons are shown in Figs 6 and 7 for 40 MHz and 140 MHz respectively. For spread F, the indexing system depending upon the virtual height extent of spread F given by Rao et al (1960) has been adopted. The time of the ionograms has been adjusted to the time corresponding to the longitude of the sub-ionospheric point of the intersection of the ray path and F region maximum.

From Fig 6, it can be seen that scintillations on 40 MHz started a little later than bottomside spread F but continued to be stronger even after spread F had become weaker, in the midnight period. Scintillations on 140 MHz (Fig 7) also are delayed with respect to bottomside spread F. It may be noted here that Krishnamurthy (1966) reported that Spread F in the topside ionosphere is delayed with respect to that in bottomside. So, it appears that only after spread F in the bottomside becomes strong and also is present in the topside, thus providing irregularities over a greater altitude range, scintillations begin to occur at VHF.

Though there is a secondary peak at midnight in bottomside spread F (Fig 7)  $S_4$  at 140 MHz continues to decrease and finally scintillations disappear at 0030 hrs whereas bottomside spread F disappears at 0100 hrs. There is a sudden burst of scintillations

during 0115 to 0200 hrs whereas bottomside spread F started again only at 0145 hrs. This again indicates that topside spread F plays an important part in producing scintillations.

The dominant periods as in the scintillations as obtained from power spectrum analysis are also shown in Fig 7. It is seen that periods are shorter when the scintillations are stronger.

Daytime scintillations: At Trivandrum, scintillations have been observed quite frequently during daytime. These are more prominent at 40 MHz than on 140 MHz and on 360 MHz, they are almost non-existing. As the raypath from Trivandrum passes through the equatorial electrojet region, we attribute the observed scintillations to equatorial sporadic E irregularities. Fig 8 shows typical daytime scintillations observed on 40 MHz and 140 MHz. Analysis of daytime scintillations is in progress.

- - -  
R e f e \_r\_e\_n\_c\_e\_s

- Briggs, B.H. and I.A. Parkin : J. Atmosph. Terr. Phys., 25, 359, (1965).
- Chytil, B. : J. Atmosph. Terr. Phys. 29, 1175, (1967).
- Krishnamurthy, P.V. : J. Geophys. Res. 71, 4527, (1966).
- Nakagami, M. : Statistical methods in Radio Wave Propagation, Pergamon Press, 3, (1960).
- Rao, M.S.V.G., B.R. Rao and P.R. Pant : J. Atmosph. Terr. Phys. 17, 345, 1960.
- Rufenach, C.L. : J. Geophys. Res. 79, 1562, (1974).
- Yeh, K.C., C.H. Liu and M.Y. Youakin. : Radio Science, 10, 97, (1975).

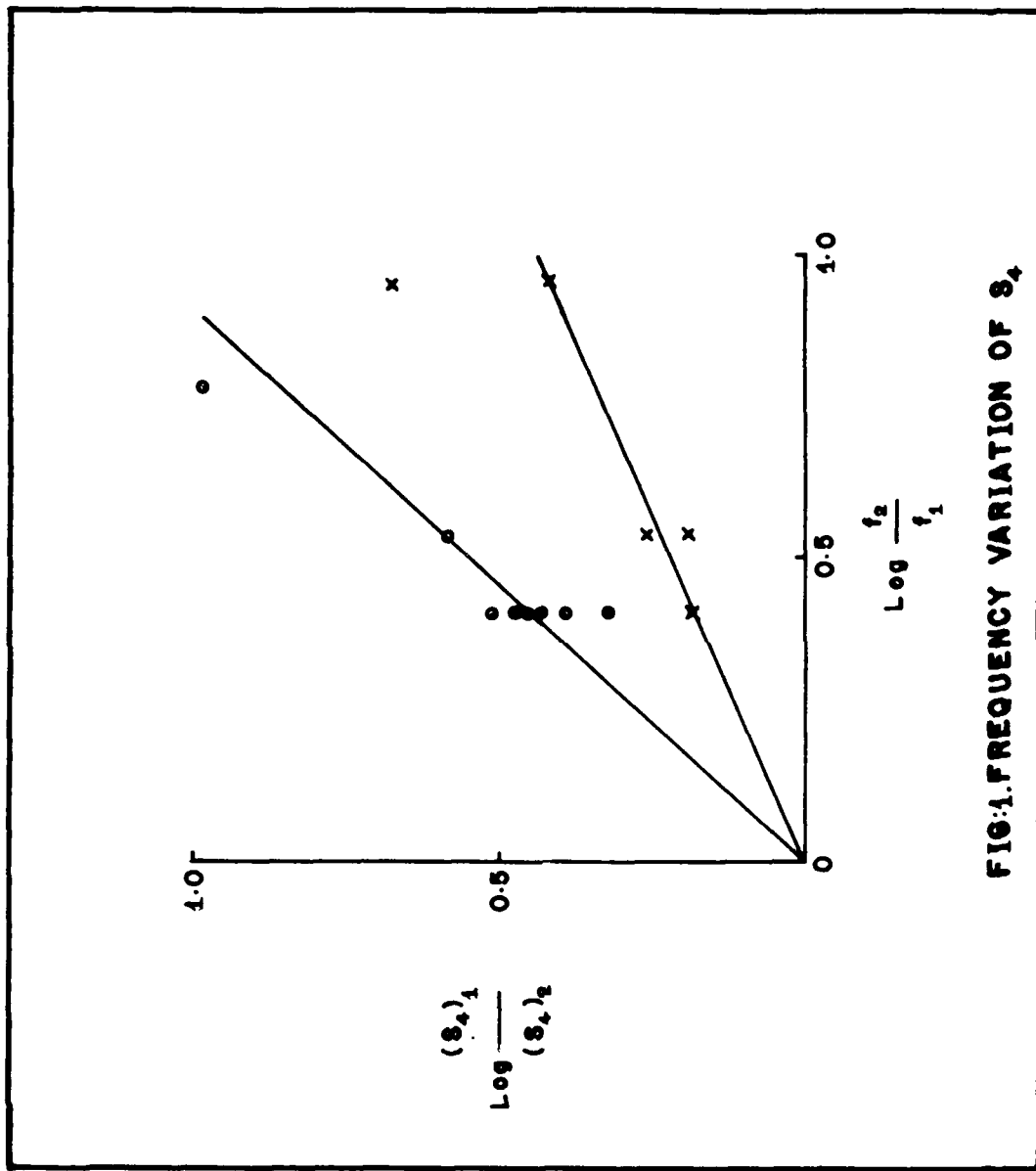


FIG:1.FREQUENCY VARIATION OF  $s_4$

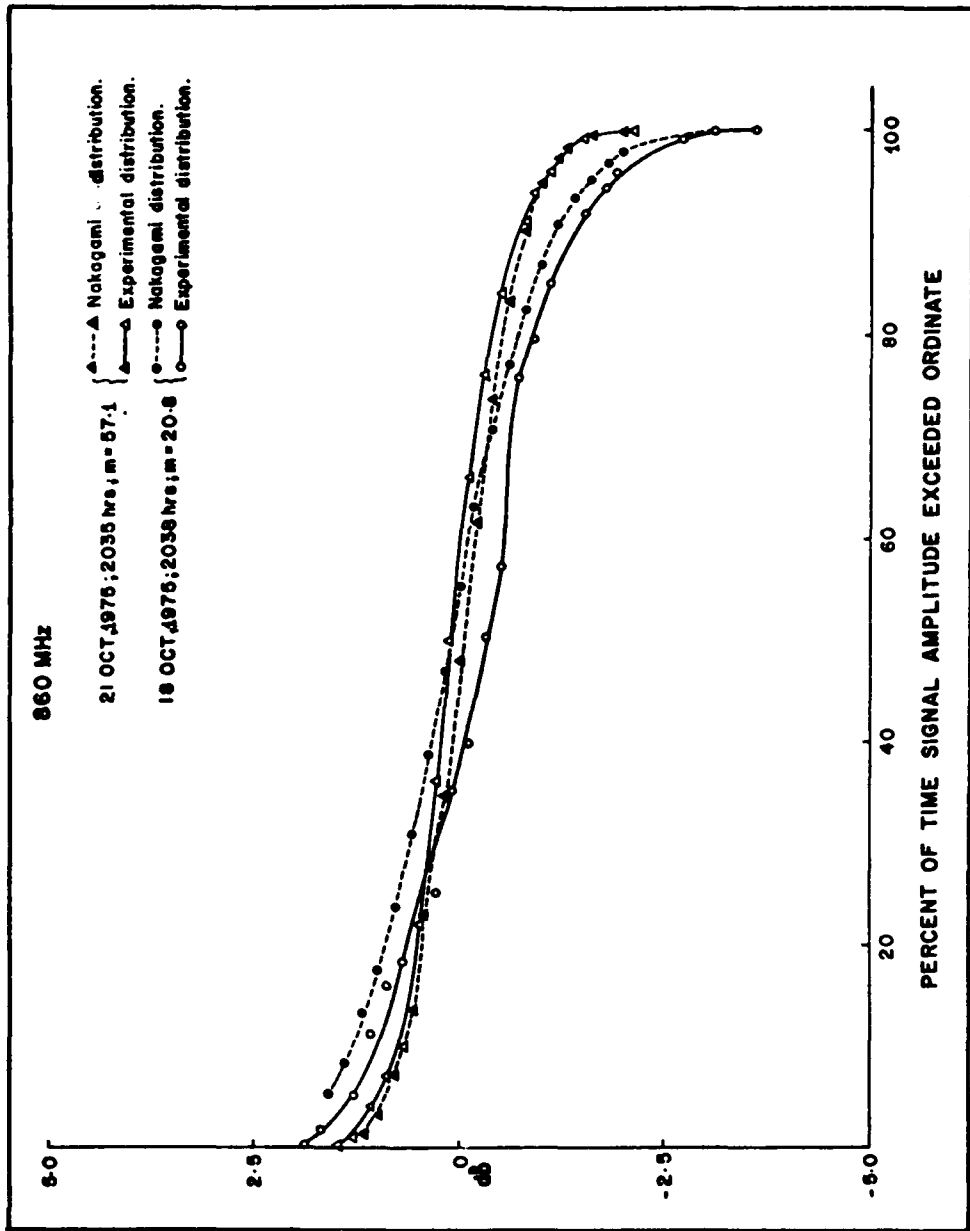


FIG:2. EXPERIMENTAL AND NAKAGAMI CDF's FOR 860 MHz

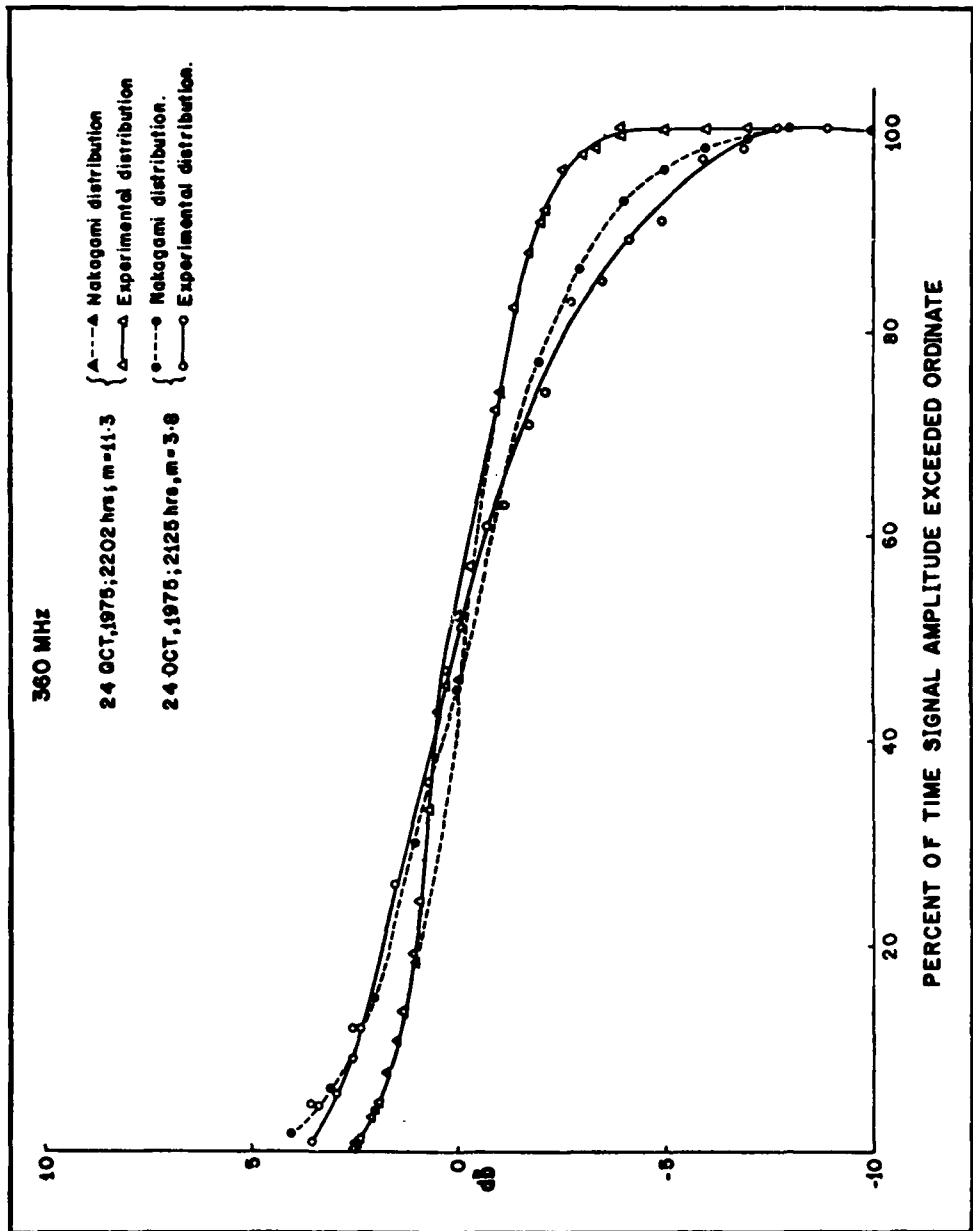


FIG:3. EXPERIMENTAL AND NAKAGAMI CDF'S FOR 360 MHz

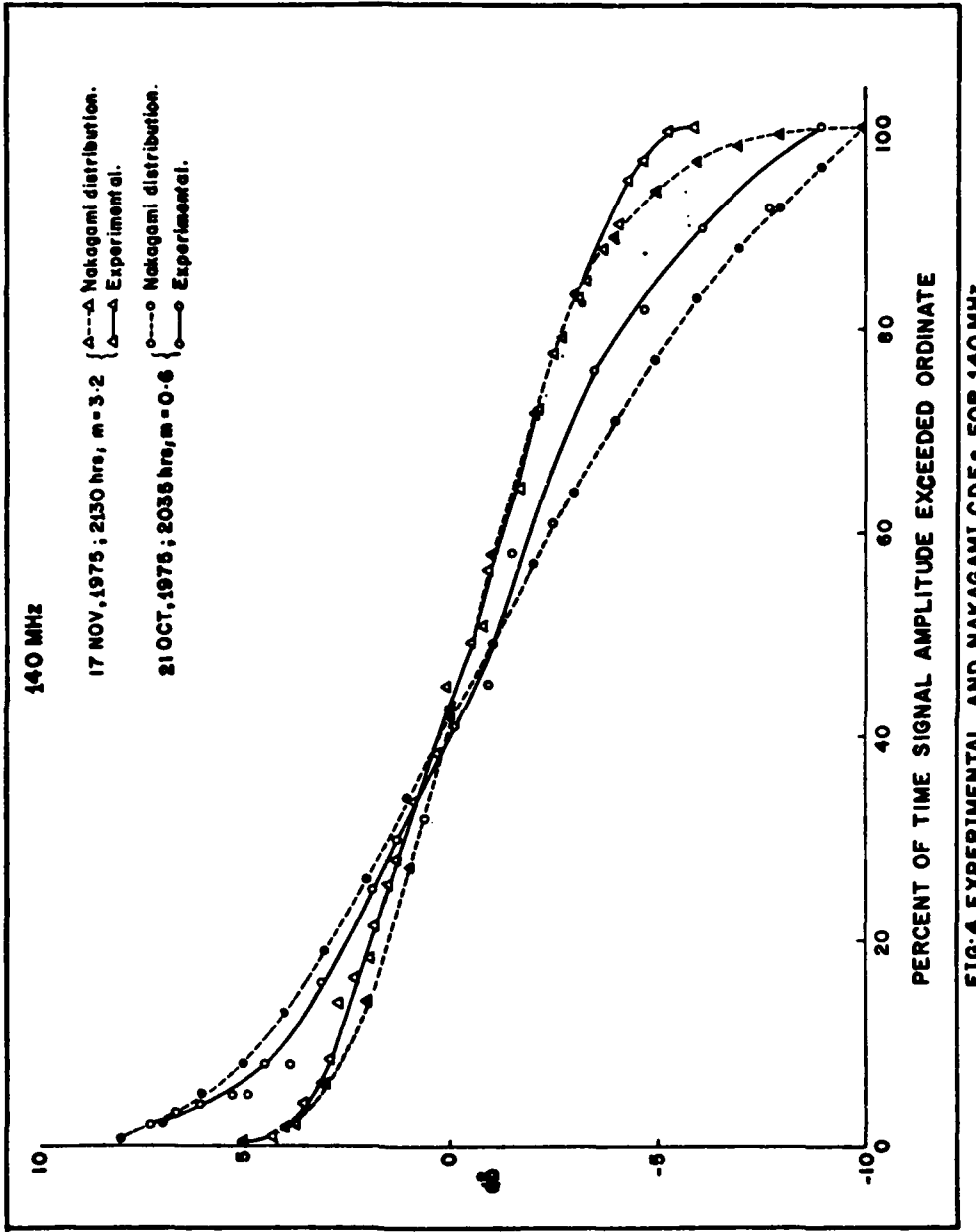


FIG:4. EXPERIMENTAL AND NAKAGAMI CDF'S FOR 140 MHz

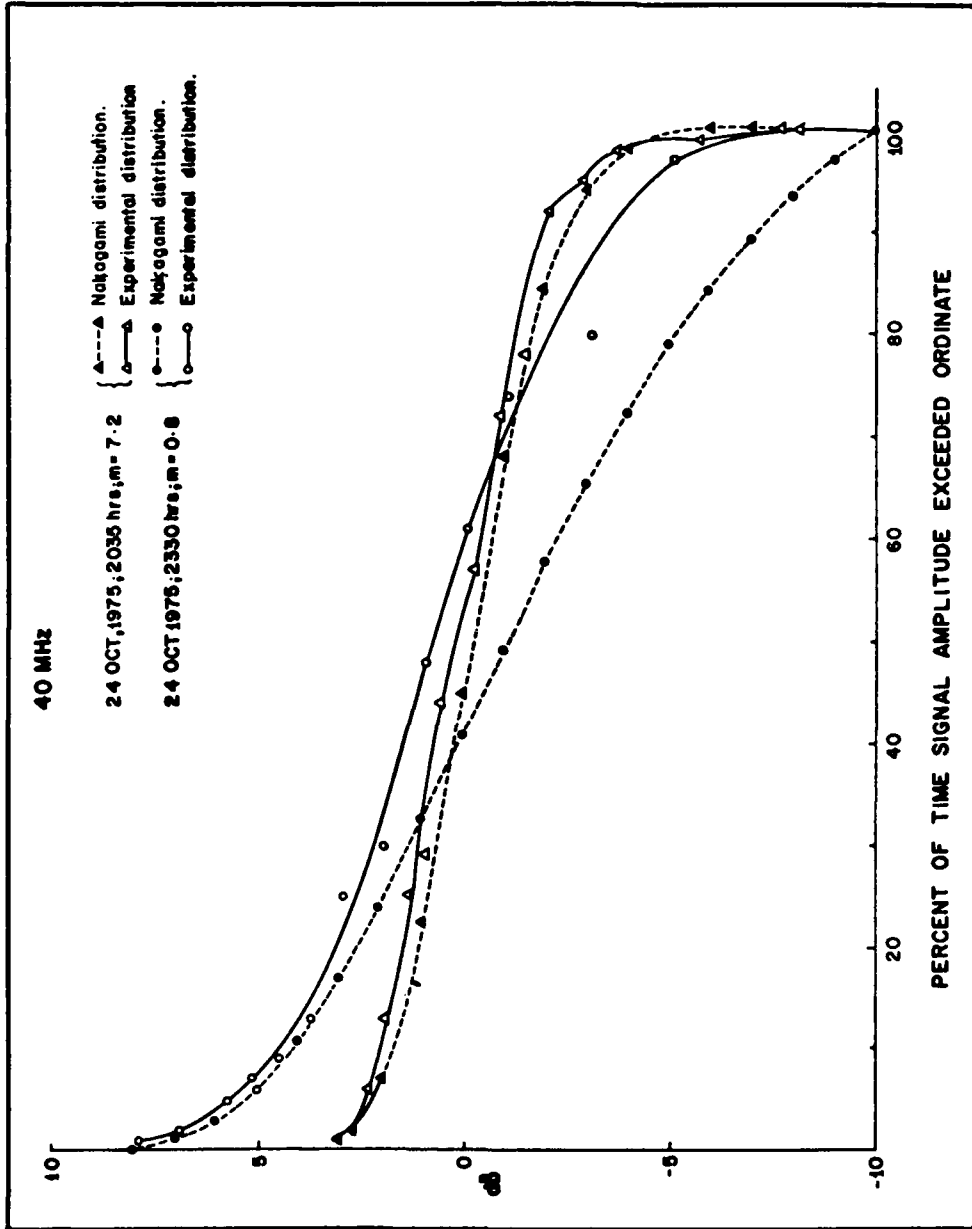


FIG:6 EXPERIMENTAL AND NAKAGAMI CDF'S FOR 40 MHz

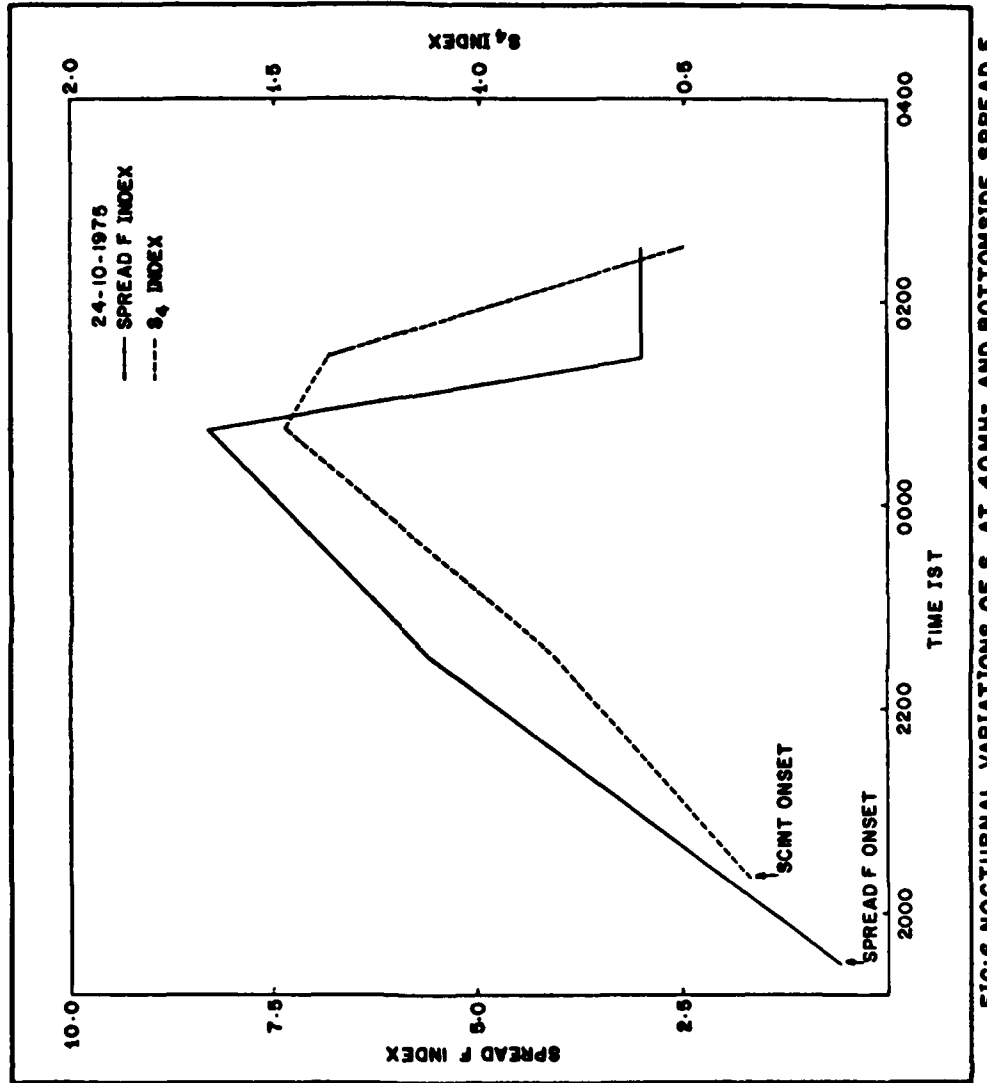


FIG:6. NOCTURNAL VARIATIONS OF S<sub>4</sub> AT 40MHz AND BOTTOMSIDE SPREAD F

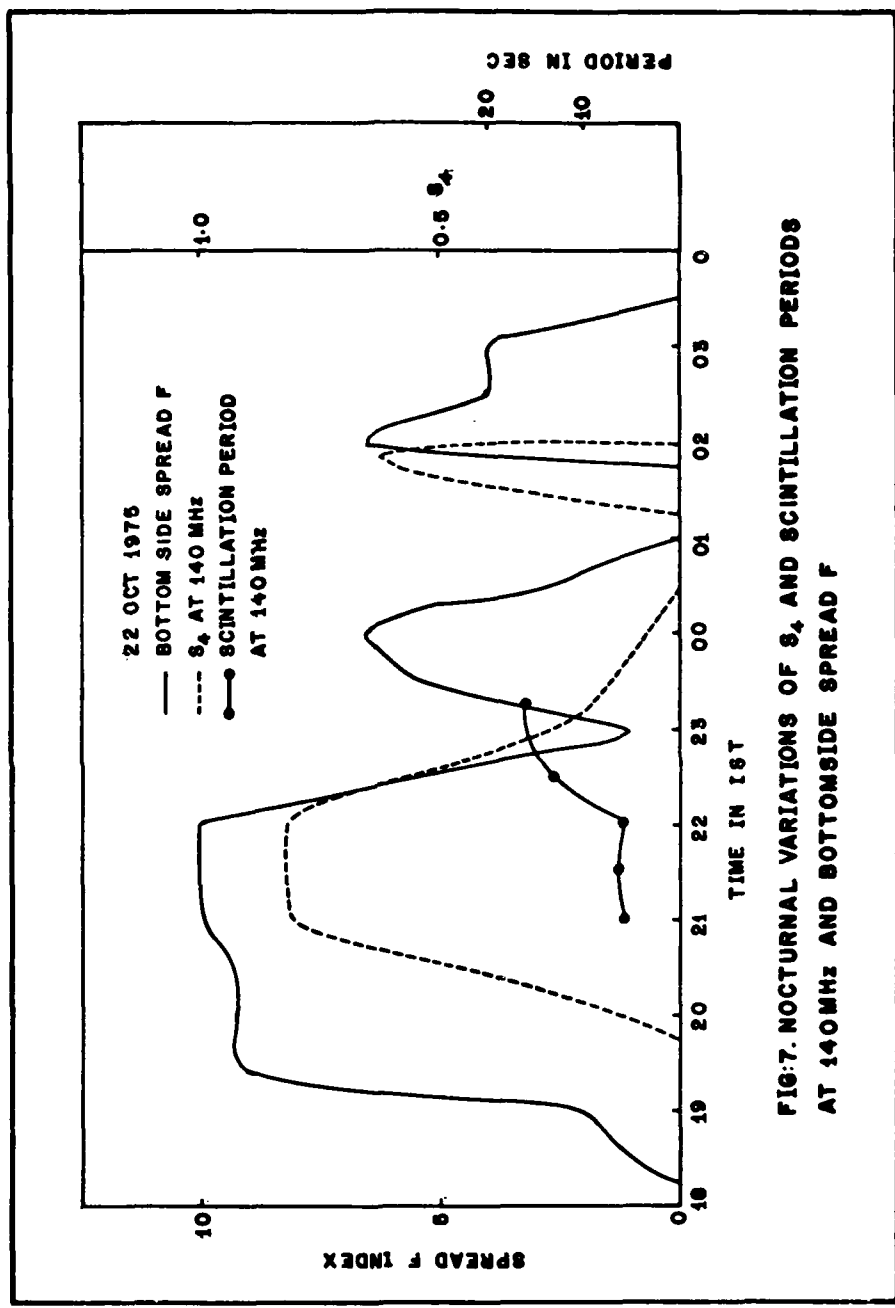


FIG:7. NOCTURNAL VARIATIONS OF  $S_4$  AND SCINTILLATION PERIODS  
AT 140MHz AND BOTTOMSIDE SPREAD F

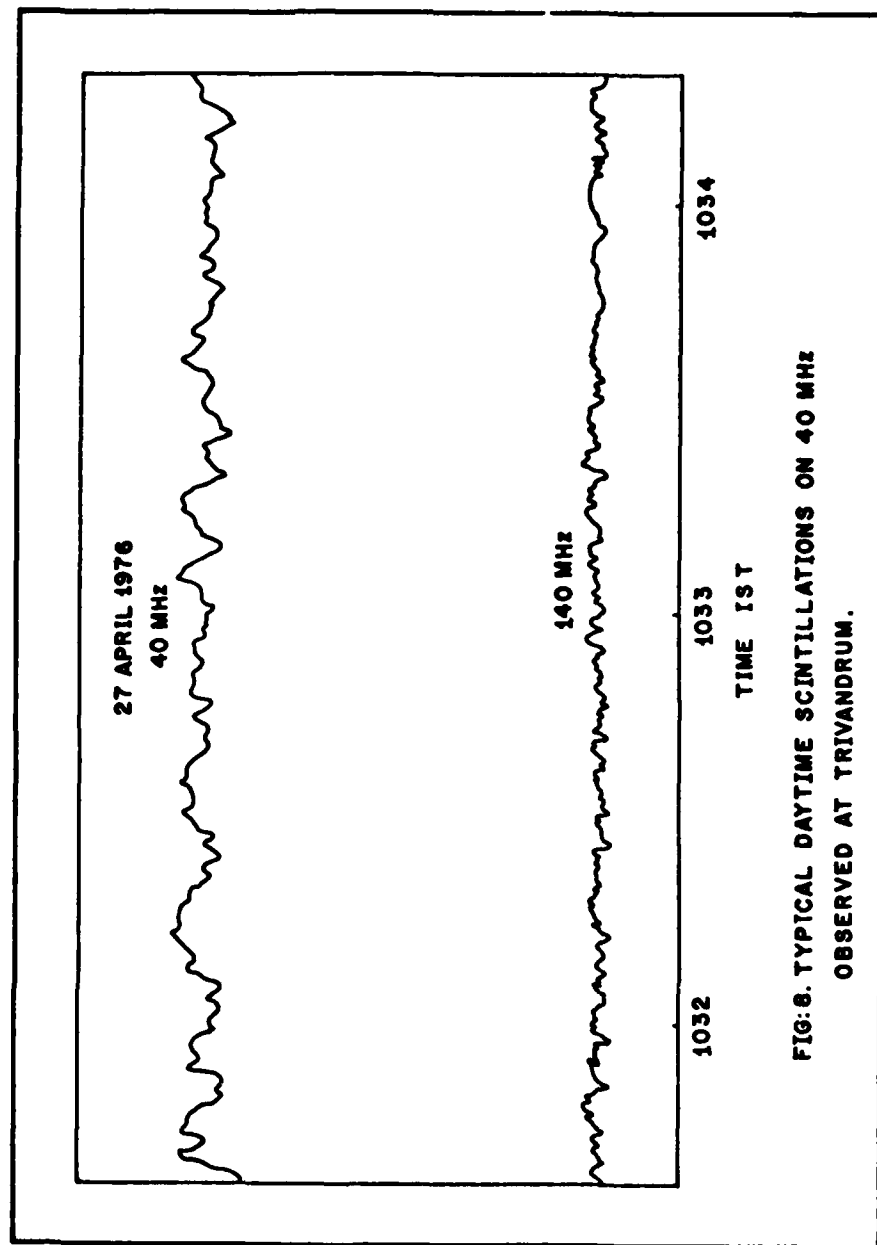


FIG. 8. TYPICAL DAYTIME SCINTILLATIONS ON 40 MHz  
OBSERVED AT TRIVANDRUM.

A NONLINEAR MODEL FOR EQUATORIAL SPREAD F:  
IRREGULARITY AND SCINTILLATION CALCULATIONS

B. E. McDonald, S. L. Ossakow  
U.S. Naval Research Laboratory  
Washington, D.C. 20375

and

A. J. Scannapieco  
Science Applications, Inc.  
Mc Lean, Va.

ABSTRACT

We show that a simple nonlinear model based upon plasma equations of motion and a wave equation for radio propagation is capable of predicting plasma irregularities and scintillations at the equator. The irregularities develop from a linear convective instability on the bottom of the F layer. Depleted regions, or "bubbles," form and rise nonlinearly through the F peak, disturbing the top of the F layer. We integrate the equations of motion numerically, and then solve the parabolic equation for propagation of a 300 Mhz wave through the plasma. We assume a modest total electron content of  $5 \times 10^{16} \text{ m}^{-2}$ . From the radio wave solution we extract scintillation indices as a function of time. Approximately two hours after the instability starts,  $S_4$  reaches 0.48, and the log power variance reaches 3.1 db.

1. The Equatorial Spread F Model.

A recent numerical investigation (Scannapieco and Ossakow, 1976) suggests the collisional Rayleigh-Taylor instability as a cause of observed topside F layer irregularities near the equator. Recent rocket measurements (Kelley et al., 1976) have in fact supported this contention. The collisional Rayleigh-Taylor instability has been suspected as a cause for a few years now (Balsley et al., 1972), but the linear theory of the instability has difficulty explaining the existence of irregularities at altitudes up to 1000 km (Farley et al., 1970). The numerical work of Scannapieco and Ossakow (1976) depicts the commencement of a linear convective instability on the bottom of the F layer, followed by formation of depleted regions, or "bubbles" which rise in a nonlinear fashion to the top of the F layer. This scenario is consistent with observed time delays between appearance of irregularities on the bottom of the F layer and their appearance on the top (Krishnamurthy, 1966).

The theoretical model consists of the following coupled equations which are two dimensional in the coordinate directions orthogonal to the magnetic field (altitude and longitude):

$$\begin{aligned} \frac{\partial n}{\partial t} + \nabla \cdot n \frac{c}{B} \left( \frac{m}{e} \mathbf{E} - \nabla \phi \right) \times \mathbf{B} \\ = -(\kappa_1 [v_2] + \kappa_2 [N_2]) (n - n_0) \end{aligned} \quad (1)$$

$$n v_{in} \nabla^2 \phi + \nabla n v_{in} \cdot \nabla \phi \\ = \left( \frac{m}{e} \nabla n v_{in} - \frac{B}{c} \nabla n \times \hat{b} \right) \cdot g \quad (2)$$

In (1) and (2) the quantities  $n$ ,  $B$ ,  $m$ ,  $g$ ,  $\phi$ ,  $\hat{b}$  and  $v_{in}$  are respectively the ion number density, magnetic field (taken to be constant), ion mass, gravitational acceleration, electrostatic potential, the unit vector in the magnetic field direction, and the ion-neutral collision frequency. The right hand side of (1) is a recombination rate involving the number densities of  $O_2$  and  $N_2$ ;  $n_o$  is an assumed ambient ion profile (a function of altitude). This recombination rate models the night time process of charge exchange followed by dissociative recombination.

Equation (1) is the ion continuity equation; (2) is the quasineutrality equation which results from setting to zero the divergence of the electric current,  $n e (v_i - v_e)$ , where the  $v$ 's are ion and electron velocities. These velocities are determined algebraically from electron and ion momentum equations in which inertia has been neglected. In (1) and (2) we have retained dominant terms, neglecting small terms due to electronic collisions, thermal effects, and ratios of collision frequencies to gyrofrequencies.

The equilibrium solution to (1) and (2) is a state in which the ions are supported against gravity by an electric field:

$$\nabla \phi_o = \frac{m}{e} g \quad (3)$$

We must also consider what the electrons are doing. The ambient electric field is of the wrong sign and magnitude to support them against gravity, so they respond by drifting horizontally. Thus viewed as a whole, the electrically neutral plasma is supported by an electron current  $J = c n_o m g / e$ . We can write (1) and (2) in the following form:

$$\frac{\partial n}{\partial t} = \frac{c}{B} \nabla \cdot n (\nabla \phi_1 \times \hat{b}) - (K_1 [O_2] + K_2 [N_2]) (n - n_o) \quad (4)$$

$$\nabla^2 \phi_1 + \frac{\nabla n v_{in}}{n v_{in}} \cdot \nabla \phi_1 = - \frac{B}{c v_{in}} \left( \frac{\nabla n}{n} \times \hat{b} \right) \cdot g, \quad (5)$$

where

$$\phi_1 = \phi - \phi_o. \quad (6)$$

The ambient profiles  $n = n_o(z)$  and  $\phi_1 = 0$  are a steady state solution to (4) and (5), as one can see by inspection. The right hand side of (5) becomes zero because the ambient  $n_o$  gradient is parallel to  $g$ .

Why is the equilibrium unstable below the F peak? The ambient plasma density profile of Figure 1 is supported against gravity by an ambient electric current. If we displace a small amount of plasma downward from region A to region B in Figure 1, the mass density near B exceeds the value which can be supported by the ambient current. Thus the mass near B falls into regions of decreasing support against gravity and a convective instability is sustained. The same type of argument predicts that the depleted region A would rise toward the F peak. However, if we were to repeat the argument for density perturbations above the peak, we would

predict that slightly depleted regions would rise only a small distance before finding insufficient ambient current to raise them further. Thus linear theory based on (1) and (2) predicts that the ambient density gradient is stabilizing above the F peak, and destabilizing below it. This can be seen in the following expression for the linear growth rate derived from (1) and (2):

$$\gamma = - \frac{g}{v_{in}} \cdot \frac{\nabla n_o}{n_o} - (K_1[O_2] + K_2[N_2]). \quad (7)$$

## 2. Computer Simulation of the Instability.

We have integrated the model equations (4) and (5) numerically using a flux corrected (diffusive-antidiffusive) method for (4) (Boris and Book, 1973) and an alternating direction implicit solver for (5) (Varga, 1962). The vertical extent of the mesh is from 250 to 450 km, with 102 points spaced 2 km apart. The horizontal mesh is 42 points spaced 200 meters apart. We assume a total electron content of  $5 \times 10^{16} \text{ m}^{-2}$ . The initial condition is a 5% density fluctuation imposed 50 km below the F peak. The initial plasma density contours are similar in shape to those of Figure 2.

The development of the instability is shown in Figures 2 through 4. One should keep in mind that the vertical scale has been compressed by a factor of 50 in these figures. By 2000 seconds (Figure 2), the 5% fluctuation has grown to about 20%, with little change in contour shapes (the growth is still approximately linear). The contour distortion at 5000 seconds (Figure 3) shows that nonlinearity has become important as the depleted "bubble" rises toward the F peak. By 10000 seconds (Figure 4) the bubble has risen through the peak and has disturbed the top of the F layer.

## 3. Radio Propagation Through the Disturbed F Layer.

Let us consider the effect of the plasma irregularities just described upon radio waves. We shall consider an incident plane wave propagating downward at zero zenith angle. The calculations presented here are for a wavelength  $\lambda$  of one meter (300 Mhz). The applicable wave equation is (Yeh and Liu, 1972)

$$[\nabla^2 + k_o^2(1 + x(\underline{r}))] E = 0, \quad (8)$$

where  $k_o = 2\pi/\lambda$  is the incident wavenumber,  $x$  is the electric susceptibility of the plasma, and  $E$  is a scalar component of the electric field. For high frequency waves we may assume a scalar susceptibility:

$$x = - \frac{\omega_{pe}^2}{\omega^2} = - \frac{\lambda}{\pi} r_e n, \quad (9)$$

where  $\omega_{pe}$  is the electron plasma frequency and  $r_e = 2.8 \times 10^{-13} \text{ cm}$  is the classical electron radius.

For solution of (8) we make the substitution

$$E(\underline{r}) = \exp \left[ i \int k_o \sqrt{1 + x_o(z)} dz \right] (1 + x_o(z))^{-1/4} F(\underline{r}). \quad (10)$$

where  $z$  is altitude and  $x_o(z)$  is the susceptibility of the ambient  $n_o$  profile. We assume

$$|x| \ll 1, \text{ and} \quad (11)$$

$$\lambda \ll L,$$

where  $L$  is the scale size of structures in the plasma. These assumptions with (8) and (10) yield the parabolic equation:

$$\frac{\partial F}{\partial z} = \frac{i}{2k_o \sqrt{1+x_o^2}} (\nabla_{\perp}^2 F + k_o^2 x_{\perp}^2 F), \quad (12)$$

where  $\perp$  refers to the coordinates orthogonal to  $z$ , and

$$x_{\perp}(r) = x(r) - x_o(z) \quad (13)$$

The parabolic approximation i.e., the neglect of a second  $z$  derivative of  $F$  in (12), introduces a fractional error into  $F$  which is on the order of  $|x_{\perp}| + 1/k_o^2 L^2$  (McDonald, 1976).

We have integrated (12) numerically through plasma density distributions produced by the spread  $F$  model described above. The integration scheme is a space centered leapfrog representation of (12), with real and imaginary parts of  $F$  defined on alternate  $z$  levels. The mesh consists of 42 horizontal points ( $x$ ) spaced 200m apart and 451  $z$  levels 1km apart.

The integration proceeds down from  $z = 450$  km, where the initial condition is  $F = 1$ . Results for  $S_4$  and  $\sigma_x$  (log power variance) appear in Figures 5 and 6. These indices are evaluated at ground level as follows:

$$S_4 = (\langle |F|^4 \rangle - \langle |F|^2 \rangle^2)^{1/2} / \langle |F|^2 \rangle \quad (14)$$

$$\sigma_x = 10 (\langle (\log_{10} |F|^2)^2 \rangle - \langle \log_{10} |F|^2 \rangle^2)^{1/2} \quad (15)$$

The brackets in (14) and (15) are horizontal averages. One sees in Figures 5 and 6 a steady increase in  $S_4$  and  $\sigma_x$  from  $t = 0$  to 7000 seconds, followed by a dropoff. This maximum is apparently due to the sudden disturbance of the  $F$  peak by the rising bubble of Figures 3 and 4. This single bubble results in modest indices:  $S_4 = 0.48$  and  $\sigma_x = 3.1$  db. We anticipate stronger scintillation to result from later phases of the instability, when the  $F$  layer is disturbed by many depleted regions. Results from the later stages of the calculation will be presented elsewhere.

#### REFERENCES

1. A. J. Scannapieco and S. L. Ossakow, NRL Memo Report 3280, May, 1976 (to appear also in Geophys. Res. Lett.).
2. M. C. Kelley, personal communication via S. L. Ossakow (1976) (to appear in Geophys. Res. Lett.).
3. B. B. Balsley, G. Haerendel, and R. A. Greenwald, J. Geophys. Res., 77, 5625, 1972.
4. D. T. Farley, B. B. Balsley, R. F. Woodman, and J. P. McClure, J. Geophys. Res., 75, 199, 1970.

5. B. V. Krishnamurthy, J. Geophys. Res., 71, 4527, 1966.
6. J. P. Boris and D. L. Book, J. Comput. Phys. 11, 38, 1973.
7. R. S. Varga, Matrix Iterative Analysis (Prentice-Hall, Inc., Englewood Cliffs, N.J., 1962). Chap. 7.
8. B. E. McDonald, "Numerical Solution of the Parabolic Equation with the PEP Code," NRL Memo Report, June, 1976 (in preparation).

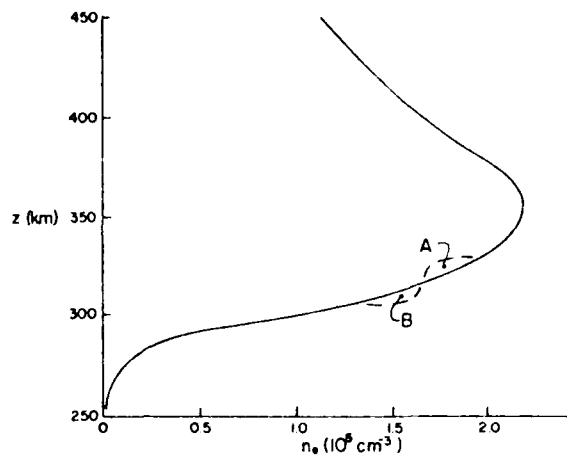


Figure 1. Ambient plasma number density profile showing displacement for Rayleigh - Taylor instability.

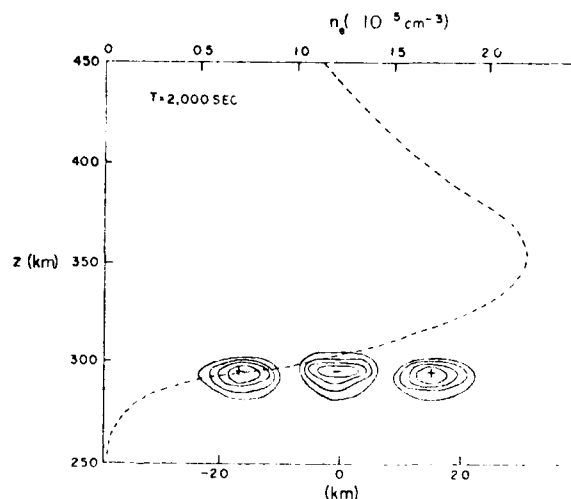


Figure 2. Contours of  $n$  relative to ambient  $n_0$  at 2000 sec. Values range from -22% to +19%.

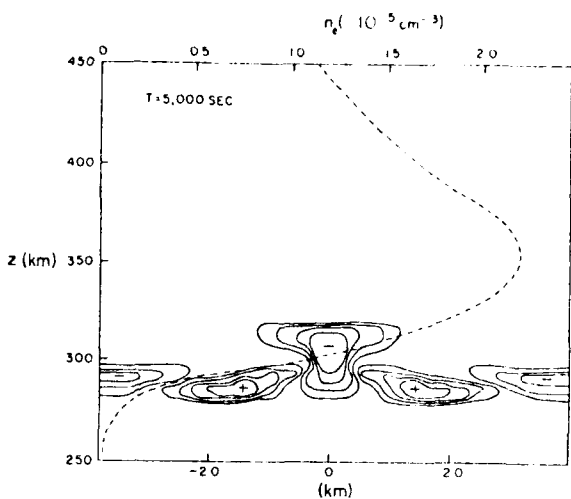


Figure 3. Contours of  $n$  relative to ambient at 5000 sec. Values range from -46% to +107%.

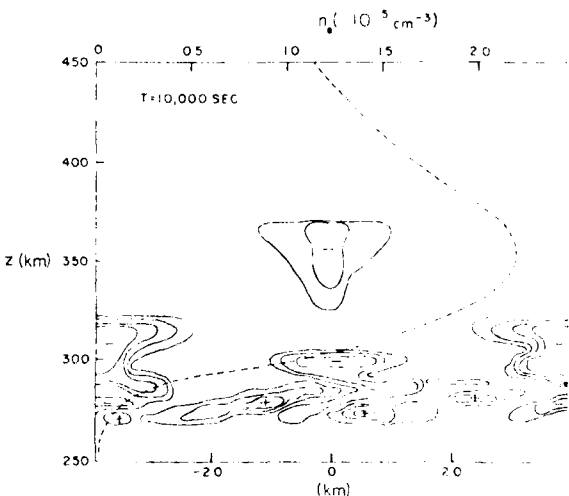


Figure 4. Contours of  $n$  relative to ambient at 10,000 sec. Values range from -58% to +28%.

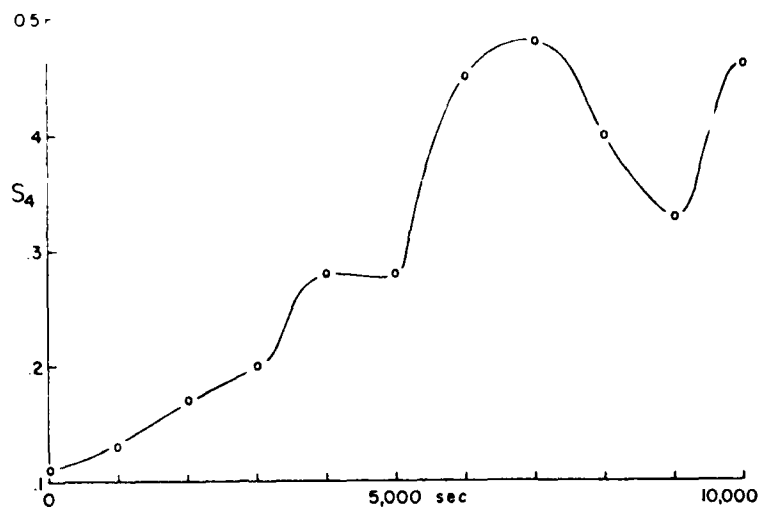


Figure 5. Scintillation index vs time at ground level for incident 300MHz plane wave.

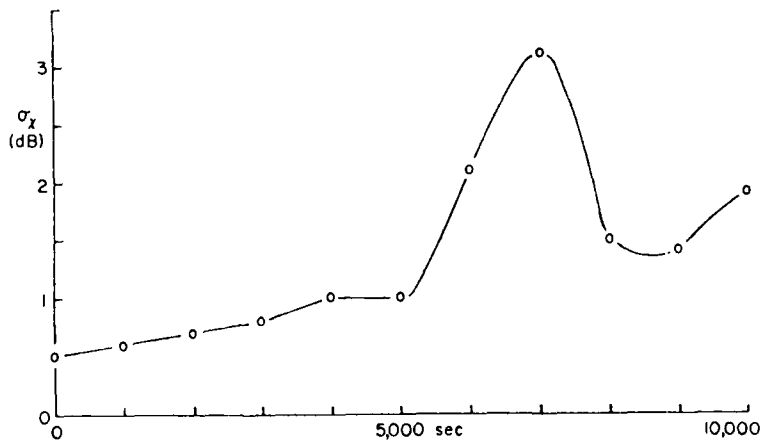


Figure 6. Log power variance vs time at ground level for incident 300MHz plane wave.

## The Stormtime Component of Scintillations

Jules Aarons and Sunanda Basu\*  
Air Force Geophysics Laboratory  
Air Force Systems Command  
Hanscom AFB, MA 01731

Eileen Martin  
Emmanuel College  
Boston, MA 02115

### Abstract

During moderate magnetic storms, scintillations from a host of synchronous satellites at auroral and sub-auroral stations show the effects of the well-known expansion of the auroral oval and the flow of field-aligned currents. The effects are particularly noticeable for stations such as Narssarsuaq ( $64^{\circ}$  A) and Goose Bay ( $60^{\circ}$  A) for storm commencements in the morning sector when severe daytime scintillations are observed in addition to an intensification of its usual nighttime pattern.

For large magnetic storms, however, when a symmetric ring current develops and the plasmapause moves well equatorward of its usual quiettime location, it is possible to recognize a stormtime component of scintillations at many midlatitude stations with invariant latitudes  $< 60^{\circ}$ . Simultaneous scintillation data from stations widely separated in local time such as College ( $58^{\circ}$  A), Sagamore Hill ( $53^{\circ}$  A), Aberystwyth ( $49^{\circ}$  A) and Lindau ( $44^{\circ}$  A) and total electron content observations at Sagamore Hill (to monitor the position of the plasmapause) were used to establish this universal time component of scintillations. The UT component could be clearly identified for the big magnetic storms of June 17, 1972, October 31, 1972 and the various storms that took place during August 4-9, 1972. It seems that this component of scintillations is associated with plasma instabilities and electron heating effects that occur in the vicinity of the stormtime plasmapause.

### Introduction

Field aligned irregularities of the order of several hundred meters to several kilometers are observed at high latitudes by a variety of techniques. They are predominantly in the 300 - 350 km range and are extant over a region from

\* NRC Resident Research Associate

below the auroral oval to over the polar cap. It has been documented (Aarons and Allen, 1971) that the intensity of the irregularities increases during magnetic storms. This intensity is measured by the fading of radio frequency signals traversing the ionosphere.

Given the recent plethora of synchronous satellite observations at 136 MHz at widely separated ground stations, our objective is to determine a stormtime component of scintillations during large magnetic storms in 1972. This universal time controlled component of scintillations is found to be superimposed on the widely known local midnight component and adds a further element of complexity to the already complex scintillation morphology during storms. Basu (1974) had earlier demonstrated the existence of this component of scintillations by utilising simultaneously obtained Sagamore Hill scintillation and total electron content (TEC) data. We wish to substantiate this concept further by utilising data from stations listed in Table I. The data are a series of amplitude fluctuations reduced by the method of Whitney et al., (1969) into 15 minute averages of scintillation index. We have not converted the empirical index  $SI_{JSSG}$  to the theory-based index  $S_4$  (Briggs and Parkin, 1963) as our object was to establish the onset time of moderately heavy scintillations at various midlatitude stations, rather than a quantitative comparison of the actual magnitudes observed.

#### Storm of January 21, 1972

The storm started with an SSC at 1151 UT on January 21 as shown in Figure 1. Dst indices for the storm show that maximum Dst attained was  $-80 \gamma$  at 1600 UT and the recovery phase started immediately afterwards. The scintillation response at a host of stations is shown in Figure 2. The striking feature of this storm is the almost immediate response at Narssarssuaq and Goose Bay, then in the morning sector. This is most probably due to the expansion of the auroral oval. The negative bay at Narssarssuaq coupled with large negative declination variation  $\Delta D$  in the St. John and Ottawa magnetograms imply the flow of field aligned current into the morning sector of the auroral oval. College, in the midnight sector, shows the expected intensification of its normal local time component of scintillations.

It is quite interesting to note that Sagamore Hill shows little response to this magnetic storm in its development phase. This is believed to be due to the fact that the plasmapause did not move equatorwards as far as

the L=2.8 intersection point of the ray path to ATS-3 as may be observed from the  $\Delta$ TEC curve of Sagamore Hill which shows positive deviations only in the development phase of the storm. Such a situation with considerable daytime scintillations at Narssarssuaq and Goose Bay with little or no response at Sagamore Hill coupled with positive TEC variation is also observed for the storms of February 24 and March 6, 1972. For both these storms the maximum Dst was approximately -80 γ also. A study of other storms in 1972 showed that similar storms in other seasons did not produce as much daytime scintillations at Narssarssuaq and Goose Bay as the winter ones. This could be due to the fact that the angle between the axis of the earth's magnetic dipole and the earth-sun line is a minimum at winter daytime as it is at summer nighttime. For summer nighttime conditions, Basu (1975) has shown that the scintillation activity peaks at Narssarssuaq in response to the dipole tilt angle orientation. Since a similar favourable orientation is attained for winter daytime, scintillations would probably increase in response to even a moderate enhancement of magnetic activity.

The Sagamore Hill data shows enhancement in scintillation activity between 2200 and 0400 LT on January 22 without any accompanying increase in magnetic activity. It is probable that this component of scintillations is associated with sharp horizontal density gradients found at times of quietening after magnetic activity. These steep gradients are found to break up into small scale irregularities (Basu, 1976) which are likely to cause scintillations.

#### Storm of June 17, 1972

This was a very large magnetic storm in which Dst reached -190 γ at 0300 hours on June 18, 1972, (Figure 3) the SSC having occurred at 1312 UT on June 17. Narssarssuaq and Goose Bay show auroral type scintillations and hence will not be discussed any further in this paper. However, the scintillation behaviour at College, Sagamore Hill and Lindau clearly exhibit a stormtime component of scintillations. Sagamore Hill shows a sharp rise in scintillations at approximately 0100 UT on June 18 when Dst increased sharply from -70 γ at midnight to -150 γ at 0100 UT. The TEC at Sagamore Hill, shown in Figure 3, decreased sharply well below its median value after showing the usual "dusk increase" (Mendillo and Klobuchar, 1974) indicating that the plasmapause had moved to the vicinity of L=2.8. Unfortunately College data was missing

till 0200 UT, so it is difficult to precisely determine the time of increase of scintillations but the station does show considerable scintillations from 0200 to 0900 UT ( $\sim$  1600-2100 LT) which is not its usual local time component of scintillations. The existence of the stormtime component becomes even more convincingly demonstrated by the 100% peak of scintillations at Lindau at 0400 UT which is much beyond its local midnight sector. It is to be noted that 0400 UT was the time of maximum Dst and, as such, it may be surmised that the plasmapause reached its maximum equatorward excursion at that time. The occurrence of scintillations near simultaneously at stations widely separated in local time such as College, Sagamore Hill and Lindau lends support to our hypothesis of a stormtime component of scintillations dynamically controlled by the position of the plasmapause.

#### The August 1972 storms

This much studied most active period of the last sunspot cycle provides us with a few classic examples of the existence of the stormtime component of scintillations. In Figures 4 and 5 are seen the Dst index, the TEC from from Sagamore Hill and the scintillations at various stations for this period. The Dst index reached peak values exceeding -100 γ on August 4-6 and after a period of relative quiet on August 7-8, again showed the large value of -150 γ on August 9. In this storm sequence, as for the storm of June 17, it is the lower latitude stations that give us a better indication of the stormtime component. This may be observed from the curve of Dst index and the scintillation history for Sagamore Hill, Aberystwyth and Lindau. All of these stations even though separated 6 hours in local time show scintillation peaks around 0400 on August 4, 0000 UT on August 5 and 0500 UT on August 6 in conjunction with Dst increases and large TEC depletions at Sagamore Hill (Mendillo and Klobuchar, 1974). The sharp peak around 1200 UT on August 9 is a rather dramatic example of this effect as it occurs in either the noon or the morning sector of these stations. The afternoon peak on August 8 at Aberystwyth and Lindau is unusual and seems to be due to localized disturbances in the European sector - the peak being absent at Sagamore Hill. Even though the data are not shown we would like to point out that LES-6 and ATS-3 data taken at Narssarssuaq shows peaks in the afternoon hours of August 8 while at Goose Bay and Sagamore Hill there is no activity at that time. Thus it seems that stations to the east of the Narssarssuaq sector showed

evidence of localized disturbances. Chappell et al. (1971) have observed such longitudinally limited disturbances in the daytime sector with Ogo-5 data. It is interesting to note that Athens at an invariant latitude of  $31^{\circ}$  does not show these UT effects indicating that the plasmapause does not move as far equatorward even during the severest disturbances. In fact, Athens, which shows a fairly high scintillation activity during quiet times in local summer, actually showed a decrease of scintillation activity during this very disturbed period (Aarons and Martin, 1975). Under the assumption that the summer quiettime maximum at Athens is caused by E<sub>s</sub> type scintillations, the negative correlation between scintillations and magnetic activity may be explained by the lower incidence of midlatitude E<sub>s</sub> during magnetic storms (Basu et al., 1973).

More detailed studies are underway to correlate the position of the plasmapause in the magnetosphere obtained by a variety of techniques and ground based scintillation during this extensively studied magnetically disturbed period.

#### Storm of October 31, 1972

The development of the high latitude irregularity region during this storm has been described by Aarons (1976). In this report we shall only discuss the stormtime component of scintillations clearly observed at Sagamore Hill (using three satellites I2F3, ATS-3 and ATS-5, and radio stars) as well as at Aberystwyth using I2F3 and ATS-3. The data from College again demonstrates that at certain times during a magnetic storm, a large negative bay in the same local time sector will give rise to a very fast longitudinally limited expansion of the irregularity region without the same effects being observed at comparable latitudes in other local time sectors (Aarons, 1976). The College scintillation data and magnetogram are shown in Figure 6 as well as the Dst for the storm and the TEC variation at Sagamore Hill.

The Dst index for this storm shows that beyond 0200 UT on November 1, there is a rapid intensification of ring current. Between 0240 and 0245, the Cygnus intersection noted a rapid increase in scintillation, the latitude of the intersection being at  $58^{\circ}$  invariant (Figure 7). In this case, the 400 MHz channel showed a dramatic increase in fading to 6 dB. Sagamore Hill observations (at  $53^{\circ}$  invariant), showed a rapid increase at 0300 UT on all three satellite ray paths. At the same time the ATS-3 TEC observations (Figure 6) showed a rapid decrease reaching 50% below its median value (Mendillo and Klobuchar, 1974). The TEC

remained below median for two hours when the SI reached saturation at Sagamore Hill. A DMSP pass at 0400 UT shown in Figure 8 did not show any visual aurora at the latitude of Sagamore Hill. Thus we have reason to believe that the high scintillations at this time are caused by the proximity of the plasmapause, the irregularities being created via the heat conduction hypothesis (Cole, 1965; Bowhill, 1966) or one of the plasma instability mechanisms (Cornwall et al., 1971; Hudson and Kelley, 1976) postulated in the literature. Beyond 0500 UT irregular positive fluctuations of TEC are observed, probably associated with auroral precipitation. The local ionograms taken at Billerica, Ma., show the presence of auroral E and a DMSP pass at 0600 UT (Figure 9) shows visual aurora at the latitude of the 3 satellite intersection points from Sagamore Hill. Intense scintillations continue through this period up to 1200 UT.

The next station where an increase in index was noted was the Aberystwyth ATS-3 ionospheric point of 49° invariant latitude at 0402 UT while a rise of I<sub>2</sub>F<sub>3</sub> point from Aberystwyth at 45° invariant was noted at 0450 UT in Figure 6. It is very significant that Aberystwyth shows the increase in scintillation well past local midnight and somewhat later than the higher latitude Sagamore Hill onset time. This gives credence to our hypothesis of a UT controlled scintillation component well correlated with the known equatorward motion of the plasmapause during storms.

#### Conclusion

With data from several midlatitude stations widely separated in longitude, we have been able to establish a stormtime component of scintillations related to the position of the plasmapause bounding a plasmasphere which is quite drastically reduced in size. It is known that SAR arcs are usually found at the equatorward edge of the stormtime plasmapause (Hoch, 1973). Thus a few of the mechanisms that are responsible for the excitation of SAR arcs may also create small scale irregularities giving rise to scintillations (Basu, 1974). Cornwall et al. (1971) and more recently, Hudson and Kelley (1976) have postulated plasma instabilities which would operate at the equatorial edge of the ionospheric plasma trough during magnetic storms. This would explain the existence of electric field fluctuations in the ionosphere in the region of SAR arcs as observed by Ogo-6 (Nagy et al., 1972, 1974). Such turbulent electrostatic field fluctuations have been previously correlated with scintillations (Kelley, 1972).

Since the existence of the stormtime component has been reasonably well established, it is important to incorporate this component into a suitably refined version of the high and midlatitude model of scintillations (Aarons, 1973). Such a refined model is currently being developed.

References

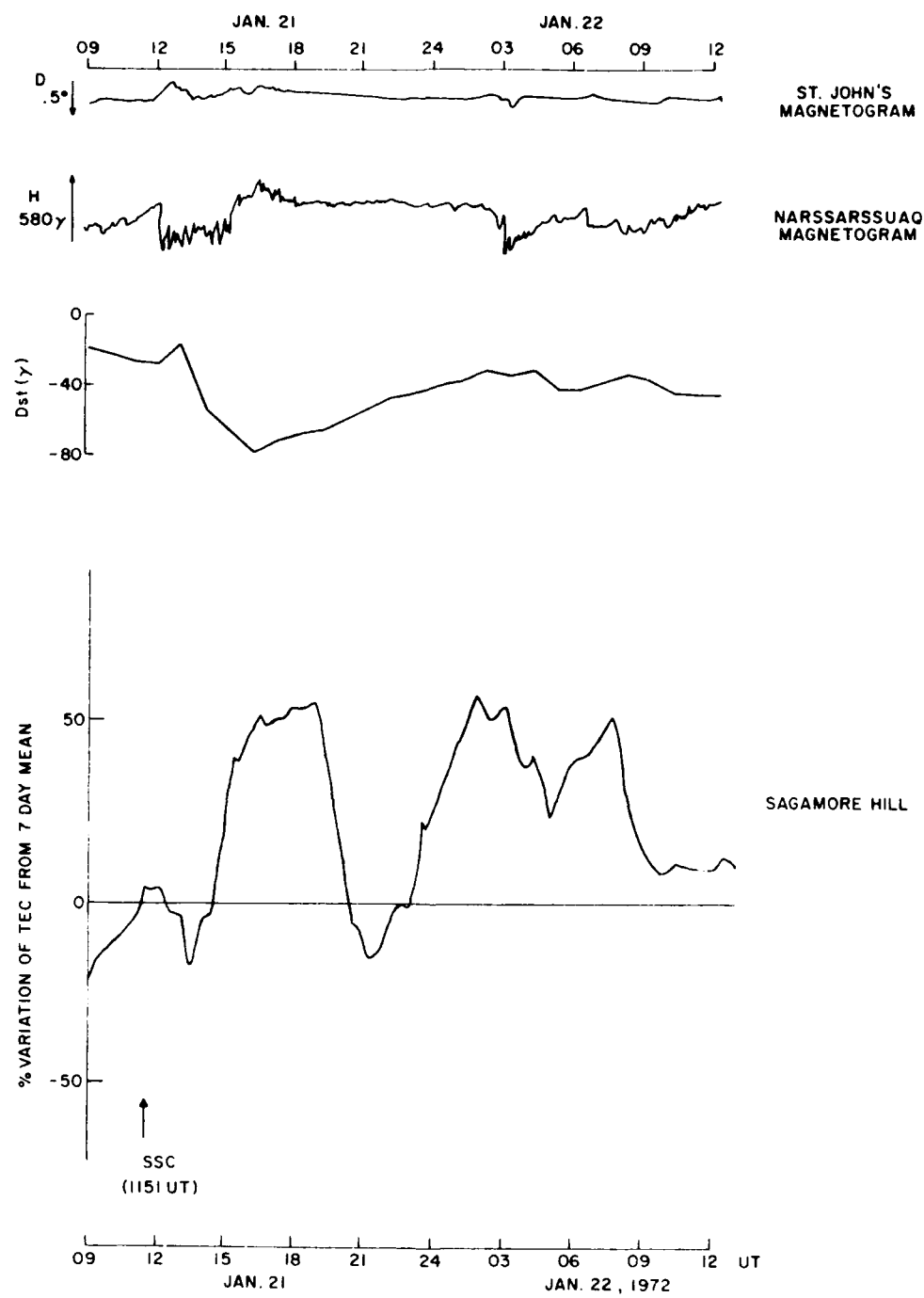
- Aarons, J., J. Geophys. Res., 78, 7441 (1973).
- Aarons, J., J. Geophys. Res., 81, 661 (1976).
- Aarons, J. and R.S. Allen, J. Geophys. Res., 76, 170 (1971).
- Aarons, J. and E. Martin, Radio Science, 10, 547 (1975).
- Basu, Sunanda, R.L. Vesprini and J. Aarons, Radio Science, 8, 235 (1973).
- Basu, Sunanda, J. Geophys. Res., 79, 3155 (1974).
- Basu, Sunanda, J. Geophys. Res., 80, 4725 (1975).
- Basu, Sunanda, EOS Abstracts, 57, 307 (1976).
- Bowhill, S.A., in Spread-F and Its' Effects upon Radiowave Propagation and Communications, edited by P. Newman, Technivision, Maidenhead, England (1966).
- Briggs, B.H. and I.A. Parkin, J. Atmos. Terr. Phys., 25, 339 (1963).
- Chappell, C.R., K.K. Harris and G.W. Sharp, J. Geophys. Res., 76, 7632 (1971).
- Cole, K.D., J. Geophys. Res., 70, 1689 (1965).
- Cornwall, J.M., F.V. Coroniti and R.M. Thorne, J. Geophys. Res., 76, 4428 (1971).
- Hoch, R.J., Reviews of Geophysics and Space Physics, 11, 935 (1973).
- Hudson, M.K. and M.C. Kelley, Evidence for a Rayleigh-Taylor type instability and upwelling of depleted density region during equatorial Spread F, Submitted to J. Geophys. Res. Letters (1976).
- Kelley, M.C., J. Geophys. Res., 77, 1327 (1972).
- Mendillo, M. and J.A. Klobuchar, An atlas of the ionospheric response to geomagnetic storms as monitored by the parameters total electron content, peak density and slab thickness, Tech. Rep., Air Force Cambridge Res. Lab., Bedford, MA (1974).

References (cont.)

- Nagy, A.F., W.B. Hanson, R.J. Hoch and T.L. Aggson, J. Geophys. Res., 77, 3613 (1972).
- Nagy, A.F., L.H. Brace, N.C. Maynard and W.B. Hanson, J. Geophys. Res., 79, 4331, (1974).
- Whitney, H.E., J. Aarons and C. Malik, Planet. Space Sci., 17, 1069 (1969).

Table I

Station	Satellite	Geographic Coord.		Invariant Latitude	Angle of Elevation
		Latitude	Longitude		
Narssarssuaq	ATS-3	54.2°N	51.0°W	64°	18.0°
	LES-6	54.4°N	43.9°W	63°	20.7°
Goose Bay	ATS-3	48.3°N	62.0°W	60°	28.8°
College	ATS-1	57.0°N	147.5°W	58°	16.9°
Sagamore Hill	I2F3	39.1°N	65.8°W	53°	28.0°
	ATS-3	39.3°N	71.0°W	53°	41.0°
	ATS-5	39.2°N	75.2°W	53°	29.5°
	Cygnus	43.5°N	75.3°W	57°	
(0240-0245 UT)					
Aberystwyth	ATS-3	46.4°N	22.1°W	49°	6.5°
	I2F3	46.5°N	12.5°E	45°	7.8°
Lindau	I2F2	46.4°N	19.9°E	44°	16.1°
Athens	I2F2	35.0°N	27.7°E	31°	33.2°



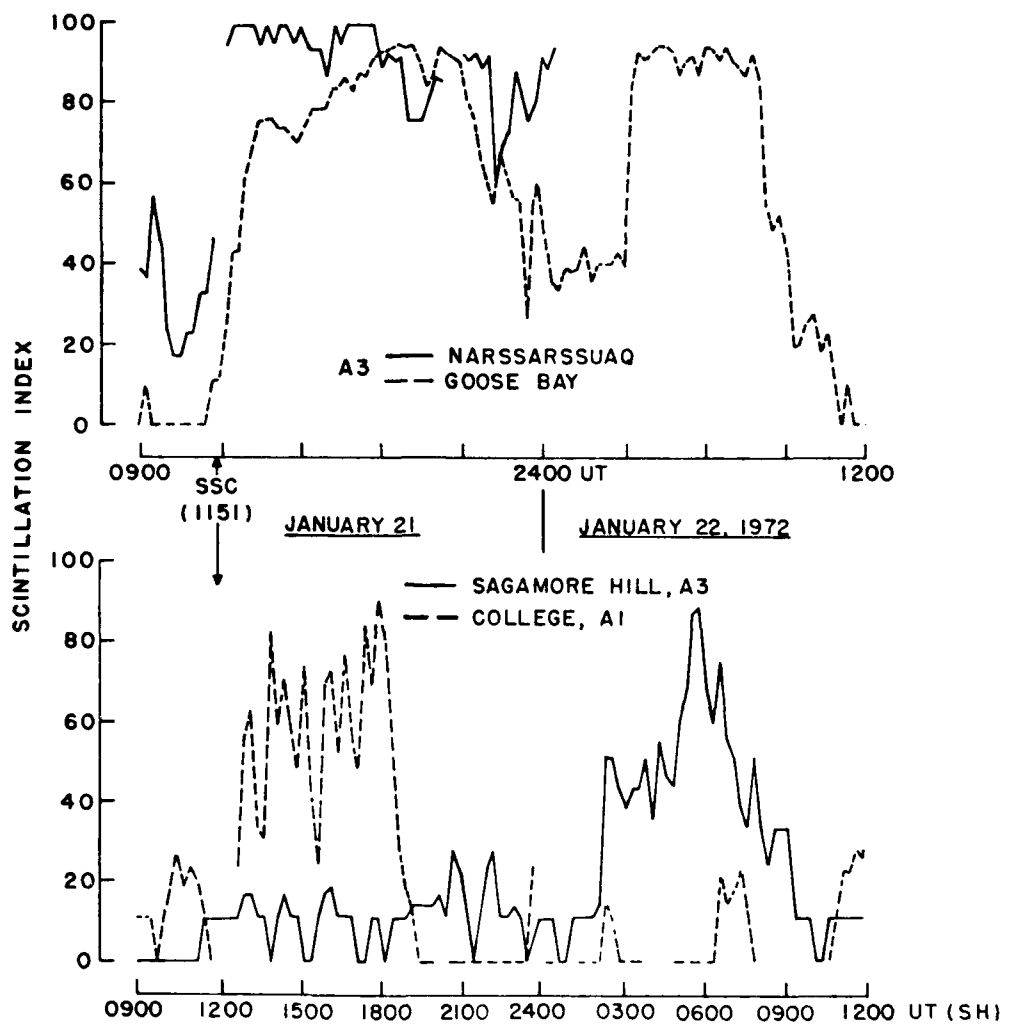


FIGURE 2.

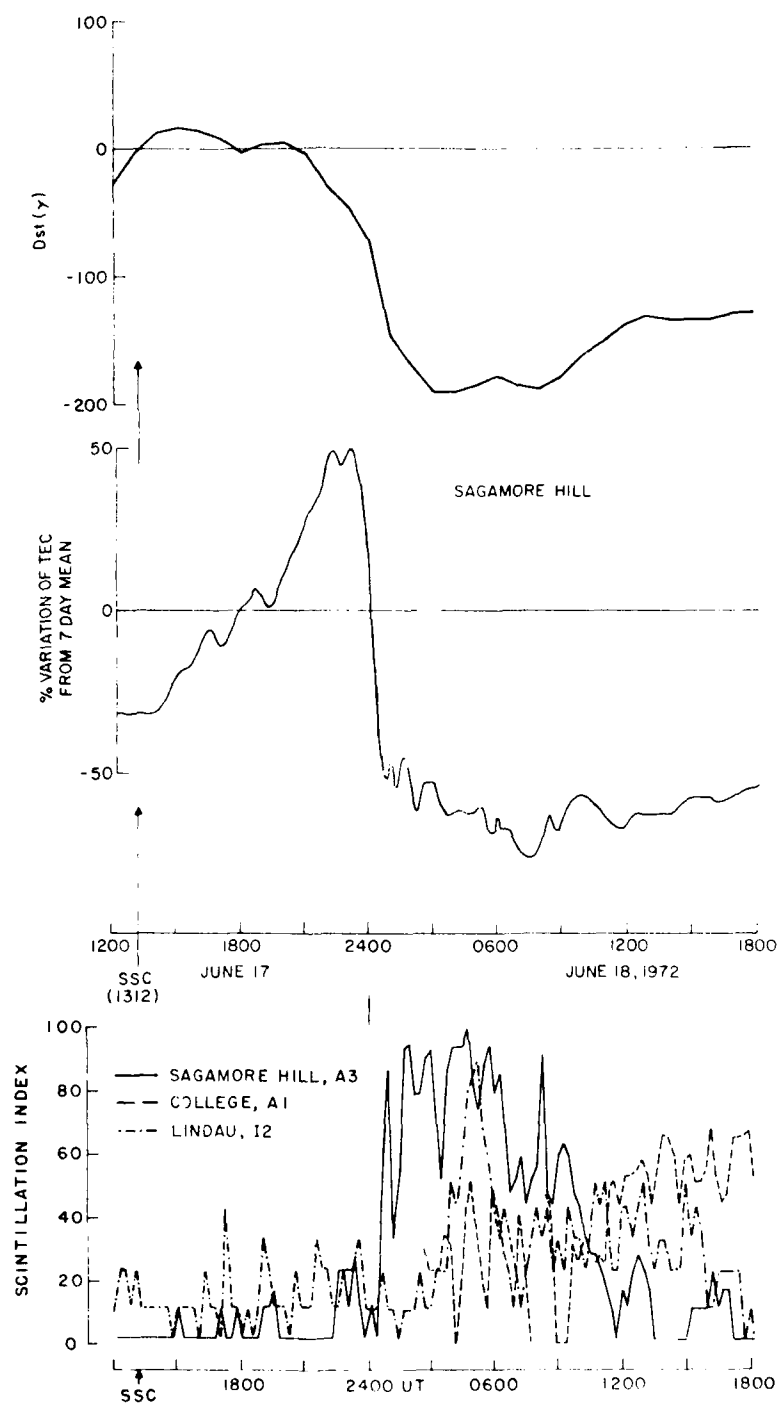


FIGURE 3.

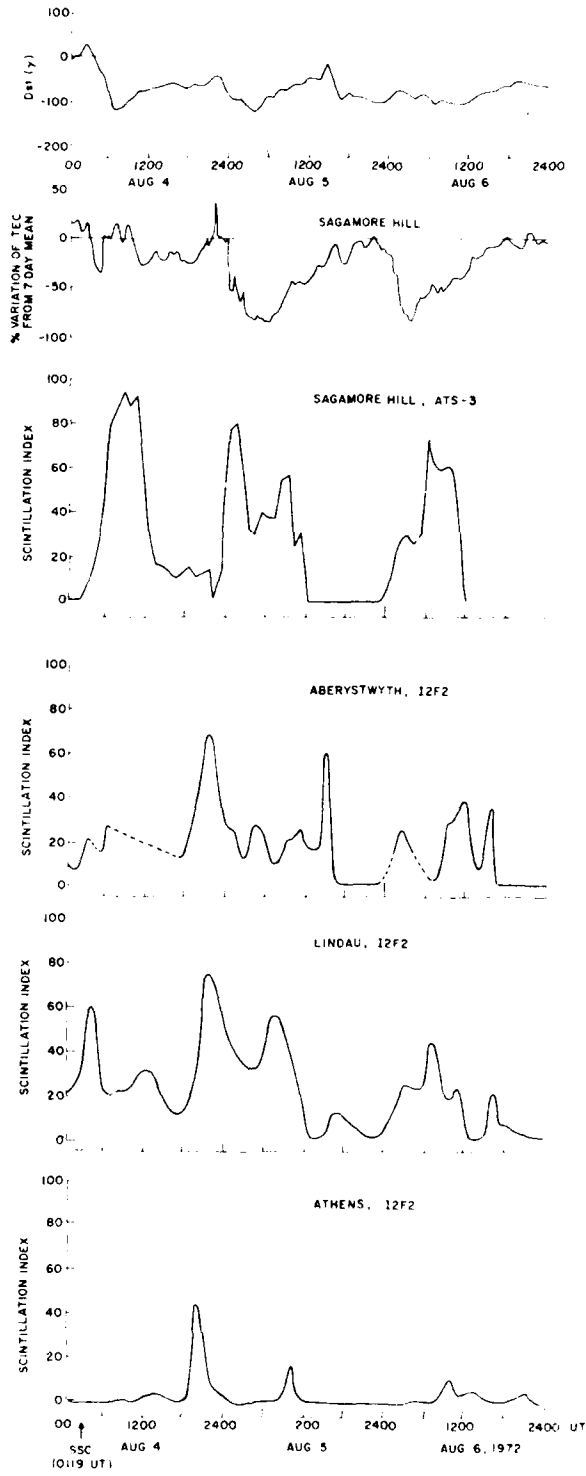


FIGURE 4

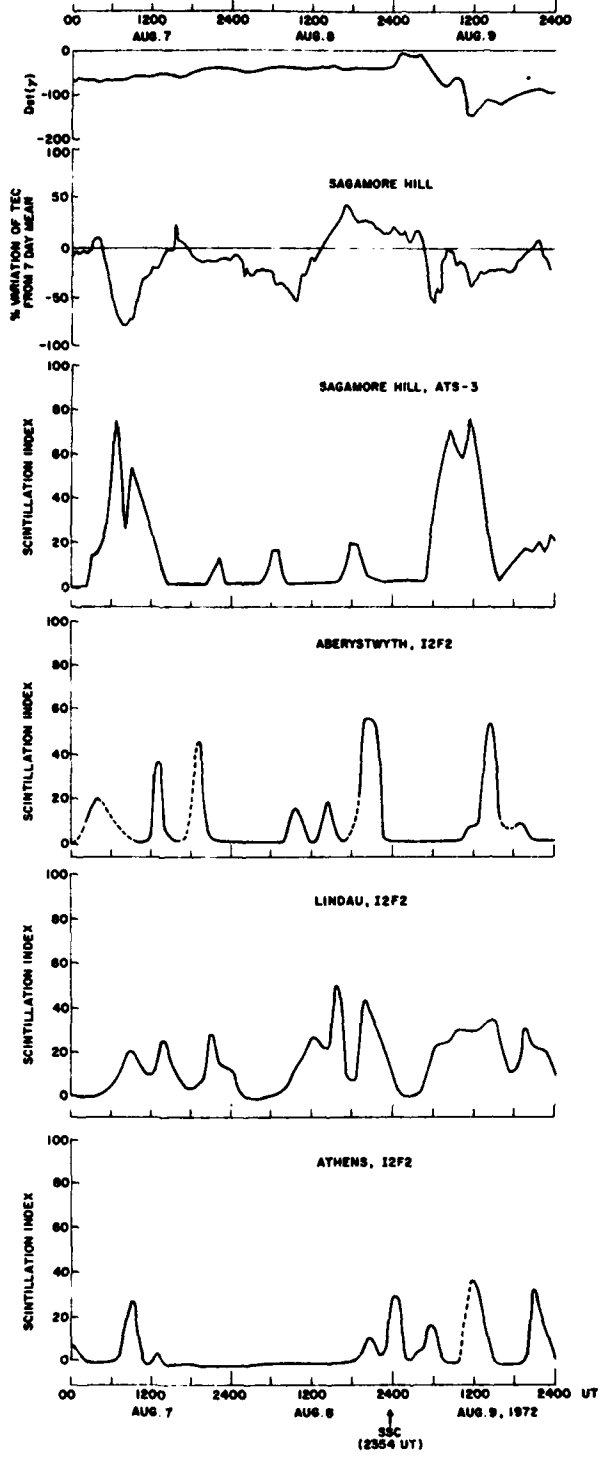


FIGURE 5.

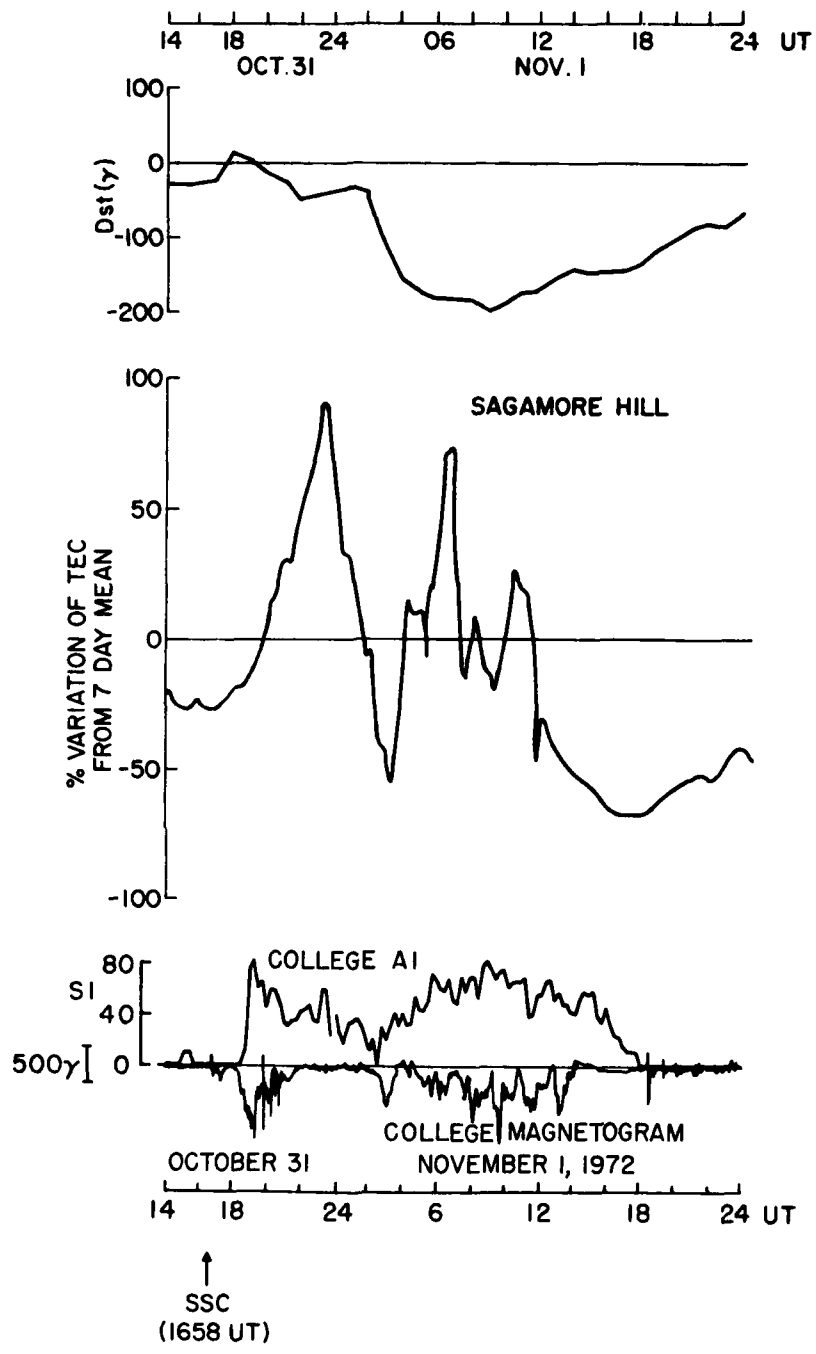


FIGURE 6.

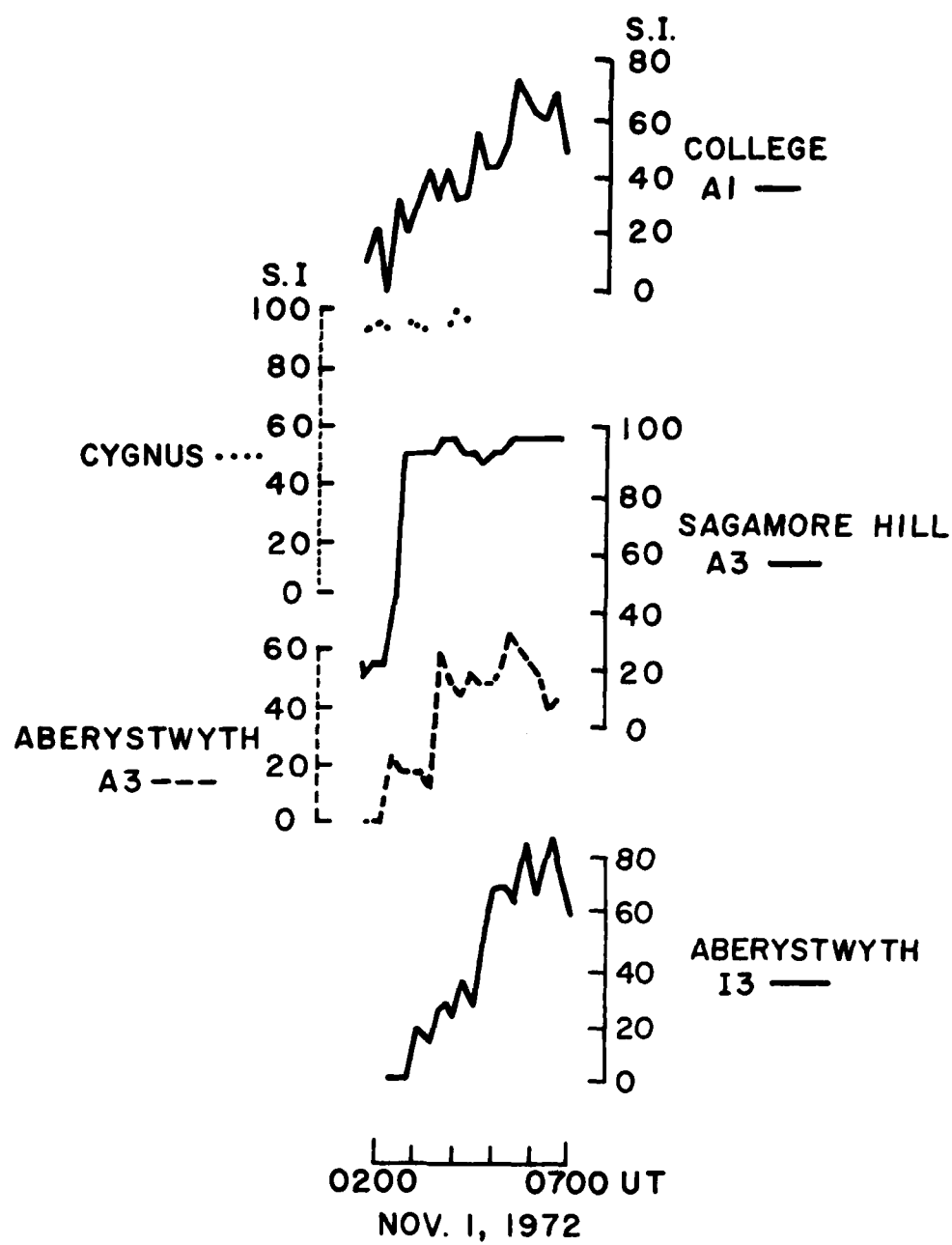
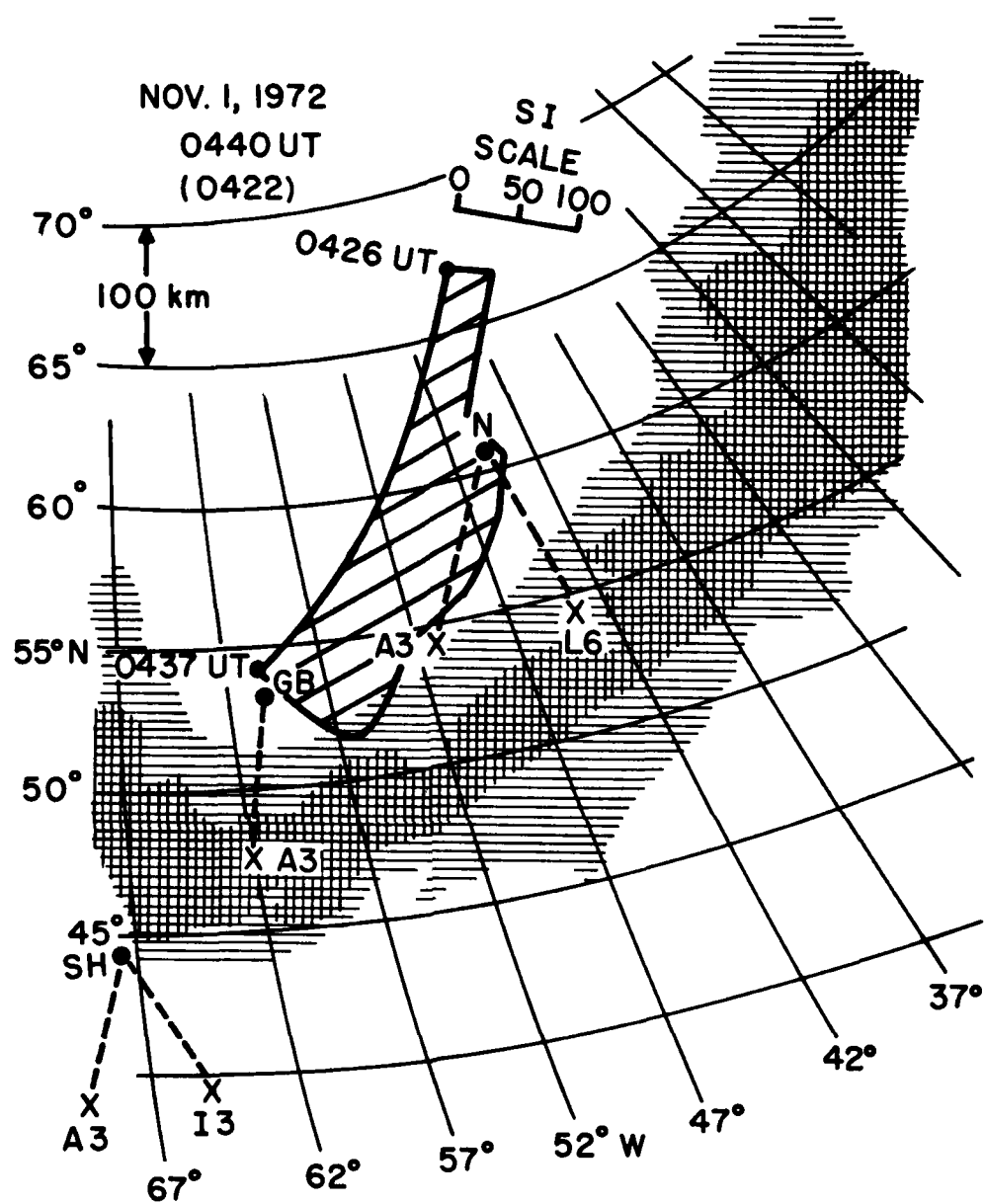


FIGURE 7.



**FIGURE 8. AURORAL TRACING WITH SATELLITE  
 INTERSECTION POINTS AND NIMBUS 4  
 PATH SHOWN.**

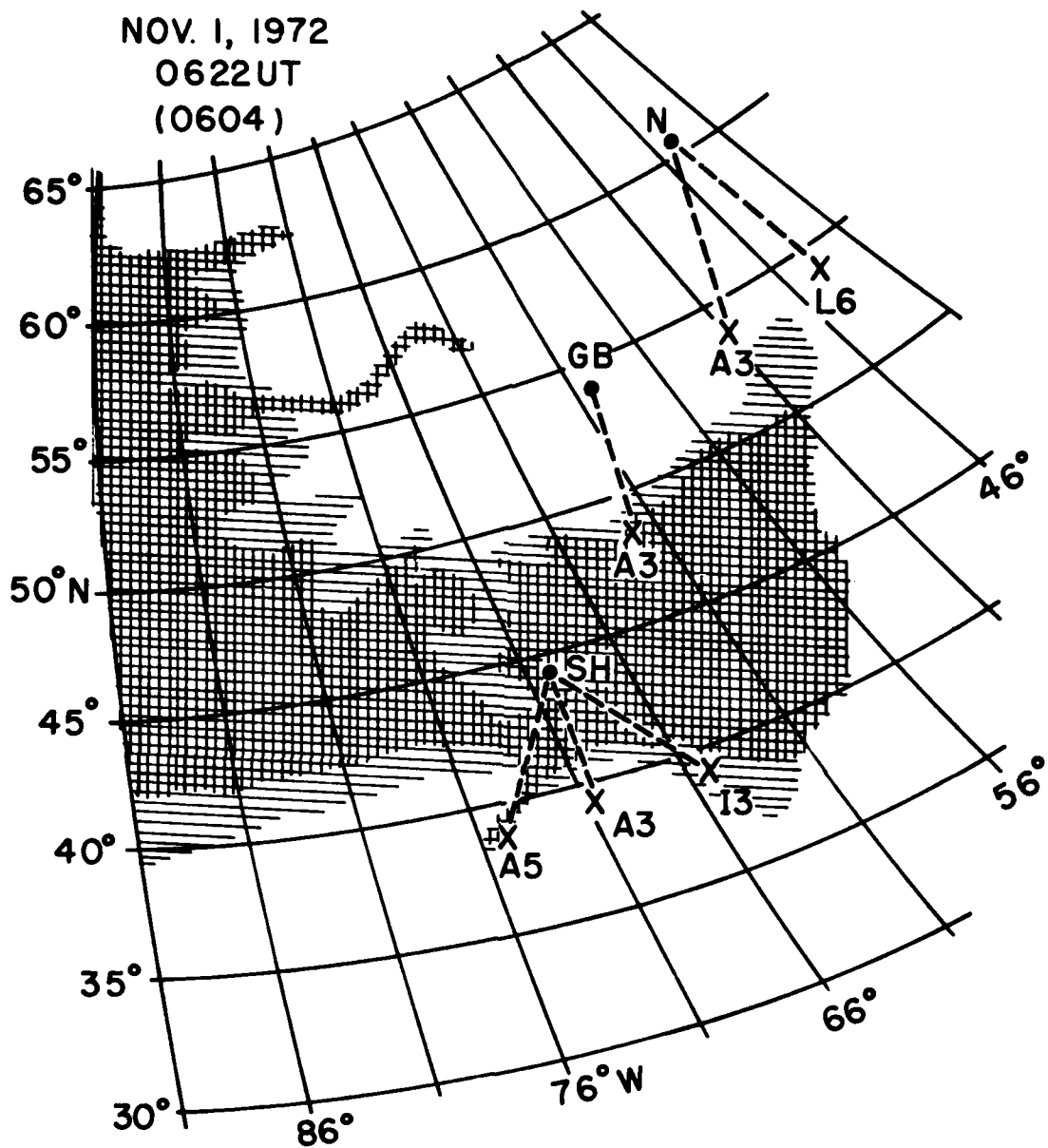


FIGURE 9. AURORAL TRACING WITH SATELLITE  
INTERSECTION POINTS SHOWN.

## Scintillations Observed Through the Magnetospheric Cleft

John P. Mullen and Jules Aarons  
Air Force Geophysics Laboratory  
Air Force Systems Command  
Hanscom AFB, MA 01731

### Abstract

Observing scintillation produced by E and F layer irregularities on 254 MHz transmissions of LES-6 over a period of years has shown a high occurrence of strong irregularities over the magnetospheric cleft before noon. A broad maximum of scintillation occurrence with S4 values greater than 0.3 was found around 1000 LMT. The observations were taken from the AFGL Geopole Observatory at Thule, Greenland with the 350 km intersection at 71° invariant and the 100 km intersection at 75°. The angle of elevation to the satellite ( $\sim 3^\circ$ ) was low and did not allow for precisely locating the latitude where the strong irregularities were observed.

Distinctive occurrence maxima were observed in summer and fall under quiet magnetic conditions. Winter and spring fail to show clear pre-noon maxima under quiet conditions which may be due to the low latitude of the intersection at 350 km, the probable height of the irregularities producing scintillation during quiet magnetic conditions. Under disturbed magnetic conditions each season shows the pre-noon maximum with S4 values before noon in each case higher than the midnight maximum. This data indicates that the irregularity region has moved to lower latitudes (and across the propagation path to the satellite) during magnetically disturbed conditions and has intensified.

The irregularities may be related to low energy cleft electrons or convective electric fields.

### Background

For the past seven years the AFGL Geopole Observatory (Thule, Greenland) has recorded the 254.140 MHz beacon on the Lincoln Experimental Satellite LES-6 (1968-081D). The equipment consisted of a stacked pair of linear yagi antennas having a total gain of 15 decibels, Vanguard converters and

R-390 receivers. The data were recorded on magnetic tape and on strip charts with a time constant of 0.5 seconds. Relative calibration was accomplished by inserting a signal into the receiving system and attenuating it in steps. In this way a relative calibration was obtained whose accuracy is dependent only on the attenuator steps, which are within  $\pm 1\%$  of nominal.

#### The Data

Due to technical difficulties in the satellite the signal was frequently below threshold from 0200-0400 UT. Other than this period, continuous recording was the rule. Approximately 8000 hours of data taken over the period 1969-1975 inclusive were manually reduced, sorted and averaged to yield the curves shown herein.

The observatory is located at  $76.40^{\circ}\text{N}$ ,  $291.3^{\circ}\text{E}$  ( $85.36^{\circ}\text{A}$ ). The elevation angles to the satellite as it moved from  $90^{\circ}$  to  $40^{\circ}$  west longitude ranged from approximately  $4^{\circ}$  to  $3^{\circ}$ . The sub-ionospheric points for the major portion of the period were as shown in Table I:

Table I

Assumed height	350 km	200 km	100 km
Geomagnetic	$61.9^{\circ}\text{N}$ $51.8^{\circ}\text{W}$	$66.1^{\circ}\text{N}$ $54.5^{\circ}\text{W}$	$69.8^{\circ}\text{N}$ $57.8^{\circ}\text{W}$
Invariant Latitude	$71^{\circ}$	$74^{\circ}$	$79^{\circ}$

Figure 1 summarizes all of the data. In magnetically disturbed ( $K_p \geq 4$ ) and quiet ( $K_p = 0-3$ ) periods minima were found near 0300 LT and 1600 LT. During quiet periods, there was a very diffuse maximum extending from 0700 LT to 1300 LT. During magnetically disturbed periods, occurrence probability of  $SI > 60$  increases almost to unity, and maximizes near 1100 LT. Indices greater than 80% ( $S4 > .43$ ) show similar times of minima outlined above. (There was unfortunately insufficient data to refine any of the seasonal curves in this manner for magnetically disturbed periods.)

Figure 2 shows the probability of occurrence of scintillation greater than 60% during quiet periods, for the different seasons. Here the seasons are defined as winter (November, December, January), spring (February, March, April), summer (May, June, July), and fall (August, September, October). Each season is the composite of three months from all the

years examined. All seasons show the minima at approximately the same times, and thus agree in that respect with the summary curves. It is the maxima which show the major seasonal variation. In summer there are maxima from 0500 LT to 1400 LT and at midnight, with the daytime maximum primary. In fall there is a single secondary maximum near 1000 LT with the primary maximum before midnight. In winter, all levels are depressed and there is little diurnal pattern. Daytime scintillation peaks at 0700 and 1200 LT. Spring daytime values are depressed. There is a clear midnight peak.

Gross features of the seasonal occurrence are as follows:

summer - high morning and midnight occurrence  
fall - high pre-midnight and moderate morning occurrence  
winter - generally low scintillation occurrence  
spring - high midnight occurrence, low daytime scintillation

#### Discussion

Using the magnetospheric model of Roederer (Figure 3) Thule looks through the cleft under moderately disturbed conditions while observing geostationary satellites. There is substantial evidence for soft particle precipitation in the cleft during daytime (Dyson and Winningham, 1974; McDiarmid, Burroughs and Budzynski, 1976). Dyson and Winningham define a severe topside irregularity zone (STIZ) generally coincident with the southern boundary of the cleft. The zone extends north of the cleft, which Dyson and Winningham attribute to magnetic convection.

It is important to bear in mind that the location of the sub-ionospheric point cannot be precisely determined because of the low elevation angle. Table I shows that the 350 km intersection point is at 71° invariant latitude. This location corresponds closely with the northern edge of the scintillation boundary (Aarons and Allen, 1971) at approximately 1000 LT and 1300 LT. This would lead one to expect a "double-humped" curve such as one sees in Figure 1. During disturbed periods the irregularity structure moves south, but additionally intensifies and spreads north as well. It is this characteristic to which we attribute the large daytime maximum when  $K_p=4-9$ .

Recent experiments of this group whose data are now being reduced have shown that over Thule ( $85.36^\circ \text{ A}$ ) scintillations do not vary as a function of  $K$  index for

moderate K groupings of 4-6. The intensification of irregularities (both day and night) occurs in the cleft region. However, a relatively high pre-noon occurrence of scintillations did take place indicating this phenomenon is associated with the cleft and the magnetospheric tail particles.

#### References

- Aarons, J. and R.S. Allen, Scintillation boundary during quiet and disturbed magnetic conditions, J. Geophys. Res., 76, 170-177, 1971.
- Dyson, P.L. and J.D. Winningham, Topside ionospheric Spread F and particle precipitation in the dayside magnetospheric clefts, J. Geophys. Res., 79, 5219-5230, 1974.
- McDiarmid, I.B., J.R. Burroughs and E.B. Budzinski, Particle properties in the dayside cleft, J. Geophys. Res., 81, 221-226, 1976.
- Roederer, J.G., Planetary plasmas and fields, EOS, Trans. Am. Geophys. Union, 57, 53-62, 1976.

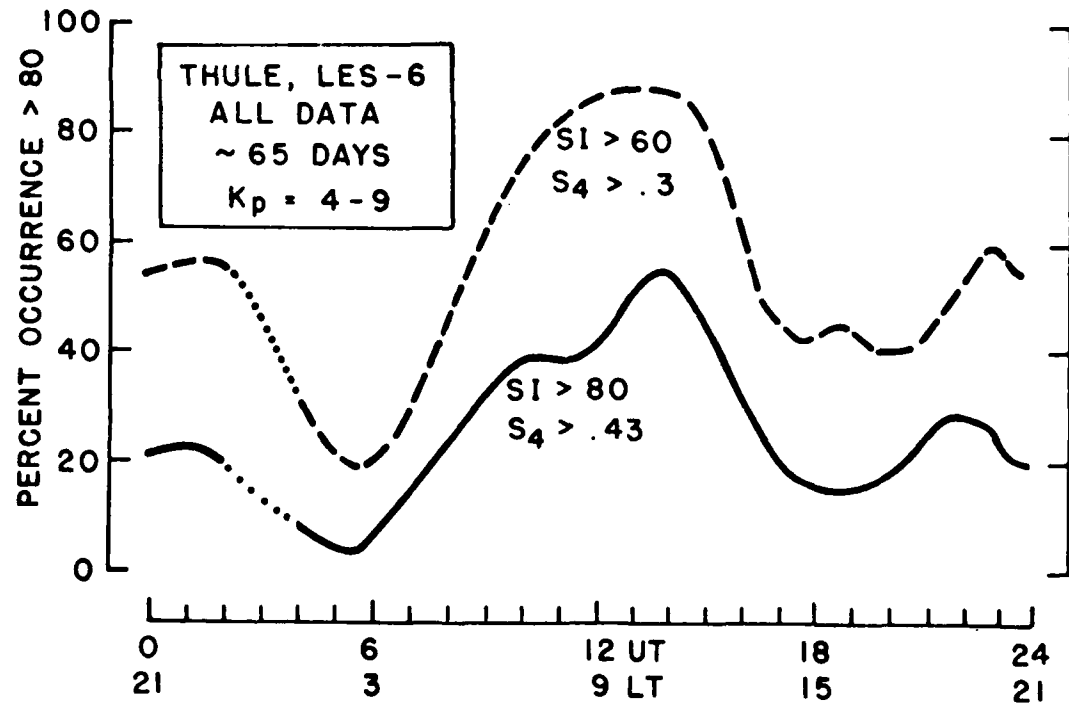
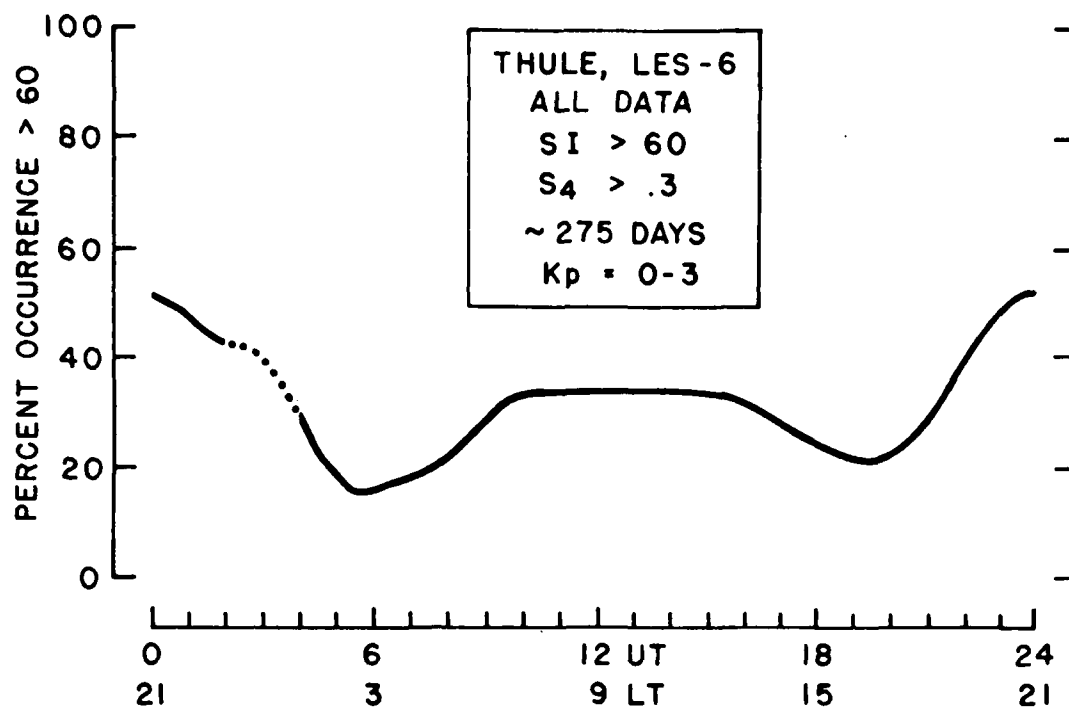
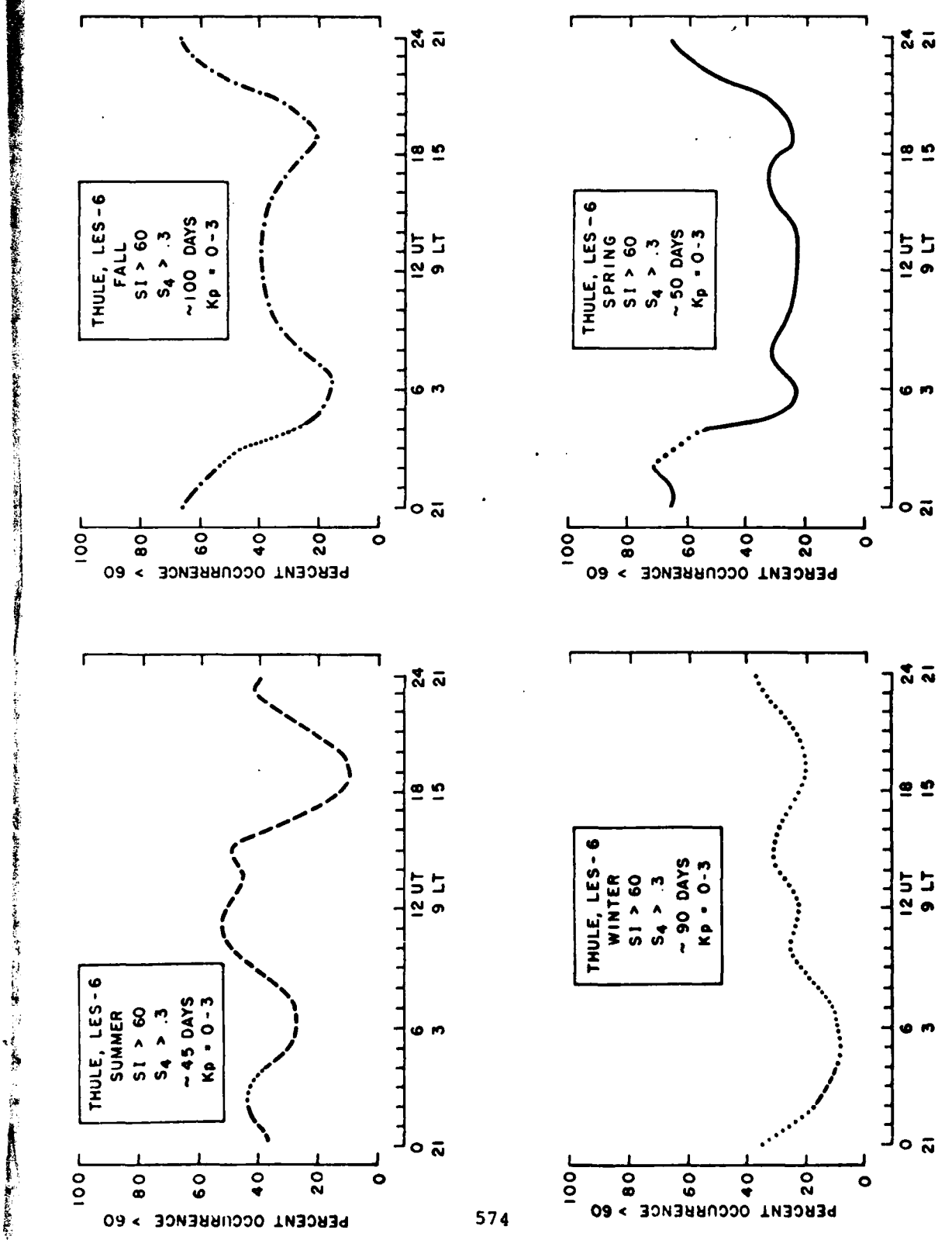


FIG. I



574

FIG. 2

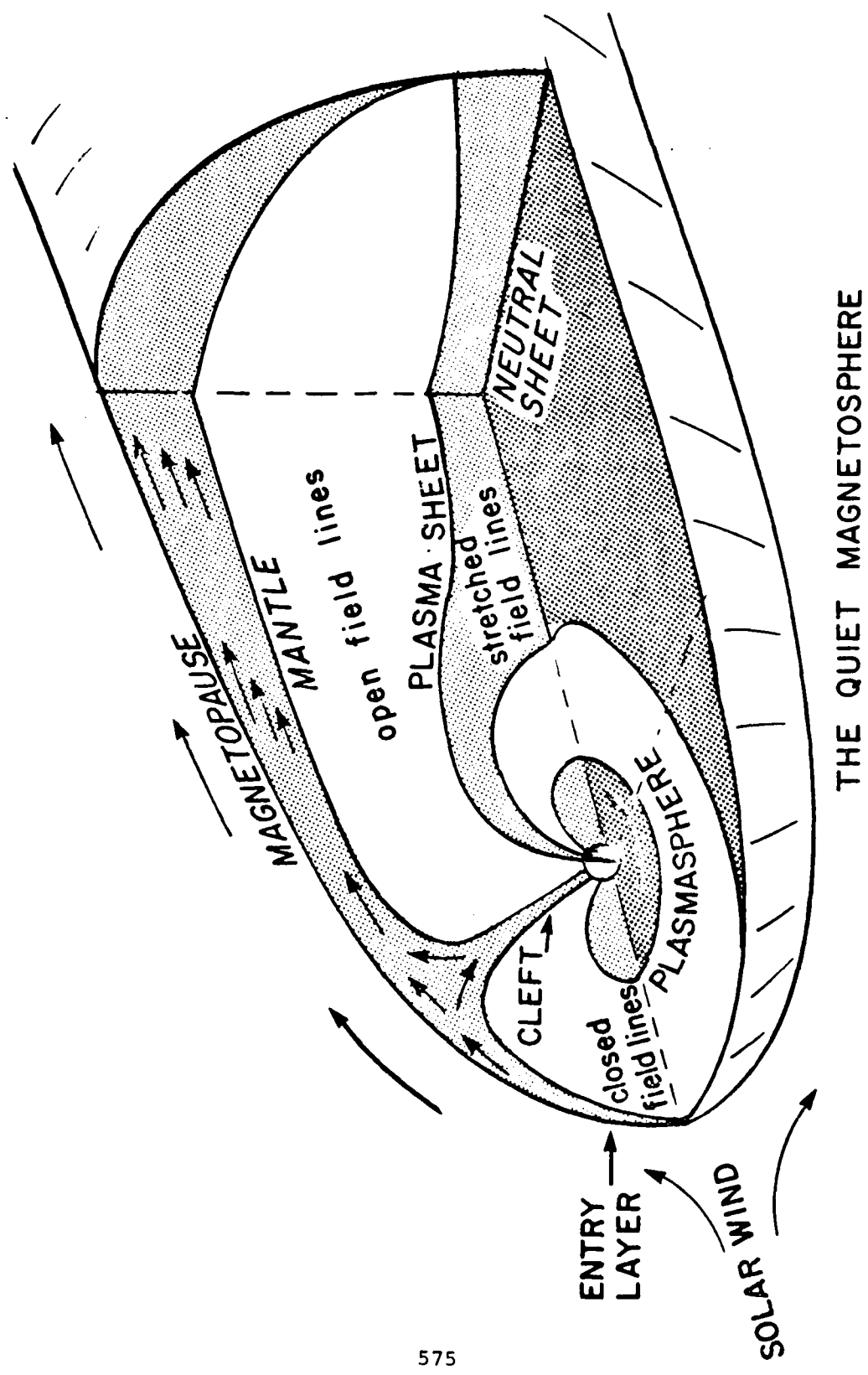


FIG. 3

THE QUIET MAGNETOSPHERE

Angle-of-arrival scintillations in the region  
of the polar cleft

J.A. Fulford and P.A. Forsyth  
Centre for Radio Science  
University of Western Ontario  
London Canada N6A 3K7

During the summer of 1975, a dual frequency (150 MHz and 400 MHz) differential angle-of-arrival system was operated at Cambridge Bay near the average position of the daytime cleft. Some 100 passes of NNSS satellites were observed. Very strong amplitude and angular scintillations were recorded at 150 MHz and on some occasions the ionospheric irregularities were sufficiently strong to produce angular scintillations at 400 MHz. The strongest amplitude and phase scintillations appeared to occur during the mid-day hours when the cleft region was overhead. At such times angular deviations as great as one milliradian at 400 MHz were seen, corresponding to lateral gradients in the total electron content of  $4 \times 10^{12} \text{ m}^{-3}$ . If it is assumed that the irregularities were cylindrical, the peak electron concentration must have been about  $10^{12} \text{ m}^{-3}$ . During the mid-day hours the regions of strong scintillation moved rapidly with respect to the observing station in a manner that is not easily characterized but which may be consistent with the known rapid motion of the cleft region.

Introduction

There is much current interest in the mechanism of formation and the morphology of the dayside magnetospheric cleft. It is known that the region is the site of complex structure in the ionospheric F-region and is probably subjected to substantial electric fields. In August, 1975 a dual frequency angle-of-arrival system was operated at Cambridge Bay, latitude  $69.1^\circ\text{N}$  and longitude  $254.9^\circ\text{E}$  (geomagnetic latitude  $76.7^\circ\text{N}$  and longitude  $296.5^\circ\text{E}$ ), under the mean position of the cleft.

The equipment consists of two phase-measuring interferometers, one operating at a frequency of 400 MHz and the other at 150 MHz, two of the frequencies radiated by beacons aboard the NNSS series of satellites. Each interferometer consists of two antennas separated in the North-South direction (parallel to the orbital plane of the satellite). The signals from the antennas are mixed with separate local oscillators to produce i.f. frequencies separated by 1 kHz and then amplified and detected in a common receiver. The resulting 1 kHz signal is then compared in phase to a standard oscillator in a digital phasemeter in order to derive the instantaneous angle-of-arrival of the incoming radio waves

relative to the antenna base-line. Since the satellite beacons are phase-coherent it is also possible to measure the phase difference between the 1 kHz signals produced in the 150 MHz and 400 MHz receivers, to produce a continuous record of the difference of angle-of-arrival as observed at 150 MHz and 400 MHz. For an orbiting satellite this is a major advantage since, provided that the two antenna base-lines are parallel and have the same electrical length, the rapid "phase ramps" which characterize the records at each frequency are eliminated and what is left is an accurate record of the angular refraction suffered by the radio waves. The refraction suffered by the 150 MHz signal is just  $400^2/150^2 \approx 7.1$  times that of the 400 MHz signal so the "differential" angle-of-arrival record represents 86% of the refraction suffered at 150 MHz. A simplified block diagram of the system is shown in Fig. 1

The system operates with a nine-channel digital magnetic tape recording system of which six channels are assigned to the three phase outputs (150 MHz, 400 MHz and "differential") in order to achieve 0.1 sec time resolution in the records and two channels are assigned to amplitude recording for the two frequencies (with time resolution of 0.2 sec). The ninth channel is used for recording time from a digital clock.

In normal use the antenna base-line at each frequency is 200 wavelengths which gives a resolution in angle-of-arrival of about  $5 \times 10^{-5}$  radians. Early in the operation at Cambridge Bay it became apparent that the angular scintillation was so strong that the phase variation sometimes exceeded  $2\pi$  (corresponding to an angular deviation of 5 milliradians) and consequently the antenna base-lines were reduced to 72.6 wavelengths. All of the records discussed in this paper were taken with this reduced value of antenna separation.

#### Refraction measurements

Of the records obtained during some 100 passes of NNSS satellites most show some angular and amplitude scintillation. The strongest scintillations seem to occur during the mid-day period within an hour or two of local magnetic noon which during the period of the observations occurred at 19 hr 32 min UT. Although the location of the magnetospheric cleft is subject to rapid deviation of the order of several degrees, the mean location of its centre is at about invariant latitude  $76^\circ$  and at about one hour after local geomagnetic noon. Several of the records taken near the expected time of passage of the cleft show exceptionally strong amplitude and angular scintillation. Part of one of these, obtained on 28 August, which shows easily measured angular scintillations at 400 MHz is reproduced in Fig. 2. These scintillations are among the

strongest that have been observed in more than ten years of angle-of-arrival measurements at lower latitudes including some made of the aurorally disturbed E-region and F-region at Fort Churchill, Manitoba (see, for example, Turnbull and Forsyth, 1965; Mason, Tull and Forsyth, 1967; Forsyth, 1968 and Palmer, Doan and Forsyth, 1970). In the complete record there were several angular scintillations but at least two represent angular deviations at 400 MHz of more than one milliradian. Only one of these will be discussed here, that (shown in Fig. 2) which took place at about 20 hr 00 min UT. This scintillation reached a maximum in about 0.2 sec and since the line-of-sight to the satellite was moving through the F-region at about 2.2 km/sec the horizontal half-width of the irregularity must have been about 450 m. The relationship between the gradient (in the direction of motion of the line-of-sight) of the total line-of-sight electron content,  $N_t$ , and the angular deviation,  $\theta$ , for 400 MHz radio waves is:

$$\frac{d(N_t)}{du} = 3.95 \times 10^{15} \theta$$

which yields a value for this scintillation of,

$$\frac{d(N_t)}{du} = 4.1 \times 10^{12} \text{ m}^{-3}$$

or a peak deviation in  $N_t$  of about  $1.8 \times 10^{15} \text{ m}^{-2}$ .

If it is assumed that the irregularity was a cylinder aligned with the local magnetic field and having a gaussian radial distribution of electron concentration (as has been verified for observations at lower latitudes) the relationship between the maximum angular deviation and the peak electron concentration,  $N_o$ , (in excess of the background concentration) is given by

$$\theta_{\max} = 3.8 \times 10^{-16} N_o \csc \gamma$$

where  $\gamma$  is the angle between the line-of-sight and the local magnetic field direction, which yields for the present case

$$N_o \approx 1.5 \times 10^{12} \text{ m}^{-3}$$

It is concluded that the F-region in the region of the magnetospheric cleft is highly disturbed and contains small irregularities with scale size of the order of 0.5 km and peak electron concentration in excess of ambient which is at least comparable in magnitude to the ambient ionization.

### Temporal behaviour of the cleft

Because the NNSS satellites are in polar orbits a high latitude station can record a large number of passes each day. This suggests the possibility of investigating the temporal behaviour of the disturbed F-region. Since nearly all the records show some scintillation at 150 MHz it is difficult to analyze these in any meaningful way. Also, because the angle-of-arrival records at 150 MHz are so disturbed (as, of course, are those for differential angle-of-arrival) it is not practical to use any form of automatic analysis for statistical purposes. The amplitude recordings at 400 MHz do show both quiet and disturbed periods so were used to determine the temporal characteristics. A preliminary analysis of the amplitude fluctuations indicated that the autocorrelation function fell to a low value for time displacements of the order of the resolution of the records (0.2 sec). It seemed appropriate therefore to derive a root mean square scintillation index. The average signal level over a period of about two seconds is derived and the index merely expresses the ratio of the root mean square deviation of the actual signal to the average signal level. This processing was carried out digitally and provides a record which is independent of signal amplitude (for all signals above a predetermined threshold level).

Again the most interesting behaviour was exhibited during the middle day-time hours. The root mean square scintillation index as a function of latitude for five satellite passes between 18 hr and 24 hr on 27 Aug. is shown in Fig. 3 and that for six passes between 17 hr and 22 hr on 28 Aug is shown in Fig. 4. Both of these days were magnetically quiet. Some of the passes occurred at some distance to the east or west of the station and in order to reveal systematic temporal changes in these two figures the time of each pass is corrected for the difference in local time between the subsatellite point and the station.

In Fig. 3 (for 27 Aug) the pass near 20 hr shows a patch of scintillation to the south and weak scintillations to the north. By 21 hr a strong patch of scintillation has developed about  $2.5^\circ$  north of the station and this patch, with a sharp southern boundary appears to be associated with the cleft. In subsequent passes the patch moves rapidly to the south. The behaviour is consistent with the known asymmetry of the cleft ionization with respect to the invariant latitude of the cleft centre as revealed by satellite observations of luminosity, although the motion appears to be more rapid than usual, and may include a true component of motion of the whole cleft region in latitude. On the 28 Aug. (Fig. 4) the behaviour seems to be more typical. There is a fairly consistent

motion of the region of maximum disturbance toward the south at about the expected rate.

Knudsen (1974) has discussed the effect of the dawn-to-dusk electric field in the polar cap on the motion of irregularities. The irregularities should be convected toward the north at rates of the order of 1 km/sec as a result of the crossed electric and magnetic fields in the region of the cleft. The irregularities should decay as they move northward from the region of formation, producing a sharp boundary to the south and a gradual decay to the north of the actual cleft region. While the few results obtained in the present experiment are not definitive there is some evidence of this type of behaviour in Figs. 3 and 4. Indeed, if interpreted in this way it would appear that the actual region of irregularity formation in the cleft is somewhat less than a degree of latitude in width and the irregularities are convected for several degrees of latitude in the northern direction before decaying below the detectable level at a frequency of 400 MHz. In any case it appears that the morphology of the cleft region can be investigated with relatively simple equipments using satellite beacon sources. It is planned to extend the observations to two stations separated in longitude operating simultaneously during the summer of 1976.

#### References

- Forsyth, P.A. 1968. Can. J. Phys. 46, 1841  
Knudsen, W.C. 1974. J. Geophys. Res. 79, 1046  
Mason, K.H., Tull, E.H. and Forsyth, P.A. 1967. Can. J. Phys. 45, 3065  
Palmer, F.H., Doan, J.W. and Forsyth, P.A. 1970. Can. J. Phys. 48, 554  
Turnbull, R.M. and Forsyth, P.A. 1965. Can. J. Phys. 43, 800

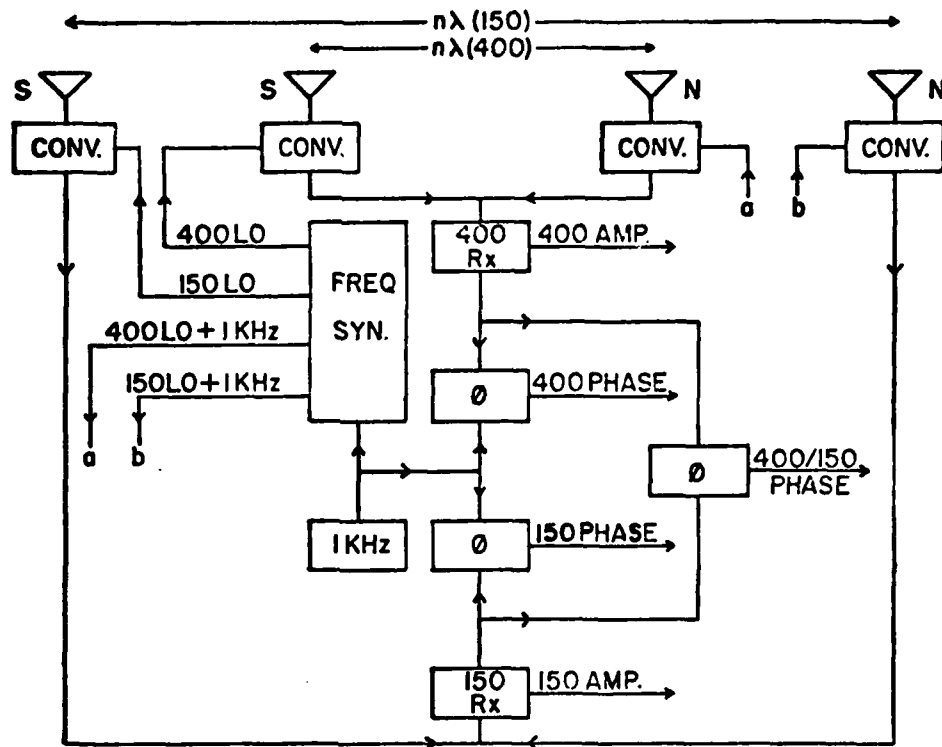


FIG.1 Simplified block diagram of the two frequency differential angle-of-arrival apparatus.

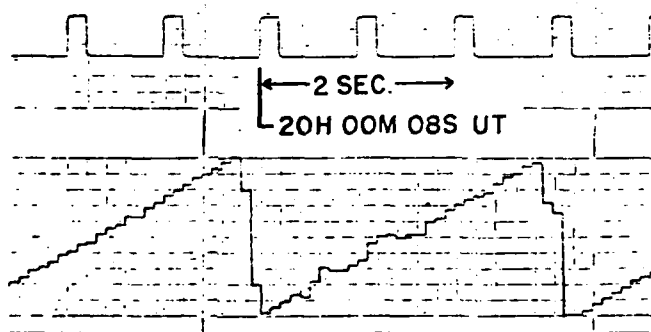
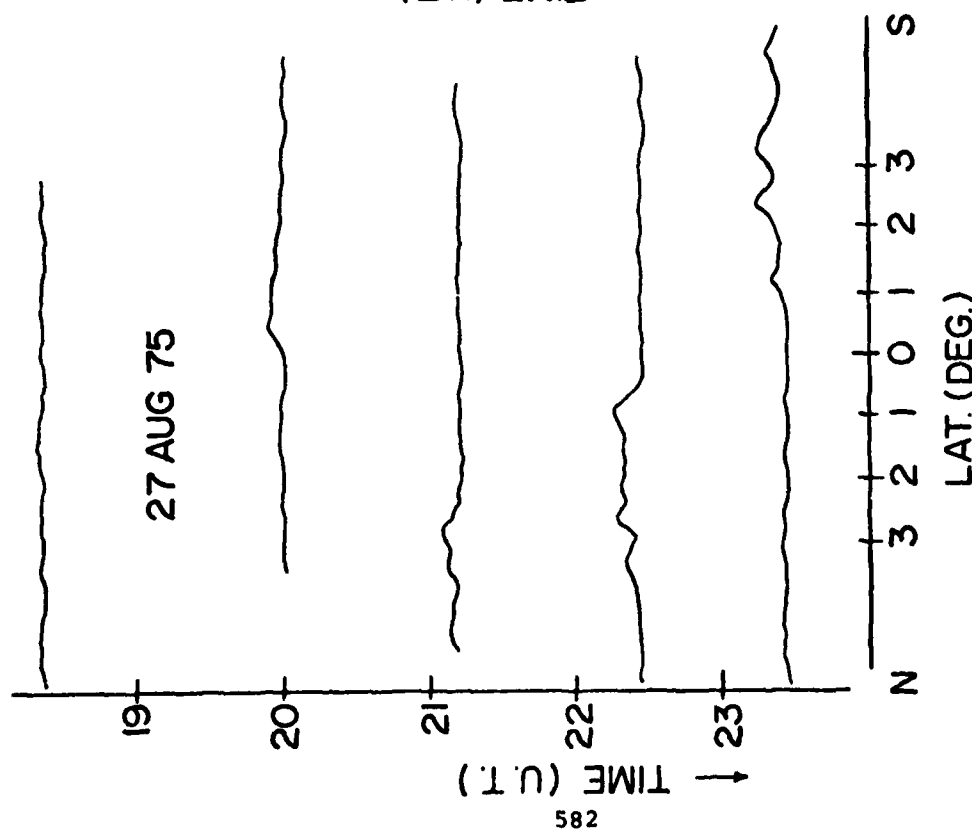


FIG.2 Two phase ramps of the 400 MHz angle-of-arrival record obtained at about 20 hr UT on 28 Aug. 1975. The second ramp, starting at 20 hr 00 min 08 sec shows strong angular scintillations including the one discussed in the text.



582

FIG. 3 The root-mean-square amplitude scintillation index (see text) as a function of latitude measured north and south from Cambridge Bay NWT for satellite passes between 18 hr and 24 hr UT, 27 Aug. 1975.

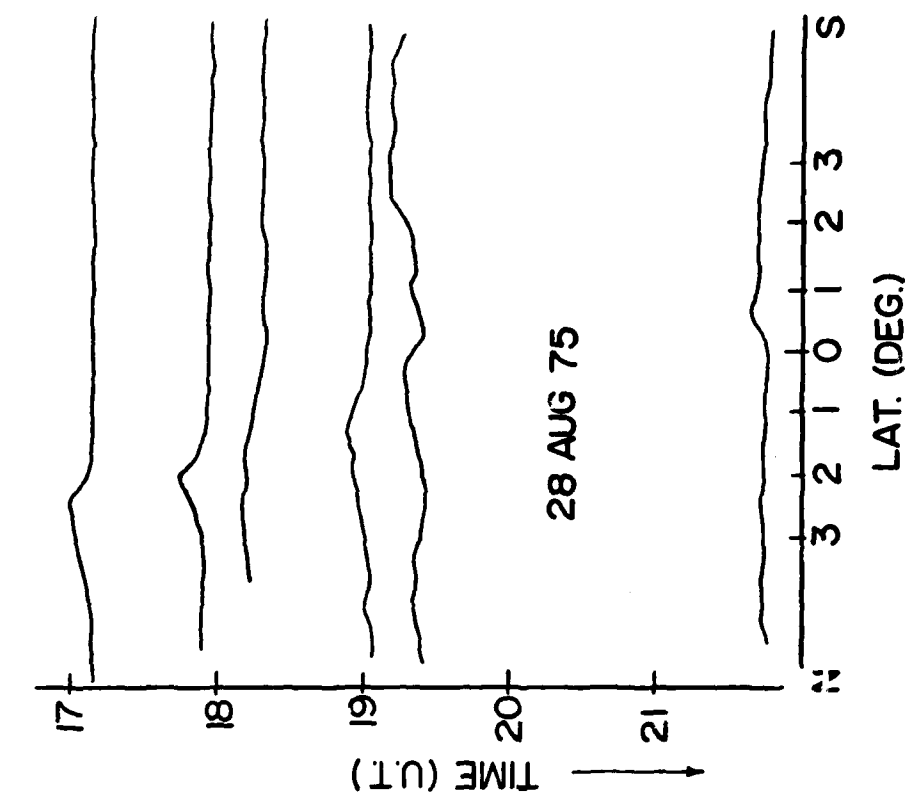


FIG. 4 Information similar to that of Fig. 3 for passes between 16 hr and 22 hr UT, 28 Aug. 1975.

## ANGLE-OF-ARRIVAL AND DOPPLER FLUCTUATIONS CAUSED BY IONOSPHERIC SCINTILLATION

Robert K. Crane

Environmental Research & Technology, Inc.

### ABSTRACT

Angle-of-arrival and doppler scintillation were observed at the Millstone Hill Radar Facility using 150 and 400 MHz transmissions from the U.S. Navy Navigation System satellites. A theoretical analysis was performed to predict the fluctuation spectra using the Rytov approximation and an anisotropic power law power spectrum to model the electron density fluctuations. The observed and predicted spectra were in good agreement.

The height and axial ratio of the irregularities were estimated using derived relationships between the rms fluctuations of doppler, elevation angle and traverse angle (azimuth  $\times \cos(\text{elevation})$ ). Data were analyzed from two magnetic storms. The observations showed E-region irregularities at 57 to 61° invariant latitude and F-region irregularities over the range 45 to 67° invariant. The axial ratios ranged from 2 to 4 south of 57° invariant to 2 to 12 north of 57° invariant.

### 1. INTRODUCTION

Ionospheric scintillation causes spatial and temporal fluctuations in the amplitude and phase of radiowaves propagating through the ionosphere. The spatial fluctuations in phase in turn cause fluctuations in the apparent angle-of-arrival of the source; the temporal fluctuations in phase in turn cause Doppler fluctuations. As a part of a radar propagation effects program at the Millstone Hill Radar Facility (Evans, 1973a) angle-of-arrival measurements were made with a single monopulse tracking system. The radar propagation study was conducted to investigate their effects on radar systems; this paper will dwell on the inferred structure of the irregularities.

In a previous paper (Crane, 1976; to be referred to as Ref. 2) spectra of log power and phase fluctuations observed at 150 and 400 MHz at Millstone were reported which show that the election density fluctuations may be modeled by a three dimensional (3-d) power law power spectrum with a -4 exponent. The observed spectra were compared with spectral estimates generated by both the Rytov and Born approximations. The results showed that the Rytov approximation was applicable over a wider range of scintillation intensities. Using the Rytov approximation, spectra and variance estimates can be derived for band limited observations of angle-of-arrival and Doppler fluctuations which may be used to calculate the axial ratio and, if the drift velocity is known, the height of the lower edge of the dominant irregularity region. Comparisons between the theoretical estimates and observed spectra show excellent agreement.

The measurements of angle-of-arrival and Doppler fluctuations were made using the U.S. Navy Navigation System satellites. These satellites are in 1100 km circumpolar orbits. The line-of-sight from a single ground station to one of the satellites moves rapidly through the ionosphere at F-region heights. For the satellite passes used for analysis, the effective drift velocities at 300 km height ranged from 1.6 to 2.7 km/sec. For these high effective drift velocities, the ionospheric irregularities may be assumed to be fixed in space. This assumption was used to calculate the heights of the lower edge of the dominant irregularity region. Detailed analysis of axial ratio and irregularity height were made for two time periods with intense scintillation, 4-5 August 1972 and 1 November 1972. The August magnetic storm observations were during times with  $3^h$  Kp average values ranging from  $6^-$  to  $8^+$ . For this storm, the axial ratio values ranged from 2 to 4 and the lower edge of the irregularity region was at E-region height for invariant latitudes between  $56^\circ$  and  $60^\circ$ .

The data for the 1 November 1972 observations were also for relatively high Kp values which ranged from  $8^-$  to  $8^+$ . For this set of observations, the irregularity heights decreased towards the north again showing evidence of E-region production at invariant latitudes between  $58^\circ$  and  $61^\circ$ . For this data set, the axial ratio values showed a trend towards larger values at higher invariant latitudes. The range of axial ratios was from approximately 2 at  $52^\circ$  invariant to between 4 and 12 at  $58^\circ$  invariant.

## 2. THEORETICAL ESTIMATION OF ANGLE-OF-ARRIVAL SPECTRA

Equations for the correlation functions and spectra for log power and phase fluctuations were developed in Ref. 2 for weak scintillation using the Rytov approximation (see also Crane, 1977). The analysis of phase fluctuations may be used as a starting point for an analysis of angle-of-arrival fluctuations. Early angle-of-arrival observations were made using interferometers. The analysis of fluctuations for a large aperture antenna with a monopulse tracking feed starts with the equations for an interferometer. The results are then specialized to those for a single antenna by letting the spacing between the interferometer elements approach zero. Interferometer observations are sensitive to spatial fluctuation in phase at scale sizes larger than the interferometer spacing. Fluctuations on scale sizes smaller than the spacing are uncorrelated and contribute to measurement noise. For a single antenna, the observations are sensitive to fluctuations at all scale sizes although the effect of scales smaller than the diameter of the receiving aperture are attenuated. The effect of aperture averaging were not considered because the fluctuations on the scale size of the receiving aperture are smaller than those masked by receiver noise.

For a two element interferometer, the angle-of-arrival is given by

$$\sin\theta = \frac{2LR + R^2 - r^2}{2Lr} \approx \frac{R}{r} = \frac{1}{kr} (\phi(r) - \phi(0)) \quad (1)$$

where

$\underline{L}$  = position vector of the source

$\underline{r}$  = positive vector of the second interferometer element

$r, L$  = magnitudes of the position vectors  $\underline{r}, \underline{L}$

$kR = \phi(\underline{r}) - \phi(0)$  = phase path difference;  $k = 2\pi/\lambda$ ,  $\lambda$  = wavelength

$\theta$  = angle of arrival measured in the plane of  $\underline{L}, \underline{r}$ ;

$$\cos\theta = \hat{\underline{r}} \cdot \hat{\delta}; \hat{\delta} = \frac{\hat{\underline{L}} \times \hat{\underline{r}} \times \hat{\underline{L}}}{|\hat{\underline{L}} \times \hat{\underline{r}} \times \hat{\underline{L}}|}$$

$\hat{\underline{r}}, \hat{\underline{L}}, \hat{\delta}$  = unit vectors in the direction of  $\underline{r}, \underline{L}, \delta$  respectively.  
Small fluctuations in the angle-of-arrival caused by phase fluctuations may be approximated by

$$\theta = \frac{1}{k(r \cdot \hat{\delta})} (\phi'(\underline{r}) - \phi'(0)) \quad (2)$$

where the instantaneous angle-of-arrival is  $\theta + \delta$  and the instantaneous phase is  $\phi' + \phi$ .

The correlation function for the angle-of-arrival fluctuations,  $B_\theta$ , can be calculated from the correlation function for phase fluctuations:

$$B_\theta(d) = \frac{1}{k^2} \left. \frac{d}{dr^2} B_\phi(d, \underline{r}) \right|_{r=0} \quad (3)$$

The one dimensional (1-d) power spectral density of angle-of-arrival fluctuation,  $S_\theta(kd)$ , is given by the 1-d Fourier transform of the correlation function in a direction transverse to the line-of-sight specified by  $\hat{d}$ .

High and low frequency asymptotes were obtained from asymptotic evaluations of the integrals implied in the expression for  $S_\theta(k)$  (see Ref. 2). The ratios between the high frequency asymptotes for elevation and traverse angle measurements can be used to determine the axial ratio if the pointing geometry relative to the geomagnetic field is known. The ratio at a fixed fluctuation frequency

$$R = \frac{S_{\theta, \text{TRAVERSE}}}{S_{\theta, \text{ELEVATION}}}$$

can be used to determine the axial ratio  $\alpha$  by:

$$\alpha = \left[ \frac{R-1}{\sin^2 \Psi [\cos^2(\xi-\phi) - R \sin^2(\xi-\phi)]} + 1 \right]^{1/2} \quad (4)$$

where  $\psi$  = propagation angle or the angle between the propagation direction  $\hat{\rho}$  and the geomagnetic field  $\hat{m}$ ;  $\cos \psi = \hat{\rho} \cdot \hat{m}$

$\xi$  = orientation angle or the angle between the normal to the plane containing the geomagnetic field and the propagation direction and  $\hat{d}$

$$\cos \xi = \frac{\hat{\rho} \cdot \hat{m}}{|\hat{\rho} \cdot \hat{m}|} \cdot \hat{d}$$

$\phi$  = direction angle or the angle between  $\hat{\delta}$  and  $\hat{d}$ ;  $\cos \phi = \hat{\delta} \cdot \hat{d}$  and the requirement that  $\kappa$  is along  $\hat{d}$  is implied

and the 3-d power spectral density for the electron density fluctuation is assumed to have a power law form with a -4 exponent. Figure 1 illustrates the theoretical spectra for an axial ratio of 2.

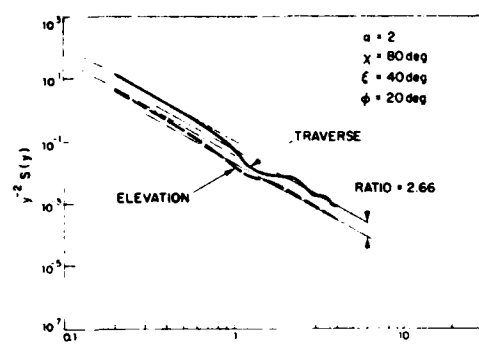


Figure 1 - Theoretical Spectra

The high frequency asymptote to  $S_\theta$  behaves as  $y^{-(p-3)}$  where  $y$  is the fluctuation frequency ( $y \propto k$ ). The high frequency asymptotes to the spectra for log power and for phase fluctuation  $S_x$  and  $S_\phi$  both have a  $y^{-(p-1)}$  behavior (Ref. 2). To give the three spectra the same appearance at high frequencies and to provide a ready visual comparison between the several spectra  $y^{-2} S_\theta$  is plotted rather than  $S_\theta$ .

### 3. THEORETICAL ESTIMATION OF DOPPLER FREQUENCY VARIANCE

Doppler frequency fluctuations occur when temporal changes in phase occur along the propagation path. For a rapidly moving line-of-sight through a fixed ionosphere, the Doppler fluctuations are caused by the rapid motion of the line-of-sight. For the general problem, the fluctuations are caused by the drift of the irregularities across the line-of-sight. For the rapidly moving line-of-sight case, the Doppler shift is given by

$$F = \frac{\phi(V\Delta t) - \phi(0)}{2\pi\Delta t} \Big|_{\Delta t \rightarrow 0} = \left( \frac{V}{\lambda} \right) \frac{\phi(r) - \phi(0)}{kr} \Big|_{r=V\Delta t} \quad (5)$$

where  $V$  represents the motion of the end point of the line-of-sight. Referring back to Eq. (1), it is evident that the Doppler fluctuations may be calculated using the expressions for angle-of-arrival. The power spectrum for Doppler fluctuations is also related to the power spectrum for phase fluctuation (Ref. 2) by:

$$S_F(\kappa) = \left(\frac{V\kappa}{2\pi}\right)^2 S_\phi(\kappa) \quad (6)$$

Noting that the spatial fluctuations may be translated into temporal fluctuations for the case of a rapidly moving satellite with  $\omega = V\kappa$ , then  $M = V/2$  where  $M$  is the fluctuation frequency and

$$S_F(M) = f^2 S_p(M) \quad (7)$$

For the case of a rapidly moving satellite, the spatial spectra for angle-of-arrival fluctuations may also be converted into temporal spectra using the substitution  $M = V\kappa/2\pi$ . For a thin scattering layer at  $\rho$  the high (or low) frequency asymptote for  $S_F$  may be simply related to the asymptote for traverse fluctuations,  $S_{TR}$ , by

$$S_F(M_1) = \frac{(\rho V)^2 S_{TR}(M_1)}{\lambda^2 (L-\rho)^2 G} \quad (8)$$

$$\text{where } G = \frac{1+(\alpha^2-1)\sin^2\psi\cos^2(\xi-\phi)}{1+(\alpha^2-1)\sin^2\psi\cos^2\xi}$$

The distance to the scattering layer,  $\rho$ , or, from the elevation angle of the line-of-sight, the height of the scattering layer can be calculated using (8) knowing  $S_F$  and  $S_{TR}$ :

$$\rho = QL/(V+Q); \quad Q = [(S_F/S_{TR})d^2(G)]^{1/2} \quad (9)$$

The variance in phase, angle-of-arrival, or in Doppler cannot be calculated unless a value of the outer scale is specified. If  $p = 4$ , an inner scale must also be specified to provide a high wavenumber cut-off to obtain a finite integral. This is evident from the form of the spectra shown in Fig. 1 where the power spectral density keeps increasing as  $\kappa$  decreases and decreasing as  $\kappa$  increases. Evaluating the variances,  $\sigma_\phi^2$ ,  $\sigma_\theta^2$ , or  $\sigma_F^2$  as an integral of  $S_\phi$ ,  $S_\theta$  or  $S_F$  over all  $\kappa$  results in an infinite value unless the outer scale and inner scale is specified. Several approaches have been used to get around the singularities implied by spectra without an outer and inner scale. Tatarski (1967) makes use of structure functions to remove the outer scale singularity. Use can also be made of band limited sets of detrended data. For samples from a low pass filtered random process with the mean value and perhaps higher order trends removed, the power spectra has fluctuation energy only in a limited frequency band. The lowest frequency corresponds to  $1/T$  where  $T$  is the total observation period. The variance of the detrended random process is given by the integral over the spectra from  $y_1 = 1/T$  to the highest frequency  $y_2 = 1/t$  where  $t$  = sampling rate. The variances calculated using bandlimited spectra are not affected by singularities at the origin (or at infinity).

The variances for band limited integrals of the spectra are proportional to the low frequency asymptotic spectral density estimates evaluated at a single fluctuation frequency. This approximation improves as the observing period is lengthened because the details of the low frequency to high frequency transition region become less important. For a thick irregularity layer, the details of the transition region are also averaged out because contributions at different frequencies originate at different heights. In practice the ratios of variances caused by traverse and elevation fluctuations or the ratios of variances caused by traverse and Doppler fluctuations may be equated to the ratios of the asymptotes to their respective spectra.

#### 4. EXPERIMENTAL OBSERVATIONS

Scintillation observations were made using phase coherent transmissions from the Navy Navigation System satellites and the 84-foot tracking antenna at the Millstone Hill Radar Facility (Gilhoni, 1973). The UHF (400 MHz) receiver system was used to track the satellite in both phase and pointing angle.

The digitally recorded data were post processed to provide rms values and spectra for the scintillation induced fluctuations about trend curves representing the best (least square) estimate of slow variations caused by satellite aspect angle variation, polarization changes, pedestal tilt, changes in the observing geometry and distance to the satellite, and background ionospheric refraction. The data were sampled at a 15 per second rate. The data were low pass filtered prior to digitizing: the error voltage channel cut-off frequencies were 7.5 Hz; the phase and Doppler observations had 250 and 7.5 Hz cut-off frequencies at 150 and 400 MHz respectively. One hundred and twenty-eight successive samples were used to estimate the trend curves and calculate the rms value. Overlapping blocks of 128 consecutive samples spaced by 64 samples were used to generate the spectra of fluctuations about the trend curves. The fluctuations were weighted by a parabolic curve with a unity value at the center and near zero values at the ends of each analysis interval prior to calculating the spectra. Thirteen successive spectra were averaged to generate power spectral density estimates for each minute of data. The resultant spectra had 21 degrees of freedom and a bandwidth of 0.14 Hz.

Figure 2 displays simultaneously obtained empirical estimates of log power ( $S_x, 400$  and  $S_x, 150$ ), differential phase, ( $S_{\phi, 150-400}$  or  $y^{-2} S_F$ , see eq. (7)), elevation ( $y^{-2} S_{EL}$ ), and traverse ( $y^{-2} S_{TR}$ ) spectra. The 150 MHz log power and the 150-400 MHz differential phase spectra have been scaled to have the same (theoretical) high frequency asymptotes as the 400 MHz log power spectrum (see Ref. 2). The axial ratio estimated using the ratio of the variances of traverse to elevation angle fluctuations is 4.8. This calculation was based upon the use of Eq. (4) with the substitution of the square of the rms values for the asymptotic spectral values. Based upon the ratio of the variance of traverse to VHF doppler, the distance to the scattering layer was 640 km and the height was 180 km.

Given the best fit of the theoretical estimate of  $S_x, 400$  to the

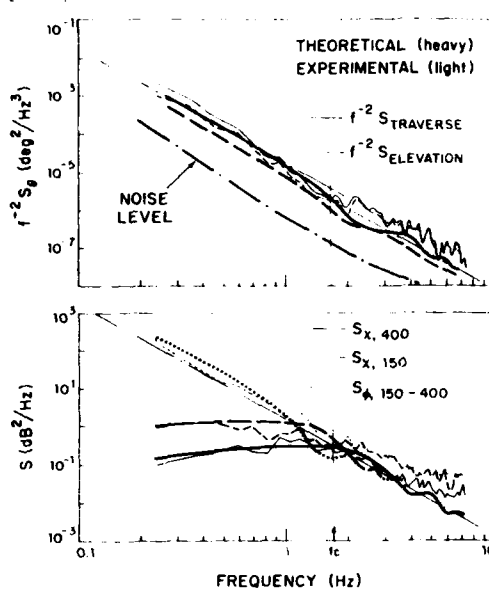


Figure 2 - Comparison Measurement  
and Theory

data on Fig. 2 and the axial ratio, all the theoretical curves on Fig. 2 are determined. Only the measured spectrum  $S_{X,400}$  and the position of  $y^2 S_{EL}$  relative to  $y^2 S_{TR}$  were constrained by the fit to  $S_{X,400}$  and the estimation of the axial ratio from the ratio of  $\sigma_{TR}$  to  $\sigma_{EL}$ . The measured spectra  $S_{X,150}$ ,  $S_{\phi,150-400}$ , and  $STR$  were not constrained. The agreement between the measured spectra  $S_{\phi,150-400}$  and  $STR$  and the calculated spectra is excellent. The rms log power fluctuations were  $\sigma_X = 4.1$  dB at 400 MHz and  $\sigma_X = 6.1$  at 150 MHz showing strong scintillation at the lower frequency. The strong scintillation is responsible for the difference in power spectral density between the measured and calculated  $S_{X,150}$  curves (Ref. 2).

## 5. ANALYSIS

Excellent agreement was shown between the theoretically estimated phase and angle-of-arrival spectra based upon the use of the Rytov approximation and the observed spectra. The low frequency asymptotes for phase, Doppler, and angle-of-arrival spectra correspond to large scale sizes (geometric optics) which are not affected by the multiple scattering process associated with strong scintillation.

The locations of the lower edge of the dominant irregularity region and the axial ratios for the irregularities were computed from data from two satellite tracking sessions. The data were from two magnetic storms, one occurred on 3-5 August 1972 and the other on 31 October, 1 November 1972. The latter storm has been described by Aarons (1976). The invariant latitude for the lower edge of the irregularity region was also computed. These data are displayed on Figures 3 through 8 together with the satellite rise time and the 3<sup>h</sup> average  $\kappa_p$  value for each of the passes. The satellites were visible for less than 18 minutes, hence, the data are for the listed times plus up to 18 additional minutes.

The data from the November storm period show zenith corrected  $\sigma_{X,400}$  values increasing toward the north, the axial ratios increasing toward the north, and both E- and F-region irregularities. The invariant latitude of Millstone (at the surface) is indicated by M. The E-region irregularities are confined to a narrow 58 to 61° A (invariant) sector and F-region irregularities occur simultaneously within, to the north, and to the south of this sector. The observation technique can only

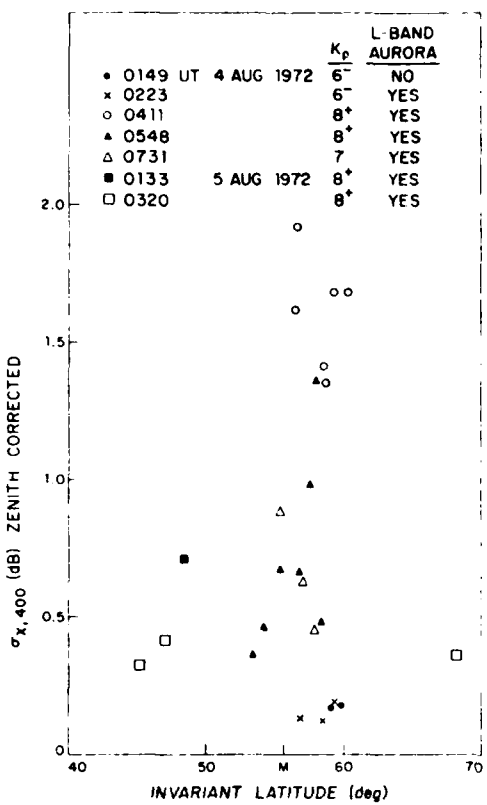


Figure 3 - Zenith Corrected  $\sigma_{X,400}$ , August

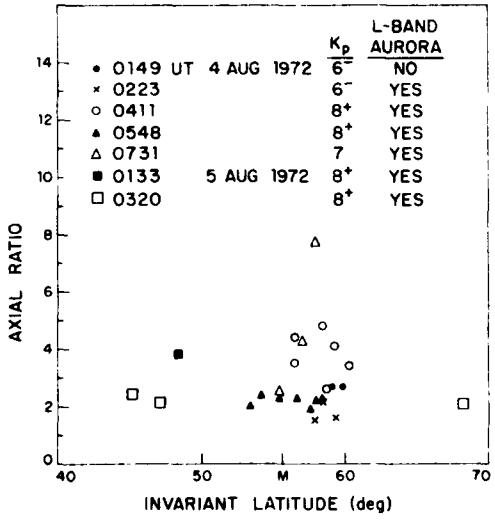


Figure 4 - Axial Ratio, August

locate the closest edge of the irregularity region, hence, F-region irregularities that may exist to the north of  $63^\circ \Lambda$  at 200 km heights are masked by the E-region irregularities. Aarons (1976) reported that during the 0300 to 0720 time period strong scintillation extended from north of  $65^\circ \Lambda$  to south of  $55^\circ \Lambda$  for  $\Lambda$  evaluated at 350 km height. He reported hourly average scintillation indices observed at 137 MHz not corrected to zenith. The zenith corrected values (Fig. (6)) show relatively intense scintillation to the north of  $55^\circ \Lambda$ . The observed values range from 0.4 to 0.9 dB (zenith corrected  $S_4$  values ranging from .65 to .95 at 137 MHz, see Crane, 1977) at 0300 UT to between .7 and 1.6 dB at 0500. At 0700 the values again were in the 0.4 to 0.9 dB range. The lower edge of the irregularity region also changed little during this time interval. Aarons reported that both auroral (spread) D and spread F were observed in the ionosonde data obtained overhead at Billerica (same  $\Lambda$  as Millstone) for the 0145 to 0300 UT time per-

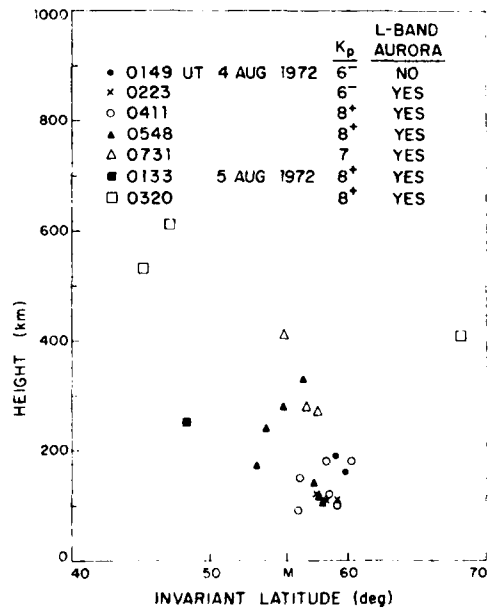
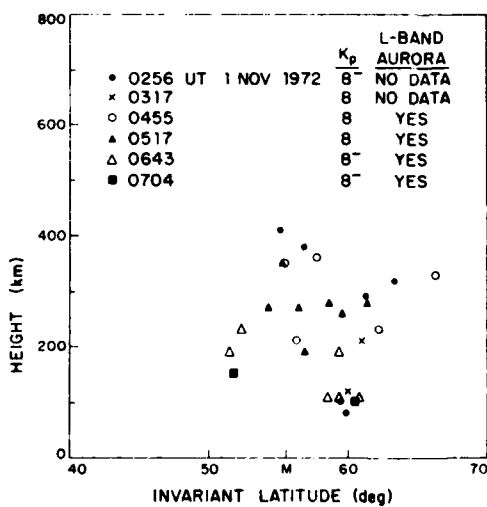
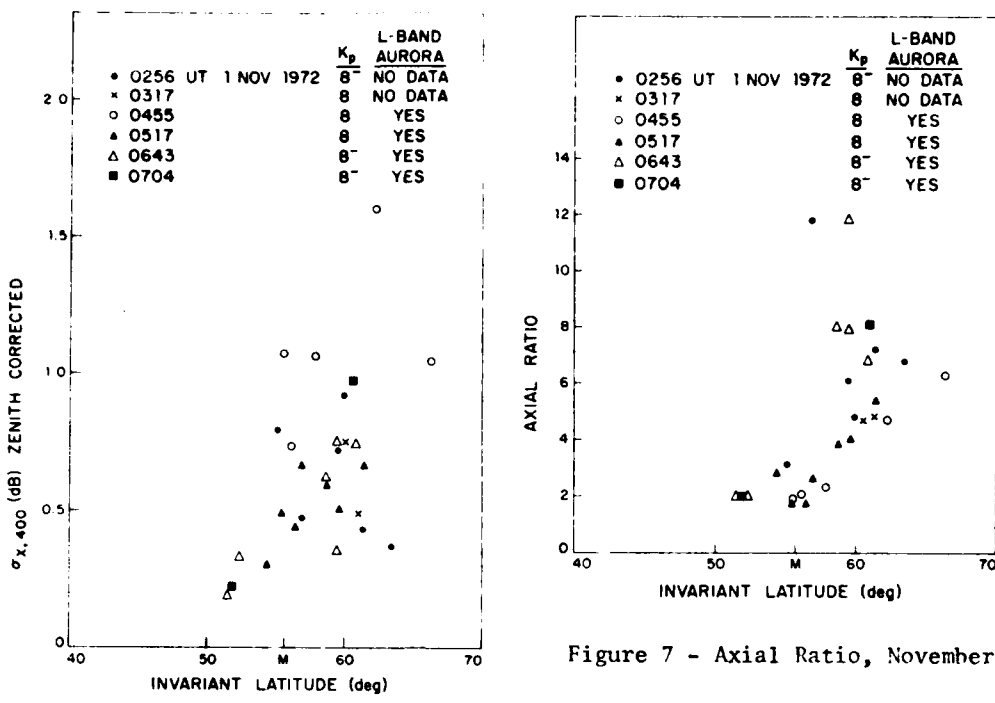


Figure 5 - Height, August



iod after which strong absorption took place. L-band radar obser-vations made at Millstone during the same period showed evidence of backscatter from field aligned irregularities in the auroral region. The radar and ionosonde data provides conformation of the E-region scintillation observa-tions.

During the 0300 to 0700 time period, visual aurora was also ob-served from the DMSP satellite (Aarons, 1976). The southern edge of the diffuse auroral region coincided with the southern edge of the E-region irregularity band. Aarons observed that scintillation was observed to the south of the visual aurora. From Figure (8) it is evident that the region to the south of the visual aurora coincides with F-region irregularities. Hook and Owren (1962) ob-served simultaneous occurrences of E- and F-region irregularities along the same field line in the

auroral region. The data in Figure (8) also show E- and F-region irregularities at the same invariant latitude.

The time history of this magnetic storm as reported by Aarons showed the irregularity region to initially occur in a thin invariant latitude band (at 360 km height) between 60 and 63°  $\Lambda$ . The irregularities region then expanded to the north and south within the F-region. These observations suggest that the irregularity production occurred in the E-region, was transferred to the F-region along the field line, and rapidly propagated to the north and south within the F-region. The E-region production appears to be associated with the optical aurora. Dagg (1957) postulated that the E-region irregularities (at large scale sizes) could be conducted up the field lines to the F-region.

The scintillation observations made during the August magnetic storm also show simultaneous E-region and F-region irregularity occurrence. L-band radar observations also revealed auroral backscatter. In this case, the intense E-region irregularity band was wider and further to the south masking a larger volume in the F-region than for the November observations. The data also showed E-region irregularities only during the 4 August time period. Although the  $\kappa_p$  values for 5 August were still high, E-region irregularities were not observed. The axial ratio observations for both the August and November periods did not show any correlation with the location of the lower edge of the irregularity region. The August data also did not show a well defined trend with either time or  $\Lambda$ .

## 6. REFERENCES

- Aarons, J. (1976) "High-Latitude Irregularities During the Magnetic Storm of October 31 to November 1, 1972", J. Geophys. Res., 81, 661-669 (1976).
- Crane, R.K. (1976) "Spectra of Ionospheric Scintillation", J. Geophys. Res.
- Crane, R.K. (1977) "Ionospheric Scintillation", Proc. IEEE (submitted 1976).
- Dagg, M. (1957) "The Origin of the Ionospheric Irregularities Responsible for Radio-Star Scintillation and Spread F, 2-Turbulent Motion in the Dynamo Region", J. Atmos. and Terr. Phys., 11, 139-150.
- Evans, J.V. (1973) "Millstone Hill Radar Propagation Study: Scientific Results", Tech. Report 509, Lincoln Laboratory, MIT, Lexington, MA.
- Gilhoni, J.C. (1973) "Millstone Hill Radar Propagation Study: Instrumentation", Tech. Report 507, Lincoln Laboratory, MIT, Lexington, MA.
- Hook, J.L. and L. Owren (1962) "The Vertical Development of E-region Irregularities Deduced from Scintillations of Satellite Radio Signals", J. Geophys. Res., 67, 5353-5356.
- Tatarskii, V.I. (1967) The Effects of the Turbulent Atmosphere on Wave Propagation, November, Moscow.

THE STRUCTURE OF SIGNALS UNDERGOING SCINTILLATION AS  
INFERRED FROM ATS-6 AND TRANSIT COHERENT BEACON TRANSMISSIONS

By

C. L. Rino, E. J. Fremouw, and R. Livingston  
Stanford Research Institute  
Menlo Park, Calif. 94025

ABSTRACT

Extensive analysis has been performed on data recorded at Poker Flat, Alaska from the Navy Navigation Satellite (TRANSIT) coherent beacon transmissions at 400 MHz and 150 MHz, and from ATS-6 transmissions at 40, 140, and 360 MHz, recorded at Table Mountain, Colorado. A phase-detrending procedure has been developed by which all phase variations that have periods larger than or comparable to the largest period in the amplitude variations are removed. The residual is then interpreted as the complex random component of the signal. This procedure admits a degree of arbitrariness but appears to be workable.

We have found that large phase variations (typically in excess of one radian) are associated with all amplitude scintillation, even for very small amplitude scintillation levels ( $S_4 < 0.25$ ). This means that the classical weak-scatter theory cannot be used to interpret the complex signal structure. Indeed, it is through multiple scattering that large phase variations develop.

Thus, we have attempted to interpret the data against a multiple-scatter theory. To obtain the irregularity spectrum, for example, one must Fourier analyze the logarithm of the mutual-coherence function. The calculated spectra show the expected power-law form with no readily identifiable outer scale within the time periods that were admitted.

## 1. INTRODUCTION

Phase-coherent beacon satellite transmissions are emerging as a powerful new tool for probing the structure of the ionosphere (Daves et al.; Schmidt and Tauriainen, 1975). By using phase-coherent signals one can measure the full complex signal. Thus, in principle, the irregularity structure can be measured undistorted by the Fresnel filter effects that complicate the interpretation of intensity scintillation data.

In this paper we present some preliminary measurements of the complex signal moments and discuss their interpretation. We begin by briefly reviewing the principle of the measurement. Consider two phase-coherent transmissions at frequencies  $f_1$  and  $f_R = n f_1$ , where  $n$  is an integer. The received signals have the form

$$S_R(t) = A_R(t) \cos(2\pi f_R t + \varphi_R(t)) , \quad S_1(t) = A_1(t) \sin(2\pi f_1 t + \varphi_1(t)) \quad (1a), \quad (1b)$$

In the receiver a reference oscillator is phase-locked to  $S_R(t)$  and then used to synchronously demodulate  $S_1(t)$ . The synchronous demodulator produces the quadrature signals

$$\begin{Bmatrix} x_1(t) \\ y_1(t) \end{Bmatrix} = A_1(t) \begin{Bmatrix} \sin \\ \cos \end{Bmatrix} (\varphi_1(t) - \varphi_R(t)/n + \varphi_o) \quad (2)$$

The constant phase offset  $\varphi_o$  is induced by the receiver, and it can generally be ignored.

A recently recorded example of a synchronously demodulated VHF signal is shown in Figure 1 together with  $A_1(t)$  and the differential phase  $\Delta\varphi(t) = \arctan [y_1(t)/x_1(t)]$ . Our first task is to isolate the coherent or nonscattered signal component. To this end, we identify three components in the differential phase by writing

$$\Delta\varphi(t) = \bar{\omega}_d(t)t + \varphi_d(t) + \left[ \delta\varphi_1(t) - \frac{\delta\varphi_R(t)}{n} \right] . \quad (3)$$

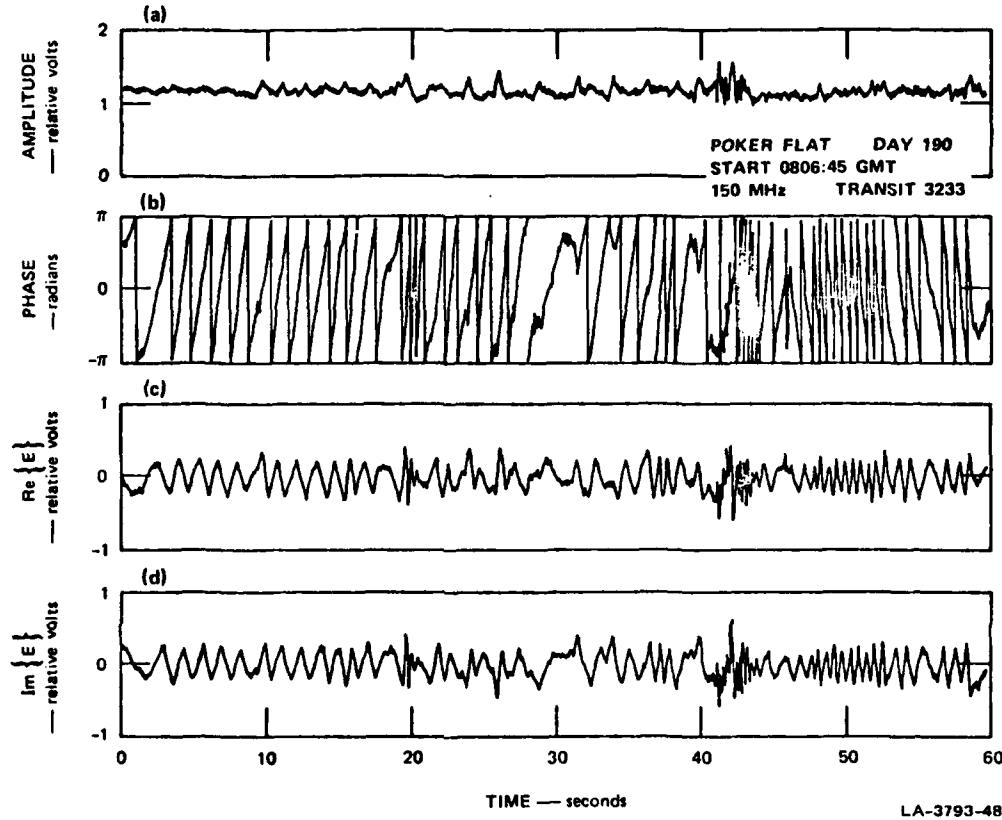


FIGURE 1 MODERATELY DISTURBED TRANSIT RECORD (after decimation) OBTAINED AT POKER FLAT ON 9 JULY 1975, SHOWING INTERESTING VARIATIONS IN (a) AMPLITUDE, (b) PHASE, AND (c and d) QUADRATURE COMPONENTS

The first term,  $\bar{\omega}_d(t)$ , is a slow phase variation induced by changes in the total electron content along the propagation path. We assume that any amplitude variation associated with  $\bar{\omega}_d(t)t$  is a pure refraction effect that can be simply calculated or ignored. Thus,  $\bar{\omega}_d(t)t$  can be extracted by low-pass filtering  $\Delta\varphi(t)$ . We then use  $\bar{\omega}_d(t)t$  to derive a reference signal to synchronously demodulate  $x_1(t) + i y_1(t)$ .

The complex signal that results has the form

$$u(t) = A_1(t) \exp \left\{ i \varphi_1(t) \right\} \quad (4)$$

where

$$\varphi_1(t) = \varphi_d(t) + \left[ \delta\varphi_1(t) - \frac{\delta\varphi_R(t)}{n} \right] . \quad (5)$$

We assume that the reference-signal term  $\frac{\delta\varphi_R(t)}{n}$  is negligible when compared to the remaining terms in Eq. (5). A scatter diagram for a typical signal phasor  $v(t)$  is shown in Figure 2.

The prominent feature of all the signals we have processed in this manner is the large phase variations that dominate the signal. Indeed, it is this fact that led us to consider two separate components in  $\varphi_1(t)$ . The rapid component,  $\delta\varphi_1(t)$ , is more closely associated with the amplitude scintillation, but we admit a small amount of amplitude scintillation with slow periods.

In the companion paper by Fremouw et al. (1976), it is shown that  $u(t)$  admits the multiplicative decomposition

$$u(t) = v(t) \exp \left\{ \Psi(t) \right\} \quad (6)$$

where  $v(t)$  and  $\Psi(t)$  are statistically independent complex Gaussian processes. The imaginary part of  $\Psi(t)$  is identified with  $\varphi_d(t)$  in Eq. (5), while the real part of  $\Psi(t)$  is generally small, at least for weak to moderate scattering.

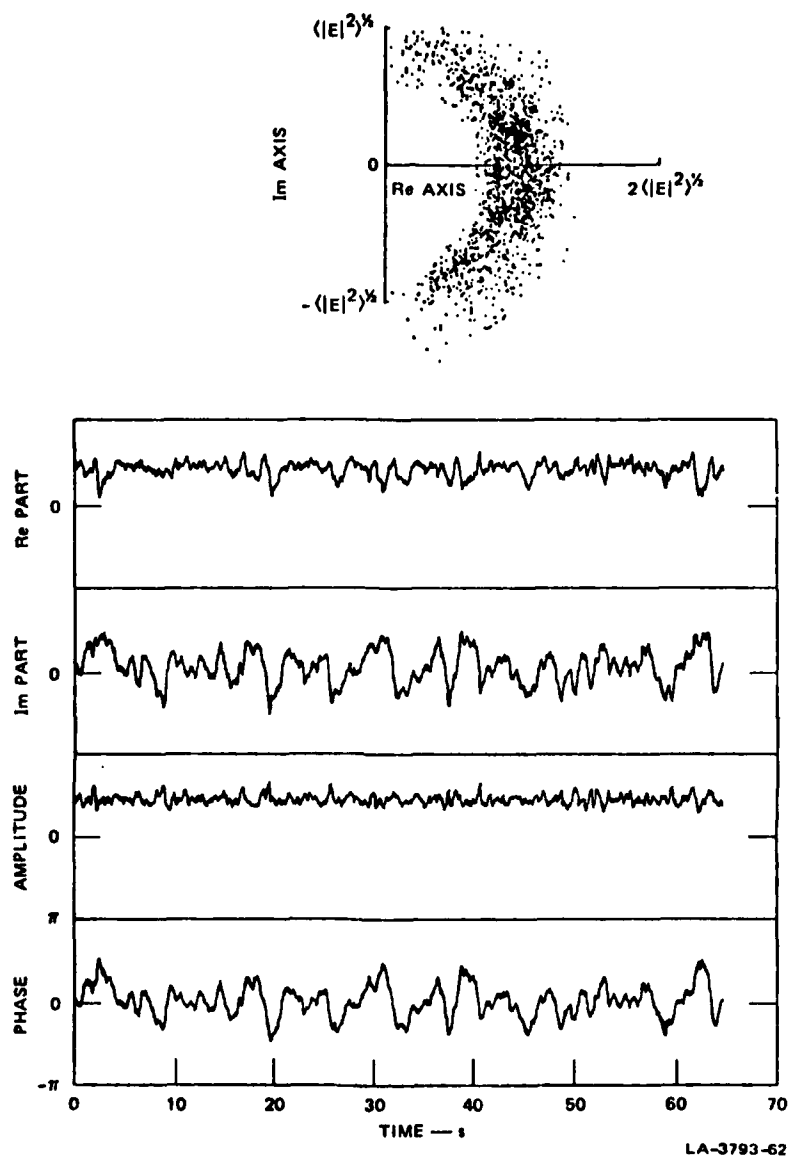


FIGURE 2 EXAMPLE OF DETRENDED SIGNAL SHOWING CHARACTERISTIC LARGE PHASE VARIATIONS

This signal structure readily explains why the intensity statistics are accurately characterized by a single-component Gaussian model (Rino et al., 1976). Indeed,  $I(t) \triangleq |u(t)|^2 \cong |v(t)|^2$ . That is, the amplitude variation associated with the log-normal component,  $\exp[\Psi(t)]$ , is small when compared with the amplitude variations associated with  $v(t)$ .

If one accepts the signal structure as shown in Figure 2, it is immediately clear that the conventional weak-scatter theory cannot be applied directly. The large phase variations exclude direct use of the Born approximation. Moreover, the Rytov solution, while admitting large phase fluctuations, is restricted to the extreme near zone.

To avoid these restrictions, we must consider the parabolic approximation to the wave equation:

$$\frac{du(\vec{r}, z)}{ds} = i \frac{\lambda}{4\pi} \nabla_T^2 u(\vec{r}, z) - i r_e \lambda \Delta N_e(\vec{r}, z) . \quad (7)$$

In Eq. (7),  $\vec{s}$  is a distance vector along the propagation direction, and  $\Delta N_e(\vec{r}, z)$  is the local electron density perturbation.

However, there is essentially no loss of generality if we take the  $z$  axis along  $\vec{k}$  so that the directional derivative in Eq. (7) involves only the  $z$  variable. Making this assumption, we can write Eq. (7) in the equivalent form

$$\frac{d \log u(\vec{r}, z)}{dz} = i r_e \lambda \Delta N_e(\vec{r}, z) - i \frac{\lambda}{4\pi} \nabla_T^2 u(\vec{r}, z)/u(\vec{r}, z) . \quad (8)$$

Going further, we integrate Eq. (8) over a short  $z$  distance,  $\Delta z$ , and neglect second-order propagation effects.

The result takes the simple form

$$u(\vec{r}, z_o + \Delta z) \cong \exp \left\{ -i r_e \lambda \int_{z_o}^{z_o + \Delta z} \Delta N_e(\vec{r}, \eta) d\eta \right\} \\ \times [u(\vec{r}, z_o) - i \frac{\lambda \Delta z}{4\pi} \nabla_T u(\vec{r}, z_o)] . \quad (9)$$

The first factor is simply the phase perturbation obtained by using the linear ray-optics approximation. The second factor is the differential approximation to the diffraction integral

$$u(\vec{r}, z_o + \Delta z) = \iint \exp \left\{ i \frac{\lambda \Delta z}{4\pi} \kappa^2 \right\} \exp \left\{ -i \kappa^2 \cdot \vec{r} \right\} d\xi(\vec{\kappa}; z_o) \quad (10)$$

where  $d\xi(\vec{\kappa}; z_o)$  is the Fourier spectrum of  $u(\vec{r}, z_o)$ .

From Eq. (9) it is clear that the interaction of a wave with a randomly irregular medium involves both a phase perturbation and diffraction. When  $\Delta N_e(\vec{r}, z) = 0$ , Eq. (9) reduces to the equation of free-space propagation. Now, for remote probing we would like to unravel the diffraction effects and extract a quantity related to  $\Delta N_e(\vec{r}, z)$  such as

$$\varphi(\vec{r}) = - r_c \lambda \int_{z_o}^{z_o+L} \Delta N_e(\vec{r}, \eta) d\eta \quad . \quad (11)$$

In the radio holographic approach (Schmidt and Tauriainen, 1975) one attempts to remove the diffraction effects directly by inverting the integral in Eq. (10). Since diffraction and scattering evolve simultaneously within the medium, however, the radio holographic technique cannot unambiguously reproduce the irregularity structure. Nonetheless, one can localize large-scale structures.

We have pursued an alternative statistical approach in which we compute the complex field moments and then use the theoretical geometrical dependence of the moments to infer the average structure of the irregularities as characterized by their autocorrelation function, or, equivalently, their spectral density function. In principle, the statistical method leads to unambiguous determination of the irregularity structures. Moreover, the large phase variations induced by multiple scattering does not impose a fundamental restriction.

## 2. SOLUTIONS TO THE PARABOLIC WAVE EQUATION UNDER THE MARKOV APPROXIMATION

We shall consider here the complex signal moments

$$R_u(\Delta \vec{r}; z) \stackrel{\Delta}{=} \langle u(\vec{r}) u^*(\vec{r}') \rangle, \quad B_u(\Delta \vec{r}; z) \stackrel{\Delta}{=} \langle u(\vec{r}) u(\vec{r}') \rangle \quad (12a), (12b)$$

The  $R_u$  correlation function is usually called the mutual-coherence function. The complementary function  $B_u$  has no accepted name, but it is sometimes referred to as the asymmetry correlation function.

We note that the complex signal mean  $\langle u(\vec{p}) \rangle$  is not subtracted from  $u(\vec{p})$ . Moreover, no normalization is used. However,  $R_u(0; z) = \langle |u(\vec{p})|^2 \rangle$  is the average signal intensity, which is unchanged by the scattering because backscattered energy is negligible as is absorption. For convenience we shall assume that  $u(\vec{p})$  is normalized to unity intensity.

To derive differential equations for Eqs. (12a) and (12b), we note that in Eq. (9),  $\Delta N_e(\vec{p}, z)$  contributes to the integral for  $z$  values greater than  $z_o$ , while the diffraction term uses only the  $u(\vec{p}, z_o)$ . Suppose now that  $u(\vec{p}, z_o)$  and  $\Delta N_e(\vec{p}, z)$  are uncorrelated for  $z > z_o$ . This assumption is essentially the Markov approximation. A sufficient condition is that the perturbation induced over a correlation distance be small (Beran, 1970).

By accepting the Markov approximation it is possible to derive differential equations for  $R_u$  and  $B_u$  directly from Eq. (9). Using a compact notation we have

$$\begin{aligned} \left\{ \begin{array}{l} R_u(\vec{p}, z_o + \Delta z) \\ B_u(\vec{p}, z_o + \Delta z) \end{array} \right\} &\simeq \langle \exp \left\{ i[\varphi(\vec{p}) \mp \varphi(\vec{p}')] \right\} \rangle \\ &\times [1 - i \frac{\lambda \Delta z}{4\pi} (\nabla_T^2 \pm \nabla'_T)^2] \left\{ \begin{array}{l} R_u(\vec{p}, z_o) \\ B_u(\vec{p}, z_o) \end{array} \right\} \quad (13) \end{aligned}$$

where the upper sign is used for  $R_u$  and the lower sign for  $B_u$ . Equation (13) is essentially equivalent to the corresponding equation given in Gurvich and Tatarski (1975).

Now for the tacitly assumed homogeneous statistics, the  $\nabla_T^2$  and  $\nabla'_T^2$  operators give identical results. Thus, for the mutual-coherence function the diffraction term has no effect. Indeed, Booker, Ratcliffe, and Shinn (1950) showed that in free space the mutual-coherence function is invariant to propagation effects.

To evaluate the expectation term in Eq. (13), we assume that  $\varphi(\vec{p})$  is Gaussian. This assumption is not strictly necessary, but it simplifies the computations. For Gaussian  $\varphi(\vec{p})$  we have

$$\langle \exp \left\{ i[\varphi(\vec{p}) + \varphi(\vec{p}')] \right\} \rangle \cong \exp \left\{ -\sigma^2_{\Delta z} \left[ (1 - \int_0^\infty p_{\Delta N_e}(\Delta \vec{p}, z) d\eta) \right] \right\} \quad (14)$$

where

$$\sigma^2 = r_e^2 \lambda^2 \Delta N_e^2 \int_0^\infty R_{\Delta N_e}(0, \eta) d\eta . \quad (15)$$

In deriving Eq. (14) we assumed that the correlation distance along  $z$  is small compared to  $\Delta z$ , which is consistent with the Markov assumption condition.

By using Eq. (14), in Eq. (13) we readily obtain the equations

$$R_u(\Delta \vec{p}; z_o + \Delta z) \cong R_u(\Delta \vec{p}; z_o) \exp \left\{ -\sigma^2_{\Delta z} [1 - \int_0^\infty p_{\Delta N_e}(\Delta \vec{p}, \eta) d\eta] \right\} \quad (16a)$$

and

$$B_u(\Delta \vec{p}; z_o + \Delta z) \cong \exp \left\{ -\sigma^2_{\Delta z} [1 + \int_0^\infty p_{\Delta N_e}(\Delta \vec{p}, \eta) d\eta] \right\} \\ [B_u(\Delta \vec{p}; z_o) - \frac{i\lambda\Delta z}{2\pi} \nabla_T^2 B_u(\Delta \vec{p}; z_o)] . \quad (16b)$$

The similarity of Eqs. (16b) and (9) can be used to immediately deduce the differential equation for  $B_u(\Delta \vec{p}; z)$ . Alternatively, under the Markov approximation, the diffraction effects apply to  $B_u(\Delta \vec{p}; z)$  in exactly the same way as the diffraction effect applies to  $u(\vec{p}, z)$  itself.

For an incident plane wave, Eq. (16a) admits the exact solution

$$R_u(\Delta \vec{p}, L) = \exp \left\{ -\sigma^2_L [1 - \int_0^\infty p_{\Delta N_e}(\Delta \vec{p}, \eta) d\eta] \right\} \quad (17)$$

where  $L$  is the length of the propagation path. If  $p_{\Delta N_e}(\Delta \vec{p}, \eta)$  varies, the effect can readily be accommodated in the integral.

In practice, we can measure only a one-dimensional scan of  $R_u(\vec{\Delta\rho}, L)$  or  $B_u(\vec{\Delta\rho}, z)$ . Nonetheless, the theory gives a direct relation between the irregularity spectrum and the measurable complex signal moments that imposes no restriction other than narrow-angle scattering and the Markov approximation. By a very similar development it can be shown that

$$\sigma_T^2 \triangleq \langle |u|^2 \rangle - |\langle u \rangle|^2 = 1 - \left\{ \exp -\sigma_L^2 L \right\} . \quad (18)$$

### 3. APPLICATIONS TO DATA ANALYSIS

In our first attempt at using these results, we measured the first-order moments  $\sigma_T^2$  and  $B_u(0; z)$ . From  $\sigma_T^2$  we could solve Eq. (18) for  $\sigma_L^2 L$ . In Table 1 we show a typical set of measured parameters for a nighttime TRANSIT pass in the auroral zone. From Point Nos. 1 through 15 there is a steady buildup of amplitude fluctuation and then an abrupt drop from Points 16 through 20.

From the complex signal moments we see that  $\sigma_T^2$  is well into the multiple-scatter regime (say,  $\sigma_T^2 > 0.2$ ) before the  $S_4$  index achieves a value of 0.3. Previously we had argued that weak-scatter conditions prevail for  $S_4$  values as large as 0.4. We also note that  $\sigma_T^2$  achieves its largest value (Point 14) before the peak value of  $S_4$  (Point 15). This shows that an intensification of the spectral density does not lead to amplitude fluctuation unless small-scale structure develops.

To show how these data can be interpreted, we have used a thick phase-screen model and assumed a field-aligned anisotropy. The calculations were performed during a  $K^{-4}$  power-law spectral shape with both an inner and an outer scale cutoff. To simplify the computations we used the near-zone approximation

$$B_u(0; z) \cong B_u(0; z_0) - iz \left[ \frac{\partial^2 B_u(\vec{\Delta\rho}, z_0)}{\partial \Delta\rho_x^2} + \frac{\partial^2 B_u(\vec{\Delta\rho}; z_0)}{\partial \Delta\rho_z^2} \right]_{\vec{\Delta\rho} = 0} . \quad (19)$$

The calculations are summarized in Table 1. To put the results in familiar terms we use the Briggs-Parkin angle  $\psi_{BP}$  and projection factor  $\beta_{BP}$ . We recall that

Table 1  
SATELLITE LOCATION AND MEASURED PARAMETERS

PASS ID POKER FLAT			PENETRATION POINT (350 km)			CALCULATED			
	START 266	9 58 0					$ B $		
	END 266	10 13 0					$\sigma_T^2$	$\sigma_L^2$	$\sigma_N^2$
		10.0							
NO.	DAY	TIME (UT)	LAT	LON	L	S <sub>4</sub>	$\sigma_T^2$	$\sigma_L^2$	$\sigma_N^2$
1	266	95921.8	56.70	-137.69	3.89	.09	.005	.0050	.00
2	266	95942.3	57.47	-138.02	4.05	.10	.006	.0060	.00
3	266	10 0 1.9	58.12	-138.32	4.19	.23	.031	.0315	.01
4	266	10 021.7	58.76	-138.64	4.34	.16	.014	.0141	.01
5	266	10 042.3	59.41	-138.94	4.50	.11	.007	.0070	.00
6	266	10 1 2.1	59.95	-139.21	4.64	.13	.011	.0111	.00
7	266	10 121.7	60.51	-139.49	4.79	.10	.006	.0060	.00
8	266	10 142.2	61.05	-139.78	4.94	.12	.020	.0202	.01
9	266	10 2 2.0	61.55	-140.03	5.09	.15	.093	.0976	.04
10	266	10 221.6	62.03	-140.28	5.24	.22	.133	.1427	.07
11	266	10 242.3	62.52	-140.54	5.40	.15	.166	.1815	.09
12	266	10 3 2.0	62.96	-140.79	5.55	.18	.239	.2731	.13
13	266	10 322.5	63.41	-141.02	5.71	.26	.716	1.2588	.63
14	266	10 342.3	63.83	-141.23	5.87	.41	.882	2.1371	1.10
15	266	10 4 1.9	64.24	-141.45	6.02	.94	.675	1.1239	.59
16	266	10 422.6	64.66	-141.65	6.20	.15	.293	.3467	.19
17	266	10 442.2	65.06	-141.89	6.37	.10	.118	.1256	.07
18	266	10 5 1.8	65.46	-142.05	6.55	.08	.127	.1358	.08
19	266	10 522.6	65.87	-142.25	6.74	.09	.102	.1076	.06
20	266	10 542.2	66.27	-142.45	6.94	.10	.126	.1347	.08
21	266	10 6 1.8	66.67	-142.62	7.15	.11	.104	.1098	.06
22	266	10 622.5	67.10	-142.82	7.38	.27	.064	.0661	.04
23	266	10 642.1	67.51	-142.99	7.62	.28	.088	.0921	.05
24	266	10 7 1.7	67.94	-143.16	7.88	.21	.105	.1087	.06
25	266	10 722.4	68.39	-143.37	8.16	.20	.109	.1154	.07
26	266	10 742.0	68.84	-143.54	8.47	.21	.174	.1912	.11
27	266	10 8 1.8	69.32	-143.76	8.81	.21	.112	.1188	.06
28	266	10 822.4	69.81	-143.93	9.18	.19	.121	.1290	.07
29	266	10 842.0	70.31	-144.15	9.59	.22	.105	.1109	.05
30	266	10 9 1.8	70.84	-144.38	10.04	.24	.157	.1708	.08
31	266	10 922.3	71.41	-144.61	10.57	.25	.089	.0932	.04
32	266	10 942.1	72.01	-144.83	11.18	.24	.122	.1301	.06
33	266	1010 1.7	72.60	-145.08	11.81	.30	.157	.1708	.07
34	266	101022.3	73.29	-145.41	12.62	.35	.149	.1613	.06
35	266	101042.0	73.94	-145.77	13.44	.25	.095	.0998	.04
36	266	1011 1.7	74.62	-146.12	14.39	.20	.085	.0888	.03
37	266	101122.4	75.43	-146.56	15.61	.18	.055	.0566	.02
38	266	101142.0	76.21	-147.08	16.91	.34	.135	.1450	.05
39	266	1012 1.6	77.02	-147.58	18.42	.50	.186	.2058	.07
40	266	101222.3	77.89	-148.33	20.19	.56	.268	.3120	.10

$$\sigma_L^2 = r_e^2 \lambda^2 \frac{\alpha a \langle \Delta N_e^2 \rangle L \sec \theta}{\beta_{BP}} N \quad (20)$$

where  $N$  depends only on the spectral shape,  $a$  is the axial ratio, and  $\alpha$  is the outer scale size. The parameter  $\sigma_N^2$  is defined as

$$\sigma_N^2 = (\sigma_L^2) \frac{\beta_{BP}}{a \sec \theta} \quad (21)$$

which is a direct measure of the spectral intensity up to the largest spatial frequency admitted by the detrend operation.

One can readily see from the data in Table 1 that whereas we observed a steady buildup in  $\sigma_T^2$ , the parameter  $\sigma_N^2$ , for a 10:1 axial ratio, shows a single symmetric peak near  $L = 5.87$ . This is very likely to be associated with auroral precipitation to the north of the receiver site. It is doubtful that such a "clean" localization could be made with intensity data alone.

#### REFERENCES

- Daves, K., R. B. Fritz, R. N. Grubb, and J. E. Jones, "Some early results from the ATS-6 Radio Beacon experiment," Radio Science, Vol. 10, pp. 785-799 (1975).
- Schmidt, C., and A. Tauriainen, "The localization of ionospheric irregularities by the holographic method," J. Geophys. Res., Vol. 80, pp. 4313-4320 (1975).
- Fremouw, E. J., C. L. Rino, and R. C. Livingston, "A two-component model for scintillation," paper presented at COSPAR Symposium, Boston, 1976.
- Rino, C. J., R. C. Livingston, and H. E. Whitney, "Some new results on the statistics of radio-wave scintillation--A. Empirical evidence for Gaussian statistics," to be published J. Geophys. Res. (1976).
- Beran, M., "Propagation of a finite beam in a random medium," J. Opt. Soc. Am., Vol. 60, pp. 518-521 (1970).
- Gurvich, A. S., and V. J. Tatarski, "Coherence and intensity fluctuations of light in the turbulent atmosphere," Radio Science, Vol. 10, pp. 3-14 (1975).
- Booker, H. G., J. A. Ratcliffe, and D. H. Shinn, "Diffraction from an irregular screen with applications to ionospheric problems," Phil. Trans. Roy. Soc. A, pp. 579-607 (1950).

# ATS-6 40 and 360 MHz Differential Phase Measurements

Frederick F. Slack  
Air Force Geophysics Laboratory  
Air Force Systems Command  
Hanscom AFB, MA 01731

## Abstract

Equipment employing new cross-correlation design concepts for receiving and processing weak R.F. signals in a noisy environment is described. It is shown how this equipment becomes an integral part of the instrumentation for measuring the differential phase between the ATS-6 satellite, 40 and 360 MHz coherent c.w. signals that have been propagated thru the ionosphere.

The relationship between 40 MHz phase and amplitude scintillation was developed using differential phase data from the ATS-6 geostationary satellite. The 40 and 360 MHz coherent signals were propagated through the ionosphere and received on the 150' radio telescope at the Sagamore Hill Radio Observatory.

The analysis of the computerized data was based on 13 consecutive days of active scintillation in November 1974. It shows that amplitude and phase scintillation occurred simultaneously only 53% of the time, indicating that application of the equivalent thin diffracting screen theory is invalid for describing the data for the remaining 47% of the time. Statistical comparisons suggest that daytime amplitude scintillations were apparently caused by ionospheric focusing mechanisms, since phase scintillation proved to be almost exclusively a nighttime phenomena.

The differential phase data from the same source is analyzed in a manner that reveals many of the ionospheric interactions that affect space communications. The interactions are further reduced into the following parameters that describe ionospheric conditions that relate to R.F. propagation:

1. Total electron content (TEC)
2. Changes in electron density, assuming height
3. Equivalent slab thickness, assuming height
4. A continuous measurement of phase velocity
5. A continuous measurement of rate of change of TEC
6. A continuous measurement of rate of change of refractive index

## 7. A continuous measurement of angle of arrival.

The influence that the travelling ionospheric disturbances (TID) have on the phase of the 40 MHz signal receives special emphasis, and it is shown how the presence of T.I.D. aids in the analysis.

### Introduction

Detection and processing of VHF and UHF Satellite C. W. signals with power levels less than -135 dbm at the antenna present difficulties when attempting to translate the processed data into meaningful measurements of ionospheric physical interactions. The principal problem is interference from extraneous signals, i.e. man-made and natural R.F. noise. For several years tracking filters have been employed to alleviate the problem by narrowing the receiver band width to a few cycles per second. The filters are required to frequency track the R.F. signal, because generally the satellite signal and the local oscillator are not sufficiently stable to allow use of a narrow band fixed filter.

Experience has shown that geo-stationary satellite UHF signals drift up to 200 Hz and orbiting satellite signals, due to the added doppler frequencies, shift many times that. Local oscillators, however, can be made extremely stable using synthesizer techniques.

The complexity of the tracking filter with the automatic search circuitry required to lock the filter onto the signal during acquisition or when it reappears after a fade is an unattractive feature of this process.

Experience has also shown that when the signal is scintillating violently the tracking filter will not stay locked. For these reasons and the difficult alignment procedure, it appears that frequency tracking is not the solution for low cost satellite monitoring receivers, although in most cases it is presently the only solution.

### Phase Measuring Equipment

Fortunately there are satellites transmitting high and low UHF signals that are coherent, i.e. both are multiples of the same crystal frequency, and as a consequence lend themselves favorably to a much more dependable, simpler and less expensive system for their detection and processing. This is a cross-correlation technique designed at the AFCRL Ionospheric Research Laboratory, Bedford, MA to measure differential phase between a 40 MHz signal and a 360 MHz signal transmitted from the ATS-6 satellite. If the use of electronic correlation is not restricted because of the required response time, it is a powerful tool capable of extracting minute but meaningful information from an exceptionally noisy

environment. The band width determined by the integration time constant can be made extremely narrow. In this system it is .5 Hz at -3 dB, this being adequate for the fastest 360° phase shift encountered.

Inspection of the cross-correlation formula,  $\phi(\tau) = 1/T \int f(t) g(t-\tau) dt$  shows that when two time varying voltages  $f(t)$  and  $g(t-\tau)$  are the same frequency and the delay time,  $\tau$  is zero, the signals will be in phase and the output voltage,  $\phi(\tau)$  will be a maximum positive DC voltage. As  $\tau$  varies the phase between the voltages increases. At 90° the average correlated output is zero. When  $\tau$  is such that the phase difference is 180°, the correlated output is a maximum negative DC voltage. If  $\tau$  is varied linearly in incremental steps, for instance using a tape loop to provide  $g(t-\tau)$ , the correlated integrated output is sinusoidal with each incremental step's worth of integrated data being produced for each cycle of the tape loop.

The use of cross-correlation to detect and process ionospheric phase data provides a compatible marriage between the processing technique and the phenomena producing the ionospheric anomalies for the following reasons:

(1) The transmitted frequencies are made coherent in the satellite, therefore, for this system no frequency locking equipment is required.

(2) The variable delay ( $\tau$ ) requires no additional equipment as it is generated naturally in the ionosphere by the diurnal variation of the total electron content with its inherent refractive effects changing the phase velocity of the 40 MHz signal.  $\tau$  is also sensitive to phase scintillations and faster changes in the total electron content (TEC) such as those caused by magnetic storms and ionospheric winds; also travelling ionospheric disturbances, i.e. acoustic-gravity waves that modulate the TEC profile as they propagate through the ionosphere (Yeh, 1974).

(3) Because the system rejects random noise and uncorrelated signals, the product of which average out to zero, the normal receiver requirements are minimal, and it is not necessary to employ a complex phase locked communications receiver.

(4) The circuitry that provides a .5 Hz band width also produces a quasi-sinusoidal integrated output voltage when the TEC is increasing or decreasing at a linear rate. This by coincidence and very conveniently satisfies the first requirement for generating a voltage proportional to phase for making a strip chart recording.

A block diagram, Figure 1, has been provided to assist in the explanation of the complete system. The receiver portion consists of blocks 1 through 7. Blocks 1 and 4 are standard preamps with a 2 dB noise figure and a 28 dB gain. The local oscillator, block 7, is tuned 2 KHz higher than the 40 MHz satellite signal, thus when mixed with the satellite signal, 2 KHz becomes the difference frequency for further processing.

When the local oscillator is mixed with the 360 MHz satellite signal it is actually the 9th harmonic that is used, thus making

the 2 KHz difference frequency 18 KHz for further processing at the mixer output.

At this point the system has produced a 2 KHz signal carrying the 40 MHz phase information and an 18 KHz signal to be used as the standard, since refractive effects on the 360 MHz frequency responsible for it are minimal.

The two frequencies have remained coherent through the heterodyning process, because the same L.O. has been employed for both; however, for cross-correlation purposes they should both be the same frequency. To accomplish this the 18 KHz could be divided down to 2 KHz or the 2 KHz could be multiplied up to 18 KHz. The latter method was chosen for two reasons. There is more stability in frequency multiplication than there is in frequency division, and it is possible to make a chart record that is nine times more sensitive, nine being the multiplication factor to bring 2 KHz up to 18 KHz. Therefore, each  $\phi(\tau)$  cycle out of the correlator represents 40° instead of 360° of the 40 MHz phase change. See Figure 2.

The increased sensitivity is valuable when measuring the time of occurrence of T.I.D.'s (Figure 2) as the phase reversals can be measured accurately to within a few degrees. Its potential value is the accuracy to be achieved in measuring T.I.D. direction and speed, if three systems are put into operation in triangulation.

For strip chart recording of phase and phase scintillation a sinusoidal function is not adequate as it is subject to ambiguity, i.e. one cannot tell if the phase is increasing or decreasing. If the system includes two correlators, one generating a sinusoidal function and the other generating a cos function, as this system does (blocks 10 through 13), the ambiguity can be eliminated through visual interpretation of the record. However, this is a tedious operation, so it is better to extend the process further and include a coordinate converter (blocks 12, 14, 15, 16, 17) that puts the data back in the form of two coherent a.c. signals still retaining the proper phase relationship that can operate a phase ramp generator. The frequency can be whatever one chooses. This system uses 60 Hz because of future intentions to drive a clock motor. It may appear at this point that nothing has been gained; we started with two 18 KHz signals, one changing phase relative to the other, and we end up with two 60 Hz signals, one changing phase relative to the other. The big difference, however, is that the unprocessed 18 KHz signals have so much phase jitter and extraneous noise that the data from a phase detector operating on these signals would be worthless. On the other hand the two 60 Hz signals are relatively noise free having gone through the correlation process with the .5 Hz band width.

Mathematical expressions describing the more complex portions of the system are as follows: Placing a 90° phase shift on one of

the 18 KHz signals and simultaneously running it through a second correlator produces a second correlated signal thus providing two output voltages,  $\sin \phi(\tau) = 1/T \int_0^T f(t) g(t-\tau) dt$  and  $\cos \phi(\tau) = 1/T \int_0^T f(t) g(t-\tau) dt$ .

When the phase between the two input signals is shifting at a constant rate, these two functions can be considered to be very low sub audio frequencies, one 90° out of phase with the other. One cycle per second is about the highest frequency so far encountered. Therefore, treating them as such yields the following expressions for the output of the modulators, box 14,  $(\sin \omega_1 t) (\sin \omega_2 t)$  and box 16,  $(\cos \omega_1 t) (\cos \omega_2 t)$ . Summing the two outputs (box 17) yields the trigonometric relation,  $\cos(\omega_1 t - \omega_2 t)$ . Amplifying this signal into saturation obliterates the cos function and the output is then  $t(\omega_1 - \omega_2)$ . Thus the output of the summer and amplifier when  $\omega_1 = K = 60$  Hz and  $\omega_2 = 1$  Hz is a 59 Hz square wave which is just another way of saying a 60 Hz constant amplitude voltage is changing phase at the rate of one cycle per second relative to the 60 Hz standard.

The multiplication by  $1/T$  is performed to normalize the data, i.e. to eliminate signal time duration as a factor in determining the amplitude of the integrated output.

Operating a conventional phase detector off of the two 60 Hz signals produces a phase ramp for each 40° phase shift between the two R.F. signals at the antenna, i.e.  $360^\circ/9$  as explained earlier in the text.

It was decided, however, not to phase detect here, but to extend the range to  $1280^\circ$  per ramp to help distinguish phase scintillations from phase ramps and also to reduce the chart speed for more economical use of chart paper. To accomplish this both 60 Hz signals are fed into 32 to 1 digital counters, boxes 19, 20. The counter output, operating from the 60 Hz oscillator, supplies a pulse to repeatedly start a very linear ramp generator (block 21). This is a sawtooth voltage with a repetition rate of approximately .5 cycles per second, i.e.  $32/60$  Hz.

The ramp generator is fed to the phase detector where it is sampled by the instantaneous pulse from the 32 to 1 signal counter. The value sampled is placed in storage on a capacitor and held constant until the next pulse 2 seconds later. If the phase is increasing the sampled values follow the ramp up in the positive direction. If the phase is decreasing, the reverse is true. For example if it takes 32 seconds for the signal to complete each cycle of the 2 second ramp in incremental stored steps, the output of the phase detector is a 32 second ramp that reverses direction when the signal reverses phase. See Figure 2.

Earlier in the text it was mentioned that there was a reason for using 60 Hz in the coordinate converter. The proposal is to

develop a complete diurnal curve of the total electron content using electro-mechanical techniques. If the two 60 Hz voltages, blocks 12 and 17, are used to drive clock motors the output shaft of the signal 60 Hz will rotate slightly faster or slower than the standard 60 Hz motor, depending on how fast the phase is increasing or decreasing. By using an appropriate gear reduction in combination with a mechanical differential coupled to a linear potentiometer it will be possible to develop a variable D.C. voltage representing a diurnal plot of the electron content, there being a direct correlation between phase shift and changing TEC. The gear reduction will have to be sufficient to keep the rotation of the potentiometer arm within the mechanical limits of the potentiometer. This will ensure a smooth curve without interruption caused by potentiometer discontinuity.

"The equivalent thin phase screen" is a popular concept used by ionospheric scientists for explaining in mathematical terms, amplitude scintillations on RF signals propagated through the ionosphere. This is a screen of negligible thickness that would produce the same phase variations on the RF signal as the actual irregular region (Briggs, 1966). The assumption is that the signal leaves the thin screen, fluctuating in phase only, but as the wave propagates beyond the screen amplitude fluctuations develop from the summation of the deviated phase signals.

Recent measurements made on ATS-6 geostationary satellite signals comparing 40 MHz phase with amplitude show that application of the equivalent thin screen theory is valid for only a portion of the data. During a 13 day active period of ionospheric scintillation in November 1974 data was computerized to make the above comparisons. The results show that during the periods of amplitude scintillation, phase scintillation existed only 53 percent of the time (Figure 4). Thus, if the amplitude scintillation at the antenna was not the result of ionospheric phase scintillation during 47 percent of the time, another theory is required to explain the results. To conform to the data as presented on the strip charts, the responsible mechanism must allow both enhancement and attenuation of the RF signal. Past investigators studying large scale irregularities have suggested marked focusing effects as the cause of scintillation. This could also explain the remaining 47 percent reported here. Concurrent cycles of the RF propagation could be focused on the antenna through lens-like structures of the irregularities, eliminating the phase deviation requirement dictated by the diffraction theory. Also, when a moving ionospheric structure focuses an increase in energy on the antenna, its refractive area that supplied the enhancement must also reduce the energy when it is appropriately positioned, resulting in moving irregularities that are equivalent to alternating convex and concave lenses.

In a similar manner moving electron gradients normal to the propagation path could deflect concurrent rays that are close

to grazing incidence resulting in alternating enhancement and fading of the signal at the antenna (Slack, 1970). An example of amplitude scintillation accompanied by phase scintillation is shown in Figure 5; amplitude scintillation without the presence of phase scintillation is shown in Figure 6.

A graph (Figure 7) was constructed showing the percentage of time the phase angle  $\phi$  was in excess of X degrees for the 13 day period. The smoothness of the curve suggests that sufficient data was analyzed to describe conditions for a high percentage of ionospheric scintillation.

Although the shape of the curve appears to indicate a near Gaussian distribution of irregularities with respect to the line of sight between the satellite and the receiver, logically there is no reason to believe there would be such a distribution at the specific region where the RF ray penetrates the ionosphere. It is more likely that, statistically, there is a linear distribution being affected by a diminishing power law.

The Fresnel formula,  $vt = \sqrt{2n\lambda r}$  states that when the lateral distance in the ionosphere between the line of sight ray and an interfering ray, or the equivalent radius resulting from diffracted or scattered rays has changed  $vt$ , it produces a difference in the arrival time required for  $n\lambda$  at the receiver distance  $r$ . If  $\lambda_0/2\pi$  is substituted for  $n$ , the equation can be solved for phase change  $\phi_0$  instead of integers of wavelengths. Thus with rearrangement and substitution, the formula becomes

$$\phi_0 = \frac{\pi(vt)^2}{\lambda r}.$$

From this it is apparent that the change in phase resulting from a linear distribution is proportional to the square of the ray separation distance  $vt$ . Looking again at the graph in the region of  $\phi_0 > 1$  rad the curve closely follows a square law indicating Fresnel action on a linear distribution of irregularity sizes. If such is the case, it supports the contention made by several investigators that some ionospheric scintillation is produced by either a superposition or a distortion of quasi-periodic events. These are the irregularities which, when isolated, develop a characteristic "ringing" Fresnel pattern as displayed on the amplitude channel of a chart recorder (Elkins and Slack, 1969; Titheridge, 1970; Kelleher and Martin, 1974). They fall in the region  $\phi_0 \gg 1$  rad, and the curve would have to be extended significantly to include the uncontaminated isolated examples.

The region of  $\phi_0 < 1$  rad is where, according to Hewish (1951) and generally accepted by others, the projected irregularities have the same scale size when measured on the ground as would be the case if measured at the ionospheric level. Here the curve is quite linear as one might expect with a linear distribution of increasing scale sizes, because the change in refractive index, and thus the change in phase, is directly proportional to the electron content in the irregularity.

Aarons et al (1962) in referring to the two regimes as weak scattering where  $\phi_0 < 1$  rad and strong scattering where  $\phi_0 > 1$  rad shows that there are periods when the two regimes exist simultaneously. The graph supports their findings by displaying a gradual transition from linear to a characteristic Fresnel curve in the region between  $57^\circ$  and  $90^\circ$ .

The recorded data does not differentiate between positive and negative phase deviations, so they have all been lumped on one side in the graph. Since  $\phi_0$  is the result of a changing refractive index about a mean level, a complete graph should include a mirror image of itself in the negative  $\phi$  direction to more accurately portray the process that produces the phase scintillations. This is taken into consideration in explaining the non-linearity of the curve close to  $\phi_0 = 0$ . It is similar to the zero beat that appears on a travelling ionospheric disturbance record (Figure 3) when the phase reverses direction, and the angular refraction goes to zero.

In comparing the information contained in Figures 4 and 7 and using a spate of speculation with at least a modicum of logic, it appears that there is a relation between  $\phi$  scintillation in the hours between sunset and sunrise and  $\phi_0 < 1$  rad. Since the electron content is decaying during this period and the electrons would be clinging to their magnetic field aligned positions, electron gradients would develop normal to the field. With the ionosphere in motion, conditions now exist for the occurrence of  $\phi$  scintillations, initially falling in the regime  $\phi_0 < 1$  rad, because adjacent areas would produce only slight differences in refraction. As the decay cycle continues electron deficient holes would likely develop because of the remaining electrons' propensity for field alignment, causing the medium to become more irregular. At this time there would be a tendency towards focusing mechanisms or grazing reflection surfaces more suitable for  $\phi$  scintillations in the regime  $\phi_0 > 1$  rad. Briggs (1966) in writing about "the equivalent thin phase screen" and its application to scintillation amplitude, summarized by saying, "This method will give useful results if  $\phi_0 < 1$  rad. When  $\phi_0$  is large there is evidence of focusing." Note in Figure 4 the negative correlation between  $\phi$  scintillation and amplitude scintillation during the daylight hours. Then compare this with Figure 7 showing that the rate of occurrence of  $\phi$  scintillation is practically zero for  $\phi_0 > 240^\circ$ . Thus the data indicates that during the daylight hours the increased electron density requires that the irregular structure instead of behaving like holes must now behave as cylinders with essentially all amplitude scintillations being caused by focusing or reflection surfaces, i.e.  $\phi$  scintillation is almost nonexistent, and when it does occur it is likely to be in the regime  $\phi_0 > 1$  rad.

It must be emphasized that the above explanation has been based on 13 active days of scintillation in November and its application to scintillation in general is a matter of conjecture.

### The Travelling Ionospheric Disturbance

One of the most outstanding features displayed by the phase data is the influence that travelling ionospheric disturbances (TID) have on the phase of the 40 MHz signal. A TID is generally thought to be an acoustic-gravity wave propagating through the vast expanse of the atmosphere including the ionosphere (Yeh, 1974).

Interpretation of the data (Figure 2) indicates that the medium is being diffused and compressed in a cyclic manner that changes its refractive index in the same fashion. Further, the data shows that the alternating diffusion and compression is in a direction that crosses the satellite receiver propagation path. To reach this conclusion consider the diurnal curve of the total electron content (Figure 8). This is the sum of all the phase ramps into one continuous 24 hour curve. Since there is a direct correlation between TEC and phase, the ordinate of the curve can be calibrated in the number of electrons per  $m^2$  column between the satellite and the receiver. Polarimeter data has been used this way for a number of years but uses the relationship between TEC and Faraday rotation and is only about 10% as sensitive to the changes in the medium. Also the polarimeter measures the Faraday rotation only to the range still influenced by the earth's magnetic field. Because of this difference the electron content, as measured by the polarimeter, should never exceed the differential phase TEC measurements. Since the figure contradicts this fact, it appears that the wrong range value was selected in the polarimeter analysis.

The figure shows that the TID produce equal deviations about the median of the curve. This indicates that there has been no net gain or loss in the total electron content, only that the electrons have been diffused away from the satellite-receiver propagation path and then compressed back again. If the compression and diffusion were in the direction of the R.F. path the data would show no change in the total electron content column when TID are present.

Since the ion gyrofrequency is much higher than both the ion neutral collision frequency and the wave frequency, the charged particles can move only along the magnetic field lines (Yeh, 1974). Thus ionospheric oscillations are induced more easily by field aligned perturbations. Combining this information with the above presents the hypothesis that the extent of TID influence on the R.F. propagation path is latitude dependent, being maximum at the equator where the satellite-ground propagation path is normal to the magnetic field lines, and minimum in the northern latitudes where the ray path and field lines are more closely parallel. This of course excludes other factors that may be more overpowering such as the TID having spent its energy by the time it reaches the equator.

The ATS-6 satellite elevation angle at Sagamore Hill, Hamilton, Massachusetts is  $36^\circ$ . The magnetic dip angle is  $73^\circ$ . Therefore the R.F. propagation path crosses the magnetic field lines at an angle of  $37^\circ$ . It follows that the magnitude of the electron flow normal to the propagation path is  $\sin 37^\circ \times$  the magnitude of the electron motion moving back and forth along the field lines as they respond to the TID wave motion. This compares with  $\sin 90^\circ$  at the equator.

It's also important to consider the TID direction component normal to the R.F. propagation path, so that the refractive process taking place can be understood, since this is what the receiver and phase detector system is measuring. If the crest of the TID wave represents the maximum electron density and the trough the minimum (Figure 2), then one can visualize this as introducing ionospheric gradients in the direction of the TID motion with maxima and minima representing positions where the rate of change of electron content goes to zero. Zero angular refraction (no bending of the R.F. ray) would appear when these points are centered on the ray, more specifically when components normal to the ray have reached this condition i.e. the integrated column of electrons are equal on opposite sides of the ray in the incident plane. It follows then that maximum refraction occurs when the rate of change of electrons is greatest during the steepest part of the TID wave. This is just what the recorded data shows, except that these conditions are slightly offset by the ever present diurnal change in total electron content.

The earlier section on the equipment shows how these physical interactions are translated into electrical measurements that are displayed on a chart recorder. A better understanding is provided by studying the diagram (Figure 3). The diagram represents conditions in the ionosphere where the satellite is directly overhead, the magnetic field lines are at right angles to the R.F. propagation path, and the TID direction is also normal to the R.F. propagation path. The figure shows what happens to the R.F. ray as a TID influenced electron gradient moves across it. No bending occurs at the maximum and minimum positions where there is zero gradient. Maximum bending occurs during the steepest portion of the gradient. Since the refractive index is less than one, the bending is always towards the greater density.

As the gradient passes across the ray, the phase velocity completes a cycle of increasing, decreasing, reversing direction then increasing and decreasing in the reverse direction. One side is a mirror image of the other except for the imbalance caused by the diurnal effect or some other natural perturbation. This action repeats for each passing TID cycle that intercepts the R.F. ray and is illustrated on the strip chart (Figure 2).

There have been pen recordings showing examples of TID electron displacements up to 20% of the ambient total electron

content at the time of the disturbance. Close inspection of the phase data 40° cycles and 1280° phase ramps shows that the refraction is causing the 40 and 360 MHz rays generally to separate and close at a constant velocity, causing typical doppler spacing of the 40° cycles. The cycles follow the square law spacing for a constant velocity fixed frequency moving at right angles to the propagation path. A mathematical solution shows that doubling the lateral distance the ray travels produces 4 times the number of cycles. Note on Figure 2 doubling 2 cycle distance produces 8 cycles, doubling the 4 cycle distance produces 16 cycles. It is assumed that the dominant action is on the 40 MHz ray, the coherent 360 MHz being high enough to be almost free of the refractive effects and is thus used as the standard reference for the phase measurement.

It should be emphasized that the number of cycles between crest and trough per unit time does not measure the velocity of the TID but relates to the rate of separation and closing of the 40 and 360 MHz rays normal to the propagation path. The number of cycles are also a measure of the TID amplitude i.e. the bigger the TID, the greater the influence on the electron density which in turn produces a larger change in refractive index, and thus an increase in phase velocity as illustrated on the chart by recording a greater number of cycles per unit time.

Doppler theory adequately explains the form of the data as displayed on the chart record, however many of the parameters that influence space communications can be gleaned from the data through the application of ray optics analysis, which then permits the use of Snell's law and the Appleton Hartree formula. A list of these parameters in addition to total electron content (TEC) are:

- 1) Changes in electron density, assuming height
- 2) slab thickness, assuming height
- 3) a continuous measurement of phase velocity
- 4) a continuous measurement of rate of change of TEC
- 5) a continuous measurement of refractive index
- 6) a continuous measurement of angle of arrival

A simple analysis can be performed on the recorded data on those sections where the chart record clearly indicates that the phase is shifting in accordance with a linear motion normal to the rays i.e. the 40° cycles follow the square law spacing mentioned earlier. There are generally several such sections to be found each day.

Ray optics analysis is valid if the following conditions are met: (1) the incident angle  $\phi_i$  is sufficiently large; (2) the medium is lossless; (3) the phase is measured at a distance sufficiently far from the inhomogeneous medium; (4) the media vary slowly compared to a wave length (R. J. Papa, private communication). These conditions exist for the data presented.

The first condition exists because gradients normal to the ray path caused by the TID are considered to be the dominant influence on the R.F. ray; therefore the incident angle  $\phi_i$  is measured from a line normal to the gradient. Figure 3 shows that  $\phi_i$  is always very large going to  $90^\circ$  at both the crest and trough of the TID. Since total reflection occurs in all dielectrics at the grazing incident angle ( $90^\circ$ ) the principal of reversibility (Jenkins and White, 1937) can be used to explain the phase reversal at both the crest and trough. The principal of reversibility states that whenever a ray is totally reflected a phase change of  $180^\circ$  occurs; also if the phase reversal does not take place when the wave passes from the lower to the higher refractive index, it will occur when the wave passes from the higher to the lower refractive index. This explains through ray optics the phase reversals appearing on the chart records at both the TID crest and trough. Thus ray optics theory provides the same answer given by the phase doppler process which shows the frequency or phase to be increasing when range of the R.F. source is decreasing and decreasing when the range is increasing with a phase reversal at or near the point of closest approach. Figure 9 depicts the geometry for the case where the satellite is directly overhead and the TID direction is normal to the R.F. ray.

$r$  = range to TID point of highest electron density

$vt$  = ray separation distance for  $n\lambda$

$n\lambda$  = number of wavelength phase change from crest or trough to max. phase velocity

Solving the geometry yields some important relationships:

$$r = \frac{(vt)^2}{2n\lambda}$$

$vt = \sqrt{2n\lambda r}$  This is recognized as the Fresnel formula when  $n = 1$  and states that the ray separation or closing must have travelled  $vt$  in order to change the phase  $360^\circ$  at the distance  $r$ .

If the incident angle  $\phi_i$  is measured from the path  $vt$ , a line normal to the TID gradient, the relationship  $vt/r = \cos \phi_i$  is important, because it accommodates the introduction of an equation derived from Snell's law,  $\cos \phi_i = f_n/f$  where  $f_n$  = plasma frequency and  $f$  = the propagation frequency. From the Appleton-Hartree equation:  $\mu^2 = 1 - 1 - (\frac{f_n}{f})^2 = 1 - K \frac{N}{f^2}$  where  $\mu$  = the refractive index  $K = (e^2/4\pi^2\epsilon_0 m) \cdot 80.6$ ,  $f$  is in Hz,  $N$  = number of electrons/m<sup>3</sup> at highest density point. Combining these equations gives:

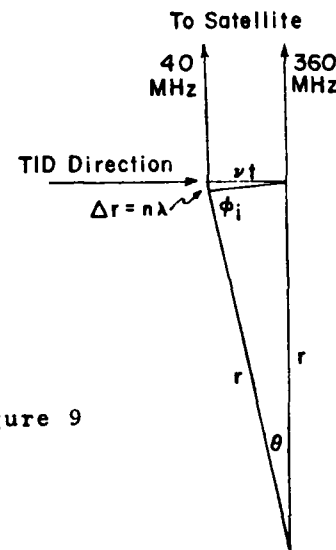


Figure 9

$$fN = \sqrt{80.6N}$$

$$\cos \phi_1 = \sqrt{\frac{80.6N}{f}} = \frac{v_1}{r} = \frac{2\pi\lambda}{vt} = \sin \theta$$

$$r = \frac{2\pi\lambda f^2}{80.6N} \text{ or } N = \frac{\pi\lambda f^2}{40.3r}$$

The last expression states that if the range to the point of highest electron density is known the change in density caused by the TID can be calculated. However it must be remembered that the equation represents conditions when the 40 and 360 MHz rays are separating at a linear rate, and it is only during the periods when the chart records show this that the analysis can be performed.

To ascertain the TID velocity 3 spaced differential phase sites could be established. The TID velocity would be calculated by making appropriate use of the time difference of the phase reversals at the 3 sites. As stated earlier these are the times when the angular refraction has been reduced to zero, thus the measurements provide accurate information regarding the TID crest or trough position, speed and direction.

Range ( $r$ ) to the area of maximum density can be measured if phase data as a function of relative TID position among the 3 sites is separated from phase data caused by ionospheric refraction. This can be accomplished using interferometer analysis on the higher frequency (360 MHz) by knowing the various distances among the 3 sites. However this is the subject for a later report, should the expanded program materialize.

Analysis of the data shows the tremendous influence a TID has over the ionospheric refraction of the lower UHF signals. In minutes it can reduce to zero the rate of change of electron content and temporarily reverse the diurnal refractive process caused by the sun. The reason for this is the dominance of the TID gradients normal to the ray path giving rise to large incident angles (including grazing) as opposed to the normal less disturbed vertical gradients with incident angles that are much more acute. This is in accordance with Snell's law, the more oblique the angle, the lower the plasma frequency resulting in greater refraction.

If one accepts the foregoing analysis, one must ask the question, how can the ramps measure the electron density per  $\text{m}^3$ , and at the same time, measure the electron content in a square meter column between the earth and the satellite? The answer

is that during TID they can't, because the formula for electron content is invalid where horizontal gradients are present. This is demonstrated in the following exercise.

Shortly before the ATS-6 satellite disappeared over the horizon, a 40 MHz polarimeter output was fed on to an adjacent pen recorder channel for comparison with the differential phase data (Figure 10). During this 9 day period there were some interesting revelations. The ratio of polarimeter ramps to differential phase ramps varied during the day. Since both were presumed to be a measure of the electron content in a square meter column between the satellite and the receiver on the ground, except for a small difference caused by the plasmasphere, it was expected that this ratio would be nearly constant. This proved to be a false assumption. The two measured extremes are 7 to 1 and 4 to 1. Shown in the figure is a ratio of 4.5  $\Delta\phi$  ramps to 1 polarimeter ramp and a ratio of 7 to 1 at an earlier time.

In terms of electron content the formula for the differential phase is:  $\Delta\phi = \frac{134 \times 10^7}{40 \text{ MHz}} \left( \frac{m^2 - 1}{m^2} \right) \text{ REC}$  where  $\Delta\phi$  = number of  $360^\circ$  phase shifted cycles between the low frequency and the high frequency and  $m = 360 \text{ MHz}/40 \text{ MHz}$ . The ramps displayed on the chart record have been divided down and represent  $1280^\circ$  of differential phase making one ramp equal to  $1.07 \times 10^{15} \text{ e/m}^2 \text{ col.}$

The formula for converting the polarimeter measurements to electron content is  $N_e \cdot \frac{(K/I^2) H \cos \theta}{40 \text{ MHz}}$  and one ramp equals  $3.7 \times 10^{15} \text{ e/m}^2$  column. The difference between the two measurements is important. The differential phase system measures the electron content in the total path (the ionosphere plus the plasmasphere) whereas the polarimeter data is a measure of the electron content only to the range still influenced by the earth's magnetic field. Thus where the ramp ratio is 4 to 1 the change in electron content measures  $4.28 \times 10^{15} \text{ e/m}^2$  column in the differential phase system for each  $3.7 \times 10^{15} \text{ e/m}^2$  column change in the polarimeter system. This leaves a change of  $.58 \times 10^{15} \text{ e/m}^2$  in the  $\text{m}^2$  column between the magnetic field and the satellite, which seems to be high but perhaps reasonable. However when the ratio becomes 7 to 1, it represents, in terms of electron content,  $7.4 \times 10^{15} \text{ e/m}^2$  to  $3.7 \times 10^{15} \text{ e/m}^2$  which states that one half of the electron change in the  $\text{m}^2$  column is in space beyond the influence of the magnetic field. This is unrealistic and requires another explanation for the inconsistency in the ramp ratio.

The reason for the inconsistency became apparent when the TID records were given closer inspection. Figure 11 is a 2 hour graph of the differential phase, polarimeter ramp ratio vs. time. Each low point corresponds with the point of zero angular refraction where the phase reverses direction and the electron diffusion is greatest (Figure 10). The high points coincide with periods of highest phase velocity (maximum angular

refraction). This gives convincing evidence that the presence of the TID is responsible for the changing ratio. It is inconceivable to think that the TID could double the influence of the magnetic field and unlikely that the TID would encounter sufficient plasmasphere electrons to produce twice the refraction. Therefore the conclusion drawn from the above exercise is that the differential phase formula for calculating electron content is not valid in the presence of TID, because they produce horizontal gradients that dominate the physical interactions, thus the angular refraction is better represented by the derived formula for electron density.

#### Additional Causes of Discrepancies in the Faraday/ $\Delta\phi$ Ratios

Smith (1970) has noted a diurnal variation in the ratio of Faraday rotation  $\Omega$  to electron content I of up to 30% at Puerto Rico. Kersley and Sawbrook (1971) report similar discrepancies in Great Britain. Davies et al (1975) are in close agreement with ATS-6 phase modulation and Faraday measurements at Boulder showing a 35% diurnal discrepancy. They suggest that the changing  $\Omega/I$  ratio may be due to the diurnal variation in the effective height of the ionosphere, the 35% representing a change from 580 km to 1200 km.

The Hamilton records were inspected for a changing diurnal  $\Omega/I$  ratio, but none was found in the 6 available June records. However it is apparent in the January 12 TEC profile comparisons (Figure 8) that in the early morning hours from 0000 to 0500 LT the phase is increasing and decreasing much faster than the Faraday rotation, showing values that indicate about 30% of the electron content is in the plasmasphere at that time. This would certainly show a much lower  $\Omega/I$  ratio and indicates a greater effective height during this period agreeing with the reports by Davies et al.

All other varying  $\Omega/I$  ratios were scattered through the records and were present as reported above only during periods of apparent horizontal gradients, except for a long term changing average ratio caused by the lowering of the elevation angle as the ATS-6 satellite moved towards the horizon (Figure 12 and Figure 13). Inspection of the TEC equations for both systems shows that the changing ratio conforms with theory, demonstrating that only the number of polarimeter ramps is related to the magnetic field or more precisely to the cos of the angle between the magnetic field and the ray path. This exercise also serves to demonstrate the validity of the overall equipment design and the field measurements.

#### Equivalent Slab Thickness

Since the form of the phase data during TID is consistent with the formula developed for calculating electron density,

calculation of equivalent slab thickness is also possible if polarimeter data is available to measure electron content.

Dividing the electron content contained in the TID wave from the trough to the crest (as measured by the polarimeter) by the electron density for the same period (measured by the  $\Delta\phi$  method) yields the slab thickness. The ratio, using the parameters given earlier, reduces to:

$$\frac{(\text{no. of } 180^\circ \text{ polarimeter ramps}) \times (3.5 \text{ h})}{(\text{no. of } 1280^\circ \text{ differential phase ramps}) \times (\text{sec } z)},$$

where  $h$  is the height and  $z$  is the zenith angle. It is suggested that this ratio is the same as the ratio of TEC to maximum electron density at the time of the measurement. This formula can be used to assign values to Figure 11, which now becomes a very graphic portrayal of the slab thickness profile showing the tremendous influence a TID has on the ionosphere. Using 400 km for  $h$  and 1.54 for sec  $z$ , it gives values of slab thickness of 126 km to 202 km. These values are practically the same as the ranges reported by Tyagi and Samayajulu (1966) using the ratio TEC/max electron density. They reported a range of values from 125 to 200 km at Delhi. However values reported by Klobuchar and Allen (1970) with combined data from two locations are higher. Their analysis on data taken for 18 months in 1967 - 1968 yield a wide range of values with an annual mean value of 261 km. They do caution that the values suffer somewhat from the fact that the TEC data were taken along the oblique path to the ATS-3 satellite from Hamilton, Massachusetts, while the  $N_{\max}$  values were derived from vertical incidence ionosondes from Fort Belvoir, Virginia and Wallops Island, Virginia.

It appears that more comparison data will be required to determine the validity of the hypothesis that the change in the TID electron content divided by the change in density is equivalent to TEC/ $N_{\max}$ . The following exercise suggests that theoretically they are the same.

In the Klobuchar, Allen analysis they showed that the propagation delay  $\Delta r = 40.3/f^2 \int N dl$  where  $\int N dl = \text{TEC in el/m}^2$  slant column.

Referring back to the formula for electron density derived here for the TID it is shown that  $N = n\lambda f^2/40.3r$  where  $N = \text{electron density} = \text{el/m}^3$ ;  $n\lambda = \Delta r$ , thus  $\Delta r = 40.3rN/f^2$ .

Since there is only one  $\Delta r$  representing the delay in propagation from crest to trough in the TID irrespective of the cause, the 2 formulas for  $\Delta r$  can be equated which yields  $r = \int N dl/N \text{ m}^3$ . Thus it is shown that such a relationship produces the formula for the equivalent slab thickness, however in this case the integration is only during the TID interval from crest to trough, and  $N$  represents the change in

electron density for the same period. This is the equivalent  $m^2$  column of length  $r$  with a uniform density of electrons that is either compressed into or diffused away from the equivalent  $m^2$  column representing the total electron content with a uniform maximum density. The question is, are they really the same length? The analysis shows that at least they are in the same ball park.

#### Electron Content in the Plasmasphere

Comparing Figure 10 with Figure 11 shows that the low points coincide with times of maximum diffusion and zero angular refraction. The indication is that all gradients normal to the R.F. ray have momentarily disappeared, so these are the periods when the differential phase formula for TEC is valid. Thus if comparisons are made between the TEC diurnal profiles of both systems to measure the electron content in the space between the ionosphere influenced by the earth's magnetic field and the satellite, the TID troughs would be accurate positions to make such measurements. As illustrated in the figure the trough positions produce the more stable and consistent values indicating that the averaged net TEC beyond the magnetic field remains quite constant even though ionospheric perturbations are present during this period.

#### A Sunrise Phenomenon

Davies et al (1975) using Faraday and modulation phase data from an ATS-6 experiment have illustrated an interesting sunrise phenomenon. They have shown that the start of the Faraday TEC increase precedes the start of the modulation phase TEC increase, varying from less than one minute to 15 minutes at sunrise. The modulation phase measurement like the differential phase measurement reported here measures the TEC all the way to the satellite.

They attributed the time difference to a lowering of the effective height of the ionosphere before the total content starts to increase.

Our records were inspected for this sunrise phenomenon. There were six available records with simultaneous recordings of both phase and Faraday. The delays varied from a few seconds to two minutes.

Comparison of the ATS-6 differential phase profile with the ATS-3 Faraday profile for January 12, 1975 (Figure 10) shows that a large portion of the electron content was in the plasmasphere for several hours before sunrise reaching a peak of approximately 30% of the total at 0315 LT. The data also

indicates a fairly sharp demarcation between the ionosphere and the plasmasphere during this period. It's reasonable to believe that the excess electrons were still flowing into the F region at sunrise thereby lowering the effective height of the ionosphere before new production had actually started as suggested by Davies et al.

In both the modulation phase measurements and the differential phase measurements  $d\phi/dt = 0$  occurs when the production rate Q equals the loss rate L. At Boulder an example was given showing L to be  $-2.16 \times 10^{12} m^{-2} sec^{-1}$  at the Faraday morning reversal. In accordance with the above statement at  $d\phi/dt = 0$ ,  $Q = 2.16 \times 10^{12} m^{-2} sec^{-1}$  just after sunrise.

Two Hamilton records were analyzed for the electron production rate. The analysis yielded values of  $Q = 2.19$  and  $Q = 2.21 \times 10^{12} m^{-2} sec^{-1}$  agreeing favorably with the Boulder measurement.

#### Phase Velocity

The lower channel in Figure 10 is the analog output of a circuit counting the number of  $40^\circ$  cycles per second. Therefore it is a measure of the phase velocity. Note that if every other peak is inverted, the trace approximates a slow sine wave  $90^\circ$  out of phase with the trace of the differential phase data, showing it to be the first derivative of the phase analog (the summation of the phase ramps). When it was first recorded, it was calibrated to read the rate of change of electron content per  $m^2$  column between the earth and satellite. However in view of the new interpretation of the phase data during the periods of TID gradients, it is more accurate to calibrate the data to read rate of change of electron density (electrons per  $m^3$ ) at highest density region.

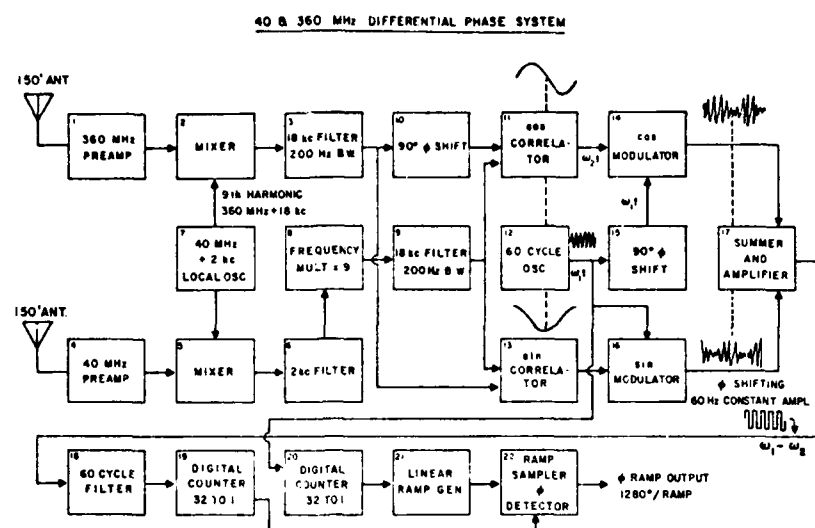


FIG. 1

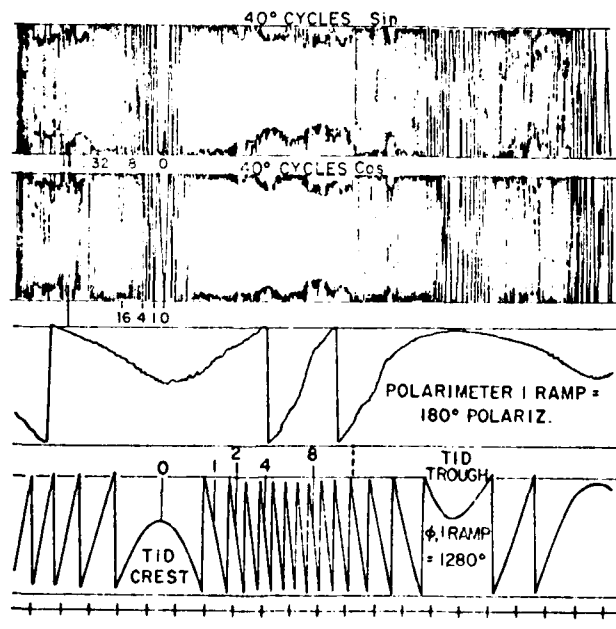


FIG. 2

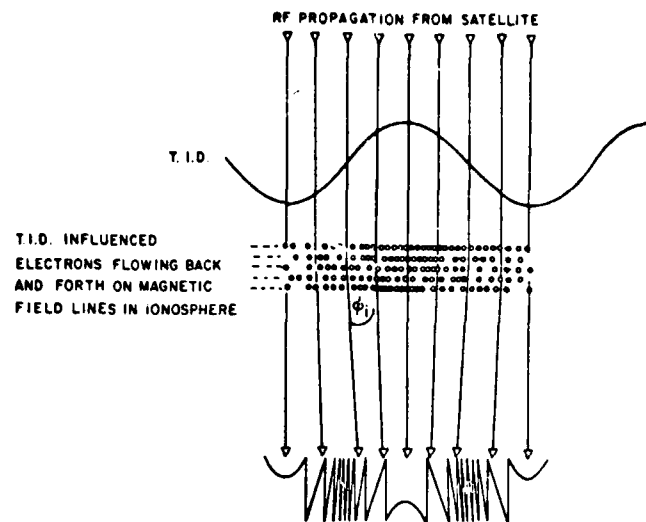


FIG. 3 INFLUENCE OF TRAVELLING IONOSPHERIC DISTURBANCE ON ELECTRON CONTENT AND R.F. PROPAGATION USING GEOMETRY AT EQUATOR FOR SIMPLIFICATION

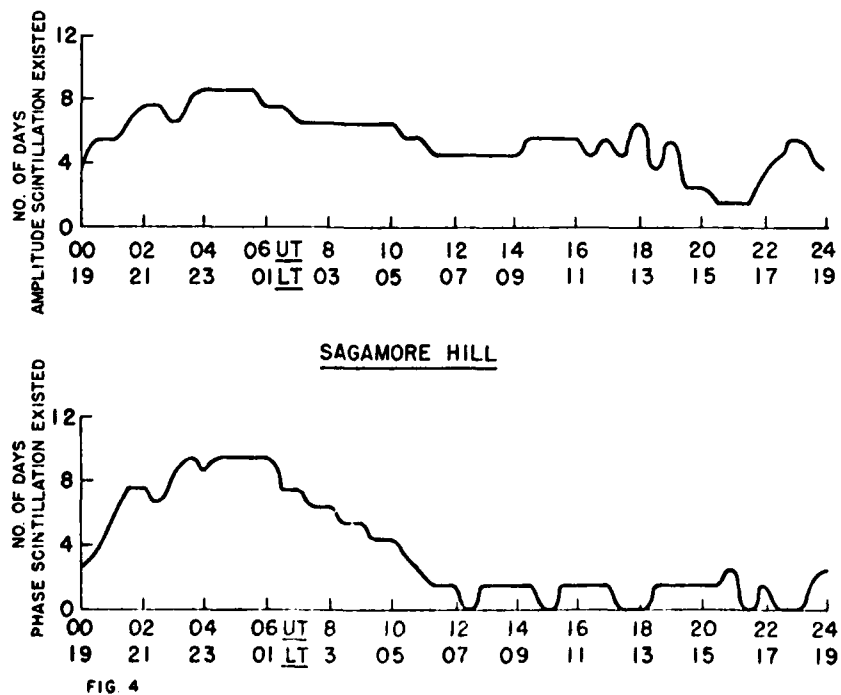


FIG. 4

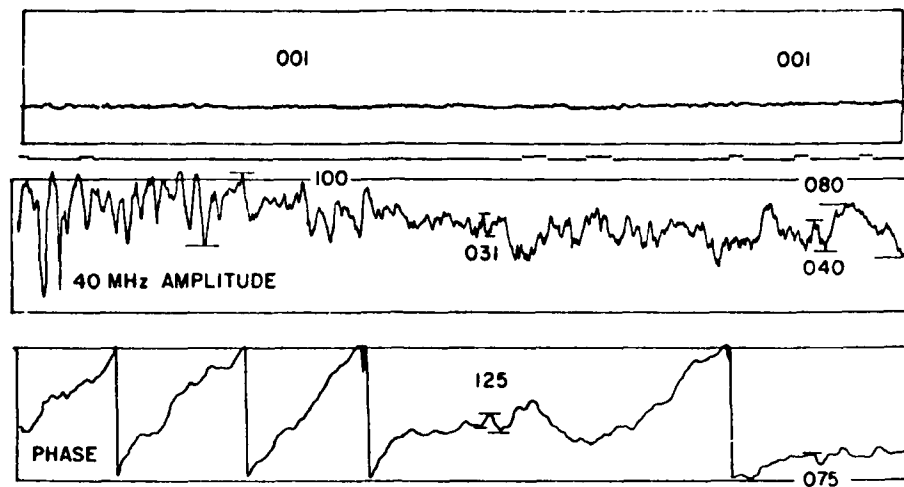


FIG. 5 AMPLITUDE AND PHASE SCINTILLATION

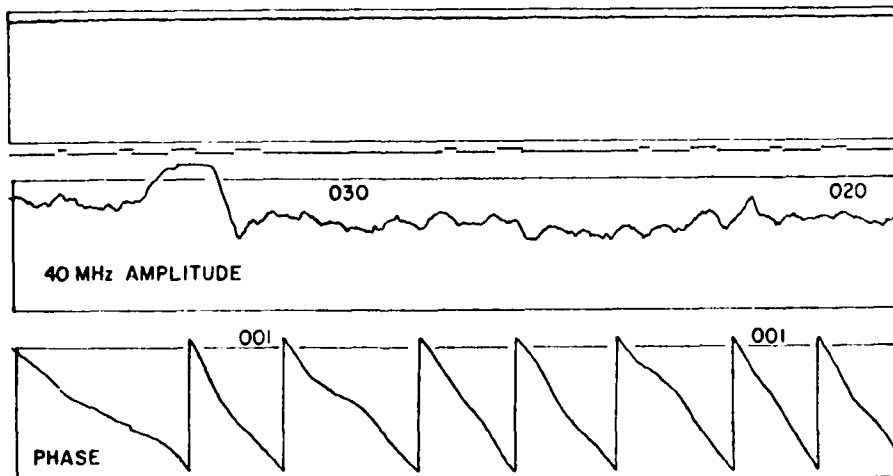


FIG. 6 AMPLITUDE SCINTILLATION WITHOUT PHASE SCINTILLATION

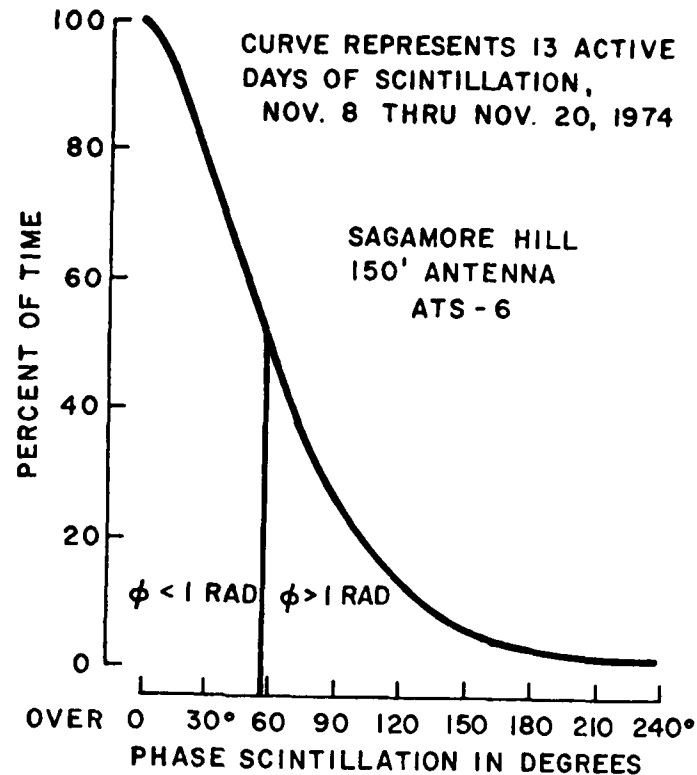


FIG. 7

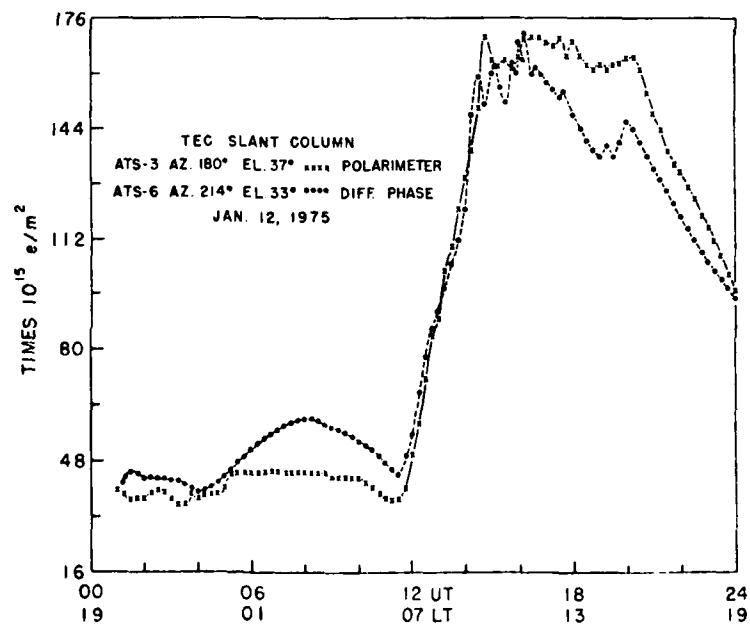


FIG. 8

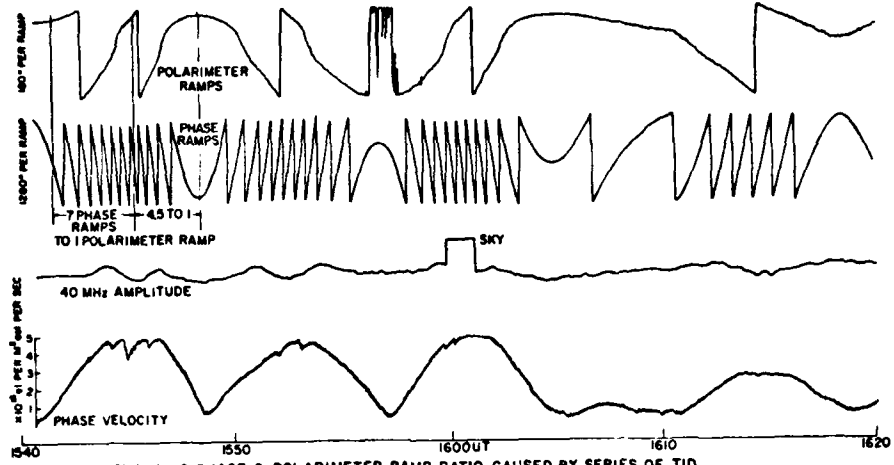


FIG. 10 CHANGING PHASE & POLARIMETER RAMP RATIO CAUSED BY SERIES OF TID

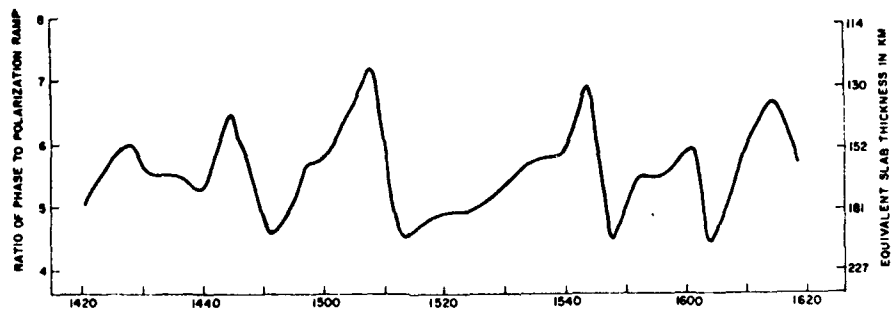


FIG. 11 CHANGING PHASE & POLARIMETER RAMP RATIO CAUSED BY TID, SHOWING INFLUENCE ON SLAB THICKNESS ALSO

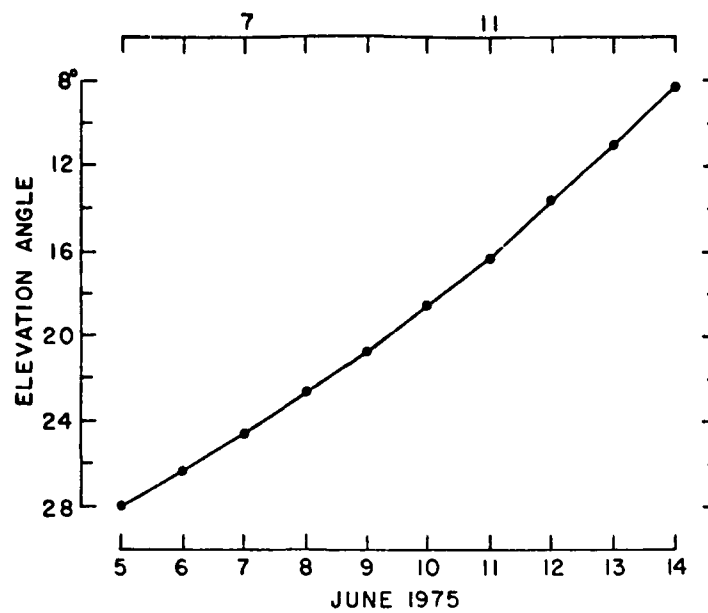


FIG. 12 CHANGING ELEVATION ANGLE AS ATS-6 MOVED TOWARDS HORIZON MEASURED ON 150' ANTENNA

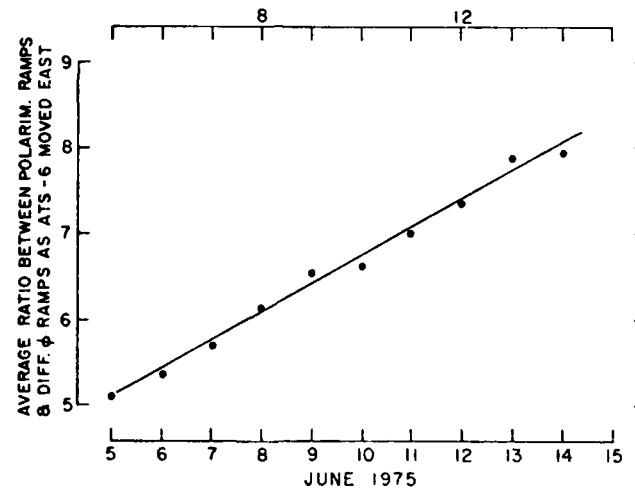


FIG. 13 THIS CHANGING RATIO CONFORMS WITH THEORY  
 $\Omega = \left( K_{f_2} \right) \int N_e H \cos \theta \, ds$  WHERE  $\Omega$  = NO. POLARIM.  
 RAMPS,  $H$  = MAGNETIC FIELD,  $\theta$  = ANGLE BETWEEN  
 $H$  AND RAY PATH.  $\theta$  WAS INCREASING, THUS  $\cos \theta$   
 WAS DECREASING. THE NUMBER OF DIFF. PHASE  
 RAMPS IS INDEPENDENT OF THE MAGNETIC FIELD.

## Review of Ionospheric Time Delay Limitations to Ranging Systems

John A. Klobuchar  
Air Force Geophysics Laboratory,  
Air Force Systems Command  
Hanscom AFB, MA 01731

### Abstract

The requirements of several present or planned satellite and astronomical distance-ranging systems include as a major source of error the time delay of the earth's ionosphere. One of these systems is an advanced navigation system which will use L band radio waves from high orbit satellites for positioning accuracy to within a few feet anywhere on the earth's surface. The ionospheric time delay and its rate of change will be important limitations for some users of this system. Another advanced engineering requirement involves the transfer of precise time via satellite, which will be also limited by ionospheric time delay. Another example is in the radar systems used for satellite orbit determination which sometimes encounter ionospheric range errors at UHF up to 1 kilometer. Still another example is in the astronomical technique of Very Long Baseline Interferometry, VLBI, in which the separation of two widely spaced points on the earth's surface is precisely measured. The differential time delay of the ionosphere, along the two stations' lines of sight, limits the measurement accuracy.

The current state of ionospheric time delay prediction models can provide corrections for ionospheric time delay up to 70-80% r.m.s., but with a relatively large computational effort. The point of minimal future ionospheric time delay model improvement, without some new external input parameter, has probably been reached. Correspondingly better time delay corrections can be made to an engineering system if a near-real-time measurement of an F2 region parameter, either TEC or f0F2, is available from a nearby location. Engineering systems designed to make use of two widely spaced frequencies can nearly eliminate the effects of ionospheric time delay.

### Introduction

With the ever increasing state of the art of navigation, timing and positioning systems, the effects of the earth's ionosphere have become a greater potential source of error in advanced system designs. Fortunately, the research in ionospheric Total Electron Content (TEC) begun in the late 1950's in a modest

way, by the measurement of Faraday polarization twist of lunar reflected radio waves, and continuing since 1964 with similar measurements from VHF radio waves transmitted from geostationary satellites, has reached a certain maturity so that sufficient data are available over several regions of the world to give advanced satellite ranging system design engineers a good numerical representation of the magnitude of the expected ionospheric time delay. In this paper the limitations to various types of ranging systems by ionospheric time delay will be reviewed and suggestions for correction schemes for this limitation will be made.

#### Transit - An Early Satellite Navigation System

A satellite navigation system begun in the 1960's and still in use is the U. S. Navy Navigation Satellite System, NNSS or TRANSIT, which employs a pair of coherent radio signals near 150 and 400 MHz transmitted from a satellite in an approximate 1000 km high polar orbit to allow a user anywhere on the earth's surface to determine his position to within a few tens of meters. The disadvantages of the system include the several minute time period required to determine a position, which limits its use to relatively slow moving vehicles and its limited time availability. Even with six satellites in spaced orbits, due to their relatively low orbital heights there are occasional long periods when no satellite is above the horizon, especially at the equatorial latitudes.

Because of the relatively low frequencies used for this satellite navigation system the ionospheric time delay errors are large, and, if uncorrected, would give position errors of up to several kilometers. Fortunately, the designers of this system included a two-frequency capability to correct for the first order ionospheric rate of change error. In fact, use has been made of the coherent pair of frequencies transmitted from the TRANSIT satellites by ionospheric researchers to make measurements of ionospheric TEC. Because the ionosphere is a dispersive medium, that is, the time delay due to the ionosphere is proportional to  $1/f^2$ , the magnitude of the ionospheric time delay is 100 times greater at 150 MHz than at 1500 MHz. Thus, due to ionospheric limitations among other considerations, advanced ranging systems are being designed for frequencies above 1 GHz. An example of a high orbit satellite positioning system, to give continuous, worldwide coverage, even to users on high velocity vehicles is the NAVSTAR-Global Positioning System.

#### NAVSTAR-Global Positioning System

The NAVSTAR-GPS is an advanced, high orbit satellite positioning system designed to give precise position and velocity information on a global basis to users. It too will use two frequencies to enable corrections to be made for ionospheric time delay; but a less expensive, single frequency receiver will

be available for users who do not require the accuracy of the two frequency capability. For single frequency receivers the ionospheric time delay will contribute a worst case vertical range error of approximately 50 meters, in the equatorial anomaly region, but with an r.m.s. ionospheric range error over the whole earth of approximately five meters. For the single frequency receiver user class a simple algorithm has been developed to provide an approximate 50 percent average correction for ionospheric time delay. The reasons for the choice of a 50 percent correction algorithm will be discussed in a later section.

#### The ASTRO-DABS Navigation System

A commercial satellite navigation system currently under study by the U. S. Department of Transportation will use a single frequency L band signal from satellites at geostationary heights for precise positioning of commercial aircraft. Because the ionospheric error will be greater than the required system positional accuracy a network of real time ground based monitoring stations has been proposed to measure and correct for ionospheric time delay effects. A major question concerns the number of necessary monitoring stations versus required TEC accuracy under worst case conditions. For instance, during a major magnetic storm, when TEC is more than twice its average value during the mid-afternoon maximum the required station spacing to accurately represent the large temporal and geographic TEC gradient over the entire continental United States may be unrealistically large. A study by Elrod (1975) concluded that a network of 21 ionospheric calibration stations located throughout the continental United States, each viewing six satellites for a total of 126 separate ionospheric time delay calibrations, was needed to satisfy the requirement that the uncorrected ionospheric time delay error not exceed 14 nsec on a worst case basis. An interesting corollary to this calibration system is that, if such a monitoring network is ever built for the proposed ASTRO-DABS system, it will represent a significant resource of new ionospheric data on a scale not previously available, and will enable detailed studies of ionospheric gradients during magnetically disturbed periods to be made. The system ionospheric monitoring network itself will be a significant new ionospheric experimental research tool.

#### Intercontinental Precise Time Transfer

The transfer of precise timing information from widely separated frequency standards has been undertaken by physically moving a single, portable clock standard among various fixed locations to establish correlations among the various world-wide time standards. Attempts have also been made to transfer precise timing information over large distances by means of satellite transponders (Hanson and Hamilton, 1974). The ionosphere is potentially a large error source in such attempts at time transfer although at present the attempts to transfer time in this manner are several orders of magnitude away from the present day clock precision and not yet at the point where ionospheric limitations have been reached.

### Very Long Baseline Interferometry

The technique of precise location determination by means of radio interferometry of astromical point sources is now well established. This technique is a potential means of measuring continental drift and relative motion across a known fault line in an earthquake zone. The differential ionospheric time delay at the two interferometer locations will give an error in positioning greater than the potential accuracy of the measurement. Various means of correcting for ionospheric time delay errors in VLBI measurements have been attempted. The method to be adopted in future experiments is to utilize two frequencies to actually measure the differential ionospheric time delay and subtract it from the experimental data to obtain a corrected position.

### Space Probe Orbit Determination

Deep space probes are tracked by measuring the frequency difference between an on-board precision oscillator and a similar oscillator on the ground. This geometric Doppler shift information is contaminated by the additional Doppler shift introduced by the rate of change of the electron content of the earth's ionosphere. Corrections are usually made for the ionospheric contribution by making measurements of Faraday rotation of VHF signals transmitted from a geostationary satellite above the horizon where the deep space probe signals are being received and using the observed rates of change of ionospheric TEC to correct the received deep space probe data.

### Correction Techniques for Ionospheric Effects on Operational Systems

There are several methods of correcting for the time delay effects of the earth's ionosphere on operational ranging systems. Fortunately the ionosphere is a dispersive medium so that, if the operational capability of utilizing two widely spaced frequencies is used, the effects of the ionospheric time retardation can be directly measured by the system and corrected for. This scheme is potentially the best method of making corrections for ionospheric effects as it uses exact system frequencies and makes measurements along the same ionospheric path as that on which the system operates. However, it may be very expensive to provide a second transmitted frequency sufficiently separated to allow a direct, accurate TEC measure to be made by the operational system.

Lacking the capability of a direct, two frequency measurement one may resort to a model, or a model updated with a nearby measurement of TEC, or with a nearby measurement of the density at the peak of the F2 region, N<sub>max</sub>, to correct for the time delay effects of the ionosphere. In all of these cases, however, the question is: How good is the correction as a function of difference in direction between the desired and the measured directions?

If the operational system cannot incorporate an ionospheric measurement technique because of the difficulty of covering a large geographic region with ionospheric sensors a model without updating may be used. Generally, the system is under a limitation of computer memory and computation time so that the best available models cannot be utilized to make this correction. A tradeoff between model capability and model difficulty is generally required. Model difficulty is defined here as the amount of computation time and memory required for each correction to be made.

As an example of a tradeoff between number of model coefficients and model accuracy, the case of the ionospheric time delay algorithm choice for the NAVSTAR-GPS is a good example. The system is a two frequency systems allowing those users who require the most accurate ionospheric time delay correction to utilize a two frequency receiver. However, for the single frequency system user, ionospheric time delay algorithm coefficients are transmitted down the satellite-user link and an algorithm designed for a 50 percent r.m.s. correction was constructed. The number of coefficients required to provide a state of the art 75 percent correction and the algorithm itself would have been much more difficult and would have required much more user computation time. With the limited single frequency user computation capability and the limitation on the number of coefficients allowed to be transmitted down the satellite to user link the 50 percent correction was decided upon. If a plot of model correctability versus difficulty is made the knee of the curve probably comes somewhere near 50 percent. A 99 percent correction for ionosphere is probably impossible to make; a 50 percent overall r.m.s. correction is relatively easy. The best state of the art models probably have an r.m.s. correction capability of from 70 to 80 percent and these require considerable computer resources.

### Conclusions

There are several different types of operational and planned systems which will have their accuracy affected by the time delay of the earth's ionosphere. With these many operational and proposed systems the requirements, and indeed, the capabilities of making some sort of correction for the ionospheric error differ. In each case there is a tradeoff between correction capability desired or required and difficulty in making the correction, whether it be real time measurements or models with no measurements. Fortunately the data taken over the past several years can be used to give the system design engineer an idea of the magnitude of the expected ionospheric error for his system and can contribute to models and techniques for error correction.

### References

Elrod, B.D., Correction for Ionospheric Propagation Delay in ASTRO-DABS - The Dual Frequency Calibration (DFC) Method, Mitre Technical Report MTR-6896, April, 1975.

Hanson, D.W. and W.F. Hamilton, Satellite Broadcasting of WWV Signals, IEEE Trans. on Aero. and Elect. Sys., Sept., 1974.

Space Variant Transfer Functions for the Characterization of  
Inhomogeneous Scattering Media

P.F.Checcacci, A.M.Scheggi

IROE/CNR, FIRENZE, ITALY

1. Introduction

The present communication is concerned with the definition of some transfer functions which can be applied to characterize any type of space variant propagation medium [1]. Assuming two reference surfaces limiting the medium, and an input field distribution, it is possible with such transfer functions to evaluate the field at the output surface in terms of elementary plane or spherical waves. In general the transfer functions are defined for linear and invariant media; however, while in the reality it is rather easy to fulfill the linearity condition, the same cannot be said for the invariance. The invariance of the medium would require that it remain constant over an infinite scale or at least over a scale very large with respect to the local wavelength. However by using a procedure analogous to that used by Zadeh and Bello [2,3] for time varying systems it is possible to define suitable transfer functions for space variant media.

2. Definition of the Different Transfer Functions

Let us now consider two parallel planes (Fig.1) and rectangular coordinate systems  $x_1, y_1$  for the input plane and  $x_2, y_2$  for the output plane limiting an inhomogeneous steady medium. A complex amplitude distribution at the input plane  $a_1(x_1, y_1)$  can be expanded in terms of Dirac functions

$$1) \quad a_1(x_1, y_1) = \iint_{-\infty}^{+\infty} a_1(x'_1, y'_1) \delta(x_1 - x'_1; y_1 - y'_1) dx'_1 dy'_1$$

The time dependence  $e^{i\omega t}$  will be omitted everywhere.

If with  $h(x_1, y_1; x_2, y_2)$  we denote the response of the medium that is the so called "Point source response" to an input  $\delta$ -function centered at  $x_1, y_1$  from expression 1), due to the linearity of the medium one gets

$$2) \quad a_2(x_2, y_2) = \iint_{-\infty}^{+\infty} a_1(x_1, y_1) h(x_1, y_1; x_2, y_2) dx_1 dy_1$$

which relates the complex amplitude distribution on the output plane to the input distribution  $a_1(x_1, y_1)$ . Hence the point source response  $h(x_1, y_1; x_2, y_2)$  characterizes any space variant

medium.

By performing the Fourier transform at each side of eq.2) and indicating with  $K(x_1, y_1; f_x, f_y)$  the Fourier angular spectrum of the point source response with respect to the coordinates  $x_2, y_2$  one has

$$3) A_2(f_x, f_y) = \iint_{-\infty}^{+\infty} a_1(x_1, y_1) K(x_1, y_1; f_x, f_y) dx_1 dy_1,$$

where

$$4) A_2(f_x, f_y) = \iint_{-\infty}^{+\infty} a_2(x_2, y_2) \exp [i2\pi(f_x x_2 + f_y y_2)] dx_2 dy_2$$

$f_x, f_y$  denote the spatial frequencies at the output plane, that is the  $x, y$  component of the wave vector of the generical scattered wave.

Analogously other transfer functions relating the input to the output field distributions can be defined either in the spatial frequency domain and/or in the space spatial-frequency domains.

For instance by writing the input function as the inverse transform of its spectrum  $A_1(l_x, l_y)$  ( $l_x, l_y$  represent the spatial frequency components at the input plane) one has

$$5) a_1(x_1, y_1) = \iint_{-\infty}^{+\infty} A_1(l_x, l_y) \exp [-i2\pi(l_x x_1 + l_y y_1)] dl_x dl_y$$

If now one indicates with  $H(l_x, l_y, x_2, y_2)$  the Fourier transform of the point source response with reference to the input coordinates  $x_1, y_1$  and substitutes eq.5) in eq.2) one obtains

$$6) a_2(x_2, y_2) = \iint_{-\infty}^{+\infty} A_1(l_x, l_y) H(l_x, l_y, x_2, y_2) dl_x dl_y$$

Finally by denoting with  $S(l_x, l_y, f_x, f_y)$  the Fourier spectrum with respect to the variable  $x_2, y_2$  of function  $H$  and by transforming each side of relation 6) one gets

$$7) A_2(f_x, f_y) = \iint_{-\infty}^{+\infty} A_1(l_x, l_y) S(l_x, l_y, f_x, f_y) dl_x dl_y$$

which is analogous to relation 2) in the spatial-frequency domain.  $S(l_x, l_y, f_x, f_y)$  is denoted as scattering function.

The above formalism can be visualized by showing that the defined functions, besides constituting an useful mathematical tool for solving propagation problems in particular media have a precise physical meaning (Fig.2). For instance eq.2) can be compared with the well known Huygens Fresnel formula and the function  $h$  which accounts for all the waves scattered by the medium can be thought as a generalization of the term  $\exp[-i(kR - \frac{t}{4})]/R$ , representing the spherical waves emitted by each elementary point source. Function  $K$  represents the angular spectrum scattered by the medium when illuminated by a point source while function  $H$  represents the complex amplitude distribution at the output plane produced by the scattering due to plane wave illumination of the medium. Finally function  $S$  yields the scattered angular spectrum due to plane wave illumination. Consequently these functions can represent all the possible experimental situations.

### 3. Practical Applications

#### 3.1 - Input plane wave and directive receiving antenna

Once the propagation medium has been characterized by means of one of the above functions it is possible to foresee the performance of the system constituted by a given source, the propagation medium and a given receiving antenna<sup>(+)</sup>.

Let us consider for example an impinging plane wave of complex amplitude  $A(l_x)$ , being  $l_x$  the x-component of its wave vector. If  $g(f_x)$  indicates the amplitude output of the receiving antenna illuminated by an unitary amplitude plane wave of spatial frequency  $f_x$ , the antenna output amplitude due to the scattered waves is

$$8) \quad u(l_x) = A(l_x) \int_{-1}^1 g(f_x) S(l_x, f_x) df_x$$

Recalling that the directivity of the antenna in free space is

$$9) \quad D = \left[ \frac{g(f_x)}{g_{\max}(f_x)} \right] \left[ \frac{g(f_x)}{g_{\max}(f_x)} \right]^*$$

<sup>(+)</sup> For the sake of simplicity we will limit to the bidimensional case; the extension to the three-dimensional case is straight-forward.

where  $g_{\max}$  indicates the maximum value of  $g$  when  $f_x$  varies, the new directivity of the antenna in the presence of the medium results

$$10) \quad D' = \left[ \frac{u(l_x)}{u_{\max}(l_x)} \right] \left[ \frac{u(l_x)}{u_{\max}(l_x)} \right]^*$$

Obviously with an analogous procedure and by using the appropriate characterizing function, similar results can be obtained for the point source.

The above considerations apply to an inhomogeneous but steady medium. Consequently it can be utilized for evaluating the performance of an antenna looking through a fixed scattering structure (Radome, window, natural obstacles). On the contrary when considering an inhomogeneous turbulent medium like the ionosphere it is necessary to characterize the medium on a statistical basis. We will assume that the medium varies in time so slowly that the output waves are still monochromatic. The mean value of the antenna output in the case precedingly considered (see eq.8) becomes

$$\langle u(l_x) \rangle = A(l_x) \int_{-1}^1 g(f_x) \langle S(l_x, f_x) \rangle df_x$$

That is the mean value of the output signal results defined by the mean value of the function  $S$  characterizing the medium. Analogously from relation 10) it is possible to derive the mean value of the antenna directivity in the presence of the turbulent medium.

Another quantity of interest for communication purposes is the variance of  $u(l_x)$

$$11) \quad \sigma_u^2 = \langle \Delta u^2(l_x) \rangle = \langle u(l_x)^2 \rangle - \langle u(l_x) \rangle^2$$

By assuming

$$12) \quad S(l_x, f_x) = \langle S(l_x, f_x) \rangle \left[ 1 + \frac{\Delta S(l_x, f_x)}{\langle S(l_x, f_x) \rangle} \right]$$

one obtains

$$13) \quad \sigma_u^2 = A^2(l_x) \iint_{-1}^1 g(f_x) g(f'_x) \langle \Delta S(l_x, f_x) \Delta S^*(l_x, f'_x) \rangle df_x df'_x$$

If one puts

$$14) f_x - f'_x = \tilde{\tau}$$

eq. 13) becomes  $\int_{-1}^1 f_x^{+1}$

$$15) \sigma_u^2 = A^2(l_x) \int_{-1}^1 g(f_x) g^*(f_x - \tilde{\tau}) \langle \Delta S(l_x, f_x) \Delta S^*(l_x, f_x - \tilde{\tau}) \rangle df_x d\tilde{\tau}$$

Under the hypothesis of an isotropic scattering eq. 15) can be written as  $\int_{-1}^1$

$$16) \sigma_u^2 = A^2(l_x) \int_{-1}^1 g(f_x) g^*(f_x - \tilde{\tau}) R(\tilde{\tau}) df_x d\tilde{\tau}$$

where  $R(\tilde{\tau})$  represents the correlation of the  $S$  function fluctuations which due to the above hypothesis is independent of  $f_x$ .

By putting  $\int_{-1}^1$

$$\int_{-1}^1 g(f_x) g^*(f_x - \tilde{\tau}) df_x = G(\tilde{\tau})$$

one finally gets  $\int_{-1}^1$

$$17) \sigma_u^2 = A^2(l_x) \int_{-1}^1 G(\tilde{\tau}) R(\tilde{\tau}) d\tilde{\tau}$$

This expression along with expression 12) can be used either for predicting the performance of an antenna looking a turbulent medium or for characterizing the medium properties having at disposal an antenna of known characteristics.

### 3.2 - Input spherical wave and receiving aperture

Let us consider a point source centered at  $x_1$  of complex amplitude  $a(x_1)$  and a receiving aperture of width  $D$  centered at  $x_2$  (with  $x_2 = x_1$ ). Analogously to the previous case the antenna output  $u(x_1)$  resulting by the summation of all the contribution across the aperture is

$$18) u(x_1) = \int_{-D/2}^{D/2} a(x_1) h(x_1, x_2) dx_2$$

Its mean value in the presence of a turbulent ionosphere is

$$19) \langle u(x_1) \rangle = \int_{-D/2}^{D/2} a(x_1) \langle h(x_1, x_2) \rangle dx_2$$

and the variance

$$20) \sigma_u^2 = \langle \Delta u(x_1) \Delta u^*(x_1) \rangle = a^2(x_1) \iint_{-D/2}^{D/2} \langle \Delta h(x_1, x_2) \Delta h^*(x_1, x'_2) \rangle dx_2 dx'_2$$

By putting  $x_2 - x'_2 = \xi$ , one has

$$21) \sigma_u^2 = a^2(x_1) \iint_{-D/2}^{D/2} \langle \Delta h(x_1, x_2) \Delta h(x_1, x_2 - \xi) \rangle d\xi dx_2$$

Under the hypothesis that the averaged expression be only function of  $\xi$ , eq. 21) becomes

$$22) \sigma_u^2 = a^2(x_1) D \int_{-D/2}^{D/2} R(\xi) d\xi$$

with  $R(\xi) = \langle \Delta h(x_1, x_2) \Delta h^*(x_1, x_1 - \xi) \rangle$

In both cases of directive receiving antenna and receiving aperture, the hypothesis that the functions  $R(\tilde{f})$  and  $R(\tilde{\gamma})$  be independent of  $f_x$  or  $x_2$  respectively is not so stringent as it could appear. In fact it is sufficient that  $R(\tilde{\gamma})$  be independent of  $f_x$  in the interval where  $G(\tilde{\gamma}) \neq 0$  while  $R(\xi)$  must be independent of  $x_2$  only in the interval  $-D/2 + D/2$ .

The application of the above formalism requires the measurement of quantities such as  $\langle S \rangle$ ,  $\langle h \rangle$ , etc. and of their autocorrelations  $R(\tilde{\gamma})$ ,  $R(\xi)$ . On the other hand the relationships found among these quantities give also an indication on the type of measurement. For instance by using an highly directive antenna pointed in a direction  $\bar{f}_x$ , for which  $g(f_x) = g(\bar{f}_x) \delta(f_x - \bar{f}_x)$  and substituting this expression in eq. 8) one obtains

$$23) S(l_x, \bar{f}_x) = \frac{u(l_x)}{A(l_x)g(\bar{f}_x)}$$

and hence

$$24) \langle S(l_x, \bar{f}_x) \rangle = \frac{\langle u(l_x) \rangle}{A(l_x)g(\bar{f}_x)}$$

With two identical antennas of the same type pointed in the directions  $f_x$  and  $f_x - \tilde{\gamma}$  and cross-correlating the fluctuations of the outputs  $u_1(l_x)$  and  $u_2(l_x)$  one obtains

$$25) \quad R(\tilde{\tau}) = \frac{\langle \Delta u_1(l_x) \Delta u_2^*(l_x) \rangle}{A^2(l_x) g(\bar{f}_x) g(\bar{f}_x - \tilde{\tau})}$$

The necessity of highly directive antenna makes this method usable only at very high frequencies. Alternatively by using a point receiving antenna from eq. 18) one can get  $h(x_1, x_2)$  and its mean value. By using two point receiving antennas spaced by  $\Psi$ , and following the same above procedure one obtains  $R(\Psi)$ . This is a measurement commonly performed with beacon satellites.

#### 4. Conclusions

The different transfer functions outlined in the present paper, whose formalism is well known for application in different fields have the main purpose of characterizing a varying propagation medium such as the ionosphere, for engineering applications.

Obviously such transfer functions, due their nature of input-output relations do not give any a priori information on the physical structure of the medium. However under certain hypotheses on the medium structure these functions can be utilized for solving the inverse problem.

The given definitions indicate also the procedures to be followed for the determination of the different transfer function in the media to be characterized. Apart from a suitable normalization these procedures result as measurements commonly made with beacon satellites.

#### Bibliography

- [1] P.F.CHECCACCI, M.NEGRIN, A.M.SCHEGGI: Analisi di Fourier di sistemi spazialmente varianti - Report CM-R.150-15.7 IROE-CNR (September 1972).
- [2] L.A.ZADEH: Frequency Analysis of Variable Networks - Proc.IRE, 38, 291 (1950).
- [3] P.A.BELLO: Characterization of Randomly Time-Variant Linear Channels - IEEE Trans. on Comm. Systems, CS-11, 360 (1963).

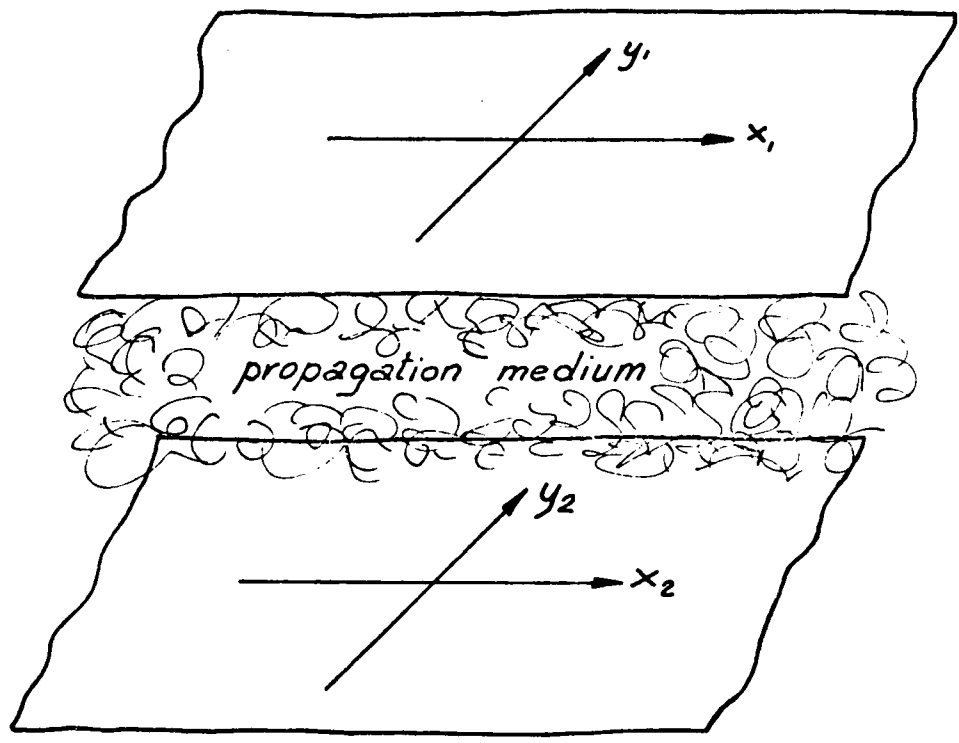


Fig.1 - Reference input and output planes

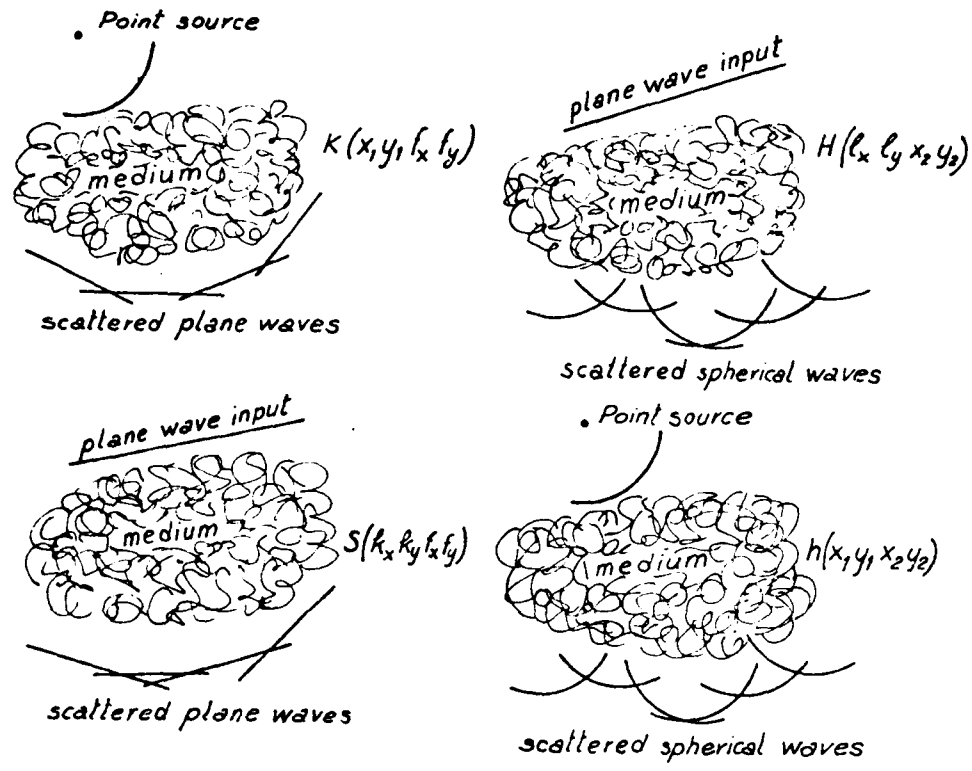


Fig.2 - Physical processes corresponding to the different transfer functions.

Solar Cycle Variations in The Total Electron Content  
at Invariant Latitude 54 Degrees

By

Yinn-Nien Huang  
Telecommunication Laboratories, M.O.C.  
Chung-Li P. O. Box 71, Taiwan  
Republic of China

I. Introduction

Studies of diurnal and seasonal variation of the total electron content of the ionosphere by use of the geostationary satellite signals have been done by many workers (e.g. Titheridge, 1966; Yuen and Roelofs, 1966 and 1967; Garriott et al., 1965 and 1970; Hawkins and Klobuchar, 1974). However, the solar cycle variations of the total electron content have been studied only by few workers (e.g. Da Rosa et al., 1973; Huang, 1975). The total electron content data obtained at Air Force Cambridge Research Laboratories station at Sagamore Hill, Massachusetts by using 136 MHz ATS-3 beacon satellite signal during the period from November 1967 to September 1973 have been published by Hawkins and Klobuchar (1974). The reduced TEC values apply to the vertical point of intersection of the ray and the 420 km layer. The coordinate of this vertical point is 38.6° N; 70.5° W, invariant latitude 54° (Hawkins and Klobuchar, 1974). The major purpose of this study is to use their published data to investigate the solar cycle variations of total electron content at invariant latitude 54 degree.

II. Solar Cycle Variation of the Monthly Mean Hourly Value

The full line in Figure 1 shows the month to month variation of the total electron content,  $I$ , at 00, 04, 08, 10, 15, 17, 20 and 23 hours in 75° W LST (LST - UT - 5 hr.). The apparent seasonal variation of  $I$  at different hours is very clear and will be discussed in section III. To eliminate the seasonal variation, 12 month running average values of  $I$ , denoted by  $\bar{I}$ , were calculated and plotted as dotted lines in Figure 1. The 12 month running average value of monthly mean sunspot number,  $R$ , denoted by  $\bar{R}$ , is also plotted at the top of the figure.

It can be seen that a positive correlation exists between  $\bar{I}$  and  $\bar{R}$ . The dependence of  $\bar{I}$  on  $\bar{R}$  can be seen more clearly in Figure 2. Although the TEC data were available only for about half solar cycle, the hysteresis variation (Huang, 1963; Huang and Jeng, 1976) of  $\bar{I}$  can be seen very clearly. However, the saturation effect of  $\bar{I}$  found for the TEC data in Hawaii (Huang, 1975) can not be found at present study.

The regression analysis was made between  $\bar{I}$  and  $\bar{R}$ . The

diurnal curves for the correlation coefficients and the slopes of the regression lines are plotted as a full line and a dashed line, respectively, in Figure 3. The correlation coefficients are found to be larger than 0.86 with a flat maximum appearing in afternoon hours and with a broad minimum appearing around the sunrise. The result is slightly worse as compared with the one obtained for Hawaii TEC (Huang, 1975). The diurnal variation of the slope of the regression line is characterized by a flat maximum around 14 hr. and a flat minimum around 0<sup>h</sup> hr. It is interesting to note that although the maximum slope at Sagamore Hill is only half of the value obtained in Hawaii (Huang, 1975), the minimum slope at Sagamore Hill is almost three time larger than that obtained in Hawaii.

The dotted line in Figure 3 shows the diurnal variation of the correlation coefficient between I and R. The correlation coefficients between I and R are much smaller as compared with those obtained between T and R, especially for the hours around sunrise.

### III. Solar Cycle Variation of the Apparent Seasonal Variation

The apparent seasonal variation of the total electron content at different hours can be seen in Figure 1. It can be seen that the amplitude of the seasonal variation decreases as the solar activity decreases showing dependence of the seasonal amplitude on the sunspot number. The seasonal patterns also change as the sunspot number decreases. Because of this solar activity dependence of seasonal variation, we call it as an apparent seasonal variation instead of merely a seasonal variation. The real seasonal variation will be given in section IV.

The major findings about the apparent seasonal variations are summarized below:

- (i) At nighttime starting from 19 hr. to 06 hr., the apparent seasonal variations are characterized by one maximum appearing around May and one minimum in January. It should be remarked that the maximum does not appear at the June solstice but about one month ahead of it.
- (ii) After sunrise, the pattern of seasonal variation gradually changes to have two maxima in March and October, respectively, and two minima in January and June or July, respectively. It is interesting to note that one of the maximum does not appear in the autumnal equinoctial month but one month later.
- (iii) The maximum value in March is much larger than that in October. The seasonal amplitude is maximum at about the same time when the diurnal peak appears.
- (iv) Winter anomaly, with electron content greater in winter than in summer at daytime, is well developed at the maximum solar activity. However, it disappears as the solar activity starts to decline.

#### IV. Real Seasonal Variations of the Total Electron Content

It should be remarked that the apparent seasonal variations described in section III include the effect of the solar activity. This is the reason why we have defined them as the apparent seasonal variations to distinguish them from the real seasonal variations described below. In order to obtain seasonal variation, we first assume that the monthly mean hourly TEC value at  $n$  hour  $m$  month, denoted by  $I(n,m)$ , and the smoothed sunspot number at  $m$  month, denoted by  $\bar{R}(m)$ , are linearly related by the following equation:

$$I(n,m) = A(n,m) + B(n,m) \bar{R}(m) \quad (1)$$

where  $A(n,m)$  and  $B(n,m)$  are constants to be determined by the standard method of regression analysis. The validity of the assumption of Equation (1) can be tested by determining the correlation coefficients between  $I(n,m)$  and  $\bar{R}(m)$ . Once the validity has been proved, Equation (1) can be used to obtain  $I(n,m)$  at  $\bar{R} = 0$ , representing minimum solar activity and at  $\bar{R} = 100$ , representing maximum solar activity. The seasonal variations constructed by these  $I(n,m)$ 's represent the real seasonal variation at constant solar activity.

Figure 4 shows the contour chart of the correlation coefficient between  $I(n,m)$  and  $\bar{R}(m)$ . It can be seen that the correlation coefficient is very large except for the time near the sunrise for each month and at nighttime in November.

The coefficient  $B(n,m)$  represents the rate of increase of  $I(n,m)$  per unit increase of  $\bar{R}(m)$ . The contour chart of  $B(n,m)$  is given in Figure 5. The dotted line represents the sunrise at 425 km height above the subionospheric point (Longitude =  $70^{\circ}$ W; Latitude =  $39^{\circ}$ N) (Hawkins and Klobuchar, 1974). The chained line represents the time when the diurnal minimum value appears. The diurnal minimum value appears about 0.5 to 1.0 hour ahead of the 425 km sunrise. The diurnal maximum value appears at the time (double chained line) when the diurnal peak of TEC appears as will be shown later. Seasonally, at daytime,  $B(n,m)$  has two minima appearing in July and December, respectively, and two maxima appearing in March and October; at nighttime, there are one maximum appearing in summer and one minimum appearing in December. The winter anomaly also appears for the seasonal variation of  $B(n,m)$ . One of the seasonal maximum does not appear exactly in September equinox but in October.

Figures 6 represents the contour chart of  $I$  for the maximum solar activity of  $R = 100$  constructed by using Equation (1). The following are its major characteristics:

- (i) The diurnal minimum value (chained line) appears at about

- 0.4 to 1.0 hours ahead of the sunrise at 425 km and almost coincides with the time of the appearance of the diurnal minimum value of  $B(n,m)$  shown in Figure 5.
- (ii) The diurnal maximum value (double chained line) appears at about the same time as the appearance of the diurnal maximum value of  $B(n,m)$ .
  - (iii) Seasonally, there are two maxima appearing in March and October and two minima in July and December at daytime; and one maximum appearing in May and one minimum in December at nighttime.
  - (iv) The October maximum is slightly smaller than the March maximum. Winter anomaly is well developed at daytime.

Figure 7 represents the contour chart of  $I$  for the minimum solar activity of  $R = 0$  constructed by using Equation (1). Unusual negative TEC values appear at daytime of November. The correlation coefficients at daytime are better than 0.8 as can be seen in Figure 4. However, the coefficients are determined by using the  $I(n,m)$  values obtained at the period in which  $R(m)$  varies from about 45 to 120. It is doubtful that the close correlation can exist between  $I(n,m)$  and  $\bar{R}$ , if the value of  $\bar{R}$  is extended down near zero value. The unusual negative TEC value may be due to the nonlinearity in the variation of TEC with respect to  $\bar{R}$  when  $\bar{R}$  becomes small. The TEC value may keep at a constant value even if the smoothed sunspot number continues to decrease. This argument should be proved by using TEC data obtained at sunspot minimum period. The coefficients  $A(n,m)$  and  $B(n,m)$  in Equation (1) obtained at present study can be used to construct our charts for the values of  $R$  ranging from about 50 to 120 only.

Figure 8 shows the contour chart of  $I$  at medium solar activity of 50 constructed by using Equation (1). It is interesting to note that the March peak at  $R = 100$  shifts to February when  $R = 50$ ; and the October peak becomes a very small one. Around 14 hr., it becomes almost a flat value starting from September until December. The sunrise time at 425 km almost coincides with the time of the appearance of the diurnal minimum in May and June.

#### V. Solar Cycle Variations of the Harmonic Components of the Monthly Mean Diurnal Variation

The harmonic components of the monthly mean diurnal variation have been calculated for each month and are shown in Figure 9.  $I_0$ ,  $I_1$ ,  $I_2$  and  $I_3$  represent the daily mean value, the 1st, 2nd and 3rd harmonic components of the monthly mean diurnal variation, respectively. The harmonic components beyond the 4th components are so small that they are not shown in the figure.  $\bar{I}_0$ ,  $\bar{I}_1$ ,  $\bar{I}_2$  and  $\bar{I}_3$  show the 12 month running average values of  $I_0$ ,  $I_1$ ,  $I_2$  and  $I_3$ , respectively. The

variation of  $\bar{R}$  is plotted at the top of the figure. It is very clear that the positive correlation exists between each smoothed harmonic component and the smoothed sunspot number,  $R$ . The solar activity dependence of each harmonic component can be seen more clearly in Figure 10. A very large positive hysteresis variation can be seen for the  $I_0$  component. Almost no hysteresis loop can be found for the components  $I_1$ ,  $I_2$  and  $I_3$ . The rate of increase of  $I_0$  with respect to  $R$  is much larger than other three components. The component  $I_1$  keep almost a constant value.

The seasonal variations of the components  $I_0$  and  $I_1$  are characterized by two maxima appearing in February and October and two minima appearing in January/December and June/July. For the component of  $I_0$ , the February maximum is much larger than October maximum. Winter anomaly is well developed only for the component  $I_1$ . The seasonal variation of the component  $I_2$  is characterized by a maximum appearing in winter and a broad minimum appearing in summer. The component  $I_3$  is characterized by two maxima appearing in equinoctial months and two minima appearing in summer and winter.

## VI. Conclusion

The following conclusions can be drawn from the present investigation:

- (1) The 12 month running average value of the total electron conternt,  $T$ , at each hour has been found to have the best linear correlation with the 12 month running average value of monthly mean sunspot number,  $\bar{R}$ .
- (2) The correlation coefficient is larger than 0.86 with a flat maximum appearing in afternoon hours and a broad minimum around the time of sunrise. The slope of the regression line varies diurnally with a flat maximum and a flat minimum appearing around 14 hr. and 04 hr. respectively.
- (3) The correlation coefficients between monthly mean hourly TEC value,  $T$ , and monthly mean sunspot number,  $R$ , is much smaller than that between  $T$  and  $\bar{R}$ .
- (4) Positive hysteresis variation has been found for the variation of  $T$  with respect to  $\bar{R}$ .
- (5) The linear correlation coefficient between  $T(n,m)$  and  $\bar{R}(m)$  is large. However, the present investigation cannot ascertain that the linearity can be extend down to the sunspot minimum period when  $R$  is very small. The appearance of unusual negative TEC value in November for  $R < 0$  seems to show that, near sunspot minimum, TEC may keep a constant value even if  $R$  continues to decreases.
- (6) At daytime, winter anomaly is present both for TEC at  $\bar{R} = 100$  and slope  $B(n,m)$ . The time for the occurrence of the diurnal maximum and minimum of  $T$  at  $\bar{R} = 100$  almost coincide with those for the slope  $B(n,m)$ .

(7) The diurnal variation of I can be well represented by a sum of its diurnal mean and first three harmonic components. The solar cycle variations of these components and their seasonal variations are quite different. The positive hysteresis variation is found only for the diurnal mean component.

#### Acknowledgement

The author is grateful to Mr. B. S. Jeng for his assistance in numerical calculation; to Mr. S. W. Chen for his preparation of the illustrations; and to Miss M. S. Hsieh for her preparation of the manuscript.

#### References

- Da Rosa, A. V., H. Waldman and J. Bendito, Response of the ionospheric electron content to fluctuation in solar activity, *J. Atmosph. Terr. Phys.*, 35, 429, 1973.
- Garriot, O. K., F. L. Smith III and P. C. Yuen, Observations of ionospheric electron content using a geostationary satellite, *Planet. Space Sci.*, 13, 829, 1965
- Garriot, O. K., A. V. Da Rosa and W. J. Ross, *J. Atmosph. Terr. Phys.*, 32, 705, 1970
- Hawkins, G. S. and J. A. Klobuchar, Seasonal and diurnal variations in the total electron content of the ionosphere at invariant latitude 54 degrees, AFCRL Environmental Research Report No. 482, June 1974
- Huang, Y. N., The hysteresis variation of the semi-thickness of the F2 layer and its relevant phenomena at Kokubunji, Japan, *J. Atmosph. Terr. Phys.*, 25, 647, 1963
- Huang, Y. N., Solar cycle variation of the total electron content at low latitude to be published in Preceeding of the 1975 Symposium on the effect of ionosphere on space systems and communications ed. by J. M. Goodman, 1975
- Huang, Y. N. and B. S. Jeng, A further study on the hysteresis variation of the F2 layer semithickness parameter  $y_{pF2}$  at Kokubunji, Japan, *J. Atmosph. Terr. Phys.*, 38, 319, 1976
- Titheridge, J.E., Continuous records of the total electron content of the ionosphere, *J. Atmosph. Terr. Phys.*, 28, 1135, 1966
- Yuen, P. C. and T. H. Roelofs, Diurnal variation of the ionospheric total electron content, *J. Geophys. Res.*, 71, 849, 1966
- Yuen, P. C. and T. H. Roelofs, Seasonal Variations in ionospheric total electron content, *J. Atmosph. Terr. Phys.*, 29, 321, 1967
- Yuen, P. C. and T. H. Roelofs, Seasonal Variations in ionospheric total electron content, *J. Atmosph. Terr. Phys.*, 29, 321, 1967

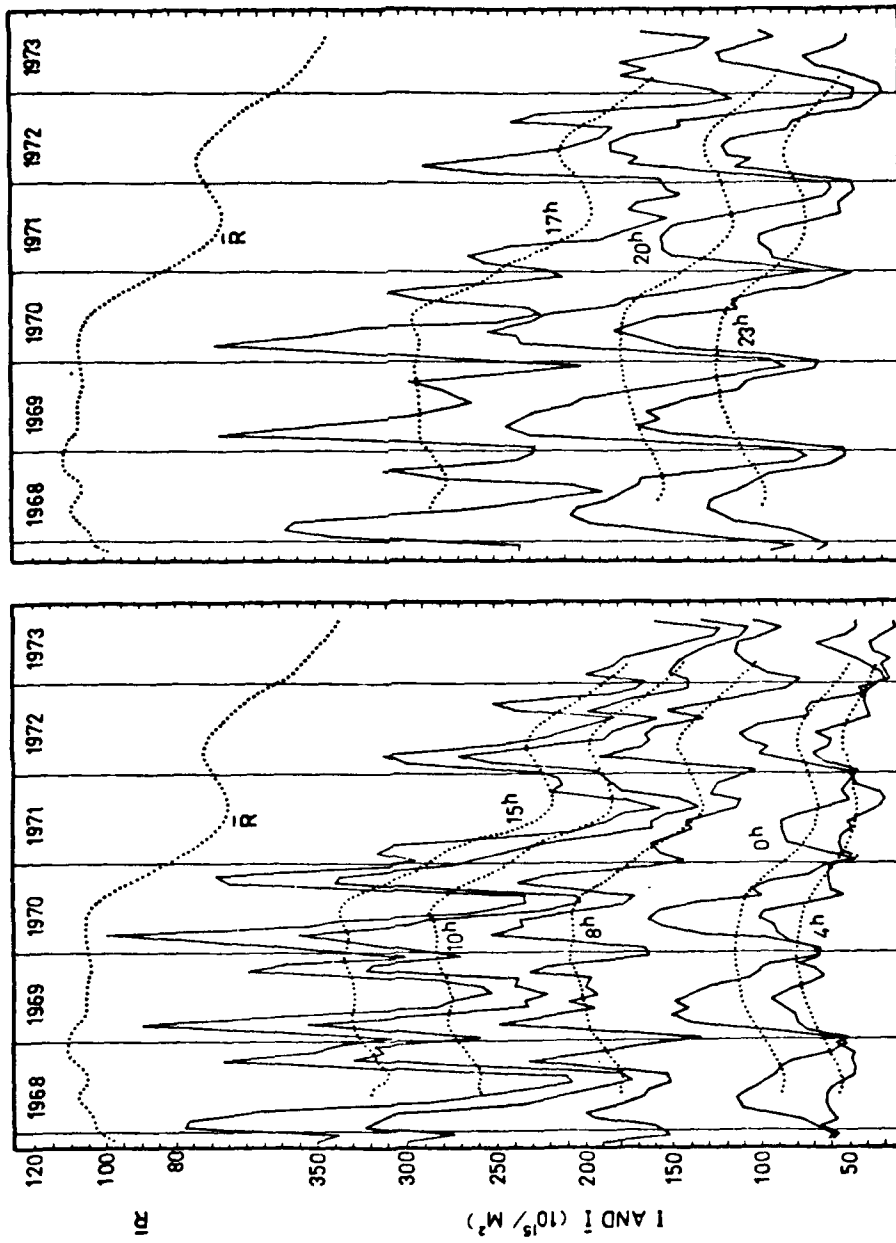


Fig.1 Variations of  $I$ ,  $i$  and  $\bar{R}$  at different hours.

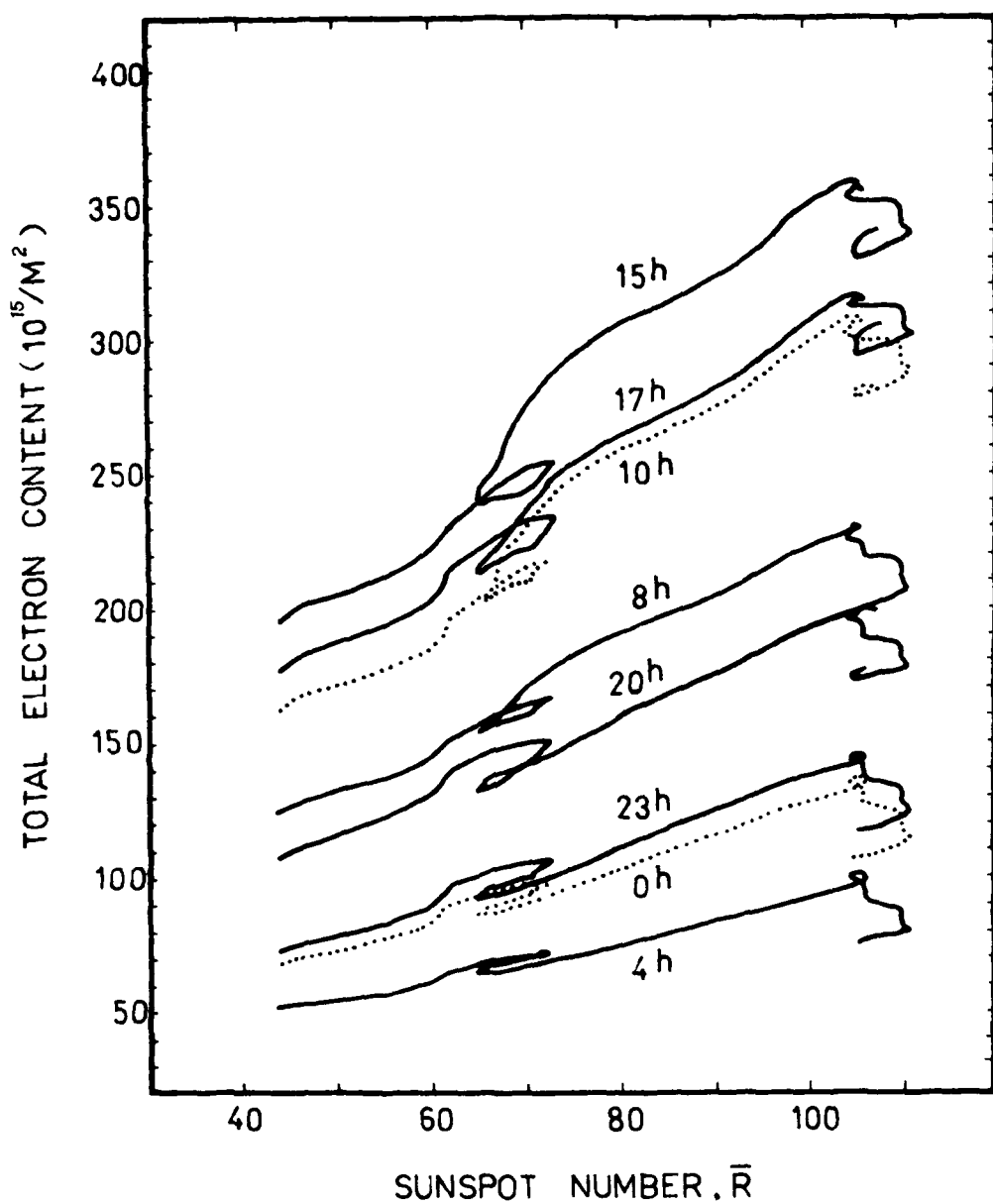


Fig.2 Variation of  $\bar{I}$  with  $\bar{R}$  at different hours.

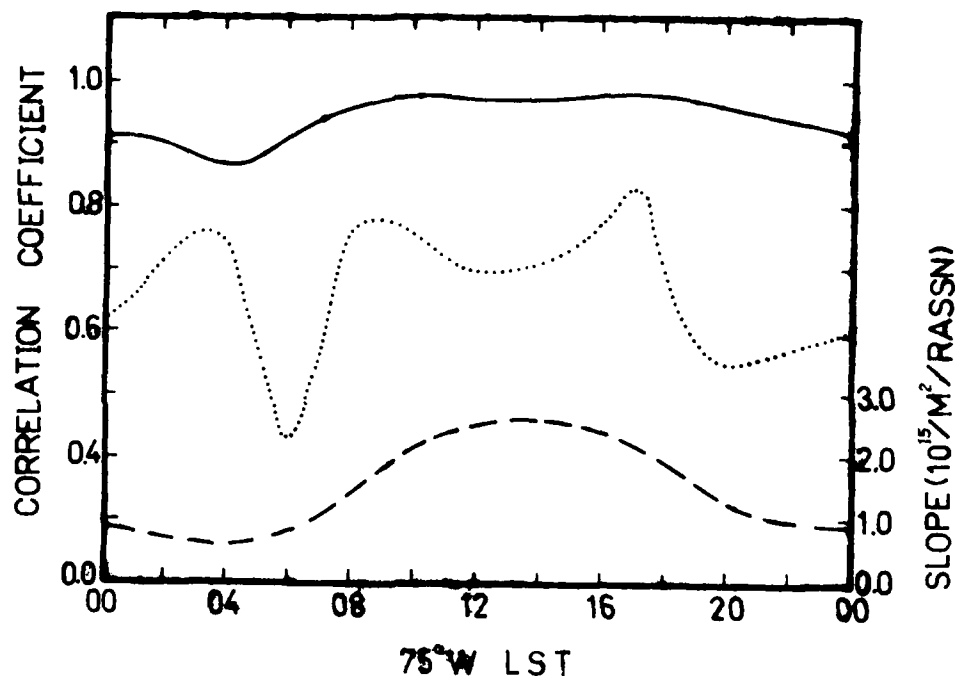


Fig. 3 Diurnal variations of the correlation coefficient between I and R (full line); the slope of the regression line (dashed line); and the correlation coefficient between I and R (dotted line).

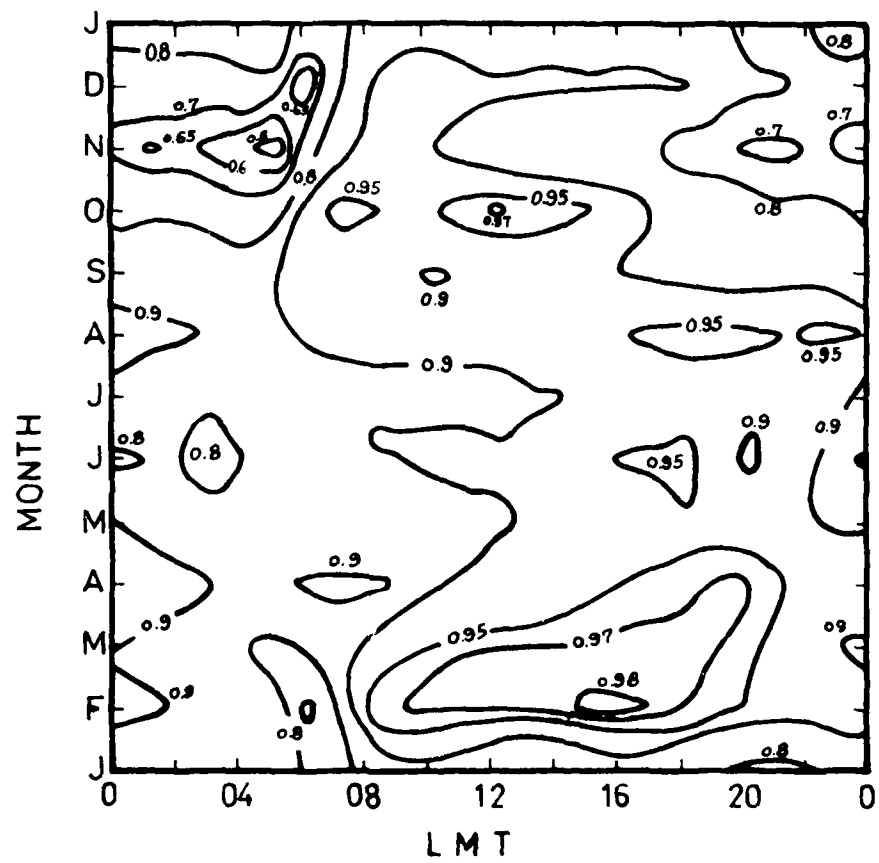


Fig.4 Contour chart of the correlation coefficient  
between I and  $\bar{R}$ .

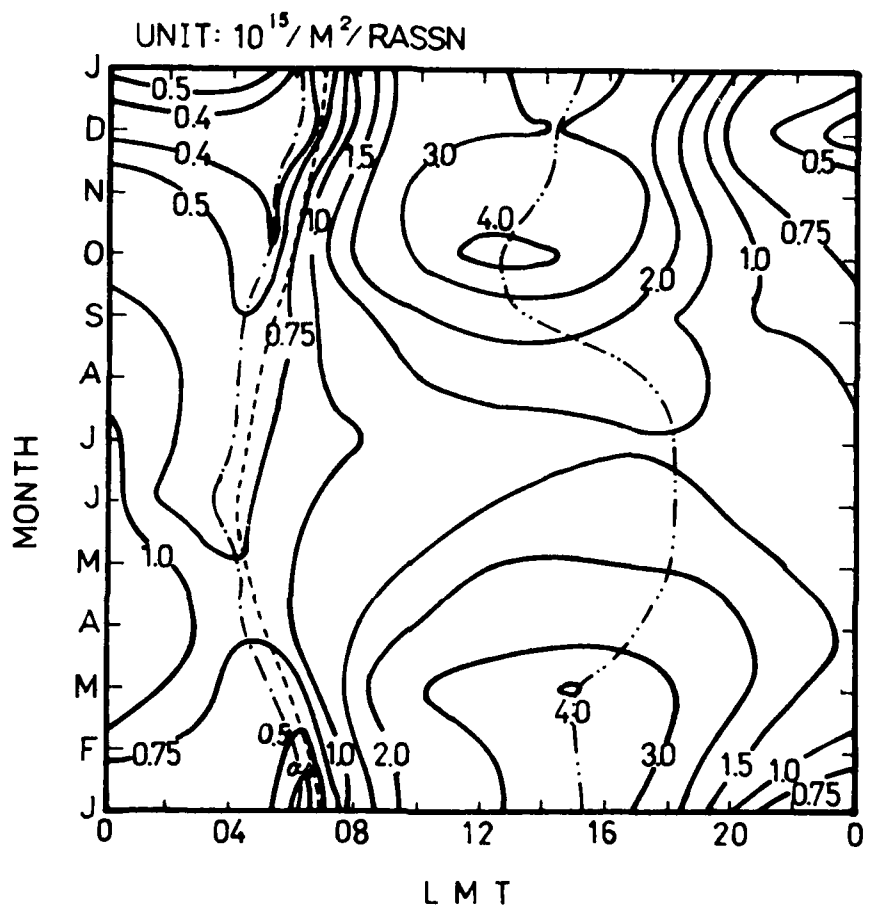


Fig.5 Contour chart of the rate of increase of  $I$  with respect to  $\bar{R}$ .

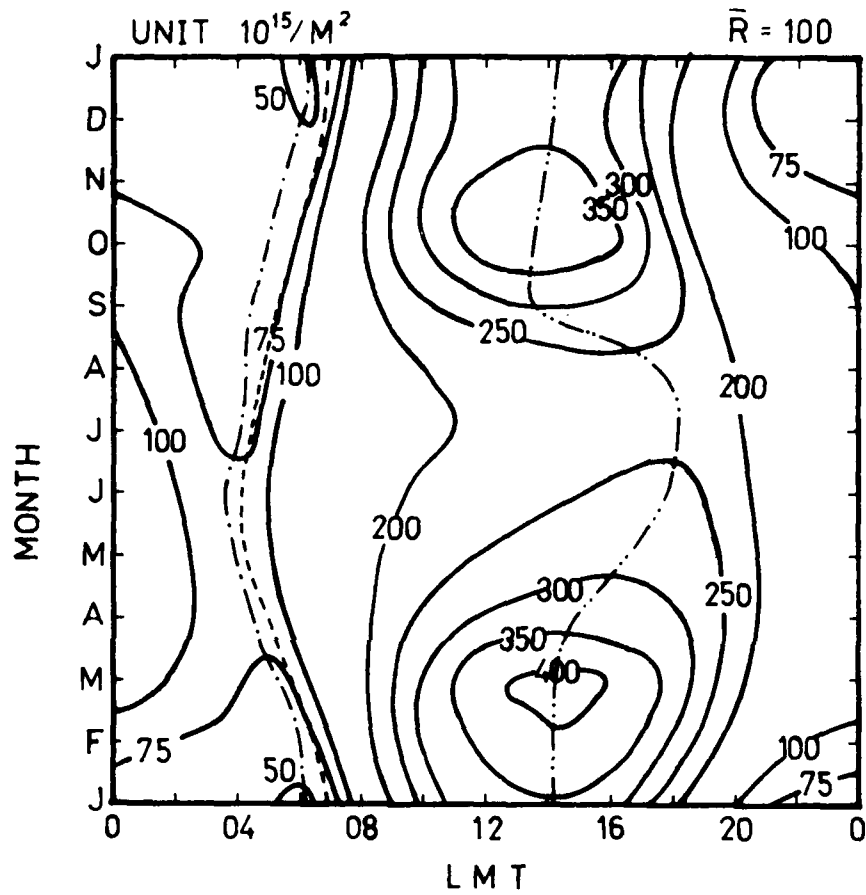


Fig. 6 Contour chart for  $I$  at maximum solar activity of  $\bar{R}=100$ .

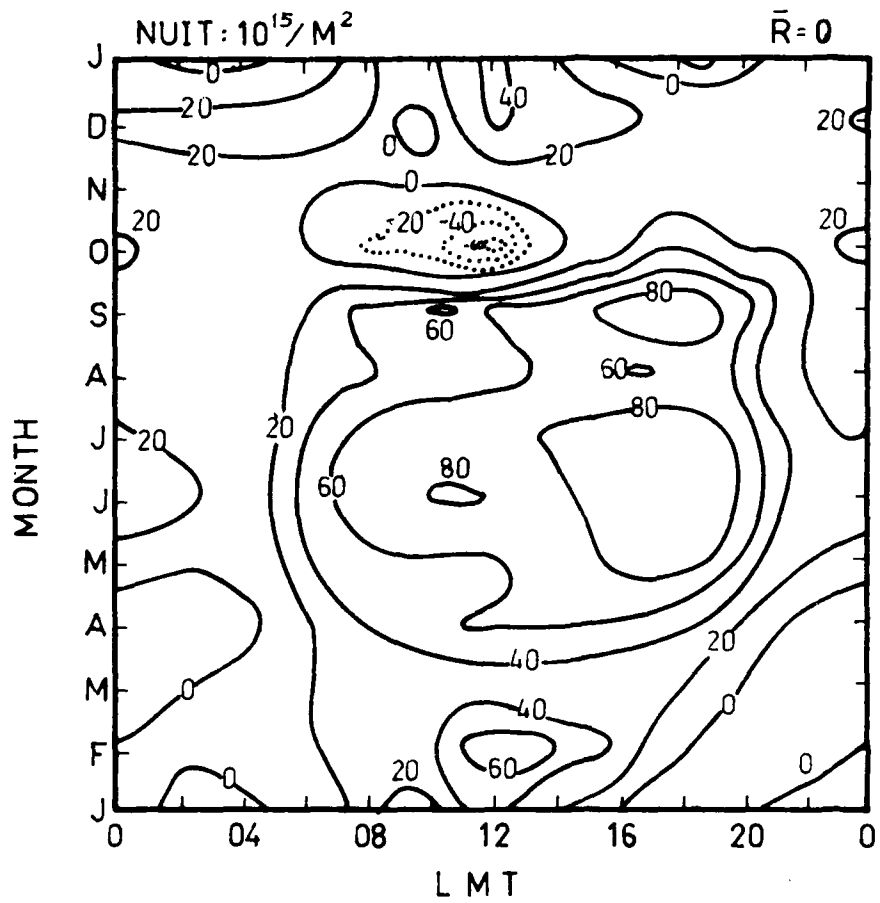


Fig. 7 Contour chart for I at minimum solar activity of  $\bar{R} = 0$ .

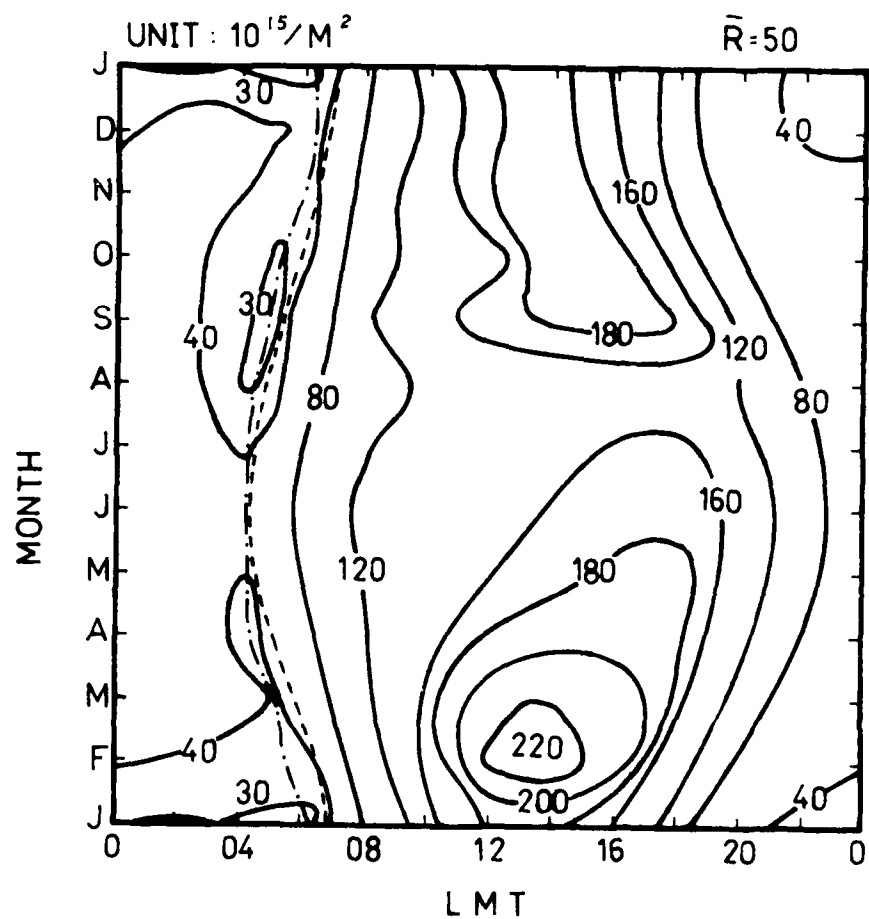


Fig. 8 Contour chart for  $I$  at medium solar activity of  $\bar{R}=50$ .

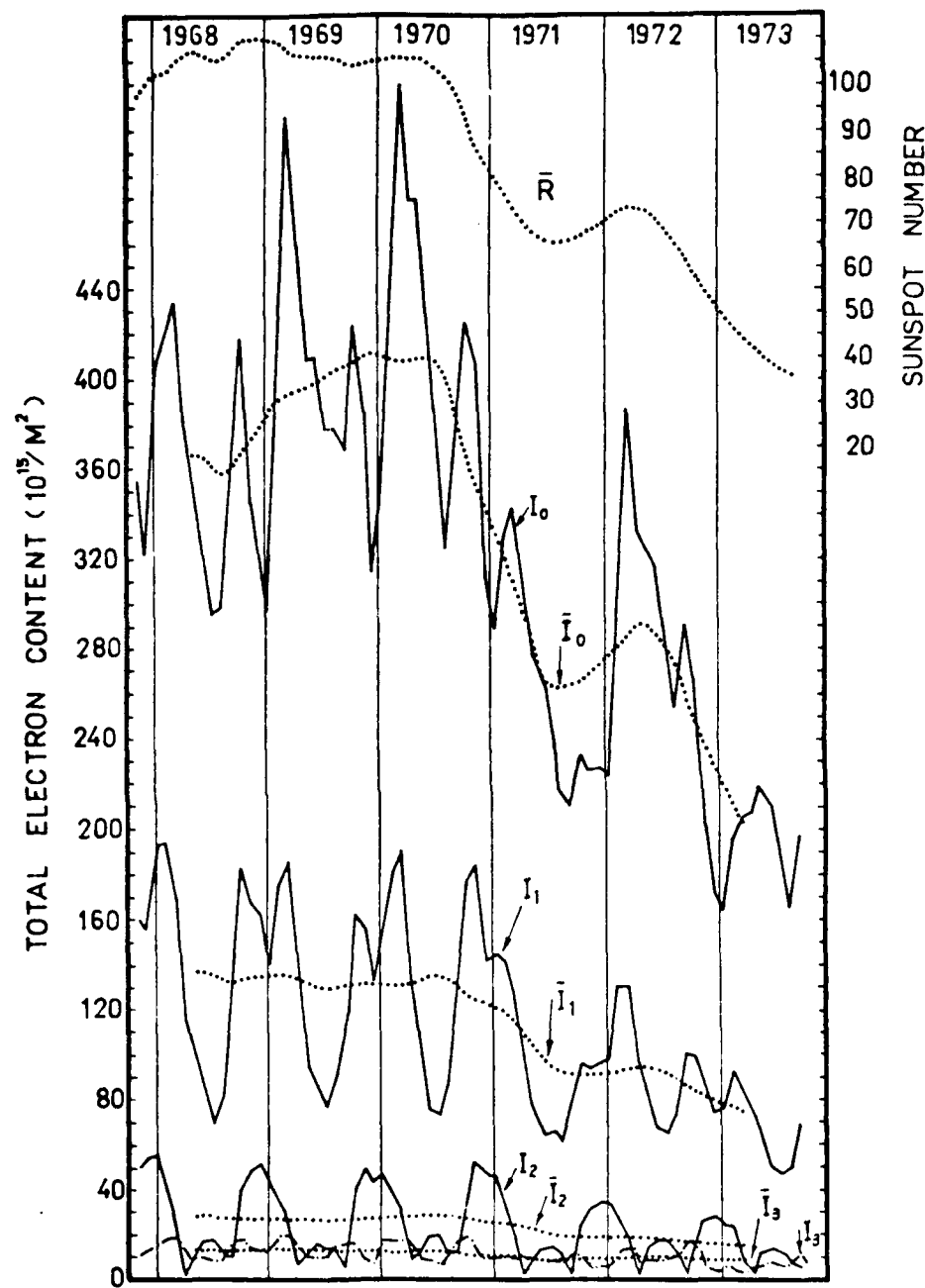


Fig. 9 Variations of the harmonic components of the monthly mean diurnal variation.

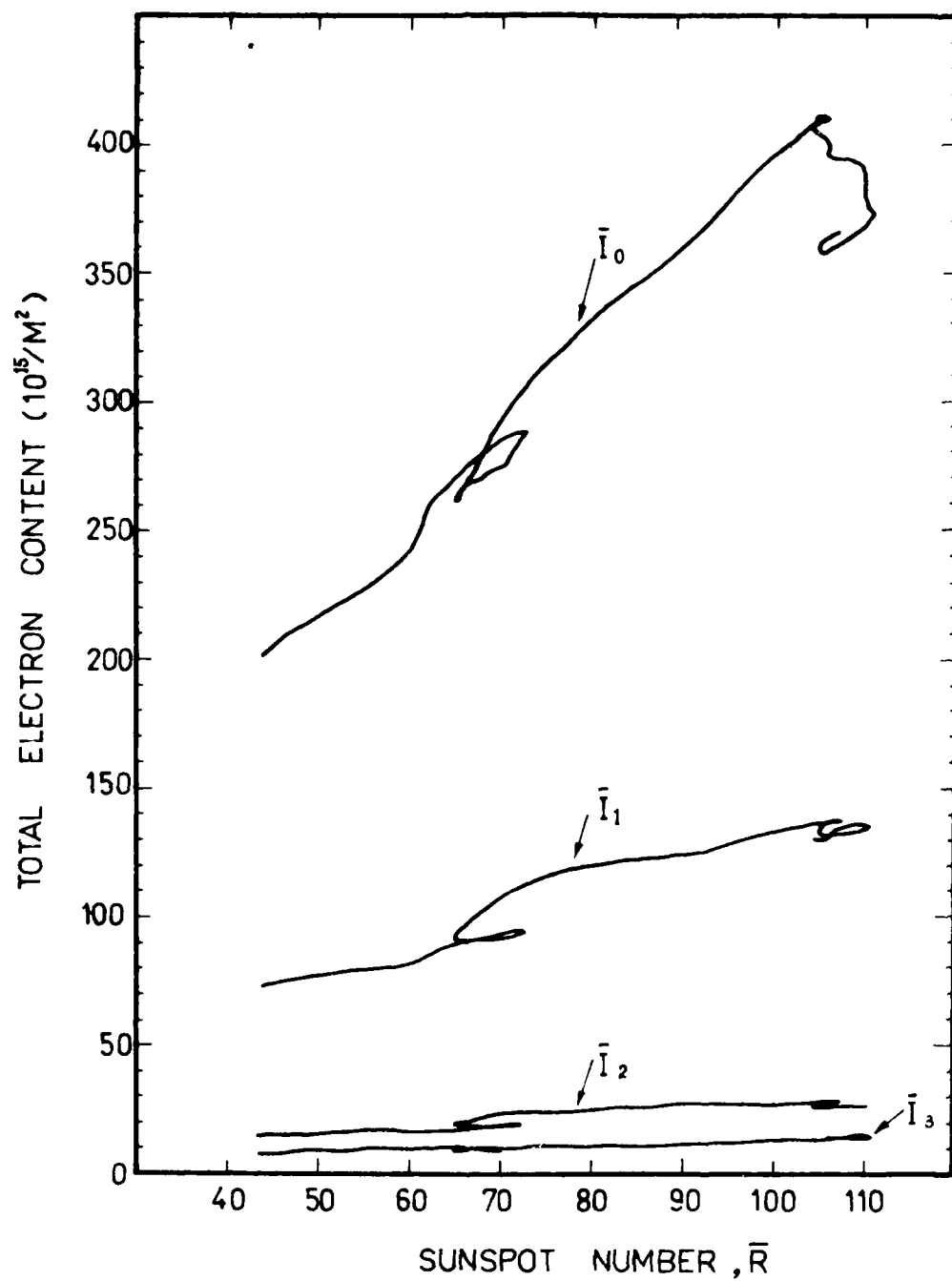


Fig.10 Variation of each smoothed harmonic component with  $\bar{R}$ .

SPECIFICATION OF NAVIGATION AND RADAR ERRORS  
CAUSED BY THE IONOSPHERE

Delia D. DuLong  
Regis College  
Weston, Massachusetts 02193

Richard S. Allen  
Air Force Geophysics Laboratory  
Hanscom AFB, Massachusetts 01731

INTRODUCTION

Our principal aim in this study is to examine the concept of making a real time correction for errors that arise when VHF/UHF radio waves pass through portions of the ionosphere. If we consider any VHF/UHF navigation, timing or radar system, the phase or the group delay of the radio waves, whichever is the basic system measurement, can be considered the sum of a part due to the distance along the actual wave path and a part due to the free electrons along that path. Making the simplifications to the steady state solutions of the wave equations that are appropriate to the earth's ionosphere and to VHF/UHF radio frequencies, a Euclidean line between source and receiver is sufficient to define the wave path to far better accuracy than the parameters that might be introduced into a 3-D ray trace program. This means that angular deviation may be ignored for first order calculations. For instance, the measured range ( $R$ ) is

$$R = R_0 + \frac{2\pi e^2}{m_e w^2} \int_{S_1}^{S_2} N_e(s) ds$$

$$= R_0 + \delta R$$

where  $R_0$  is the free space distance and  $\delta R$  is the ionospheric contribution.  $\delta R$  is directly proportional to the total number of electrons per unit cross sectional area along the ray path, and may be calculated piecewise along the line of sight ( $\theta$ ) through a model of the electron density vs height.

$$\delta R = \frac{k}{f^2} \sum_{h=h_1}^{h_2} \sec \theta(h) N_e(h) \Delta h$$

Alternatively, it may be estimated as a fractional portion ( $\rho(h_1, h_2)$ ) of the vertical total electron content (TEC) of the entire ionosphere

$$\delta R = \frac{k}{f^2} \rho(h_1, h_2) \overline{\sec \theta} TEC$$

The frequency dispersion, the time dependence of phase, and the correction for angle of arrival also depend, to first order, on the integrated electron content along the slant path.

In theory, any system could be devised to use measurements at several radio frequencies to make a correction for the contribution due to the ionosphere. In practice, however, most systems use single radio frequencies and therefore, a correction must be estimated from a model ionosphere. There is now a world data pool of systematic observations of equivalent vertical electron content which has been measured using the Faraday rotation of beacon signals from synchronous satellites. This archive data demonstrates that, over the latitude range from Hong Kong to Nar-sarsuaq, Greenland, and over the most recent solar cycle, the expected monthly variability (r.m.s. deviation from monthly mean TEC) is 20 to 25 percent of the monthly mean TEC. This is consistent with the observations from world data that the variability of  $f_0 F2$  is 10 to 12 percent of monthly mean daytime  $f_0 F2$ .

For perspective, consider a 400 mhz radar situated at Hamilton, Mass. To estimate the range error for a space vehicle orbiting well above the peak of the F2 region, we reference the archive data from local measurements of the Faraday rotation of ATS-3. At mid-latitude the largest monthly median values occur during solar maximum, the equinoxes, and local daytime. Table 1 gives representative values of range error at 400 Mhz scaled from daytime values of TEC for these conditions. Note, the range between largest and smallest observations at a given hour, over the calendar month, is about 75 percent of the hourly mean.

Table 1 Range Errors (Meters, one way) at 400 Mhz

Median TEC  $33 \times 10^{16}$ (for 1968)	Max Mean Min	90°	Elevation Angle		
			45°	0°	0°
			280 210 140	595 443 395	

Alternatively, a model profile could be constructed from ionospheric parameters. Choosing a form for the profile, monthly median values of  $f_0 F2$ , hmF2 and various thickness parameters could be used to derive electron content along the ray path. If a very good median model is constructed, the r.m.s. variability about the prediction should be the same as the variability found in the archive data - about 20 to 25 percent of the monthly median value. Many systems would like to reduce this variability by using a local measurement. For example, from the signals of a beacon satellite, such as one of the Navy TRANSIT series, the differential doppler observed between two radio beacons could be used to estimate the equivalent vertical electron content along the sub-ionospheric path of the satellite. This estimate could then be used to specify an area model.

### SPATIAL VARIABILITY

An example of the potential of this specification technique to remove spatial variability is shown in Figure 1. Differential Doppler records, taken at Millstone Hill, Mass. using one of the TRANSIT satellites of the Navy Navigation Satellite System, were reduced to equivalent vertical electron content (N. Tomljanovich, preliminary data). A standard Air Force prediction program, used to estimate the median value of TEC along the satellite path, and separate measurements of TEC from Hamilton, Mass. and from Goose Bay, Labrador, using Faraday rotation measurements of ATS-3 signals at the time of the pass, were compared with the TRANSIT observations. There is a general fit of the latitude gradients along the path for both the predicted median and the two sets of observations.

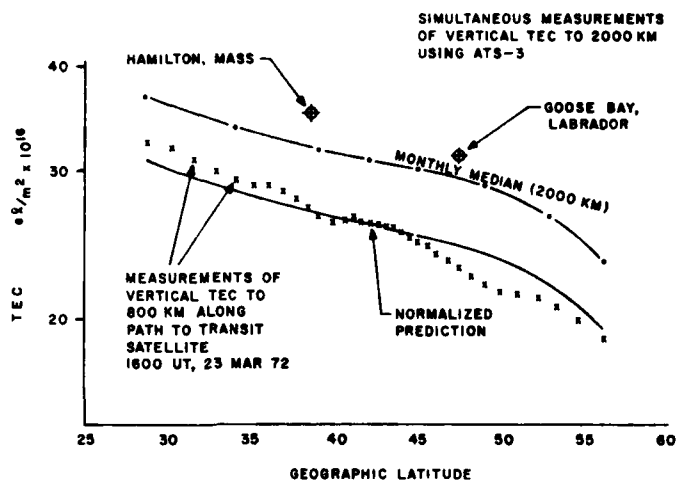


FIGURE 1 SPECIFICATION OF MEDIAN LATITUDE VARIATION OF VERTICAL CONTENT BY A LOCAL MEASUREMENT.

From the TRANSIT pass, the value of TEC at closest approach was used to scale the predicted median at this point, and this correction factor was applied to the predicted median along the entire path. The resultant normalized prediction has a spatial variability of less than 5 percent within a few degrees of the central scaling region. The maximum deviation increases with distance along the path, to about 10 percent at the extremes. Figure 2 is a representative daytime sample with a TRANSIT pass from each of five different months selected using the criteria that it fall within  $\pm 0.5$  degrees longitude of the sub-ionospheric point of the ATS-3 measurements made from Hamilton, Mass. The initial results for specification of the daytime ionosphere are consistent, and indicate that the proposed technique of adaptive modeling of the median range error by normalization to

the central region of a satellite pass track can produce a ten-fold reduction of the variability from monthly median observations.

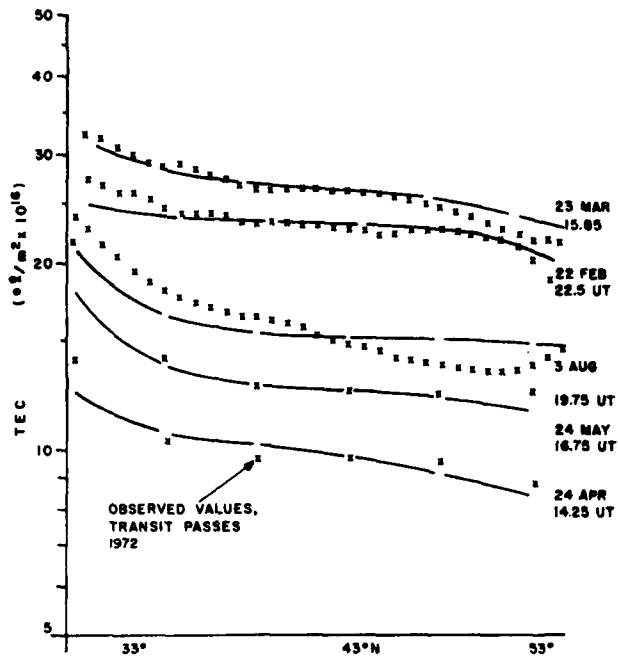


FIGURE 2 COMPARISON OF NORMALIZED PREDICTION OF MEDIAN GRADIENT WITH OBSERVED TOTAL CONTENT TO 800 KM.

The median range errors expected during night hours are about a magnitude less than those expected during the day. Although the 30 percent day to day variability about the median for nighttime is only slightly worse than the 20 percent for daytime, sharply localized features in the ionosphere may make it just as necessary to use an adaptive modeling technique during the night. Figure 3 illustrates a local nighttime feature. The steep gradient of electron content found over small latitude intervals along the TRANSIT path is confirmed by the gradient measured simultaneously, with the ATS-3 beacon at Hamilton, Mass. and at Goose Bay, Labrador. The prediction of the monthly median, which has not been normalized to the observations, has only a slight gradient at this time, but the absolute error between prediction and observation is of the same order as the absolute daytime error using the scaled median. We have not yet had sufficient data to determine whether the observed gradients are a consistent nighttime feature. If they are, scaling could introduce new errors and an improvement in prediction would have to result from improved modeling of these features.

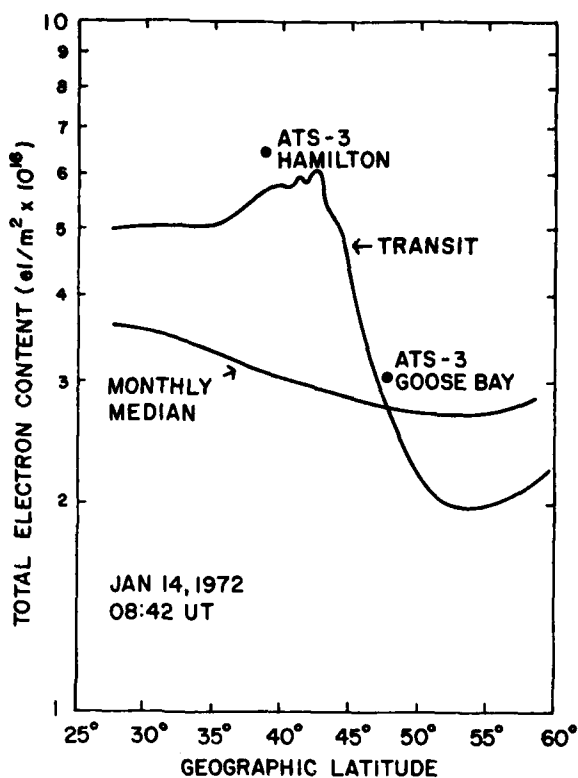


FIGURE 3 COMPARISON OF PREDICTED MEDIAN GRADIENT WITH OBSERVED NIGHTTIME GRADIENT IN TOTAL CONTENT

#### TEMPORAL VARIABILITY

In parallel with the spatial variability, the temporal variability, using a similar scheme for scaling the predicted median, is being examined. The values of TEC, as determined from measurements of ATS-3 signals taken at Hamilton, Mass. in 15-minute intervals for the year 1972, have been used for the local observations. The effectiveness of the predicted 10-day median was examined by comparing the standard deviation of the observations with the rms deviation from the predicted median. The errors are equivalent, one of the indications that the observed mean is being successfully modelled.

To simulate adaptive updating of a model ionosphere, the ATS-3 measurements in TEC units and the predicted median TEC were used to determine a scaling factor at each hourly observation. The resultant factor was then used to scale the prediction at 15 minute intervals for the succeeding 12 hours.

The monthly mean of this scaled prediction was determined, and the rms deviation of the observations from the new prediction was calculated. Figure 4 shows the error, in TEC units, for: the hourly-based 12-hour predictions for 2-hour intervals for the month of September, 1972; the observations from the monthly mean of the observations; and the observations from the predicted median. Some of the constraints in this technique are apparent here, particularly at sunrise. The new prediction, which tends to have errors less than those that would result from using the monthly mean or the predicted median throughout the nighttime hours, rapidly exceeds that error near sunrise. There is a similar, though less extreme, occurrence in the late afternoon. A scaled prediction from a measurement at 1600 hours or later up to sunrise is at least as good, and usually better than, the predicted median up to this point, but cannot be used beyond sunrise. An update made after sunrise, up to 1600 hours, is better than the predicted median throughout this period and is no worse than the median for the hours between 1600 and sunrise. The September results for the period between 1600 hours and sunrise are consistent throughout the year, but the results after sunrise vary. For some months an observation between sunrise and 1600 can only be used for periods of 2 to 3 hours before the error exceeds the error using the predicted median. Further examination will determine whether this is a seasonal diurnal variation.

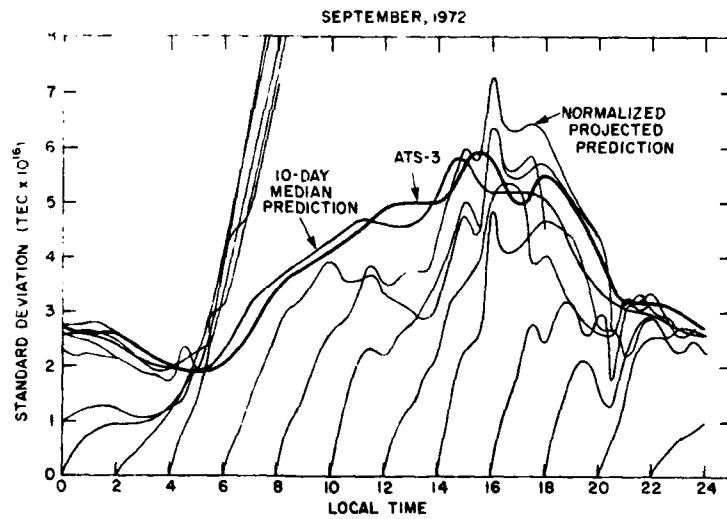


FIGURE 4 COMPARISON OF STANDARD DEVIATION OF OBSERVED TOTAL CONTENT FROM MONTHLY MEAN, 10-DAY MEDIAN PREDICTION, AND NORMALIZED PREDICTION UP TO 12 HOURS FROM NORMALIZATION POINT

The potential effectiveness of this technique depends on the time interval between local TEC measurements. Figures 5, 6, and 7 summarize the results of predictions based on 15-

minute, 1 hour and 2-hour observations, respectively, for the year 1972. The dashed lines approximate sunrise and sunset, the contours are the rms percent error. To reduce the rms error to 5% or less for most of the daytime, measurements would have to be made in intervals of about 15-minutes. The error rarely exceeds 10% at anytime other than the period near sunrise, but even at these times, the absolute error does not exceed the maximum daytime error.

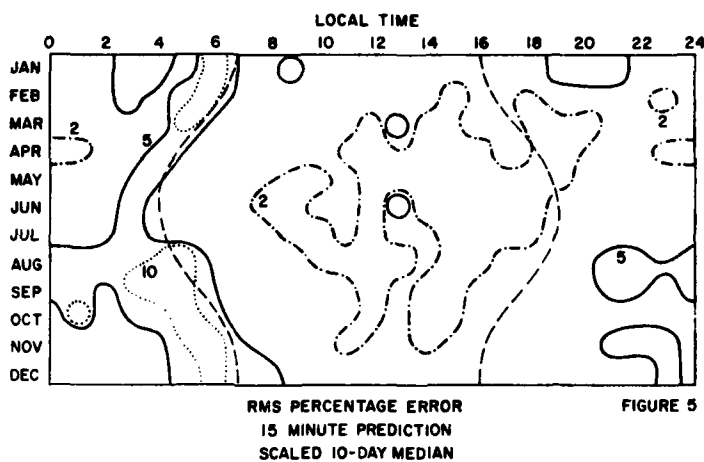


FIGURE 5

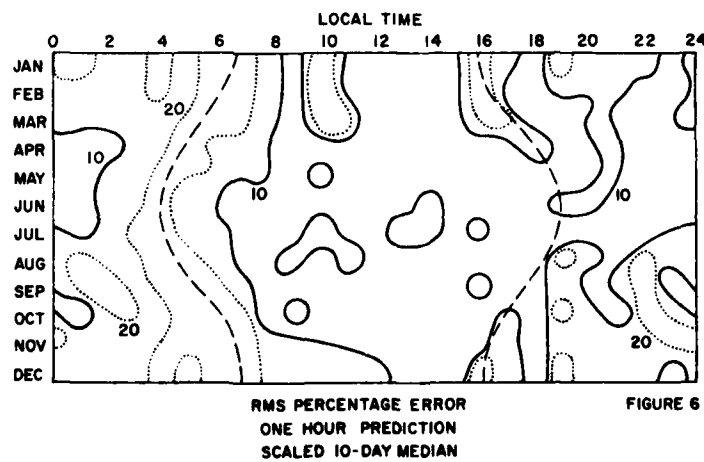


FIGURE 6

For a prediction based on a 1-hour observation, the rms error is less than 10% throughout most of the day time hours, less than 20% through most of the year, but exceeds 20% rms near sunrise. Using a 2-hour observation, there can still be a significant reduction in error. The rms error is on the order of 15% or less for most of the daytime hours and near sunrise

it exceeds 25% error, but for most of the year it is less than the 20 to 25% expected rms error using the predicted median.

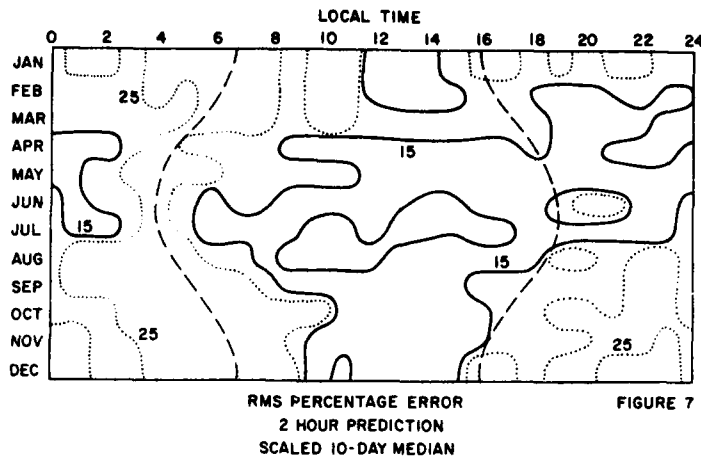


FIGURE 7

#### VARIABILITY OF MODEL PARAMETERS

The previous reductions apply to specification of the error contributed by the total ionosphere along the slant path to the calibration vehicle. (SLANT TEC). If a target vehicle is embedded in the ionized region, only a portion of the slant content contributes to the range error and that portion can be sensitive to the parameters used to model the vertical distribution of electron density.

The relative change in slant content can be estimated in the following manner:

$$\begin{aligned}\Delta \text{TEC} &= \text{Actual} - \text{Predicted} \\ &= \int_{h_1}^{h_2} N_1 P_1(s) ds - \int_{h_1}^{h_2} (N_0 + \Delta N) P_0(s) ds \\ &= N_0 \sec \theta_1 \int_{h_1}^{h_2} P_1(h) dh - (N_0 + \Delta N) \sec \theta_0 \int_{h_1}^{h_2} P_0(h) dh\end{aligned}$$

where the normalized profiles ( $P$ ) are slightly different and the density ( $N$ ) at the peak of the F2 region, in the median model, has been adjusted so that the model content matches the electron content observed with the calibration vehicle. If the difference between the actual hmF2 and the predicted median hmF2 is small compared to the local scale height of electron density, then, the difference in the profiles is just a vertical shift of  $P_0(h)$  to produce  $P_1(h)$ , and the geometric factors of the slant paths remain nearly identical. In that case,  $\Delta \text{TEC}$  maximizes at hmF2 where  $P(h)$  is unity, so that

$$\Delta \text{TEC} \approx (N_0 + \Delta N) \sec \theta \Delta h$$

Normalized to the equivalent slant content used in calibration,

$$\frac{\Delta \text{TEC}}{\text{TEC}} \approx \frac{(N_0 + \Delta N) \sec \theta_0 \Delta h}{N_c \sec \theta_c \tau} \approx \frac{\Delta h}{\tau}$$

where  $\tau$  is the integral of the normalized vertical profile. Over most conditions at mid-latitudes,

$$hmF2 < \tau \leq 2 hmF2$$

so that

$$\frac{\Delta h}{2hmF2} \leq \frac{\Delta \text{TEC}}{\text{TEC}} < \frac{\Delta h}{hmF2}$$

From this we conclude that if there is an uncertainty in  $hmF2$  alone, a worst case would be a target near the peak of the F2 region and the error would be approximated by

$$\Delta R \approx \frac{k}{f^2} \text{ SLANT TEC } \left( \frac{\Delta hmF2}{hmF2} \right)$$

Since the rms percentage variability of  $hmF2$  is about 7 percent of the monthly mean  $hmF2$ , the r.m.s. error for targets near the peak of the F2 region would be about 7 percent of the range error to the calibration vehicle.

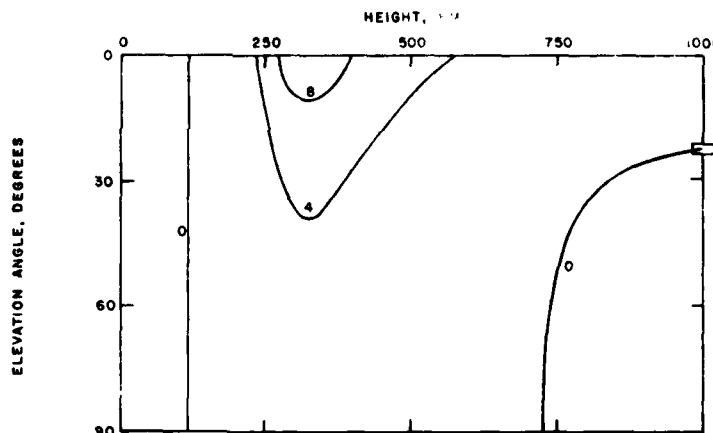


FIGURE 8 RANGE ERROR, IN FEET, FOR AN L-BAND RADAR AT MID LATITUDES  
WORST MEDIAN CONDITIONS WHEN SPECIFIED BY A SLANT OBSERVATION  
TO A TARGET AT 22 DEGREES, 1000 KM ALTITUDE, IF THERE IS A 5  
PERCENT ERROR IN THE HEIGHT OF THE F REGION.

Figure 8 illustrates a comparison made when the actual ionosphere is assumed to differ from the median ionosphere only in the height of the F2 region. A model of the actual ionosphere was integrated to provide a measure of slant TEC at a sample location for a calibration satellite of 1000 km, 22 degrees

elevation. Then a normalization factor was applied to the median ionosphere to provide the same slant TEC at that point, and this factor was used to scale the median model at all other points. Note that the difference between the range error to a target at various positions in the actual ionosphere and in the median ionosphere approaches a maximum for target vehicles near the peak of the F region and at low elevation angles. Simultaneous errors in foF2 and profile thickness parameters have to be considered in a similar manner, along with hmF2, to specify the range error for target vehicles embedded in the ionosphere.

#### CONCLUSION

Examination of the spatial and temporal variability of foF2, hmF2 and the thickness parameters used to derive electron content along the ray path may be necessary for systems which wish to specify propagation corrections to vehicles within the ionosphere. The expected variability of these parameters from their monthly mean values is about 10 percent for foF2, 7 percent for hmax, and 15 percent for the thickness parameters. A local measurement of one or several of these parameters, coupled with a specification technique similar to that discussed here for measurements of total content, may be required for reductions in error to the same order that is possible for vehicles in the topside ionosphere.

For a target in the topside ionosphere, initial results indicate a local measurement of total electron content is sufficient for a significant reduction in range error. From the comparison of the TRANSIT passes with their corresponding normalized median predictions it was shown that a reduction in error to less than 5 percent is possible, in daytime, within a few degrees latitude of the normalization point. This error in spatial variation increases to about 10 percent over 15 degrees latitude. These errors are equivalent to the daytime rms error in temporal variability using 15-minute and 1-hour observations, respectively, to scale the median prediction. This is an indication that mean spatial and temporal variations are comparable in magnitude. Also, since the TRANSIT passes are effectively north-south, and the temporal variations can be considered east-west, it would appear that direction is not a primary consideration in determining variation on a mean basis.

## IONOSPHERIC REFRACTION ERRORS IN SATELLITE TRACKING AND NAVIGATION IN LOW LATITUDES

Y.V. Somayajulu and A.B. Ghosh  
Space Research Section, Radio Science Division,  
National Physical Laboratory, New Delhi-110012

### ABSTRACT

Satellite tracking and navigation systems use radio beacons to measure the range and elevation angle for position fixing. However these values differ from the true values due to refraction effects of the intervening troposphere and ionosphere. This paper deals with the ionospheric problem. In order to correct for the refraction effects, one has essentially to utilize a three dimensional tracing of the ray path from receiver to the satellite which requires a knowledge of the electron density distribution along the ray path. The present technique of building up electron density profiles is essentially based on the method proposed by Somayajulu et al (1965). The region around hmF2 is built by assuming an  $\epsilon$ -chapman layer extending to 1.5 scale height above hmF2. The topside region above ( $hmF2 + 1.5H$ ) is divided into two exponential decaying regions, the lower one corresponding to heavy ion ( $O^+$ ) as the dominant constituent and the upper one corresponding to lighter ions ( $He^+$  or  $H^+$ ) as the dominant constituent. The two constraints put on the development of topside electron density profile are electron content obtained from satellite beacon experiment and electron density at 1000 Km. obtained by satellite probes.

## 1. INTRODUCTION

Satellite radio beacons are used for position fixing in various applications such as satellite tracking, navigation, geodesy etc. In these systems the elevation angle, range and range rate are measured for position fixing of fixed location on the earth or overland, sea, air or spacecrafts. However, it is well known that the measured range and elevations angle determined using radio transmissions, differ from the true values due to the refraction effects of the intervening troposphere and ionosphere. With increasing demand on the accuracy of position fixing, there is need first to evaluate the errors introduced by ionospheric & tropospheric refraction for proper choice of the beacon frequency and the transmitter-receiver geometry to minimise the refraction effects. Next there is need to develop correction techniques so that from measured values of range and elevation angles, the true values may be computed very quickly. Such methods require three-dimensional ray-tracing of the ray-path from the receiver to the transmitter with appropriate ionospheric and tropospheric inputs. This requires the specification of the refractive index profiles in the troposphere and the ionosphere. In this paper we restrict the ionospheric refraction errors only. In the ionospheric case the input becomes one of specifying the electron density distribution along the ray path. The electron density distribution along the ray path which is slant is not readily available and has to be derived from vertical electron density profiles upto satellite altitudes for a grid of latitudes and longitudes. Thus there is need for modelling of electron density profiles. In low and equatorial latitude region such as the electron density profiles have a strong longitude dependence, particularly, during daytime. This paper is mainly concerned with development of modelling technique for building electron density profiles with application to low latitude region such as the Indian subcontinent. The main requirement for satellite navigation would be that the methods to correct for refraction effects should be fast, using on board minicomputers so that the true range and elevation angle values could be recovered in a matter of minutes. The primary ionospheric inputs could then be either real time data, such as  $f_{oF2}$ , the F2-region critical frequency,  $h'F$ , the minimum F-region virtual height and/or the total electron content. If real time data are not readily available, the predicted  $f_{oF2}$ ,  $h_{mF2}$  or  $M(3000)F2$  factor and the electron content could be used. In a practical situation the inputs may be a combination of real time data and predicted values. The problem then is one of generating a family of electron density profiles at, say, 50 latitude intervals and with local time dependence to represent longitude effects.

## 2. METHODS OF BUILDING ELECTRON DENSITY PROFILES

Several methods have been developed to generate electron density models using  $f_{oF2}$  and  $h_{mF2}$  values. The bottomside profile can be accurately generated because a substantial amount of work has been put into such work and a wealth of bottomside data is available on a global basis over several solar cycles. The analyses show that the bottomside F-region electron density profile may be represented accurately by an  $\alpha$ -Chapman distribution (Rishbeth and Barron 1960, Seddon 1963).

Several empirical worldwide ionospheric models are in use for uses in space communication navigation and tracking and other purposes. These include

- {1} Penn State MK-I Model
- {2} AFCRL Model
- {3} Aerospace Model
- {4} Bent Model

All these models more or less describe the bottomside profile by an  $\alpha$ -Chapman distribution. The  $f_{oF2}$  and  $h_{mF2}$  are specified externally to describe the solar activity and latitude variations. Major differences come in generating the topside electron density distribution. However, these methods are useful mainly for midlatitudes and there is need for models for low latitudes such as the Indian subcontinent.

The method described in this paper is based on the one proposed by Somayajulu et al (1965) for building electron density profiles upto 1000 Km. by making use of the bottomside ionograms and the electron content measurements. Certain improvements are incorporated in the present paper.

The technique of building the electron density profiles is as follows:

### (A) Bottomside Profile

- (i) The first step is to locate the height  $h_{mF2}$  of the F2 - region peak and  $N_{mF2}$  its peak electron density

The peak electron density,  $N_{mF2}$ , can be readily obtained from the  $f_{oF2}$  values, using the relationship,

$$N_{mF2} = 1.24 \times 10^{-2} (f_{oF2})^2 \quad \dots (\text{el/m}^3) \dots (1)$$

where  $f_{oF2}$  is in MHz

To obtain  $h_{mF2}$ , the F2-region height the predicted values of  $M(3000)F2$  from standard "ionospheric data" publications may be used using the Appleton-Beynon formula:

$$h_{mF2} = \frac{1346.92 - 526.40M + 59.825M^2}{MUF(3000)F2} \quad \dots \quad (2)$$

where  $M = M(3000)F2$  factors =  $\frac{1}{f_{oF2}}$

where  $hmF2$  is in Km.

The M-factor itself is derived from  $h'F$  values from the ionograms.

- (ii) It has been shown by Sedden(1963) that the F2-region can be represented by an  $\zeta$ -chapman layer from one-scale height( $Hm$ ) below  $hmF2$  to about  $1.5Hm$  above the peak.  $Hm$  is the value of the scale height at the F2-region peak. Thus

$$N=NmF2 \ ch(z) \quad \begin{cases} -1 \leq z \leq 1.5 \text{ for day} \\ z \leq 1.5 \text{ for night} \end{cases} \quad \dots \quad (3)$$

where  $\frac{zsh-hmF2}{Hm}$  and

$ch(z)$  is the Chapman function given by  $\exp^{-\frac{1}{2}(1-z-e^{-z})}$

From one -scale-height below  $hmF2$ , down to the E-region the profile for daytime is represented by

$$\begin{aligned} N=Nm(E)e^{\frac{h-100}{100}} \quad & Nm(E) \leq N \leq 0.7NmF2 \\ & 1000Km \leq h \leq hmF2 - Hm \end{aligned} \quad \dots \quad (3a)$$

The parameters  $Hm$  and  $s$  are functions of localtime, latitude and solar activity. From analysis of past data from various ionospheric observations the values of  $Hm$  and  $s$  can be predicted for a given set of conditions.

Using equation(3) the profile is extended upto a height of  $1.5 Hm$  above  $hmF2$  and down to a height of  $1.0 Hm$  below  $hmF2$ .

- (iv) The bottomside electron content upto  $hmF2$  is obtained by using the relation

$$Nb=1.31 HmNmF2 \quad \dots \quad \dots \quad (4)$$

where  $Hm$  is the scale height at  $hmF2$

- (v) The value of electron content upto a height of  $1.5 Hm$  above  $hmF2$  is then obtained by integrating equation (3).

#### (B) Topside Profile

- (vi) Above the height ( $hm+1.5Hm$ ), the electron density is assumed to fall off exponentially as

$$N=N_0 e^{-kh} \quad \dots \quad \dots \quad (5)$$

where  $h$  is height measured from the height of ( $hm+1.5Hm$ ) and  $N_0$  is the electron density at this height( $N_0=0.7 Nm$ ).

The major ionic constituent in the topside is O<sup>+</sup> upto 1000Km during the day for solar maximum conditions. However, at night the light ions become important and there is a transition from O<sup>+</sup> to lighter ions as the major ionic constituents below 1000Km. During solar minimum conditions even during day time the O<sup>+</sup> to lighter ion transition occurs below 1000Km. Further the plasma temperature is also height dependent. In order to take into account these effects it is considered necessary to build up the topside profiles using two decay exponents K<sub>1</sub> and K<sub>u</sub>. It is assumed that during solar minimum daytime the transition occurs at a height of 750Km and at night for all conditions at a height of 500Km. Thus the profile is built from h<sub>m</sub>+1.5H<sub>m</sub> to the transition height using an exponent K<sub>1</sub> and above this height upto 1000Km using K<sub>u</sub>.

The value of the exponents K<sub>1</sub> and K<sub>u</sub> are chosen such that the topside electron content obtained from the model profiles matches the average electron content data appropriate for the location. A further constraint used is that the electron density at 1000Km from the model profile should also match the average value of N at 1000Km observed by satellite probes. Fig. 1 illustrates the details of this technique.

### 3. RESULTS AND DISCUSSION

Using the technique described in the previous section, electron density profiles have been built upto 1000Km. altitudes. The profiles have been built for the locations of Delhi, Ahmedabad, Calcutta, Hyderabad and Kodaikanal covering a large latitude range to determine the accuracy of topside profiles. These are compared with the available topside profiles from the Alouette I and Alouette II satellites.

The model electron density profiles built for summer and winter day time and for minimum and maximum solar conditions for the stations Delhi, Ahmedabad, Calcutta, Hyderabad and Kodaikanal covering a geomagnetic latitude range from 20°N to about 1°N are shown in figures (2), (3), (4) and (5).

The values of K<sub>1</sub> and K<sub>u</sub> for solar minimum condition and K for solar maximum condition determined to give the best match are summarised in tables I, II, III & IV. It may be noted that the K<sub>1</sub> for solar minimum and K for solar maximum conditions mostly decreases as the geomagnetic latitude decreases.

Recently Bent et al (1971) described a method of building an ionospheric model profile upto 1000Km. using the topside and bottom-side profiles covering almost one solar cycle. The model profile can be predicted for a particular time, location and solar activity.

The present technique differs from Bent's model in the following ways:

- i) The profile from h<sub>m</sub> to h<sub>m</sub> + 1.5 H<sub>m</sub> based on the work of Seddon is built using -chapman layer making use of bottomside profile while in Bent's model he uses a biparabolic model.

- ii) Bent divides the topside exponential profile into three arbitrary height ranges and adjusts the decay constant K to match the observed profile. In our work the topside region is divided on physical grounds into two altitude ranges, the lower one corresponding to heavy ion( $O^+$ ) as the dominant constituent and the upper one corresponding to lighter ions as the dominant constituents. The transition height between the lower and the upper regions is chosen based on the experimental data on the transition altitudes from  $O^+$  to lighter ions as discussed earlier.
- iii) In addition to foF2 data we also have used electron content data as a constraint on the profile.
- iv) Another important difference is that in Bent's model, he divides the whole latitude range into 3 groups,  $0^\circ$  to  $30^\circ$ ,  $30^\circ$  to  $60^\circ$  and  $60^\circ$  to  $90^\circ$ . It is well known that in the  $0^\circ$  to  $30^\circ$  latitude range there is a strong latitudinal dependence of ionosphere due to the presence of equatorial anamoly. In our model the latitudinal dependence at low latitudes is explicitly introduced in the profile building.

According to Bent's model for low solar activity (flux value 120) and for ( $0^\circ$  to  $30^\circ$ )N latitude region, the decay constants for the lower, middle and upper portion of exponential profiles are:

$$K_l = 7.5 \times 10^{-8} \text{ cm}, K_m = 7.3 \times 10^{-8} \text{ cm}, K_u = 4 \times 10^{-8} \text{ cm}$$

while from our model we obtain for low solar activity during summer daytime:

$$K_l = 8.23 \times 10^{-8} \text{ cm}, K_u = 3.42 \times 10^{-8} \text{ cm}$$

and for low solar activity during winter daytime:

$$K_l = 9.19 \times 10^{-8} \text{ cm}, K_u = 3.43 \times 10^{-8} \text{ cm}$$

Thus our model is expected to be more accurate for application in the tropical regions.

It is considered that the technique described in this paper enables one to build electron density profiles when the ionospheric parameters such as foF2, h'F, and electron content are available as inputs. Further work on refinement of the modelling technique described here is in progress.

#### 4. EVALUATION OF IONOSPHERIC ERRORS IN RANGE AND ELEVATION ANGLE

Using the profiles built as described above, the range and elevation angle errors at various frequencies (20MHz-5GHz) and for different zenith angles ( $10^\circ$ - $80^\circ$ ) using the 3-dimensional ray tracing program developed based on a modified version of Jones' Ray tracing program have been computed. Some sample calculations for Delhi, Ahmedabad, Calcutta, Hyderabad, Kodaikanal are shown in figures (6), (7), (8) and (9).

**REFERENCES:**

1. Bauer, S.J.  
J. Atmospheric Sci., (1962), 19, 17-19
2. R.B. Bent, Sigrid K. Llewellyn and P.E. Schmid  
Space Research XII, (North-Holland Publ. Co.,  
Amsterdam, 1972).
3. R.M. Jones, ESSA Technical Report IER, 17-ITSA 17, 1966
4. R.M. Jones, ESSA Research Laboratories Technical  
Memorandum ITS-134, 1968
5. J.C. Seddon, J. Geophys. Res., 68, 1339(1963).
6. Y.V. Somayajulu, Tuhi Ram Tyagi and V.P. Bhatnagar  
Space Research V, ed. P. Muller(North-Holland Pub., Co.,  
Amsterdam, (1965) 641.

**T A B L E - I**

**K VALUES FOR SOLAR MINIMUM SUMMER DAYTIME**

Station	Geomagnetic Latitude	K <sub>1</sub> (cm)	K <sub>u</sub> (cm)
Delhi	19°11'N	8.23x10 <sup>-8</sup>	3.42x10 <sup>-8</sup>
Ahmedabad	14°01'N	7.34x10 <sup>-8</sup>	3.39x10 <sup>-8</sup>
Hyderabad	07°39'N	6.58x10 <sup>-8</sup>	3.35x10 <sup>-8</sup>
Kodaikanal	0°44'N	7.30x10 <sup>-8</sup>	3.4x10 <sup>-8</sup>

**T A B L E - II**

**K VALUES FOR SOLAR MINIMUM WINTER DAYTIME**

Station	Geomagnetic Latitude	K <sub>1</sub> (cm)	K <sub>u</sub> (cm)
Delhi	19°11'N	9.32x10 <sup>-8</sup>	3.45x10 <sup>-8</sup>
Ahmedabad	14°01'N	8.10x10 <sup>-8</sup>	3.4x10 <sup>-8</sup>
Hyderabad	07°39'N	7.86x10 <sup>-8</sup>	3.38x10 <sup>-8</sup>
Kodaikanal	0°44'N	7.44x10 <sup>-8</sup>	3.35 x10 <sup>-8</sup>

TABLE - III

## K VALUES FOR SOLAR MAXIMUM SUMMER DAYTIME

Station	Geomagnetic Latitude	K(Cm.)
Delhi	19°11'N	6.41x10 <sup>-8</sup>
Ahmedabad	14°01'N	6.35x10 <sup>-8</sup>
Calcutta	12°15'N	7.73x10 <sup>-8</sup>
Hyderabad	07°39'N	6.19x10 <sup>-8</sup>
Kodaikanal	0°44'N	6.19x10 <sup>-8</sup>

TABLE - IV

## K VALUES FOR SOLAR MAXIMUM WINTER DAYTIME

Station	Geomagnetic Latitude	K(Cm.)
Delhi	19°11'N	6.76x10 <sup>-8</sup>
Ahmedabad	14°01'N	6.67x10 <sup>-8</sup>
Calcutta	12°15'N	6.54x10 <sup>-8</sup>
Hyderabad	07°39'N	6.47x10 <sup>-8</sup>
Kodaikanal	0°44'N	6.25x10 <sup>-8</sup>

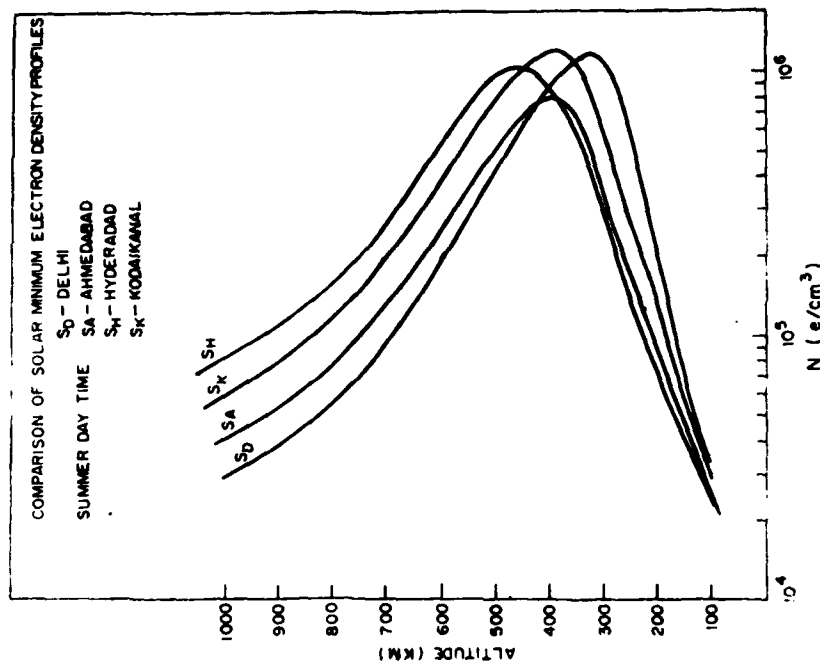


Fig.2 Electron density profiles for  
 Solar minimum summer daytime.

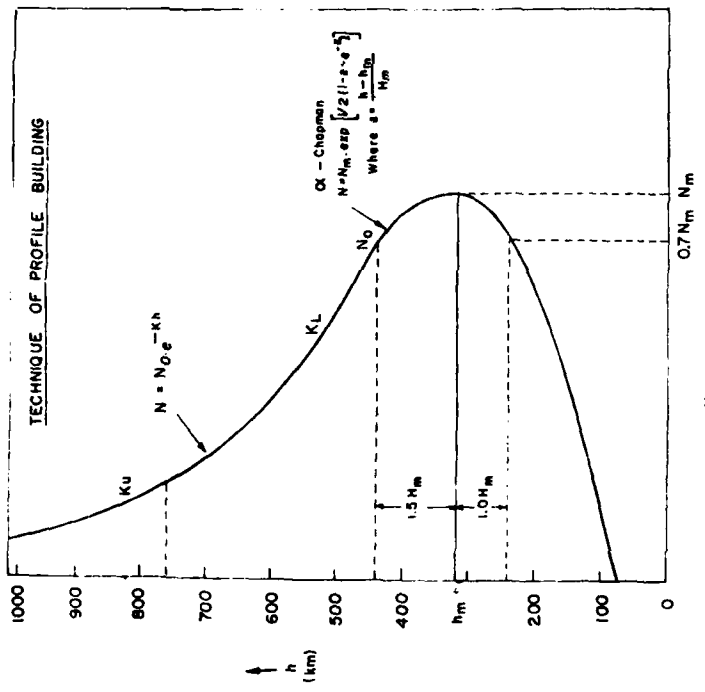


Fig.1 Technique of profile building.

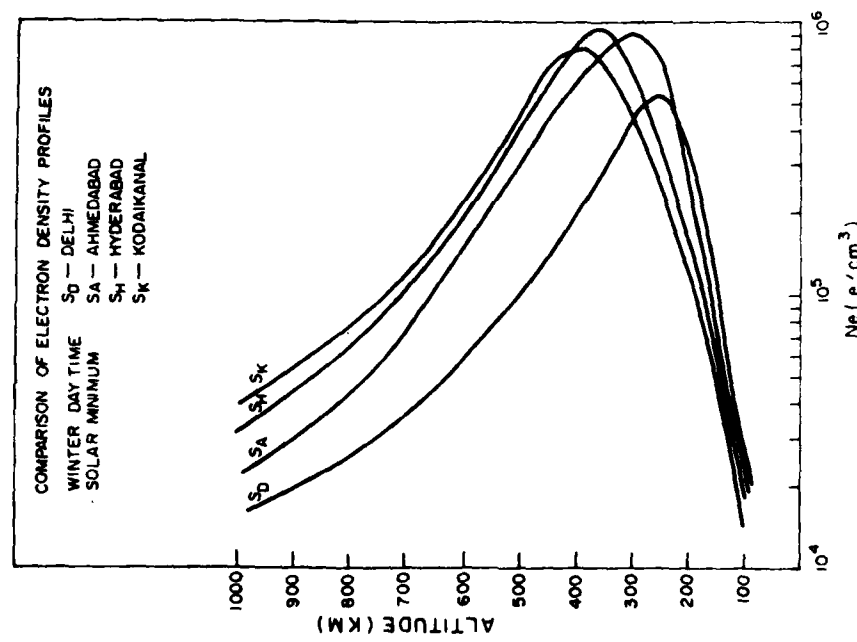


Fig.3 Electron density profiles for solar minimum winter daytime.

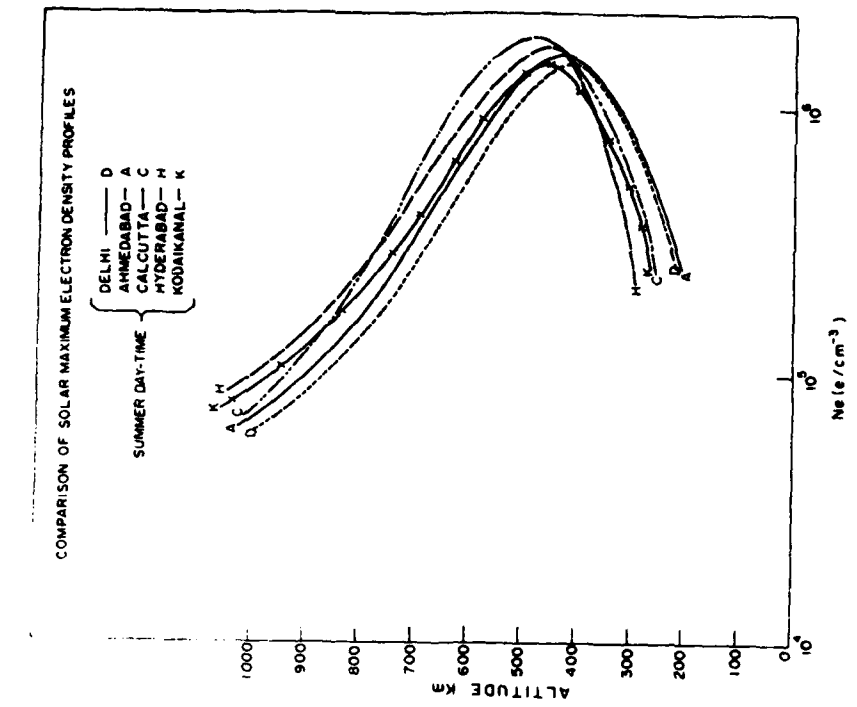


Fig.4 Electron density profiles for solar maximum summer daytime.

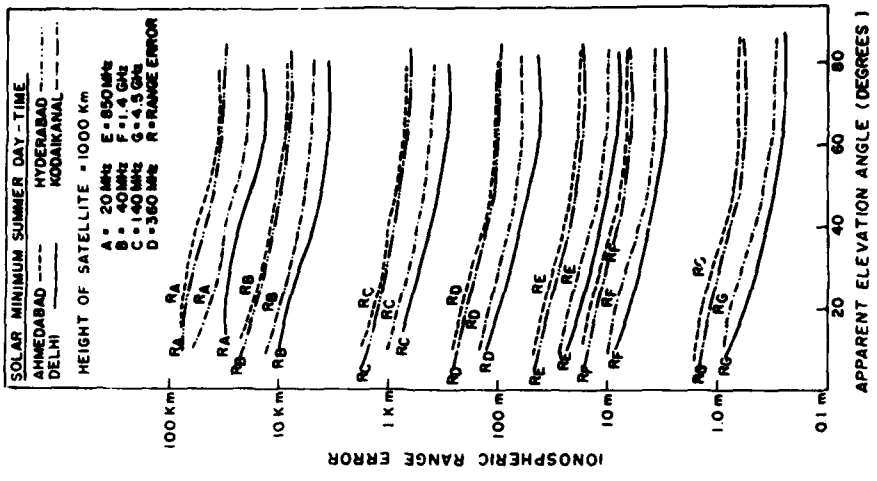
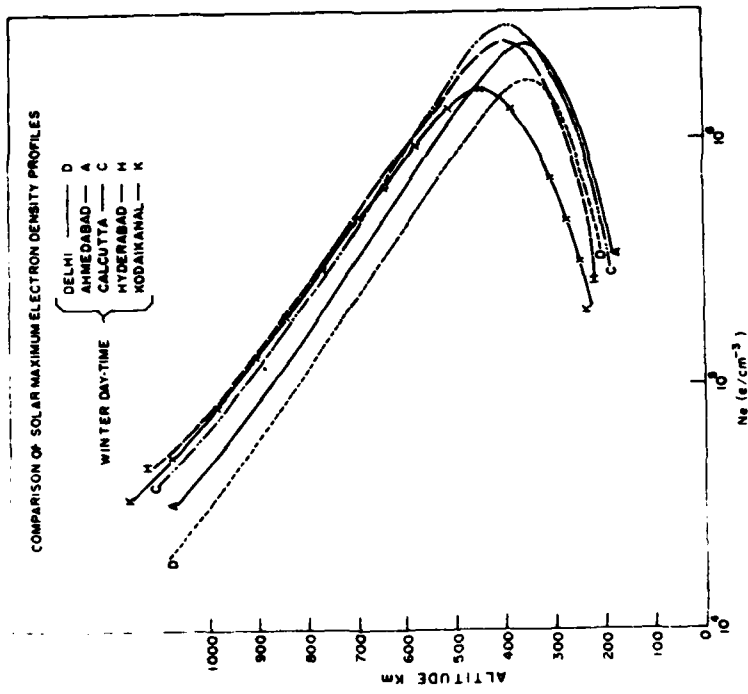
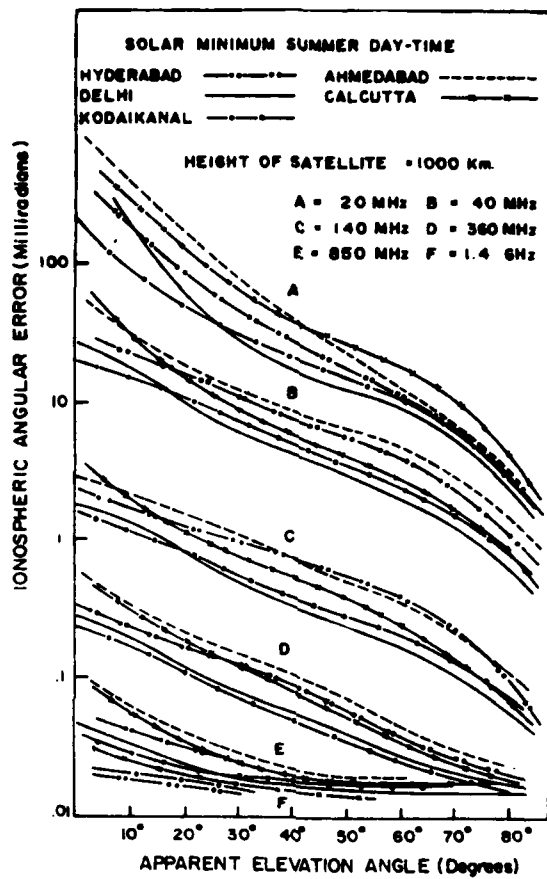


Fig.6 Ionospheric range errors for solar minimum summer daytime.





**Fig.7** Ionospheric angular errors for solar minimum summer daytime.

## MONITORING OF THE TROPOSPHERE USING LOW ELEVATION SATELLITE RADIO BEACONS

Y.V. Somayajulu, Tuhi Ram Tyagi & A.B. Ghosh  
Space Research Section, Radio Science Division  
National Physical Laboratory, New Delhi-110012

**Abstract:** In this paper some effects of characteristic enhancements and/or fluctuations of the amplitude of the satellite radio beacon transmissions are described. It is convincingly shown that these effects are of tropospheric origin. The characteristics and the detailed statistics of the occurrence of these effects is described based on the 40-41 MHz transmissions of the satellite INTASAT recorded for the period Nov. 1974 to March 1976.

### 1. INTRODUCTION

Anomalous enhancements of the signal amplitude of the radio beacons received from the satellites at low elevations have been reported in literature. MASS and HOUNINER (1967) observed signal amplitude enhancements on two successive satellite passes and concluded that the effect resulted from the multipath propagation caused by field-aligned ledges. On the other hand, HARTMANN (1967, 1969) reported sudden increases in signal amplitude on a considerable number of occasions when the satellite was at low elevation angles in the range 2-28°. Normally at low elevation angles the signal strength was 2-3 dB above the noise level. However, when the effects occurred, the field strength suddenly increased upto 15 dB shortly after satellite rise or shortly before satellite set. The enhancements also showed amplitude fluctuations with quasi-periodicity ranging between 0.3 to 8 Hz and the durations of 3-20 seconds. HARTMANN observed that the occurrence of these effects coincided with strong gradients of the tropospheric refractive index and showed that these could be explained theoretically if the troposphere is considered to act like an echelle grating causing diffraction of the signal. Such effects sometimes occurred upto three times in succession in the same pass. KERSELEY and EDWARDS (1970) reported some characteristic low angle enhancements of signal strength, which they called 'tail bursts' and concluded that they appeared to be ionospheric in nature resulting from multipath propagation.

In this paper we first present the results of a co-ordinated set of observations including satellite radio beacons carried out during a large tropospheric event and convincingly demonstrate the feasibility of detection of tropospheric changes using the satellite radio beacon technique and then present the details of

all the events recognised using the 40-41 MHz Faraday fading records from the 'INTASAT' transmissions obtained at Delhi ( $28.63^{\circ}\text{N}$ ,  $77.22^{\circ}\text{E}$ ) during the period November, 1974 to March, 1976.

## 2. DESCRIPTION OF THE COORDINATED PROGRAMME OF OBSERVATIONS FOR MONITORING THE TROPOSPHERE

A coordinated programme of multi-technique monitoring of the troposphere has been started recently at the National Physical Laboratory (NPL), New Delhi. The techniques currently employed are:

- (i) radio beacon signals received on 40 and 41 MHz frequencies from the orbiting satellite INTASAT (1450 Km nominal circular, sun-synchronous orbit);
- (ii) acoustic sounding radar (SODAR) located in NPL; and
- (iii) a line-of-sight (LOS) microwave link operating on a frequency of 7.2 GHz between Delhi and Sonepat (50 km. path)

In addition, meteorological data from the radiosonde measurements regularly carried out by the India Meteorological Department is also available. The satellite radio beacon technique provides a measure of the total or integrated effect of the entire troposphere and the ionosphere. Techniques (ii) and (iii) provide monitoring of the troposphere upto heights of about 500 m. The tropospheric effects dominate over the ionospheric effects for satellite elevation angles less than  $15^{\circ}$ . Therefore the satellite radio beacon recordings are extended to cover the entire pass almost from horizon-to-horizon in order to include the ionospheric as well as tropospheric effects. INTASAT is a sun-synchronous satellite and the satellite passes over the observing station around the same diurnal hour once in the forenoon and once in the late evening. The pass-times for Delhi are around 08-10 hours and 20-22 hours local time. These times are convenient for tropospheric studies as the changes in troposphere are frequently observed following the rising and setting of the Sun.

In order to distinguish and demonstrate the tropospheric effects, a typical example, showing the ionospheric effects of normal satellite passes is exhibited in Fig. 1. Fig. 1(a) shows the record of 41 MHz signal received on 15th Dec., 1974. This is typical of normal amplitude variation at the end of a record after the Faraday fadings have lost their identity and the signal dropped to below the noise level. Fig. 1(b) shows the satellite spin effect super-imposed over the normal Faraday fading.

## 3. DESCRIPTION OF THE TROPOSPHERIC EVENT OF DEC. 19-21, 1974

A rather unusual and strong tropospheric event occurred during the period 19-21 December, 1974. SODAR gave the first warning that a major disturbance was underway. The SODAR happened to be in round-the-clock operation during the period of growth of the disturbance.

During the day all through the period of disturbance the SODAR facsimile record showed the usual formation of the thermal plume structure. Normally during nights, laminated stratified stable structure characterise the records. However, a strong wind shear appeared on the night of 17-18 December at a height about 300 meters and developed into a large wave motion, by the night of December 19-20 December, super-imposed on the laminated stable structure. The wave motion broke into ripples during the later part of the night (Mitra et al, 1976). Though the SODAR provides information on the general structure of the troposphere upto about 500 m altitude its usefulness is limited only to night hours. The evidence of strong tropospheric activity was also recorded by the 7.2 GHz LOS link signal intensity. The microwave-link signal variations are available on continuous basis and are directly relevant for comparison with satellite beacon observations reported here.

The microwave-link signal strength recordings are shown in Fig.2. Under normal tropospheric conditions the microwave signal strength is steady as shown in Fig. 2(a). When there are abnormal tropospheric conditions such as high gradients, the signal strength decreases by several db as shown in Fig2(b). (Mitra et al, 1976).

The SODAR observations during December 19-21, showed that the general inversion structure formed during the night has been disturbed on several occasions. The extent of this disturbance determines the extent of clear atmospheric turbulence. On December 20, when the effect was largest on the satellite beacon and the LOS-microwave-link signal intensities, the SODAR data showed plumes revealing that the troposphere thermal structure was broken into oscillations. ( Mitra et al, 1976).

Radiosonde data from India Meteorological Observatory, Delhi, were used to derive the radio refractivity profiles for December 19 and 20, 1974, for 0430 and 1630 hrs.(Mitra et al, 76) and are shown in Fig. 3. It may be noted that on both these days the initial gradient during nighttime was about -130 N units/Km which is high in comparison to normal (daytime) gradient which is usually about -40N/Km.

#### 4. RESULTS OF THE SATELLITE RADIO BEACON MONITORING OF THE TROPOSPHERIC EVENT OF DECEMBER 19-21, 1974.

The amplitude of the 40 and 41 MHz radio beacons from the INTASAT orbiting satellite were being regularly recorded at the National Physical Laboratory, New Delhi, since its launch on 14 November, 1974. Several cases of amplitude enhancements and/or fluctuations have been observed and examples are shown in Figs. 4 and 5. The recordings made on the morning hours of December 14 and 16, 1974 show abrupt amplitude fluctuations for about 40 secs. (fig. 4a, 4b). It may be noted that on December 14, the fluctuations occurred in the beginning, while on Dec. 16, these occurred towards the end of the record, thus showing that the effects may occur at low elevation angles both towards north as well as south of the observing station (Somayajulu et al,1975),

The more interesting examples recorded on December 19, 20 and 21 are shown in Figs. 5a, 5b, and 5c. In all these cases the amplitude enhancements occurred twice in succession and heavy fluctuations are superimposed over them. We have seen earlier from Fig. 1(b) that the spin introduces modulation on the amplitude. One must, therefore, consider these cases carefully. The point under consideration is whether the amplitude enhancements have really occurred twice in each case or a single effect is split into two due to spin effect. On careful examination one notes the following points: Firstly, the time period of the enhancement effects is different from the spin period. Secondly, the enhancement disappears abruptly at least in three cases while the effect of the spin is more gradual. Therefore, we are led to the conclusion that these enhancements in fact have occurred twice in each case.

The amplitude effect on 20th December was largest of all the three cases described above. Further it may be interesting to note that the time of this effect coincided with the maximum depression observed on microwave link record shown in Fig. 2(b). On SODAR the atmosphere was found to be broken into oscillations on this night.

#### 4.1 ORIGIN OF AMPLITUDE EFFECTS DURING THE EVENT OF DEC. 19-21'74

KERSLEY and EDWARDS(1970) noted that a feature of the records containing 'tail bursts' was an irregular variation in the Faraday fading period throughout the pass indicating strong horizontal gradients in ionisation. However, in the present case the records containing amplitude enhancement and/or fluctuations do not show the fluctuations in Faraday fading periods throughout the pass, though in some case few fades did show fluctuations in the fading period. Secondly, no 'tail burst' was observed to the north of the station by KERSLEY and EDWARDS while in our case the amplitude effects have been noted both towards north and south for low elevation angles. As the present data is limited to four months only no seasonal effects can be considered. The above considerations indicate that these effects could be of tropospheric origin. Further, in general, these effects are only rarely observed. However during the period 14-21 December, 1974 which was meteorologically active such effects were observed on 5 out of 8 days. Moreover, the effects on 20th December which were the largest coincided with the peak of the effects on microwave link. The SODAR observations also showed that on 20th December, 1974 the atmosphere was broken into oscillations. Also, the tropospheric refractivity profiles showed very large initial refractivity gradients. Therefore, it may be concluded that these effects are of tropospheric origin. This large tropospheric event lasted from 14th to 21st December, 1974 and the growth and decay of the disturbance through the various techniques is given in Fig. 6. In this representation the day is used as one block and night as another. The effects noted on satellite radio beacons are shown at corresponding hour of the day. The correspondence between the difference observations is obvious. It appears

that the disturbance maximised around 20th of December, 1974. An important point to note is while the disturbance lasted for a week the effects were strong only during nighttime conditions, during the day, they were subdued. This was the case for radio refractivity, for microwave propagation characteristics, for SODAR characteristics and for the satellite beacon transmissions. This also seems from this diagram that the satellite beacon technique is a little more sensitive to such disturbances in comparison to other techniques used. And hence it may be stated now that the satellite radio beacon amplitude recordings can be used to monitor the tropospheric events. The statistical morphology of these effects is given in the next section.

#### 5. STATISTICAL MORPHOLOGY OF TROPOSPHERIC EFFECTS MONITORED USING 40-41 MHz INTASAT TRANSMISSIONS DURING THE PERIOD NOVEMBER'74 TO MARCH 1976

Apart from the strong tropospheric event on 19-21 December'74, such effects were observed on several other occasions. During the period November 1974 to March 1976 about 45 cases were identified. The effects were more towards the north than towards south. However, this inference could be misleading because the satellite INTASAT crosses Delhi in the direction south to north in the evenings and north to south in the mornings. It is shown in the previous section that the tropospheric disturbances occur more during the nights than during days. Because of the manual operation the effects occurring shortly after the rise of the satellite are likely to be missed. Therefore there is more weightage for the events occurring towards north than towards south. Elevation angles were calculated for all the cases identified so far. These are summarised in Table 1. It may be seen from the table that most of these cases occurred when the elevation angle was within  $10^{\circ}$ . This is in agreement with the expectation that tropospheric effects dominate the ionospheric effects at low elevation angles.

The occurrence of these effects seems to be quite random and no seasonal effect can be identified except that the cases were very few during the months of April to June.

The recordings with INTASAT are made with fixed antenna system and so the sensitivity at low elevation angles is poor. Therefore only large tropospheric events can be recorded. If the system sensitivity can be increased by using an antenna which can follow the satellite, even the weaker events can be monitored. The recordings from orbiting satellites are also limited in diurnal coverage as only 2-4 passes can be recorded per day. Continuous coverage is possible if a geostationary satellite at a low elevation angle can be used. A 140 MHz phase lock receiving system was set up at Gauhati to record ATS-6 transmissions at about  $20^{\circ}$  elevation on a continuous basis. The results from this study will be presented elsewhere.

REFERENCES

- |   |      |   |
|---|------|---|
| Hartmann, G.  | 1967 | "Die Amplitudenregistrierungen des Satelliten Explorer 22, Unter besonderer Berücksichtigung der Effekte, die bei Mitteilungen aus dem Max-Planck Institut für Aeronomie, Rep. No. 31(I). |
| Hartmann, G.  | 1969 | J. Atmosph. Terr. Phys., 31, 663  |
| Kersley, L. and Edwards, KG.  | 1970 | "A low angle propagation effect of Satellite transmissions" - Proceedings of the symposium on the Future Application of Satellite Beacon Experiments 18-1, Lindau, W. Germany.            |
| Mass, J., Houminer, Z.  | 1967 | J. Geophys. Res., 72, 1, 243  |
| Mitra A.P., Somayajulu, Y.V., Singal S.P., Mazumdar, S.C., Tyagi, T.R., Reddy B.M., Aggarwal, SK, Gera B.S., Ghosh A.B. and Sarkar S.K. | 1976 | "Tropospheric Disturbance of Dec. 17-21, 1974 and its effect on microwave propagation" Centre of Research on Troposphere, NPL, New Delhi, India<br>Sci. Rep. No. 22                       |
| Somayajulu Y.V., Tyagi T.R. and Ghosh A.B.  | 1975 | J. Atmosph. Terr. Phys., 37, 1603   |

T A B L E - 1

Time period - November 1974 to March 1976				
Total number of cases identified -- 44				
Effects north of Station -- 38				
Range of elevation angle -- ( $0^{\circ}$ - $5^{\circ}$ ) ( $6^{\circ}$ - $10^{\circ}$ ) $10^{\circ}$				
Number of cases	--	17	25	2

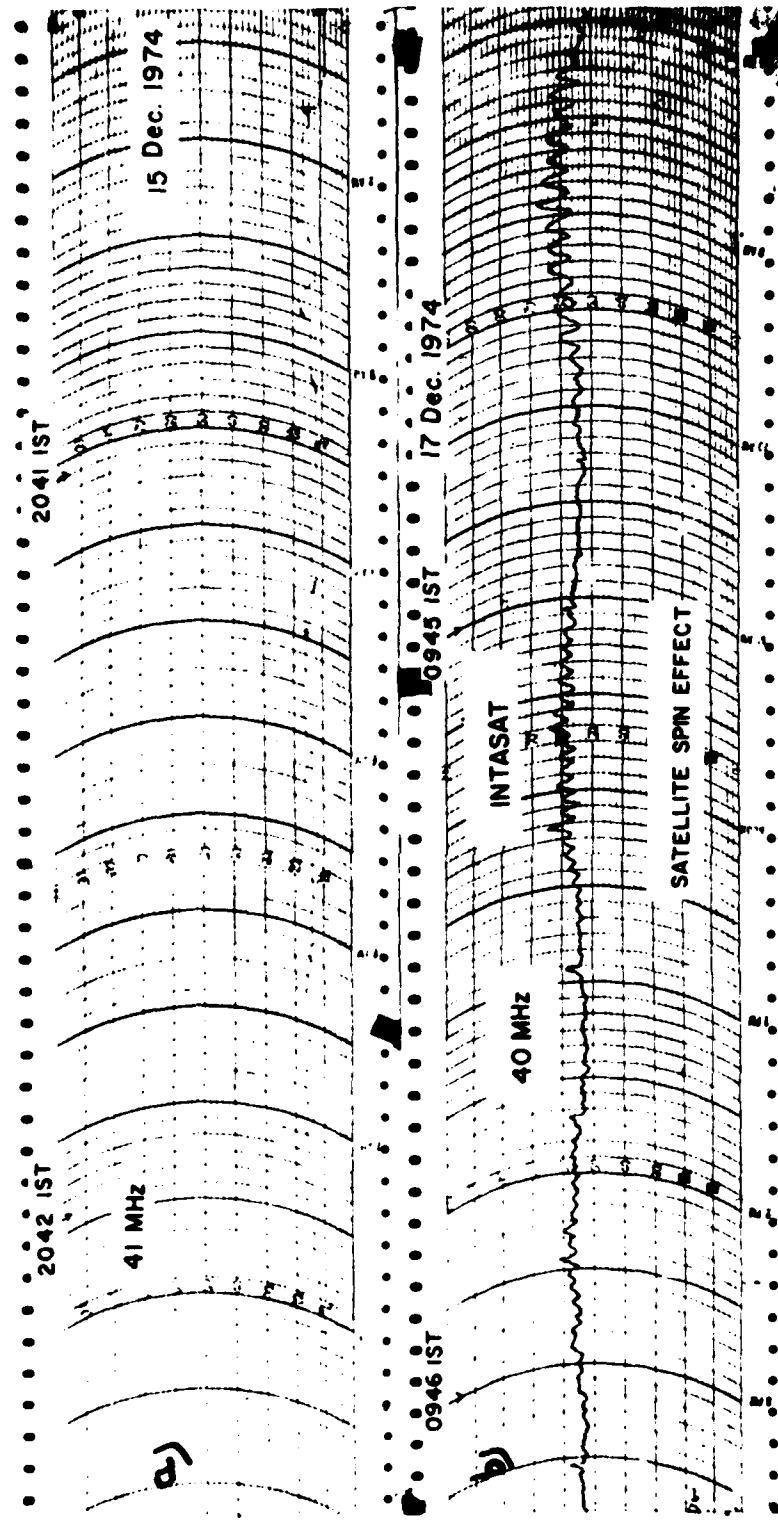


Fig.1(a) A typical satellite beacon record showing normal amplitude variation at the end after the Faraday fades lost their identity.  
 (b) A typical Faraday fading record. The spin of the satellite is clearly evident.

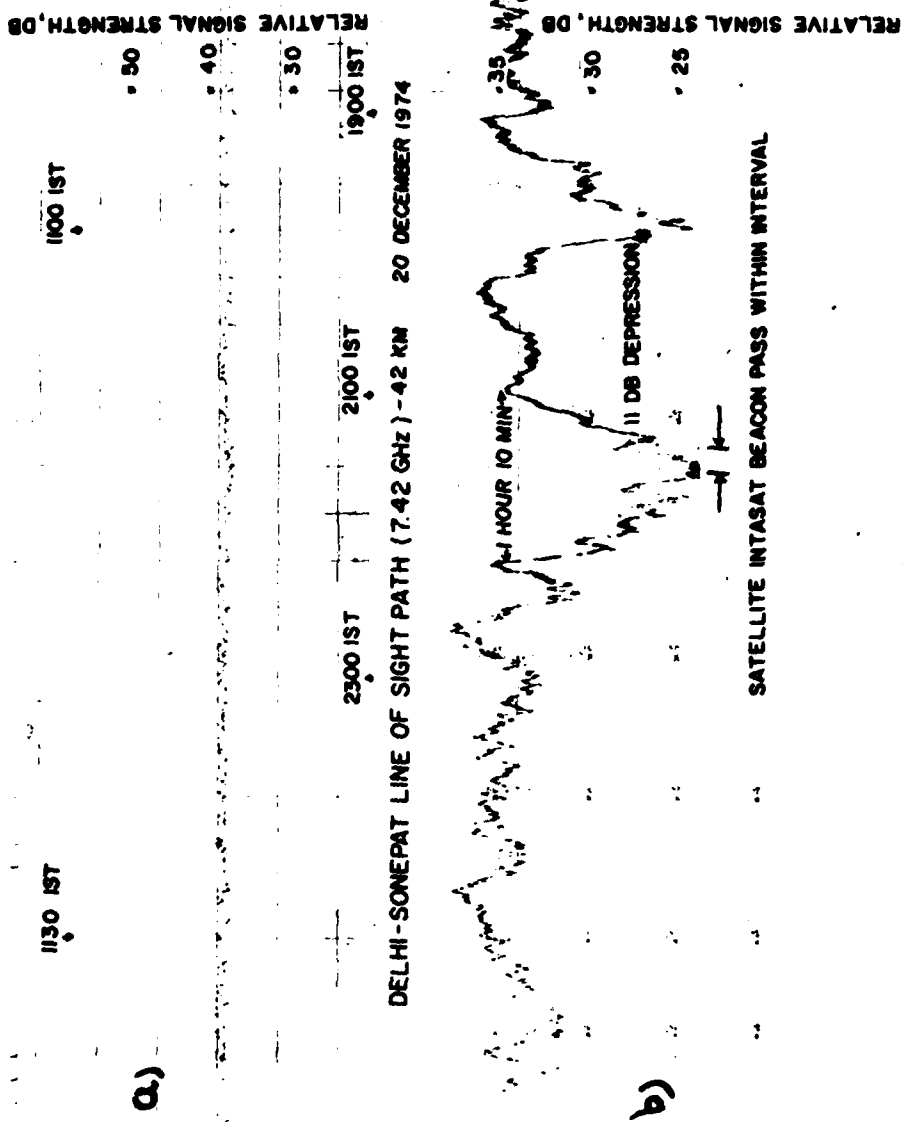
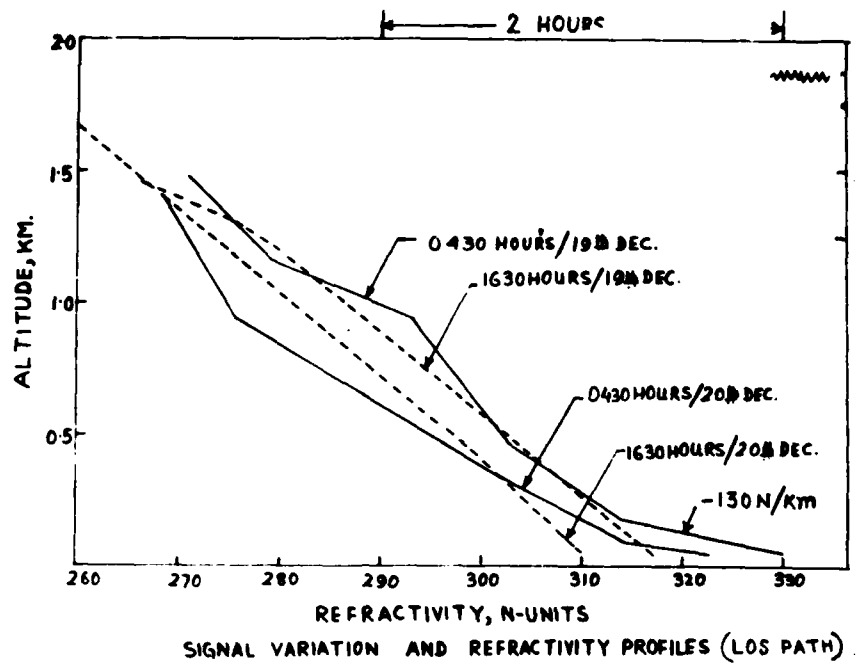


Fig. 2 (a) 7.42 GHz normal daytime record for December 20, 1974 (LOS)  
 Fig. 2 (b) 7.42 GHz nighttime LOS record on December 20, 1974  
 at NPL New Delhi showing 11 db depression around 21  
 to 22 hrs. IST; the duration of INTASAT amplitude  
 record made on the same day is also marked.



**Fig.3** Tropospheric refractivity profiles showing very high initial gradients during night on 19th and 20th Dec. '74

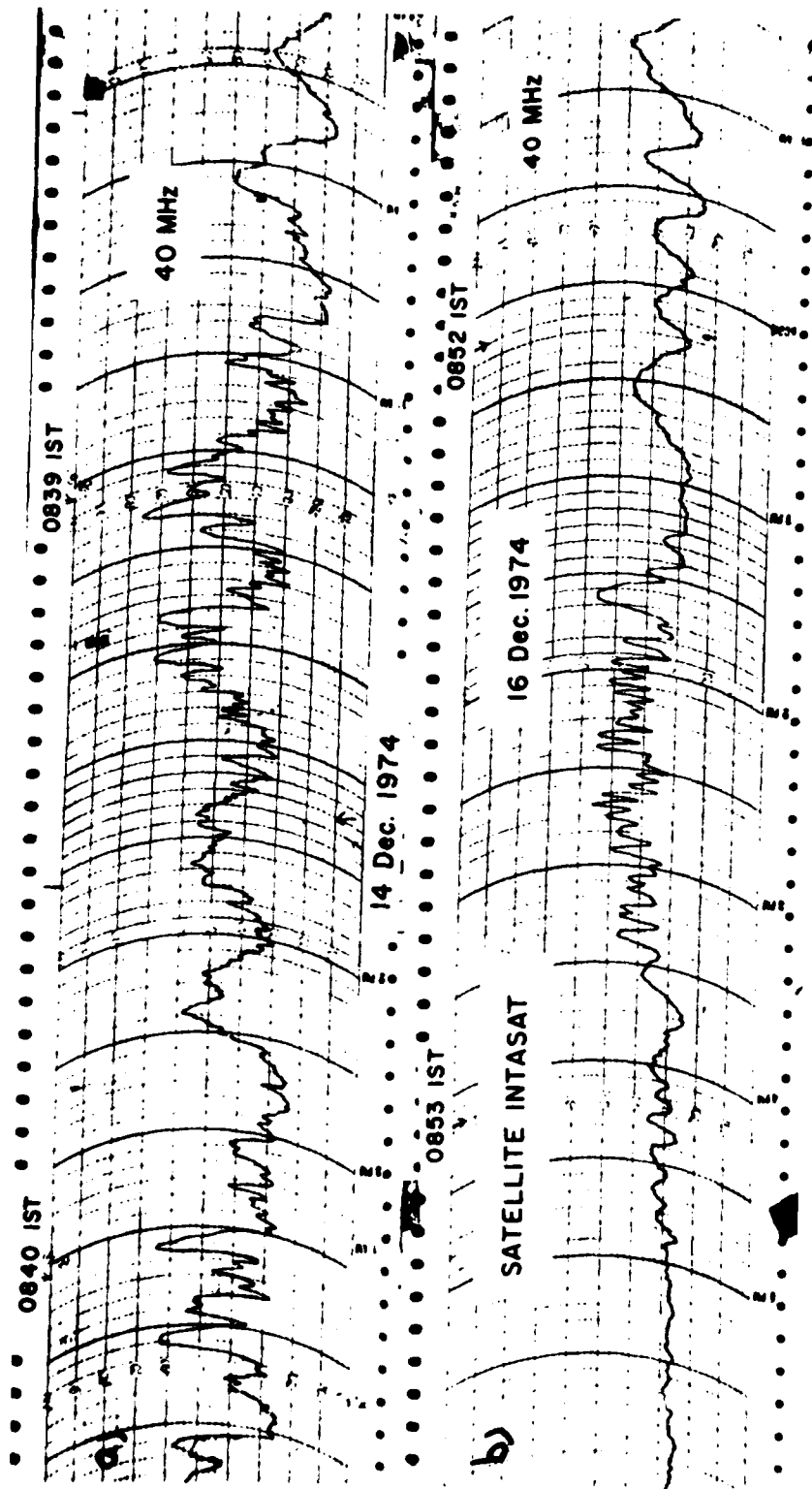


FIG.4 Characteristic amplitude enhancements/fluctuations can occur both towards the beginning (a) and end (b) of the records during low elevation angles.

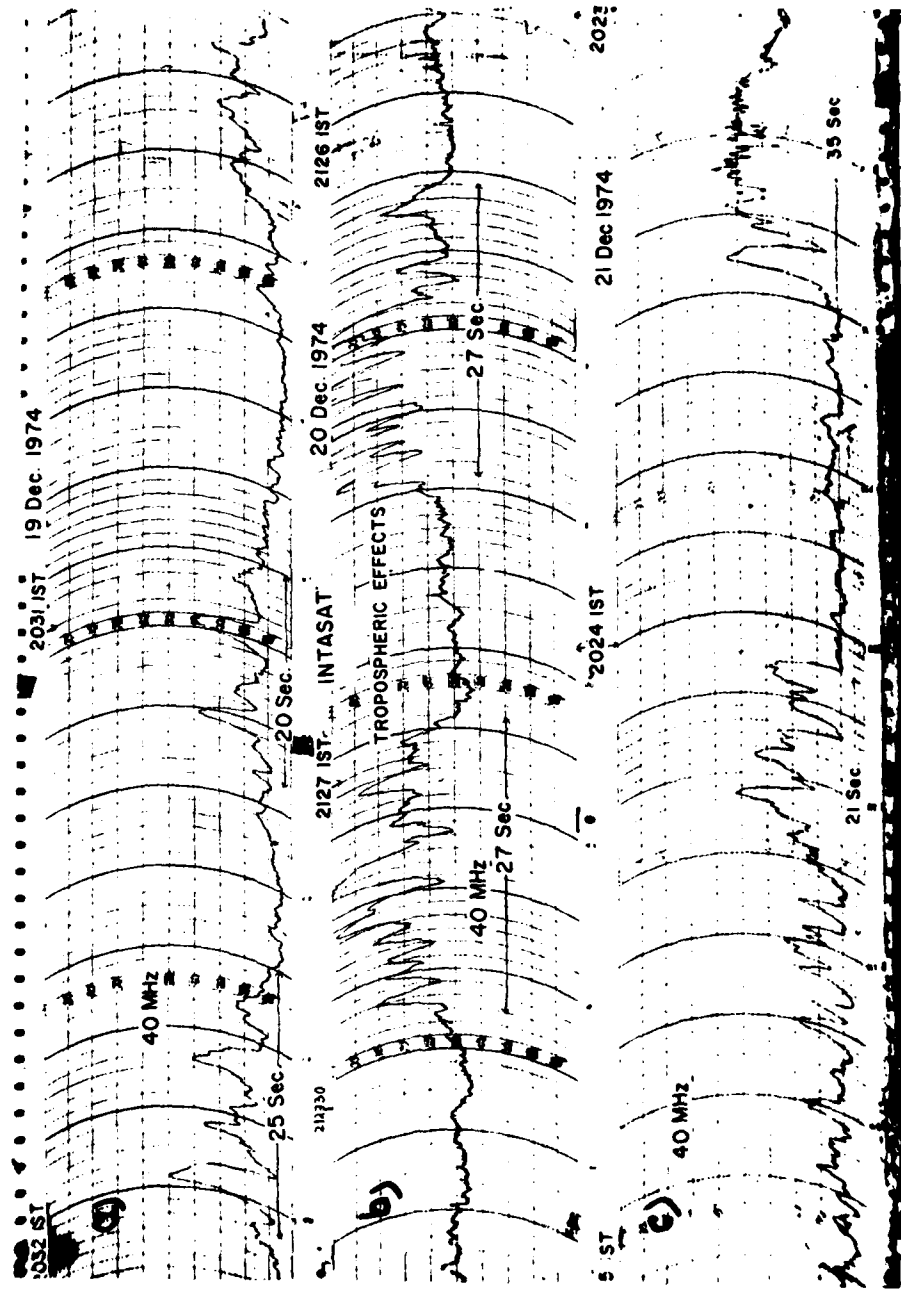
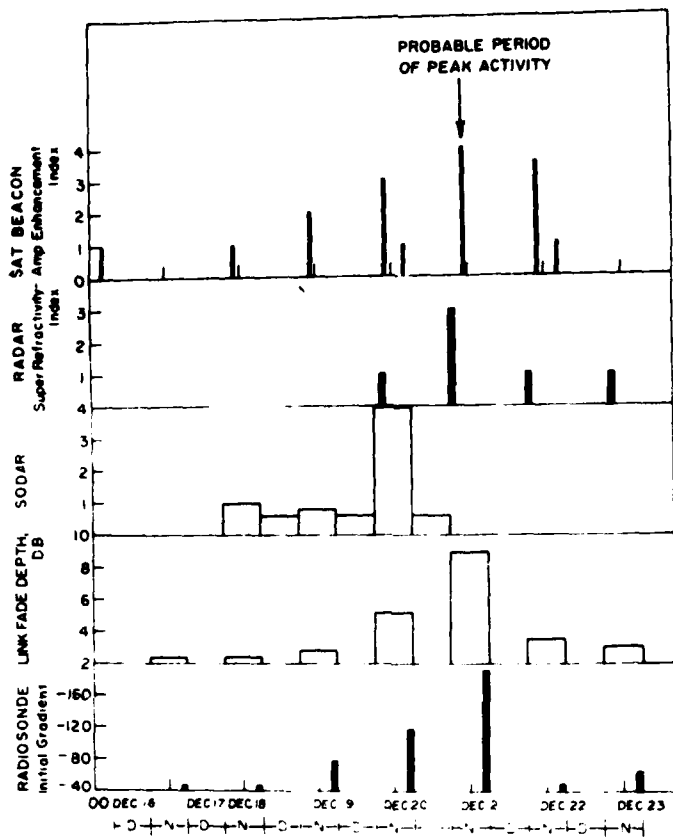


FIG. 5  
a,b,c      40 MHz amplitude recording from the satellite INTASAT  
showing that amplitude enhancements have occurred  
twice in succession on 19th, 20th and 21st December '74.



**Fig.6** Growth and decay of the tropospheric disturbance as seen through different techniques: SODAR, RADAR, Satellite Radio Beacon, Radiosondes and Microwave Radio Propagation characteristics.

## TROPOSPHERIC EFFECTS ON SATELLITE-EARTH LINKS

Claus Fengler

Department of Electrical Engineering

McGill University, Montreal, Quebec

**ABSTRACT** Effects in satellite-earth links in the VHF and UHF range caused by the troposphere are considered. It is found that these effects occur in particular at weather situations which are associated with ground inversions, cold fronts, and elevated discontinuities.

### 1. INTRODUCTION

In ionospheric research satellite-earth links are used to study the structure of the ionosphere. But not only effects due to the ionosphere were recorded on these links but also effects caused by the troposphere. Very long periodic fadings (5-30 min) were observed at the 136 MHz and 400 MHz transmission of stationary satellites which were not related to ionospheric activity (T.J. Elkins; M.D. Papagiannis; J. Aarons, 1967). G.K. Hartmann (1969) found satellite rise effects (SRE) and satellite set effects (SSE) at 20 MHz, 40 MHz, 136 MHz, and 400 MHz which are the result of diffraction of the radio waves by structures within the troposphere. Satellite radio beacons are used at 40 MHz to monitor the troposphere (Y.V. Somayajulu; Tuhi Ram Tyagi; A.B. Ghosh, 1976). Amplitude and phase fluctuations caused by the troposphere were observed at 140 MHz and 360 MHz (W. Degenhardt; G.K. Hartmann, 1967). These results show that the troposphere cannot be approximated for this type of links as homogeneous medium. In order to find the specific tropospheric structures influencing these links other observations at 136 MHz and 35 MHz were evaluated in respect to the tropospheric structure existing at the time of observation.

### 2. EVALUATION OF 136 MHz AND 35 GHz DATA

For more than 5000 cases the difference between observed and calculated rise time of orbiting satellites was analysed by determining the beginning of the audibility of the 136 MHz transmission (G. Fengler, 1971). The result of the analysis shows in 13.2% of all cases an anticipation of the audibility of more than 30 sec (in 4.5%) or a delay of more than 60 sec (in 8.7%) occur. These very strong effects were correlated with the simultaneously existing tropospheric structure. It was found that anticipation effects were related to situations with ground inversions and cold fronts whereas the delay effects were related to situations with strong elevated discontinuities.

A similar investigation was performed for 35 GHz radiation of the sun playing the part of a satellite. The attenuation of this radiation is fairly good correlated (depending on elevation angle) with the absolute humidity if cases with precipitation are excluded. (E.E. Altshuler; V.J. Falcone, Jr.; K.N. Wulfsberg, 1968; and L.E. Telford; E.E. Altshuler, 1975). The evaluation of 230 cases with 5° elevation angle yields that 20% of all cases have a large derivation from the regression line. (Fig.1). It was found that 77% of these runaways with larger attenuation related to the absolute humidity were in these cases when the rays from the sun pass through cold fronts. The runaways (23%) with a smaller attenuation related to the absolute humidity were associated with strong high pressure areas, situations which have a tendency to produce pronounced elevated discontinuities (Fig.2).

### 3. THE CORRESPONDING TROPOSPHERIC STRUCTURE

The correlation of the 136 MHz and the 35 GHz data with simultaneously existing tropospheric structure yields the common result that cold fronts and strong elevated discontinuities produce a strong effect. The profile of the refractive index of a cold front and the following region of cold air is equivalent to the profile of ground inversions (Fig.3) which produce good ducting properties for VHF and UHF what the anticipation at 136 MHz explains. Otherwise cold fronts are associated with regions of strong precipitation (Fig.4) which lead to a larger attenuation at 35 GHz. Strong elevated discontinuities can be considered at 136 MHz as reflecting boundaries. The coefficient of reflection becomes high at grazing incidence which occur in particular at low elevation angles at the satellite. The rays are deflected and a delay of audibility is observed. The smaller attenuation at 35 GHz can be explained by refraction processes in the layered medium or simply as a stronger decrease with height of absolute humidity in extensive high pressure areas.

Discontinuity layers are in motion and give rise to long periodic fading known on earth VHF and UHF links. Discontinuity layers embedded in less stable air may act as duct for gravity waves which have periods between 2 and 20 minutes (G. Fengler; G. Stilke, 1968). This is in agreement with the interpretation of the fadings of the transmission from stationary satellites by gravity waves (T.J. Elkins; M.D. Papagionnis; J. Aarons, 1967).

### 4. CONCLUSIONS

Long periodic fluctuations of the received field strength in satellite earth links in the VHF and UHF range can be explained by the impact of cold fronts, ground inversions and elevated

inversion. These tropospheric structures have also an influence on the attenuation of wave at frequencies greater than UHF.

### 5. ACKNOWLEDGEMENTS

The writer is indebted to Dr. E.E. Altshuler(AFCRL) for discussions and leaving of parts of his observations for further evaluation. Furthermore the author expresses his gratitude to SIGMA e.V. Hamburg, supporting this work.

### REFERENCES

- |   |      |  |
|---|------|--|
| E.E. Altshuler<br>V.J. Falcone, Jr.,<br>K.N. Wulfsberg. | 1968 | Atmospheric effects on propagation at millimeter wavelength, IEEE spectrum July 83-90  |
| W. Degenhardt,<br>G.K. Hartmann.                        | 1976 | Periodic amplitude and phase fluctuations ranging from 1 sec. to 30 min. observed with the ATS-6 RBE at Lindau Proc: Geophys. Use of Satellite Beacon Obs. (URSI-COSPAR), Boston, paper II,-5. |
| T.J. Elkins<br>M.D. Papagiannis                         | 1967 | Studies of irregular atmospheric refraction using stationary satellites.<br>Space Research VIII, Amsterdam, 405-412  |
| C. Fengler  | 1971 | Tropospheric effects on the propagation of VHF-satellite signals Kleinheubacher Berichte 14, 59-66.  |
| C. Fengler  | 1968 | Microwave propagation influenced by interval gravity waves AGARD CP 37, paper 21   |
| G.K. Hartmann   | 1969 | Tropospheric diffraction phenomena of radio signals from the beacon satellite  |

G.K. Hartmann (cont'd)	1969	Explorer 22 J. Atmos. Terr. Phys. 31, 663-669
Y.V. Somayajula Tuhi Ram Tyagi A.B. Ghosh	1976	Satellite radio beacon monitoring of the troposphere
L.E. Telford E.E. Altshuler	1975	Proceedings of The Geophysical Use of Satellite Beacon Obser- vations, Boston, V - 6, (URSI - COSPAR)

Atmospheric attenuation  
at 15 and 35 GHz for  
slant paths near the  
horizon.

1975 URSI Meeting  
Urbana, IL., 32-33.

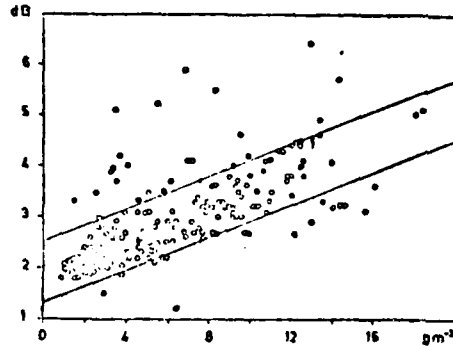


**Figure 1**  
Attenuation [db] against  
humidity  $[gm^{-3}]$

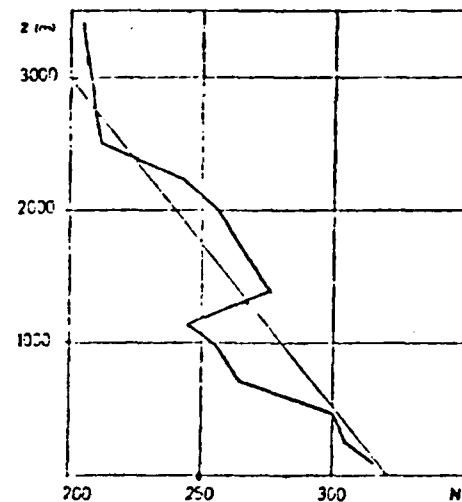


**Figure 2**  
Profile of refractivity N of  
pronounced elevated discon-  
tinuities    z:height

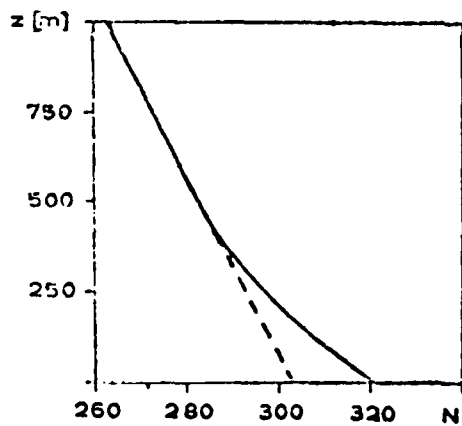


**Figure 3**  
Profile of refractivity N  
in presence of ground  
inversion  
z:height  
---- without ground  
inversion

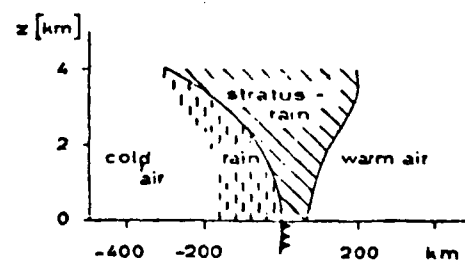


**Figure 4**  
Cross section of idealized  
cold front

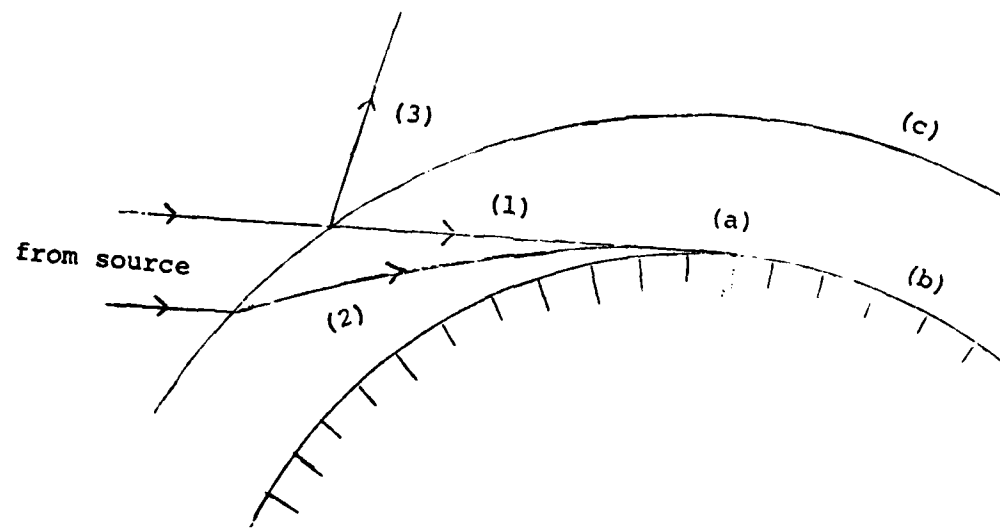


**Figure 5**  
Path geometry (idealized)

- (1) without discontinuity
  - (2) refraction due to ground inversion
  - (3) reflection at elevated discontinuity
- (a) receiving station
  - (b) surface of the earth
  - (c) upper boundary in case (2)  
elevated discontinuity in case (3)

TRANSIONOSPHERIC LONG RANGE PROPAGATION STATISTICS THROUGH THE  
FIRST CHINESE SATELLITE TRANSMISSION

P.Beni, F.Bertini, P.F.Pellegrini

Istituto di Ricerca sulle Onde Elettromagnetiche, C.N.R.  
Firenze, Italy

Abstract

Results are presented of a research on HF long range propagation obtained at IROE, Firenze by using the radio signal radiated by the first Chinese satellite (1970-34 A).

Three phases of the work were developed.

- 1) Study and realization of a crosscorrelation receiving system, which is able to measure the level of the received signals down to a post detection S/N ratio of -27 dB.
- 2) Statistical analysis of the received signals as a function of the geometry of the radio link, geographic coordinates of the satellite and station, local solar time etc.
- 3) Interpretation of the results on the basis of the actual ionospheric conditions by means of ray-tracing techniques.

The signal at 20.009 MHz, has allowed the study of transionospheric propagation beyond the horizon.

Particular attention has been given to the quantitative determination of the parameters characterizing this kind of propagation.

Ray-tracing techniques analysis have verified that partially-guided low-loss paths are consistently available.

Measured values of path losses over ranges up to the antipodal point of the ground station are varying between 120 and 150 dB. An improvement over free-space propagation losses of the order of 4 dB over ranges of 12000 Km, and up to 8 dB for nearly antipodal satellite passes have been observed.

During the total of 142 revolutions the signal was received for 20 per cent of the orbits from ranges greater than 10000 Km. The received level shows in particular that its distribution cannot be considered stationary as the distance varies.

Statistical analysis of data on long range HF transionospheric propagation was performed using the radio signals emitted by the first Chinese satellite (1970-34 A) and received in

Firenze [1]-[5]. The satellite orbited above the maximum of the F2 region (perigee 445 Km, apogee 2400 Km, inclination  $68.44^\circ$ ). The results refer to an observation period of 12 days from April 27, 1970.

As first work the satellite emission characteristics, unknown a priori, were determined.

The 20.009 MHz signal was AM modulated (modulation index  $\approx 1$ ) by audio synthesized tones of the theme "The East is Red" and by telemetric informations in one minute frame. The most frequent tone of the theme is at 784 Hz.

To perform careful measurements of the received signal intensity, in spite of the involved low signal-to-noise ratios, a suitable correlation receiving system was designed and set up [6]. The receiving system consisted of an horizontal dipole antenna which feed a receiver operating in AM (NGC mode, IF bandwidth 5KHz), whose audio output was connected to a crosscorrelation detection system to determine the presence or the absence of the 784 Hz tone and its intensity.

A decision device discriminates the 784 Hz tone sequence allowing the signal identification.

The overall detection system allows to determine the presence or the absence of the satellite-earth link typically with a probability of error of 1% with AF signal-to-noise ratios of about -27 dB.

During the 250 hours of the experiment, the signal was frequently received for long time period when the satellite was beyond the station horizon thus showing the existence of steady long range propagation condition. A considerable amount of long-range propagation data is available from both the North-Atlantic and South-Atlantic regions in addition to the antipodal zone.

The overall description of the propagation data obtained in terms of reception occurrence, versus the subsatellite-station range, is shown in the map of constant reception occurrence curves of Fig.1.

From North-Atlantic zone ( $50^\circ$ - $68^\circ$ N) propagation paths extending on range up to 8000 Km take place between 20 and 00 station LST, and 10-20 satellite LST (satellite altitude 445-1500 Km).

The sunset region in the vicinity of the ground receiving station results to be favorable for the reception. Propagation from South on ranges between 7000 and 12000 Km during descending passes takes place at 2100-2330 station LT (satellite altitude 800-1600 Km).

Propagation paths extending along the sunset transition further demonstrates as the twilight belt plays an important role

in the long range propagation. Propagation from antipodal region has been observed between 06 and 10 station LT (20-22 satellite LST, satellite altitude 1250-1450 Km); the propagation paths westward crossed the sunset transition near the equatorial anomaly then the signal via ducting propagates in northern hemisphere and was received at ground.

To the purpose of analyzing the paths through which guided propagation may occur, a three-dimensional ray-tracing procedure on a world-wide scale was applied [5]. This procedure is based on the numerical integration of the ray canonical equations originating from geometric optics and uses a three-dimensional model of the ionospheric electron density constructed from experimental data (NOAA Boulder, Colorado).

As a result when the satellite was in the antipodal region at an height above that of the F2  $h_{\max}$  (1250-1450 Km) at 2030-2200 LT partially-guided paths westward were found. The encountered sunset transition allows the conversion from multihop to guided propagation as shown for example in Fig.2 for revolution 111.

Satellite-to-ground station path loss measurements were taken on the 142 observed revolutions.

For satellite-station ranges from 6000 Km up to 14000 Km several measured path losses values are lower than free-space propagation losses from 2.5 to 4 dB. An improvement over free-space propagation losses up to 8 dB characterizes the received signals from the antipodal region.

This turns out to be in good agreement with that found by H.T.Chang [7], by using the waveguide mode theory of whispering-gallery propagation in the F region.

The analysis of the distribution function of the received levels (see Fig.3) shows that for different ranges: a) the distribution behavior is approximately of the same type and it is in agreement with a distribution derivable from Rayleigh, b) the value of the average level varies only slowly with the range interval, c) the reception probability varies as a function of the range interval.

This means that for greater ranges the obtained distribution cannot be considered as the tail of a single distribution.

This proves that the mechanisms which supports beyond the horizon transitionospheric propagation are different for different range intervals.

In other words, the distribution of the levels of the signal cannot be considered stationary as the distance varies. The amplitude distributions obtained can be considered an estimation of the distributions  $P_d(s_d)$  which can be obtained from theo-

retical consideration on Rayleigh law. Tacking into account the threshold of the receiving system it results:

$$P_d(s_d) = \frac{2 s_d}{\overline{s}^2} \exp\left[-(s_d^2 - s_t^2)/\overline{s}^2\right]$$

where:  $P_d(s_d)$  is the probability density of reception of a signal level  $s_d$   
 $\overline{s}^2$  is the mean square value of the signal that should have been received from a system without threshold  
 $s_t$  is the threshold level of the receiving system.  
 $s_d$  is the detected signal.

#### References

- [1] N.Carrara, M.T.De Giorgio and P.F.Pellegrini: " Guided Propagation of HF Radio Waves in the Ionosphere" , Space Sci. Rev. 11, 555-592, (1970)
- [2] M.D.Grossi, B.M.Langworthy: " Geometric Optics Investigation of HF and VHF Guided Propagation in the Ionospheric Whispering Gallery" , Radio Sci. 1, 877, (1966)
- [3] P.Beni, P.F.Pellegrini: " Beyond the Horizon Iospheric Propagation Experiment from an Equatorial Orbiting Satellite to a Middle Latitude Station" , Planet.Space Sci. 20, 1984-1996, (1972)
- [4] P.F.Pellegrini, M.T.De Giorgio: " Studies on the Ionospheric Guided Propagation of Satellite Transmissions at IROE" , Alta Frequenza vol. XLIII, n.10, (October 1974)
- [5] F.Bertini, M.T.De Giorgio, P.F.Pellegrini: " Ray-Tracing in the Ionosphere for Long Range Propagation Studies" Submitted to Alta Frequenza, (1975)
- [6] P.Beni, P.F.Pellegrini: " Correlation receiving System for Detection of the First Chinese Satellite Signals" Alta Frequenza vol. XLIV, n.8 (August 1975)
- [7] H.T.Chang: " The Waveguide Mode Theory of Whispering Gallery Propagation in the F Region of the Ionosphere" Radio Sci. 6, 475-482, (1971).

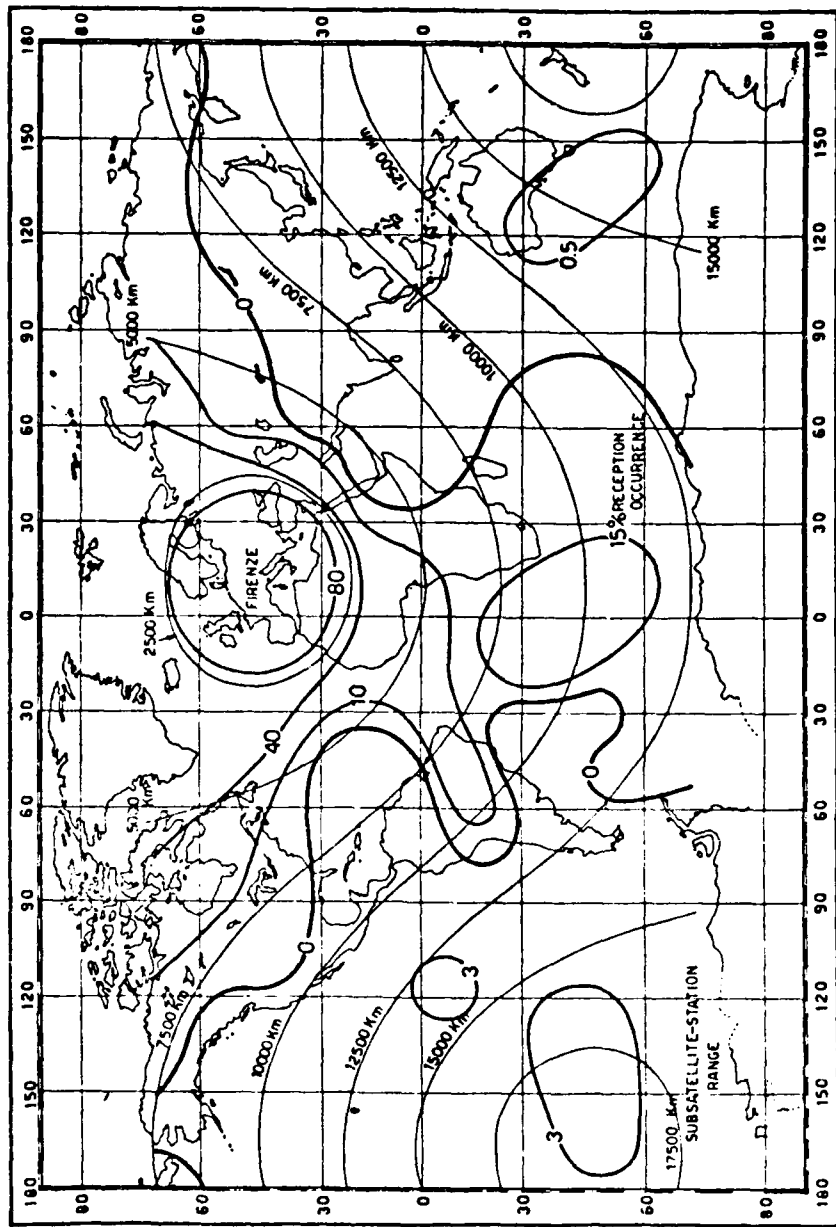
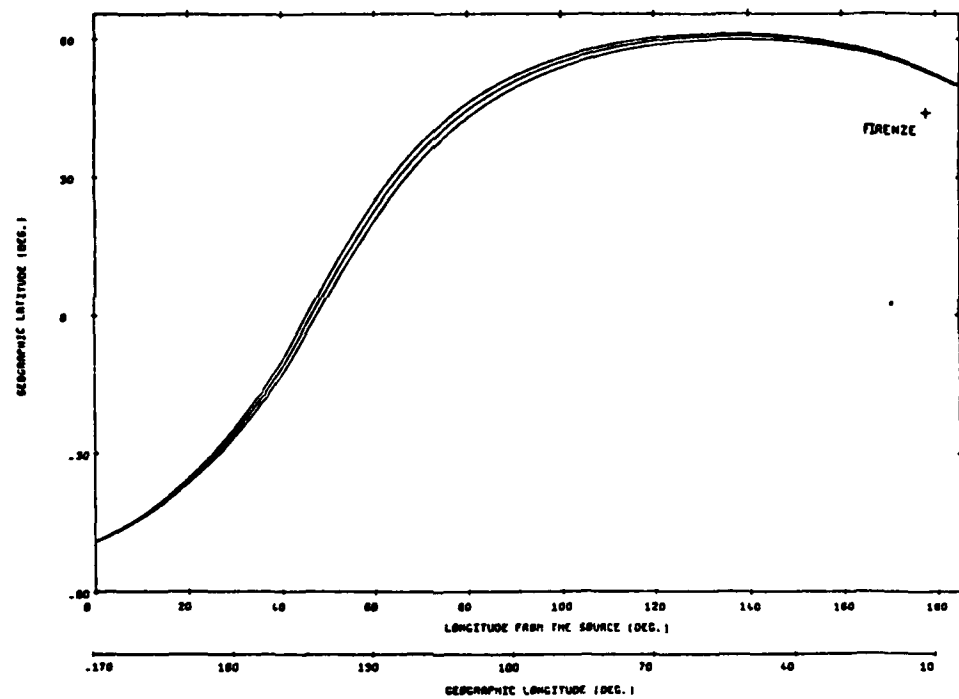
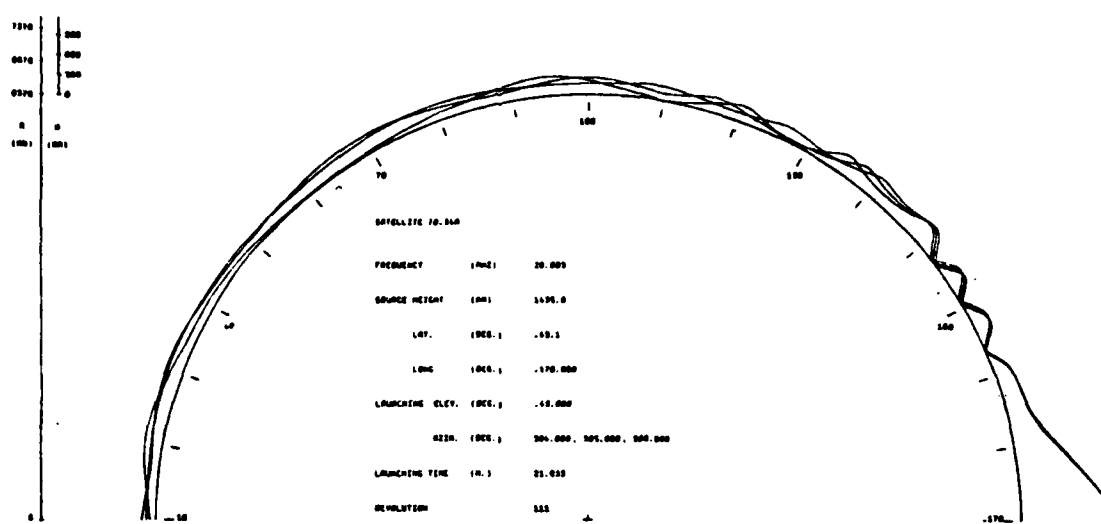


Fig.1 - 1970-34A satellite-to-ground relative reception occurrence observed at Firenze. The transmitted frequency is 20.009 MHz.



**Fig.2** - Ray-tracing example of partially-guided propagation from antipodal region of Firenze. The projection of the ray-path on the equatorial plane is presented (geographic longitude is indicated, -w; +E). The lower diagram indicates the projection of the ray-path on the earth surface.

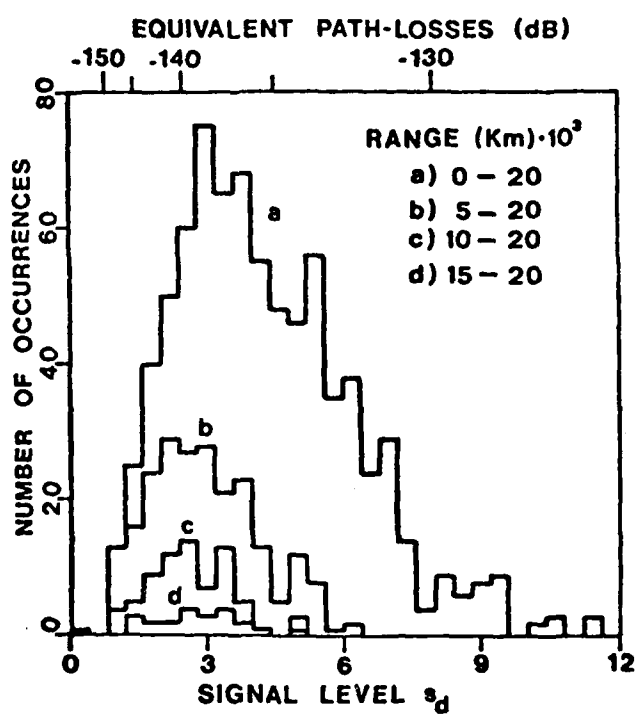


Fig.3 - Probability density diagrams of the received signal levels of the 1970-34A satellite.

LINE-OF-SIGHT ELECTRON DENSITY GRADIENTS  
AS DEDUCED FROM AN EMPIRICAL IONOSPHERIC MODEL

George Nesterczuk, Jerry K. Kozelsky

Atlantic Science Corporation

Riverdale, Maryland, USA

and

John A. Behuncik

NASA/Goddard Space Flight Center

Greenbelt, Maryland, USA

I. INTRODUCTION

The need for a good model of the ionosphere on a global scale has existed for some time. Such a model would find application in a number of areas including communications and satellite tracking. It is for the latter reason that work was undertaken at NASA which led to the development of the Bent Ionospheric Model, an empirical worldwide model of the ionosphere. The model is used to compute ionospheric refraction corrections to range, range rate, and angular satellite tracking data. As orbit determination requirements become more demanding, the ionospheric model must be equal to the task. The model has to be able to provide the refraction corrections needed in geodetic work as well as for satellite to satellite configurations.

A global model is absolutely essential for such applications. Models of the behavior of the ionosphere above one site with the implicit assumption of homogeneity throughout the visible sky obviously will not do for these global requirements. One must concede, however, that there are inherent computational difficulties in working with a model on a global scale and this has been partly the reason for using more localized versions of ionospheric models. With our current generation of high speed computers this need no longer be a problem.

The results presented here are only a portion of a larger effort to develop the techniques required to compute satellite to satellite refraction corrections in an operational orbit determination environment. In this paper we will look at the effects of line of sight gradients, as predicted by the worldwide Bent Ionospheric Model, on ground to satellite measurements. The results and conclusions apply equally to transitionospheric satellite beacon measurements of total electron content (TEC) as well as range and range rate measurements in satellite tracking.

II. THE IONOSPHERIC MODEL

A. Model Development

The model was developed from a global data base of bottomside

and topside soundings. Data was acquired for the years 1962 through 1969, which includes a solar maximum year. Bottomside data was available in the form of hourly profiles to the height of the f0F2 peak. A total of over 400,000 of these soundings was included in our analysis. The topside model was deduced from over 60,000 topside Alouette and ISIS satellite soundings and an additional 6000 density probe measurements from the Ariel 3 satellite. Though the data was not evenly distributed around the world it did span a range of from +85 degrees to -75 degrees magnetic latitude and covered a wide span of local time. The topside data enabled us to model the ionosphere to a height of 3500 km. No attempt was made to model the detailed structure in the bottomside, for the intended purpose of this model was to provide an accurate prediction of integrated electron content. Hence the bottomside model is more a "bottomside content" model than a proper profile.

#### B. Density Profile

To facilitate the analysis of the large volume of data available, an assumption as to the shape of the profile was made. The assumed profile is shown in figure 1. Correlation and recursive analysis was then used to model each of the parameters  $k_1, k_2, k_3, k_4, k_5, Y_t, Y_b, f0F2$  and Hmax. The equations governing the various segments of the profile are exponential in the topside, biparabolic in the bottom and parabolic around the nose.

$$\text{Topside layers: } N = N_i e^{-k_i a} \quad (1a)$$

$$\text{Topside, near peak density: } N = N_s \left(1 - \frac{b_1^2}{Y_t^2}\right) \quad (1b)$$

$$\text{Bottomside: } N = N_b \left(1 - \frac{b_2^2}{Y_b^2}\right)^2 \quad (1c)$$

Where  $N_i$  is the electron density at maximum.  $Y_b$  and  $Y_t$  are thickness parameters of the lower and upper parabolic layers, respectively.  $k$ 's are decay constants for each of the five topside exponential layers.

The topside parabola extends from the height of maximum electron density up to the point where the slope of the parabola matches the slope of the lowest exponential layer.

#### C. Topside Ionosphere.

The initial analysis was performed on the profile from 1000 km down to the height observable by the sounders. Later two more layers were added from 1000 km to 2000 km and 2000 km to 3000 km. Considerable effort was expended in trying to model the region below 1000 km using a single value of the exponential decay constant  $k$  (eq. 1a). This was found to

be impossible and this region of the ionosphere was then divided into three equal segments with decay constants  $k_1, k_2, k_3$  (Fig. 1). The wide variations in the  $k$  values as shown in Figures 2a and 2b are a clear indication of the impossibility of modelling the topside with a single exponential constant.

In correlating the  $k$ 's against a number of variables, strong correlations were found to exist with variations in solar flux, magnetic latitude, and critical frequency f0F2. No explicit dependence on local time was found, but an implicit dependence exists by way of the correlation with f0F2. The resultant dependences of the  $k$ 's on all these parameters are displayed graphically in Figure 2b. A north-south symmetry was also noted in the latitudinal dependence of the  $k$ 's as evidenced in Figure 2a. This figure is a plot of the mean values of the  $k$ 's for all values of solar flux and critical frequency. It is interesting to note that the equatorial anomaly and the mid-latitude trough are both quite evident in this plot. This observation supports the view that large scale empirical models can be quite useful in theoretical studies of the ionosphere.

In addition to these basic variations in the  $k$ 's a seasonal dependence was also found and modelled. Summer and winter adjustments to the  $k$  values were found to be as large as  $\pm 15\%$  of the spring and fall values.

The most difficult region of the ionosphere to model was the portion connecting the lowest measurable point in the topside sounding with the maximum density from the bottomside. Little or no data was available in this domain hence a parametric representation had to be improvised. Comparisons of the modelled TEC against measured TEC indicated that a parabola having a thickness parameter of  $Y_t$  (eq. 1b) provided the "best fit".  $Y_t$  is set equal to the more extensively modelled bottomside  $Y_b$  for values of f0F2 up to 10.5 MHz, and thereafter takes on larger values as f0F2 increases. The lowest exponential layer and this parabolic "nose" are then matched at a height  $H_{max} + d$  where the slopes of the two curves are equal, thus producing a smooth, continuous profile.

#### D. The Bottomside

No attempt was made to model the bottomside profile exactly, but the general shape is that of a bi-parabola (eq. 1c) and this is what was chosen. For each bottomside profile the electron content was integrated up to the maximum electron density.  $Y_b$  was then chosen such that the TEC from the bi-parabola would match the TEC from the observed profiles. Correlation analysis was performed on  $Y_b$  against 10.7 cm solar flux, f0F2, local time, and season. No direct solar flux dependence was found, but a high degree of correlation was discovered with variations in f0F2 and local time. The resultant dependence of  $Y_b$  on these quantities is illustrated in figure 3. The local time dependence for values of f0F2 greater than 10 MHz follows the 10 MHz curve in that figure. A weaker, though still significant, correlation with season was also noted and is included as an update in the calculation of  $Y_b$ .

#### E. Critical Frequency ( $f_{0F2}$ ) and Height of Maximum Density ( $H_{max}$ )

By far, the most important parameter needed to predict an ionospheric profile, using the Bent Ionospheric Model, is the critical frequency  $f_{0F2}$ .  $f_{0F2}$  is obtained, as a monthly median prediction, by using a method developed at NOAA. The technique, described by Jones, Graham and Leftin (1969) and generalized by Jones and Obitts (1970), was developed from a worldwide data base of  $f_{0F2}$  observations collected over a period of several years.  $f_{0F2}$  is represented by a series containing diurnal and geographic terms. The time variations are given by a Fourier series of harmonic terms up to the sixth order. The geographic variations in latitude were found to correlate well with the geomagnetic field, hence the "modified" magnetic dip " $x$ " (eq. 2) is used to define the primary latitudinal dependence of  $f_{0F2}$ .

$$x = \tan^{-1} \frac{I}{\sqrt{\cos \lambda}} \quad (2)$$

where       $I$  = magnetic dip angle  
               $\lambda$  = latitude

The longitudinal variations as well as additional latitude terms are expanded to the eighth order. A map of the worldwide distribution of  $f_{0F2}$  predicted by this technique is illustrated in figure 5a.

The series representation of  $f_{0F2}$  produces a monthly median value, but day to day excursions of  $f_{0F2}$  from the mean can be quite large. A procedure was devised to update the median  $f_{0F2}$  using the daily value of solar flux, thus, in effect allowing a "daily" prediction of  $f_{0F2}$ . For work requiring great accuracies, the predicted  $f_{0F2}$  can be replaced with measurements from ionospheric sounders.

The height of maximum electron density,  $H_{max}$ , is given by

$$H_{max} = 1346.92 - 526.40(M3000) + 59.825(M3000)^2 \quad (3)$$

where       $M3000 = \frac{MUF(3000)F2}{f_{0F2}}$

and  $MUF(3000)F2$  is the maximum frequency which can be used to propagate a signal over a distance of 3000 km by reflection from the F2 layer. Equation (3) was derived from the Appleton-Beynon (1940, 1947) equations. The  $M3000$  ratio is predicted on a monthly mean basis, in a manner similar to  $f_{0F2}$  but using fewer terms and a different set of Fourier coefficients in the time series.

#### F. Comparison With Chapman Profile

The Chapman profile is the most commonly used profile in ionospheric work today. A study was undertaken to compare the Bent and Chapman profiles at several locations on the globe and under varied ionospheric conditions. An example is illustrated in figure 4, for location Quito, Ecuador on 15 January 1969. Two Chapman curves are plotted, differing from each other in the scale height, as indicated below.

Chapman 1	H=1.66 (30+.075 (Hmax-200))
Chapman 2	H=1.66 (30+.200 (Hmax-200))

All three profiles are normalized to Nmax at Hmax.

The Bent profile was found to be consistently denser than the Chapman profile at heights above 1000 km. Below 1000 km the results varied with the Bent profile sometimes thinner than Chapman, and at other times denser than Chapman. The profile identified as Chapman 1 gave the best agreement with the Bent profile. In the sample illustrated in figure 4, the TEC from the Chapman 1 and Bent profiles are in excellent agreement. This was not always the case, for the two profiles generally disagreed by 10% to 20% in TEC and in some cases by as much as 50%. The Chapman 2 profile was consistently thicker (denser) than the Bent profile and produced TEC values from 1 to 7 times larger than the Bent TEC.

#### G. Accuracy Of The Model

Numerous evaluation tests of the model were made, primarily comparing predicted TEC values against Faraday rotation measurements. It was found that in general, TEC can be predicted, using the Bent model, with RMS residual error of 20% - 25%. This error can be reduced to 10% - 20% if measured values of f0F2 are used as input to the model, to override the predicted f0F2.

A sample comparison between measured TEC and modelled TEC can be seen in figure 6. The plot is of ionospheric group delay at 1600 MHz for each day of November 1968 at 0<sup>h</sup> UT. The measurements were taken from Honolulu to the ATS-1 satellite, and observations of f0F2 were obtained from a sounder station at Maui. The Maui f0F2 were used in the model in place of predicted f0F2 to generate "updated" profiles and TEC. Note the excellent agreement between measured delay and modelled delay.

A more detailed discussion of the model development, evaluation and its applications can be found in Bent et al (1975) and Llewellyn and Bent (1973).

### III. THE RAY TRACING PROGRAM

For our comparison standard, TEC was obtained by ray tracing

through the ionospheric profiles predicted by the Bent model. The ray tracing program is a double precision arithmetic application of Snell's Law in spherical form. Numerical integration of the equations, relating ray bending and electron content to changing local elevation angle and refractivity, was performed layer by layer through the ionosphere to provide the TEC. The program is capable of using electron densities predicted by either a Chapman profile or the profile predicted by the Bent Ionospheric Model.

To define the electron density variations along each line of sight, up to 150 density points were used for low elevation cases. At higher elevations this number was gradually reduced to 50 points. The densities were generated prior to the ray tracing process, and during the generation procedure straight line propagation was assumed. Values of the density were computed at 20 km intervals along the path from the bottom of the ionosphere up to a height of 1000 km. Thereafter the interval was increased to 200 km up to the top of the ionosphere, which for this study was set at 3500 km.

Electron densities were provided to the ray trace program at specified heights by interpolating between these 50 to 150 precomputed density points. Below the maximum density the interpolation was of fourth order. Above maximum density, quadratic interpolation was used in the parabolic region of the profile, and logarithmic interpolation in the exponential layers. Integration steps were 1 km in height below 1000 km and 5 km for heights above 1000 km. Integration of the density through each step was performed with a 3 point Simpson's rule. Tests of the numerical stability of this approach indicated that TEC at vertical incidence was accurate to 1 part in  $10^8$ . This was deemed more than adequate for the purposes of this study, since we were looking for TEC effects of order 5 parts in  $10^3$  or larger.

#### IV. EVALUATION CONDITIONS

Our first requirement was to select a time and place at which severe horizontal density gradients could be expected to exist. By examining available maps of ionospheric characteristics such a site was selected at Kashima, Japan (lat =  $35^{\circ} 95'$ , lon =  $140^{\circ} 7'$ ) for 12 h U.T. on 15 January 1969. Worldwide maps of f0F2 and vertical electron content  $N_v$  corresponding to that date and time are reproduced in figures 5a and 5b. The f0F2 gradients in the visible sky over Kashima are shown in figure 7. These severe gradients are typical of the ionosphere in low latitude regions.

Lines of sight were chosen at  $30^{\circ}$  intervals in azimuth for elevations from  $0^{\circ}$  to  $90^{\circ}$ . From 50 to 150 electron density points were computed for each line of sight, and TEC was then integrated by ray tracing through these precomputed points. Results of the ray trace integration for several elevation angles are plotted in figure 8. TEC was also calculated analytically using equation 5, below.

$$TEC = \int N(s)ds = \int N(h) \sec \varphi(h) dh \quad (4)$$

$$\text{where } \sec \varphi (\bar{h}) = \left( 1 - \left( \frac{R_e}{R_e + h} \right)^2 \cos^2 El \right)^{-1/2}$$

$$TEC = \overline{\sec \varphi (\bar{h})} \cdot \int N(h) dh = G \cdot N_v \quad (5)$$

Equation 5 is derived from equation 4 by postulating the Mean Value Theorem for integrals. The value of  $\overline{\sec \varphi (\bar{h})}$  was evaluated for each line of sight at a height corresponding to the mean of the density distribution, i.e. the height below which half the TEC is contained. In effect  $\overline{\sec \varphi}$  acts as a geometric scaling factor, which maps the vertical electron content  $N_v$  into TEC along the line of sight. Typical values of  $\overline{\sec \varphi}$  as a function of elevation are shown in figure 9.

The density profile  $N(h)$  was defined for each line of sight at the point at which maximum density occurs. By recomputing a new profile for each line of sight, the gradients in the visible sky (figure 7) were thus taken into consideration. This approach can be considered to correct for "first" order horizontal gradient effects on TEC. "Second" order effects arise from neglecting these same gradients along the line of sight.

## V. RESULTS

The first order gradient effects, alluded to above, are very large indeed for this test case. In figure 7 we note that f0F2 varies in the visible sky from 2.5 MHz to over 10.0 MHz. This gave rise to  $N_v$  values from .25 to  $3.5 \times 10^{17} \text{ el/m}^2$ , and a variation in TEC across the visible sky (fig. 8) by a factor of 30!

The second order gradient effects, due to line of sight gradients, are shown in figure 10. In this figure we have plotted the percent error resulting from comparisons of ray trace results to TEC obtained from equation 5 (i.e. assuming a homogeneous profile along the line of sight, scaled by a geometric factor). The percent error  $\Delta N_t$  is defined in equation 6.

$$\Delta N_t (\%) = \frac{TEC(\text{eq. 5}) - TEC(\text{ray trace})}{TEC(\text{ray trace})} \times 100 \quad (6)$$

Referring to figure 10, we note that  $\Delta N_t$  can be as large as 20%. Looking north (azimuth 300° to 60°) at elevations above 20°, the homogeneous profile leads to an overestimate of the actual TEC by up to 18%. Looking south (azimuth 120° to 240°), at these elevations, we get up to 20% underestimate with the homogeneous profile. In the east direction the ionosphere appears to be homogeneous ( $\Delta N_t = 0\%$ ) at all elevations, while in the west inhomogeneities begin to appear at elevations below 20°. As indicated by the low elevation curves in figure 10, the effects of line of sight gradients become less systematic the longer the path traversed through the ionosphere. This is

to be expected, for the ionosphere is a highly inhomogeneous medium with multiple density inversions (figures 5a and 5b), and the longer the line of sight, the more these inversions will be encountered.

Let us correlate the results of figure 10 with the ionospheric state depicted in figures 5a and 5b. At elevations above  $20^{\circ}$  we are limited to a local ionosphere over Kashima. The underestimates of TEC indicated for southward directions in figure 10 correspond to increasing density gradients in figure 5. The overestimates to the north are due to decreasing density gradients. At the lower elevations, the line of sight pierces further away from Kashima. The reversal in  $\Delta N_t$  noted at  $5^{\circ}$  and  $10^{\circ}$  elevation fits in with the reversal in f0F2 gradients at latitude  $+55^{\circ}$  and longitude  $150^{\circ}$ . The inversion in  $\Delta N_t$  looking south corresponds to the entry of the line of sight into the equatorial anomaly.

## VI. CONCLUSIONS

The conclusion to be drawn from these results is that  $N_v$  or slab thickness values, deduced from standard analysis of equatorial Faraday rotation or group delay measurements, may at times be in error by as much as 20%. In the presence of increasing density gradients, deduced values of  $N_v$  or slab thickness will be too large, while for decreasing gradients the values of  $N_v$  or slab thickness will be smaller than they should be. This applies to observations through the east-west gradients at times of sunrise as well as through the north-south gradients of the equatorial anomaly.

An interesting implication of these results is that observations from stations north and south of the equatorial anomaly should give overestimated values of  $N_v$  for directions toward the equator. Looking away from the equator the  $N_v$  values would be biased lower than they should be. Stations situated within the equatorial itself, will in general experience predominantly decreasing density gradients. Hence, transionospheric observations from these stations, when reduced to  $N_v$  or slab thickness, should be consistently biased to the low side. This hypothesis lends itself to experimental confirmation using data taken simultaneously from opposite directions of a gradient region. The INTASAT beacon satellite, in a high inclination orbit, may be an ideal satellite to use for such an experiment since a large number of stations currently tracking it, are located in low latitudes.

Further work of this nature using the Bent Ionospheric Model could be carried out with more stations, to examine latitudinal, diurnal, seasonal, and solar flux dependences of line of sight gradient effects. Only then will we have a proper insight into the severity of the gradient problem, including its magnitude and frequency of occurrence.

Acknowledgement--The efforts of two of the authors (G.N. and J.K.K.) were funded by the National Aeronautics and Space Administration under contract number NAS 5-22302. We wish to express our appreciation to our colleagues at NASA/GSFC and at Atlantic Science Corporation for their continued help and cooperation.

## REFERENCES

1. R. B. Bent, S. K. Llewellyn, G. Nesterczuk, P. E. Schmid, "The Development of a Highly Successful Worldwide Empirical Ionospheric Model and its Use in Certain Aspects of Space Communications and Worldwide Total Electron Content Investigations", Proceedings of the 1975 Symposium on the Effect of the Ionosphere on Space Systems and Communications, Naval Research Laboratory (January 20 - 22, 1975)
2. S. K. Llewellyn, R. B. Bent, "Documentation and Description of the Bent Ionospheric Model," AFCRL TR-73-0657, SAMSO TR-73-253 (July 1973)
3. W. B. Jones, D. L. Obitts, "Global Representation of Annual and Solar Cycle Variation of f0f2 Monthly Median, 1954-1958," OT/ITS Research Report No. 3 (October 1970)
4. W. B. Jones, R. P. Graham, M. Leftin, "Advances in Ionospheric Mapping by Numerical Methods," ESSA Technical Report ERL 107, ITS 75 (May 1969)
5. (a) E. V. Appleton, W. J. G. Beynon, Proc. Physical Society 52, Pt. I, 518 (1940)  
(b) E. V. Appleton, W. J. G. Beynon, Proc. Phys. Soc. 59, Pt. II, 58 (1947)

FIGURE 1. THE EXPONENTIAL PARABOLIC & BI-PARABOLIC PROFILE

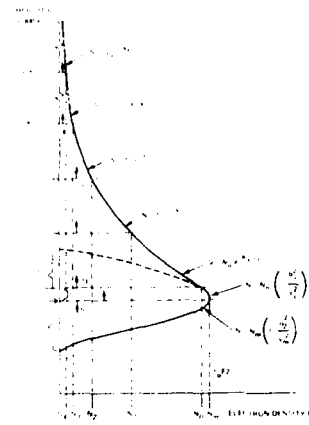


FIGURE 1a. VARIATION OF  $\lambda$  FOR THE UPPER (U), MIDDLE (M) AND LOWER (L) TOPSIDE PROFILE BELOW 1000 km AND THE LAYERS FROM 1000 TO 2000 AND 2000 TO 3000 nm DUE TO SOLAR FLUX,  $F_2$  AND MAGNETIC LATITUDE.

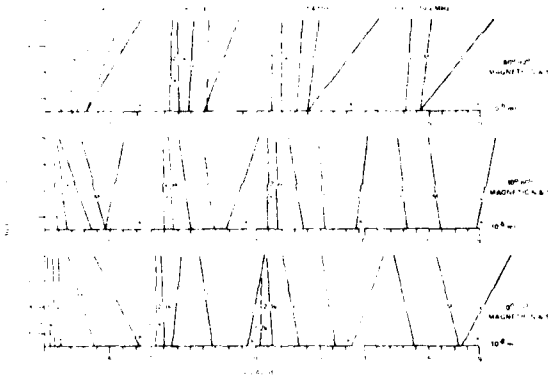


FIGURE 4. COMPARISON OF BENT IONOSPHERIC PROFILE WITH CHAPMAN PROFILES

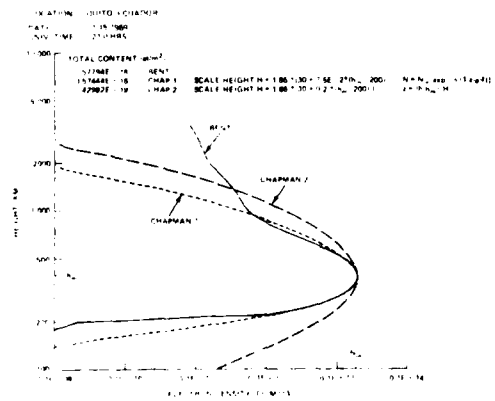


FIGURE 2a. THE MEAN FLUCTUATION OF THE DECAY CONSTANT  $\lambda$  WITH MAGNETIC LATITUDE FOR THE UPPER (U), MIDDLE (M) AND LOWER (L) PORTIONS OF THE TOPSIDE IONOSPHERE BELOW 1000 km AND FOR THE LAYERS FROM 1000 TO 2000 AND 2000 TO 3000 km.

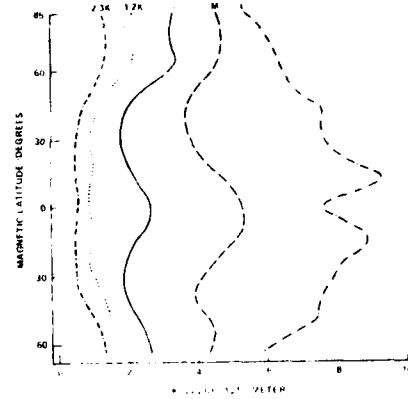


FIGURE 3. VARIATION OF BOTTOMSIDE THICKNESS PARAMETER  $y_m$  AS A FUNCTION OF  $f_{0}F_2$  AND LOCAL TIME.

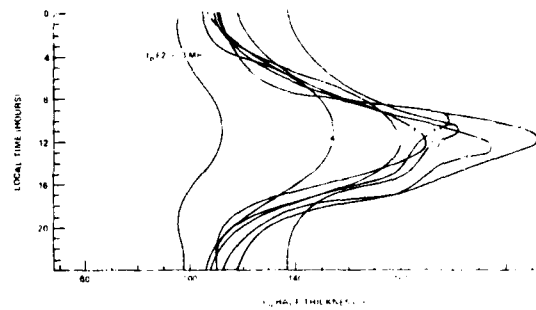


Fig. 5a. World Map of Ionospheric Critical Frequency  $f_{0}F_2$  in MHz at 12 h UT on 15 January 1969  
Contours are Plotted Every 1.0 MHz.

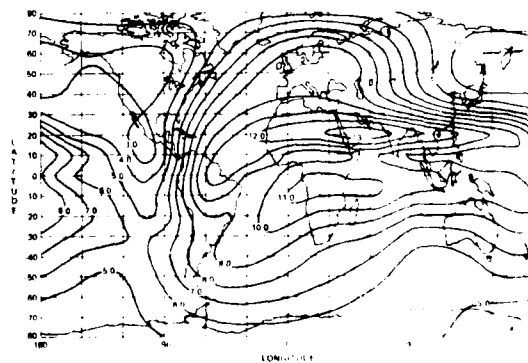


Fig. 5b. World Map of Integrated Vertical Electron Content  $N_v$  as Predicted by Bent Ionospheric Model in Units of  $10^{17}$  el./sq. meter at 12 h UT on 15 January 1969. Contours Every  $5 \times 10^{16}$  el./sq.m.

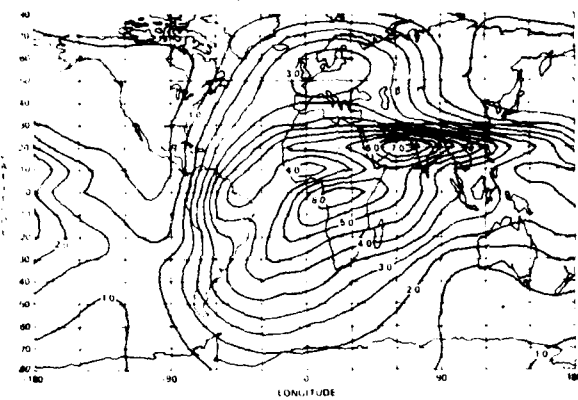


Fig. 7. Ionospheric critical Frequency  $f_{0F2}$  in the Visible Sky Over Kashima, Japan (lat:  $35^{\circ} 35'$ , long:  $140^{\circ} 7'$ ) at 12 h UT (21 h LT) on 15 January 1969. Units are MHz.

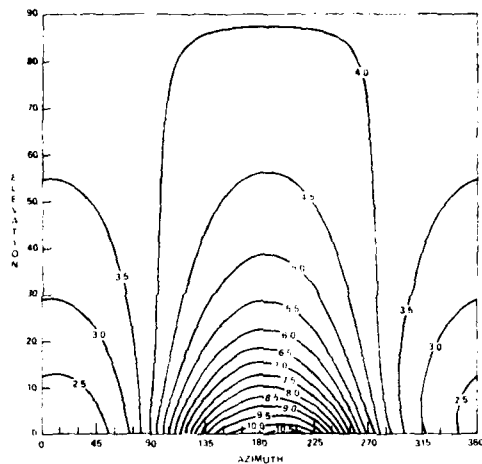


Fig. 9. Scale Factor  $\cdot N_v(E)/N_v(E = 90^\circ)$  - Showing Contribution to TEC from Increasing Path Length as Line of Sight Moves off the Vertical. Ionosphere was Assumed to be Homogeneous. Calculations were Performed for Typical Daytime (—) and Night Time (---) Profiles.

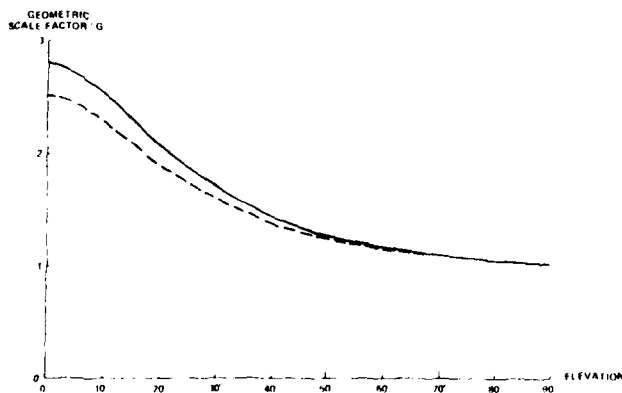


FIGURE 6. IONOSPHERICAL DELAY AT 1800 MHZ HONOLULU ATS-1, NOV 1968 0 HOURS UT

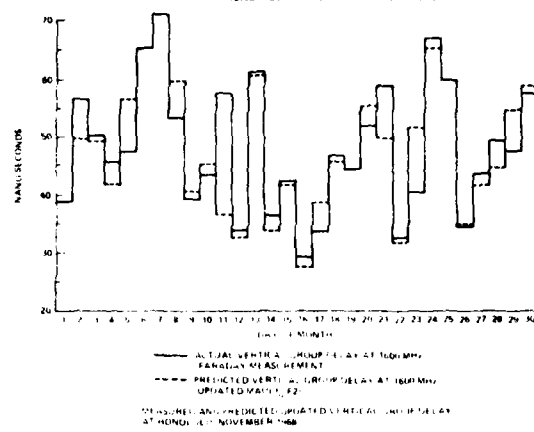


Fig. 8. Predicted Integrated Electron Content for Various Elevation Angles (as Labeled on the Curves) Kashima, Japan at 12 h UT on 15 January 1969. The Integrated Content was Obtained by Ray Tracing Through up to 150 Separate Ionospheric Profiles Evaluated from the Bent Ionospheric Model.

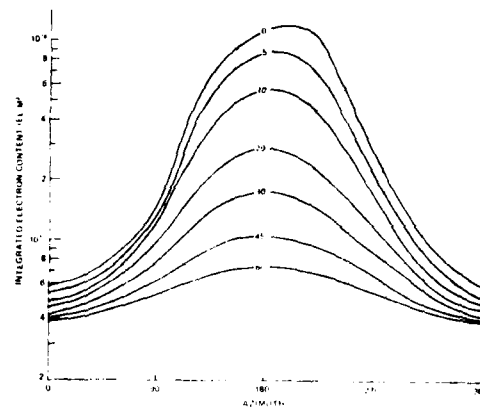
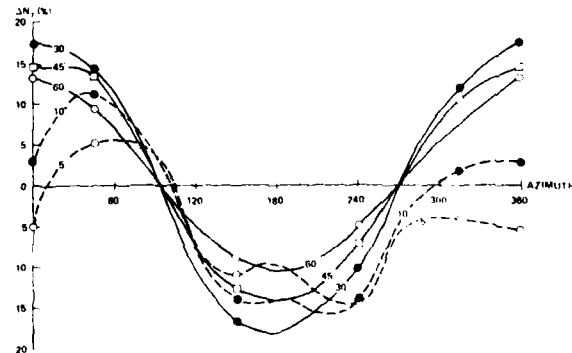


Fig. 10. Percentage Difference Between TEC Obtained by Ray Tracing Through an Inhomogeneous Ionosphere and TEC Obtained by Assuming a Homogeneous Ionosphere with Geometric Scaling Equal to the Secant of the Local Zenith Distance. The Homogeneous Ionospheric Profile Chosen for each Line of Sight is the Profile Occurring at the Maximum Density Along the Line of Sight. The Local Zenith Distance was Evaluated at the Mean of the Density Distribution and is the Angle Between the Local Vertical and the Line of Sight. Elevation Angles are indicated for each Curve. Evaluated for Kashima, Japan at 12 h UT on 15 January 1969.



## THE PERFORMANCE OF THE ATS-6 RADIO BEACON AS A MEASUREMENT SYSTEM

R. N. Grubb, R. B. Fritz, and J. E. Jones  
NOAA Environmental Research Laboratories  
Boulder, Colorado 80302

The overall system performance of the ATS-6 Radio Beacon transmitter in orbit and the Boulder ground receiver will be considered. In particular, the calibration accuracy and stability of the system will be described in terms of the observed difference in total content measured by the 360 to 140 MHz differential group delay and the 360 to 40 MHz differential group delay during the first year of operation. A summary of the transmitter housekeeping data and of the ground data collected on the EIRP and satellite antenna polar diagrams will also be presented.

### 1. INTRODUCTION

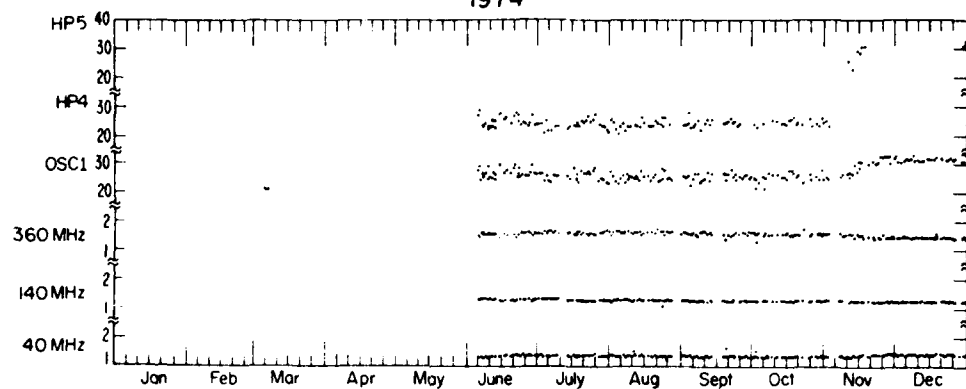
The design of the ATS-6 Radio Beacon Experiment (RBE) transmitter, transmitting antennas, and the Boulder receiving installation have been previously described (Davies, 1975; Grubb, 1972a and b). The objective of this paper is to summarize the performance actually observed from the system in orbit and the Boulder ground receiver system in actual operation.

### 2. TRANSMITTER PERFORMANCE

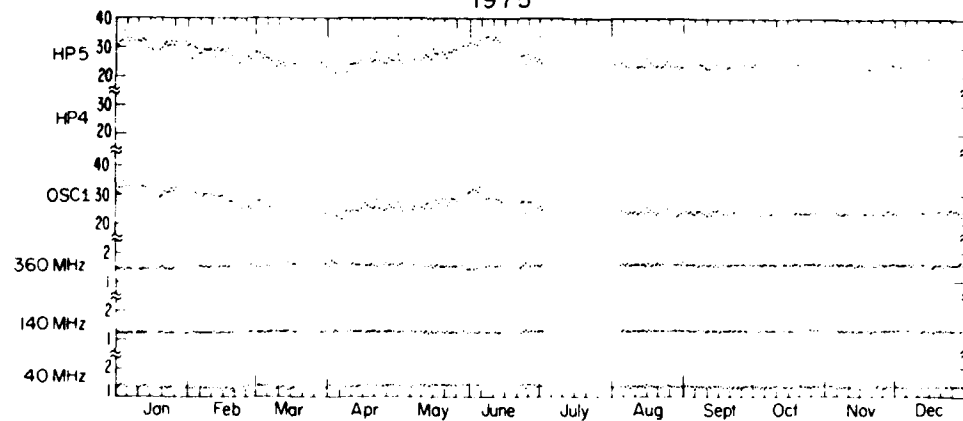
The ATS-6 satellite with the transmitter and antennas aboard was launched on May 30, 1974. The RBE transmitter was first turned on in orbit a few days later and has been in semicontinuous operation using oscillator 1 of the redundant pair of oscillator synthesizers since that time.

The basic performance of the transmitter itself appears to have been excellent. The satellite telemetry data received continuously indicates total forward RF power to the RBE antennas close to the prelaunch test values, with the exception of that at 40 MHz, and shows that very little, if any, drift has occurred over the nearly two years of operation. Figure 1 shows the forward power over the period plotted on a single point per day basis together with the crystal oscillator temperature and the local structural temperature. The major anomaly indicated by telemetry is that the 40 MHz Automatic Level Control (ALC) voltage is out of range (below 0 V), and the 40 MHz forward power telemetry indicates higher than the prelaunch values. Tests using the Engineering Model Transmitter and a full scale mock-up of the satellite and the RBE antennas show that this is consistent with an out of specification VSWR on the 40 MHz antenna. The ALC system was intended to maintain the 40 MHz carrier level constant to  $\pm 0.1$  dB to enable ionospheric absorption to be measured more accurately. Figure 2 shows a typical 12 hour plot of the telemetered 40 MHz total power and the transmitter temperature. The power is normally stable to a few tenths of a dB if turn-on transients and periods of abnormal temperature fluctuation are excluded. However, it is not possible to separate changes of carrier level from changes in sideband level from this telemetry value. Over the small range of temperature observed in orbit, the rate of variation of telemetered 40 MHz total

1974



1975



1976

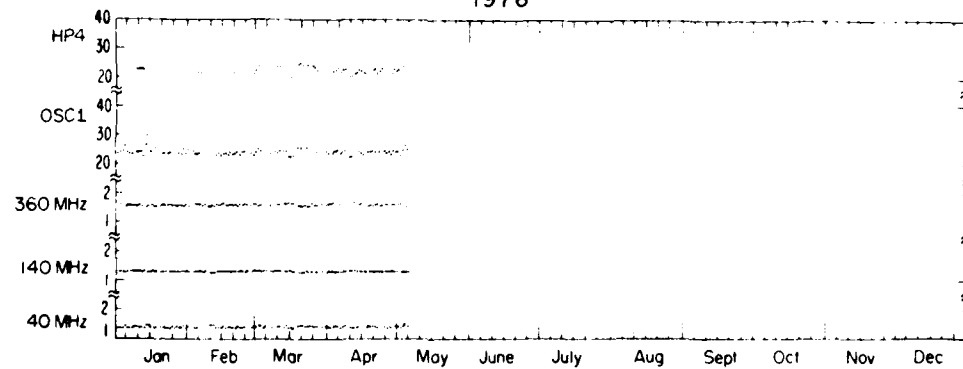


Figure 1. RBE transmitter telemetry data.

Radiated power in watts. Temperatures in °C. HP4 and HP5 are temperatures adjacent to the RBE transmitter.

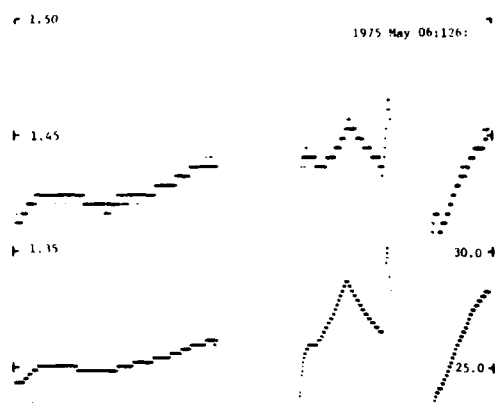


Figure 2. Telemetered total forward power at 40 MHz (watts, upper trace, left scale) and Oscillator 1 temperature over a typical 12-hour period ( $^{\circ}\text{C}$ ).

power is similar to that observed in prelaunch ground tests. Since the operation of the ALC circuit influences this temperature behavior, this tends to suggest that the ALC may in fact be working, although it is out of its intended range of operation. It is not possible to determine this unambiguously from the received signal on the ground unless an alternative measurement of ionospheric absorption is available for comparison.

### 3. TRANSMITTING ANTENNA PERFORMANCE

The EIRP\* of the RBE measured by a number of groups is very close to the prelaunch predictions. These measurements are shown in Table 1. The sideband levels at 40 MHz are somewhat unbalanced, but this is consistent with the other abnormalities at 40 MHz which are interpreted as a high VSWR on the 40 MHz antenna. The small variations observed in the 40 MHz and 140 MHz signal levels when the satellite pointing direction is changed are reasonably consistent with the polar diagrams obtained by the RBE contractor. However, large variations in 360 MHz field strength have been observed in both the carrier and sideband components during quite small satellite pointing angle changes. Difficulties were experienced by the contractor in developing the 360 MHz RBE antenna in obtaining a sufficient front-to-back ratio to avoid illumination of the satellite dish antenna and the resultant interference between the main forward radiation and the focused back radiation. It appears that, as in the case of the 40 MHz antenna problem, the transfer of the antenna design from the satellite mock-up to the final flight model spacecraft was not accurate enough. An example of variations in 360 MHz carrier field strength observed on the ground during satellite maneuvers is shown in Figure 3 together with the group delay measured by comparison of 360 and 140 MHz, 1 MHz modulation. Small correlated changes in group delay are observed particularly during the earth edge-to-edge scan at approximately 1330. The variations of the group delay for more normal maneuvers are negligible.

Signal Component	Preflight		Ground Measurement	
	Nominal	Predicted	Avg. $\pm$ Std. Dev. ***	SIL Boundary****
40 MHz	+27	+28.6	+26.9	+27
40 MHz 100 kHz USB	+24	+25.8	+23.9	+24.7
40 MHz 100 kHz LSB	+24		+24.9	+24.1
40 MHz 1 MHz USB	+27	+26.8	+29.6	+27.2
40 MHz 1 MHz LSB	+27		+25.7	+28.5
140 MHz	+32	+32.5	+31.6	+32
160 MHz 100 kHz USB	+26	+26.2	+29.4	+25.9
160 MHz 1 MHz USB	+26			+26
360 MHz	+33	+32.6	+34.1	+32
360 MHz 100 kHz USB	+24	+25.6	+24.4	+23.1
360 MHz 100 kHz LSB	+24		+25.6	+22.9
360 MHz 1 MHz USB	+24	+26.7	+21.9	+22.6
360 MHz 1 MHz LSB	+24		+22.7	+22.7

\*Based on a radiometric measurement calibrated against TASS 3 sources.  
\*\*Based on nominal illumination efficiency for a parabolic antenna.  
\*\*\*Based on nominal ALC/RI pattern integration series for RBE array antennas.  
\*\*\*\*Absolute values are dB. Relative side band amplitudes are +10 dB.

\*Effective Isotropic Radiated Power

The polarization of the transmitted signals were measured before launch by the RBE contractor using a full scale mock-up of the satellite. Our confidence in these values is quite high, since major mechanical damage would be required to change the transmitted polarization significantly. Good agreement was obtained between the Faraday ionospheric electron content measurements made at 40 MHz and 140 MHz. The ambiguity was checked using the 40, 41 MHz differential rotation which is independent of the transmitted polarization. The radiated polarization at 140 MHz has been checked by the VHF lunar radar technique and found to agree with the prelaunch calibration within the accuracy of the measurement (Klobuchar, 1975).

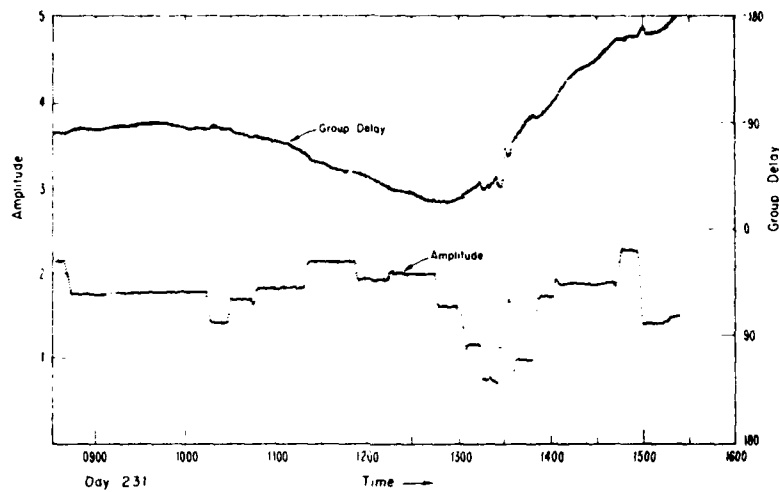


Figure 3. 360 MHz field strength variations observed during satellite maneuvers (linear voltage scale) and corresponding group delay variations at 140 MHz (phase in degrees of 1 MHz modulation).

#### 4. MODULATION PHASE CALIBRATION AND STABILITY

The radiated modulation phase of the RBE transmitter was calibrated before launch by a combination of measurements of the transmitter, under test conditions, working into resistive loads and measurements of the transmitting antennas using a full scale mock-up of the satellite. The group delay experiment basically depends on the stability of the radiated modulation phase in orbit. However, the consistency of the radiated modulation phase can be checked by comparing the total electron content  $N_T$  derived from differential group delay measurements using the 40/360 [ $N_T(41)$  and  $N_T(40.1)$ ] and the 140/360 [ $N_T(141)$ ] pairs of transmissions. The magnitudes of the various corrections to the group delays are given in Table 2. From this, it can be seen that the magnitude of the calibration corrections involving the transmitter and the transmitting and receiving antennas are about the same for  $N_T(41)$  and  $N_T(140)$  but are about ten times as large in proportion to the group delay actually being measured in the case of  $N_T(140)$ . Table 3 separates the various possible sources of drift and error and tries to assign worst case error estimates to them.

Table 2. Differential Group Delay Magnitudes				
	Typical Total Content $5 \times 10^{17} e/m^2$	Typical Plasmaspheric Content (10% Total)	Transmitter Group Delay (Inc. Ant.)	Receiving Antennas
140 1 MHz	3400 ns	340 ns	175 ns	9 ns
40 100 kHz	42000 ns	4200 ns	222 ns	46 ns
40 1 MHz	42000 ns	4200 ns	203 ns	46 ns

Table 3. Calibration Worst Case Error Estimates								
Signal	1 Year Prelaunch Transmitter History $\sigma$	Transmitting Antennas ( $\pm 10\%$ )	Receiving Antennas Group Delay $\pm 50\%$	Receiver Antenna Position $\pm 1^\circ$	Receiver Phase Linearity $\pm 5^\circ$	Worst Case Total	Percentage of Typical Content ( $5 \times 10^{17} e/m^2$ )	Percentage of Typical Plasmaspheric Content ( $5 \times 10^{17} e/m^2$ )
140 MHz	4 ns	$\pm 2$ ns	$\pm 5$ ns	$\pm 4$ ns	$\pm 15$ ns	27 ns	0.8%	82
1 MHz								
40 MHz	13 ns	$\pm 19$ ns	$\pm 23$ ns	$\pm 1$ ns	$\pm 150$ ns	276 ns	0.6%	67
100 kHz								
40 MHz	8 ns	$\pm 24$ ns	$\pm 21$ ns	$\pm 1$ ns	$\pm 15$ ns	71 ns	0.1%	22
1 MHz								

The measurements at Boulder shortly after launch showed good agreement between values of  $N_T$  calculated using the three available sideband frequencies 141, 40.1, and 41 MHz. It is convenient in considering the transmitter stability to calculate new values of transmitted phase  $\theta_T$  for 141 which force  $N_T(141)$  to equal  $N_T(41)$ , since  $N_T(41)$  would be expected to be the most accurate if we assume there is an equal probability of a phase change in any of the transmissions. The prelaunch calibration value for  $\theta_T(141)$  was  $-63^\circ$ . Table 4 shows the values of this quantity calculated from the  $N_T(41)$  and  $N_T(40.1)$  data for the period October, 1974, through May, 1975. With the exception of three values, these lie between  $-65^\circ$  and  $-69^\circ$ .  $1^\circ$  corresponds to an electron content of  $\approx 4 \times 10^{14} e/m^2$ . The reason for the three anomalous values of  $\theta_T$  of about  $74^\circ$  is not clear. These calibration checks will be continued to track any long term changes which occur. Our preliminary conclusion, however, is that the total measurement system is showing satisfactory stability. The original proposal goal was to measure the 1 MHz modulation phase at 40 MHz with an accuracy of about  $\pm .05$  cycles or  $\pm 18^\circ$  giving an error in plasmaspheric content measurement of about  $\pm 3\%$ . It would appear that the accuracy of calibration of modulation phase more than meets this goal.

Table 4. ATS-6 RBE Modulation Phase Calibration Consistency Check Calculation Summary

Date	Day No.	UT	F MHz	$N_T(40.1)$ $\times 10^{-16}$	$N_T(41)$ $\times 10^{-16}$	$\theta_T(41)$ from 40.1	$\theta_T(41)$ from 41
17 Oct 74	290	085959	.81	4.55	4.24	-68°	(-75°)
7 Nov 74	311	061455	.64	7.15	7.15	-67°	-67°
6 Dec 74	340	060051	.60	5.27	5.09	-69°	(-73°)
13 Jan 75	013	060011	.63	5.65	5.55	-65°	-67°
11 Feb 75	042	060031	.77	6.30	6.30	-68°	-68°
16 Mar 75	075	090008	.76	6.91	6.92	-67°	-67°
13 Apr 75	103	085836	.73	4.75	5.05	(-74°)	-68°
16 May 75	136	090335	.76	4.84	4.82	-65°	-65°
Prelaunch Calibration				$\theta_T = -63^\circ$			
Mean $\theta_T$ (41) from 41				$\theta_T = 67.0^\circ$			$N_T(40.1)$ and $N_T(41)$ include the effects of refraction

## 5. BOULDER RECEIVER SYSTEM PERFORMANCE

At the time that the Boulder receiver design was proposed, the use of phase-locked loop technology in Beacon reception was in some disrepute both because of the complication and expense compared with envelope detection systems and because of poor operating experience with the acquisition and maintenance of lock. However, the use of phase-locked tracking loops has the great advantage of preserving receiver linearity and, therefore, permitting more effective use of post detection integration. The technology available for implementing tracking loops has improved considerably, and it was felt that the potential advantages were well worth any small risk. The receiver design employs 5 separate tracking loops, three carrier and two sideband, to make the complete set of Faraday and modulation phase measurements. Its actual performance has been very close to theoretical expectations. No difficulties have arisen whatsoever with loop acquisition or maintenance of lock. The elaborate control system planned using software control of a sequential search and lock procedure proved quite unnecessary in practice. All that was required was a simple amplitude threshold detector operating on the 360 MHz carrier amplitude which enabled a periodic reset of the loop filter integrators whenever a loss of signal occurred. The basic receiver design described in the literature has been extended to provide measurements of differential carrier phase using a carrier reconstruction technique.

The use of a linear receiver together with comparatively large aperture receiving antennas has resulted in data whose "signal-to-noise" ratio is apparently limited more by ionospheric fluctuation than by thermal noise. Table 5

shows the calculated and measured signal-to-noise performance of the receiver evaluated using the 1 second sampled data output of the three carrier amplitude outputs. The calculated signal-to-thermal noise ratios for typical sky temperatures agree well with the observed ratio of "signal on" to noise with signal off or to the signal-to-noise observed on a local calibration signal equal in amplitude to that of the satellite. The "signal-to-noise" ratio observed on the satellite signal is always limited, even under quiet conditions at 360 MHz by ionospheric scintillation.

This order of receiver performance has made possible the measurement of small magnitude ionospheric effects. For example effects due to solar flares, sudden commencements, and plasma oscillations representing only a few hundred picoseconds change per second in differential group delay can be readily detected in the 40 MHz carrier phase. An example is shown in Figure 4. The power spectrum of ionospheric scintillation can be obtained over a 40-50 dB range.

One danger in overreliance on post detection filtering is the possibility of predetector receiver overload occurring due to local interference or other phenomena producing a large increase in signal power within the predetection bandwidth. Some examples of this did occur during the large solar radio noise

Table 5. Receiver Carrier Signal-to-Noise Comparison

	60 MHz	140 MHz	360 MHz
EIRP dBm	+27	+32	+33
Free Space Loss dB	-156	-167	-175
Polarization Loss dB	-3	-3	-3
Antenna Gain dB	+13	+19	+21
Received Power	-119 dBm	-119	-124
Receiver Noise Temp.	300°K	300°K	300°K
Typical Sky Temp.	3000°K	300°K	40°K
System Temp. dB°K	+35	+27.8	+25.3
Boltzman's Constant dBm/Hz/°K	-198.6	-198.6	-198.6
Bandwidth 0.17 Hz	-7.5	-7.5	-7.5
Noise Power dBm	-165.1	-178.3	-180.8
Calculated S/N dB	+52.1	+58.3	+56.8
Observed S/N* dB	48-50	51-59	53-58
Observed S/N** dB	-13 dB	20 dB	-25 dB

\*Ratio of "carrier on" output to noise with "carrier off," quiet sun, winter conditions.  
 \*\*Typical quiet carrier to "noise" ratio. Noise is due to scintillation.  
 Signal-to-noise ratio is computed in both cases from the sampled data output as the ratio of the 5 minute mean to the standard deviation.

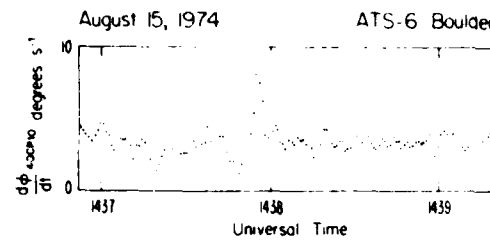


Figure 4. 40 MHz differential carrier phase transient occurring during a magnetic sudden commencement.

bursts accompanying the solar activity in the summer of 1974 where the solar flux reached  $10^{-19} \text{ W/m}^2/\text{Hz}$  or greater at 40 MHz and caused a suppression of the amplitude of the satellite 40 MHz signal. The response of the receiver to an actual solar noise burst and to artificial increases in input noise level is shown in Figure 5. Although the noise level was normally about 20 dB below the phase detector 1 dB compression level, a complete loss of signal occurred for several of the larger solar flares.

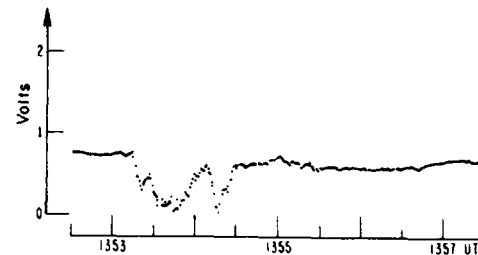
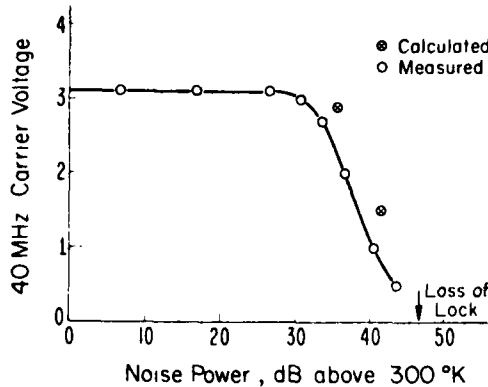


Figure 5. Response of the Boulder receiver. 40 MHz amplitude channel during the July 4, 1974, flare (right) and to an artificial increase in noise temperature (left).

The accuracy of the polarimeters in the Boulder receiver system were checked by making direct comparisons between the receiver O-X phase comparison and the polarization measured by a dipole manually rotated for a signal strength null. A peak-to-peak error of  $\approx 5^\circ$  was observed with a form generally consistent with the effects of the ground reflection on the rotating dipole measurement.

## 6. CONCLUSIONS

The engineering performance of the ATS-6 Beacon transmitter and the Boulder Beacon receiver system appears to have exceeded the basic requirements of the proposed experiment by a comfortable margin. The high performance of the receiver system has enabled a number of new phenomena to be investigated.

#### ACKNOWLEDGMENT

The ATS-6 RBE transmitter was developed under contract to the NASA Goddard Space Flight Center ATS Program Office by the Aeronutronic Division of Aeronutronic Ford Corporation. The Boulder Ground Receiver development and operation was funded by the ATS Program Office. Contributions to the ground receiver design and development were made by Mr. Prentice Orswell and Mr. John Taylor of SEL in addition the present authors.

#### REFERENCES

- Davies, K., R. B. Fritz, R. N. Grubb, and J. E. Jones (1975), The ATS-6 Radio Beacon Experiment: Technique and Some Early Results, Proc. on the Beacon Satellite Investigations of the Ionosphere Structure and ATS-6 Data, Vol. II, IZMIRAN, Moscow.
- Grubb, R. N. (1972a), The ATS-F Radio Beacon--A Progress Report, Proc. of the Symposium on the Future Applications of Satellite Beacon Measurements, Graz, Austria (R. Leitinger, Ed.).
- Grubb, R. N. (1972b), A Receiver Design for the ATS-F Radio Beacon Experiment-- Proc. of the Symposium on the Future Application of Satellite Beacon Measurements, Graz, Austria (R. Leitinger, Ed.).
- Klobuchar, J. A. (1975), Polarization of VHF Waves Emitted from Geostationary Satellites, J. Geophysical Res. 80, No. 3, 4387-4389.

I.R.O.E. Ground Equipment for ATS-6

P.F.Checcacci, E.Capannini, P.Spalla  
I.R.O.E./CNR, FIRENZE, ITALY

The present communication is concerned with the description of an apparatus recently completed and put in operation for the ionospheric program with the ATS-6 geostationary satellite.

The design criteria for such apparatus have been reported previously [1]. The basic concept is that of a general purpose apparatus constituted by a number of identical receiving channels which can be arranged to perform the basic propagation measurements that is: polarization, differential phase, angle of arrival, amplitude and cross correlation on the incoming wave. Fig.1 sketches this basic principle.

Let us now look in detail at the features. Fig.2 shows the block diagram of one of the receiving channels. Double conversion superheterodyne scheme was used along with Phase Lock detector. Phase coherence among the various channels is assured by using as local oscillator sources, a synthesizer for all the channels. All the synthesizers are driven by a common standard frequency oscillator thus assuring accurate and very stable tuning. The use of connectors between the basic functional blocks offers a great flexibility in changing the configuration of the apparatus. Such blocks are either constructed on purpose and commercial ones.

Referring to the above mentioned receiving channel, the RF amplifier mixer, built at I.R.O.E., has a noise figure of about 3.5 dB at 40 MHz and overall gain of 35 dB with an output at 10.7 MHz.

The IF amplifier also built at I.R.O.E. has a gain of 45 dB; its typical bandwidth is 4 or 8 KHz. The IF includes a second mixer stage with an output in the range 100-10 KHz.

The Phase Lock is an HP3410A microvoltmeter. It can lock and track a signal in the range 5 Hz + 600 KHz with a tracking speed and range depending on the input frequency range. The second mixer allows to choose the optimum working frequency of the PL for the different signals. Typically the value of 10 KHz is used which gives a PL bandwidth of about 1 Hz. The first mixer local oscillator is an Adret Mod. CS.202 while the second is a Schomandl Mod.BN-B.synthesizer.

Fig.3 shows the polarimeter configuration. The antenna is a double polarization crossed yagi. The output phase difference is measured between the two PL-VCO by means of a time interval meter Eldorado Mod.784. Using an averaging mode over 1000 periods it is possible to appreciate about  $10^\circ$ .

Analogic (O and X amplitude) and digital (phase) data are sent to an on line computer (shown in all the described configuration) of which we will refer later.

Fig.4 shows the configuration for amplitude occurrence or cross correlation of two signals. An HP3721A real time correlator is used. Either signal or signal envelope cross correlation can be performed.

Fig.5 is the configuration for the dispersive Doppler. A third mixing is used to increase the frequency measurement accuracy. As all the local oscillator frequency are exactly known and coherent it is possible to evaluate at the computer the exact incoming frequencies and the dispersive Doppler.

Finally Fig.6 shows the interferometer configuration. Here a Lock-in Detector Tekelok Mod.9822 supplies the quadrature component of the interferometer output using the VCO of the PL of the central antenna as reference signal.

The use of all the above described configurations requires in practice only six channels as some ones are common to the different schemes. A small on line computer Laben 701 with suitable interfaces collects all the analogic data (amplitude) through an A/D converter and digital data (phase, correlator output, time) and after suitable formatting, records them on a digital magnetic tape. Time information is supplied by a time code generator driven by the standard frequency oscillator.

The data listed in Table I are taken at 1 minute intervals with the exception of the correlator output which is taken at 15 minutes intervals. A tape reel contains 10700 records and lasts for 7 days.

The Laben 701 computer was also used for solving the problem of power interruption during the unattended operation. With a suitable software and hardware the computer, at the power restart, resets the tape, records the interruption on the TTY and restarts the recording. The time code generator and the frequency standard are kept running during the interruption by two alkaline batteries. A thermal safety device switches off the apparatus in case of over-heating.

To the purpose of easily moving the apparatus in a different geographical location, the apparatus itself and all the items necessary for its operation are housed in two standard freight containers of 10'x10'x20'.

Fig.7 shows an overall view of the containers along with the antennas at the operation site. The container near the antennas is isothermal and houses the apparatus. It is fitted with instrumentation racks, air conditioning, electrical wiring.

Fig.8 shows the instrumentation racks in the container: from the right to the left there are the stabilized AC supply, the time and frequency rack, two racks for the receiving channels and the Laben 701 computer.

The second container at left (Fig.7) is of the dry, not insulated type and houses the antenna parts, and the service vehicle equipped with electric crane for erecting the antenna, during transportation. It also carries all the spare parts, the inverter for operation at power frequency different from 50 Hz, the main power switches, and a small workshop for mechanical repair on the spot.

The used antennas at 40 and 140 MHz are 6 element crossed yagis supplying both O and X components. The 40 MHz antenna is very large (about 12 m lenght) (Fig.7) and has a gain of about 12 dB.

The described apparatus is now operative with the ATS-6 signal since October 1, 1975. It is located in a site on the Tirrenian Coast near Piombino ( $42^{\circ}57'N$ ,  $10^{\circ}40'E$ ).

The surveillance is limited to change the tape once a week.

Fig.9 shows a typical polarimeter output after pre-processing in the main I.R.O.E. computer.

Work is in progress to reduce all the data taken up to now.

The work was supported by C.N.R. through I.R.O.E. Operation of the station is supported by Servizio Attività Spaziali (S.A.S.) of the C.N.R.

- [1] P.F.CHECCACCI: Ground Equipment for ATS-F Ionospheric Beacon - COSPAR Information Bulletin n.66, p.26 (June 1973).

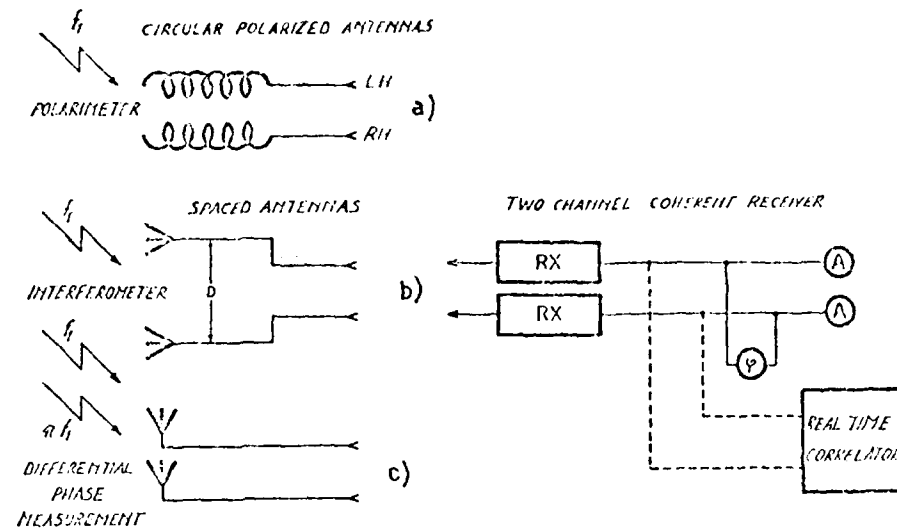


Fig.1 - Basic principle of operation

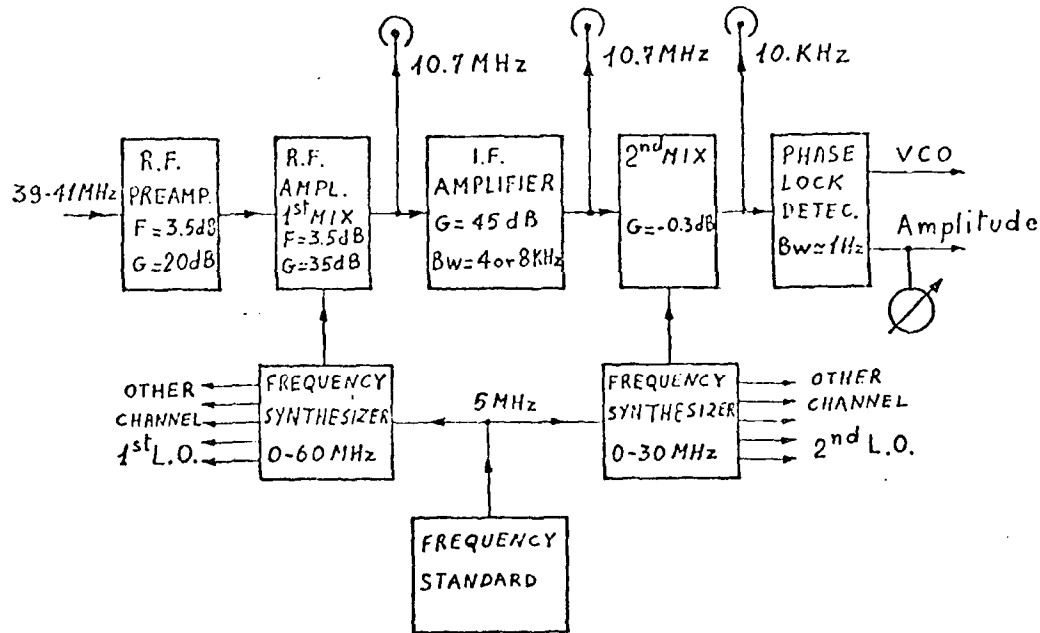


Fig.2 - Receiving channel block diagram

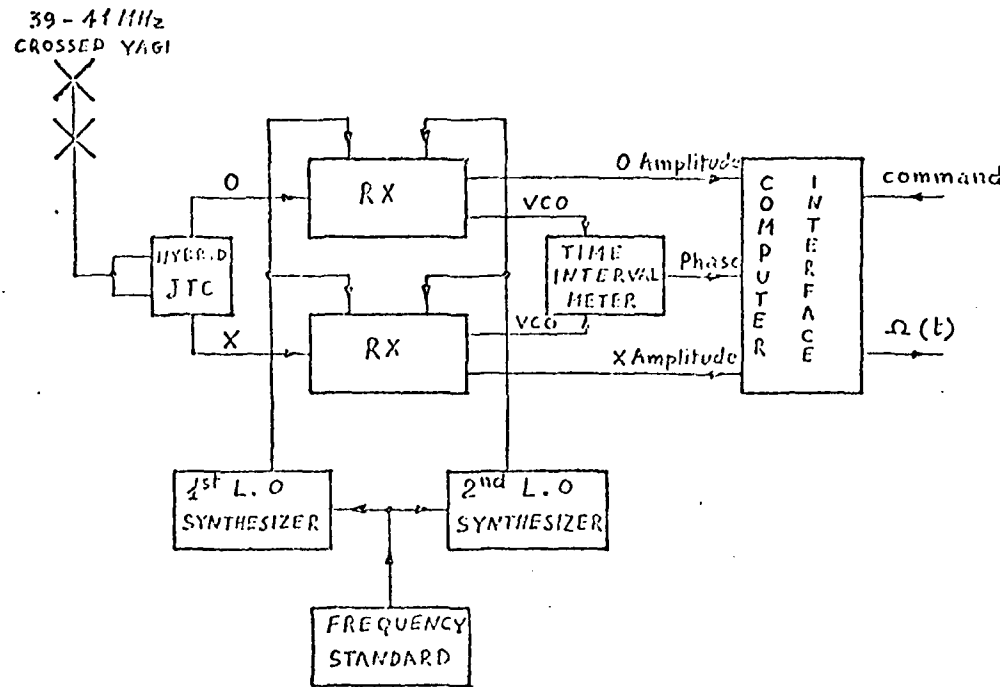


Fig.3 - Polarimeter configuration

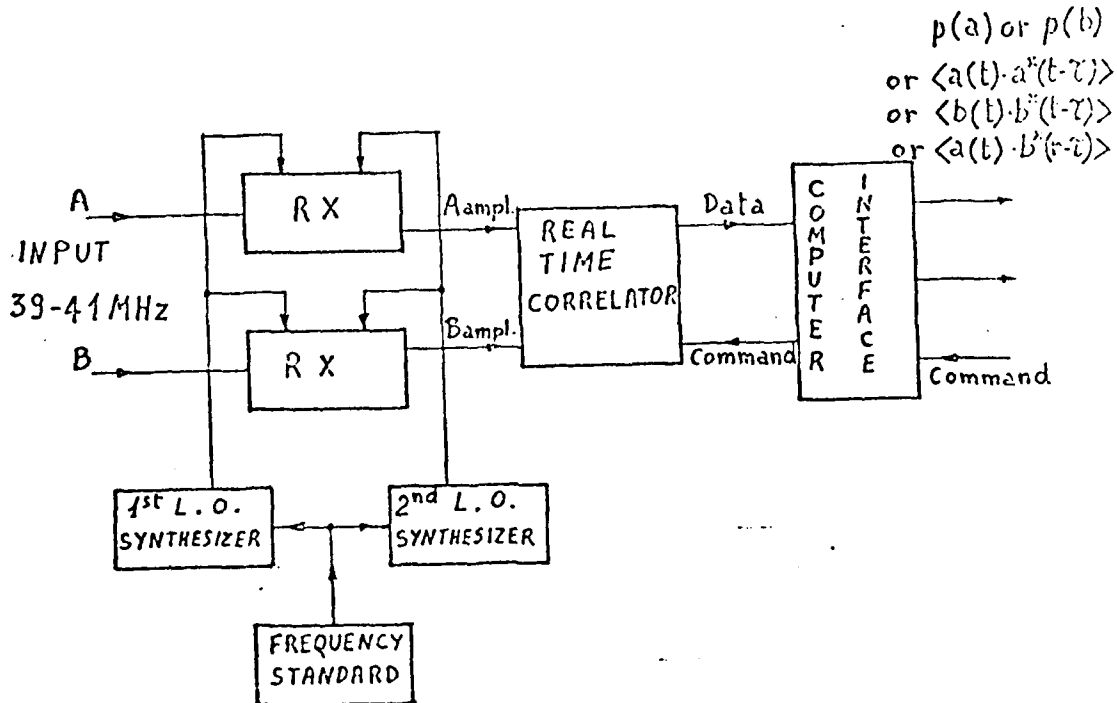


Fig.4 - Amplitude occurrence and cross correlation measurement configuration

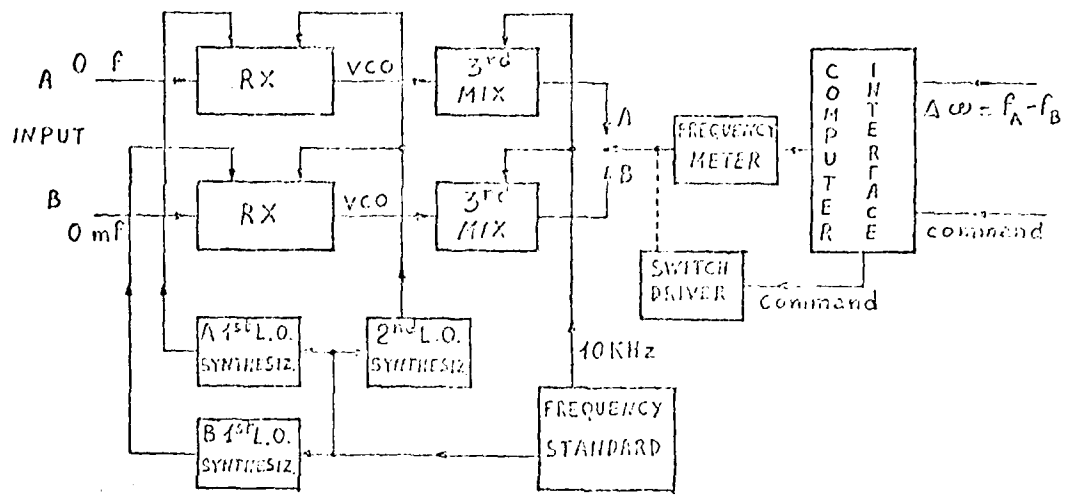


Fig. 5 - Dispersive Doppler measurement configuration

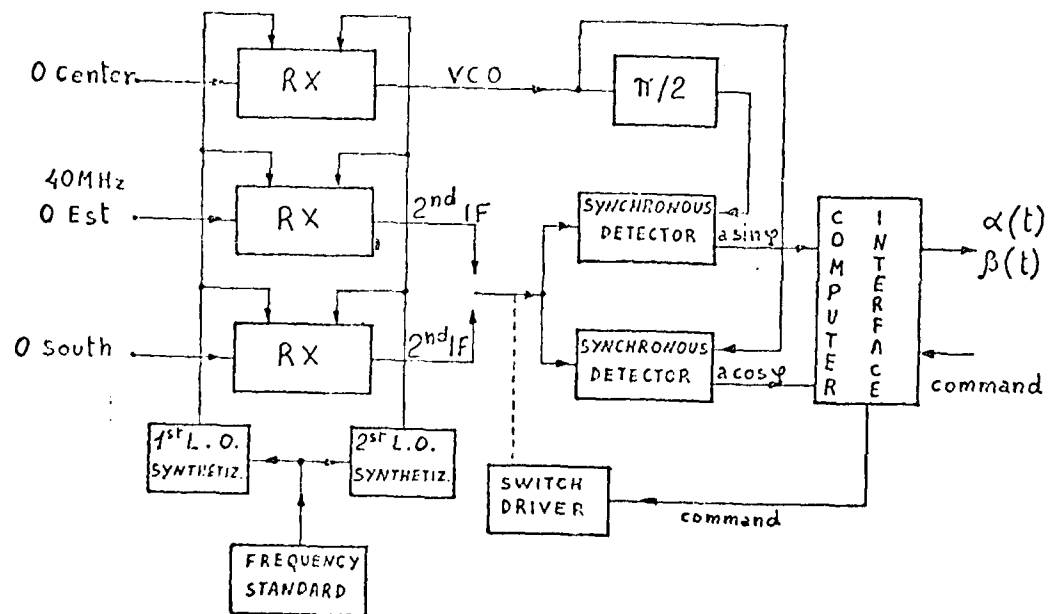


Fig. 6 - Interferometer configuration



Fig.7 - Overall view of the station in the operative site

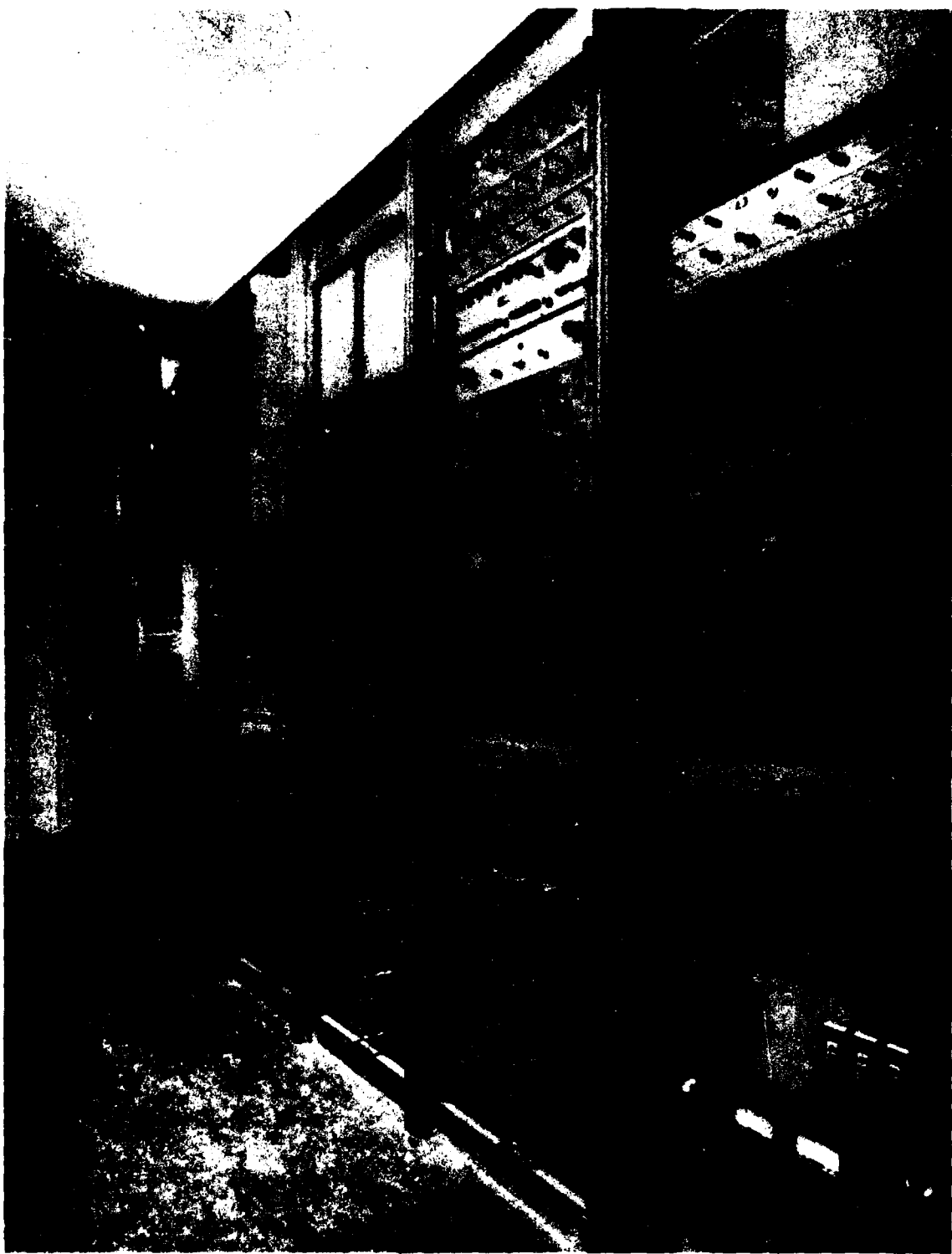
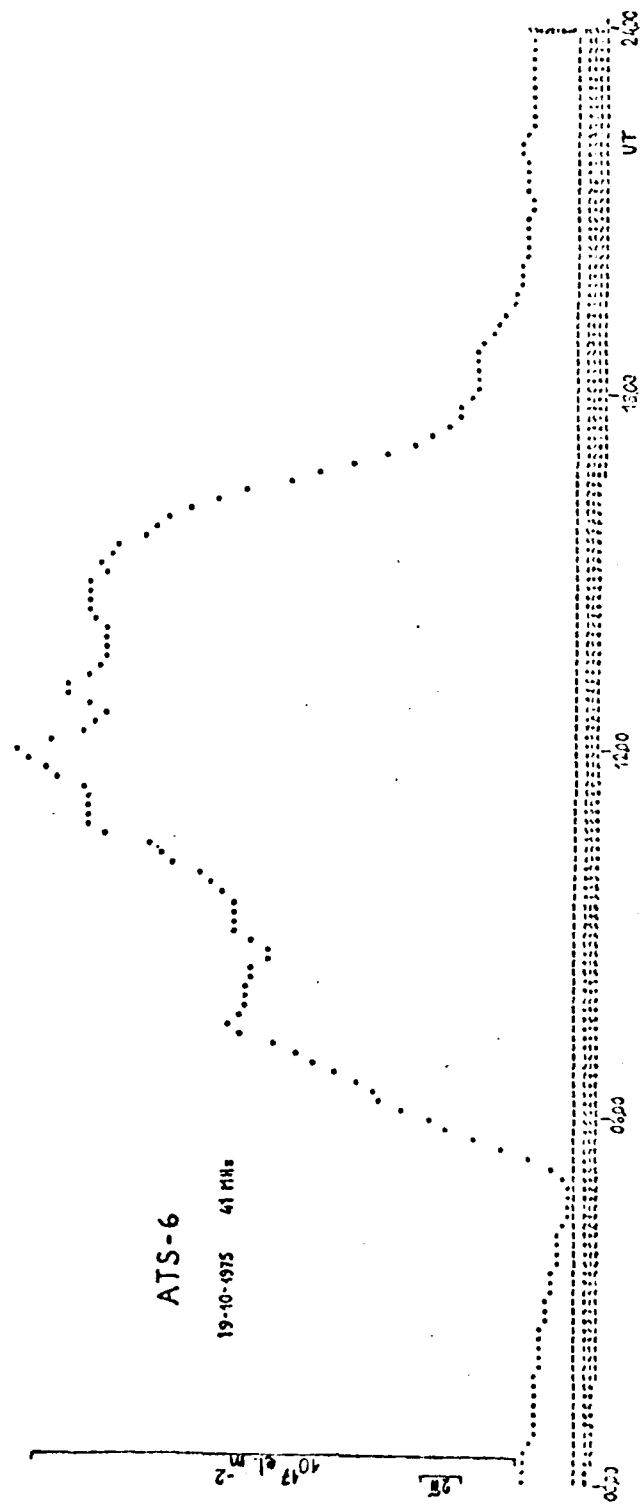


Fig.8 - Interior of the instrumentation container



734

Fig.9 - Measured polarization angle at 41 MHz

Table I

RECORD N. 6222		Polarization angle at 240 MHz												
11A	1A	INTERV. 1	MICROSEC	• 3536015E+02										
Time		INTERV. 2	MICROSEC	• 4082060E+02	"	"	"	"	"	"	"	"	"	
11B	1A	INTERV. 3	MICROSEC	• 7708789E+03	Doppler	"	"	"	"	"	"	"	"	
Time		INTERV. 4	MICROSEC	• 5128515E+03	"	"	"	"	"	"	"	"	"	
11B	1A	INTERV. 5	MICROSEC	• 7317679E+03	"	"	"	"	"	"	"	"	"	
Time		LIVELLO CANALE 1	VOLT	• 1522797E+00	Amplitude	O}	X}	"	"	"	"	"	"	
11B	1A	LIVELLO CANALE 2	VOLT	• 3214799E+00	"	"	"	"	"	"	"	"	"	
Time		LIVELLO CANALE 3	VOLT	• 9670799E+00	"	"	"	"	"	"	"	"	"	
11B	1A	LIVELLO CANALE 4	VOLT	• 4635599E+00	"	"	"	"	"	"	"	"	"	
Time		LIVELLO CANALE 5	VOLT	• 3615599E+00	"	"	"	"	"	"	"	"	"	
11B	1A	LIVELLO CANALE 6	VOLT	• 3124559E+01	A Cos	O}	X}	"	"	"	"	"	"	
Time		LIVELLO CANALE 7	VOLT	• 4024079E+01	A Sin	O}	X}	"	"	"	"	"	"	
11B	1A	LIVELLO CANALE 8	VOLT	• 2400000E-02	N.C.	"	"	"	"	"	"	"	"	
11A	17	53	43	1										
0	0	0	0	0	0	0	0	0	0	0	0	0	0	
0	0	0	0	0	0	0	0	0	0	0	0	0	0	
0	0	0	0	0	0	0	0	0	0	0	0	0	0	
29	70	63	53	75	75	61	67	52	56	56	56	56	56	
62	43	62	96	87	90	107	110	223	263	263	263	263	263	
165	150	112	103	100	51	37	49	49	49	49	49	49	49	
3	0	0	0	0	0	0	0	0	0	0	0	0	0	
0	0	0	0	0	0	0	0	0	0	0	0	0	0	
7	0	0	0	0	0	0	0	0	0	0	0	0	0	

## RESEARCH PROGRAM AT IROE WITH THE DNA-002 EXPERIMENT

F.Bertini, P.F.Pellegrini

Istituto di Ricerca sulle Onde Elettromagnetiche del C.N.R.  
Firenze

P.Bruscaglioni, M.Pieralli  
Università degli Studi - Firenze

A research program will be performed with the DNA-002 experiment to be performed in 1976 with the P76-5 satellite.

The program will be carried out by the high atmosphere propagation group of IROE in cooperation with the University of Firenze, by using a special receiving station assembled for this experiment. This station is placed in a standard container to be easily transported to suitable locations.

The station allows the reception of all the emissions of the DNA-002 beacon.

The block diagram of the system is shown in Fig.1

The different frequency bands (namely VHF, UHF, L, S bands) are converted to the HF bands in order to be commutated by a multiplexer to the input of two RF channels utilizing two 651-S4 Collins receivers.

The output signals of the receivers are detected to obtain the amplitude and the phase of the signals (actually the real and immaginary part of the complex envelope) which are then sampled and recorded in digital form on a 9 tracks magnetic tape.

All the station is synthetised and controlled by a HP 2100 A computer.

The computer controls and commands varieus apparatuses and functions also including the sequencies for frequency translation of the received signals (in particular the sequency F3 for receiving all the 7 equispaced lines in the UHF band), the filter for UHF band, the Multiplexer, the receivers and the reference frequencies for the amplitude and phase detectors (Complex envelope detectors: C.E.D.).

In the normal mode of operation the two receiving channels: ch A and ch B (see Fig.1) are tuned: one on a fixed frequency corresponding to S1 or S2 signals, the other one is sequentially commutated to the other lines.

The overall bandwidth is of the order of some hundreds Hz, and the computer, by evaluating the received signals on line, operates a discrete frequency tracking to follow doppler shift. Informations on the doppler shift are also recorded on magnetic tape as well as time informations.

Some quick loock information are also obtained on a video

terminal and on a graphic plotter.

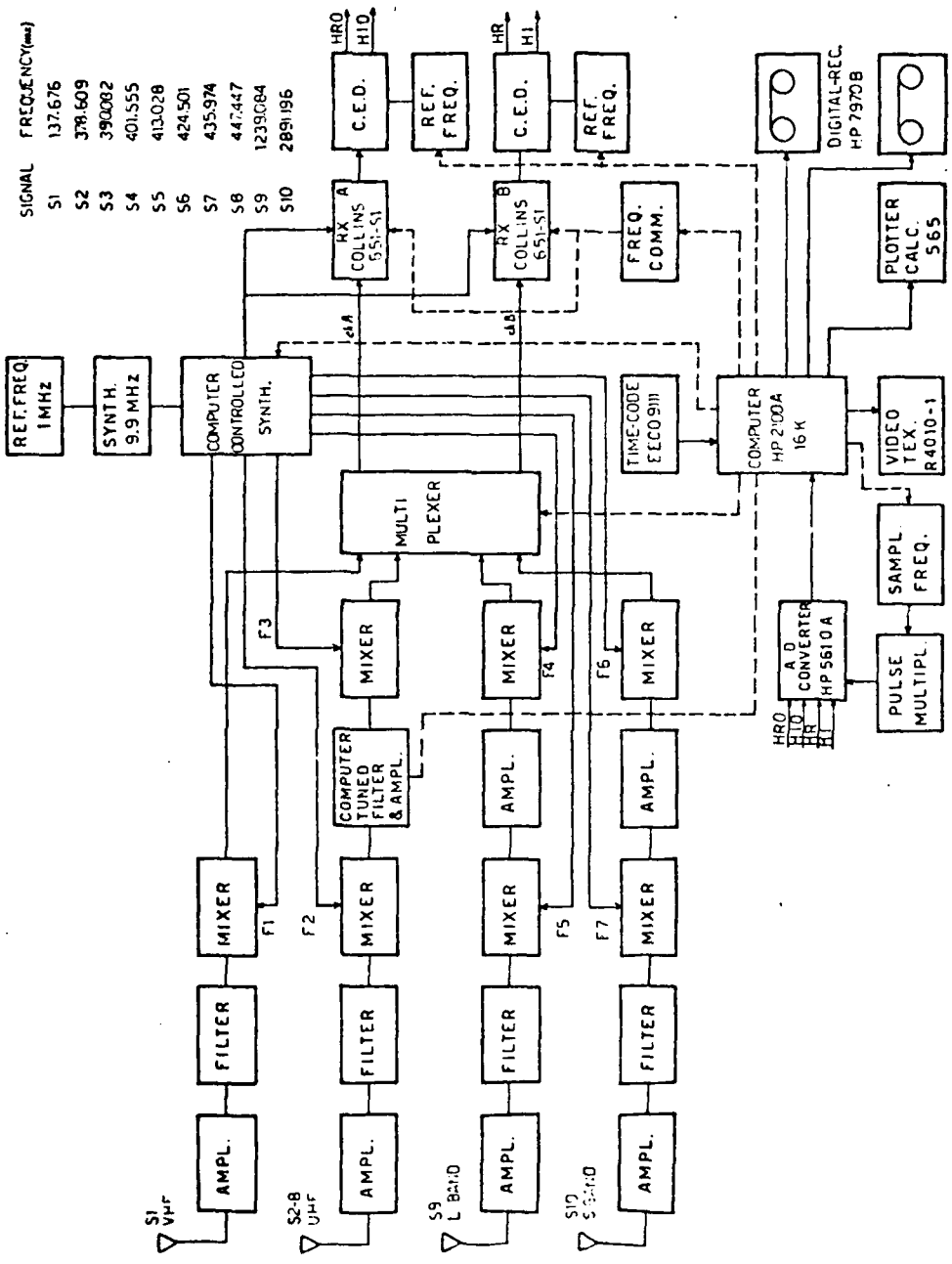
Data analysis will be oriented to the determination of the bi-dimensional time and frequency spread, channel correlation function and scattering function.

Amplitude and phase fluctuations at different frequencies will be also studied to obtain informations on the ionospheric time varying structure.

Combined observations could be performed also on emissions of other satellites to investigate different zones of the propagation medium.

Particular data format can be chosen and measurements of other parameters can be planned for data interchange and research cooperation with other laboratories.

The campaign will be carried out in San Rossore ( $10^{\circ}20'E$ ,  $43^{\circ}41'N$ ) near Pisa.



-Block diagram of the station-

## LIST OF PARTICIPANTS

- Dr. Jules Aarons  
AFGL (LIR)  
L.G. Hanscom AFB  
Bedford, Mass. 01730
- Dr. M. Ahmed  
Research Center  
Regis College  
Weston, Mass. 02193
- Mr. R. S. Allen  
AFGL (LIR)  
L.G. Hanscom AFB  
Bedford, Mass. 01730
- Dr. Roy E. Anderson  
Bld. 37 Rm. 559  
General Electric Co.  
Schenectady, N. Y. 12301
- Dr. D.A. Antoniades  
Radioscience Laboratory  
Stanford University  
Stanford, California 94305
- Dr. S. Basu  
Emmanuel College  
400 The Fenway  
Boston, Mass. 02115
- Dr. Sunanda Basu  
AFGL (LIR)  
Hanscom AFB  
Bedford, Mass. 01730
- Dr. P.A. Bernhardt  
Radioscience Laboratory  
Stanford University  
Stanford, California 94305
- Dr. F. Bertin  
CNET  
Issy les Moulineaux  
FRANCE
- Dr. E. W. Bramley  
Appleton Laboratory  
Ditton Park  
Slough SL 39 JX  
Berkshire  
UNITED KINGDOM
- Dr. Piero Bruscaglioni  
IROE - CNR  
Via Panzatichi 65  
50127 Firenze  
ITALY
- Mr. Michael Buonsanto  
Dept. of Astronomy  
Boston University  
Boston, Mass. 02215
- Eng. A. Bushby  
Geophysical Institute  
P.O. 3747  
Lima  
PERU
- Dr. C. Chacko  
Dept. of Astronomy  
Boston University  
Boston, Mass. 02215
- Prof. P. F. Checcacci  
IROE CNR  
Via Panzatichi 5a  
I-50127 Firenze  
ITALY
- Dr. Edwin J. Chernosky  
AFGL (LIR)  
L.G. Hanscom AFB  
Bedford, Mass. 01730
- Major John G. Clark  
Defense Nuclear Agency  
Washington, D.C. 20305
- Prof. R. R. Clark  
Department of Electrical  
Engineering  
University of New Hampshire  
Kingsbury  
Durham, N.H. 03824
- Dr. Robert Crane  
Environmental Research  
and Technology, Inc.  
996 Virginia Road  
Concord, Mass. 01742

Dr. W. Degenhardt  
Max-Planck-Institute  
fur Aeronomie-IFL  
D-3411 Lindau/Harz  
P.O. Box 80  
West Germany

Dr. M. R. Deshpande  
Physical Research Laboratory  
Navrangpura, Ahmedabad 380009  
INDIA

Dr. Richard F. Donnelly  
Space Environment Lab  
NOAA Environment Research Labs  
Boulder, Colorado 80302

Mr. Richard Dubroff  
Dept. of Electrical Engineering  
University of Illinois  
Urbana, Illinois 62801

D. D. Dulong  
Regis College Research Center  
Weston, Mass. 02193

Dr. J. V. Evans  
MIT/Lincoln Lab.  
Lexington, Mass. 02173

Dr. Claus Fengler  
Dept. Elect. Eng.  
Mc Gill University  
Montreal, Quebec  
CANADA

Dr. P.A. Forsyth  
Centre for Radio Science  
University of Western Ontario  
London  
CANADA N6A 3K7

Prof. A. Frost  
Dept. of Elect. Eng.  
University of New Hampshire  
Durham, N. H. 03824

Dr. J.A. Fulford  
Physics Dept.  
University of Western Ontario  
London, Ontario N6A3K7  
CANADA

Dr. Mario D. Grossi  
Smithsonian Astrophysical  
Observatory  
60 Garden St.  
Cambridge, Mass. 02138

Mr. Richard N. Grubb  
Space Environment Lab  
NOAA  
Boulder, Colorado 80302

Capt. B. Halcrow  
SAMSO  
Los Angeles, California

Dr. Rudi Hanbaba  
Departement Mesures  
Ionospheriques  
et Radioelectriques  
CNET  
22301 Lannion  
FRANCE

Major Martin S. Harris  
European Office of Aerospace  
Research and Development  
223-231 Old Marylebone Road  
LONDON, NW1 5th  
ENGLAND

Dr. J.K. Hargreaves  
Dept. of Environmental Sciences  
University of Lancaster  
Lancaster  
ENGLAND

Dr. G. Hartmann  
Max-Planck-Institute  
fur Aeronomie-IFL  
D-3411 Lindau/Harz  
P.O. Box 80  
WEST GERMANY

Mr. Philip A. Hicks  
Program Manager  
Teledyne Micronetics  
P.O. Box 20396  
San Diego, California 92120

Mr. Julian Holmes  
Naval Research Laboratory  
Code 7127.1  
Washington, D.C. 20375

Dr. Z. Houniner  
Radio Observatory  
P.O.B. 4055  
Haifa  
ISRAEL

Dr. Yinn-Nien Huang  
Telecommunications Lab.  
P.O.Box 71, Chung-Li  
Republic of China  
TAIWAN

Mr. James M. Johanson  
Emmanuel College Physics  
Research Division  
430 Marrett Road  
Lexington, Mass. 02173

Prof. L. Kersley  
Department of Physics  
University College of Wales  
Aberystwyth  
WALES

Dr. I. Keroub  
Radio Observatory  
P.O.B. 4055  
Haifa  
Israel

Mr. J. Klobuchar  
AFGL (LIR)  
L. G. Hanscom AFB  
Bedford, Mass. 01730

Rev. Prof J.R. Koster  
Department of Physics  
University of Ghana  
P.O. Box 63  
Legon, Accra  
GHANA

Dr. Duchesne Lassudrie  
CNET Route de Tregastel  
M.I.R.  
22301-Lannion  
FRANCE

Dr. R. Leitinger  
Institute f. Meteorologie  
u. Geophysik  
Universitat  
A-8010 Graz  
AUSTRIA

Ms. Virginia Lincoln  
Director, World Data Center-A  
for Solar-Terrestrial Physics  
NOAA  
Boulder, Colorado 80302

Dr. C.H. Liu  
60 Electrical Engineering  
Building  
University of Illinois  
Urbana, Illinois 61801

Prof. G. F. Lyon  
Physics Dept.  
University of Western Ontario  
London, Ontario N6A3K7  
CANADA

Mrs. Eileen Mackenzie  
Emmanuel College  
Boston, Mass. 02115

Mr. Chester Malik  
AFGL (LIR)  
L. G. Hanscom A.F.B.  
Bedford, Mass. 01730

Dr. Dimitris Matsoukas  
University of Athens  
Department of Physics  
Division of Electronics  
144 Solonos St.  
Athens  
GREECE

Dr. B. E. Mc Donald  
Plasma Dynamics, Code 7750  
U.S. Naval Research Lab.  
Washington, D.C. 20390

Prof. Michael Mendillo  
Astronomy Department  
Boston University  
Boston, Mass. 02215

Dr. I. S. Mikkelsen  
Danish Meteorological Institute  
Lynglyvej 100, DK 2100  
Copenhagen  
DENMARK

Ms. Florence A. Mulkern Regis College Research Center Wellesley St. Weston, Mass. 02193	Lalitha Emmanue Boston,
Mr. John P. Mullen AFGL (LIR) Hanscom AFB Bedford, Mass. 01731	Dr. Bod Universi Research 450 Alki Lowell,
Dr. B.V. Krishna Murthy Physics and Applied Mathematics Division Vikram Sarabhai Space Centre Trivandrum INDIA	Dr. Chai Stanford 335 Rave Menlo Pa
Dr. George Nesterczuk Atlantic Science Corporation 5711 Sarvis Avenue Suite 502 Riverdale, Maryland 20840	Ms. Rita Chief, I Branch Air Force Hanscom Bedford,
Dr. Elaine Uran Naval Research Lab. Code 7750 Washington, D. C. 20375	Dr. Jose INTA Paseo Pi Madrid - SPAIN
Prof. K. H. Pai National Taiwan University Department of Elect. Eng. Taipei, Taiwan	Prof. A. IROE CNR Via Panc i-50127 ITALY
Prof. M. D. Papagiannis Astronomy Department Boston University Boston, Mass. 02215	Dr. Abhi Physical Navrang Ahmedabi INDIA
Dr. Pier Franco Pellegrini IROE-CNR Via Panclatichi 64 50127 Firenze ITALY	Mr. Abr. Nationa
Lt. Erle Pettus Room 1, 1911 Maxwell Ave. Kirtland AFB, N.M. 87118	P.O. Bo Haifa ISRAEL
Dr. G.W. Prölss Institut fur Astrophysik D-5 Bonn, Federal Republic of GERMANY	Mr. Fre AFGL (L Hanscom Bedford,

Dr. Haim Soicher  
US Army Electronics Command  
AMSEL - NL - H - 4  
Fort Monmouth, New Jersey 07703

Mr. R. Umeki  
Dept. of Electrical Engineering  
University of Illinois  
Urbana, Illinois 62801

Dr. A. Wernik  
Institute of Geophysics  
Polish Academy of Sciences  
Warszawa 22, Pasterua 3  
POLAND

Mr. Herbert Whitney  
AFGL/LIR  
Hanscom A.F.B.  
Bedford, Mass. 01731

Dr. Peter Wildman  
AFGL  
L. G. Hanscom A.F.B.  
Bedford, Mass. 01730

Dr. Gordon Willey  
Defense Documentation Center  
Analysis Branch  
Cameron Station  
Alexandria, Virginia 22314

Dr. K.C. Yeh  
Dept. of Electrical Engineering  
Building  
University of Illinois  
Urbana, Illinois 61801

SELECTED TELEX NUMBERS

AHMEDABAD, India	953 - 012 - 397
APPLETON LABORATORY Slough, England	851 - 848 - 369
BOSTON UNIVERSITY Boston, MA, USA	940 - 439
C.N.E.T. Paris, France	842 - 250 - 317
GEOPHYSICAL INSTITUTE Lima, Peru	394 - 25507
I.R.O.E. Florence, Italy	843 - 57231
I.Z.M.I.R.A.N. Moscow, U.S.S.R.	871 - 7523
UNIVERSITY OF GRAZ Graz, Austria	847 - 31105